Anatoly Belous

Handbook of Microwave and Radar Engineering

Springer

Handbook of Microwave and Radar Engineering

Anatoly Belous

Handbook of Microwave and Radar Engineering

Springer

Anatoly Belous
Integral
Minsk, Belarus

ISBN 978-3-030-58698-0 ISBN 978-3-030-58699-7 (eBook)
https://doi.org/10.1007/978-3-030-58699-7

© The Editor(s) (if applicable) and The Author(s), under exclusive license to Springer Nature Switzerland AG 2021
This work is subject to copyright. All rights are reserved by the Publisher, whether the whole or part of the material is concerned, specifically the rights of translation, reprinting, reuse of illustrations, recitation, broadcasting, reproduction on microfilms or in any other physical way, and transmission or information storage and retrieval, electronic adaptation, computer software, or by similar or dissimilar methodology now known or hereafter developed.
The use of general descriptive names, registered names, trademarks, service marks, etc. in this publication does not imply, even in the absence of a specific statement, that such names are exempt from the relevant protective laws and regulations and therefore free for general use.
The publisher, the authors, and the editors are safe to assume that the advice and information in this book are believed to be true and accurate at the date of publication. Neither the publisher nor the authors or the editors give a warranty, expressed or implied, with respect to the material contained herein or for any errors or omissions that may have been made. The publisher remains neutral with regard to jurisdictional claims in published maps and institutional affiliations.

This Springer imprint is published by the registered company Springer Nature Switzerland AG
The registered company address is: Gewerbestrasse 11, 6330 Cham, Switzerland

Foreword

Over the past decade, we have observed an intensification of the convergence process (mutual penetration) of various previously unrelated trends in the development of science and technology, producing a synergistic effect—the rising effectiveness of various research and development projects as a result of the integration of individual elements into a single system. This tendency also fully applies to the convergence of two independent trends in science and technology—Microwave Electronics and Radar Engineering.

Indeed, each of those trends in science and technology was developing according to its own laws, considering a wide spectrum of specific scientific and complex practical problems. Specifically, Microwave Electronics is a field of science and technology that uses the general laws of electrodynamics and is associated with the study and use of the properties of electromagnetic waves in the frequency range from approximately 300 MHz to 300 GHz.

Radar Engineering is a field of science and technology that combines the methods and means of detecting and measuring coordinates, determining the properties and characteristics of various objects, also based on the use of electromagnetic waves (radiation).

Modern microwave devices and systems today use an extremely wide range of electromagnetic wave frequencies, where the lower frequencies lie close to zero Hertz, and the highest ones come close to the light waves.

The scope of application of modern radars and other devices of microwave technology has also significantly expanded from radiolocation, radiometry, and radio communications to radio navigation, radio astronomy, telecommunications, Earth remote sensing satellites, geolocation, microwave weapons, etc.

In other words, over the past decade we have observed the process of technical symbiosis of those two trends in scientific and technological progress, where Microwave Electronics is the technological platform (base) of Radar Engineering. At the same time, successes in the development of the first trend stipulate an improvement in the technical and economic characteristics (performance, accuracy,

functionality) of the second trend, and the requirements for the continuous improvement of those characteristics pose the corresponding tasks regarding the development of the technological platform.

This concept of technical symbiosis of the two trends was developed by the author during his participation in the project of creating the Soviet Volga Radar Station in the period from 1980 to 1995.

Hantsavichy Radar Station (Russian: Gantsevichi Radar) (also described as Gantsevichi) is a 70M6 Volga-type radar near Hantsavichy (48 km from Baranavichy in Belarus). It is an early warning radar, which is run by the Russian Aerospace Defence Forces. It is designed to identify launches of ballistic missiles from Western Europe and can also track some artificial satellites.

During participation in the Volga project, the author was the chief designer regarding developing and organizing the production of the basic set of high-speed chips for this radar. On the basis of the requirements for technical parameters of the radar and the operation algorithms of the major devices received from the designers of the radar, dozens of original, unparalleled in the world, high-speed integrated circuits of the 1815xx series were designed under the guidance of the author, on which the Volga Radar was subsequently built. Upon completion of all the tests, this radar was introduced into the composition of the Russian Space Forces and put on combat duty in a missile early warning system in 2003.

In Chaps. 2, 4, 9, and 10 of the book, the author discusses some results of theoretical research studies and technical solutions that have been tested in this Radar Station.

The valuable experience acquired by the author during the project indicated that the major factor regarding the success of the Volga project was the organization of the synchronous work of two large teams of specialists—in Microwave Electronics and in Radar Engineering—because the specialists in the first area understood the basics of the theory and practice of Radar Engineering well, and the developers of the radar knew well the real capabilities and limitations of Microwave Electronics.

Subsequently, based on the experience obtained at that time, in collaboration with Merdan Merdanov, the General Director–General Designer on Radar Engineering of the Russian holding company "Electronic Instrument Engineering," the book "Microwave Electronics in Radar and Communication Systems. Technical Encyclopedia in one books" (1520 pages) was prepared and published in Moscow in 2016 by the publishing company TECHNOSPHERA. Then and there, for the first time in the scientific and technical literature in the volume of one book, the theoretical foundations, physical mechanisms, and operating principles of all known microwave devices and typical devices based on them, calculation and design methods, basic technological, circuit design particularities and engineering specifications of each class of microwave devices, as well as the most common technical solutions to electronic systems based on them, from radar and telecommunication devices for various purposes to microwave weapons for ground and space applications, were reviewed in great depth.

At the request of the publisher, since the book was in high demand among engineers, we supplemented certain chapters, and in 2018, the second revised edition of this book was published.

In this book, both individual materials of the above-noted technical encyclopedia and additional materials obtained by the author in the course of his own theoretical research and practical development in the field of Radar Engineering are used.

When writing this book, the author was guided by the following basic principles.

1. Future research and development engineers of commercial and military radars, students and their teachers always need to have "at hand" a sort of systematized collection of reference materials on such devices.
2. In order to become quite popular among a broad audience of scientists, specialists, and students, this book must simultaneously fulfill the integral functions of both a classical textbook and a short scientific practical manual-reference book, as well as simply be a fascinating book.
3. The book should provide sufficiently voluminous reference material, but unlike classical textbooks with an abundance of formulas and mathematical expressions, it should try to explain in as simple language as possible the basic theoretical aspects of the problem under study, and to give specific practical examples.
4. The book should only include those methods, technical means, and technological solutions whose effectiveness were previously confirmed by the practice of their application.
5. In the text of the book, it is necessary to use the maximum possible amount of graphic materials that reflect the effectiveness of various working scenarios.

How well and to what extent the author has managed to put those principles into practice is to be judged by the reader.

Minsk, Belarus Anatoly Belous

Introduction

The First Chapter "Theoretical Basics of Radiolocation"

This introductory chapter is dedicated to concise presentation of the theoretical basics of radiolocation. Here, in synopsis, the theoretical basics of functioning of the radiolocation devices are represented, starting with the chronology of the historical events, related to creation of the first radiolocation stations, description of the basic functional principles of radars, typical algorithms of signal processing (from measurement of the distance to the target, determination of the angle of the target elevation and of the radar definition as per the target), characteristics of aerials (signal amplification, aperture of the aerial, radar's cross-section, noises, and echo-signals), as well as the general information about the radiolocation stations: classification, frequency ranges of work, performance parameters, comparison of the activity zones of the passive range-difference detection systems of the various radio irradiation sources, differences between the military and civil radars.

Individual paragraphs of the chapter are dedicated to a more detailed investigation of the basic principles regarding construction of the various program complexes intended for simulation of the radiolocation signals, including typical compositions of such complexes, particularities of the design engineers' work regarding the "radiolocation objects," and particularities of setting up the spatial configuration of the object. For the first time, a new method is introduced to enhance the interference resistance of the contemporary radiolocation stations with application of the auto-compensators of the "obstructive irradiations" based on applying the coherence principles for compensation of the active noise interferences, including the specific recommendations on the technical implementation of such auto-compensators. The special procedures used to assess the applied methods of compensation of the active noise interferences of the contemporary radiolocation stations are provided.

The Second Chapter "Specific Features of Designing Digital Processing Systems for Radiolocation Systems Based on Microprocessor VLSI Sets"

The chapter is dedicated to investigation of the construction particularities of the systems for the radiolocation signals digital processing (SDP) based on the microelectronic element base—special purpose microprocessor complexes of the very large scale integrated circuits (VLSIs).

Here the main tendencies and influence particularities are considered regarding the contemporary microelectronic technologies in progress related to the informational and control structures of the modern radars: the standard SDP algorithms and methods of their practical implementation, including for the primary signal processing that is especially important for the contemporary theater of warfare and for the secondary signals processing elements, illustrating both the high efficiency and precision of determining the targets of the contemporary radiolocation stations of the ground borne and space echelons of the counter missile defense (CMDS).

The major interest of the design engineers (electronic engineers and software engineers) of the contemporary radiolocation stations is attributed to the hierarchy of tasks of the SDP operations as applied to the tasks of the contemporary radiolocation stations, as well as the typical procedures and optimum hardware structures of the SDP systems as applied to the specific tasks of the radiolocation stations.

The IC structures of the Russian microprocessor set of the 1815 series radiolocation station are viewed as a concrete example, on whose basis the radiolocation station "Volga" was developed with the active phased array antenna.

The chapter concludes with the analysis of the various methodological approaches for constructing the special purpose microelectronic base for the SDP systems overall and for the purposes of radiolocation and communications in particular.

The Third Chapter "Ground Penetrating Radars" (Ground Penetrating Radars)

The chapter is dedicated to consideration of specific independent trends regarding radiolocation devices such as ground penetrating radars.

Here are presented the most widely known radars of the Earth remote probing and the specific geo-radars with enhanced resolution capacity, geo-radars used to search for mines, field charges, and unauthorized planted explosive devices in buildings, structures, on automobiles and railways, and the routes of military convoys under different environmental conditions.

Special attention from the readers should be paid to the sections dedicated to analysis of the contemporary status and development tendencies of the super wideband devices of the radio systems of the various (civil and military) applications.

Here the analysis results are listed regarding the development of the super wideband technology of the radar equipment in the world and in Russia, including the main features and technical solutions for construction of the radio locators of the ground penetrating probing with enhanced resolution capacity (structure, design particularities, methods of formation and processing the super wideband frequency modulated signals, etc.).

For the first time in the open scientific–technical printed media here in detail the particular features to apply the radars for ground penetration when airborne (aircraft, helicopter, airship, air balloon, etc.) are provided.

The chapter conclusion lists the main technical parameters of the most widely used geo-radars (series "Loza," "OKO," "Zond," etc.)

The Fourth Chapter "Antennas and Antenna Devices for Radar Location and Radio Communication"

The chapter is dedicated to the interrelated issues of design development, fabrication, and application of the various antennas and antenna devices for the systems of radiolocation and communications. Here are listed the basic parameters and types of systems produced in the world and in Russia, examples are cited of the most effective design solutions—including antennas for the portable wireless systems of the standard WIMAX/WLAN; wideband micro strip antennas with enhanced gain ratio; wideband microwave antennas of the running wave, clipped directly to garments and even borne on the human body; multiband PAT antennas; micro strip antennas on the thin substrate; flat reflecting printed antennas for the cellular communications systems; triple range antennas for the systems of uninterrupted communications; original wideband antennas on the ceramic substrate; wideband multi-spiral antennas with polarization, etc.—with the detailed consideration of the computing methods of these antennas using the contemporary means of the automated design development.

A special section of the chapter is dedicated to the phased-array antennas' classification, structure, and particularities of application.

An individual section of this chapter comprises also the specific issues of design development and reliability evaluation of one of the most vital components of the phased-array antennas—power supply systems. In addition, analysis of the status and major problems is indicated regarding the development of various components required for the successful solution of the task to ensure the mechanical positioning of the aerial systems of the radiolocation stations and different devices and systems of radio communications. These are the object location sensors (encoders), various "revolving" elements of the positioning systems of the radiolocation stations, and other components.

The chapter is concluded with the analysis of the current status and the closest prospects for developing the contemporary devices for radiolocation, systems of

communications, as well as the main tendencies and the means of solution regarding the concrete technical tasks for developing the aerial systems, both for the radiolocation stations and the commercial systems of wireless communications.

The Fifth Chapter "Features of Organizing the Process of Designing Radar Microcircuits"

The chapter is dedicated to the specific problems and particularities regarding the process of designing the radiolocation integrated circuits.

The beginning of the chapter considers the specific particularities of designing the radio frequency integrated circuits, especially the simulation stages of the HF-integrated circuits composing the radio electron system being designed and the existent radio electronic system, formation methods of the required sequences of test signals with the acceptable parameters, and an analysis was made regarding the equipment and the software required to arrange the working place of the designer of the radio frequency circuits and others.

Under the spotlight are also the various types of microelectronic technologies used to fabricate the HF devices.

In the special section dedicated to the software for designing the microwave integrated circuits, a detailed analysis is provided of the potentialities and specific features of the most widely applied in practice software products of the company Cadence Design System, a comprehensive list of the required design libraries, their functional purpose and description, with an indication of the basic specific features of the design methods of the digital systems using the language VHDL, a detailed description is offered on the design routes of the integrated circuits.

One of the specific examples under scrutiny involves the particularities of the schematic designing of phase shifters for the radiolocation stations.

The Sixth Chapter "Power Electronics Devices Based on Wide-Gap Semiconductors"

The chapter focuses on the physical fundamentals of the semiconductor microwave electronics. An abridged history of the development of microwave electronics as one of the branches of microelectronics is presented, and the structure and properties of the basic semiconductor material—gallium arsenide—and major types of semiconductor devices that use it (diodes, field transistors, bipolar transistors with heterojunctions, new types of GaAs-devices) are reviewed.

In detail are reviewed the status and development prospects of the comparatively new type of GaAs-devices of the microwave monolith integrated circuits (MIC),

including the particularities of design and fabrication technology, main materials used for their fabrication, design specific features of the MIC active elements and problems of ensuring their reliability, and prospective design-technological solutions of microwave MICs.

A concise comparative review is presented of the designs of the world market leaders, as well as the major trends of applications of MICs in the Western and Russian space military hardware.

The Seventh Chapter "Vacuum Electronics"

The chapter is entirely dedicated to one of the most "aged" directions of the microwave electronics—vacuum electronics.

Here at the beginning of the chapter are considered principles of operation, classification, and technological particularities of both "classic" and the new types of vacuum electronic devices, as well as the main values of the attained parameters of the devices.

A thorough coverage was provided regarding the specific features of the design, technology, and circuitry engineering related to the innovative direction of the vacuum microwave electronic devices—power microwave modules, vacuum microwave devices of the centimeter, millimeter, and terahertz bands.

The Eighth Chapter "Semiconductor SHF Devices for Radar Sets"

The chapter is dedicated to analysis of the semiconductor microwave devices, purposed directly for construction of the electronic modules of the modern radar sets and systems of communications.

Here in detail is considered the element base of the combined modules of AFAR (attenuators, phase shifters, switches, fore amplifiers, low noise amplifiers, and power amplifiers), as well as a wide spectrum of the noise suppression devices for AFAR.

The nomenclature and the basic technical parameters of the major Russian manufacturers (JSC "Microwave Systems," CJSC RPA "Planet-Argall," RPA "Pulsar," and others) are indicated. Additionally under consideration are the basic "Western" integrated circuits for the combined modules of the radar sets, based on gallium nitride, in particular from the manufacturers Mini-circuits, Hittite Microwave, and others. The important specific features for selection of the element base for the systems of the secondary power supply of AFAR are also considered.

The Ninth Chapter "HF and SHF Components for Radar Sets"

The chapter is dedicated to consideration of high frequency and microwave electronic components for radar sets—micro strip filters, microwave filters on the surface acoustic waves (SAW-filters), cable seals, power strip microwave resistors, high frequency connectors, and ceramic microwave components for radar sets (ceramic and film capacitors, network filters, special connectors, and cable "assembly sets").

The chapter concludes with a section dedicated to the design evolution of packages for the electronic devices and blocks of radio electronic equipment of radar sets.

The Tenth Chapter "Methods and Means of Ensuring Reliability of Radar and Communication Systems"

The chapter is dedicated to consideration of complex methods and means of ensuring reliability of the radio location systems and means of communications. Here in detail are presented the physical and technical aspects of the problem of ensuring the electromagnetic compatibility (EMC)—the nature of the electromagnetic interferences, types and classification of EMC, norms and standards, technical solutions of the tasks of ensuring the electromagnetic compatibility of the microprocessor control units of radar sets and means of communications.

The classification is listed along with the basic technical characteristics of the protective microwave devices for radar sets and systems of communications.

A section worthy of special attention is dedicated to the particularities of evaluating the service life of the microwave devices of radar sets considering the reliability of the mechanical components, which were earlier not regarded by the design engineers of radar sets, resulting in the artificial rise of the calculated reliability of radar sets. The specific features of arrangement of the internal and external power supply circuitry of the microwave devices of the contemporary radar are considered in detail.

The types and the basic parameters of a number of special high frequency and microwave components for suppression of the electromagnetic interferences are listed.

The chapter concludes with consideration of a complex issues related to the test methods of microwave devices, including for resistance to electrostatic discharges (test standards both at the level of an individual microwave device and at the system level).

The Eleventh Chapter "Radiophotonics in Telecommunication and Radar Location Systems"

The chapter is dedicated to the relatively new and rapidly developing scientific–technical direction—the issues of application of radiophotonics in telecommunication and radiolocation devices and systems.

Under the spotlight are the physical principles of operation, design, and technological aspects of fabrication and application of the photonic devices based on the surface irradiating lasers with the vertical resonator, the irradiating laser of the alloyed structural design (electric and energy parameters, noise and low signal frequency modulated parameters, linearity in the mode of a strong signal, spectral and tuning characteristics of the lasers of the continuous (VECSEL, MEMS-VCSEL, LICSEL) and pulse (VECSEL-SESAM, MIXSEL) generation).

The specific technical solutions are indicated regarding the application problems of the radiophotonic devices in the radiolocation systems (active delay lines, transmission channels of microwave signals for great distances, systems for signal distributions along the curtain of the AFAR radar sets, measuring–calibration complexes, and means for such radar sets).

The chapter concludes with an analysis of the microwave photosensors for the systems of radiophotonics, radiolocation, and optical fiber communications.

The Twelfth Chapter "Measurement of Electrophysical Parameters of Dielectric and Semiconductor Materials and Structures of Microwave Electronics"

The chapter is dedicated to the theoretical aspects of interaction between the electromagnetic irradiation of the microwave range with the photon structures, including the nano-metric metal, dielectric, and semiconductor layers.

The original results represent the analysis of the contemporary status of research in the sphere of technologies and control methods of parameters of the dielectric and conductive materials (measurement of the electrophysical parameters using the waveguide, bridge resonator methods, waveguide–dielectric resonance methods, methods applying the synchronized generators of microwave irradiation, etc.)

A description is provided of the complex mathematical model, including depiction and analysis of the computer simulation results of the reflection spectra dependence of the waveguide photonic structures on the position of defect ("disruption") in the structure of a photonic crystal, on the parameters of the specific defect, and results of the reflection spectra simulation of the waveguide photonic structures for the various frequency bands.

The last section of the chapter is dedicated to analysis of both the previously known and the obtained by the author results of the experimental investigations of the interaction of the microwave irradiation with the 1-D waveguide photonic structures and the measurement results of the different parameters of the microwave materials with application of the waveguide photonic structures.

The Last Chapter "Radiation Stability of SHF Devices"

The chapter is dedicated to analysis of the actual problems of ensuring the radiation stability of the modern microwave devices.

Here in detail are reviewed the influence particularities of the various kinds of ionizing irradiations on the operational parameters of the silicon–germanium microwave devices (heterogeneous bipolar transistors, integrated circuits of low noise and broadband microwave amplifiers and voltage controlled generators).

The particular features of designing the radiation stable design library of the microwave functional blocks based on the Russian CMOS

S-on-I technology of the JSC "RIM Micron" (transistors, MOS-varicaps, R, C, L-elements) are reviewed.

The chapter concludes with a section dedicated to the particular features of designing the passive elements for the radiation stable monolithic silicon–germanium microwave integrated circuits (micro-strip transmission lines, integrated inductances, transformers).

Contents

1 Theoretical Basics of Radiolocation 1
1.1 Physical Basics of Radiolocation 1
1.2 Basic Tactical and Technical Parameters of Radars 4
1.3 Classification of Radar Devices and Systems 7
1.4 Comparative Analysis of Effective Areas of Passive Range-Difference Systems of Detection of Radio Frequency Sources . . 8
1.4.1 Passive Range-Difference System of RFS Detection with Minimization of Observation Interval in Terms of Travel Difference 8
1.4.2 Comparative Analysis of Spatial and Energy Characteristics of Various Implementations of Frequency-Difference Cross-Correlation Processing Algorithms 9
1.5 Features of Application of Millimeter and Sub-millimeter Waves 14
1.5.1 Introduction 14
1.5.2 Development of Technology of Millimeter and Sub-millimeter Waves 16
1.5.3 Fields of Application of Millimeter and Submillimeter Waves in Science and Technology and Main Directions of Developments 20
1.5.4 Transmission Lines of Millimeter and Sub-millimeter Waves 23
1.6 Main Principles of Building Software Complexes for Simulation of Radiolocation Signals 27
1.6.1 Typical Composition of a Software Complex for Modeling of Radiolocation Signals 27
1.6.2 Features of Implementation of the Construction Set of Radiolocation Objects 31

1.6.3 Features of Setting Spatial Configuration of the Object . . . 32
1.6.4 Calculation of HT Projections to the Line of Sight . . . 33
1.7 Increasing Noise Immunity of the Radar Using Automatic Compensators of Perturbing Radiators . . . 37
1.7.1 Principle of Coherent Compensation of Active Noise Interferences . . . 38
1.7.2 Features of Technical Implementation of the Design of Automatic Compensator of Perturbing Radiations . . . 41
1.7.3 Assessment of Efficiency of Active Noise Interference Suppression . . . 44
References . . . 50
Further Reading . . . 52

2 Features of Designing Digital Processing Systems for Radiolocation Systems Based on Microprocessor VLSI Sets . . . 53
2.1 Features of Designing DSP Systems . . . 53
2.2 Effect of Microelectronic Technologies on the Structure of Computing Systems of Radars . . . 57
2.3 DSP Algorithms and Methods of Their Implementation . . . 74
2.3.1 Primary and Secondary Signal Processing . . . 74
2.3.2 Hierarchy of DSP Tasks and Operations . . . 76
2.3.3 Typical DSP Procedures and Hardware Structures . . . 79
2.4 General Questions of Building Microelectronic Element Base for DSP Systems . . . 92
2.5 Certain Practical Aspects of Designing Microprocessor Sets for Radars . . . 95
2.6 Features of Implementing the Algorithm of Synthesis of Linear Antenna Arrays with Required Directivity Pattern and Integer Amplitude Coefficients . . . 97
References . . . 103

3 Ground Penetrating Radars . . . 107
3.1 Design Features of Ground Penetrating Radars . . . 107
3.1.1 Traditional Procedures of Formation and Interpretation of Radio Images . . . 108
3.2 Radar Stations of Earth Remote Probing . . . 114
3.2.1 ERS (European Remote Sensing Satellite) System . . . 117
3.2.2 Space ERS Vehicle ENVISAT-1 . . . 120
3.2.3 ERS-1 (Japan Earth Resources Satellite; Japanese Name – Fuyo-1) . . . 120
3.2.4 Japanese Advanced Land Observation Satellite (ALOS) . . . 120
3.2.5 Canadian System of Survey of Earth's Natural Resources Radarsat (Radar Satellite) . . . 121

3.2.6 Russian Program "Almaz" . . . 121
3.2.7 Russian Module of Earth's Remote Sensing "Priroda" ("Nature") . . . 122
3.2.8 ERS Space Vehicles COSMO (Italy, Spain, Greece) . . . 122
3.2.9 Double-Purpose ERS SV COSMO-SkyMed (Italy) . . . 123
3.2.10 Radar Intelligence System Lacrosse . . . 123
3.2.11 Radar Location Complex SIR-C/X-SAR . . . 123
3.2.12 French ERS Space Vehicle Osiris Based on Radar 2000 Project . . . 124
3.3 Ground Penetrating Radars with Increased Resolution . . . 126
3.4 Ultra-Wideband Devices of Radar Systems . . . 132
3.4.1 Basic Characteristics of UWB Devices . . . 132
3.4.2 Classification of US UWB Radars . . . 133
3.4.3 Development of UWB Technology in Russia . . . 138
3.5 Linear FM Ground Penetrating Radar with Increased Resolution . . . 140
3.5.1 Structure of a Ground Penetrating Radar with Ultra-Wideband Quasi-Continuous Linear FM Signal . . . 140
3.5.2 Path of Generation and Processing of Ultra-Wideband Quasi-Continuous Linear FM Signals of Ground Penetrating Radar . . . 142
3.6 Features of Using Ground Penetrating Radars from Aircrafts . . . 147
3.7 Russian Georadars . . . 150
3.7.1 Ground Penetrating Radars of the "Loza" Series . . . 151
3.7.2 "Zond-2" Georadars . . . 158
3.7.3 "OKO" Georadars . . . 160
References . . . 163

4 Antennas and Antenna Devices for Radar Location and Radio Communication . . . 167
4.1 Main Parameters and Types of Antennas . . . 167
4.1.1 Introduction . . . 167
4.1.2 Characteristics of Radar Set Antennas . . . 168
4.1.3 Basic Antenna Types and Technical Characteristics . . . 192
4.2 Examples of Design Concepts of Antennas for Radio Communication Systems . . . 207
4.2.1 Small-Sized Antenna for Portable Wireless Systems of Thee WIMAX/WLAN Standard . . . 207
4.2.2 Wideband Microstrip Antenna with Increased Gain Factor . . . 210
4.2.3 Wideband SHF Travelling-Wave Antenna . . . 215
4.2.4 Man-Portable Antennas . . . 226
4.2.5 Multiband Patch Antenna . . . 230
4.2.6 Microstrip Antennas on Thin Substrate . . . 234

4.2.7 Flat Reflective Printed Antenna for Cellular Communication Systems . . . 243
4.2.8 Features of Designing Mirror Reflector Phased Antenna Arrays . . . 248
4.2.9 Three-Range Slot Antenna for Wireless Communication Systems . . . 253
4.2.10 Wideband Vivaldi Antenna on Ceramic Substrate for 60 GHz . . . 255
4.2.11 Methodological Basis of Calculation of Mirror Dish Antennas Using Modern Microwave CAD Systems . . . 264
4.2.12 Wideband Log-Spiral Antenna with Circular Polarization . . . 281
4.3 Phased Antenna Arrays . . . 288
4.3.1 Classification, Structure and Features of Application of Phased Antenna Arrays . . . 288
4.3.2 Detailed Description of the Structure and Operating Principles of PAA Without a Single Formula . . . 292
4.4 Design Features and Reliability Assessment of Power Supply Systems of Active Electronically Scanned Arrays of Radar Stations . . . 301
4.5 Components for Provision of Mechanical Positioning of Antenna Systems of Radars and Radio Communication . . . 310
4.5.1 Position Sensors (Encoders) . . . 311
4.5.2 Rotary Junctions of Positioning Systems . . . 314
4.6 Condition and Prospects of Development of Antenna Devices for Radars and Communication Means . . . 320
4.6.1 Analysis of the Current State of Development of Antenna Devices in Radar Sets . . . 320
4.6.2 Main Directions of Development of Antenna Systems of Radar Sets . . . 323
4.6.3 Ways of Solving Technical Problems of Development of Advanced Antenna Systems of Radar Sets . . . 325
References . . . 328
Further Reading for Chapter 5 . . . 333

5 Features of Organizing the Process of Designing Radar Microcircuits . . . 335
5.1 Features of Organizing the Process of Designing Radio Frequency Microcircuits . . . 335
5.2 Possible Types of Technologies Used for Production of RF and SHF Products . . . 347
5.3 Software Means for Designing SHF ICs . . . 348
5.3.1 Analysis of Possibilities and Advantages of Software Products of Cadence Design Systems, Inc. . . . 348

5.3.2 List of Necessary Design Libraries and Their Functional Description . . . 353
5.3.3 Features of Teaching Methods of Designing Digital Systems Using VHDL Language . . . 353
5.3.4 Detailed Description of an IC Design Process . . . 358
5.3.5 Multisim Blue Software for Modeling of Radioelectronic Devices . . . 366
5.4 Features of Circuit Modeling of Phase Shifters for Radar Sets . . . 380
5.4.1 Basic Parameters of a Standard Phase Shifter . . . 380
5.4.2 Phase Shifter Designing Using CAD Means . . . 383
References . . . 388

6 Power Electronics Devices Based on Wide-Gap Semiconductors . . . 389
6.1 Main Properties of Materials Based on Large Gap Semiconductors . . . 389
6.2 Evolution of Silicon Carbide Production Technology . . . 394
6.3 Main Manufacturers of SiC-Based Power Electronics Devices . . . 397
6.4 Designs of GaN-Based Power Devices . . . 400
6.4.1 Diode structures . . . 402
6.4.2 MOSFET . . . 403
6.4.3 Structures Based on 2D Electron Gas . . . 404
6.4.4 Lateral Structures . . . 404
6.4.5 Vertical Structures . . . 405
6.5 State and Trends of Development of the Technology of Powerful GaN-Based SHF Transistors and MICs . . . 406
6.6 Wideband Transistor Power Amplifiers of the Microwave Range . . . 416
6.7 Features of Basic Process Operations of Production of GaN Device Crystals . . . 427
6.7.1 Epitaxy . . . 428
6.7.2 Formation of Contacts . . . 429
6.7.3 Lithography . . . 431
6.7.4 Etching and Groove Production Processes . . . 431
6.7.5 Surface Formation and Device Passivation . . . 432
References . . . 434

7 Vacuum Electronics . . . 437
7.1 Operating Principle, Classification and Technological Features of Vacuum Electronic Devices . . . 437
7.2 Application of Vacuum Electronics in US Military Equipment . . . 439
7.3 Main Values of VTD Parameters Achieved by 2000 . . . 443

7.4 Microwave Integrated Vacuum Electronics 445
7.5 High-Power SHF Modules 453
7.6 Vacuum SHF Devices of Centimeter, Millimeter and Terahertz Ranges 459
7.6.1 Vacuum SHF Devices of the Centimeter Range 459
7.6.2 Vacuum SHF Devices of Millimeter and Terahertz Ranges 460
References 463

8 Semiconductor SHF Devices for Radar Sets 467
8.1 Element Base of TRMs for Phased Antenna Arrays 467
8.1.1 Attenuators for Transceiver Modules of Active Electronically Scanned Arrays 467
8.1.2 Two-Pole Switches for AESA 470
8.1.3 AESA Phase Shifters 474
8.1.4 Preamplifiers of Transceivers for AESA 476
8.1.5 Low Noise Amplifiers and Power Amplifiers for AESA 476
8.1.6 Noise-Suppressing Filters for AESA 478
8.2 Russian Element Base of SHF Devices for Radar Sets 482
8.2.1 Russian Active GaAs Elements for Transceiver SHF Modules of the Centimeter Range 482
8.2.2 SHF Devices by JSC "Microwave Systems" 490
8.3 Russian GaAs Based Microwave Components by "Planeta-Argall" 499
8.3.1 Transistor Amplifiers 499
8.3.2 Protective Devices 504
8.3.3 Microwave Transistors 506
8.4 Features of Designing SAW Frequency Selective Microcircuits 511
8.5 Microwave Radio Receivers by RSE "Pulsar" 518
8.6 High Speed Hybrid Converters for Radar Sets 525
8.7 Foreign Microcircuits for GaN-Based Transceiver Modules of Radar Systems 529
8.7.1 GaN-Based AESA TRMs 529
8.7.2 Monolithic GaN Microwave Power Amplifiers 531
8.7.3 GaN-Based SHF Microcircuits of Switches 533
8.7.4 Optimization of Design of GaN SHF Transistors 535
8.7.5 SHF Microcircuits by RFHIC 535
8.8 HF and SHF Devices by Mini-Circuits 543
8.8.1 Integrated Monolithic Amplifiers of the VNA Group 543
8.8.2 Double Balanced Mixers of the MCA1 Group 545
8.8.3 Series of Multi-purpose High-Frequency Amplifiers . . . 546

8.8.4 Frequency Mixers . . . 548
8.8.5 Attenuators of HF and SHF Ranges . . . 549
8.9 SHF Chips by Hittite Microwave . . . 550
8.9.1 SHF Chips of Attenuators by Hittite Microwave . . . 550
8.9.2 Monolithic SHF Microcircuits of Full Synthesizers by Hittite Microwave . . . 572
8.10 Specifics of Selecting Element Base for Secondary Power Supply Systems of AESA Transceiver Modules . . . 594
8.10.1 Principles of Building Power Supply Systems for AESA TRMs . . . 594
8.10.2 Technological Features of Production of DC/DC Converters . . . 597
8.10.3 Features of SynQor Converters of the Hi-Rel Series . . . 600
8.10.4 Electromagnetic Processes in the Power Supply System of AESA Transceivers . . . 602
References . . . 605

9 HF and SHF Components for Radar Sets . . . 611
9.1 Microstrip Filters for SHF Systems . . . 611
9.2 Features of Using Acoustic Wave-Based Microwave Filters . . . 614
9.3 Features of Using Special Design Solutions of Cable Sealing Glands for SHF Devices . . . 618
9.4 Russian Powerful Stripline SHF Resistors . . . 623
9.5 High Frequency Connections for Active Phased Antenna Arrays . . . 625
9.6 HF and SHF Components of Spectrum Advanced Specialty Products . . . 630
9.7 Ceramic SHF Components for Radar Sets . . . 649
9.7.1 Ceramic Capacitors . . . 649
9.8 Line Filters and Film Capacitors for Radar Sets . . . 651
9.9 Special Connectors and Cable Assemblies . . . 654
9.10 Evolution of Packages for Devices and Units of Radioelectronic Equipment . . . 657
References . . . 659

10 Methods and Means of Ensuring Reliability of Radar and Communication Systems . . . 661
10.1 Electromagnetic Compatibility: Terms, Definitions, Classification . . . 661
10.1.1 The Nature of Electromagnetic Interference . . . 661
10.1.2 EMC Terms, Definitions and Classification . . . 666
10.1.3 Regulations and Standards for Electromagnetic Compatibility . . . 670

10.2 Ensuring Electromagnetic Compatibility of Microprocessor Control Units of Electronic Devices 680
10.2.1 Design Features of Printed Circuit Boards Optimized in Terms of Electromagnetic Compatibility 680
10.2.2 Measurement of the Level of Interference Emitted by Microcontrollers 687
10.2.3 Ensuring Electromagnetic Compatibility in Wired Communication Systems 696
10.2.4 Design of Printed Circuit Boards for High-Speed Communication Systems 698
10.3 Protective SHF Devices for Radar Stations and Communication Systems 710
10.3.1 Classification and Features of Creation of Protective SHF Devices for Radar Location and Communication 710
10.3.2 Gas Discharge Protective Devices 712
10.3.3 Semiconductor Protective Devices 714
10.3.4 Vacuum Protective Devices 721
10.4 Features of Assessment of the Resource of SHF Devices Considering the Reliability of Mechanical Components 723
10.5 Features of Organizing Electric Power Supply Circuits of Radar Set Microwave Devices 728
10.6 HF and SHF Components for Suppression of Electromagnetic Interference 736
10.7 Assessment of Resistance of Microcircuits to the Effect of Electromagnetic Interference 745
10.8 Standard Methods of Testing SHF Devices for Resistance to Electrostatic Discharges 752
10.8.1 Standards of Tests at the Device Level 753
10.8.2 Comparison of Test Methods at the Device Level 755
10.8.3 Standards of Tests at the System Level 755
10.9 Passive Intermodulation in SHF Circuits 761
10.9.1 Mechanisms of the Occurrence of Passive Intermodulation 761
10.9.2 Causes of the Passive Intermodulation and Methods for Reducing its Level in RF Connectors 763
10.9.3 Passive Intermodulation in the Printed Circuit Board Material 764
10.9.4 PIM in Band, Coaxial and Waveguide Transmission Lines 764
10.9.5 PIM in Directional Couplers, Frequency Duplexers and Transformers 765

10.9.6 External PIM Sources 766
10.9.7 PIM Level Evaluation Methods 767
10.9.8 Specialized Equipment for PIM Testing 769
References 772

11 Radiophotonics in Telecommunication and Radar Location Systems 777
11.1 Photonic Devices Based on Surface-Emitting Lasers with Vertical Resonators 777
11.2 Design of a Long-Wave Alloyed Surface-Emitting Laser 780
11.3 Basic Technical Characteristics of a Long-Wave Alloyed Surface-Emitting Laser 782
11.3.1 Electrical and Power Characteristics 782
11.3.2 Low-Signal Frequency-Modulation Characteristics 782
11.3.3 Noise Characteristics 783
11.3.4 Linearity in High Signal Mode 784
11.3.5 Spectral and Tuning Characteristics 784
11.4 Continuous Generation Lasers: VECSEL, MEMS-VCSEL, LICSEL 786
11.5 Pulse Generation Lasers: VECSEL-SESAM, MIXSEL 796
11.6 Main Directions of Fundamental Studies in the Field of Component Base of Radiophotonics and Functional Devices Based on It 799
11.7 Examples of Use of Radiophotonic Devices in Radar Location 800
11.7.1 Active Delay Lines 801
11.7.2 Channels for Long-Distance Transmission of Microwave Signals 803
11.7.3 Systems of Distribution of Radio Signals over Radar AESA Curtain (Figs. 11.34, 11.35, 11.36, and 11.37) 805
11.7.4 Measurement and Calibration Means for Radar Sets 807
11.8 Microwave Photodetectors for Radiophotonics, Radar Location and Optic Fiber Communication Systems 809
11.8.1 Physical Principles of Operation of Microwave P-I-N Photoelectric Detectors 809
11.8.2 Physical Mechanisms of Limiting Photocurrent of a P-I-N-Photodiode 814
11.8.3 Design Features of Photodiodes 817
References 821

12 Measurement of Electrophysical Parameters of Dielectric and Semiconductor Materials and Structures of Microwave Electronics 827
12.1 Analysis of the Modern State of Studies in the Field of Technologies of Parameter Control of Dielectric and Conductive Materials at SHF 827
12.1.1 Features of Using Microwave Measurement Methods in Semiconductor Microwave Electronics 827
12.1.2 Measurement of Electrophysical Parameters of Materials by Waveguide Methods 830
12.1.3 Measurement of Semiconductor Parameters by Bridge Methods 833
12.1.4 Measurement of Semiconductor Parameters by Cavity Methods 834
12.1.5 Measurement of Material Parameters by Waveguide Dielectric Resonance Method 840
12.1.6 Measurement of Parameters of Materials and Structures by Autodyne Methods 841
12.1.7 Measurement of Material Parameters Using Synchronized Oscillators 842
12.1.8 Near-Field SHF Microscopy of Material Properties 843
12.1.9 Measurement of Thickness of Nanometer Metal Layers and Conductivity of Semiconductor in Metal-Semiconductor Structures Based on Reflection and Transmission Spectra of Electromagnetic Radiation 847
12.2 Mathematical Model and Results of Computer Modeling of the Interaction Between Microwave Radiation with One-Dimensional Waveguide Photonic Structures Including Nanometer, Metal, Dielectric and Semiconductor Layers 849
12.2.1 Interaction of SHF Radiation with Multi-Layered Structures with Planes of Layers Perpendicular to the Radiation Propagation Direction 849
12.3 Theoretical Basis for the Method of Measurement of SHF Material Parameters Using One-Dimensional Waveguide Photonic Structures 866
12.3.1 Measurement of Permittivity of Materials 866
12.3.2 Measurement of Complex Permittivity of Materials with Losses 869
12.3.3 Measurement of Thicknesses of Nanometer Metal Films on Dielectric or Semiconductor Substrates 871

12.4 Results of Experimental Study of Interaction of SHF Radiation with One-Dimensional Waveguide Photonic Structures 875
12.4.1 Results of Experimental Study of Reflection and Transmission Spectra of Waveguide Photonic Crystals 875
12.4.2 Use of Waveguide Photonic Structures for Measurement of Parameters of Nanometer Metal Layers on Semiconductor and Dielectric Substrates 877
12.4.3 Use of Waveguide Photonic Structures for Measurement of Parameters of Dielectric Materials 884
References 894

13 Radiation Stability of SHF Devices 909
13.1 Impact of Ionizing Radiation on the Characteristics of Silicon-Germanium Integrated Circuits of the SHF Range . . . 909
13.1.1 Heterostructural Bipolar Transistors 910
13.1.2 SHF LNA and WBA Chips 912
13.1.3 SHF VCG Chips 917
13.2 Design Features of the Radiation-Resistant Library for Designing SHF Functional Units Based on CMOS SOI Technology 922
13.2.1 High-frequency and Noise Properties of Domestic SOI MOS Transistors 923
13.2.2 Instrument Modeling of SOI MOS Transistors 925
13.2.3 MOS VVCs 928
13.2.4 *R, C, L* Elements 930
13.2.5 Design of Functional Elements of SHF Path 932
13.3 Features of the Mechanisms of Influence of Space Factors on the Formation of Local Radiation Effects 937
13.4 Features of the Design of Passive Elements for Radiation-Resistant Monolithic Silicon-Germanium SHF ICs 944
13.4.1 Microstrip Transmission Line 945
13.4.2 Integral Inductances 946
13.4.3 Balance-to-Unbalance Transformers 947
References 953

Index 957

Chapter 1
Theoretical Basics of Radiolocation

1.1 Physical Basics of Radiolocation

Radiolocation in the common sense is the detection of various objects with the help of microwaves, as well as their identification and detection of their position and movement parameters. Objects of radiolocation are known as *radar targets.* As a rule, radiolocation makes use both of signals reflected from the target and signals radiated by the target itself and radio devices installed on it.

Electronic systems and devices solving the tasks of radiolocation are known as *radiolocation systems*, *radiolocation stations* or *radio locators* (*radars*).

Radar systems perform search and detection of radar signals with subsequent measurement of their parameters containing useful information.

Determination of a target position in a radar requires measurement of the object's (target's) coordinates. In certain situations, it is also necessary to know components of the object (target) velocity vector. Geometrical or mechanical characteristics that characterize position and movement of the object or target are known as *location elements* (W).

Radars are usually used as data processing signals (data sensors) in more complex multi-layered complexes.

Complexes are combinations of functionally connected sensors, systems and means designed to solve a specific tactical task. A complex usually includes the following elements:

- information sensors (IS), both radioelectronic and non-technical (e.g., inertia-based);
- computers or specialized calculators;
- communication and data exchange system (cable, optic fiber/optic and other communication devices between parts of the complex);
- information display system (display, monitor);
- control and diagnosis system designed to eliminate the possibility of using a faulty complex.

© The Editor(s) (if applicable) and The Author(s), under exclusive license to Springer Nature Switzerland AG 2021

A. Belous, *Handbook of Microwave and Radar Engineering*,
https://doi.org/10.1007/978-3-030-58699-7_1

The use of a radar set as one of the main parts of a complex requires systemic approach to the selection of its operational characteristics, in particular – in terms of accuracy and reliability.

Physical basis of radiolocation is the effect of dispersion of radiowaves by object with electrical characteristics (electric permittivity ε, dielectric permittivity μ and conductivity σ) different from corresponding characteristics of the environment during irradiation.

Intensity of dispersion or reflection of radiowaves (secondary field intensity) depends on multiple factor – degree of difference of electrical characteristics of the object and environment, the radio of its dimensions *I* and wavelength λ, polarization of radiowaves, etc. Resulting secondary electromagnetic field consists of the field of reflection propagating in the direction of the radiating primary field, and the shadow field propagating behind the object (in the same direction as the primary field).

Receiving antenna and receiver can be used to receive a part of the dispersed signal, convert and amplify it for subsequent detection. Therefore, a basic radar consists of a transmitter (generates radio signals), a transmitting antenna (radiates these signals), a receiving antenna (receives reflected signals), a radio receiver (amplifies and converts signals) and an output device detecting reflected signals (Fig. 1.1).

As a rule, amplitude (or power) of the received signal is low, and the signal itself is random in nature. Low signal power is explained by long distance to the object (target) and absorption of signal energy during its propagation. Moreover, the intensity of the reflected signal is heavily influenced by dimensions of the target. Random nature of the signal is the consequence of fluctuation of the reflected signal due to: random movement of elements of a complex target during reflection of radio waves; multi-beam propagation of radio waves; chaotic changes in the signal amplitude during propagation and a number of other factors. As a result, the received signal resembles noise and interference in the receiving path in terms of intensity and character of variation. Therefore, the main and most important task of any radar is to detect useful radio signal against the background of interferences. This technical task is solved by special device included in the radar – detector, which uses special algorithms of optimal (best) detection. Quality of the detection process is

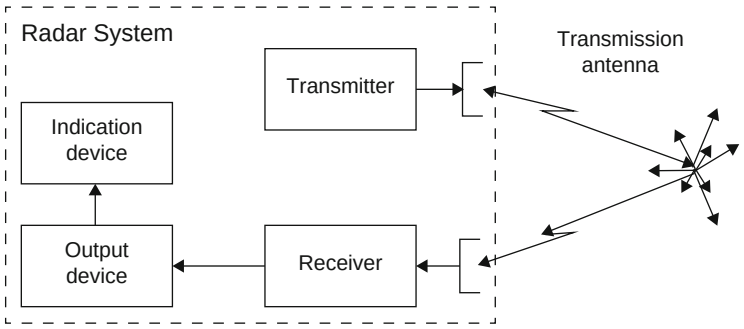

Fig. 1.1 Operating principle of a basic radar [2]

characterized by the probability of correct detection D, when the signal present in the input information is detected, and the probability (rate) of false alarm F, when an interference is mistaken for the useful signal, and the signal itself is absent. A good detector has a high D value and a low F value.

Since most parameters of the received signal are unknown a priori, during detection it is necessary to perform search of the required parameter of the radio signal, which distinguishes it from the accompanying noise and interference.

Construction of radars based on modern digital-analog technologies of data processing suggests the use of a phased antenna array (PAA) as an antenna, a synchronizer as a generator of drive pulses of the frequency synthesizer, and a digital processor as an output device.

Depending on the type of antenna used in the radar set, the transmitter can be implemented in modular version and integrated into active PAA, or in the form of modulator and single-stage or multi-stage generator of radio frequency for passive PAA or mirror antenna. Therefore, an advanced radar set (Fig. 1.2) consists of a PAA, a synchronizer, an analog processor (receiver), a digital processor and a data visualization device.

The antenna uses the signals received from the EDC to generate beams and move them for observation of space. Radio transmitter forms probing signals radiated by the antenna. Radio receiver amplifies weak signals reflected by the target and received by the antenna. Since these signals arrive mixed with noise and interference, their extraction is performed with the help of matched filters of concentrated selection and digital filters. As a rule, the signal processor (receiver) produces electrical signals in digital code. Further processing of signals is performed in the data processor based on embedded programs of processing algorithms. Operating frequencies and time intervals in a radar are set with the help of a synchronizing synthesizer. Data display device is usually designed on an indicator with electron beam tube or on the processor screen.

The number of simultaneously detected and tracked targets is determined by the operational speed of data processing systems – the output device, which is usually represented by a digital processor.

Typical image in the screen of p-display of an UWB radar set is shown in Fig. 1.3a. Here, light-emitting radial and circular marks can be seen. The radar is in the center of the screen. Highligts are the marks of the target. Radius can be used

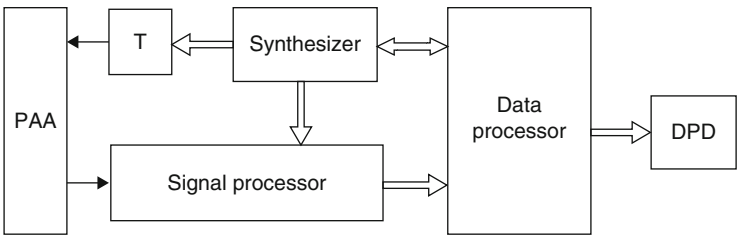

Fig. 1.2 Design of a modern pulse radar [2]

Fig. 1.3 Screen of an air traffic control radar: (**a**) – general view of the screen; (**b**) – zoomed-in image of a screen fragment with log [1]

to calculate the range, rotation angle of the radius passing through the target mark relative to the vertical line passing through the center of the screen – to calculate target bearing. A log is attached to each mark on the screen, which contains the necessary information about the flight number, altitude, range and bearing of the plane (Fig. 1.3b). Figure 1.3 shows inverted image for better clarity.

1.2 Basic Tactical and Technical Parameters of Radars

Tactical and technical parameters are a combination of values characterizing quality of the radar set.

Tactical parameters determine the importance and possibilities of the system, the most important of which are: field of view (work area), resolution, precision, noise immunity, precision, noise immunity, throughput capacity, reliability and operational efficiency.

Field of view is an area in space within the limits of which a target with certain reflecting properties can be detected with the probability of correct detection and false alarm rate not worse than the set values. This critical parameter of a radar is characterized by detection limits in terms of range, bearing and angle of location, i.e. minimum and maximum detection ranges and observation sectors by bearing and location angle (this region sometimes referred to as detection area).

Field of view can be replaced with work area, e.g. the area within which the error of position finding with the help of radar set does not exceed the given σ3 value with known probability. In the plane, the notion of the work zone corresponds to the work area. Work area is characterized by the range of system *R*max, i.e. maximum distance from the radar set at which the given accuracy of finding target (object) coordinates is ensured.

Resolution determines the possibility of separate detection of coordinates of objects (targets) located close to each other. The measure of range resolution is the

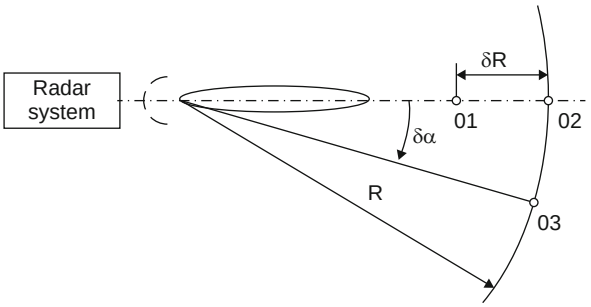

Fig. 1.4 Range and bearing resolution of targets

minimum distance δR between two objects $O1$ and $O2$ with equal angular coordinates α, β, at which separate detection and determination of coordinates of these objects is possible (Fig. 1.4).

The measure of angular coordinate resolution is the minimum difference between angular positions $\delta\alpha$ ($\delta\beta$) of the objects $O1$ and $O2$ with equal R, α (R, β), at which separate detection and determination of angular coordinates of these targets is possible. Speed resolution δV is the minimum difference between speeds of objects with equal R, α, β, at which separate detection and measurement of speed of these objects is possible. Enhancement of resolution, i.e. reduction of δR, $\delta\alpha$, etc. is achieved by corresponding selection of signal and parameters of the antenna system.

Accuracy reflects closeness of measurement results to the true value of the measured parameter and is characterized by values of systematic and random errors.

Systematic errors are determined by characteristics factors and therefore can be estimated by calculations or experiments and, therefore, eliminate or take into account during measurements. As a rule, measurement result is a value free from systematic error.

Random errors are caused by a large number of factors that cannot be accounted for precisely and act differently during each measurement operation; therefore, it is usually considered that random measurement errors x are distributed according to Gaussian (normal) law (Fig. 1.4):

$$w(x) = \frac{1}{\sqrt{2\pi\sigma}} \exp\left\{\frac{x^2}{2\sigma^2}\right\}, \tag{1.1}$$

where σ^2 is the dispersion of the random value x.

Root-mean-square σ, average (probable) δ or maximum $x_{\max}$ error is used as the measure of accuracy.

RMS error is calculated as square root from dispersion of measurement results. The probability that the measurement error will not exceed σ with Gaussian law $w(x)$ amounts to 0.683. In international practice, doubled RMS error 2σ is often used; 95% of all measurements have an error within 2σ. For systems with increased accuracy, maximum error $x$max is usually used, which is equal to 3σ (99.7% of all measurements have error under 3σ).

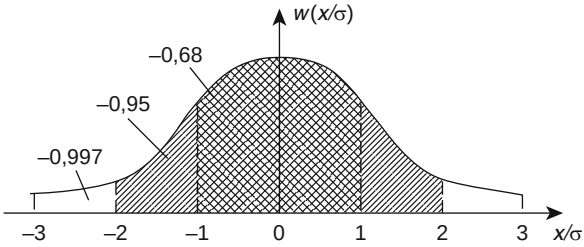

Fig. 1.5 Distribution density of probabilities of random measurement errors

Median (probable) error is linked to the average squared error in case of Gaussian distribution of errors by the ratio $\delta = 0.67449\sigma$. The probability of absolute value of the measurement error being less or more than δ is equal to 0.5 (Fig. 1.5).

Interference immunity is the ability of a system to detect signals and receive information about position of objects (targets) with the required probability and accuracy under the effect of natural or artificial radio interferences of a certain type. The measure of interference immunity is the threshold value of one of interference parameters (e.g., power) and stability of its other characteristics, at which the radar remains serviceable.

Throughput capacity is the ability of a radar to ensure operation simultaneously with a number of objects. Measure of the throughput capacity can be, for example, the number of simultaneously tracked targets or simultaneously controlled objects.

Reliability is the ability of a radar to preserve tactical parameters within the set limits and operating conditions during the required period of time. For the purpose of simplification, reliability is usually determined in the absence of interference. Change in the system state accompanied by the loss of the indicated property (loss of workability) is known as *failure*. Commonly used reliability indicators are the probability of system success, i.e. the probability that the system failure will not occur within a given time, and the so-called mean time between failures.

Operational efficiency (E_o) characterizes average time costs for setting (T_s), adjustment (T_a) and maintenance (T_m) of the system compared to the time of its utilization (T_u) according to its purpose:

$$Э_ф = T_{исп} / (T_н + T_р + T_о). \tag{1.2}$$

Technical parameters characterize the technical means required to ensure given technical parameters. They include value and stability of the carrier frequency; type and parameters of modulation of the radiated oscillations; beam patterns of antenna devices; transmitter power; receiver sensitivity; reliability of system devices; weight and dimensions of the system, etc. Deviation of any technical parameter from the given value affects a certain tactical parameter (or a group of parameters), which can cause tactical parameters of the radar to go beyond the set limits, i.e. lead to system failure.

1.3 Classification of Radar Devices and Systems

The main classification parameters of radiolocation devices and systems are their purpose, character of the received signal, type of the measured element W and, sometimes, the level of self-sufficiency.

In terms of purpose, surveillance and tracking radars are identified.

Surveillance radars are used for determination and measurement of coordinates of all targets in the given area of space or ground surface, as well as for air traffic control of air (missile) defense, reconnaissance, obtaining metrological information, etc.

Tracking radars perform the function of accurate and continuous detection of coordinates of one target or a number of targets. Information received by the radar is used, for example, for aiming or object control.

Standalone (autonomous) and on-line (non-autonomous) systems and devices are distinguished.

Standalone devices and systems operate independently, without the help of other radioelectronic devices, and use no radiolines connecting onboard equipment of the object to external systems and devices. Such radiosystems use the principle of single-position radiolocation, i.e. information about W elements is extracted from the signal reflected from the ground surface or the signal target.

On-line options include both onboard equipment installed on the object and connected equipment of special radio devices installed in ground points or at other objects, i.e. multi-position radiolocation principle is implemented.

The main characteristic features of a signal are the type of the radiated (probing) signal (continuous or pulsed), modulation type, dynamic power range, spectrum width, etc.

Based on the type of the measured element W, azimuth, range and range-difference devices, as well as speed measurement devices, are distinguished.

Azimuth devices of radars determine the angle between the reference direction and the direction of the object in horizontal ($W = \alpha$) or vertical ($W = \beta$) plane (bearing) in the corresponding coordinate system. These devices (direction-finding) sets include the means that help find angular coordinates of the source of electromagnetic interference based on the results of measurement of radiowave receipt direction.

Distance gauges (radio range finders) are designed for measurement of distance to the target ($W = R$). As a rule, radio range finders are used to measure the delay of the signal reflected by the object relative to their own emitted (probing) signal. Distance gauges are included in most radars; they are also used independently, for example, o find the altitude of a plane flight (radar altimeters). Distance gauges can operate on the call and response principle, when the range is measured based on the retranslated signal.

Range-difference devices help find the element $W = R\Delta = R1–R2$, where $R1$ and $R2$ are ranges to the object from two radiating (re-radiating) devices in a multi-positional radar system determined by comparison of informative signal parameters.

1.4 Comparative Analysis of Effective Areas of Passive Range-Difference Systems of Detection of Radio Frequency Sources

Below are the results of analysis of areas of effect, precision and energy characteristics of various implementation of the range-difference algorithm for detection of spatial coordinates of radio frequency sources with cross-corelation processing in the frequency domain and minimization of the observation interval in terms of difference of delay times compared to other passive systems [2].

1.4.1 Passive Range-Difference System of RFS Detection with Minimization of Observation Interval in Terms of Travel Difference

Multi-positional passive radar sets provide the possibility of solving the entire range of ensuring aerospace safety and air traffic control. Moreover, MPP radars have a number of advantages as compared to single-position radar systems, such as covertness, noise immunity, durability, etc. [3–8]. Due to this reason, the studies aimed at simplification of organization of space survey in radar surveillance in multi-positional passive complexes, reduction of the number of receiving stations (RS) and volume of the equipment are relevant today.

The article presents the method of calculation and the results of comparison of areas of effect of passive location complexes (PLC) with various methods of determining spatial coordinates: azimuth, range-difference (RD) and various combinations of these two methods. The article also demonstrates the prospects of using minimization of the observation interval in terms of difference of delay time values between receiving stations in a PLC due to the use of a priori information about angular position of a real or virtual antenna directivity pattern (DP). Such method of PLC building makes it possible to significantly simplify designs of radar surveillance space observation devices, system of detection of radio frequency sources (RFS) and measurement of their spatial coordinates.

Complex use of azimuth and range-difference methods can make it possible to increase the accuracy of detecting positions of radiating targets and enhance the PLC range [8–12]. The role of the central receiving station (CRS) can be performed by an RS with high-directional directivity pattern (DP) and linear azimuth scan. Peripheral positions are receiving stations with non-rotary, low-directional DPs.

The value of difference of delay times of RFS signals relative to RSs of the system is functionally dependent on the angular position of the RFS, which makes it possible to observe not the entire range of possible values of delay time difference, but only a small part of it [13, 14]:

$$\Delta\tau_k(r,\beta) = \frac{1}{c}\cdot\left[r - \sqrt{r^2 - 2r\cdot d_k\ \cos\ (\beta - \beta\ d_k) + d_k^2}\right],$$

where β is the value of the current RFS azimuth, $\beta\ d_k$ ισ τηε azimuth of the k th RS, d_k ισ τηε distance from the CRS to the k th RS, r ισ τηε current range, c ισ τηε speed of light, $\Delta\tau_k(r,\beta)$ ισ τηε delay time difference of complex RFS signal envelopes between CRS and the k th RS. Finding this value will make it possible to significantly reduce the interval of observation in terms of time difference at the output of the device for calculation of maximum of the cross-correlation function (CCF).

The use of a priori information about angular position of the RFS can make it possible to significantly reduce time and computing costs for signal processing [15] and solve the problems of ambiguity of assessment of spatial RFS coordinates in a multi-task situation; moreover, due to high potential of the CRS receiving station, it is possible to obtain CCF at lower values of the signal-to-noise ratio at the RS input. All this can provide an advantage in terms of detection range comparable with the range of action of an azimuth system with preserved precision of detection of RFS coordinates typical of a range-difference PLC [12].

However, insertion of a directional antenna system (AS) with linear azimuth scan into an MPP radar significantly complicates the design of the system in general. The cost of a directional AS with the possibility of spatial scan in modern complexes reaches 70% of the total cost of the product. Moreover, due to linear azimuth scan, the probability of detection of signals from RFSs emitting short-term radiation decreases (Fig. 1.6).

Implementation of electronic azimuth pseudo-surveillance in base-correlation PLC in combination with the use of cheap non-directional ACs at all RSs of the system can make it possible to preserve a relatively low cost of MP PLC and at the same time reduce the interval of possible delay time differences with regard to spatially distributed RSs and eliminate the ambiguity of measurements in a multi-task situation [16].

Continuous observation based on pseudo-angular coordinate also makes it possible to obtain the estimate of its value in the absence of a real direction finder in the system [17].

1.4.2 Comparative Analysis of Spatial and Energy Characteristics of Various Implementations of Frequency-Difference Cross-Correlation Processing Algorithms

In order to perform comparative analysis of precision capabilities of detection of spatial coordinates by various methods, radar developers usually conduct a modeling calculating experiment applied to passive location complexes implemented on the basis of azimuth, range-difference and combined azimuth-range-difference methods.

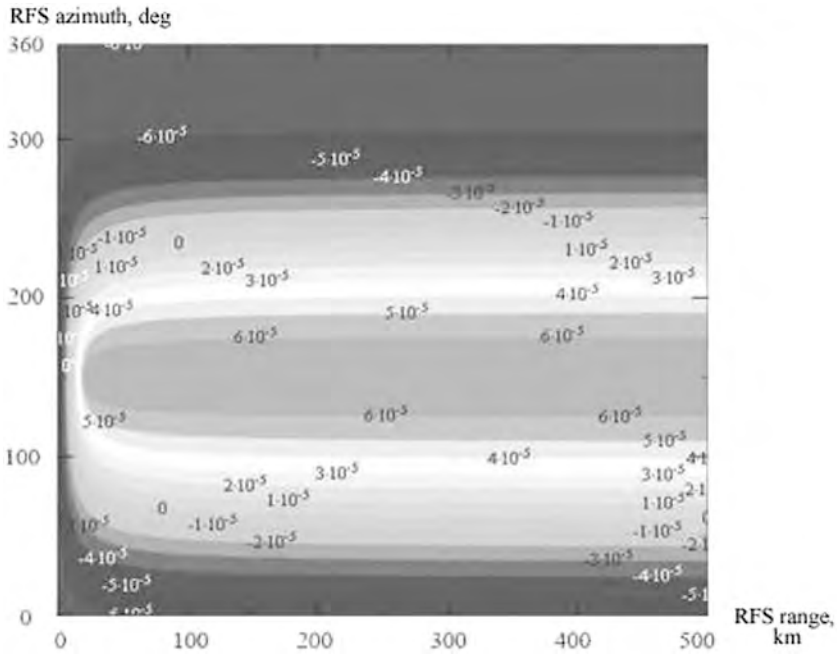

Fig. 1.6 Dependence of the delay time difference on the azimuth and range to the RFS for one pair of receiving stations [2]

The most common integral characteristics of a processing method is the PLC work area – a part of space within which the deviation of estimates of target coordinates from their actual values does not exceed the maximum permissible Δ_{max} values at least with the given probability P_{Δ}. During calculations, it is usually assumed that for a horizontal plane, $\Delta_{max} = 2500$ m at $P_{\Delta} = 0.9$.

Characteristics of antennas and receiving devices of direction finder with narrow directivity pattern and RSs with non-directional antennas usually remained unchanged. If azimuth or azimuth-range-difference methods are used, such system consists of two RSs placed at a distance of 20 km from each other. In case of calculation of effective areas of range-difference PLCs with directional and non-directional AS at CRS, geometry of the system includes three RSs in angles of an equiangular triangle with distances to the CRS equal to 12.5 km. As radio sources, the researches considered the responders of the Mk-12 system (wavelength – 0.3 m, transmitter power – 500 W, non-directional antenna) and more covert multi-functional (MF) radar of a fighter jet (wavelength – 0.03 m, transmitter power – 100 W, radiation is received by side lobes of the DP). All work (control) areas were built in idealized conditions, in which curvature of the Earth's surface, coverage angles and other factors were not taken into account. Signal-to-noise ratio values were accepted for processing without taking into account limitedness of the linear section of signal processing path.

The mehod of performing such calculation experiment usually includes the following steps [2].

1. Spatial configurations of PLC RCs on a plane is set;
2. Study area is determined in the form of a square with the size of $\pm X_{\max}$ and $\pm Y_{\max}$;
3. Multiple serial generation of coordinates of the radiation source is performed evenly across the entire area with coordinates $\pm X_{\max}$ and $\pm Y_{\max}$;
4. Signal-to-noise ratio at the output of the linear part of the processing path is calculated for each of the generated RFS coordinates [9–11]: $y = P_{per}G_{per}G_{pr}\lambda^2 T_0/N_0(4\pi)^2 r_c^2 K_z$, where P_{per} is the transmitter pulse power, G_{per} is the gain of the transmitting antenna, G_{pr} is the gain of the receiving antenna, N_0 is the spectral density of power of intrinsic noises of the receiver, K_z is the coefficient of attenuation of radio waves in the atmosphere, λ is the wavelength, T_0 is the pulse duration, r_c is the range to the RFS.
5. Fluctuation errors of angle measurements are calculated [9–11]: $\sigma_{fl,\beta} = \sqrt{\Delta\theta(1+y)/4\pi y^2}$, where $\Delta\theta$ is the azimuth resolution, y is the signal-to-noise ratio.
6. Fluctuation errors of path difference measurements are calculated [9–11]: $\sigma_{fl,\beta} = \sqrt{c^2\Delta\alpha^2\left(1+y_{pp}y_{cpp}\right)/4\pi\left(y_{pp}y_{cpp}\right)^2}$, where $\Delta\alpha$ is the path difference resolution, y_{pp} is the signal-to-noise ratio at the peripheral RS input, y_{cpp} is the signal-to-noise ratio at the CRS input.
7. Measurement of errors in calculation of position lines of azimuth RSs is performed [9–11]: $\sigma_\beta = r_c\sigma_{fl,\beta}$;
8. Measurement of errors in calculation of position lines of RD RSs is performed [9–11]: $\sigma_\Delta = \sigma_{fl,\Delta}/[2\sin(\phi/2)]$, where ϕ is the angle between directions to RSs from RFS.
9. Errors of measurement in determination of spatial RFS coordinates are calculated [8–10]:

– for azimuth PLC (APLC):

$$\sigma_\Sigma = \frac{1}{\sin(\phi)}\sqrt{\sigma_{1\beta}^2 + \sigma_{2\beta}^2 + 2\cos(\phi)\sigma_{1\beta}\sigma_{2\beta}\rho},$$

– for range-difference PLC (RDPLC):

$$\sigma_\Sigma = \frac{1}{\sin(\phi)}\sqrt{\sigma_{1\Delta}^2 + \sigma_{2\Delta}^2 + 2\cos(\phi)\sigma_{1\Delta}\sigma_{2\Delta}\rho},$$

– for azimuth-range-difference PLC (ARDPLC):

$$\sigma_\Sigma = \frac{1}{\sin(\phi)} \sqrt{\sigma_{1\Delta}^2 + \sigma_{2\beta}^2 + 2\cos(\phi)\sigma_{1\Delta}\sigma_{2\beta}\rho},$$

where ρ ισ τηε correlation coefficient of measurements of position lines. For all considered scenarios, ρ was accepted as equal to zero due to actual absence of correlation between the measured parameters.

10. After that, calculated value of error in measurement of RFS spatial coordinates is compared for each generated point in the plane with maximum permissible value $\Delta_{\max}$. If for the ith position of the source the condition $\sigma_\Sigma \leq \Delta_{\max}$ was true, such point was included in the work area and displayed in the figure.

An example of results of such mathematical modeling is shown in Fig. 1.7 [2].

Calculation of the signal-to-noise ratio value (Fig. 1.8) and values of root-mean-square (RMS) error in measurement of spatial coordinates (Fig. 1.9) are usually stages of building working areas of PLCs. Conditions of calculation of signal-to-noise ratio and root-mean-square errors are specific for each option. However, in combination with the analysis of the results of modeling work areas of various PLC types, presentation of dependencies of signal-to-noise ratio and RMS errors in measurement of the range to the RFS received in PLCs of various types provides additional information for comparative analysis of various methods of measurement of spatial coordinates in PLC.

The presented dependencies demonstrate that an azimuth PLC is the most precise option. Range-difference PLC is a high-precision complex; however, when the signal-to-noise ratio drops below 16 . . . 15 dB, measurement errors increase sharply. For Mk-12 signals, it is manifested at distances of over 300 km, in the 3-centimeter range of wavelengths – at distances of up to 100 km. The use of a direction finder with narrow DP as a part of the complex makes it possible to increase the accuracy of coordinate detection and enhance the range of detection of RFS signals.

Based on the above comparative analysis of obtained characteristics and dependencies, the following conclusions can be made. The range of RFS detection by azimuth complex (Fig. 1.7a) is the smallest of all the analyzed methods. The cost of such complex, on the other hand, can be the highest due to the need to use two or more direction finders. In addition, the need to match radar navigation space observation in terms of angular coordinates increases the complexity of the system.

Spatial possibilities of RFS detection can be improved by implementing azimuth-range-difference method of detection of space coordinates. However, the range of detection of low-energy signals increases insignificantly and amounts to about 250 km (Fig. 1.7b). Moreover, due to the use of a high-directional antenna system, cost and complexity of implementation will most likely exceed similar complexes with the use of omnidirectional antennas.

Modern complexes of passive radiolocation, which use the range-difference method of detection of space coordinates, make it possible to determine RFS positions with high accuracy. However, the range of detection of signals with low energy levels does not exceed 270 km (Fig. 1.7c) and is insufficient for a number of tasks.

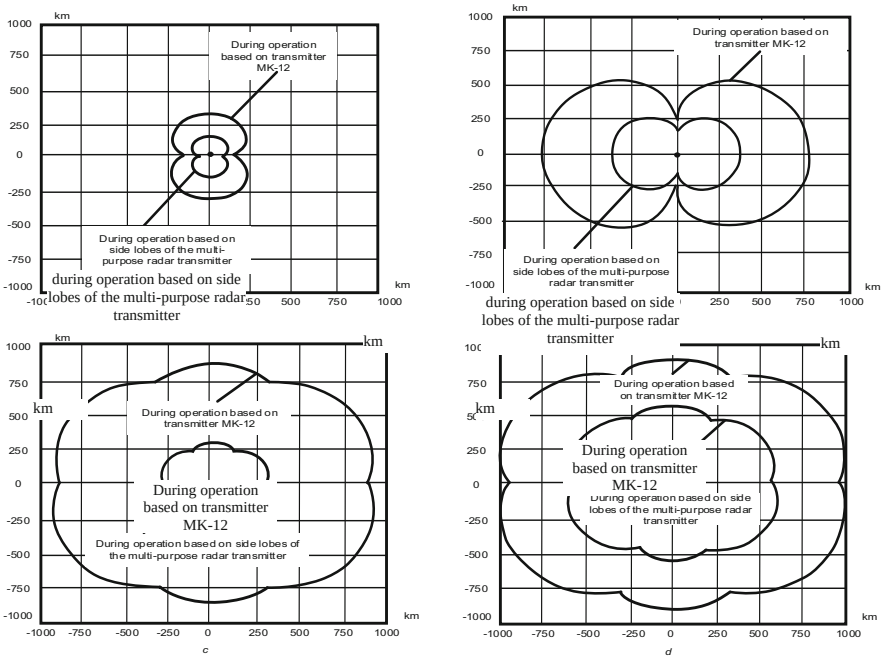

Fig. 1.7 Examples of work areas of PLCs with various methods of determining RFS spatial coordinates: (**a**) – azimuth; (**b**) – azimuth-range-difference; (**c**) – range-difference; (**d**) – range-difference with high-directional antenna system at CRS

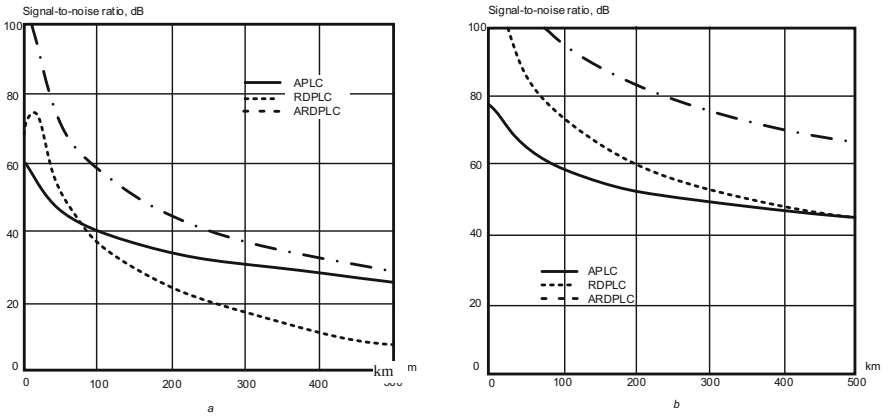

Fig. 1.8 Dependence of the value of the signal-to-noise ratio on the distance to RFS for APLC, RDPLC and ARDPLC: (**a**) – during operation based on side lobes of MF radar DP; (**b**) – during operation based on specific transmitter Mk-12

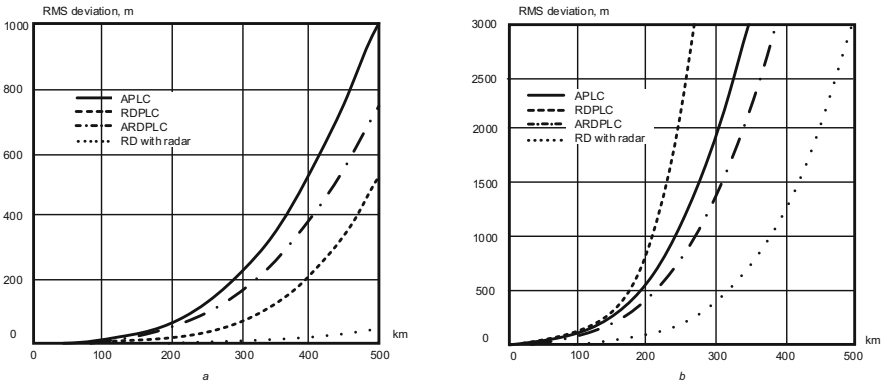

Fig. 1.9 Typical dependence of the value of signal-to-noise ratio of errors in measurement of spatial coordinates on the distance to RFS for APLC, RDPLC and ARDPLC: (**a**) – during operation based on side lobes of MF radar DP; (**b**) – during operation based on specific transmitter Mk-12

The use of a high-directional antenna system as one of the receiving points during implementation of the range-difference method can improve possibilities of detection of low energy signals (Fig. 1.7c). The information about angular RFS position also helps minimize the observation interval in terms of delay time difference values, eliminate ambiguity of estimates of RFS spatial coordinates in a multi-task situation due to radar image redundancy. Implementation of this method will make it possible to provide the range of action of about 580 km for all radiation sources.

It is clear that supplementation of the base-correlation system with determination of delay time difference by virtual antenna system with rotation simulation can make it possible to significantly simplify and reduce cost of the system due to abandoning the real direction finder and preserving the advantages of its use. The range of detection in this case is reduced and becomes comparable to the range of detection of a RD PLC with non-directional antenna; at the same time, the above advantages of using a direction finder remain.

1.5 Features of Application of Millimeter and Sub-millimeter Waves

1.5.1 Introduction

Modern radio electronics is an extensive field of science and technology, which penetrates into new spheres and embraces new fields of knowledge, determining the progress of science and technology in general to a significant extent. Radioelectronics is developing in many directions, including:

- creation and development of new technologies, new generations and new types of element base within wide frequency ranges;
- exploration of new frequency ranges, including creation of radioelectronic systems with new properties and characteristics, as well as element base and metrological provision means for them;
- increasingly wide use of DSP means in radioelectronic and weapon means;
- intense development of antenna-waveguide technology, including in new frequency ranges, creation of new types of radar systems with phased antenna arrays, etc.;
- the use of new physical principles and phenomena for creation of more advanced radioelectronic devices and the use of radar methods for study and research of various physical processes and phenomena (astronomy, biology, plasma diagnostics, study of high-temperature hyperconductivity, etc.).

A special place in the field of radioelectronics is occupied by the creation and use of radioelectronic microwave systems and facilities, including centimeter, millimeter, and in recent years, submillimeter wavelengths. When creating such systems a variety of microwave devices and their connections is used. The study of the characteristics and parameters of microwave devices during their creation and verification of the compliance of such devices with the specification requirements during production, as well as many other tasks and studies require appropriate tools for instrumental analysis of microwave devices and their connections.

The variety of types of transmission lines and devices used in the microwave ranges results in a variety of parameters and characteristics that describe their properties and require experimental definition. This, in turn, makes it necessary to solve a variety of measuring problems that are solved using appropriate measuring tools. The range of existing and newly created measuring instruments is very large, since it must ensure measurements of all parameters and characteristics of microwave devices of interest for developers of systems, as well as of interest for other consumers in different frequency ranges and for different types of transmission lines used.

Modern methods of analysis and calculation of microwave devices and their connections are largely based on their "chain" representation, when a microwave device seems to be a equivalent multi-terminal described by a certain system of parameters. Connecting microwave devices to the desired microwave circuit is respectively considered as a connection of such equivalent multi-terminals. When studying such devices and connections it is important to know the extend of efficiency and amount of loss during transmission of microwave signals carrying useful information through them (how coordinated are the devices, what are the losses, etc.).

Therefore, along with other measurement tasks (measurement of power, frequency, spectrum, etc.), the task of measuring the parameters of microwave circuits in various frequency ranges was initially and continues to be one of the main and most important measurement tasks.

Of particular note is the significant progress achieved recently in the industrial development of the millimeter-wave range, including its short-wave part (with a wavelength of 3 and 2 mm), which has stimulated the accelerated creation of various radiolocation systems in this wave range.

Progress in the field of radioelectronics and weapon systems is largely determined by the development of new higher frequency ranges. In this regard, researchers, developers and customers of radioelectronic equipment are increasingly interested in the range of submillimeter waves, which are intermediate between millimeter and optical waves.

Exploration of millimeter and sub-millimeter wave ranges opens wide prospects for many fields of science and technology. This applies primarily to the most important areas of physics that study the atomic nucleus, phenomena occurring at low temperatures, high-temperature superconductivity, gas discharge, physical properties of solids, plasma physics and related conditions for the implementation of controlled thermonuclear reactions, as well as to such areas of technology as radiolocation, radio communications, radio telemechanics, radio navigation, high-precision weapons and systems of defense from such weapons, etc.

Taking into account further exploration of these frequency ranges, new fields of their application, features of propagation and transmission of millimeter and sub-millimeter waves, as well as features of the applied technologies during creation of elements, paths and radio means of these ranges, it is necessary to consider the problems of development and use of these regions of wavelengths in practice in detail.

1.5.2 Development of Technology of Millimeter and Sub-millimeter Waves

Let us consider features of propagation and application of millimeter and submillimeter waves.

In recent years, one of the most important directions in development of commercial and military microwave electronics has been the advance into the region of millimeter and submillimeter wave bands.

In accordance to the applied specification of wavelengths, millimeter range includes radiowaves with the length of 10^{-2}–10^{-3} m, or the frequency band of 30–300 GHz; sub-millimeter, or decimillimeter range includes radiowaves with the length of 10^{-3}–10^{-4} m, or the frequency band of 300–3000 GHz.

As a rule, division of the entire area of electromagnetic waves into ranges takes into account physical passage, specifics of propagation, methods of generation and reception. However, there are no clear physical boundaries between ranges, and they are conventional to a great extent.

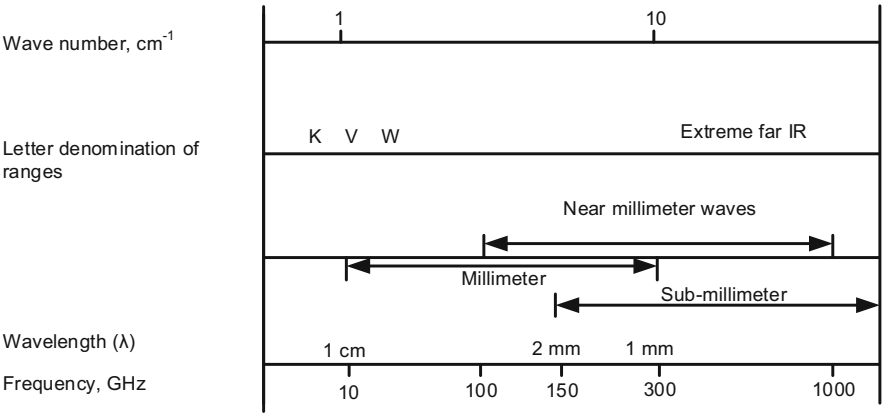

Fig. 1.10 Boundaries of the range of near millimeter waves and neighboring frequency ranges [2]

Certain scientific and technical literary sources use the term "near millimeter wave range", which covers the wavelengths of 0.3–3.0 mm, i.e. the frequency range of 100 GHz–1 THz.

Since the range of frequencies near the 94 GHz frequency is often used in practice, frequencies of 90–100 GHz are usually also attributed to the near-millimeter range.

Figure 1.10 shows names and conventional boundaries of frequency intervals of the near millimeter wave range and neighboring ranges.

Millimeter and decimillimeter waves occupy the intermediate position between radio waves of the centimeter range and infrared radiation (3–400 GHz). The limit between the ranges of radio waves and infrared radiation waves is unclear. However, the technology of generation and receipt of millimeter and decimillimeter range in the currently used methods are closer to radio equipment than infrared equipment.

Intensive exploration of the ranges of millimeter and sub-millimeter waves in recent years is due to the rapid growth in the number of radioelectronic devices and systems, due to which the lack of free frequencies in the range of less than 30 GHz ($\lambda < 1$ cm) has become sensible. The interest in these ranges is also caused by a number of special properties of millimeter waves, which distinguish them from waves of the centimeter range:

- reduction of dimensions and weight of devices and systems, in particular, reduction of size of antennas of radar stations; possibility of installation on rockets and mobile means;
- extension of the frequency band and the possibility of increasing information capacity of communication channels;
- improvement of antenna beam patterns, great resolution and possibility of detection of small objects;
- better penetration through dust and fog through the optical range and during radiation of SHF oscillations with greater wavelengths;

- increase in the noise immunity of communication lines and minimum interception possibilities;
- lower attenuation during passage through ionized medium as compared to waves of centimeter and decimeter ranges;
- great change of absorption in the atmosphere with relatively low frequency change.

It should be specifically noted that the interest in short millimeter wave range is largely determined by difficulties faced during the use of optical waves. Infrared systems, capable of operating during night and day, are often inefficient in case of presence of clouds, fog or smoke in the path of propagation of waves. At the same time, radiation of the near millimeter range can penetrate through such clouded areas and ensure sufficient range and angular resolution.

Selection of working frequencies in the ranges of millimeter and sub-millimeter waves is mostly determined by conditions and characteristics of propagation of these waves in the atmosphere. In this region, atmospheric attenuation increases significantly due to molecular absorption, which is insignificant in the range of centimeter waves. Absorption in the range of millimeter waves is mostly due to interaction with molecules of O_2 and H_2O water vapor. O_2 molecules are characterized by presence of magnetic moment, H_2O molecules – by presence of electrical moment. Interaction of the electromagnetic wave with magnetic moment of O_2 molecules causes emergence of a number of absorption lines near 60 GHz as well as the 118.8 GHz line. Water vapors similarly create absorption lines at 22.2 and 183.3 GHz frequencies, as well as at higher frequencies. Figure 1.11 shows characteristics of absorption in water vapors and molecular oxygen depending on frequency.

The first attenuation maximum (about 20 dB/km) is at the frequency of 60 GHz. Along with attenuation peaks, there are several transmission bands (windows), including at the frequencies of 94 GHz (attenuation about 0.6 dB/km), 140–150 GHz (about 2 dB/km), 230–240 GHz (about 7 dB/km), 500 GHz (about 10 dB/km). At higher frequencies, attenuation increases to values of about 1000 dB/km near the infrared region, and then passes through several maximums and minimums in the short-wave region and drops to 0.05 dB/km in the region of visible light.

Important conditions of propagation of millimeter and sub-millimeter waves are atmospheric phenomena, such as rain of various intensity, fog, snow and dust. The effect of rain and fog is illustrated by curves in Fig. 1.12.

Features of millimeter and submillimeter features described above, as well as successes and achievements in the field of electronics and microelectronic technology, which would allow, regardless of significant technical difficulties, to create sufficiently reliable semiconductor and other components of this range with identical parameters and characteristics (power sources, detector-mixer, control and isolation devices, various elements of the microwave path: splitters, phase shifters, switches, attenuators, etc.) have led to the situation in which many systems and devices of the millimeter wave range are currently transitioning from the development stage to the

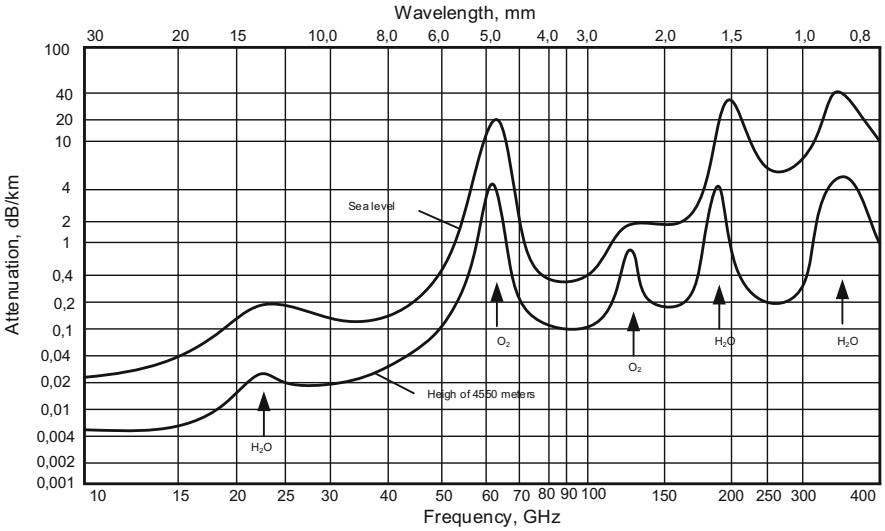

Fig. 1.11 Average absorption of millimeter waves by the atmosphere during horizontal propagation [2]

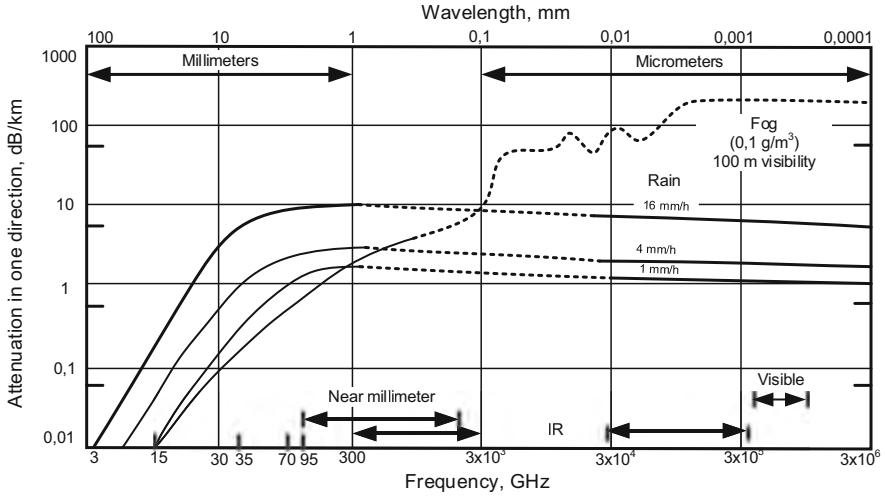

Fig. 1.12 Effect of rain and fog on propagation of millimeter and submillimeter waves [2]

production stage. The trend of exploration and practical use of the short-wave part of the millimeter ($f \geq 75$ GHz) range is becoming more and more obvious.

The main directions in the millimeter range of wavelengths are associated with creation of various systems and equipment for military purposes, as well as for scientific and industrial purposes [1].

1.5.3 Fields of Application of Millimeter and Submillimeter Waves in Science and Technology and Main Directions of Developments

The main fields of application of millimeter and submillimeter waves in science and technology are [2]:

- radiolocation;
- radio navigation;
- radio communications;
- radio control;
- electronic countermeasures;
- radio astronomy;
- radiometry;
- medicine;
- atmospheric meteorology;
- computing equipment means;
- modeling of radiotechnical systems;
- scientific studies of different directions.

Modern radioelectronics, which is an advanced technical field, is characterized by presence and development of many radiosystems, which differ significantly in terms of their purpose, principle of operation, used frequency range, complexity, cost, weight and dimensions, scale of production, etc. A radiosystem is any technical system in which the main function is performed by radioelectronic means.

It turn, the systems are divided into several categories based on their purpose: systems of radio communication, radio location, radio navigation, radio control, radio telemetry, radio aiming, electronic countermeasures, etc. The main components of any radiosystem include radio transmitting and receiving devices, antenna feeder devices, as well as devices for power supply, data display, electronic calculation devices, etc.

In the radio receiver of any system, encoded message is used for modulation of oscillations of the carrier frequency, which are more and more often represented by oscillations of millimeter and sub-millimeter waves. Accordingly, receiver and antenna feeder devices are build with the paths of the millimeter range and its elements, and the systems in general belong to the systems of millimeter and sub-millimeter wave ranges.

Certain preferable sections of frequency bands are assigned to radio systems of various purposes in regulatory and legislative order.

The main radiosystems of the millimeter range, actively developed by many companies (first of all – Russian and American) in recent years, include:

- high-resolution radar stations, including radar sets for detection and location of space objects from Earth and satellites, radar sets for detection and tracking of low-flying targets for anti-aircraft missile systems and ships, airborne plane radar sets, etc.;

- various communication systems, including Earth-space communication (e.g. at frequencies around 60 GHz due to the presence of atmospheric peak of up to 20 dB/km, it is possible to ensure long-range communication in space between satellites that is hidden from ground-based observations), super-long range communication systems, hidden operative and tactical communication at ranges of up to 5–8 km in stop bands, etc.;
- aiming means, including systems of passive and active guidance, target seekers, etc.;
- radio navigation systems of various purposes, including aircraft, satellite, marine and other systems performing navigation and identification;
- systems of electronic countermeasures used in electronic surveillance, communication and signal radio surveillance, etc.;
- a number of other systems, including control and management systems.

Modeling is one of important fields of application of millimeter and submillimeter waves.

Laboratory models operating at significantly higher frequencies then the actual stations are created for better presentation and study of properties of developed radar stations and reflection characteristics of detected targets. During this process, the modeled targets are reduced in size on the relevant scale. Normal values of reduction rates are within 1/4–1/20 for planes and within 1/100–1/200 for ships. Since the most commonly used operating frequencies of radars are the frequencies of 3–10 GHz, radar models are designed for frequencies of 10–200 GHz (there is information about development of such model for the frequency of 890 GHz).

Wide prospects of further works are associated with the use of millimeter and sub-millimeter waves in scientific studies, for probing of atmosphere in meteorology, medicine, radio astronomy and other fields.

For example, the past few years saw a significant increase in radio astronomy studies, which make it possible to obtain information not only about distribution of radiation sources in space, but also about their physical nature. The studies now extend into the region of sub-millimeter waves. Problems associated with atmospheric attenuation of signals are eliminated due to the use of space devices (placing radar telescopes outside the atmosphere on satellites, space stations, etc.).

Today, there are already registered extragalactic sources in the sub-millimeter wave range at wavelengths of 1 mm, 350 μm and 100 μm. Development of studies in this field was aided by creation of special sensitive radiometers.

Great successes have been achieved in radiospectrometry of the millimeter and sub-millimeter ranges, including for creation of equipment designed for studies of absorption spectra. Studies are performed related to interaction of electromagnetic radiation with the substance in liquid, solid and gaseous states. Such materials as germanium, silicon, gallium arsenide and some others are studied.

More and more advanced equipment and radiation sources in the short-wave part of millimeter and sub-millimeter ranges are used during plasma heating and diagnostics, for determination of electronic concentration, collisional frequency and electronic temperature.

The range of millimeter and submillimeter waves is also used in biology and medicine. Microwave thermograph for chest and spine imaging is currently being developed. Biological effects within these frequency ranges are studied. Works on creation of radiometers for diagnostics of tumors (e.g. breast cancer) are currently being performed. Radiation of millimeter waves can be used for destruction of tumors (by heating) without surgical interference.

Other fields of application of millimeter and submillimeter waves are being developed: in radio relay communications, in transport, agriculture, etc.

Frequency distribution of the millimeter range for different fields of application used in the USA is presented in Table 1.1 [2].

Distribution includes satellite communication, radiolocation, various forms of radio navigation, radio astronomy, studies of Earth's surface from satellites and so on and covers the entire continuous range of frequencies between 30 and 300 GHz, both regions of transmission windows and stop bands of the atmosphere (for

Table 1.1 Frequency distribution of the millimeter range in the USA

No.	Application	Frequency range
1	Fixed	36–43;50–51;54,25–58,2;59–64;76–86;92–95;102–130;140–142;150–165;170–182;185–190;200–230;265–300
2	Fixed satellite	30–31;40–41;50–51;92–95;102–105;140–142;150–152;220–230;265–275
3	Radiolocation	33,4–36;48–50;70;71–76;94;140;165–170;230;240–250
4	Radio astronomy	31,2-31,5;86–92;130–140;230–240
5	Space research	31,5-31,8;51–54,25;58,2–59;64–66;86–92;101–102;130–140;182–185;230–240
6	Mobile	31;36–43;50–51;54,25–64;76–86;92–95;102–130;140–142;150–165;170–190;200–230;265–300
7	Aeronautical mobile	
8	Maritime mobile	
9	Aeronautical mobile satellite	43–48;66–71;95–101;142–150;190–200;250–265
10	Maritime mobile satellite	
11	Radionavigation	31,8–33,4
12	Aeronautical Radionavigation	
13	Maritime Radionavigation	
14	Radionavigation satellite	43–48;66–71;95–101;142–150;190–200;250–265
15	Aeronautical Radionavigation satellite	
16	Maritime Radionavigation satellite	
17	Intersatellite	54.25–64;105–130;170–182;185–190
18	Broadcasting satellite	41–43;84–86
19	Amateur	48–50;71–76;165–170;240–250
20	Earth exploration satellite	51–52

example, sections of the stop bands at 54.25–64; 105–130; 170–180 and 185–190 GHz are allocated for intersatellite communication and radio navigation).

1.5.4 Transmission Lines of Millimeter and Sub-millimeter Waves

Developments of various systems and equipment, i.e. practical use of short millimeter and sub-millimeter waves, require creation of waveguide systems and various elements included in the waveguide path and fitted for effective operation in these frequency ranges. Serious attention is paid to such works in the USA, Russia, Japan and other countries.

The most commonly used model of the waveguide path for millimeter range systems in the USA for the frequency band of up to 325 GHz is represented by hollow metal single-mode waveguides with rectangular cross-sections.

Table 1.2 contains designations, dimensions, frequency ranges (and their designations) of standard waveguide foreign companies.

Table 1.3 contains values of frequency rages of waveguides of standard sections for the millimeter range used in Russia.

In ranges of millimeter and sub-millimeter waves, in addition to hollow metal waveguides with rectangular and cylindrical cross-sections, in which waves of a single type propagate, other types of waveguides are used to solve various tasks, including waveguides with extended cross-section, groove waveguides, microstrip lines, radial and dielectric waveguides, etc.

Formulas for the main H_{10} (TE_{10}) wave type of a rectangular waveguide:

$$\Lambda = \frac{\lambda}{\sqrt{1 - \left(\frac{\lambda}{2a}\right)^2}} = \frac{1}{\sqrt{\left(\frac{f}{c}\right)^2 - \left(\frac{1}{2a}\right)^2}} \tag{1.3}$$

where Λ is the wavelength in the main mode waveguide;

λ is the wavelength in free space;
f is the frequency (Hz);
c is the speed of light in free space;
a is the size of the wide wall of the waveguide.

$$f_{\text{кр}}\left(H_{10)} = \frac{C}{2a} \text{ or } f_{\text{кр}}\left(H_{10)} = \frac{149.9}{a}(\text{ГГц}),\right. \tag{1.4}$$

where $f_{kp(\mathbf{H10})}$ is the critical (cutoff) frequency of the main type of wave.

Table 1.2 Standard waveguides of the most famous manufacturers [2]

Designations of the frequency range					Frequency range, GHz	Waveguide cross-section, mm (inch)	Cutoff frequency, GHz	Waveguide designation			
TRG, USA	Hughes, USA	Millitech (BCJ), USA	H/P, USA	Hitachi, Japan				IEC	EIA	JAN	Brit
K	K	K	K	K	18.0–26.5	10.67×4.32 (0.420×0.170)	14.8	R220	WR-42	RG-53/V	WG-20
A	Ka	Ka	R	R	26.5–40.0	7.11×3.56	21.10	R320	WR-28	RG-96/V	WG-22
B	Q	Q(B)	Q	Q	33.0–50.0	5.69×2.84 (0.224×0.112)	26.35	R400	WR-22	RG-96/V	WG-23
V	V	V(Q)	V	F	40.0–60.0	4.78×2.39 (0.188×0.094)	31.41	R500	WR-19		WG-24
V	V	V	V	M	50,0–75,0	3.76×1.88 (0.148×0.074)	39.90	R620	WR-15	RG-98/V	WG-25
E	E	E	E	E	60,0–90,0	3.10×1.55 (0.122×0.061)	48.40	R740	WR-12	RG-99/V	WG-26
W	W	W(R)	W	W	75.0–110.0	2.54×1.27 (0.100×0.050)	59.05	R900	WR-10		WG-27
F	F	F(N)		V	90.0–140.0	2.03×1.02 (0.080×0.040)	73.84	R1200	WR-08	RG-138/V	
D	D	D(T)		T	110.0–170.0	1.65×0.83 (0.065×0.0325)	90.85	R1400	WR06, WR07	RG-136/V	
G	G	G			140.0–220.0	1.30×0.65 (0.051×0.0255)	115.75	R1800	WR-05		
		Y			170.0–260.0	1.10×0.55 (0.043×0.0215)	137.52	R2200	WR-04		
		D			220,0-325,0	0.86×0.43 (0.034×0.017)	173.28	R2600	WR-03		
					325.0–400.0	0.71×0.355 (0.028×0.014)	211.00		WR-2.8		
					400.0–500.0	0.56×0.28 (0.022×0.011)	268.0		WR-2.2		

Table 1.3 Standard cross-sections of waveguides and their operating frequency ranges [2]

Row I		Row II	
Waveguide section a×b, mm	Frequency range, GHz	Waveguide section a×b, mm	Frequency range, GHz
0.9×0.45	218.8–315.6	0.7×0.35	258.4–405.1
1.3×0.65	142.8–218.8	1.1×0.55	178.4–258.4
2.0×1.0	94.28–142.8	1.6×0.80	118.1–178.4
3.0×1.50	63.79–94.28	2.4×1.20	78.33–118.1
4.4×2.2	44.09–63.79	3.6×1.80	53.57–78.33
6.2×3.1	30.91–44.09	5.2×2.60	37.50–53.57
9.0×4.5	21.43–30.93	7.2×3.40	25.95–37.50
13.0×6.5	14.71–21.43	11.0×5.50	17.44–25.95
19.0×9.5	9.93–14.71	16.0×8.00	12.05–17.44
28.5×12.6	6.85–9.93	(17.0×8.00)	11.55–16.66
40.0×20.0	4.80–6.85	23×10.0	8.15–12.05
58.0×29.0	3.20–4.80	35×15.0	5.64–8.15
90.0×45.0	2.14–3.20	48×24.0	3.94–5.64
130.0×65.0	1.45–2.14	72×34	2.59–3.94
		110×55	1.72–2.59
		(120×57)	1.56–2.38
		160×80	1.16–1.72

$$\alpha = 2,3273\sqrt{\frac{\rho}{\rho_0}}\frac{1}{b\sqrt{a}}\frac{\left(\frac{f}{f_c}\right)^2 + \frac{2b}{a}}{\sqrt{\frac{f}{f_c}\sqrt{\left(\frac{f}{f_c}\right)^2 - 1}}}\,(\text{дБ/м}) \tag{1.5}$$

where α is the attenuation in rectangular waveguide;

ρ is the specific resistance of internal non-magnetic metal wall;
ρ_0 is the specific copper resistance $= 1.7241 \times 10^{-8}$ Ohm/m;
a is the internal waveguide width in mm;
b is the internal waveguide height in mm;
f_c is the critical frequency determined by the expression (1.2);
f is the frequency at which attenuation is calculated.

$$P_{\text{пред}} = \frac{abE^2_{\text{пред}}}{1,51}\sqrt{1 - \left(\frac{\lambda}{2a}\right)^2}\ (\text{KW}) \tag{1.6}$$

where P_t is the threshold power of the waveguide;

$E_t = 29$ kV/cm (for air).

With transition to short waves, properties of single-mode waveguides deteriorate: dimensions decrease, dimension tolerance become stricter, and losses increase. With wavelength of 1 mm, losses in rectangular waveguide in which the wave H_{10} propagates exceed 20 dB/m. With reduction of the wavelength, the losses quickly increase.

Figure 1.13 shows frequency dependencies of typical loss values of standard US waveguides (from WR-28 to WR-3).

In technically reasonable cases, waveguides in the frequency range of (1.25–1.90) $f_{\mathbf{kp(H10)}}$ can be used.

Practical implementation of waveguide devices with waveguide cross-section less than 1.6 × 0.8 or 1.3 × 0.65 mm becomes a difficult task due to increased

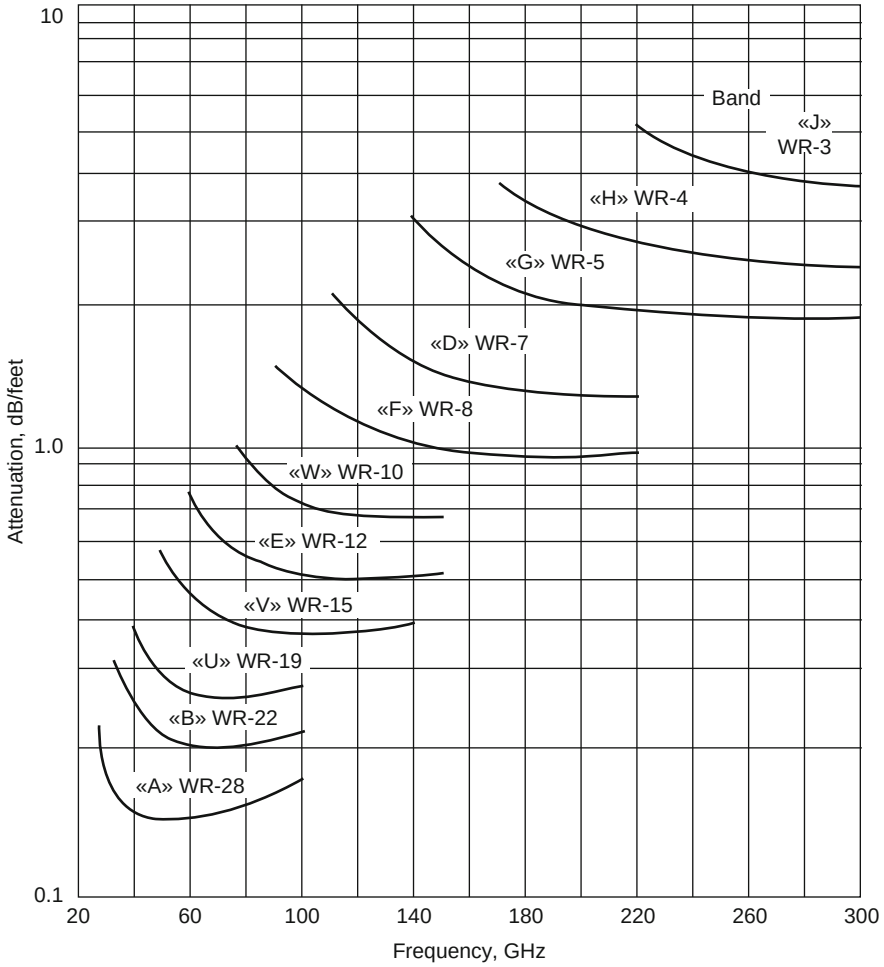

Fig. 1.13 Frequency dependencies of losses in standard waveguides [2]

losses in them, significant reduction of all linear dimensions and the necessity of significant toughening of tolerances for these devices. A significant problem for these sections of waveguides is provision of reliable flanged connections without skews and displacements of apertures of the coupled waveguides, which has a significant effect on the parameters of the measuring path.

Certain practical use is found by waveguides with increased cross-sections, in which oscillations of higher types can exist. Losses in them are significantly lower. At $\lambda = 0.8$ mm, attenuation in waveguide with cross-section of 7.2×3.4 mm amounts to 1.4 dB/m; at $\lambda = 0.65$ mm, attenuation in waveguide with cross-section of 23×10 mm amounts to 1.65 dB/m.

Waveguides of other types, such as H-waveguides, grooved waveguides (with grooves along wide walls) are suggested and studied in the examined ranges. Different variants of dielectric waveguides are studied, but the losses in such waveguides are fairly high.

The impossibility of creating = waveguides with low losses led to the use of quasi-optical technology in the submillimeter wavelength range. Beam waveguides with lenses and mirrors are also used. Their disadvantages include relatively high loss levels and the necessity of careful adjustment of mirrors.

At the moment, the following types of transmission lines of quasi-optical path can be identified:

- oversize multimode metal rectangular waveguide with the main wave type H_{10};
- groove waveguide;
- quasi-optical beam guide;
- metal-dielectric waveguide (MDWG) of circular cross section;
- quasi-optical transmission line of the "channel in dielectric" type;
- metal-dielectric waveguide (MDWG) of rectangular cross section.

According to a number of studies performed, the best option for use in equipment and various systems of the short-wave region of millimeter and sub-millimeter band (above 150 GHz) is the use of an oversized metal-dielectric waveguide (MDWG).

Comparison of the main characteristics of quasi-optical transmission lines of the closed type is presented in Table 1.4.

1.6 Main Principles of Building Software Complexes for Simulation of Radiolocation Signals

1.6.1 Typical Composition of a Software Complex for Modeling of Radiolocation Signals

Solution of the problems of radar surveillance (detection, measurement, identification) suggests processing of implementations of the received signal [18, 19]. At the stage of creation of the radiolocation path of signal processor, the task of performing

Table 1.4 Characteristic of transmission lines [2]

Line type	Losses per unit length in sub-millimeter band	Self-filtering level	Polarization immunity	Producibility	Possibility of building of path elements	Disadvantages
Single-mode rectangular waveguide	30 dB/m; ($f = 300$ GHz)	Single mode	Stable	Possibility of production of single samples	Possibility of building elements with low parameters	High losses per unit length, lack of produceability
Oversized rectangular waveguide; waveguide length 10×23 mm; $\lambda = 1$ mm	$\alpha = 1$ dN/m	Absent	Possibility of conversion at irregularities	High	Possibility of building a wide set	Absence of self-filtration and excitation of parasite modes at irregularities of the path
Dielectric beam guide $\lambda = 0.8$–1.7 mm; $\varepsilon = 1.4$–2.3	$\alpha = 1.2$–5 dB/m	High	Low	Medium	Examined the possibility of building a wide class of elements	High losses, stability of polarization, excitation of parasite modes at irregularities
MDWG (rectangular)	$\alpha = 0.03$ dB/m	Medium	Stable	High	Possibility of building of a wide class of elements	Excitation of parasite modes at irregularities
MDWG (circular)	$\alpha = 0.0037$ dB/m; KA = 40, $\lambda = 2$ mm	Medium	Non-fixed	High	Possibility of building of a wide class of elements	Excitation of parasite modes, irregularities, instability of polarization
Groove waveguide	$f = 230$ GHz; $\alpha = 0.07$–0.08 dB/m	High	Stable	High	Insufficiently studied	Absence of shielding, radiation at irregularities
Channel in dielectric (square and round)	Depends on the dielectric material	High	Stable for square and non-fixed for circular	High	Possibility of building of a wide class of elements	Weak shielding and high specific attenuation for dielectrics with high tg

multiple experiments associated with adjustment of algorithms of the designed devices. Debugging process suggests presence of implementations of random signals adequately characterizing the examined objects. Such implementations can be obtained by several methods: by recording real signals of the observed objects; as a result of iron bird tests; with the help of systems of imitational mathematical modeling.

At the modern stage of development of computing means, the method of mathematical modeling becomes especially relevant. Being the most advantageous from the point of view of economy, it helps form implementations of random processes in accordance with the needs of tasks to be solved: ensures the following precision of description of physical processes and takes into account characteristics and features of radar objects in given surveillance conditions [20, 21].

In this section we will consider specific features of building a software complex [18] ensuring modeling of signals reflected from radar objects under surveillance. The main focus in on the principles of creation of the construction set of simulated radiolocation targets ensuring the required distribution of local reflection areas on the object surface.

Such software complex makes it possible to imitate implementations of reflected radiolocation signals from the observed water, ground and air objects. When modeling signal implementations, it is necessary to take into account spatial position of the target, its geometrical dimensions and shape, design features and the presence of observed rotating components, as well as the value of effective dispersion surface relative to given probing parameters.

As is known, any object of radar observation can be presented as combination of local reflection areas (highlights, HL) arranged in space in a certain manner [19] (Fig. 1.14).

In general case, temporal structure of the reflected signal (RS) is a result of coherent adding of signals reflected from separate elements of the target structure [2]:

$$m(t) = \sum_{x=1}^{N_\chi} m_\chi(t) = \sum_{x=1}^{N_\chi} E_\chi(t) U_L\left(t - t_{r_\chi}\right) e^{\,j2\pi f_0\left[t - t_{r\chi}(t)\right] + \varphi_{\text{эс}}}, \qquad (1.7)$$

where $N\chi$ is the quantity of local reflection areas on the surface of the object (HT number); $m_\chi(t)$ is the temporal structure of the signal reflected from the χth local reflection area; $E_\chi(t) = \sqrt{2\sigma^2_{c\chi}(t)}$ is the amplitude of the signal reflected from the xth HL; $U_L(t - t_{r\chi})$ is the complex law of modulation of limited sequence L of single radio pulses taking into account the current RS delay time; $t_{r\chi}(t) = \frac{2r_{u\chi}(t)}{c}$ is the current RS delay time defined by the range $r_{u\chi}$ (t) from the radar to the xth HL; $\omega_0 = 2\pi f_0$ is the circular carrier frequency of the probing signal; φ_{ps} is the initial phase of the radiated probing signal.

Approximated presentation of the observed radiolocation object with the combination of highlights distributed in the observation space is physically reasonable, as it makes it possible to take into account the main features of reflection typical of

Fig. 1.14 Representation of a target as a combination of local reflection areas

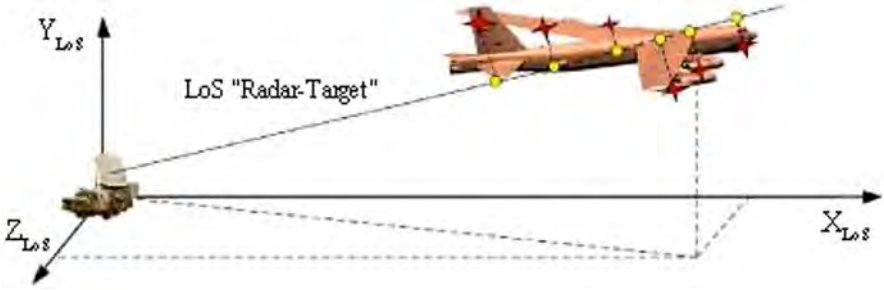

Fig. 1.15 HL projection to LoS

signals from real objects during modeling. Moreover, significant simplification of the modeling process makes this approach extremely attractive from the point of view of practical implementation.

The examined approach makes it possible to form the resulting signal as a combination of reflections from the combination HLs projected to the line of sight (LoS) between the radar station and the target (Fig. 1.15).

The developed modeling software complex shall make it possible to generate implementations of signals reflected from the simulated target of any required class. At the same time, it is necessary to ensure imitation of discrete RS counts taking into account the features of spatial movement of the target, conditions of its observation and the values of radar parameters. Generalized structural diagram explaining the RS modeling process is shown in Fig. 1.16.

A standard software complex usually includes the following components:

- object trajectory generator (uses source data at required moments for output of current coordinates and movement parameters of the object);
- construction kit for radiolocation objects (uses set characteristics of the modeled object to imitate its geometrical shape and spatial distribution of the regions of local reflection);
- reflected signal generator (takes into account tactical-technical characteristics of the radar, movement parameters and characteristics of the target to perform vector

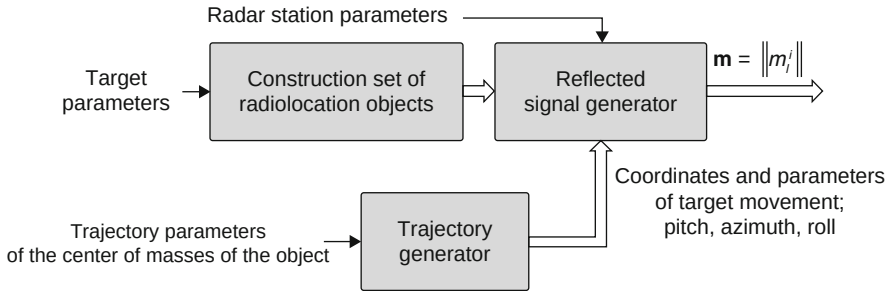

Fig. 1.16 Generalized structural diagram explaining the process of RS modeling

addition of reflections from projections of the combination of highlights to the line of sight between the radar and the target).

One of the most important components of a software complex is the object constructor. Due to this fact, it will be reasonable to consider principles of its building relative to the task of RS generation.

1.6.2 Features of Implementation of the Construction Set of Radiolocation Objects

Construction set of radiolocation objects makes it possible to use the set characteristics of the target to form the spatial distribution of HL combination determining reflective properties of the surface of simulated object. The shape of surface of the observed target is approximated by the combination of elementary geometric components. Adter determination of projections of the selected HL combination to the LoS, RS implementation is calculated.

During modeling, the simulated radiolocation object is presented by a set of highlights distributed within the area limited by dimensions of the target (Fig. 1.17). Geometrical volume occupied by the modeled complex radiolocation object is formed with the help of m typical elementary components (EC) – geometrical figures: rectangle, ellipsoid and elliptical cylinder. For example, the glider of an aircraft can be represented by an ellipsoid, its wings – by rectangular parallelepipeds, engine nacelles – by cylinders (Fig. 1.17).

Each EC of the object, which is a combination of connected reflectors, is set in its own local coordinate system (CS) Xv Yv Zv (Fig. 1.17b).

In order to ensure imitation of reflections from rotating elements of the target structure, the object construction set shall provide the possibility of synchronous rotation of the selected combination of reflectors ("rotary component"). This approach allows simulating reflections from rotary propeller blades, turboprop blades and turbojet engines observed on the object's surface during calculations.

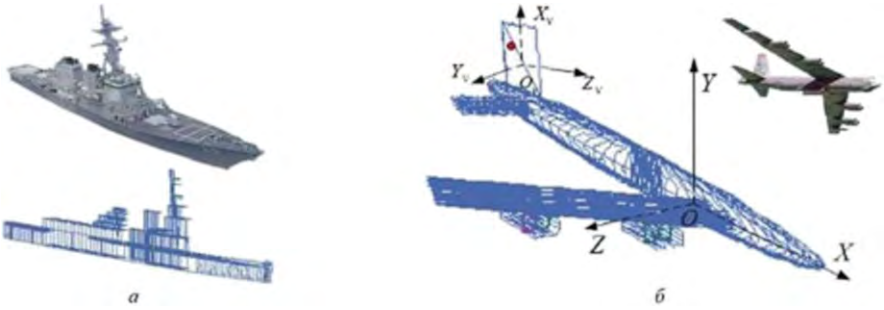

Fig. 1.17 Setting a complex modeled object with the help of elementary components: (**a**) – model of the Arleigh Burke class destroyer presented as a set of elementary components; (**b**) – position of the elementary components in the coordinate system of the modeled object (strategic bomber B-52H) [2]

1.6.3 Features of Setting Spatial Configuration of the Object

Imitation of spatial configuration of each elementary component (EC) of the object is ensured by generating the combination of n distributed highlights (HT). HT of the *v*th ($v = 1 \ldots m$) surface is said to belong to the modeled object if it is located inside the elementary component describing a certain part of the modeled object (Fig. 1.17b). Distribution of highlights within the volume of an elementary component is random. This distribution can be selected in accordance with uniform or Gaussian distribution laws. During modeling, distribution of HLs along each coordinate of the space is considered independent.

It should be noted that the radar cross-section RCS of the radiolocation object is the sum of RCSs of elementary components. PCS of each HL within the limits of EC remains the same and is determined by the ratio of RCS of the elementary object component σ_k to the HL quantity: $\sigma^k_{HL} = \sigma_k/n$. The number of highlights shall allow their combination to visually determine contours of the object (Fig. 1.18).

Construction set of radiolocation objects shall make it possible to model both symmetrical objects (plane, missile) and asymmetrical objects (e.g., helicopter, surface vessel, certain types of ground objects). In case with simulation of symmetrical objects (Fig. 1.17b), only configuration of the right side of the object is modeled in order to reduce computational costs. Left part of the object is usually formed by symmetrical display of the obtained part of the model relative to the symmetry plane (construction plane XOY).

After obtaining the required distribution of the combination of elementary reflectors, the calculation of their projections to the sight line is performed.

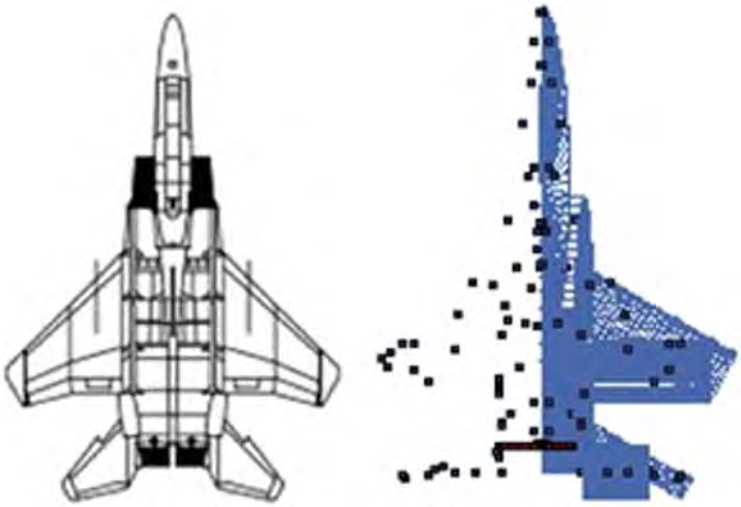

Fig. 1.18 Draft model of the F-15SE fighter jet represented by a combination of highlights (HL) [2]

1.6.4 Calculation of HT Projections to the Line of Sight

Practical solution to this engineering problem suggests consequent analysis of reflectors of all elementary components of the object. For this purpose, each HL set in the coordinate system of the elementary component of the target is recalculated in the CS of the center of masses of the target, after which it is converted into the CS associated with the radar.

Main operations of coordinate recalculation process are [21]:

- shift of the center of the analyzed coordinate system;
- rotations of the analyzed coordinate systems.

The process of transfer of a local CS is explained in Fig. 1.19a.

For transmission of coordinates of the analyzed point $P_v = (x_v, y_v, z_v)^T$ along the axes *OX, OY, OZ*, the corresponding transition (shift) matrices are used:

$$M_X = \begin{pmatrix} 1 & 0 & 0 & x_v \\ 0 & 1 & 0 & 0 \\ 0 & 0 & 1 & 0 \\ 0 & 0 & 0 & 1 \end{pmatrix} M_Y = \begin{pmatrix} 1 & 0 & 0 & 0 \\ 0 & 1 & 0 & y_v \\ 0 & 0 & 1 & 0 \\ 0 & 0 & 0 & 1 \end{pmatrix} M_Z = \begin{pmatrix} 1 & 0 & 0 & 0 \\ 0 & 0 & 1 & z_v \\ 0 & 0 & 0 & 1 \\ 0 & 0 & 0 & 1 \end{pmatrix}$$

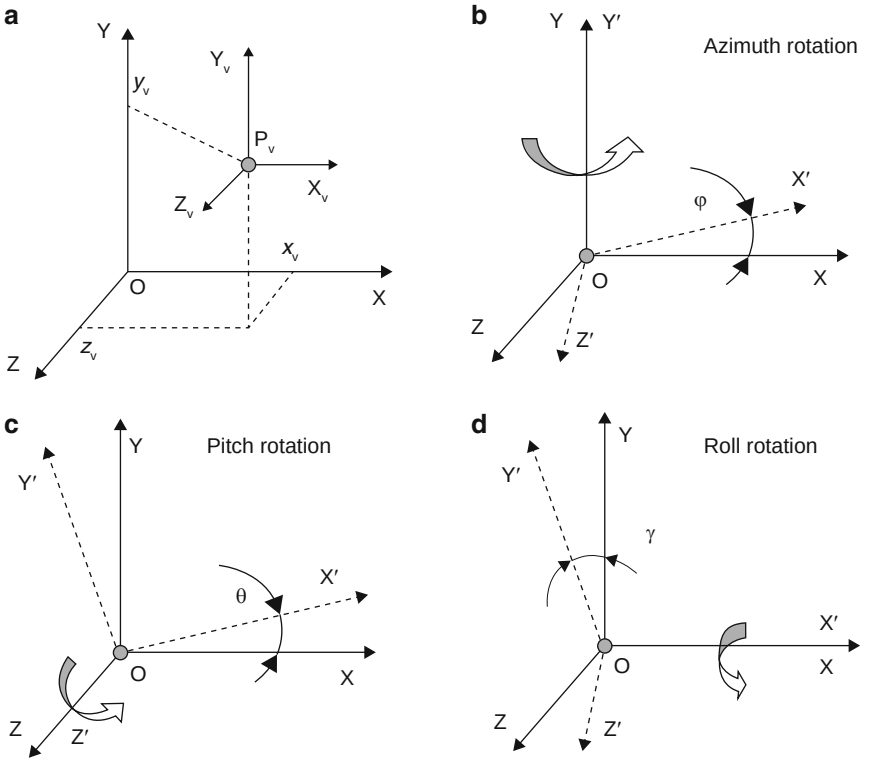

Fig. 1.19 Basic operations of coordinate recalculation process: (**a**) – transfer of coordinate system; (**b**) – azimuth rotation of coordinate system; (**c**) – pitch angle rotation of coordinate system; (**d**) – roll angle rotation of coordinate system

During calculations, it is convenient to use the transition matrix that takes into account combined shift of coordinates along three axes:

$$M(P_v) = M_X M_Y M_Z = \begin{pmatrix} 1 & 0 & 0 & x_v \\ 0 & 0 & 1 & z_v \\ 0 & 0 & 0 & 1 \\ 0 & 0 & 0 & 1 \end{pmatrix} \tag{1.8}$$

where x_v, y_v, z_v are the required values of coordinate shift along each axis.

During modeling, the following parameters are used to describe orientation of the object in space [21]:

– azimuth φ (measured by rotation of the model around the OY axis);
– pitch angle θ (measured by rotation of the model around the OZ axis);
– roll angle γ (measured by rotation of the model around the OX axis);

Possible rotations of the local coordinate system are explained in Fig. 1.19b–d.

During modeling, all rotations (angle changes) are clockwise. For rotation around the OY axis by the azimuth φ, around the OZ axis by the pitch angle θ and around the OX axis by the roll angle γ, corresponding rotation matrices are used [21]:

$$
\begin{aligned}
M_{OY} &= \begin{pmatrix} \cos\varphi & 0 & -\sin\varphi & 0 \\ 0 & 1 & 0 & 0 \\ \sin\varphi & 0 & \cos\varphi & 0 \\ 0 & 0 & 0 & 1 \end{pmatrix} M_{OZ} \\
&= \begin{pmatrix} \cos\theta & \sin\theta & 0 & 0 \\ -\sin\theta & \cos\theta & 0 & 0 \\ 0 & 0 & 1 & 0 \\ 0 & 0 & 0 & 1 \end{pmatrix} M_{OX} \\
&= \begin{pmatrix} 1 & 0 & 0 & 0 \\ 0 & \cos\gamma & \sin\gamma & 0 \\ 0 & -\sin\gamma & \cos\gamma & 0 \\ 0 & 0 & 0 & 1 \end{pmatrix}
\end{aligned} \tag{1.9}
$$

The examined transforms make it possible to determine coordinates of the analyzed HL of the reflection surface of the imitated object in the CS of the radiolocation station (Fig. 1.20).

For calculation of HL projections to the sight line, the following sequence of events is performed:

1. The ith HL is transfered, which is characterized by the coordinates

$P_i^\circ = (x_i^\circ \; y_i^\circ \; z_i^\circ \; 1)^{\mathrm{T}}$ in CS of *k*th EC from the local CS of the analyzed component to the CS of the modeled object. For this, rotations are performed around the axis OY_k by the angle φ, around the axis OZ_k by the angle θ_k, around the axis OX_k на угол γ_k, after which the elementary *th* component is shifted to the point $P_k = (x_k \; y_k \; z_k \; 1)^{\mathrm{T}}$.

Matrix of transformation of coordinates for *k*th EC in this case has the following form:

$$M_k = M(P_k) \cdot M^{OX}(\gamma_k) \cdot M^{OZ}(\theta_k) \cdot M^{OY}(\varphi_k), \tag{1.10}$$

Coordinates of the *i*th HL in the target CS are calculated as the product of the vector of coordinates and the conversion matrix $P_i^{\mathrm{t}} = (x_i^{\mathrm{t}} \; y_i^{\mathrm{t}} \; z_i^{\mathrm{t}} \; 1)^{\mathrm{T}} = M_k \cdot P_i^\circ$.

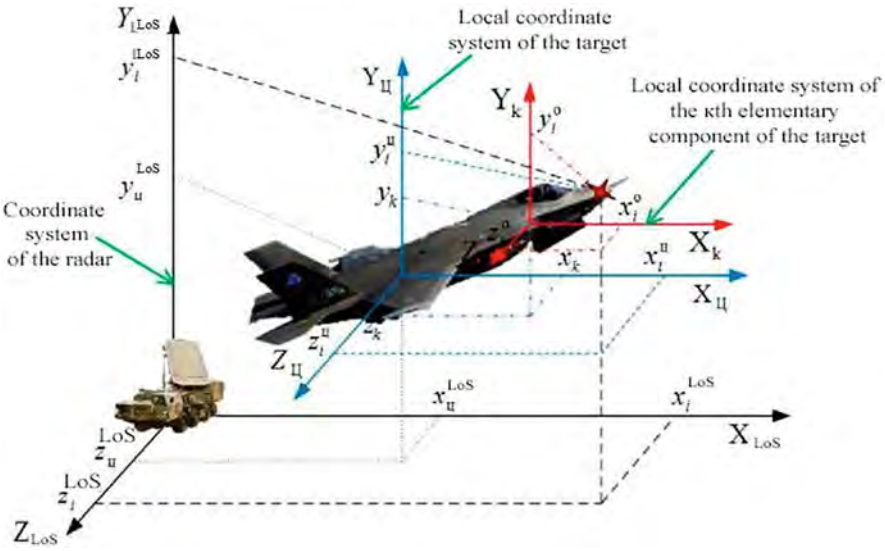

Fig. 1.20 Production of HL projection to LoS [2]

2. Coordinates of HLs in radar CS are found with the help of coordinate conversion matrices

$$M_{\text{ц}} = M(P_{\text{ц}}) \cdot M^{OX}(\gamma_{\text{ц}}) \cdot M^{OZ}(\theta_{\text{ц}}) \cdot M^{OY}(\varphi_{\text{ц}}), \tag{1.11}$$

where $P_{\text{t}} = (x_{\text{t}}^{\text{RS}}\ y_{\text{t}}^{\text{RS}}\ z_{\text{t}}^{\text{RS}}\ 1)^{\text{T}}$ are the coordinates of the mass center of the object in the radar CS.

As a result, coordinates of the *i*th HL in the radar coordinate system are found

$$P_i^{\text{RS}} = \left(x_i^{\text{RS}} y_i^{\text{RS}} z_i^{\text{RS}}\ 1\right)^{\text{T}} = M_{\text{t}} \cdot P_i^{\text{t}}.$$

3. Projection of HLs on the line of sight is determined as scalar product of two vectors:

$$r_i^{\text{ЛБ}} = \frac{x_i^{\text{РЛС}} + x_{\text{ц}}^{\text{РЛС}} + y_i^{\text{РЛС}} + y_{\text{ц}}^{\text{РЛС}} + z_i^{\text{РЛС}} + z_{\text{ц}}^{\text{РЛС}}}{\sqrt{\left(x_{\text{ц}}^{\text{РЛС}}\right)^2 + \left(y_{\text{ц}}^{\text{РЛС}}\right)^2 \left(z_{\text{ц}}^{\text{РЛС}}\right)^2}}. \tag{1.12}$$

After determining projections of all observed HLs on the line of sight, addition of complex signals reflected from each HL is performed according to the expression (1.7). During this, amplitude and phase relations are taken into account, which are defined by the presence of the Doppler frequency of signals reflected from the combination of highlights for the current radar parameters.

The developed modeling complex makes it possible to form random implementations of the signal reflected from the observed object, taking into account its dimensions and structural features of spatial movement of the target, presence of rotating reflectors and characteristics of the radar radiation.

Therefore, we have considered the features of building a typical software complex for modeling of signal implementations reflected from the simulated radiolocation object. Such complex shall include: an object trajectory generator, a construction kit of radiolocation objects, and a reflected signal generator (conditioner). Object of radar observation is approximated by a set of elementary components (rectangle, ellipse and elliptical cylinder). Within the EC volume, highlights are randomly distributed, the combination of which visually determines configuration of the object. RS is the sum of signals reflected from the observed projections of highlights in the line of sight between the radar and the target.

This approach helps ensure the required accuracy of calculations with significant reduction of computing costs (as compared to faceted reflection models [19]). RS model developed with the help of this method makes it possible to take into account the main features of reflections of radiolocation objects for the given observation conditions.

1.7 Increasing Noise Immunity of the Radar Using Automatic Compensators of Perturbing Radiators

Detection of the reflected signal is usually performed against the background of noises and interference. Interferences are clutter reflections or radiations, which can be natural or artificial, created deliberately to disrupt or fully suppress normal operation of the radar station.

Extraction of the useful signal from interference is performed on their determined and statistical differences, which can be related to energy, frequency, time, spectrum, space or polarization [24].

Automatic compensation of perturbing radiations is based on spatial differences between useful signal and interference [25], since the useful signal is received in the main lobe of the antenna directivity pattern, and the interference signal – in side lobes of the same antenna.

The influence of interferences received in the side lobes affects signal-to-noise ratio and thus greatly reduces the radar detection area. This causes appearance of uncontrolled areas in the radiolocation field and reduces the probability of target detection.

The need to increase noise immunity of radars is due to constant development of technical means of electronic countermeasures and improvement of the tactics of their use. The most efficient method of protection from electronic countermeasures for radars based on active location principle consists in ***using automatic compensators of perturbing radiations*** [26]. Increased efficiency of interference

compensation directly enhances abilities of the radar in terms of timely detection of radar targets and accuracy of determining coordinates and parameters of the targets.

1.7.1 Principle of Coherent Compensation of Active Noise Interferences

Coherent compensation of perturbing radiations (CCPR) consists in balancing of the amplitude and phase of the signal of perturbing radiations in the main and compensating channels and their subsequent inter-channel subtraction [27]. Figure 1.21 shows a coherent compensator of clutter radiations.

As a result, compensation of perturbing radiations is ensured at the output of the adder of the CCPR device. From the point of view of the directivity pattern, this means that the resulting beam pattern forms a minimum in the direction of the source of perturbing radiations, which is shown in Fig. 1.22.

Due to quick movement of the main antenna beam due to its scanning and variations in both amplitude and phase of the required weighting coefficient, as well as the need for simultaneous compensation of signals from several interference sources, manual adjustment of the weighting factor ω in the CCPR device is impossible.

In this regard, the device of coherent compensation of clutter interferences shall ensure automatic adjustment of the weighting factor ω without participation of the operator, which is implemented in automatic compensators of clutter radiations.

Automatic compensator of perturbing radiations (ACPR) is a tracking gauge of the weighting factor ω, the operating principle of which is based in integration (smoothing) of the measurement error signal [24]. Automatic compensator is designed for suppression of active noise interferences received in side lobes of the beam pattern of the main antenna.

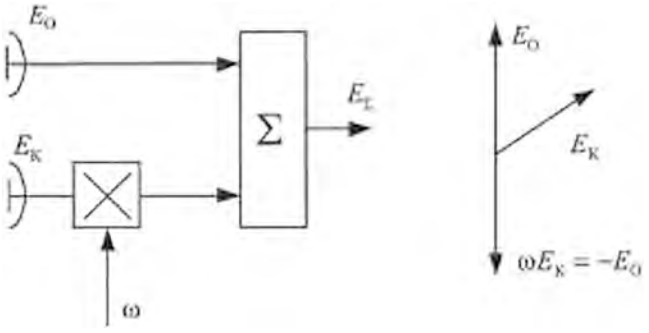

Fig. 1.21 Coherent compensator of clutter radiations
E_c is the complex amplitude of the interference signal in the compensating channel; E_m is the complex amplitude of the interference signal in the main channel; E_Σ is the complex amplitude of the interference signal at the output of the automatic compensator; ω is the complex weighting factor

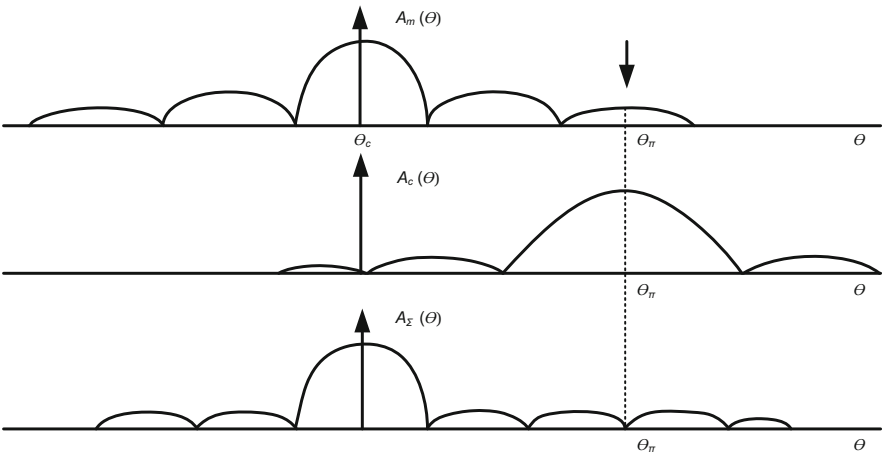

Fig. 1.22 Beam patterns
A_m (θ) is the beam pattern of the main antenna; A_c (θ) is the beam pattern of the compensating antenna: A_Σ (θ) is the directivity pattern at the output of the automatic compensator; θ_j ~ is the angular coordinate of the jammer

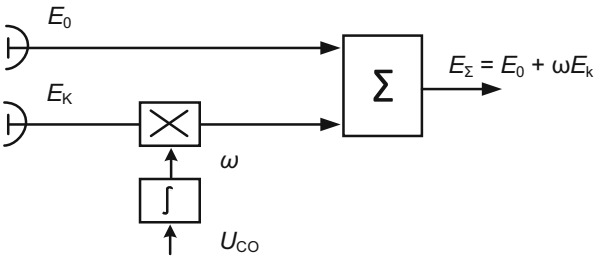

Fig. 1.23 Automatic compensator of clutter radiations

Generalized block diagram of the ACPR is shown in Fig. 1.23.

The error signal is the derivative of the processing device quality criterion in terms of the measured parameter [25]:

$$U_{\text{CO}} = \pm \frac{dF(\omega)}{d\omega}, \tag{1.13}$$

where $F(\omega)$ is the criteria of quality of the device operation.

The derivative $dF(\omega)/d\omega$ is taken with the "−" sign if the quality criterion needs to be minimized, and with the "+" sign if the quality criterion needs to be maximized.

Criterion of minimum output signal power $P_{out}(\omega)$ is used as a criterion of operation of the ACPR [11]:

$$F_{\text{АКМИ}}(\omega) = P_{\text{вых}}(\omega) = |E_\Sigma|^2 = E_\Sigma + E_\Sigma^* \tag{1.14}$$

Graphs explaining the operating principle of the tracking gauge of weighting factor ACPR are shown in Fig. 1.24.

The figures show that when an error signal is supplied to the integrator, the weighting factor is automatically tuned to its optimal value regardless of the magnitude and sign of de-tuning.

ACPR operation algorithm is determined by the operating algorithm of the discriminator of error signal of weighting factor measuring device [26]:

$$U_{CO} = \frac{dP_{\text{вых}}}{d\omega} = \frac{d|E_0 + \omega E_k|^2}{d\omega} = -2E_\Sigma \cdot E_k^* \tag{1.15}$$

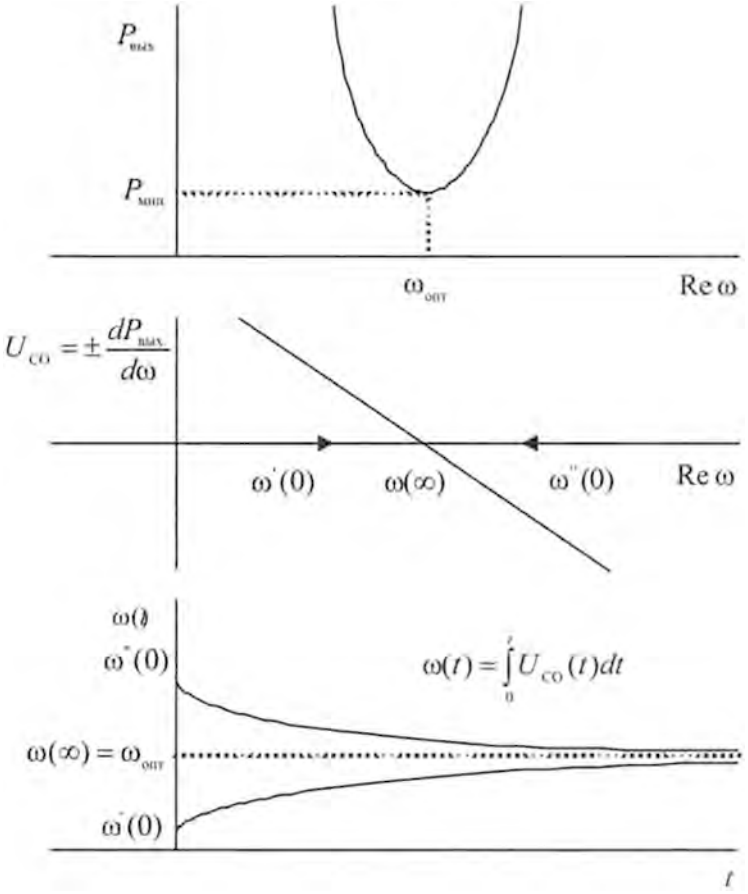

Fig. 1.24 Operating principle of a tracking measuring device of the weighting factor
P_{out} is the power of the output signal of automatic compensator; P_{min} is the minimum power of the output signal of automatic compensator at optimal value of the weighting factor ω_{opt}

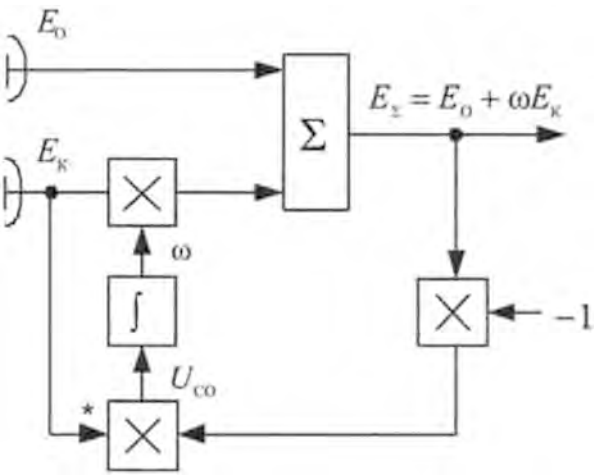

Fig. 1.25 ACPR with correlation feedback

Taking into account expression (1.15), ACPR operating algorithm can be explained with the help of Fig. 1.25. Signal of the error in measurement of the weighting factor in a particular case with the accuracy of up to an insignificant constant factor is equal to the derivative of the output signal power of the processing device in terms of the measured weighting factor and is implemented due to correlation feedback.

1.7.2 Features of Technical Implementation of the Design of Automatic Compensator of Perturbing Radiations

ACPR operating algorithm suggest multiplication of the received signal (its complex amplitude) by complex weighting factor [22, 23].

Depending on the method of implementing multiplication of the received signal by complex weighting factor, there are heterodyne and quadrature automatic compensator [29].

In a heterodyne ACPR, the multiplier is represented by the mixer, output signal of which is described by the expression:

$$U_{вых} = |U_{вх1}| \cdot |U_{вх2}| \cdot cos\left((\omega_1 - \omega_2)t + \varphi_1 + \varphi_2\right) \tag{1.16}$$

where $|U_{вх1}|$, ω_1, φ_1 are the amplitude, frequency and phase of the first input; $|U_{вх2}|$, ω_2, φ_2 are the amplitude, frequency and phase of the second mixer input.

It should be noted that the operation of multiplication of complex amplitudes of input signals in this case is also accompanied by transition to the intermediate (differential) frequency. Diagram of a heterodyne ACPR is shown in Fig. 1.26.

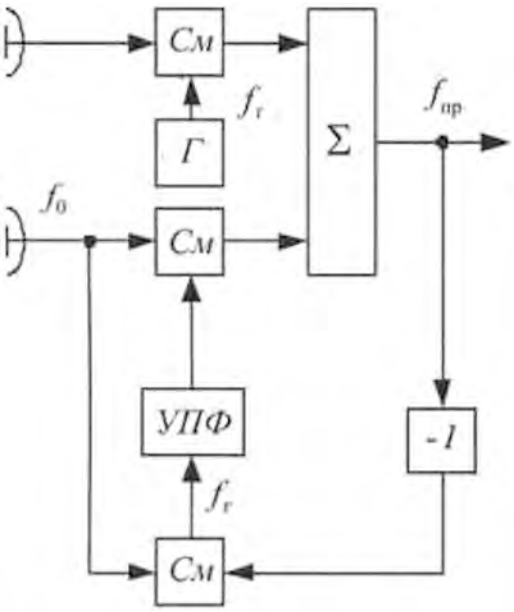

Fig. 1.26 Heterodyne ACPR
f_0 is the carrier frequency of the signal at the input of the automatic compensator, f_h is the carrier frequency of the heterodyne and the error signal, f_{out} is the carrier frequency of the output signal of the automatic compensator

In a heterodyne ACPR, the error signal is produced at the radio frequency (heterodyne frequency f_h); the role of integrator of the error signal is performed by the narrow-band filter (NBF); the role of multiplicator – by the mixer (M).

In a quadrature ACPR, multiplication by complex weighting factor is ensured by addition to different amplitudes of phase-shifted original oscillations. It is illustrated in Fig. 1.27.

Adjustment of the amplitude of original oscillations is performed in balanced amplifiers (BA), which ensure inversion of input signals in case of change in the polarity of control voltages. Diagram of a quadrature ACPR is shown in Fig. 1.28.

In quadrature ACPRs, multiplicators in circuits of correlation feedback processing are represented by phase detectors (PD), while formation of error signals and weighting factors is performed at the video frequency. The role of error signal integrators is performed either by RC chains or integrators on operational amplifiers [29].

Based on the type of the element base used, it is possible to identify analog (voltage and current can change continuously on it) and digital circuits (the signal can only perceive several different discrete states).

Based on the number of processing channels, single-channel and multi-channel compensators can be identified. Single-channel automatic compensator has one auxiliary channel and is capable of suppressing active interference acting from a single direction. In case of simultaneous effect of several interference sources from different directions in the radar detection area, multi-channel automatic compensators shall be used.

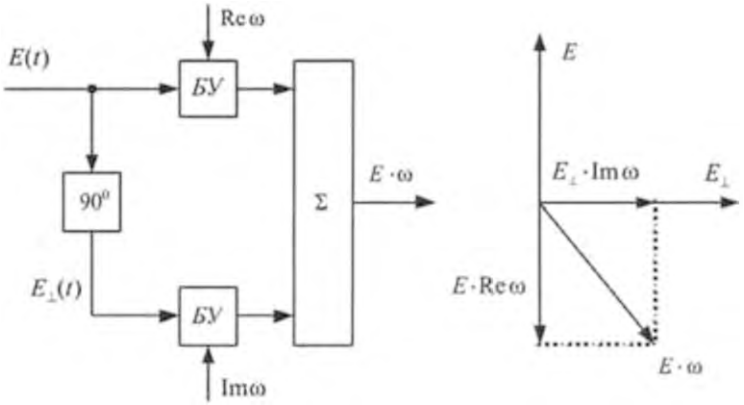

Fig. 1.27 Quadrature phase shifter

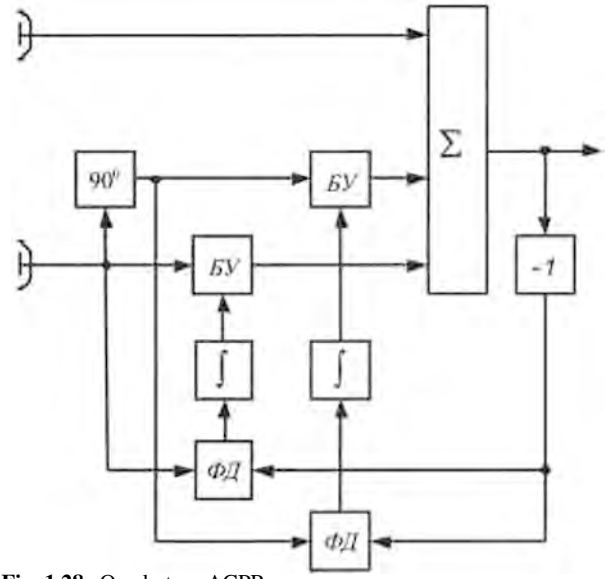

Fig. 1.28 Quadrature ACPR

Depending on the place of implementaiton of multipliers, automatic compensators at radio frequency, intermediate frequency and video frequency are distinguished. In automatic compensators at radio frequency, multiplication by complex weighting factors is performed directly at the frequency of received signals.

In automatic compensators at intermediate frequency, multiplication by complex weighting factors is performed after conversion of the received signals to the intermediate frequency.

In automatic compensators at video frequency, multiplication by complex weighting factors is performed after conversion of the received signals to the video frequency. Autocompensators at video frequency can be both analog and digital. Conversion of the received signals to video frequency suggest generation of two quadrature components (x, y) of each received signal characterizing real and imaginary parts of its complex amplitude.

Quadrature components are formed as a result of filtration in low pass filters (LPF) of the output signals of the pair of phase detectors (PD); heterodyne voltages at the frequency of received signals are supplied to second inputs. The second phase detector, which forms the imaginary part of the complex amplitude, receives the reference voltage with the phase shift of π/2, which is shown in Fig. 1.29 [2].

1.7.3 Assessment of Efficiency of Active Noise Interference Suppression

1.7.3.1 Effect of the End Radius of Spatial Field Correlation

The main problem in compensation of interference is the increase in efficiency. The main indicator of compensation efficiency is the potentially possible interference suppression coefficient.

Efficiency of an automatic compensator is the ratio of power of the interference power at the input of the compensator to the power of residual interference signal at the output of the compensator [27, 28]:

$$\upsilon_{\text{ми}} = \frac{|\bar{E_0}(t)|^2}{|E_0(t) + \bar{\omega} \cdot E_k(t)|^2}, \tag{1.17}$$

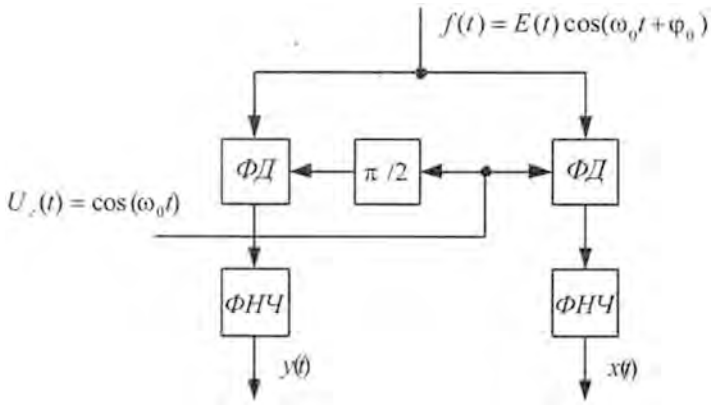

Fig. 1.29 Formation of quadrature components

where $E_m(t)$ is the complex amplitude of the main channel signal; $E_c(t)$ is the complex amplitude of the compensation channel.

Optimal value of the weighting factor ω_{opt}, at which the minimum power of perturbing radiations at the processing device output is ensured, can be obtained from the condition:

$$\frac{d|E_o + \bar{\omega}E_k|^2}{d\omega} = E_k^*(E_0 + \bar{\omega}E_k)_{\omega=\omega_{опт}} = 0 \tag{1.18}$$

From which:

$$\omega_{опт} = \frac{E_0\bar{E}_k^*}{E_k E_k^*} = -\frac{\sigma_0\sigma_k}{\sigma_k^2} re^{i\Delta\varphi} = \frac{\sigma_0}{\sigma_k} re^{i\Delta\varphi}, \tag{1.19}$$

where r – is the absolute value of the coefficient of inter-channel correlation of the PR signal; $\Delta\varphi = 2\pi\Delta R/\lambda$ is the inter-channel phasing constant of the PR signal; ΔR is the difference between the paths of interference signal received by the main and compensation channels; $\omega_m{}^2$, $\omega_c{}^2$ are the values of the PR signal power in the main and compensation channels respectively.

In this case, it can be demonstrated that the power of PR residues at the ACPR output taking into account self-tuning errors ($\omega = \omega_{opt} + \Delta\omega$) is described by the expression [24]:

$$\begin{aligned} |E_\Sigma(t)|^2 &= [E_0 + (\omega_{опт} + \Delta\bar{\omega})E_k]\bar{[}E_0 + (\omega_{опт} + \Delta\omega)E_k] \\ &= 2\sigma_0^2(1 - r^2) + 2\sigma_0^2|\Delta\omega|^2\frac{\sigma_k^2}{\sigma_0^2} = 2\sigma_0^2\left(1 - r^2 + \frac{\sigma_k^2}{\sigma_0^2}|\Delta\omega|^2\right), \end{aligned} \tag{1.20}$$

Taking into account the obtained expression for the power of PR residues, the following expression can be obtained for determining ACPR efficiency:

$$\upsilon_{ми} = \frac{|\bar{E}_o|^2}{|E_o + \bar{\omega}E_k|^2} = \frac{1}{1 - r^2 + \frac{\sigma_k^2}{\sigma_0^2|\Delta\omega|^2}} \approx \frac{1}{1 - r^2 + \left|\frac{\Delta\omega}{\omega_{опт}}\right|^2}. \tag{1.21}$$

Potential efficiency of the automatic compensator is observed in the absence of self-tuning of the weighting coefficient and described by the known expression [24]:

$$\upsilon_{ми\ макс} = \frac{1}{1 - r^2} \tag{1.22}$$

Potential efficiency depends only on the absolute value of the coefficient of inter-channel correlation of the interference signal. The closer the coefficient of inter-

channel correlation is to zero, the higher is the compensation efficiency. Interchannel correlation coefficient is determined by the following factors:

- end radius of the spatial correlation of the interference signal;
- influence of intrinsic noises of receipt channels;
- inter-channel temporal delay of the signal;
- non-linear distortions in processing paths;
- non-identity of frequency characteristics of receipt channels;
- effect of self-tuning errors of the automatic compensator.

In the following, effects of each of the above factors on efficiency are considered.

With regard to the component of ACPR efficiency defined by incomplete spatial correlation of perturbing radiations, the following should be noted. First of all, the interval of spatial correlation of the interference signal δI_{i} determined by the end dimensions of the jammer antenna and atmospheric turbulence, significantly exceeds the variation of main and compensating antennas. Moreover, when assessing this component, it is necessary to take into account that ACPR, being a tracking gauge of the weighting factor and having a relatively high operating speed, manages to track a significant share of fluctuations of the setting effect caused by incomplete spatial correlation of the interference signal. The effect of end radius of spatial correlation of the interference field is detailed in [13], the results of which demonstrate that with different approximations of spatial correlation function of the interference field, potential efficiency of compensation remains at least equal to 50 dB. Therefore, this component can be practically disregarded during analysis of potential efficiency of compensation in real conditions.

1.7.3.2 Effect of Intrinsic Noises of Receiving Channels

Component of CCPR efficiency determined by de-correlating effect of intrinsic noises of receipt channels [24]:

$$\nu_\gamma = \frac{1}{1 - r_\gamma^2} \approx \frac{\gamma_h}{2}, \tag{1.23}$$

where

$\gamma_h = \frac{\sigma_h^2}{\sigma_{h0}^2}$ is the ratio of the interference-uncorrelated background; $\sigma^2{}_h$, $\sigma^2{}_{h0}$ are the power values of interference and intrinsic noises respectively. The expression (1.23) means that in the absence of other de-correlating factors, almost complete suppression of the external interference is ensured, and only the sum of intrinsic noises of the main $\sigma^2{}_{\text{h00}}$ and compensating $\sigma^2{}_{\text{h01}}$ channels remains at the output of the automatic compensator:

$$P_{\text{вых}} = \sigma_{h00}^2 + \sigma_{h01}^2 = 2\sigma_{h0}^2, \tag{1.24}$$

$$\nu_\gamma = \frac{\sigma_h^2 + \sigma_{h0}^2}{2\sigma_{h0}^2} \approx \frac{\sigma_h^2}{2\sigma_{h0}^2} = \frac{\gamma_h}{2}. \tag{1.25}$$

The expression (1.25) is obtained based on suggestion that the level of intrinsic noises of the main and compensation channels at the adder input is equal. Therefore, in the absence of self-tuning error of the weighting coefficient, intrinsic noises will not affect suppression of an external correlated interference; however, signal-to-noise ratio at the automatic compensator output is reduced due to addition of intrinsic noises of the additional (compensation) receipt channel. It should be noted that intrinsic noises affect fluctuation self-tuning errors of the weighting coefficient due to non-compensated part of the output ACPR signal.

In practice, intrinsic noises of receiving channels limit efficiency at the level of 60–70 dB [31].

1.7.3.3 Effect of Delay of Received Signals

Partial CCPR efficiency caused by temporal delay of the PR signal is determined by the expression:

$$\nu_\tau = \frac{1}{1 - r_H^2\left(\frac{\Delta R}{c}\right)}, \tag{1.26}$$

where $r_{\text{H}}(\tau)$ is the specified correlation function of time fluctuation of the PR signal; ΔR is the difference of electrical lengths of the main and compensating receipt channels.

As a rule, width of the energy spectrum of the CR signal exceeds the pass band of receiving devices. In this case, specified correlation function of the CR signal at the output of the processing channel is determined as the amplitude-frequency characteristic (AFC) of the processing channel.

For single resonant circuit, it is possible to obtain [25]:

$$r_H(\Delta\tau) = \exp\left(-\frac{|\Delta\tau|}{\tau_{\text{п}}}\right) = \exp\left(-2\Delta f_{np}|\Delta\tau|\right) \approx 1 - 4\Delta f_{np}|\Delta\tau|, \tag{1.27}$$

where Δf_{r} is the pass band of the receiver.

Partial CCPR efficiency:

$$\nu_\tau = \frac{1}{1 - r_H^2(\Delta\tau)} = \frac{1}{1 - \exp\left(-4\Delta f_{np}|\Delta\tau|\right)} \approx \frac{1}{4\Delta f_{np}|\Delta\tau|}. \tag{1.28}$$

For a channel with Gaussian frequency characteristic (number of resonance circuits connected in series approaches infinity) [26]:

$$r_H(\Delta\tau) = \exp\left(-\frac{\pi\Delta\tau^2}{4\tau_{\text{п}}}\right) \approx 1 - \frac{\pi\Delta\tau^2}{4\tau_{\text{п}}^2} = 1 - \pi\left(\Delta f_{np}\Delta\tau\right)^2, \tag{1.29}$$

$$\nu_\tau = \frac{1}{2\pi}\left(\frac{1}{\Delta f_{np}\Delta\tau}\right)^2. \tag{1.30}$$

For channel with rectangular frequency characteristic [26]:

$$r_H(\Delta\tau) = \frac{\sin\left(\frac{\pi\Delta\tau}{2\tau_{\text{п}}}\right)}{\left(\frac{\pi\Delta\tau}{2\tau_{\text{п}}}\right)} \approx 1 - \left(\frac{\pi}{2}\right)^2\frac{\Delta\tau^2}{6\tau_{\text{п}}^2} = 1 - \frac{\pi^2}{6}\left(\Delta f_{np}\Delta\tau\right)^2, \tag{1.31}$$

$$\nu_\tau = \frac{3}{\pi^2}\left(\frac{1}{\Delta f_{np}\Delta\tau}\right)^2. \tag{1.32}$$

Therefore, with an increase in rectangularity of frequency characteristics of receiving channel, critical importance of operation of the automatic compensator of perturbing radiations to the difference of electrical lengths of receipt channels is reduced, which is explained by the smaller contribution of the off-frequency radiation to the total signal power.

1.7.3.4 Effect of Non-linear Distortions

Specific efficiency of compensation defined by non-linear distortions is determined by the expression [26]:

$$\nu_{\text{нэ}} = \frac{1}{1 - r_{\text{нэ}}^2}, \tag{1.33}$$

The process of determining temporal correlation of signals at outputs of non-linear channels is lengthy and complex. Results of calculation of the Gaussian interference passage through channels with limitation can be used as an example. Calculation results [32] demonstrate that achievement of partial efficiency of automatic compensation $\nu_{\text{пе}}$ of more than 25÷30 dB suggest provision of dynamic range reserve of the receiver: limitation level shall exceed maximum effective values of the interference at least 3 times (10 dB). In order to meet this requirement, each receipt channel shall include the circuit of automatic gain adjustment, which prevents the

signal from exceeding the level of limitation and reserve of the bit grid of the analog-to-digital converter (ADC). Modern element base makes it possible to obtian partial compensation efficiency v_{ne} at the level of 45÷55 dB [30, 31].

1.7.3.5 Effect of Mismatch of Frequency Channel Characteristics

Effect of mismatches of frequency characteristics on compensation efficiency is described in [24, 25]. The main effect of mismatches of frequency characteristics consists in reducing the coefficient of interchannel interference correlation.

With Gaussian frequency characteristics and small de-tuning values, it is possible to obtain [26]:

$$\frac{1}{\nu_{\text{нчх}}} = \frac{1}{\nu_{\xi}} + \frac{1}{\nu_{\eta}} + \frac{1}{\nu_{\sigma a}} + \frac{1}{\nu_{\sigma\varphi}}, \tag{1.34}$$

where $\nu_{\eta} = 2\left(\frac{\Delta f_{np}}{\delta f_{np}}\right)^2$ is the partial efficiency of the automatic compensator defined by de-tuning of the pass bands of receipt channels; Δf_r is the pass band width of the main receipt channel; δf_r is the de-tuning of pass bands of the receipt channels; $\nu_{\xi} = 2\left(\frac{\Delta f_{np}}{\delta f_0}\right)^2$ is the specific efficiency of the automatic compensator caused by de-tuning of central frequencies if receipt channels; δf_0 is the de-tuning of central frequencies of receipt channels; $\nu_{\sigma a} = \frac{1}{2\sigma_a^2}$ is the partial efficiency of the automatic compensator caused by irregular AFC distortions of receipt channels; $\sigma^2{}_a$ is the dispersion of random AFC deviations; $\nu_{\sigma\varphi} = \frac{1}{2\sigma_{\varphi}^2}$ is the partial efficiency of the automatic compensator defined by irregular AFC deviations of receipt channels; $\sigma^2{}_{\varphi}$ is the dispersion of random AFC distortions.

Mismatches of frequency characteristics of receiving channels often contribute the most to reduction of compensation efficiency [31]. For example, in order to obtain efficiency of suppression of interferences of at least 30 dB, relative de-tuning of parameters of the frequency characteristics of receipt channel shall not exceed at least 3%, which is a fairly strict requirement in practice, especially with significant width of the pass band of channels [27].

1.7.3.6 Effect of Self-tuning Errors

Efficiency of ACPR operation depends on self-tuning errors. In real conditions, efficiency will be reduced due to the effect of self-tuning errors of the weighting coefficient [24]:

$$\nu_{\text{ми}} = \frac{1}{1 - r^2 + \left|\frac{\Delta w}{w}\right|^2} \tag{1.35}$$

or

$$\frac{1}{\nu_{\text{ми}}} = \frac{1}{\nu_{\text{ми}_{\text{мах}}}} + \frac{1}{\nu_{\Delta\text{w}}}, \tag{1.36}$$

where $\nu_{\Delta\text{w}} = \left|\frac{w}{\Delta w}\right|^2$ is the partial ACPR efficiency caused by self-tuning errors of the weighting factor; w, Δw are the absoulte values of the weighting factor and the errors of its calculation respectively.

Self-tuning errors contain three main components [26]: transitional period errors, dynamic tracking errors and fluctuation errors.

Dynamic errors are caused by variations of the setting action of the automatic compensator and its limited speed of operation. Fluctuation errors are caused by perturbing effect of residues of the interference compensation. Errors of the transient process are caused by initial conditions and limited speed of operation of the automatic compensator. After completion of transient processes in the established mode, only dynamic and fluctuation errors are observed.

Dispersions of the measurement error of weighting factor:

$$\sigma^2_{\text{фл w}} = \left(1 - r^2\right)|w|^2 \frac{\Delta f_{\text{w}}}{2\Delta f_{\text{ш}}} = \left(1 - r^2\right) \frac{|w|^2}{4\Delta f_{\text{ш}} T_{\text{экв}}} = \frac{1}{\nu_{\text{ми}}} \frac{|w|^2}{4\Delta f_{\text{ш}} T_{\text{экв}}}, \tag{1.37}$$

where r is the coefficient of inter-channel correlation of the PR signal; $\Delta f_w = \frac{1}{2\pi} \int\limits_{-\infty}^{\infty} K_0^2(\omega) d\omega$ is the effective pass band width of the closed-loop weighting factor measuring device; Δf_{w} is the width of the energy spectrum of the perturbing effect; T_{eq} is the equivalent time constant of the weighting factor measuring device.

In order to minimize dynamic errors of ACPR self-tuning, self-tuning systems with second order of astatism can be used in radars with quick scanning [25]. Selection of self-tuning circuits shall ensure minimization of accumulated filtration errors.

References

1. Белоус, А. И., Мерданов, М. К., & Шведов, С. В. (2018). СВЧ-электроника в системах радтолокации и связи. Техническая энциклопедия в 2-х книгах. Книга 1, Москва, Техносфера, 817 с.
2. Belous, A., Merdanov, M., & Shvedov, S. (2018). *Microwave electronics in radar and communication systems* (Technical Encyclopedia in 2 volumes, 2nd ed., revised, 1520 p). Moscow: Tekhnosfera.
3. Dave, H., & Philip, G. (2008, July). *Multi-static primary surveillance radar – An examination of alternative frequency bands*. Roke Manor Research Limited. Report № 72/07/R/376/U. July, 2008. Issue 1.2 (p. 186).
4. Kaczur, M. (2010). Passive coherent location. Brno.
5. Radioengineering, B. P. (2008). Vol. 17, № 3, 53–59.

6. Zubkov, A. (2010, February 23–27). *Information aspects of multispectral active-passive radio monitoring system*. TCSET'2010 (pp. 96–97). Ukraine: Lviv-Slavske.
7. Special Report. (2011). *Iran tests passive radar in aerial drill. [Electronic resource]*. Mode of access: http://English.news.cn. Date of access: 05.01.2012.
8. Savenko, S. A. (2000). *Theory and technology of combined adaptive processing of signals in surveillance active-passive radar systems*. Minsk.
9. Ohrimenko, A. E. (1983). *Radiolocation basics and radar electronics warfare* (Radiolocation Basics, p. 1). Moscow.
10. Ohrimenko, A. E. (1990). *Basics of information processing and transmission*. Minsk.
11. Shirman, Y. D., Bagdasaryan, S. T., Gorshkov, S. A., et al. (2007). *Radar electronic systems: Building basics and theory. Reference book*. Moscow.
12. Peretyagin, I. V., & Polukhin, I. F. (2006). *Collection of reports of the international science and technology conference "radiolocation, navigation, communicatio"* (p. 2, 10). Voronezh.
13. Dmitrienko, A. A., Sedyshev, S. Y., & Gorshkov, S. A. (2012). *Collection of Scientific Works of the SE "Research Institute of the Belarusian Armed Forces"* (pp. 104–109, No.1 (1)).
14. Dmitrenko, A. A. (2012). *Comparative analysis of methods for constructing complexes for passive location*. Dissertation of the Master of Technical Sciences. Minsk.
15. Dmitrienko, A. A., Sedyshev, S. Y., & Gorshkov, S. A. *Device for quick observation based on delay time differences in base-correlation complexes of passive location*. RB Patent No. 9543.
16. Dmitrenko, A. A., & Sedyshev, S. Y. (2014). *PSU Bulletin*. No. 4. Series S. Fundamental Sciences.
17. Dmitrienko, A. A., Sedyshev, S. Y., & Gorshkov, S. A.. *Device for determination of angular coordinate of radio frequency source in correlation-base passive location complexes*. RB Patent No. 9864.
18. Solonar, A. S., Yarmolik, S. N., Khramenkov, A. S., Mikhalkovskiy, A. A., & Khmarskiy, P. A. (2014). *Construction set of objects of the software complex of radiolocation signal modeling*. *BSUIR Reports, 6*, 60–66.
19. Ohrimenko, A. (1983). *Radiolocation basics and radar electronics warfare* (Radiolocation Basics, p. 1). Moscow.
20. Sukharevskiy, O. I. (2009). *Dispersion of electromagnetic waves by air and ground radar objects*.
21. Leonov, A. I., & Vasenev, V. I., & Goydukov, Y. I. (1979). *Modeling in radar location*. Moscow.
22. Gorbatenko, S. A., Maksimov, E. M., & Polushkin, Y. F. (1969). *Flight mechanics. General information. Movement equations* (Engineering Reference Book). Moscow.
23. Sidorevich, A. N., & Davydenko, I. N. (2015). *Problems of spatial compensation of clutter radiations* (Electronics-Info, No. 3, pp. 30–36). Minsk.
24. Monzingo, R. A. (1986). *Adaptive antenna arrays* (R. A. Monzingo & T. U. Miller, Eds., 448 p). Moscow: Radio and Communication.
25. Losev, Y. I., et al. (1998). *Adaptive compensation of interferences in communication channels* (Y. I. Losev, Ed., 208 p). Moscow: Radio and Communication.
26. Pistolkors, A. A. (1991). *Introduction to the theory of adaptive antennas* (A. A. Pistolkors & O. S. Litvinov, Eds., 200 p). Moscow: Science.
27. Shirman, Y. D. (1981). *Theory and technology of processing of radiolocation information against interference background* (Y. D. Shirman, Ed., 416 p). Moscow: Radio and Communication, .
28. Gonorovskiy, I. S. (1986). *Radiotechnical circuits and signals: Study book for higher educational institutions* (I. S. Gonorovskiy, Ed., 4th ed, Revised and Expanded, 512 p). Moscow: Radio and Communication.
29. Baskakov, V. I. (2000). *Radiotechnical circuits and signals* (V. I. Baskakov, Ed., 3rd ed., 462 p). Moscow: High School.

30. Chernyak, V. S. (1987). Multi-position detectors of fluctuating signals against the background of spatial correlated interferences (V. S. Chernyak, Ed.). *Radiotechnics and Electronics*, *32*(2), 334–346.
31. Efimenko, V. S. (2002). Potential characteristics of adaptation of space-time processing for SRNS (V. S. Efimenko & V. N. Kharisov, Eds.). *Radiotechnics*, *7,* 82–87.
32. Marchuk, L. A. (1995). *Potential efficiency of adaptive spatial processing in the presence of non-linearities* (L. A. Marchuk, News of Higher Educational Institutions. Radioelectronics, No. 10, pp. 46–52).

Further Reading

33. Grishin, Y. P., Ipatov, V. P., et al. (1990). *Radio systems* (Y. M. Kazarinov, Ed.) (Study Book, 496 p). Moscow: High School.
34. Gryanik, V. N., & Pavlikov, S. N. G. (2009). *Theory and technology of radar location and navigation* (Teaching Materials, 132 p). Vladivostok: VSUES.
35. Gulshin, V. A. (2006). *Book of radiolocation problems* (60 p). Ulyanovsk: UlSTU.
36. Demidenko, P. P. (2004). *Vessel navigation radiolocation stations* (163 p). Odessa: Study Book.
37. Dudnik, P. I., Ilchuk, A. R., & Tatarskiy, B. G (2007). *Multi-functional radar systems* (283 p). Moscow: Drofa.
38. Eroshenkov, M. G. (2004). *Radiolocation monitoring* (452 p). Moscow: MAX Press.
39. Zaytsev, D. V. (2007). *Multi-position radiolocation systems. Methods and algorithms of information processing in conditions of interference* (114 p). Moscow: Radiotechnics.
40. Kanaschenkov, A. I., & Merkulov, V. I. (2003). *Aviation systems of radio control* (in 3 volumes). Publishing: Radiotechnics.
41. No Author, K. (2011). *Kolchuga – Best Compex of Radio-Technical Surveillance in the World*.
42. Kondratenkov, G. S., & Frolov, A. Y. (2005). *Radiovision. Radar systems of Earth's remote sensing* (G. S. Kondratenkov, Ed., 368 p).Moscow: Radiotechnics.
43. Perunov, Y. M., Matsukevich, V. V., & Vasliyev, A. A. (2010). *Foreign radioelectronic means*. In 4 volumes. Moscow: Radiotechnics.
44. History of Russian Radar Aircraft Technology / Ed. by Director of the Department of Radioelectronic Industry of the Ministry of Industry and Trade of the Russian Federation S.V. Khokhlov. (2015). Moscow: LLC "Capital Encyclopedia Publishing House" (400 p).

Chapter 2
Features of Designing Digital Processing Systems for Radiolocation Systems Based on Microprocessor VLSI Sets

2.1 Features of Designing DSP Systems

The use of methods of digital signal processing (DSP) makes it possible to relatively easy ensure high noise immunity of data processing systems, necessary accuracy and resolution, interface of the data processing subsystem with the control computer, stability of data processing path parameters and a number of other advantages. Therefore, over the last 30–35 years DSP processors have, in one form or another, become an integral part of computing complexes designed to solve the tasks of information processing and control in various radar systems and devices [1–24].

The trend towards paralleling of calculations observed in digital computing equipment in recent years is associated with continuous growth of requirements towards performance of computing means of radar systems. The best data processing methods for microelectronic implementation are the methods known under the common name of systolic [16, 22, 24]. These methods are oriented on parallel-pipeline performance of the most labor-consuming computing operations and make it possible to effectively implement a wide class of computing algorithms and tasks by ensuring limit performance of computing device for this level of technology and maximum density of circuit package. Several hundred thousand types of microcircuits implementing the systolic data processing principle are currently developed and produced abroad; however, they are mostly field-specific devices, which limits the possibilities of their use.

Practical aspects of development of the element base for parallel-pipeline DSP systems include a wide range of problems, such as:

1. Determination of the list of basic operations that shall be implemented in VLSIs.
2. Development and selection of the algorithms of performance of basic operations and the corresponding structures of processor elements.
3. Identification of the possible structures of systolic networks, the implementation of which shall be ensured by the created element base and the selection of the

© The Editor(s) (if applicable) and The Author(s), under exclusive license to Springer Nature Switzerland AG 2021

A. Belous, *Handbook of Microwave and Radar Engineering*,
https://doi.org/10.1007/978-3-030-58699-7_2

corresponding protocols of data exchange between PE within the structure and between the structure and external devices.
4. Selection of formats of data presentation during their input, output and processing.
5. Development of the problems of data presentation accuracy, scaling and data normalization for the purpose of eliminating possible overfills during performance of fixed point operations.

When solving these problems, it is necessary to take into account the specifics of the identified field of application of the created DPS system. The main criterion for selection of certain solutions is the level of performance achieved by the data processing system or its separate unit implemented on the basis of the given technology. This parameter is closely connected to the efficiency of use of hardware resources, i.e. the relation of the accumulated time during which system unit or node performs useful function of data processing to the accumulated time during which this unit or node remains idle, waiting for the moment of receipt of input data or the moment when it will be possible to supply the result of the operation to the next processing unit.

Performance of the system, its overall dimensions and power consumption are closely connected to the required computing accuracy, which is defined by the formats of data used, range of frequencies of input signals, volumes of processed information and types of used algorithms.

Let us consider certain most characteristic ***fields of application of DSP methods from this point of view*** [2].

1. ***Processing of sound signals***, including analysis, recognition and synthesis of speech, telecommunications and data compression during their transmission via communication channels. In most cases, satisfactory results are provided by the data format with fixed point and the word length of 32 bits. In the event of higher requirements for processing quality, transition to 64-bit format with floating point is possible. The range of input signal frequencies for the tasks of speech processing is only 100 Hz – 4 kHz, and the selected sampling rate in many cases is around 8 kHz. During processing and transmission of sound signals in general, including music, the upper limit of frequency range is extended to 20–40 kHz. Sampling rate in such cases reaches 112 kHz and more. The applied algorithms include digital filtration, spectral signal analysis (calculation of fast (FFT) or discrete (DFT) Fourier transforms), correlation analysis, reverse convolution, as well as special algorithms like linear prediction, dynamic programming for the tasks of recognition, etc. [25–28]. If block algorithms of data processing are implemented, each block includes 128–256 samples. Minimum performance in the tasks of sound signal processing can reach $6 \cdot 10^5$–$6 \cdot 10^6$ multiplications per second, which suggests development of parallel structures based on special element base.
2. ***Image processing***. The goals of image processing are enhancement of images containing noise, compression of information for transmission and storage and sample recognition. Recovery and improvement of images is performed by

filtration with the help of inverse convolution. Since the sizes of the processed data in this case are farily big (typical values: 256x256 samples, 512x512 samples), FFT algorithms are widely used for the tasks of linear image filtration. During image processing, algorithms of filtration, calculation of convolution and FFT are two-dimensional. An important class of tasks associated with recovery and enhancement of images arises during analysis of objects of various nature by penetrating radiation methods. Recovery of the 3D structure of an object based on its projection is performed by calculation of ***Fourier transforms*** from projections, formation of the set of object sections and calculation of inverse Fourier transform. Enhancement of such images is performed by spatial frequency filtering methods. Another class of algorithms of image enhancement is formed by point operations, such as contrast conversion, outlining and methods of statistical image processing.

Various transforms are used for data compression during transmission and storage of images. The most statistically effective method is the ***Karhunen-Loeve transform***; however, it requires large volumes of calculation operations and has no quick performance algorithms. Unlike Karhunen–Loève transform, orthogonal transforms like ***Fourier, Hadamard and Walsh transform*** allow quick implementation and ensure sufficiently effective compression of original images, which is the reason behind their wide popularity for solving such tasks.

The tasks of pattern recognition for image processing are solved by the same methods as speech recongition, but data array volumes in this case increase to 10^5–10^6 counts. Data capacity is typically low – 16 or even 4–8 bits. Required performance is estimated by values of at least 10^9–10^{12} and is ensured in real time scale only with the help of parallel-pipeline methods.

3. ***Radar systems*** perform search and detection of objects in space, determination of coordinates and dynamic parameters of these objects and their classification. Decisions are made and the corresponding complexes are controlled based on the obtained data. The main content of data processing in a radar is matched filtration of signals received from the antenna sensor. The frequency range of input signals is 10 MHz – 10 GHz. In many cases filtration is performed in the frequency domain based on FFT algorithms. Conversion sizes can reach 2^{14} complex dots; however, there are tasks in which data arrays have moderate dimensions of 1024, 512 dots and less. In systems with phased antenna arrays, directivity pattern is formed with the help of the scalar vector product operation (sometimes referred to as weighting addition). The capacity of input data is currently 6–8 bits; however, there is a trend towards its increase to 10–12 bits and more. Requirements for the speed are around 10^8–10^9 multiplications per second.
4. ***Hydrospace detection*** tasks mostly include the same operations as the tasks of radiolocation, i.e. generation of the directivity pattern, spectral analysis, correlation analysis and convolution, secondary processing of signals for data output to display devices and control tasks. Therefore, used algorithms include scalar product of real and complex vectors, one-dimensional direct FFTs and reverse FFTs, two-dimensional (space-time) FFTs, calculation of correlation functions,

one-dimensional and two-dimensional convolutions and matrix operations, including matrix multiplication and inversion and solving systems of linear equations. Hydroacoustic signals are characterized by their lower frequency range (2–40 kHz). On the other hand, high noise level in these signals requires building of multi-channel AA systems; therefore, the volume of computing operations in modern hydrolocation systems has the same order as in radar sets (10^6–10^8 operations per second). Sizes of data arrays during block processing are relatively small (2^6–2^{10}), but the number of parallel channels reaches 2^6–2^7. The used data representation includes samples with fixed point with the length of 12–16 bits in primary processing devices and data with floating point in the 16-bit format for algorithms of FFT, correlation and convolution and 32 bits for matrix operations. In the latter case, performance requirements are much lower and amount to 10^3–10^5 operations per second.

Analysis of the above requirements for functional possibilities of DSP equipment, data formats and performance allows us to identify the following basic matters that are frequently found and the implementation of which is necessary during the first stage of works [29].

Applied algorithms: filtration, convolution calculation, FFT. Data formats: 8-bit and 16-bit fixed point formats. Performance – 10^8–10^{10} addition-subtraction operations per second.

Microcircuits of K588, K1800 and K1802 series were among the first Soviet microprocessor kits used to solve practical DSP tasks, which is due to the presence of first Russian specialized multiplier LSICs in these kits. These multipliers made it possible to design specialized DSP processors with acceptable parameters, in which operations were performed mostly in sequence. Accordingly, the speed of these processors was relatively low, which limited the range of the processed signals by low frequency regions exclusively (acoustic signal processing). *Building of parallel systems based on such components was associated with great difficulties of implementing the necessary number of links between elements of a parallel system (since data input, output and processing are performed in the parallel code).* Moreover, the effectiveness of using hardware resources in such systems was extremely low due to principal impossibility to ensure continuous performance of useful functions by all elements of the system typical of von Neumann type machines.

The possibility of increasing speed occurred due to transition to parallel and conveyor methods of data processing. This approach was used in [29] to built the processor element of specialized FFT computers. The same paper contains timing diagram of operation of this PE during performance of basic FFT operation, which shows that the main hardware resources of the processor element (multiplier and adder) mostly remain idle. For example, the multiplier operates only during 4 out of 10 clock cycles; the load on the adder is even smaller. All this indicates that the element base shall be optimized to solve task of a specific problem field, in this case – the DSP field. The main optimization criterion shall be the increase in the load on hardware resources on chip. In this case, specialization will allow to increase the

speed of operation of DSP systems and reduce hardware costs of their implementation several tasks, which is especially relevant for parallel systems.

This chapter presents the results of the first actual national specialized element base for parallel-pipeline DSP systems, which made it possible to practically solve issues of effective implementation of such systems with acceptable parameters in terms of overall dimensions and power consumption.

2.2 Effect of Microelectronic Technologies on the Structure of Computing Systems of Radars

Technology of production of the electronic component base (ECB) of computing systems determines their main technical characteristics: speed, overall dimensions, power consumption, functional possibilities and, ultimately, architecture of the designed architectural systems of various purposes. On the one hand, the constant growth of requirements to technical and economic characteristic of modern equipment calls for improvement of the known algorithms and structures of calculation systems and development of new ones. In turn, new architectural solutions stimulate development of works in the field of creating a corresponding microelectronic element base. The problems of selection of the element base for creation of modern DSP systems have great scientific and practical importance; high requirements for performance of these systems can only be provided with non-traditional parallel methods and means of data processing. The achieved progress and rates of development of the VLSI technology are widely known. On the other hand, the possibilities of microelectronic element base of modern computing and control devices by ensuring effective implementation of traditional computing structures (single-processor machines with von Neumann architecture) inversely affect principles of organization of digital devices and methods (algorithms) of data processing in these devices. This influence is manifested in activation of works in the field of searching for new architectural solutions of data processing systems and new methods of organization of parallel calculations allowing for maximum use of all possibilities of the modern microelectronic technology. Let us consider the main aspects of this mutual influence manifested both during early stages of VLSI design and during the stages of production and debugging of VLSI-based computing systems.

In general case, it is believed that effectiveness of a certain VLSI-based system is determined, first of all, by the cost of this system compared to the importance of tasks solved by this system. Total cost of the system C_S consists of the cost of its development C_d, cost of its production C_p and operation C_l: $C_S = C_d + C_p + C_l$.

Production C_p and operation C_l costs of a system are insignificantly related to the structure of the computing system. The main factors influencing C_p, C_l include size of the crystal, used technology, percentage yield and reliability of microcircuits.

Let us consider the main factors influencing C_d in detail. Development of microcircuits, despite the great progress achieved in this field, is still a very labor-

consuming procedure. This labor intensity required is primarily determined by the cost of the integral system, i.e. the number of its elements (LSIC integration degree) that increases constantly as the technology is improved. The cost of designing a system of n elements in general case is determined by the relation [29]:

$$C_{\boldsymbol{d}} = kn, \tag{2.1}$$

where k is the proportionality factor, which corresponds to the labor costs of placing one element (transistor) on the LSIC chip. Values k and $C_{\boldsymbol{d}}$ are usually measured in man-hours, man-days, etc. Implementation of systems containing several dozen or hundred thousand transistors on LSIC chip suggest corresponding arrangement of each of these transistors on the chip, determination of electrical modes of operation of this transistor and its links to other LSIC elements. In terms of integration degree, which exceeds 10^4 transistors on chip, this task is beyond psychophysiological abilities of a human developer. The value C_d for modern microprocessors is expressed in several hundreds of man-years. The use of CAD systems helps reduce the time and increase the quality of LSIC design. The review of the main principles of organization and architecture of systems in which these LSIC are used helps generally reduce the production cycle. The essence of the method that allows to sharply reduce the cost and terms of designing VLSI consists in using uniform computing structures including small numbers of basic types of elementary modules connected by means of short and regular links. This approach makes it possible to develop one or several basic functional modules and multiply them for formation of the system implementing the necessary function. The cost of design in this case is reduced dramatically and depends on the number of module types, dimensions of these modules and their total quantity. For example, if N elements of the system consist of l identical modules with $n_{\mathbf{l}} = N/\mathrm{l}$ elements each, the expression (2.1) takes the following form:

$$C_{\boldsymbol{d}} = kn_{\mathrm{l}} + kl. \tag{2.2}$$

Here, it is assumed that the labor costs of placing the element inside the module and placing the module on the crystal are equal. It follows from the expression (2.2) that at fixed N, there is a certain optimal size $n_{\mathbf{l}}$ of modules forming the system, as well as their optimal number 1 at which the value $C_{\boldsymbol{d}}$ is minimal: $1 = n_1 = \sqrt{N}$. Figure 2.1 shows the dependence of $C_{\boldsymbol{d}}$ (1) at fixed N.

If the system contains t various types of functional modules, the expression for evaluation of the design cost $C_{\boldsymbol{d}}$ takes the following form:

$$C_d = \sum_{i=1}^{t} k_i n_i + \sum_{i+1}^{t} k_i l_i, \tag{2.3}$$

where $n_{\boldsymbol{i}} = \mathrm{N}_{\boldsymbol{i}}/l_{\boldsymbol{i}}$ – the number of elements in one module of the ith type; $l_{\boldsymbol{i}}$ – the number of modules of the ith type; $\sum N_i = N$. In this case, it is also possible to build

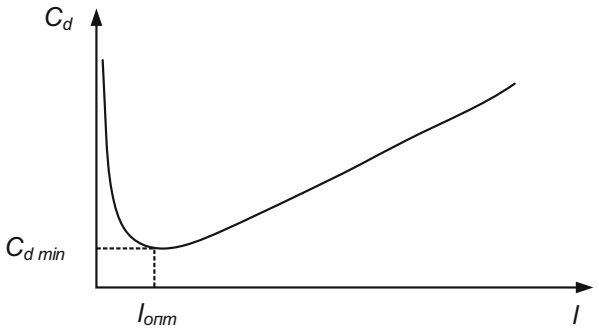

Fig. 2.1 Development of the cost of development Q on the number of identical functional modules in the system [2]

the dependence of C_d on the number of modules in the system; however, such dependence is multi-dimensional and therefore more difficult to analyze. For example, $t = 2$ function $C_d(l_1, l_2)$ will be set by certain surface in 3D space. Expressions (2.2), (2.3) can be used to build optimal strategy of system design, for which $N(N_i)$ and values of k_i coefficients are known.

During the stage of production and operation, modularity and regularity of a computing system structure make it possible to easily adapt it for effective solving of tasks processing varied data volumes with different speeds. This means that the cost of such system can be made proportional to the required performance, and that this cost can be distributed between multiple consumers solving various tasks, which will further increase economical efficiency of development, since the end cost of the product will be lower.

An important aspect of the influence of microelectronic technology on the architecture of calculation systems is the fact that the traditional approach to estimation of efficiency of a certain computing system based on taking into account only the number of active components in this system (transistors, logic elements, etc.) will no longer reflect the real state of things after transition to VLSI. Several analytical qualitative models of VLSIs are known that are used for evaluation of efficiency of various architectural solutions in case of their implementation on chip, and comparisons between these solutions [2, 3] *and all these models take into account geometrical, dynamical and other parameters of both active elements and links between them.*

For example, LSIC model suggested in 1972 by Thompson [2] contained the following basic provisions:

1. The width of any link on a chip is equal to one.
2. At least two links can intersect in any point of a chip.
3. The area of an active transistor element is equal to one. A link cannot pass through an active element region, and an active element cannot be located in the region of the link.
4. Each link ensures transfer of one bit of information per unit of time equal to the time of switching of an active component.
5. The delay in link switching is negligible.

6. N input variables are supplied to system inputs, each of which can take one of M various values. Total number of equally possible combinations of input variable values is M^N.
7. The value of N is an integer power of 2.
8. Values of input variables are presented by words with the length of $\log_2 M$ bits. Standard binary codes are used: direct, reverse, additional, etc.
9. Each input variable is supplied to the system input and recorded in the input register only once at the beginning of each calculation cycle. Each input variable is supplied only to one input register.
10. Cycle time T of the system consisting of a set of active elements and link is determined by the minimum possible value of time intervals between supply of two sequential sets of input data to system inputs for performance of two sequential cycles of calculations and supply of two sets of output results to the outputs.

This model and similar models are still widely used to obtain asymptomic assessments of parameters of various architectural solutions based on the possible area A_S of the chip required for their implementation and the suggested speed T_S that can be ensured by this structural solution [29]. It is clear that the results of assessment of the chip area A_S obtained on the basis of such models will depend on the number and size of active elements as much as on the number and dimensions of links between active elements. In practice, links can take up more than 50% of the chip area, which accordingly increases the cost of VLSI design, production and operation.

It should be noted that the presented VLSI model is a simplified one; therefore, it is necessary in each specific case to take into account how accurately the used model corresponds to the specific physical and structural parameters and limitations of the used technology, specifics of the tasks that is intended to be solved using this system, data I/O protocols, etc. For example, with the reduced dimensions of active elements, their speed increases proportionally, and in this case delays in switching between links (interconnects) become comparable to the time of switching between active elements and start playing a significant role. In these conditions, provision 5 of the Thompson model is not true. With transition to faster components, such as CaAs-based ones, delays in propagation along longer links also start limiting the speed of the system, while the attempt to reduce these delays by using more powerful generators working for longer links increase the area of the chip and total power consumption of the microcircuit. Consideration of all these moments can significantly alter the values of parameters (A_s, T_s, etc.) obtained on the basis of analytical VLSI model. Therefore, it is necessary to use a number of other parameters as well for more accurate assessment and comparison of architectures of various computing systems. In particular, it is always useful to specify the task for the search of the optimal solution, since the criterion of the minimum value of product $R = A_s T_s$ (also referred to as total hardware and time costs) can lead to selection of such system

structure that is not be able to solve the set task or cannot be implemented on the basis of the available technology. In this case, two approaches can be applied [29]:

1. the best option is the one ensuring the required speed of operation T_s and at the same time requires minimum hardware costs A_s (implemented on the chip with minimum area);
2. the best option is the one ensuring minimum time of solving the task T_s with acceptable hardware costs A_s.

Moreover, in practice it is necessary to assess such parameters as total performance P_Σ of hardware resources that can be placed on a LSIC chip using given technical solution, load factor K of hardware resources of the computing system and data I/O speed [29]:

$$G_s = (1/T_s)(l_F + V_F) \tag{2.4}$$

where l_F is the quantity of information (in bits) in the input data array, on which the system S performs the operation F, V_F is the quantity of information in the output data array formed by the system S as a result of performance of operations F. In order to determine the load coefficient K, it is considered that the system S solving a certain task F during the time interval T_s contains l hardware modules M_i, $i = 1, 2, \ldots, l$. Each module M_i is characterized by hardware costs (area) A_i and can perform a certain operation f_i over time t_i, at the same time, the task F is the superposition S of operations f_i:

$$F = S\left(f_i^{(n_i)} \right), \tag{2.5}$$

where n_i is the number of operations f_i performed by the module M_i over the time t_i when solving the task F. It is clear that the total hardware costs are $A_s = \sum_{i=1}^{l} A_i$, and the level of accumulated hardware costs is determined by the relation

$$R = T_s \sum_{i=1}^{l} A_i, \tag{2.6}$$

In this case, it is plausible to additionally introduce the parameter of useful hardware and time costs

$$r = \sum_{i=1}^{l} n_i t_i A_i, \tag{2.7}$$

and determine the load factor of system hardware resources:

$$K_s = \frac{r}{R} \frac{\sum_{i=1}^{l} n_i t_i A_i}{T_s \sum_{i=1}^{l} A_i}. \tag{2.8}$$

It can be easily seen that with given hardware costs A_s, the higher the value of K_s is, the higher the performance P_Σ of the system is (the less the time of the cycle T_s is).

The parameter G_s takes part in assessment of structural solutions of the computing system in the form of peak limitation of the maximum acceptable I/O speed determined by characteristics of external devices interacting with the designed system, as well as the speed and number of system I/O ports.

The computing speed shall be matched with the possible speed of data input and output operations and not exceed it. There is no point in increasing computing power at the VLSI chip if the possibility of sufficiently quick data input and output is absent. VLS I/O speed is also limited by the number and quality of primary microcircuit outputs. The influence of primary VLSI outputs (first of all, the delay in switching of external links loaded to these outputs) is beginning to play a significant role for super quick systems. It is known that the problems of matching between relatively slow external devices and connections with high operating speed of internal units of microcircuits is solved in GaAs-based MDs by using the pipeline principle of memory addressing, sampling and presentation of data, which helps increase efficiency of input and output [30–34].

Figure 2.2a demonstrates the MD in which the cycle time is determined by three main values: t_1 – switching time of address buses, t_2–time of supply of information to the MD output; t_3– switching time of output data buses of the MD: $T_i = t_1 + t_2 + t_3$.

If the matrix of memory cells of the MD is based on GaAs, GaAs $t_2 \approx 0.5$–2.0 ns [5], while values of t_1, t_3 can reach 10–20 ns and more depending on the capacity of external buses connected to the circuit. Inclusion of buffer registers RA and RV at the address input of the MD and its output (Fig. 2.2b) makes it possible to reduce the cycle of addressing MD to the value $T_1 = \max(t_1 + t_2 + t_3)$, where $t_1 = t_1 + t_{su}$; $t_2 = t_p + t_2 + t_{su}$; $t_3 = t_p + t_3$. Here, t_{su} is the time of presetting information at the register input relative to the front of the clock signal SYN, which is used to write

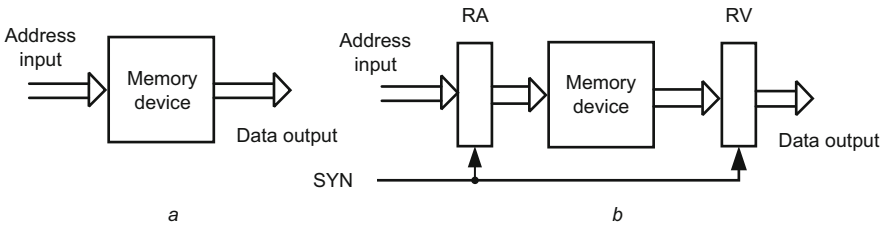

Fig. 2.2 Principle of organization of a pipeline MD

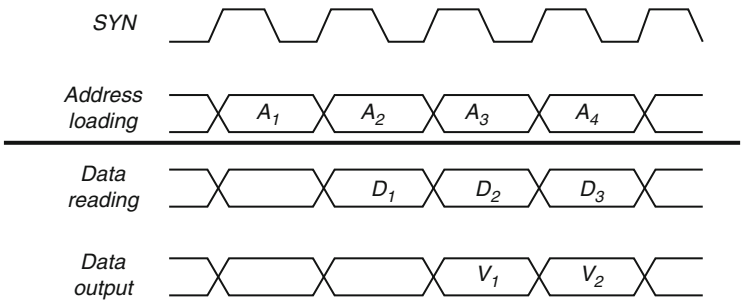

Fig. 2.3 Time diagrams of operation of memory devices with pipeline principle of performance of micro-operations

information into the register; t_p is the time of presentation of information to the register output relative to the clock signal front.

Since registers are also implemented on the basis of GaAs, t_{su} and t_p are negligible as compared to t_1 and t_3, i.e. $t_1 \approx t_1$; $t_3 \approx t_3$. The time of internal MD cycle (t_2') is slightly increased but still remains less than t_1, t_3. Therefore, the cycle of addressing the MD T_1' (assuming that $t_1 \approx t_3$) will be reduced nearly two times due to pipeline performance of micro-operations, data reading from MD and data supply to the output of the microcircuit (Fig. 2.3).

The second field where the presented approach can be useful and effective includes devices implemented with traditional silicon technology, in which pipeline organization of calculations leads to extremely short cycle of data processing both inside VLSIs and in system based on these VLSIs. Such devices include parallel-pipeline microcircuits of the K1815 set, the principles of building of which are the main subject of this book. The use of pipeline approach has made it possible to significantly increase the values of dynamic parameters of input and output LSICs of the set by using buffer memory elements. Reduction of numerical values of such dynamic parameters as the time of presetting, hold and presentation of information at LSIC inputs and outputs simplifies organization of the pipeline mode of operation of the systems in which such microcircuits are used.

As for the number of primary outputs of a microcircuit, it mostly depends on the method of dividing the task into parts (even though there are tasks that cannot be divided using an acceptable number of primary microcircuit outputs), as well as on the method of organization of data exchange between microcircuits that is determined by the data format and the necessary data input and output rates. The attempts to find a compromise between the requirement to ensure maximum possible data I/O speed and the limitation of the permissible number of external pins of the microcircuit package often causes multiplexing of data paths. Input and output efficiency can also be increased by combining input and output with computing operations.

In many cases, it is fairly difficult to determine the possible rate of exchange in a complex computing system in advance; therefore, it is necessary to provide for the

possibility of changing the rate of calculation by changing the number of modules performing calculations. This is another argument in favor of modularity of the structure.

System input and output characteristics also determine the volume of LSIC internal memory. In this regard, it is necessary to note that the problems of input and output become especially important when a computing task with large data volumes is solved with the help of VLSIs, each of which doesn't have internal memory of the sufficient capacity to store the entire volume of the necessary data, or doesn't have the sufficient quantity of computing resources to carry out the entire volume of calculations. In this case, the computing task is divided into parts and solved with the help of several VLSIs implementing various stages of the task in sequence and transmitting data to each other in pipeline mode, or by means of a single VLSI performing various stages of the task regarding entered data in sequence. The advantage of the second approach as compared to the first one is the significantly smaller total volume of input and output operations. However, if in the first case the task can be solved by using a set of microcircuits, each of which performs a certain fixed algorithm, the second approach suggest using a programmable structure.

Moreover, a system of several specialized VLSIs ensures significantly higher performance when solving the set task than a single programmable microprocessor. For example, FFT algorithm can be implemented on the basis of the widely known LSIC of TMS 320 digital signal processor; calculation of 64 bit-long FFT will require 740 μs. The processing speed can be increased by organizing the computing pipeline through introduction of buffer memory devices that will make it possible to perform data exchange between processor units simultaneously with arithmetic operations. A possible structure of such microprocessor is shown in Fig. 2.4 and contains elements included in most existing DSP processors: data I/O bus DIO, multiplier-accumulator MAC, subtracter-adder SM, data, program and coefficient memories DM, PM and KM respectively, address unit AU, program counter PC and the clock signal generator SG.

The MP additionally contains three buffer memory devices DB1– DB3. For FFT calculation with the help of such microprocessor, it is necessary to load the input data array with the length of N real words during N clock periods into data memory DM,

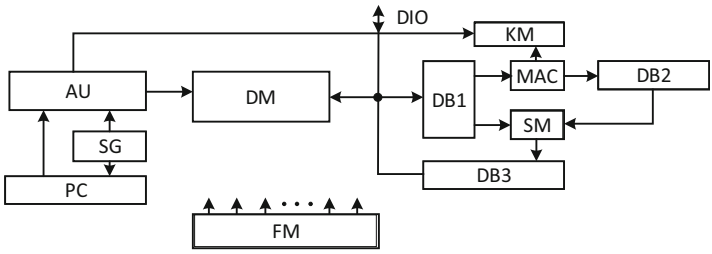

Fig. 2.4 Structure of microprocessor with pipeline organization of calculations based on buffer MDs [29]

perform $(N/2)\log 2N$ cycles of calculation of the basic FFT operation (if the algorithm for base 2 is used), and during 2 N clock cycles unload N complex samples of the calculated Fourier coefficients of the input data array. Basic FFT operation (butterfly) has the following form

$$\begin{aligned} A^{(2)} &= A^{(1)} + B^{(1)}W, \\ B^{(2)} &= A^{(1)} - B^{(1)}W, \end{aligned} \tag{2.9}$$

where
$A^{(1)}$, $B^{(1)}$ – input complex data; $A^{(2)}$, $B^{(2)}$ – output complex data; W – complex rotating coefficient;

$$\begin{aligned} A^{(1)} &= a_R^{(1)} + ja_I^{(1)}, & B^{(1)} &= b_R^{(1)} + jb_I^{(1)}, \\ A^{(2)} &= a_R^{(2)} + ja_I^{(2)}, & B^{(2)} &= b_R^{(2)} + jb_I^{(2)}, \\ & W = w_R + jw_I. \end{aligned} \tag{2.10}$$

One cycle of calculation of butterfly by the microprocessor shown in Fig. 2.4 in this case will require eight clock periods, during which the following operations are performed:

1. Output of $b_R^{(1)}$b jf* from DM to DB1.
2. Output of w_R from KM to MAC input, generation of $b_R^{(1)}\, w_R$, output of $b_I^{(1)}$ from DM to DB1, recording of $b_R^{(1)}\, w_R$ in the MAC register.
3. Output of w_I from KM to MAC input, generation of $b_R^{(1)} w_I$, generation of $S1 = b_R^{(1)} w_R - b_I^{(1)} w_I$, recording of S1 in DB2, output of $a_R^{(1)}$ DM to DB1.
4. Output of w_R from KM to MAC input, generation of $b_I^{(1)}\, w_R$, recording of $b_I^{(1)} w_R$ in the MAC register, output of$a_I^{(1)}$ from DM to DB1, calculation of $a_R^{(2)} = a_R^{(1)} + S1$ in SM, recording of $a_R^{(2)}$ in DB3.
5. Output of w_I from KM to MAC input, generation of $b_R^{(2)} w_I$ generation of $S2 = b_R^{(1)} w_I + b_I^{(1)} w_R$, recording of S2 in DB2, calculation of $b_R^{(2)} = a_R^{(1)} - S1$, recording of $b_R^{(2)}$ in DB3, output of $a_R^{(2)}$ from DB3 to DM.
6. Calculation of $a_I^{(2)} = a_I^{(1)} + S2$, recording of $a_I^{(2)}$ in DB3, output of $b_R^{(2)}$ from DB3 to DM.
7. Calculation of $b_I^{(2)} = a_I^{(1)} - S2$, recording of $b_I^{(2)}$ in DB3, output of $a_I^{(2)}$ from DB3 to DM.
8. Output $b_I^{(2)}$ from DB3 to DM.

Timing diagrams of the basic FFT operations performed by device in Fig. 2.4 are shown in Fig. 2.5. Total number of clock periods for FFT calculation will therefore be equal to $L = 3\ N + 4\ N \log_2 N$. At $N = 64$, $L = 1728$, i.e. with clock duration $T = 200$ ns (TMS 320 [1, 21] has the same clock period), the time T_s of execution of

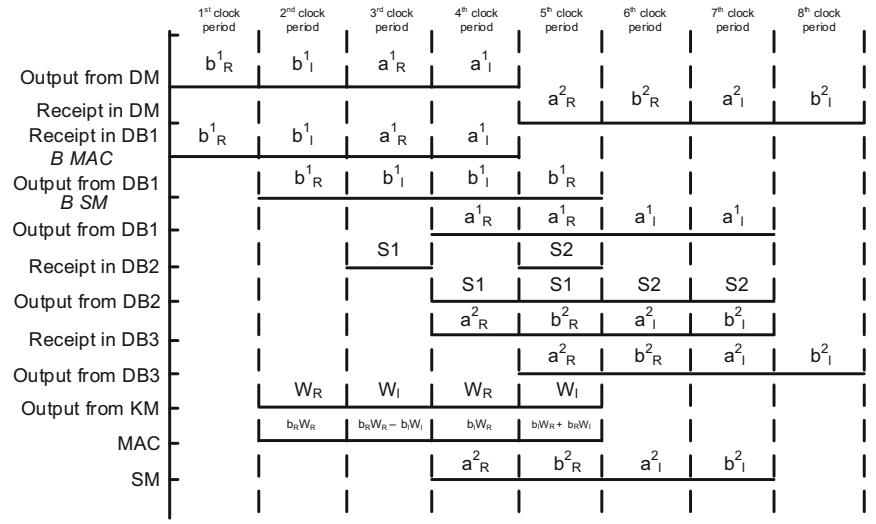

Fig. 2.5 Timing diagrams of performance of fast Fourier transform operations

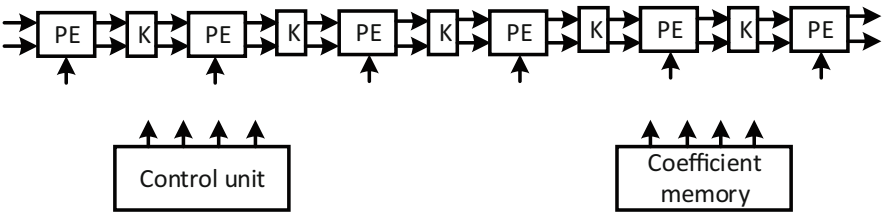

Fig. 2.6 Structure of linear parallel-pipeline process of fast Fourier transform [29]

a 64-bit long FFT will amount to approximately 345 μs, which is more than 2 times less than for TMS 320. It should be noted that further increase in performance is possible for the structure in Fig. 2.4, since it can be clearly seen from timing diagrams in Fig. 2.5 that arithmetical units of the MP MAC and SM perform useful functions only during four out of eight clock periods, i.e. load coefficients $K_{MAC} = K_{SM} = 1/2$. Limit performance at $K_{MAC} = K_{SM} = 1$; time of calculation of a 64-dot FFT will amount to $T_s = 173$ μs.

Further increase in performance can be achieved by rejecting programmable single-processor architectures and transition to parallel-pipeline specialized processes. One of the options of such processor for FFT algorithms is shown in Fig. 2.6. The processor consists of $\log_2 N$ processor elements (PE) performing the butterfly and $\log_2 N - 1$ switching units K performing data rearrangements in accordance with the graph of the implemented algorithm. It ensures continuous processing of the sequence of input data arrays, N samples each, and formation of the corresponding sequence of output arrays of complex Fourier coefficients, N complex samples each. If we assume that hardware costs of the processor in

Fig. 2.4 are equal to 1, i.e. $A_s = 1$, rough estimate for the system in Fig. 2.6 produces the value $A_p = 4\ 1\log_2 N$, since each PE in the most basic case contains four multipliers and six adders, i.e. requires approximately four times greater hardware costs than the processor in Fig. 2.4. Speed of operation of pipeline systems is estimated by the period of entering two sequential arrays of input data with which the system ensures correct performance of the given operation. For the system shown in Fig. 2.6 the period $T_p = Nt$, where t is the duration of the clock period. At $t = 200$ ns, $N = 64$, $T_p = 12.8$ μs.

Operating speed is increased due to parallel operation of $\log_2 N$ PEs; load coefficiencts of all PEs $K_{PE} = 1$. The second important moment that determined the rapid leap in performance was narrowing of specialization of the data processing system. If the MP in Fig. 2.4 can be used for implementation of other DSP algorithms (e.g., for filtration), the structure in Fig. 2.6 can only be used for FFT calculation. In this regard, it should be noted that another problem to be solved during development of VLSI-based systems is the necessity to determine the acceptable balance between rigid specialization of the system for a specific algorithm or a class of algorithms and the possibility of programming such systems for implementation of various algorithms. This issue will be considered in detail in the following; for now, let us note that specialized devices make it possible to achieve maximum performance in solving the task they are designed for, but the cost of their development satisfies a relatively narrow circle of consumers, which is economically ineffective and only justified in exceptional cases. On the other hand, programmable systems allow for solving a wide range of tasks but at the same time have their disadvantages that consists in lower performance and more complex hardware implementation of such systems. In this regard, it should be noted that most algorithms that shall be performed by DSP systems can be summarized as a certain basic set of operations. This generality can be studied and then used to simplify the aperture, simultaneously preserving the sufficient degree of flexibility.

When examining general issues of designing VLSIs and VLSI-based systems, it is necessary to single out the problem of synchronizing a great number of functional modules operating parallel to each other in a VLSI-based computing system and interacting with each other. Two aspects of this problem can be identified: synchronization of separate modules on the LSIC chip and synchronization of LSIC chips between each other. The simplest way of synchronization is global synchronization; however, it is necessary to take special measures in case with large structures in order to ensure workability of the entire system. This is due to the fact that different interacting modules can receive clock signals via different circuits, due to which there is a possibility of failure due to variation of dynamic parameters of these circuits. This fault can be eliminated by reducing the clock signal frequency and/or adding delays to the chain connecting the modules to each other, which reduces the speed of operation. The task of implementation of large systems controlled by global clock signal is, therefore, a challenging one; however, with existing densities of VLSI packaging this problem can still be solved by various means of improving dynamic parameters of synchronization chains and using multi-layered metallization. For certain specific structures, such as linear module chain, it is demonstrated

that global synchronization can be effectively implemented even in case of great delays in propagation through the sync circuit in systems of any size [6]. Specific issues and difficulties arising in case of organization of synchronization circuits on LSIC chips, as well as the means of overcoming these difficulties, are examined further in the context of K1815VF1 LSIC.

An alternative solution to the synchronization problem is the technical solution where modules synchronize exchange between each other locally, using one of the acknowledgement options [7]. The term "module" here is used to refer to the PE or any other device implemented as VLSI. Self-synchronizing systems require additional hardware costs and increase delays in each module, but these disadvantages are compensated by the fact that the time required for data exchange between two modules does not depend on the size of the entire system and variation between dynamic parameters of the elements of its component parts.

Thus, it is possible to identify a number of basic problems associated with implementation of VLSI-based computing systems, which can be briefly formulated as follows:

1. Ensuring modality, regularity and uniformity of the computing structure.
2. Ensuring local links inside the structure.
3. Ensuring the best balance between possibilities of I/O interface of the system and its computing capabilities.
4. Solving the complex of tasks associated with ensuring programmability of the system and organization of its synchronousness.

While solving issues mentioned in item 4 depends on the class of the specific task to be solved, the first three items are general and mandatory to achieve the most effective implementation of a VLSI-based computing structure. Analysis of the known architectures of computing systems from these positions makes it possible to single out parallel-pipeline systems, in particular systolic systems, as the most suitable for microelectronic implementation [8].

A systolic structure is a multitude of identical functional PE modules interconnected as a network by local links; each PE is connected only to the nearest PEs for data transmission. For implementation of various calculations, data flows in systolic system can move in the pipeline manner in different directions with different (fixed) speeds, intersecting and interacting inside PEs. The main principle of a systolic system is that all data passing through the PE array regularly and rhythmically are used multiple times. This makes it possible to significantly increase the efficiency and achieve high computing performance by paralleling calculations and reducing exchange of the systolic system with external devices performed through the limited number of borderline PE located at the edges of the array. Calculations in parallel-conveyor systems are organized in a similar manner; however, in this case there are no strict requirements for the architecture of the computer regarding uniformity of composition of hardware resources and locality of links between PEs. The requirements given are a theoretical idealization which is difficult to achieve in practice, especially if the task is to build a processing device that will

most effectively used all available resources. In the following, when talking about systolic structures, we will also refer to parallel-pipeline structures, unless otherwise specified. For correct operation of a systolic system, it is necessary to ensure organization of the computing process at which all operands to be processed by PEs are in their corresponding PEs within the corresponding computing cycle. This computing process is known as systolic processing.

Mathematical algorithms that can be implemented on systolic architectures are known as systolic algorithms. These algorithms shall have the following basic qualities.

1. The algorithm can be described using a small number of operator types.
2. The algorithm provides the possibility for wide use of multi-processing and pipeline methods. As a result, the great number of PEs implementing operators of the algorithms are active at each moment, which makes it possible to match the computing rate with the data supply volume and rate.
3. Data flows and control links between operators are simple and regular in order for PEs to be combined in a network with local regular interconnects.

As a rule, systolic algorithms can be recorded as a recursive expression. In a specific implementation of a systolic system, PE functions and their interconnections are determined by the class of tasks to be solved. Each PE can, for example, perform addition-subtraction function and consist of multiplier, adder and several registers. For other applications, it is possible to use a much simpler cell containing several gates. Typical systolic structure performing the operation of multiplication and summation of matrices C = AB + D is shown in Fig. 2.7. It contains the network

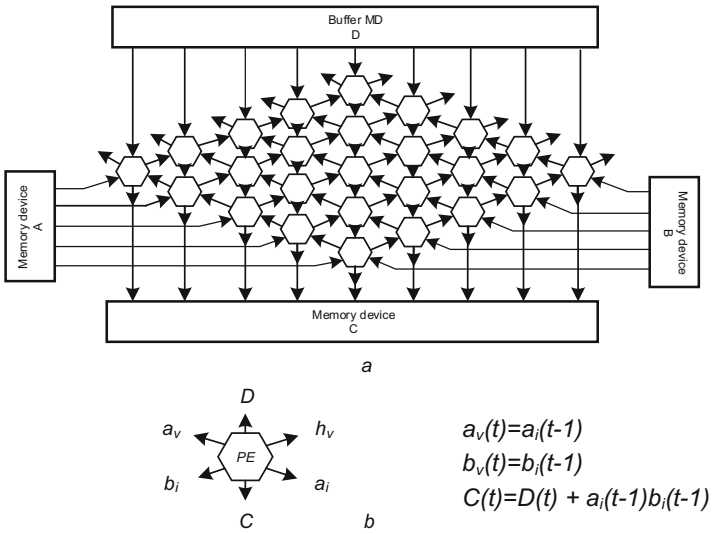

Fig. 2.7 Typical systolic structure performing the operation C = AB + D

of processor elements PE connected by local linkages and buffer memory devices at inputs and outputs of this networks designed for organization of the required order of data input and output in the structure.

There are many currently known systolic algorithms and structures designed for solving various data processing tasks. All these structures can be classified from the point of view of their flexibility (programmability), data presentation and processing formats, topology of arrangement of PEs and connections between them. When examining effectiveness of implementation of VLSI-based systolic (parallel-pipeline) methods of data processing, it is necessary to consider these characteristics of systolic systems in more detail.

Problems of programmability of systolic systems can be considered on the system level and on the level of its components (PEs). The most obvious method of implementation of a systolic algorithm is building of a specialized processor performing this algorithm exclusively. An example of such processor is considered above (Fig. 2.7) [2]. This approach is plausible if at least one of the following conditions is met.

1. Performance of the processor plays the definitive part, and the importance of tasks performed by the processor makes it possible to disregard its cost.
2. The processor will be used widely despite its narrow specialization.
3. The cost of development and production is low; this is possible for systolic matrices consisting of a small number of types of simple cells and in the presence of a developed computer-aided design (CAD) system.

The intermediate position between specialized and programmable processors is taken by multi-purpose (problem-oriented) systolic systems capable of implementing a certain set of systolic algorithms. The possibility of such solution follows from the fact that many systolic algorithms (calculations of convolution and multiplication of matrices) can be performed on systolic systems with very similar internal structure. In this case, such structure with small additional costs to ensure the necessary flexibility can perform a fairly wide range of functions.

Even more flexible programmable systolic systems can be built at the expense of programmability of PEs, links between them or both.

The problem of programmability of systolic system PEs shall also be solved based on the specific implemented task or a class of tasks. The search of the ways of creation of programmable PEs is stimulated, in particular, by the necessity to ensure the possibility of implementation of a wide range of systolic systems, each of which in itself is not important enough to justify individual custom design. Moreover, in certain systolic structures the operation to be performed by a cell depends in a complex manner on the information at the inputs of the cell and the state of the cell. Certain general functions, such as multiplication with subsequent summation, are necessary for a great number of systolic systems. Therefore, it is possible to build elementary processors that will perform several widely used functions and subsequently connect these PE in order to obtain various parallel processors of various shapes and sizes. This approach seems the best option from the point of view of unification of the element base and leads to the concept of macro-programmable

PEs. Here, correct selection of the multitude of implemented functions is extremely important from the point of view of achieving efficient PE design. The main criterion for such selection shall be formed by minimum difference in the composition and configuration of connections between hardware means ensuring implementation of the selected functions.

Topological structures of systolic and parallel-pipeline systems can be very different – linear, orthogonal, hexagonal, triangular, ringular, etc. Nevertheless, it is possible to single out three types of topology structures that are distinguished by the relation of the number of calculation operations performed by the system per unit of time to the number of input and output operations with external devices over the same time.

1. Two-dimensional systolic structures like orthogonal and hexagonal matrices. In each such cycle in these systems of n PEs, about n (hereinafter we will use the designation O(n)) PEs perform calculations, while O($\sqrt{n}$) boundary PEs perform functions of data exchange with external devices. The relation between the number of computing operations and the number of input-output operations is O($\sqrt{n}$).
2. Degenerate two-dimensional systems, i.e. one-dimensional PE chain in which O(n) PEs perform calculations and O(n) PEs perform I/O operations during each cycle. The relation of calculation operations to I/O operations is O(1).
3. Linear systolic systems, for which O(n) PEs perform calculations and only two extreme PEs perform I/O operations during each cycle, i.e. the relation of calculation operations to I/O operations is O(n).

In cases where the possibilities of data exchange between external devices and the systolic system are limited, linear systolic system which facilitates I/O organization is preferred. Moreover, linear systems are easier to synchronize. In order to facilitate solving of input and output tasks in two-dimensional systolic systems, PEs responsible for input and output can be fitted with buffer memory.

The main principle, according to which this topological structure of a multiprocessor system makes it possible to classify this system as a systolic one as compared to parallel-pipeline system is the locality of links between PEs and regular structure of these links. Locality of links in a multi-processor system of n PEs $P_i\left(i = \overline{1,n}\right)$ means that there is a certain constant C independent of n, at which for any pair of PEs P_i and P_j linked to each other the length of this link d_{ij} does not exceed $C(d_{ij} \leq \mathrm{C})$. However, there are situations where the locality condition is not met, but the system nevertheless ensures the limit performance during implementation of the selected algorithm. For example, introduction of one or several global (translation) links ensuring simultaneous transmission of data or intermediate data to inputs of multiple PE in certain cases help increase the efficiency of the system dramatically as compared to a purely systolic structure. In this relation, it is necessary to single out tree-like structures, which are linked to quick calculation algorithms and are not systolic in terms of locality of links, i.e. the length of links between PEs in the system of n PEs is proportional to $\sqrt{n}$. However, for moderate values of $n(n \leq 2^{10})$ the length

of links in tree-like structures has no significant effect on the speed of exchange between PEs, and effective pipeline implementation of such structures is allowed for execution of parallel-pipeline algorithms as an alternative to linear and matrix structures. At the same time, tree-like structures have fairly uniform composition of processor elements, the complexity (number) of operations of data exchange with external devices for tree-like structures is the same as for linear ones, and, which is extremely important in a number of cases (e.g. during summation of multiple numbers), tree-like structures make it possible to greatly reduce requirements for accuracy of data presentation (capacity of numbers) and ensure effective implementation of scaling operations.

For parallel structures like systolic ones, very important in practice are the problems of selection of data presentation, overfilling, scaling and round of the calculation results formed by PEs. These issues are not considered in most known theoretical works; it is believed that the data is presented in the format preventing the possibility of overfilling. It is true if floating point or fixed point data format with sufficient redundancy (great number of most significant redundant bits) is used. Presentation of data in the floating point format makes it possible to achieve fairly satisfactory results in such application as processing of speech signals, which require high accuracy of calculations associated with great dynamic range of input signals, while the volume of calculations is relatively large but does not require maximum limit performance of computing means (signal capture size is 2^5–2^6, and the input signal frequency does not exceed 20–40 kHz). As for most radar-related tasks and image processing, the use of floating point arithmetics in them is not justified by requirements for accuracy of calculations. In particular, 6-bit presentation of input data is sufficient to solve the task of detecting ground objects with dimensions of 10–30 m from the satellite moving at the speed of 6800 m/s 700 km above the ground surface by radiolocation methods. Clearly, the use of floating point arithmetics in such cases will reduce the data processing speed dramatically, and the fixed point arithmetics is used instead.

Another aspect in the problem of selection of data presentation format is associated with the choice between data representation in serial and parallel code. Most known works dedicated to the problems of building parallel-pipeline systems indirectly imply that the data are presented in parallel code. At the same time, there is a number of considerations, according to which it is plausible to use serial code for data presentation and processing in such systems. First of all, it is due to the limited number of primary outputs of microcircuits, which reduces dramatically the possibility of implementation of a finished parallel-pipeline structure consisting of multiple PEs on a single chip. For example, a processor element performing basic FFT function shall have six data inputs and four outputs. If the 16-bit data presentation format is used, the microcircuit will have to have at least 160 pins in addition to control, synchronization and power supply inputs. The achieved degree of integration makes it possible to place two of such PEs on one crystal; however, it is obvious that production of a microcircuits with about 350 pins is much more difficult than production of a microcircuit with 30–40 pins (with the parallel code used).

Placement of such microcircuit on the board and proper routing of all these 350 pins are also problematic tasks. Moreover, the use of serial code makes it possible to reduce dramatically the hardware resources necessary to perform a single data processing operation. For example, addition of two number in serial code is ensured by a single-digit full adder regardless of their capacity; in a parallel code, it will require a device consisting of at least n such single-digit adders, where n is the data capacity. It can be demonstrated that the reduction of total performance of computing resources on chip in case of use of the serial code will not occur due to the fact that the number of simultaneously performed operations is increased; at the same time, conveyor processing of serial codes can be performed with the maximum speed for this technology. On the other hand, data processing in a serial code is more complex in terms of management and synchronization of computing operations.

In recent times, the possibilities of creating microelectronic DSP systems of the next generation, the so-called ultra-LSIC containing 5–100 million transistors and more placed on a single silicon substrate are actively studies. The only way to achieve percentage yield other than zero for such super-systems consists in ensuring redundancy of all elements (both processing modules and communication channels between them) and reconfiguration of systems for deactivation of failed units. Of course, the attempt to provide redundancy of exchange ways with data presented in parallel code, the area taken by these ways will increase catastrophically along with the complexity of circuits ensuring reconfiguration. All this can negate the effect of redundancy; therefore, for ULSICs implemented as systems on chips or as superchips, the only acceptable form of data presentation for exchange between system units and for processing is the serial code. In this regard, it is practical to use serial code for data processing at the level of LSICs and VLSIs in order to ensure continuity of the already achieved technical solutions during transition to creation of ULSICs in the future.

Therefore, it is possible to single out parallel-pipeline (systolic) systems as the best option for implementation using microelectronic technology. These systems are characterized by properties of regularity, modality, uniformity and locality of links. They can be easily tested in the process of production and operation. High regularity and uniformity make it possible to use simple means to ensure high fail-safety of systolic systems and in certain cases allows to increase percentage yield due to addition of redundant PEs on the crystal. Due to the aforementioned reasons, parallel-pipeline principle of data processing is usually selected as the main principle during development of specialized sets. In order to increase the efficiency of using hardware resources on chip, most VLSIs of such set are specialized and perform a small number of basic operations selected on the basis of analysis of typical DSP algorithms in parallel-pipeline mode (see below). Parallel-pipeline processing is performed on the level of data layers and on the level of separate bits. Synchronization of operations between LSICs and within a single LSIC is performed by common global clock signal. Three types of data formats are used: serial-parallel code (input, output and processing are performed with the rate of two bits per clock period), serial signed-digit code and parallel code.

2.3 DSP Algorithms and Methods of Their Implementation

2.3.1 Primary and Secondary Signal Processing

A signal is known to carry information. Due to this fact, the main content of signal processing, including digital processing, is the extraction of useful information related to the signal source object or the environment through which the signal propagates. The complexity of algorithms used for signal processing is determined by such factors as the structure of signals, their quantity, frequency range, necessary resolution, type of sources of the processed signals, conditions of propagation (transmission) of signals from sources to the input of the processing system, etc. The signal structure is the combination of all its parameters and connection to the information contained in the signal. It is obvious that the signal in the general case has a fairly complex structure, since during all stages of signal's passing from the source through the propagation environment and input data into the processing system, the signal parameters are changed in a certain manner.

Let us consider the process of formation of an input signal for active radar system with separate receiver and transmitter modules (Fig. 2.8) as an example [2]. In the following, S_0 is the combination of parameters of the signal radiated by the transmitting module antenna, S_t is the combination of parameters of the probed object, S_I is the combination of parameters of the signal carrying information about the object. Clearly, S_I is a certain superposition of S_t and S_0:

$$S_I = S_t * S_0. \tag{2.11}$$

In order to take into account the characteristic of the propagation medium, it is possible to introduce the function $_t$ describing variation of signal parameters depending on parameters of the medium along the trajectory T of signal passage. In this case, the expression (2.11) will look as follows:

$$S_I = \varphi_{AC}[S_t * \varphi_{AB}(S_0)]. \tag{2.12}$$

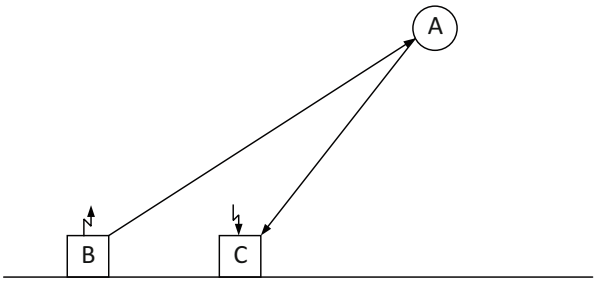

Fig. 2.8 Formation of the structure of radiolocation signal at the input of the radar receiver module: (**a**) probed object; (**b**) radar transmitter module; (**c**) radar receiver module

If there are multiple objects in the radar set surveillance area, the signal at the input of the receiving station will look as follows:

$$S_I = \sum_i \varphi_{A_i C}\left[O_{t_i} * \varphi_{A_i B}(S_0)\right]. \tag{2.13}$$

Similarly, we can examine operation of several radars (ground and air-based) in the same region, consider interferences (natural and artificial), etc. Ultimately, signal parameters at the processing system input can be recorded as follows:

$$S_I = \Phi(S_t); \tag{2.14}$$

and in this case the DSP system shall implement the inverse operation

$$S_t = \Phi^{-1}(S_I) = R(S_I), \tag{2.15}$$

where
the operator $R = F^{-1}$ determines the data processing algorithm.

From the point of view of useful information with regard to the radiated (observed) object or environment, operation (2.15) can be presented as two stages.

1. Extraction of the certain multitude of parameters S^*_I from the combination of parameters of the S_I signal supplied to the system input; these multitude includes parameters that directly depend on the parameters of the object of interest or parameters of the environment of interest:

$$S^*_I = R^*(S_I). \tag{2.16}$$

2. Using S^*_I to find target parameters S_t.

$$S_t = R^t\left(S^*_I\right). \tag{2.17}$$

Operation (2.16) is usually known as the primary signal processing, operation (2.17) – as secondary signal processing. Accordingly, system processing signals usually contain primary and secondary processing subsystems. Primary processing subsystems perform extraction of signals from noise, transformation of signals from one type to another, elimination of the existing redundancy (data compression), determination of spectral, phase, power, statistical and other parameters of signals. Secondary processing subsystems perform recognition and classification of information data received from the output of the primary processing subsystem, transform the form of representation of data into the form convenient for viewing on the display device and the resolver. Most data processing operations (90% and more) are performed by the primary processing system, due to which the requirements for

performance of these subsystems are always extremely high. If digital signal processing methods are used, in most practically significant cases primary processors (subsystems) can ensure the required performance only with the specialized element base, while secondary processing tasks in many cases can be implemented with the help of general purpose MPs. Therefore, problems of implementation of primary data processing algorithms will be mostly considered in the following.

2.3.2 Hierarchy of DSP Tasks and Operations

Instead of trying to cover the entire variety of applications of DSP method and means described in classic literature on digital signal processing [1, 9–12], which is constantly expanding, we will introduce the ***notion of a system task*** solved by this complex of hardware and software DSP means. A system task directly or indirectly reflex the purpose of the specified complex, volume and types of signals supplied to the input, source of signals, type and form of presentation of information at the output of the complex, etc. Typical examples of system tasks include tasks solved by the radar complex of the airport flight service; tasks solved by the system of speech signal processing and analysis; tasks of obtaining images of hidden objects in digital tomography systems, etc. Therefore, a system task is a complex program of the highest hierarchy level determined by the operator R based on the expression (2.15) and solved by the entire combination of hardware and software means of the data processing system. It should be noted that one of the main advantages of DSP methods is the fact that various system tasks can be solved based on identical or very similar hardware and software means that will actually differ in terms of types of sensors at system inputs and the structure of the secondary processing subsystems. This aspect is extremely important from the point of view of developing an element base for DSP systems, since it allows to consider and solve problems of creation of a unified element base ensuring creation of systems (or at least primary signal processors) to solve the widest range of DSP tasks.

System problem set by the operator R is solved by performing certain DSP procedures, which form the following level of hierarchy of DSP tasks. In terms of primary processing of signals the number of procedures used for these goals is not very high. Four basic and most frequency applied categories, the implementation of which is especially important, can be singled out: convolution and filtration; Fourier transforms; matrix calculations.

These procedures are performed in operational devices included in primary processors. Depending on the requirements (performance, permissible hardware costs, power consumption, etc.), operational devices (ODs) can be implemented on the basis of programmable signal processors like TMS 320 parallel-pipeline specialized structures, or modular microprocessor sets oriented on DSP tasks (like AMD 29500).

tDSP procedures are a combination of arithmetic operations on input and intermediate data. Arithmetic operations form the third level of hierarchy of DSP

tasks. The most commonly used operations are multiplication and addition. Separate procedures connected to solving systems of linear equations and generalization of matrices use operations of division and square rooting, but the percentage of such operations is extremely low. Below we will only consider the procedures using multiplication and addition/subtraction operations. In terms of hardware, arithmetic operations are implemented by means of corresponding arithmetical devices (ADs), the structure of which is determined by formats of input and output data, protocols of data exchanges as well as algorithms of performance of arithmetic operations implemented in ADs. Typical DSP macro-operations, which are a combination of ordered arithmetical operations, can be singled out as intermediate hierarchy level. Examples of macro-operations include basic FFT operation, digital filter links of the 1st and 2nd order, weighting addition and operations with complex numbers. Identification of macro-operations as a separate level of hierarchy is due to the fact that modern microelectronic technology helps install several interconnected ADs performing same or different arithmetical operations on a VLSI chip. Such possibilities require solution to the problem of optimal selection of composition and structure of hardware resources on chip, which consists in analysis of typical DSP procedures and their division into a combination of marco-operations, implementation of which is possible on a VLSI chip. Parallel-pipeline system contain multiple interconnected ADs that usually perform user-defined macros and are referred to as PEs.

The next hierarchy level contains arithmetical and logical operations on separate data bits. This level includes basic boolean functions of bit variables (conjunction, disjunction, negation, XOR) as well as more complex operations, such as addition of several bit variables with equal or different weights, majorization, formation of high-speed carry signals, etc. Hardware means at this level are gates and their combinations – combinational circuits of limited size.

Any information system (including any DSP) system, in addition to data processing operations, always also performs operations of storage of input and output data, intermediate results, coefficients and programs. In accordance with the above hierarchy of processing in DSP systems, it is possible to present hierarchy of data storage means as follows.

1. System level. Includes the main memory of the complex that constantly stores applied control software, necessary constants and coefficients, general purpose operating system and other components ensuring solving of a system task in general. At this level, it is also possible to identify random-access data memory devices for temporary storage of input and output information and intermediate results, as well as random-access memory devices for temporary storage of currently performed software modules.
2. Level of operational devices. On this level, MD structure is determined by the OD type. If a single-processor OD is used, the memory structure is the same as the memory structure on the system level and contains the main OD memory storing the OD operating program, necessary data and coefficients (in certain cases, main

Table 2.1 Hierarchy of DSP operations and hardware means [2]

DSP operation levels	Hardware means of data processing	Hardware means of data storage
System task	System DSP complex including the controlling computer, primary and secondary processors, input signal sensors, display and control devices, resolvers and executive devices	Main memory of the complex (program memory, constant and coefficient memory), RAM devices of programs and data
DSP procedures	ODs including modules of data exchange with other units of the system complex, arithmetical devices (one or many) or PEs, control and synchronization circuits	Memory devices for storage of programs, data and coefficients, working and buffer registers, addressing and synchronization units
Arithmetical operations (macro-operations)	Arithmetical devices (multipliers, adders, subtractors, code transformation units, etc.), processor elements	Registers
Operations on data bits	Logic gates, combinational circuits	Triggers

OD memory can correspond to operative MDs on the system level) and means of operating data storage in the form of general-purpose working registers and buffer registers included between OD units. If the OD implements parallel-pipeline data processing methods, the main memory as such is absent, and the storage medium is distributed and implemented as pipeline registers, the limited number of which is contained in each PE of the OD.

3. Level of arithmetical devices (PEs). Data are stored in working registers of ADs (PEs). Structure of working registers, their number and the order of data receipt and supply are determined by the used data formats and operations performed by ADs or PEs.
4. Level of bit operations. Trigger devices of various types are used for storage of minimal data units – data bits.

The described hierarchy of DSP operations and corresponding hardware means in the compressed form is given in Table 2.1. In the remaining part of the paragraph we will consider the second and the third levels of this hierarchy in more detail, since the specifics of DSP as a technical and scientific field is most prominent on these levels, and the problems of creating an effective element base are most relevant for them. Moreover, the main volume of computing operations necessary to solve system tasks is performed on these levels, and analysis of different methods of performance of DSP operations on the level of operational and arithmetical devices will allow to choose the most effective approaches in terms of the given criteria, after which it will be possible to solve the problems of building the system complex and design on the lower level of hierarchy taking into account the selected methods of implementation of DSP procedures and arithmetical operations.

2.3.3 Typical DSP Procedures and Hardware Structures

Tasks of signal filtering are performed in one form or another by any signal processing system. In general case, the filter in a DSP system is the device, the input of which receives the signal a_{in} with a certain combination of parameters $\overline{S_{in}} = \{S_1, S_2 \cdots\}$, and the values of these parameters are within set ranges $d_i = \overline{(d_{i1}, d_{i2})}$, i.e. $d_{i1} \le S_i \le d_{i2}$; at the output of this device, the signal $A_v = f(a_{in})$ is formed, and the signal A_v has the same combination of parameters $\overline{S_v}$ as the input signal$\overline{S_v} = \overline{S_{in}} = \overline{S}$. The values of these parameters are withn the ranges $D_i = \overline{(D_{i1}, D_{i2})}$, and there is at least one parameter $S_F \in \overline{S}$ for which $d_f \ne D_F$. The aim of filtration is to divide a complex parametric structure of the input signal into components and deletion of components with the parameters that do not contain useful information (e.g. noise, interference). For these purposes, it is sufficient in primary signal processing signals to manipulate parameters of signals presented as functions of time t or frequency w. Time and frequency filters are used accordingly.

Time filters can be considered as amplifiers with variable gain factor set by the function $f(t)$. The signal $y(t)$ at the output of the temporal filter is equal to the input signal $x(t)$ multiplied by function $f(t)$:

$$y(t) = x(t)f(t). \tag{2.18}$$

In DSP devices, input and output signals and the function $f(t)$ are discrete, and the expression (2.18) takes the form.

$$y(nT) = x(nT)f(nT), \tag{2.19}$$

where T is the sampling period.

Operation (2.19) is sometimes referred to as signal weighting, and the function f in this case is known as weighting function. Temporal filtration ensures extraction of the samples over the given period of time (Fig. 2.9a) from the signals supplied to the input. Weighting function can have a rectangular shape and amount to 1 in the given time interval T and to 0 outside the time interval T. In this case, time filtration is implemented by means of the basic switch N, one input of which receives the signal x, and the other input – function f (Fig. 2.9b). Such approach with minimum hardware costs, however, introduces additional high-frequency components into the output signal spectrum.

Therefore, weighting function with suppression at the edges of the interval T is often used (Fig. 2.10a). In this case, temporal filtration is performed with the help of multiplier (Fig. 2.10b). Temporal filtration is mostly used at the inputs of primary processing system for formation of input data arrays. Frequency filtration, in case of which the signal at the input and output of the filter as well as the filter characteristic are considered as the function of frequency w is much more useful for extraction of information parameters of the signal. In this case, we will denote them with the help

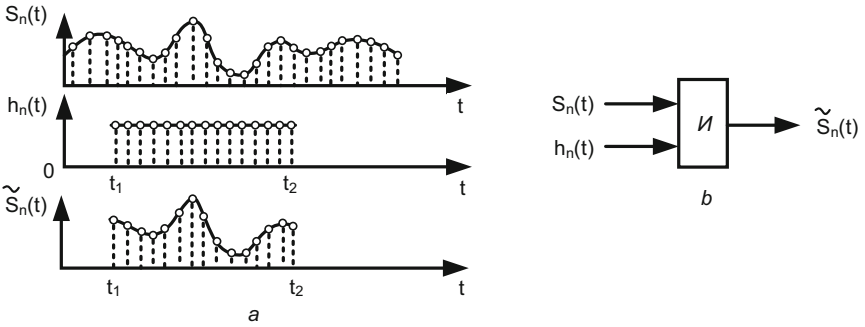

Fig. 2.9 Timing filtration of the sampled signal $S_n(t)$ with rectangular weighting function $h_n(t)$: (**a**) diagrams of input $S_n(t)$, and output $\check{S}_n(t)$ signals and weighting function $h_n(t)$; (**b**) basic time filter

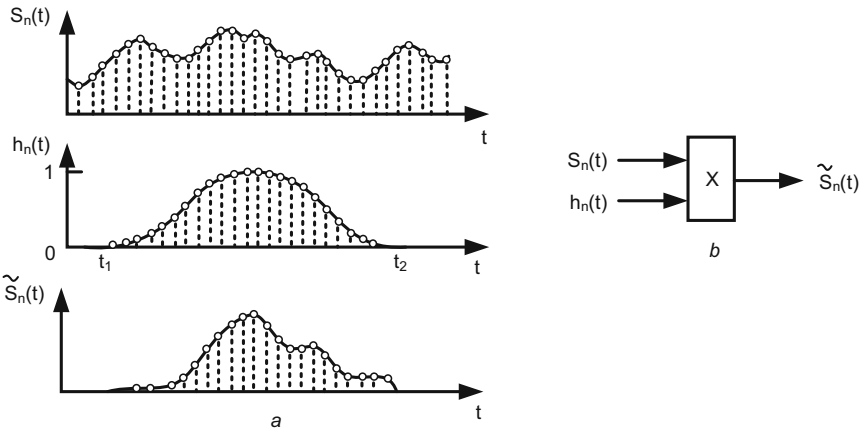

Fig. 2.10 Temporal filtration with suppression of high-frequency components in the output signal spectrum: (**a**) diagrams of input $S_n(t)$ and output $\check{S}_n(t)$ signals and weight function $h_n(t)$; (**b**) hardware implementation of multiplier-based filter

of Latin capital letters $X(w)$, $Y(w)$ and $F(w)$, and the equivalent of the expression (2.18) for frequency filtration has the form.

$$Y(w) = X(w)F(w). \tag{2.20}$$

Since the signals supplied from input sensors are always a time function and not a frequency function, in order to perform frequency filtration in the form of expression (2.20), it is necessary to switch from temporal presentation of the signal to its frequency presentation (spectrum) with the help of Fourier transform (see below). However, in some cases it is more convenient to use convolution for frequency filtration. The possibility of such approach is based on the well-known Plancheral theorem, according to which the Fourier transform from convolution of two

functions is equal to point-by-point product of each function included in the convolution, and vice versa, i.e. if we denote convolution as * and the Fourier transform as Ψ, then

$$Y(w) = X(w)F(w) = \Psi[x(t) * f(t)]. \tag{2.21}$$

Taking the reverse Fourier transform from both parts of the Eq. (2.21) and proceeding with discrete presentation of signals, we obtain that

$$y(nT) = x(nT) * f(nT) = \sum_{i=1}^{n} x(iT)f[(n-1)T], \tag{2.22}$$

where $x(nT)$, $n = 0, 1,..., N-1$ is the sequence of samples of the signal supplied to the filter input; $f(nT)$, $n = 0, 1,..., L-1$ is the sequence of samples of the pulse characteristic of this filter; $y(nT)$, $n = 0, 1,..., L+N-1$ is the sequence of samples of the signals formed at the filter output. Thus, convolution is a method of calculation of the signal at the input of the device performing filtration in the frequency domain. Pulse characteristic $f(nT)$ of the filter is the signal at its output (filter response), which is formed when the pulse with single amplitude of vanishing duration is supplied to its input. Pulse characteristic $f(nT)$ fully determines parameters of the filter during consideration of its operation in temporal domain. Analysis of operation of the filter in frequency domain is based on amplitude-frequency characteristic (AFC) of the filter, which is the Fourier transform from the pulse characteristic $f(nT)$ and is set by function $F(w)$ in the Eq. (2.21).

In general case, main parameters of digital filters determining their speed of operation and hardware costs are the length L of the pulse characteristic (filter order), counting rate N of the input signal $x(nT)$ received for processing, capacity of coefficient and data and data presentation method. Specified parameters are determined during designing of digital filters satisfying the established requirements for AFC, accuracy of calculations and so on. Methods of design of digital filters have been extensively studied and described in literature [11, 12, 15]; therefore, in the following we will only present a brief overview of widely used algorithms of digital filtration and corresponding hardware structures in order to form requirements for element base of digital filtration devices.

Figure 2.11 shows possible option of implementation of serial specialized processor of digital filtration, which implements the expression (2.22) by means of multiple performance of the basic operation of multiplication with accumulation

$$S_t = S_{t-1} + a_t b_t, \tag{2.23}$$

where S_t is the intermediate sum formed by the adder (summator) SM and stored in the buffer register R2; a_t, b_t are successive counts of input data and coefficients supplied to inputs of the multiplier MP from the data memory DM and coefficient memory CM. Pipeline buffer register R1 makes it possible to reduce the time of the

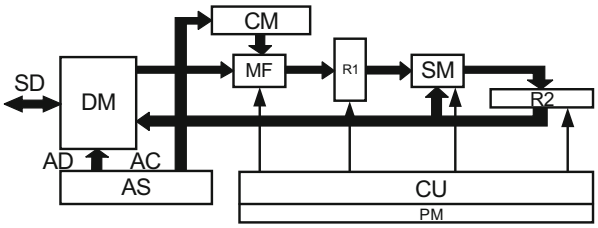

Fig. 2.11 Serial digital filtration processor [2]: *DM* data memory, *CM* coefficient memory, *PM* program memory, *SD* data I/O bus, *AD* data address bus, *AC* coefficient address bus, *AS* generator of address sequences, *JCU* control unit, *MP* multiplier, *SM* adder, *Rl, R2* buffer registers

processor cycle by parallel performance of multiplication and summation operations. Micro-program of operation of the specialized processor is determined by the structure of the control unit CU, which generates address sequences for loading and unloading of data and coefficients and also generates control and synchronization signals for arithmetical units and processor registers. Another possible variant of the special processor capable of solving filtration tasks was considered above (Fig. 2.4). Several other options of such devices are considered in [1]. The time of calculation of each output sample by means of such processor is determined by the number of necessary multiplication operations. For input array of N samples, total number of multiplications will amount to LN, time of processing of such array (without taking into account time costs of data input and output) – LNT, where T is the processor cycle time determined by the speed of operation of the multiplier and adder. Hardware costs necessary for implementation of such specialized processor allow for its single-chip implementation for moderate values L, N (L, $N = 2^6$–2^8).

Parallel-pipeline (systolic) structures, several variants of which are shown in Fig. 2.12, are used to achieve higher performance. The structure in Fig. 2.12, a [13] contains a linear pipeline of multipliers and adders processing data and coefficients in parallel code. Input counts x_n are supplied in continuous flow; input speed is determined by the speed of one pipeline stage. Output counts y_n are formed with the same speed. Coefficient memory can be implemented on the basis of registers loaded before the beginning of operation of the system, which makes it possible to easily change parameters of the implemented filter.

2D systolic structure in Fig. 2.12, b performs block data processing. Each PE contains a multiplier and an adder, as well as conveyor registers at inputs (outputs). For the purpose of processing input data vector $X = (x_0, x_1 \ldots, x_{N\text{-}1})$ the structure contains the matrix NxL of processor elements, where L is the length of the pulse characteristic of the implemented filter. Vector of samples of the input signal is inserted into the PE matrix from the bottom and transmitter from one PE to another along diagonal links. Coefficients of pulse characteristic are entered from the left and transmitted between PEs through horizontal links. Results of calculation of convolution are formed by accumulation of intermediate results along vertical links upwards and returned from outputs of top PEs in each column. In this case, the pipeline is organized on the data word layer.

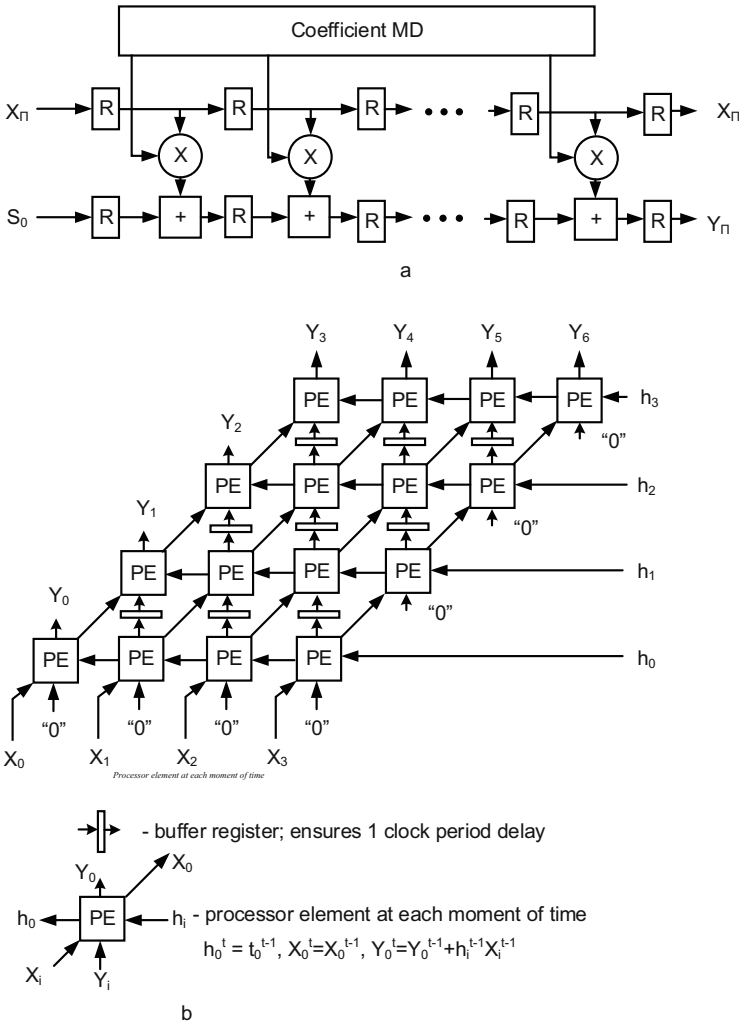

Fig. 2.12 Parallel-pipeline structures of digital filters [2]: (**a**) linear PE circuit, data presented in serial code; (**b**) two-dimensional PE matrix, data presented in parallel code; (**c**) two-dimensional matrix of one-bit PEs, serial code is used; (**d**) device for calculation of convolution with tree-like structure of multi-input adder

Implementation of the convolution operation by means of systolic structure designed as pipeline on the level of separate bits is shown in Fig. 3.12 in [14]. Each PE in this structure contains a full one-bit adder, a chain of generation of bit-by-bit products of the processed operands and pipeline registers (triggers). Input samples are entered in the sequential code starting from the less significant bit and sequentially pass through all PEs interacting with bits of coefficients of the pulse characteristics. The given coefficients are uploaded into the system before the

beginning of operation and circulate in the corresponding pipeline registers of PEs of each line. One PE line is, in fact, multiplier of numbers in serial code, and the result of multiplication is added to the results received from the previous (upper) line and sent to the following (lower) line. Addition is performed without reduction of transfers, which makes it possible to increase clock frequency of the system to the limit; final result is formed by a separate adder in the bottom line of the matrix.

Finally, Fig. 2.12, d shows another parallel-pipeline structure for calculation of convolution, which contains a set of multipliers forming products of input samples xn by coefficients of the pulse characteristic hi, pipeline registers and pipeline multi-input adder. Input data xn are supplied to the input of the first multiplier and then transmitted in series from one multiplier to another through pipeline registers ensuring required synchronization of data streams. h_i coefficients are supplied to inputs of multipliers of coefficient registers, which are loaded before the beginning of operation and can change their contents during calculations (if adaptive filtration algorithms are implemented). The result is formed at the output of the multi-input adder, which has a tree-like structure in this case. It is possible to consider at least two variants of the structure in Fig. 1.12d, which process data in parallel or serial code.

The presented structures and their various modifications can be compared to each other. It should be noted that the comparison of parallel conveyor processors in Fig. 2.12a–d based on the above criteria demonstrates preferability of tree-like structures processing data in serial code (Fig. 2.12d).

Equation (2.22) describes the so-called finite impulse response (FIR) filter [15]. Also widely used are infinite pulse response (IIR) filters, or recursive filters set by expression

$$y(n) = \sum_{i=0}^{n} x(n-i)f(i) + \sum_{k=1}^{n} y(n-k)g(k), \tag{2.24}$$

where $f(i)$, $i = 0, 1,\ldots, \mathrm{I}-1$, $g(k)$, $k = 0,1,\ldots K-1$ are the coefficients of the pulse characteristic of the filter, $x(n–i)$ are the input samples determined for $0 \leq \mathrm{n}-\mathrm{i} \leq 1$, $y(n–k)$ are the output samples determined for $0 \leq n-k \leq K$.

Algorithms of calculation of expressions (2.22), (2.24) can be presented with the help of graph structures containing operations of multiplication, adding and delay located in the nodes of the oriented graph, edges of which determine the order of performance of these operations; i.e., for each operation, preceding operations are determined, the results of which are input arguments for this operation, and following operations, which use the result of this operation as their input arguments. Figure 2.13 [3] shows variants of such graph structures describing the algorithms of calculation of (2.22), (2.24). These graphs can be used for direct synthesis of hardware structures implementing (2.22), (2.24) by replacing operations with the relevant hardware units with preservation of the structure of connections (compare Figs. 2.12 and 2.13). This helps obtain combinational (non-pipeline) processes of digital filters.

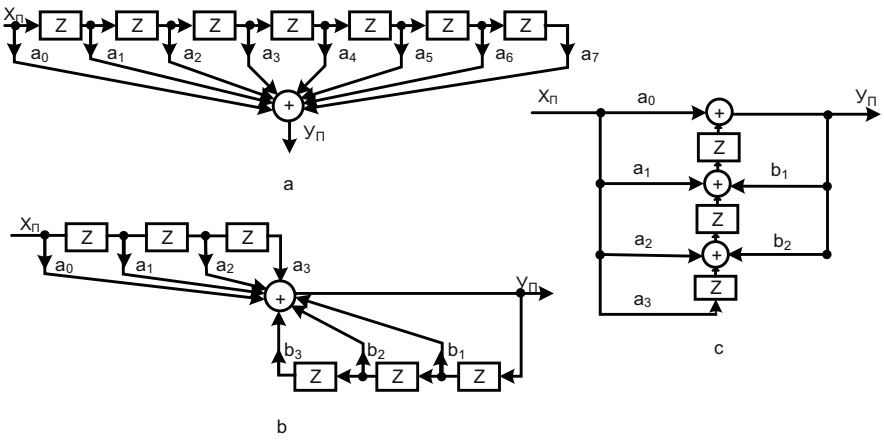

Fig. 2.13 Graph presentations of digital filtration algorithms: (**a**) finite (non-recursive) impulse response filter; (**b**) infinite (non-recursive) impulse response filter; (**c**) canonical structure of a recursive digital filter

Synthesis of conveyor structures for non-recursive filters is performed by placing pipeline buffer registers inside combination chains with a high switching delay in order to minimize the total cycle time of the device. It should be noted that pipeline registers can simultaneously perform functions of delay elements. Correct synchronization of data flows inside such pipeline structures is ensured fairly easy due to absence of reverse links. Implementation of pipeline computers based on structures shown in Fig. 2.13 for recursive filters is severely complicated by the presence of reverse links, due to which the cycle time for such devices cannot be shorter than the delay in reverse link switching. Accordingly, it is preferred to use recursive filters with short reverse link, i.e. with small K values in pipeline systems. Development of this idea is the method of implementing digital filters based on standard low-order links, which is also attractive from the point of view of reducing the list of element base components.

As noted above, another approach to implementation of digital filters is based on the use of DFT determined by the expression [2];

$$X(k) = \sum_{n=0}^{N-1} x(n) \exp\left(-j\frac{2\pi}{N}nk\right), \tag{2.25}$$

where $X(k)$, $k = 0{,}1\ N - 1$ are Fourier transforms; $x(n)$, $n = 0,\ 1,\ldots,\ N - 1$ are input signal samples. Coefficients $X(k)$ are, in fact, amplitudes of sinewaves with frequencies $w_k = 2\pi k/N$, the sum of which exactly defines the input signal, i.e. the following relation is true

$$x(n) = \frac{1}{N}\sum_{k=0}^{N-1} X(k)\exp\left(j\frac{2\pi}{N}nk\right). \tag{2.26}$$

The Eq. (2.26) sets the reverse Fourier transform. Coefficients $X(k)$ can be interpreted as spectral components of the signal $x(n)$, due to which the Fourier transform is also often used for spectral analysis.

DFT algorithms in DSP tasks can be implemented both directly, by calculation of (2.25) for each Fourier transform $X(k)$ an on the basis of quick algorithms (FFT algorithms) using the properties of symmetry and periodicity of functions $\exp(-j(2\pi/N)nk)$ relative to indices k and n.

In the first case, calculation of N-dot DFT will require $(N-1)^2$ operations of complex multiplication and $N(N-1)$ operations of addition of complex numbers. If we record the expression (2.25) in the recursive form, it is easy to notice that the operation analogous to (2.23) can be calculated as the basic operation for implementation, the difference being that the operands and the result of operation become complex values. In general case, during calculation of DFT based on direct methods, the indicated basic operation shall be extracted N times for each of N calculated Fourier transforms. For values of N reaching 2^{10} and more, the volume of calculations in case of using direct methods turns out to be excessive, which limits the speed of operation of the system, the range of frequencies of processed signals, accuracy of calculations, etc. In FFT algorithms, the basic operation is (2.9), (2.10), considered above from the point of view of its implementation on the basis of a programmable processor (Fig. 2.4). In general case, performance of FFT of the array of samples of the input signal containing N points requires $(N/b)\log_b N$ base operations, where b is the FFT algorithm base. Most frequently used values of b are 2, 4, 8. Expression (2.9) determines the basic FFT operation for base 2, which consists of one multiplication of complex numbers and two complex additions. It is easily to find that for $N = 2^{10}$, the volume of calculation in case of use of the FFT algorithm for base 2 was reduced approximately 200 times in terms of number of complex multiplication operations and about 100 times in terms of number of complex addition operations as compared to direct algorithm of DFT calculation. The disadvantage here lies in more complex organization during FFT calculation and, accordingly, more complex control over the calculation process.

From the point of view of hardware structures, for calculation of the Fourier transform it is possible to consider methods of implementation of both examined approaches based on serial programmable processors and parallel-pipeline structures. Programmable specialized processor for effective implementation of the basic FFT operation using base 2 helps fully implement the FFT algorithm and can also be programmed for performance of basic operation of the (2.23) type with complex data and implementation of direct algorithms of DFT calculation. Let us consider several parallel-pipeline structures for calculation of Fourier transform in detail.

Figure 2.14 shows an option of the linear systolic structure containing N processor elements, each of which performs basic operation (2.23) with complex values.

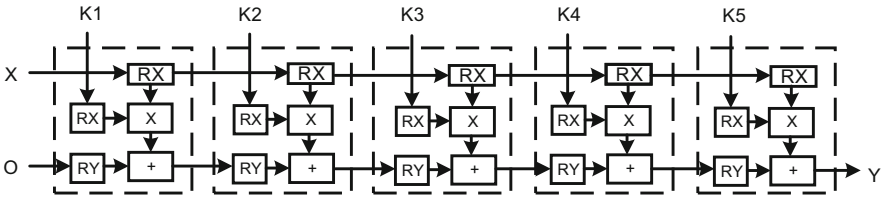

Fig. 2.14 Linear systolic structure for calculation of discrete Fourier transform [2]

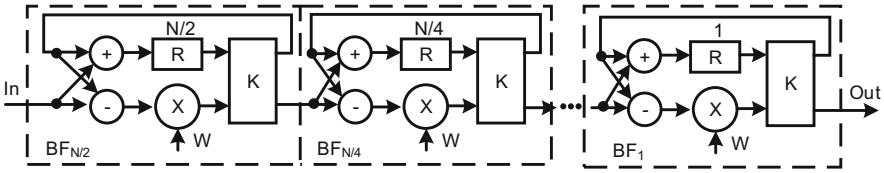

Fig. 2.15 Pipeline specialized processor of fast Fourier transform: K – switch; W – rotating coefficients; BF_L- unit performing basic operation in which the shift register R ensures a delay of L clock periods

Counts of the input signal $x(n)$ are entered in series to the input of the extreme left PE and then systolically transmitted from one PE to another. The matrix of $\left[\exp\left(-j\frac{2\pi}{N}\right)\right]^{nk} = w^{nk}$ values is entered into the PE from the top; results of intermediate calculations are transferred from the left to the right in such manner that the final results of $X(k)$ (Fourier coefficients) are accumulated during calculations and returned from the output of the Nth PE. Different modifications of this structure are possible, distinguished by the direction of data flows, organization of storage and movement of intermediate result, order of input and output of data and results, PE loading, format of data used, etc. Many systolic structures for FFT calculation are considered in [16].

Parallel-pipeline FFT implementation suggest presence of arithmetical devices performing the basic operation and certain means for organization of the necessary permutations of the intermediate calculation results in the system. Figure 2.15 [2] demonstrates the specialized FFT processor containing $\log_2 N$ processor elements, in which permutations of intermediate results are performed by shift registers of different lengths and switches controlled by the corresponding signals.

Parallel-pipeline structure in Fig. 2.16 ensures required data permutations due to the corresponding layout of connection between PEs. This structure ensures maximum parallelism during performance of FFT algorithm, but the problems of data input/output for it are fairly complex. Quite a lot of parallel-pipeline structures for FFT calculation have been suggested [17]. Selection of a specific structure is determined by the specifics of the solved task and lies within the hardware designer's scope of responsibility.

As for determination of requirements for the element base, the performed brief analysis the main requirements of DSP and hardware structures for their

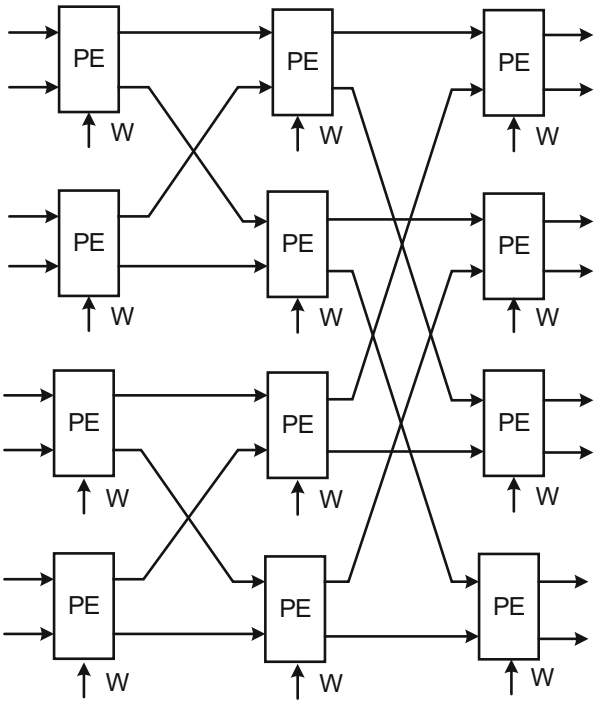

Fig. 2.16 Two-dimensional parallel-pipeline structure for FFT calculation: *PE* processor elements performing basic FFT function

implementation allows us to single out the main used arithmetic operations – multiplication and addition, as well as their certain combinations (user-defined macros) used in the considered DSP algorithms.

Macro-operations include basic FFT operation, complex addition and subtraction, operation (2.23) for real and complex data, operation for calculation of the sum of products (as a component of complex product and algorithms of digital filtration). It is also necessary to mention macro-operations of standard links of low-order digital filters, which make it possible to build efficient parallel and cascade structures of digital filters. The following types of standard links can be singled out, which in combination ensure implementation of nearly any digital filters that can be presented as (2.22), (2.24) [2].

1. Non-recursive link of the 1st order (NRF1) determined by the expression

$$y(n) = x_n + ax_{n-1}. \tag{2.27}$$

2. Non-recursive link of the 2nd order (NRF2)

$$y(n) = x_n + a_1 x_{n-1} + a_2 x_{n-2}. \tag{2.28}$$

3. Recursive link of the 1st order (RF1)

$$y_n = x_n + by_{n-1}. \tag{2.29}$$

4. Recursive link of the 2nd order (RF2)

$$y_n = x_n + b_1 y_{n-1} + b_2 y_{n-2}. \tag{2.30}$$

5. Bi-quadratic link

$$y_n = x_n + a_1 x_{n-1} + a_2 x_{n-2} + b_1 y_{n-1} + b_2 y_{n-2}. \tag{2.31}$$

Figure 2.17 present possible options of hardware structures ensuring implementation of (2.27), (2.28), (2.29), (2.30), (2.31). Specified hardware structures consisting of multipliers, adders and delay units can be implemented as separate VLSIs, which shall be combined into cascade (Fig. 2.18a) and parallel (Fig. 1.18b) structures for building of digital filters of higher orders. Transfer functions of such composite filters are described by expressions [29].

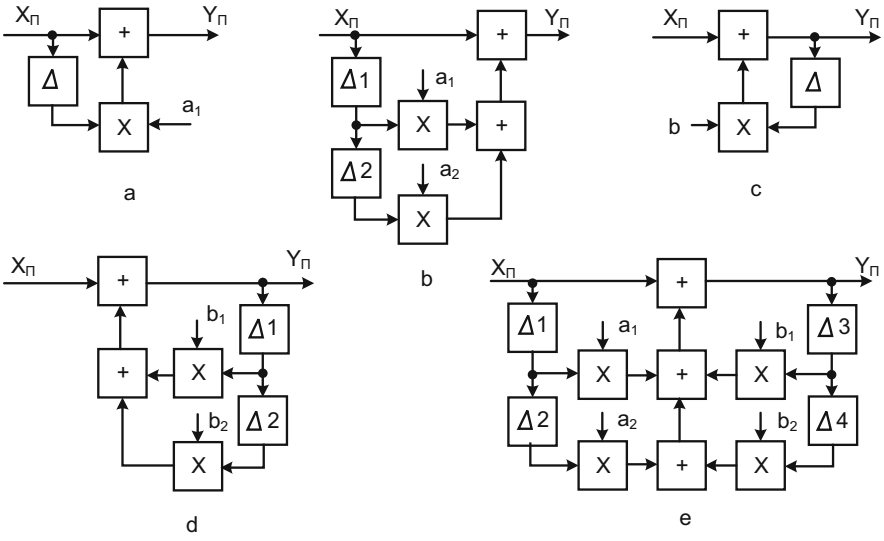

Fig. 2.17 Hardware implementation of standard links of digital filters: (**a**) non-recursive link of the first order; (**b**) non-recursive link of the second order; (**c**) recursive link of the first order; (**d**) recursive link of the second order; (**e**) bi-quadratic link

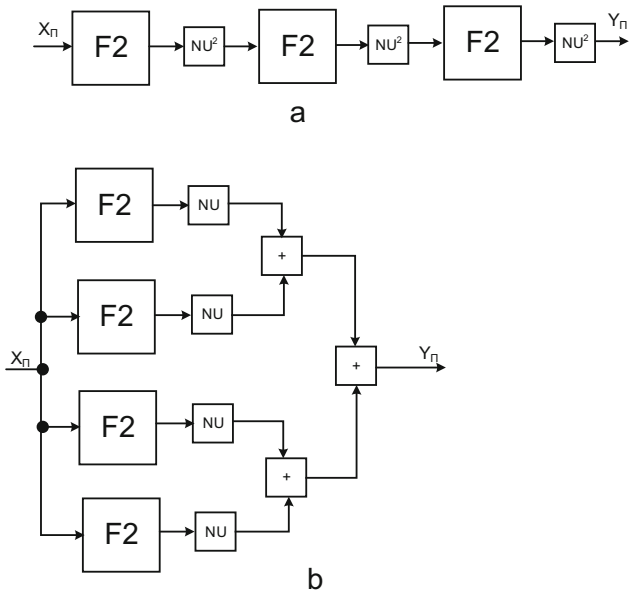

Fig. 2.18 Building of a high-order digital filter based on standard links: (**a**) cascade structure of a 6th order filter based on bi-quadratic links; (**b**) parallel structure of an 8th order filter based on bi-quadratic links. *NU* normalization units

$$H_S = \prod_{i=1}^{n} H_i \tag{2.32}$$

for staged structures and

$$H_P = \sum_{i=1}^{n} H_i \tag{2.33}$$

for parallel structures, where H_i – are transmission functions of separate standard links.

Coefficients in standard links are determined on the basis methods of digital filter designing in such manner that would ultimately ensure implementation of the given AFC with the required accuracy. Also possible are combined staged-parallel structures based on typical links of low orders. It is clear that the use of the considered approach to construction of a digital filtration device makes it possible to use pipeline methods to increase the speed of calculation. The pipeline can be organized both at the level of standard links (buffer pipeline registers are introduced between separate units of cascade structures of digital filters) and at lower levels (at the level of arithmetic operations or even operations of processing of separate data bits when using serial codes).

The described possibility is determined by the fact that in digital filters (2.27), (2.28), (2.29), (2.30), (2.31) the feedback chain is either absent or short enough, which facilitates synchronization of data flows during transition to pipeline processor and in the general case allows to achieve the highest performance of parallel-pipeline digital filtration devices.

To summarize the results of analysis of typical DSP algorithms, it is possible to form multiple macro-operations ensuring performance of these algorithms, for which it is reasonable to consider the possibility of developing specialized VLSIs for their implementation. This multitude is presented in Table 2.2, which contains the list of macro-operations, data types (real and complex) and the formats of input and output data, which are used to perform these macro-operations. Minimum capacity of input data shall be set as 8 bits.

Accuracy of presentation of input samples can be increased to 16 bit due to unification of two 8-bit modules (for example, two 8-bit multipliers) into a single 16-bit one; this will accordingly reduce the quantity of functional resources. Moreover, when solving filtration tasks (macro-operations 4–8), capacity of the input data depending on the field of application can amount to 16 and 32 bits. Output data can be presented with single or double precision, i.e. with the precision of 8, 16 or 32 bit depending on the capacity of input data and calculation mode. In this case, it is possible to identify five combinations of formats of input and output data presented in Table 2.3. Analysis of macro-operations from the point of view of possible and required formats of input and output data during their performance gives the results presented in the 3rd column in Table 2.2.

Table 2.2 Typical macro-operations of DSP [2]

Performed macro-operation	Data type	Formats
Weight addition $y_n = \sum_i x_i a_i$	Real, complex	F1, F2, F3, F4
Convolution $y_n = \sum_i a_i x_{n-1}$	Real, complex	F1, F2, F3, F4
Set of multipliers $y_i = x_i a_i + c_i$	Real, complex	F1, F2, F3, F4
Non-recursive filter of the 1st order $y_n = x_n + ax_{n-1}$	Real	F3, F5
Non-recursive filter of the 2nd order $y_n = x_n + a_1 x_{n-1} + a_2 x_{n-2}$	Real	F3, F5
Recursive filter of the 1st order $y_n = x_n + ax_{n-1} + by_{n-1}$	Real	F3, F5
Recursive filter of the 2nd order $y_n = x_n + b_1 y_{n-1} + b_2 y_{n-2}$	Real	F3, F5
Bi-quadratic link $y_n = x_n + a_1 x_{n-1} + a_2 x_{n-2} + b_1 y_{n-1} + b_2 y_{n-2}$	Real	F3, F5
Type 1 butterfly $E = A + BC, \quad D = A - BC$	Complex	F1, F3
Type 2 butterfly $E = (A + B)C, \quad D = A - B$	Complex	F1, F3

Table 2.3 Formats of input and output data

Designation	Input data formats, bits	Output data formats, bits
F1	8	8
F2	8	16
F3	16	16
F4	16	32
F5	32	32

2.4 General Questions of Building Microelectronic Element Base for DSP Systems

During evolution of approaches to the principles of building microelectronic element base of DSP, the following approaches were used::

1. custom-made microcircuits oriented on performing a specific set DSP macro-operations (e.g. filter link [18], correlator [19], complex multiplier [20]);
2. programmable DSP processors like TMS320, MPD7720, etc. [21];
3. components of DSP signals in the form of separate microcircuits (multipliers, adders, ALUs) or microprocessor kits, such as 29,500 by AMD [2, 3].

Clearly, the highest efficiency of implementation of DSP algorithms is ensured by the first approach, in which the principles of specialization and parallel-pipeline processing as the main methods of increasing performance of data processing systems can be implemented in the fullest and most consistent manner.

However, from the point of view of variety reduction, the most preferable solution is the development of a single VLSI ensuring performance of all the mentioned operations for all necessary data formats. Such tasks was solved 30 years ago by programmable DSP processors of the TMS320 type (second direction); however, performance of these processors in many cases is insufficient due to the fact that calculation algorithms in them are mostly performed in a serial manner. Known are the attempts to combine the principle of programmability of data processing means and parallel-pipeline methods of organization of calculations [22]; however, the attempts to ensure maximum versatility led to the necessity to build programmable structures and create the corresponding mathematical support and at the same time to extreme excessiveness of hardware means implemented in the computing system. At the same time, it is obvious that such multi-purpose VLSIs during performance of each given operation will not use a part of their resources designed for implementation of other operations. Moreover, this approach greatly complicates the control unit and switching system used to set VLSI to the given operation.

The alternative solution consists in dividing the original multitude of user-defined macros into small number of groups based on structural feature and develop a

separate VLSI for each group. The main feature based on which a macro-operation can be attributed to this group: minimum number of changes to be introduced in a certain basic hardware structure to provide this macro-operation. Analysis of the contents of Table 2.2 [2] from these positions makes it possible to identify the following groups of operations:

1. Calculations of sums of products of real numbers – weight summation, convolution, set of multipliers.
2. Calculations of sums of products of complex numbers – weight summation, convolution, set of multipliers.
3. Set of real digital filters – NRF1, NRF2, RF1, RF2, bi-quadratic link.
4. Basic FFT operation with complex numbers.

Tasks of signal processing that require building of complex digital filters are known; however, these algorithms have their own specifics. The best option is implementation of the four identified groups of macro-operations with corresponding formats of input and output data with the help of 4 VLSIs that can be referred to as VLSI of weight summation of real numbers, VLSI of weight summation of complex numbers, VLSI of real filters and VLSI of basic FFT operation.

In order to create complete DSP systems containing ODs based on parallel-conveyor specialized processors, except for multi-functional PEs listed above, it is necessary to create a number of specialized VLSIs, the use of which will allow a significant increase in the efficiency of implementation of specialized processors. For example, in certain cases it may be necessary in DSP tasks to perform addition and subtraction operations only (without multiplication). Such situation occurs, in particular, during building of parallel-pipeline filters of high order ($N = 2^6$–2^{12}), when products of counts of input data by coefficients can be calculated using VLSI of weight summation of real numbers and partially added, after which the real sum of these products must be formed. Another example is connected to implementation of FFT algorithms, when during the first or the last of log N calculation stages the rotating coefficients degenerate into a unit, and the basic FFT operation consists in addition-subtraction of complex numbers. In such cases, it is plausible to use special PEs performing only addition and subtraction operations.

In addition to multiplication, addition and subtraction, division operation is also found in DSP algorithms. Therefore, it is necessary to provide for VLSI performing subtraction operation in the element base for DSP systems. Specific configuration of such PE can be determined as a result of the additional analysis of algorithms using this operation.

Finally, it should be noted that, while solving the task of development of the element base for parallel-conveyor DSP systems and aiming to effectively implement calculation complexes solving a system task (the task of the highest hierarchy level), it is also necessary to provide for means of organizing data input and output in

parallel-conveyor specialized processors, means of control of processor state (workability) and initialization of the processor, as well as means of pairing the specialized processor with the main computer of the system. The most necessary of these means are VLSIs of the specialized controller of parallel-pipeline specialized computers and VLSIs of multi-purpose buffer memory device. Buffer MD receives data from sensors or the main computer, converts data formats and organizes data input to the specialized processor and data output from the processor to the main computer. The number of ports in a buffer memory device shall be not less than 2. In separate cases, buffer MD can store constant coefficients used in the implemented DSP algorithm. Structure of the VLSI of the specialized controller shall be optimized for control of buffer Md in order to perform regular or continuous monitoring of workability of the processor and maintain interface between the main computer and the specialized processor.

Another class of tasks, the solution of which shall be provided by the corresponding element base, includes various conversions of data formats: from parallel code to serial code and back, from fixed point format to floating point format and back, from additional code to direct code and back, scaling, normalization, etc. Availability of specialized elements ensuring performance of these operations will help select the data presentation methods during each stage in the best possible manner during each processing stage, taking into account given requirements for speed, accuracy of calculations and hardware costs.

Therefore, the use of the following VLSI types as microelectronic element base of parallel-pipeline DSP processors is most necessary.

1. Macro-programmable VLSIs of processor elements performing basic macro-operations and containing multipliers, adders-subtractors, means for reduction of the formed calculation results to basic applied data formats (units of rounding, normalization, code transformation, etc.) and switching circuits for PE setting to one of typical operations (Table 2.2).
2. Special processor elements for performance of addition, subtraction and division operations.
3. Special processor of parallel-pipeline processors.
4. Means for data storage (multi-purpose buffer MD) and conversion from one format to another.

Such set can also include specialized VLSIs performing one of the widely used DSP operations (convolution, correlation, etc.).

It is clear that the ways of creating a sufficiently complete list of microelectronic elements ensuring practical implementation of the general algorithms, structures and principles of creation of data processing devices described above are determined by the specific task to be solved (end goal of the project) and the level of the specific applied technology.

2.5 Certain Practical Aspects of Designing Microprocessor Sets for Radars

Below we will consider certain practical aspects of designing microprocessor sets for radar devices in a specific context. As an example, we will use the project of creation of K1815 microcircuits produced by Belarusian holding "Integral". The authors of this book directly participated in this project as heads of microcircuit developer teams. The end goal of the project was the creation of a number of special processors, high requirements for performance of which were due to the necessity to use parallel-pipeline methods of data processing. During creation of this set, we had to take into account a number of limitations regarding speed and functional possibilities of the developed element base imposed by the technological basis level. Let us consider these limitations and the means of neutralizing them in the context of central LSIC of the K1815 series – processor element K1815VF1, the structure of which largely determined the structure of other LSICs of the set.

During creation of the K1815VF1 microcircuit, we had the specific task of creating a processor element (PE) for parallel-pipeline DSP systems that would process data in serial code and ensure carrying out of typical DSP operations (first of all, calculation of convolution, summation of products, etc.). Additional requirements: PE shall ensure processing of the continuous flow of input operands supplied with the speed of at least one 8-bit word per 0.5 μs; it is also necessary to ensure a number of additional functional possibilities of the PE, including the possibility of loading coefficients into internal registers of microcircuits and their storage inside, the possibility of performing summation of results supplied from PE outputs and the possibility of reconfiguration for processing of 16-bit words. Another significant limitation during development of the circuit was power consumption of not more than 1 W. This limitation in combination with functional possibilities with given operating speed parameters determined the selection of bipolar technology of integrated injection logic (I2L) as the technological basis. CMOS basis at the time could not ensure the required speed of data processing in parallel code and did not meet requirements for maximum power at limit frequency – at least 50% of all LSIC elements are switched in a pipeline circuit during each clock period. The speed of I^2L basis also proved insufficient for data processing in purely serial code. Logic gate switch delay within the range of temperatures and supply voltages for branching coefficient $n = 4$ amounted to $\tau = 15$–18 ns, therefore, minimum cycle time $T_{\min} = 6\tau = 90$–108 ns, i.e. time of processing of 8-bit words reached $T = 8T_{\min} = 720$–800 ns and more. This called for the use of presentation and processing of data in serial-parallel code.

Another technological limitation that influenced the VLSI architecture was the limitation of the integration level existing at the moment of development: 3.5–4.0 thousand gates for serializable LSICs. Due to this fact, the developers were forced to give up the attempts to implement the full set of user-defined macros and limit functional possibilities of PEs for macro-operations of calculating the added products of two pairs of 8-bit numbers with the possibility of reconfiguration for

processing of 16-bit numbers. Limitations in terms of integration levels also made it impossible to implement number multiplication in additional code in the K1815 kit, which called for introduction of direct-to-additional code converters into LSIC K1815VF1 as well as into the kit (LSIC K1815PR1). In this scheme, multiplication operation is performed in direct code with minimum hardware costs, subsequent addition operations – in additional code. Thus, the main operation performed by LSIC K1815VF1 is

$$S = \sum_{i=1}^{n} a_i b_i \tag{2.34}$$

for $n = 2$. For $n > 2$, the operation (2.34) is performed with the help of LSIC of the multi-input adder K1815IM1 with tree-like structures. LSIC K1815IA1 can be used to build cascade tree-like structures of multi-input adders with any numbers of inputs. Conversion of data formats from parallel code to serial code and back is performed by the orthogonal memory LSIC K1815IR1. The four microcircuits listed above (K1815VF1, K1815IM1, K1815IR1, K1815PR1) form the core of the K1815 and jointly ensure performance of the first group of operations from the Table 1.2 [2], i.e. operations associated with calculation of sums of products of real numbers. The described microcircuits can also be used for implementation of other user-defined macros from Table 1.2 (operations with complex data and digital filtration operations); however, in this case it is necessary to use additional external elements of low degree of integration in order to organize management of computing and data flow synchronization processes [23], which reduces the effectiveness of computations with regard to the relation between the achieved performance and hardware costs required to build the processing devices.

In addition to microcircuits performing basic operations of arithmetical processing and data conversion, the kit also included two auxiliary microcircuits: LSIC of accumulating adder K1815VF2 and LSIC of specialized ALU K1815IA1 [30–37].

The main operations performed by LSIC K1815VF2 included loading of data supplied in 8-bit parallel code to the input highway and input registers, summation of the contents of input registers and supply of the result to the 12-bit output highway. LSIC K1815VF2 can be used in output stages of primary data processing devices for performance of adding of output results. Moreover, this microcircuit can be used to form regular address sequences in subsystems of output of processing results to display devices, etc. K1815IA1 includes 4 one-bit ALUs supplemented with registers for receipt and storage of processed data. The system of commands implemented by this ALU is a subset of the system of commands of the widely known microcircuit K155IP3. The LSIC is designed for performance of bit operations in secondary processing subsystems, in particular, in image generation and enhancement subsystems.

LSIC K1815VF3 deserves a special mention; it includes a fairly wide range of the most commonly used DSP operations, including multiplication, addition, scaling,

determination of the absolute value and so on, as well as various combinations of these operations. This LSIC was designed during the aforementioned studies for creation of multi-processor systems with reconfigurable architecture [22] as an attempt to combine versatility of the element base with parallel-pipeline methods of data processing. Elementary analysis of the system of commands of LSIC K1815VF3 confirms the previously made conclusion on redundancy of hardware resources present in the circuit during performance of separate commands from their available combination. However, LSIC K1815VF3 makes it possible to built fairly effective specialized processor for performance of FFT algorithms and digital filtration algorithms in which redundancy of hardware resources of this LSIC is minimal. Another feature of K1815VF3 LSIC is the use of signed-digit serial code for data presentation and processing. This code requires doubled (as compared to regular binary code) hardware costs for implementation of corresponding processing devices but allows for data processing starting from most significant bits and makes it possible to ensure minimum (1–3 clock periods of the main clock signal) delay in presentation of results. The latter allows for improving speed of data processing systems in a number of cases.

Basic list of microcircuits of the K1815 set and brief description of their main functions and characteristics are given in Table 2.4 [29].

Figure 2.19 [2] shows an example of implementation of the device for calculation of convolution of continuously supplied 8-bit input signal counts with 16-dot pulse characteristics on the basis of a K1815 LSIC. Implementation of the device requires four K1815IR1 microcircuits, eight K1815VF1 microcircuits, two K1815IM1 microcircuits, coefficient memory with the volume of 16X8 bits and simple control chains, i.e. the unit can be implemented on a 10x10 cm^2 board. In this case, total performance $P_\Sigma \approx 65$ million operations per second is achieved, and processing of input data supplied at the rate of over two million counts per second is ensured.

2.6 Features of Implementing the Algorithm of Synthesis of Linear Antenna Arrays with Required Directivity Pattern and Integer Amplitude Coefficients

The trend for development of stationary and mobile small-size communication systems with mobile objects led to strengthening of requirements for mass and dimension parameters of modern antenna devices. It should be noted that implementation of the given functions of antenna directivity with preservation of high directivity factor jointly with the task of their miniaturization and adaptability to manufacture is a fairly task both in theoretical and in practical terms [38].

The main problem in solving tasks of synthesis of antenna arrays (AA) based on the required directivity pattern (DP) is the necessity of complex presentation of the amplitude-phase distribution of the field along the array, which usually ultimately leads to difficulties in technical implementation of attenuators and phase shifters.

Table 2.4 Basic parameters of LSICs of the K1815 series [2]

LSIC type	Functional purpose	Data formats	Cycle time, ns	Technology	Power supply voltage	Power consumption, MW	Degree of integration	Number of leads	Package type
K1815VF1	PE LSIC	Input: 8, 16 bits, serial-parallel direct code; output: 16, 32 bits, serial-parallel additional code	118	I^2L	+5 V ± 10%; +3 V ± 5%	1275	13,520	24	Flat, ceramic-metal 4131.24-3
K1815IM1	LSIC of 8-input adder	Any capacity, serial-parallel code	118	Schottky TTL	+5 V ± 10%	770	2079	24	Flat, ceramic-metal 4118.24-3
K1815PR1	Code converter LSIC	8, 16, 32 bits, serial-parallel code	118	Schottky TTL	+5 V ± 10%	660	1172	16	Flat, ceramic-metal 402.16-21
K1815IR1	LSIC of orthogonal register memory	4, 8 bits	118	Schottky TTL	+5 V ± 10%	990	1770	28	Flat, ceramic-metal 4119.28-1
K1815VF2	LSIC of accumulating adder	Input: 24 bits; output: 12 bits, parallel additional code	472	I^2L	+5 V ± 10%	907	5610	28	Flat, ceramic-metal 4119.28-1
K1815IA1	LCIS of specialized ALU	Single-bit logic variables	120	Schottky TTL	+5 V ± 10%	825	1371	42	Flat, ceramic-metal 429.42-1
K1815VF3	LCIS of FFT microprocessor	Serial signed-digit code, length of input and output layers of up to 24 bits	100	I^2L	1.0–1.7 V	420–510	14,098	24	Flat, ceramic-metal 405.24-2

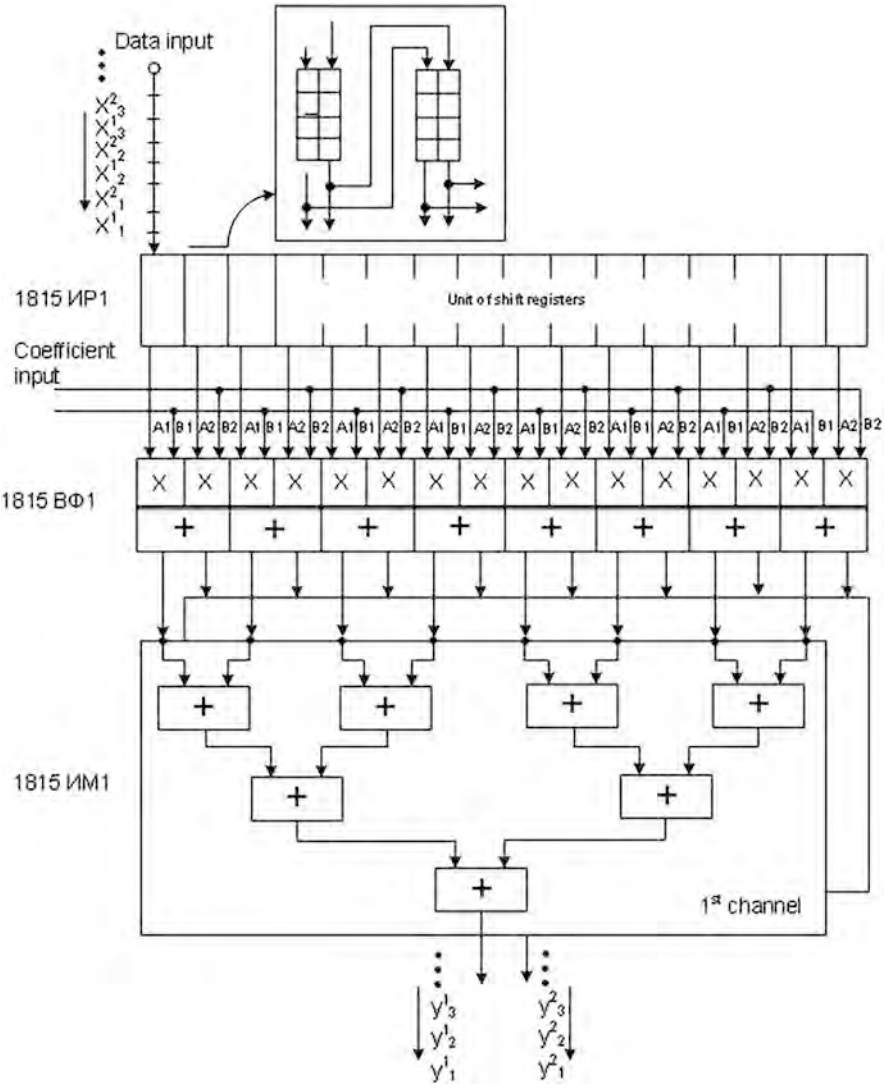

Fig. 2.19 Device for calculation of convolution based on K1815 LSIC at $P_{\Sigma} \approx 65–10^6$ operations per second [2]

One of the ways of solving this problem is development of the algorithm for synthesis of antenna array with discrete elements with approximation of complex amplitude-phase field distribution by the real one.

In general case, AA synthesis based on set function consists in finding the array of amplitude and phase coefficients [39, 40]. In this case, accuracy of approximation of the directivity pattern largely depends on the length of the array or on the number of radiators in the given plane.

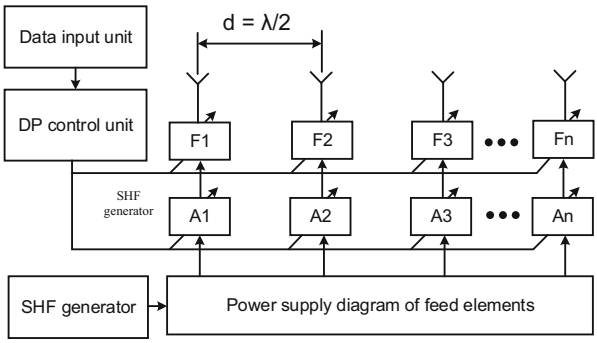

Fig. 2.20 Structural diagram of a linear antenna array [41]

Typical structural diagram of an AA shown in Fig. 2.20 [38] contains a set of permanent calibrated attenuators A1 ... An and phase shifters P1 ... Pn, which are switched with the help of a multi-position switch [40].

Depending on the requirements for DP tuning speed and accuracy of its generation, electronically controlled attenuators can be implemented as one of two options:

– with continuous adjustment, when the resistance of the p-n-junction of the microwave transistor or diode is used, which depends on displacement voltage;
– with discrete adjustment, when sections of the transmission line with calibrated attenuation are used, and the required attenuation value is achieved by corresponding switching of these sections using p-i-n-diode-based switches [41].

Similarly to attenuators, phase shifters can also have continuous curve dependence of the phase shift on control voltage (provided with the help of ferrites) or be discrete, with pre-calibrated parameters. Temperature parameters and temporal stability of discrete attenuators and phase shifters is usually better than in elements with continuous curve characteristics.

Synthesis of antenna array depending on the given directivity pattern is implemented by the DP control pattern. As demonstrated above, amplitude distribution of the field in the aperture of the antenna array and the directivity pattern are connected by the Fourier transform, when amplitude and phase coefficients are calculated with the help of Fourier transform and then processed based on the selected circuitry implementation of attenuators and phase shifters. Calculation of reverse Fourier transform for modified coefficient makes it possible to calculate the synthesized directivity function.

When developing the algorithm for the search of amplitude and phase coefficients, it is necessary to take into account the fact that integer values of attenuation are easier to implement than fractional ones.

Standard source data for array synthesis – operating frequency f, discrete or continuous directivity function $F(\Theta_i)$, $i = \overline{0, N-1}$, and permissible value of root-mean-square deviation ε.

Algorithm for synthesis of equidistant linear array with a pitch of radiators equal to $\lambda/2$ (where λ ισ the operating wavelength) has the following form.

Step 1. Determine the number of radiators of the array: N=Int(90°/$\Delta\varphi$), where $\Delta\varphi$ is the phase shift between fields of radiators.
Step 2. If the function $F(\Theta)$ is set in continuous form, divide it into N samples.
Step 3. Find direct discrete Fourier transform $F(\Theta)$:

$$C(k) = \sum_{i=0}^{N-1} F(\Theta_i) \exp\left(-j\frac{2\pi ik}{N}\right), \quad k = \overline{0,\ N-1}. \tag{2.35}$$

Step 4. Find amplitude coefficients using the formula

$$A(k) = \sqrt{\mathrm{Re}\left\{C(k)\right\}^2 + \mathrm{Im}\{C(k)\}^2}. \tag{2.36}$$

Step 5. Round amplitude coefficients to the nearest integer:

$$A'(k) = \mathrm{Int}[A(k)]. \tag{2.37}$$

Step 6. Allocate phase equal to π radians to all even phase coefficients:

$$B(2i) = \pi, \quad i = \overline{0,\ (N-1)/2} \quad \text{или} \quad i = \overline{1,\ N/2}. \tag{2.38}$$

Step 7. Allocate phase equal to 0 radians to all odd phase coefficients:

$$B(2i+1) = 0, \quad i = \overline{1,\ (N-1)/2} \quad \text{или} \quad i = \overline{1,\ N/2}. \tag{2.39}$$

Step 8: Find modified Fourier coefficients:

$$C(k) = \mathrm{Re}\,[A(k) \cdot \exp(\ j \cdot B(k))] + \mathrm{Im}[A(k) \cdot \exp(\ j \cdot B(k))] \cdot j. \tag{2.40}$$

Step 9. Calculate reverse discrete Fourier transform:

$$F'(\Theta_i) = \frac{1}{N} \sum_{i=0}^{N-1} C(k) \exp\left(\ j\frac{2\pi ik}{N}\right), \quad i = \overline{0,\ N-1}. \tag{2.41}$$

Step 10: Calculate root-mean-square deviation between $F(\Theta)$ and $F'/(\Theta)$:

$$\delta = \sqrt{\frac{\sum_{i=0}^{N-1} \left(F(\Theta_i) - F'(\Theta_i)\right)^2}{\sum_{i=0}^{N-1} F^2(\Theta_i)}}. \tag{2.42}$$

Step 11. Check if δδε: if yes, synthesis is complete; otherwise, increase the number of radiators N=N + 1 and proceed with step 2.

Let us consider a specific example.

Suggest that we need to synthesize a printed antenna array with the directivity function of the following form:

$$F(\Theta) = \begin{cases} 1 \quad npu \quad -4^\circ < \Theta < 4^\circ; \\ 0 \quad npu \quad |\Theta| > 4^\circ \end{cases} \tag{2.43}$$

with the phase shift $\Delta\varphi = 1^\circ$.

Determine the number of radiators of the array: N=Int(90°/ $\Delta\varphi$) = 90. As the function $F(\Theta)$ is set in continuous form, divide it into 90 samples. After performing steps 3, 4 and 5 of the above algorithms, we obtain the amplitude coefficients. Phase spectrum of coefficients shall be set in accordance with steps 6 and 7.

Figure 2.21 shows exact (A_mt) and rounded (A_mp) values of the obtained amplitude coefficients depending on the specified length m of the antenna array, i.e. amplitude distribution of the field in the array. The value m was calculated using the formula [38]:

$$m = \frac{l}{N\frac{\lambda}{2}}, \tag{2.44}$$

where l is the actual array length.

The results obtained after performing reverse discrete Fourier transform are shown in Fig. 2.22 [42].

Analysis in Fig. 2.22 demonstrates fairly good coincidence of the given and synthesized beam patterns in the area of the main lobe and increased level of side level of the obtained diagram, which can be considered a disadvantage. Relative level of side lobes in this case is $\xi = 20\lg 0.08 = -21.9$ dB, RMS deviation $\delta = 0.15$.

Thus, the algorithms of synthesis of linear antenna arrays with integer amplitude and binary phase coefficients suggested in [43], which is based on using fast discrete Fourier transform, makes it possible to ensure set root-mean-square deviation from the original directivity pattern. Directivity function here can be set either by analytical expression or in discrete form. The suggested algorithm can also be used for

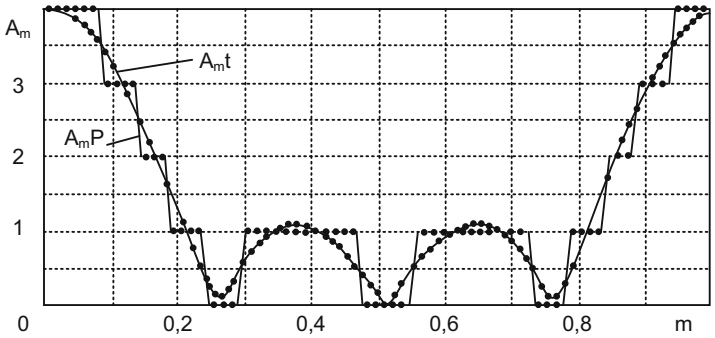

Fig. 2.21 Exact (A_mt) and rounded (A_mp) values of amplitude coefficients depending on the specified length of the antenna array m

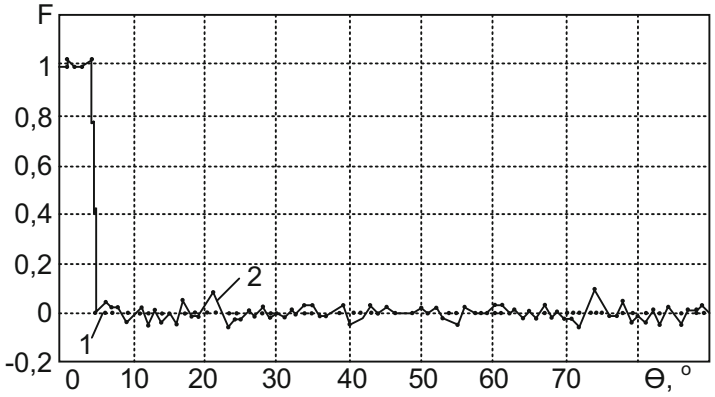

Fig. 2.22 Set (1) and synthesized (2) antenna patterns

calculation of coefficients determining the antenna directivity pattern, which is especially important in connection with emergence of controlled integrated phase shifters and attenuators, as shown further in Chap. 6.

References

1. Petrovskiy, A. A. (1988). *Methods and microprocessor means of processing wideband and high-rate processes in real time scale*. Minsk: Science and Technology. 272 p.
2. Belous, A., Merdanov, M., & Shvedov, S. (2018). *Microwave electronics in radar and communication systems* (Technical Encyclopedia in 2 volumes, 2nd edn, revised, 1520 pages). Moscow: Tekhnosfera.
3. Thompson, C. D. (1979, September). *A complexity theory for VLSI*. PhD thesis. Department of Computer Science, Carnegi-Mellon University, Pittsburgh.

4. Gilbert, B. K., Naused, B. A., Hartley, S. M., & Van Nurden, W. K. (1983, October). Exploitation of parallelism and ultraspeed integrated circuits in the next generation of distributed super signal processors. *IEEE computer society workshop on computer architecture*. Pattern Analysis and Image Database Management, Pasadena, pp. 87–92.
5. Multinovic, V., Fura, D., & Helbig, W. (1985, October). Impact of GaAs on microprocessor architecture. In *Proceedings of the 1985 IEEE international conference on computer design: VLSI in computers*. Port Chester, New York, pp. 30–40.
6. Fisher, A., & Kung, H. T. (1983). Synchronizing large VLSI processor arrays. *Conference Proceedings of the 10th annual international symposium on computer architecture*, Stockholm, pp. 54–58.
7. Wann, D. F., & Franklin, M. A. (1983). Asynchronous and clocked control structures for VLSI based interconnection networks. *IEE Trans, on Computers, C-32*(3), 284–293.
8. Foster, M. J., & Kung, H. T. (1980). The design of special purpose VLSI chips. *Computer, 13*, 26–40.
9. Rabiner, L. R., & Gold, B. (1978). *Theory and application of digital signal processing* (Trans. from Eng., Ed. Y. N. Aleksandrov, 848 p.). Moscow: Mir.
10. Oppenheim, A. (Ed.). (1980). *Application of digital signal processing* (Trans. from Eng., Ed. A. M. Ryazantsev, 552 p). Moscow: Mir.
11. Oppenheim A., & Schafer R. (1979). *Digital signal processing* (Trans. from Eng., 416 p). Moscow: Communication.
12. Vysotskiy, F. B., Alekseev, V. I., Pachin, V. N., et al. (1984). *Digital filters and devices of signal processing on integrated microcircuits*. Moscow: Radio and Communication. 216 p.
13. Williams, F. (1983). Digital integrated circuit for video signal filtration. *Electronics, 20*, 74–79.
14. Wood, D., Evans, R. A., & Wood, K. W. (1983, May). An 8-bit serial convolver chip based on a bit level systolic array. In *Proceedings of the IEEE international custom circuits conference*, pp. 256–261.
15. Bogner, R., & Constantinides, A. (1976). *Introduction to digital filtering* (Trans. from Eng., 216 p). Moscow: Mir.
16. Kukharev, G. A., Tropchenko, A. Y., & Shmerko, V. P. (1988). *Systolic processors for signal processing*. Minsk: Belarus. 127 p.
17. Wold E.H., Despain A.M. Pipeline and Parallel-Pipeline FFT Processors for VLSI Implementation IEEE Transactions on Computers. - 1984. - Vol. C-33, N 5. - P. 414–426.
18. Adams, P. F., Harbridge, J. R., & Macmillan, R. H. (1981). An MOS integrated circuit for digital filtering and level detection. *IEEE Journal of Solid-State Circuits*, *SC-16*(3), 183–190.
19. Lan, B. K. (1987). CMOS building blocks shrink and speedup FFT systems. *Electronic Design* (August), 101–106.
20. Corry, A., & Patel, K. (1983). Architecture of a CMOS correlator. *The GEC Journal of Research*, *1*, 35–38.
21. TIIER. (1987). Hardware and software means of digital signal processing, *75*(4), 212 p.
22. Kalyaev, A. V. (1984). *Multi-processor systems with reconfigurable architecture* (240 p). Moscow: Radio and Communication.
23. Podrubny, O. V., & Lapitskiy, R. E. (1987). Parallel-pipeline implementation of recursive digital filters during data processing in serial code. *Abstracts of 6th All-Union Seminar "Paralleling of Data Processing"*, p. 2. Lviv, pp. 222–224.
24. Avgul, L. B., Belous, A. I., & Grechishnikov, A. I. et al. (1988). *Parallel data processing. Vol. 4. High-performance systems of parallel information processing* (V. V. Gritsyk, Ed., 272 p). Kiev: Navukova Dumka.
25. Belous, A. I., Podrubny, O. V., Zhurba, V. M., et al. (1986). LSIC of the multi-purpose processor element K1815VF1. *Microprocessor Means and Systems, 2*, 9–13.
26. Bobkov, V. A., Kalyaev, A. V., Stanishevskiy, O. B., et al. (1986). Microprocessor K1815VF3 for digital processing of signals. *Microprocessor Means and Systems, 2*, 21.
27. Belous, A. I., & Gorovoy, V. V. (1989). *Microprocessor systems of digital signal processing* (Precis Articles. Series 50.33.39 processors, 53 p). Minsk: BelNIINTI.

28. Abraitis, B. B., Averyanov, N. N., Belous, A. I. et al. (1988). *Microprocessors and microprocessor sets of integrated microcircuits* (V. A. Shakhnov, Ed., vol. 1–2). Moscow: Radio and Communication.
29. Belous, A. I., Podrubny, O. V., & Zhurba, V.M. (1992). *Microprocessor LSIC set of K1815 series for digital signal processing: Reference book* (256 p). Moscow: Radio and Communication.
30. Silin, A. V., Milovanov, A. I., & Pribilskiy, A. V. (1986). LSIC of Code Converter K1815PR. *Microprocessor Means and Systems, 2*, 14.
31. Medvedev, V. I., & Pribylskiy, A. V. (1986). LSIC of specialized ALU K1815IA1. *Microprocessor Means and Systems, 2*, 20.
32. Belous, A. I., Vainilovich, O. S., Zhurba, V. M., et al. (1986). LSIC of accumulating 24-digit adder with interface. *Microporcessor Means and Systems, 2*, 19.
33. Smolov V.B., Khvosch S.T., Belous A.I. Injection Microprocessors in Industrial Equipment Control. - L.: Engineering, 1985. - 182 p.
34. Belous, A. I., & Vainilovich, O. S. (1988). Circuitry Features of Microprocessor Injection LCISs of the Second Generation. *Microprocessor Means and Systems, 4*, 79–82.
35. Belous, A. I. AC 1508929 USSR. Integrated circuit protection device. Published in 1989, Bulletin No. 13.
36. Silin, A. V., Belous, A. I., & Pribylskiy, A. V. et al. AC 1503930 USSR. Matching device with tree output states. Published in 1988, Bulletin no. 21.
37. Belous, A. I., Sukhoparov, A. I., Boldyrev, V. P., & Savotin, Y. I. AC 646698 USSR. I^2L Microprocessor. Published in 1979, Bulletin No. 37.
38. Zelkin, E. G., & Sokolov, V. G. (1980). *Antenna synthesis methods: Phased antenna arrays and antennas with continuous aperture*. Moscow: Soviet Radio.
39. Kravchenko, V. F. (Ed.). (2011). *Digital processing of signals and images in radiophysical applications*. Moscow: Fizmatlit.
40. Zelkin, E. G., Kravchenko, V. F., & Gusevskiy, V. I. (2005). *Design methods of approximation in antenna theory*. Moscow: Science Press.
41. Voskresenskiy, D. I. (Ed.). (2012). *SHF devices and antennas. Design of phased antenna arrays*. Moscow: Radio and Communication.
42. Voskresenskiy, D. I., & Kanaschenkov, A. I. (Eds.). (2004). *Active phased antenna arrays*. Moscow: Radiotechnics.
43. Sadchenko, A. V., Kushnirenko, O. A., & Troyanskiy, A. V. (2015). Algorithm of synthesis of antenna arrays with required directivity pattern and integer amplitude coefficients. *Technology and Engineering in Electronic Equipment, 2–3*, 15–17.

Chapter 3
Ground Penetrating Radars

3.1 Design Features of Ground Penetrating Radars

Ground penetrating radars (GPR) are designed for monitoring of various hidden objects. The spectrum of their application is fairly wide – they help perform diagnosis of underground lines, souls for construction sites, road surfaces and air strips of airfields, local irregularities in the soil, identify masked mines and explosive devices, detect points and levels of leaks from underground fuel storages, level of ground waters, and so on. A significant feature of GPRs consists in using short-pulse ultra-wideband (UWB) signals propagating in media with pronounced attenuation and dispersion. Bandwidth factor $\mu = \Delta f / f_0$ (Δf – signal frequency band, f_0 – average frequency) for UWB signals is equal to $0.5 \leq \mu \leq 2$. This field overseas is developed by over a hundred companies, including such large institutes as GSSI and Penetradar (USA), ERA Technology and Redifon (England), Sensor and Software (Canada), NTT (Japan), MALA (Sweden), Radar Company (Latvia) and many others [1–7]. In particular, they are used to solve the relevant task of detection and identification of modern anti-personnel and anti-tank mines with guaranteed probability of 99.6% (and low false alarm rate).

Development of any GPR includes the following main stages: creation of electrodynamical models of the probed sub-surface regions and objects taking into account the specifics of UWB signals; selection of the frequency range of radio probing (in this case, it is necessary to ensure the compromise between the required resolution and attenuation in this specific environments), selection of the specific form of the probing signal (linear FM, with step-wise frequency change and UWB short-pulse signals), development of the data collection algorithm, selection of the aperture formation methods, calculation of resolution and dynamic range of the system, development of the algorithms of formation of radio images taking into account the specifics of using UWB signals, creation (in case of necessity) of the

© The Editor(s) (if applicable) and The Author(s), under exclusive license to Springer Nature Switzerland AG 2021

A. Belous, *Handbook of Microwave and Radar Engineering*,
https://doi.org/10.1007/978-3-030-58699-7_3

element base, design and technological development of main units (antenna, receiver, transmitter, as well as data processing and display module).

Ground penetrating radars based on UWB video pulse signals are most widely used in industrial countries. A wide range of such GPRs with central frequencies from 80 MHz to 2.5 GHz have been developed: including low-frequency (80...120 MHz, video pulse width – 12...8 ns); medium-frequency (350...500 MHz, video pulse width – 3...2 ns) and high-frequency (0.9...2.5 GHz, video pulse width – 1.1...0.4 ns) models.

In the following, we will consider features of implementation of one of critical stages – formation of radio images (recording-recovery-interpretation) with the use of traditional processing algorithms, as well as methods of solving the reverse problem – formation and interpretation of radio images based on the so-called space and time samples of evanescent field, which qualitatively increase informational value and reliability of interpretation of environments and objects.

3.1.1 Traditional Procedures of Formation and Interpretation of Radio Images

The process of formation of radio images is usually implemented according to the following sequence: "recording-recovery-interpretation" [5, 8] (Fig. 3.1). The first stages usually includes purely hardware-related tasks associated with electrical isolation of the receiver and transmitter modules, selection of the specific polarization basis and the algorithm (strategy) of scanning of the surveyed area. Preliminary processing procedures are used to reduce the effect of noise (by averaging N signals in the current position of the recorder) and the level of noise due to irregularity and

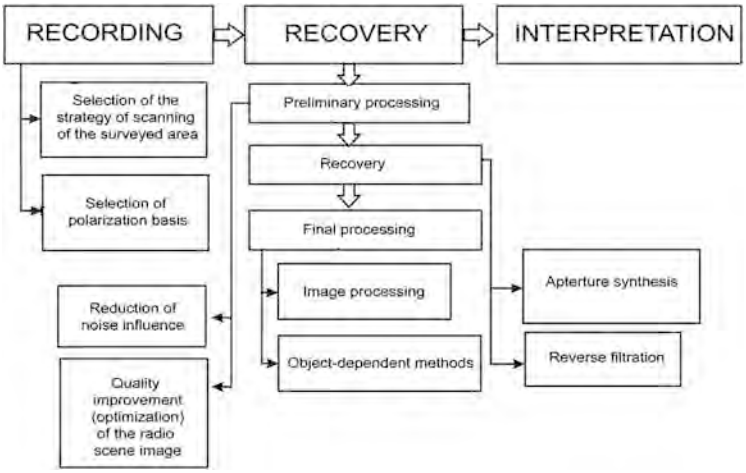

Fig. 3.1 Main stages of formation and interpretation of radio images [1]

reflections from the environment surface. These procedures of noise suppression usually use a priori data about the object, probing signal and the nature of noise (intrinsic, caused by reflections from ground surface and irregularity of the ground surface).

When such information is known a priori, developers (and customers) attempt to improve the quality of the obtained image of sub-surface radio scene, usually based on the fact that the received signal $e(R,t)$ is a convolution of the transmitter signal $s_0(t)$ and pulse characteristics of the transmitting (receiving) h_{a12} antennas, direct leakage h_b and reflections from the ground surface h_g and object h_{ts}, which, taking into account the noise $n(t)$, results in [1]:

$$e(R,t) = s_0(t) \times h_{\mathrm{a1}} \times h_{\mathrm{b}} \times h_{\mathrm{g}} \times h_{\mathrm{ts}} \times h_{\mathrm{g}} \times h_{\mathrm{a2}} + n(t) \tag{3.1}$$

After that, in order to improve spatial resolution, aperture synthesis is implemented by equalizing delays of signals from the analyzed space points. In this, known values of averaged radio waves in the soil are used, and preliminary testing of the environment is performed in most cases. In order to facilitate interpretation of the radio scene, more sophisticated algorithms are used: 3-dimensional migration procedures, construction of 2D and 3D images of sub-surface radio scene, etc.

Algorithms of subsequent processing are mostly used to enhance the quality of formed radio images and present the results of their interpretation accordingly, using characteristic data about the object and classic methods of image processing (smoothing, increasing contrast, emphasizing borders, etc.). Traditional procedures of interpretation of sub-surface probing and object identification results are usually performed by the operator, which always introduces elements of subjectiveness and reduces reliability of interpretation and monitoring speed (Figs. 3.2 and 3.3).

A number of approaches to solving reverse problems of formation and interpretation of radio images have been suggested for qualitative increase in informational value and reliability of interpretation of radio images. Let us note some of them: spectral method of reconstruction of objects in holographic and tomographic interpretations [3] based on transition to frequency region and the use of convolution algorithm; method of intrinsic resonance frequencies of objects depending of geometrical and electro-physical parameters of the object [5, 6]; building of horizontal pattern of sub-surface radio scene with subsequent use of correlation processing procedures [2]; methods of solving inverse dispersion problems [8–15]. The latter category seems to be the most promising. In turn, two groups of methods are used in their implementation. The first group includes precise methods, which use mathematically strict procedures of recovering coefficients of differential equations based on measured samples of dispersed fields using asymptotic properties of solving these equations in the spectral region. Methods of the second group are based on minimization of deviations between the results of experimental tests and numerical modeling for simple but sufficiently adequate models of probed environments and objects.

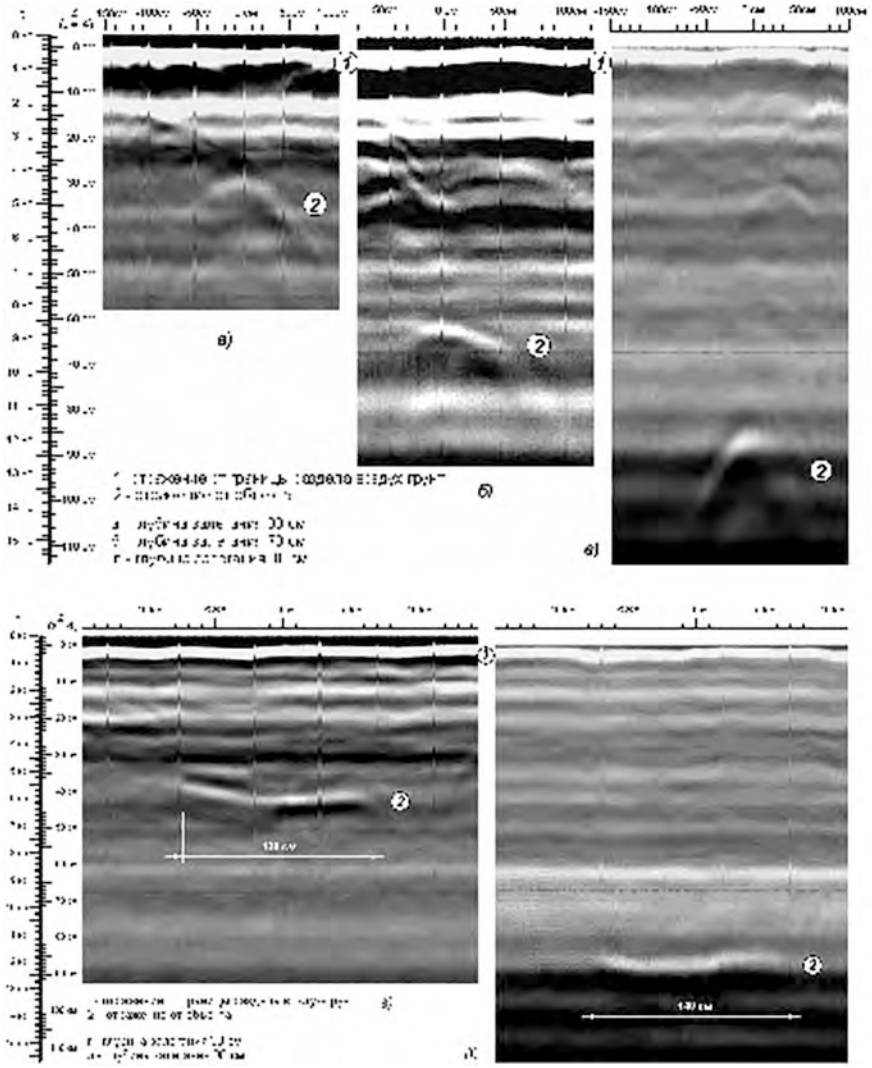

Fig. 3.2 Sub-surface image (B-scan) during movement of the GPR perpendicularly to (**a**–**c**) and along (**d**, **e**) a section of metal pipe [1]

Let us explain one of the variants of the calculation diagnostics method (CDM) for determination of geometrical and electro-physical parameters $x(\varepsilon,\sigma)$ of environments and objects in the tasks of structural (monitoring of road surfaces, air strips) and detection (underground communications, irregularities, mines) diagnostics [8, 13–15]. CDM is based on minimization of the common "smoothing" functional consisting of the functional of differences (residual) $\|Ax - u\|_u^2$ between the measurement results of samples of the electromagnetic field u dispersed by objects and

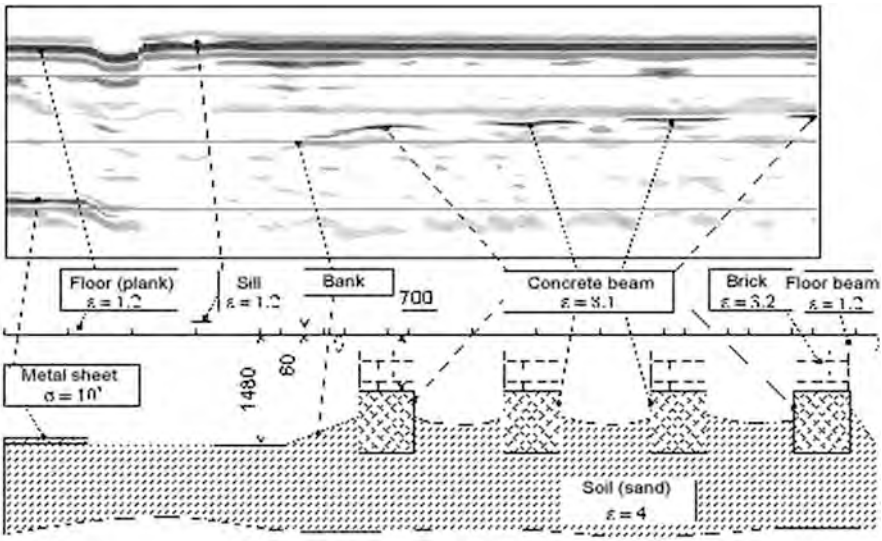

Fig. 3.3 Probing of a building structure

the modeling direct problem Ax, as well as the stabilizing functional, which takes into account a priori information about electrophysical and geometrical parameters of sub-surface radio scene ~x(a is τηε regularization parameter; q ισ τηε parameter characterizing accuracy of the a priori information). A significant problem arising during solving of the reverse task by CDM is related to the necessity to have efficient algorithms of solving direct tasks for a wide frequency range, as well as to the complexity of finding the global minimum of x caused by multiextremal nature of the functional F_a (x, A, u). Therefore, it is necessary to perform its minimization for different initial approximations in order to find its global minimum with maximum reliability. This is illustrated by the graph in Fig. 3.4 for four-layer medium (Fig. 3.5), parameters of which are presented below for different operating frequency bands on the probing signal.

$$\Phi_a(x, A, u) = \|Ax - u\|_u^2 + a \cdot \|q(x - \widetilde{x})\|_x^2, \tag{3.2}$$

Figure 3.4 shows that convergence of the algorithm to the true value depends on initial approximation; otherwise, the algorithm gives one of many false solutions. In order to extend the region of reliable search of the global minimum, it is plausible to increase the range of frequencies of the probing signal, which is illustrated by curve 1 in Fig. 3.4.

An example of numerical modeling for recovery of electrophysical and geometrical parameters of a flat-layered structure of four layers with the help of a video pulse ultra-wideband GPR is shown in Fig. 3.5 (without irregularity – Fig. 3.5, a;

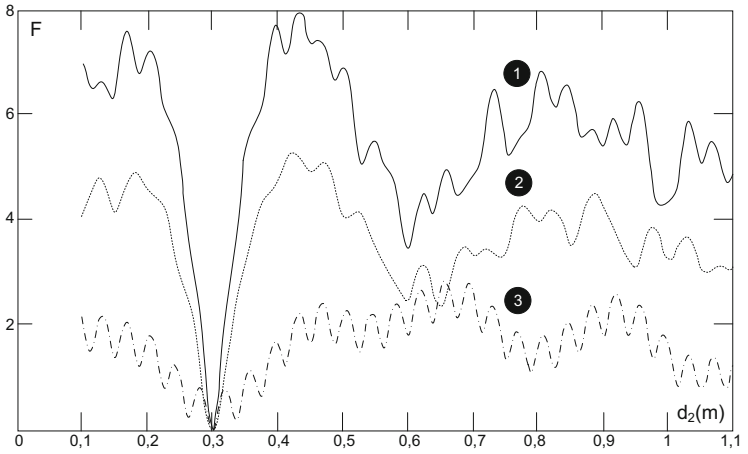

Fig. 3.4 Minimized function for four-layered medium depending on the thickness of the second layer d2: 1 — $\Delta f = 180...2000$ MHz, $Nf = 20$; 2 —$\Delta f = 500...1500$ MHz, $Nf = 20$; 3 — $\Delta f = 180...2000$ MHz, $Nf = 5$

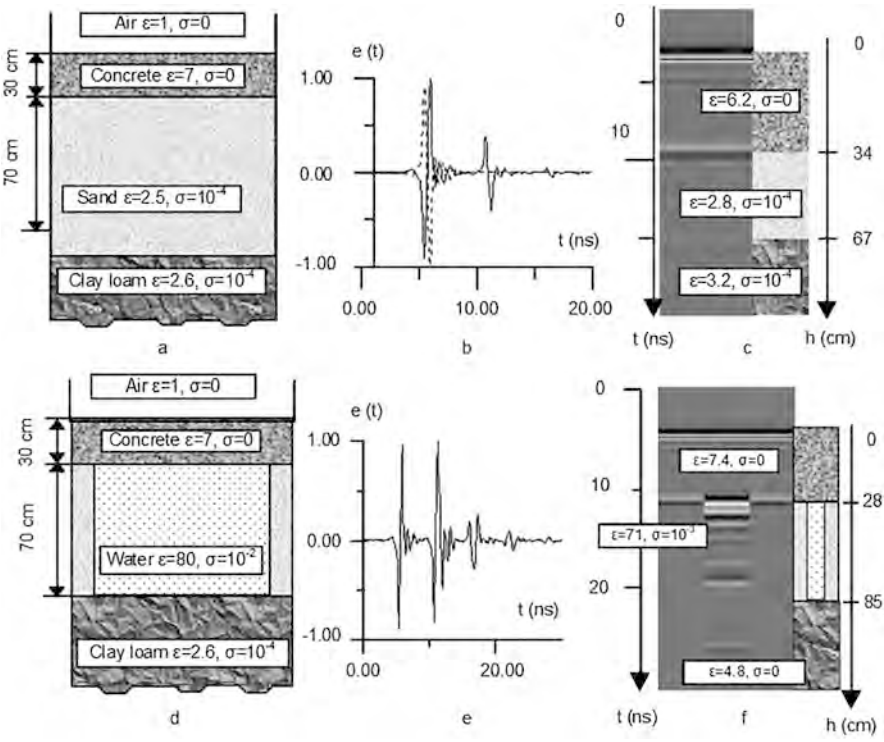

Fig. 3.5 Results of numerical experiment for recovery of parameters of a four-layer environment [1]

with irregularity of rectangular shape in the third layer (Fig. 3.5) simulating defect of the layered surface in the form of a gall filled with water).

As a rule, GRP structure includes a transmitting module (forming a single-period probing signal with duration of 1 ns and amplitude of 50 V at load of 50 Ohm at the output); an antenna module containing a transceiver T-shaped horn antenna operating within the frequency range of 150...1500 MHz; a receiver module uniting a strobing converter, a recording device and a device for temporal automatic amplification adjustment with the range of −55 dB to +20 dB; and two modules of digital procession and visualization of the radio images.

In terms of prospects and main trends in development of ground penetrating radars, the following shall be noted. For qualitative increase of informativeness and reliability of interpretation of radio images, sub-surface environments and objects and for reduction of the monitoring time, it is necessary to develop, study and practically implement new technologies related both to the algorithms of reconstruction and improvement of the software complex and the modules of UWB short-pulse ground penetrating radars. These technologies include:

- development of small-sized antennas radiating ultra-wideband video pulses with low ringing values adapted to electrophysical parameters of the probed sub-surface region, as well as methods of their electrodynamical analysis;
- creation of metrological means for measurement of antenna and radar characteristics in general for different parameters of soils and depths of objects;
- creation of GPRs with multi-element recorders and polarization processing forming stable 2D and 3D images of the sub-surface radio scene;
- development of new electrodynamical models, algorithms and software means to solve direct tasks of dispersion of ultra-wideband short pulse signal from complex sub-surface objects (local irregularities in the soil, mines, cables, etc.), e.g. based on the finite difference algorithm in time domain;
- development of methods, algorithms and software for solving reverse tasks of reconstruction of geometrical and electrophysical parameters of environments and objects based on the results of ultra-wideband short-pulse probing (minimization of corresponding functional of difference between test and received signals);
- development of methods, algorithms and software for automated procedure of identification of sub-surface objects with specific attributes (polarization, resonance, etc.);
- development of software for complete electrodynamical modeling of the GPR functioning process in general taking into account actual conditions of using GPRs;
- performance of complex experimental studies of GPRs based on new equipment and software-based technologies to obtain corresponding statistics.

It should also be noted that engineering and technological problems, which determine design of the device and convenience of operation, are very important during development of GPRs.

3.2 Radar Stations of Earth Remote Probing

Of all air vehicles of radiolocation remote Earth sensing, the most commonly used in practice are space vehicles equipped with synthesized aperture radars (SAR) [1, 16]. Such radars make it possible to obtain radar images of **extremely high quality, since their resolution is increased significantly compared to system with real dimensions of antenna apertures.**

This section of the technical encyclopedia is based on the materials of a brief yet high-quality overview of ERS space vehicles equipped with basic surveillance radar sets with SARs [16, 17].

Analysis of these materials have demonstrated that there are already many space systems with remote probing devices fitted with SARs, which make it possible to receive high-quality radar images comparable to photographs of surface of the Earth taken by optical and optical-electronic systems.

Modern radars of Earth sensing with synthesized antenna aperture, as shown in Sect. 3.1, have extensive informational capabilities on condition of further improvement as methods of remote probing, algorithms and technical means of processing and interpretation of the received information, as well as improvement of the element base for implementation of global aerospace system of continuous monitoring of natural and man-made dynamic processes, control of the state of ecosystems and monitoring of armed conflicts.

Already available is the extensive Russian hardware base for implementation of space SARs meeting the requirements of both civilian and military information consumers within the framework of Russian limitations of the regulations on radio communication in dedicated frequency bands for Earth remote sensing from space.

An important factor of the process of extraction of thematic information based on radar probing results is the use of special measuring technologies.

For example, in addition to the use of classic amplitude (energy) images, which make it possible to measure radar cross-section (RCS) of objects and specific RCS of surfaces of the Earth in conditions of different levels of polarization, the so-called interferometric processing of complex images (topographic mapping, differential interferometry, change of speed of small-sized and distributed object, polarimetric interferometry, etc) is becoming more and more popular [17].

Probing in different wave ranges with the help of SARs installed on various space vehicles is actively used across the world. It is possible to get radiolocation images with a fairly high resolution (0.5–1.5 m) in the 3 cm wave range, in particular – for imagery intelligence tasks, detection of small-sized objects in open areas, as well as with resolution of 3 m and higher in wave bands of 3 and 5.6 cm for monitoring of vegetation state and other standard tasks of Earth remote sensing (ERS). As compared with centimeter ranges, probing in the decimeter range (23 cm) with resolution of 3–7 m has its advantages: for military specialists, they include the ability to detect hidden equipment items under leaves; stability of the signal phase for interferometric processing (topography and detection of changes in the operative situation using the differential interferometry method); advantages for specialists of the agricultural

sector and environmental expert are the ability to estimate the biomass volume and determine the type and state of the vegetation in the surveyed area.

Another important direction in the obvious tendency of SAR modernization defined by improvement of spatial and radiometric resolution is the wide introduction of methods of radio vision and multi-positional probing with production of three-dimensional object patterns that detect their shape in detail, as well as the use of automatic methods of object classification based on radiolocation patterns and image texture.

Multi-positional probing and miniaturization of receiver sensors on relatively cheap mini-satellites and remotely piloted aircrafts helps ensure permanent control of local areas both for support and provision of military operations and for monitoring of emergencies (fires, floods, earthquakes, etc.).

As a rule, advanced means of remote Earth sensing by means of multi-channel multi-functional SARs developed by the leading electronic companies are usually integrated into functionally complete geoinformation system (GIS), which allows geology specialists to carry out more precise calculations of the geoid shape for accurate digital mapping of relief and provides meteorologists with the possibility to perform climatic research and studies of the interaction in the ocean-atmosphere system.

Cardinal problem of Earth remote sensing, in which only the first steps have been implemented, consists in solving the complex reverse problem of defining and describing basic properties of the observed surface, as well as ground and underground (underwater) objects using radar data. The latter is extremely important for military specialists.

Practical possibilities of remote surveying of the Earth appeared in the end of the 1960s with first practical application of radar location and scanning methods, which were initially developed for military intelligence, in civilian studies. At the time, they made it possible to perform surveys in previously unused ranges of electromagnetic waves and obtain qualitatively new information, including images of different regions of the Earth's surface with different areas. Such survey methods as multizone and infrared (IR) photography appeared, along with thermal and passive methods of mapping in the microwave range. Multiple electronic systems, operation of which is based on these methods, allows civilian and military specialists to collect information about the surface of the Earth by analyzing its SHF and IR radiations and reflected electromagnetic oscillations in visible and near IR regions of the spectrum. It should be noted that all sensors of these systems are passive, i.e. only register the energy radiated by the surface of the Earth or re-radiated by it during reflection of solar radiation.

Brand new possibilities are provided to specialists by the use of new radar location systems operating within the microwave band of electromagnetic radiation. The principle of operation of such systems is as follows: Side-looking radar installed on an ERS SV sends a narrowly directed high-frequency electromagnetic pulsed signal focused by the antenna to the Earth's surface. After being reflected from the scanned area, it is received by the receiving antenna once again and automatically registered on the space vehicle by receiving hardware. Since such systems use their

own radiation energy and work at relatively long waves, such surveys can be performed at any time of the day, in any weather and cloud conditions, as the stream of electromagnetic radiation in a certain range of wavelength directed by the system antenna easily passes through clouds, rain and fog. Moreover, such systems provide the unique possibility of continuous control over the state of various dynamic processes taking place on the surface of the Earth.

Due to the reasons listed above, radar location methods of remote probing of Earth are extremely widely used. In practice, both side-looking radars with real apertures (known as non-coherent side-looking radars) and radar stations with synthesized antenna apertures (coherent side-looking radars) are used [18]. Resolution of non-coherent side-looking radars is determined by the dimensions of the actual antenna aperture, and their advantage consists in relative simplicity of design of the radar itself and the data processing system, as well as in wider swath. The disadvantage of these systems consists in their low resolution. Coherent side-looking radars help achieve higher resolution, but require the use of a fairly complex electronic system of signal control and processing.

Side-looking radars are one the most universally applicable and informative systems of remote probing in the microwave range. Spatial resolution of ERS radars (10–100 m for SARs and 1–2 km for non-coherent side-looking radars) is commensurate with the resolution of optical systems [19].

Radars with synthesized antenna aperture are also widely used in practice today. Their operating principle is based on movement of the vehicle radar antenna for sequential formation of the antenna array in the flight trajectory. The airborne antenna itself has relatively small dimensions and wide directivity pattern. At each point of the carrier flight trajectory, SAR forms definite amplitude and phase information about the surveyed areas and objects corresponding to immediate values of their current coordinates relative to the SV. This information (RF hologram) is automatically extracted from the combination of received pulse radio signals [20].

Despite complexity and high cost of space-based SARs, their development and operation help solve multiple important tasks often available only for this method of remote probing. In particular, these very systems are also used to solve navigation tasks. Successful solutions to this tasks for the purpose of obtaining the most accurate referencing of the radar image to real objects require production of radar images with the highest possible spatial resolution, which currently can only be ensured by aperture synthesis.

Due to this fact, of all variety of ERS SVs, in the following we are only going to consider systems equipped with SARs. As is known to specialists, in addition to orbital parameters of movement, each ERS SV has many different technical characteristics and parameters of functioning of the target equipment installed on board (radiated power, frequency range, signal polarization, scan swath width, etc.). However, one of the most important characteristics of any probing system is its resolution. It can be spatial and radiometrical (brightness-based). Radiometric resolution is determined by the number of brightness sampling levels and depends on the width of the dynamic range.

Spatial resolution depends on the wavelength, size of the aperture and orbit height as follows [19]:

$$r(\lambda\tilde{/}D)H, \tag{3.3}$$

where r is the spatial resolution; λ is the wavelength; D is the size of the antenna aperture; H is the orbit height.

The presented ration shows that in order to achieve high spatial resolution, equipment developers shall aim to increase the size of the antenna aperture and have the smallest possible working wavelength. Since wavelength is determined by the operating frequency band of electromagnetic radiation of the radar and has a relatively high value as compared with the light range of optical means, in order to increase spatial resolution of a side-looking radar, it is necessary to increase the dimensions of the antenna aperture. However, this is nearly impossible to implement from the technical point of view, as in order to receive the required resolution, it is necessary to have very large overall dimensions of the real antenna aperture in non-coherent radar sets.

Therefore, specialists use the principle of aperture synthesis, in which the size of the aperture increases due to movement of a relatively small antenna along the surveyed surface. In such (coherent) radar sets, resolution of two neighboring targets is ensured by differences in time delays of reflected signals and Doppler frequencies changing in time. An important fact is that these differences do not depend on the distance to the target, and due to this fact the resolution of side-looking radars with SAR does not depend significantly on the ERS SV orbit height.

As of the moment of publication of this book, different types of ERS systems with aperture synthesis are used in space: ERS, Radarsat, IGS-3R, Yaogan, COSMO SkyMed, TerraSAR-X, SAR-Lupe, TECSAR, ENVISAT, ALOS, SIR-X SAR, etc. (Table 3.1).

Basic technical characteristics of some of these systems are presented below [19].

3.2.1 ERS (European Remote Sensing Satellite) System

Target equipment of ERS space vehicles includes AMI (Active Microwave Instruments) installed on both space vehicles (ERS-1 and ERS-2) and ensures different modes of operation. The mode of creation of radiolocation images of the underlying surface with the help of aperture synthesis (AMI-SAR image mode) has the following characteristics:

- radiated power: 1270 W;
- radiation frequency: 5.3 GHz;
- radiated signal spectrum width: 15.5 ± 0.06 MHz;
- polarization of radiated and received waves: vertical linear;
- pulse duration: 37.1 μs;

Table 3.1 Values of basic orbital parameters and technical characteristics of various RS SVs with SARs [16]

Space vehicle	SV orbit height, km	SV orbit inclination	Operating frequency length (frequency, GHz)	SAR functioning mode	Spatial resolution (bearing-range), m	Swath width (frame size), km
ERS-1	782 × 785	98.5*	(5.3)	–	30	100
ERS-2	782 × 798	98,54*				
ENVISAT-1	820	98.55*	7.69–4.84 (3.9–6.2)	7 selected bands	30	100
				Surveillance	100	400
				Global	1000	400
JERS-1	567 × 569	97,7*	(1.275)	–	18	75
ALOS	700	98.1*	(1.275)	High resolution	5–10	70
				Low resolution	–	250
Radarsat	743	98.6*	(5.263)	Standard	28 × 25	500
				Wide observation area	28 × 35	300
				High resolution	9 × 10	200
				Surveillance	30 × 35	300
				Surveillance	50 × 50	300
				Surveillance	55 × 32	500
				Surveillance	100 × 100	500
				Experimental	28 × 30	300
				Experimental	28 × 40	170
Almaz-1A	280	72,7*	(3)	–	15	30
Almaz-1B	400	–	3.5	–	5–7	20–35
			9.6	Detailed	5–7	30–55
				Intermediate	15	60–70
				Surveillance	15–40	120–170
			70	–	20–40	120–170
COSMO	600–650	98″*	(9,65)	–	3	40
					6–12	100–120

COSMO- SkyMed 1	614.4 × 633	97.86′*	3,1 (9,6)	Depending on the required resolution*	Less than 1	(10 × 10)
					3–15	40
					30	100
					100	200
Lacrosse	676 × 696	68*	(9.5–10.5)	Detailed	Less than 1	(2–4 × 2–4)
				Surveillance	2–3	(6–20 × 6–20)
					10–15	100
SIR-C/X-SAR (Space Shuttle)	233 × 240	57*	(5.298)	–	30 × 13–26	15–90
			(9.6)			15–40
			–	Telescopic	8–10	–
Osiris	600–800	90*	3	–	3–5	30–50
TerraSAR-X	507.7 × 512.5	97,45*	(9,65)	Projector	1–2	(5–10 × 10)
				Routing	3	(30 × 50)
				Surveillance	16	(100 × 150)
				Super-detailed	0.5–1	–

- spatial resolution: 30 m;
- precision of determining height of ground object during interferometric measurements: 10 m;
- radiometric resolution: 2.5 dB (with space resolution of 30 m) and 1 dB (with space resolution of 100 m);
- scanning band width: 100 km with the angle of incidence of radiated EMW on the Earth's surface of 23° in the center of the swath.

3.2.2 Space ERS Vehicle ENVISAT-1

Remote probing equipment of the ESV ENVISAT-1 includes an improved ASAR (Advanced Synthetic Aperture Radar) system, which is a modification of the SAR used on ESV of the ERS series. ASAR system operates at frequencies of the C-band (3.9–6.2 GHz or 7.69–4.84 cm) and ensures all-weather observation of up to seven selected bands along the ESV track with the common width of 100 km and resolution of 3 m or one band with the width of 400 km and resolution of 100 m. In global observation mode, the swath width equals to 400 km, resolution – to 1 km. Radiometric accuracy of measurements equals to 0.65 dB, radiometric resolution – to 1.5–3.5 dB.

3.2.3 ERS-1 (Japan Earth Resources Satellite; Japanese Name – Fuyo-1)

Radar system with synthesized antenna aperture (real dimensions of the antenna array – 11.9 × 2.5 m) is designed for all-weather survey of the Earth's surface and coastal area of the sea with production of high-quality radar images. It has the following characteristics:

- operating frequency: 1275 MHz;
- spatial resolution: 18 m;
- swath width: 75 km, edge of the swath is shifted to the right of the ESV route by 326 km;
- power in pulse: 1.3 kW;
- pulse duration: 35 μs.

3.2.4 Japanese Advanced Land Observation Satellite (ALOS)

The ESV is eqiupped with high-resolution radar system VSAR, which has the following technical characteristics:

- operating frequency: 1.275 GHz;
- radiated signal spectrum width: 15 MHz;
- limit spatial resolution: 10 m (for line-of-sight distance), 5 m (along the ESV track);
- accuracy of measurement of surface RCS: ±1 dB;
- swath width: 70 km (in high resolution mode), 250 km (in low resolution mode).

3.2.5 *Canadian System of Survey of Earth's Natural Resources Radarsat (Radar Satellite)*

Dimensions of the radar antenna – 15 × 1.5 m. Multi-functional radar system with synthesized antenna aperture installed on Radarsat ESVs is designed for all-weather survey of the planet surface, observation of movement of ships and ice, mapping of the Earth's surface and many other purposes.

SAR of the Radarsat space vehicle has the following basic characteristics:

- operating frequency: 5.263 GHz;
- spatial resolution: 9–100 m (depending on the operation mode);
- polarization of radiated and received signals: linear horizontal;
- mean radiated power: 300 W;
- pulse radiated power: 5 kW;
- pass band width: 11.6, 17.3 and 30 MHz;
- sampling rate: 12.9, 18.5 and 32.3 MHz;
- pulse duration: 42 μs;
- pulse repetition frequency: 1270–1390 GHz.

The radar can measure position of the swath relative to the space vehicle path. Swath width varies within 45–500 km in accordance with the required sector of observation angles and spatial resolution.

3.2.6 *Russian Program "Almaz"*

The "Almaz" program, or, specifically, its national economy-related part for the survey of Earth's resources by means of space vehicles with SARs used the radiolocation system with synthesized aperture of space vehicles "Almaz-1A" and included two waveguide antenna arrays with the size of 1.5 × 1.5 mm generating two separate beams.

Basic technical specifications [1]:

- operating frequency: 3 GHz;
- spatial resolution: 15 m;
- polarization of transmitted and received signals: linear horizontal;

- radiated power: 190 W (pulse), 80 W (average);
- duration of probing pulses: 0.07 and 0.1 ms;
- pulse repetition frequency: 3 kHz;
- SAR beam width on the ground: 30 km;
- swath width: 350 km;
- length of recording of the radiolocation image along the ESV track: 20–240 km.

"Almaz" program was continued by "Almaz-1B" space vehicle, onboard radar location complex of which is designed for all-weather observation of the Earth's surface and consists of three different subsystems ensuring surface probing at different frequencies and in different modes [1]:

- SAR-3 operating frequency length – 3.5 cm, ground resolution – 5-7 m, swath width – 20 to 35 km;
- SAR – 10 operating frequency length – 9.6 cm, ground resolution – 5 to 7 m, swath width – 30 to 55 km (detailed mode); ground resolution – 15 m, swath width – 60 to 70 km (intermediate mode); ground resolution – 15 to 40 m and swath width – 120 to 170 km (survey mode);
- SAR-70 operating frequency length – 70 cm, ground resolution – 20 to 40 m, swath width – 120 to 170 km.

Russian Scientific and Production Enterprise "Vega" designed a multi-functional radiolocation complex of the new generation "Ekor-1 V" for SV "Almaz-1 V" [1]. This three-part radar complex "Ekor-1 V" operates in the centimeter range: 3.49 cm (resolution 5–7 m at swath width of 20–35 km); 9.58 cm (range resolution: 5–7 m and 22 m, bearing resolution: 5 m and 15 m at swath width of 25–100 km); 69.8 cm (resolution: 20–40 m with swath width of 100–150 km).

3.2.7 Russian Module of Earth's Remote Sensing "Priroda" ("Nature")

"Priroda" ("Nature") module was a space platform fitted with various ERS equipment, which operated as a part of the Mir Orbital Station since April 1996. Radar system with synthesized antenna aperture "Travers" had the following main characteristics: operating frequency length – 9.3 and 23 cm, space resolution – 50 to 150 m, swath width – 50 km.

3.2.8 ERS Space Vehicles COSMO (Italy, Spain, Greece)

COSMO ERS SVs are equipped with SARs operating at the frequency of 9.65 GHz, which ensures spatial resolution of 3 m at swath width of 40 km and 6–12 m at 100–120 km accordingly [19].

3.2.9 Double-Purpose ERS SV COSMO-SkyMed (Italy)

Orbital group of double-purpose COSMO-SkyMed ERS SVs includes six space vehicles [21]. In 2010, SAR-2000 synthesized aperture radar with antenna dimensions of 5.7 × 1.4 m was installed on COSMO-SkyMed 1. The radar operates in the X-range of wavelengths (6.2–10.9 GHz or 4.84–2.75 cm) at the frequency of 9.6 GHz (wavelength 3.1 cm). In different operation modes, they ensure ground resolution less than 1, 3–15, 30 and 100 m with the corresponding swath width of 10 × 10, 40, 100 and 200 km.

3.2.10 Radar Intelligence System Lacrosse

A typical example of a military-purpose ERS SV is the Lacrosse system created by Martin Marietta in the USA. It should be noted that the original cost of development of the system amounted to about $3 billion, the cost of one SV – $0.5 to 1 billion. It was planned that the orbital group would include six SVs. According to experts (the information is not available in open print), operating frequency range of the Lacrosse SV radar is within the band of 9.5–10.5 KHz; ground resolution of a radar image in the detailed mode is under 1 m, frame size – 2 to 4 by 2 to 4 km; in survey mode, resolution is 2–3 m, and the frame size is 6–20 per 6–20 km. Also possible is survey with swath width of about 100 km; resolution in this case will amount to 10–15 m. Reconnaissance performed by Lacrosse is clearly strategic in nature, and this SV is designed for high-resolution long-term observation of small areas, mostly in regions of local military conflicts and man-made catastrophes.

3.2.11 Radar Location Complex SIR-C/X-SAR

The complex was developed by orders of NASA (USA) and military departments of Germany and Italy. Jet Propulsion Laboratory, Ball Communication (USA), Domier (Germany) and Selena (Italy) companies designed the equipment. The complex consists of three radars with aperture synthesis operating in L (1248 MHz), C (5298 MHz) and X (9600 MHz) bands. Radiation power in the pulse is 4.3, 2.25 and 3.3 kW accordingly. Swath width – 15 to 90 km (SIR-C) and 15–40 km (X-SAR). Bearing resolution is 30 m, range resolution – 13 or 26 m (two options). In the telescopic mode, range resolution of 8–10 m can be achieved [22].

3.2.12 French ERS Space Vehicle Osiris Based on Radar 2000 Project

Customer – French Department of Defense, contractors – Matra Marconi Space and Alcatel Espace. This space vehicle is equipped with SAR of the centimeter range, which ensures resolution of 3–5 m at swath with of 30–50 km.

An example of a modern commercial ERS SV with SAR capable of solving a wide range of tasks, including military ones, is the German satellite of radiolocation Earth survey TerraSAR-X, which was placed in the sun-synchronous orbit on June 15, 2007 and is still successfully working. German space agency DLR defrayed most of the expenses for TerraSAR-X and became the partner of the German branch Astrium GmbH of the European concern EADS. An important fact for understanding the financial side of the project that the share of DLR in this project amounted to €102 million, the share of EADS – to €28 million with the total project cost of €130 million. Target equipment of the satellite was presented by the synthesized aperture radar TSX-SAR – polarimetric multi-channel complex with a weight of 394 kg with active PAA of the X-band (9.65 GHz frequency) with high spatial and radiometric resolution comparable to resolution of aviation SARs. The radar was created on the basis of technologies obtained by Europeans during flights of shuttles with SIR-C and SRTM radars in 1994 and 2000. Onboard active PAA has overall dimensions of 4.8 × 0.8 × 0.15 mm and consists of 384 transceiver modules.

This radar complex ensures survey of surface of the Earth in three main modes: projector, routing and scanning ScanSAR. Spatial resolution characteristics (by bearing):

- 1–2 m (projector);
- 3 m (routing);
- 16 m (scanning ScanSAR).

Frame size:

- (15–10) × 10 km (projector);
- 30 × 50 km, route length 1500 km (routing);
- 100 × 150 km, route length 1500 km (scanning ScanSAR).

Swath width: 463 (up to 622) km (projector); 287 (up to 622) km (routing); 287 (up to 577) km (scanning ScanSAR).

TSX-SAR also has several so-called experimental modes:

1. Super-detailed mode with range resolution under 1 m (up to 0.5 m) with the use of radio signals with spectrum width of 300 MHz.
2. ATI (Along Track Interferometry) mode in which, due to redundancy of electronic PAA modules, this radar can receive signals through separate channels from two PAA sub-arrays (Dual Receive Antenna, DRA) 2.4 m long each, and after comparing signals from two sub-arrays, specific moving objects can be identified. In continuation of this project, Germa space agency DLR began

development of two additional projects (TanDEM-X and TerraSAR-X2) in 2010. TanDEM-X project (EUR 85 mln.) is also funded by partnership: €56 million is provided by DLR, €26 million – by Astrium EADS, €3 million – by other investors.

Taking into account high cost of ERS SVs with SARs, a promising direction is creation of light space-based SARs with high resolution for small SVs. Speaking of Russian projects in this direction, it should be noted that the Russian scientific and production enterprise "Vega" is designing light space-based SARs, which can be put into orbit by ballistic missiles, including the ones removed from combat duty. Such super-high resolution SARs for small SVs can operate at wavelengths of 9.6 cm, cover the redirecting band of 500 km and ensure the following resolution:

– 2 m (during detailed observation and with swath width of 10–20 km);
– 5–7 m (during observation with reduced resolution and with swath width of 50–100 km);
– 15 m (during observation with low resolution and with swath width of 150–200 km).

At the same time, total weight of the radar equipment does not exceed 250 kg, while its power consumption remains at the level of 1300 W.

Based on the above, we can draw up the following basic conclusions [1].

1. Requirements for engineering of SAR are specific and often contradictory, since they depend on many factors [20]. When using radar information of ERS for navigation tasks, coverage of greater planet areas is required, and it is necessary to achieve the best possible resolution. However, high resolution can usually be ensured only with small swath width and frame dimensions. For most space-based SARs, the ratio of the swath width to resolution in the bearing direction is less than 10,000; i.e., resolution of 5 m cannot ensure swath width greater than 50 km.
2. Brief overview of ERS space vehicles with SARs presented in this section demonstrates great interest of space nations in such systems, which have been developing rapidly in recent time despite their extremely high cost. Directions of further development of ERS space vehicles with SARs are determined by requirements of data consumers to a great extent, but have significant theoretical and technical limitations caused, for example, by the diffraction limit of achieving high resolution, energy resource of the radar set, complexity of data processing algorithm and speed of operation of computing machines, throughput capacity of the data transmission line, etc.
3. Taking into account the technical contradiction between achievement of high resolution and the desire to obtain great swath width, it is possible to predict the trend for development of SAR in the direction of increasing their resolution, which significantly expands possibilities of such systems. This contradiction can be practically resolved by transition from narrowband signals to wideband ones with simultaneous use of wide-angle apertures. Since the theoretical resolution

limit has not been reached yet, it is necessary to continue scientific studies and search for new methods and means of increasing resolution.

Achievement of high SAR resolution is especially relevant for the use of radar location information to solve military tasks, as well as navigation and traffic control tasks.

It is clear that the problem of further development of this advanced technical direction can only be solved with the help of latest achievements of microwave electronics, using modern electronic component base.

3.3 Ground Penetrating Radars with Increased Resolution

Ground penetrating (sub-surface) radar is a radar which, unlike classic device, is used for probing of the *surveyed medium* instead of *air space*. The studied medium can be ground (hence the most popular name of this device – ***georadar***), water, building walls, etc. The most widely known use of ground penetrating radars is the search for anti-personnel and anti-tank mines and various explosive devices planted by the enemy [23, 24].

Figure 3.6 shows general appearance of one of these non-secret products – Russian georadar "OKO-2".

The design of this ground penetrating radar consists of three main parts: antenna part, recording unit and control unit. It is known that the main electronic unit of any GPR consists of standard electronic components, which usually perform the following main functions: generation of pulses radiated by the transmitting antenna, digital processing of signals received from the receiving antenna and synchronization of operation of the entire system. The antenna part usually includes receiving and transmitting antennas. Recording unit is usually represented by a standard digital control unit, which includes microelectronic devices, system of cables and optical-electrical converters.

Fig. 3.6 Russian georadar "OKO-2" [1]

As is known from the history of development of georadars, first serial georadars appeared in the beginning of the 1970s; in the middle of the 1980s, the interest in georadiolocation increased due to emergence of a new generation of microcircuits and semiconductor devices. However, the costs of their production at that time could not pay off, and the interest in georadiolocation disappeared again. In the 1990s, when highly integrated analog-digital VLSIs appeared, and personal computers became more available, the interest in georadiolocation increased once again and still remains high. As of the moment of publication of this book, there are over a hundred manufacturers of georadars in the world.

The largest foreign manufacturers of georadars are GSSI (New Hampshire, USA), Sensor and Software Inc. (Canada), Era Technology (Great Britain), Geoscanners AB and MALA (Sweden), Radar Systems (Latvia), OYO corporation (Japan), Geozondas (Lithuania) and Transient Technologies (Ukraine).

In Russia, development of georadar technologies is carried out by LLC "VNII SMI" – LOZA georadars, CJSC "TIMER" – Grot georadars equipped with antennas for various purposes, as well as LLC "LOGIS" (officially represented by Scientific and Production Center of Georadar Technologies, SPC LLC "GEOTECH") – OKO-2 georadars (shielded and horn antennas with a wide range of frequencies).

Ground penetrating radars are usually used for monitoring of objects, detection of hidden underground objects, soil waters, etc.

Operating principle of ground penetrating radars is the same as in regular radars. Two types of ground penetrating radars are identified: these are pulsed radars and frequency-modulated radars (including with stepwise frequency variation).

Let us consider the main design features, structure and ways of hardware implementation of georadars with increased resolution [24].

As is known, ultra-wideband (UWB) radar location has achieved great success over the last few decades. Since the fields of application of georadars are always expanding [25], requirements for qualitative parameters and characteristics of such georadars are also constantly increasing.

From the practical point of view, two parameters of a GPR are most important: probing depth and resolution. In order to estimate the maximum probing depth, the following ratio is usually used [26]:

$$H_{\max} = \sqrt[4]{\frac{P_{\text{пд}} G^2 \lambda^2 \sigma_{\text{ц}}}{(4\pi)^3 P_{\text{ш}}}} \times \exp^{-0{,}115 H_{\max} \Gamma}, \tag{3.4}$$

where A is the attenuation in the medium, dB/m; P_t is the pulse power of transmitter radiation, W; λ is the wavelength, m; σ_T is the target RCS, m^2; G is the antenna gain; P_n is the noise power supplied to the receiver input, W.

This ratio was first obtained for narrowband sinewave signal (this is why the λ parameter is used) if the radar operates in the far field.

If the georadar operates in the near field, there is no solution of the known Maxwell equation for this case at the moment, and specialists use the reduced ratio in the first approximation by replacing the wavelength λ with $c/2\tau_p$ (τ_p is the pulse duration).

As follows from (3.4), possible ways of increasing probing depth are limited. For example, increase in $H_{\max}$ at the expense of the wavelength λ is impractical, since in causes a significant reduction in the resolution of the georadar, while the possibilities of increasing probing depth at the expense of increasing the transmitter power have mostly been tested and proven ineffective.

In this regard, increase of the probing depth without affecting georadar resolution, according to specialists [24], can mostly develop in the direction of reducing the power of noise supplied to the input of the UWB radar receiver.

The main function of receiver of any radar system with UWB signals consists in reception, amplification and registration of changes in time of strength of the magnetic field dispersed by the probed object. Therefore, radar receivers with pulsed UWB radio signals are usually designed as linear wideband amplifiers. The required pass band width of such amplifier shall conform to the width of the spectrum of the probing UWB radar signal, which reaches several GHz in the centimeter band.

Wideband amplifier installed directly at the input of the receiver determines the level of noise of the entire receiver supplied to the input. Suggesting that the gain factor of the wideband amplifier is constant within the entire frequency range, the power of the noise supplied to the receiver input can be approximately estimated as follows:

$$P_{\text{ш.пр}} \cong N_0 \Delta f_{\text{сшп.рлс}}, \tag{3.5}$$

where

N_0 is the spectral density of the noise supplied to the input of the receiver; $\Delta f_{\text{uwb rs}}$ is the pass band of the UWB radar station.

Noise power P_{nr} is extremely significant due to the required large pass band width $\Delta f_{\text{uwb rs}}$, and if special measures are not used, the only method of reduction of P_{nr} clear from (3.5) is the use of wideband amplifiers with minimum possible noise temperature T_{n} in the georadar receiver.

As a rule, TWTs with noise factor of about 3–5 dB, which corresponds to $T_{\text{n}} \approx 500$–1000 K, are used in the SHF range as wideband amplifiers of such devices. The use of TWTs as wideband amplifiers of the microwave range at frequencies about 10 GHz with frequency band $\Delta f \approx 5$ GHz gives $P_{\text{rn}} \approx 10^{-10}$ W, which is 4–5 orders of magnitude worse than the corresponding parameter for traditional (narrowband) radars.

It should be noted that further reduction of TWT noise factor values beyond these values is extremely problematic, and they are therefore threshold values for wideband amplifiers of the microwave range in UWB radars. The presented estimated calculations demonstrate that the value of P_{rn} can only be reduced by using the filter matched with the received signal [24]. However, these ideas are debatable, since several papers [24, 25] state that matched filtration can destroy the waveform, which contains information about geometrical parameters of the object. Therefore, complex solution to the problem based on methods of matched filtration, increase in probing depth and resolution of the georadar is of interest.

When building the structure of the receiver of such UWB radar, it is necessary to take into account that both radiated and reflected signals are UWB signals of the SHF range with complex waveforms.

The main ways of implementation of matched filtration ensuring an increase in resolution and depth of ground penetrating probing of a georadar are detailed in [24].

For example, it is known that a classic matched filter can be practically implemented on the basis of a linear parametric oscillation system, and the calculation of synthesis of the pumping signal of the parametric selective filter shall ensure emission of a complex signal supplied to input of the georadar receiver by the matched filter. In other words, the procedure of processing of the signal reflected from the object in the modernized receiver of the georadar shall use the structure of the received reflected signal itself to form the pumping signal. Since the reflected signal is usually unknown a priori, setting of the parametric selective filter of the microwave range (formation of the pumping signal) shall be preceded by preliminary and at least approximate determination of the signal reflected form the object and supplied into the receiver of the georadar.

This requirement can be met by using additional receiver of the classic (without matched filter) design as a part of the modernized receiver. Practical implementation of the pumping signal synthesis procedure shall be based on the following baselines:

– Pumping signal is formed as a set of sinewaves of frequencies divisible by the signal radiated by the transmitter, amplitude and phase, which are determined by the signal subject to filtration according to the algorithm described in [27].
– Frequency values of pulses radiated by the transmitter and received by the receiver coincide.

Thus, in such modernized georadar, the signal received from the output of the classic receiver is first used as a basis for formation of the pumping signal of the parametric selective filter of the microwave range [27], after which parameters of the studied object are measured with the help of the receiver based on the matched filter. These measurements shall give clearer and more detailed information about the studied object.

Figure 3.7 shows the approximate structural diagram of such modernized receiver of a GPR.

In the following, we are going to take a detailed look at purpose and features of specific hardware implementation of the structural diagram of georadar modernized receiver described above.

As can be seen from this structural diagram, organization of the pumping signal is performed according to the following algorithm.

First, the signal from the output of the scale-time converter of the georadar receiver designed according to the classic circuit is supplied to the computer. The computer (microcomputer) uses the algorithm described in [27] to calculate amplitudes and phases of harmonics of the pumping signal. From the computer output, the signal is supplied to the pumping signal conditioner, which simultaneously receives

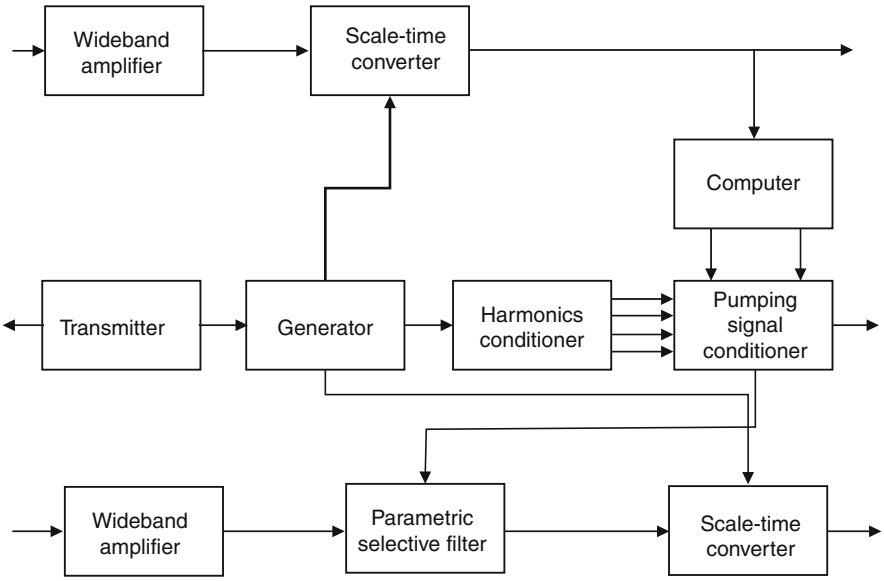

Fig. 3.7 Approximate structural diagram of a modernized georadar receiver [1]

the signal from the pumping signal harmonic conditioner. The conditioner is a system of resonators to which the signal from the transmitter pulse generator is supplied. Pumping signal conditioner is a system of controlled attenuators and phase shifters of the SHF range, the aim of which is to ensure organization, management and control of the pumping signal. From the conditioner output, the pumping signal is supplied to the parametric matched filter of the SHF range, where it is used to control parameters of the matched filter. Pumping signal conditioner is the most critical and complex unit of the modernized georadar receiver. Its organization is associated with solving a significant number of complicated engineering tasks and thus requires to be considered separately.

Structurally, parametric selective filter of the microwave range can be implemented by various means. One of these means is the use of one-dimensional, spatially uniform wave systems (UWS) with non-stationary conditions at one of the borders. Such parametric filter of the microwave range consists a spatially uniform autonomous UWS without dispersion as the main element. Examples of such UWS include coaxial wave structures, symmetrical strip lines and other similar structures.

A very important task is the creation of non-stationary boundary conditions for the UWS class described above. In fact, the studied class of linear parametric oscillation systems (LPOS) with distributed parameters includes devices containing of a stationary oscillation system, which in our case is based on a section of spatially uniform independent UWS, in which creation of periodic boundary conditions ensures effective control over the frequency of self-oscillation of this stationary

oscillation system. In order to achieve parametric effect, control (pumping) frequency shall have the order of intrinsic oscillation of the stationary system; moreover, in case of such periodic control of the frequency of intrinsic oscillations certain requirements shall be met.

The most significant requirements are:

- Independence of parameters of elements of LPOS with distributed parameters controlling frequencies of intrinsic oscillations of the system on the field of the selected signal.
- The possibility of achieving the required range of frequency variation of intrinsic oscillations of LPOS with distributed parameters.
- Ensuring the possibility of influencing the control element by pumping field without affecting the structure of fields (characteristics, parameters) of UWSs, on the basis of which the LPOS with DP is organized.

As is known, the listed requirements in practice can be met with a certain degree of accuracy.

Currently available methods of organization of periodic boundary conditions can be divided into two categories:

- The first one includes methods of organizing periodic boundary conditions at the limits of UWS based on the use of electronic circuits with quasi-concentrated active and passive elements. Such methods of organization of periodic boundary conditions are possible in the low-frequency part of the microwave range (from hundreds of MHz to several GHz).
- The second category includes the methods of organization of periodic boundary conditions at the limits of UWS based on the use of controlled active elements (materials), which change their properties (such as dielectric or magnetic permittivity) under the effect of foreign electrical fields, the frequency of which is higher than the pumping frequency by several orders of magnitude. Pumping control signal in this case is used as the signal modeling the side electrical field. This method of organization of periodic boundary condition is preferable and can be used within the entire microwave frequency range where LPOSs with distributed parameters are applicable. One of the most promising directions in the creation of LPOSs with distributed parameters for the microwave range consists in using dielectrics with controlled permittivity as active elements in resonators. The use of active dielectrics helps solve the entire range of problems associated with the need to satisfy the above special conditions, which ensure the possibility of practical implementations of LPOS with distributed parameters. The use of new active materials here looks very promising for microwave equipment.

It should be noted that linear parametric oscillation systems (LPOS) are most effective in building matched filters for narrow-band signals. With extension of the band of the signal to be filtered, complexity of the pumping structure signal increases together with complexity of hardware implementation of LPOS.

3.4 Ultra-Wideband Devices of Radar Systems

3.4.1 Basic Characteristics of UWB Devices

As is known from print, over ten years ago a decision was made in the USA to legalize operation of ultra-wideband (UWB) radiosystems on a non-licensing basis [28–30]. After that, operation of UWB devices has been legally allowed in the Russian Federation, Canada, Europe, Japan, South Korea, Taiwan and other countries. Features of such UWB devices are described below.

First of all, it is necessary to consider the specifics of development of UWB devices in the USA.

According to part 15F, Volume 47 of the US Code of Federal Regulations [31], a UWB transmitter ıσ a radiator that at any moment in time has the relative band equal to or wider than 0.20 or an absolute band equal to or wider than 500 MHz regardless of the relative band. Absolute frequency band in this case is measured at the −10 dB level relative to the radiation maximum. As follows from the definition, this requirement applies only to radiating UWB devices. If the device is a receiver of UWB signals, its operation is regulated by other parts of the American legislation. In addition to the bandwidth, a UWB transmitter is characterized by the operating frequency range, radiated power, level of parasite radiation and the field of application.

US rules also establish requirements for wideband devices, frequency band of main radiation of which shall be not less than 10 MHz (part 15C, §15.252) or 50 MHz (part g15C, §15.250) with disabled modulation, with step-wise tuning of the carrier frequency and can exceed 1 GHz, including effects of frequency modulation and other types of modulation.

It should be noted that wideband signals today are mostly used in the frequency range of up to 10 GHz; UWB radiation is a sequence of short radio pulses with the duration of 1.0–5.0 ns. The spectrum can include local maximums of high amplitude, e.g. to the right of the main maximum (Fig. 3.8) [32].

Frequency bandwidth Δf of such UWB radiation is determined taking into account the local maximum.

The procedure of device registration in the USA consists of the following stages:

- determination of the class of the UWB device;
- measurement of the basic parameters by authorized companies; parameters include: main radiation bandwidth, medium and peak power radiated by the device, parasite radiation, etc. in accordance with the requirements for this class of devices;
- gathering of documents, which shall include: report on measurement of device parameters; photographs of the device during measurement (general view); enlarged photographs of the device on the inside and on the outside including its identification number registered by the committee; block diagrams; description of the operating principle; operation manual; confidentiality request if the

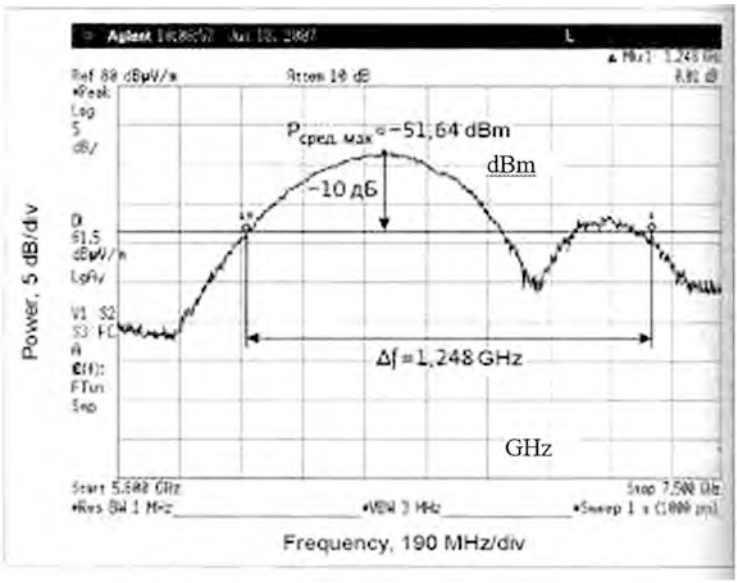

Fig. 3.8 Radiation spectrum of the RAD635 UWB radar by Zebra Technologies (USA) [1]

provided documents constitute a commercial secret. In addition to the above, the commission can also demand provision of specification documents;
– registration of the submitted documents by the USA Federal Communications Commission.

Let us take a look at the classification of UWB devices, as well as certain specific features of each class.

3.4.2 Classification of US UWB Radars

According to the US Code of Federal Rules mentioned above, the following types of ultra-wideband penetrating radars are identified.

3.4.2.1 Radars of Sub-surface Probing of Building Structures

Radiation of these radars can have any band and be within any frequency range from zero to 10.6 GHz. Permitted radiation power varies depending on the used frequency range.

3.4.2.2 Through-The-Wall Radars

The use of such devices is limited by state law enforcement structures, fire and emergency services.

3.4.2.3 Stationary Surveillance Radars

Similarly to the previous case, the use of stationary radars is permitted only to state structures, as well as separate communal services and industrial enterprises.

3.4.2.4 Medical Visualization Systems

They can only be used under control or supervision of practicing medical specialists.

3.4.2.5 Automobile Radars

Frequencies allocated for operation of such devices are within the range of 22–29 GHz. Operation of the radar is allowed only on ground vehicles with engines on.

3.4.2.6 Stationary UWB Systems (for Indoor Applications)

As a rule, these are stationary systems with limited mobility connected to the electrical network. They include modules for wireless UWB communication integrated into stationary computers and laptops, radio access points, demonstration UWB equipment, and beacons of local equipment positioning systems.

3.4.2.7 Mobile (Portable) UWB Systems

Small-sized devices that are not linked to a fixed infrastructure. They include wireless adapters for UWB communication connected, for example, to USB ports of personal computers, beacons of local equipment and personnel positioning systems with autonomous power sources, etc. These devices have their specifics in terms of signal transmission mode. If the confirmation from the receiver for which the transmission is designed is not received within 10 sec, the transmission stops. Such confirmation shall be received by the device at least every 10 sec. Vast majority of these UWB devices are designed for provision of wireless communication services.

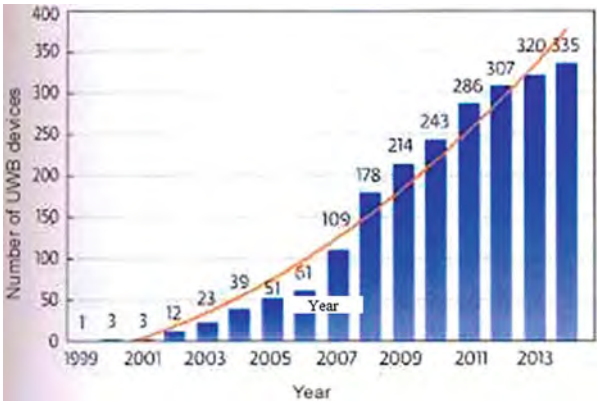

Fig. 3.9 General dynamics of changes of UWB devices in the US market [1]

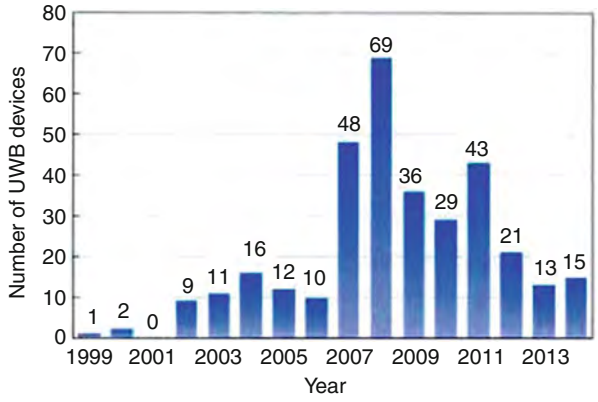

Fig. 3.10 Number of new types of UWB devices annually appearing in the US market [1]

As of the beginning of 2015, over 350 types of UWB devices were presented in the US market [33], and the dynamics of their growth (Fig. 3.9) shows that the market is far from being saturated. A number of new UWB devices appear every year (Fig. 3.10), and their functional possibilities and technical characteristics are constantly improving. The USA is the undisputed leader among the countries offering their products – 223 device types as of the end of 2014; other countries offer significantly smaller numbers (Fig. 3.11).

Also interesting is the distribution of the number of device types attributed to different paragraphs in accordance with the above classification, as well as described in paragraphs 15.250, 15.252 of the US Federal Code (Fig. 3.12). §15.250 includes tags of UWB system of local positioning operating outdoors. Formally, these devices cannot be attributed to any of the paragraphs of section 15F. The closest is §15.517; however, according to it, operation of UWB devices outdoors is not allowed. Requirements of §15.519 are not met by these devices either, since some beacons of UWB positioning systems are only used as transmitters and cannot ensure confirmation about receipt of the transmitted information.

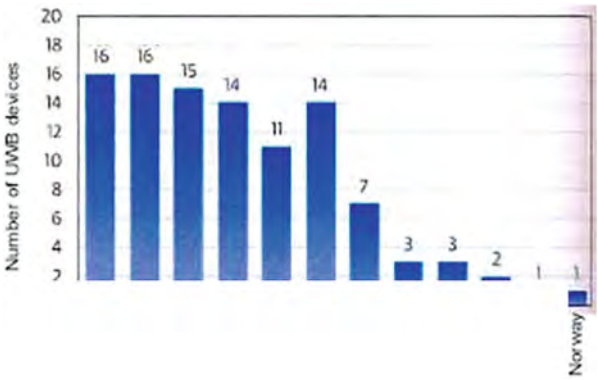

Fig. 3.11 Distribution of the number of sold UWB devices in the US market (2016) [1]

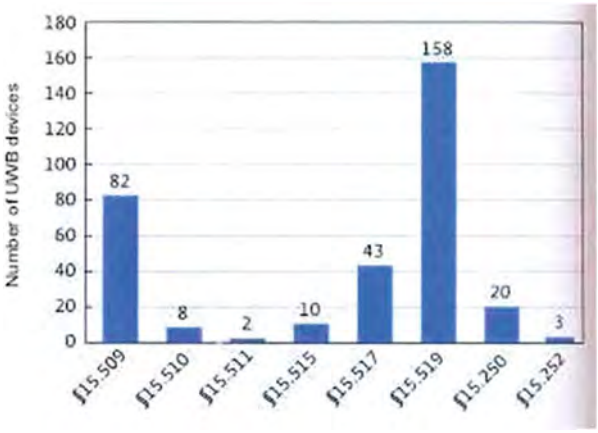

Fig. 3.12 Number of types of UWB devices in the US market operating in accordance with different paragraphs of Part 15 of the United States Code (2016) [1]

As of today, no medical devices have been submitted for operation in accordance with the requirements of §15.513. There was a Canadian company [34] that entered the US market with a medical device, but it was submitted for operation in accordance with the conditions of §15.517. This circumstance is due to duration and high cost of clinical tests of devices for medical applications.

All UWB devices registered in the USA can be divided into three categories – devices for radiolocation, radio communication and radio navigation (Fig. 3.13). Most devices (56.4%) are used to solve radio communication tasks.

Today, UWB radio communication is used at distances of up to 10 m in the following applications (Fig. 3.14): for organization of wireless interface USB 2.0; in wireless local area computer networks of data transmissions with speeds of up to several GB/s (by mini PCI modules); in modern VGA and audio adapters, as well as in multi-purpose multi-functional devices for transmission of different data types (e.g., designed for translation of high-definition images from the X-ray apparatus). This category also includes specialized devices – generators of UWB signals with the possibility of reception and analysis of received signals and data protocols.

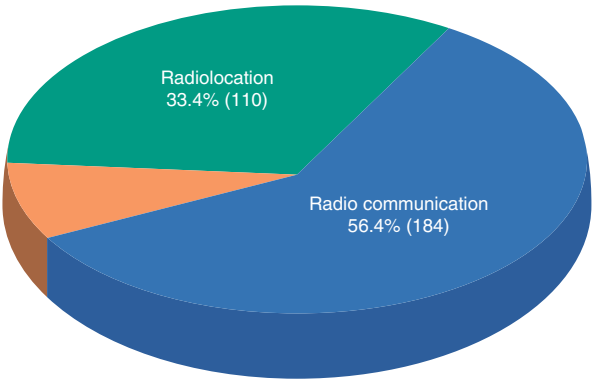

Fig. 3.13 Classification of UWB devices. The absolute number of device types of the specific category is given in brackets [1]

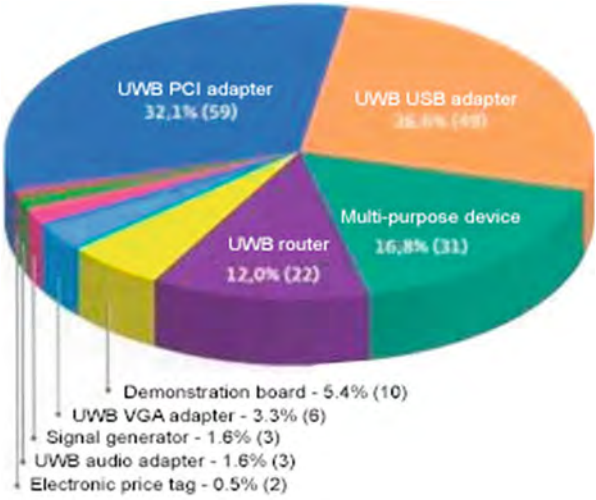

Fig. 3.14 Main fields of application of radio communication UWB devices in the USA [1]

Unlike radio communication devices, which solve a limited set of tasks, radar UWB devices are used in many applications (Fig. 3.15). Non-destructive testing is implemented by system of UWB geolocation and location of construction objects. UWB radars installed on vehicles perform functions of automatic cruise control and control of blind spots. Through-the-wall UWB radars are used to ensure security in civilian and military purposes. Portable (consumer) UWB devices of detection of reinforcing elements and foreign objects in walls are used in the field of repair and construction. UWB radars of perimeter and territory control are used for protection of commercial and private objects. UWB radars for measurement of levels of liquids (including toxic) and bulk products are used in industry. In medicine, UWB radars are used to diagnose lungs and cardiovascular system of patients.

Radio navigation UWB signals are represented by tags (reference signal transmitters), as well as systems for demonstration of possibilities of the UWB

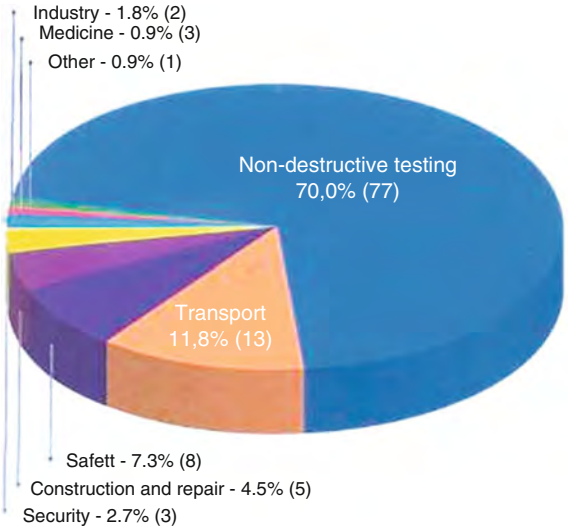

Fig. 3.15 Main fields of application of radar UWB devices [1]

technology in this field. It should be noted that UWB radio navigation for indoor applications is considered as the basis for the system expanding and supplementing possibilities of global navigation systems GLONASS/CPS.

It is interesting that not all UWB devices presented in the US market strictly follow the requirements of the applicable legislation. If necessary, a petition is filed to the Federal Communications Commission of the USA with substantiation of the exception that shall be made for this device. After reviewing the substantiation, Commission issues a resolution on its partial or full approval or rejection.

3.4.3 Development of UWB Technology in Russia

Products of Russian companies are not directly presented in the world market; however, Russian engineers widely participate in the development of UWB technology. Today, there are more than ten companies in Russia [35–41], the activities of which relate to all fields of application of UWB technology: sub-surface probing radars, through-the-wall radars, area protection radars, medical UWB devices of various purposes and UWB radio communication systems (Table 3.2).

Therefore, the number of new UWB devices in markets of different countries is increasing every year. Many companies extend the areas of their business after achieving success in their countries. In general, recent years can be considered successful for the UWB technology, which has demonstrated its consistency and is not going to give in to other quickly evolving technologies, constantly finding new niches for application in civilian and military spheres.

Table 3.2 Main Russian manufacturers of UWB devices [1]

Company	The list of produced UWB devices
Scientific and Research Center for Ultra-Wideband Technologies of the Moscow Aviation Institute	System of territory protection from unauthorized entrance of people and vehicles system of exact positioning of staff and (or) equipment in a building or within an area
	Radar for detection of people behind optically non-transparent obstacles
	Radar for remote monitoring of psychophysiological indicators
	Radar for round-the-clock monitoring of breath and heart rate of patients in reanimation, burn wards of hospitals and children's wards of maternity houses
	Device for measurement of pulse wave velocity and heart rate variability, etc.
LLC Smolensk Science and Innovation Center for radioelectronic systems "ZAVANT"	Ultra-wideband radio line of high-speed data transmission; measuring complex for study of reflection of UWB signals; UWB radar for detection and monitoring of human breath; UWB radar for control of filling of marshalling tracks; UWB radiolocation device for UWB antenna range measurement, etc.
IZMIRAN, Troitsk	Georadars of the "Loza" series (Loza-V, Loza-N), including radars for river and marine applications.
LLC "Nanochaos"	Ultra-wideband small-sized transceiver PPS-40 for wireless personal communication systems
	Ultra-wideband transceiver PPS-50 for creation of wireless sensor systems
	Active ultra-wideband radio tags (RFID)
	Educational and Scientific Complex "Ultra-Wideband Wireless Sensor Networks" UWB micro-transmitter "KROSH"
	UWB wireless sensor network.
NPP "TRIM"	UWB digital strobing recorders, oscillographs and S-parameter gauges
	Generators of ultra-short video- and radio pulses of UWB antennas
	Automated UWB complexes for measurement of antenna parameters (in far field, in near field and with the use of collimator)
	Automated UWB complexes for measurement of radar location characteristics of objects (in far field and with the use of collimator)
LLC "LogiS"	OKO-2 georadars
LLC "NanoPulse"	Baby sleep guard bedside monitor monitor for maby incubators sleep apnea detector pneumothorax detector pulse wave velocity meter

(continued)

Table 3.2 (continued)

Company	The list of produced UWB devices
OJSC Design Center for Pilot Works	Ice thickness measuring device Pikor-Led 2M
	Device for road surface monitoring Pikor-Avtodor
	Device for detection of movement behind obstacles Pikor-Bio
	Set of search georadar Pikor-Geo
	UWB antennas
	UWB modules
	UWB developer sets, etc.

3.5 Linear FM Ground Penetrating Radar with Increased Resolution

3.5.1 Structure of a Ground Penetrating Radar with Ultra-Wideband Quasi-Continuous Linear FM Signal

Frequency method of altitude metering [41, 42] along with traditional use during creation of radio altitude gauges [42–45] and short-range radar systems [45–49] is also actively used for implementation of ground penetrating probing systems [49–53]. Operational specifics of such systems is associated with work in the near zone. Express multi-beam character and high value of signal attenuation in solid media are observed [54]. At the same time, requirements for revolution can be equal to single centimeters. Moreover, there are limitations on the size of the antenna system structure, while compliance with sanitary norms determines the permissible power of the probing signal. Ultimately, parameters of the path shall conform to special requirements [55, 56]: generation and processing of the microwave signal by linear frequency modulation (linear FM signal) in the microwave range with pass band of about 1 GHz; isolation between receiving and transmitting channels – not less than 30 dB; dynamic range of the signal processing path – over 60 dB; sensitivity of the receiving path – below 60 dBm.

The paper [57] suggest an original design of a linear FM ground penetrating radar with increased resolution, including specifics of technical implementation of the path of formation and processing of ultra-wideband quasi-continuous linear FM signals.

Classic structure of the ground penetrating radar [53, 58, 59] using frequency method of measuring distance to the object and time diagrams explaining its operation are shown in Fig. 3.16.

Voltage-controlled oscillator (VCO) ensures formation of the probing wideband linear FM signal with the modulation law set by the control voltage at its input (Fig. 3.16, b, full line), which changes in a linear manner according to the sawtooth-

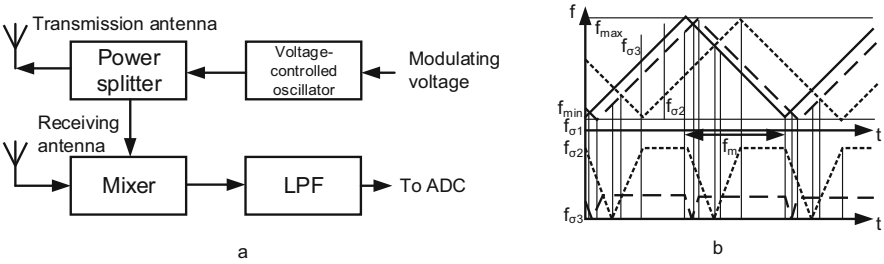

Fig. 3.16 Frequency method of range determination: **a** – classic radar structure; **b** – functioning diagram

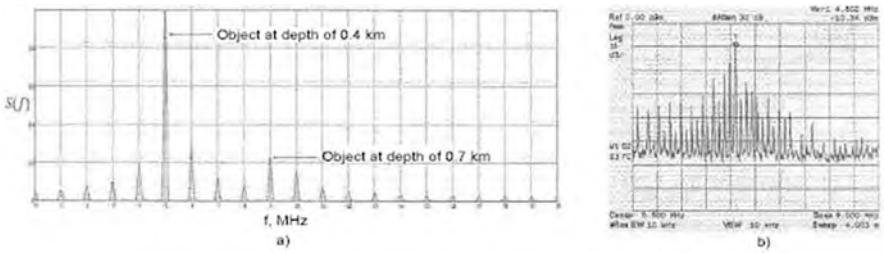

Fig. 3.17 Spectrum of differential frequencies: **a** – modeling results; **b** – experimental data

like law. The generated signal is divided into reference and probing components with the help of the power splitter and supplied to the heterodyne input of the splitter and the transmitting antenna. The signal reflected from the object (Fig. 3.16, b, dashed lines) is received by the receiving antenna and supplied to the signal input of the mixer, where it is multiplied by reference component. As a result, frequency components of beating are extracted (Fig. 3.16, b, $f_{\delta 1}$ and $f_{\delta 2}$), which are proportional to the distance to objects. Low pass filter (LPF) at the output of the mixer prevents overlapping of high-frequency components with the low-frequency component of beating during analog-digital conversion.

Figure 3.17 shows examples of spectral patterns of radio observation of sub-surface objects, obtained by modeling and experimental studies of the classic structure described above [55].

Clearly, the implemented classic structure of a ground penetrating radar makes it impossible to form clear depth pattern of the object due to insufficient resolution of the system.

One of promising ways of solving this problem consists in using adaptive algorithms of superresolution, which can increase radio location pattern resolution up to five times depending on the signal-to-noise ratio at the input of the system [60]. However, their practical implementation demands synchronization of operation of the transceiver path and spectrum analyzer to ensure possibility of analysis of one period of the received signal as digitalized implementation, which is strictly linked to the probing signal in the time domain.

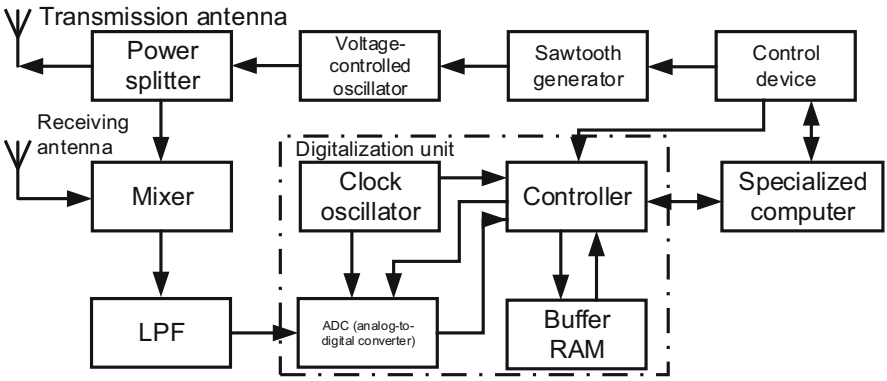

Fig. 3.18 Structure of ground penetrating radar with formation and processing of ultra-wideband quasi-continuous linear FM signals [1]

The structure of ground penetrating radar, which makes it possible to form single linear FM pulses and process them as quasi-continuous oscillation is shown in Fig. 3.18. Here, similarly to the classic circuit shown in Fig. 3.16, beating frequencies are formed at the output of the mixer, which contain information about the probed object, and the characteristic feature consists in the presence of the sawtooth generator synchronized with the digitalization unit. Control device sets the operation mode of the radar by forming drive pulses of the sawtooth generator and digitalization unit with the required period and helps set timing position of the analysis window relative to the moment of beginning of probing pulse generation. Upon receipt of the clock pulse, the sawtooth generator generates one period of linearly changing voltage, which serves as a modulating pulse for the VCO, and the RAM records the given number of samples of implementation of the mixer output signal. AD converter is launched by highly stable clock generator ensuring fixed duration of the analysis window. After the memory buffer is filled, digitalization unit transmits the obtained implementation of the signal to the specialized computer, where it is digitally processed in order to form a depth pattern of the tested environment.

As a result, due to synchronization of the digitalization unit with the transmitting path, obtained implementation of differential oscillations are fixed to frequency deployment, which makes it possible to analyze a single signal period containing full information about the depth pattern. Therefore, it becomes possible to apply algorithms of superresolution operating in real time scale.

3.5.2 Path of Generation and Processing of Ultra-Wideband Quasi-Continuous Linear FM Signals of Ground Penetrating Radar

Transceiver path of the developed ground penetrating radar is designed using integrated microcircuits of the microwave range (Fig. 3.19, a).

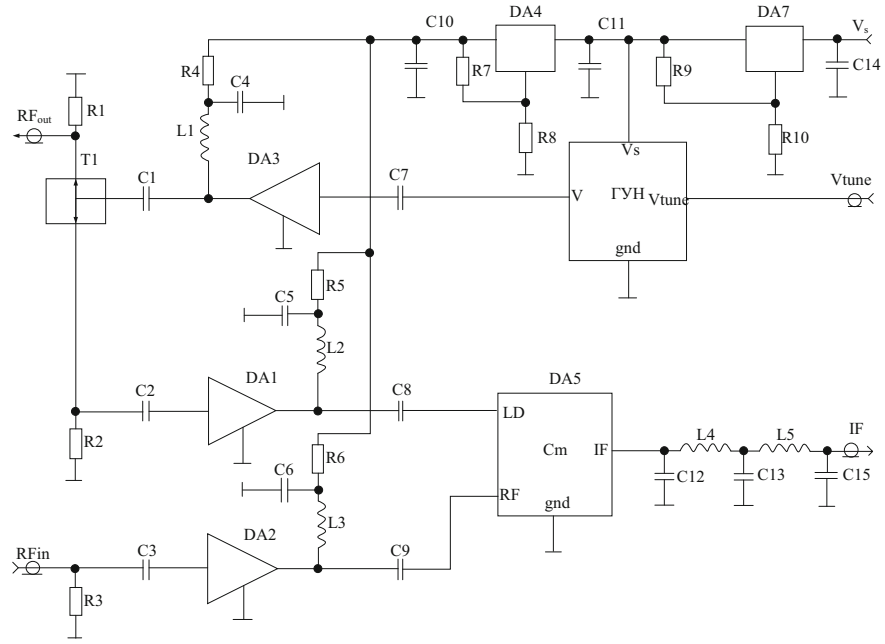

a)

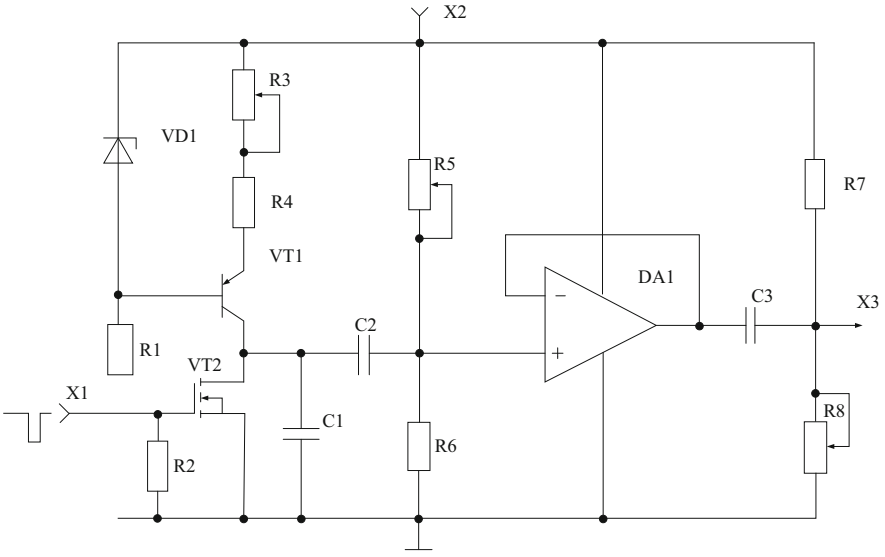

b)

Fig. 3.19 Diagram of a ground penetrating radar: **a** – transceiver path; **b** – sawtooth pulse generator with synchronous launch [1]

Modulating voltage formed by the sawtooth generator is supplied to the modulation input of the VCO DA6 microassembly. The obtained wideband linear FM signal is amplified by the micro-module DA3 and supplied from the RFout output through the power divider to the radiating antenna; from the other output of the divider, the signal is supplied to the heterodyne input of the integrated mixer DA5 through the integrated amplifier DA1. RFin input is connected to the receiving antenna recording reflected signals, which are supplied to the signal input of the mixer DA5 through the low-noise integrated amplifier DA2 and then sent to the output of the transceiver path after multiplication by reference oscillation through the low pass filter. Integrated voltage stabilizers DA4, DA7 generate supply voltages required in the circuit.

Diagram of the sawtooth generator of ramp voltage driven by clock pulse is shown in Fig. 3.19, b. Ramp voltage is formed due to charging of the capacitor C1 with stable current, the source of which includes elements VD1, VT1, Rl, R3, R4. Fine-tuned resistor R3 makes it possible to change the capacitor charge current and adjust the pulse amplitude. Operational amplifier DA1 includes a buffer used to exclude the effect of subsequent stages with low input resistance on the capacitor charging process. Circuit C2, R5, R6 and C3, R7, R8 are used for shift tuning. VT2 transistor serves to ensure zero level of the charge of the capacitor C1 until the control pulse is received. Duration of the pulse is determined by the duration of the clock pulse generated by the control device.

Figure 3.20 shows experimental spectrogram of the radar probing signal obtained in the mode of accumulation of samples with saving of the maximum value [57].

It can be seen that the developed path makes it possible to form a pulse with *linear frequency modulation* with duration of 10 μs and frequency variation range

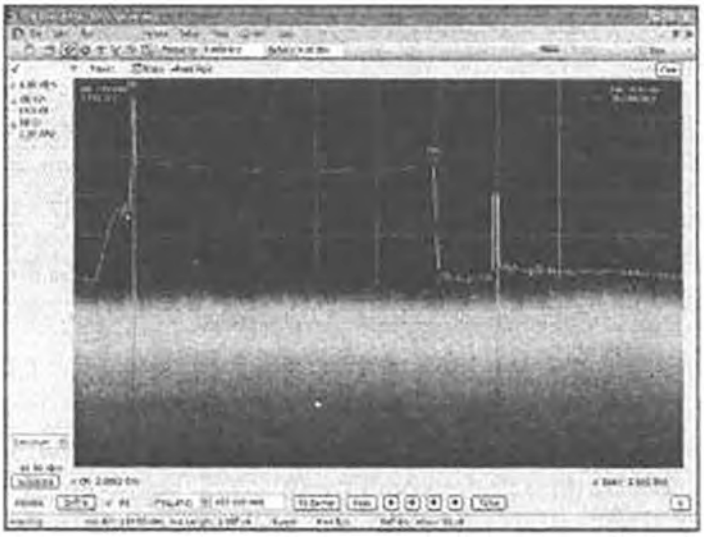

Fig. 3.20 Probing signal spectrum

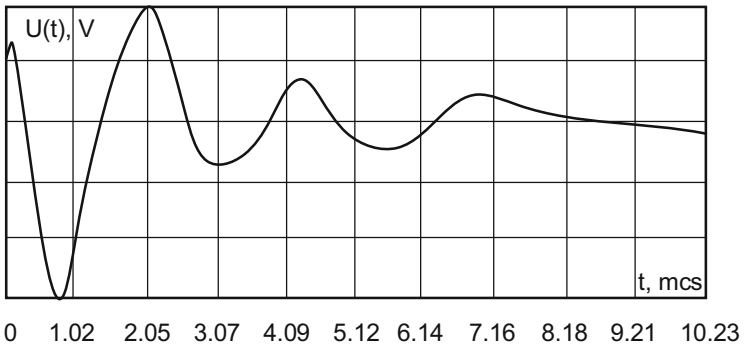

Fig. 3.21 Implementation of the signal at the mixer output

of 1200–2200 MHz, with irregularity of 3 dB. The signal received at the RFin input $u(t) = n(t) + m(t) + h(t)$ is the additive mixture of the interference $h(t)$ (white noise and signal leakage from the transmitting antenna to the receiver antenna), the signal reflected from the ground surface $n(t)$ and buried object $m(t)$. After conversion, differential oscillations $u_r(t)$ are formed at the output of the mixer, the frequency of which is proportional to the distance to reflecting objects. Figure 3.21 shows digitalized implementation of the signal at the output of the mixer in the scale of duration of the probing pulse, achieved during sub-surface detection of the dielectric object.

Design value of the differential frequency is determined by the expression [55]:

$$f_{r_m} = \frac{4\Delta f_0}{T_0 c}\left[r_z + r_m\sqrt{\varepsilon}\right], \tag{3.6}$$

where Δf_0 ισ τηε width of the probing signal spectrum; c ισ τηε speed of propagation of electromagnetic wave in vacuum; ε ισ τηε dielectric permittivity of the tested medium; T_0 ισ τηε duration of the radio pulse; r_z ισ τηε elevation of the antenna module above the ground; r_m ισ τηε depth of the observed object.

Radiolocation pattern P is formed in accordance with the classic Fourier transform or by adaptive algorithm based on the ML (maximum livelihood) method [60]:

$$P = \left[S_O^{\langle n\rangle^T} Q \overline{S_O^{\langle n\rangle}}\right]^{-1}, \quad n = \overline{0,\ N_f - 1}, \tag{3.7}$$

where $Q = R$ ισ the direct covariation matrix obtained for differential frequencies by Fourier transform; $Q = R^{-1}$ ισ the inverse covariation matrix obtained for differential frequencies; N_f *is the* number of elements of the formed depth pattern; S_O *is the* matrix of reference frequencies.

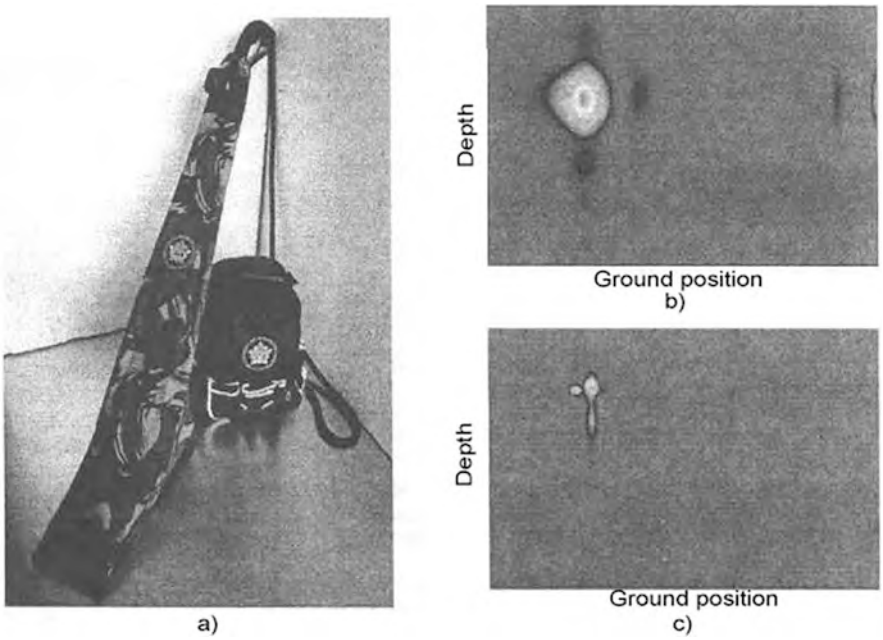

Fig. 3.22 Ground penetrating radar: **a** – structural design; **b** – depth pattern obtained by Fourier transform; **c** – depth pattern obtained by using ML method

Figure 3.22 b, c demonstrates depth patterns of the sub-surface object obtained with the help of the designed radar (Fig. 3.22, a) implementing the described signal processing. The obtained images are an interpretation of combination of the correlation matrix spectra of the received signal during horizontal scanning of the space above the location of the buried object by the radar system antenna.

The presented depth patterns demonstrate efficiency of the considered structure of the linear FM radar and the possibility of adaptive processing of the received signal in real time scale. Also demonstrated was the qualitative increase in the resolution due to use of super-resolution ML algorithms (Keypon's methods [42], which, as opposed to Fourier transforms, make it possible to observe upper and lower boundaries of the buried object and, therefore, classify it based on linear dimensions.

Therefore, the paper [57] suggest an original design of the ground penetrating radar, which makes it possible to implement frequency method of range measurement using ultra-wideband quasi-continuous signal with linear frequency modulation. Unlike traditional frequency distance gauges, this structure is optimized taking into account the need to obtain information about objects embedded in solid media (soil). The main advantage in comparison with other means of short-range sub-surface radiolocation is the possibility of applying methods of increasing resolution in real time scale.

3.6 Features of Using Ground Penetrating Radars from Aircrafts

We will consider the possibility of using a ground penetrating radar installed on an aircraft, as well as the optimal characteristics of radars used in such situations and possible types of other applied aircrafts [61].

Englishman A. Wait was one of the first to notice the effect of reflection of pulsed electromagnetic waves from sub-surface irregularities in 1957 at the ice airfield in Antarctic, when he discovered that the radar altimeter of the plane showed the altitude of 900 feet before take-off. The initial suggestion about malfunction of the altitude gauge, which was a pulse radar, was not confirmed; it was found out that the radar was registering a signal from the foot of the glacier. Further experiments demonstrated that the use of a pulsed radar makes it possible to determine the thickness of the ice layer both directly from its surface and from air [62–64].

However, the use of ground penetrating radars from aircraft vehicles is still not widely used. There are only single cases of successful use of aircrafts for sub-surface probing [64–68], which is due to a number of practical problems arising during installation of ground penetrating radars on aircrafts. Let us enumerate only the most important ones:

- antennas of most georadars are designed for operation at the air-ground interface – with the distance between the antenna and soil exceeding the wavelength of the radiated signal, directivity pattern of the antenna becomes nearly circular, which reduces efficiency of the antenna, increases the number of reflections from objects on the surface and subsequently complicates detection of comparatively weaker signals reflected from under the surface;
- at the air-ground interface, the strongest reflection of the signal is observed; therefore, significantly lower power penetrates into the soil as compared to the case with radar installed on the surface, which makes it necessary to expand the dynamic range of radar amplification, as it is necessary to detect signals from under the surface that are orders of magnitude lower than background of high-power reflection from the surface;
- most modern georadars operate according to the strobing principle – in order to form a sample of N points, it is necessary to emit N probing pulses (it is suggested that during sampling formation, the form of the reflected signal changes so insignificantly that this change can be disregarded);
- most georadars compensate attenuation of the signal in the environment by accumulating a great number (100 and more) pulses to increase the signal-to-noise ratio, also suggesting that the signal will not change during the time of accumulation.
- when the radar is raised dozens of meters above the ground surface and placed on a quickly moving carrier, the condition of permanence of the signal during strobing and accumulation of the signal is nearly impossible to meet – in this case, other means of signal generation and registration are required;

– any change in the aircraft height during probing causes a change in the amplitude and the delay time of the reflected signal, which complicates its registration;
– orientation of the signals obtained from a quickly moving aircraft is a fairly difficult task.

In order to find successful solution to the problem of using a ground penetrating radar from an aircraft, it is necessary first to deal with several specific technical tasks:

– increase average power of the radiated signal;
– reduce the signal registration time;
– ensure synchronization of the initial moment of signal registration with readings of the altitude gauge;
– enure geo-tagging of the radiolocation data with maximum accuracy;
– create an antenna system with narrow DP in which the reflection area will be commensurate with the Fresnel area.

As demonstrated, an increase in the average power of the radiated signal can be achieved by transition from ultrashort ultra-wideband (UWB) signal to the so-called organized signals: signal with linear frequency modulation (LFM) or phase-code frequency modulation (PCM). Improvement of the signal-to-noise ration in this case will be directly proportional to the duration of the LFM signal (or number of sub-pulses of the PCM signal). The use of such signals makes it possible to perform immediate registration of the received signal instead of accumulation and strobing, which will reduce the time of registration to an acceptable level. Another method consists in using high-power kilovolt super-short pulses at a resistively loaded antenna.

Any altitude gauge can be used to ensure that the signal registration begins immediately at the moment of receiving reflection from the surface. This can be a laser distance gauge or a high-frequency radio distance gauge operating alternately with the ground penetrating radar. After measuring the distance to the distance, launch of the data registration procedure of the ground penetrating radar is delayed for the time of its propagation to the surface and back. In this case, data will be recorded only in important moments of time.

Mapping can be performed by means of high-precision GPS receivers. Moreover, to increase accuracy of detecting direction to sub-locator point, it is possible to use a gyro-stabilized platform, the coordinates of which are determined and recorded at each moment of measurement.

In order to obtain a narrow beam pattern, it is necessary to use a dish antenna with resistively loaded dipole as a radiator [64], or a more complex specially designed antenna system.

A helicopter (manned or unmanned) is usually used as an aircraft. Both options have their disadvantages: in piloted helicopters, there are limitations on operation at low heights; in remotely piloted helicopters, the weight of the useful load is usually limited. An alternative consists in using a helium-filled zeppelin: autonomous (remotely controlled) or towed at a given height by ground transport (kite-type);

the dish radar antenna can also be made in the form of an inflatable structure with a metallized reflective working surface.

A number of countries (USA, Britain, France, China) are developing such specialized air-based radar complexes designed for installation on remotely piloted aircrafts. Unfortunately, most of such projects are not covered in detail in open print, and only separate aspects of them are known. For example, it is suggested that the package of the SABRC developed in the USA shall include a laser distance gauge for measurement of relief of the surveyed surface or the upper boundary of the snow, a high-frequency scanning radar for determination of radiophysical properties of the surface and the lower boundary of the snow, a sub-surface probing radar for study of the soil structure and detection of irregularities (decompactions, pipelines, cables, underground communications and elements of building structures, water-containing layers, etc.). One of the possible SABRC compositions:

High-frequency scanning radar with the following characteristics:

- central frequency – 3 to 5 GHz (specified during development);
- beam width – 0.5° (clutter spot size – 0.1 m from the height of 10 m);
- scanning area size – 10 m (from the height of 10 m);

The second variant of high-frequency scanning radars is characterized by the following parameters:

- beam width – 0.5° (clutter spot size – 1 m from the height of 100 m);
- scanning area size – 20 m (from the height of 100 m);

Basic characteristics of the ground penetrating radar:

- central frequency – 150 to 200 MHz;
- observed area size – 20 m (from the height of 100 m);
- probing depth – not less than 5 m (in dry sand);

Laser distance gauge with the possibility of determining range at altitudes up to 150 m with accuracy of at least 1 cm.

Complex processing of data obtained by such technical objectives makes it possible to acquire additional information about the structure of the examined soil or objects hidden under the soil layer.

The range to the surface and relief are determined by a scanning laser and confirmed by a high-frequency radar with an antenna array. If the results of laser scanning and radar probing differ significantly, the surveyed area is covered with a thick layer of snow (in the winter) or vegetation.

Soil structure and its density can be estimated based on the data of the ground penetrating radar. For this, moisture of the underlying surface shall be estimated based on the data from laser distance gauge and high-frequency radar. Since the reflective capacity of loose soil is lower than in firm soil, it is possible to experimentally find dependence of power of the reflected signal on height for different types of soils and then, comparing the received signal with the reference value, receive probability estimate of soil density.

Moreover, SABRS can be used for monitoring of forest areas (assessment of timber volumes), prevention of forest fires (based on forest dryness), ice reconnaissance before moving icebreaker for selection of the best path.

The possibility of detection of hidden cables, bunkers and underground communications makes SABRCs irreplaceable in the field of security and counter-terrorist measures.

The work was performed with partial support from the Program of the Branch of Physical Sciences of Russian Academy of Sciences "Radioelectronic Methods in Studies of Natural Environment and Human".

3.7 Russian Georadars

Russia boasts its own authoritative scientific school of creation and serial production of a series of georadars – digital portable geophysical devices, the operating principle of which is based on radiation of pulses of electromagnetic waves and recording of signals reflected from the boundaries between media with different values of dielectric permittivity.

Russian georadars are designed for a wide range of geotechnical, geological, ecological, engineering and other tasks, where there is a need for non-destructive and operative electromagnetic monitoring of the environment.

Main fields of application of Russian georadars:

Geology – creation of geological sections, determination of the position of the groundwater level, ice thickness, depth and profiles of the bottoms of rivers and lakes.

Transport construction – determination of thickness of structural layers of road surfaces and quality of compaction of road construction materials.

Industrial and civil construction – determination of quality and state of concrete and brick structures (bridges, buildings, etc.), condition of dams, identification of landslide areas, location of engineering communications.

Environmental protection – assessment of contamination of soils, detection of leaks from oil and water pipelines.

Archaeology – detection and mapping of buried buildings and burial sites. Building of detailed cross-sections of the excavation site with the minimum number of earth works. Identification of irregularities and cross-ditches in cultural level.

As a search technical and forensic tool – detection of objects (including non-metallic ones) hidden in the structures of buildings and structures or in the ground, voids and irregularities in brick and concrete structures.

3.7.1 Ground Penetrating Radars of the "Loza" Series

"IZMIRAN" Company is the main developer and manufacturer of one of the first modifications of georadars in the USSR. In the following, we will present a brief overview of the history of creation of first "Loza" radars, since this history is also characteristic of other Russian enterprises currently working in this field.

"IZMIRAN" first faced the problems of sub-surface probing in the beginning of the 1990s, when it began a member of the famous ambitious project of the flight to Mars "Mars-94". In accordance to this project, a Mars research vehicle was supposed to move over the surface of the planet, fitted with the device that would probe Martian soil at depths of up to 500 meters and detect presence or absence of ice at these depths, which would help answer the famous question: is there life on Mars? The conditions of creation of this device were fairly strict in terms of both mass and power consumption from the in vehicle network, which called for revision of certain construction principles existing at the moment.

Since a half of kilogram of weight and a half of watt of consumption from the in vehicle network – these were the operating conditions of the future device – were too hard to achieve, the Department of Radiolocation of the Riga Institute for Civil Aviation Engineers, which was the leader in the USSR in terms of georadars, refused to participate in the project. By that time, many companies, including RIIGA, had been producing ground radars (georadars); these companies clearly understood that the task set for Mars was impossible to solve, at least in the field of universally known circuitry solutions of georadars. Analysis of all publications and patents performed by "IZMIRAN" specialists demonstrated the same: the generally accepted design solution of a sub-surface radar cannot be fitted into the specified parameters in terms of weight and power consumption, and it was necessary to look for another option. And such solution was found. It can be referred to as photoflash principle. Basics of radar location state that probing range depends on the energy of the received signal. In the generally accepted circuit of georadars, a transistor transmitter with power of about 100 W and a sensitive receiver with accumulation of signal energy are used.

Specialists of "IZMIRAN" decided that the signal energy shall be accumulated in the transmitter instead of receiver. Such energy accumulation is simpler in terms of design, and the design is lighter. Low-power high-voltage supply source shall be used to charge the capacitor to several thousand volts and short-circuit to the antenna through the arrester. Power of the transmitter will be increased about 10,000 times and amount to 1 MW. In this case, it is possible to use a basic low-sensitivity light receiver. That is, to implement the photoflash principle, which is known to all photography amateurs: energy is accumulated from a low-power battery during long time and then turns into a powerful flash of light.

This feature, along with a number of other original circuitry-related solutions, made it possible to build the device with the required characteristics within the limits of weight and consumption; moreover, an additional function of the device appeared, which allowed to use it as an ion probe for sensing of the Martian

ionosphere. The same transmitter pulse was used for it. Signals from under the surface of Mars were received at short time intervals, signals from the ionosphere of Mars – at long time intervals. Well-known events in politics and economics of the USSR in the beginning of the 1990s led to cancellation of the Mars-94 project. It can be said metaphorically that ground devices of Martian origins are georadars of the "Loza" series.

Since after cancellation of the project and general deterioration of the economic situation in the country the future of the groups as a scientific department was in question, a decision was made to test these Martian development in conditions of the Earth. The developers had a brand new circuitry solution of the georadar – and the task was to check whether it would be useful on Earth.

It was known that all georadars were practically based on the same circuit published in literature. Actual potential of these devices amounts to 20–40 dB. This means that the device detects an underground object only when the amplitude attenuation of the signal does not exceed 10–100 times. Such attenuation makes it possible to probe environments with low conductivity to depth of several dozens of centimeters. Such environments include dry sand, permafrost, snow and ice. In wet clays, which prevail in the Moscow region and generally in midland Russia, these devices do not work. Manufacturers and users of georadars at the time were certain that georadars could not work in clayey soils.

The experiments performed by specialists of "IZMIRAN" demonstrated that the new approach to radar engineering could prove useful. In order to increase the probing depth without losing resolution, it is necessary to stay within the same frequency range but sharply increase the transmitter power, as it was done in the design of the radar for the Martian program.

All georadars of the Loza series are built according to the circuit which was previously designed for the Mars research vehicle. The main differences of devices of this series from all ground penetrating radars consisted in the following [69]:

Pulse power of the transmitter was increased about 10,000 times and amounts to 1 MW. It should be specifically noted that the average power was reduced about 10 times as compared to standard ground penetrating radars due to reduced repetition frequency of probing pulses.

Strobing method of signal registration after its conversion into low frequency is replaced with registration in the range of operating frequencies with the help of high-speed comparators.

The transmitter operates in asynchronous mode. Synchronization is performed in the receiver.

Measured real potential of Loza georadars amounts to at least 120 dB. This means that the device responds to the signals with amplitude attenuation of one million times.

The listed parameters implemented in the medium-frequency (50–300 MHz) version of the "Loza-V" georadar made it possible to achieve the real probing depth of 10 m in conditions of Moscow region and midland Russia.

Below are several basic examples of practical applications of the "Loza" radars [69].

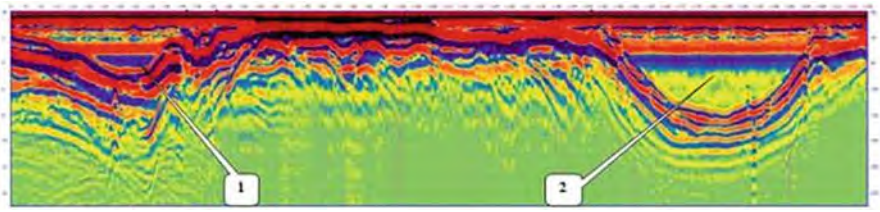

Fig. 3.23 Radarogram (without processing) obtained at the crossing of the floodplain of the Dnieper River (Smolensk) (1) and (2) ancient paleochannels of the Dnieper River filled with river deposits [69]

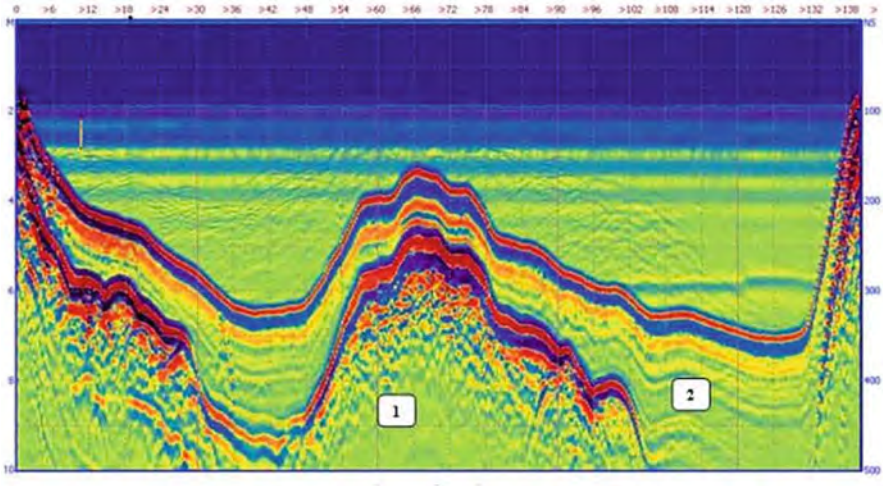

Fig. 3.24 Radarogram (unprocessed) obtained at the intersection of the lake at Mount Golgotha on the island of Anzer, Solovki. (1) – granite bed of the lake, (2) – sand and gravel deposits [69]

Figure 3.23 shows a georadar section made along the Dnieper River valley with the help of ***Loza-V*** (150 cm (100 MHz) antennas, 256 ns sweep). Probing depth – over 10 m. Soils – layers of sand, silt and loam.

High potential of the "Loza-V" radar makes it possible to probe geostructures through the water layer from the surface. Figure 3.24 shows the profile of the bottom of lake with maximum depth of more than 6 m and geological structure of near-bottom soil layers at the depth of 4–6 m. Probing was performed with the help of "Loza-V" with 150 cm (100 MHz) antennas installed on small raft on the water surface. Sweep – 512 ns.

Figure 3.25 shows one of the georadar cross-sections (1205 profile), the data of which were used to excavate previously unknown tombs at the depth of 4–5 m. The survey was carried out during an expedition of the Institute of Oriental Studies of the Russian Academy of Sciences using a Loza-V georadar with 100 cm (200 MHz) antennas with 256 ns sweep.

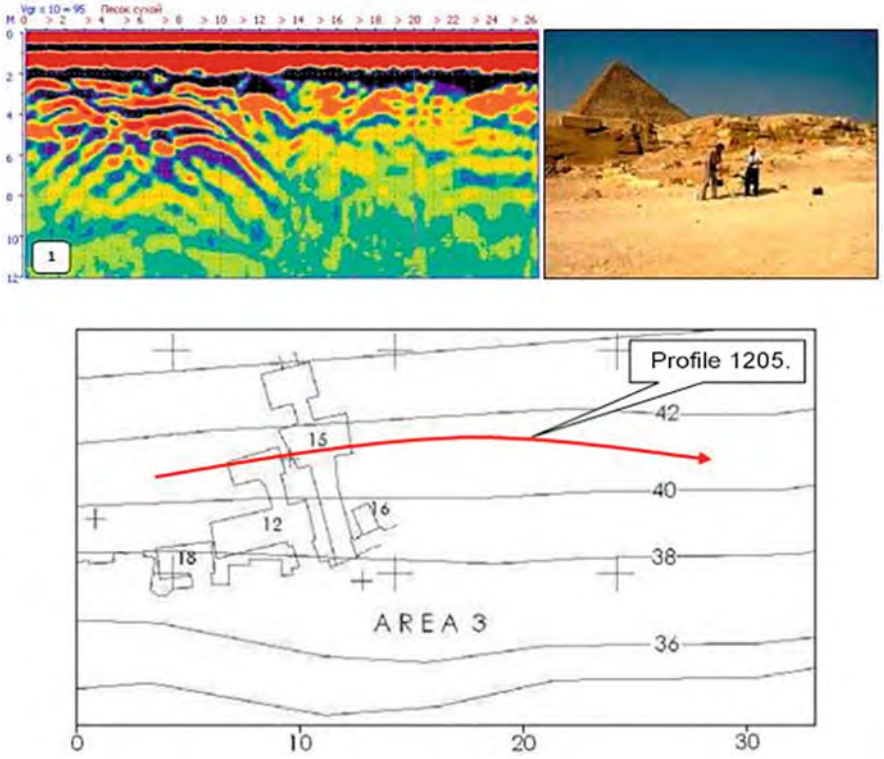

Fig. 3.25 Radarogram made on the Giza plateau in the eastern part of the necropolis. (1) – radarogram. (2) – plan of excavated tombs [69]

Probing depths of over 10 m can be reached by two methods – reducing frequency of the probing signal and increasing power of the georadar. In the "***Loza-N***" georadar, both these methods of achieving maximum probing depth are implemented. Frequency band of "Loza-N" is 1–50 MHz, which makes it possible to apply antennas of 300 cm (50 MHz), 600 cm (25 MHz) and 1000 cm (15 MHz). Georadar of the N model in extended version is fitted with the transmitter with power of 10 MW (18 kV). The use of a super high-power transmitter and low-frequency antennas made it possible to increase the maximum probing depth significantly.

Figure 3.26 shows one of cross-sections performed during the survey of the karst-hazardous section of the railroad. The presence of karst is confirmed by boring. The work was performed with the help of "Loza-N" georadar (600 cm (25 MHz) antennas, 1 MW transmitter). Scan – 1024 ns, probing depth – 60 m.

Figure 3.27 shows one of the sections made in Nagatinsky Pool during survey of geology of bottom deposits for project 4 – ring. The work was performed with the help of "Loza-N" georadar (300 cm (25 MHz) antennas, 1 MW transmitter). Scan – 1024 ns, probing depth – about 30 m. The use of low-frequency antennas in the water made it possible to study geological structures at previously unavailable depth in bottom layers of bodies of water.

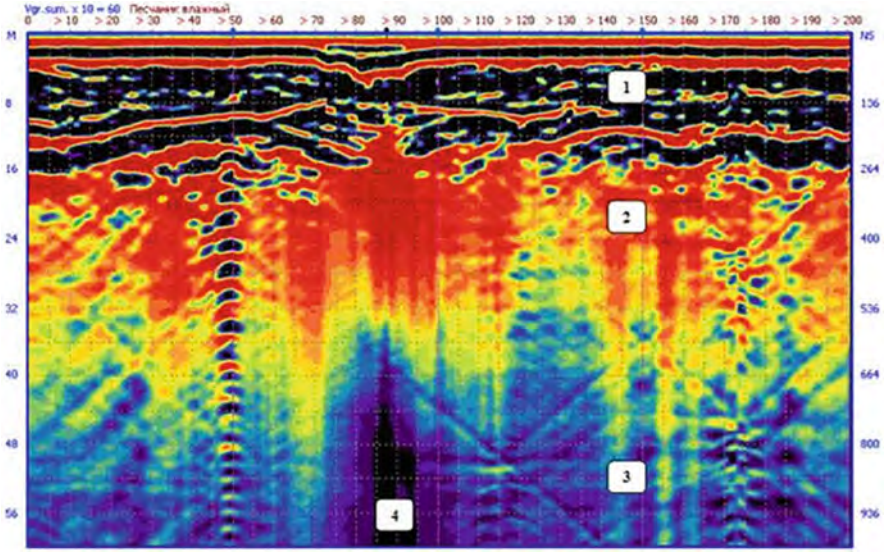

Fig. 3.26 Radarogram of the area along the railway track in the Dzerzhinsk – Nizhny Novgorod section. (1), (2) – sand layers, (3) – limestone, (4) – karst remaining under the ground surface [69]

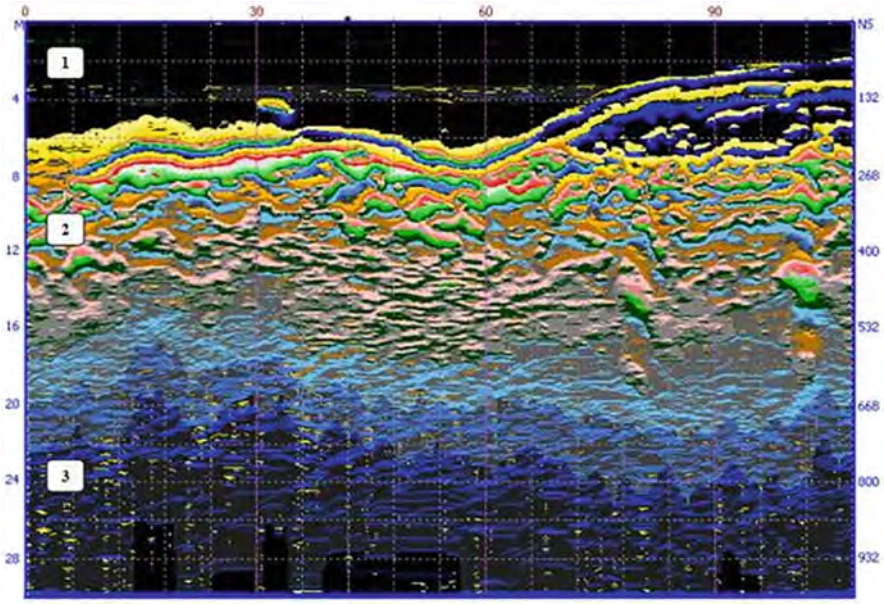

Fig. 3.27 Georadar cross-section performed in Nagatinsky Pool (Moscow River). (1) – water, (2) – sand layers, river deposits, (3) – limestone [69]

The use of the super high-power transmitter increases the probing depth approximately 1.7 times. Low-frequency georadar "Loza-N" with 10 MW transmitter helps reach probing depths of 150–200 mm depending on the absorbing properties of soil. This makes it possible to use the georadar to solve tasks of classic geology and search for natural resources at low depth.

Figure 3.28 shows a georadar section reflecting a deep fault of the Earth's crust. Surface layers of river deposits are registered at the depths of 40–60 m. The profile was made in the Oka River valley in the Stupino Disctrict, Moscow region. 600 cm (25 MHz) antennas with 10 MW transmitter were used in the work. Scan – 2048 ns, probing depth – over 100 m.

Another interesting application of georadars of this series – archaeological studies – shall also be mentioned. In 2000, representatives of the underwater archaeological expedition of the RF IAN to Taman (Krasnodar Territory) asked the georadar group of the enterprise to help in the search of Greek cities of the

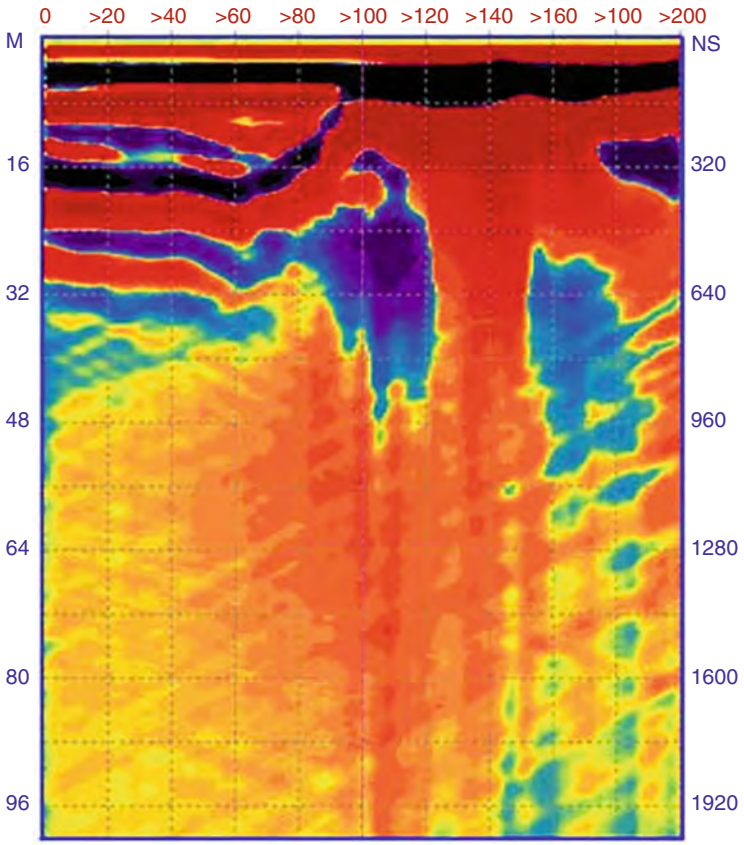

Fig. 3.28 Radar cross-section performed in the Oka River valley (Stupino Disctrict, Moscow region) [69]

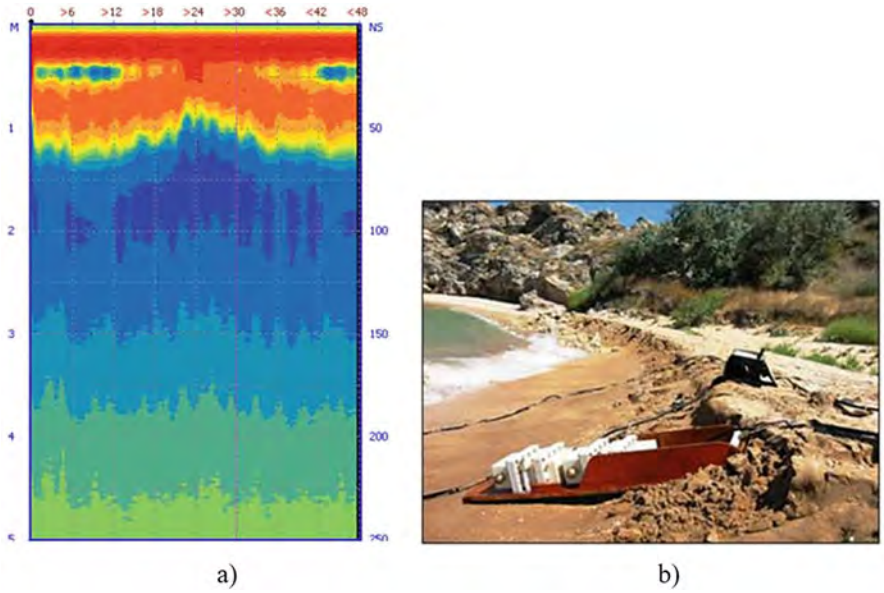

Fig. 3.29 Georadar section (**a**) and appearance (**b**) of the underground sea version of the georadar "Loza-V" [69]

Bosporus kingdom (fifth century BC). The problem consists in the fact that most Greek settlements of that period remained under the bottom of the sea at low depth due to mud-volcanic activity. The method used in fresh water (probing directly from the water surface) cannot be used for salty sea water. Radio waves used by the radar (50–300 MHz) are almost completely absorbed by sea water at distances of about 40 cm, even with the transmitter power of 1 MW. However, this means that if we place the device directly on the bottom and move it along the surface, the task still can be solved. As a result of multiple experiments, ***marine configuration of the radar was created***, the appearance of which is shown in Fig. 3.29. Georadar section shows a section of the base of the eastern part of the fortress wall of Phanagoria – the capital of the Bosporus kingdom. The study was performed by the expedition of the RF IAN to Taman (headed by the Doctor of Historical Sciences V.D. Kuznetsov) in 2008. The survey area was the underwater part of the Phanagoria settlement (Taman Bay of the Black Sea (salinity 14‰), water depth 1–1.5 m). Probing depth – 2 to 3 m under the sea bottom.

The practice of work in large areas made the enterprise face the questions about air-based georadars. Unlike ground-based georadars, where directivity pattern is formed by the soil, for air-based georadars this problem shall be solved differently. There are several such ways, including the use of a dish antenna with resistive-loaded reflectors. Specialists of the company have performed the first successful

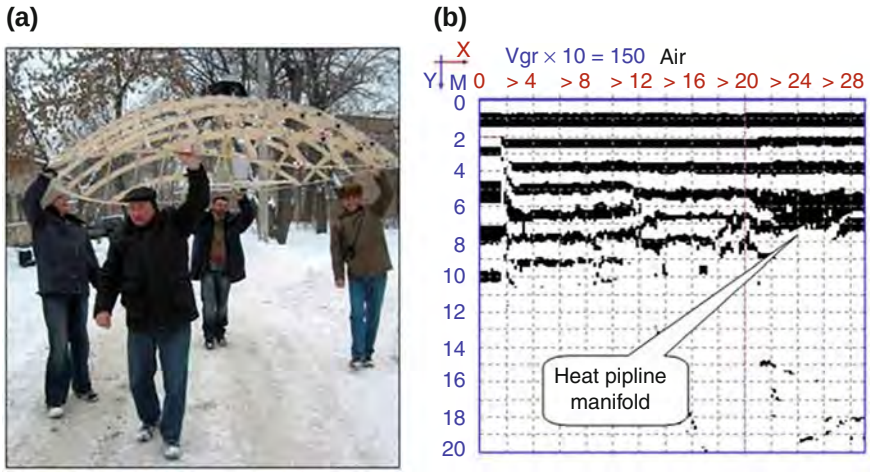

Fig. 3.30 Model of air suspension of the Loza-V georadar (**a**) and georadar section of the road base and manifold of the heating pipeline at the depth of 50 cm (**b**) [69]

experiments in this direction. Figure 3.30 shows the model of a dish antenna with resistively loaded reflectors, the focus of which contains antennas of the georadar (300 MHz). Recorder of the georadar is installed in the top part of the reflector and operates in automatic mode. Section 0–20 m of the georadar section shows the structure of the road base; section 20–24 mm contains the manifold of heating pipeline (depth: 50 cm) and the soil defrosting zone. During profiling, antennas of the georadar were at the height of about 2 m. Probing depth was up to 1 m.

Based on the above examples, we can conclude that georadars, according to the prospects of development, will become the most informative and popular device in geophysics. Its value will increase in studies of the Moon and other planets. Contactless quick method of determination of the soil structure makes it possible to use this method both from the orbit and from the planet surface.

3.7.2 "Zond-2" Georadars

Zond-12 (Zond-12e) georadars αρε digital, single- or double-channel portable sub-surface probing radars, each of which can be carried by a single operator. Full set of the georadar includes the central unit with portable computer fixed on the special platform (the computer is usually not included in the supply package), set of antennas for different probing frequencies and software [70].

The central unit is supplied in firm plastic case together with accessories.

During profiling, radar location profile in real scale is displayed on the screen of a portable computer; at the same time, data are recorded to the hard drive for further use.

Main features of georadars of this series:

- all parameters of the georadar are controlled with the help of computer, which determines the simplicity of operation;
- software supports many types of color and monochrome data and allows to display data in various forms;
- the number of paths in the profile is unlimited;
- the set of replaceable antenna modules ensures the possibility of probing within the frequency range of 38 MHz–2 GHz;
- Probing depth: 6 cm–30 m;
- Measuring wheel or GPS can be used for orientation of the profile obtained during probing;
- antennas are dust- and spray-proof and can even be submerged into water for a short time;
- surface antennas have fluoroplastic substrates, which are extremely resistant to abrasion;
- Design of the georadar and antennas makes it possible to perform studies using the common depth point method.

Prism 2 software is used for work with radars of this series.

Prism 2 software is designed for control of parameters of the "Zond-12e" georadar, receipt of probing data with simultaneous display on the computer screen and recording to the hard drive in the form of a file, as well as for processing of files and their printing.

Software features:

- Reception of data from the georadar is possible in the continuous mode (main mode) and in stepwise accumulation mode. Continuous mode provides maximum spatial (horizontal) resolution. Stepwise accumulation is used to achieve the maximum possible probing depths and solve specific tasks (tomography, etc.), but requires more time for probing.
- Supported languages: Russian, English, German, Greek; switching between languages is possible without restarting the program.
- All parameters of the georadar (except on/off switching) are controlled with the help of a computer.
- For orientation of the profile obtained during probing, the operator can use the button to enter markers when passing through pickets or any marks. These markers will be displayed in the profile as vertical lines with corresponding numbers at the top.
- Upon completion of probing (or after that at any moment) it is possible to add a text comment to the file, which can contain the following: probing location, purpose, etc.
- During radar setting and probing the software issues warnings if incorrect parameters are set and provides its recommendations.

3.7.3 "OKO" Georadars

Basic kit of the most popular georadar of this series "OKO-2" includes: control unit, suspension for portable computer (PC is not included in the kit), handle bar, optical converter, power supply units ((BP-2.0/12 – 2 pcs. (for operation ONLY with antenna units AB-1700, AB-1700У, AB-1200, AB-12200У), BP-9/12-1 pc.), chargers for power supply units (3 pcs.) set of cables and basic version of the software [70].

The following can be supplied additionally: antenna units, specialized processing unit with field bag, set with radio modem for remote operation of the georadar, movement sensor with wheel and optical cable, automobile movement sensor, path meter with coil and optic cable, power supply units and chargers, professional version of control and processing software.

Features of "OKO" georadars:

- For operation in field and unfavorable climate conditions the georadar is fitted with the special field version of the indication and processing unit replacing the portable computer.
- All units of the GPR are optically isolated (receiver, transmitter, control unit, movement sensor). This reduces intrinsic noise level of the system and helps achieve more stable signals when moving antenna units point-to-point.

The radiomodem makes it possible to control the device remotely and retrieve information from antenna units within the radius of up to 100 m.

- The set of antenna units ensures the possibility of probing within the frequency range of 50 MHz–1.7 GHz.
- Probing depth: 3 cm–24 m.
- High strength of antenna units made of aluminum alloys. All antennas except the dipole are shielded.
- Three types of movement sensors can be used for orientation of the profile obtained during probing.
- Low power consumption – one set of accumulators ensures operation for 4–8 h.
- Small size – device set fits into a comfortable transport bag. Large antennas ABD, AB-150 AB-250 are modular.

"OKO" georadars are operated with the help of **GeoScan32** software.

GeoScan32 is designed to organize control over OKO series radars, as well as for further mathematical processing and demonstrative visualization of information obtained during probing.

The program allows to save images of the sub-surface environment obtained by the user on the hard drive and insert them into MS Word documents, as well as print them out.

Software features:

- Help file and screen tips facilitate work with the program.

– GeoScan32 records accompanying information, which makes it possible to create extensive archives of ground penetrating probing data.
– A special operating mode "Reinforcing Elements Search" is available for detection of point objects.
– The number of paths in the profile is set as 100–65,000.

It is also necessary to mention the possibility of using other programs during work with georadars.

For example, **RadExplorer** – specialized program for interactive processing and interpretation of georadiolocation data (development of "DEKO-Geophysics").

RadExplorer software is specially designed for processing and interpretation of georadar data. The set of possibilities optimized for georadiolocation and convenient and clear interface in Russian make it possible to process data in a quick, simple and efficient manner.

Software features:

– Automatic selection of optimal processing parameters depending on recording parameters.
– Interactive building of processing flows with the possibility of saving them on the drive for further use.
– Possibility of canceling applied operations with unlimited number of steps.
– Possibility of interactive determination of layer speeds and depths of local objects.
– Correlation of reflections (picking) with saving of the obtained picks in a text file.
– User-friendly environment model editor.
– 3D Gazer – instrument for 3D visualization of georadar data.

3D Gazer is another frequently used program. Its specific feature is the use of 3D visualization of images, which helps get a better idea of the structure of the examined object.

The possibility of tracking of linear objects is also provided: pipes, cables and other lines.

In the special program mode of partial transparency, only high-amplitude sections of profiles are displayed.

Additional convenience: on top of the radarograms, the user can display a semi-transparent shooting scheme or a plan of the premise in which the work was carried out.

When choosing the suitable type of Russian georadars, the potential customer can refer to Table 3.3, which contains comparative technical characteristics of "OKO-2" and "Zond-12e" georadars.

Table 3.3 Comparative technical characteristics of "OKO-2" and "Zond-12e" georadars [70]

Characteristics	OKO2	Zond-12e
Capacity, bits	16 or 32	16
Probing time interval, ns	25–1500	1–2000 with a pitch of 1
Number of points per path	127, 255 or 511	512
Data transmission rate, paths per second	40	56 (single channel) and 40 or 80 (double channel)
Number of accumulations	1–10,000, hardware and software	1–1024, hardware
Repetition frequency of transmission pulses, KHz	20–400, depends on the antenna unit type	115
Gain, dB	Linear or exponential (80), AGC	Based on 10 points (0–80)
Filtration	–	Switched high-frequency filter: 0.00; 400; 800 Hz
Data recording modes	Continuous or point	Continuous or point
Data orientation	Manually or automatically (using measuring wheel, movement sensor or automobile movement sensor)	Manually or automatically using odometer, measuring thread or GPS
Multi-channeling	–	1 or 2 channels (depending on the version of the device)
Data transmission	Ethernet	Ethernet
Internal memory volume, Mb	256 in spec. Processing unit	–
External memory volume	Depends on external memory	
Visualization	Depends on external memory	
Graphic data presentation	Color or monochrome	
Power supply, V	12, antennas are powered by individual accumulators	12, antennas are powered via cable from the control unit
Dimensions, cm	27.3 × 17.2 × 5.5	35 × 50 × 5.5
Weight, kg	2.2 (weight of the processing unit without computer)	3.2 (weight of the control unit without computer)
Operating temperature, °C	0 to +30 (−20 to +50 in climatic configuration)	−10 to +40 (with relative humidity of up to 95%)

References

1. Belous, A., Merdanov, M., & Shvedov, S. (2018). *Microwave electronics in radar and communication systems. Technical encyclopedia in 2 volumes*. Second edition, revised, Moscow, Tekhnosfera, 2018. 1520 pages.
2. Proceedings of 9th Internanional Conference on Ground-Penetrating Radar, Santa Barbara, California, USA, April 29–May 2, 2002. 608p.
3. Proceedings of Millennium Conference on Antennas & Propagation, Davos, Switzerland, April, 2000, v.1. 663 p.
4. Abstracts of the Conference "Georadar in Russia – 2000", Moscow, MSU, May 2000. 61 p.
5. Daniels, D. J. (1996). *Surface-penetrating Radar*. London: The Institution of Electronical Engineers.
6. Finkelshtein, M. I., Karpukhin, V. I., Kutev, V. A., & Metelkin, V. N. (1994). *Subsurface radiolocation*. Moscow: Radio and Communication. 216 p.
7. Taylor, J. D. (Ed.). (2001). *Ultra-wideband radar technology* (p. 424). New York: CRC Press.
8. Immoreev, I., Grinev, A., Vovshin, B., & Zaikin, A. (1996). *Videopulse radar for subsurface penetrating: Signal processing, experiment*. In Proceedings of 6th International Conference Ground Penetrating Radar, Sendai, Japan (pp.103–106).
9. Tikhonov, A. N., & Goncharskiy, A. V. (Eds.). (1987). *Incorrect problems of natural science*. Moscow: Moscow University Publishing.
10. Batrakov, D. O., & Tarasov, M. M. (1999). Algorithm of solving reverse dispersion tasks based on the principles of Pontryagin maximum. *Radiotechnics and Electronics, 44*(2), 137–142.
11. Borovikov, I. P., Obukhov, Y. V., Borovikov, V. P., & Pasechnik, V. I. (1999). New algorithms of recovery of signals and images modeled with the help of differential equations. *Radiotechnics and Electronics, 44*(8), 982–987.
12. Alifanov, O. M., Artukhin, E. A., & Rumyantsev, S. V. (1988). *Extreme methods of solving incorrect tasks*. Moscow: Science.
13. Grinev, A. Y. (2001). *Recovery of geometrical and electro-physical parameters of objects in sub-surface probing tasks*. In Works of the XI All-Russian School-Conference on Diffraction and Propagation of Waves, Moscow, December, 2001 (Vol. 1, pp. 30–42).
14. Grinev, A. Y., Zaikin, A. E., & Chebakov, I. A. (2001). Application of computational diagnostics in sub-surface radio probing tasks. *Radiotechnics, 3*, 21–27.
15. Sablin, V. N., Grinev, A. Yu, & Chebakov, I. A. (2002). *Detecting and classifying of physical and geometrical characteristics of the subsurface through the use of computing diagnostics method for ground penetrating radar*. In Proceedings of 9th Internanional Conference on Ground-Penetrating Radar, Santa Barbara, California, USA, April 29–May 2, 2002.
16. Shpenst, V. (2013). Spase-based radiolocation stations of Earth remote sensing. *Components and Technologies, 3*, 154–158.
17. Guschin, V. N. (2003). *Basics of design of space vehicles: Study book for higher educational institutions*. Moscow: Engineering.
18. Kashkin, V. B., & Sukhinin, A. I. (2001). *Earth remote sensing from space. Digital image processing: Study book*. Moscow: Logos.
19. Garbuk, S. V., & Gershenzon, V. E. (1997). *Space systems of Earth remote sensing*. Moscow: A & B Publishing.
20. Antipov, V. N., Goryainov, V. T., Kulin, A. N., et al. (1988). *Radar stations with digital synthesis of antenna aperture*. Moscow: Radio and Communication.
21. Kopik, A. (2007). In space – Italian radiolocation reconnaissance device. *Cosmonautics News, 8*, 295.
22. Cantafio, L. J. (1989). *Space-based radar hand book*. Norwood: Artech House.
23. Grinev, A. Y. (Ed.). (2005). *Problems of ground penetrating radar location. Joint monograph*. Moscow: Radio Technology. 416 p.: il. ISBN 5-88070-070-4.

24. Germanovich, O., Liferenko, V., Katsan, I., & Tebuev, M. (2014). Georadar with enhanced resolution. Structure and hardware implementation means. *Components and Technologies, 6*, 166–168.
25. Grinev, A. Y. (Ed.). (2000). *Problems of sub-surface radiolocation: Monograph*. Moscow: Radiotechnics.
26. Dudnik, A. V. (2008). Influence of radiated power on the depth of georadiolocation probing. *Mineral Exploration and Protection, 1*.
27. Germanovich, O., Katsan, I., & Parantaev, G. (2007). Synthesis of a parametric selective filter of the SHF range. *Components and Technologies, 11*.
28. Sudakov, A. (2014). Ultra-wideband devices – Classification and application/electronics. *NTB, 3*, 98–105.
29. D0C-22000. (2002). *New public safety applications and broadband internet access among uses envisioned by FCC authorization of ultra-wideband technology*. FCC, February 14, 2002.
30. FCC 02-48. (2002). *Revision of part 15 of the commission's rules regarding ultra-wideband transmission systems. First report and order*. FCC, April 22, 2002.
31. FCC, CFR Title 47. (2010). Chapter I, Part 15. In *Radio frequency devices* (pp.752–871), 10-01-2010.
32. FCC ID QCJRADEKL. (2007). Electro *Compatibility test report for the Multispectral Solutions, Inc. Model RAD635* (MET Laboratories, Inc. Report № EMC22474-FCC250 REV. 2. August 7, 2007) (p. 55).
33. www.fcc.gov. Federal Communication Commission web site (March 1, 2014).
34. www.wireless2000.com. Wireless 2000 UWB and RF Technologies web site (March 1, 2014).
35. http://www.uwbgroup.ru. Scientific and Research Center for Ultra-Wideband Technologies of the Moscow Aviation Institute (March 1, 2014).
36. http://www.zavant.ru. LLC Smolensk Science and Innovation Center for Radioelectronic Systems "ZAVAT".
37. http://www.nanoxaos.ru. LLC "NanoChaos".
38. http://www.trimcom.ru. NPP "TRIM" (March 1, 2014).
39. http://www.logsys.ru. (March 1, 2014).
40. http://www.nanopulse.ru. LLC "NanoPulse".
41. http://www.kbor.ru. JSC "Design Center for Pilot Works".
42. Speranskiy, V. S. (2011). *Radiolocation, systems and devices*. Moscow: Russian Federation.
43. Shirman, Y. D. (Ed.). (2007). *Radioelectronic systems: Building basics and theory. Reference book*. Moscow: Russian Federation.
44. Devine, P. (2000). *Radar level measurement: The user's guide*. West Sussex: Burgess Hill.
45. Komarov, I. V., Smolskiy, S. M., & Barton, D. K. (2003). *Fundamentals of short-range FM radar*. Norwood: Artech House.
46. Dong-Hun, S. (2011). *Park Seong-Ook II Intelligent Radio for Future Personal Terminals (IMWS-IRFPT)* (pp. 1–2). Daejeon, 24–25 August, 2011.
47. Woods, G. S., Maskell, D. L., & Mahoney Michael, V., II. (1993). *IEEE Transaction on Instrumentation and Measurement, 42*(4), 812–816.
48. Cooper, K. B., II. (2008). *IEEE Microwave and Wireless Components Letters, 18*(1), 64–66.
49. Brooker, G. (2009). *Sensors for ranging and imaging*. Raleigh: SciTech Publishing, Inc.
50. Finkelstein, M. I. (Ed.). (1994). *Sub-surface radiolocation*. Moscow: Radiotekhnika.
51. Finkelstein, M. I. (Ed.). (1997). *Radiolocation of layered ground surfaces*. Moscow: Radiotekhnika.
52. Grinev, A. Y. (Ed.). (2005). *Problems of ground penetrating radar location*. Moscow: Radiotechnika.
53. Mikhnev, V. A. (2002). *Reconstructive microwave structural studies of multi-layered dielectric media: Monograph*. Minsk: Laserscom LLC.
54. David, J., & Daniels, I. I. (2009). *Unexploded ordnance detection and mitigation* (pp. 89–111). New York: Springer-Verlag.

55. Savenko, S. A., Malevich, I. Y., Grinkevich, A. V., Lopatchenko, A. S., & Kalenkovich, E. N. (2013). Problems of building a radar for a ground penetrating system. *Science and Military Defense, 3*, 20–27.
56. Shirman, Y. D., & Manzhons, V. N. (1981). *Theory and technology of processing radiolocation information against the background of interferences*. Moscow: Radiotekhnika.
57. Lopatchenko, A. S., Malevich, I. Y., & Savenko, S. A. (2015). LFM ground penetrating radar with increased resolution. *BSUIR Reports, 3*(89), 43–48.
58. Sinan, K., Demir, Ş., & Hizal Altunkan, I. I. (2008). *Turkish Journal of Electrical Engineering & Computer Sciences, 16*(2), 125–132.
59. Graham, M. B. (2005). *1st internationals conference on sensing technology* (pp. 152–157).
60. Grinkevich, A. V., Grinkevich, A. V., & Savenko, S. A. (2006). Improving effectiveness of a ground penetrating radar using non-traditional methods of spectral analysis. *Science and Military Defense, 4*, 38–41.
61. Marchuk, V. N., Smirnov, V. M., & Yushkova, O. V. (2014). *Possibilities of using a sub-surface radar from an aircraft*. In Proceedings of the XXIV All-Russian Scientific Conference "Propagation of Radio Waves" dedicated to the 100th anniversary of Prof. V.M. Polyakov, June 29–July 5, 2014, Irkutsk, pp. 219–221.
62. Finkelstein, M. I., Mendelson, V. L., & Kutev, V. A. (1977). *Radiolocation of layered soils* (174 p). Soviet Radio: Moscow.
63. Evans, S. (1963). Radio techniques for the measurement of ice thickness. *PolarRec, 11*, 406–410.
64. Episode 27. Air-based georadar//LLC "VNII SMI" Foundation for underwater geophysical studies, http://www.geo-radar.ru/stories/story27.php
65. Andrianov, V. A., Nazarenko, S. D., Marchuk, V. N., & Shtern, D. Y. (1990). *An experiment in sub-surface radiolocation of frozen soils*. In 3rd International Conference on Sub-Surface Radiolocation, Lakewood, Colorado, USA.
66. Andrianov, V. A., Nazarenko, S. D., Marchuk, V. N., & Podborny, E. E. (1991). *Experimental results of remote radiolocation probing of a gas pipeline in soil*. In Abstracts of all-union science and technology conference "application of wideband signals in radioelectronics and geophysics", Krasnoyarsk, August 26–30, 1991.
67. Semeikin, N. P., Monakhov, V. V., Zverev, E. O., & Eremenko, A. V. (2004). Georadiolocation studies of freshwater river ice. Ice thickness measurement. In *Abstracts of the 4th International Scientific and Practical Conference on Georadiolocation "Georadar-2004"*. Moscow: MSU.
68. Harry, M. J. (2008). *Ground penetrating radar theory and applications*. Amsterdam: Elsevier. 544 p.
69. Kopeikin, V. V., Morozov, P. A., Popov, A. V., Kuznetsov, V. D., Berkut, A. I., & Kozlyakov, A. N. (2008). *Ground penetrating radars "Loza" and their application*. In Proceedings of the Russian-Bulgarian Conference "Fundamental Space Studies. Remote Sensing of Earth and Planets", Sunny Beach, Bulgaria, September 23–28, 2008.
70. Ground penetrating radars, http://www.topcon.by/resource/upload/doc157.pdf

Chapter 4
Antennas and Antenna Devices for Radar Location and Radio Communication

4.1 Main Parameters and Types of Antennas

4.1.1 Introduction

The term "Antenna" originates from the works of Italian inventor Marconi. During his experiments with electromagnetic waves, he used a wooden rod for the tent with the radiating wire placed along it. In Italian, this rod is known as ***l'antenna.*** The wide use of this term in description of Marconi's experiments ultimately led to emergence of the popular term "antenna" used to denote one of the elements of a classic transmitter.

An antenna receives or transmits electromagnetic waves. In fact, antennas are used to transform electromagnetic waves into high-frequency electric currents and vice versa. Mechanical dimensions of an antenna depend on the used wavelength. There are both large antennas with lengths exceeding hundreds of meters using long-wave frequencies and antennas with wavelengths of only several millimeters for microwave ranges. In this chapter, we will mostly consider antennas used in radar equipment of various purposes, as well as in SHF radio systems.

After reading this chapter, the reader shall be able to:

- describe directivity of a basic antenna and gain characteristics;
- describe the focusing effect of a basic dish antenna;
- describe the basic directivity pattern of the most common dish reflectors;
- describe basic characteristics of a horn radiator;
- describe the design of a monopulse antenna.

Antenna is one of the main working elements of a radar. As a rule, it performs the following important functions:

© The Editor(s) (if applicable) and The Author(s), under exclusive license to Springer Nature Switzerland AG 2021

A. Belous, *Handbook of Microwave and Radar Engineering*,
https://doi.org/10.1007/978-3-030-58699-7_4

– transmits the transmitter energy in the form of certain signals in space with the required distribution and efficiency. This process is applied in the same manner during reception.
– ensures the required spatial beam pattern. In general case, it shall be sufficiently narrow in terms of bearing in order to ensure the required bearing resolution.
– shall ensure the required frequency of updating the target position. In case with antenna with mechanical scanning, this is equivalent to the rotation speed. High rotation speed can pose a significant mechanical problem due to the fact that antenna can have a reflector with large dimensions within certain frequency ranges and weigh several tons.

Antenna design shall ensure preservation of working parameters under heavy duty conditions.

Speaking of structural design of antennas, two configurations are normally used:

– parabolic dish-shaped antenna;
– array-shaped antenna.

4.1.2 Characteristics of Radar Set Antennas

At first, let us consider the list and brief descriptions of the basic characteristics of radar antennas.

4.1.2.1 Antenna Gain

An important characteristic of any antenna is its gain factor, regardless of whether the antenna is a transmitting or a receiving one.

Certain antenna sources radiate energy evenly in all directions. Radiation of this type is known as isotopic radiation. It is known that the Sun radiates energy in all directions. The energy radiated by the Sun measured at any fixed distance and at any angle will be approximately the same. Let us assume that the metering device revolves around the Sun – in any point of this circumference, the distance between the metering device and the Sun will be the same. Measured radiation values will also be equal. Therefore, the Sun is considered an isotopic radiator.

Since all antennas, as opposed to isotropic radiators, amplify signals, more energy is propagated in certain direction than in other ones.

The ratio of values of energy propagating in these directions to the energy that would propagate if the antenna was not directional is known as gain. When a transmitting antenna with a certain gain factor is used as a receiving antenna, it will have the same gain factor during reception.

4.1.2.2 Antenna Beam (Directivity) Pattern

Radiation of most radiators is stronger in a certain direction than in other directions. Such amplifiers are known as anisotropic. However, the standard method makes it possible to mark positions around the source in such manner that makes it possible to compare one beam pattern with another.

Energy emitted by the antenna forms the field with a certain directivity (beam) pattern. Radiation pattern is a means of graphic representation of the radiated antenna energy. This energy is measured at different angles and at constant distance from the antenna. The shape of this radiation pattern depends on the type of the antenna used.

Two different types of graphs are used to draw up this pattern: in orthogonal coordinates and in polar coordinates.

The form of presentation in polar coordinates is used to study radiation beam patterns. In a graph with polar coordinates, position of a point is set by projection along the rotation axis (radius) to intersection with one or several concentric circumferences with equal intervals. Typical graph in polar coordinates for measured radiation is shown in Fig. 4.1.

- Main beam (lobe) is the region around the direction with maximum radiation (usually located within 3 dB from the peak value in the main beam). Main beam in Fig. 4.1 is directed to the north.
- Side lobes are weaker beams located outside the main lobe. These side lobes usually present radiation in undesirable directions, which cannot be completely

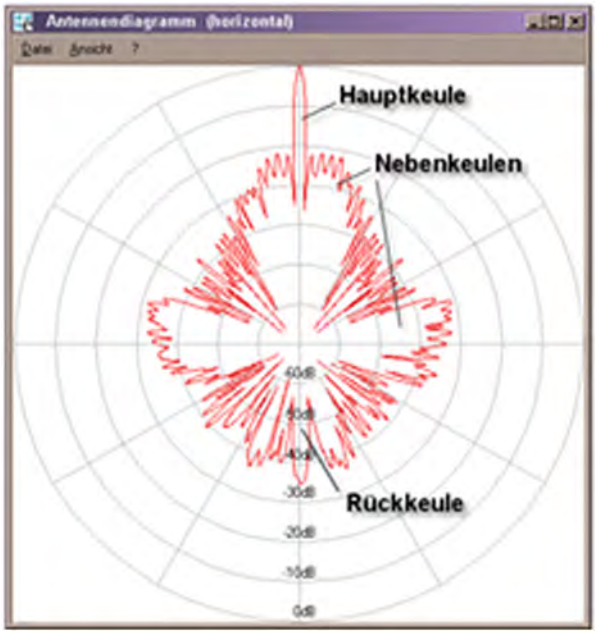

Fig. 4.1 Graph in polar coordinates for measured antenna radiation

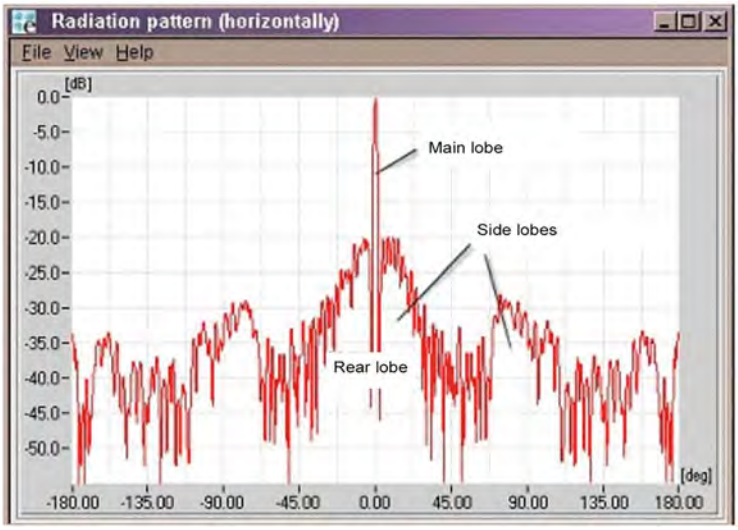

Fig. 4.2 Graph in orthogonal coordinates for the same source of radiations

excluded. Level of side lobe radiation is an important parameter used to describe beam radiation pattern.

– One of side lobes is referred to as rear lobe. This is the part of the beam pattern directed opposite to the main direction.

Figure 4.2 shows the graph in orthogonal coordinates for the same source. In a graph in orthogonal coordinates, point coordinates are set by projections on a pair of stationary perpendicular axes. Horizontal axis on the graph with orthogonal coordinates corresponds to circumferences on the graph in polar coordinates. Vertical axis in the orthogonal graph corresponds to the rotation axis (radius) on the polar graph. Graph measurement scales can be linear or logarithmical.

The obtained beam pattern of the antenna can be used to measure certain important characteristics of the antenna:

– ratio of power gain between front and rear lobes for a directional antenna (in Fig. 4.3, the value for the side lobe at 180 °: 34 dB);
– ratio for the side lobe, maximum value for the side lobes removed from the main beam (Fig. 4.3 shows the value of the side lobe at +6 °: 20 db).

The following conventions and terms are used for radiation pattern analysis:

4.1.2.3 Beam Width

Angular distance of the antenna radiation pattern at which at least a half of the maximum power is still radiated is described as beam width. Boundary points of this main lobe are therefore the points in which field strength is reduced in space

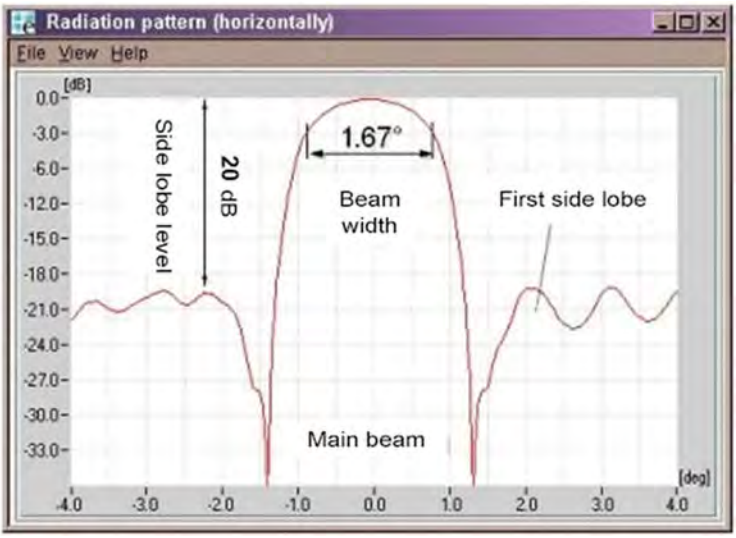

Fig. 4.3 Antenna directivity pattern in orthogonal coordinates in small scale

approximately by 3 dB relative to the maximum field strength. This angle is then described as beam width or aperture angle (or half-power angle, – 3 dB) denoted as Θ (or φ). Beam width Θ is the angle between two marked black power levels in Fig. 4.3. The angle Θ can be determined in horizontal plane (denoted as Θ_{AZ}), as well as in vertical plane (denoted as Θ_{EL}).

4.1.2.4 Aperture

Isotropic radiator disperses all energy over the sphere surface. Power has a certain density at the given distance. Directed (directional) antenna concentrates energy in a narrower region, while its power is higher than in an isotropic antenna. Density is usually characterized as power per unit of area. Received power can be compared to the connected surface. This area is known as effective aperture.

Therefore, effective antenna aperture A_e is the surface provided for the radiated or received signal. This is the main parameter determining characteristics of an antenna. Antenna gain factor is connected to effective area by the following relation:

$$G = \frac{4\pi \cdot A_e}{\lambda^2}; \quad A_e = K_a \cdot A \tag{4.1}$$

where λ is the wavelength; A_e is the effective antenna aperture; A is the physical antenna area; K_a is effective antenna aperture

Aperture effectiveness depends on the character of distribution of radiation density in the aperture cross-section. If it is linear, then $K_a = 1$. This high

effectiveness is shifted relative to high levels of side lobes obtained by linear radiation. Therefore, aperture efficiency in antennas with more practical levels of side lobes is less than one ($A_e < A$).

4.1.2.5 Main and Additional Lobes

The radiation pattern shown in the figures above describes the radiation concentrated in several lobes. As a rule, radiation intensity in one of the lobes is significantly higher than in other ones. The strongest beam is called the main beam; other (additional) ones are referred to as side lobes. Generally, main lobes are the lobes with the maximum radiation density. Side or additional lobes are the ones in which radiation intensity is lower.

4.1.2.6 Front to Back Intensity Ratio

Front to back intensity ratio is the relation between the gain of the front part and the back part of a directional antenna. For the case when the lobe is not exactly opposed to the main beam, the ratio of the front to rear relates to the highest side lobe within the area of $+-10$ to $+-30$ ° around the direction opposite to the main beam. It is desirable to ensure high ratio of the front intensity to back intensity; otherwise, minimum amount of energy is radiated in the unwanted direction.

4.1.2.7 Polarization

The field of antenna radiation consists of electric and magnetic power lines passing at right angles to each other. Electrical field determines the direction of polarization of the wave. When a single-wire antenna is used for extraction of energy from the passing radiowave, maximum extraction will occur if the orientation of the antenna coincides with the electrical field in terms of direction.

Electric field oscillations can be oriented in one direction (linear polarization) or rotate during passage of the wave (circular or elliptical polarization).

4.1.2.8 Linear Polarization

Vertically and horizontally mounted receiving antennas are designed for receipt of vertically and horizontally polarized waves respectively; therefore, any changes in polarization correspondingly cause changes in the level of the received signal.

Generally, the following polarization planes are used in practice:

- in a vertically polarized wave, electric power lines lie in vertical direction;
- in a horizontally polarized wave, electric power lines lie in horizontal direction.

When a single-wire antenna is used to retrieve energy from the passing radio wave, the best result is achieved if the antenna is oriented in the same direction as the electric field. Therefore, vertical antennas are used for effective reception of vertically polarized waves, while horizontal antennas are used for reception of horizontally polarized waves.

4.1.2.9 Circular Polarization

Circular polarization has power lines rotating by 360 ° at each cycle of RF energy. Circular polarization results from addition of two input signals with phase shift by 90 ° and simultaneous movement of the antenna with flat polarization by 90 °. Electrical field is selected as the basic field as the intensity of the wave is usually measured in the units of intensity of electrical field (volts, millivolts or microvolts per meter). In certain cases, orientation of the electric field does not remain constant – the field rotates as the wave passes through space. In these conditions, both horizontal and vertical components are present, and the wave has the so-called elliptical polarization (Fig. 4.4).

Circular polarization can be right-sided and left-sided. The disadvantage of an antenna with circular polarization is that it depends on the state of the atmosphere and is reflected with the opposite orientation for transmission. During reception, the antenna suppresses waves of the following orientation in case of spherical polarization, thus minimizing the effect of rain.

For maximum reception of energy of electromagnetic fields, the receiving antenna shall be in the same polarization plane. If an incorrectly polarized antenna is used, significant losses occur, in practice – between 20 and 30 dB.

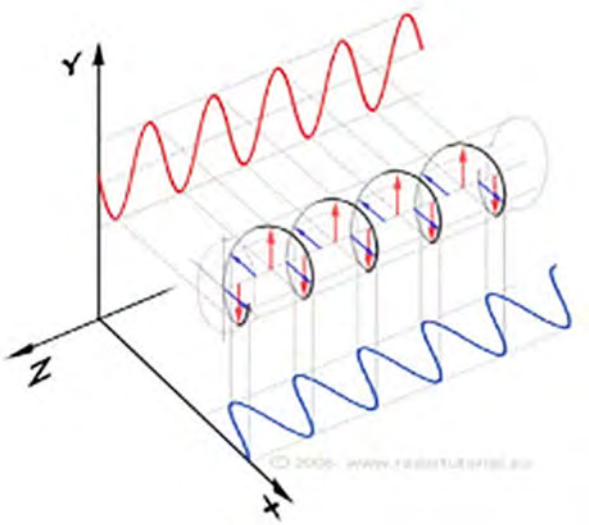

Fig. 4.4 Occurrence of circular polarization

In practice, in the event of emergence of meteo objects extremely complicating the situation, air traffic control services prefer to use circular polarization. In this case, masking effect of targets caused by meteorological objects will be reduced.

4.1.2.10 Half-Wave Antenna

Half-wave antenna (also known as a dipole, a Hertz, or a symmetrical vibrator) consists of two pieces of wire or pipe with the length of each equal to ¼ of the wavelength at certain frequency. This is a basic element used to build many complex antennas. For a dipole, current is maximum in the center and minimum at the ends. Voltage is minimum in the center and maximum at the ends.

Energy can also be supplied into a dipole in case of division of the dipole in the center and connection of the transmission line from the output stage of the end transmitter with two central ends of the dipole. Since the antenna is powered in the center (the point of low voltage and high current), this power supply is known as center feed method. Feed point is important for determining the type of the transmission line to be used in the designed device (Figs. 4.5 and 4.6).

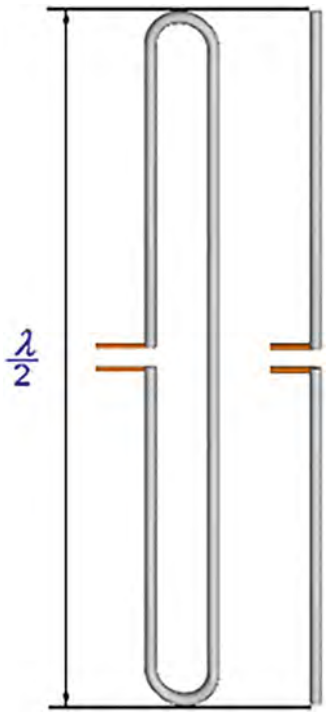

Fig. 4.5 Bent dipole and half-wave dipole

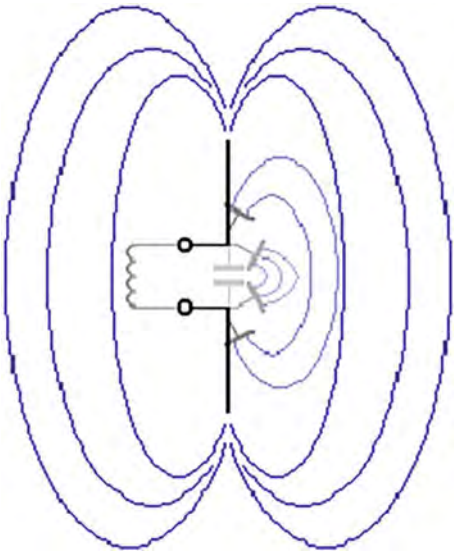

Fig. 4.6 Formation of a dipole from compressed oscillator circuit

4.1.2.11 Parabolic Antenna

Parabolic (dish) antenna is the shape most commonly used in radar equipment for installed (stationary) types of antennas. Figure 4.7 shows an example of a dish antenna. Dish antenna consists of one round dish reflector and the point source located in the focal point of this reflector. This point is known as (primary) radiator.

In turn, round parabolic reflector is made of metal frame covered with metal lattice on the inside. Width of the metal lattice slot shall be less than λ/10. This metal coating forms a reflector, acting like a mirror for radiated radar energy.

According to the laws of optics and analytical geometry, for this type of reflector all reflected beam will be parallel to the paraboloid axis, which produces one perfectly reflected beam parallel to the main axis without side lobes. Horn radiator ensures spherical wave front. Since each element of the wave front reaches the reflecting surface, its phase is shifted by 180 °, and it is emitted outside at angles that ensure parallel movement of all field elements.

This is an idealized model of the radar antenna, which forms a thin beam. If the reflector is elliptical, it will form a divergent beam. Typical serial surveillance radars use two different curvatures in horizontal and vertical planes in order to achieve the required bearing directivity of the beam and classic diverging beam with cosecant squared directivity pattern.

Of course, the perfect scenario shown in Fig. 4.8 is not found in practice. Beam pattern of actual dish antennas always has a conical shape due to structural imperfections in course of their production. Angular width of this main lobe can change within 1–2 ° in all special radar devices and within 15–20 ° in all other radars.

Fig. 4.7 Dish antenna of the Gematronic weather radar

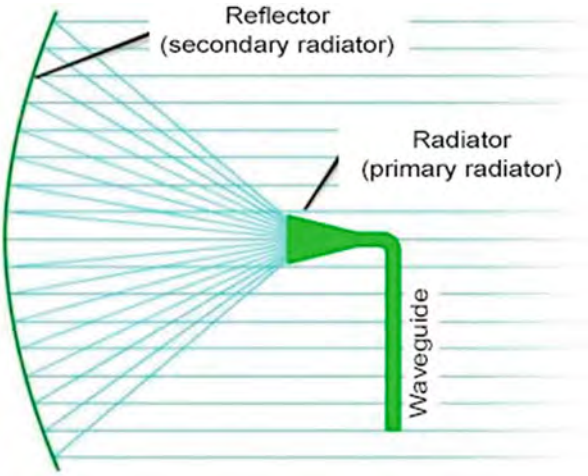

Fig. 4.8 Principle of building a dish reflector

Beam pattern of such dish antenna contains the main lobe that is directed along the propagation axis, as well as several side lobes. This type of reflector makes it possible to produce extremely narrow beams.

Gain G of an antenna with dish reflector can be determined as follows:

$$G \approx \frac{160^2}{\Theta_{Az} \cdot \Theta_{El}} \tag{4.2}$$

where

Θ_{Az} is the beam bearing width; Θ_{El} is the beam elevation width.

This is an approximate formula, but it gives good results for many targets, demonstrating that gain can change with the radiation function.

4.1.2.12 Blade Beam Antenna

A blade beam antenna is a directional antenna forming main lobe with narrow beam in one direction and wide beam in the other direction (Fig. 4.9). This pattern can be achieved by irradiating assymetrical section of a paraboloid, e.g. a truncated dish reflector. Since the reflector is narrow in vertical plane and wide in horizontal plane, it creates a beam that is wide in vertical plane and narrow in horizontal plane.

This type of antenna systems is usually used in the equipment of target height detection (if the reflector rotates by 90 °). The shape of a height finding radar resembles a horizontal blade shown in Fig. 4.10. Horn radiator is slightly shifted to the side from the center, as in an receiver antenna dish of a commercial satellite. This type of design is known as offset antenna.

4.1.2.13 Offset Antenna

One problem associated with feed element consists in the effect of shadow created by feed element located in the way of the beam. This shadow is a blind spot located directly in front of the horn radiator. As a rule, the horn radiator is an obstacle for beams received from the reflector in the dish antenna.

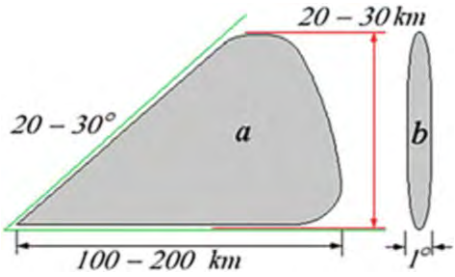

Fig. 4.9 Beam pattern of a blade beam antenna: (**a**) cross-section; (**b**) front view

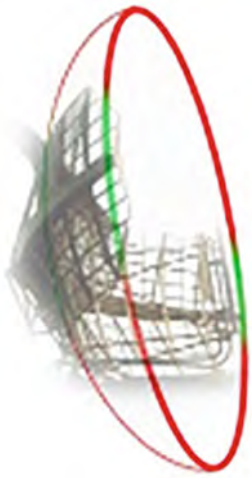

Fig. 4.10 Reflector of a cut paraboloid forming a blade-shaped beam

In order to solve this structural problem, horn radiator can be slightly moved away from the center. In this case, the horn will be outside the path of the wave, and there will be no deterioration of the beam pattern caused by aperture overlapping. The horn is directed backwards relative to the parabola axis, and the bottom half of the parabola is removed. The resulting effect is that the parabola has smaller depth at greater focal length. Therefore, the horn radiator is located at a greater distance from the reflector and requires greater directivity to prevent energy loss. This, this design requires bigger horns and is more expensive and difficult to produce (Fig. 4.11).

4.1.2.14 Cosecant-Squared Antennas

Cosecant-squared antennas were specifically designed for air surveillance radars.

Cosecant-squared beam pattern is a method of achievement of uniform signal strength at the input of the receiver, when the target moves at constant height within the limits of the beam. There are several possibilities of structural changes to achieve the cosecant-squared beam pattern in practice:

– deformation of the dish reflector;
– layered beam due to several horns feeding the dish reflector (Fig. 4.12).

In practice, cosecant-squared beam pattern can be achieved by modernizing the structure of the parabolic reflector accordingly: the radiator is in the focal point of the dish reflector and forms a relatively sharply compressed radiation lobe; all beams in perfect conditions shall be emitted from the reflector in parallel.

In order to obtain a cosecant-squared beam pattern, a part of the radiated energy shall be rotated upward, which can be done with smaller bend of the top part of the radiator. Some of the beams incident on the region with smaller curvature (at the top) are now reflected upwards. Another possible method consists in providing greater curvature of the bottom part of the reflector (Fig. 4.13).

Fig. 4.11 Standard antenna of a height finder with the offset antenna forming the blade beam

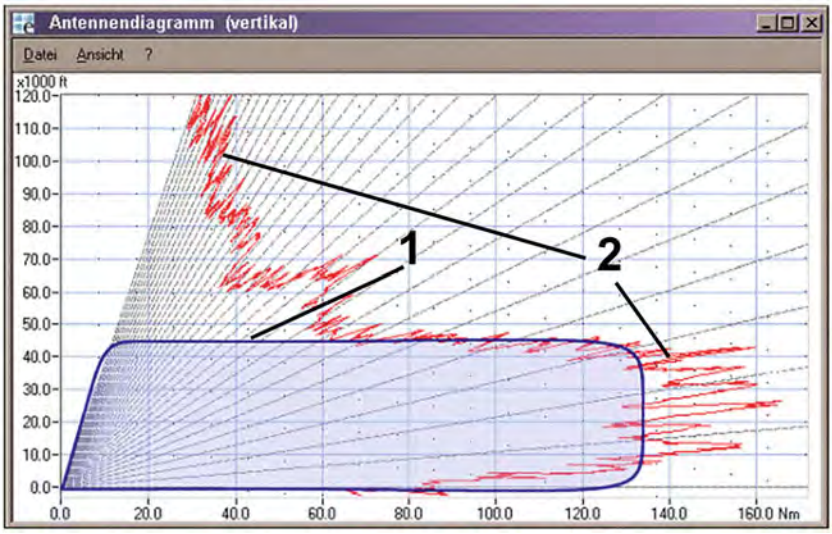

Fig. 4.12 Vertical projection of the beam pattern of a cosecant-squared antenna: graph 1 shows the theoretical shape, graph 2 – the shape measured in practice

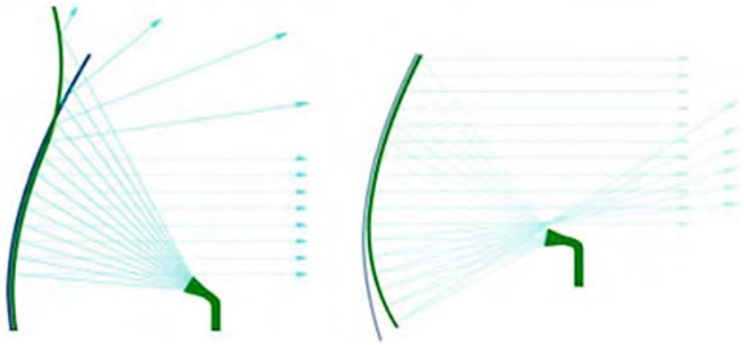

Fig. 4.13 Various modernizations to achieve cosecant-squared beam pattern reflector

The lobe of the radiator is also weaker at the border, and therefore borders of the reflector are irradiated with lower intensity than its center. Since the beams directed upwards don't have high power density, the maximum range of target detection in case of greater height is limited by this factor.

4.1.2.15 Inverse Cosecant-Squared Beam Pattern

Mobile radars and ship movement control systems usually used antennas for inverse cosecant-squared coverage ensuring direction of energy mostly towards the surface.

Coverage diagram in Fig. 4.14 shows directivity pattern of the antenna of a basic ship radar with inverse cosecant-squared antenna beam pattern. The antenna is designed for preferable irradiation below 0 ° (line of the horizon) to ensure constant detection of targets approaching by the sea surface.

4.1.2.16 Cosecant-Squared Antenna with Layered Beam

Cosecant-squared beam pattern can be achieved using two or more horns feeding the dish reflector.

Each feed element already has its own fixed radiation direction. If the transmission power is distributed unevenly between single radiators, the beam pattern approaches a cosecant-squared beam pattern.

With several receiving channels, it is possible to determine position by height. Here, targets can be set for beams with certain given elevation angles (Figs. 4.15 and 4.16).

Cosecant-squared pattern is not limited by dish reflectors – it can also be implemented in different types of antennas. In antenna arrays with waveguide antennas (Yagi antennas), directivity pattern is formed by interference of the direct wave with its parts reflected from the ground surface.

Here, a short explanation of terms used shall be provided.

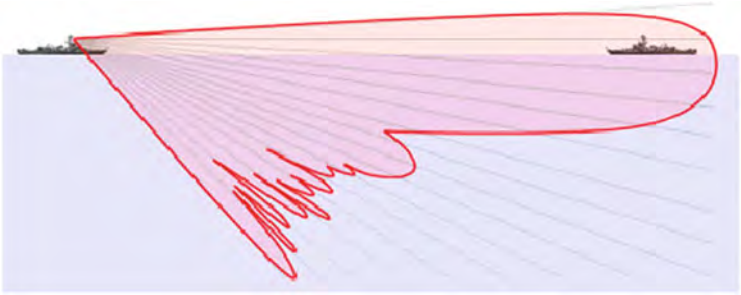

Fig. 4.14 Directivity pattern with the reverse cosecant-squared coverage

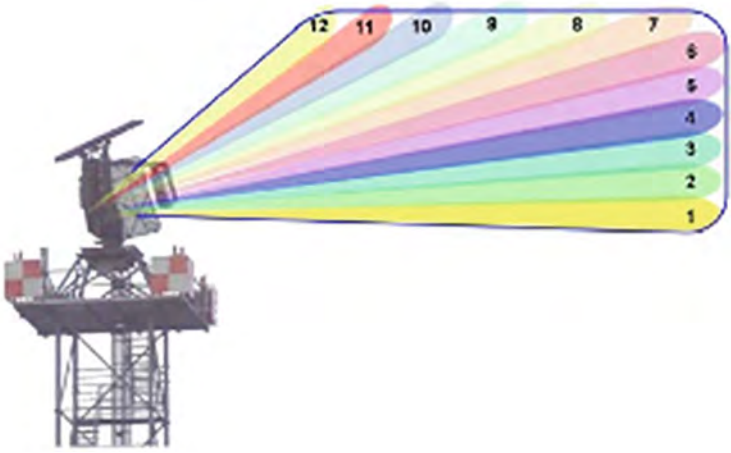

Fig. 4.15 Operating principle of a cosecant-squared antenna with layered beam

Fig. 4.16 An example of arrangement of twelve horn radiators on the antenna of the ASR 910 radar, which produces cosecant squared directivity pattern with layered beam

The term "cosecant" does indeed sound very similar to the name of a trigonometric function. This is true. But what's the connection between this term and an antenna?

As is known, the height H and the range R determine the value of the elevation angle ε using a simple formula:

$$\sin \varepsilon = \frac{H}{R}. \tag{4.3}$$

Cosecant-squared beam pattern means achievement of uniform signal strength at the input of the receiver, since the target moves at constant height within the limits of the beam.

If we transform the formula as:

$$H = R \cdot \sin \varepsilon, \tag{4.4}$$

and use the known trigonometric ratio mentioned above, the terms "sine" and "cosine" appear.

$$R = \frac{H}{\sin \varepsilon} = H \cdot \cos \varepsilon, \tag{4.5}$$

Use the main radar equation:

$$P_e \frac{\tilde{G^2}}{R^4} \quad |P_e = const, \tag{4.6}$$

If the echo has uniform signal strength at the input of the receiver, the range depends on the squared value of antenna gain in proportion to the fourth power:

$$\begin{aligned} &G^2 \tilde{R^4}, \\ &G\tilde{R^2}. \end{aligned} \tag{4.7}$$

For further simplification, we can arithmetically simplify the power and replace the range with the expression from the previous formula for cosecant. According to the above definition, the height will also be constant:

$$G(H \cdot \tilde{\cos} \varepsilon)^2 | H = const. \tag{4.8}$$

It means that the height can be reduced without measuring the dependence:

$$G \tilde{\operatorname{cosec}}^2 \varepsilon. \tag{4.9}$$

As a result, we get the basic mathematical description of the cosecant-squared antenna using the trigonometric function of cosecant.

4.1.2.17 Phased Antenna Arrays

Phased antenna array consists of multiple radiating elements, each with its own phase shifter. The beam is formed by means of phase shift of the signal emitted by each radiating element for ensuring amplifying/attenuating interference in order to control the beams in the required direction.

In Fig. 4.17a both radiators are formed in the same phase. The signal is amplified due to amplifying interference in the main direction.

In Fig. 4.17b, the signal is radiated by the lower radiating element with the phase shifted by 10 ° with upper radiating element phase lead. Due to this, main direction of the accumulated signal radiation moves upwards.

In Fig. 4.17 radiating elements are used without a reflector. Therefore, the reverse lobe of the demonstrated beam pattern has the same size as the main lobe (Fig. 4.18).

The main beam is always pointed in the direction of the phase shift increase. If the signal to be radiated is supplied through the electronic phase shifter ensuring constant phase shift, the direction of the beam will be measured electronically. However, this process is not unlimited. The greatest value that can be achieved for the field of view (FOV) for a phased array antenna is 120 ° (60 to the left and 60 to the right). The necessary phase change can be calculated with the help of the theorem of sines.

For an antenna with phased array, important fact is that single radiating elements are controlled with the help of regular phase movement, which changes the main direction of the beam. For example, antenna of the German defense radar RRP-117 consists of 1584 radiating elements.

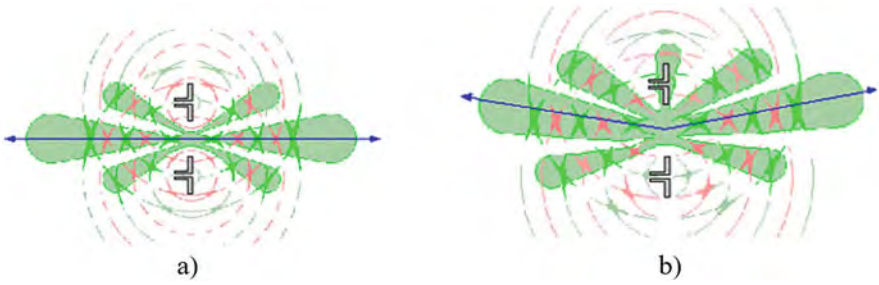

Fig. 4.17 Electron beam deflection

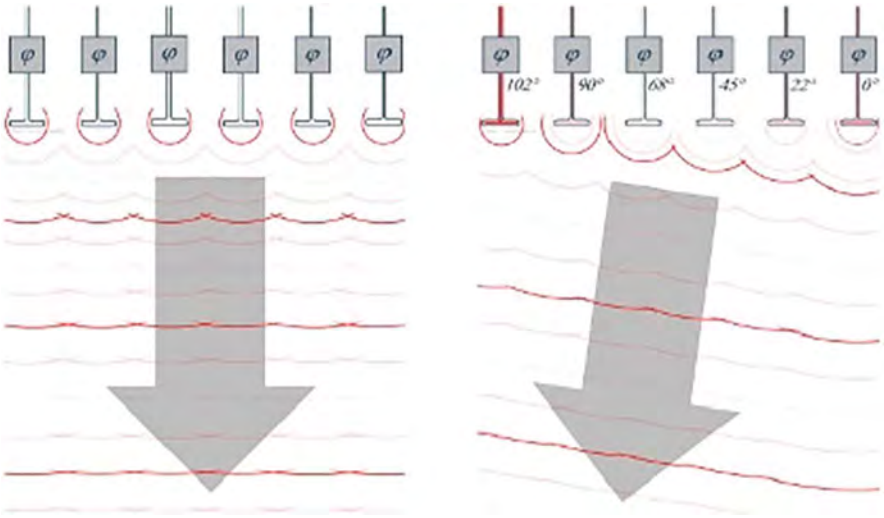

Fig. 4.18 Electron beam deflection caused by phased antenna array, left: without deflection, right: deflection

4.1.2.18 Linear Antenna Array

Such antennas consist of lines, the elements of which are controlled by a single common phase shifter. A row of horizontal antennas vertically mounted next to each other forms a flat antenna.

Typical examples:

- Precise approach radar PAR-80 (horizontally deflected electron beam).
- Air defense radar RRP117 (vertically deflected electron beam).
- Antenna with large vertical aperture (LVA) (fixed beam direction) (Fig. 4.19).

This type of phased antenna array is widely used if it is necessary to ensure beam deflection in one plane due to the fact that the entire antenna is rotated in any case.

4.1.2.19 Planar Array

These antenna arrays fully consist of single reflectors, and each of them has its own computer-controlled phase shifter. Elements are arranged in a matrix array. Planar arrangement of all elements forms a finished phased array antenna.

- Advantage: formation of beam direction in two possible planes
- Disadvantages: complex design concept and the need to use complex electronic devices (processors) for controlled phase shifter.
- Examples: AN-FPS-85 and Thompson Master-A (Fig. 4.20).

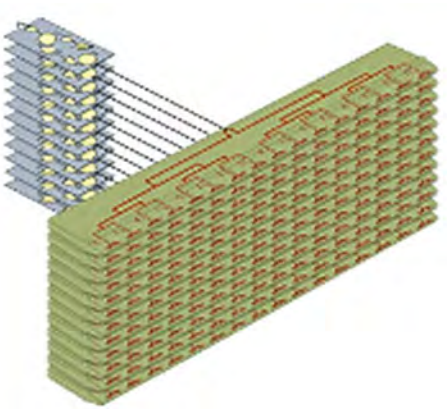

Fig. 4.19 Linear matrix of a phased array antenna; each row of reflectors requires its own phase shifter

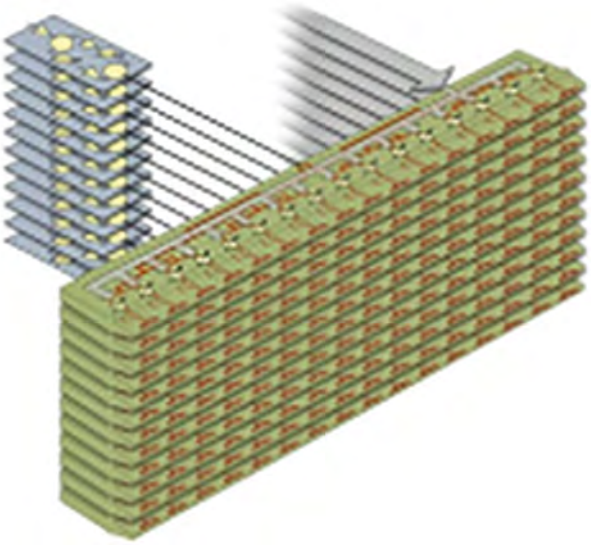

Fig. 4.20 Planar lattice of a phased array antenna; each reflector requires its own phase shifter

The processor providing control over the beam deflection requires high processing speed. Phase shifters are often controlled by a serial system of buses. Additional individual attenuators, one per each radiator, allows creating different beam shapes. If the radar is mobile and mounted on a moving platform, the processor shall also take into account the height and movement speed of the carrying platform (chassis) for calculation of deviation.

4.1.2.20 Frequency Scanned Antenna Array

Frequency scanned antenna array is the phased array antenna design in which the main beam is controlled by frequency scanning of the radiator. Beam control is the function of the transmitted frequency. This type of antennas is referred to as frequency scanned antenna array. Here, different radiating elements are powered from one bent waveguide (Fig. 4.21).

By changing the radiation frequency, the angle Θ_s between the axis of the main beam and normal to the antenna matrix is altered. Height information is generated using the following technique:

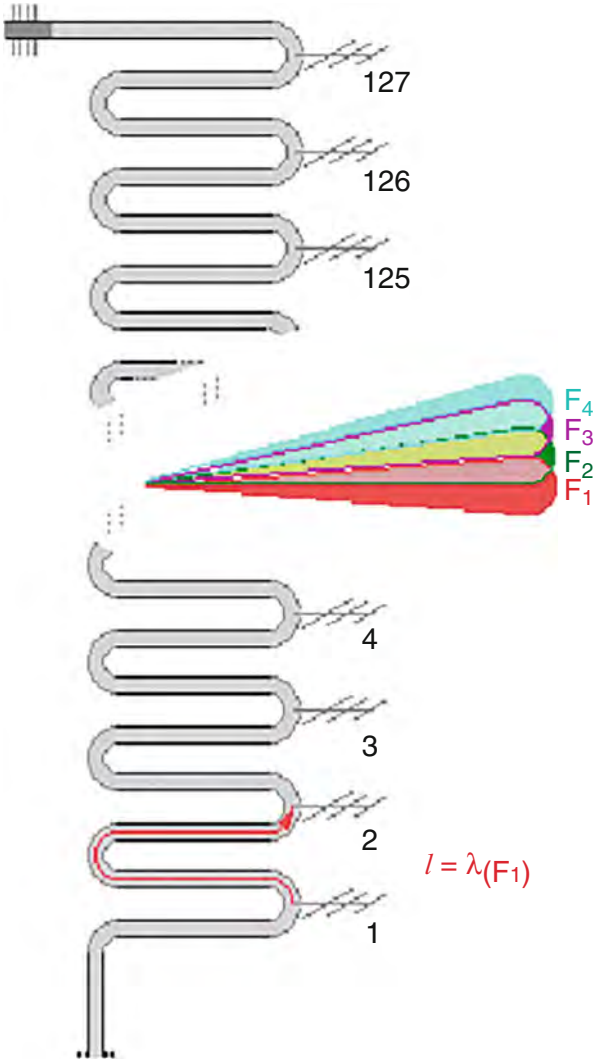

Fig. 4.21 Frequency scanned antenna array

– if the transmitted frequency is increased, the beam passes upwards relative to the front part of the antenna;
– if the transmitted frequency is reduced, the beam passes downwards relative to the front part of the antenna.

If the frequency changes, beam axis will change as well, and scanning can be performed with elevation. Design of the radar ensures tracking at frequencies at the moment of their transmission and detection and converts the returned frequencies into data for 3D display.

4.1.2.21 Phase Shifter

Various bypass switching circuits of phase shifters have greater operational speeds than regulators. Figure 4.22 shows a phase shifter with 4-bit switching, which is used in a basic radar. Various bypass circuits are included in the signal chain, which forms 16 different phase angles between 0 and 337.5 ° with a pitch of 22.5 °.

Inductances (thin meander-shaped circuits as components of low frequency filters) can also be used in feed with switching voltages for all 24 pin diodes.

Since this phase shifter module operates both for transmission and for reception, branching between these two paths is performed by means of pin diode-based switches on ceramic plate (at the input and output of the module).

The same data word shall be used both during reception and during transmission. This one radiator, which transmits the very last phase shift, first receives the echo signal. Its phase shifter shall have the largest bypass circuit to form the beam pattern in the required direction. The same bypass circuit is necessary to add the received energy and the video pulse.

Phase shifter traces the microwave signal that is transmitted to each radiating elements through cables of variable length. Cables delay the waves, thus shifting relative phase at the output. Figure 4.23 shows three basic delays that can be

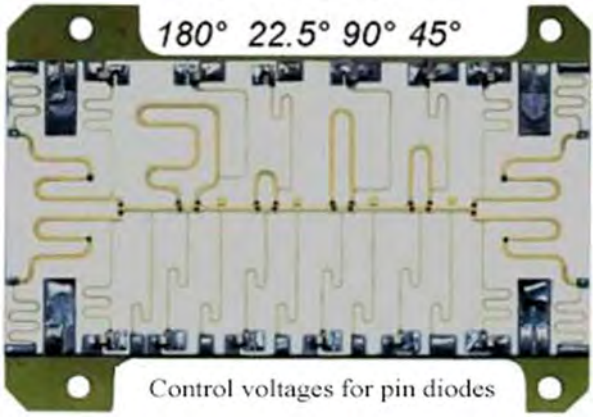

Fig. 4.22 Board with phase shifter routing with switching bypass circuits

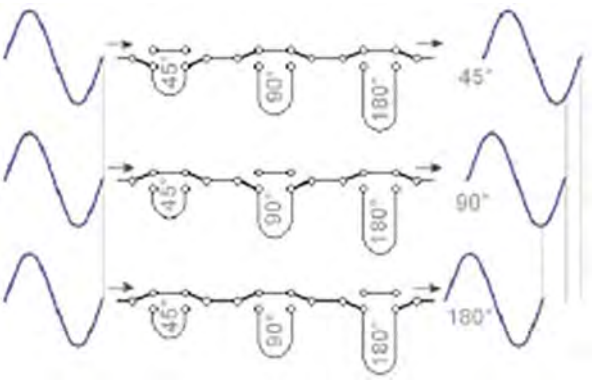

Fig. 4.23 Routing of phase shifter delay chains

introduced by each phase shifter. Switches are based on quick pin diodes. Central computer calculates the required phase delay for each radiating element and switches the phase shifter paths in the corresponding combination.

4.1.2.22 Monopulse Antennas

These antennas are combined; they are built as antenna arrays and have a special feed method: single elements of an antenna are not always switched together in phase. Various sums and differences can be formed based on the received energy for different purposes.

In primary radars using monopulse antennas all elements of the antenna are fed in a single phase, and their beam patterns are added. Certain groups are added only during reception, and their sums or differences are supplied to their individual receipt channels. All signals are then processed by the videoprocessor, and their difference is used for a more precise assessment of the target bearing. Therefore, it can operate at significantly lower speed of data coincidence per one scan.

In secondary channels with monopulse antennas, a group of pulses is transmitted via the accumulated channel, special additional channel – to the difference channel. The monopulse antenna here is used to suppress the side lobe.

These two examples demonstrate that: a monopulse antenna is not a basic antenna model; it can be built as a group of logarithmic periodic antennas, a set of simple dipole radiators or fields of radiating antennas (Fig. 4.24).

In terms of structure concept, these monopulse radars determine their initial coordinate points in tracking systems. Since the end of the 1970s, the monopulse principle has been introduced in well-known PSR and SSR systems and is now widely used around the world.

The target becomes visible on radar screens as soon as in enters the main beam of the radar antenna (Fig. 4.25).

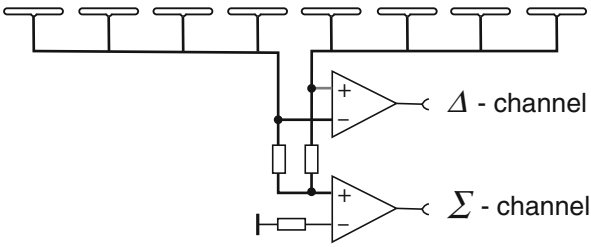

Fig. 4.24 Monopulse antenna principle

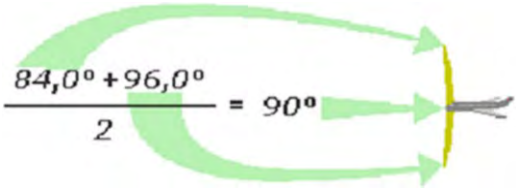

Fig. 4.25 Assessment of angular position of classic radars at high speed of target irradiation

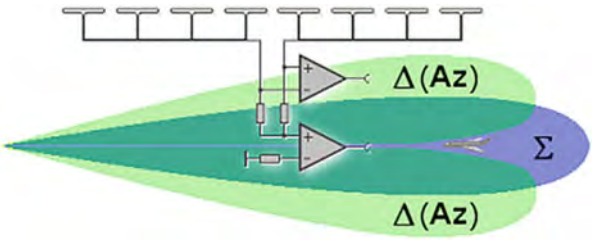

Fig. 4.26 The processor uses monopulse antenna to calculate the position of targets in the beam based on the data received from the radar

Such radar always introduces a small error in determining the target direction, since it assumes that the target is located in the direction of the main antenna beam axis. This is an error of the order of the main antenna beam width.

Unfortunately, estimated bearing position of the target will always be subjected to errors caused by thermal noise and errors due to target fluctuation (scintillation). Target fluctuation errors are caused by the change in cross-section during aiming of the antenna, which causes deviation of the envelope of the reflected pulse train.

Monopulse ensures much more accurate measurements of the target bearing than the assessment of angular position shown in Fig. 4.26. It also can operate at significantly lower request speed. Monopulse systems usually contain improved processing for presentation of information of higher quality about the target code. Single pulse is sufficient for monopulse measurements (hence the name).

All elements in a linear antenna array are usually divided into two halves. These two separate antenna arrays are placed symmetrically in the focal plane at each side of the radar antenna (often referred to as the reference direction axis). In the transmission mode (Tx), both antenna arrays will be powered in phase, and the directivity pattern is presented by region 1, known as Sigma or $\sum$ (sum – diagram – top graph), as shown in Fig. 4.27.

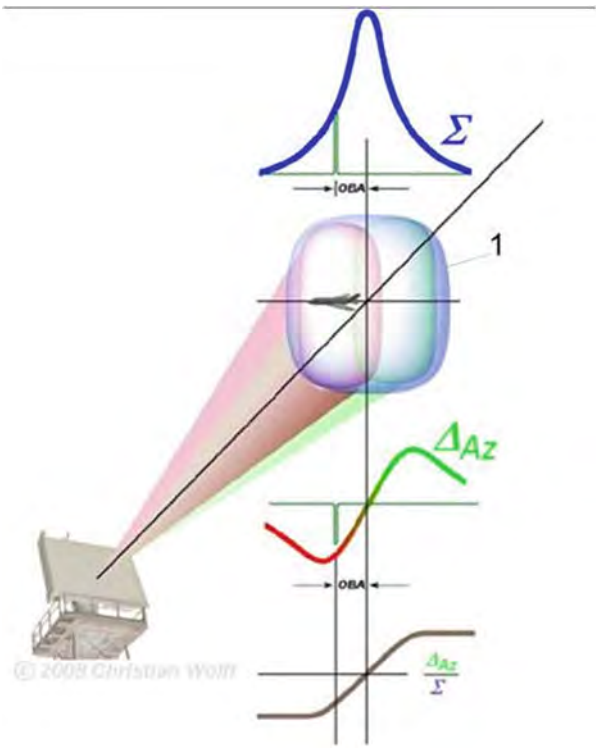

Fig. 4.27 Operating principle of a monopulse system

Additional reception path can be used in the reception mode (Rx). Received signals of both separate antenna arrays can be used to calculate Σ (in the same manner as the transmitted sum diagram) and the difference Δ_{Az}, the so-called delta azimuth diagram. Beam pattern is indicated by two separate regions in the same figure. Both signals are then compared as a function of the response processor, and their difference is used for more precise assessment of the target bearing.

The angle between the antenna axis (boresight axis) and the target direction is also known among specialists as the Off-Boresight Angle (OBA).

Elevation angle is also measured in 3D radars as the third coordinate, and the measurement procedure is used twice. Here, antenna is installed in the top half and in the bottom half. The second difference channel (Δ_{EI}) is now referred to as "Delta Estimate".

Such monopulse antenna is divided into four quadrants:

From received signals of these four quadrants, the following signals are formed:

Sum – signal Σ [I + II + II + IV];
Difference – signal Δ_{Az} [(I + IV) – (II + III)];
Difference – signal Δ_{EI} [(I + II) – (III + IV)];
Additional signal Ω.

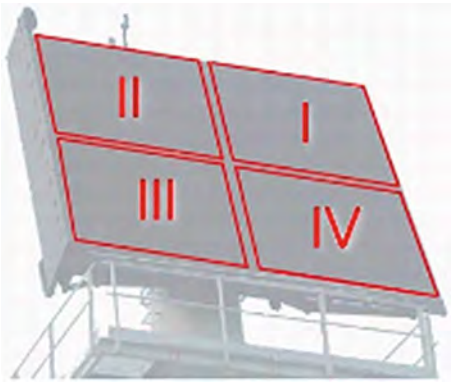

Fig. 4.28 Four parallel receiver channels

Fig. 4.29 During conical scanning, the radar tracks the conical diagram around the central axis

It should be noted that the signal is not additionally linked to the monopulse antenna. This channel for compensation of side lobes always has its practically individual small antenna and a very wide beam pattern; it is also used for active interference functions.

All these signals require an individual receiver channel. Therefore, all modern radars have at least four parallel receiver channels (Fig. 4.28).

4.1.2.23 Conical Scanning

In some older radars, conical scanning principle is used for target tracking.

Conical beam pattern can be generated as shown in Fig. 4.29 by using a rotating radiator driven by encased engine at the rear part of the dish. Axis of the radar lobe is deployed in a cone in space; the top of this cone is, of course, on the transmitter antenna or reflector.

Trajectory of the lobe axis usually has a circular shape at any given distance from the antenna. Within the useful beam range, inner edge of the lobe always overlaps the scanning axis. Now, let us suggest that we are using a beam with conical scanning for target tracking. If the target is in the scanning axis, then the strength of reflected signals remains permanent (or changes gradually together with distance). However, if the target is slightly outside the axis, the amplitude of reflected signals will change together with the scanning speed. For example, if the target is located to the left of the scanning axis, as shown in Fig. 4.30, the reflected signals will have the

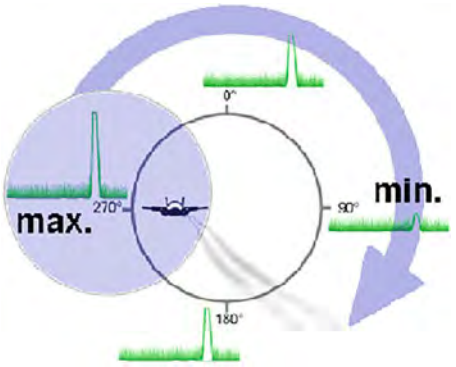

Fig. 4.30 Conical scanning principle: if the target is not in the reference direction, maximum reflection power in the direction of eccentric movement will be used. The antenna then shall follow in this direction

maximum strength, since the lobe passes through the right part of its cone. Information about immediate position of the beam relative to the scanning axis and the strength of reflected signals is supplied to the computer. Such computer in radar systems with angle tracking is known as angle tracking circuit (or an angular error detector). If the target leaves the scanning axis, the computer immediately determines the direction and the value of displacement of the antenna required to continue tracking. Computer output is used to control servo mechanisms, which move the antenna. Therefore, the target is tracked precisely and automatically.

Widely used structure of the conical scanning radar includes the Conical Scan on Receive Only mode (CORSO), in which the structure of conical scanning is only used when the radar is in the reception mode.

Therefore, we have examined the main principles of operation and typical designs of radars on the level that can be easily understood even by unprepared readers, school and college students. In the following, we will present a more in-depth description of the main antenna types and their technical characteristics, using stricter definition, physical formulas and mathematical expressions.

4.1.3 Basic Antenna Types and Technical Characteristics

As demonstrated above, all antennas, regardless of their varieties and types, generally convert radio-frequency electrical oscillations into the energy of electromagnetic field (radiowaves) and back (Fig. 4.31) [1].

Receiving and transmitting antennas are practically identical in terms of their operating principles due to reciprocity of electromagnetic field conversion efficiency. Nevertheless, technical features of receiving and transmitting antennas can differ significantly both in terms of purpose and in terms of operational requirements (limit power, bandwidth, noise, etc.).

The most basic classic example of an antenna is a resonant LC circuit (Fig. 4.32 – left). If the capacitor plates are separated and the inductance of the wire itself is considered as the choke, we get a basic dipole antenna shown in Fig. 4.32 (right).

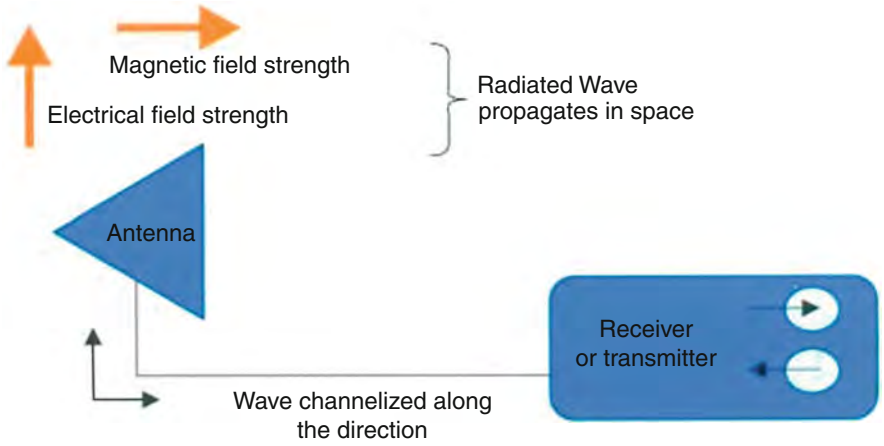

Fig. 4.31 Purpose of an antenna

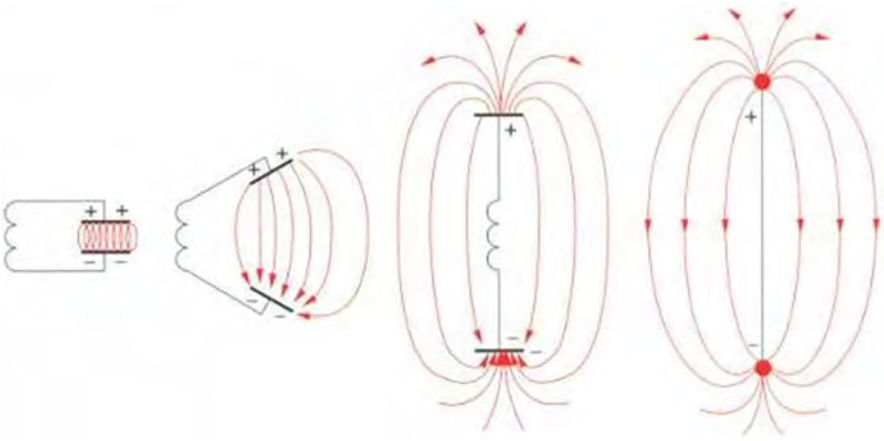

Fig. 4.32 Operating principle of a symmetrical Hertz vibrator (dipole)

In the transmission mode, alternating source current (e.g., current of a radio transmitter) generates alternating magnetic field around itself. This magnetic field changing in time, in turn, not only affects the electrical current that created it in accordance with the Faraday's law, but also creates an electrical field changing in time around itself. It creates an alternating magnetic field, etc.; as a result, an interconnected magnetic field is created, which forms the electromagnetic wave propagating from the antenna into space. Energy of the electric current source is transformed into electromagnetic wave energy by the antenna and transmitted through space. In reception mode, alternating magnetic field of the wave incident on the antenna induces currents on current-conducting elements of the antenna structure, which are supplied to the load (feeder, radio receiver).

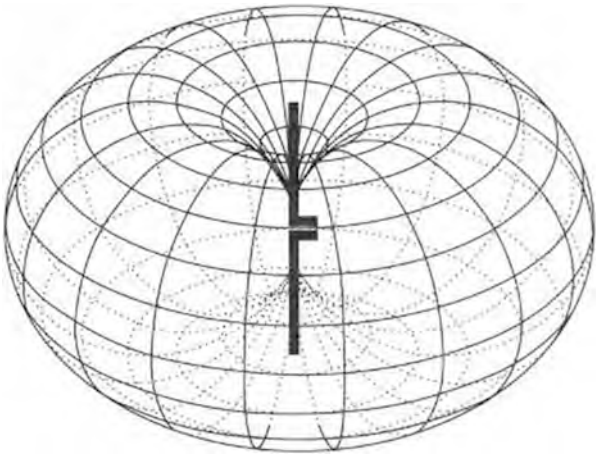

Fig. 4.33 3D presentation of dipole radiation pattern

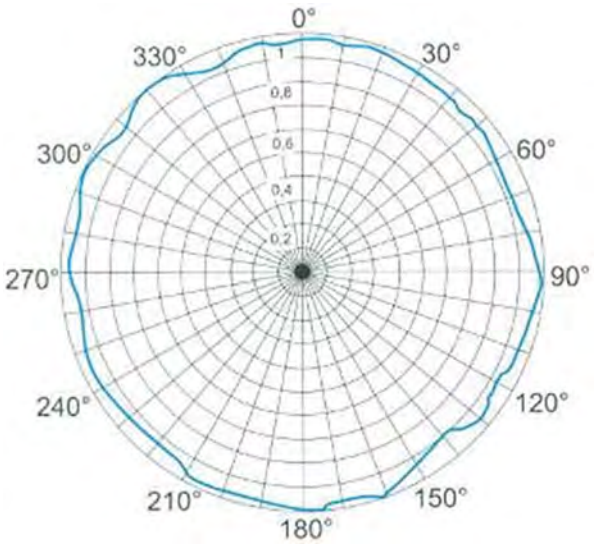

Fig. 4.34 Dipole beam pattern in horizontal plane (azimuth)

One of the most important characteristics ***of an antenna*** is its directivity, i.e. the ability of the antenna to focus its radiation in space.

Directivity pattern is the graphic representation of the dependence of antenna gain or directivity on the direction of the antenna in the given plane. Pattern of radiation of a dipole antenna in space is shown in Fig. 4.33. The corresponding radiation pattern is shown in Figs. 4.34 and 4.35.

As a rule, manufacturer documentation for each antenna includes the beam pattern in horizontal (bearing) and vertical (elevation angle) planes. This diagram is often built in the planes of directivity vectors of electrical and magnetic fields E

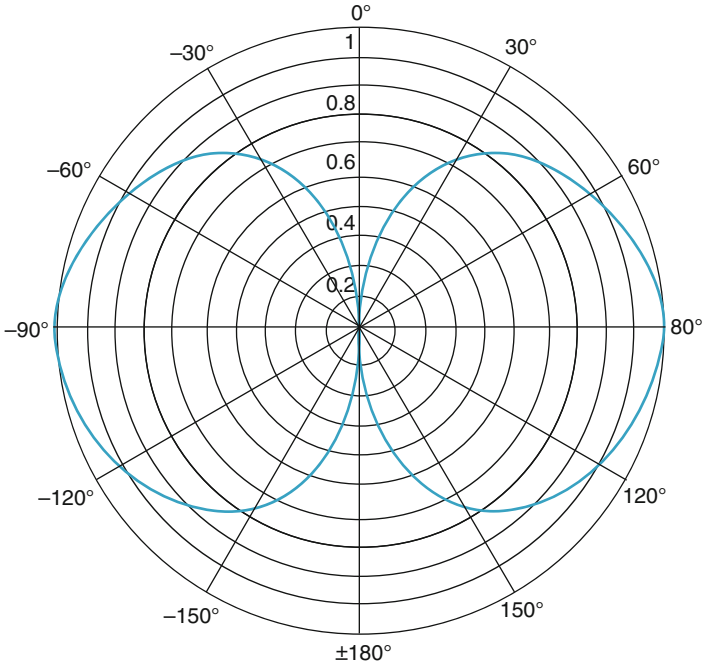

Fig. 4.35 Dipole beam pattern in vertical plane (rotation angle)

and H. Such diagrams depend on orientation of radiators and do not depend on orientation during antenna mounting. For special narrowly directed antennas, directivity pattern is usually built in rectangular coordinate system (Fig. 4.36).

The following parameters are determined using the beam pattern.

1. Suppression of side lobes – relation between main lobe and biggest side lobe.
2. Beam angle at half power – the angle between two points of the main lobe removed from the maximum by – 3 dB. It is determined for both planes.
3. Front-to-back ratio – the ratio of the peak gain in the forward direction to the gain in the reverse direction (180°), dB.

Directivity *D* is the ratio of the intensity of radiation $F_{\max}$ in the main direction to the intensity of radiation F_i of the perfect isotropic radiator with the same radiated power P_t. Radiation intensity can be replaced with power density:

$$D = \frac{F_{MAX}}{F_i}, \quad \text{where} \quad F_i = \frac{P_t}{4\pi}. \tag{4.10}$$

Gain *G* is the ratio of the intensity $F_{\max}$ of radiation in the main direction to the intensity F_i0 of radiation generated by the perfect isotropic radiator with the same input power P_t0.

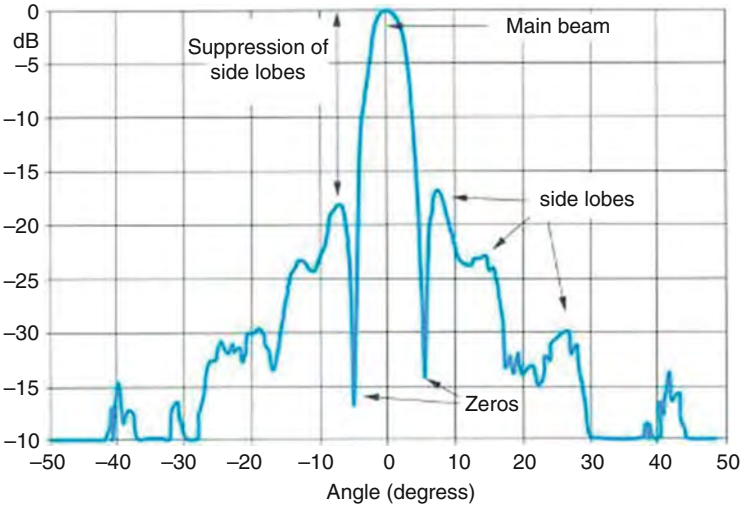

Fig. 4.36 Beam pattern in rectangular system of coordinates (for narrow-beam antennas)

Degree of coincidence of D and G coefficients is characterized by the antenna efficiency

$$D = \eta \cdot G \tag{4.11}$$

If ŋ = 100%, gain and directivity factors are equal.

Effective antenna area is the value characterizing ability of a receiving antenna to gather incident electromagnetic radiation, i.e. its efficiency.

Effective area is introduced by the following formula:

$$A_w = P_r/S, \tag{4.12}$$

where A_w is the effective area; P_r is the received power (usually measured in watts); S is the radiation stream (W/m^2).

Even though effective area of the antenna can be considered as real area perpendicular to the direction of incident wave propagation, it does not necessarily coincide with geometrical dimensions of the antenna A_g. Aperture effectiveness q is the value characterizing the relation between the effective and geometrical area:

$$q = \frac{A_w}{A_g}. \tag{4.13}$$

Effective area of an antenna can be expressed through the gain factor as follows:

$$A_w = \frac{\lambda^2}{4\pi} G. \tag{4.14}$$

Of course, it is necessary to understand that due to diffraction of radio waves effective area of an antenna is always smaller than its geometrical area: waves of excess length bypass the antenna, waves of insufficient length are sensitive to irregularities of the antenna surface. It is usually considered that the operating range of the antenna is:

$$20\sigma < \lambda > 120D, \tag{4.15}$$

where λ is the wavelength; σ is the surface precision; D is the aperture diameter.

Outside this wavelength range, effective area of any antenna is reduced significantly. If the antenna operates at fixed wavelength, its design ensures that its effective area at the given wavelength is maximum. Effective area of the antenna is connected to its beam pattern by the following formula [1]:

$$\begin{aligned} &A_{eff}\,\frac{\lambda^2}{\Omega_a} \\ &\Omega_a = \int\limits_{4\pi} A(\theta,\varphi)d\Omega, \end{aligned} \tag{4.16}$$

wheere Ω_a is the effective solid angle; $A(\theta, \varphi)$ is the directivity pattern.

Aperture efficiency is the non-dimensional value equal to the ratio of the effective antenna area to its geometrical area:

$$\varepsilon = \frac{A_{eff}}{A_{geom}}. \tag{4.17}$$

Since effective area of an antenna is always smaller than the geometrical area, aperture utilization factor is within the range of 0–1.

Input impedance (resistance) of the antenna is the main characteristic of transmitting and receiving antennas, which is determined as the ratio of high-frequency voltage and supply current. Input impedance of the antenna Z is determined as the sum of resistance of radiation R1 and resistance of antenna losses R_2:

$$Z = R_1 + R_2. \tag{4.18}$$

Radiation resistance is usually defined as the quotient of the radiated power and the square of the average squared current value, and its value depends on the position on the antenna. Resistance of losses R_2 includes ohmic losses in antenna elements and wires, losses in insulation (due to leaks), resistance of losses in the ground and heat losses in the surrounding objects located in the near field of the antenna.

In case of resonance, imaginary part in the expression for impedance disappears. In order to increase antenna efficiency, it is necessary to aim for matching of the input impedance Z of the antenna with wave resistance of the line, i.e. their equation,

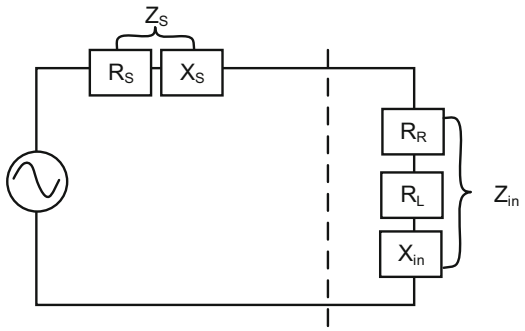

Fig. 4.37 Simplified equivalent electrical circuit of a transmitting antenna

as well as reduction of losses in the antenna. In case of mismatch, parasite effects occur, including reflection. Reflected power is easily calculated with the help of equivalent circuit characteristic of a transmitting antenna (Fig. 4.37).

In order to obtain optimal antenna characteristics, transmitter impedance Z_s shall be matched with the input antenna impedance Z_{in}. In this case, the transmitter power is maximum.

Matching condition can be described as follows:

$$\begin{aligned} Z_{in} &= Z_s \\ Z_{in} &= R_{in} + jX_{in} \\ Z_s &= R_s + jX_s. \end{aligned} \tag{4.19}$$

If tihs condition is not met, the signal is reflected, and a part of power is lost. This effect is characterized by so-called *voltage standing-wave ratio* (VSWR). It is defined as relation of maximum voltage to minimum voltage in the transmission line. For practical calculation of the numeric value, two-link formula can be used:

$$\begin{aligned} a_r &= -20\lg|r| = -20\lg\left(\frac{V_{refl}}{V_{form}}\right) = -10\lg\left(\frac{R_{refl}}{R_{form}}\right) \\ s &= \frac{V_{\max}}{V_{\min}} = \frac{I_{\max}}{I_{\min}} = \frac{|V_{form}| + |V_{refl}|}{|V_{form}| - |V_{refl}|} = \frac{\sqrt{P_{form}} + \sqrt{P_{refl}}}{\sqrt{P_{form}} - \sqrt{P_{refl}}} \end{aligned} \tag{4.20}$$

Another parameter, antenna reflection coefficient, is closely connected to VSWR. It is determined as the ratio of amplitudes of the reflected V_{refl} and forward V_{forw} waves:

$$r = \frac{V_{refl}}{V_{form}}. \tag{4.21}$$

Table 4.1 Interconnection of parameters characterizing matching of antenna impedances

VSWR	r	a, dB	Reflected power, %
1.002	0.001	60	–
1.01	0.005	46	–
1.1	0.05	26	0.2
1.2	0.1	20	0.8
1.5	0.2	14	4
2.0	0.33	9.5	11.1
3.0	05	6	25
5.0	0.67	3.5	44.4

From this, it is possible to calculate the reverse loss coefficient:

$$s = \frac{1 + |r|}{1 - |r|}. \tag{4.22}$$

Therefore, antenna impedance matching is described by several interconnected parameters. In order to simplify transition from one parameter to another, it is recommended to use data from Table 4.1.

Antenna efficiency (in the transmission mode) is the ratio of power of antenna radiation to the power of the supplied radio frequency signal. Efficiency of the transmitted antenna (η_a) the ratio of the power radiated in space (P_Σ) to the value of full power (P_{tr}) supplied from the transmitter to the antenna input:

$$\eta_a = P_\Sigma / P_{nep}. \tag{4.23}$$

This full power supplied to the antenna in the general case is spent for antenna radiation and energy losses in the antenna:

$$P_{tr} = P_\Sigma + P_F \text{ and } \eta_a = P_\Sigma / (P_I + P_F).$$

Power losses of any antenna are formed by losses in the ground, various wires of the antenna, isolators for suspension of the antenna curtain and even in the ropes supporting the antenna. It should be noted that the main energy losses are usually losses in the ground.

Due to the principle of reciprocity of antennas, efficiency of a receiving antenna is estimated by the value of its efficiency when used as a transmitting antenna. Since the power of received waves is always very low, efficiency of the receiving antenna can be low, but not lower than 10–15%.

The range of operating frequencies in which the characteristics of an antenna can be considered practically unchanged is called bandwidth. The antenna operates with the highest efficiency in this range. As a rule, it is located near the central (resonant frequency). In turn, bandwidth depends on the type of the antenna and its geometry. In practice, band pass is determined by the VSWR level. For wideband antennas, the

ratio between the frequencies of the top limit of the pass band to the bottom limit of the pass band is determined. The ratio of 2:1 is called an octave, 10:1 – a decade. In general case, the frequency band can be described by the expression:

$$BW = \frac{f_H}{f_L}, \tag{4.24}$$

where f_H is the higher boundary of the pass band; f_L is the lower boundary.

The antenna is considered wideband if $BW \geq 2$. For narrowband antennas, bandwidth is determined as follows:

$$BW = \frac{f_H - f_L}{f_C} \cdot 100\%, \tag{4.25}$$

where f_C is the central frequency.

Numeric values are within the range of 0–200%. As a rule, this definition is used only for BW under approximately 100%. The permissible value of radiated power is an extremely important parameter of any transmitting antenna. If the current-carrying parts of the transmitting antenna are surrounded with air, then at $E > 30$ kV/cm (and normal atmospheric pressure) electrical breakdown is inevitable. Therefore, the limit permissible radiation power (which is 2–3 times higher than the operating frequency) is determined from the condition $E < 30$ kV/cm in the point of maximum field strength near the antenna.

Below we will briefly examine the basic most commonly used antenna types.

4.1.3.1 Dipole Antenna

Dipole antennas are the type of antennas that is most widely used in radioelectronics. The most well-known example is a half-wave dipole (symmetrical vibrator). Dipole length is slightly smaller than the wavelength.

Since the input impedance in case of resonance is within 50–70 Ω (depending of the length/diameter ratio), in practice it is usually recommended to connect the feeder cable with typical nominal impedance. In this case, current distribution (red line on the graph in Fig. 4.38) is a sinewave in approximation. Beam pattern is presented in the E-plane, i.e. in the plane where the dipole axes are located. In the perpendicular plane (H) radiation has no specific direction.

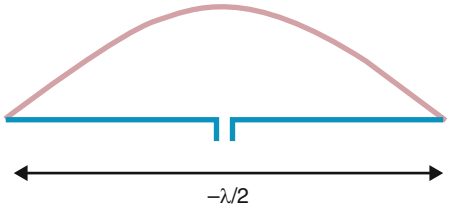

Fig. 4.38 Current distribution on a half-wave dipole

Half-wave dipople, as follows from the name, is made only for one frequency. However, multiple experiments demonstrate that such dipoles can be used for reception within a wider frequency range, i.e. at a distance from resonant frequency. Since the input impedance of the antenna greatly depends on the ratio between the antenna length to the wavelength (Fig. 4.39), correct matching is extremely important for operation at a distance from the resonant frequency. It is especially true for the so-called thin dipole, in which the ratio of length l to diameter d is high. Mismatch decreases together with this ratio.

Several standard shapes of thick dipoles are shown in Fig. 4.40. When matching the dipole impedance with the feed cable, it is necessary to take into account that the developers of radioelectronic equipment almost always use balance-to-unbalance converters. For the purpose of material saving and weight reduction, all wideband dipoles are usually designed as lattices. Another popular type of test antennas is presented by the so-called biconical antennas shown in Fig. 4.40 (right).

Directivity pattern depends on the relation of the dipole length to wavelength (Fig. 4.41).

Due to imperfect current distribution on the dipole, when the ratio of dipole length to the wavelength is too high, the energy is dissipated. This can be avoided by using a rod antenna, which operates as telescopic, and the length of which varies in accordance with operating frequency. However, a more practical solution consists in changing the distribution of current on the antenna in such manner that only a part of the antenna is activated at high frequencies – e.g., with the help of reactive elements, resonance circuits, ferrite rings, etc. In this case, the ratio of dipole length to wavelength can remain almost unchanged even if the frequency is changed.

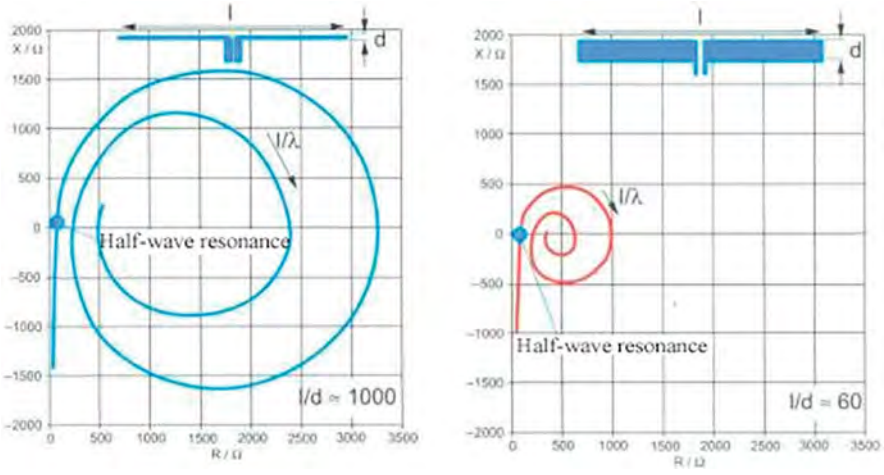

Fig. 4.39 Input impedance of the dipole antenna for different ratios between the dipole length and its diameter

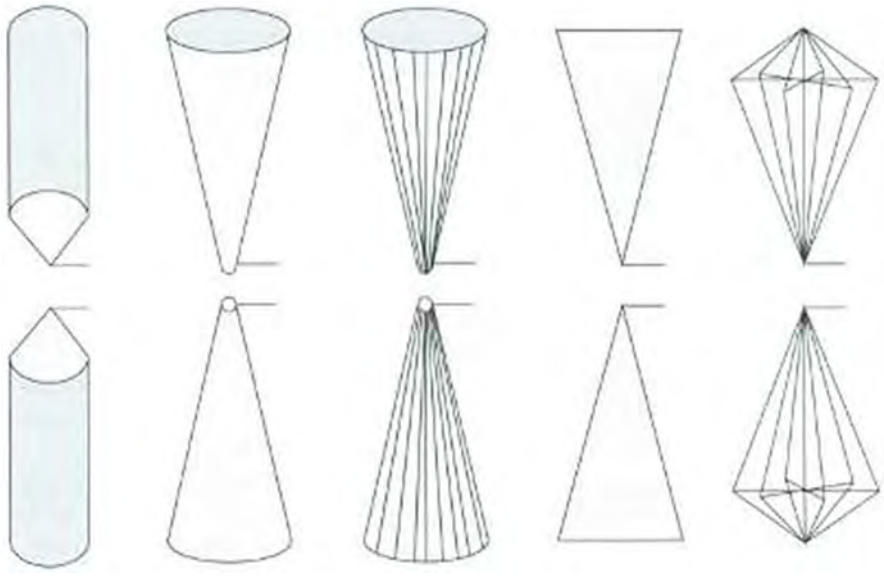

Fig. 4.40 Shapes of wideband dipoles

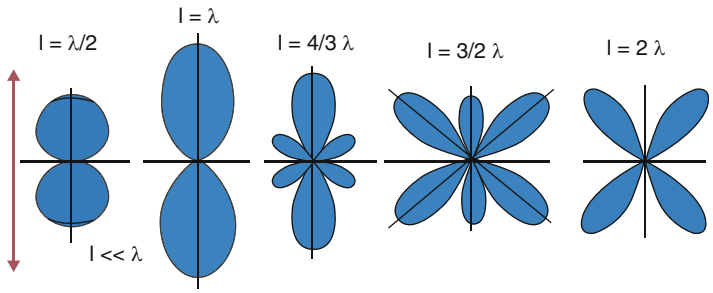

Fig. 4.41 Beam patterns for half-wave dipoles with different ratios between dipole length and radiation wavelength (the arrow is used to indicate the desired transmission direction)

When the SHF line is turned into a radiating system (antenna), irreversible energy losses increase, since heat losses P_{F} are added to radiation losses P_{Σ}. Therefore, the total power consumption of the antenna is:

$$P_{\text{A}} = P_{\text{F}} + P_{\Sigma}. \tag{4.26}$$

In practical applications of this rule, the increase of irreversible losses in the system can be considered as an increase in its active resistance, i.e. it is possible to say that the full active resistance of the antenna is:

$$R_{\mathrm{A}} = R_{\mathrm{T}} + R_{\Sigma}., \tag{4.27}$$

where
R_{T} is the resistance of thermal losses; R_{Σ} is the intrinsic resistance of the radiator.

Since antenna operates as an energy converter, its efficiency, which is the ratio of the radiation power to the supplied power, is an extremely important characteristic:

$$\eta_a = \frac{P_{\Sigma}}{P_{\Pi} + P_{\Sigma}} = \frac{1}{1 + \frac{R_{\Pi}}{R_{\Sigma}}}. \tag{4.28}$$

It follows, therefore, that the antenna efficiency increases together with an increase in the the resistance R_{Σ} compared to the resistance of heat losses. However, absolute value of radiation resistance is also of great significance. As with any oscillation system, current and voltage during resonance, as well as resonance properties of the antenna greatly depend on active resistance. The higher it is, the smaller is the current amplitude in the antenna during resonance at set power. However, the smaller the current value is, the lower the voltage in the antenna is. The latter is beneficial, since with the given radiation power it helps soften the requirements for resistance of the antenna insulation.

High radiation resistance increases the width of the antenna pass band and reduces the sharpness with which its input impedance changes when the operating frequency of the transmitter is altered. This facilitates matching of the antenna with the feeder and generator at all frequencies at which the antenna shall operate. During calculation of an antenna, it is necessary to know the value of its input resistance during resonance, since in this case the input resistance of the antenna is purely active, and the antenna power consumption is calculated as follows:

$$P_A = \frac{1}{2} I_{inA}^2 R_{inA}, \tag{4.29}$$

From which:

$$R_{inA} = \frac{2P_A}{I_{inA}^2}. \tag{4.30}$$

4.1.3.2 Asymmetrical Vibrator (Monopole)

In essence, this is a rod antenna in the form of a half of a vertically installed symmetrical vibrator (Fig. 4.42). Vibrator length is 1, 1/2 or 1/4 of the wavelength. Beam pattern is shown in Fig. 4.43. It is an eight cut along. Due to the fact that the second half of the eight is absorbed by the ground, directivity of a monopole is usually twice higher than in a dipole, since all power is radiated in a narrower direction.

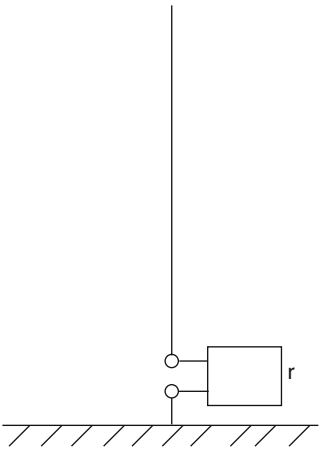

Fig. 4.42 Monopole (unbalanced vibrator)

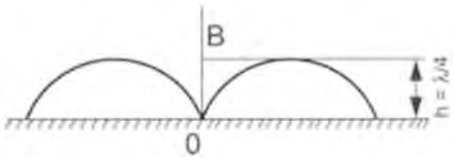

Fig. 4.43 Monopole beam pattern

In general, vibrators in LF, HF and MF ranges are used as transport antennas. Input impedance of a monopole is two times smaller than the input impedance of a dipole and amounts to 30–40 Ω.

4.1.3.3 Directional Antennas

It is impossible to manufacture a perfect directional antenna. Nevertheless, there are antennas that focus the radiated power in one direction with maximum efficiency. The simplest directional circuit consists of two asymmetrical vibrators with power supplied with different phases (Fig. 4.44). Such antennas are sometimes referred to as director antennas. In the examined case, the distance between vibrators amounts to A/4, phase shift – to 90°. The radiation pattern is shown in Fig. 4.45. Even though such radiation cannot be called narrow, there is a region in which antenna emits no radiation.

This feature can be used in practice to suppress the interference phenomenon.

Combinations of several vibrators are used to obtain narrowly directed radiation. Of course, power supply in practice is performed not as shown in Fig. 4.44. As a rule, connection through radiation is used: only one radiator receives power through the cable and activates the other radiators. In director-type antennas (Fig. 4.45) (waveguide antennas, Yagi antennas), 4–30 elements are used. Gain factor, as a rule, exceeds 10 dB.

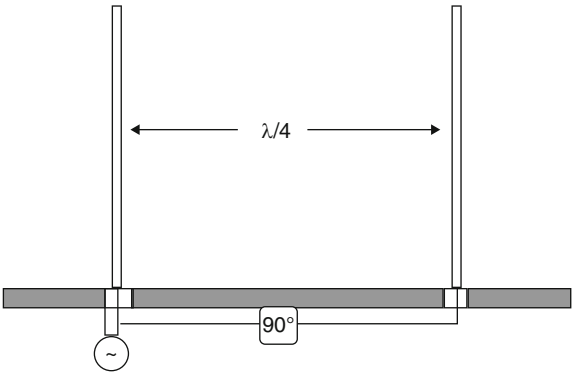

Fig. 4.44 Director antenna

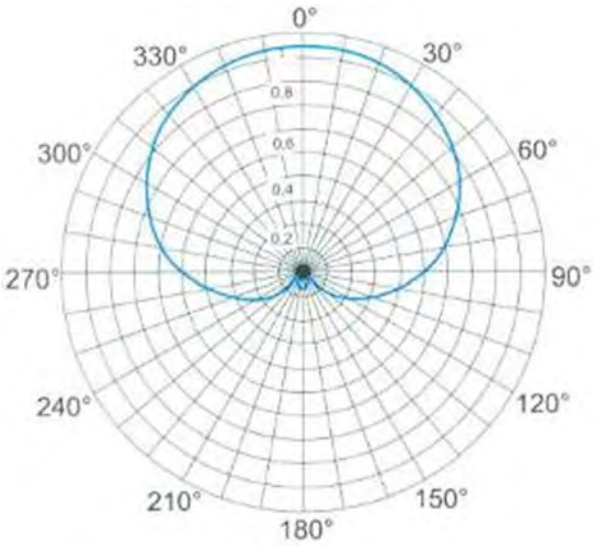

Fig. 4.45 Director antenna beam pattern

4.1.3.4 Log-Periodic Antenna

Log-periodic antenna is a wideband directed antenna operating within ten-fold or wider wave range. In terms of gain, this antenna is equivalent to a three-four-element waveguide antenna. Log-periodic antennas are usually used for reception of television signals.

One of the basic versions of this antenna is shown in Fig. 4.46. The antenna consists of a row of parallel vibrators connected to the two-wire line with serial polarity reversal of vibrator feed points. Values of vibrator lengths and distances between them reduce in geometrical progression in the direction of the feeder connection points. A short-circuiting link improving matching of the antenna with the feeder and ensuring symmetry is installed behind the longest vibrator.

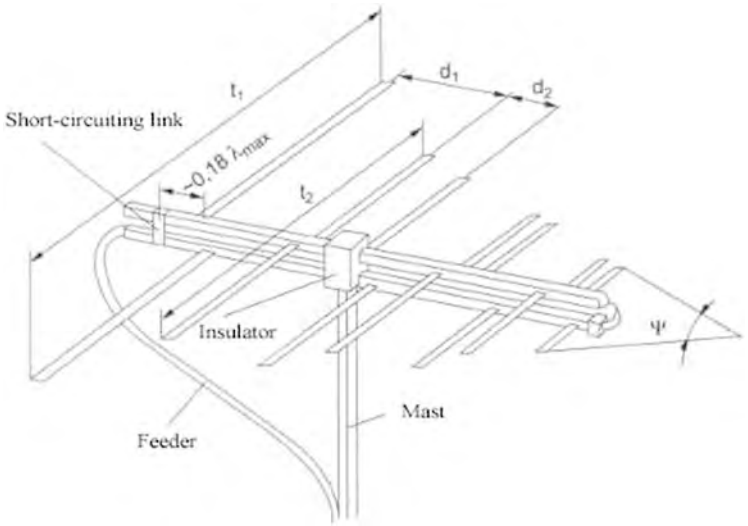

Fig. 4.46 Typical design of a log-periodic antenna

The cable is put through one of the pipes of the two-wire line and welded at the side of the shortest vibrator. Characteristics of the antenna depend on the denominator of the geometrical progression τ characterising the rate of decrease of vibrator lengths and distances between them and the angle φ at the top of the triangle into which the vibrators are inscribed. The closer τ is to one, and the less φ, the greater is the gain of the antenna; however, its dimensions and weight also increase. In practice, as a rule, $\tau = 0.8$–0.9 and $\varphi = 30$–$40°$, which helps achieve a relatively high gain with relatively small dimensions and weight.

Since not all radiators emit power at each frequency, log-periodic antennas cannot ensure high directivity. The radiation pattern is practically the same across the entire frequency range. As a rule, the width of the beam at half power is about 120 ° in the H plane and 60. . .80 ° in the E plane.

4.1.3.5 Active Antennas

According to the definition, active element of an active antenna is directly connected to the dipole with small electrical length (Fig. 4.47). They are not to be confused with systems in which the output signal of the passive antenna passes through the amplifier. It clearly follows from the definition that active antennas can only be receiving.

The advantage of active antennas lies in the fact that their radiation pattern is not the function of frequency, and they include elements with small electric length.

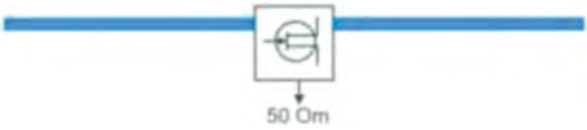

Fig. 4.47 Building principle of an active antenna

Active antennas are most widely used for reception of low-frequency signals (up to 200 MHz), since for them the threshold atmospheric noise is high. However, due to wide frequency band, they are also applied at higher frequencies.

One of the most important advantages is small size. The length of active antennas can be smaller by an order of magnitude. As opposed to other types of antenna, when selecting the design of an active antenna, it is necessary to distinguish between electronic gain GT and practical gain Gpract. The first is the ratio of the received signal at nominal resistance to maximum power of the received signal, which can be received by an antenna with equivalent directivity. The second coefficient characterizes the ratio of the received signal power at nominal resistance to maximum power of the signal received by a perfect non-directional antenna.

Maximum disadvantages of active antennas are more narrow dynamic range, sensitivity to interference and mounting specifics.

4.2 Examples of Design Concepts of Antennas for Radio Communication Systems

Let us consider a number of specific design concepts of SHF antennas designed for use in radio communication and telecommunication systems.

4.2.1 Small-Sized Antenna for Portable Wireless Systems of Thee WIMAX/WLAN Standard

Antennas that not only cover the required band but also have the minimum linear dimensions are widely used in popular wireless systems WiMAX and WLAN. In practice, in order to reduce the size of the antenna unit, developers often use one two-band antenna instead of two one-pole ones.

Let us consider features of engineering and technical characteristics of one of the options of a small-sized two-band antenna for portable devices for frequency bands 3.1. . .3.8 GHz (WiMAX) and 5.0. . .5.8 GHz (WLAN) [6].

There are many configurations of multi-band antennas [6]. Here, we are going to consider the antenna, the configuration of which is shown in Fig. 4.48. Structures of the top and bottom layers are identical. The antenna is made on the FR-4 substrate with the size of 20 × 20 × 1 mm. It operates within the range of

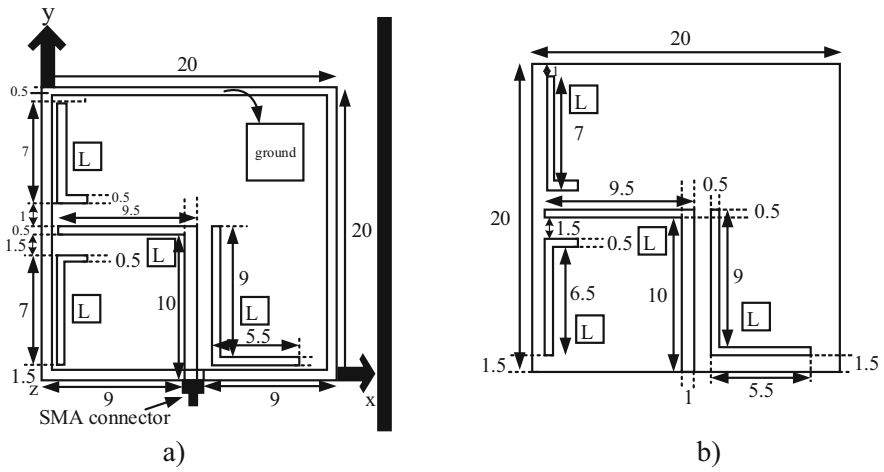

Fig. 4.48 Antenna configuration: (**a**) top view; (**b**) bottom view

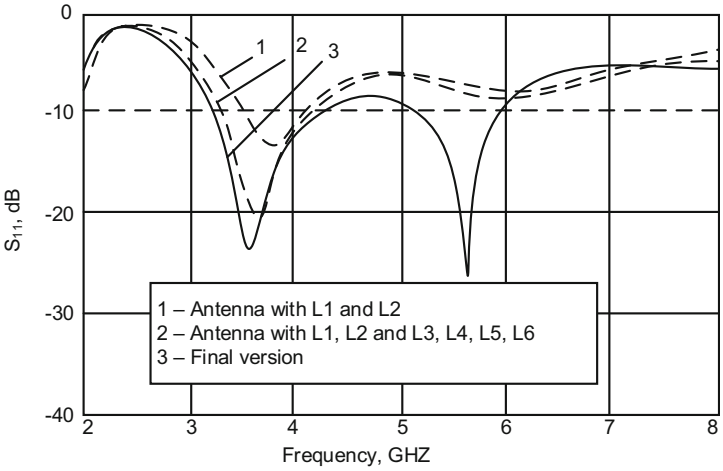

Fig. 4.49 Modeled dependence of VSWR on frequency at different stages of antenna production

3.1. . .3.8 GHz (WiMAX) and 5.0. . .5.8 GHz (WLAN). The process of production of such antenna consists of three stages.

First, the feeder (L1) and L-shaped radiating plate are made. Parasite element of the same shape (L2) is placed at the back side of the substrate. During the second stage, 4 L-shaped elements are installed on top and bottom sides of the substrate (L3-L6). After that, parasite elements L7 and L8 (next to the radiating plate) are added.

Results of modeling of this antenna in the High Frequency Structure Simulator (HFSS) ANSYS environment are shown in Fig. 4.49 [2]. This antenna with L1 and

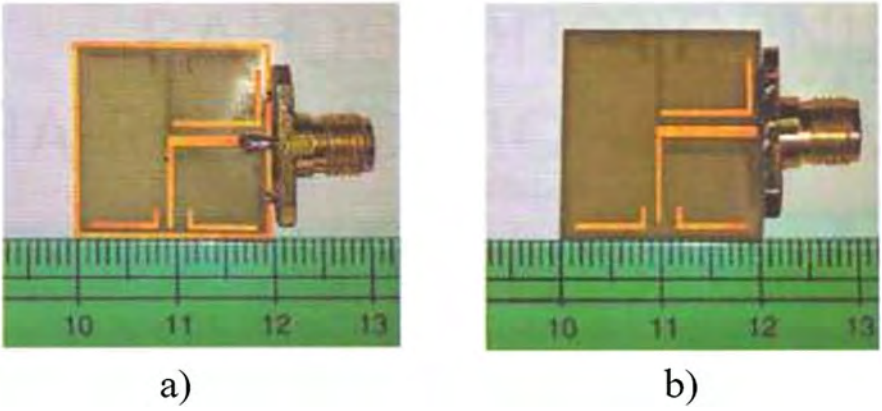

Fig. 4.50 Appearance of the antenna: (**a**) top view; (**b**) bottom view

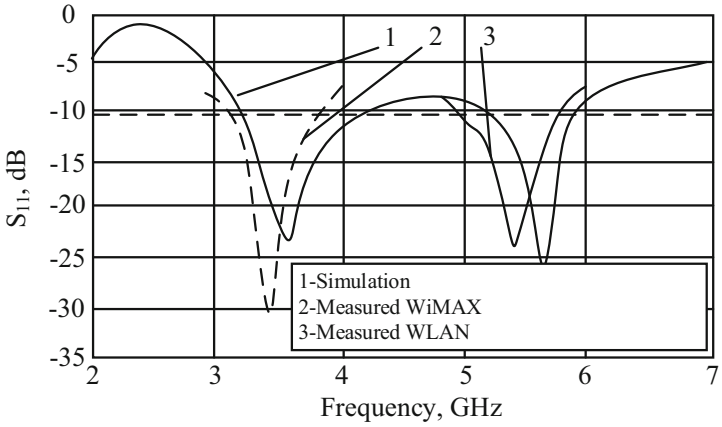

Fig. 4.51 Theoretical and measured dependencies of the reverse loss factor on frequency [6]

L2 elements operates at frequencies of 3.5. . .4.0 GHz, which does not conform to WiMAX requirements. Therefore, addition of the elements L3-L6 reduces resonant frequency to 3.5 GHz; at the same time, the covered frequency range is extended to the required 3.2. . .4 GHz. Elements L7 and L8 ensure another resonant frequency of 5.5 GHz (bandwidth 5.2. . .5.9 GHz).

In order to determine characteristics in real operating environment, the developers have designed a prototype (Fig. 4.50). Figure 4.51 shows comparison between simulated and real antennas. This structure operates within the band of 3.1. . .3.8 GHz (WiMAX) and 5.0. . .5.8 GHz (WLAN). Figure 4.52 demonstrates dependence of the antenna gain factor on frequency. It can be seen that relatively stable and acceptable in terms of value peak gain factor is ensured at both bands.

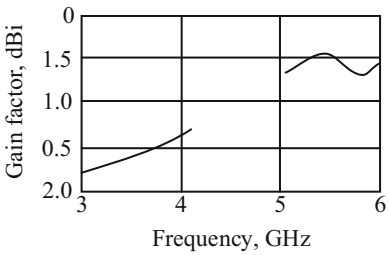

Fig. 4.52 Dependence of peak gain factor on frequency in WiMAX and WLAN ranges

Comparison of characteristics (size, ground plane area, operating frequency range) of the considered antenna to characteristics of [3, 4, 5] clearly shows that the described antenna has smaller dimensions.

For example, in antennas [3, 4, 5], the ground plane area is 390.6, 514.8 and 495 mm^2 respectively. In the examined antenna, it is smaller by an order of magnitude – only 38 mm^2. Therefore, it is suitable for use in mobile devices using WiMAX and WLAN protocols for data transmission. The users need to be aware of the fact that characteristics of this antenna depends on the position of L-shaped elements and selection of their parameters.

The described antenna ensures proper characteristics at 3.1…3.8 and 5.0…5.8 GHz frequency bands. Its difference from similar antennas consists in small area of the ground plane, which makes it possible to use this antenna in devices where small size is an important criterion.

4.2.2 Wideband Microstrip Antenna with Increased Gain Factor

As is known [2], antennas with very wide bands and coplanar waveguides have good beam pattern suitable for wideband transmission systems. They can be used in such fields as SHF visualization, pulsed radio communication and biomedical equipment. For further increase of numerical values of the gain factor, it is necessary to ensure greater signal-to-noise ratio, which is provided by non-directional or semi-directional radiation. It is also possible to increase effectiveness of the antenna or use a reflecting screen. In particular, one of the solutions that are most frequently used by designers is the use of thinner substrates, which generate less surface waves.

Microstrip antennas have a number of advantages, including small size and weight and even the possibility of integration into SHF microcircuits. They are suitable for transmission of data, voice and video image in wireless systems but don't have high gain required to provide communication at large distances. In order to eliminate this disadvantage and increase the gain factor, coplanar waveguide (Fig. 4.53) was used in the examined antenna [2].

Fig. 4.53 Configuration and parameters of a wideband microstrip antenna

The radiation plate itself is star-shaped. Pass band, which is determined by full input resistance, amounts to 3...11.7 GHz; three-layer frequency-selective frame increases gain by 4–5 dB, preserving wide pass band and attenuating rear lobe of antenna radiation.

If the radiating plate lies on dielectric substrate, pass band of the antenna is narrowed due to emergence of additional surface waves. There are multiple ways of expanding the band (some of them will be considered in the following), such as cuts in the ground lever, use of frequency selective screens, formation of the ground layer in the form of meander, etc.

The design of this antenna is characterised by the frequency-selective screen, which is a passive periodic structure of metal or dielectric elements used to control propagation of electromagnetic waves. It has high surface impedance and delays propagation of surface waves, supporting in-phase reflected waves, due to which the antenna gain factor increases. As a rule, the screen for antennas with low profile shall be small-sized, simple and reasonable from the economic point of view.

Using such frequency selection screen, it is possible to adjust beam pattern, polarization and pass band of the antenna. Such screen can be used as a filter, a reflector, a polarizer or a magnetic conductor.

Typical elements of a classic frequency-selective screen are a rectangle, a ring, a contour, a dipole and a fractal. Characteristics of the screen are determined by the size, shape and geometrical structure of the sell, as well as their periodicity.

During creation of the design of microwave antenna, developers used the frame composed of square cells to demonstrate efficiency of frequency-selective screens. It increases the antenna gain factor within the range of 3.0...11.7 GHz. Modeling was performed in the CST Microwave Studio Environment.

Figure 4.53 shows simplified structure of the antenna. The substrate is made of 1.58 mm thick material FR-4 with dielectric constant $\varepsilon = 4.3$. Scatter factor is 0.019 in the Z plane. Initially, simple rectangular cut was made in the ground layer. It is excited by the coplanar waveguide with the width W_{lf} and W_{uf} in the narrow part. The end of the waveguide contains a radiating star-shaped plate. Figure 4.53 shows the principle of formation of such star-shaped plate: two equicrural triangles with height T_h and base width T_b are taken; one of them is turned around and superimposed on the other.

The cut is designed asymmetrical in order to increase the bandwidth – a rectangular section is added at one side (Fig. 4.53). This asymmetry increases the inductances, which compensates for unwanted parasite capacity links with the radiating plate. Pass band also depends on the size and shape of the cut. Parameters of the antenna were optimized in order to minimize its size (Table 4.2).

Reverse loss factor of the antenna was measured using vector network analyzer R&S ZVA-40 Rohde&Schwarz. Figure 4.54 shows comparison of measured and

Table 4.2 Basic antenna parameters

Parameters	G_{pg}	G_{fg}	W_{uf}	W_{lf}	A	V	C
Values, mm	0.70	0.30	0.82	1.73	14.97	4.20	10.10
Parameters	A1	A2	B1	B2	Sl	Sw	–
Values, mm	1.5	9.10	8.20	7.50	10.50	14.30	–

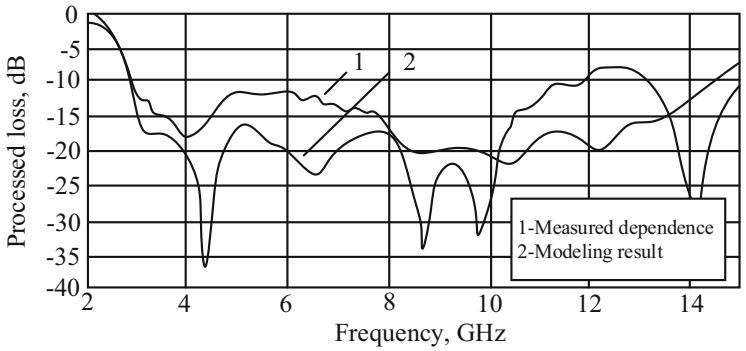

Fig. 4.54 Dependence of reverse loss factor on frequency

calculated dependencies. Measured pass band width determined from full input resistance amounts to 8.7 GHz (3.0...11.7 GHz). It can be seen that dependencies are similar, except for separate frequencies at which deviations are probably caused by dirt on the substrate or interference from SMA connectors.

Dependence of the reverse loss factor on frequency depending on changes in length A2 and width B2 for the considered antenna design is shown in Fig. 4.55. As we can see, with an increase in A2, the reverse loss factor is increased, and the frequency is reduced.

The interaction between ground layer and radiating plate enhances with an increase in the cut length A2, which ensures greater matching of impedances and increases the reverse loss factor. However, the reverse loss factor decreases starting from certain A2 value, thus the designer of the antenna needs to find the optimal cut length. Figure 4.55b shows that the reverse loss factor depends on the width of the cut in a similar manner (optimal B2 value – 7.50 mm).

If the cut is symmetrical, the reverse loss factor will be lower even with optimal parameters. The study [6] was based on the anaylsis of distribution of surface current across the antenna. High current density was observed at the frequency of 4.3 GHz with resonant frequency of 6.5 GHz and pitch of 3.2 GHz.

The first resonant frequency is approximately equal to:

$$f1 = \mathrm{c}/\left[\mathrm{SL}\left(\varepsilon_{eff}\right)^{1/2}\right], \tag{4.31}$$

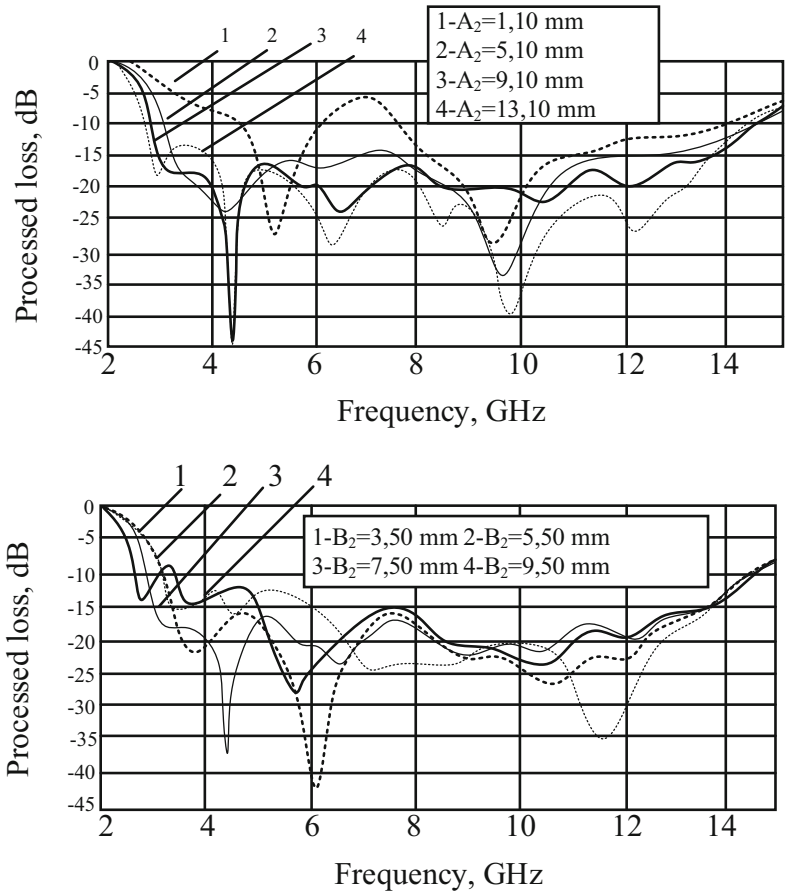

Fig. 4.55 Dependence of the reverse loss factor on frequency for different values of cut length and width

where $f1$ is the lowest resonant frequency in Hz; SL is the length of the cut in meters (0.065 m); c is the speed of light in vacuum in m/s; ε_{eff} is the effective dielectric constant, which is approximately equal to $(\varepsilon_r + 1)/2$.

Approximated condition for the second resonant frequency on condition of the height of the radiating plate being equal to $\lambda/4$ has the form:

$$f2 = c/\left[4\mathrm{L}\left(\varepsilon_{eff}\right)^{1/2}\right], \tag{4.32}$$

where L is the height of the star-shaped plate.

Fig. 4.56 Cell size on two internal layers (**a**) and in the external layer (**b**)

Fig. 4.57 Possible configurations of the frequency-selective screen of the microstrip antenna

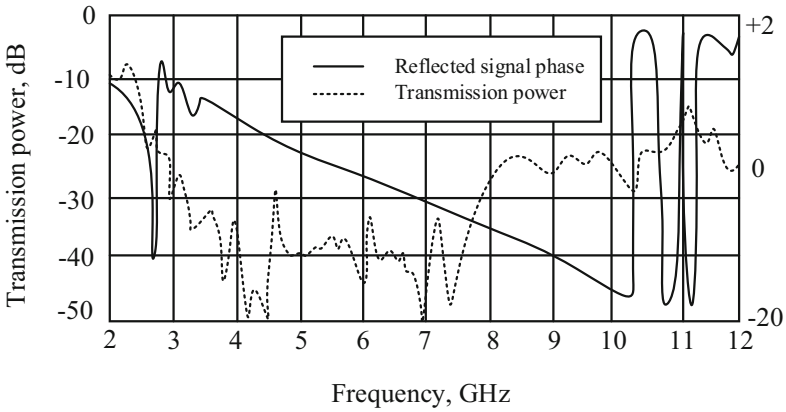

Fig. 4.58 Characteristics of transmitted and reflected signals

The cell of the frequency-selective screen mentioned above is shown in Fig. 4.56. The screen itself consists of three layers separated by substrates. In the upper layer, the cells are larger than in two bottom ones, since this structure makes it possible to achieve a wider stop band. Substrate thickness is 1.6 mm, and dielectric constant of the material is 4.4. Two bottom layers have the 6x6 lattice structure (Fig. 4.57); external layer at each side of the screen contains up to 5 cells.

Figure 4.58 [2] shows simulated dependencies of the transmitted signal amplitude and the reflected signal phase on frequency. Stop band at the transmitted signal power of not more than – 20 dB is 8.3 GHz (2.6. . .10.9 GHz). The frame is installed under the antenna and used as a reflector. If the signal emitted by the antenna and its reflection from the frame are in phase, the gain increases. Condition of in-phase state of the signals:

$$\Phi_{\text{FSS}} - 2\beta h = 2n\pi, \tag{4.33}$$

where $n = \ldots -2, -1, 0, 1, 2, \ldots$; P_{FSS} is the phase of the reflected signal; β is the constant of signal propagation in free space; h is the distance between the screen and the antenna.

From the Eq. (4.33), we can find this distance – $h = 26.13$ mm. The prototype produced by the authors of [2] is shown in Fig. 4.59. It should be noted that the

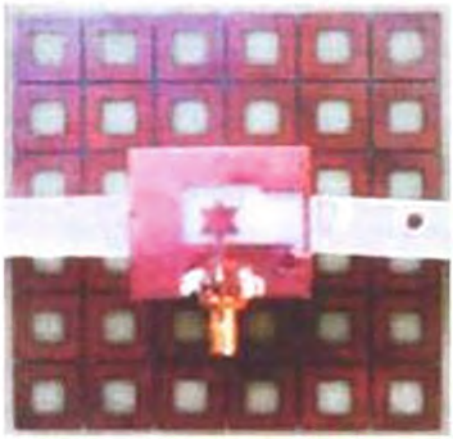

Fig. 4.59 Appearance of the prototype

presence of a frequency-selective screen has almost no effect on the pass band width determined by full input resistance. It amounts to 8.7 GHz (3.0. . .11.7 GHz).

Small difference between reflection coefficients in Fig. 4.58 was caused by reflection of the signal from the screen. Antenna beam patterns in E and H planes with and without the frame are shown in Fig. 4.60. It can be seen that the addition of a screen makes radiation of this antenna more directional. At 7.5 GHz, the rear lobe is reduced approximately by 10 dB when the screen is used.

Figure 4.61 [2] shows peak antenna gain factors with and without the screen. The use of the frame makes it possible to increase the gain by 4–5 dBi within the entire band.

Therefore, the considered small-sized antenna with non-symmetrical cut and frequency-selective screen has a fairly high gain in a wide frequency band. Measured pass band width determined from full input resistance amounts to 102% at 7.5 GHz. In order to increase the gain factors, designers use three-layered frequency-selective screen as a reflector, which provides additional 4–5 dBi of gain.

4.2.3 Wideband SHF Travelling-Wave Antenna

In this section, we will consider one of effective design solutions of a high-power SHF travelling wave antenna. Recently, scientific institutes and industrial companies have become increasingly interested in SHF sources and radiating elements of high power for use in military and civil radio communication systems.

Radiating elements are integral components of SHF systems; therefore, great attention shall be paid to their development. The main difficulty here is the effect of the radiated energy on the system itself. Since the radiation has high power, it can disrupt operation of equipment located close to the antenna, if the radiation is directed at it.

Fig. 4.60 Beam pattern

Fig. 4.61 Antenna gain factor

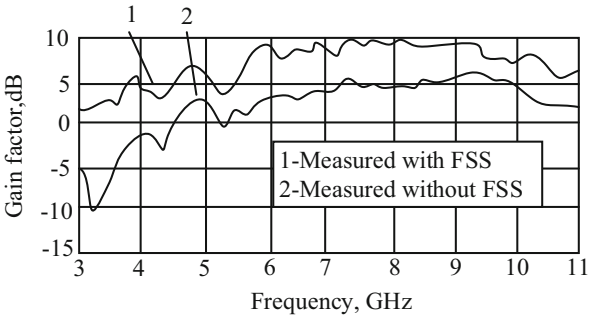

In order to ensure high efficiency during radiation of powerful pulses, it is necessary to take several important aspects into account.

1. Wide frequency band. Radiated pulses are very short and therefore occupy a wide band. The antenna shall work in the corresponding frequency range.
2. Directivity. The antenna needs to be directed in order to prevent incidence of energy on the staff or equipment in immediate vicinity.
3. High efficiency. Operation of the radiating element and feed element shall be matched in order to prevent formation of standing waves that can ultimately cause electrical breakdown.
4. Power dissipation Antennas shall be massive enough in order to ensure proper power dispersion and avoid electrical breakdown.
5. Dispersion. In certain applications, such as wideband radars considered in Chap. 1, it is necessary to take radiation dispersion into account, since these systems are based on correlation between transmitted and received signals. Radiation dispersion characterizes the degree of spread of the pulse due to deviations of the phase center of an antenna in a wide frequency band.

The design of the considered antenna [7] consists of two parallel plates bent away from each other during radiaton (Fig. 4.62). This antenna is a modified version of the antenna consisting of two co-planar sickle-shaped vibrators (valentine antenna), which is, in turn, a variation of the TEM horn.

There are multiple antennas in the market that conform to the basic requirements in terms of frequency band and directivity; however, they are difficult to produce and require the use of numerical control (NC). Development of a simple antenna design is the priority criterion, followed by technical characteristics of the work. They can be non-optimal and require modernization, but shall conform to the stated requirements.

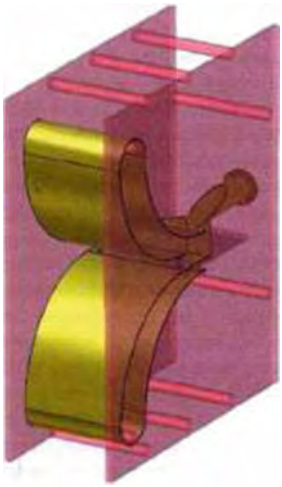

Fig. 4.62 3D model of a wideband SHF travelling-wave antenna

Radiation mechanism of this antenna is similar to the one used in classic travelling wave antennas and consists in the following. First, electrical field is created between two parallel plates at the input of the antenna. When the plates are displaced, wave resistance changes, and radiation begins. Radiation is formed as the pulse passes between two displaced plates. Each spectral component is radiated when the distance between plates is equal to the half of its wavelength. In this region, wave resistance is the same as in case with open space, i.e. $120\pi\ \Omega$. Due to this reason, high frequencies are radiated at the beginning of the antenna, and low frequencies – at its end, as shown in Fig. 4.63.

The diameter of the rounded part of the antenna is increased in order to reduce the current reflected from the antenna end and increase effectiveness of low frequency radiation. Non-radiated currents are dispersed by ohmic resistance of metal (aluminum); otherwise, they return into the generator, and the second parasite pulse is possible if no proper protection has been provided by the designer of the antenna.

Figure 4.64 is a conventional graphic representation of distribution of the electrical energy over the radiating element obtained with the help of the well-known T-solver tool of the CST Studio Suite software. Here, low frequency pulses are generated at the far end of the radiating element, while high frequency pulses are formed at its close end.

In order to avoid the effect of dispersion of modes, the design of the waveguide ensures excitation only by TEM modes, while modes of higher orders are extremely weak. Antenna polarization is vertical, and therefore the antenna is mounted vertically.

Figure 4.65 shows basic parameters of radiating element of this wideband microstrip SHF antenna. Simulation was performed in the band of 0.2. . .5 GHz. Pure TEM mode cannot be obtained in the upper band (above approximately 2.5 GHz), since modes of the higher order are excited simultaneously. Due to this

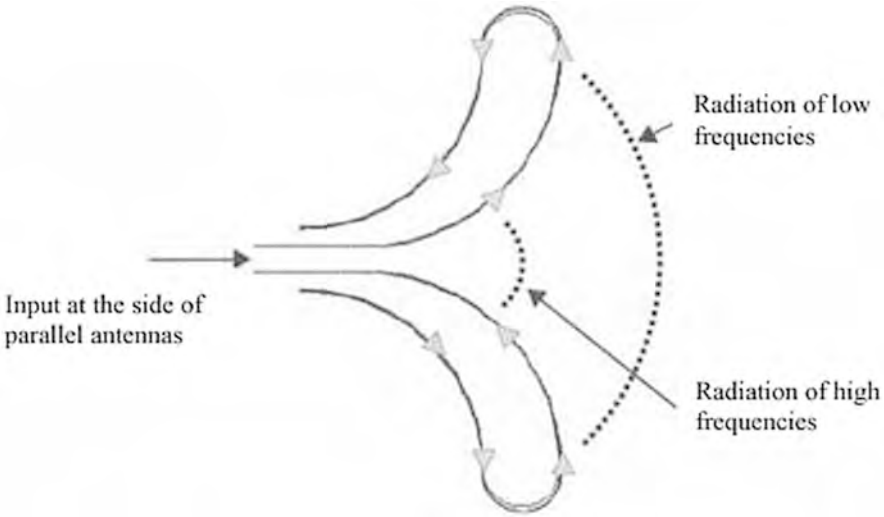

Fig. 4.63 Distribution of currents (current directions are indicated with arrows)

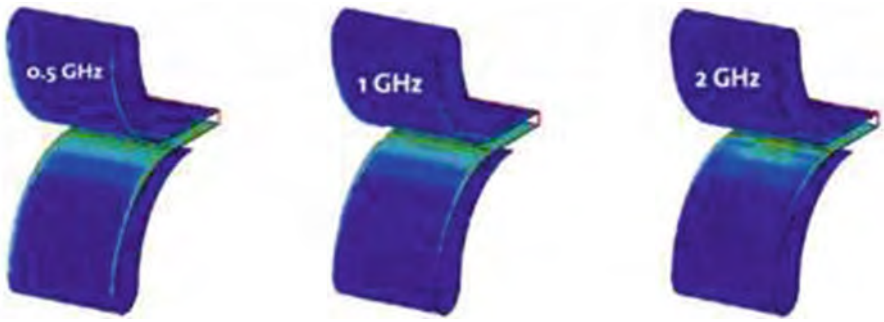

Fig. 4.64 Distribution of electrical power over radiating element

reason, simulation was performed differently: the excited field is the superposition of the fields produced by simultaneously emitted first, second and third modes. Reflection coefficient in this case is referred to as active S-parameter (Fig. 4.66). Parameters of far field modulation important for the antenna designer are shown in Figs. 4.67, 4.68 and 4.69.

In the E plane $\Theta = \pi/2$, $\varphi = [0.\ 2\pi]$; in the H plane $\varphi = \pi/2$, $\Theta = [0.\ 2\pi]$. Figure 4.70 shows the directivity pattern (in dBi) as a frequency function. As expected, directivity increases together with frequency.

Certain design features of organizing transition between waveguides shall be noted here.

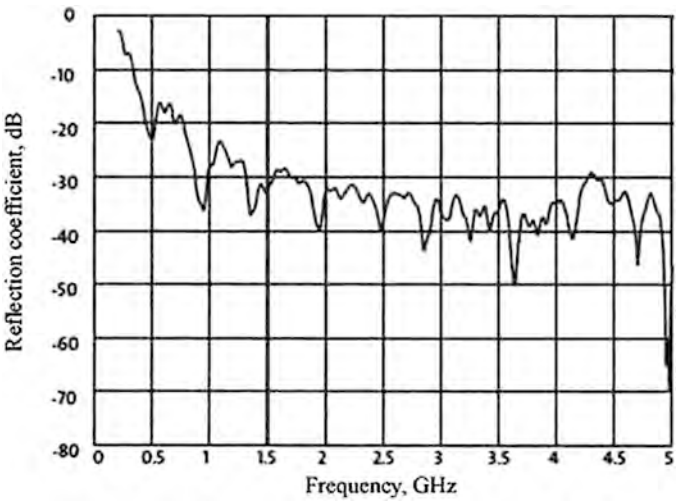

Fig. 4.65 Typical dependence of the reflection coefficient of wideband microstrip antenna on frequency

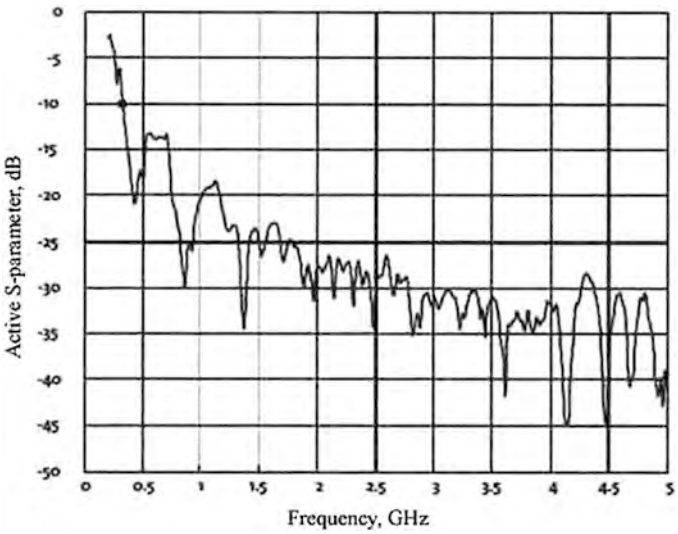

Fig. 4.66 Dependence of the active reflection coefficient of microstrip antenna on frequency

In the point of connection of the coaxial waveguide with parallel plates, the top part of the coaxial waveguide is cut off, and the central conductor has a conical shape (Fig. 4.71). The radiation is provided by the differential mode, which create the potential difference between the plates of the TEM horn. In-phase modes are radiated in the unwanted direction and only cause the loss of energy. The energy

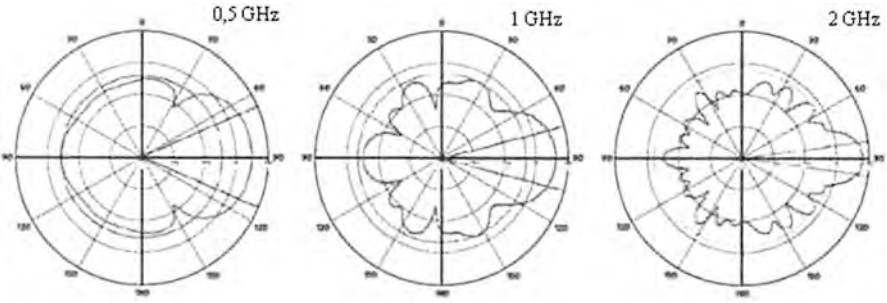

Fig. 4.67 Antenna beam pattern in the H-plane

Fig. 4.68 Beam pattern in the E-plane

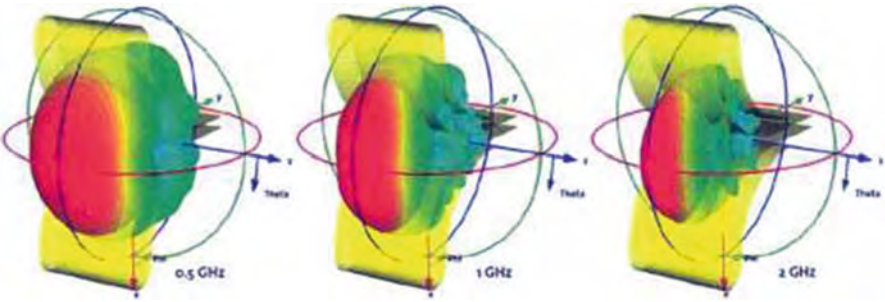

Fig. 4.69 3D beam pattern of a microstrip SHF antenna

of in-phase modes shall be reduced by selecting the best cross-section angle. Figure 4.72a, b shows distribution of charge for in-phase and differential modes.

Unlike previously considered design options, the configuration of the adapter suggested in [7] is much simpler and does not require the use of expensive CNC. The developers performed parametric analysis to determine the degree of matching of energy depending on the section angle. Cross-section angle varied within 15. . .25°. The found optimal value is 21°. With higher values, in-phase modes occur; with

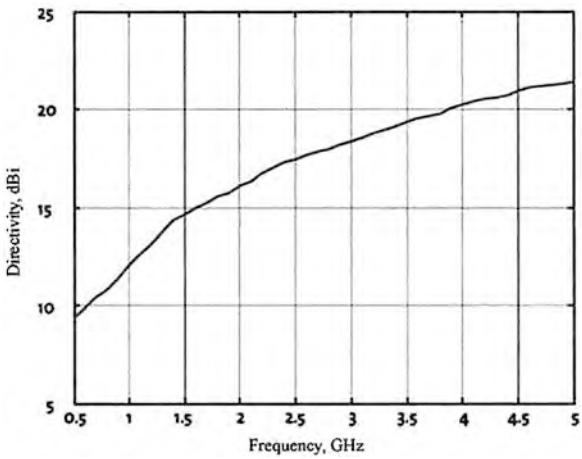

Fig. 4.70 Dependence of the degree of directivity on operating frequency of the antenna

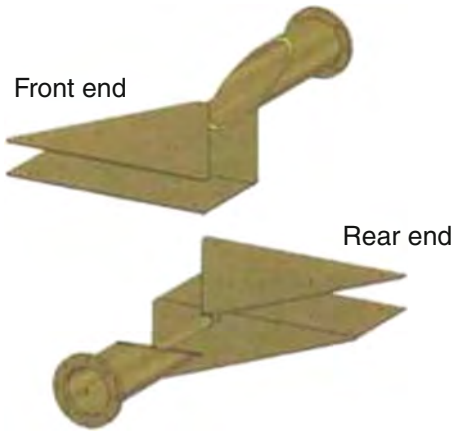

Fig. 4.71 Schematic drawing of the transition region between waveguides

lower values, the reflection coefficient increases. The next parameter to be analyzed is the radius of the internal conductor at its thick end.

As the external conductor becomes smoother, the thickness of the central wire increases (Fig. 4.73). This is done to compensate for the reduction in the equivalent capacity caused by the change in the shape of the external conductor.

Figure 4.74 shows that the electrical matching becomes more accurate as the radius of the internal conductor increases. Increase by 2 mm (from 3.5 to 5.5 mm) already provided significant improvement, especially in the top frequency band.

Development of the design of this antenna is concluded by electrical and mechanical connection of the transition region from the coaxial waveguide to displaced plates (Fig. 4.75). An important fact for the engineer is that the internal conical conductor is connected to parallel plates by means of a small socket, which is screwed to the top plate by two screws. Let us note that parallel plates in this point are narrow and adiabatically expand to the value received in each specific case based

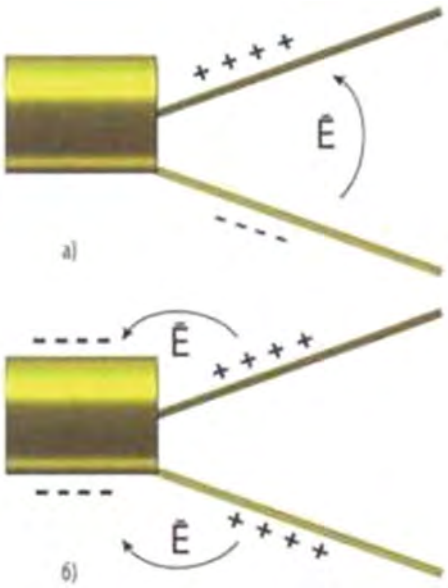

Fig. 4.72 Charge distribution diagram for differential modes (**a**) and in-phase modes (**b**)

Fig. 4.73 Possible configurations of the internal conductor

on the results on computer modeling. In order to ensure the required gap between plates, four plexiglass separators are inserted between them and screwed; they are located along the line of fixed wave resistance.

Figure 4.76 presents the reflection coefficient of the considered antenna. Precise matching is achieved at central frequency $f_c = 1$ GHz, which corresponds to the pulse width of 1 ns. It is sufficient for this matching to be ensured within the frequency range of 0.3…3 GHz; however, it should be noted that the transition region preserves matching at higher frequencies as well. In this higher band, modes of higher order will be excited not only in a waveguide made of parallel plates, but in a coaxial waveguide as well. Of course, it is necessary to understand that we are talking about the modes of TE11 and singular TE11. Their angular frequency $f_{\text{cutoff. TEio}} = 2.25$ GHz, which is much higher than the range usually used by military.

An example of the design of microwave microstrip antenna with the package made of plexiglass is shown in Fig. 4.77.

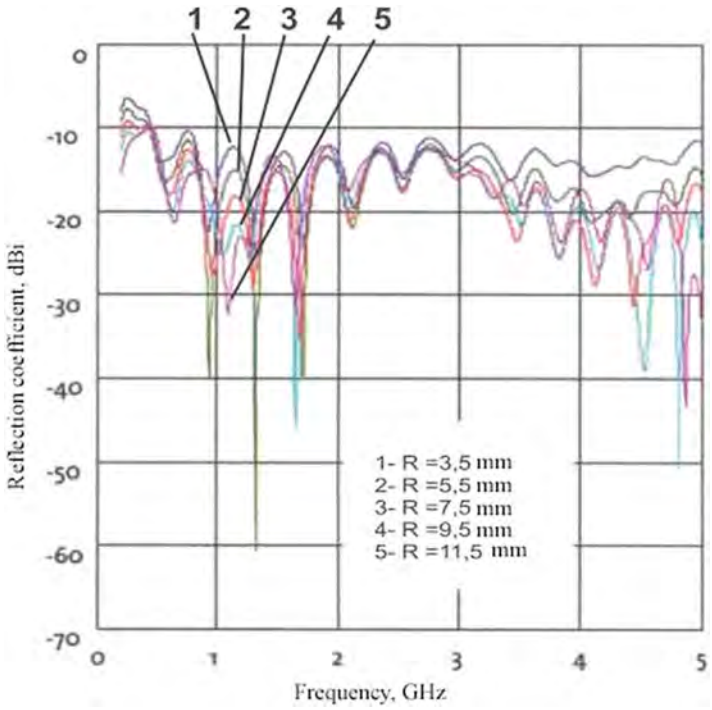

Fig. 4.74 Reflection coefficient for different values of the radius of bigger section of the central conductor

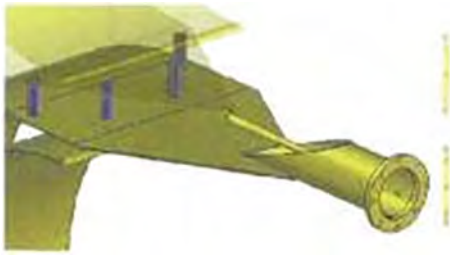

Fig. 4.75 Connection between coaxial waveguide and parallel plates

Figures 4.78, 4.79 and 4.80 show directivity pattern of the analyzed packaged antenna.

Figures shown above demonstrate that the in-phase component is slightly excited in the lower band, but it has no significant effect on the directivity pattern, especially near the central frequency. The package itself does not reflect energy or provoke occurrence of surface waves.

It would be plausible to provide brief recommendations for practicing engineers concerning features of measurement of characteristics of this antenna [7–14].

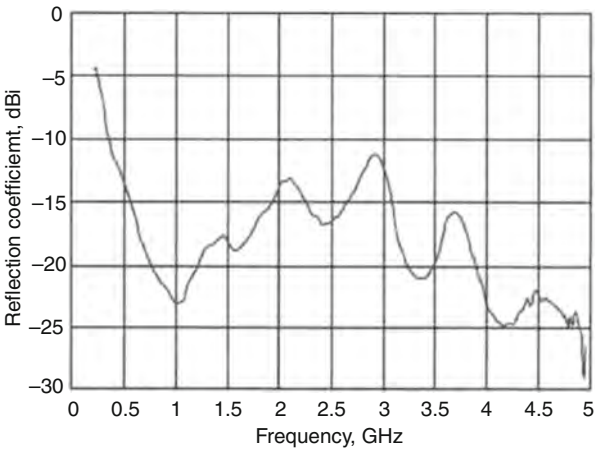

Fig. 4.76 Characteristic of the dynamics of reflection coefficient of a finished antenna

Fig. 4.77 Packaged antenna appearance

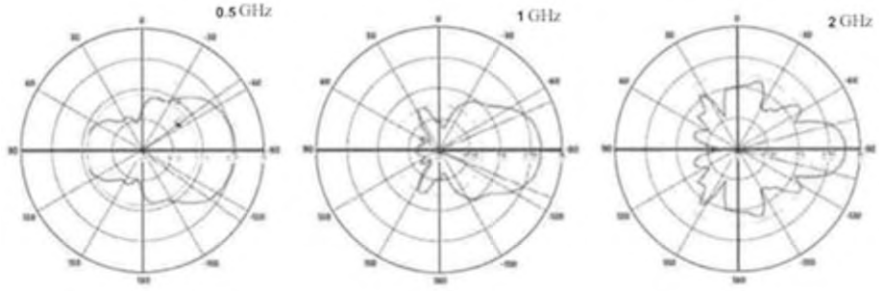

Fig. 4.78 Antenna directivity pattern in the H-plane

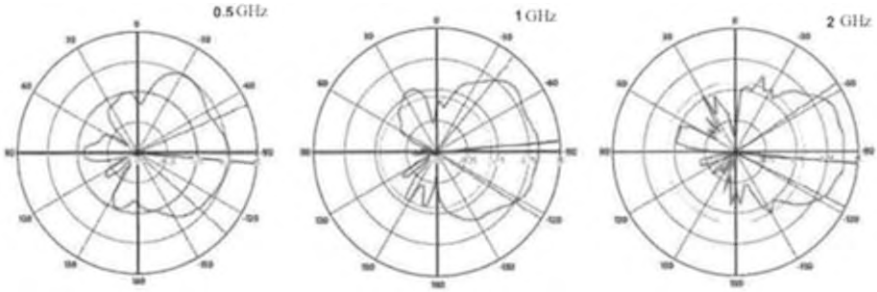

Fig. 4.79 Antenna directivity pattern in the E-plane

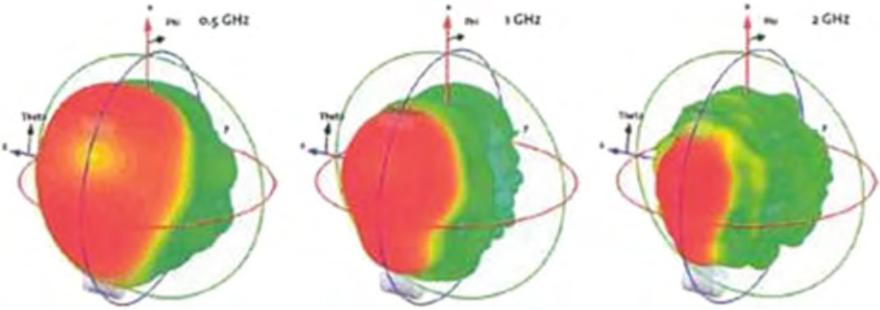

Fig. 4.80 3D antenna beam pattern

In order to transmit powerful signals, developers of radio communication systems shall pay special attention to energy absorption in order to avoid damaging the equipment placed nearby. Measurements shall be performed in a shielded environment isolated from external electromagnetic effects. At the same time, it is necessary to remember that the beam pattern is not affected by the energy reflected from surrounding objects, especially if they are made of metal.

It is recommended to test the antenna using one of the two methods: with the help of a capacitor voltage divider or a D-Dot-sensor. In order to measure the transmitted signal, the capacitor voltage divider shall be installed in the point where the waveguide ends and parallel plates begin. Capacitive voltage divider is made of a thin dielectric intermediate layer attached to the bottom plate of the antenna at one side and to the copper plate at the other side.

In fact, this is a condenser with voltage measured by means of directly connected measuring rod of the oscillograph.

Oscillogram of voltage at such divider is shown in Fig. 4.81. Pulse rise time is about 1.2 ns. Measurements shall be performed at the point of end of the transient region between waveguides; in this case, the signal is not distorted, and the transient region does not affect the quality of work.

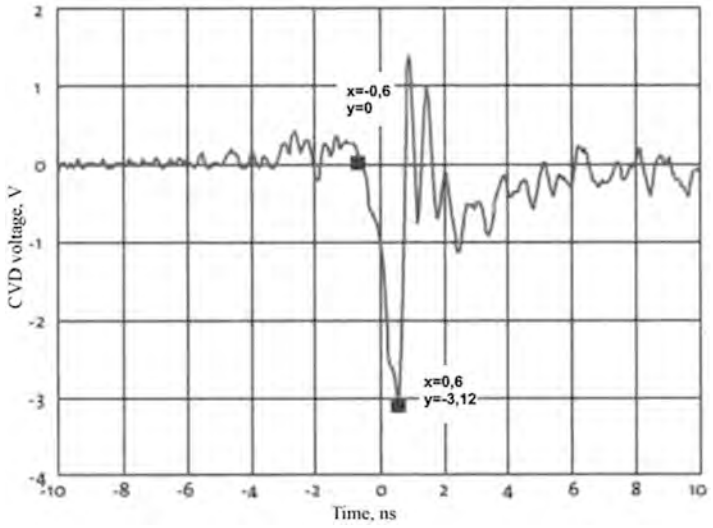

Fig. 4.81 Measured voltage at capacitance divider

For measurement of the electrical field at various distances, it is recommended to place the antenna in an echo-free room with the D-Dot sensor (the difference between them shall be 270 cm). Electrical field intensity at this distance is 156.87 kV/m^2, received signal power is proportional to 1/r^4.

4.2.4 Man-Portable Antennas

As is known, networks of multiple wireless man-portable devices (WBAN) are widely applied in different fields and especially relevant *in* military communications. Units of such military network usually include elements of clothing (vests, watches, bands, etc.) fitted with sewn-in antennas. During development of such antenna, it is necessary to take into account that it will operate near the human body or on it. This imposes limitations on the level of radiation; moreover, it is necessary to take into account several important parameters, first of all – operating frequency and pass band [15].

Even if the designers of the system have performed separation between ultra-wideband and narrowband antennas, *in* both cases it is necessary to study the effects of curvature and jamming, which inevitably occur during movement of the object observed by the radar. Moreover, frequency tuning of such radio system shall be acceptable for the target pass band.

The next line of crucial parameters for designers includes the radiation pattern, coverage area and polarization.

In most applications, so-called "quasi-directional" transmission is required to ensure maximum coverage. A configuration with several antennas can be used for this purpose.

With regards to the power of the absorbed dose, it is necessary to understand that, similarly to the situation with radio frequency wireless devices, the level of electromagnetic energy absorbed by the body *must* stay within the regulated value. Of course, special protective devices can be used in specific cases.

Of course, during implementation of a specific design of portable antenna, it is necessary to take into account the features of the used technological process, as well as mechanical properties and geometric dimensions of materials, thickness of metal parts, conductivity, thermal properties, etc.

As a practical example, we will briefly consider the main provisions of the concept of implementing man-portable antennas by one of the world leaders – Giante.

Giante's concept is easy to implement and ensures the acceptable level of power of the absorbed dose; its main principle consists in creating the filed in which the radiated electromagnetic field is significantly reduced.

According to the fundamental laws of physics, an object placed in a zero-dimensional field will have no significant effect on the distribution of the field and will not be subjected to radiation.

In our case, it is necessary to ensure the required amplitude and phase distribution similar to the one observed in antenna arrays by connecting several antennas. The difference is only that they have no periodic structure, antenna array can be non-uniform, and antennas do not have to be in the same plane.

Configuration of the designed antennas shall ensure the possibility of printing on or embedding in clothes; therefore, the antennas shall repeat the natural inflection of a human (animal) body. As an example, Fig. 4.82 shows a group of three antennas of the same type arranged in an arc. Radiation inside the convex region formed by them is weak; therefore, if human body is placed inside this region, distribution of the field will change insignificantly, and the dose absorbed by the body will be small. Figure 4.83 shows modeling results for two groups of such antennas, each of which consists of three dipole elements placed directly on human body. In this case, electromagnetic field is usually weak, and the absorbed dose is 2 W/kg. With total power of 1 W, design value of the absorbed dose is 0.62 W/kg, which conforms to all European standards.

As a specific example of structural design, we will consider the well-known transceiver Giante WBAN, which has a bulk structure but is mostly implemented as a planar circuit. Due to this fact, it can be easily attached to clothes. Specific configuration of a group of such antennas depends on the working frequency, features of the drive circuit, which independently controls each element in the group, type of antennas and parameters of the human body.

As a rule, monopole antenna help obtain acceptable directivity pattern on condition that their orientation relative to each other is optimal. In order to ensure full aperture angle of radiation, two groups of antennas are usually required: for the left and right sides, as shown in Fig. 4.83.

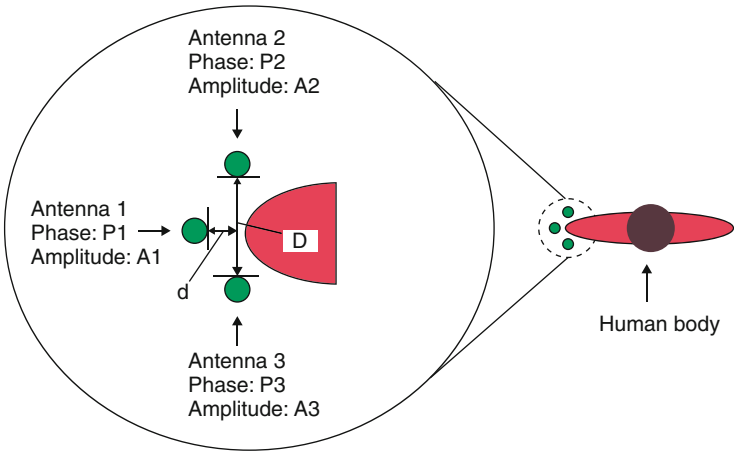

Fig. 4.82 Arrangement of antennas shall ensure a weak field region between them

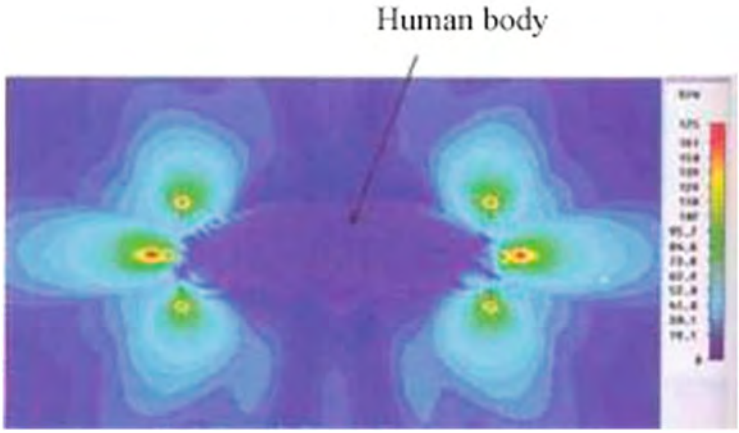

Fig. 4.83 Distribution of electric field of two antenna groups obtained in the CST Microwave Studio 3D simulator

The main technical characteristics of Giante WBAN transceivers include the matching factor, directivity patterns and communication range. It should be noted that their antennas are designed for the range of 2–2.1 GHz, and the radiating element is presented by a simple dipole antenna.

Figure 4.84 demonstrates measured dependence of the reflection coefficient on frequency. It can be seen that it is much lower than – 15 dB at the wide band – almost within 2–2.4 GHz. Figure 4.85 shows design and experimentally obtained beam patterns (measurements were performed in a nonreflecting room). Close coincidence of results can be seen, even though significant differences are observed in several

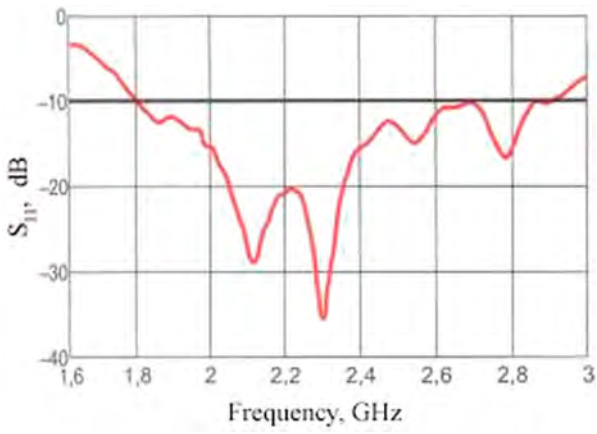

Fig. 4.84 Dependence of the reflection coefficient on radiation frequency

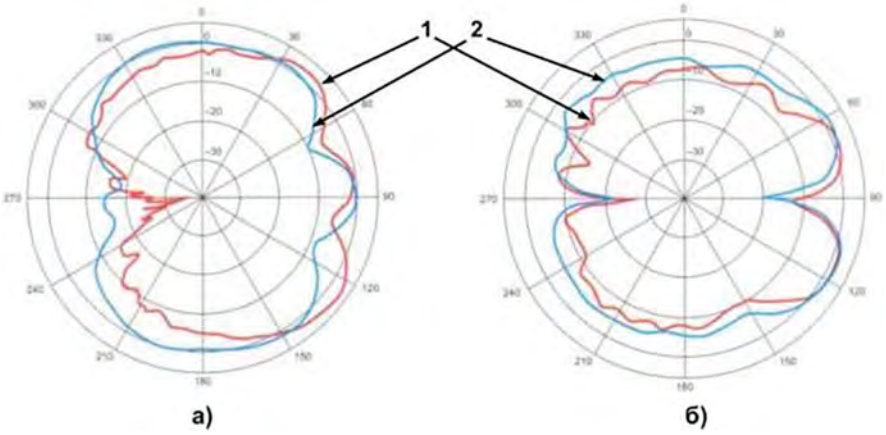

Fig. 4.85 Measured (1) and modeled (2) beam pattern: (**a**) for co-polarisation option; (**b**) for cross-polarisation option

directions, which are mostly caused by imperfection of the test station. The authors of [7] performed modeling of the numerical value of the absorbed dose in the CST environment.

Especially important for decision-making is the results at power below 1 W: SAR_{local} for 10 g of fabric = 1.24 W/kg. This is much lower than the maximum permitted values of SAR_{max} for human body (2 W/kg) and limbs (4 W/kg). The range of communication in real open environment was also measured experimentally. It has been demonstrated that the range of communication between two vests equipped with Giante transmitters usually exceeds 1400 m in all directions with power of 1 W; in conditions of a forest or urban development, the range of communication is 500 m.

The advantage of these antennas is their fairly high ergonomics and compatibility with digital print technology, which makes it possible to install them on clothes or directly on human skin.

4.2.5 Multiband Patch Antenna

As demonstrated above, the main structural element of any small-sized antenna is usually made on substrate made of reinforced and wear-resistant glass fiber, which provides the necessary mechanical strength to the microstrip antenna. It is necessary to remember that the dielectric material also influences electrical properties of the antenna and its cost. In the following, we will consider the main results of modeling of a standard small-sized microstrip antenna, published in [16] for the antenna shown in Figs. 4.86 and 4.87.

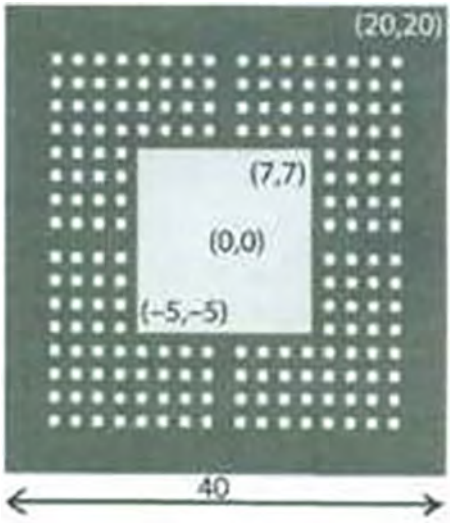

Fig. 4.86 Design of a multi-pole antenna (top view)

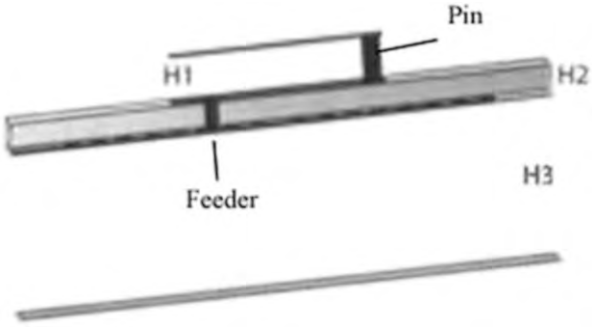

Fig. 4.87 3D image of a multistrip antenna design

In the examined specific example, square radiators with a side of 16 mm were installed on the 40 × 40 mm substrate. Thickness of the top radiator is 2.6 mm, thickness of the bottom one – 1.6 mm. Feeder line is connected to the bottom radiator point. Radiators are connected by a 01 mm pin in the point of (7;7 mm). 40 × 40 mm metal plate is placed under the bottom substrate to ensure grounding. Square holes (1 × 1 mm) with a distance of 2 mm between them are cut in the plate.

Air intermediate layer was used as the top dielectric; for the bottom layer, designers alternated between materials listed in Table 4.3. It can be seen that an increase in dielectric permittivity reduces the resonance frequency. The highest directivity of an antenna is ensured by widely used foam plastic; however, it is inferior to all other examined materials in terms of other parameters.

In the following, we will consider an antenna based on glass fiber and epoxy resin composite, since this material is distinguished by its low cost.

When designing multiband small-sized microstrip H-shaped antenna, environment OriginPro 8.5 OriginLab and simulators 3D, FEM, EM and HFSS Ansoft were used in [16].

Antenna characteristics:

- pass band width determined from full input resistance amounts to 3.25 GHz: 9.75. . .13.0 GHz at VSWR <2.0:1;
- maximum gain factor: 8.5 dBi;
- gain – 0.63 dBi, efficiency – 96% at 10.3 GHz; gain – 6.03 dBi, efficiency – 84.2% at 12.5 GHz;
- radiator length: 5 mm;
- size: 12 × 15 mm.

Appearance of this antenna is shown in Fig. 4.88, and optimized antenna parameters are given in Table 4.4 [16, 17].

The current in a H-shaped radiator passes a slightly longer path to the opposite end of the antenna as compared to a rectangular radiator, even though the size of the radiator in all cases remains the same.

The antenna is made on a substrate of hardened glass fiber with thickness of 1.6 mm, relative dielectric permittivity of 4.6 and loss tangent of 0.023 (Fig. 4.89). It should be noted specifically that the choice of the substrate material greatly influences technical parameters of the antenna. Substrate material is usually made of 60% glass fiber and 40% epoxy resin; it is easy to make and has low cost.

Theoretical and experimental dependencies of VSWR on frequency for the considered antenna design are shown in Fig. 4.90. Pass band width determined from full input resistance amounts to 3.25 GHz with VSWR <2.0:1. Lower resonance frequency shifted from 10.5 GHz to 10.3 GHz, while the upper frequency increased from 12.3 GHz to 12.5 GHz.

Figure 4.91 shows the dependence of the gain factor of this antenna on frequency, which is important for practical applications; Fig. 4.92 shows the efficiency of radiation of a multi-band patch antenna at top and bottom resonant frequencies.

Table 4.3 Characteristics of a wideband portable antenna depending on the substrate material

Material	Dielectric permittivity	Tangent of losses	Resonant frequency, GHz	Coefficient of reverse losses	Antenna efficiency, %	Gain factor, dBi	Directivity, dBi
Foam plastic	1.05	0	2.707	−4.145	61	2.99	5.09
Duroid	2.2	0.0009	2.64	−11.88	93.51	4.47	4.76
Benzocyclobutene	2.6	0	2.636	−14.01	96.51	4.63	4.78
Roger 4350	3.48	0.004	2.586	−25.29	99.66	4.62	4.63
Epoxy resin	3.6	0	2.576	−17.37	98.34	4.54	4.61
FR4	4.4	0.018	2.556	−24.08	99.6	4.54	4.56
Glass	5.5	0	2.535	−19.14	98.88	4.44	4.49
Duroid 6010	10.2	0.0023	2.455	−9.449	88.64	4.02	4.55

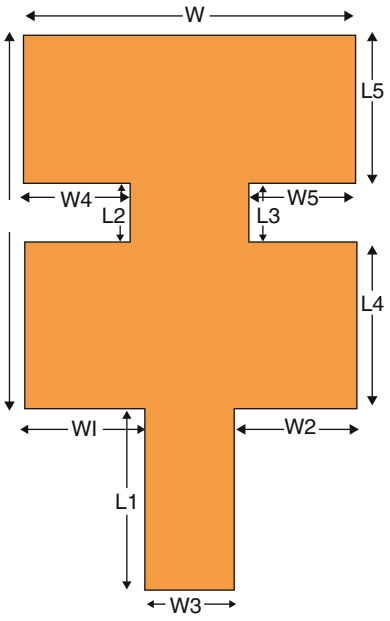

Fig. 4.88 Typical configuration of an antenna

Table 4.4 Basic antenna parameters

Parameters	Values, mm	Parameters	Values, mm
L	15	W	12
L1	5	W1	4.5
L2	2	W2	4.5
L3	2	W3	3
L4	6.5	W4	4
L5	6.5	W5	4

Fig. 4.89 Appearance of the antenna

Figure 4.93 shows the typical graph of changes in the input impedance of this multiband antenna showing that the real part of impedance is very close to 50 Ω, which is extremely important for practical implementations.

Figure 4.94 shows the circular diagram of full resistances of this antenna.

Standard beam pattern of this antenna is shown in Figs. 4.94 and 4.95.

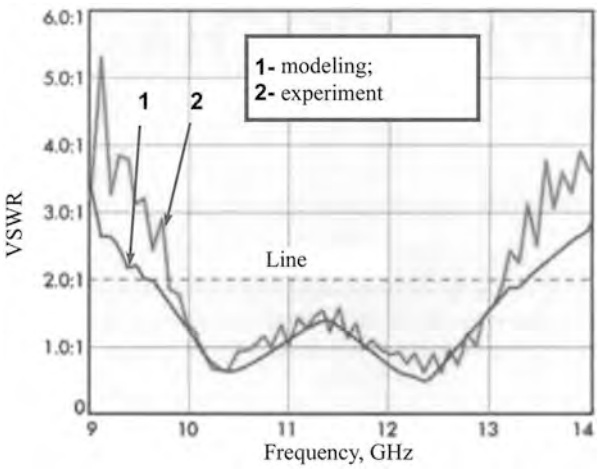

Fig. 4.90 Dependence of the Voltage Standing-Wave Ratio (VSWR) on frequency

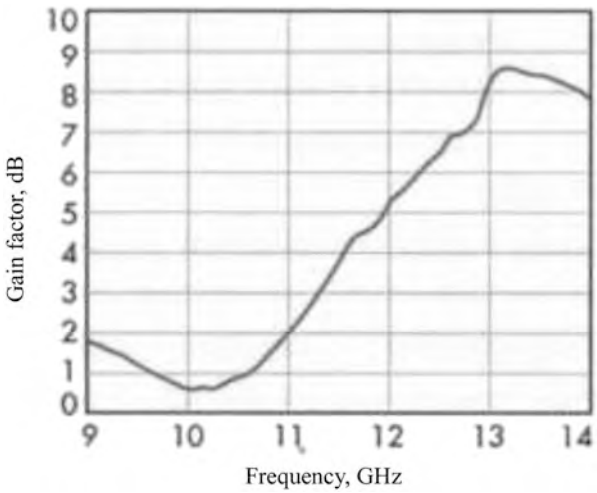

Fig. 4.91 Multiband antenna gain factor

Therefore, the antenna considered above is characterized by fairly small dimensions (15 × 12 mm). Pass band width determined from full input resistance amounts to 3.25 GHz (9.75. . .13.0 GHz at VSWR <2.0:1). Peak gain factor is 8.5 dBi.

4.2.6 Microstrip Antennas on Thin Substrate

Even though all microstrip antennas for SHF radio systems have small dimensions and weight and are easily integrated with other RF components, their field of application is limited significantly due to narrow pass band.

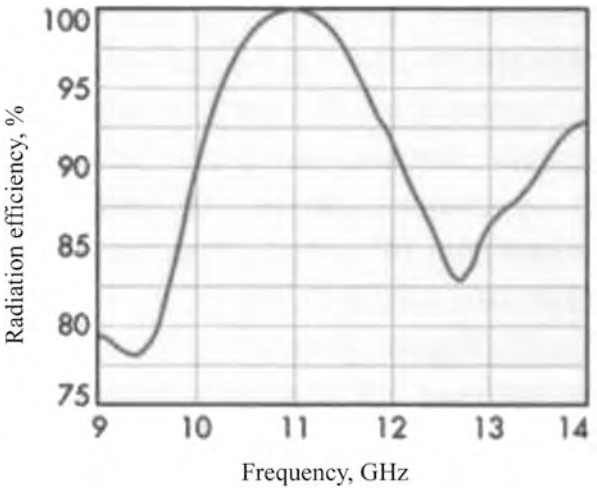

Fig. 4.92 Multiband antenna radiation efficiency

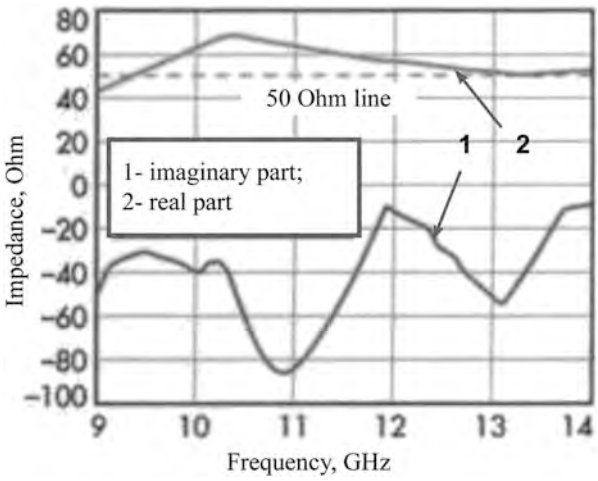

Fig. 4.93 Input impedance of microstrip antenna

As already noted above, there are several known and widely used technological and structural methods of expanding the pass band:

– increasing substrate thickness;
– using special methods of matching impedances and feed;
– using several radiators;
– production of cuts.

However, the use of the above measures in practice often leads to an increase in overall dimensions of the antenna, its cost and weight. In order to avoid it, U-shaped patch antenna are used, as well as U-shaped and L-shaped antennas with shorting links (or walls). As a rule, they are manufactured on a thick substrate. Therefore, in

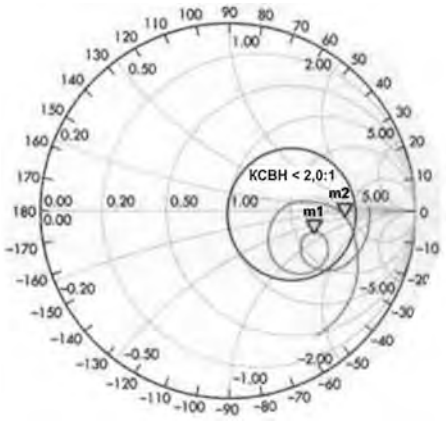

Name	Freq	Angle	Value	Power
m1	10,3	-12,15	0,95	1,02-0,89
m2	12,5	-6,568	1,02	1,18-0,9

Fig. 4.94 Smith chart (polar impedance chart)

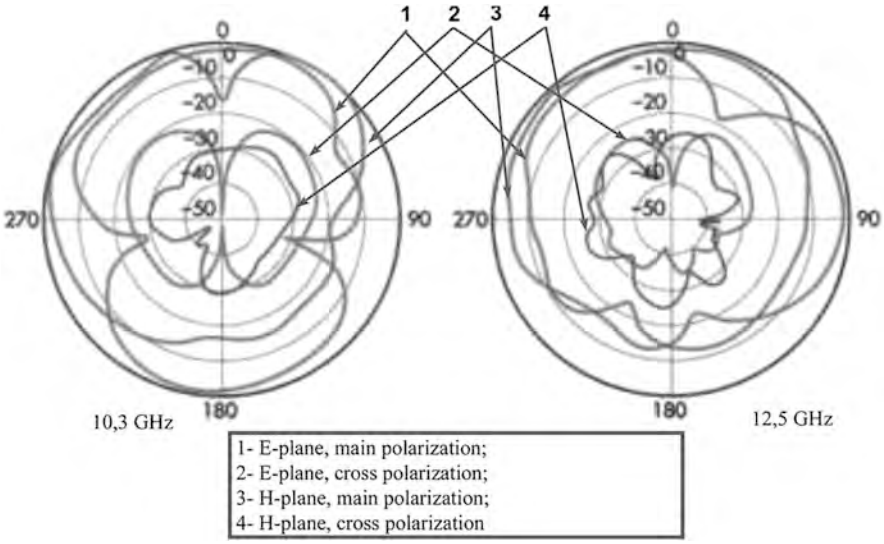

Fig. 4.95 Measured beam pattern

the following we will consider a standard antenna on thin substrate (with thickness of $0.008\lambda_0$, where λ_0 ισ τηε wavelength in air at central frequency of 2.45 GHz).

Figure 4.96 shows the general top and side views of such modified antenna. As can be seen from previous sections of this book, in order to ensure matching of impedances in a wide frequency band, resonance modes shall be excited simultaneously at central frequency, and the reverse loss factor at resonant frequencies shall be below 10 dB.

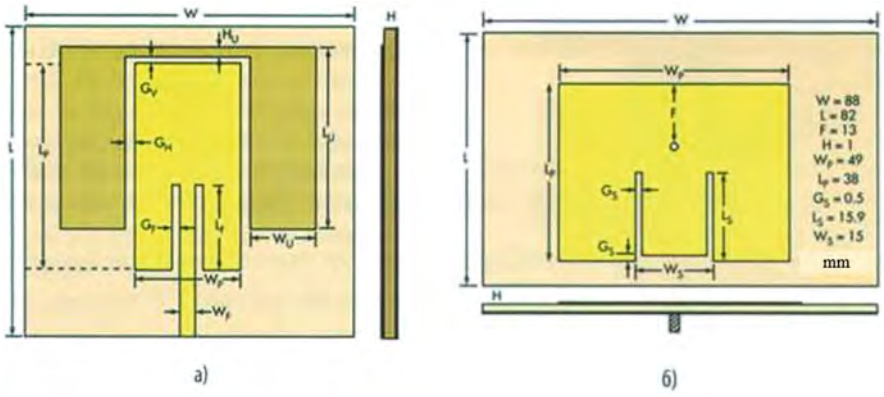

Fig. 4.96 Configuration of (**a**) modified and (**b**) classic antennas

The configuration of SHF microstrip antenna suggested in [18] is distinguished from the classic model by the presence of parasite U-shaped radiator. Resonant frequency of the main rectangular radiator is lower than resonance modes. If the length of the main radiator L_P is 0.5 and the width is 0.25 λ^L_g, where λ^L_g ισ τηε wavelength at the lower frequency, then the resonant wavelength is ensured by a smaller antenna than the classic one.

In this antenna design, upper resonant frequency is ensured by using a U-shaped element placed around the main element (Fig. 4.96). Resonant wavelength of such U-shaped radiator is determined by its length L_U and width W_U. Electromagnetic interaction between radiators is ensured with the help of horizontal and vertical gaps (G_H and G_V accordingly).

This antenna is designed for the working range of 2420. . .2484 MHz. Of course, in order to fully cover this range, resonant frequencies of the antenna shall be close to the limits of the desired operating range. In other words, length and width of the main antenna radiator shall be $0.5\lambda^L_g$ and $0.25\lambda^L_g$ respectively (lower resonance frequency – 2430 MHz), as well as length and width of the U-shaped radiator $L_U + 0.5W_U - 0.5H_U$ shall be about 0.5 at the upper resonance frequency (2474 MHz).

This antenna design was modeled by the developer [18] in the High Frequency Structure Simulator Ansoft environment. Final dimensions of the antenna are as follows: $L_P = 38.5$ mm; $W_P = 19.4$ mm; $U = 33.6$ mm; $W_Y = 11.9$ mm; $H_R = 1.7$ mm; $G_V = 0.8$ mm; $G_H = 1{,}8$ mm; $L_F = 15.5$ mm; $W_F = 2.73$ mm; $G_F = 0.5$ mm; $H = 1$ mm. Substrate size is 66x60 mm.

It should be noted that the authors of [18] performed detailed parametric analysis of this design; in particular, the effect of geometric parameters on the antenna reverse loss value was analyzed. Figure 4.97 shows the dependence of the numerical value of the reverse loss factor on frequency for different length of structures of the main

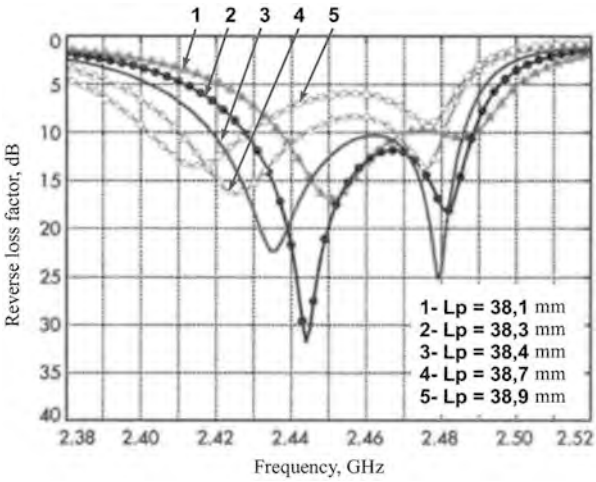

Fig. 4.97 Effect of the main radiator length on the antenna reverse loss factor

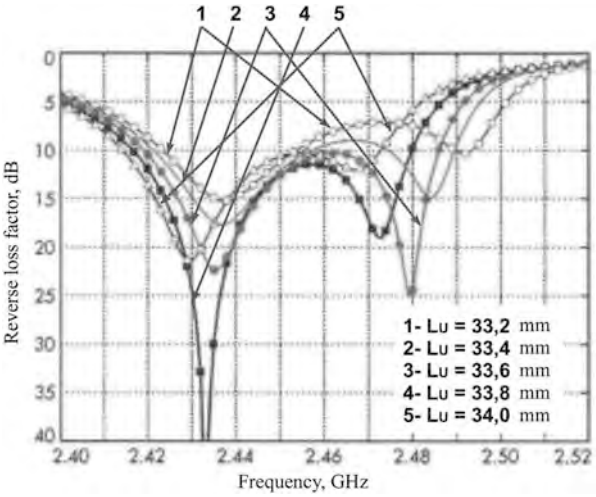

Fig. 4.98 Effect of the parasite radiator length on the antenna reverse loss factor

radiator. It can be seen that the lower resonant frequency is shifted downwards when the geometrical dimension L_P is increased. At the same time, it should be noted that the upper resonant frequency remains nearly unchanged and determined by the length of the U-shaped radiator (Fig. 4.98).

Dependencies of the reverse loss factor on the width of gaps and cuts are shown in Figs. 4.99, 4.100 and 4.101. E.g., Fig. 4.102 shows the dependence of the reverse loss factor on the location of the feeder line attachment point. As we can see, change in the numerical value of L_F causes a very significant change in the impedance value at the upper resonance frequency, since the point of connection of the feeder line is closer to the bottom edge of the U-shaped amplifier.

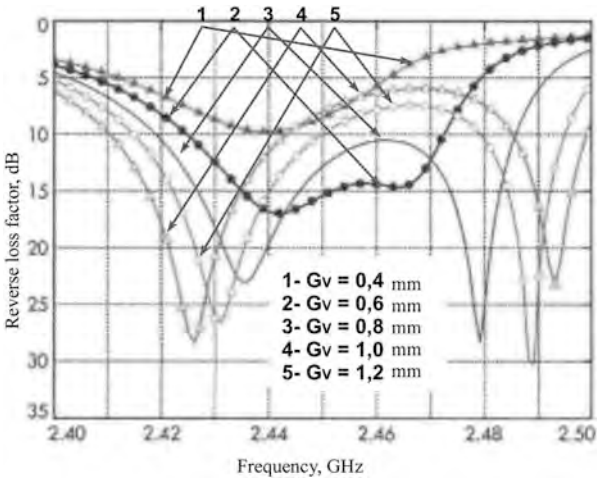

Fig. 4.99 Effect of the vertical gap width on the antenna reverse loss factor

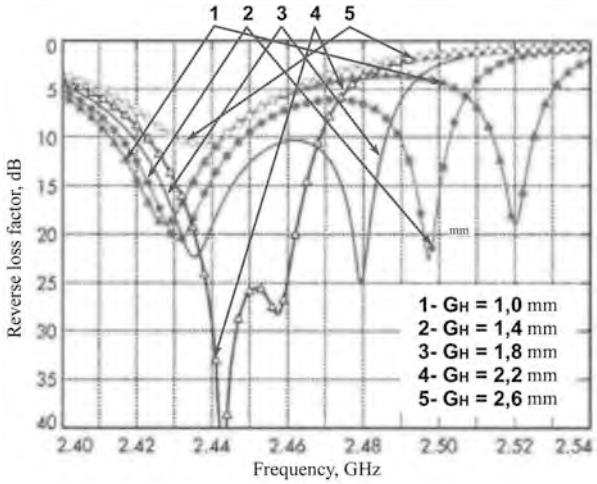

Fig. 4.100 Effect of the horizontal gap width on the antenna reverse loss factor

At the same time, Fig. 4.102 shows that the increase in L_F from 14.5 to 15.5 mm causes a significant reduction in the lower resonance frequency due to narrowing of the resonance range at the lower frequency. In this case, parasite radiator of the antenna operates only at higher resonant frequency.

Figure 4.103 shows experimental dependencies of the reverse loss factor for classic and modified microstrip antennas. Losses at resonant frequencies are 23.03 and 28.34 dB. Bandwidth is equal to 67 MHz (within the range of 2419. . .2486 MHz).

Figure 4.104 shows the structure of the analyzed microstrip antenna on thin substrate. Parameter measurements were performed with the help of network

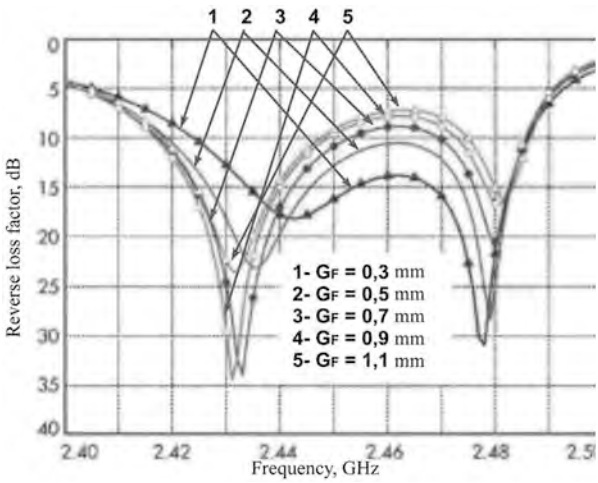

Fig. 4.101 Character of effect of L_F on the reverse loss factor of the antenna

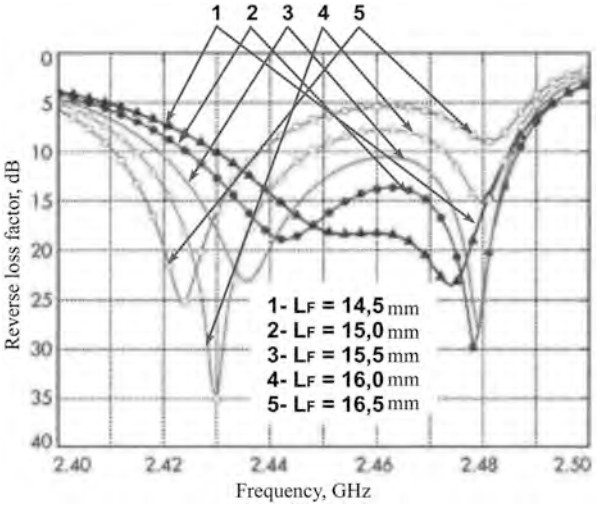

Fig. 4.102 Effect of the point of application of feeder on reverse loss factor for an antenna on thin substrate

analyzer 37269A Anritsu. Measured pass band determined by full input resistance is 66 MHz (within the range of 2421. . .2487 MHZ), resonant frequencies – 2441 and 2480 MHz. Reverse loss factor at top and bottom resonant frequencies amounts to 41.6 dB and 22.2 dB respectively (see Fig. 4.105). Beam patterns are shown in Fig. 4.106.

As we know, classic microstrip antenna with thin substrate has narrow pass band determined based on full input resistance. U-shaped parasite radiator is added to expand it. Comparison of characteristics of classic and modified antenna is given in

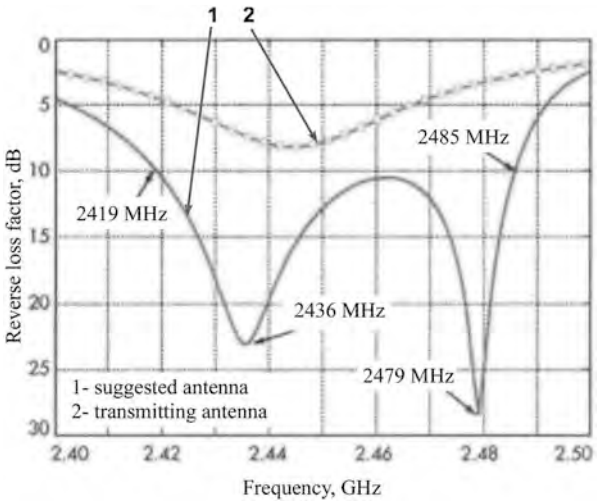

Fig. 4.103 Comparison of characteristics of classic and modified transmitting antennas on thin substrate

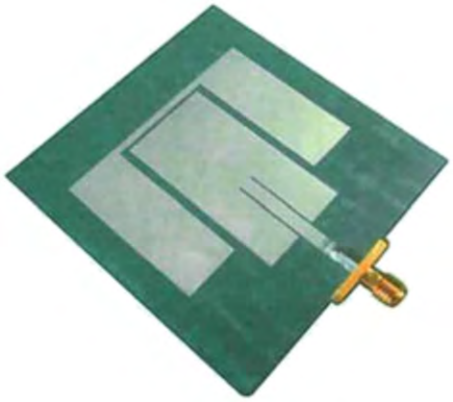

Fig. 4.104 Appearance of microstrip antenna on thin substrate

Tables 4.5 and 4.6, which shows that the modified antenna is characterized by 2.747 times wider operating frequency. Directivity patterns of both antennas are similar, except for the fact that the gain of the modified antenna is slightly lower due to greater ground range [18, 19].

It should be noted that in vertical section the 3 dB pass band is equal to 83° at the frequency of 2441 MHz and 84° at the frequency of 2480 MHz. It can be seen that the peaks are slightly shifted from the Z axis due to position of the feeder line on the main radiator. In horizontal section vertical section the 3 dB pass band is equal to 93° at the frequency of 2441 MHz and 86° at the frequency of 2480 MHz. Directivity pattern is symmetrical, since the antenna has bilaterally symmetrical configuration. Maximum gain factor of the antenna is 5.6 dBi at 2.45 GHz.

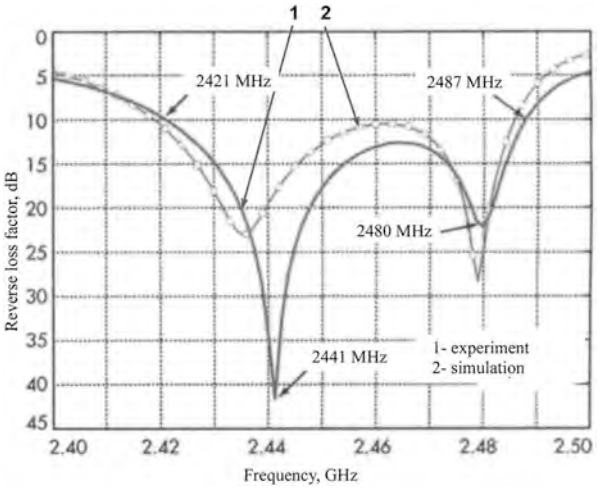

Fig. 4.105 Dependence of reverse loss factor on frequency for microstrip antenna on thin substrate

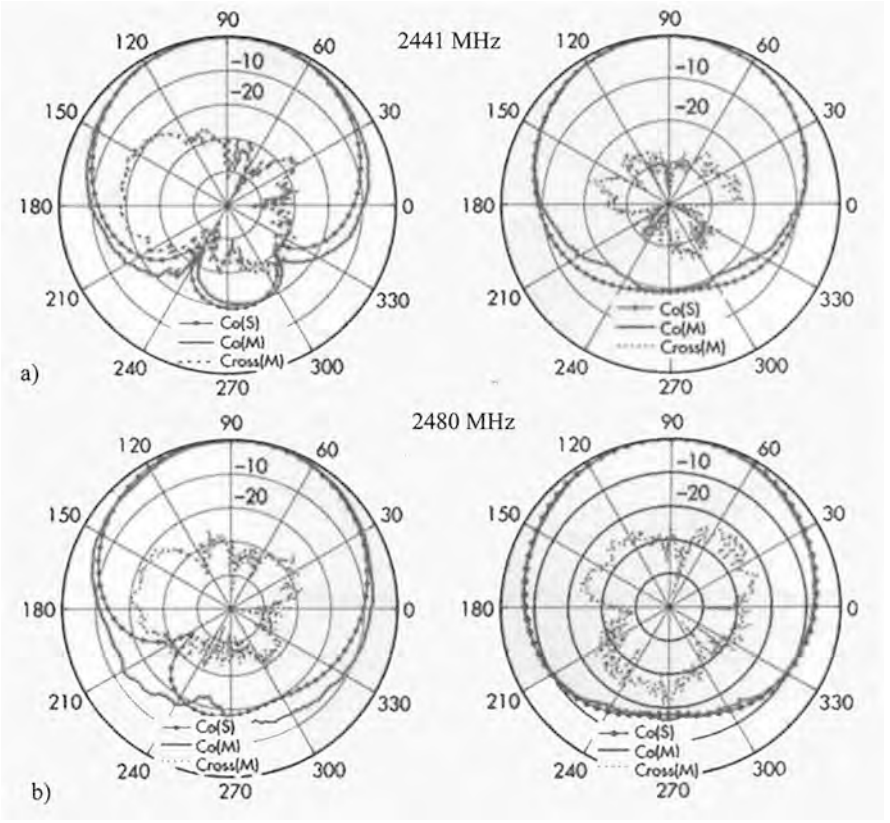

Fig. 4.106 Beam pattern at frequencies of 2441 MHz (**a**) and 2880 MHz (**b**): Co(S) – main polarization (modeling); Co(M) – main polarization (experiment); Cross (M) – cross polarization (experiment)

Table 4.5 Results of simulation and experimental measurements of the pass band width determined from full input resistance

	Modeling		Experimental measurements		
Antenna	Range, MHz	Band	Range, MHz	Band	Advantage, times
Classic	2438. . .2463	25 MHz (1.75%)	2440. . . .2464	24 MHz (0.979%)	1
Modified	2419–2485	66 MHz (2.694%)	2421. . .2487	66 MHz (2.689%)	2.747

Table 4.6 Comparative results of modeling and measurement of antenna gain factors

	Modeling		Experimental measurements	
Directivity pattern	3 dB band	Gain factor	3 dB band	Gain factor
Classic antenna	83°(E), 88° (H) at 2450 MHz	5.82 dBi	88°(E), 88° (H) at 2450 MHz	5.6 dBi
Modified antenna	83°(E), 93° (H) at 2441 MHz	5.5 dBi	90°(E), 89° (H) at 2441 MHz	5.3 dBi

4.2.7 Flat Reflective Printed Antenna for Cellular Communication Systems

4.2.7.1 Principle of Operation of a Parabolic Dish Printed Antenna

Transmission of wideband digital signals on the Internet or in systems of communication between base stations of cellular phones requires the use of small-sized cheap antennas capable of operating in the millimeter frequency range with gain of at least 30 dB. Planar reflector antenna [20], which combines properties of a parabolic mirror and a planar structure of strip resonators, meets these requirements to the greatest extent. Similarly to dish mirror, which transforms spherical front of the wave emitted by the primary radiator into the flat front forming high-directional radiation of the antenna, planar structure of strip resonators also performs the main task of the antenna and converts spherical front of the primary radiator into flat phase front of the antenna wave. At the same time, planar structure of strip resonators has small weight and dimensions and is easy to manufacture. Antenna designed as planar structure of strip resonators is usually referred to as planar printed antenna [20].

Planar printed antennas with different radiator feed circuits have been developed for a long time; however, printed antennas to replace dish mirrors appeared relatively recently [21, 22]. A significant contribution to the development of this direction was made by Russian companies St. Petersburg State Electrotechnical Institute LETI and LLC “Resonance” [22, 23].

Figure 4.107 shows the basic design of a planar reflecting antenna. Here, the flat reflecting surface contains planar elements, the dimensions of which ensure that the phase of the wave reflected from each element compensates the difference of phases

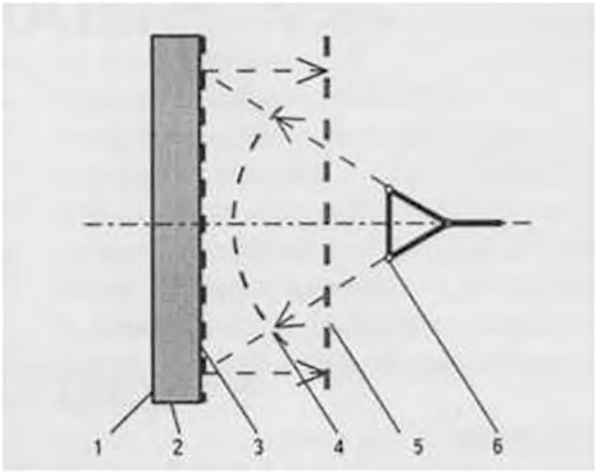

Fig. 4.107 Principle of building a planar reflector antenna: 1 – metallization, 2 – dielectric substrate, 3 – reflector array, 4 – spherical phase front, 5 – flat phase front, 6 – primary radiator

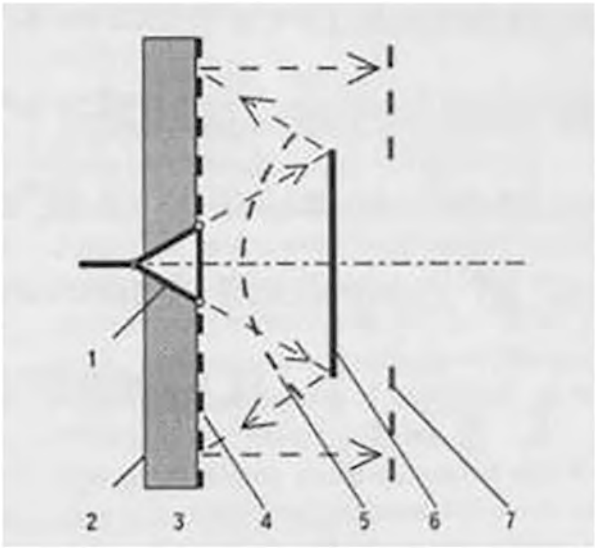

Fig. 4.108 Diagram of a planar reflecting antenna with flat counter-reflector: 1 – primary radiator, 2 – metallization, 3 – dielectric substrate, 4 – reflector array, 5 – spherical phase front, 6 – counter-reflector, 7 – flat phase front

between the spherical and flat fronts of the waves. As demonstrated in previous sections of this chapter, compensation of the phase difference causes the spherical front of the primary radiator of this antenna to turn into standard (classic) flat phase front after reflection from planar elements. Slightly modified version of this design of a planar reflector antenna is shown in Fig. 4.108. In the examined case, primary radiator of the antenna is placed directly in the plane of reflectors, and the so-called counter-reflector is introduced into the circuit of the primary radiator wave propagation. In this case, antenna thickness is reduced twice, but the counter-reflector shades a part of the aperture.

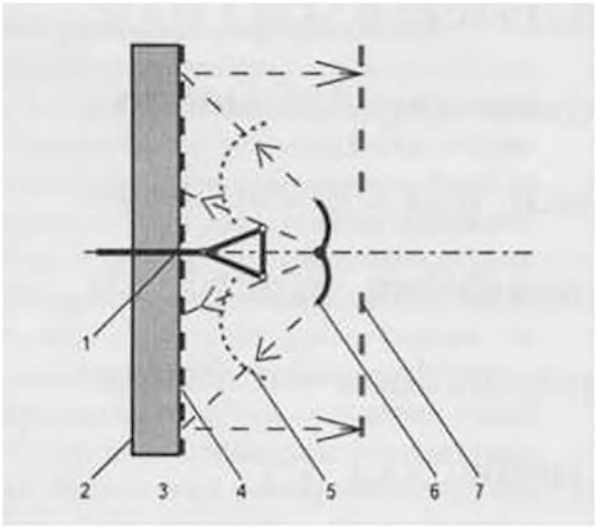

Fig. 4.109 Diagram of a planar reflector antenna with the counter-reflector formed by a half of elliptical toroid: 1 – primary radiator, 2 – metallization, 3 – dielectric substrate, 4 – reflector array, 5 – phase front of the wave reflected by counter-reflector, 6 – counter-reflector, 7 – flat phase front

For deeper understanding of the problem, Fig. 4.108 shows the cut central part of flat phase front on the radiating antenna surface. As is known to specialists, distortions of the flat phase front on the radiating surface of the antenna reduce gain and increase the level of side lobes. Figure 4.109 shows a new version of a modern planar reflector antenna, in which the counter-reflector is formed by a half of elliptical toroid. In this case, the wave reflected by counter-reflector does not illuminate the central part of the reflecting antenna surface. Shading caused by presence of the counter-reflector is not manifested, and the distribution pattern of radiating currents on the illuminated part of the reflecting surface is more uniform [25]. Since the front of the wave reflected by the counter-reflector is not spherical, change in the configuration of the front of the wave incident of the main reflecting surface would complicate the design of the mirror antenna, since the mirror shall not be parabolic. However, in case with reflecting surface formed by such array of reflectors, adjustment of the phase shift occurring during reflection of the wave from the reflecting surface is easily taken into account during calculation of mismatch elements of various reflecting elements of such antenna.

One of the multiple known designs of such planar reflecting antenna is shown in Fig. 4.110. In this case, aperture of the antenna is formed by the polarizer, which in turn is formed by a system of parallel conductors. In order to simplify presentation of the material, let us suggest that the conductors are located in a horizontal plane. Since the primary antenna radiator emits a wave with horizontal polarization, this wave is reflected from the polarizer and falls on the plane carrying reflectors. Dimensions of reflectors shall not only provide the phase difference required for formation of a flat phase front, but also ensure rotation of the polarization plane of the reflected wave by 90° – in this case, the reflected wave becomes vertically polarized and freely passes through the polarizer. In this case, antenna thickness is also reduced twice, and

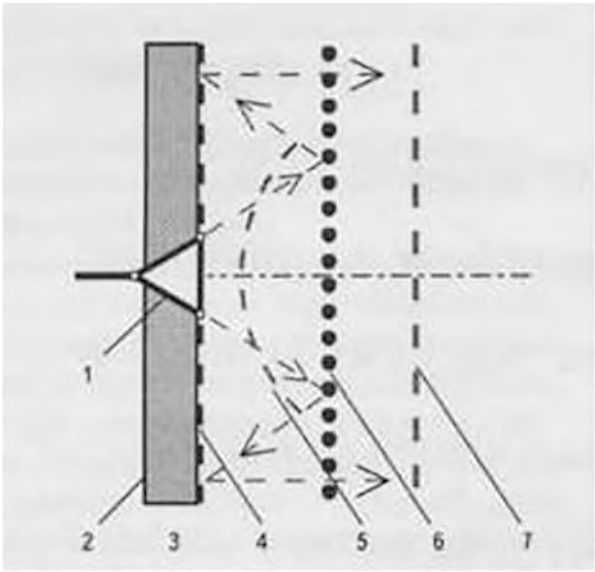

Fig. 4.110 Equivalent circuit of a planar reflecting antenna with polarization counter-reflector: 1 – primary radiator, 2 – metallization, 3 – dielectric substrate, 4 – reflector array, 5 – spherical phase front, 6 – polarizer used as counter-reflector, 7 – flat phase front

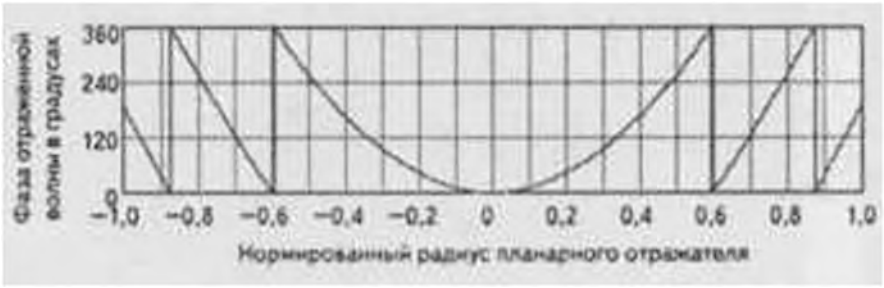

Fig. 4.111 Absolute phase value of the wave incident on the reflector taking into account subtraction of the excess phasing constant equal to n 360°, where n is an integer

shading effect of the counter-reflector is not observed. However, this design of planar mirror antenna has a disadvantage. Carefully selected dimensions of reflectors, which shall ensure the required difference between phases and rotation of the polarization plane during wave reflection are effective only within a limited frequency band, which narrows the pass band in which the maximum gain factor is ensured.

Designer of the radio communication system needs to understand that a greater angle of deflection of the primary radiator from the antenna axis increases the phase difference obtained by this beam when passing the direction to the reflecting surface. This difference between phases shall be compensated during reflection of the wave from the reflector. Central part of Fig. 4.111 shows the absolute value of phase

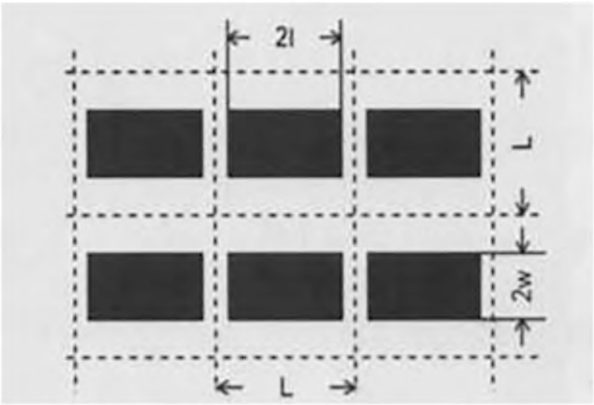

Fig. 4.112 Appearance of a part of the antenna reflector system placed on dielectric substrate

difference that shall correspond to the phase shift occurring during reflection of the wave from the reflector. When the beam deflection angle becomes sufficient, compensation phase difference exceeds 360°. The real phase difference is calculated after subtracting 360° from excessive compensating phase difference. Figure 4.111 illustrates the graph of dependence of compensating phase difference on the radius of the reflection point on flat reflecting surface taking into account subtraction of the excess phasing constant equal to n 360°, where n is an integer. Reflecting surface that provides phase shift corresponding to Fig. 4.111 is known as Fresnel mirror. It is clear that a Fresnel mirror ensures perfect transformation of spherical wave front into flat wave front in a fairly wide but limited frequency band.

Thus, the reflecting surface shown in Figs. 4.107, 4.108, 4.109 and 4.110 is formed by a system of reflectors installed on dielectric substrate with high-conductivity metallized base. A part of the reflecting surface is shown in Fig. 4.112. The reflecting surface is designed as a square lattice of reflectors with a pitch of LxL (reflector size – 2l × 2w). Reflectors are formed on dielectric substrate with the thickness of H, where dielectric permittivity of the substrate material is equal to ε_d.

Figure 4.113 shows the dependence of the reflection coefficient phase of the wave incident on the reflecting surface on the size of the reflector. Here, the frequency of the supply wave is 25 GHz, electrical field vector is parallel to the side of the reflector with the size 2 l, and the substrate is made of a widely known material – foam ethylene with low dielectric permittivity ($\varepsilon_d = 1.06$), substrate thickness H = 2 mm. In the analyzed antenna structure, these reflectors are implemented by means of photolithography on the surface of the foiled lavsan (polyethylene-terephthalate) placed directly on the surface of the polyethylene foam substrate: lavsan thickness = 0.1 mm; copper foil thickness on the lavsan surface −0.035 mm.

As can be seen from graphs in Fig. 4.113, change in geometrical dimensions of the antenna reflector causes the phase shift from 135° to −200°, which leads to phase control span of 335°. Since it is 25° less than the required span of 360° (Fig. 4.111),

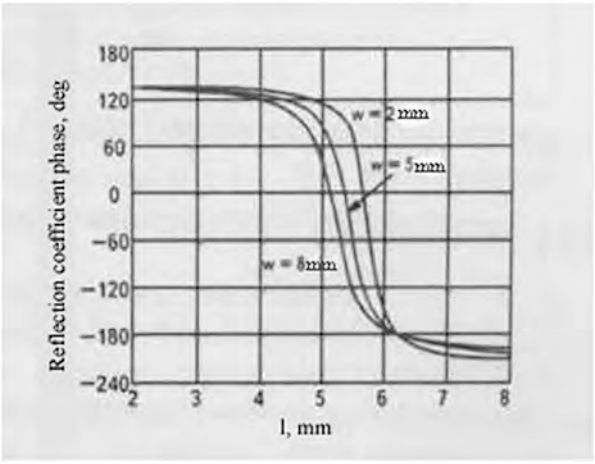

Fig. 4.113 Dependence of the reflection coefficient phase of the wave incident on the reflecting surface on the size of the reflector

it will cause a phase error at insignificant portion of reflectors within ±12.5°, which in turn can reduce gain by 0.5 dB and increase the level of side lobes by 2–3 dB [26].

4.2.8 Features of Designing Mirror Reflector Phased Antenna Arrays

Based on the theory of phased antenna array [26], linear size of reflecting (radiating) elements of low directivity shall amount to $L = (0.65–0.6S)\ \lambda_0$, where λ_0 is the length of the wave in free space surrounding the antenna. In particular, at 10 GHz $\lambda_0 = 30$ mm and $L = 20$ mm [20]. Design of such antenna array consists in calculation of dimensions of the reflectors that shall perform phase shift of the reflecting wave ensuring transformation of the spherical phase front of the primary radiator wave into the flat phase front radiated by the antenna array and detection of distribution of reflector dimensions on the surface of the planar antenna.

Below is the list of basic design solutions recommended for developers of modern PAAs.

4.2.8.1 Calculation of Dimensions of PAA Reflectors

For the purpose of simplifying the calculation, it is suggested that mutual influence of reflectors is quite low [21–24]. Therefore, calculation of reflection from each separate reflector is entirely possible. The array is divided into a system of virtual waveguides, each of which contains one reflector. Virtual waveguide is formed by electric and magnetic walls. Power lines of the electrical field are normal to the electrical walls, and the power lines of the magnetic field are normal to magnetic

walls; cross size of the waveguide – LxL. In this case, we assume that purely transversal wave with zero indices propagates in the waveguide along both coordinate axes T_{00}.

Then the standard algorithm of calculating dimensions of reflectors, which shall ensure the required phase shift of the reflected wave, is down to two ways:

1. Finding the reflected wave phase based on analytical (phenomenological) model of reflection of the wave from the vibrator placed inside the waveguide.
2. Finding the phase of the reflected wave based on electrodynamical calculation of the field structure in the waveguide containing the vibrator with set dimensions.

It should be noted that electrodynamical calculation of the field structure in the waveguide is known in English as Full Wave Analysis. Analytical model helps perform calculation with the help of MATCAD within a short period of time; however, the model cannot provide high accuracy of the obtained result. Therefore, two-stage process is implemented in designing the reflector array. At first, calculation based on analytical model is performed, and graphs (Fig. 4.113) and corresponding data tables are obtained. After that, graphs and tables are made more exact by means of full wave analysis.

Known dependence of the phase of reflected wave on the dimensions of the reflecting element based on the analytical model shall be specified with the help of full wave analysis. In each specific case, this stage of engineering of a reflector array shall be performed using an original software product which uses the method of moments in relation to multi-layered reflecting structure [23, 24].

One of the main parameters is the distribution of sizes of reflector elements over the surface of the planar reflector antenna.

As noted above, in this practical example we are using two stages of calculating dimensions of the elements forming the reflector array. (1) analytical calculation of the vibrator model, (2) full wave analysis of the field structure excited by the presence of vibrator. After implementation of two calculation steps, we obtain the phase value of the reflected wave depending on the size of the reflecting element. On the other hand, knowing the position of reflecting elements on the surface of the planar reflector antenna and the distance between the primary radiator to the antenna surface, we can calculate the phase shift to be ensured by each reflecting element (Fig. 4.111). Knowing the required phase shift and dependence of the phase shift on the dimensions of the reflecting element, it is easy to find distribution of dimensions of reflecting elements across the surface of the planar reflecting antenna. As can be seen from the presented transforms, phase front of the wave emitted by the primary radiator turns into flat phase front as a result of reflection, which ensures high-directional beam pattern of the antenna.

Each of such reflecting elements ensures one-directional radiation and has gain factor of about 3 dB. Let us suppose that the designed antenna shall ensure amplification of 35 dB. Then, taking into account certain irregularity of distribution of radiating currents over the antenna surface, we obtain the required number of reflecting elements N = 1400–1600. Antenna design is implemented as a result of repeated multiplication of the structure shown in Fig. 4.112, taking into account

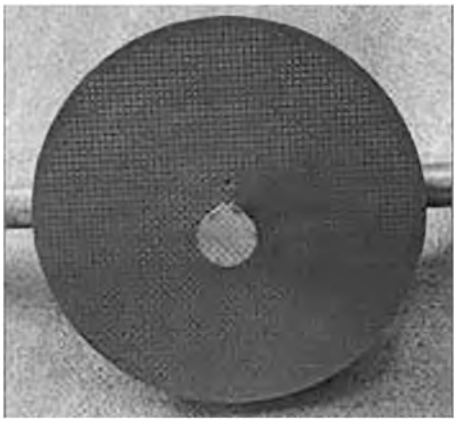

Fig. 4.114 Planar printed structure that ensures transformation of the spherical front of the primary radiator wave without rotation of the polarization plane into the flat phase front of the wave radiated by the antenna

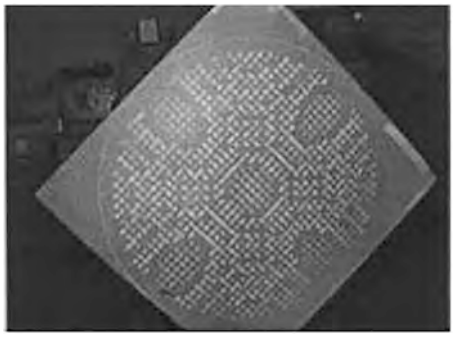

Fig. 4.115 Planar printed structure that ensures transformation of the spherical wave front of the primary radiator with rotation of the wave polarization plane by 90°

correction of dimensions (1, w). This procedure is performed with the help of the specially designed system, which implements the design of the antenna with subsequent formation of the mask.

Figure 4.114 shows the photograph of the known [26] planar printed structure that ensures transformation of the spherical front of the primary radiator wave without rotation of the polarization plane into the flat phase front of the wave radiated by the antenna. In the arrangement of reflecting elements in the photo (Fig. 4.114) one can see rings corresponding to zones of the Fresnel mirror.

Figure 4.115 shows the photograph of the planar printed structure that ensures transformation of the spherical wave front of the primary radiator with rotation of the wave polarization plane by 90°. Several words shall be said about how the polarization plane rotation is formed. Let us suggest that the primary radiator wave has vertical polarization. Symmetry axes of reflecting elements (1, w) are rotated by 45° relative to the vertical axis. Vector of electrical field strength of the wave incident on reflecting elements can be broken down into components parallel to the axes of reflecting elements: E_l and E_w Each of these components will excite the reflecting

Fig. 4.116 General view of a planar reflector antenna in a radio-transparent package

element according axes 1 and w respectively. Phase shift of reflected waves depends on dimensions of 1 and w. With correct dimensions, electrical field strength vectors E_1 and E_w will have the phase difference of 180°. This will cause rotation of the polarization plane.

4.2.8.2 Structure and Parameters of a Planar Reflector Antenna

Figure 4.116 is the photograph of a planar reflecting antenna designed according to diagram in Fig. 4.109. This antenna is structurally designed in radiotransparent package ensuring protection of structural elements from negative atmospheric effects. In particular, in 2015 this antenna (RA 42 model) is produced by the "Resonance" company.

Basic technical characteristics of this antenna:

- operating frequency range: 40.5–42.5 GHz:
- polarization: linear (vertical):
- gain factor −34 dB min;
- beam width: (bearing) 2.3°, (location angle) 2.3°;
- VSWR (maximum): 1.5:
- permissible input power: 10.0 W (average):
- level of side lobes: – 15 dB (in horizontal plane):
- cross polarization: – 25 dB;
- reverse radiation level: – 30 dB;
- dimensions: 220 × 220 × 60 mm;
- weight: 1 kg:
- operating temperature: −30 to +60°C:
- permissible wind speed: 150 km/h.

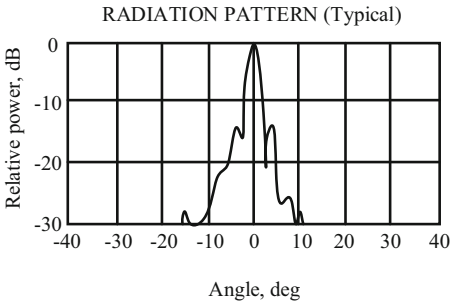

Fig. 4.117 Antenna directivity pattern in horizontal plane

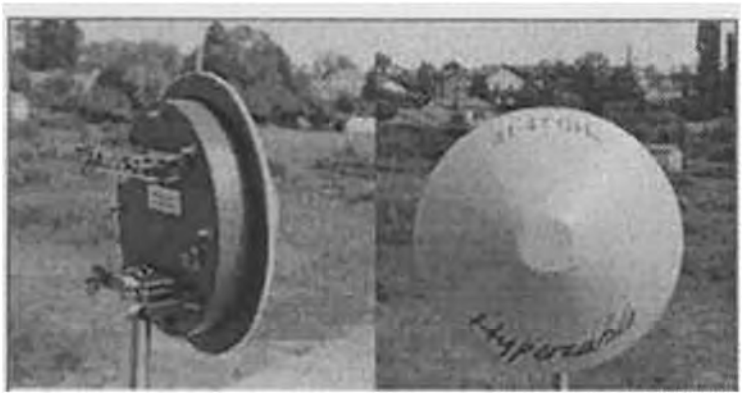

Fig. 4.118 Photograph of the antenna in working conditions

Figure 4.117 shows the beam pattern of this antenna in horizontal plane; Fig. 4.118 is the photograph of the actual design of this antenna in real operating conditions. Design of the antenna here was created by the Russian developer in cooperation with the foreign company MDS (France).

Figure 4.119 shows recommended installation dimensions of this antenna in combination with the volume allocated for placement of the transceiver unit. It should be noted that the electronic unit was designed by the Russian company in cooperation with the French company Thales (France).

Of course, it should be noted that the examined planar reflector antenna is mostly designed for the use in communication systems, the Internet, civilian radars (protection of vehicles from collisions, short-range navigation for small ships, etc.) operating at the waves of centimeter and millimeter ranges. Simplicity of the antenna structure and the use of standard technology ensure its low cost in mass production. Development of the antenna is based on original mathematical models and corresponding software, which cover the entire design cycle ending with production of data required for manufacturing of the mask and performance of process

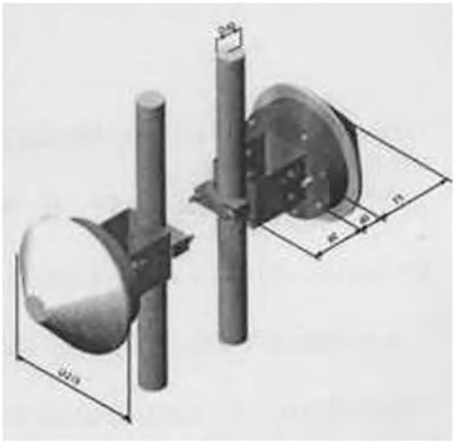

Fig. 4.119 Installation dimensions of the antenna in combination with the volume allocated for placement of the transceiver electronics

operations of photolithography. Developers have created specialized equipment for testing of electrodynamical characteristics of manufactured reflecting surfaces.

4.2.9 Three-Range Slot Antenna for Wireless Communication Systems

The antenna has two U-shaped cuts, due to which it operates in three frequency ranges: 2.45; 2.64 and 3.44 GHz.

Since several frequency bands are allocated for wireless data transmission, communication systems shall be equipped with several antennas if they support two or more communication standards. The second option, which is more compact, suggest the use of antennas operating within several frequency ranges.

Let us consider design features of the three-range antenna shown in Fig. 4.120 [27]. The top side is a rectangular plate with two U-shaped cuts ensuring two frequency bands. The bottom side of the antenna contains the ground plane and the Z-shaped metal element providing one more resonant frequency. Two L-shaped cuts at the grounding section are designed to expand the pass band determined by input impedance. Supply line impedance: 50 Ω.

This antenna is built of FR-4 substrate with thickness of 0.8 mm (relative dielectric permittivity: 4.3; loss tangent: 0.02); size: 34.5 × 40.0 mm.

Modeling and experimental results demonstrate that this antenna can be applied in wireless network equipment (2.45 GHz), 4G cell phones (2.60 GHz) and WiMAX devices (3.3–3.6 GHz).

Modeling and optimization of parameters was performed in the HFSS (High-Frequency Structure Simulator) software using the Finite Element Method (FEM). Antenna parameters are given in Table 4.7 [27]. Distribution of currents for all operating bands is shown in Fig. 4.121a, b.

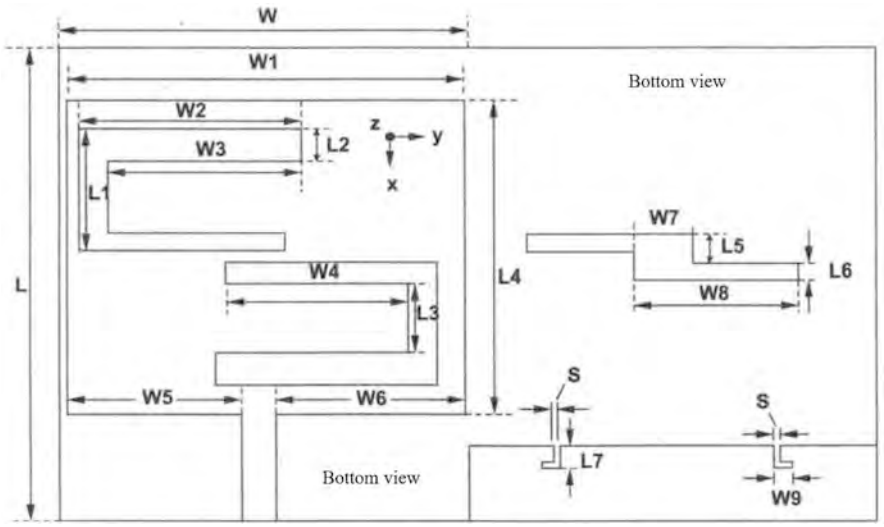

Fig. 4.120 Slot antenna design: top view (left) and bottom view (right)

Table 4.7 Optimal antenna parameters, mm

W	L	s	W1	W2	W3	W4	W5	W6	W7
34.5	40.0	0.3	33.6	18.9	16.4	14.9	14.7	16.0	5.0
W8	W9	L1	L2	L3	L4	L5	L6	L7	
14.1	1.5	6.3	2.7	6.3	26.7	2.3	1.5	2.0	

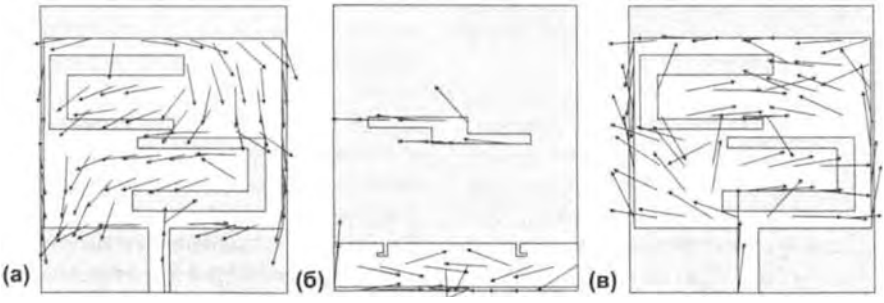

Fig. 4.121 Distribution of current over the antenna surface for the ranges of (**a**) 2.45 GHz; (**b**) 2.64 GHz and (**c**) 3.44 GHz

Figure 4.122 shows the dependence of the standing-wave ratio (SWR) on frequency. It can be seen that design-based and experimental results are similar. Figure 4.123 shows radiation pattern for all three frequency ranges. Plane xz corresponds to the E vector plane, plane xy – to the H vector plane.

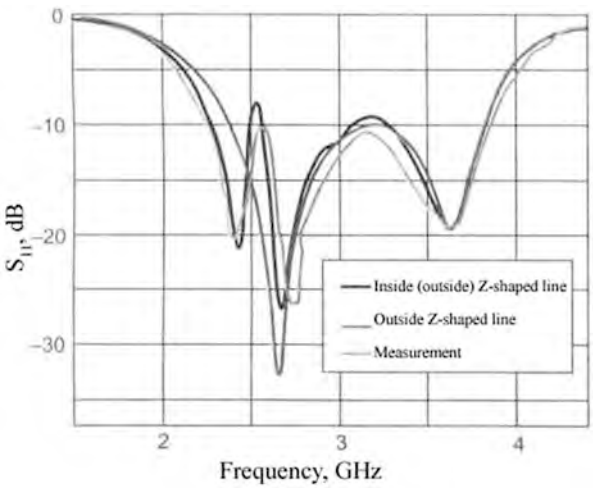

Fig. 4.122 Modeled and experimental dependencies of the standing wave ratio (S_{11}) on frequency

In the lower operating range, the directivity pattern looks like an 8 in the E plane and is almost round ιν τηε H plane. This indicates that the antenna works in a fashion similar to a monopole, even though the characteristics of the latter are slightly better.

Figure 4.124 shows the results of measurement of the gain factor. It takes values of 2.24–4.89 dBi in the first band, 1.71–4.70 dBi in the second band and 3.12–4.19 dBi in the third band.

The considered antenna supports three operation modes and is distinguished by its small size. Selection of frequency ranges shall ensure support of the main types of wireless communication by the antenna: local wireless networks (2.45 GHz), 4G cell phone communication (2.60 GHz), WiMAX networks (3.3–3.6 GHz). The antenna ensures proper matching of impedances and stable beam pattern within the entire range of operating frequencies.

Modeling and experimental results are nearly identical, which proves the possibility of using this antenna in wireless communication systems.

4.2.10 Wideband Vivaldi Antenna on Ceramic Substrate for 60 GHz

With development of wireless communication and internet, total volume of transmitted data will grow and eventually overcome the available capacity of communication channels [28]. Capacity inside the frequency band designed for mobile wireless communication can be increased by improving efficiency of use of the

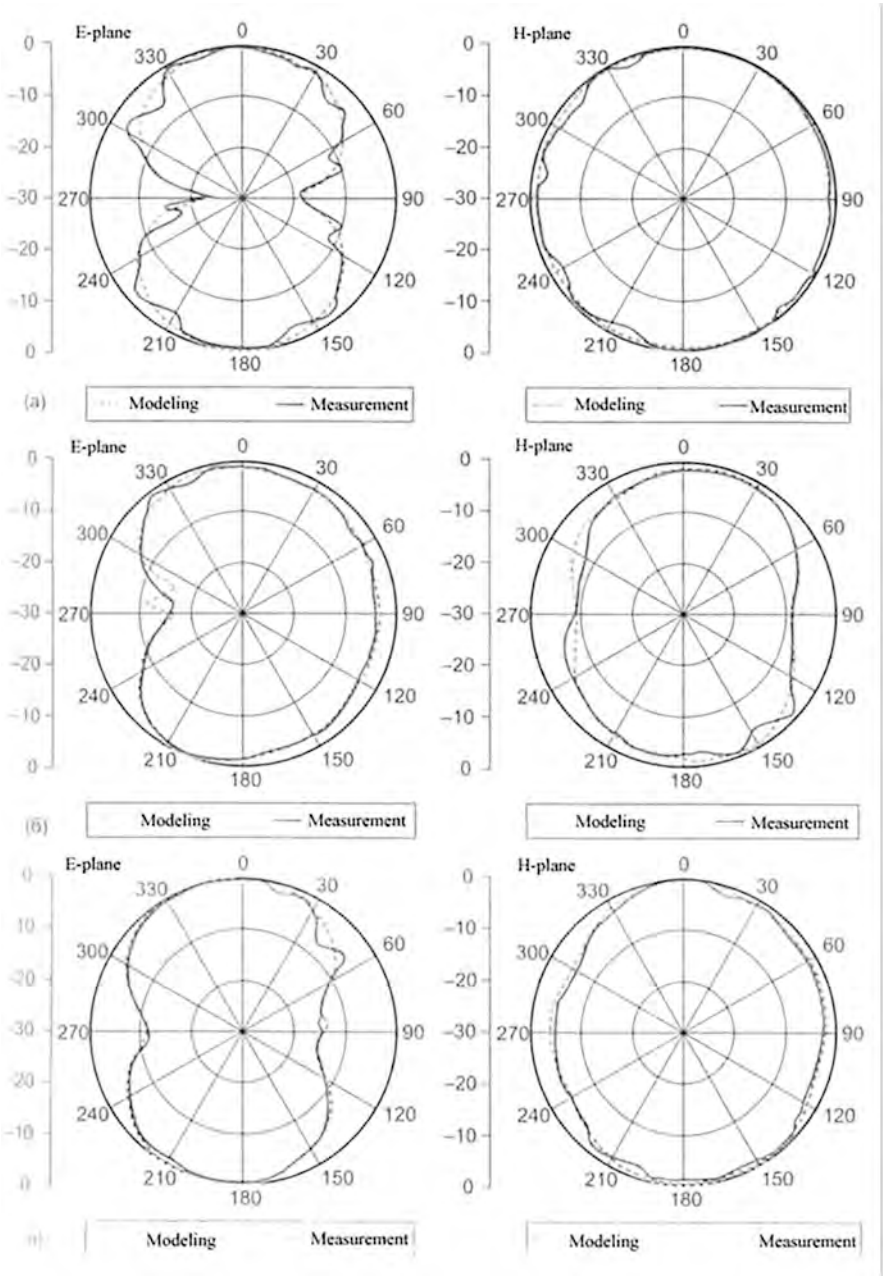

Fig. 4.123 Antenna beam patterns at the bands of 2.45 GHz (**a**), 2.64 GHz (**b**) and 3.44 GHz (**c**)

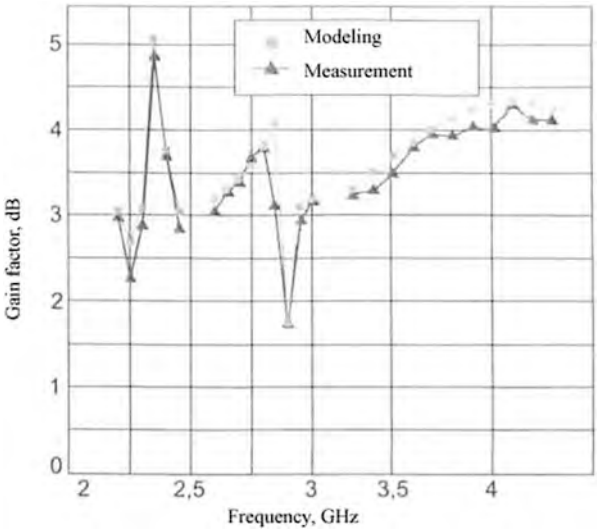

Fig. 4.124 Frequency dependence of the gain factor on frequency

spectrum and transition to smaller cells. At the same time, it is not enough to simply meet the requirements; it is necessary to start using higher frequencies in order to avoid overloading of communication channels in the future.

At the moment, wireless communication at the speed of several Gb/s based on the IEEE 802.1 lad standard is being developed. This technology is expected to form the basis for devices of the fifth generation (5G). Implementation of this idea requires antennas with the function ensuring beam scanning that would follow movement of a mobile subscriber or change the directivity pattern for the purpose of interference attenuation. The antenna described below can be used in 60 GHz wireless communication systems.

In SHF range, effectiveness of the antenna is the definitive factor. Operation of antenna is affected by such factors as losses in substrate and interconnects, mismatch of impedances and proximity of foreign materials. Due to area saving, antennas are implemented as integrated and are already included in the transmitting chip.

This requirement is mandatory in certain devices. In the range of 60 GHz, basic radiators can be used, such as dipoles, patch antennas, slotted and folded antennas and inverted F-shaped antennas. If a higher gain is required, Yagi antennas, horn antennas and Vivaldi antennas are used. The latter are characterized by several advantages: bandwidth, simplicity of design and production. They are recommended for use in the 60 mm range. As a rule, antennas are designed as a part of the crystal substrate. When the operational frequency increases, electrical characteristics of the crystal become as important as the possibility of integration and the problems of general cost. Table 4.8 contains comparison of the existing solutions.

Paper [28] examines the Vivaldi antenna on FerroA6S substrate made of LTCC with dielectric permittivity $\varepsilon_r = 5.9$ and loss tangent of 0.002. Substrate thickness –

Table 4.8 Comparison of antenna manufacturing technologies

Base layer	Quantity of layers	Max. frequency, GHz	Loss tangent at 60 GHz	Passive elements	Percentage yield	Cost
Rogers Duroid	4	~40	0.01	–	Medium	Low
Low Temperature Cofired Ceramics (LTCC)	24	~100	0.002	Resistors, capacitors, ferroelectrics, heat removal circuits	High	Medium
Integrated configuration (IPD)	3	~100	0.009	Resistors, capacitors	High	High

97 μm, silver-plating line parameters: $t = 9$ μm, specific conductivity – $\sigma = 5.5 \times 10^7$ cm/m. Substrates of low temperature cofired ceramics have the following advantages:

– maturity of production process;
– good electrical characteristics of antennas;
– extended integration capabilities;
– small tolerances.

Metallization consists of three layers: the first and the third are placed on top and bottom surfaces of the substrate, while the second is between them in the substrate itself.

Production of a Vivaldi antenna includes several stages. During the first stage, substrate size is set. In the first approximation it is considered rectangular with the width equal to the half of the plate length. The length of the rectangle shall be not lower than one wavelength at the lowest operating frequency.

In our case, this length is equal to 6 mm. Unless otherwise specified by the manufacturer, substrate thickness shall ensure characteristic impedance of 50 Ω and acceptable line width. Let us suggest that the substrate is 0.388 mm thick and has the relative dielectric constant equal to 5.7. Now, we will apply classic formula for characteristic resistance of the strip line and find the width of the line.

$$\frac{W_{stripline}}{H_{stripline}} = \frac{30\pi}{\sqrt{\varepsilon_r} Z_0} = -0,441. \tag{4.34}$$

As a result, we get $W = 0.135$ mm. From this, we can calculate the remaining geometrical parameters.

During the second stage, cavity for the middle metallization layer is manufactured, to which the supply line is connected. The supply line has a non-linear shape (Figs. 4.125, 4.126 and 4.127). Elliptical shape ensures proper results and is easily

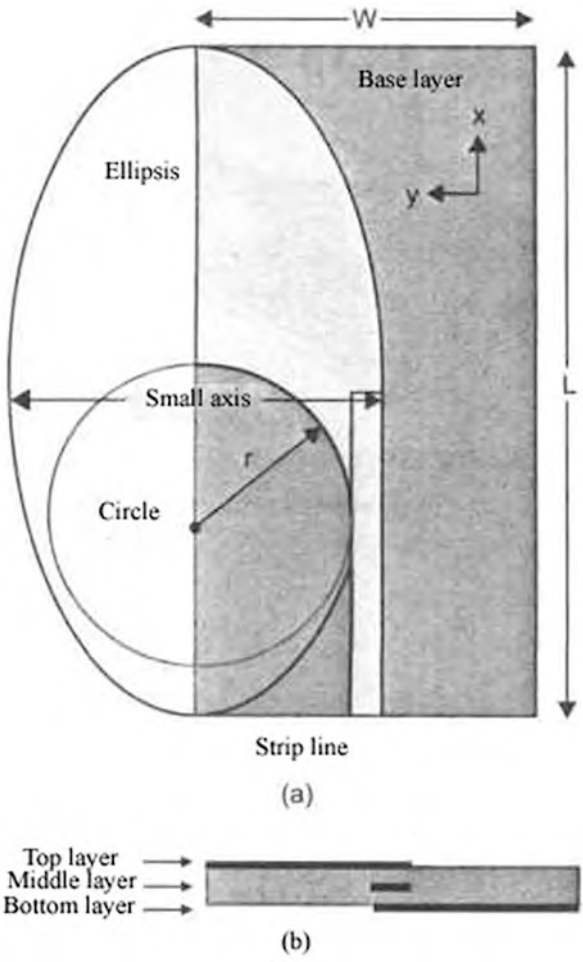

Fig. 4.125 Antenna structure: (**a**) top view, (**b**) front view

created in most CAD systems with the help of Boolean operations, even though other shapes can be used if necessary, such as exponential or linear.

The following designations are used in Fig. 4.125: W – substrate width, L – substrate length, r – circle radius. We can see that this layer consists of three basic shapes: ellipse, circle and rectangle. Length of the rectangle is about a half of the substrate's length, and the rectangle is located in the middle of the board.

The ellipse is located in the middle of the left part of the substrate. Its major axis and relation of axis are calculated according to the formula:

$$\textit{Большая} \quad \textit{ось} = \frac{L}{2}; \quad \textit{отношение} \quad \textit{осей} = \left(W + W_{stripline}\right)/L. \tag{4.35}$$

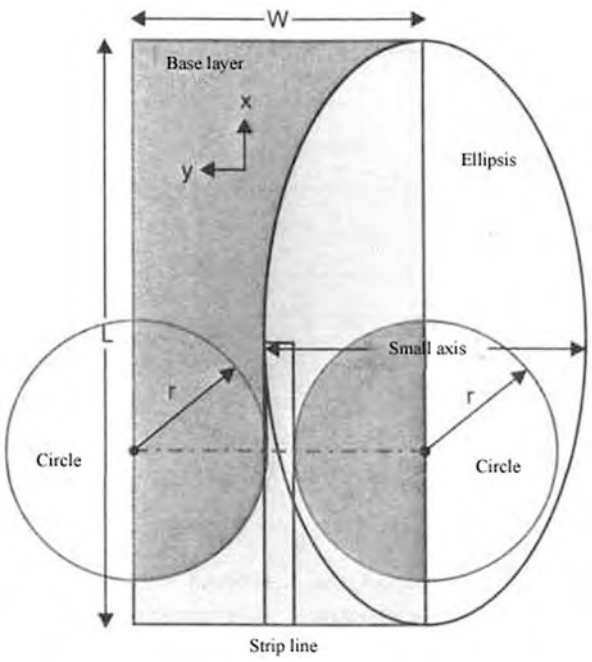

Fig. 4.126 Land plan

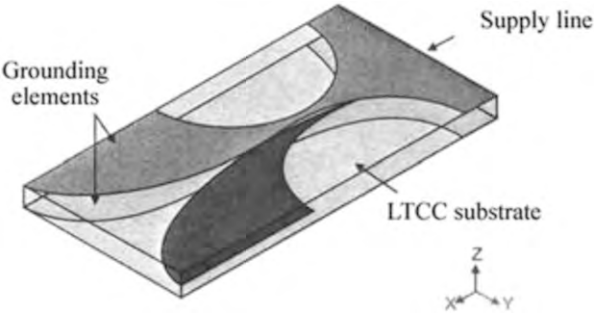

Fig. 4.127 Antenna model for HFSS CAD system

Inserting the values, we get 3 mm and 0.5225 respectively. Center of the circle is at the distance: $(W - W_{stripline})/3$ from the horizontal line passing through the center of the substrate, i.e. 0.955 mm in our case. Circle radius is calculated according to the formula:

$$r = \left(W - W_{stripline}\right)/2. \tag{4.36}$$

We get 1.4325 mm. After application of the mask, the circle is subtracted from the ellipse, and the obtained figure is connected to the rectangle (feed line). The curved element is complete. It is hashed in Fig. 4.125. Excess material is removed.

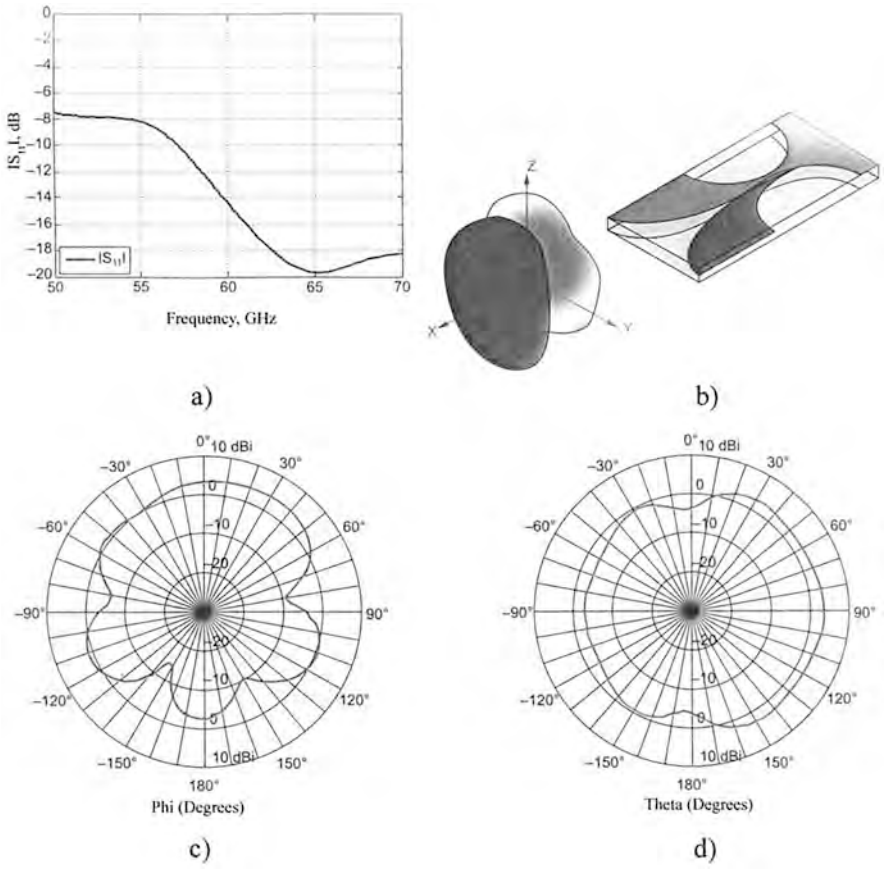

Fig. 4.128 Modeling results: (**a**) matching of impedances; (**b**) volumetric radiation diagram; (**c**) radiation by bearing; (**d**) radiation by elevation angle

Ground layers at the top and bottom of the substrate are manufactured in the same manner. The procedure is simplified by the fact that radiating elements are identical reflections of the middle plate with feeder, i.e. additional calculations are not required.

The rectangle in Fig. 4.126 outlines the area in which the land plan is formed. The width of the rectangle is W, and the length exceeds the radius of circles. Circles are cut out, and a free line is used to connect the plate elements.

Modeling was performed in the Ansys HFSS environment. Antenna model is shown in Fig. 4.127, and simulation results are shown in Fig. 4.128. According to primary modeling results, the width of the pass band determined on the basis of input impedance covers the entire band of the V range (50…75 GHz). This proves applicability of Vivaldi antennas manufactured using the described method.

Obtained far-field beam patterns are typical of most Vivaldi antennas, and the peak gain factor is 4 dBi. Antenna parameters are satisfactory but can be improved

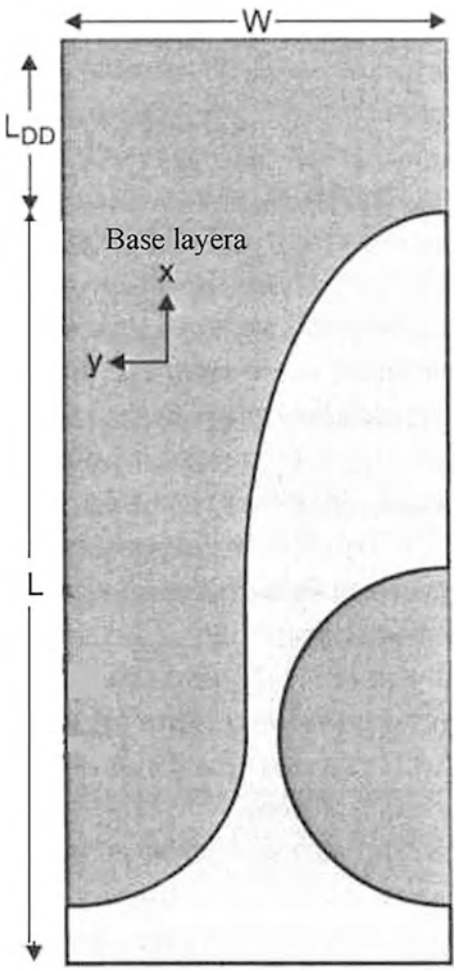

Fig. 4.129 Addition of director to increase the gain factor

by several means. The first of these means is the alteration of geometric parameters. For example, an increase in the plate length or width increases the gain factor. The second method consists in adding a dielectric director.

Vivaldi antennas have many advantages as compared to other antenna types; however, there is one significant disadvantage: low gain factor. Its increase is achieved by addition of the dielectric director at the edge of the substrate in the form of an extension that covers the aperture (Fig. 4.129). At LDD = 2 mm, gain factor is increased by 2.5 dBi and reaches 6.5 dBi. Profiling of the director height helps achieve an even better result.

Parameters of the antenna in paper [28] were measured using metal exciter with coaxial V connector. The exciter consists of two parts: base and holder. The base sets the antenna level. The holder ensures reliable connection of the antenna feed line through the V-shaped connector. At microwave range frequencies, the size of the

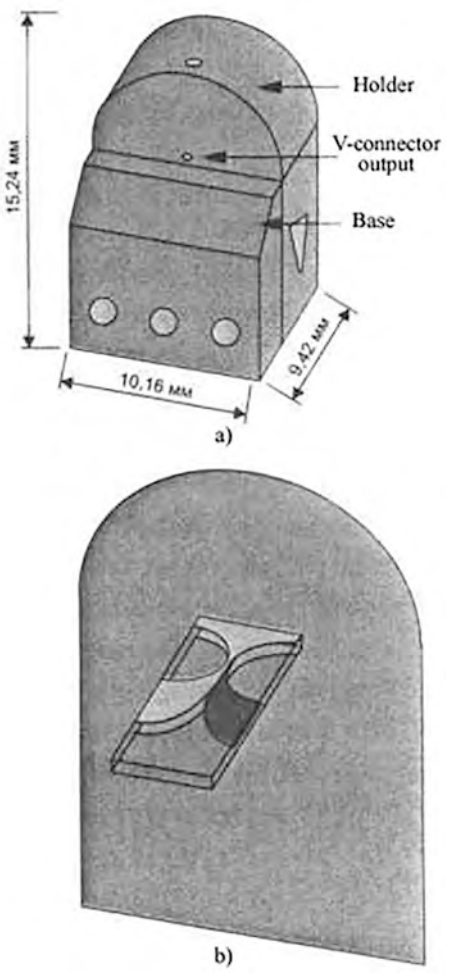

Fig. 4.130 Exciter model: (**a**) full, (**b**) simplified

exciter becomes commensurate with the wavelength, and it operates as a reflector, increasing gain factor of the tested antenna.

Figure 4.130 shows the corresponding model of the system and its simplified version. When the simplified exciter model is used, gain factor increases by 0.7 dBi at 60 GHz. This value shall be taken into account when matching design and experimental data.

The following main conclusions can be drawn up when summarizing the results of consideration of this antenna. During the first stage, the size of antenna is selected. The length of a radiating element is approximately equal to one wavelength, the width – about a half of it. Strip technology is selected in order to reduce losses and increase the quality of insulation. Production of antenna elements is relatively easy, since simple masks that do not require multiple calculations are used. Antenna gain

factor can be increased if necessary. Modeling and experimental results prove the possibility of using this antenna in wireless communication systems.

4.2.11 *Methodological Basis of Calculation of Mirror Dish Antennas Using Modern Microwave CAD Systems*

As is known, hundreds of wavelengths and more fit into the dimensions of modern mirror antennas for satellite communication and radio astronomy (from dozens of centimeters to hundreds of meters [29, 30]). Calculation of such large structures by strict electrodynamic methods requires significant computing costs. Therefore, analysis and calculation of radiation characteristics of mirror antennas of large electrical dimensions is usually performed using approximate methods of geometrical optics and geometrical diffraction theory, as well as methods of physical optics and physical diffraction theory [31–33].

In most cases, the developers use the most effective and accurate method of physical optics, which provides approximation of surface electrical current for perfectly conducting scatterers (reflectors). Key algorithm of numerical calculation of this method is based on the classic formula:

$$\overline{J}^{э} = 2\left[\overline{\mathrm{H}},\ \overline{\mathrm{n}}\right], \tag{4.37}$$

where $\overline{\mathrm{n}}$ ισ τηε normal vector for each point of the reflector surface, $\overline{\mathrm{H}}$ ισ τηε vector of the magnetic field created in this point by the primary emitter ([A/m]), $\overline{J}^{э}$ ισ τηε surface electrical current on metal reflector.

After that, known electrical current (4.37) is used to calculate the field of radiation of the mirror antenna (secondary field). Calculation of the secondary field consists in calculating corresponding two-dimensional Fourier integrals from the surface electric current.

This method does not require solving a complex system of linear algebraic equations of high order, which is necessary in most known electrodynamical methods of solving a system of Maxwell equations.

Moreover, the use of the method of physical diffraction theory [32, 33] makes it possible to take into account even subtler (as compared to physical optics method) effects of diffraction of the primary radiator field at the edge of the mirror. As a rule, it helps specify the level of far side lobes of the antenna radiation field. However, it is well known that numerical implementation of the physical diffraction theory method is more complex and not universal. Therefore, this method is rarely used in practice for analysis of large antennas.

It should be noted that during analysis of mirror antennas the method of geometrical optics is less accurate than the physical optics method, since it does not take into account polarization effects – in particular, during analysis of mirror antennas with

aperture method, even though it is approximately equivalent to the physical optics method in terms of accuracy.

Analysis and design of mirror antennas is usually performed by developers with the help of unique programs specifically designed to solve specific tasks. It is recommended to use commercially available program GRASP developed by TICRA for precise simulation of mirror antennas [34]. Another Russian program for such specialized tasks known as Mirror [35] was developed in the experimental design bureau of the Moscow Energy Institute. It is designed to solve the task of irradiating the reflector with a system of radiators. These specialized programs are capable of solving tasks with very high speeds, which helps calculate multiple variants as early as during front-end engineering of antenna systems.

Modern powerful microwave CAD system FEKO [36] can also be effectively used for calculation of mirror antennas. This is a multi-purpose system, which makes it possible to create, design and optimize various radiating structures. However, as demonstrated by experience, calculation time in these multi-purpose systems can be significant. Physical optics method is used in GRASP, Mirror and FEKO programs for calculation of mirror antennas.

Let us consider a specific example of calculation of a circular mirror antenna using this well-known program. Mirror software is designed for calculation of radiation characteristics of reflector antennas with single-element or multi-element feed systems (Fig. 4.131). Work with the program usually begins with selection of the problem parameters. Dialog window with parameters (Fig. 4.132) is called by the Reflector menu option.

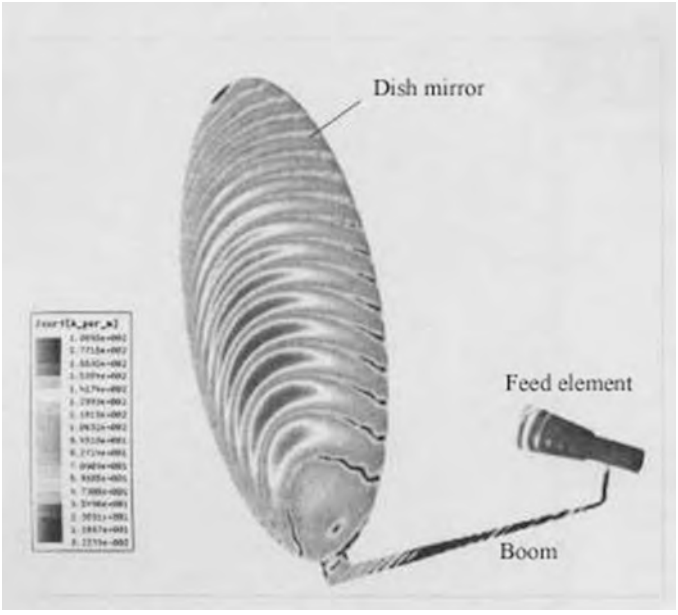

Fig. 4.131 Mirror dish antenna with calculated surface currents irradiated by horn

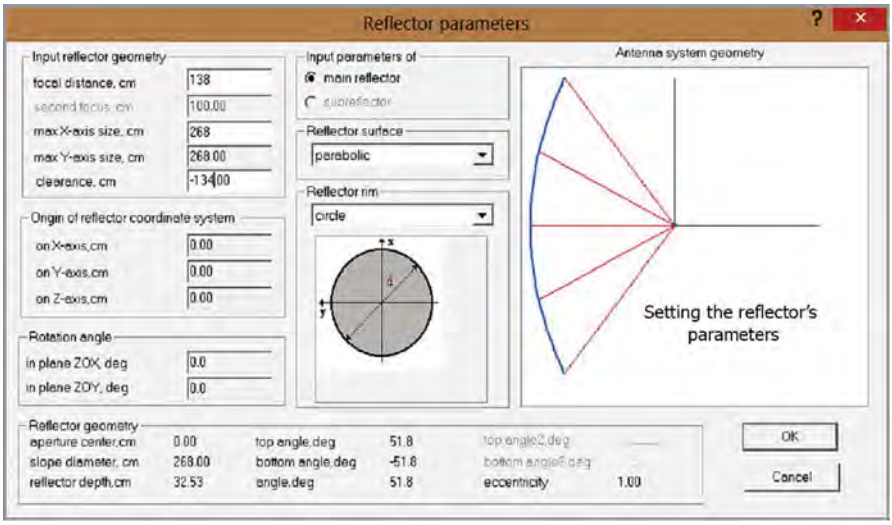

Fig. 4.132 Reflector geometry selection window in Mirror software

Mirror diameter of 268 cm and focus distance of 138 cm are selected in our case for analysis of the antenna similar to the one described in [39] in terms of dimensions. After that, the Array Feed System command is used to call the window (Fig. 4.133), in which the methods of exciting the mirror antenna are set.

As is known, Mirror allows to create up to 32 arbitrarily arranged and oriented objects of the Feed class (feed antennas). Each of these objects, similarly to elements of phased antenna arrays (PAA), can be set by one of the following means:

- tabulated directivity pattern (DP), e.g. obtained experimentally;
- directivity pattern approximated by analytical function;
- simple model of pyramidal horn;
- electrodynamical model of a smooth conical horn and a conical horn with a fracture;
- electrodynamical model of multi-sectional circular and rectangular waveguides, which makes it possible to obtain any geometry of horn radiator, including grooved horn radiator.

Functions of this class calculate the electrical current induced by the object to reflector surfaces and the object radiation field in near-field or far-field (for electrodynamical models) and display the results in the window (Fig. 4.134).

Calculated radiation pattern of the excitation element can be saved in a .dat file. This file can be subsequently used for calculation in other programs. Obtained feed element fields are used for calculation of currents on the mirror (Fig. 4.134).

After calculation of distribution of currents, beam pattern is calculated, which is built in the directivity pattern display window. For its cross-section, co-polarisation and cross polarisation elements are built.

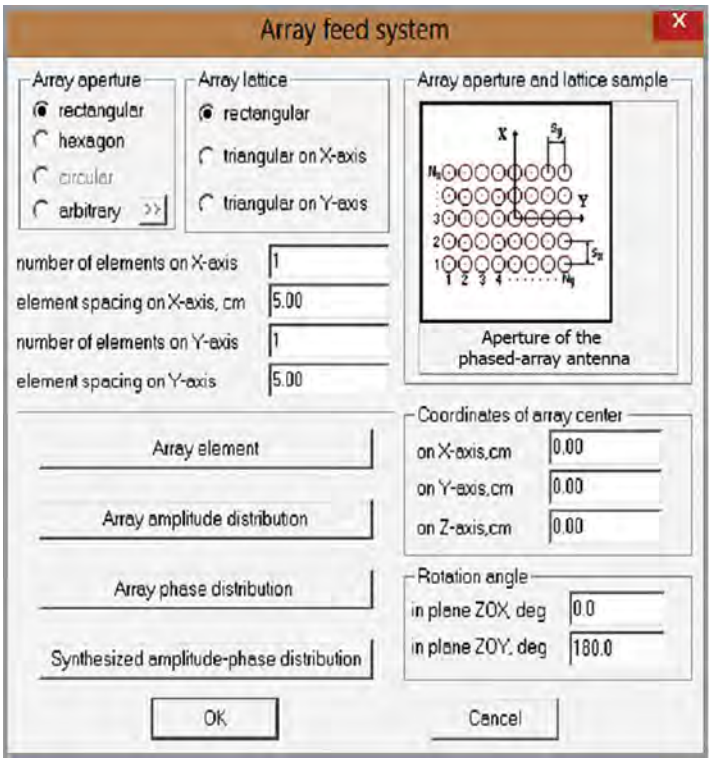

Fig. 4.133 Setting the characteristics of the antenna array irradiating the mirror antenna

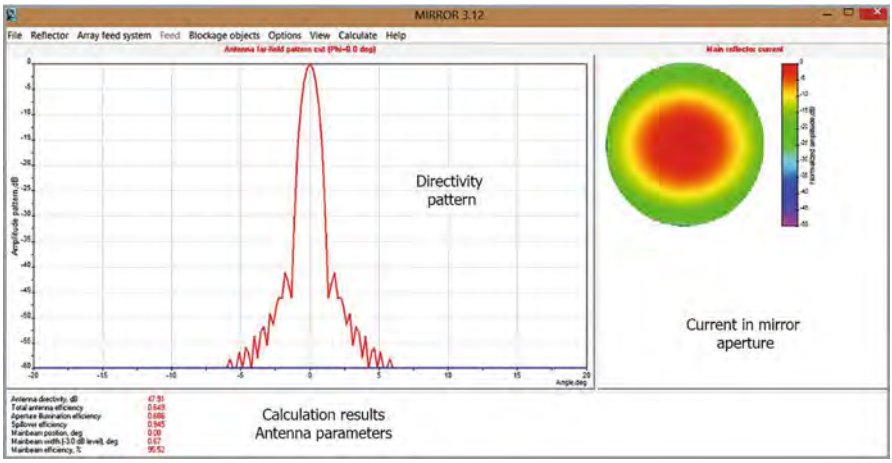

Fig. 4.134 DP section (left) and current in the mirror antenna aperture (right) calculated by Mirror

The window displays the beam pattern, current in the mirror section and mirror antenna parameters. Antenna directivity is equal to 47.9 dB for the given dimensions and parameters.

As the second alternative example, we are going to examine features of calculating offset mirror antenna using the Mirror program.

Classic mirror antenna with circular arrangement of the radiator has a single but significant disadvantage: its radiator and booms shade beams of direct passage, affecting the efficiency. Therefore, offset mirror system is often used in practice.

The analyzed offset mirror antenna [39] is illuminated from the bottom at an angle of about 50°. The angle between antenna section and the vertical plane is about 26°. Operating surface of the reflector is a cut from the rotation paraboloid described by the equation $z = (x^2 + y^2)/4F$, where $F = 138$ cm. Cut-out center is located 134.5 cm away from the focal axis.

The antenna has the following parameters according to the data sheet:

- dimensions 240 × 267 cm, aperture diameter 240 cm;
- frequency range – 10.97–12.75 GHz;
- beam width – 0.7 deg;
- gain factor of 47.6 dB (10 GHz);
- level of side lobes – not more than 25 dB.

Let us calculate an offset antenna irradiated by the open end of a round waveguide.

Mirror software takes into account the far-field effect. First, the radiating element is calculated together with its far field at each element of the mirror antenna array. Calculation result can be displayed as directivity pattern of the mirror antenna and as its cross-polarization component [37, 38] in the directivity pattern cut window (Pattern Cut, Fig. 4.135).

Calculation of the offset antenna helped find its directivity (48.35 dB), surface utilization factor (67.6%) and the beam width at the level of – 3 dB (0.72°).

Data calculated by Mirror corresponds to the values presented by antenna manufacturer [39]; the calculated directivity exceeds the design value by 0.75 dB.

Calculation in FEKO program is another example that is useful for system designers.

FEKO also allows to calculate a larger mirror antenna, such as a circular mirror antenna irradiated by a round waveguide, using the *classic method of physical optics* [31]. In this example, currents on the surface of the mirror antenna are calculated using the formula (4.37). Currents are calculated in the center of each element of decomposition of the mirror antenna (triangle), from which FEKO calculates the normal. Finite size of the triangle and replacement of the smooth surface of the paraboloid with cut planes are the sources of errors of numerical calculation by physical optics method.

Use the Draw -» Paraboloid command to draw a paraboloid with the diameter of 240 cm. Let us enter its focal length (138 cm) in the displayed window (Fig. 4.136).

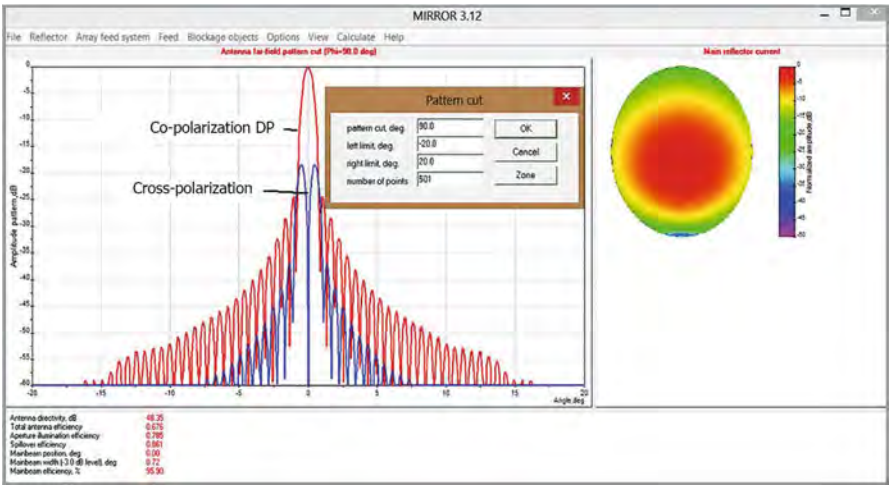

Fig. 4.135 Calculation of cross polarization. Calculated value – 20 dB

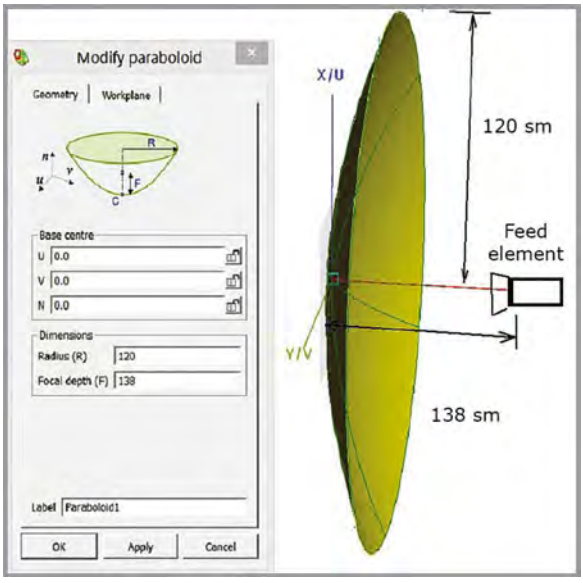

Fig. 4.136 An example of drawing a paraboloid with focal distance of 138 cm and diamter of 240 cm in the FEKO software

For drawing, the designer usually creates another working system of coordinates displaced by 138 cm relative to the global one. To reduce calculation time, open end of the round section is analyzed and near field in the raster cross-section is calculated during the first stage. The density of point in which the near field is calculated depends on the Increment value (Fig. 4.137). In order to save E and F calculated in these points of the field for further calculation, select saving of parameters of the field

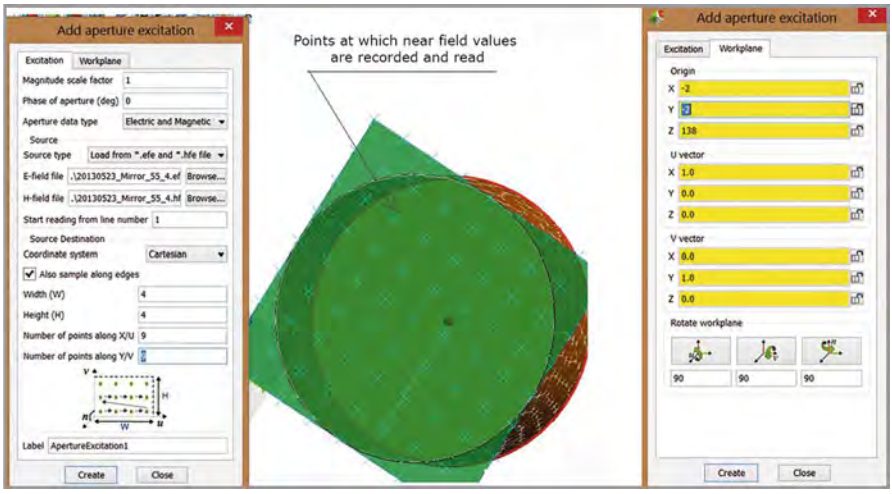

Fig. 4.137 Dialog windows of feed element aperture setting

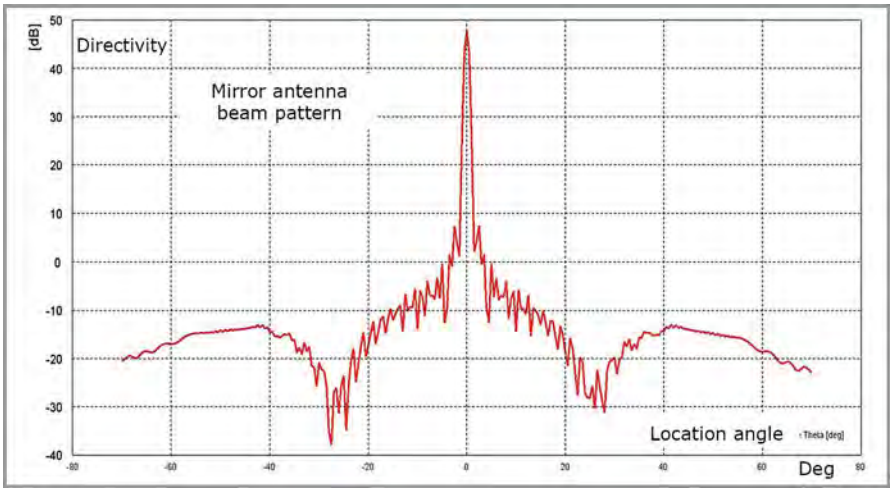

Fig. 4.138 Directivity pattern of a circular mirror antenna calculated in FEKO

in these points into files with .efe and .hfe extensions in the Advanced tab. Now, we will use these data to create flat aperture for mirror excitation; aperture points will be placed in the points where near field was calculated.

FEKO divides the metal mirror into triangles. Of course, it can take a lot of time. The beam along which the H wave creating currents on the mirror propagates is calculated from each aperture element (intersections in Fig. 4.137). Using integrated equations, FEKO calculates far-field characteristics. Calculated beam pattern is

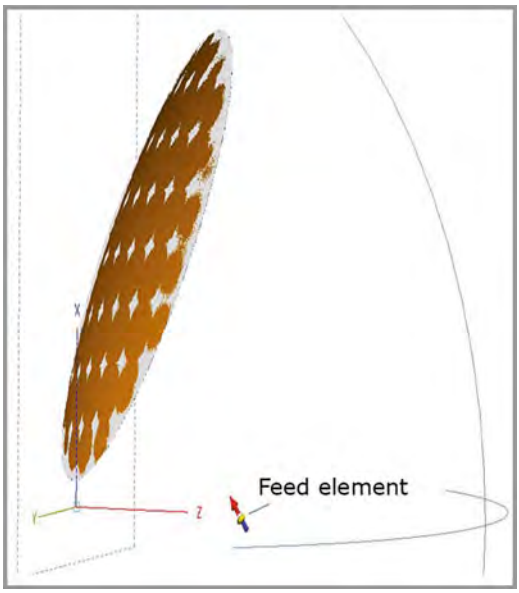

Fig. 4.139 Mirror antenna with displaced feed element

shown in Fig. 4.138. It is used to calculate directivity of the mirror antenna – 48 dB. Calculation results for the mirror antenna shown in Figs. 4.135 and 4.138 coincide with the calculations performed in Mirror.

As is known from the experience of use, when working on the same computer, calculations in Mirror were performed five times faster than in FEKO. However, FEKO is more flexible in solving such tasks; this program makes it possible to calculate structures with dielectrics and losses in metal and dielectric environments.

Finally, let us consider the features of calculating specific structure of the offset mirror antenna, the structure of which is shown in Fig. 4.139. Here, the radiator is in the focus of the paraboloid, and the mirror is cut from the paraboloid with the help of a 3D cylinder and becomes elliptical.

In order to divide the task being solved into two parts (calculation of feed element and building of the field incident on the mirror with these data), it is necessary to describe the sphere, on the surface of which the near-field value can be saved, in section of the round waveguide (feed element). In FEKO, just like in Mirror program described above, division of this task can also be performed for the far field.

Of course, the developer can also calculate this system in full, isolating the radiator and the mirror – here, the radiator is formed by a section of round waveguide (Fig. 4.137), for which the DP section is also calculated, and the width at the level of – 3 dB equal to 80° is calculated.

Standard results of calculation of beam pattern based on main polarization of such antenna are shown in Fig. 4.140.

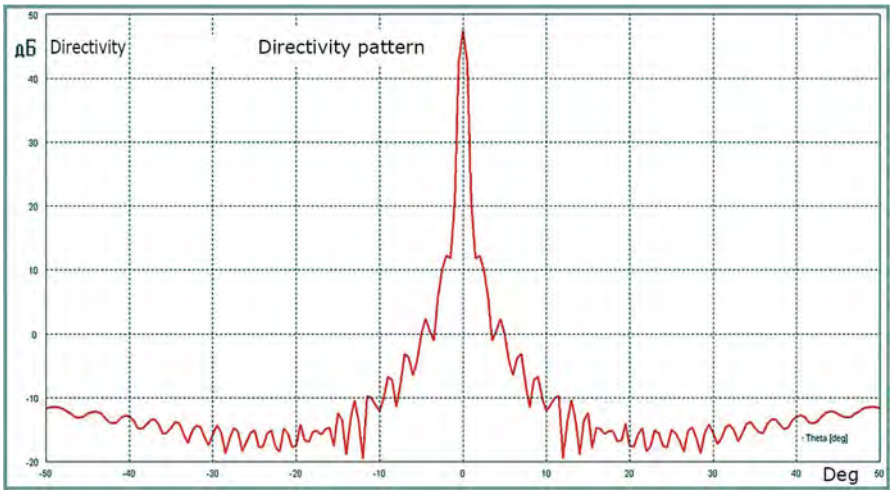

Fig. 4.140 Beam pattern of offset mirror antenna [37] calculated in FEKO

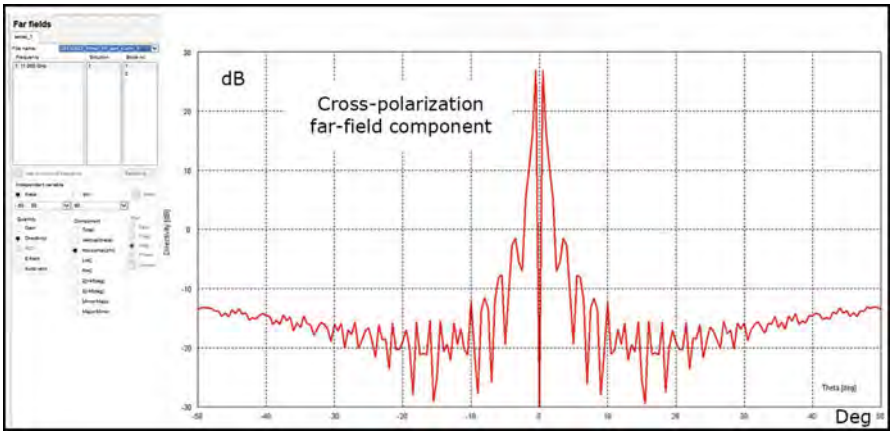

Fig. 4.141 Cross-polarization component of the directivity pattern of an offset mirror antenna (calculation in FEKO)

For antennas of communication systems with polarization multiplexing, it is always important to take ino account the so-called cross-polarization, since the parasite signal can affect the quality of reception. Typical requirement for the level of this cross-polarization in the maximum of the antenna directivity pattern is usually equal to – 30 dB (for systems with two linear orthogonal polarizations).

The value of cross-polarization in the maximum obtained by the calculation [26] is equal to 28 dB (Fig. 4.141), which is less than the signal in the maximum of the main polarization DP by 20 dB.

The coincidence of the results of calculation in Mirror and FEKO programs and the data presented by the antenna manufacturer was confirmed on the basis of the demonstration examples of calculation of circular and offset mirror antennas. All the programs described above are flexible modern tools for designing complex antenna systems, and their additional possibilities make it possible to calculate other complex tasks as well.

Let us consider certain important features of modeling a mirror antenna using HFSS ANSYS [40].

Therefore, analysis and calculation of radiation characteristics of mirror antennas of large electrical dimensions can be performed using approximate methods of geometrical optics and geometrical diffraction theory, as well as methods of physical optics and physical diffraction theory [41–43].

The method of physical optics, which is highly efficient and accurate and provides approximation of surface electrical current for perfectly conducting scatterers (reflectors), is the most popular. In the physical optics method, the key algorithm of numerical calculation is the above formula:

$$\bar{J} = 2\left[\overline{H}, \bar{n}\right], \tag{4.38}$$

where

$\bar{n}$ ισ τηε normal vector for each point of the reflector surface, $\overline{H}$ ισ τηε vector of the magnetic field created in this point by the primary emitter ([A/m]), J^{-3} ισ τηε surface electrical current on metal reflector. After that, known electrical current (4.38) is used to calculate the field of radiation of the mirror antenna (secondary field). Calculation of the secondary field consists in calculating corresponding two-dimensional Fourier integrals from the surface electric current.

Algorithm of implementation of the physical optics method in HFSS [43] consists in that vector of the magnetic field is found from each elementary current in the direction of each elementary area of the metal mirror; the product of this vector by area normal determines the current according to the formula (4.38). Therefore, physical optics method does not require solving a complex system of linear algebraic equations of high order, which is necessary in most known electrodynamical methods of solving a system of Maxwell equations.

The use of the method of physical diffraction theory [41–43] makes it possible to take into account even subtler (as compared to physical optics method) effects of diffraction of the primary radiator field at the edge of the mirror. As a rule, it helps specify the level of far side lobes of the antenna radiation field. However, it is well known that numerical implementation of the physical diffraction theory method is more complex and not universal, and the use of this method from the practical point of view is not necessary for analysis of large antennas.

It should be noted that during analysis of mirror antennas the method of geometrical optics [41–43] is less accurate than the physical optics method, since it does not take into account polarization effects – in particular, during analysis of mirror

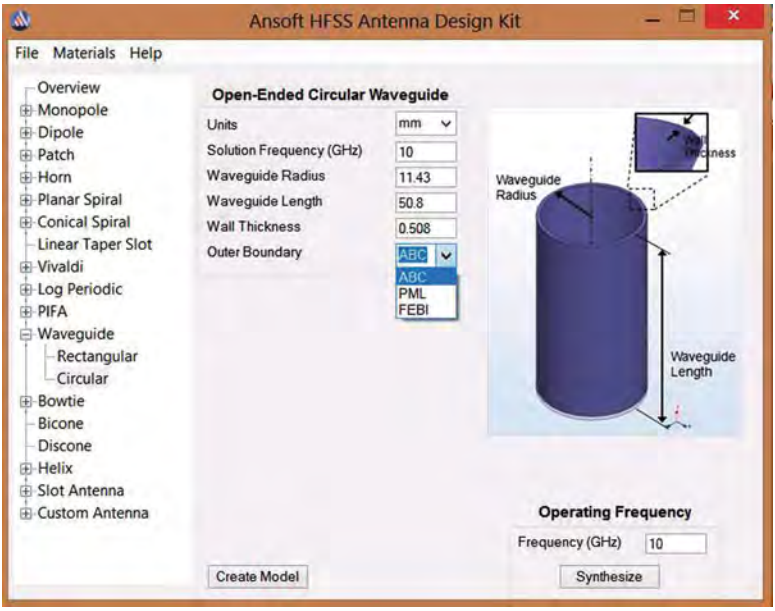

Fig. 4.142 ADK HFSS interface

antennas with aperture method. The method of geometrical diffraction theory is approximately equivalent to the method of physical optics in terms of accuracy.

Below we are going to consider two main modeling options: circular mirror and offset mirror antennas.

4.2.11.1 Modeling of a Circular Mirror Antenna

For illustration purposes, we will provide the solution to the problem of irradiation of dish mirrors of different sizes and compare the results of calculation by two methods: integral equations (IE) and physical optics (PO). Both methods are implemented in the HFSS ANSYS software. Calculations are performed at one frequency of 10 GHz. A section of round waveguide is used as the radiator. Radiating antennas can be designed in the ADK HFSS program (Fig. 4.142).

The port is installed on one of the sections of the waveguide serving as the radiator; the other section becomes a radiating raster. The profile of the mirror antenna corresponds to the formula:

$$Z = \frac{1}{4F}\left(x^2 + y^2\right), \tag{4.39}$$

where

x, y and Z αρε coordinates of each point of the mirror, F ισ τηε focus of a parabolic mirror in which the radiator is placed (Fig. 4.143).

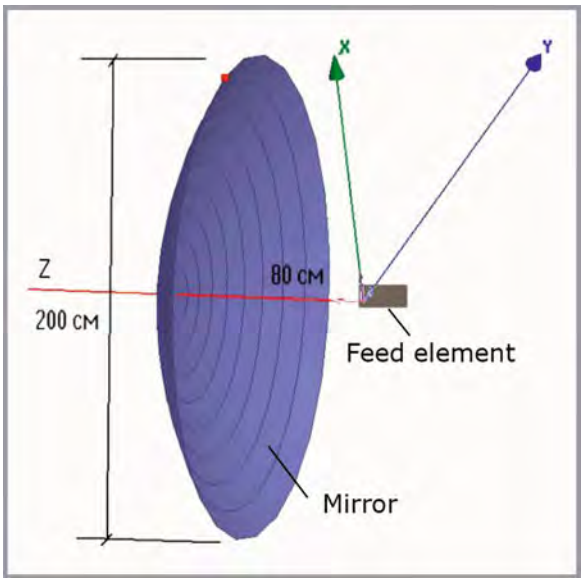

Fig. 4.143 Mirror antenna with diameter of 200 cm

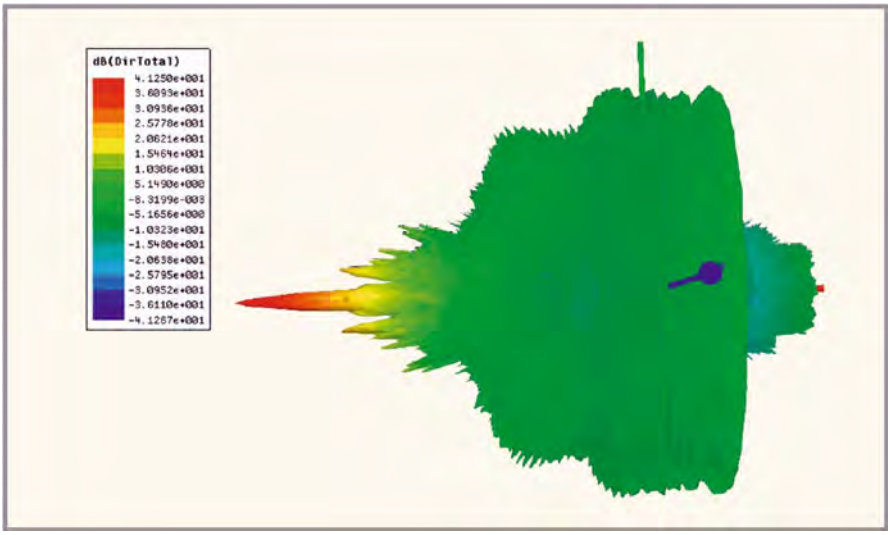

Fig. 4.144 3D directivity pattern of a circular mirror dish antenna irradiated by circular waveguide

Results of calculation of a circular antenna with the diameter of 2 mm are shown in Figs. 4.144 and 4.145. Figure 4.145 shows sections of the directivity pattern performed by solving integral equations and by physical optics method on the same reference grid.

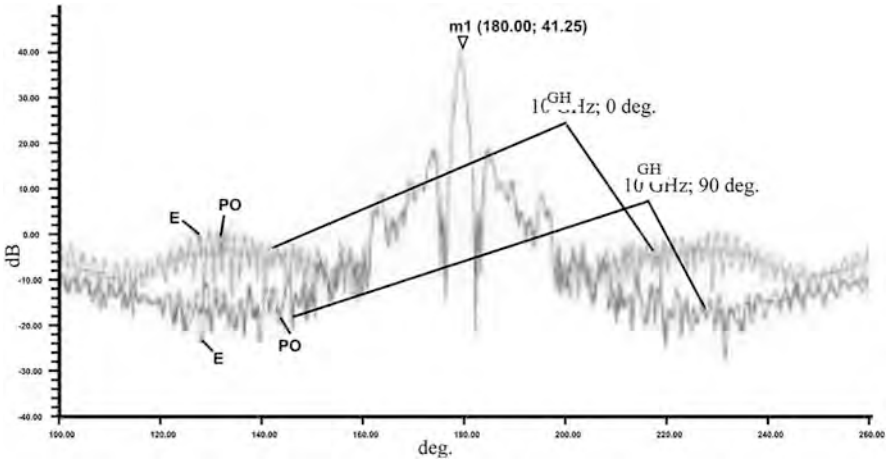

Fig. 4.145 Cross-section of the DP of a mirror circular antenna with diameter of 200 cm irradiated by the waveguide section in two perpendicular planes (Phi = 0 and Phi = 90)

As can be seen from the figure, methods of physical optics (PO) and integral equations (OE) for antennas with large diameters differ only in the levels of side lobes. These calculations coincide in the region of the main lobe. In order to confirm this fact, which was first noted in the work of E.N. Vasilyev [41], a number of calculations has been performed for mirrors with diameters of 0.5–40λ (Table 4.9).

It should be noted that in case of large antenna sizes the developer has to face difficulties related to gridding and calculation duration. Of course, this can be avoided by abandoning selection of the grid size based on frequency, exclusion of adaptation (grid compaction process), as well as import of the grid from the project previously solved, the grid of which has been obtained in another example.

For practical applications, it is possible to use the results of calculation of several dimensions of a circular mirror antenna (with focus to diameter ratio F/D = 0.4), which are summarized in Table 4.9.

These calculations were performed on a personal computer with 4-core processor with clock frequency of 2 GHz and 16 Gb RAM. The table shows that the time of calculation using the physical optics method is 50 times smaller than when using the method of integral equations. Analysis of possible errors in calculation (different values of directivity and the level of side lobes) demonstrates that they are caused by geometric building errors in the PO method and errors in building the system of equations in the IE method.

Of course, the physical optics method provides high accuracy for metal models; however, starting from certain dimensions of radiating structure, when the problem cannot be solved by the method of moments due to the impossibility to solve the system of equations, the method of physical optics shall be used.

Table 4.9 Results of calculation of offset mirror antennas with different sizes

Calculation No.	D, cm	F, cm	Directivity, dB	Level of side lobes, dB	Calculation time	
					IE, s	PO, s
0	1.5	0.6	2.5 (P0)	-4 (P0)	20	1
			2.5 (IE)	−6 (IE)		
1	3	1.2	9.2 (P0)	−8 (P0)	20 (1000 tr.)	1
			9.4 (IE)	−11 (IE)		
2	6	2.4	14.5 (P0)	−26.7 (P0)	24 (1500 tr.)	1
			14.6 (IE)	−32.2 (IE)		
3	15	6	20.9 (P0)	−32 (P0)	500 (22 thous. tr.)	1
			22.3 (IE)	−35 (IE)		
4	30	12	28.2 (P0)	−34.2 (P0)	2100 (80 thous. tr.)	7
			29 (IE)	−39.2 (IE)		
5	45	18	30.5 (P0)	−25 (P0)	3300 (100 thous. tr.)	–
			31.6 (IE)	−30 (IE)		
6	90	36	36.94 (P0)	−37.5 (P0)	3020 (30 thous. tr.)	10
			37 (IE)	−42.5 (IE)		
7	200	80	41.25 (PO)	−39 (P0)	3300 (50 thous. tr.)	90
			41.29 (IE)	42 (IE)		

4.2.11.2 Offset Antenna Modeling

The disadvantage of a mirror antenna with circular position of the radiator is that the radiator and booms shade the beams of direct passage and thus deteriorate the efficiency. Therefore, offset mirror system is often used in practice (Fig. 4.146).

The analyzed offset mirror antenna [44] is illuminated from the bottom at an angle of about 50°. Antenna section is also rotated relative to vertical plane approximately by 26°.

Operating surface of the reflector is a cut from the rotation paraboloid described by the equation $Z = (x^2 + y^2)/4F$, where $F = 138$ cm. Cut-out center is located 134.5 cm away from the focal axis.

The antenna has the following parameters [44]:

- dimensions – 240 × 267 cm (aperture Ø240 cm);
- frequency range – 10.95–12.75 GHz;
- beam width – 0.7 deg;
- gain factor – 47.6 dB (11 GHz);
- level of side lobes – not more than 25 dB.

An offset antenna irradiated by the open end of a round waveguide shall be calculated. Calculation is performed by the methods implemented in HFSS-15 [43] (Table 4.10).

Mirror of the offset antenna has parabolic shape regardless of its diameter. Area of the mirror can be selected by changing diameter of the cut-out cylinder. In this case,

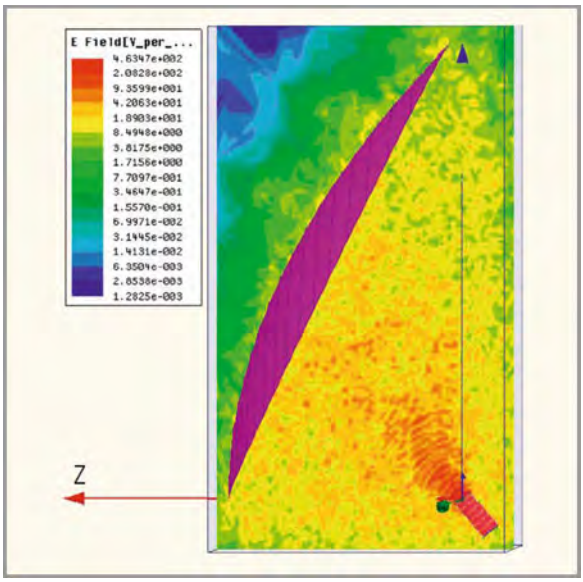

Fig. 4.146 Near field radiating parabolic mirror of the offset antenna

Table 4.10 Solving methods and means of building these methods

Section	Method	Description
1	FEM	Finite element method. Both parts of the antenna (mirror and radiator) are placed in a box with radiate boundary conditions
2	IE method	Method of integral equations. The model only contains the mirror; calculation volume is not set. A wave is incident on the mirror that is equivalent to the far field of the radiator
3	FBIE method	Each part of the structure is covered by a separate box, inside which the space is counted by FEM method; for these boxes, IE boundary conditions are set
4	IE-P0 method	Method of physical optics combined with the method of integral equations

focus of the parabolic mirror remains in the same place. Directivity of the mirror antenna can be estimated using the formula:

$$КНД = \frac{4\pi S}{\lambda^2} КИП, \tag{4.40}$$

where S ισ τηε mirror area, λ ισ τηε wavelength (for the frequency of 11 GHz, $\lambda = 2.7$ cm), E ισ τηε aperture efficiency [42].

Assuming that the mirror area in an offset antenna is approximately equal to

$$S = \pi D^2/4 \text{ [3]}, \text{we obtain directivity equal to 38.9 dB.} \tag{4.41a}$$

Finite Element Method (FEM, Table 4.10) requires the use of supercomputer to solve the electrodynamical problem; therefore, this method is not used for antenna dimensions exceeding 5λ.

Method of integral equations IE (Table 4.10) implemented in HFSS ANSYS IEDesign 1 demonstrated significant mistakes (up to 200%) when calculating far-field characteristics.

At the same time, it demonstrates significantly greater calculation speed than FEM. However, high error values prove that this method is effective only when used together with the method of physical optics (PO).

In the FEBI method (Table 4.10), the task is solved in the HFSS HFSSDesignl (DrivenModal) project; the horn antenna is counted by FEM method and covered by the box of radiation with IE condition set. Parabolic mirror is covered by the volume of radiation also restricted by the IE condition. This hybrid method combines positive sides of both FEM and IE methods. The analyzed volume, which is divided into tetrahedrons, is reduced significantly (up to 10 times), and the precision of far-field calculation corresponds to the FEM method.

Finally, let us not a number of parameters of analysis of an offset mirror antenna using physical optics method that are important for developers.

For example, the hybrid method IE-PO (Table 4.10) implemented in HFSS makes it possible to replace the feed element (Fig. 4.146) with the saved solution obtained in another project in advance. Therefore, interconnected tasks can be solved in sequence. When the data on far field of the feed element have been obtained, solution for the mirror is calculated, while the solution obtained earlier serves as the feed element. The volume of the task in this case is reduced, which helps solve a more difficult problem on PC. In this case, shading caused by the radiator is ignored.

This method is implemented in the same structure with one nuance: PO option is set in the Solve section [43]. In this mode, a path is traced from the phase center to the center of each triangle of the mirror, the angle between the exciting segment and the triangle plane is found, and these data are used to calculate the current on the surface of the irradiated mirror antenna.

For large mirror systems, it can be considered that the optimal option is the system with maximum directivity.

Directivity of the modeled offset mirror antenna can also be increased by changing position of the feed element within narrow limits. Another method is optimization of the mirror surface division. Division can be optimized in such way that large groups of triangles will have normals pointed towards the emitter of the mirror antenna. Calculation of the beam pattern and directivity (Figs. 4.147 and 4.148) was performed for the frequency of 11 GHz.

As demonstrated by Fig. 4.148, the level of side lobes during calculation with the help of physical optics method (20 dB) is worse than the design data (25 dB). Taking into account analysis of the data presented in Table 4.9, it can be demonstrated that the level of side lobes in the PO method shows an increase in the level of side lobes to 5 dB.

The time of calculation of the directivity pattern shown in Fig. 4.148 for the given conditions amounted to 8–10 min.

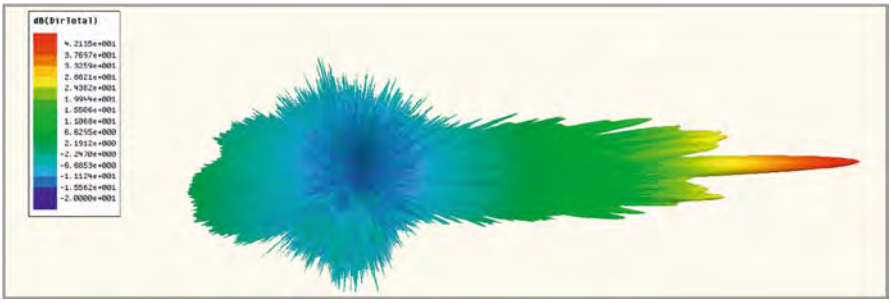

Fig. 4.147 3D directivity pattern calculated by PO method

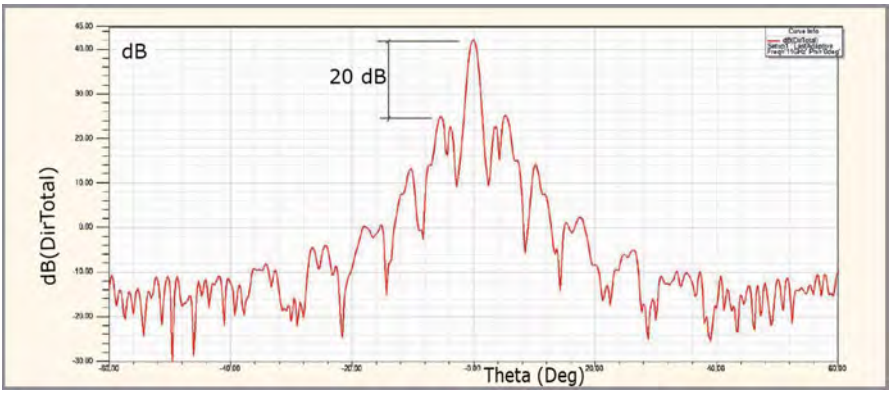

Fig. 4.148 Directivity pattern section, solution by PO method

Therefore, the presented specific examples taken from practical experience of developers [40] demonstrate that the calculation of offset mirror antennas allowed the author to achieve correspondence of the results of calculation in the HFSS program and the data provided by the manufacturer of the antenna. HFSS ANSYS as a flexible modern tool used to design complex antenna systems has various options, which make it possible to calculate tasks involving large geometrical dimensions. This paragraph demonstrates how one big task is divided into several smaller ones. The most universal hybrid method EI-PO makes it possible to calculate parts with the size commensurate with the wavelength by finite element method or by method of integral equations, while large parts can be calculated by physical optics method.

The performed comparison of the results of calculation by method of integral equations demonstrated that the physical optics method provides approximately the same accuracy as the method of integral equations, but with the counting time increased significantly.

4.2.12 *Wideband Log-Spiral Antenna with Circular Polarization*

As is known, one of relevant directions of development of information and communication technologies is the creation of hardware-software complexes (HSC), navigation modules and navigation equipment operating on the basis of global navigation satellite systems (GNSS). An important task here consists in increasing efficiency of navigation provision means and reliability of results of evaluation of these characteristics [45].

In particular, an important unit of such an HSC determining its basic navigation abilities is a wideband antenna radiating and receiving GNSS signals in the gigahertz frequency range. For these wideband antennas for HSCs, system developers often use log-spiral antennas operating within the frequency range between hundreds of megahertz and dozens of gigahertz (Fig. 4.149). The log-spiral antenna consists of a double helix and a matching transformer and is in fact designed as two metal strips wrapped around and attached to dielectric cone ($e = 1...3$). Width of the vibrators increases exponentially in the direction of the cone base. Such shape of flat helical vibrators ensures wide band, as well as wide angle of one-directional radiation with circular polarization in the direction of the cone top.

The first log-periodic antenna with permanent aperture angle in the form of planar spiral wrapped around dielectric cone was created by American scientist D. Dyson in 1958 [46]. The feature of this log-spiral antenna is that the width of each of its arms increases logarithmically starting from the feed point, and the directivity pattern (DP) depends on the value of the angle at the cone top and the winding angle.

The article [45] contains detailed examination of the problems of designing such wideband antenna radiating and receiving signals of global navigation satellite systems; the developers used a helical log-periodic antenna as a wideband antenna. Calculation, modeling and study of the antenna were performed in the electrodynamic modeling software HFSS.

Three models of such antennas (3101, 3102 and 3103) are produced in lots by Electro-Mechanics Company (EMCO) [47], member of ETS-Lindgren corporation;

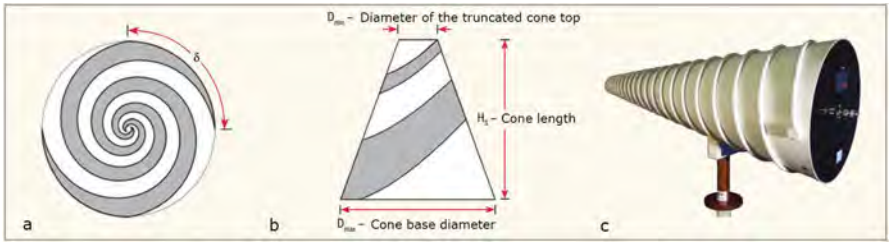

Fig. 4.149 Log-spiral antenna: (**a**) top view; (**b**) coil winding angle; (**c**) side view (model EMC0-3101)

Table 4.11 Characteristics of log-spiral antennas

Characteristic	Model		
	1301	1302	1303
Polarization	Circular left/circular right		
DP	One-directional		
Directivity (dBi)	10; 5-min.; 15- max.	–	–
Bandwidth	Multi-octave, depends on geometry of arms		
Complexity	High		
Input impedance, Ohm	150; 100 – min.; 280 – max.		
Operating frequency range, GHz	0.2...1	1...10	0.1...1
Input power, W, max	100 (150-peak)	50 (100-peak)	100 (150-peak)
VSWR	2.4:1	1.6:1	1.9:1
Impedance, Ohm	50		
Connector type	N		
Length (Ns), mm	813	381	1020
Diameter (D), mm	330	127	660
Weight, kg	4.5	3.6	10.0
Operating temperature range, ° C	−50... + 50		

therefore, designations like EMCO-3101 and ETS-Lindgren-3101 can simultaneously be found in articles and various antenna catalogs, even though they are used to refer to the same model. Figure 4.149c shows the log-spiral antenna 3101. Operating frequency range of this antenna is 0.2...1 GHz. Other antennas have the same structure but are designed for operation in other frequency ranges; therefore, their only significant difference from the 3101 model is their size. Operating frequency ranges and other characteristics of log-spiral antennas are presented in Table 4.11.

Let us briefly consider the main results of modeling of this log-spiral antenna in the HFSS ANSYS system [48] for the frequency range of 1...20 GHz.

One of the main distinguishing features is the method of power supply to the log-spiral antenna.

There are several methods of feeding a wideband log-spiral antenna; however, conical log-spiral antennas are most frequently powered with the help of a coaxial line or a coaxial cable applied to spiral surfaces. A two-wire line can also be used for this.

The developers usually use a wideband converter designed as a wedged coaxial line (Fig. 4.150) with smoothly changing characteristic impedance [49]. This is achieved by the fact that the structure of lines in different sections changes smoothly – from round coaxial line (A-A section) it transforms into two-wire line with small dielectric intermediate layer (section B-B). Coaxial cable of the UT-141-SA type (Fig. 4.151) is used here for transition from non-symmetrical line to symmetrical line. Diameter of its inner strand is 0.91 mm, diameter of outer braid – 2.98 mm. Coaxial line is filled with material with e = 2.2. The transition is a radiating line. At one side, an asymmetrical waveguide port is created, at the other side – a symmetrical discrete port.

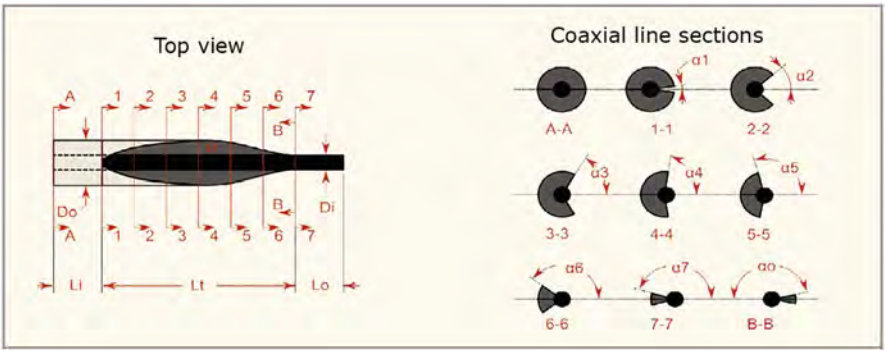

Fig. 4.150 Cross-sections of a wedged coaxial line

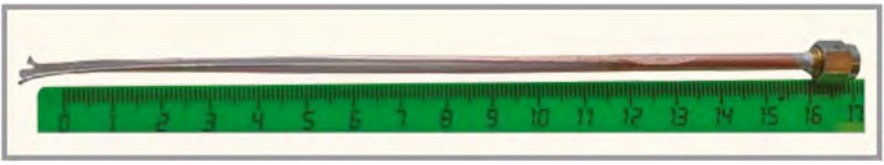

Fig. 4.151 Transition of coaxial line into two-wire line

Software complex HFSS ANSYS [50] is a powerful system for designing and 3D modeling of HF and SHF devices and electromagnetic fields. So-called S-parameters are used for analysis of behavior of electrical circuits during transmission of SHF signals. They are determined as input reflection coefficients (S11 and S22) and coefficients of transmission from the second input to the first one (S12) and vice versa (S21) during connection of matched loads to all other inputs.

Such created transition usually has the length of 160 mm (Fig. 4.151). In order to ensure travelling-wave mode in the line, it is recommended to set resistance at the output of two-wire line equal to 100 Ω (Fig. 4.152), which is the input resistance of a typical log-spiral antenna.

Therefore, calculation and measured characteristics of the antenna (Fig. 4.153) demonstrate that the transmission line performs matching functions from the levels of signals of the standard unbalanced line (coaxial input) to the levels of balanced load (resistance of 100 Ω) within the band of 1. . .20 GHz with the voltage standing-wave ratio (VSWR, ratio of the maximum voltage in the microwave path to the minimum voltage) < 3.

The considered conical log-spiral antenna is the slowing structure for the surface wave passing from the feed point to the top of the cone. However, in the space of the wide section of the cone it becomes an accelerating structure, due to which radiation direction and beam pattern change towards the top of the cone. Cone log-spiral antenna radiates in this direction with circular polarization.

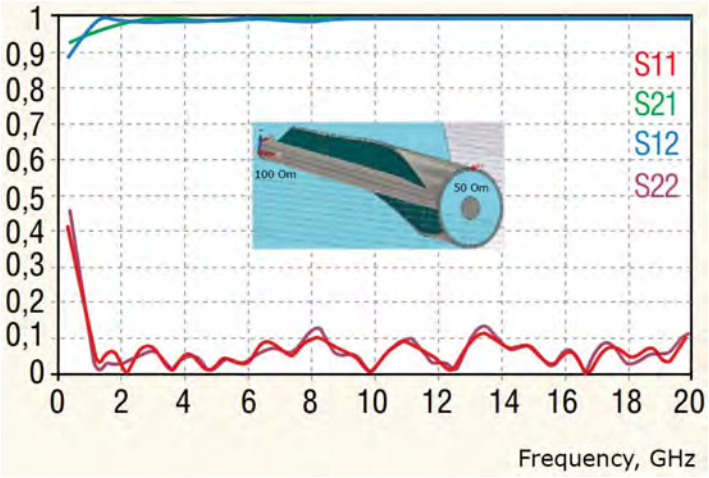

Fig. 4.152 Frequency characteristic of transmission line for the frequency range of 0. . .20 GHz

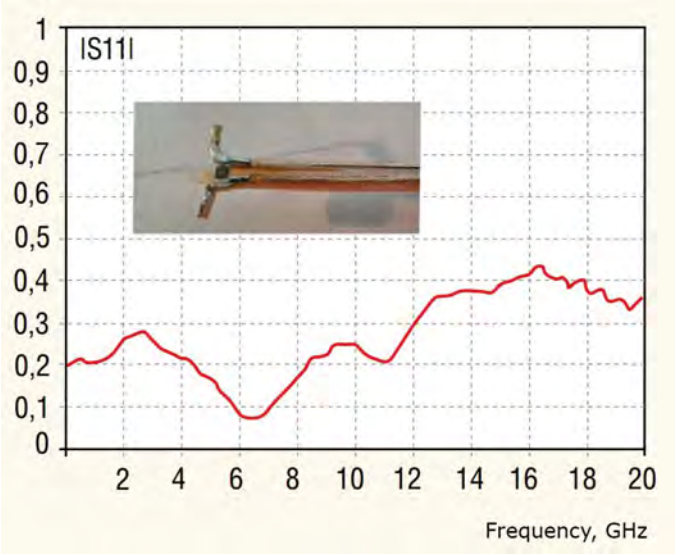

Fig. 4.153 Frequency characteristic of the balancing transformer S11 in the form of wedged coaxial line for the frequency range of 1. . .20 GHz

The model of a log-spiral antenna is shown in Fig. 4.154. Diameter of the cone base is 43 mm, and its length is 145 mm. Feed point of the log-spiral antenna is at the top of the cone. In this point, symmetrical input of the wideband junction shown in Fig. 4.151 is soldered to outputs of the log-spiral antenna.

Fig. 4.154 Model of a log-spiral antenna

Pass band width of such conical log-spiral antenna is determined by the ratio of the base diameter Dmax (about a half of the wavelength at lowest frequency) to the diameter of the truncated top Dmin (about a quarter of the wavelength at highest frequency). According to Babinet's principle, input resistance of 188 Ω is predicted for a planar log-spiral antenna. Connection between spirals on the cone reduces this value to 150 Ω and less.

Frequency characteristics of any log-spiral antenna depend on the geometry of the cone and the winding angle of the spiral. The lowest operational frequency of a log-periodic antenna is connected to the maximum diameter of the cone base Dmax, while the maximum frequency is connected to the minimum diameter of the truncated cone Dmin, on which the log-spiral antenna is formed. Polarization can be changed by coiling direction. Log-spiral antenna gain increases with an increase in the spiral angle; width of the beam is reduced together with the spiral angle (Fig. 4.149).

Input impedance of the antenna is increased with a reduction of the angle between antenna arms. Experimental frequency characteristics of SWR of the tested antenna measured with the help of Agilent network analyzer is shown in Fig. 4.155.

In order to understand the features of using the recommended software complex, we are going to consider the procedure of calculating a log-spiral antenna by IE method, which does not require coverage of the antenna with absorption box using the electrodynamic modeling software HFSS. The time of calculation of such antenna, the size of which can be considered to be more than 10 wavelengths at the highest frequency (20 GHz) usually amounts to 2 min in one frequency point (2 GHz 2 Gb computer). HFSS program calculates impedance frequency characteristics and radiation characteristics of radiation at each frequency point. Recalculation of the S11 reflection coefficient and SWR is performed according to the formula: $S11 = (SWR - 1)/(SWR + 1)$. Results of measurement and calculation of the |S11| parameter are shown in Fig. 4.156.

Let us consider certain features of calculating far-field characteristics of a log-spiral antenna.

For example, the HFSS ANSYS complex provided possibilities for solving multiphysical tasks. Here, it is also possible to solve one problem by different methods (for example, by FEM and IE methods). To calculate far-field characteristics of the log-spiral antenna we will use the method of integral equations, since it requires less computer resources.

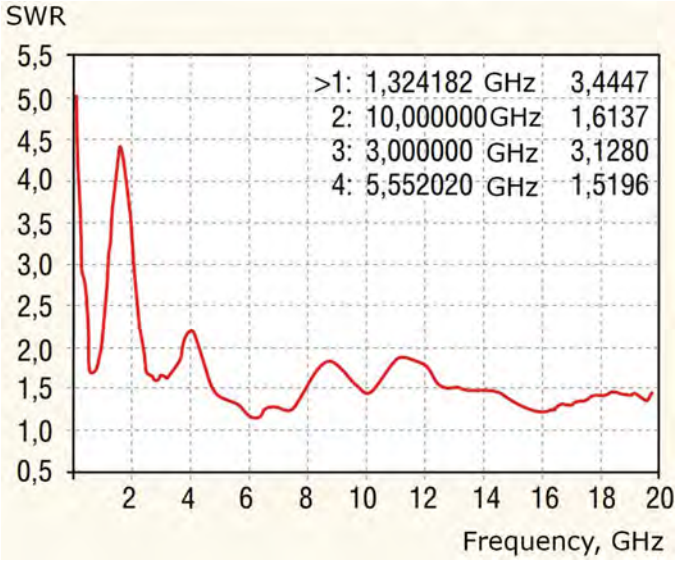

Fig. 4.155 Measured frequency characteristic of a log-spiral antenna SWR within the frequency range of 1. . .20 GHz

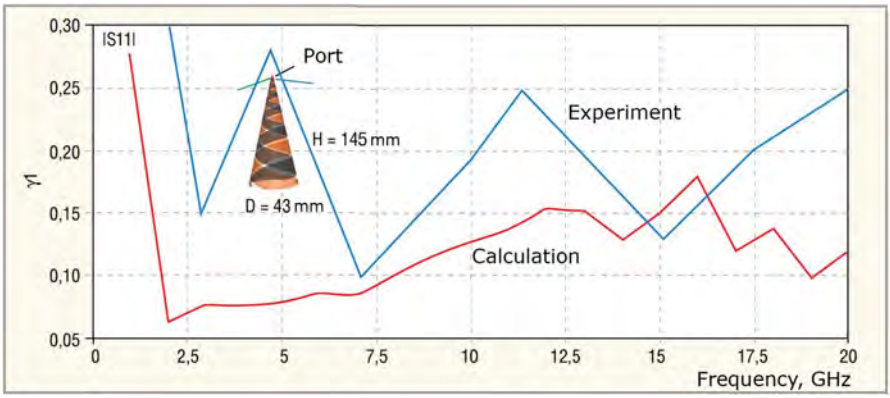

Fig. 4.156 Frequency characteristic IS11 of the log-spiral antenna

Frequency properties of a wideband antenna are estimated mostly by its matching in a wide range of frequency ranges and stability of its far-field characteristics (gain, axial ratio, phase center, etc.). Far-field frequency characteristics calculated at each frequency point are shown in Fig. 4.157 (axial ratio, AR) and Fig. 4.158 (directivity).

Figure 4.157 shows that in the frequency range of 1. . .14 GHz the axial ratio describing circular polarization of the log-spiral antenna is <3. This is a good result. Frequency dependencies of directivity in the direction of the radiation axis are

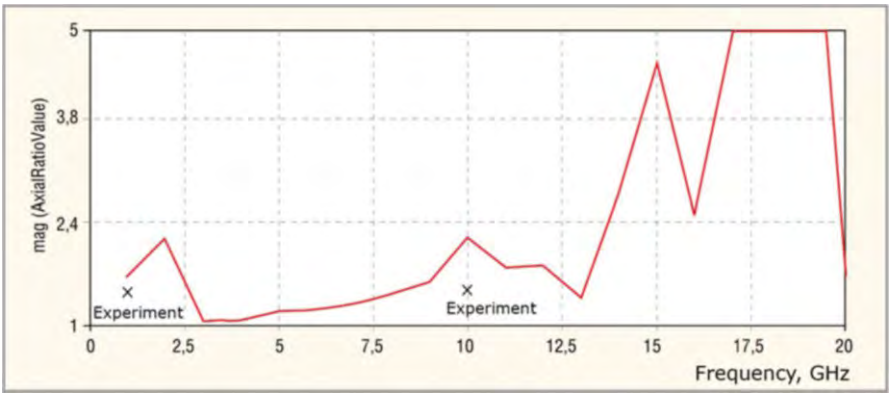

Fig. 4.157 Axial ratio of a log-spiral antenna within the frequency range of 1...20 GHz

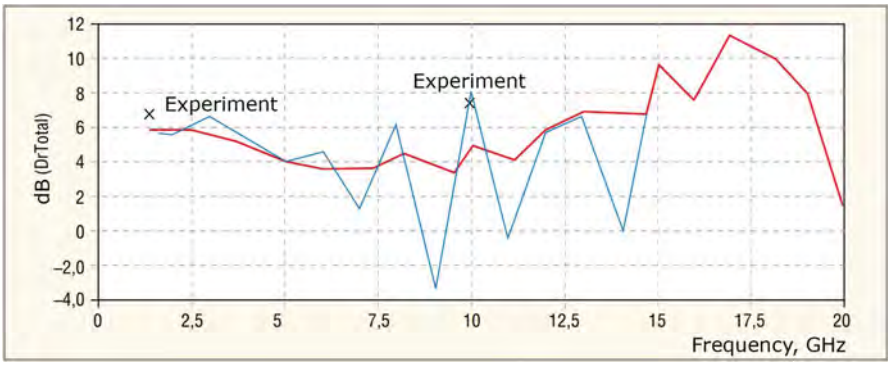

Fig. 4.158 Log-spiral antenna gain in the direction of the main beam pattern maximum within the frequency range of 1...20 GHz

shown in Fig. 4.157, in 3D presentation for frequencies of 1–10 GHz – in Fig. 4.159, which shows that radiation in the direction of axis Z changes insignificantly, but the shape of the 3D DP suffers significant deformation. The study of far-field characteristics of the log-spiral antenna is performed in an echo-free chamber. Crosses in the figures mark the results of parameter measurements in specific points of the frequency range.

Characteristics of log-spiral antennas make it possible to use them in navigation tasks. The log-spiral antenna has circular polarization within a wide range of radiation angles and operating frequencies. Modeling of such complex wideband antenna, the dimensions of which exceed wavelengths of the operating (centimeter) range, performed with the help of the software complex HFSS ANSYS, demonstrated qualitative and quantitative coincidence of design and measurement antenna characteristics.

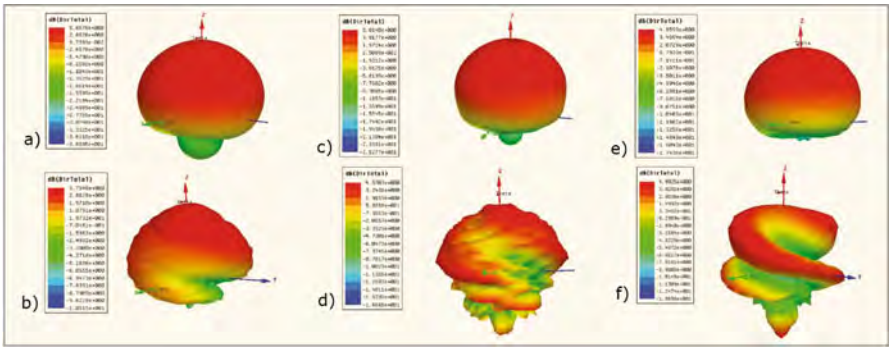

Fig. 4.159 Change in the shape of 3D beam pattern of log-spiral antenna within the frequency range of 1…10 GHz: (**a**) 1 GHz; (**b**) 2 GHz; (**c**) 4 GHz; (**d**) 6 GHz; (**e**) 8 GHz; (**f**) 10 GHz

4.3 Phased Antenna Arrays

4.3.1 Classification, Structure and Features of Application of Phased Antenna Arrays

The main technical element of the ground echelon of missile warning systems as well as other ground-based and space-based system is the antenna array – the type of antennas structurally designed as a group of antenna radiators, in which relative signal phases are measured in an integrated fashion so that the effective antenna radiation is amplified in a certain desired direction and suppressed in all other directions.

Phase control (phasing) allows a radar with a PAA to:

- form (with extremely varied arrangements of radiators) the required directivity pattern (DP) of the antenna (e.g. high-directional, beam-shaped DP);
- change the beam direction of a fixed antenna, thus performing quick (in most cases, almost inertia-free) scanning – beam swinging;
- control the shape of the directivity pattern within certain limits – change the beam width, intensity (levels) of side lobes, etc. (for this purpose, control of wave amplitudes of separate radiators is sometimes also implemented in PAA).

These (and some other) properties of PAAs, as well as the possibility of using modern automatics and computing electronics for PAA control, defined the prospects and wide use of these arrays in radio communication, location, navigation, astronomy, etc. PAAs with large numbers of controlled elements are included in various ground-based (stationary and mobile), ship-based, aerial and space radio devices.

The use of such antenna arrays provides the following advantage.

An array of N elements helps increase the directivity (and, accordingly, gain) of the antenna as compared to a single radiator and narrow the beam to increase accuracy of determination of the angular coordinates of the radiation source in navigation and radar location.

The array helps increase electrical strength of the antenna and the level of emitted (received) power by placing independent amplifiers of high-frequency energy in the channels of the array.

An important advantage of the array is the possibility of quick (inertia-free) observation of space due to beam swinging by electrical methods (electronic scanning).

There is a number of structural and technological advantages in comparison with other antenna classes. For example, weight and dimensional characteristics of onboard equipment are improved due to the use of printed antenna arrays. Reduction of cost of large radio astronomy telescopes is achieved by using mirror antenna arrays.

Until the end of the 1980s, creation of such system required the use of a large number of devices, due to which phased arrays fully controlled by electronics were mostly used in large stationary radars, such as massive BMEWS (Ballistic Missile Warning Radar) and slightly smaller American marine-based air defense radar SCANFAR (modification of AN/SPG-59) installed on American heavy nuclear powered guided missile cruiser "Long Beach" and nuclear aircraft carrier "Enterprise". Its "descendant" SPY-1 Aegis was installed on Ticonderoga cruisers and later on Arleigh Burke torpedo boat destroyers. The only known aircraft applications were the large-sized "Zaslon" radar installed on the Soviet interceptor MiG-31 and the B-1B Lancer attack radar [51]. Today, it is used in Su-35 and F-22.

Such radar were not installed on plains mainly due to their heavy weight, since the first generation of the phased array technology used simple radar architecture. While antenna was changed, everything else remained the same, but additional computers were added in order to control phase shifters of the antenna. This lead to an increase in the quantity of computing modules and the load on the power supply system.

The following classification of antenna arrays is considered generally accepted; (a) linear; (b) arc; (c) ring; (d) flat; (e) cylindrical; (f) conical; (g) spherical; (h) non-equidistant.

In terms of excitation type, the following AA types are distinguished:

- with serial feed;
- with parallel feed;
- with combined (serial-parallel) feed;
- with spatial (optical, aerial) excitation method.

Active Electronically Scanned Array (Fig. 4.160) is a type of phased antenna array (PAA), in which each element of the array or a group of elements have their own miniature microwave transmitter instead of using one large transmitter tube

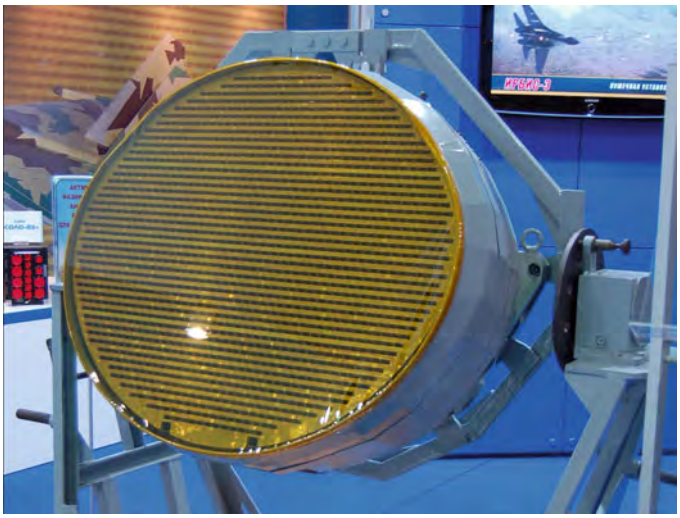

Fig. 4.160 Active Electronically Scanned Array (AESA)

used in radars with passive phased arrays. In an active phased array, each element consists of a module which contains a slot of the antenna, a phase shifter, a transmitter and often a receiver.

In a regular passive array, one transmitter with power of several kilowatts feeds several hundreds of elements, each of them emits only dozens of watts of power. A modern microwave transistor amplifier can also produce dozens of watts, and a radar with active phased antenna array contains several hundred modules with power of dozens of watts each, which create a high-power main beam of the radar with a power of several kilowatts.

While the results are identical, active arrays are much more reliable, since the failure of a single transceiver distorts the antenna directivity pattern, which slightly affects characteristics of the radar, but it remains generally serviceable. Catastrophic failure of the transmitter tube, which is a problem of regular radars, is simply impossible. The additional advantage consists in reduced weight due to the absence of a large high-power tube, a cooling system connected to it, and a large high voltage power unit.

Another feature, which can only be used in active arrays, is the possibility to control amplification of individual transceiver modules. If this can be done, the range of angles through which the beam can be deflected is increased significantly, and it is therefore possible to bypass many limitations of array geometry that are typical of standard phased arrays. Such arrays are known as supergain arrays. Unfortunately, further development of PAAs depends on solving two power-related problems – power dissipation and cost reduction.

The first problem is power dissipation. Disadvantages of modern transistor amplifiers of the microwave range (MMIC) include the low efficiency of the module transmitter – usually lower than 45%. As a result, AESAs emit large volumes of heat

that needs to be dissipated to prevent chips of the transmitter from melting – reliability of GaAs MMIC chips increases at low operating frequencies. Traditional air cooling, which is used in regular computers and avionics, is not suited well in case of high density of AESA elements, due to which modern AESAs are cooled by fluid; in American projects, polyalphaolefin (PAO), cooling agent similar to synthetic hydraulic fluid, is used. Typical liquid cooling system uses pumps supplying cooling agent through the channels in the antenna and then to the heat exchanger – it can be an air cooler (radiator) or a heat exchanger in fuel tank – with second fluid cooling the heat exchange loop in order to remove high temperature from the fuel tank.

In comparison with a regular air-cooled radar of a fighter plane, AESA is a more reliable option that will, however, consume more power and require more intensive cooling. AESA, on the other hand, can ensure a much higher transmitting power, which is required for greater range of target detection (an increase in the transmitting power, however, has a disadvantage – it increases the trace which can be used by the enemy radar surveillance or RWR to detect the radar).

Another problem is the cost of mass production of modules. For the radar of a fighter plane, which usually requires 1000–1800 modules, the cost of AESA becomes unacceptable if the modules cost more than 100 dollars each. First modules were priced around 2000 USD, which made mass production of AESA impossible. However, the cost of such modules and MMIC chips is constantly reducing, since the cost of their development and production becomes lower and lower, as will be demonstrated in one of the chapters.

Regardless of all disadvantages, active phased arrays are superior to regular radar antennas almost in every relation, ensuring higher tracking capacity and reliability, even if with a certain increase in complexity and cost.

Figure 4.161 shows typical structure of the main element of an AESA – transceiver module.

Transceiver module is the basis of the space signal processing channel in any AESA.

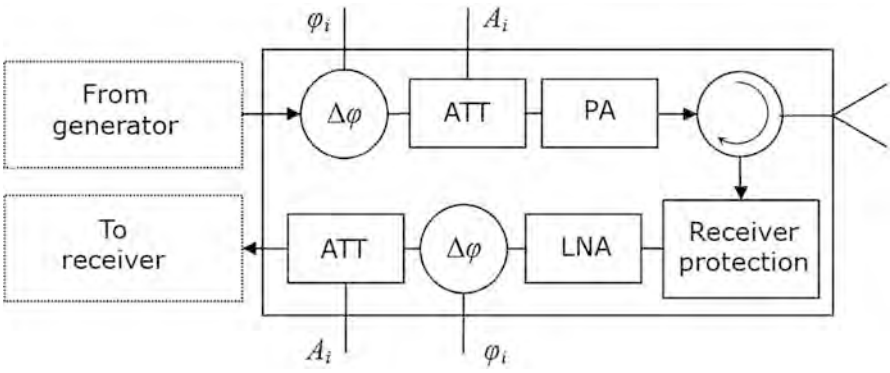

Fig. 4.161 Structure of an AESA transceiver module

Its design includes an active element – an amplifier, which makes this device electrodynamically unilateral. Therefore, in order to ensure possibility of operation of the device both for receipt and for transmission, transmitting and receiving channels are separated inside it. Separation is performed by a switch or a circulator.

The receiving channel contains the following devices:

Receiver protection device is usually an arrester or another threshold device preventing overloading of the receiving channel.

Low noise amplifier – two or more stages of active signal amplification.

Phase shifter is the device for phase delay of the signal in the channel for setting phase distribution across the array aperture.

Attenuator is a device used for signal amplitude setting (reduction, attenuation) for amplitude distribution in the antenna aperture.

Composition of the transmitting channel is similar to the receiving channel. The difference lies in the absence of the protection device and lower requirements to the amplifier in terms of noise. However, the transmitting amplifier shall have higher output power than the receiving one.

4.3.2 Detailed Description of the Structure and Operating Principles of PAA Without a Single Formula

In this section, we will try to provide a detailed description of functioning of antenna arrays on the level that can be easily understood even by novice radio amateurs, without using a single formula or mathematical expression [52].

Constantly rotating antenna of the radar sending high-frequency signals to the line of the horizon for the purpose of detection of remote objects is an integral element of the panorama of any modern airfield. However, in many of the most popular fields of application of radar location, such as aviation, air defense and reconnaissance, mechanically controlled antenna mirrors are being replaced with devices of the new type. A set of small identical plates located in the same plane, each of which is capable of transmitting and receiving signals, replaces a concave reflector. The beam created by this set of antennas moves, observing the air space, and the antenna system itself remains fixed. The direction of electromagnetic radiation generated by the radar is set by the special electronic device; beam control is based on using the phenomenon of interference of electromagnetic waves.

Operation of all radar location stations is based on directed radiation of radio signals. As a rule, radiation frequency lies within the microwave range from 3×10^8 to 10^{10} GHz, even though some types of radar stations with extremely high operating range work in the ranges of high frequencies or super-high frequencies, or in the ranges of 3×10^6–3×10^7 Hz and 3×10^7–3×10^8 Hz respectively. Depending on the shape, antenna radiates a narrow high-directional beam suitable for precise target tracking, or a wide fan-shaped beam most suitable for observation of wide regions of air space [52].

When the signal sent by the antenna reaches the object, it is reflected. If the power of the transmitted pulse, sensitivity of the antenna and the reflecting capacity of the object are high enough, the reflected signal received by the antenna can be detected by the radar station. The reflected signal may contain different information about the target, which is determined by the type of the radar and the form of the radiated pulse.

The direction from which the reflected signal arrives determines the position of the object; if the radar station radiates energy pulses instead of a continuous signal, the time of delay between pulse transmission and the receipt of the reflected signal can be used to estimate the distance to the object. Some radar stations provide the possibility of measurement of the Doppler frequency shift of the reflected frequency shift (i.e., difference between frequencies of direct and reflected signals), which occurs when the radiation source (in this case – the target) and the receiver (radar) move in relation to each other. The value of Doppler shift is used to calculate the speed of the object in the direction of the antenna or in the reverse direction.

For the given distance to the object, intensity of the reflected signal presents a certain general idea of the object dimensions. The word "presents" is used here for a purpose: two objects of the same time that have different shapes or are made of different materials will sent reflected signals with significant differences in intensity. In order to obtain more accurate information about the dimensions of the objects, certain radar stations transmit such short pulses that are physically shorter than the targets they can meet in the way of propagation. If a radar station radiates energy only during several parts per billion of a second, by the time pulse transmission is completed, its front will pass a distance of one or several meters. Such pulse has smaller length in space than, for example, a plane. Radar signals are reflected from far and near surfaces of the target; if the pulse is extremely short, two reflected signals are formed. The time interval between these two reflected signal correspond to the length of the target [52].

Since a regular radar observes wide areas of the air space, it can collect information about many objects. However, there is also a time interval between consequent moments at which the same target appears in the field of view of the radar, which is sometimes significant. The rate of updating information about the target, i.e. the frequency with which the same target is fixed by the radar does not exceed the speed of rotation of the antenna mirror around its axis for most stations with rotating antennas. In radar stations of air traffic control systems, for example, green line of radial scanning, which moves on the screen and leaves marks characterizing new position of the plane and carrying other information about it, rotates with the same speed as the antenna mirror itself. The information about the observed object in such radar stations is usually updated every 6 s; even in the most advanced military stations, information is rarely updated with higher frequency than twice per second.

There are circumstances in which it is required to receive new information on position and movement of targets more often. One radar with mechanically controlled antenna can provide continuous retrieval of information about one or several closely located objects by permanent tracking with the help of rotation of the antenna system. However, to solve many combat and reconnaissance tasks, such as tracking

several missiles moving towards a warship from different directions from this warship, or careful observation of the flight of several components of a divided warhead during testing of intercontinental ballistic missiles, each of the large number of targets shall be observed continuously. Until recently, several radar stations were used in such cases, each of which was designed for surveillance over one or several targets. After invention of radar stations with phased antenna arrays, the use of several radars with mechanically controlled antennas in such cases became irrelevant. Now they can be replaced with a single station equipped with the new antenna system. As an example, we can cite one of the first old-fashioned radiolocation stations under the codename of COBRA DANE equipped with phased antenna array; in the previous century, it was installed on the shore of the Bering Sea; this radar station is capable of tracking hundreds of targets dispersed in a space limited by 120 ° in azimuth and about 80 ° in elevation angle. In reality, the radar station tracked these targets simultaneously by automatically throwing its beam from one target to another over time measured in microseconds [52].

Electronic control of the beam, due to which such excellent possibilities are achieved, is based on using a simple physical phenonemon. When sources located close to each other radiate energy simultaneously at the same frequency, the waves emitted from these sources are combined. This phenomenon is known as interference. The character of interaction of two waves from two sources separated in space depends on the phase shift between these waves. If peaks and troughs of one wave respectively coincide with peaks and troughs of the other wave (phase shift is equal to 0), the resulting oscillation will have an accumulated amplitude. If the waves are not in phase, and their peaks and troughs do not coincide, the resulting signal will be attenuated or (with phase shift of 180°) equal to 0.

As noted 4.5.1, a phased antenna array is usually composed of radiating elements located in the same plane and at equal distances from each other, to which signals of the microwave range with equal amplitudes and phases are supplied. The master oscillator generates the signal, while microcircuits and special lamps designed for operation in the microwave range, such as travelling wave tubes, amplify it. If the signals are emitted in phase from all array elements, their amplitudes are added in separate points of space along the line perpendicular to the array plane. Therefore, the radiated signal will be strong, and the signal reflected from the objects in the way of its propagation along the axis and perpendicular plane of antenna array and within the small sidewise angles will have the intensity sufficient for its detection.

In case of wide angles of deflection from the perpendicular axis of the antenna array, signals from different radiating elements shall pass different distances to the target. As a result, the ratio of their phases changes, and they interfere, attenuating or fully eliminating each other. Therefore, outside the narrow cone, the axis of which coincides with perpendicular axis of the antenna array, and in which interference with amplification of amplitude of the resulting wave takes place, signals reflected from objects have low intensity and cannot be detected. Underlying physical principles of formation of fringe patterns make it possible to determine the width of this cone. It is directly proportional to the operating wavelength and inversely proportional to the size of the antenna array. If each element of the antenna array radiates

signals in phase with other signals, propagation of the radar beam is strictly perpendicular to the array plane.

Now, let us suggest that the signals of each radiating element are delayed for the time that evenly increases from one element to another along the plane of the array. The signal radiated by each element will be delayed from the signal of the next element by a part of the wavelength. As a result, all signals will be shifted in phase relative to each other. Now, the area in which separate signals coincide in phase and during addition produce the signal of accumulated amplitude with the help of which it is possible to detect targets is located not along the perpendicular axis of the array and shifted towards an increase in the signal delay. Beam deflection angle depends on the phase shift of signals radiated by neighboring elements of the antenna array, size of the array and the wavelength. In this case, the beam takes the shape of a narrow cone surrounded by destructive interference regions. Therefore, the radar beam is deflected without changing the antenna position.

When the reflected signal returns from the target located in this new direction determined by rising phase shift, the circuit ensuring time delay of the transmitted signal introduces a new series of delays of separate signals received by each of the radiating elements. Since the front of the returning wave reaches the antenna array at an angle to its plane, the antenna elements that radiated the signal the last (located closer to the target) will be the first to receive the reflected pulse. Therefore, the same series of delays used to create set direction of radiation ensures transmission of all components of the reflected signal to the receiver in a single phase, which makes it possible to process them and receive information about the target.

Phase delay control makes it possible to deflect the beam of a regular antenna array by an angle of up to 60° from the perpendicular axis, which ensures the bearing field of view of 120°; i.e., while retaining the antenna in fixed state, the radar observes one third of the circular line of the horizon; if the array plane has a sufficient inclunation, the field of view extends from the horizon to the zenith and far beyond. Since beam control in this case is not connected to any mechanical tuning, and the movement of the beam within the entire field of view takes only several microseconds. With the help of a computer for calculation of the required phase shifts for the purpose of deflecting the beam by the required angle and control of the signal delay circuit, radar stations with phased antenna arrays, such as COBRA DANE, could perform tracking of several hundreds of targets at the same time [52].

The electronic device that ensures control of the radar beam and creates the required delay of the microwave signal during supply to each element of the antenna array is known as *phase shifter*. It consists of sections of cable or waveguide with very exact dimensions. An increase in the length of the cable used to transmit the signal from the generator or the amplifier to the radiating element causes a delay in the signal pass time. It practice, it is impossible to ensure the length of all cables used to transmit signals to radiating elements of the phased antenna array that would change smoothly, providing continuous change of phase delays. Therefore, the phase shift is step-wise. Each element of the antenna array is connected to several cables of different lengths. In order to obtain phase shifts ensuring the given beam deviation, a certain combination of cables is included in each circuit.

In the old radar station COBRA DANE used for intelligence tasks, for example, three-element phase shifters were used. Each of such devices had three strip lines of various lengths (similar to waveguides), which ensured transmission of oscillations of the microwave range along the thin metal strip located between two grounded copper plates. One of the strip lines increased the length of the signal pass by the value equal to the half of the wavelength (about 15 cm), since the operating frequency of the radar station COBRA DANE amounted to about 1 GHz. This ensures phase shift of the signal by 180° relative to the non-delayed signal. The second strip line ensured delay of the signal by a quarter of the wavelength, i.e. phase shift by 90°. The length of the third strip line ensured the delay equal to one eights of the wavelength (which corresponds to the phase shift by 45°). In different combinations, these three strip lines made it possible to change the signal phase by any number of degrees multiple of 45, from 0 up to 315° [52].

Step-wise change in the phase delay value, as demonstrated in Chap. 1, shall cause formation of blind spot. How is it possible to ensure continuous movement of a radar beam using eight different values of phase delay with a pitch of 45°? The answer to this question can be found in the properties of interference patterns. Every time when the phase difference between signals radiated at opposite sides of the antenna array reaches 360° or one wavelength, the region of interference where the beam with combined amplitude is formed will be displaced by the distance approximately equal to its own width. Therefore, in order to move the beam perpendicular to the antenna array plane (it has this direction when all signals are emitted in phase) to the next position without formation of a blind area between these two position, accumulated phase shift along the antenna array plane shall amount to about 360°.

Whether an increase in the phase shifts along the plane of the array is continuous or step-wise (with a step of 45°), it doesn't matter. Stepwise modification of phase shifts causes only slight reduction of the radiation power and certain loss of sensitivity of the antenna system. In order to ensure smoother movement of the beam of the antenna array with three-element phase-shifting devices, it is possible to set smaller total value of phase shift, for example, 180°, i.e. four times 45°.

If the beam needs to be deflected from the perpendicular direction by value greater than its width, total phase shift along the antenna array plane shall exceed 360°. Due to periodic character of electromagnetic oscillations, phase shift by multiple number of waves is equivalent to 360°. For total phase shift by more than 360°, linear increase in the phase delay from zero to 360° shall be repeated several times across the plane of the antenna array. The first series of delays ensures accumulated phase shift by one wavelength, the second series increases it to two wavelengths, etc. Graphically, the change in the phase shift value along the plane of the antenna array is presented as saw teeth: the steeper are their skews and the greater is their number, the sharper is the beam deflection.

It follows from simple geometrical rules that the effective antenna area is reduced with an increase in the beam deflection from the perpendicular direction. As a result, sensitivity of a phased antenna array to signals reflected from the target is quickly reduced with angles of beam deflection from perpendicular axis exceeding 60°.

Therefore, one phased antenna array cannot ensure the same possibility of observation in all directions as mechanically rotated antennas. One of the solutions to this problem is the use of several antenna arrays with planes set in different directions. Another method of expanding the field of view of a phased antenna array is placing it horizontally under a dome-shaped lens, which reflects the radiation; due to this, deflection angle of the radar beam increases. When an antenna array forms a beam at an angle of 60° to zenith, the use of a lens can increase its deflection even more, up to 90° to zenith, i.e. in the direction of the horizon. Therefore, the lens makes it possible to observe the entire hemisphere of the aerospace using the antenna array. The lens can be made of special ceramics or plastic, which reflects microwave radiation. It can also serve as the phase-shifting device of the second stage in order to additionally delay the phase of the signal radiated by the antenna array [52].

When phase control is used to send a short pulse at high angle to perpendicular axis of the antenna array, the radiated pulse will inevitably be distorted – stretched in time and space. Let us suggest that the antenna radiates a pulse with a duration of 5 ns. If radiation of the radar station is strictly perpendicular to the antenna array plane, the pulse has rectangular longitudinal section in space; its width is equal to the width of the antenna array, its length – to the distance passed by electromagnetic wave during 5 ns, i.e. 1.5 m. On the other hand, if the beam is significantly deflected from the perpendicular axis due to phase shift, then the longitudinal section of the pulse will have the shape of a parallelogram. With regard to the target, the length of the pulse will exceed 1.5 m, since the signals radiated by separate elements of the antenna array reach the target in series and not simultaneously. The reflected pulse returning to the antenna array will also be stretched.

Detection and tracking of targets is usually performed with pulses of much greater duration, such as 1000 ns, and distortions within several nanoseconds are insignificant. Pulse stretching, in turn, has no significant effect on the ability of the radar station to determine location and speed of the target based on the character of the reflected signal. However, separate tracking of targets moving close to each other requires radiation of short pulses. They are also required to determine dimensions of the target based on signals reflected from its front and rear surfaces. If the transmitted short pulse is stretched, reflected signals are merged instead of arriving separately, which complicates retrieval of the required information.

The method similar to one used for control of the beam with the help of signal phase shift proves useful in this case as well; it helps preserve the shape of the pulse. In order to ensure the required phase shifts, it is necessary to delay the signals only for the time corresponding to parts of the wavelength. The delays necessary to avoid stretching of the pulse are equivalent to the integer of wavelengths. In this case, emission of signals by separate elements of the antenna array is performed in series, while the lead in radiation of each signal relative to the next one is in proportion to the distance that the signal must pass to reach the target. As a result, the same effect is achieved as if the antenna array was rotating, holding the target in the direction of the perpendicular axis. This method is known as beam control with the help of time delays. Similarly to the method in which phase delays are increased, it makes it possible to send the signal of coherent and thus powerful radiation in the given

direction. Such long delays equivalent to distances of several meters passed by the signal require inclusion of cable sections of the corresponding length in the circuit of signal pass from the generator or amplifier to the radiating element. A large antenna array can include many thousands of radiating elements, and if each of them had its own temporal delay circuit, the radar unit would be extremely complex and expensive. Therefore, designers of radar stations are trying to find the compromised solution that would simultaneously ensure the required pulse length even at great angles of displacement of the radiation direction from the perpendicular axis of the antenna array and the structural simplicity. As a result, beam control in modern radars with phased antenna arrays is controlled with the help of phase shift as well as time delays.

For example, in the radar station COBRA DANE mentioned above, each of 15,360 radiating elements was connected to a separate phase-shifting device, and therefore phase of each device was shifted separately. In the target detection mode, the radar station radiated pulses with the duration of 1000 ns, and the beam was controlled only by introducing phase delays. Since the purpose of the radar station consisted in tracking ballistic missiles, it needed to ensure acquisition of information about their dimensions after detection. For this purpose, the antenna array was divided into 96 section, each of which included 160 radiating elements. After detection of the target, the station started radiating pulses of extremely small length, and the signals supplied to each section of the antenna array first passed the time delay circuit. These circuits are similar to phase-shifting devices but have much greater dimensions. They consist of sets of coaxial cables of various lengths, and any combination of them can be included in the circuit for creation of time delays corresponding to signal passing the distance of 1–64 wavelengths, or about 19.2 m, since the operating frequency of the COBRA DANE radar station is about 1 GHz [52].

As the cross size of separate sections of the antenna array is 2.7, which is little compared to its diameter equal to 29 m, distortions that arise in each array section at great angles of displacement of the beam from the perpendicular axis lie within permissible limits. Each section of the antenna array radiates the signal occupying the volume with rectangular section shaped like a parallelogram. Due to time delays, these signals are summarized, and distortions of separate signals are not added. As a result, the shape of the pulse is preserved well enough, and only 96 devices providing time delays are used instead of 15,360.

Replacement of a moving antenna with a set of fixed radiating elements can provide additional advantages besides the possibility of electronic control of the beam. One of these advantages is ensuring high operational reliability. Operation of a fixed antenna array does not depend on condition of such wearing mechanical components as bearings and motors. Moreover, most radar stations with mechanically controlled antennas contain one or several extremely large electronic tubes for amplification of the microwave range signals.

Another example is the Marconi Martello radar station, which was produced in Great Britain in the end of the previous century and designed for use in an air defense system. The main circuitry element of this station was the electronic lamp with the output power of about 3 MW. Its malfunction caused failure of the entire system. It should be noted, however, that in such radar stations designed for

operation in intelligence and air defense systems there is always a possibility of quickly switching to auxiliary sources of microwave radiation.

By contrast, radiated power in the COBRA DANE radar station was produced by 96 tubes with the power of 160 KW each. Output signal from each tube was supplied to the divider and then to 160 radiating elements, which formed one section of antenna array. Failure of one tube in this case caused malfunction of only one of 96 parts of the antenna array, and the radar station remained generally serviceable, even though the quality of its work slightly decreased. Moreover, smaller lamps are easier to replace in case of failure than the single large lamps used in the Martello radar station.

Radars with phased antenna arrays based on semiconductor elements demonstrate even higher reliability and simplicity of use. Microelectronic circuits of generators and amplifiers are used, for example, in radar stations under the code name PAVE PAWS designed for detection of ballistic missiles launched from ships and submarines. Four parallel transistors with power of 100 W each are mounted in separate modules. Each module ensures excitation of one radiating element. Thus, signals supplied to each of the two surfaces of the double antenna are simultaneously amplified by 1792 modules in the chain of antenna elements instead of 96 tubes, and failure of a single element has even weaker effect on the characteristics of the radar station in general [52].

In the PAVE PAWS radar station, like in many other stations built on semiconductor elements, amplification of signals is performed after they are distributed between antenna elements and shifted by phase. Therefore, power losses that occur when the amplifier passes through the divider and the circuits of the phase shifter are excluded. However, along with this increased efficiency and all other advantages, semiconductor technology also has a downside. It generally provides lower values of peak power than the ones achievable with the help of electronic tubes.

Limitations related to the possibility of obtaining high power signals in radars based on semiconductor elements have increased the importance of the so-called pulse coding and compression method, which makes it possible to simulate high-power short pulses during radiation of less powerful and longer signals. This technique remains important in case of using powerful radar stations both with mechanically controlled antennas and with phased antenna arrays when it is necessary to gather certain information about distant objects.

The range at which a radar station with the set sensitivity of the receiving path can detect objects of a certain size and with defined reflective power depends on the total pulse energy. The shorter the pulse, the higher shall the peak radiation power be with set range. Theoretically, the radar station COBRA DANE could detect a metal object the size of a grapefruit at a distance of about 2000 km. However, for this the peak power of radiation shall be not less than 3×10^{12} W at the pulse length of 5 ns, which is more than enough to destroy all circuits of the radar station [52].

Still, it is possible to determine dimensions of an object or separately observe several objects flying close to each other only using short pulses. The fact that the range of a radar station is determined by the total pulse energy and not by the peak

power helps find the solution. It consists in the following. When a radar operates in the transmission mode, the radiated pulse is stretched, and the peak power is therefore reduced. This technique is known as pulse coding (encoding). In the reception mode, the reflected signal is compressed for the purpose of extracting of all information that could be received in transmission of an actually short pulse. In the radar station COBRA DANE, for example, a 5 ns pulse was stretched 200 thousand times before being amplified and radiated, and its duration became equal to 1 ms. The required peak power is reduced as much – from 3×10^{12} W to 15 MW, which is the actual radiation power of COBRA DANE [52].

When standard coding technique is used, the pulse with a duration of 5 ns, which includes the frequency spectrum, passes through the dispersion delay line, which causes varied delays of separate components of this spectrum: the higher frequency of the component, the greater is the delay; signal component with the lowest frequency is radiated without a delay, while the component with the highest frequency receives the maximum delay equal to 1 ms. After that, the pulse with new duration of 1 ms is amplified and radiated; the received reflected signal has the same duration.

The received signal passes through the compression chain, which introduces a number of additional delays. This time, the duration of delays is in reverse proportion to frequency. Pulse component with the lowest frequency receives the delay equal to 1 ms, while the component with the highest frequency receives no delay at all. Therefore, in the process of pulse coding and compression, each component of the signal spectrum receives the same accumulated delay. As a result, the reflected signal is not distorted and has the duration of 5 ns.

If the reflected pulse with a duration of 1 ms, which has the length of 300 km in space, meets an object significantly shorter than the pulse during propagation, the pulse returns in the form of two overlapping reflected signals. These reflected signals cannot be separated by conventional method, and it is impossible to determine dimensions of the object based on their relative position. However, when reflected overlapping coded signals are compressed, two different signals with the duration of 5 ns are received at the output [52].

Coding and compression of pulses perform the same function in radar stations built on semiconductor elements. Even if it is not necessary to determine the distance to the object from which the signal is reflected, precise determination of the distance to the object requires the use of fairly short pulses. Without using compression, pulses with the duration of 1 ms only allow determining the distance to the object with accuracy up to 150 km. Moreover, radiation of long pulses is affected by local interferences caused by reflection from precipitation and ground surface. At the same time, semiconductor equipment cannot ensure such powers that are necessary during operation with short pulses to make the range of radar station the same as during radiation of pulses with greater duration. Therefore, in order to achieve great range and high resolution at low power, it is necessary to use coding and compression of pulses in radar stations based on semiconductor elements.

First radar stations with phased antenna arrays, used in the 1960s and 1970s, were designed for military and reconnaissance purposes. There are circumstances in

which civil fields of economics dictate the needs stimulating development of military equipment. In particular, civil aviation needs to obtain data on rapidly moving objects in the area of the aerodrome, where arriving aircrafts adjust their course for approach. Radar stations controlling approach of planes to the strip send them for landing, simultaneously tracking the distance to the planes and their position relative to the air field strip. The increasing intensity of air traffic creates urgent need for fitting civil aviation with radars with phased antenna arrays.

With the reduced quantity of radiating elements the cost of phased antenna array is decreased. In most fields of application of radar equipment, antenna systems shall have great numbers of radiating elements. A small antenna array has a less focused and therefore a wider beam. It reduces its resolution by angular coordinates, while small area cannot ensure high sensitivity to reflected signals. When observation of a large area of air space is not required, both these disadvantages of a small antenna array can be rectified by uniting the antenna with a large reflector.

4.4 Design Features and Reliability Assessment of Power Supply Systems of Active Electronically Scanned Arrays of Radar Stations

Today, developers of radar stations are becoming increasingly interested in radar complexes based on active phased antenna arrays, which have significant advantages compared to passive arrays [53]; this is mostly due to the development of solid-state microwave equipment and appearance of small-sized transceiver modules (TRM) placed directly on the antenna curtain. Power supply of these modules can be implemented by various means but shall conform to the following basic requirements:

- minimum weight of the power supply system (especially its part placed on the antenna curtain);
- maximum reliability of the system;
- maximum efficiency of the power supply system.

AESA system is usually powered by pulse power system with high efficiency, which does not depend greatly on the source power and structure of the power supply system.

Reliability requirements for the AESA power supply system are usually set during the design stage and determined by the resource of operation of the station. Increasing reliability of power supply system above the set value is practically useless.

Therefore, the most effective is the power supply system that has the minimum weight with the given reliability. We are going to use this criterion below when comparing various power supply systems.

Building of the most effective power supply system consists in the selection of the type, number and arrangement of secondary power sources and means of connecting them. In this case, it is necessary to take into account the following circumstance.

Since the bodies of powered devices are usually connected to the package of the carrier, in any configuration of power supply system it is necessary to ensure galvanic isolation between output terminals of secondary power sources and the in vehicle network of the carrier. Moreover, TRMs are usually characterized by pulse character of supply current, which requires inclusion of energy storage devices into the power supply system.

Power supply system of the AESA antenna curtain significantly increases weight and dimensions of the station and has a much more complex structure than the power supply system of other parts of the station. Due to this fact, only power supply system of the AESA antenna curtain will be considered in the following.

AESA transceiver modules usually require one voltage of 10–50 V in the main channel (the one with the highest power) depending on the range of working frequencies and the output power of the transmitter. Moreover, operation of TRMs usually requires two or more auxiliary voltages with power values significantly lower than in the main channel.

Weight and dimensions of pulse power sources significantly depend on the presence of galvanic isolation of output voltages from the supply chain; therefore, two types of pulse sources will be considered in the following.

Balanced Voltage Converter (BVC) is a pulsed secondary voltage source in which input and output circuits are galvanically isolated. Pulsed Voltage Stabilizer (PVS) is a pulsed secondary voltage source in which input and output circuits have a common output.

It is known that any power supply system can be built according to one of the three basic circuits [54–57]:

– fully centralized system, where consumers are powered by one or several power sources;
– fully decentralized system, where each consumer has its own power source;
– partially centralized system, which contains both high-power supply sources and sources powering individual consumers.
– selection of one of the above circuits for building of the power supply system depends on the following main factors:
– Carrier type (space-based or airplane-based complex);
– shape and dimensions of the antenna array;
– number and principle of arrangement of TRMs on the AESA curtain;
– rated values of supply voltages and current consumption of TRMs;
– voltage and current type of the primary supply network.

As an example, we will consider power supply system of the A-band AESA of a space radar with specific parameters (element numbers, consumption currents, supply line voltage). Power supply of this AESA shall ensure power supply to the curtain of the antenna array and the distribution system. AESA is powered by the 28 V DC onboard network.

Standard requirements for power sources of the antenna array of such system are as follows:

- transmitting curtain of the antenna array consists of 504 transceiver modules grouped in 18 columns, 28 TRMs per each column. Moreover, 10 TRMs are placed in the distribution system;
- TRM powering requires three voltages, the main one of which is +10 V voltage with the following characteristics: instability – not more than ±4% in all operating conditions, setting precision – not more than 1%, pulsation at the conversion frequency (effective value) – not more than 0.1%;
- pulsed load current;
- current amplitude in the pulse $I_M = 7A$;
- maximum pulse duration $t_I = 40 \cdot 10^{-6}$ s;
- output voltage split at the end of the pulse – not more than 1%;
- average consumption current $I_A = 0.28$ A.

Moreover, power supply system of TRMs usually requires two additional voltages (+5 V and − 5 V) with the following characteristics:

- maximum load current for the +5 V channel – $I_1 = 0.2$ A;
- maximum load current for the −5 V channel – $I_2 = 0.08$ A;
- requirements for instability and pulsation of the output voltage in both channels are the same as the requirements for the main channel (+10 V).

Load in the +10 V supply channel is pulsed; therefore, in order to ensure normal operation of the secondary power source and reduce pulsation of the consumption current from the network, inductance-capacitance energy storage devices must be installed at inputs of each TRM.

Energy storage devices shall be installed near each TRM in any configuration of the power supply system; therefore, when comparing power supply systems of the antenna array curtain, we will suggest that they are not included in the power supply system and belong to TRMs.

Assessment of reliability of an AESA is a complex task. Failure of a single TRM on the array will not cause failure of the entire AESA. Therefore, in order to assess reliability of an AESA, it is necessary to determine the permissible number of failed TRMs and points of their possible location on the array.

In decentralized and partially centralized supply systems, come of the power sources only supply power to one TRM. Moreover, each TRM has its own energy storage device. In this case, from the point of view of reliability, TRM, its supply sources and the energy storage device form a single object, the failure rate of which is equal to the sum of failure rates of the TRM, its supply sources and the energy storage device.

This section does not include assessment of reliability of the entire AESA; therefore, when comparing different configurations of antenna array curtain power systems, we will only estimate reliability of the central part of the power supply system, malfunction of which causes failure of the entire AESA, in accordance with the methodology described in [53].

The following source data are usually used for assessment of reliability of power supply systems:

- total time of operation under current (in enabled state) – $t_p = 3000$ h;
- total storage time (in disabled state) – $t_{XP} = 40{,}000$ h;
- success probability of the centralized part of power supply system shall be not lower than 0.99;
- reliability of power buses, connecting wires, contacts, connectors, etc. is usually not taken into account.

Specialists usually use the following denotations during calculation: n is the number of columns in the antenna array ($n = 18$); m is the number of TRMs in one column (for calculations, we will use $m = 29$, i.e. 28 TRMs on the antenna curtain and 1 TRM from the distribution system); N is the total number of TRMs in the antenna array and the distribution system ($N = 514$).

It should be noted that the selection of power sources is greatly limited due to heavy duty operation conditions and reliability requirements.

We will use the series of BVC (SPN) power modules produced by Russian CJSC "Electroinvest" as a prototype for further calculations in this chapter. These power modules are single-channel balanced DC converters with the range of input voltage within 18–40 V. Modules are fitted with integrated protection from short circuits and overloads in load lines and the possibility of remote activation/deactivation. Input and output circuits of the modules are galvanically isolated from each other and from the casing. Each module is placed inside a sealed metal rectangular enclosure, the bottom surface of which ensures heat removal.

The modules have the following characteristics in terms of reliability:

- failure rate in enabled state during operation in nominal mode with package temperature of 85°C – $\lambda_P = 1 \cdot 10^{-6}$ 1/h;
- failure rate in enabled state during operation in simplified mode with load coefficient 0.8 and at package temperature of not more than 70°C –$\lambda_P = 0.68 \cdot 10^{-6}$ 1/h;
- failure rate in storage mode, including disabled integrated modules $\lambda_{XP} = 11.6 \cdot 10^{-8}$ 1/h.

It is necessary to perform a number of calculations for assessment of attestation of the centralized power supply system of a typical AESA based on the above criteria.

For example, to build a fully centralized power supply system, it is necessary to use three high-power supply sources that will ensure power supply to all TRMs of the AESA and the distribution system. Power values of such power sources will amount to 1462, 522 and 209 W for +10 V, +5 V and − 5 V channels respectively.

Of course, supply sources of higher power shall usually have slightly better values of weight and dimensions, but building of a fully centralized AESA power supply system is always limited by the following circumstance:

- in case of relatively low supply voltage in the main TRM channel (+10 V) and significant geometrical dimensions of the AESA curtain it is impossible to ensure

the required value of instability of TRM supply voltages due to voltage drop in the wires.

Let us consider the basic option of the centralized power supply system in which each column of the array is powered by three high-power SPN (BVC) modules.

Power consumption for each module can be determined using the source data provided above.

Power consumption in the +10 V channel:

$$I_{+10} = I_A n = 0.28 \cdot 29 = 8.12 \text{ A}; P_{+10} = 10 \cdot 8.12 = 81.2 \text{ W}.$$

Power consumption in the +5 V channel:

$$I_{+5} = I_1 n = 0.2 \cdot 29 = 5.8 \text{ A}; P_{+5} = 5 \cdot 5.8 = 29 \text{ W}.$$

Power consumption in the −5 V channel:

$$I_{-5} = I_2 n = 0.08 \cdot 29 = 2.32 \text{ A}; P_{-5} = 5 \cdot 2.32 = 11.6 \text{ W}.$$

Standard power sources of the SPN (BVC) type, also produced by "Elektroinvest", can be selected for such system:

- for +10 V channel – SPN100 10-V-1 KTsAYA.436434.001 TC;
- for +5 V channel – SPN50 05-V-1 KTsAYA.436434.001 TC;
- for −5 V channel – SPN 15 05-V-1 KTsAYA.436434.001 TC.

In this case, the total weight of all sources according to the data presented in Table 4.12 will amount to 10.4 kg (without taking into account the weight of energy storage devices installed in TRMs). Structural diagram of such power supply system is shown in Fig. 4.162.

Table 4.12 Types of modules by CJSC "Electroinvest"

Serial SPN (BVC) sources	Output power, W	Range of output voltages, V	Weight kg	Overall dimensions, mm
SPN03	3	5; 6; 9; 12; 15	0.042	50 × 32 × 12
SPN05	5	2.5; 3.3; 5; 6; 9; 12; 15; 27	0.052	58 × 34 × 12
SPN 10	10	2.5; 3.3; 5; 6; 9; 12; 15; 27; 36	0.064	64 × 40 × 12
SPN 15	15	2.5; 3.3; 5; 6; 9; 12; 15; 27; 36	0.086	71 × 44 × 14
SPN25	25	3.3; 5; 6; 9; 12; 15; 27; 36	0.160	89 × 54 × 16
SPN50	50	5; 6; 9; 12; 15; 27; 36	0.210	98 × 61 × 16
SPN10	100	36	0.280	122 × 84 × 1

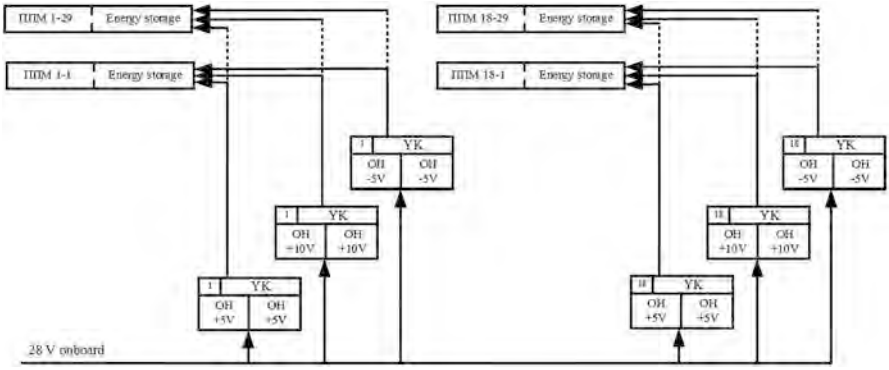

Fig. 4.162 Diagram of centralized power supply system of the antenna array curtain and distribution system

Let us assess the reliability of such system. Probability of success of one SPN source:

$$p = e^{-\lambda_P t_P} e^{-\lambda_{XP} t_{XP}} = e^{-1 \cdot 10 - 6 \cdot 3000} e^{-11,6 \cdot 10 - 8 \cdot 40000} = 0,992. \quad (4.41b)$$

In this system, failure occurs in case of malfunction of any source. Since the total number of sources k = 3xn = 54, the probability of success of a centralized power supply system is as follows:

$$P_{\ddot{O}N} = p^k = 0,992^{54} = 0,648. \quad (4.42)$$

It is clear that the obtained value of system success probability is very low. At the same time, redundancy of power sources in this system is practically impossible due to the following reasons.

First of all, it is necessary to switch output circuits of power sources when performing backup. This switching cannot be performed using an electromechanical relay due to low reliability of such relays. Second, the use of isolating diodes is also impossible, since with low output voltages observed in this case it is impossible to ensure the required values of magnitude and instability of output voltages of power sources.

To compare parameters of this power supply circuit with other options, let us assume that the relability of the switching unit (SU) is equal to one. In this case, reliability of the centralized power supply system with redundancy will amount to $P_{\text{CSred}} = 0.996$.

If the weight of a switching unit is 0.15 kg, the weight of such system will be equal to 28.9 kg.

Let us estimate the decentralized power supply system (DS). In such system, each TRM is powered by its low-power supply source, which in turn is powered directly

by the onboard circuit. This system contains no centralized part of the power supply system; therefore, its reliability during comparative analysis is equal to zero.

According to the requirements for TRM supply voltages, three SPN converters can be used here as power sources:

- for +10 V channel – SPN 03 10- V-1 KTsAYA.436434.001 TC;
- for +5 V channel – SPN 03 05- V-1 KTsAYA.436434.001 TC;
- for −5 V channel – SPN 03 05-V-1 KTsAYA.436434.001 TC.

Total weight of power sources in this case will be determined as follows:

$$M = N\text{x}3 \times 0.042 = 64.76 \text{ kg}.$$

Structural diagram of such power supply system is shown in Fig. 4.163.

Therefore, the weight of power supply system with decentralized circuit will amount to 64.8 kg excluding the weight of energy storage devices installed in TRMs.

Let us consider a power supply system with partial centralization (PC). With this design, power supply of TRMs can be ensured by several methods.

Let us consider the option (first method) in which additional voltages +5 V and − 5 V are formed from sources powered by the main channel circuit (+10 V). In this design, +5 V and −5 V sources do not require galvanic isolation of input and output circuits, and they can be based on pulse stabilizers, which have significantly smaller weight and higher efficiency as compared to SPN (BVC), since their control circuit is simpler and does not contain a transformer. Preliminary calculations have demonstrated that PVS board with two output voltages (+5 V and −5 V) installed inside a TRM will have the weight of 0.025 kg and overall dimensions of 50 × 35 × 10 mm. Efficiency of such PVS will be not less than 80%. Heat emission of this board will not exceed 0.35 W. In this case, TRM is powered only from +10 V voltage with the current consumption I+ = 0.28 + 0.175 = 0.455 A and power consumption of 4.55 W.

When the second option of the circuit with partial centralization is used, auxiliary voltages −5 V and + 5 V for each TRM are produced by the pulsed voltage stabilizer installed inside the TRM enclosure, while the +10 V voltage is provided by high-power BVC that supplies power to the entire column. According to the calculations

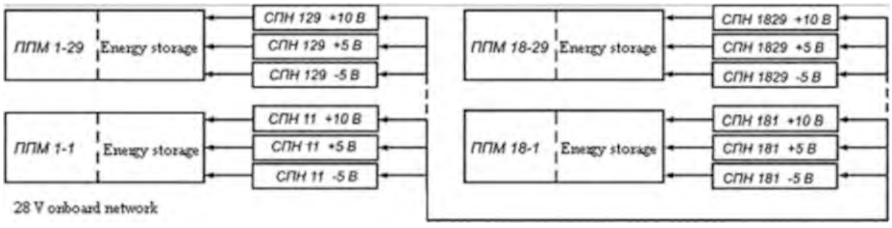

Fig. 4.163 Diagram of decentralized power supply system of the antenna array curtain and distribution system

provided above, power consumption of one TRM is equal to 4.55 W. The power of the BVC then will amount to $4.55 \times 29 = 132$ W.

BVCs for such power are not produced in lots; therefore, such source shall be specifically designed for the new system.

At first, we will assess reliability of the entire system without redundancy, accepting the probability of success of this BVC equal to 0.992 similarly to standard BVCs. Probability of system success in this case will be determined by the following expression:

$$P_{\times \mathrm{N}} = p^n = 0,992^{18} = 0,865. \tag{4.43}$$

Intensity can be increased by using passive redundancy, which is possible if all eighteen BVCs powering TRM columns have parallel outputs. In this case, control circuit of each BVC shall also include the special current balancing device ensuring uniform distribution of the load current between two running BVCs [56]. When such redundancy is used, in case of failure of one or several power sources, the load is redistributed among the remaining serviceable sources. Of course, in this case BVCs shall have a certain power margin, which depends on the permitted number of faulty sources.

Thus, probability of success in case of passive redundancy is determined by the expression

$$P_{\times Đ\ddot{O}} = \sum_{i=0}^{n-l} p^{n-l}(1-p)^l \frac{n!}{i!(n-i)!} \tag{4.44}$$

where n is the number of parallel sources (number of columns); l is the number of sources with which the system preserves its workability.

Table 4.13 shows that even with $l = 17$ (failure of one BVC is allowed) reliability of the system corresponds to the set value. BVC power in this case is equal to 140 W. Taking into account possible irregularity in distribution of currents between BVCs, let us assume that the power required by each BVC is equal to 150 W. The weight of such source will be 0.42 kg.

Table 4.13 Values of probability of system suffers and required BVC power for different values of l

Number of sources	BVC power, W	Probability of system success
18	132	0.8650
17	140	0.9910
16	148	0.9996
15	158	0.9999

Let us estimate the weight of the system sources installed inside each TRM:

$$M = 0.025\text{x}N + 0.42\text{x}n = 20.4 \text{ kg}.$$

Here, each TRM consumes 0.455 A, and one TRM column will consume 13.2 A. Based on this, the weight of wires is 2.2 kg.

Thus, the weight of the power supply system of the antenna array curtain and the distribution system will amount to 22.6 kg without taking into account the weight of energy storage devices installed in TRMS and with the system success probability of at least 0.99%. Such design of the power supply system ensures the smallest weight with given reliability.

Structural diagram of power supply system with partial centralization is shown in Fig. 4.164. As can be seen from the figure, PVS for production of auxiliary voltages +5 V and − 5 V is installed inside the sealed TRM package. The storage can be placed inside and outside the TRM. In the latter case, it is necessary to ensure the minimum length of wires between TRM and the storage. All 18 power TRMs operate for the common bus. Uniform load distribution is ensured by paralleling devices installed in each TRM.

Fuse links are installed at the output of each TRM. Installation of fuses is due to the following circumstance.

Failure of power sources is often connected to breakdown and short-circuiting of the output capacitor. In the absence of special protective measures, it can cause failure of the entire power supply system. If fuses are installed, short circuits at the BVC output leads only to blowing of the corresponding fuse and automatic disconnection of the faulty BVC from the common bus (Table 4.14).

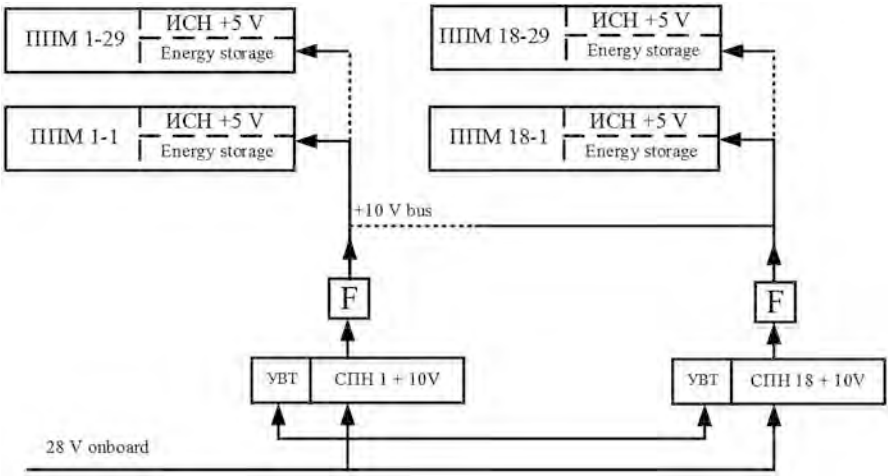

Fig. 4.164 Diagram of partially centralized power supply system of the antenna array curtain and distribution system

Table 4.14 Parameters of the described power supply systems

Power supply system type	Design weight of the system[b], kg	Reliability of the system
Centralized	29.8	0.996[a]
Decentralized	64.8	1
Partially centralized with passive redundancy	22.6	0.991

[a]This probability of system success cannot be achieve in practice due to low reliability of switching units required for redundancy of power sources
[b]Without the weight of memory storage devices

It must be noted that a centralized power supply system has good weight and dimensional characteristics, but is difficult to implement due to low reliability of switching devices required for redundancy of power sources; a decentralized system ensures maximum reliability of the AESA power supply system, but at the same time has the worst values of weight and dimensions.

Partially decentralized power supply system with passive redundancy has the best mass-dimensional characteristics while ensuring the given reliability. The main problem associated with building of systems with passive redundancy is the necessity of balancing current load between sources. Therefore, the best option of power supply system for this AESA is partially decentralized power supply system with passive redundancy. Such system has the smallest weight while ensuring the given reliability. Even though implementation of such power system is associated with problems of balancing current loads between sources, this task can be solved.

4.5 Components for Provision of Mechanical Positioning of Antenna Systems of Radars and Radio Communication

Even though radar systems with phased arrays make it possible to perform electronic scanning of space, the range of movement of the beam remains limited as a result of the structural design. Moreover, radar characteristics are significantly reduced at boundary angles. Therefore, in accordance with the required sector of view, developers of such systems are often forced to use mechanical systems of orientation of the antenna plane in space.

Depending on the tasks, positioning systems shall conform to various requirements in terms of technical characteristics; however, two basic principles can be identified that are practically important for any such system: exact determination of the relative position (angle in relation to a certain axis) of the antenna at each moment of time and the range of possible variation of this angle.

Let us consider only two main types of devices designed to solve such tasks – position sensors (encoders) and rotary junctions ensuring combined antenna rotation

angles of up to 360° (continuous full rotation) and exact finding of the current value of rotation angle. The material is based on technical data of widely used components of leading companies of this field – Netzer (Israel) and Spinner (Germany) designed for precision positioning of the antenna system and provision of its observation within the required range of angles.

4.5.1 Position Sensors (Encoders)

Netzer Precision Motion Sensors Ltd. (Israel) is one of the main leaders in designing and manufacturing such products for radar sets and radio communication systems. This company, which was founded in 1998, engages in development, production and supplies of efficient electrical sensors of absolute angular and linear movements (Fig. 4.165) based on the patented solution Electric Encoder [58–70].

Widely known patented solution Electric Encoder is a contactless technology of measurement of angular and linear position based on periodic change of the electrical field in case of change in the rotor position, which helps achieve a number of advantages as compared to optical and magnetic sensors. Simple and reliable design, high accuracy, low inertial characteristics, low profile height (less than 10 mm), high degree of protection from condensate and dirt, immunity to electromagnetic interferences, low power consumption and high degree of adaptability to customer requirements – here are only several advantages that have made Netzer sensor popular across the globe. Sensors designed for heavy duty operation conditions are successfully used in such fields as:

- remotely controlled weapon systems;
- avionics, aerospace robotics and drive mechanisms;
- panoramic installations of video surveillance and aiming;
- industrial equipment and medical devices;
- medical products, geophysical devices;
- renewable power sources.

Fig. 4.165 Netzer products

Another important advantage of rotating Netzer sensors is the possibility of individual calibration within the device for compensation of radial beat and misalignment with recording of calibration data in the nonvolatile memory of the sensor.

Netzer capacitance sensors are high-precision capacitance-type angular sensors (AS) including coarse and fine channels of angle measurement. Rotary part of the AS is a dielectric toothed disc (Fig. 4.166a) with two sets of teeth (poles) for fine and coarse channels. Stator part contains two boards with fixed AS electrodes. The bottom board contains two sets of radially arranged electrodes for the fine and coarse channels, the top board – two ring electrodes. The number of radial electrons is four times greater than the number of teeth for each channel. Each of the first four electrodes is connected to each following fourth electrode, thus forming four sets of electrodes for each of the two channels.

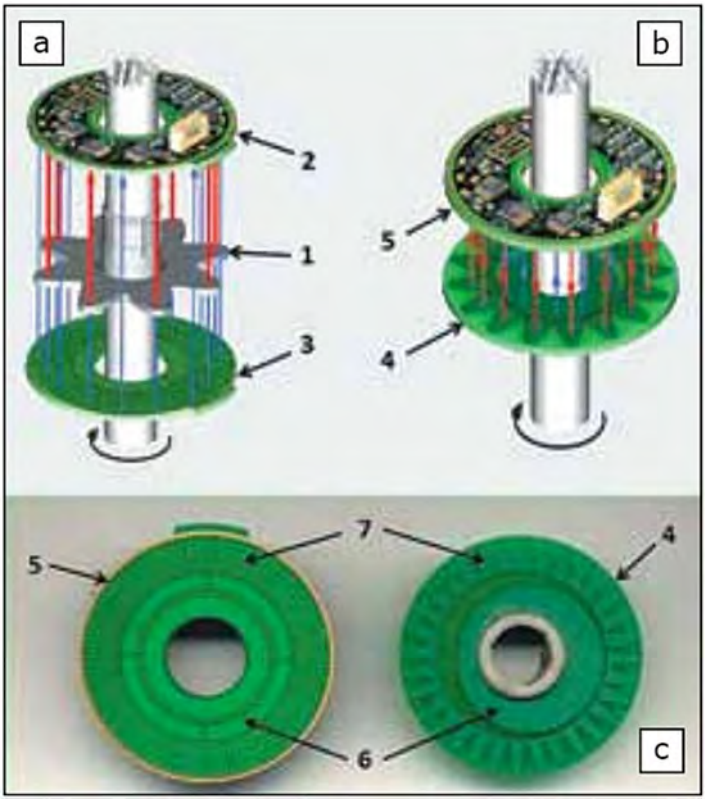

Fig. 4.166 Netzer angular sensor design options: (**a**) with dielectric rotor; (**b**, **c**) with rotor combined with bottom board: 1. dielectric rotor; 2. top plate with electronics; 3. bottom plate; 4. rotor combined with bottom plate; 5. top plate with electronics; 6, 7. electrodes of coarse and fine channels respectively

Rotation of the rotor changes combination of open fixed electrodes and electrodes covered with dielectric teeth, as well as the degree of their coverage, which causes a change in the electrical field between electrodes of the top and bottom plates. Electrical field changes are measured by the electronics installed on the upper board, which forms four analog output signals of direct current (two for each channel) proportional to sine and cosine of the rotation angle. Absolute rotor angle is calculated based on the combination of the obtained signal values.

The second widely used design option is shown in Fig. 4.166c. The stator part here is presented by the upper plate; the lower plate with tooth-shaped electrodes performs the function of the rotor part. The sensor operates according to similar principle, except for the fact that variations in the electrical field during rotor rotations occur due to changes in the electrode coverage area on top and bottom plates.

Depending on the rotor angle, output analog signals change according to the sine law. One rotation of the rotor includes a certain number of electric cycles of coarse M and fine N channels equal to the number of rotor teeth (poles) in fine and coarse channels respectively. For example, Fig. 4.166 shows the case where $M = 1$, and $N = 8$. It is obvious that one pair of values of output signals of the fine channel can correspond to eight values of angles; therefore, a pair of signals from the coarse channel is used to eliminate ambiguity. As a rule, the number of electrical signals in the coarse channel M is within 1–7, and the number of signals in the fine channel N – within 16–128. If L4 is greater than 1, indeterminedness appears once again, which is eliminated by choosing such M and N values that do not have a common denominator. Therefore, any rotor angle will correspond to a unique combination of signals of coarse and fine channels (Fig. 4.167).

In practice, the coarse channel is only used during activation of the AS for determination of the initial position of the rotary part; after that, angular position is determined by increment of signals in the fine channel. The user can select between the analog output sin/cos, which requires additional post-processing for determination of the absolute angle, and digital outputs SS1 and AqB + I providing information about the absolute angle and angle increment respectively.

AS resolution depends on the number of electrical cycles of the fine channel N (and, subsequently, on the number of rotor teeth) and capacity of the ADCs (L), to

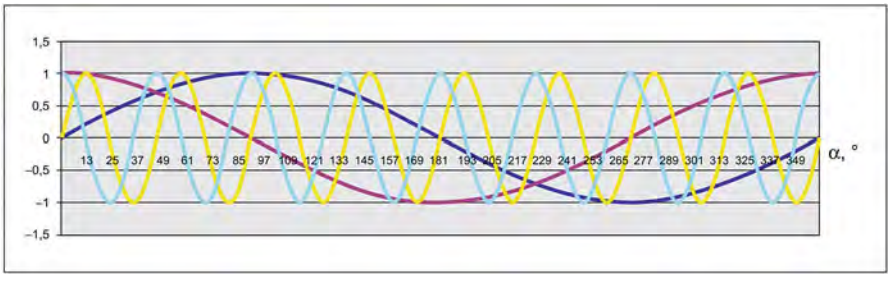

Fig. 4.167 Output signals of coarse and fine channels depending on the angular sensor rotor angle

which analog output signals of the sensor are supplied. Taking into account the fact that in case of change in the rotation angle, sinewave output signal passes through the ADC range 2 times per electrical cycle, resolution within one electrical cycle will amount to $L + \log_2(2)$ bits, and resolution across the entire range of angles from 0° to 360° will amount to $L + \log_2(2xN)$ bits. For example, for sensor DS-70 with N of 64 and with the use of 12-bit ADC, resolution will be equal to 19 bits.

From Table 4.15, we can see the trend for increase in resolution with an increase of outer diameter of sensors. This is explained by the fact that resolution can be improved by increasing either the capacity of the ADC (which is already limited by the intrinsic sensor noise level) or the number of teeth, which increases the outer diameter of the sensor.

Netzer product line is presented by the range of different configuration of angular sensors, sensors of linear displacement and the set of tuning equipment. Sensors can be produced with IP65 protection class (full protection from dust).

Netzer development kit (Fig. 4.168) includes a demonstration rotary table with installed angular sensor of the DS line, interface converter and software (Fig. 4.169 shows some of the functional abilities), which includes a set of tools for sensor testing and calibration.

Designers of antenna devices shall also pay attention to Netzer's experience in development of sensors for various operating conditions and environments. For example, angular sensor DL-25 (Fig. 4.170) has the IP65 protection level by default. Humanoid robot "Robonaut-2" (R2), designed for operation both inside and outside the International Space Station, includes 25 Netzer angle sensors which are made in radiation-resistant configuration designed for operation in outer space.

4.5.2 Rotary Junctions of Positioning Systems

For systems (Fig. 4.171) with phased antenna arrays designed for continuous circular surveillance of space, the problem of data transmission from moving part to fixed part is becoming one of the primary tasks.

These components have been successfully developed since the 1960s by Spinner Group (Germany). Today, the company is able to offer a wide range of such solutions to its potential customers:

1. coaxial transducers;
2. waveguide transducers;
3. optical transducers;
4. sliding contacts (transmission of low-voltage, digital and power signals);
5. rotary junctions for transmission of cooling liquids (this possibility is especially relevant for high-power AESAs, in particular – ship-based);
6. complex systems that make it possible to combine all previous types of transducers.

Table 4.15 Basic characteristics of Netzer angular sensors

Plastic package	DS-25	DS-37	DS-58(20)	DS-70	DS-90	DS-130	DS-247	–
Metal package	DM-25	DM37	DM-58(20)	DM-70	DM-90	DM-130	–	DL-25
Number of electrical cycles per 1 rotor rotation	16	16	32	64	64	64	128	16
Resolution (with 12-digit ADC), bits	17	17	18	19	19	19	20	17
Accuracy	<±0.015	<±0.015	<±0.01	<±0.01	<±0.01	<±0.01	<0.006	<0.04
Limit operating speed, rpm	3000	1500	750				375	750
Measurement range	360° – full rotation							
Total weight (plastic package), g	4	10	36	50	50	65	665	25
Outer diameter/inner diameter/height, mm	25/6/7	37/10/8	58/20/10	70/30/10	90/50/10	130/90/10	247/170/10	25/–/20, ~ 4 nm
Protection class	IP40 (by request – up to IP65)							IP65
Operating temperature range, °C	−40. . . + 85							
Relative humidity	<98% without condensation							
EMC	IEC 6100-6-2, IEC 6100-6-4							
Impact resistance	IEC 60068–2-27; 100 g 11 ms							
Vibration resistance	IEC 60068–2-6; 20 g within the range of 10–2000 Hz							
Supply voltage, V	+4.6. . .5.5							
Power consumption, mA	10 (analog), 160 (digital)							180

Fig. 4.168 Netzer development kit

Each rotating transducer, as a rule, is a custom product with individual functions and specific characteristics. Therefore, we will only provide several examples of the solutions already implemented by this company and describe general possibilities of developing new ones (Table 4.16).

Such solution as optical rotation transitions shall be mentioned separately (Fig. 4.172). According to the modern trend, developers try to perform conversion of analog signals from air into digital code at the rotary part and ensure transmission of information to the centralized processing unit via optic fiber line. It helps achieve a number of advantages as compared to traditional coaxial or waveguide transmission lines:

1. Reduction of dimensions of the rotary junction; e.g., 12-channel optical junction BN 54 9582 has the following dimensions: length of 118.2 m and outer diameter of only 60 mm.
2. For applications where relatively long-range transmission of the signal from the antenna system is required (ship equipment, aviation, equipment of air field observation, etc.), the use of optic fiber lines makes it possible to perform such transmission almost without negative consequences, while the use of coaxial or waveguide lines leads to significant limitations due to losses in the transmission lines. Improvement of electromagnetic compatibility of such transmission line in terms of electromagnetic field emission and noise immunity is an important factor.
3. Signal transmission in the digital form excludes the possibility of its distortion in the line and significantly improves its noise immunity. Spinner engineers employ the technology of transmission of the optical stream through the rotary element by using the Dove prism and reduction gear (Fig. 4.173). During rotation of the

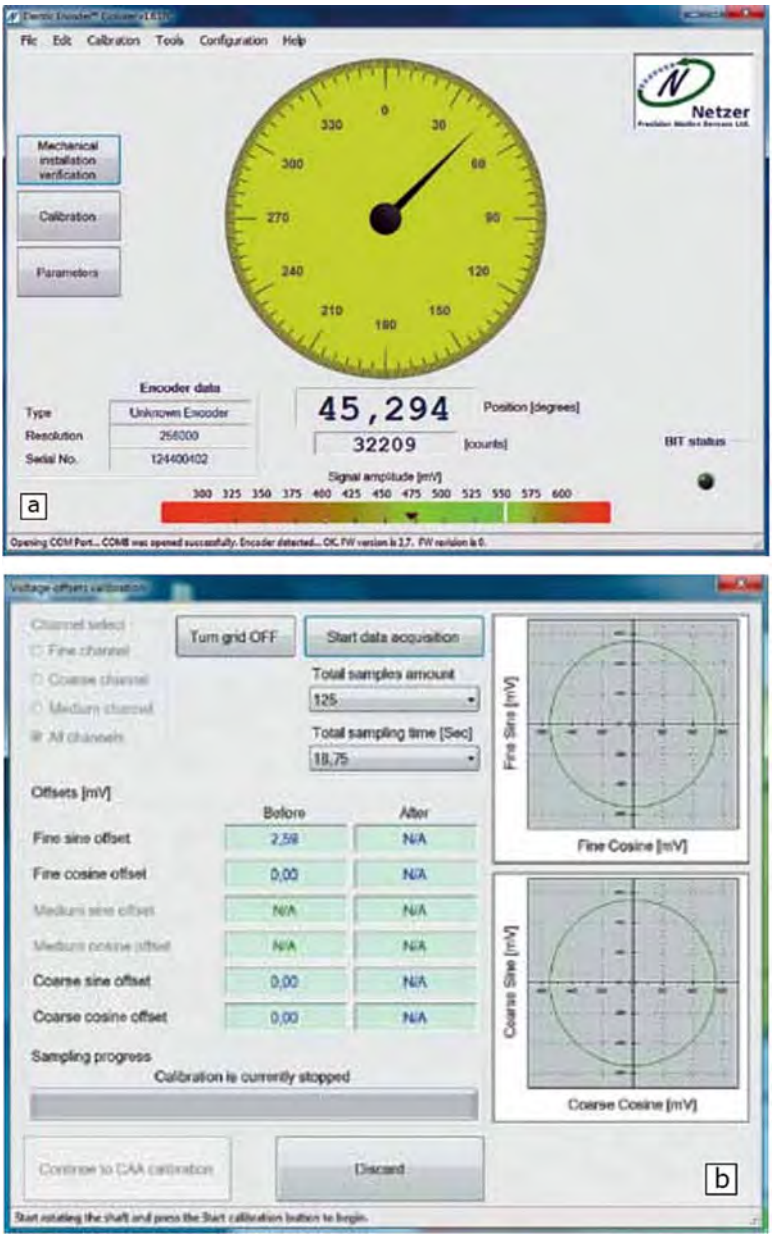

Fig. 4.169 Software equipment of Netzer development kit. (**a**) main window; (**b**) calibration window; (**c**) output signal analysis window

Fig. 4.170 Netzer DL-25 angular sensor with IP65 protection class

Fig. 4.171 Examples of application of rotating antenna systems

Table 4.16 Examples of solutions implemented by Spinner for AESA models of European and American origin

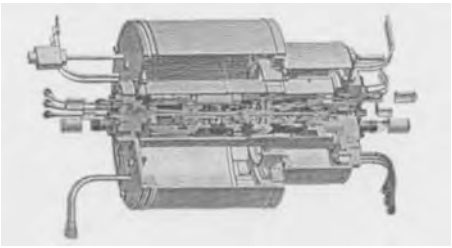	3 channels of HF signals: CH1:9–10 GHz; CH2, CH3: 1–1.1 GHz As well as 18 channels for transmission of control and power supply signals
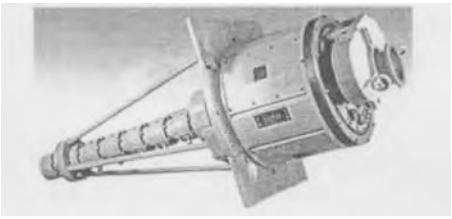	9 channels of HF signals: CH1:2.85–3.35 GHz (1500 kW/20 kW); CH2, CH3:2.85–3.35 GHz (20 kW/200 W); CH4-CH7:2.85–3.35 GHz (10 kW/100 W); CH8, CH9:1–1.15 GHz (10 kW/70 W) As well as 51 channels for transmission of control and power supply signals
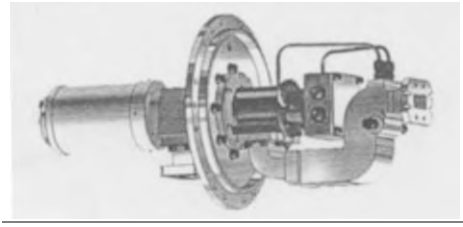	3 channels of HF signals: CH1:X-range (1500 kW/20 kW); CH2, CH3:L-range (20 kW/200 W)

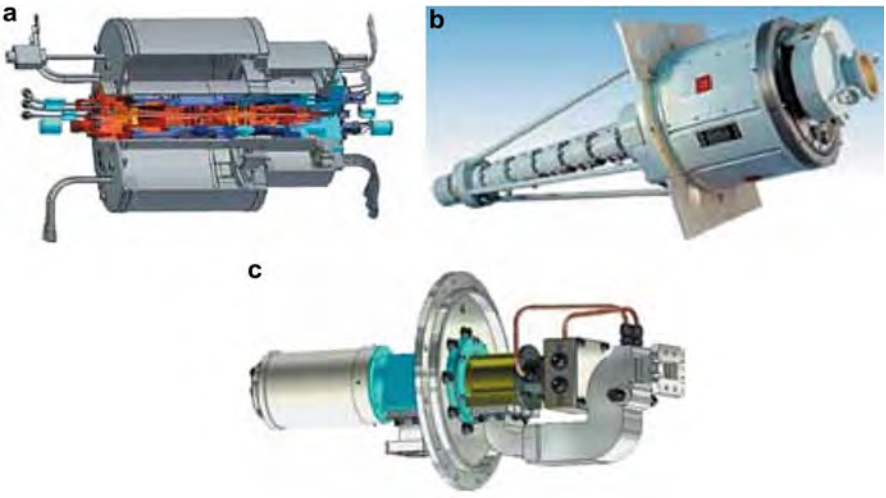

Fig. 4.172 Multi-channel rotating joint for transmission of optical signals: (**a**) appearance; (**b**) design

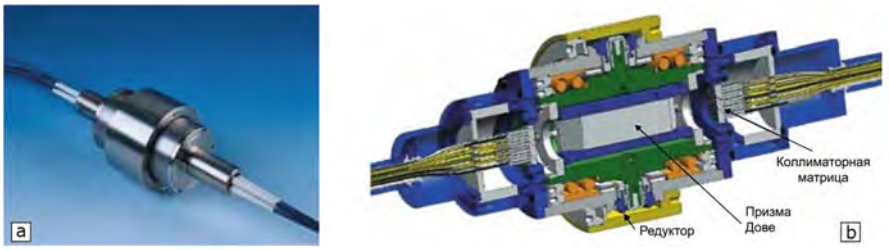

Fig. 4.173 Beam passing through Dove prism

Table 4.17 General characteristics of optical rotating junctions by Spinner

Parameter	Value
Number of channels	1–42
Wavelength, nm	850, 1310, 1550,
	Single- or multi-mode modes
Types of input/output connectors	FC/PC, FC/APC, ST/PC, SC/PC,
	SC/APC, LC/PC, LC/APC,
	E-200/PC, E-2000/APC,FSMA
Return loss for reflection, dB	55
Inserted losses for passage, dB	1
Deviation of inserted losses during rotation, dB	0.5
Maximum rotation speed, rpm	2000
Guaranteed service life, rotations	200 mln

Dove prism, image rotation angle is doubled, which helps ensure any required direction of image rotation. Therefore, the use of the reduction gear made it possible to achieve exact positioning of beams in the responding part of the junction and the possibility of implementing up to 42 channels per one rotary junction (Table 4.17).

4.6 Condition and Prospects of Development of Antenna Devices for Radars and Communication Means

4.6.1 Analysis of the Current State of Development of Antenna Devices in Radar Sets

The most important factors influencing consistent development of modern radar systems include correct determination of the technical implementation and substantiation of the main technical requirements of systems. Creation of such technology will help ensure effective functioning in difficult condition of electronic countermeasures. The basis for the successful implementation of the radar technology of the

future is the presence of an advanced scientific and technical base. The achievements of the last 50 years in this field made it possible not only to create brand new types of radar equipment, but also led to creation of new forms and methods of application of such systems [71–74].

At the same time, it should be noted that brand new technical characteristics of radar systems of any purpose are achieved, first of all, due to optimal design and engineering of antennas with transmitting and receiving devices accompanied by more advanced space-time signal processing based on modern computer equipment [75].

Let us consider the most important directions of development and improvement of antenna systems and separate functional devices of radar equipment.

It is generally recognized that all modern achievements in technology of antennas and microwave devices are based on the latest developments in electronics. Brand new characteristics of radars of any purpose are usually achieved by natural merging of the antenna with transmitting and receiving devices and the system of time and space processing of signals. An inevitable increase in the number of simultaneously operating radar stations already leads to extreme saturation of the surrounding space by various radio signals, which complicates the problem of electromagnetic compatibility of these systems. Antenna systems capable of adapting to environment are created for this purpose [76–79].

It can be stated that the common problem in development of highly efficient antenna and functional SHF devices is the development of new methods and means of their creation and modernization based both on advanced developments in the field of electronics, semiconductor equipment, technical cybernetics, coherent radio-optics and nanotechnologies, as well as on modern calculation equipment, which helps ensure development of advanced highly effective radar systems of various basing and purpose.

Today, antenna devices are already widely used in various fields of national economy – radiolocation, communication, radio control, automatic landing of aircraft vehicles, EW, targeting and control systems of high-precision weapons, radio telemetry, etc.

As noted above, high-directional scanning antennas are the most popular type today. Scanning allows for efficient observation of space, operative tracking of various mobile objects and determination of their angular coordinates. Replacement of low-directional (or non-directional) antennas in used radars with modern high-directional scanning antenna helps not only to get an advantage due to improvement of antenna gain, but also to reduce mutual effects of simultaneously operating systems in a number of cases. This can allow for significant improvement of interference immunity, operational security and other important characteristics of radar stations.

The use of modern technologies for phased antenna arrays (PAA) to build scanning high-directional scanning antennas helps ensure high speed observation and contributes to an increase in the volume of information obtained about the actual

distribution of sources of radiation (reflection) of electromagnetic waves in space [80–100]. The progress in the field of microwave technology helps not only to create controlled phase space in the antenna array (i.e. implement electronic scanning, but also preprocess the received information (add the fields, convert the frequencies, amplify the signal, etc.) directly in the SHF path of the antenna.

In [80], mathematical expressions are presented, which make it possible to calculate the values of mutual resistances of the antenna array of cruciform radiators. The feature of the suggested method consists in taking into account the end thickness of the vibrator, as well as identification of the specifics of the Green's function, which makes it possible to create effective calculation algorithms. In addition, results of numerical stuides of the effect of not taking into account electrodynamical effects on the SNR value of adaptive antenna array with exclusion of the useful signal during the stage of formation of the vector of weighting factors.

For example, [81] contains a study of a small-sized ultra-wideband antenna designed for operation as part of two-polarization antenna array within the range of 3.1...10.6 GHz. This antenna is a combination of electrical and magnetic radiators printed on 20 × 30 mm dielectric plate. The antenna was studied in the time domain as an independent radiator as well as a part of antenna array.

Further improvement of important characteristics of radars with PAA, such as resolution, speed of operation, throughput capacity, range, noise immunity, etc. can be ensured by improving methods of space-time processing of signals radiated and received by the antenna. In this case, the antenna becomes the primary processing link and largely determines main characteristics of the radar. Depending on the purpose of the radar station and requirements for its characteristics, antennas with different methods of signal information processing are developed. The most commonly used antennas in advanced radar systems are antennas with signal processing: self-tuning, with synthesized aperture (SAR, ISAR), with timing modulation of parameters, with digital processing, with analog space-time processing by coherent optics method, etc. With exploration of the range of shorter waves, holographic methods of transformation of received electromagnetic waves are gaining popularity in antenna systems.

Currently, active phased antenna arrays (active electronically scanned arrays, AESA), which are combinations of small-sized radar transceivers (active elements), are widely used in radar location [101].

Each element of such array contains, for example, a dipole antenna, a reception/transmit switch, a power amplifier, a mixer, an intermediate frequency amplifier, phase shifters and control circuits. Basic units of a modern radar (radar set) are a ***synchronizer, a high-frequency distribution device, a beam control computer, data converters*** and an ***indicator***. Active elements help reduce power losses and increase sensitivity of devices. Moreover, all elements of the beam control device during search and tracking can operate at the optimal working frequency.

Further development of radar stations with active arrays in the nearest future will make it possible to create surface arrays that can be placed along the front edge of wing of the plane (winged missile), clearing the fuselage nose for other sensors. Such PAAs are often referred to as *conforming*.

In latest AESA modifications, further development of reception of pulses with arbitrary polarization is used.

For example, [102] presents the results of studies of an ultra-wideband receiving dualpolarized antenna array designed for study of the polarization structure of electromagnetic pulses with nano- and subnanosecond duration. Each element of the antenna array consists of two crossed dipoles, the arms of which are loaded on amplifiers based on field transistors. Presented are the results of experimental studies of directivity pattern, operating length and shape of recorded pulses, studies of noise characteristics and workability of the antenna under the effect of high-power electromagnetic pulses.

At the moment of publication of this book, many various designs of antenna systems are in development, the most advanced of which are presented in the general system of classification of modern antenna based on the signal processing method [76, 79].

Therefore, antennas used in radars have turned into extremely complex devices with dozens of thousands of radiators, active elements and radiators, which are controlled by powerful means of computing equipment.

4.6.2 Main Directions of Development of Antenna Systems of Radar Sets

The main direction of development of radar antenna systems consists in ***increasing their efficiency based on: introduction of advanced technologies with synthesized aperture, with time modulation of parameters, with digital processing, with analog space-time processing; use of the methods of coherent optics, as well as development of phased antenna arrays with dozens of thousands of radiators, active elements and phase shifters with controls based on modern computing equipment with various power levels.***

Depending on the radar basing (space, aerial or ground), corresponding methodologies of development and improvement of antenna devices are used for creation of antenna systems.

First of all, it is necessary to mention rapid development of technology of the so-called large space antennas (LSA) deployed (or mounted) in near-Earth orbits, designed for operation in radiotechnical space-based complexes, where radar location systems are extremely widely used. Table 4.18 contains the list of only the main national economy and military tasks solved with the help of LSAs [103–107].

Development of the methodology for development and improvement of space-based antenna devices is associated with solving scientific and technical tasks of creation of geostationary space antennas (SA) and low-orbit SAs, including large space antennas (LSAs) deployed or mounted in low Earth orbits.

These antenna devices shall meet the following requirements: *transportability and small volume in folded state; small weight; high operational characteristics;*

Table 4.18 Space-based radiotechnical systems using large space antennas and adaptive antennas

National economy tasks:	Military tasks:
Connected ESVs in geostationary orbits and low-orbit ESVs;	Military satellite communication systems;
Side-looking radars, radar systems with synthesized aperture, radiometric and interferometric systems;	Reconnaissance (radio mapping);
	Radiotechnical intelligence;
	Navigation systems;
GPS and GLONASS satellite navigation systems;	Aerospace control;
Weather satellites and analysis of the atmospheric condition;	Satellite means of electronic warfare (EW);
Geological ESVs for sub-surface probing, analysis and prediction of the seismic situation;	Satellite means of electronic countermeasures (ECM);
Solar-space power stations;	Means of missile and air defense;
Scientific studies of Earth, planets and aerospace	Space electromagnetic weapons

rigidity of the structure in operating state; reliability of triggering of deployment mechanisms; preservation of the set geometry after deployment; low cost and simplicity of production; stability of adjustment.

Depending on the functional purpose of radar systems, it is necessary to provide for creation of antennas in the following constructive species: *with deployable mirror aperture of large diameter (dozens and hundreds of meters), with support platform and installed elements with adjustable transmission coefficients in partial channels (phased antenna array) with combined system using both these principles.*

Methodology of development and improvement ***of air-based antenna devices*** for advanced radars (detection and guidance radars), where there are strict limitations in terms of weight and longitudinal dimensions of antenna aperture are based on solving tasks of development of PAAs and AESAs ensuring high aperture efficiency with low level of side lobes of the directivity pattern and at relatively high values of pulse power per one PAA channel.

Finally, creation of ***antenna devices of ground-based radars*** is currently performed in the direction of implementation of the following science and technology tasks:

- creation of active PAAs (flat and on complex surfaces) for the ranges of millimeter and centimeter waves;
- modernization of currently used designs of high-directivity antennas with electrical scanning within the wide sector of frequency ranges of 60. . .100 GHz;
- development of multi-frequency (with coverage of at least an octave) and wideband antennas with electrical scanning within a wide range of angles for highly informative systems with maximum noise immunity (use of ultra-wideband and wideband signals, frequency tuning within a wide range, polarization selection and adaptation of the diagram depending on the target and interference environment).

4.6.3 Ways of Solving Technical Problems of Development of Advanced Antenna Systems of Radar Sets

General directions of the ways of solving technical problems of development of advanced antenna systems can be formulated as follows.

4.6.3.1 Technical Solutions for the Direction of Development of Large Space Antennas

The following main directions of development of technical solutions in the field of creation of large space antennas (*LSA)* can be formulated based on the analysis of special literature:

- creation of rigid thermally stable structures that preserve the given surface shape and antenna geometry during extended time of operation;
- development of new and optimization of known algorithmic solutions and technical options of hardware implementation of the tasks of stabilizing characteristics of high-precision LSA beam guidance in the conditions of factors of threshold thermal deformations and partial failures of separate elements of the antenna system;
- development of methods for constructing large-sized sparse non-equidistant phased arrays with wide-angle scanning for civil and military communication systems;
- exploration of the millimeter range of radiowaves in space antenna systems;
- development and optimization of specific variants of SAR and ISAR antennas for provision of tasks of Earth remote sensing with high resolution (0.1...0.3 m) and recording of stereo images.

As demonstrated by the analysis of modern state and prospects of development of this science and technology direction, development of advanced antenna devices of radar stations will be based on:

- semiconductor strip and microstrip phase shifters for frequency ranges up to 30...40 GHz;
- mirrors with locally adjustable phase of the reflection coefficient for mirror high-directivity electrically scanned antennas within a wide sector of angles operating within frequency ranges up to 100 GHz. Mirrors for single-band antennas with relative low mirror radiation power are designed on the basis of microstrip vibratory structures with semiconductor switches. For multi-range wideband antennas emitting high powers in the transmission mode, the mirrors are made using ferrite heterogeneously magnetized plates;

- lenses with electrically controlled refraction index for electrical beam scanning within frequency ranges of 60. . .140 GHz;
- wideband (ultra-wideband) strip and microstrip switches;
- antennas with electrical dimensions of about 0.01. . .0.005 of the wavelength (small-sized active antennas) for communication and navigation systems, including cellular communication.

4.6.3.2 Main Advanced Directions of Studies for Creation of Highly Efficient Antennas with Signal Processing

The main directions of studies and developments for creation of advances antenna system of various purpose, classification, design and fields of application are shown in Fig. 4.174.

Let us consider and comment on certain independent directions of these studies and developments.

Multi-element and multi-beam radar antenna system:

- multi-frequency antennas with synthesized aperture and circular polarization for ECVs ensuring higher resolution and data gathering speed, more flexible changes in the image formation modes and the possibility of changing swath width;
- slot antenna arrays with equiphase voltage distribution across the slots and with matched input;
- microstrip antenna systems for installation on missiles, planes and other objects without impairing aerodynamical qualities of these objects due to their small weight, low silhouette, conformity and cheapness;
- antenna systems with wideband PAAs with pass bands of at least two octaves of the directivity pattern and maximum dimensions equal to 0.2 of the maximum operating wavelength, as a rule, for multi-beam radars.

Electrically scanned antenna systems:

- PAAs with electronic scanning of the directivity pattern based on application of solid-state active scanners, where transceiver and radiating modules are based on

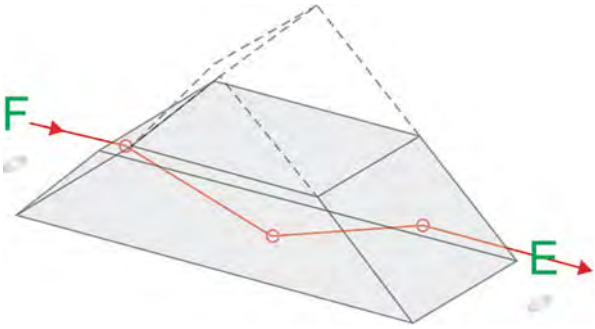

Fig. 4.174 Structural diagram of the main directions of developments of advanced antennas in the generally accepted classification system

the technology of production of monolithic microwave ICs in the millimeter range and are the main element of radars of military purpose installed in ground-based and airplane-based systems;
- antenna arrays with electronical scanning and phase correction for fields of application in passive homing heads for attacking emitting radars of the enemy.

Antenna systems of aperture synthesis:

- SARs for high-resolution radiotechnical systems for remote probing, mapping, detection of ground and water objects in conditions of impaired visibility from aircrafts (air or space vehicles) by coherent addition of images obtained in SAR during repeated observation and compression of signal lengths [108–111].

Radio-optical antenna systems:

- based on the use of optical, acoustic-optical spectrum analyzers for processing of radio signals, based on methods with spatial-panoramic or spatio-temporal observation, as well as with spatial interference rejection and focusing in the near field [112–116].

Adaptive antenna systems:

- PAA with signal processing and increased noise immunity (adaptation) under the effect of external sources of active interference, the function of which provides application of: maximization of the signal-to-noise ratio, minimization of the root-mean-square deviation, minimization of the accumulated power of noises and interference, self-focusing, combination of criteria, etc. (are widely applied in radars for detection and tracking of ground objects in conditions of natural and organized interferences);
- systems consisting of several PAAs and allowing formation of the beam directed towards the signal source and ensuring suppression of background interferences; adaptation of antenna parameters is performed by forming weighting factors at the demultiplexor input with the help of of a system of filter rows (with switched capacities) controlled by digital processor with pipeline signal processing (usually installed on planes and satellites and used in implementation of underwater communication devices).

Active antenna systems:

- based on PAAs with active amplifiers;
- with the possibility of simultaneous generation of several independent beams for irradiation of given space regions without irradiating other regions;
- with directivity pattern scanning;
- with PAA thermal adjustment system with alloyed elements fitted with memory storage, which simultaneously perform functions of sensors and actuators, increasing reliability of the system and reducing its weight and cost efficiency.

Digital antenna systems with high-speed signal processing:

- two-antenna (two-port) and three-antenna (three-port) SARs ensuring detection of small-sized objects, measurement of their radial speeds and angular coordinates by processing of echo signals;
- with PAAs, in which digitalization and adaptive formation of beams are performed at the level of sub-arrays.

References

1. Geiryaev, G. (2014). Main parameters and types of antennas. *Electronic Components*, (12).
2. Khabarov, A. (2014). Small-sized antenna WIMAX/WLAN. *Electronic Components*, (8), 22–23.
3. Xu, Y., Jiao, Y. C., & Luan, Y. C. (2012). Compact CPW-fed printed monopole antenna with triple-band characteristics for WLAN/WiMAX applications. *Electronics Letters, 48*, 1519–1520.
4. Hua, M. J., Wang, P., Zheng, Y., & Yuan, S. L. (2013). Compact tri-band CPW-fed antenna for WLAN/WiMAX applications. *Electronics Letters, 49*, 1118–1119.
5. Wu, T., Shi, X. W., Li, P., & Bai, H. (2013). Triband microstrip-fed monopole antenna with dual-polarization characteristics for WLAN and WiMAX applications. *Electronics Letters, 49*.
6. Kumar, R. (2014). Broadband microstrip antenna. *Electronic Components*, (8), 24–26.
7. Panin, N., & Wideband, S. H. F. (2014). Travelling wave antenna. *Electronic Components*, (8), 27–21.
8. MATLAB, Ver. R. (2011a). The MathWorks Inc.
9. CST Studio Suite 2011, Ver. 2011. CST – Computer Simulation Technology, AG.
10. Cadiihon, B., Pecastaing, L., Reess, T., Silvestre de Ferron, A., Pignolet, P., Vauchamp, S., Andrieu, J., & Lalande, M. (2010, October). Fligh pulsed power sources for broadband radiation. *IEEE Transactions on Piasma Science, 38*(10).
11. Baum, C. E.. (1989, November). Radiation of impulse-like transient fields. *Sensor and Simulation Notes*, Note 321.
12. Farr, E. G., Sower, G. D., & Buchenaur, C. J. (1994, October). Design Considerations for ultra-wideband, high-voltage baluns. *Sensor and Simulation Notes*, Note 371.
13. Cadiihon, B., Pecastaing, L., Vauchamp, S., Andrieu, J., Bertrand, V., & Lalande, M. (2009, October). Improvement of an ultra-wideband antenna for high-power transient applications, Microwaves, Antennas & Propagation, IET., *3*(7).
14. EG&G, Division of URS Corporation. ADC D-Dot (Free field).
15. Tedjini, S., & Lemaitre-Auger, P. (2014). Man-portable antennas. *Electronic Components*, (10), 22–23.
16. Mazurenko, E. (2014). Multiband patch antenna. *Electronic Components*, (5), 27–29.
17. http://arxiv.org/ftp/arxiv/papers/1002/1002.3337.pdf
18. Yaol, Z., Lil, M., Wang, D., & Chen Lin, L. (2014). Microstrip antenna on thin substrate. *Electronic Components*, (5), 30–32.
19. http://mwrf.com/passive-components/microstrip-antenna-maintains-low-profile
20. Vendik, O., Parnes, M., Korolkov, V., & Shifman, R. (2007). Flat reflecting printed antenna. *Wireless Technologies*, (1), 26–29.
21. Menzel, W., Pilz, D., & Al-Tikriti, M. (2002, June). MM-wave folded reflector antennas with high gain, low loss, and low profile. *IEEE Antennas and Propagation Magazine, 44*(3), 24–29.
22. Tsai, F. E., & BialkowskiM, E. (2003, October). Designing a 161-element ku-band microstrip reflectarray of variable size patches using an equivalent unit cell waveguide approach. *IEEE Transactions on Antennas and Propagation, 51*, 2953–2962.

23. Parnes, M. . D., Korolkov, V. D., Gashinova, M. S., Kolmakov, I. A., Kolmakov, Y. A., & Vendik, O. G. (2005). Planar printed mirror antenna. *News of Higher Educational Institutions: Radioelectronics*, (1).
24. Gashinova, M. S., & Vendik, O. G. (2006). Modeling of low-profile reflectarray antenna. In *Proceedings of Progress In Electromagnetics Research Symposium, PIERS 2006*, March 26–29 2006, Cambridge, USA.
25. VFH Antennas. (1977). Ed. by G.Z. Aizenberg. Part 2. Moscow: Communication.
26. Vendik, O. G., & Parnes, M. D. (2002). *Electrically scanned antennas* (Introduction to theory). Ed. by Corresponding Member of RAS Bahrah L. D. M.L Science Press.
27. Maoven, V., Jinzhong, K., & Wenzhuang, P. (2015). Three-vand slot antenna. *Electronic Components*, (1), 26–27.
28. Brzezina, G., Amaya, R., Petosa, A., & Roy, L. (2015). 60 GHz Vivaldi antenna. *Electronic Components*, (1), 28–30.
29. Kurushin, A., Lavretskiy, E., & Chadov, S. (2014). Calculation of mirror parabolic antennas using modern SHF CAD systems. *Electronics: NTB, 3*(00134), 126–131.
30. Baars, J. (2007). *The paraboloidal reflector antenna in radio astronomy and communication*. New York: Springer.
31. Henl, H., Maue, A., & Westphal, K. (1964). *Diffraction theory*. Moscow.
32. Ufimtsev, P. Y. (1962). *Edge wave method in physical diffraction theory*. Soviet Radio, Moscow.
33. Shore, R. A., & Yaghjian, A. D. (1988). Incremental diffraction coefficients for planar surfaces. *IEEE Transactions on Antennas and Propagation, 36*(1), 55–70.
34. GRASP – Program for Designing Mirror Antennas, -ticra.com.
35. Mirror Program (developers: Chadov S.E., Kondratiev A.S., Lavretskiy E.I.).
36. feko.com.
37. Parkinson, I. R., & Mehler, M. (1986). Convergence of PO integrals by Ludwig technique. *Electronics Letters, 22*(22), 1161–1162.
38. Ludwig, A. C. (1973, Janurary). The definition of cross polarization. *IEEE Transactions on Antennas and Propagation, AP-21*, 116–119.
39. STV-2.4-11 AUM offset mirror antenna by JSC “Almet”, description. Ulyanovsk.
40. Kurushin, A., Lavretskiy, E., & Dergachev, S. (2015). Modeling of mirror antenna with the help of HFSS ANSYS. *Modern Electronics*, (2), 58–61.
41. Vasilyev, E. L. (1987). *Excitation of solids of rotation*. Moscow: Radio and Communication. 272 p.
42. Sazonov, D. M., & Markov, G. T. (1977). *Antennas*. Moscow: Energy. 528 p.
43. www.orcada.ru
44. STV-2.4-1.1 AUM offset mirror antenna by JSC “AlMet”. Ulyanovsk, www.supral.ru
45. Vyugin, P., & Kurushin, A. (2014). Wideband log-spiral antenna with circular polarization. *Modern Electronics*, (8), 74–77.
46. Dyson, J. D. (1958, July 10). *The unidirectional equiangular spiral antenna*. Antenna laboratory technician report, № 33. Ohio: University of Illinois.
47. www.ets-lindgren.com. Manufacturer of conical log-spiral antennas.
48. www.ansys.com. Developer of the HFSS ANSYS System.
49. Zhen-Yu Zhang, Yong-Xin Guo, Ong, L. C., & Chia, M. Y. W. (2005). A new planar Marchand Baiun. *IEEE Transactions on MTT-53*, (4).
50. Bankov, S. E., Gutsait, E. M., & Kurushin, A. L. (2012). *Solving optical and microwave tasks using HFSS*. Moscow: Orkada. 240 p.
51. Belous, A. I., Solodukha, V. A., & Shvedov, S. V. (2015). *Space electronics* (Vol. 2). Moscow: Tekhnosfera. 1184 p.
52. http://www.airbase.ru/hangar/equipment/radars/far/
53. Bratchikov L.I. et al. Active phased antenna arrays. Moscow. Radio Technology, 2004.

54. Integrated Microcircuits. (2000). *Microcircuits for pulse power sources and their application* (2nd ed.). Moscow: DODECA. 608 p, ISBN 5-87835-055-6.
55. Lukin, A. V. (1997). Distributed electric power supply systems. *Electronic Components*, (7).
56. Laszlo, B. (2003). *Paralleling power choosing and applying the best technique for load sharing*. Texas Instruments Incorporated, 2003 Power Seminar.
57. Kazenkov, D. (2004). Selection of the power source architecture. *Electronic Components*, (6).
58. Pavlov, S., & Ponomarev, Y. (2014). Components for ensuring mechanical positioning of antenna systems. *Components and Technologies*, (11).
59. Pat. US 6492911 Bl. Capacitive displacement encoder. Netzer Y.; Assignee: Netzer Motion Sensors Ltd.; Date of patent: December 10, 2002; Appl. No.: 09/294794; Filed: April 19, 1999.
60. Pat. US 6788220 B2. Multi-speed capacitive displacement encoder. Netzer Y.; Assignee: Netzer Motion Sensors Ltd.; Date of patent: September 7, 2004; Appl. No.: 10/282890; Filed: October 29, 2002.
61. Pat. US 7126495 B2. Linear electric encoder with facing transmitter and receiver. Netzer Y.; Assignee.
62. Sick Sensors Ltd.; Date of patent: October 24, 2006; Appl. No.: 10/822094; Filed: April 8, 2004.
63. Pat. US 8567229 B2. Method for calibrating a rotational angle sensor. Netzer Y.; Assignee: Sick Sensors Ltd.; Date of patent: October 29, 2013; Appl. No.: 12/907057; Filed: October 19, 2010
64. www.netzerprecision.com
65. www.bastion-karpenko.narod.ru
66. www.militaryrussia.ru
67. www.spinner-group.com
68. Pavlov, S., & Filippov, A. (2014). Phased antenna arrays. A review of component base for implementation of transceiver modules. *Components and Technologies*, (7).
69. Efremov, V. (2014). Component base for APAA – High-frequency connectors. *Components and Technologies*, (9).
70. Vorobyev, S. (2014). Selection of element base for secondary power supply systems of APAA transceiver modules. *Components and Technologies*, (10).
71. Bystrov, R. P., & Potapov, A. A. *Functional devices and element base of radar systems*. http://www.uran.donetsk.ua/~masters/2012/frt/zaitseva/library/article7.pdf
72. Bystrov, R. P., Kann, E. V., Sadykov, R. R., & Frolov, S. S. (2005). Analysis of modern methods of radar location and substantiation of directions of their further development. *Problems of Defense Technology, series 16*(3–4), 6–11.
73. Bystrov, R. P., Sokolov, A. V., & Chesnokov, Y. S. (2004). Methods of modern Russian radar location. *Weapons Politics Conversion*, (5), 36–40.
74. Bystrov, R. P., Kuznetsov, E. V., & Sokolov, A. V. (2004). Functional devices and element base of radio devices. *Weapons Politics Conversion*, (6), 30–35.
75. Akinshin, R. N., Bystrov, R. P., Kuznetsov, E. V., Mikhailov, D. Y., Sokolov, A. V., & Chesnokov, Y. S. (2005). Development of radioelectronics in radar location systems. *Achievements of Modern Radioelectronics*, (10), 24–58.
76. Akinshin, N. S., Rumyantsev, V. L., & Prtsiuk, S. V. (2000). *Polarization selection and recognition of radar signals*. Tula: Lidar. 310 p.
77. Vystavkin A. N., & Kovalenko A. G. et al. (2009, October 26–30). Superconductive Nanobolometers – Hot Electron-based sensors for extremely sensitive matrix radio meters of the terahertz frequency range. In *Proceedings of the 3rd All-Russian Science and Technology Conference (ARSTC) "Radar location and radio communication"* (pp. 378–381). V.A. Kotelnikov IRTE, RAS.

78. Khlopov, G. I. (1999). Coherent radar location in the millimeter range. In *Achievements of modern radioelectronics* (pp. 3–27).
79. Belotserkovskiy, G. B. (1962). *Antennas*. Moscow: Oborongiz. 492 p.
80. Zvezdina, Y. A., & Labunko, O. S. (2009, October, 26–30). Assessment of influence of mutual resistances of cross-shaped vibrators on the signal-to-noise+interference ratio in PAAs. In *Proceedings of the 3rd ARSTC "Radar location and radio communication"* (pp. 26–31). V.A. Kotelnikov IRTE, RAS.
81. Balzovskiy, E. V., Buyanov, Y. I., & Koshelev, V. I. (2009, October 26–30). Small-sized flat antenna as an element of an ultra-wideband double-polarization array. In *Proceedings of the 3rd ARSTC "Radar location and radio communication"* (pp. 77–82). V.A. Kotelnikov IRTE, RAS.
82. Krakhin, O. I., & Zenin, V. A. (2009, October 26–30). Thermal energy plant for PAAs. In *Proceedings of the 3rd ARSTC "Radar location and radio communication"* (pp. 749–751). V.A. Kotelnikov IRTE, RAS.
83. Mischenko, S. E., Makhov, D. S., & Starchenko, A.V. (2009, October 26–30). Method of antenna array synthesis based on requirements of directivity pattern shape and variation of current norm in the aperture. In *Proceedings of the 3rd ARSTC "Radar location and radio communication"* (pp. 100–103). V.A. Kotelnikov IRTE, RAS.
84. Prilutskiy, A. A. (2009, October, 26–30). Radiation from periodic system of waveguides with multi-layered magnetodielectric filling in cross-section. In *Proceedings of the 3rd ARSTC "Radar location and radio communication"* (pp. 58–61). V.A. Kotelnikov IRTE, RAS.
85. Christoph, H., & Jurgen, L. (1998). *The LightSAR X-band sensordesign and performance*. EUSAR'98: European conference on synthetic Apreture radar, Friedrichshafen, 25–27 May, 1998. Berlin/Offenbach: VDE, pp. 79–82.
86. Carande Richard, E. (2000). Adding value to next generation SAR data: A remote sensing business imperative. EUSAR 2000: 3rd European conference on synthetic aperture radar, Munich, 23–25 May, 2000. Berlin/Offenbach: VDE, c. 61.
87. Shanwei, L., Wenjun, G., Sichao, L., & Hainan, D. (1998). Beijing hangkong hangtian daxue xuebao. *Journal of Beijing University of Aeronautics and Astronautics, 24*(2), 133–136.
88. Uematsu Masahiro, Ojima Takashi, Takahashi Nobuharu, Goto Naohisa, Hirokawa Jiro, Ando Makoto. Slotted leaky waveguide array antenna: Pat. 5579019 USA, IPC 6 H 01 A 13/10/; Nippon Steel Corp., Naohisa Goto. No. 580787; Application date: December 29, 1995. Publication date: November 26, 1996. Priority dated 7.10.93, No. 5-276152 (Japan); IPC 343/771.
89. Loman, V. I., Ilyinov, M. D., & Gotsuliak, A. F. (1985). Microstrip antennas. *Foreign Radioelectronics*, (10), 99–115.
90. Menzel, W., & Wolff, I. (1979). Nachrichtenelektronik, № 1.
91. Dianzi xuebao. Acta Electron., 1996, 24, 6, p. 5-9.
92. Electronics Letters. (1996), 32, № 19, pp. 1741–1742.
93. Suckrow, S. (1998). Microstrip-Antennen. Funkschau, № 6, p. 67–68.
94. IEEE Proceedings – Microwaves, Antennas & Propagation. 1995-142, № 6, pp. 495–497.
95. Buyanov, Y. I., Bulbin, Y.V., Dirin, V. N., Supgko, V. P., Tschuikov V. D. (1998). Pat. 2111584 RF, IPC 6 H 01 Q 9/02/. Engineering and Radiophysical Center of Siberia Physical and Technical Institute, Dirin V.N. – No. 96123317/09. Application date: December 16, 1996. Publication date: May 20, 1998. Bull. no. 14.
96. Rau Richard, McClellan James H. Analytic models and postprocessing techniques for UWB SAR. IEEE Transactions on Aerospace and Electronic Systems, 2000, 36, 4, p. 1058–1074.
97. Ishkova, E. A., & Evsikov, M.V. (1998). *Antennas*, *1*, 36–42.
98. Lihoshi Akira, Tohya Ken-ichi; Honda Giken Kogyo K.K. Multibeam radar system: Pat. 5579010 USA, IPC 6 G 01 S 13/60/—No. 449822. Application date: May 24, 1995. Publication date: November 26, 1996. Priority 27.5.94, No. 6-137993 (Japan); NPC 342/70.

99. Anders, S., Raju, D., Norbert, G., Yanting, D., & Lawrence, C. (2000). Ultrawide-band synthetic aperture radar for detection of unexploded ordnance: Modeling and measurements. *IEEE Transactions on Antennas and Propagation, 48*(9), 1306–1315.
100. Sherwood William, J., Rodeffer Charles, E., & Rodeffer Mark, A. (1995). Winegard Co. Deployable satellite antenna for use on vehicles. Pat. 5528250 USA, IPC 6 H 01 Q 1/32/- No. 400333. Application date: March 3, 1995. Publication date: June 18, 1996; IPC 343/711.
101. Bystrov, R. P., Sadykov, R. R., & Sokolov, A. V. (2005). *Development of antenna systems for radiotechnical systems of various basing*. Radioelectronics (Electronic Version), RAS IRTE, p. 28.
102. Balzovskiy, E. V., Buyanov, Y. I., & Koshelev V. I. (2009, October 26–30). Active antenna array for reception of pulses with random polarization. In *Proceedings of the 3rd ARSTC "Radar location and radio communication"* (pp. 36–41). V.A. Kotelnikov IRTE, RAS.
103. Sherwood William, J., Rodeffer Charles, E., & Rodeffer Mark, A. (1995). Deployable satellite antenna for use on vehicles: Pat. 5528250 USA, IPC 6 H 01 Q 1/32/; Winegard Co. No. 400333. Application date: March 3, 1995. Publication date: June 18, 1996; IPC 343/711.
104. Tanaka Masato, Matsumoto Yasushi, Takahashi Takashi. Tsushin sogo kenkyujo kiho. Review of Communication Research, 1997, 43, 3, p. 417–426.
105. Matsumoto Yasushi, Kozono Shinichi. Tsushin sogo kenkyujo kiho. Review of Communication Research, 1997, 43, 3, p. 391–395.
106. Smith Bruce A. Large deployable antenna developed for Thuraya. Aviation Week and Space Technology, 1998, 148,№ 14,p.72–73.
107. Herique, A., Phalippou, L., & Ramongassie, S. (2000). High resolution SAR constellation for risk management. CEOS SAR Workshop, Toulouse, 26–29 October, 1999. Noordwijk: ESTEC, pp. 287–292.
108. Suess, M., Vb'lker, M., Wilson, J. J. W., & Buck, C. H. (1998). Superresolution: Range resolution improvement by coherent combination of repeat pass SAR images. In *EUSAR'98: European Conference on Synthetic Apreture Radar, Friedrichshafen*, 25–27 May, 1998. Berlin/Offenbach: VDE, pp. 565–569.
109. Lohner, A. (2000). Application and characteristic of high resolution estimation techniques for range compression in SAR systems. In *EUSAR 2000: 3rd European conference on synthetic aperture radar, Munich*, 23–25 May, 2000. Berlin/Offenbach: VDE.
110. Vignaud, L. (2000). Target features extraction in SAR/ISAR images: High resolution bright points extraction and wide angle tracking techniques. In *EUSAR 2000: 3rd European conference on synthetic aperture radar, Munich*, 23–25 May, 2000. Berlin/Offenbach: VDE, pp. 595–598.
111. Berizzi F. ISAR imaging of targets at low elevation angles. IEEE Transactions on Aerospace and Electronic Systems, 2001, 37, № 2, p.419–435.
112. Introduction into Integral Optics: Collection of Articles, Transl. from Eng., ed. by T.A. Shmaonov. Moscow: Mir, 1977.
113. Cayrefourca, I., Schaller, M., & Fourdin, C. (1998). Optical switch design for true time delay array antenna. *IEE Proceedings – Optoelectronics, 145*(1), 77–82.
114. Kleev, A. I., & Yamala, K. (1997). Radio-optical antenna systems. *Radiotechnics and Electronics, 42*, 801–807.
115. Cai, Y., Brener, I., Lopata, J., Wynn, J., Pfeiffer, L., & Federici, J. (1997). Design and performance of singular electric field terahertz photoconducting antennas. *Applied Physics Letters, 71*(15), 2076–2078.
116. Levshin, V. P., & Struchev, V. F. (1982). Adaptive active electronically scanned arrays with limited number of control stages. *Foreign Radioelectronics*, (1), 31–42.

Further Reading for Chapter 5

117. Fedorov, Y. V., Maltsev, P. P., Matveenko, O. S., Gntatiuk, D. L., Krapukhin, D. V., Putintsev, B. G., Pavlov, A. Y., & Zuev, A. V. (2015). MICs of amplifiers with integrated microwave antennas on Nanoheterostructures. *Nanoindustry*, (3), 44–51.
118. Maltsev, P. P., Matveenko, O. S., Fedorov, Y. V., Gnatiuk, D. L., Krapukhin, D. V., Zuev, A. V., & Bunegina, S. L. (2014). Monolithic integrated circuit of amplifier with integrated antenna for five-Millimeter wavelength range. *Nano- and Microsystem Equipment*, (9), 12–15.

Chapter 5
Features of Organizing the Process of Designing Radar Microcircuits

5.1 Features of Organizing the Process of Designing Radio Frequency Microcircuits

Modeling is the key stage in the process of designing any radiolocation or radio frequency microcircuits. Here, two primary approaches are applied: simulation of radio-frequency VLSI as a part of radioelectronic system under design; and simulation of analog/radio-frequency VLSI as a part of existing radioelectronic system.

The end-to-end simulation of element base, modules and systems is a means of presentation of development results which is generally accepted in the global electronics industry; and it ensures vertical integration and compatibility at different levels. Here, the prime tool is a ***model*** (of component, device, system). For fast, exact and unambiguous usage of the results of design of lower level, each developed component, block or system should be described by a model which can be used when designing a system of higher level. The model involves the description of functions, parameters and behavior of the described element (component, system) when exposed to signals, temperatures, radiation and other factors. Spice and VHDL descriptions serve as an example of commonly used formats of models compatible to many CAD-tools.

Vertical integration and high efficiency of use of ECB development results can be ensured if such model formats are selected that:

– are widespread and supported by many existing CAD-tools;
– allow to simulate devices (components, systems) of different degree of complexity;
– allow all types of the description - text, schematic, physical, etc.;
– can be used for analog, digital and mixed chips.

© The Editor(s) (if applicable) and The Author(s), under exclusive license to Springer Nature Switzerland AG 2021

A. Belous, *Handbook of Microwave and Radar Engineering*,
https://doi.org/10.1007/978-3-030-58699-7_5

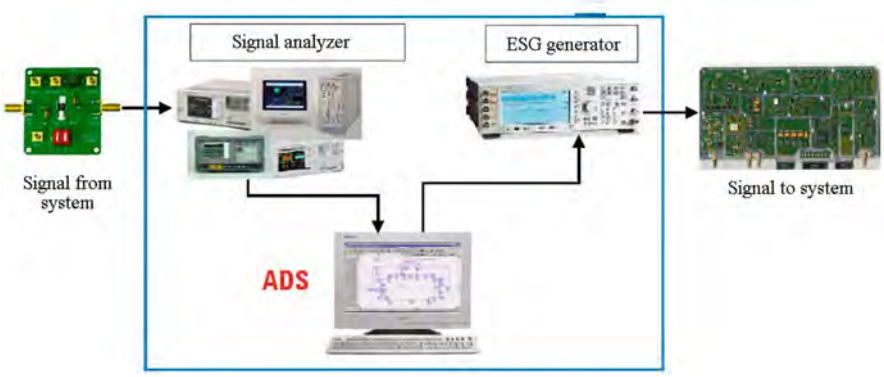

Fig. 5.1 Example of connection of ADS model to the physical model of radioelectronic system [1]

Such approach to the vertically-integrated design based on models is not only standard now, but also the only one possible in the modern conditions of the electronic equipment market.

In case when the system is at the stage of mathematical simulation, the model of the existing large-scale integrated circuit can be built in the system model that reflects the principle of vertical integration. Algorythmic (VHDL, Verilog A) or in-circuit approaches, can be used to describe model along with complex simulation system Agilent ADS or others.

When the system is at the stage of physical breadboarding, the LSI model is usually described in the ADS system (structural, schematic, physical, VHDL methods and their combinations can be used for the model description). If this LSI is made by the third-party developer or vendor, then its description can be provided by the developer. Signals of the existing physical radioelectronic system (a system prototype) which should arrive at LSI inputs are supplied to the analyzer, then the digital data stream from its output is entered into the LSI computer model. The digital data stream from the output of computer model arrives at the generator; electrical signals are generated at the generator output and then they arrive at the physical system again. Thus, the LSI model is connected to the circuit breaking where the physical LSI should be installed. It allows to perform debugging of the internal structure of LSI as well as to debug the system at the physical level with no need for available LSI produced (Fig. 5.1).

This approach can be used when the system is at the stage of mathematical modeling. It proves useful in solving two problems such as check of manufactured electronic unit being a part of virtual system, or simulation of the system, a part of units for which already exists.

The device that already physically exit is selected in the system simulated in ADS. The model of a signal in input of this device is downloaded via interface into the generator. The electric signal is supplied from the generator output to the physical device; and then this signal arrives from the device output to the analyzer (Fig. 5.2). The digital data stream being signal mathematical description is

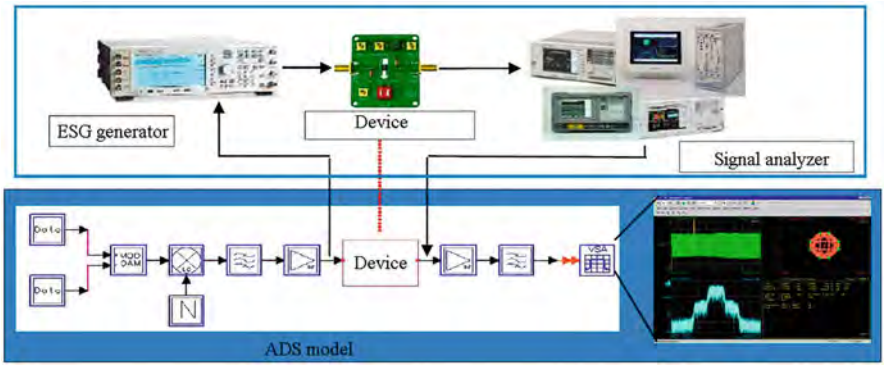

Fig. 5.2 Demonstration of the principle of including a physical device (mock-up) into the model of a radioelectronic system [1]

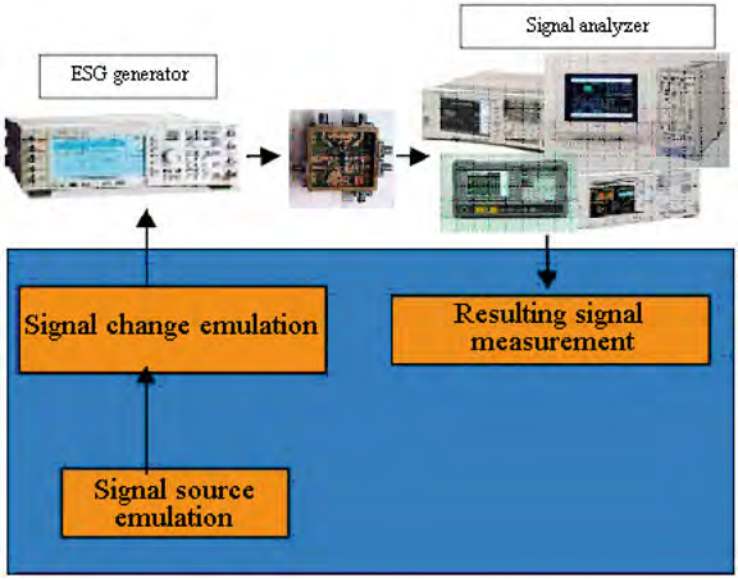

Fig. 5.3 The structure of a typical test system with random tuning of test signal [1]

downloaded in the model from generator output via the interface. Thus, the physical device (model) is connected to the model of radioelectronic system (Fig. 5.3).

An important stage of the design process is generation of test signals with variable parameters.

This approach is usually used when a developer has no standard solution for generation of a test signal with the specified characteristics. An example of this approach is addition of narrow-band interference with the specified power and spectrum to satellite navigation signal.

Automatic formation of component models based on instrument measurements is generally used for fast and exact description of behaviour of components and devices that have already been produced (Fig. 5.4 and 5.5).

From a practical point of view, the internal information control and exchange systems should be used for efficient monitoring of the project and planning of occupation of separate developer teams, as well as for effective coordination of departments of standard design center. Most objectives of such system are solved by specialized software package such as Microsoft Project Manager. The additional important functions of this project are prediction of design time and calculation of

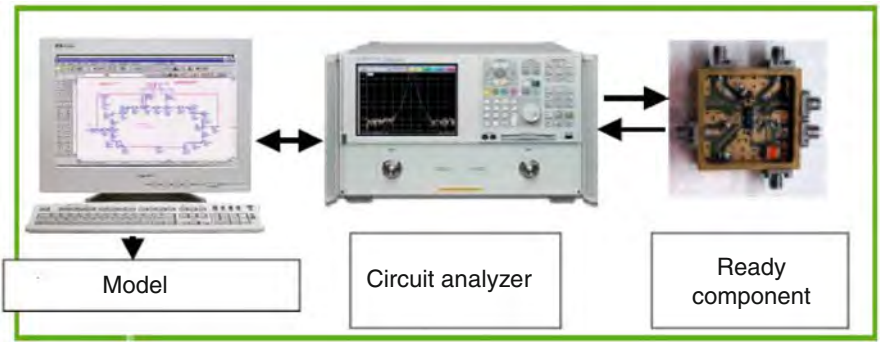

Fig. 5.4 Principle of automated generation of the model of a radioelectronic component [1]

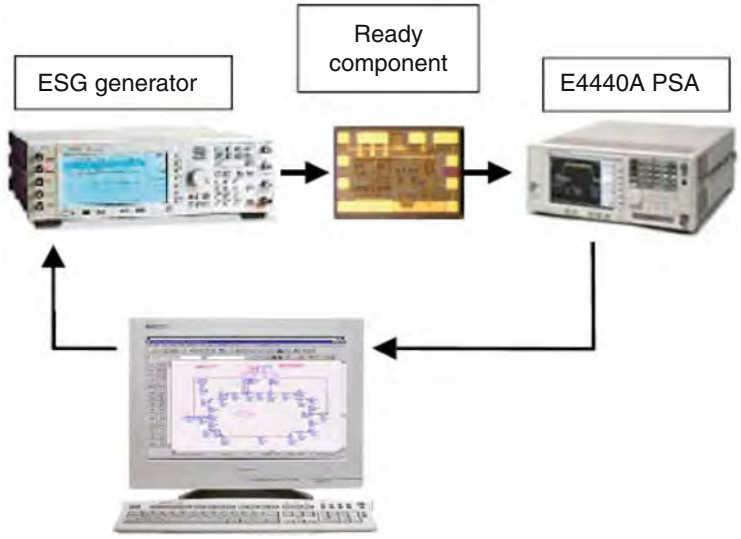

Fig. 5.5 Principle of automated generation of the model of a radioelectronic device [1]

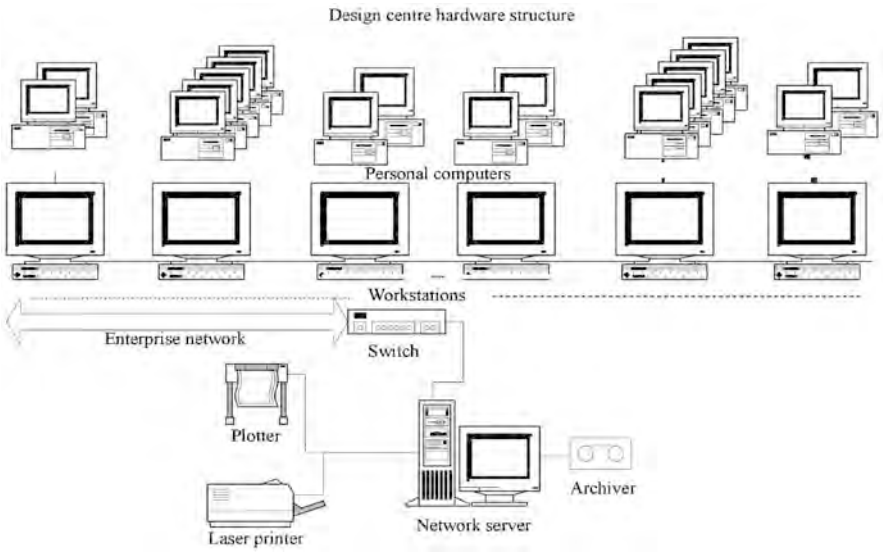

Fig. 5.6 The hardware structure of a typical chip design center

design cost based on salary of each involved participants and on time required for solution of sub-tasks.

It is necessary to review a standard structure of equipment and software required for tooling of standard design workstation.

The design department is the foundation of any design center for radar microcircuits.

The typical design departments should be equipped with the world's leading CAD-tools providing different chip design techniques:

- semicustom analog-digital integrated circuit based on master matrix crystal;
- semicustom digital IC based on master matrix crystal;
- digital custom VLSI (ASIC) based on design kit library and IP-blocks;
- analog full custom chips (ASIC) based on design kit library and IP-blocks;
- digital-analog full custom chips (ASIC);
- digital custom VLSI based on FPGA;
- custom HF- and SHF-chips.

Figure 5.6 [1] shows the structure of base content of such typical hardware of High-Speed Chip&Device Design Center.

All computing resources and peripherals of the center should be connected in local area network. The network includes a network server, print server, compute server, application and database server, workstations, personal computers, admin terminals, network devices, peripheral devices for obtaining hard copies of

documents and archiving of information. For cost optimization, some servers can be physically localized in one server without compromising the total operating performance. The server features depend on information flows in network and resources required for implementation of mission critical applications such as crystal simulation at the transistor level. Resources for such application essentially depend on software used, quantity of transistors and design techniques; and they can be rather different in some cases.

When drawing up the detail specifications, specialists optimize not only server features but also the quantity of workstations, personal computers and terminals. PC workstations can be used either as remote terminals workstations under the operating system HP-UX, or as an independent workstation under the operating system MS Windows or Linux. Increasing of the functional capabilities of CP hardware is possible due to increase in the number of workstations and PC connected to them, as well as due to additional connection and/or replacement of processor boards and other options of workstations.

Installable software (floating licences of software units) is located on the server and downloaded to the specific workplace on developer's command. In addition, these programs can be downloaded to computers with different operating systems.

Instrumental-process simulation software is installed to support the process of development and adoption of new process technologies of production of IC crystals. In this case, it will be necessary to deal with the challenges of adaptation and/or adjustment of element base SPICE-models during modification of process technology.

As a rule, for organization of effective work of design departments, the executive staff of design center installs special software for design process management, statistics collection, and quality control. It allows to solve the following tasks:

- collection on data on terms of completion of separate designing stages, the use of resources and the volume of works performed;
- design flow tracking with the appropriate recording of objective signs of completion of each procedure;
- quick training of new developers in specific design flow and reporting requirements, as well as transfer of best practices of lead specialists to young specialists.

Distribution of computing resources within a typical department is shown in Fig. 5.7.

The Table 5.1 [1] below presents and example of computing equipment and software used by design departments.

Measurement and test department of standard design center is equipped with appropriate inspection, measuring and testing equipment having the required software, measuring and testing design hardware, metrology and validation means.

First of all, these are testing complexes by such companies as: Teradyne, Agilent, Sentry and others. The department should also be equipped with modern probers for measurement of HF and SHF chips like EM6520 or EM6520–1 by the Belarusian company "Planar" and foreign probers for measurement of HF and SHF

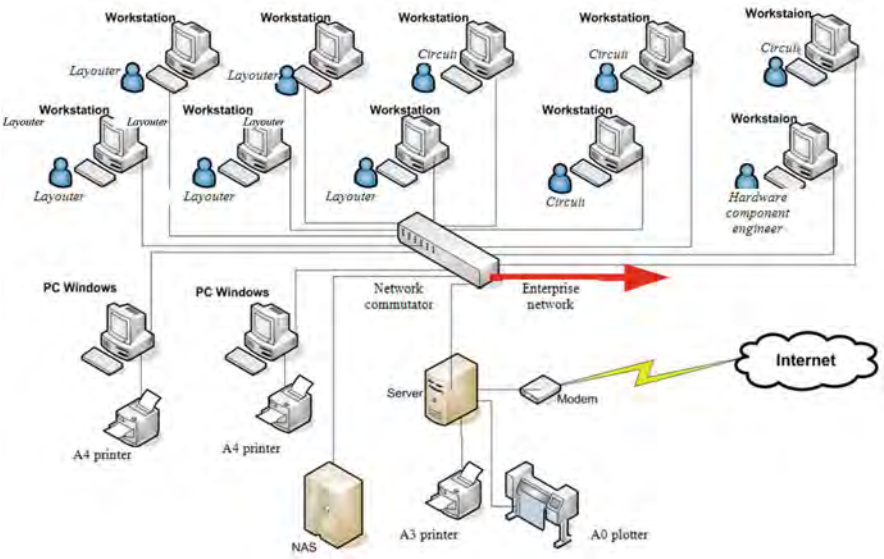

Fig. 5.7 Typical structure of computing resource distribution within the chip design department [1]

microcircuits, such as ones made by CascadeMicrotech company with full tooling package, as well as with instrumentation kits produced by such companies as Agilent Technologies, Hewlett-Packard, Fluke, DMT, Hart Scientific, Tektronix, Keithley, QualMark, National Instruments. The part of this equipment will be used in analytical laboratories of the design departments.

It should be noted that the top priority in the instrumental infrastructure of the Measurement and test department is a complex measurement system of IC functional control made by above-said companies. It is offered to use a Flexible Measurement System (a measurement system of resource type) that includes standard measuring tools with switching elements. And it is controlled by dedicated software via standardized interface.

Software shell of flexible systems provides fast transfer of measuring programs to the high-performance industrial testers. A wide choice of hardware components (voltage/current sources, generators, measuring tools, electronic loads, switching apparatus, and etc.) controlled by single software shell enables implementation of functional tests of any devices in the wide range of supply voltages and load currents. Figure 5.8 shows structural diagram of organization of the measurement process.

Further, it's worth noting the significance of such measurement element as adapter. The key component of qualitative measurements is a test adapter implementing an interface "measured device - measuring system". Figure 5.9 [1] shows the generalized process of production of such adapter and specifies the required standard software and hardware, as well as the process equipment for adapter production.

Table 5.1 Computing equipment and software used by design departments

No	Name	Quantity, pcs
Hardware		
1	PC or workstation for workplace	17
2	24″ monitors	32
3	2012 Server Std-based server	2
4	Network switch 1 Gigabit Ethernet	1
5	Set of network accessories	1
6	16 GB Fibre Channel (FC) network switches	2
7	Data storage system NAS	1
8	A3 laser printer	1
9	Color large-format printer A0	1
System software		
1	MS Windows XP Pro or 7	50
2	MS Windows 12 Server Std	1
3	Full office software of 2010 version or newer, with client licenses +50 clients	1
4	Linux Red Hat	15
5	Antivirus software. Server +50 clients	1
Application software		
	IC design software by Cadence	
1	Development of behaviour model, modeling, synthesis	2
2	Generation of functional control tests	2
3	Development of electrical circuits	4
4	Modeling of digital circuits	4
5	Modeling of analog circuits	4
6	Combined digital and analog modeling	3
7	Custom layout designing	5
8	Automated design of layouts of digital circuits, chip planning, arrangement and tracing, layout compression	2
9	Layout verification, check of design rules and comparison of layout with the diagram of electrical extraction of parasite parameters	5
10	Kit of design data recording programs Software filters for Postscript, HPGL, HPGL2 formats. Software for data translation into exchange formats GDSII, CIF, EDIF, VHDL, Verilog.	1
	IC design software ADS	
11	Set of programs for instrumental and technical modeling versions ADS 2011.01; ADS 2011.05 and ADS 2011.10	1

The next important set of equipment for the section of measurements and tests includes heat and cold chambers, ETT chambers and vibratory stands.

Table 5.2 [1] contains an approximate list of equipment for measurement and testing department.

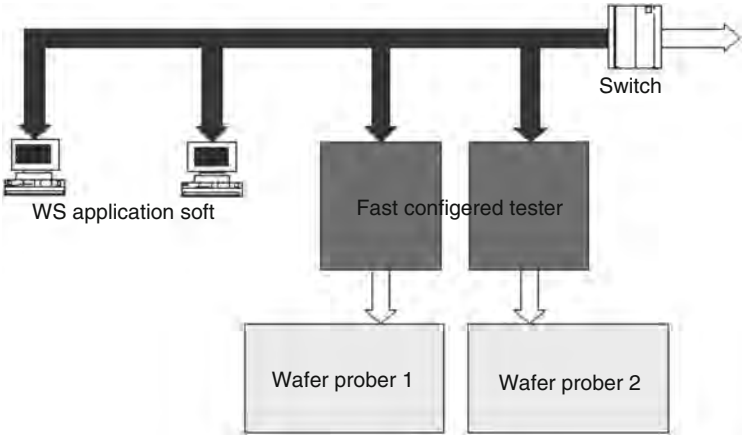

Fig. 5.8 Structural diagram of organization of the measurement process [1]

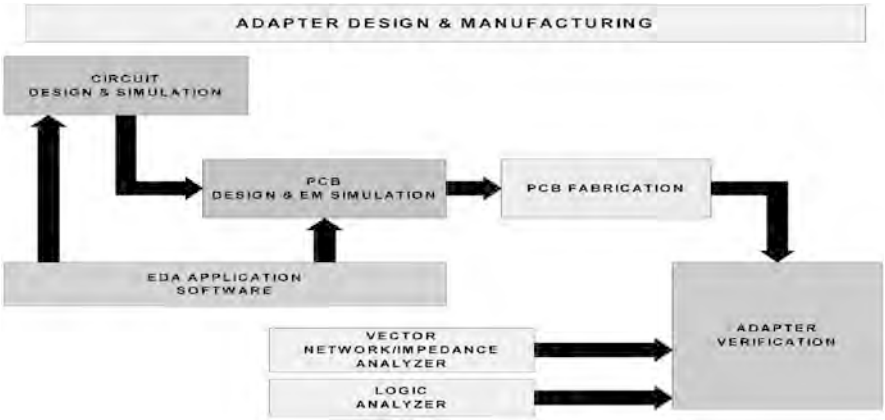

Fig. 5.9 Flow diagram of organization of adapter production and debugging

Cloning Department equipped with best expensive analytical equipment. Table 5.3 [1] contains the list of basic equipment for this department.

Two Analytical Laboratories of typical design departments are usually equipped with the most advanced tools for measurement and analysis of all possible parameters of chips in plates and devices. Such tools include high-precision testers of transistor current voltage characteristics, LCR testers including for HF and SHF ranges, multibeam HF- and SHF-oscilloscopes and spectrum analyzers, transistor characteristic monitoring devices, high-stable voltage sources and wide-band generators, and etc. Two laboratories should be equipped with probe fine manipulators for analysing of crystals on the plate.

Table 5.2 Standard list of equipment for measurement and testing department

No	Name	Qty, pcs.	Including the first stage	Including the second stage
TEST STRUCTURE MEASUREMENT SECTION				
1	Testing system	1	1	–
2	Probe station	1	1	–
IC FUNCTIONAL CONTROL SECTION				
3	Flexible measurement system	2	1	1
4	Probe station	2	1	1
5	Specialized software	2	1	–
6	Thermostatic device	1	1	–
7	Tunnel chamber	1	–	1
8	Controlling PC	2	1	1
TOOL SECTION				
9	Special software for design of test adapters and electromagnetic simulation	3	1	2
10	Impedance analyzer	1	1	–
11	Logic analyzer	1	1	–
12	Set of cables, connectors and adapters	1	1	–
13	Controlling PC	3	1	2
TESTING LABORATORY				
14	Heat/cold chamber	3	1	2
15	Electrotraining bench with a set of boards	1	–	1
16	Vibratory stand	2	1	1
17	Controlling PC	1	1	–
METROLOGY				
24	Multi-purpose calibration device	2	1	1
25	Reference 81/2 multi-meter	2	1	1
26	Controlling PC	1	1	–

The laboratories should be equipped with such optical equipment as ^{1000}-power microscopes capable of being connected to the computer, taking photos of image and its digitizing.

As well, special equipment is required for research of SHF chips.

Quality Control Department is equipped with computer equipment and special programs for collection and processing of statistics.

Documentation Development and Archiving Department is equipped with computer equipment and safe information storage devices LAN-connected to the server.

Figure 5.10 shows the main fields of application of SHF chips developed by the center [1].

Table 5.3 Approximate list of equipment for the cloning department

No	Name	Qty, pcs	Including the first stage	Including the second stage
Electrophysical analysis section				
1	1st analyzer of parameters of semiconductor structures	1	1	–
2	LCRZ meter	1	1	–
3	Switching matrix	1	–	1
4	2nd analyzer of parameters of semiconductor structures	1	–	1
5	Multipole parameter analyzer	1	–	1
6	Analytical probing station for DC/CV measurements	1	1	–
7	Analytical probing station for measurement of S-parameters	1	–	1
8	Set of cables, connectors and adapters	1	1	–
9	Extraction/generation software	1	1	–
10	Workstation	2	1	1
Chemical analysis section				
11	Exhaust cabinet	2	2	–
12	Ventilated pressurized suit	3	3	–
13	Slanting unit	1	1	–
14	Abrasive machine	1	1	–
15	Plasma etching unit	3	3	–
16	Microscope 100X – 1000X	1	1	–
17	Interference microscope	1	1	–
18	Analytical scales	1	1	–
19	Thermostat 200°C	1	1	–
20	Electrical hot plate 300°C, 500°C	1	1	–
21	Set of tools and consumables.	1	1	
Section of optical studies				
22	Microscope (UV-option / Precision Scanning Stage 8″*8″ / Confocal Module) with precision motorized scanning table	1	1	–
23	Digital color photo camera for UV microscopy and microscopy in the visible light spectrum with the possibility of micro photography	1	1	–
24	Computer with 24″ high resolution monitor	1	1	–
25	Color laser or sublimation printer	1	1	–
26	Software for automated digital step-by-step photography.	1	1	–
27	Software for stitching, viewing, printing of images	1	1	–
REM analysis section				
28	DualBeam™ FIB/SEM Workstation with EDX,Gas Enhanced Etch, and Metal Deposition Capabilities	1	–	1
29	Scanning electronic microscope 8500 FE- SEM	1	–	–

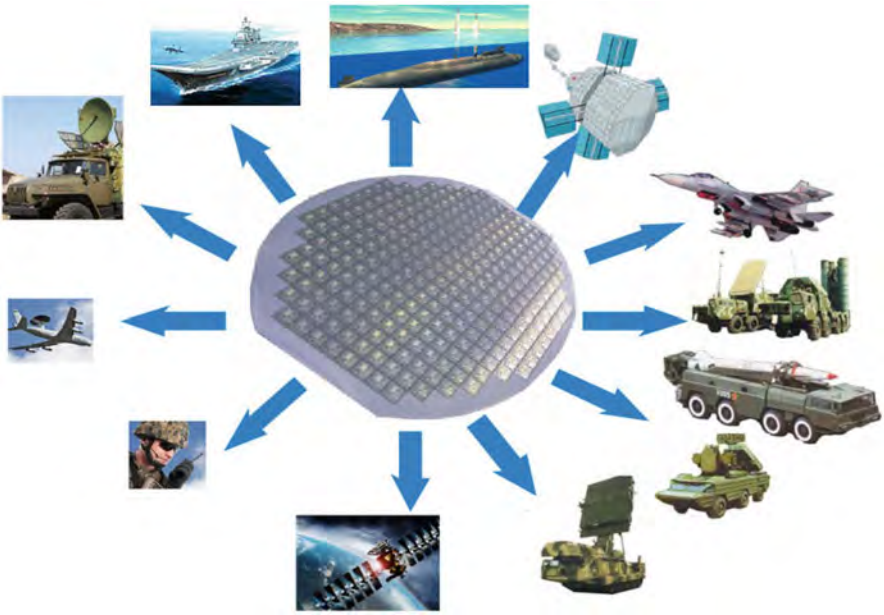

Fig. 5.10 Spheres of application of radio frequency chips

The main trends in military equipment where SHF and RF chips are used today:

Missile guidance and launch control systems, anti-missile systems.

Radars:

- multiple-target tracking systems built on AESA;
- electronic control of data arrays (AESA).

Aerospace monitoring and control systems.

Communications system:

- satellite communications;
- software defined radio;
- voice recognition and recording systems.

Electronic security systems and electronic countermeasure means:

- high-speed data transmission;
- image output for high-precision displays of different class (military imaging);
- munitions and targeting;
- hyper-spectral imaging.

Avionics, ground infrastructure and battle-field:

– individual navigation aids (GLONASS);
– portable enciphered communication systems
– motor system monitoring;
– visualization.

The latest technologies with dimensions of 180 nm, 90 nm and smaller based on the most advanced materials of GaN, SiGe, GaAs, Si-on-isolator types and others should be used to implement chips for the above-listed applications.

5.2 Possible Types of Technologies Used for Production of RF and SHF Products

All technological processes used by developers can be divided into several main groups:

CMOS - technological process, the element base of which consists of N-channel and P-channel MOSFETs. Diodes, resistors and condensers are additionally formed on structural layers. Bipolar transistor can be additionally formed depending on the substrate type - NPN for substrate with N-type conductivity or PNP for substrate with P-type conductivity. In turn, CMOS technological process is subdivided into low-voltage and high-voltage components. As a rule, only low-voltage N-channel and P-channel transistors are implemented in the low voltage process. In the high-voltage process, along with low-voltage transistors, high-voltage transistors of various designs for operating voltage of 15–800 V are implemented.

BJT - technological process, the element base of which consists of bipolar NPN and PNP transistors. Diodes, resistors and condensers are additionally formed on structural layers. Bipolar technical processes are subdivided into low-voltage with supply voltage up to 15 V and high-voltage with supply voltage up to 100 V.

BiCMOS - technological process, the element base of which consists of N-channel and P-channel MOSFETs, as well as bipolar NPN and PNP transistors. Diodes, resistors and condensers are additionally formed on structural layers. The most multi-purpose technology for implementation of a wide range of ICs.

BCDMOS - technological process, the element base of which consists of N-channel and P-channel MOSFETs, DMOS transistors, as well as bipolar NPN and PNP transistors. Diodes, resistors and condensers are additionally formed on structural layers. BCDMOS technological processes are divided into low-voltage with breakdown voltage of DMOS transistors up to 30 V, medium-voltage with breakdown voltage of DMOS transistors up to 100 V and high-voltage with breakdown voltage of DMOS transistors up to 1200 V.

BiCMOS technology is mostly used for complex functional ICs uniting multiple various units in a single chip. For example, single-crystal circuit simultaneously performing functions of calculation and control of LED display or other indicators.

Complex functional ICs like Systems-on-Chip (SoC) are designed for CMOS process with EEPROM forming unit.

In terms of application, technological processes can be divided into several main groups:

Digital ICs (microprocessors, microcontrollers, AD and DA converters, logic ICs, etc.) are usually implemented with the help of CMOS process. Analog ICs (amplifiers, voltage stabilizers, voltage regulators) are implemented using bipolar technology.

DC/DC and AC/DC voltage converters, ICs with high operating voltages up to 1200 V and high currents up to 100 A are mostly implemented using BCDMOS technological process.

5.3 Software Means for Designing SHF ICs

Main packages of CAD software means used throughout the world for design of digital, analog and mixed VLSIs are presented in Table 5.4 [1] with indication of the specific stage of design process. Here, the design process is divided into nine main stages, from development of the behavior model to verification of layout of the designed microcircuit.

In the following we will consider possibilities, disadvantages and advantages of these software products supplied by the largest CAD developers: Mentor Graphics, Cadence, Synopsys, ADS.

5.3.1 Analysis of Possibilities and Advantages of Software Products of Cadence Design Systems, Inc.

5.3.1.1 Analog Artist Design System

Interactive circuit of designing analog and digital-analog RF ICs. Provides automated comprehensive solutions to the tasks of designing custom, semi-custom analog, analog-digital and RF integrated circuits. Analog Artist integrates a wide range of powerful and field-proven tools to satisfy specific design needs in such spheres as telecommunication, computing equipment, multi-media, automation, space and military instrumentation. The tools are closely connected to the general structure of the Cadence Design Framework II™ shell. Analog Artist gives access to popular means of editing, modeling, analysis of electrical circuits and topology development.

Interactive environment Analog Artist provides the following for electrical design:

- all-round possibilities for inputting and editing analog and mixed circuits;
- interactive modeling environment with integration of many popular IC modeling systems;

Table 5.4 Main packages of microwave IC CAD systems

Route stages	Mentor Graphics	Cadence	Synopsys	ADS
Development of behavior model, modeling, synthesis	HDL Designer Leonardo Spectrum ModelSim	Virtuoso Schematic Composer VHDL Interface Virtuoso Schematic Composer Verilog Interface NC-Verilog, NC-VHDL, NC-Sim	HDL Compiler Design Compiler LEDA	
Generation of functional control tests	FlexTest FastScan	Incisive Coverage	Test Compiler	Test Compiler
Development of electrical circuits	Design Architect Renoir	Virtuoso Schematic Composer	Saber System Studio Module Compiler	S-Edit
Modeling of digital circuits	QuickSimII QuickSim Pro ModelSim	NC-Verilog Simulator NC-VHDL Simulator Verilog-XL	Formality ESP	
Modeling of analog circuits	ADi TURBO MS_Architect /Eldo Eldo RF Eldo RF	Spectre Circuit Simulator Spectre RF Virtuoso Multimode Simulation	Saber HSPICE	T-Spice W-Edit
Combined digital and analog modeling	Questa ADMS Dual Lang Continuum ADVance MS	Spectre Circuit Simulator Verilog-XL Virtuoso AMS Designer Encounter Digital Implementation System XL	NanoSimHSPICE	
Custom layout designing	IC Station Layout SDL Pyxis Custom Router Pyxis Pre Wire	Virtuoso Layout Suite XL	Chip Architect Physical Compiler	L-Edit Layout Editor
Automated design of layouts of digital circuits, chip planning, arrangement and tracing, layout compression	IC Station Layout SDL IC assemble	Encounter Digital Implementation System XL Virtuoso Custom Router	Physical Compiler Astro FlexRoute	L-Edit SPR

(continued)

Table 5.4 (continued)

Route stages	Mentor Graphics	Cadence	Synopsys	ADS
Layout verification verification of design rules and comparison of topology with electrical circuit of extraction of parasite parameters	Calibre Calibre PVS Calibre xRC	Assura Virtuoso QRC Extraction DIVA Dracula	Star-RCXT Hercules PVS	L-Edit IDRC L-Edit LVS HiPer Verify

- all-round analysis of RF circuits;
- modeling of parasite effects of hybrid systems;
- powerful means of display of modeling results;
- exhaustive means of analysis of modeling results.

5.3.1.2 Composer IC Design Environment

Logical, analog and digital-analog design

- Composer™. Basic software shell for a wide range of powerful design means.
- Integrated with Cadence layout design tools.

Simplification

- Simplification of design due to the use of descriptions in HDL languages,
- Flexible combination of any project presentations in the form of electrical circuits, block diagrams and HDL descriptions.

Increasing performance of group design

- Coordinated management of all design data,
- Helps identify both individual work spaces and separated spaces of the common project.

Early detection of errors

- Automatically highlights places of the detected errors,
- Identification of rules simplifying rectification of electrical design errors.
- Determination of individual rules for any design methodology.

Composer IC design system shell provides powerful and flexible possibilities for creation and setting of a wide range of circuit designs. From definition of architecture to detailed structural embodiment. Both novices and experienced designers will find Composer useful in creating correct hierarchical descriptions in VHDL® and

Verilog® HDL languages. Composer tracks every design step, providing a wide choice of automated solutions. Hybrid and analog design is additionally offered.

5.3.1.3 The Use of HDL Blocks Makes Design Real

Creation of modern circuits containing many millions of transistors is sometimes impossible at the gate level. Therefore, designers require flexibility of using different presentations and technologies able to reduce design cycles many times. In Composer, developers can start with block diagrams or high-level HDL descriptions, verify correctness of the project and only then select the circuit version applicable in this specific situations. During development of the design, developers arbitrarily mix HDL and structural descriptions. Description with the help of HDL preserves resources during creation of the project and its transition to other silicon technologies. Integrated means of verification of HDL descriptions significantly simplify generation of an electrically correct description.

5.3.1.4 Real Designing in a Team

Increase in size and complexity of modern projects forces the developers to attract developer teams to work. For management of complex project, Composer offers Team Design Manger™ - the program that automatically selects finished versions and presentations of design blocks and saves previous versions for sample analysis or recovery. (Other program shells force designers to group specific versions manually). Since Composer can provide access to the design base only to team members, designers can effectively separate data or work jointly with them.

5.3.1.5 All-Round Software Shell for IC Design

Open structure and data format in Cadence allow developers to set the shell and the design route according to their requirements. Composer provides a set of high performance means for end-to-end IC design. These are:

5.3.1.6 Synthesis Means

Integration of means of synthesis of logic systems and tests make it possible to optimize the design without leaving Composer. Cadence offers an exhaustive set of synthesis means of the Synergy family. The kit includes synthesis of ASIC and FPGA circuits from Verilog and VHDL descriptions, synthesis of tests, arrangement-based synthesis, which combines technologies of logical and temporal optimization. Optimization of the speed of operation satisfies modern requirements

of submicron design. Interface is provided to synthesis means Synopsys Design Compiler and Test Compiler.

5.3.1.7 Modeling

Modeling in Composer supports various description levels. Level of behavior, level of register transmissions, gate and transistor levels. Such simulators as Leapfrog VHDL™, Verilog-XL™ and Spectre™ are available through the Composer shell.

5.3.1.8 Timing Analysis

Integrated static timing analysis system Pearl™ helps identify critical paths and characterize performance of the project. Limitations determined during analysis are used in microcircuit design.

5.3.1.9 Calculation of Time Delays

Unique delay calculator Central Delay Calculator is accessible from all programs of the design route. The calculator can be set to calculate timing characteristics using any formula.

5.3.1.10 Layout Planning

Layout planner Preview™, guided by timing limitations, helps predict and control layout design results.

5.3.1.11 Test Synthesis

Synthesis of tests, generation of test vectors and simulation of failures help easily integrate testability into the design process. Such design with parallel testing ensures maximum covering of mistakes and has no such strong effect on dimensions and speed of the project as traditional design-for-test (DFT) methods.

5.3.1.12 Arrangement and Routing System

Arrangement and routing system for custom and semi-custom layouts with three or more routing levels presents such advanced technologies as arrangement controlled by time delays and synthesis of the frequency tree. Includes such products as Cell Ensemble®, Cell3 Ensemble®, Gate Ensemble™ and Block Ensemble™.

5.3.1.13 Physical Verification

To conclude the designing route, DRACULA® and DIVA® suggest the standard of layout verification tested on the largest and most complex projects. VAMPIRE® is the new, self-adjusting technology for automatic hierarchy verification.

5.3.1.14 Adaptation Means

Through the set of means ASIC Design Kit Composer can be adapted to the technology of the IC manufacturer. This set includes libraries and symbols of elements for technologies and routes of the manufacturer and is created in close cooperation with the manufacturer.

5.3.2 List of Necessary Design Libraries and Their Functional Description

Figure 5.11 [1] shows the structure of an analog design library.

Design route of mixed-signal ICs is shown in Fig. 5.12 [1].

Design route of a technology using CAD means of instrumentation and technical modeling is shown in Fig. 5.13.

In order to design GaN-based ICs, developers need to use special software design system ADS, which provides special software support for design of custom and semi-custom microwave ICs.

Due to this fact that this design system was mastered by developers only recently, special training of other specialists is required in order for them to be able to work with this software product.

Approximate program of training of engineers and additional training of engineers in design in VHDL language is presented below.

5.3.3 Features of Teaching Methods of Designing Digital Systems Using VHDL Language

Purpose of Studying the Discipline The discipline "Basics of Digital System Design in VHDL"is aimed at preparation of specialists in the field of automation of design of digital electronic devices and very large integrated circuits (VLSI). The course includes information about VHDL (**V**ery high speed integrated circuits **H**ardware **D**escription **L**anguage). VHDL language is the international standard in design automation system and is used for specification, modeling and synthesis of digital systems based on custom and user-programmed VLSIs.

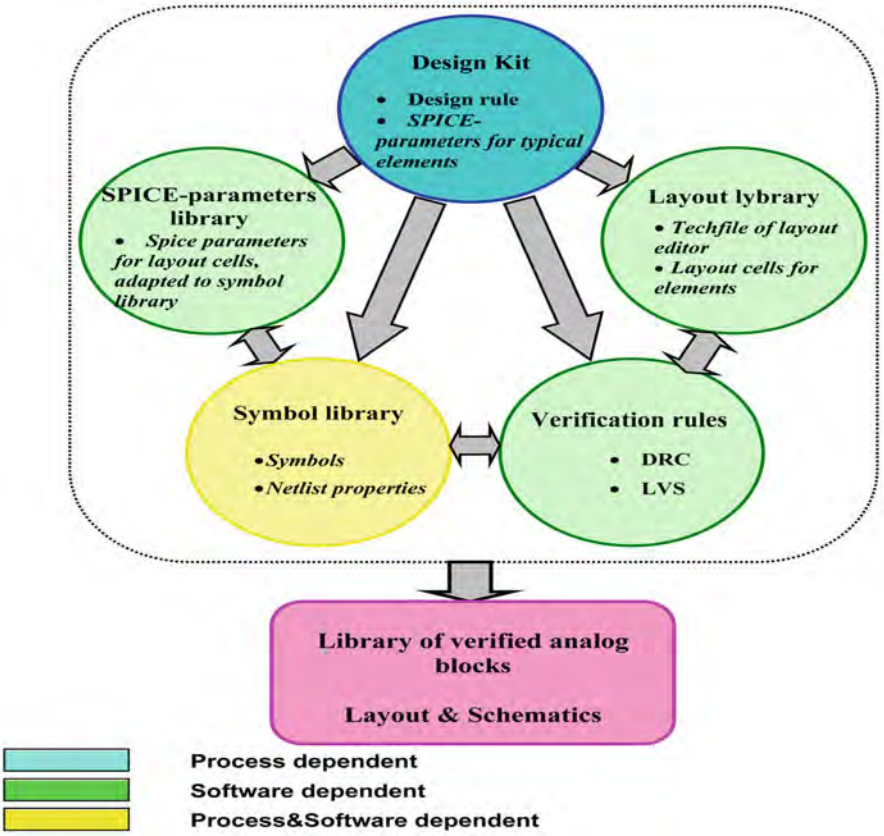

Fig. 5.11 Structure of an analog design library

Tasks of Studying the Discipline After studying the discipline, the students shall:

know:

- VHDL language of description, modeling and synthesis of digital systems;
- VHDL-models of typical circuits and algorithms;
- methods and means of synthesis of digital devices based on field programmable gate arrays (FPGAs) and custom VLSIs;

be able to:

- synthesize combinational circuits and digital machines;
- analyze work of combinational circuits and digital machines;
- develop digital devices on the set element base with the given optimization criterion;
- use VHDL language for description of original specifications of designed digital systems;

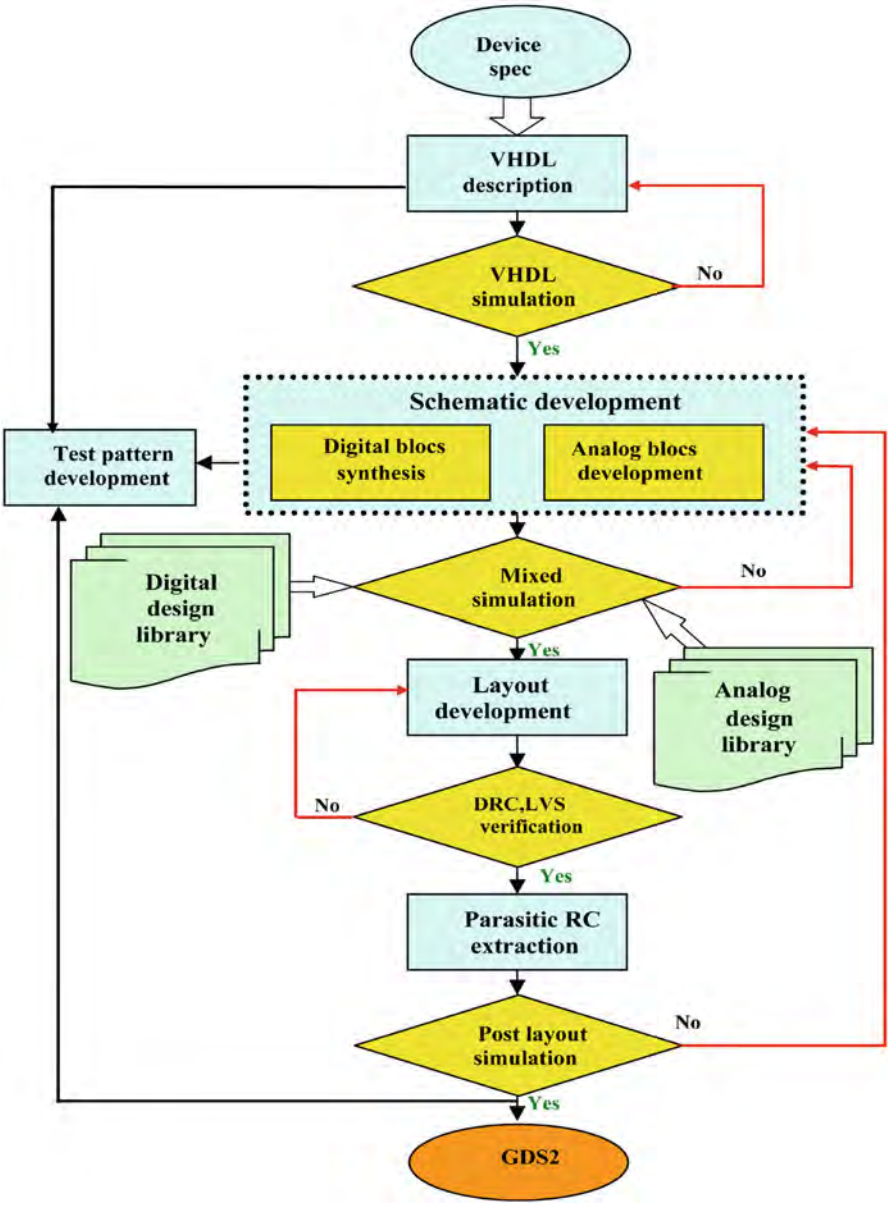

Fig. 5.12 Design route of mixed-signal ICs

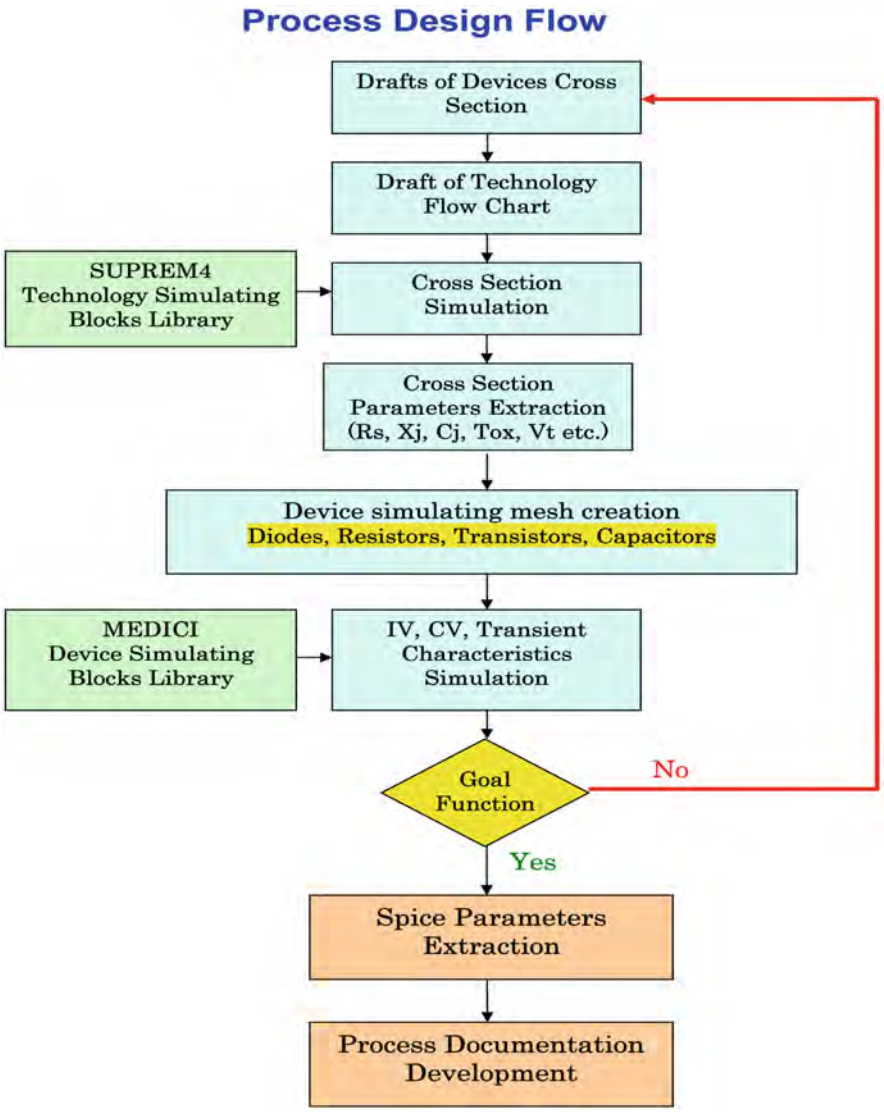

Fig. 5.13 Design route of a technology using CAD means of instrumentation and technical modeling [1]

– use VHDL language for modeling of digital devices;
– synthesize digital devices based on FPGAs and custom VLSIs;
– ***have experience*** in development of functional nodes and devices with the help of application software packages (Tables 5.5 and 5.6).

Table 5.5 Recommended subjects of lectures, their content and number of hours [1]

No	Subject	Contents	Number of hours
1	VHDL language for description of digital circuit designs	Concept of a digital circuit design. Structure and behavior. Hierarchy of structural and behavioral descriptions. Description of interface and architecture. Language objects. Lexical elements, data types, signals, variables and constants. Declarations of language objects. Arithmetical and logical operations. Serial and parallel operators. Parallel processes and their performance on computers. Units. Functions and procedures. Packages. Configurations.	24
2	Description of description and structures of digital circuits	Multiple-valued logic. Decision functions. Description of mounting connections. Packages for multi-valued logic. Description of elements and schemes of combinational logic. Description of logic elements and irregular logic circuits. Description of adders, decoders, multiplexers, FPGAs, ROMs. Description of sequential logic circuits. Description of triggers, finite state machines, microprogram automaton. Description of regular schemes.	20
3	Automatic synthesis of logic circuits based on VHDL descriptions	High-level and logical synthesis. Compilatory approach to high-level synthesis. Generated modules. Logical synthesis task. Synthesis stages: Optimization and technological display. Data coding during synthesis. Coding of logical, arithmetical and symbolic types. Coding of array elements. Synthesized and non-synthesized operators and structures. Synthesized subset of the VHDL language. Synthesis control.	6
Total:			50

One of the critical parameters of work in CAD systems is the ability to work with SPICE parameters - the basis of any design system. It would be plausible to present examples of using SPICE parameters for design of various IC classes. Since all operations using these parameters are performed in English, the examples will be given in the original language.

ADS Software Package was specially designed by Agilent Technologies for designing of microwave microcircuits on GaAs, GaN and other modern materials. This software package makes it possible not only to design microcircuit structures, but also assess their behaviour under the effect of various external factors that are important for use in special systems, such as EMR. Table 5.7 contains a brief list of subprograms.

Table 5.6 Approximate list of subjects of laboratory classes, their names and numbers of hours [1]

No	Subject	Contents	Number of hours
1	Study of the ModelSim system for modeling of VHDL descriptions	Initial design route, basic types of modeling, design creation and modeling.	2
2	Description and modeling of a system of logic functions	Development of a simple VHDL model of minimized system of logic functions	2
3	Description and modeling of irregular logic circuits	Development of a structural model of logic circuit, modeling, determination of circuit delay based on time diagram and critical path in the circuit.	8
4	Description and modeling of regular logic circuits	Hierarchical and parametrized description of regular circuits. Equivalence of VHDL models for limited dimensions of circuits	8
5	Description and modeling of triggers and finite state machines	Structural and algorithmic description of triggers of various types using multi-valued logic. Algorithmic description of finite mealy and Moore machines set by transition tables	8
6	Description of algorithmic descriptions of digital circuits based on functions and procedures	Algorithmic description of type conversion functions and procedures, processing of various presentations of numbers, arrays and matrices	6
7	Study of synthesis systems LeonardoSpectrum (by Mentor Graphics), ISE (by Xilinx). Synthesis of logic circuits.	Synthesis of VHDL projects designed in the course of laboratory works 2–6.	8
Total:			42

Table 5.7 Brief list of subprograms [1]

Software package	Number of licenses
W2213, including	5
ADS core	
Harmonic Balance Element	
Transient Convolution Element	
Layout Element	
Momentum G2 Element	
Design Rule Checker Element	5

5.3.4 Detailed Description of an IC Design Process

In this section, we will focus on the main stages of the standard design process for digital and analog microcircuits, including the list of input data required to start implementation of a stage, brief description of the works performed at this stage and

their required results upon completion of the stage, as well as the minimum required volume of output data concluding each stage.

Taking into account the specifics of this section, it would be most convenient to present the information as a table, which is more bulky but at the same time more convenient for practical use.

Table 5.8 [1] contains a more detailed description of all main stages of IC design process.

Table 5.8 Detailed description of IC design stages

No.	Stages and sub-stages of IC development	Input data	Works performed, result	Output data
1	2	3	4	5
1.	**Preliminary analysis**			
1.1.	Preliminary stage - analysis of the IC analog (for ICs with functional analogs); coordination of the set of functions and structural IC diagram with the consumer (for IC without a functional analog)	- IC-analogs (3 pcs.); - analysis program	Analysis results: - designs and assembly technologies; - production technologies and VAC of the element base of the crystal; - layer-by-layer digital photography of the crystal layout, from passivation to the decorated crystal; - detailed analysis of crystal layers and element base (if necessary): depths of p-n-junctions, thicknesses and types of layers, profiles of distribution of inclusions (on condition of availability of places for analysis), type and orientation of the substrate, type of the epitaxial layer, main layout dimensions	- analysis program; - report on IC analog analysis (examination act)
1.2.	Preliminary stage - analysis of possibility of IC production; TA development	- IC analog; - specification for IC analog; - report on IC analog analysis; - offers from potential customers	- description of the technology of element base formation with indication of type of coatings, possible production location, production features and	- generalized report on the analysis including the conclusion on the possibility of IC production; - pilot project (in the absence of IC

(continued)

Table 5.8 (continued)

No.	Stages and sub-stages of IC development	Input data	Works performed, result	Output data
			problems to be solved; - determination of possibility of parameter measurement and performance of functional control (FC); - determination of assembly possibilities; - development and approval of business plan; - analysis of the possibility of production using basic technologies and basic libraries; - development and approval of TA	analog); - business plan; - TA for R&D
2.4	Development of EC (FC)*	TA for R&D	- development of EC; - division of EC into functional units; - description of EC (FC) for CAD systems; - development of FCT (for digital ICs); - preparation of the sheet of conformity to TA; - development of modeling plan and/or method allowing to determine the field of workability within the VAC variation of the element base in accordance with TRTP and variation of external parameters in accordance with TA, including ranges of temperatures, supply voltages, etc., as well as radiation effects	- EC (FC); - BE composition; - FCT with explanatory note and reference file (for digital ICs); - modeling plan and/or method; - modeling report with the sheet of conformity to TA; - draft project (for products of the VP quality category)

(continued)

Table 5.8 (continued)

No.	Stages and sub-stages of IC development	Input data	Works performed, result	Output data
			(on condition of presence of such requirements in the TA); - modeling (for non-basic technological processes, this stage includes BE assembly, VAC measurement during CT, specification of Spice parameters). Additionally for devices of the VP quality category: - modeling (specification of Spice parameters with adjustment of TRTP - if necessary); - development of draft design	
3.	**Development of design and technology**			
3.1.	BE development (this stage can be performed separately at the discretion of the chief R&D engineer / chief research officer, or included in the stage 1.6)	- EC (FC); - BE composition; - TRTP; - composition of the library of the transistor level	- BE layout development; - development of graphic symbols; - development of DRC rules; - development of rules of LVC verification (recovery and comparison) of EC from layout; - performance of DRC and LVS verification of BEs; - modeling of BEs (critical according to expert estimate) in accordance with modeling method; - optimization of the BE layout until acceptable modeling results are obtained;	- layout of BEs, GC - DRC rules; - LVS verification rules; - report on BE modeling with determination of the field of workability

(continued)

Table 5.8 (continued)

No.	Stages and sub-stages of IC development	Input data	Works performed, result	Output data
3.2.	Development of IC layout	- TA for R&D; - TRTP; - layout of BEs, GC - DRC rules; - LVS verification rules; - EC (FC)	- unit layout development; - development of crystal assembly layout; - LVS verification; - DRC performance; - extraction of element parameters; - extraction of parasite elements (RC circuits for digital ICs); - control modeling of critical blocks or the entire IC (based on expert review) in accordance with the modeling method; - optimization of the IC layout until acceptable modeling results are obtained; - development of the assembly module layout with test ruler; - development of layout of test elements; - introduction of additional bonding pads in the text element or designing one of the crystals as test module, or placement of separate functional units and BEs in the test crystal (if necessary); - project review	- IC layout; - results DRC and LVS verification; – verdict of the expert committee on acceptance of IC design stage
3.3.	Magnetic output, DDD, DTD development	results of the previous stage	- Magnetic output for image generator; - documentation for chip manufacturing; - list of basic critical process parameters - development of DDD and DTD	- documents for magnetic output - list of basic critical process parameters; -DDD; -DTD

(continued)

Table 5.8 (continued)

No.	Stages and sub-stages of IC development	Input data	Works performed, result	Output data
			including the process route of plate production, schedule of electrical parameter with the measurement method, FCT (for digital ICs), methods for VAC measurement during the AIK test, assembly route, test methods according to the program approved by the chief design and development engineer	
3.4.	Project verification: - production of experimental specimens (plates); - assembly of experimental specimens, analysis, preliminary tests	- DDD, DTD; - TA for R&D, specification for IC analog	- performance of control matching of photomasks; - technical support of production of experimental samples (plates); - gathering of data on passage of plates through the route and VACs; - analysis of VAC and typical structure for conformity to TRTP and analog; - specification of Spice parameters; - analysis of the results of control of electrical parameters for conformity to TA, specification of the IC analog and modeling results. Determination of critical parameters of functioning and critical parameters of VAC (if decided so by the chief R&D engineer, can be performed	- report on passage of plates through the route, VACs and assembly operations; - experimental sample testing program approved by the head of the department; - report on the results of the study of experimental samples; - conclusion on the developed design of test specimens and conformity to TA requirements; - conclusion on the values of critical VAC parameters providing the workability region; - results of preliminary testing; - consumer resolution; - recommendations for adjustment of DD and TD;

(continued)

Table 5.8 (continued)

No.	Stages and sub-stages of IC development	Input data	Works performed, result	Output data
			after assembly of devices); - secondary modeling: specification of the area of workability based on results of testing of experimental IC samples; - technical support of performance of crystal assembly operations; - performance of tests according to the program approved by the chief R&D engineer; - analysis of results of preliminary testing; - analysis of consumer test results; - scheduling of production preparation (for R&D works performed with development in mass production); - development of the list of parameters of basic (critical) operations	- list of parameters of basic (critical) operations
4.	**Development of working DD and TD for production of IC test samples**			
4.1.	Development of working DD, TD	recommendations for development of DD and TD	- development of DD, TD and TR project; - calculation of parameters of the unification level of the designed IC	- working DD, TD, TR project; - schedule adjustment; - order for pilot batch testing
5.	**Production of test samples and performance of preliminary testing of ICs**			
5.1.	Production of test samples, assembly, analysis of reproducibility of parameters, tests			

(continued)

Table 5.8 (continued)

No.	Stages and sub-stages of IC development	Input data	Works performed, result	Output data
6.	**Acceptance of work**			
6.1.	Preparation of materials for presentation, R&D submission	recommendations for development of DD and TD	- development of DD, TD and TR project; - calculation of parameters of the unification level of the designed IC	- working DD, TD, TR project; - schedule adjustment; - order for pilot batch testing
6.2.	Preparation of production for serial IC production (for R&D works performed without development in mass production)			
	* These design stages are used for non-basic technological process. When the basic technological process and basic BEs are used, these design stages can be excludes from the design draft stage; the works of the excluded stages are included in the stage of structure and technology development.	- conclusion on conformity of test specimens to TA requirements; - consumer resolution; - TS project; - order for pilot batch testing; - letter-free working DD and TD; - TA for R&D, specification for IC analog	- gathering of data on passage of plates (VACs, analysis of reproducibility of critical parameters); - collection of data on assembly operations; - collection of data on IC parameters; - determination of basic (critical) operations and parameters for designed IMCs; - analysis of reproducibility of critical parameters, specification of the workability region; - analysis of consumer test results; - analysis of economic indicators, development of TD, DD of the O letter; - R&D presentation; - issuance of the order on appointment of commission; - performance of works in accordance with the production preparation schedule (for R&D works performed with development in mass production)	- report on the results of pilot batch testing; - assessment of reproducibility of critical parameters; - specification of values of critical parameters and VACs ensuring the field of IC workability in accordance with TA; - protocols and act of preliminary testing; - consumer resolution; - sheet of conformity to TA; - order on appointment of commission; - program of works (if required); - DD, TD, TC

5.3.5 *Multisim Blue Software for Modeling of Radioelectronic Devices*

Let us consider the features of work with the circuitry design program Multisim Blue (N1 Multisim Component Evaluator Mouser Edition) [1].

When the program is launched, the loading option selection window is displayed (Fig. 5.14).

One of the two options can be selected. The first difference of this software version from all previous versions is the Mouser Product Finder button on the work sheet screen; this button sends the user to the Mouser Electronics product page (Fig. 5.15). All the rest looks the same as in older versions of Ni Multisim software.

The program has significantly less analysis tools available in earlier versions. The user is provided with only a multimeter, a function generator, a wattmeter,

Fig. 5.14 Loading option selection window [1]

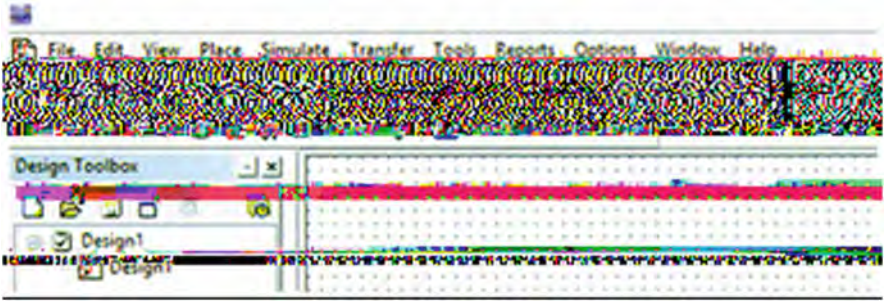

Fig. 5.15 Multisim Blue worksheet

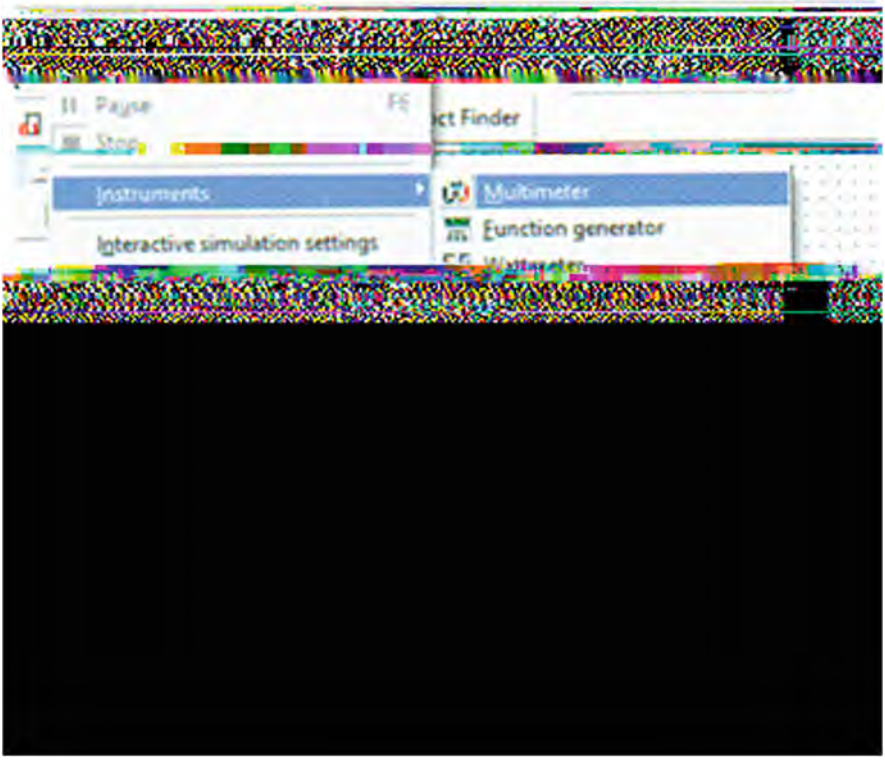

Fig. 5.16 Multisim Blue analysis tools

two-channel and four-channel oscilloscopes, a Bode plotter, a word generator, a logic analyzer, a semiconductor device parameter meter, measuring and current probes (Fig. 5.16) and Lab VIEW tools (Fig. 5.17).

Main possibilities of these analysis tools are detailed in [2, 3]. Also noticeable is the absence of tools for spectral analysis and analysis of distortions of the examined

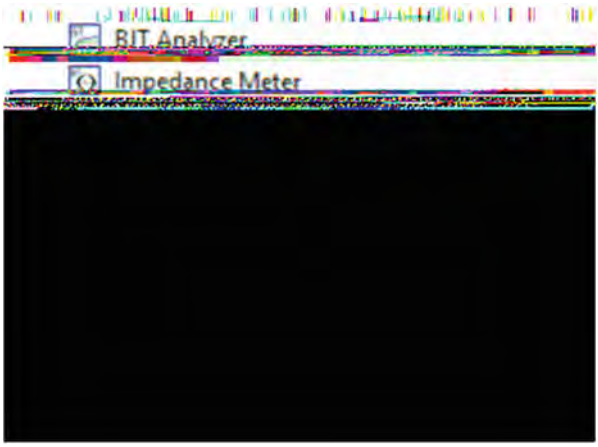

Fig. 5.17 Multisim Blue LabVIEW analysis tools

Fig. 5.18 Analyses menu of the N1 Multisim Component Evaluator Analog Devices Edition program [1]

signal. Freeware version of the N1 Multisim™ Component Evaluator-Analog Devices Edition 2013 program [2] has no such tools either, but it allows for performance of 8 options of studies using the Simulate/Analyses menu (Fig. 5.18). In addition to analysis of alternate and direct current at permanent and variable parameters of components and temperature, they include noise analysis and Fourier analysis, which helps study the signal spectrum and obtain the value of non-linear

distortions. Multisim Blue, on the other hand, has no Analyses menu. In the full version of N1 Multisim 2013, 19 analysis options are available in the Analyses menu.

Let us analyze the composition of Multisim Blue libraries. In order to compare the possibilities of freeware versions of Evaluator-Analog Devices Edition 2013 and Multisim Blue, let us consider the total quantity of available elements for each type of signal sources and components.

The library of power sources and signals in Multisim Blue only contains 28 elements, while N1 Multisim Component Evaluator-Analog Devices Edition 2013 has 68 such elements (Fig. 5.19). The numbers of voltage and current sources as well as controlled sources are reduced significantly.

Libraries of Basic elements in Multisim Blue contain two databases - Master Database and Mouser Database. As for Master Database libraries, they include (except for Basic library) very few components. On the other hand, Mauser Database libraries include much more of these elements than N1 Multisim Component Evaluator-Analog Devices Edition 2013. For example, there are 53,212 of the Basic library (Fig. 5.20).

This library is oriented more on the use as part of the Ultiboard software for design of printed circuit boards. For example, indications for each capacitor include capacitance, capacitance deviation percentage, TCC value and package type for SMD components.

The same is the situation with other libraries. Master Database libraries have very few elements, while Mauser Database libraries have enormous numbers of them: 6653 diodes; 2940 transistors; 1515 operational amplifiers, comparators and reference voltage sources; combined library of digital elements contains 1067 EEPROM ICs; Mixed library contains 37 AD and DA converters by Maxim and Texas Instruments.

Other libraries TTL, Indicator, Misc, Electromechanical and Connector contain no Mauser Database elements and very few Master Database elements. For example, TTL microcircuits are presented only by two components - multi-purpose binary-to-decimal reversible programmable counter and seven-segment decoder. Modeling of digital circuits is only allowed using virtual components from the Misc Digital library (87 elements). The user is able to change parameters of these virtual digital elements. For simple logic elements, these are front and drop durations; for complex elements, they include also the switch time delay, which helps partially compensate for the absence of component base for modeling of devices based on digital ICs. For reference, Misc Digital library in N1 Multisim Component Evaluator-Analog Devices Edition 2013 contains 146 components.

For new users, the site of Mouser Electronic offers the base of knowledge (**http://www.mouser.com/multisim-blue/support/knowledge-base**), which contains multiple articles with recommendations for the use of Multisim (in English). Video lessons for the program can be found at **http://www.mouser.com/multisimblue/support/support/video-tutorials**.

It should be noted that files created in any other version of Multisim cannot be loaded into Multisim Blue. Several examples of models for Multisim Blue can be

Fig. 5.19 Elements of Sources libraries of Multisim Blue (**a**) and N1 Multisim Component Evaluator-Analog Devices (**b**)

downloaded from **http://www.mouser.com/multisimblue/support/downloads/mouser-sample-circuit-library**. One model is given in the examples to the program.

Let us consider this model to analyze the possibilities of altering notations of components and printed circuit board design. To load a sample, it is necessary to simply click the Open Samples button (blue folder image in the standard menu in Fig. 5.15). Figure 5.21 shows the circuit from a Mouser Getting Started Final file. The circuit is in accordance with the ANSI standard.

To change the view of an element, it is necessary to double-click on its image and press Replace in the window that appears. The window of components is opened, in

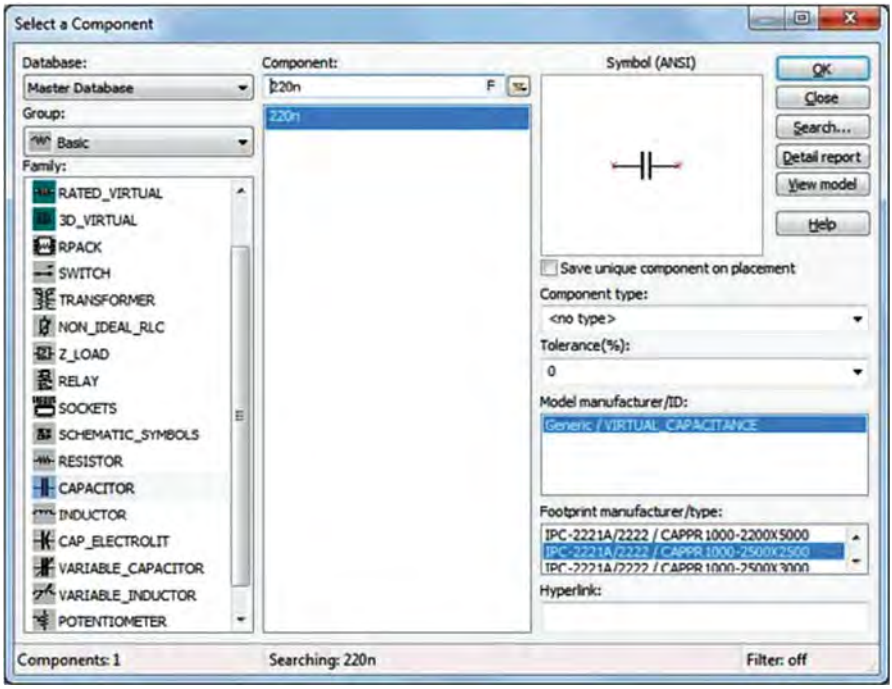

Fig. 5.20 Elements of Basic library (Mauser Database) of Multisim Blue

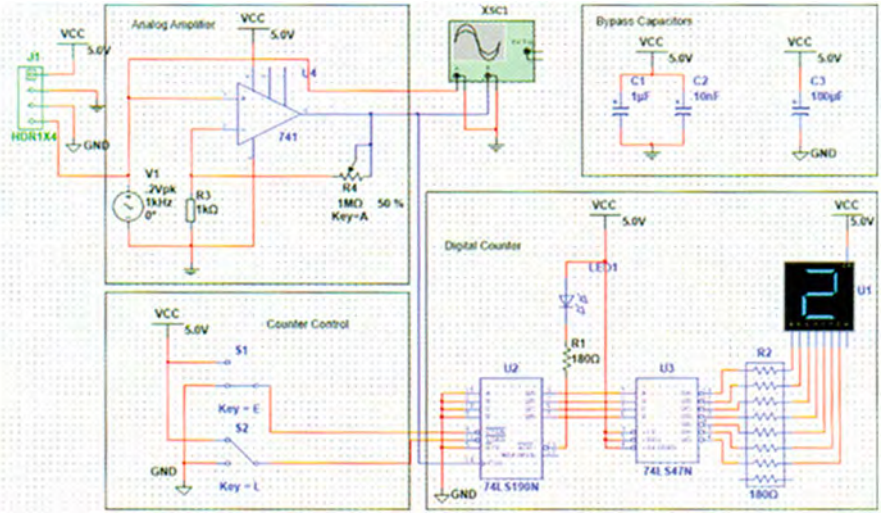

Fig. 5.21 Sample circuit from Mouser Getting Started Final file in ANSI standard

which it is necessary to select the identical element. If it is absent in the Master Database, switch to the Mouser Database and find the component there. After pressing the OK button, the image of the element will be changed (Fig. 5.22) [1]. This does not apply to such elements as common wire, power and signal sources.

To replace them, delete the element in the ANSI standard and insert it once again in the IEC 60617 standard. Circuit transformed in this way is shown in Fig. 5.23[1].

4 units are highlighted in the circuit. Analog Amplifier units performs the comparator function, transforming input harmonic signal into rectangular pulses with the amplitude of 5 V. Digital Counter unit contains a reverse programmable counter U2, a seven-segment decoder U3, a set of resistors R2 limiting output current of the decoder, a Counter Control unit and a unit of isolating capacitors for power supply circuits of the operational amplifier U4 and power supply circuits of digital microcircuits.

In order to design printed circuit board of this device, several simple steps shall be performed:

1. In Transfer menu, select Transfer to Ultiboard/Transfer to Ultiboard Component Evaluator 13.0 (Fig. 5.24).

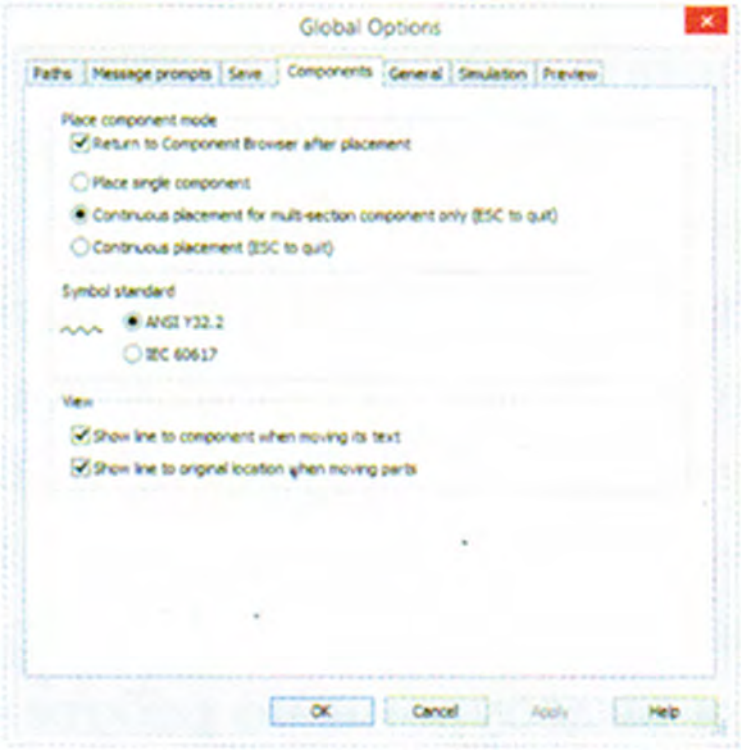

Fig. 5.22 Menu window Options/Global Options/ComponentsDevices Edition 2013

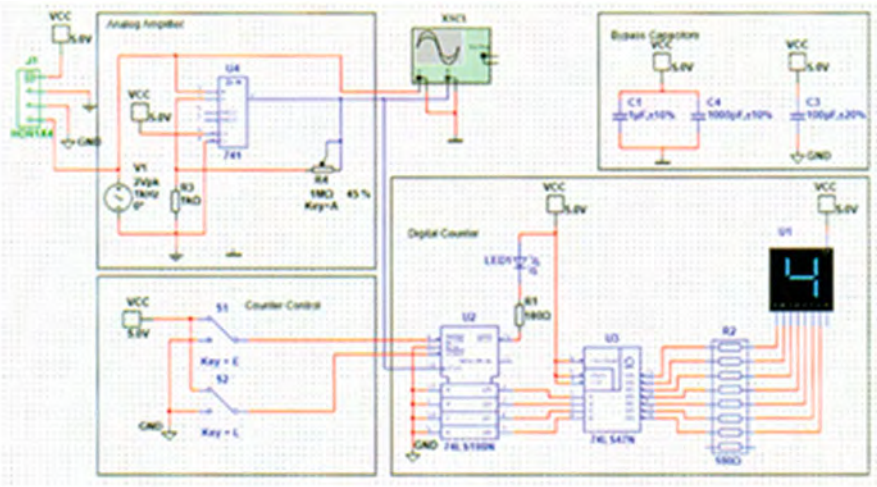

Fig. 5.23 Sample circuit from Mouser Getting Started Final file in IEC 60617 standard

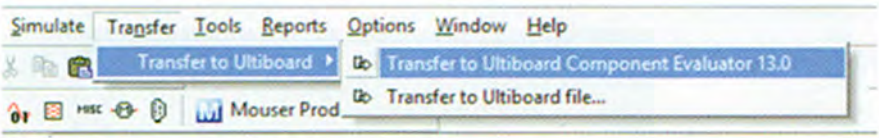

Fig. 5.24 Selection of the mode of transition to printed board design

2. In the displayed window, the program prompts the user to save the file in the Ultiboard format - Mouser Getting Started Final.ewnet. File name can be changed if necessary. Accept and press Save. The program can display a message stating that certain components have no footprints and therefore cannot be imported (Fig. 5.25).

If the user ignores this message and presses "OK", the window Ultiboard Component Evaluator will be displayed, indicating the number of remaining days of the trial period of the software (Fig. 5.26) and the Launch Ultiboard button.

After Launch Ultiboard button is pressed, the list of connections (Fig. 5.27) imported from Multisim will be displayed on the screen. After pressing OK, Ultiboard work window will appear on the screen (Fig. 5.28).

3. Similarly to Multisim, it is possible to perform user interface setting and select the color of the displayed elements, conductors, etc. Without going further into it, let us consider the process of designing the printed circuit board. In the worksheet (Fig. 5.28), the printed board is outlined in yellow; dimensions of the board are set by the program by default. This dimension can be changed during customer

Fig. 5.25 Ultiboard message on the impossibility of export of certain components

Fig. 5.26 Ultiboard Component Evaluator software message

interface setting; however, this is not required as it is easier to change the size after completion of arrangement of elements on the board and routing of connections.

In order to place components of the circuits that are located at the top of the worksheet beyond the contour of the board on the board, select Autoplace Part in the Autoroute Menu (Fig. 5.29) or press the Autoplase Part on the tool bar.

As a result, all components will be densely arranged on the printed board (Fig. 5.30).

If necessary, all components can be easily moved. Just select the required component and drag it where necessary.

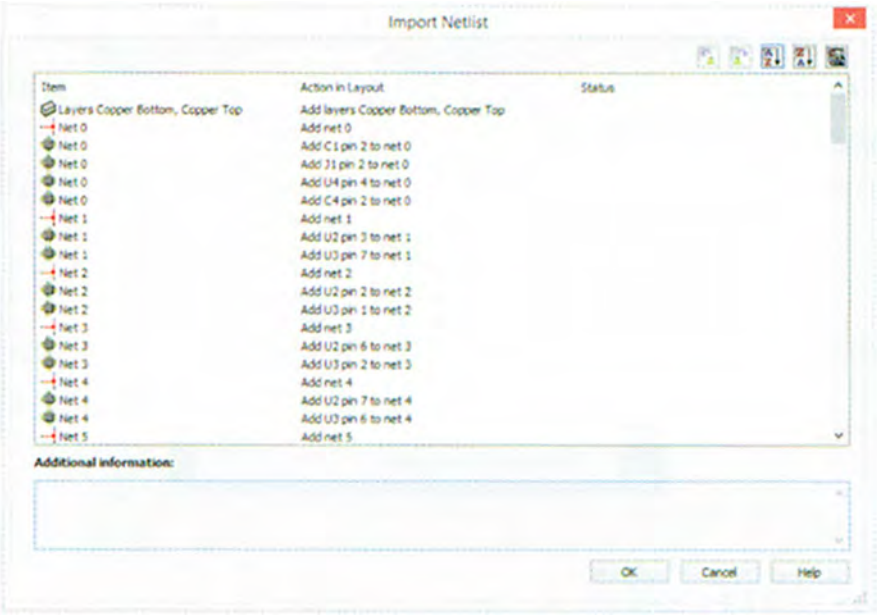

Fig. 5.27 List of connections imported from Multisim

4. For automatic tracing, select the menu item Autoroute/Start/resume autoroater. Autoroute results are shown in Fig. 5.31. After routing is complete, it is possible to set the required dimensions of the board. For this, press the right mouse button and click on "Select All" item in the context menu. Markers will appear on the image of the printed board contour, which can be used to transform its dimensions.

Colors of layers and board elements are shown to the left of the working window (Fig. 5.31). Display of a certain layer or board element can be disabled. For example, printed conductors of the top layer or contour of the board. 3D image of the designed board.

The program allows the user to view the board in 3D format. For this, select View 3D in the Tools menu. The image of the designed board will be displayed on the screen as shown in Fig. 5.32.

Display of separate elements of the printed circuit board can be switched on and off in the left part of the window. Figure 5.33 shows 3D image of a printed circuit board without installed components, Fig. 5.34 – 3D image of conductors of a printed circuit board.

In addition to the drawing of the circuit board, lower part of the screen contains additional information in the Spreadsheet View window, which contains 5 tabs. The first tab, Results, displays current information about the results of the user's actions (Fig. 5.35).

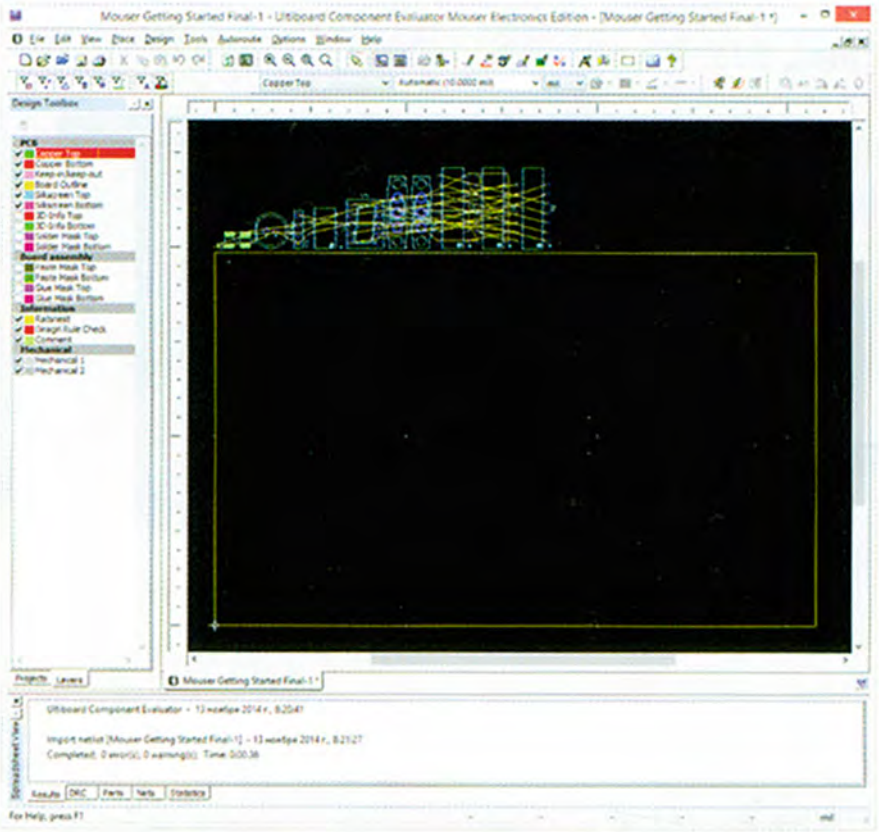

Fig. 5.28 Ultiboard work window

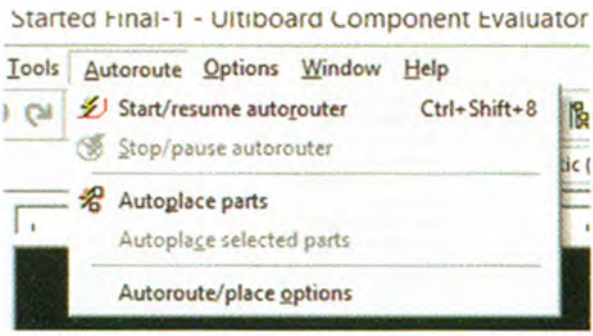

Fig. 5.29 Menu of selection of automatic arrangement of the components on the board

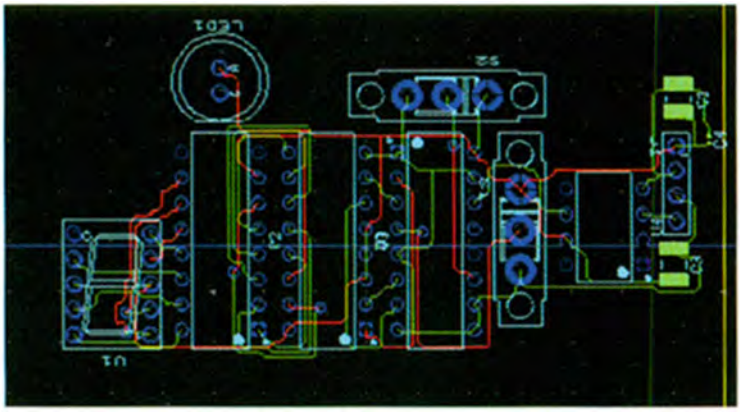

Fig. 5.30 Results of automatic arrangement of the components on the board

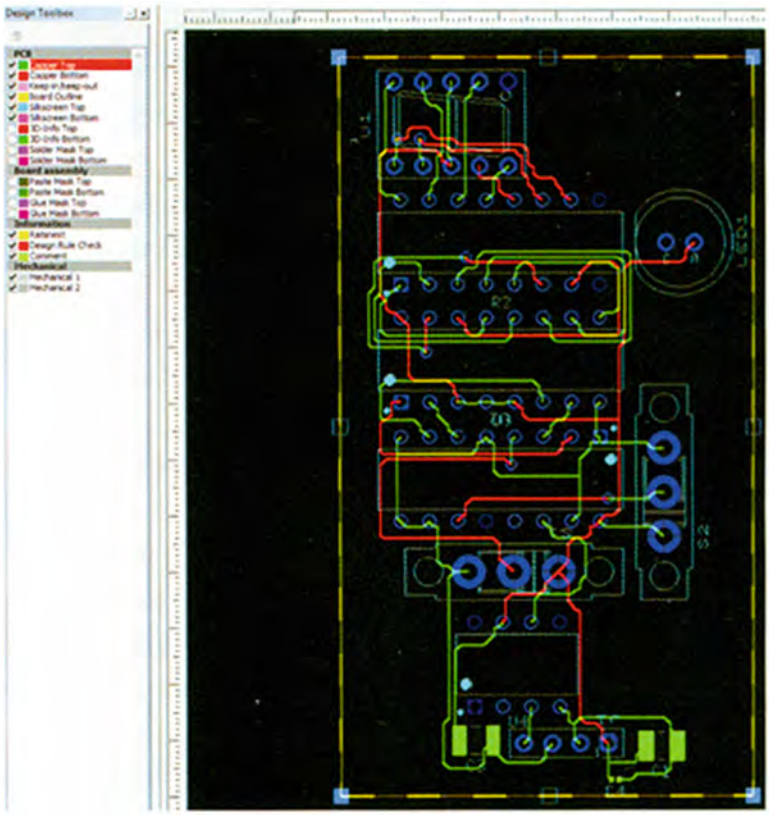

Fig. 5.31 Results of automatic routing of the board

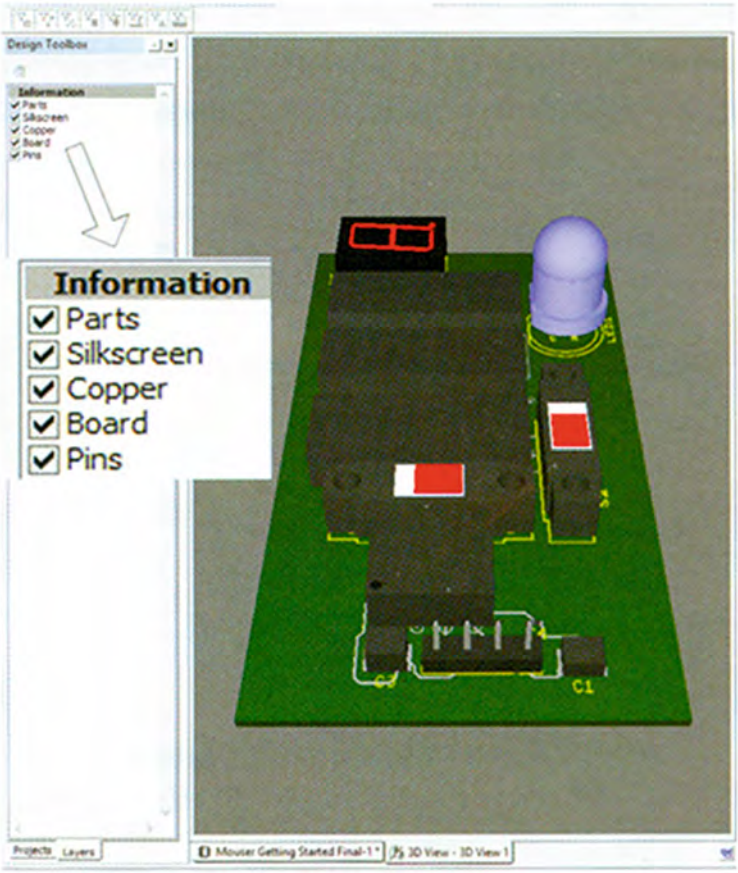

Fig. 5.32 3D image of the designed board [1]

The Parts tab contains information of all elements of the printed circuit board (Fig. 5.36).

Figure 5.37 shows information about printed circuit board conductors in the "Nets" tab; Fig. 5.38 - general information about printed circuit board in the Statistics tab. This window displays information about the number of connected and disconnected pins, number of elements, conductors, etc.

Of course, this brief overview does not contain even one tenth of information about the possibilities of the Ultiboard information, but this is enough to make a conclusion on the plausibility of its use.

When comparing possibilities of various free versions of the Multitsim program, it can be noted that the N1 Multisim 10 Analog Devices Edition program had the fullest range of possibilities in terms of tools and analysis. However, this version has

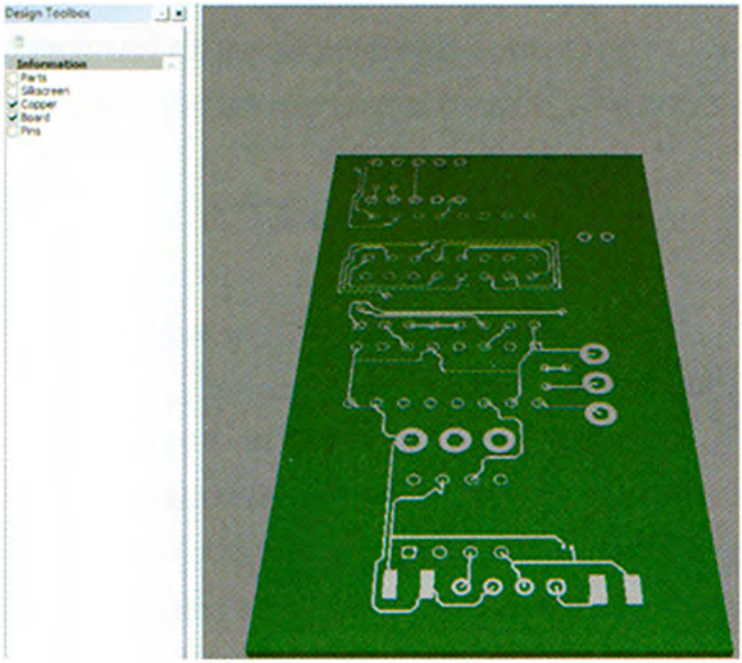

Fig. 5.33 3D image of a board without installed components

a very significant disadvantage - limited number of elements of the modeled circuit. The number shall not exceed 25. This number is absolutely insufficient for development of complex devices; however, the program can be successfully used for modeling of separate nodes. But the most efficient use of this version of the program is for study purposes. This is due to the fact that it supports all analysis functions and tools found in commercial professional versions of the program.

Summarizing the above, the following general conclusions can be made:

1. This program is convenient for verification of workability of analog devices and separate simple units of digital circuits.
2. The possibility of development of printed circuit boards using the Ultiboard program included in Multisim Blue makes it possible to quickly design the model of the device and does not require participation of a qualified design engineer for development of a printed circuit board.
3. Incompatibility with any other versions of Multisim software makes the use of previously designed models of various devices impossible, which certainly increases the time required for development of a new model.
4. Absence of tools for temperature and spectral analysis limits the possibilities of the program significantly.

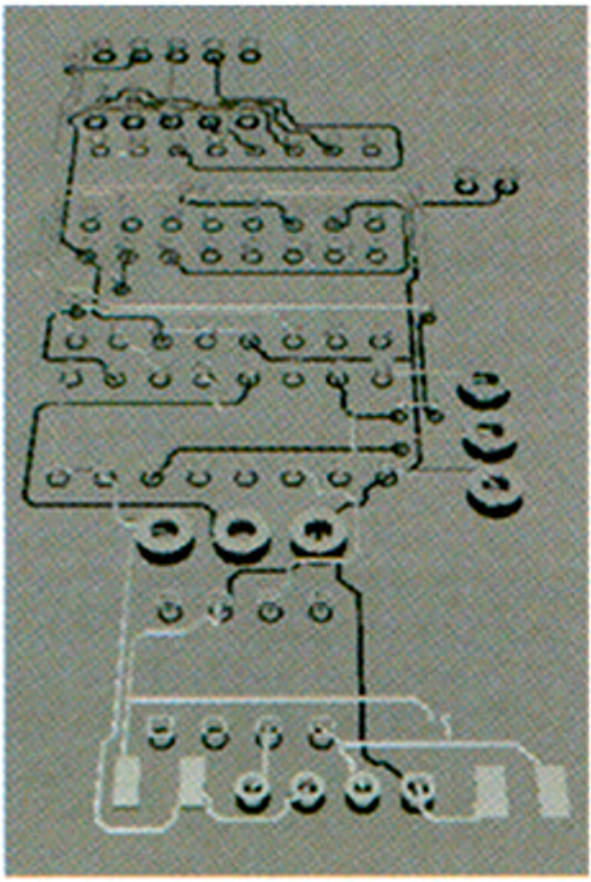

Fig. 5.34 3D image of conductors of a designed circuit board

5.4 Features of Circuit Modeling of Phase Shifters for Radar Sets

5.4.1 Basic Parameters of a Standard Phase Shifter

Phase shifters are critically important elements of many modern multi-channel transceiver paths of communication systems, since they make it possible to control position of the beam pattern in space and process the received signal based on given algorithm [4, 5].

The principle operation of the phase shifter is based on change in the complex resistance of the elements included in the control device under the effect of external electrical or magnetic fields, as well as current or voltage. In varactors and varicaps, when the control voltage changes at the reverse-biased p-n junction, the reactive capacitive component of the complex resistance changes as well. Change in the capacity occurs slowly, which determines the use of these control elements for phase

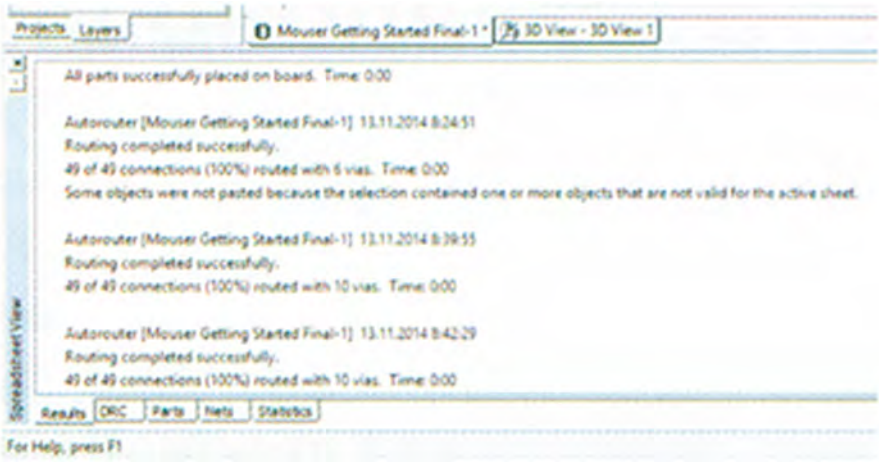

Fig. 5.35 Viewing design results in the Results window

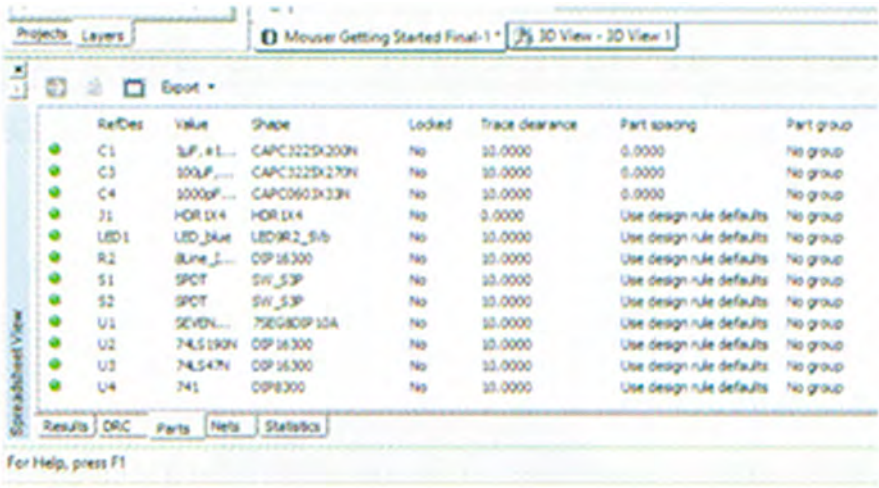

Fig. 5.36 Information about components located on the board in the Parts window

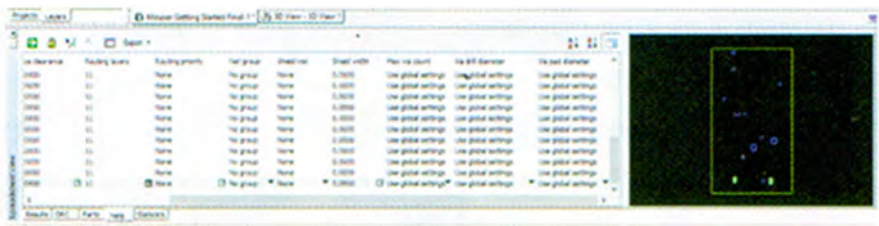

Fig. 5.37 Information about conductors in the Nets window

Fig. 5.38 General board information in the Statistics window

shifters with smooth phase adjustment. The use of pin diodes for such phase shifters is limited by the fact that the active component of resistance changes in discrete steps under the effect of control voltage.

Phase shifters with smooth phase adjustment can be separated into two types: transmitting and reflecting. Main elements of reflecting PSs are short-circuited sections (reflecting links) of lines with varactors included by various methods. They can be connected to the common path of the transmission line either directly or via four-pole circuits. In transmitting phase shifters, varactors are connected directly to the path of the transmission line. Control elements adjust the signal phase on the way to the short-circuiting device and back.

Quality of the phase shifter F is determined as the ratio of the phase shift $\Delta\varphi$ (degrees) to inserted losses L (dB) [6]:

$$F = \Delta\varphi / L.$$

Maximum achievable F value is determined by the expression:

$$F = (6 \ldots 9)\sqrt{K},$$

where K is the switching quality factor (SQF) of the active element.

Simplifed equivalent circuit of the varactor consists of resistance and capacitance connected in series respectively for zero and non-zero permanent displacement voltage: R1, C(U = 0) and R2, C(U). When the control voltage changes from 0 V to Umax, varactor resistance remains almost unchanged (R1 = R2 = R), and SQF is determined as:

$$K = \frac{\left(\frac{C(U_{\max})}{C(0)} - 1\right)^2}{(\omega C(U_{\max})R)^2},$$

where ω is the operating frequency of the phase shifter. With the help of this ratio, it is possible to select the varactor, combining its capacitances in order to achieve maximum K value.

The main advantage of the varactor as configurable capacitance is the parameter of controllability equal to $\frac{C(U_{\max})}{C(0)} = 10$ and more, which ensures a wide range of adjustment. Moreover, varactors are distinguished by high values of the Q-factor, and their control voltages will amount to single volts at current power of dozens of microamperes. The latter means that devices with varactor control can be overtuned with high speed and low power consumption.

5.4.2 *Phase Shifter Designing Using CAD Means*

One of promising ways to reduce labor costs and increase efficiency of designing of microwave devices consists in the use of computer-aided design packages [7–9]. Existing programs make it possible to model single- and multi-layered passive components, such as transmission lines, inductance coils, capacitors, resistors, vias, air bridges, transformers, etc. They make it possible to calculate electromagnetic fields in any structure, as well as estimate the effect of process tolerances and variation of electrical parameters of elements of the device on its characteristics.

SHF CAD system packages for electromagnetic modeling (Table 5.9) [10–13] are based on different methods: Method of Moment (MoM) for planar structures, Finite Element Method (FEM) and Finite Integration Technique (FIT) for arbitrary structures. Analysis in the frequency domain is performed based on these methods. Moreover, there are several methods of analysis in the time domain: Transmission Line Method (TLM) and Finite Difference Time Domain (FDTD), while transition to the frequency domain is performed by means of fast Fourier transform.

Design of SHF microstrip devices includes stages of circuitry design (selection of operating principles and structural diagrams of devices); circuitry and/or electrodynamical design (selection and calculation of the principal circuit of the device, modeling); engineering design (development of the phase shifter layout); technological design (development of the technological process of device production).

Table 5.9 Main types of CAD systems for analysis of strip SHF devices [1]

Company	Software name	Analyzed structure type	Analysis method
ANSYS	HFSS	3D-arbitrary	FEM
EM Software & Systems-S.A.	FEKO		MoM FEM
Zeland Software	IE3-D		MoM
CST	CST Studio		MoM FIT

Source data for modeling include basic PE architecture with indication of electrophysical parameters of applied materials and parameters of the equivalent circuit of varactors used as variable capacities. Characteristics of the device received during analysis are compared to the specified technical requirements. If the obtained results are not in line with the requirements, device parameters can be changed using a certain algorithm or optimized with the help of integrated software. Optimisation method is selected based on the condition of achieving the target function and can change in the process of design; the obtained parameter values are considered as source when using the next optimization method. Optimized functions are elements of S-matrix of the device, i.e. transmission coefficient, voltage standing-wave ratio (VSWR) or other characteristics. If the phase shifter model is selected correctly, fairly high coincidence between characterstics of the design and manufactured device is ensured.

Let us take a look at the examples of phase shifter simulation. Basic tasks of simulation are research and optimization of one stage (T-equivalent) (Fig. 5.39). After that, it is possible to proceed with designing of a multi-link PS module consisting of several stages. In this paper, six-link PS based on T-bridges was considered (Figs. 5.40 and 5.41 [1]).

The link of an electrically controlled microwave PS consists of dielectric substrate, lower surface of which is fully metallized and grounded; upper side of the substrate contains a strip structure designed as a non-uniform microstrip line (MSL) with varactors connected to its breaks. Microstrip stubs are connected to the section of this line adjacent to varactor connection points. In a multi-link structure, change in the varactor capacitance shift the signal phase at the input of the next T-bridge, which causes the corresponding phase shift at the output. Therefore, the device can operate in the operating frequency band of T-bridges as a controlled PS with smooth phase adjustment.

During simulation, the following structural parameters of the device were taken into account: substrate length - 45.8 mm, width - 22.7 mm, thickness - 1 mm; relative dielectric permittivity of the material RF4 $\varepsilon = 4.6$; dielectric loss tangent $\mathrm{tg}\delta = 0.001$; MSL section width - 0.9 mm; length of input and output sections - 3.2 mm; length of connecting sections - 4.1 mm; length of sections included in T-bridges - 1.5 mm; stub length - 16.8 mm; stub width - 0.961 mm. Characteristics are calculated for five values of control voltage implementing varactor capacities $C_{\mathbf{var}}$ equal to 0.5; 1.8; 3; 5.1 and 7.5 pF.

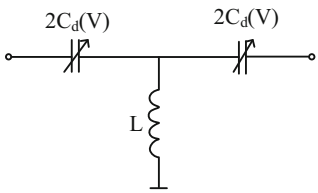

Fig. 5.39 Single PS stage with varactors connected in passage mode

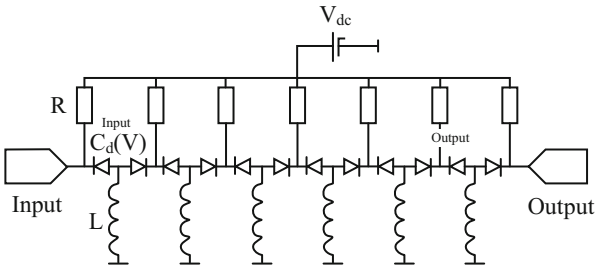

Fig. 5.40 Six-link PS built according to T-shaped scheme

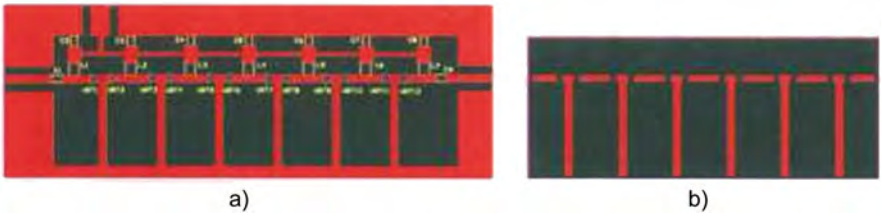

Fig. 5.41 Layout of phase shifter with control circuits (a) and without them (b) [1]

Digital simulation of the device was performed in the electromagnetic simulation software FEKO by EM Software. As a result of optimization, phase shift of one stage (T-circuit) amounts to about 60° within the band of 1.4–1.6 GHz. Phase change is linear in nature, both depending on frequency (within the range of 1.2–2.5 GHz) and during variation of the control voltage on the varactor. Maximum VSWR in the frequency band of 1.4–1.6 GHz does not exceed 2. PS reflection coefficient at the input (S_{11}) does not exceed −12 dB. Increase in the varactor capacity leads to expansion of the frequency band in which VSWR does not exceed 2. However, phase change speed reduces as the capacity increases. Maximum losses (S_{21}) in the operating frequency range of 1.4–1.6 GHz, which amounted to 0.3 dB are characterized by low irregularity. With an increase in frequency, the level of losses increases in reverse proportion to the varactor capacitance and amounts to −1 dB for 7.5 pF and to −2 dB for 1.8 pF.

In order to ensure greater phase shift, PS in the form of a staged connection of six T-bridges was used (see Fig. 5.3). Clarifiers are added to PS input and output, which ensure power supply isolation from other devices of the SHF path. Each cell is equipped with a pair of capacitances and inductances for blocking of the microwave signal to the control device. Power supply to the stages is organized in parallel;

current-limiting resistances for protection of varactors are installed in the power supply circuit in series. Simulation of this module resulted in the following.

When capacitance values are changed, oscillation phase shift occurs (Fig. 5.42). Phase difference between values of 1.8 and 7.5 pF exceeds 360°. Phase change is almost linear both in the voltage change range and in the frequency range. VSWR of the PS at the frequency of 1.5 GHz does not exceed 3 (Fig. 5.43); maximum reflection coefficient (S_{11}) at the PS input (Fig. 5.44) is −8 dB, and maximum inserted losses are equal to −3 dB (Fig. 5.45) with varactor capacitance change from 1.8 to 5.1 pF (further increase in capacitance leads to unacceptable growth of S_{11} and S_{21}).

Results of numerical modeling were compared with experimental data (Fig. 5.46) for frequency characteristic of inserted and reverse losses of the PS connected in forward (S_{21}, S_{11}, curve 1) and reverse (S_{12}, S_{22}, curve 2) directions. It was found that experimental and design characteristics are fairly close to each other. The

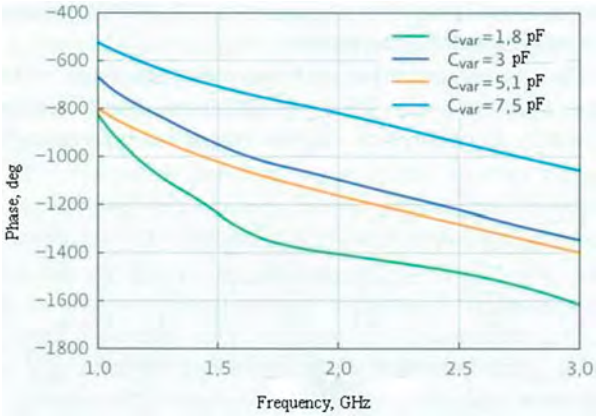

Fig. 5.42 Frequency dependencies of phase shift for different varactor capacities

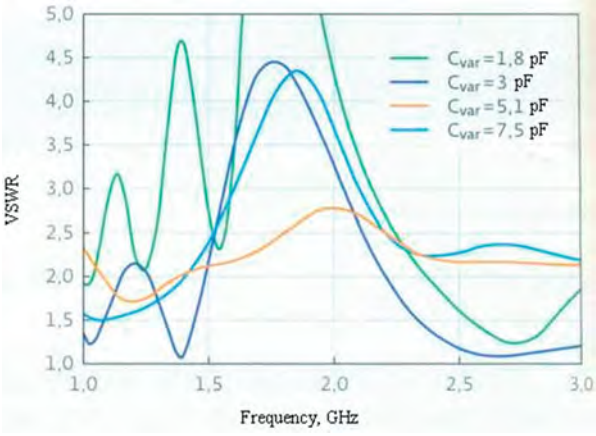

Fig. 5.43 Frequency dependencies of VSWR

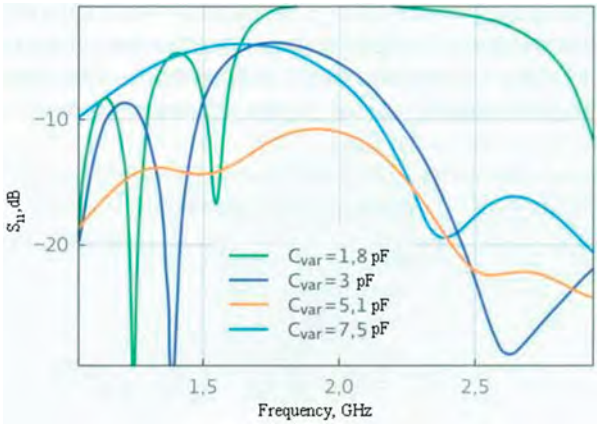

Fig. 5.44 Frequency dependencies of PS reverse losses

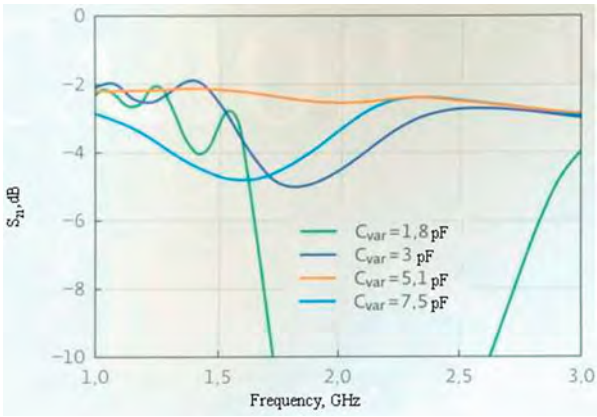

Fig. 5.45 Frequency dependencies of PE inserted losses (S_{21})

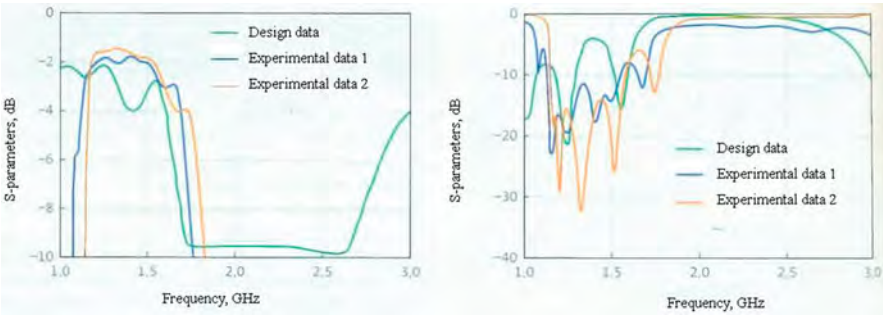

Fig. 5.46 Comparison of results of numerical modeling and experimental study of inserted (**a**) and reverse (**b**) losses with varactor capacity of 3 pF

differences are explained by inconsistencies between the real PS architecture and design parameters, as well as possible variation of electrophysical parameters of the substrate.

Therefore, the studies performed confirm efficiency of using CAD systems for development of phase shifters with smooth phase adjustment.

References

1. Belous, A., Merdanov, M., Shvedov, S.. (2018). *Microwave electronics in radar and communication systems*. Technical Encyclopedia in 2 Volumes. 2nd ed., revised, Moscow, Tekhnosfera, 1520 pages.
2. Makarenko, V.. (2013). New Versions of N1 Multisim Modeling Software. *EKiS - Kiev: VD MAIS*, 12. http://www.ekis.kiev.ua/UserFiles/Image/pdf Articles/12_2013/V. Makarenko_New_Multi- sim_EKIS_12_2013–5.pdf.
3. Makarenko, V.. (2013, April). Modeling of Radioelectronic Devices Using N1 Multisim Software. *Electronic Magazine "Radio Annals"* 23, 141–267. http://www.rlocman.ru/book/book.html?di=148191
4. Kisel N., Grischenko S., & Derachits D. (2014). Design of phase shifters - CAD-based modeling. *Electronics: NTB*, 8, 148–152.
5. Hizha, G. S., Vendik, I. B., & Serebryakova, E. A. (1984). *SHF phase shifters and switches*. Moscow: Radio and Communication.
6. Vendik, L. B., Vendik, O. C., & Kollberg, E. L. (2000). Commutation quality factor of two-state switching devices. *IEEE Trans, on Microwave Theory and Tech, 48*(5), 802–808.
7. K. Gupta, R. Garg, R. Chadha. (1987). Computer-aided design of microwave circuits (Transl. from Eng). Moscow: Radio and Communication.
8. Nikolski, V. V., Orlov, V. P., Feokistov, V. G., et al. (1982). In V. V. Nikolski (Ed.), *Computer-aided design of SHF devices*. Moscow: Radio and Communication.
9. Fusko, V. (1990). *Microwave circuits: analysis and computer-aided design* (Transl. from Eng). Moscow: Radio and Communication.
10. www.appwave.com/products/si
11. www.ansys.com
12. www.cst.com
13. Kisel, N. N. (2013). *Modeling of applied tasks of electrodynamics and antennas on supercomputing system in FEKO package: Study book*. Taganrog: YFU Publishing.

Chapter 6
Power Electronics Devices Based on Wide-Gap Semiconductors

6.1 Main Properties of Materials Based on Large Gap Semiconductors

The use of advanced production technologies and precision control methods, as well as miniaturization of semiconductor structures have caused the properties of modern power semiconductor devices to approach the limits set by physical properties of silicon. This calls for the search of alternative semiconductor materials, which started in the beginning of the 1950s and recently became especially active [1].

Main requirements and directions of development of power electronics devices can be formulated as follows:

- increasing limit values of switched current and voltage;
- reducing the level of static and dynamic losses;
- expanding the range of working temperatures;
- increasing reliability, improving resistance of components in emergency modes, extending service life;
- reducing specific cost;
- increasing radiation immunity.

Attempts to solve the above problems is closely linked to improvement of technology and causes a new generation of power devices to appear approximately every 20 years:

– 1970–1990 – silicon MOSFETs and thyristors;
– 1990–2010 – silicon IGBTs;
– 2010 and later – power SiC and GaN devices (see Fig. 6.1) [1].

Brief explanations of Fig. 6.1 are presented below.

GTO (Gate Turn Off). Regular thyristors are set to the closed state by reducing current flowing through the thyristor to the value I_h or changing the polarity of

© The Editor(s) (if applicable) and The Author(s), under exclusive license to Springer Nature Switzerland AG 2021

A. Belous, *Handbook of Microwave and Radar Engineering*,
https://doi.org/10.1007/978-3-030-58699-7_6

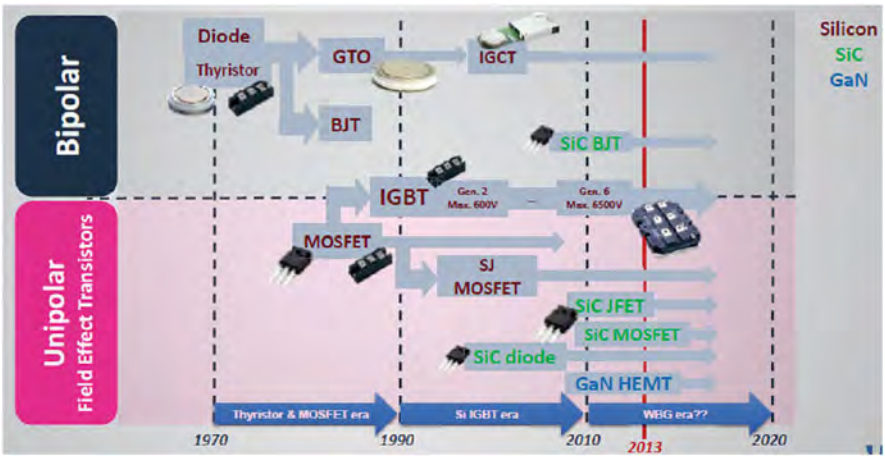

Fig. 6.1 Lifecycle of semiconductor devices of power electronics [2]

voltage between the cathode and the anode. Turnoff thyristors, unlike regular thyristors, can be switched form closed state to open state and vice versa under the effect of the control electrode current. In order to close a gate turn-off thyristor, it is necessary to transmit current with the polarity opposite to the one that caused its opening through the control electrode. It is recommended to use thyristors and turn-off thyristors in slow yet powerful power stages.

IGCT (Integrated Gate-Commutated Thyristor). IGCT is a modified (modernized) version of GTO [3].

BJT (Bipolar Junction Transistor) [4].

JFET *(Junction-Field-Effect-Transistors-FET)* [5].

HEMT (High Electron Mobility Transistor) is a field emission transistor, in which the channel is created not with the help of a doped region, like in regular MOS-transistors, but by the contact between two semiconductor materials with different gap width values (the so-called heterojunction). Other names of these transistors: field transistors with controlling metal-semiconductor junction, heterostructure FET (HFET), modulation-doped FET (MODFET). In foreign literature, they are referred to as HEMT; the following names are also used, depending on the structure: HFET, HEMFET, MODFET, TEGFET, SDHT [6, 7].

The attention of manufacturers of power semiconductors is mostly focused on two materials with extended gap – silicon carbide (SiC) and gallium nitride (GaN). As compared to silicon, they have much wider power gap between valence and the conductivity area, which helps reduce conductivity and switching losses, expand the thermal range and improve heat exchange. Table 6.1 contains qualitative characteristics of semiconductor materials, while Fig. 6.2 [1, 8, 9, 11, 12] demonstrates their effect on physical properties of devices. Table data demonstrate comparison of

Table 6.1 Comparison of properties of semiconductor materials

Parameter	Si	GaAs	GaN	3C-SiC	4H-SiC	6H-SiC	Diamond
Band gap width, E_g, eV	1.12	1.42	3.39	2.2	3.26	3.0	5.5
Breakdown field strength, E_c, MV/cm	0.3	0.4	3.3	2.0	3.0	3.0	6.0
Electron mobility, μ, $cm^2/V\ s$	1400	8500	900	800	1000	460	2200
Drift speed of electrons (saturation), V_{sat}, cm/s	10^7	$2{\cdot}10^7$	$2.5{\cdot}10^7$	$2.7{\cdot}10^7$	$2.7{\cdot}10^7$	$2.0{\cdot}10^7$	$2.7{\cdot}10^7$
Dielectric constant, ε_r	11.8	11.1	9.0	9.7	9.7	9.7	5.5
Heat conductivity, λ, W/cm K	1.5	0.5	1.3	3.6	3.7	4.9	20
Density, ρ, g/cm^3	2.33	5.32	6.15	3.21	3.21	3.21	3.51
Melting temperature, Tm, °C	1414.85	1238	2500	2730	2730	2730	3700

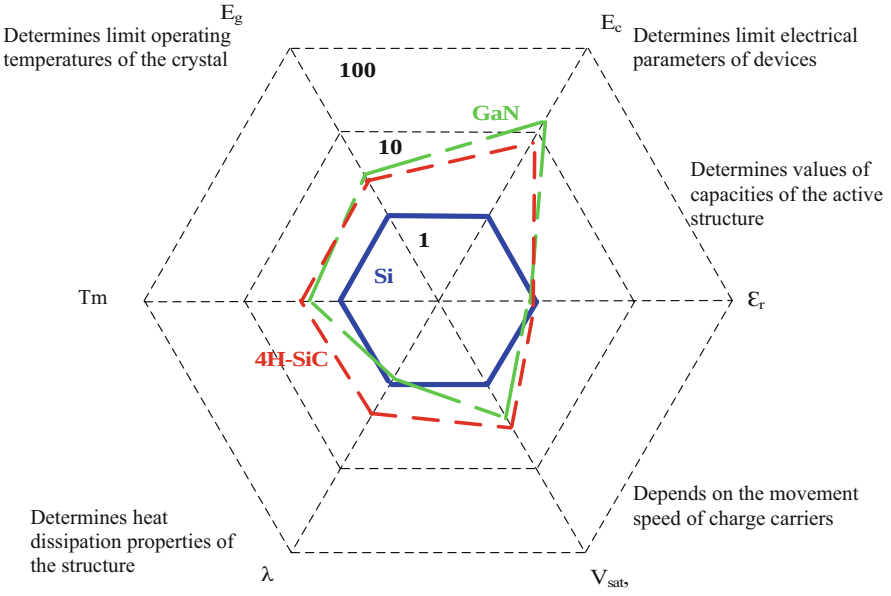

Fig. 6.2 Physicla properties of semiconductor materials Si, GaN and SiC

possible fields of application of Si, SiC and GaN in physical coordinates: gap width, strength of the electrical breakdown field, mobility of electrons, drift speed, dielectric constant, heat conductivity, density and melting temperature.

As can be seen from Fig. 6.2 and Table 6.1, GaN and 4H-SiC are characterized by the high strength of breakdown field E_c, high drift speed of charge carriers V_{sat}, good (GaN) and very good (4H-SiC) thermal conductivity λ, low dielectric constant ε_r, high melting temperature T_m and great width of the gap E_g.

The above characteristics make it possible to develop and produce more powerful and faster devices based on GaN and SiC as compared to Si-based devices.

Fig. 6.3 shows the fields of recommended use of Si, GaN, SiC and other types of power semiconductor devices in the frequency-power axes [10].

Gallium nitride is widely used for creation of LEDs, semiconductor lasers and SHF transistors.

High-quality crystalline gallium nitride can be produced at low temperature by deposition from steam-gas phase on buffer AlN layer [11]. Production of high-quality gallium nitride crystals made it possible to create p-type conductivities and create highly effective LEDs and laser diodes radiating in the blue and violet regions of the spectrum. This also led to development of nitride-based devices, such as UV radiation detectors and high-speed field transistors.

Highly effective LEDs emitting radiation in red and yellow-green regions of the spectrum were created in the 1960s-1970s.

Creation of GaN-based blue LEDs with high luminous brightness was the last stage in development of LEDs of basic colors, which made it possible to create full-color LED screens. The first blue LED was made by Shuji Nakamura on March 28, 1991.

Nitrides (semiconductors) of the third group are considered to be among the most advanced materials for production of optical devices in the visible shortwave and UV regions. Potential markets for high-power and high-frequency GaN-based devices include SHF (radio frequency amplifiers) and high-voltage switching devices for electrical circuits. Great width of the gap means that workability of GaN transistors is preserved at higher temperatures as compared to silicon transistors. In 1993, first experimental field transistors made of gallium nitride were produced. This field is currently actively developing [11].

A promising direction of development of gallium nitride is military electronics, in particular – solid-state GaN-based transceiver modules of an active electronically scanned array (AESA). Airbus Defence and Space is the leading European company in development and application of GaN-based transceiver modules (TRMs) in AESA [11].

Silicon carbide is used in super-fast high-voltage Schottky diodes, n-MOSFETs and in high temperature thyristors [12]. As compared to silicon and gallium arsenide devices, silicon carbide devices have the following advantages:

– several times greater gap width;
– 10 times greater electrical conductivity;

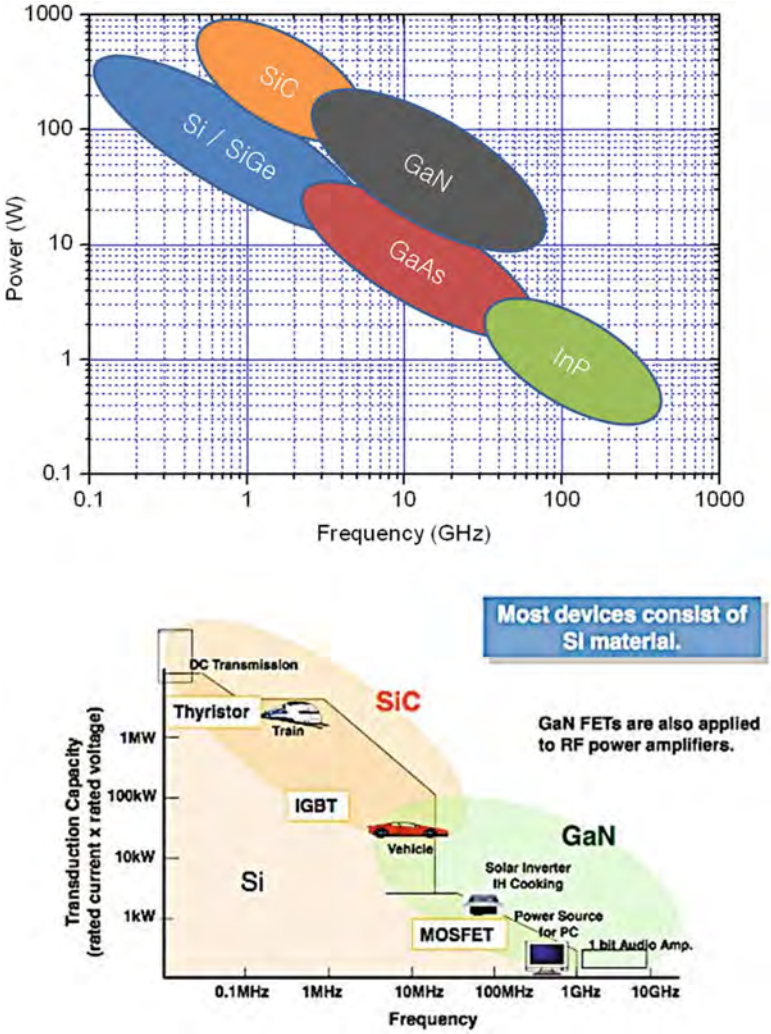

Fig. 6.3 Recommended fields of application of Si, GaN, SiC and other types of powerful semiconductor devices [10]

- high permissible operating temperatures (up to 600 °C);
- heat conductivity 3 times higher than in silicon and almost 10 times higher than in gallium arsenide;
- resistance to the effect of radiation;
- stability of electrical characteristics during temperature variation and absence of drift of parameters in time.

6.2 Evolution of Silicon Carbide Production Technology

The history of discovery and industrial production of silicon carbide is described in [13, 14]. Let us consider only its main stages.

First SiC crystals were found during studies of meteorites in the Canyon Diablo Crater in the Arizona Desert by Henry Moissan. In 1905, the mineral was named after its discoverer – moissanite. Due to natural rarity, silicon carbide is usually produced artificially.

Growing of single crystals of silicon carbide is a fairly complex technical task. The main problem during production of SiC crystals is the absence of its liquid phase at technically possible pressure levels, as well as high temperatures of synthesis of this diamond-like material. The most popular method of growing semiconductor chips of silicon carbide is sublimation, i.e. evaporation and condensation of the synthesized material [14]. Evolution of the technology of silicon carbide production looks as follows.

1893. Acheson Method. Acheson E.G. US Patent No. 492767, Feb. 28, 1893.

The simplest production method is sintering of silica SiO_2 with carbon in Acheson graphite electrical furnace at high temperature of 1600—2500 °C:

$$SiO_2 + 3C = SiC + 2CO$$

The method suggested by Edward Acheson with slight modification is still used to produce crystalline silicon carbide for production of abrasives.

Purity of the silicon carbide formed in the Acheson furnace depends on the distance to graphite resistor in tubular electric heater (TEH).

Colorless, pale yellow and green crystals of high purity are closest to the resistor. At greater distances from the resistors, the color changes to blue or black due to impurities. Nitrogen and aluminum are the most commonly found contaminants affecting conductivity of the produced material [12].

Silicon carbide produced by the Acheson method has two main disadvantages preventing its use in electronics: uncontrollable structure and shape formation of crystals and their significant contamination.

It has been found that there are different types of silicon carbide with similar chemical nature but different electrophysical parameters. It turned out that SiC specimens can have different crystalline structures – cubical (3C-SiC), hexagonal (2H-SiC, 4H-SiC, 6H-SiC and nH-SiC), rhombohedric (15 R, 21 R, etc.). As of now, there are about 200 known crystal modifications of SiC. Therefore, silicon carbine is one of the most prominent representatives of polytype compounds. The term "polytypism" was specifically introduced for carborundum [13].

1907. Electroluminescence of Silicon Carbide. ROUND H.S. "A note on carborundum", Electrotechnical World 49, 308, 1907.

H. Round observed luminescence during passage of electrical current through a SiC crystal.

1922. First Patent for an Electroluminescence Source**.** Losev O.V. "Detector-Generator, Detector-Amplifier", 1922, 14, 374.

Oleg Losev carried out more detailed studies of electroluminescence of silicon carbide in 1922–1940. He established the presence of connection between rectification and electroluminescence and observed changes in the luminescence color with increased density of current passing through the crystal. Thus, two phenomena that are critical for semiconductor electronics, electroluminescence and rectifying properties of p-n-structures, were first discovered in SiC crystals. However, electrovacuum devices were widely applied in radio engineering during that time, and these discoveries remained unnoticed [13].

1955. Lely Method Lely (Germany).

Pure silicon carbide can be produced with the help of the so-called Lely sublimation process, suggested by Lely in 1955, in which SiC powder is sublimated in the argon atmosphere and deposited on colder substrate in the form of scale monocrystals with dimensions of up to 2 × 2 cm. This process produces high-quality single crystals formed by quick heating to high temperatures and mostly composed of the 6H-SiC phase. Improved Lely process aided by induction heating in graphite crucibles produces even larger monocrystals with diameters of up to 10 cm [12].

It was determined that silicon carbide is a semiconductor with indirect band structure, i.e. the possibility of radiating recombination in it is low, and the efficiency (quantum output) of SiC LEDs shall be three-four orders of magnitude lower than in devices based on direct-band semiconductors. The width of SiC gap here depends on the polytype and varies between 2.39 eV for 3C-SiC and 3.3 eV for 2H-SiC. Many optical, electrical and other parameters of the material were determined [13].

1964. First Industrial Production of SiC Single Crystals in the USSR. Podolsk Chemical and Metallurgical Plant.

1970. Sublimation Sandwich Method of Growing Epitaxial SiC Layers. Y.A. Vodakov and E.I. Mokhov suggested sublimation sandwich method of growing epitaxial SiC layers, according to which the process occurred during approach of the vapor source and the substrate. This method allowed for controlled creation of epitaxial SiC layers with both n-type and p-type conductivity, i.e. create SiC p-n-structures [13].

1976. LETI Method. First results of growing bulk SiC crystals wer presented by employees of St. Petersburg State Electrotechnical Institute LETI Y.M. Tairov and V.F. Tsvetkov at the First European Conference on Crystal Growth (Zurich, Switzerland, 1976), while the first full-scale publication dedicated to growth of SiC crystals, referred to as LETI method, appeared in 1978 [14].

This method was based on: classic scheme of condensation of oversaturated vapor on single seed crystal (control of the nucleation process), limitation of the crystallization speed during the initial stage due to implementation of this stage in the atmosphere of inert gas (suppression of spontaneous generation and formation of a polycrystal) and pumping of the inert gas from the chamber for achievement of sufficiently high vacuum (ensuring gradual increase in the growth speed up to several millimeters per hour). Hexagonal monocrystals with dimensions of not more than 20x20 mm2 obtained by the Lely method were used as seeds; polycrystal silicon carbide synthesized from silicon and carbon of the semiconductor purity was used as the material source [14]. Growth was performed at temperatures about 2000°C.

Based on these technologies and their modifications, laboratories of Y.A. Vodakov and V.E. Chelnokov of the A.F. Ioffe PTI by the middle of the 1980s developed several SiC-based semiconductor devices and performed extensive studies of electro-physical properties of silicon carbide. It was established that introduction of certain impurities or change in the Si/C ratio in the growth area may lead to change in the polytype of the growing epitaxial layer as compared to the substrate [13].

1982. LETI method was introduced in serial SiC production**.** Podolsk Chemical and Metallurgical Plant. In 1987, production of silicon carbide was paused.

1983. **Chemical Vapor Deposition (CVD).** The interest in SiC as a promising material for semiconductor electronics was fully renewed after development of the method of gas-transport epitaxy (CVD) of 3C-SiC films on silicon substrate by S. Nishino. The use of standard technological equipment and large substrates made it possible to use the obtained results for creation of commercial products. Several types of field transistors were soon created on the basis of epitaxial films grown with this method. However, parameters of these devices and the quality of the films remained quite low. As a rule, these films are used in production of membranes or tension sensors. Since 3C-SiC (SiC polytype with the narrowest gap) has maximum operating temperature only slightly higher than in gallium phosphide (GaP), modes of CVD growth of 6H-SiC films on 6H-SiC substrates were quickly developed. The use of the modified Lely method (substrate), CVD epitaxy (epitaxial layers) with subsequent plasma-chemical etching (formation of mesa-type structures) and surface metallization made it possible to create a number of SiC devices: LEDs of the blue spectrum region, photo receivers of the UV range, rectifying diodes, field and bipolar transistors, thyristors [13].

Pure silicon carbide can also be produced by means of thermal decomposition (pyrolysis) of polymethylsilane $(SiCH_3)_n$ in the atmosphere of inert gas at low temperatures [12].

1987. Creation of Cree Research Inc. North Caroline, USA.
In 1991 Cree Research Inc. launched commercial production of bulk SiC crystals using the LETI method.

Unfortunately, in the 1990s the works of Russian scientists and the scientific potential in the field of silicon carbide physics created by the were mostly in demand by Western companies and universities. Scientists from the USSR became crystallization centers for companies and research groups in the countries of the USA and the Western Europe. In Cree (USA), the world leader in production and development of silicon carbide-based devices, almost a half of the scientific specialists in the beginning of the 1990s were natives of the USSR. Unfortunately, in the 1990s the works of Russian scientists and the scientific potential in the field of silicon carbide physics created by the were mostly in demand by Western companies and universities. [13].

In 1993, the first SiC-based IC was produced in the USA.

2001. Infinion (Germany) produces a line of 300 V and 600 V Schottky diodes.

Europe aims at using SiC in industry. USA is aimed at the defence applications, while Japan is developing applications in car industry [15].

2002. Cree (USA) produces a line of 300 V, 600 V and 1200 V Schottky diodes.

6.3 Main Manufacturers of SiC-Based Power Electronics Devices

In subsequent years the number of companies in the world engaged in research works in the SiC field increased significantly (see Table 6.2).

The list of Russian enterprises and companies involved in theoretical and applied studies in the field of SiC is fairly short: [16, 17]:

- A.F. Ioffe PTI, Saint Petersburg;
- St. Petersburg State Electrotechnical Institute LETI;
- CJSC "Svetlana", Saint Petersburg;
- JSC "Research Institute of Electronic Technology" (JSC "NIIET"), Voronezh;
- CJSC "Electro-Rectifier Research and Production Complex", Saransk;
- RAS Institute of Applied Physics, Nizhny Novgorod;
- Bryansk CJSC "Silicon EL Group";

Table 6.3 illustrates fields of application of SiC-based power electronics.

The history of SiC diodes is very noteworthy: luminance in SiC was first discovered by H. Round in 1907. First commercial LEDs were also based on silicon carbide. Yellow 3C-SiC diodes were produced in the USSR in the 1970s, while blue 6H-SiC diodes were manufactured in the 1980s across the globe. The production quickly stopped, as gallium nitride demonstrated emission that was 10–100 times brighter. This difference in efficiency is associated with unfavorable indirect SiC gap, while gallium nitride has direct gap that contributes to an increase in luminous intensity. However, SiC today is still one of important components of LEDs; it is a popular substrate of growing of gallium nitride devices and a heatspreader used in powerful LEDs.

Table 6.2 Companies engaged in research activities in the SiC field

Company profile	Company		
	USA	Europe	Japan
Military/aerospace devices	Norhrop Grumman, HRL, NASA (Glen Research Center)	Thales, AMS, EADS, Ericsson MW	–
High-frequency/ power semiconductor devices	Triquint	Infineon, STM, Philips, Dynex	Hitachi, Toshiba, Toyota/ Denso, Fujitsu/Eudyna, Oki, NEC, New Japan Radio
Vertically integrated devices (substrates, chips, packaging)	Cree, Semisouth, Astralux, Intrinsic, TDI, LCermet, Nitronex	Siced/Sicrystal, Linkopings University/TRANSIC	Large companies
Substrate layers	Dow Corning, Cree	–	–
Automation, power electronics	General Electric, Rockwell	Siemens, ABB, Alstom	Matsushita Electric, Mitsubishi Electric
Car electronics	–	–	Toyota/Denso
Optoelectronics	Lumiteds, Cree, Gelcore, Kopin	Osram Opto Semiconductor	Nichia, Toyoda Gosei, Sony, Rohm
Equipment	Veeco	Aixtron, Epigress, Thomas Swan, Riber, Jipelec, EMF	Takeuchi, Nippon Sanso

Wide use of silicon carbide is prevented by the absence of economically effective technology of production of single crystals, which makes it possible to produce plates with dimensions optimal for serial production. Silicon devices are currently produced on plates with diameter of 150, 200 and 300 mm with specific cost of 0.1 €/ cm^2, while the percentage yield exceeds 90%. Percentage yield of SiC crystals on plates with 100 and 150 mm diameters is still lower by an order of magnitude, while their cost is higher by an order of magnitude. At the same time, popularity of SiC diodes and transistors is aggressively growing due to their unique characteristics, in particular – increased speed of operation due to the absence of recovered charge [1].

Gallium nitride GaN has slightly lower characteristics than SiC and is mostly used in optical electronics. Since non-conductive sapphire Al_2O_3 is currently used as GaN substrate material, active and passive GaN elements shall have planar structures.

The use of wide-gap materials makes it possible to increase the limit operating temperature of crystals to at least +200°C. However, in order for these possibilities to be implemented without deterioration of reliability indicators, it is necessary to introduce the relevant technologies of module packaging, find new interface materials, reject standard materials of soldering of crystals on board or in package and ultrasound welding of crystal pins. These processes largely determine physical limits of power density and temperature range of power modules [1].

Table 6.3 Fields of application of SiC-based power electronics [15]

	Power supply (fuel electric cells)	UPS (mobile power sources)	HEV (hybrid cars)	Solar b atteries	Turbines of wind power stations	Electric motors	High-voltage power transmission lines, railroad and water transport
Main devices	MOSFET, Schottky diodes	MOSFET, IGBT, Schottky diodes	MOSFET, IGBT, Schottky diodes	MOSFET, IGBT, Schottky diodes	IGBT, Schottky diodes	IGBT, Schottky diodes	GTO, IGBT thyristors, pin diodes
Voltage	600 V	600/1200 V	650–1200 V	600–1200 V	690–4000 V	600–1200 V	>1700 V
Peak current per one chip	0.5–10 A	2–100 A	50–200 A	75 A	150 A	3–100 A	10–200 A

One of the possible radical solutions to this problem consists in introduction of the low-temperature sintering process by SEMIKRON and development of the SKiN technology [1, 18, 19].

6.4 Designs of GaN-Based Power Devices

Gallium nitride is mostly preferred to other semiconductor materials suitable for production of powerful devices (GaAs, SiC, diamond) due to high parameter values of GaN-based devices and relatively low production costs.

Silicon carbide and diamond are expensive materials, and the volume of their supply is limited. Moreover, there are currently no large substrates based on these materials. At the same time, due to improvement of processes of epitaxial growth of gallium nitride on silicon substrates (the cost of which is approximately two orders of magnitude lower than the cost of silicon carbide substrates), it becomes possible to produce high-quality GaN transistors on plates of large diameters.

One of the promising properties of gallium nitride from the point of view of creating powerful devices for power electronics is the possibility of formation of AlGaN/GaN heterostructural field transistors with low resistance in open state (R_{dsON}) (Fig. 6.4). Due to high values of mobility and concentration of 2D electron gas (2DEG) charge carriers formed at the border of heterostructure separation, saturation current of such structure is high, while the output power of devices based on AlGaN/GaN appliances is also increased due to great width of the material

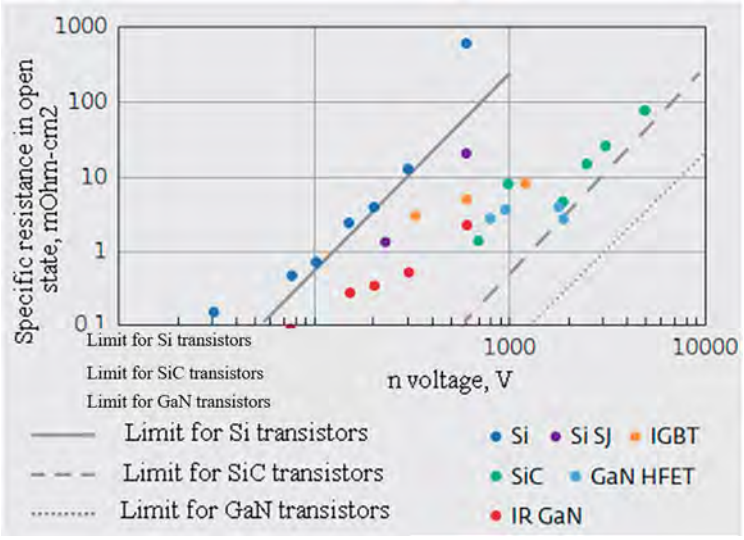

Fig. 6.4 Comparison of resistance R_{dsON} of GaN heterostructural field transistors on silicon substrates by IR and high-power Si- and SiC-based transistors

gap. At the same time, total gate charge and gate charge relative to drain (Qg and Qgd) respectively required for transistor switching are lower than in silicon devices of the same power. Low Qgd value increases the switching speed and reduces the transistor losses.

However, unlike silicon field devices, electrons in GaN HEMT are present in the channel even if there is no voltage at the gate, i.e. the transistor is a normally closed device or a device operating in the depletion mode, and its control requires a specialized driver circuit different from circuits of drivers of high-power silicon MOSFETs. Therefore, one of the main tasks of developers of power GaN transistors is the creation of normally open devices, i.e. devices in the saturation mode, which can be controlled by driver circuits of regular CMOS microcircuits.

Over the last few years, GaN- and SiC-based devices have become commercially available, but their wide introduction was prevented by high costs and experimentally unconfirmed reliability as compared to silicon element base. However, in terms of key characteristics wideband semiconductor-based devices greatly surpass silicon devices. GaN demonstrates excellent electrical strength and mobility of electrons, which helps achieve higher quality indicators than in SiC. This is true for most applications requiring transformation of electrical energy, excluding modes of operation at high temperatures, where SiC surpasses all materials used in production.

Price balance with silicon devices is achievable in case of production of GaN HEMT devices on silicon epitaxial plates; in this case, however, voltage levels are limited by 650 V or less. Higher voltages require transition from Si-substrates to SiC substrates, but this causes raise in price of the products due to increased cost of the substrate and longitudinal dimensions of the device necessary to ensure operation at high frequencies.

The best option is transition to devices with vertical structure. They will conform to the requirements for characteristics and cost due to significant reduction of the size of the crystal, but will require GaN substrate to support vertically flowing current. The task is to develop GaN-based switching elements with vertical structure. The solution to this task will make it possible to create devices for energy transformation that will have high efficiency and cost less than the existing devices.

Thus, device structures of gallium nitride-based power electronics have the following advantages as compared to silicon:

– higher blocking voltages;
– higher density of dissipated power
– lower values of R_{dsON};
– better frequency characteristics;
– radiation immunity;
– high operating temperature.

The possibility of operation of GaN field transistors at temperature of 300°C, as well as at 1000°C in vacuum (maximum operating temperature of silicon transistors – 140–150 °C) have already been demonstrated.

Analytics confirm that in the near time power electronic devices based on gallium nitride will continue to drive out silicon analogs for applications with blocking

voltage of up to 1000 V, especially in end products with high added value, including special purpose devices.

Design and operating principle of device structures of power electronics with properties of bulk gallium nitride are equivalent to those based on silicon. The use of diode structures as rectifiers and MOSFETs as key elements can be interesting for the purposes of power electronics.

6.4.1 Diode structures

Most diodes can be classified as Schottky diodes (Fig. 6.5a), Schottky barrier diodes (Fig. 6.5b) and P-N diodes (Fig. 6.5c).

The main advantage of Schottky diodes (Fig. 6.5a) consists in low forward voltage drop and short switching time; however, on the other hand, these structures are characterized by high leaks due to the low barrier. The use of Schottky diodes based on bulk gallium nitride is unreasonable, since their characteristics are inferior to those of their analogs based on silicon and silicon carbide.

Schottky barrier diodes (Fig. 6.5b) in case of forward shift demonstrate advantages of Schottky diodes in tersm of low voltage drop, in case of reverse shfit – advantages of P-N-diodes in terms of . However, there are no currently GaN diodes with Schottky barriers due to the fact that no one has yet achieved efficient post-implantation activation of magnesium, which is a p-type impurity for GaN.

The advantage of GaN P-N-diodes as compared to SiC-based devices is the significantly lower drop in direct voltage, which is due to greater mobility of carriers and the absence of degradation of the crystalline structure during current flow. However, it is currently impossible to achieve low alloying levels required for high voltages in GaN. Moreover, GaN P-N-diodes cost more than silicon carbide ones.

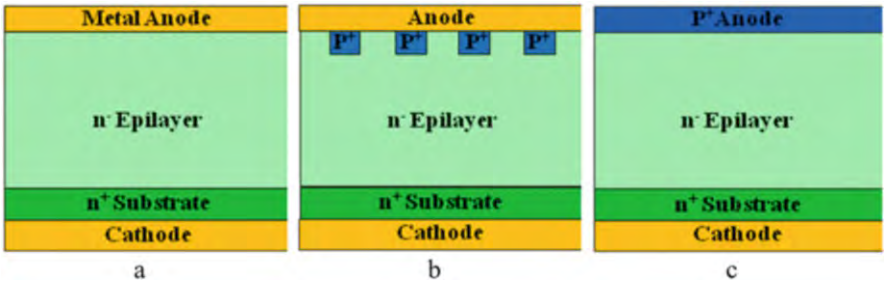

Fig. 6.5 Diode structures: **a** – Schottky diode, **b** – Schottky barrier diode, **c** – P-N-diode

6.4.2 MOSFET

Structure of a vertical GaN MOSFET is shown in Fig. 6.6. The obvious advantage of such structure consists in the possibility of creating normally closed transistors. However, this requires creation of a relatively thin p-channel that would be able to include depletion regions of both p-n-junctions in case of zero shift. However, unlike SiC, GaN technology does not allow additional alloying of surface by ion implantation. In addition, maximum current in structures of this type is limited by the fact that the mobility of carriers in 3D GaN is lower than in 2DEG.

Vertical GaN MOSFET with locally grown GaN layer under the gate (OG-FET) (Fig. 6.7) is a modification of trench GaN MOSFET but has the following advantages as compared to the latter. First, non-alloyed GaN layer used as the conducting

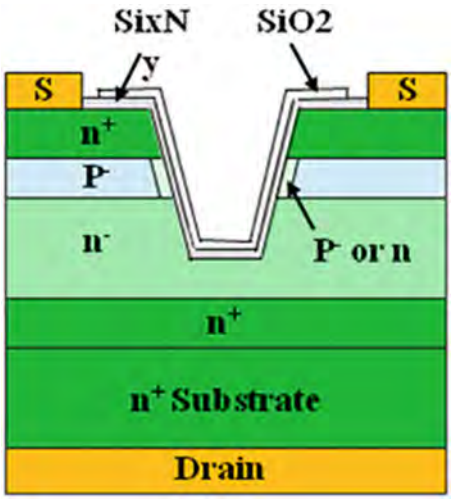

Fig. 6.6 Structure of a GaN trench MOSFET

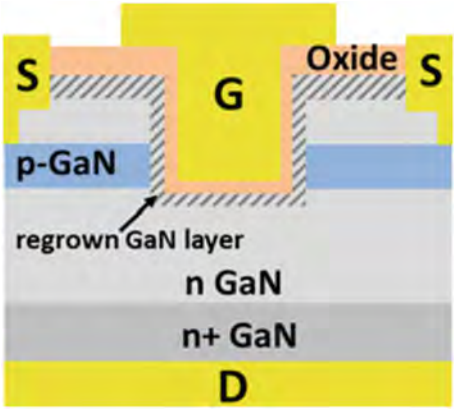

Fig. 6.7 Structure of a trench GaN MOSFET with local GaN epitaxy under the gate

channel has enhanced mobility of carriers due to their reduced dispersion on impurities. Second, gate oxide is grown in-situ with the channel layer in the MOCVD process, which reduces density of surface states and increases reproducibility of gate characteristics.

It should be noted that improvement of characteristics of the channel occurs without deterioration of behavior of normally closed device. In OG-FET structures, depletion of the channel with zero displacement at the gate is ensured by depletion region created in it by p-GaN region, and the channel is opened by positive potential of the gate.

6.4.3 Structures Based on 2D Electron Gas

Structures with 2D electron gas, also referred to as HEMT structures, make it possible to overcome the contradiction between high concentration of carriers and their mobility typical of 3D material. This makes it possible to achieve brand new characteristics both for SHF devices and for power electronic devices.

6.4.4 Lateral Structures

Structure of a lateral HEMT is schematically presented in Fig. 6.8. The function of conducting channel between source and drain is performed by 2DEG in the n⁻⁻GaN layer at the border of division with AlGaN. Its conductivity is modulated by the gate voltage; the role of the gate is performed by a metal electrode of the MOS structure or the control Schottky junction. Effectiveness of such transistor due to properties of 2DEG is significantly higher than in Si or SiC MOSFET structures, as the parameter R_{dsON} in HEMT will always have significantly lower values. However, unlike MOSFETs, in which the conducting channel is formed by voltage at the gate, the conducting channel in HEMT is formed during the growth of the heterostructure, and therefore HEMT is a normally open structure.

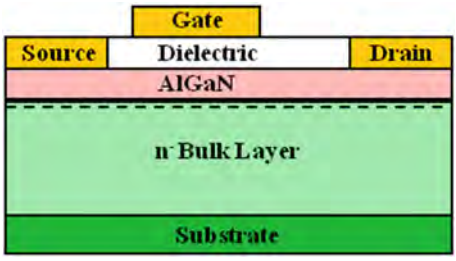

Fig. 6.8 Lateral HEMT structure

Lateral HEMTs are widely found in microwave electronics. For power electronic devices, these structures occupy large areas per current unit, especially for high reverse voltages. For example, for the source-drain distance of 16 μm, maximum reverse voltage shall amount to 1580 V, for the source-drain distance of 125 μm – 10,400 V. Therefore, it becomes more difficult to control electrical field profile of lateral structures. Moreover, lateral HEMTs are heavily exposed to heating, since all heat during operation of the structure is emitted in its sub-surface region.

6.4.5 *Vertical Structures*

These disadvantages are eliminated in vertical HEMT structures (Fig. 6.9a, b), which are widely applied for devices with forward current of more than 100 A and reverse voltage of more than 2000 V regardless of their complex formation technology.

Vertical GaN HEMT is placed in lightly doped n^--GaN layer applied over heavily doped n^+-GaN layer and separated from the region of 2D electron gas by Current Blocking Layer (CBL) with aperture that allows the current to flow vertically from 2D electon gas to the drain on the reverse side of the substrate (Fig. 6.10)

Better ratio of reverse voltage to the R_{dsON} parameter compared to vertical HEMT can be achieved in vertical heterotransition field-emission transistors (VHFET) with 2D electron gas AlGaN/GaN formed on the surface of the mesa recess in GaN substrate (Fig. 6.11). In VHFET structures, the value of threshold voltage can be controlled by changing thickness of the AlGaN layer, including creation of normally open devices.

At the moment, the best combination of characteristics in vertical GaN HEMTs is achieved by PolarMOS technology (Fig. 6.12).

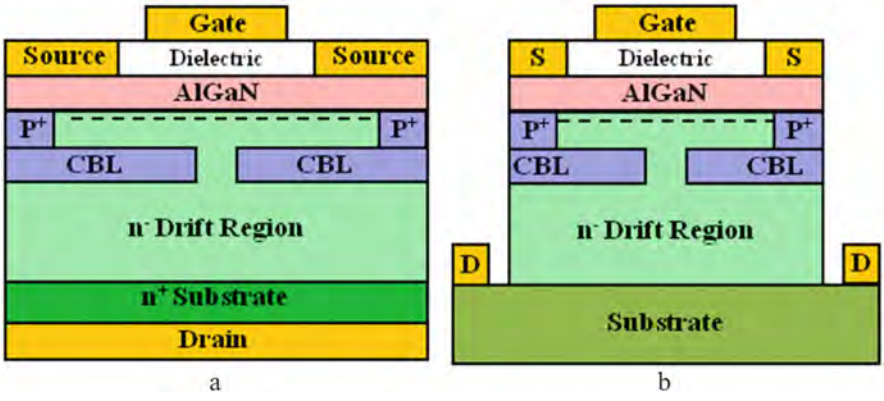

Fig. 6.9 Vertical HEMT structures: **a** – contact on reverse side, **b** – contact on planar side

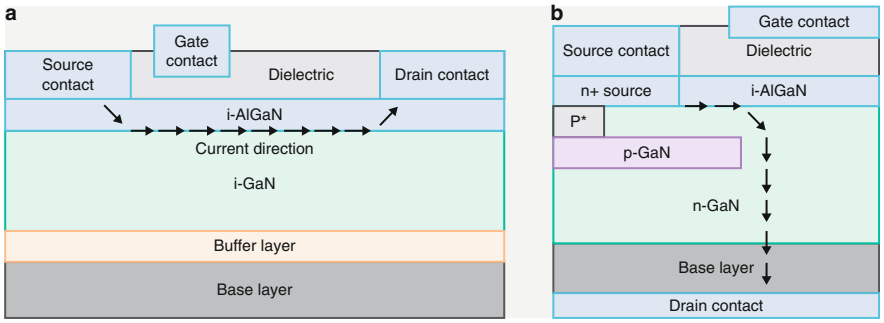

Fig. 6.10 – Current transport in HEMT: **a** – with lateral structure, **b** – with vertical structure

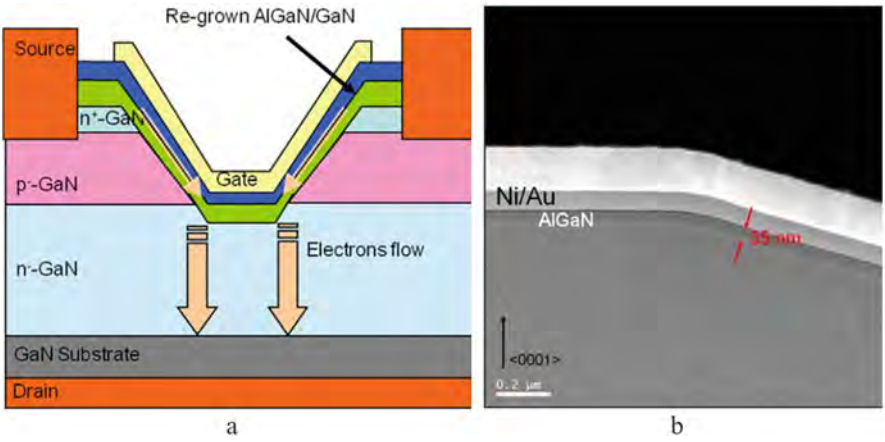

Fig. 6.11 Vertical heterojunction FET: a – structure, b – PEM image of heteroepitaxial AlGaN layer on the surface of mesa-groove in GaN substrate

6.5 State and Trends of Development of the Technology of Powerful GaN-Based SHF Transistors and MICs

Development of the technology of SHF devices on wide-gap semiconductor materials lead to exploration of design of microwave power transistors and monolithic integrated circuits (MIC) based on Gallium Nitride (GaN) in serial commercial production. Below we are going to consider the level of basic technical parameters of GaN-based transistors and MICs, as well as transistor amplifiers of high power level (10–100 W and more) based on them, as well as the main trends in development of this class of microwave devices.

The interest of developers of high-power semiconductor amplifiers in GaN transistors (or, to be more precise, in transistors based on AlGaN/GaN

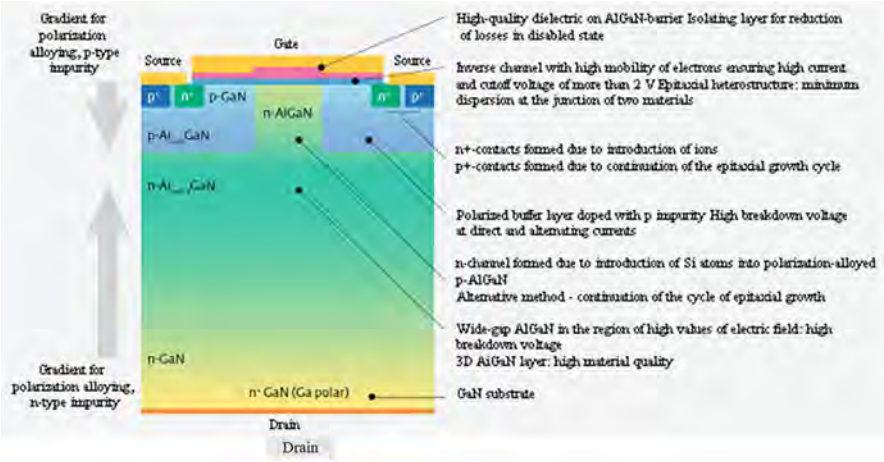

Fig. 6.12 Structure of vertical HEMT according to the PolarMOS technology

heterostructures) is due to a number of important properties of wide-gap semiconductor compounds in general and gallium nitride in particular, which are presented in the summary Table 6.4.

Presented are the main parameters of compound semiconductors used in the technologies of production of SHF devices (Si, SiC, GaAs, GaN, InP).

It is known that the maximum width of the semiconductor material gap determines the possibility of operation of the transistor at high levels of external effects (temperature, radiation). Extremely high electron concentration in the field of 2D electron gas in combination with acceptable electron mobility make it possible to implement high current density in the cross-section of the transistor channel and high gain factor. Maximum critical strength of the electrical field makes it possible to implement breakdown voltages of 100–300 V and raise operational voltage of the drain to 50–100 V, which in combination with high current density ensures specific output power of industrial GaN transistors of 3–10 W per 1 millimeter of the gate width (up to 30 W/mm in laboratory specimens), which increases specific output power of gallium arsenide (GaAs) transistors by an order of magnitude. Problems hindering further development of GaN devices include the task of ensuring efficient heat removal from the active structure and the necessity to grow epitaxial GaN structures on allogenic (with different parameters of the crystal lattice, thermal expansion, etc.) substrates due to the impossibility to implement high-resistance substrate of GaN.

First examples of effective transistor AlGaN/GaN heterostructures demonstrating their main advantages appeared in 1991–1994. In the end of the 1990s, the first examples of GaN MIC amplifiers appeared; at the same time, military and national programs of development of this direction [20] were formed and implemented, such as American WBGSTI program, followed by European MARCOS, TIGER, KORRIGAN and Japanese NEDO programs. At the same time, nearly all leading

Table 6.4 Properties of wide-gap semiconductor compounds [20]

Main parameters of semiconductor connections	Si	AlGaAs/ InGaAs	SiC	AlCaN/ GaN	InP HS
The band gap width, electron volt	1.1	1.4	3.2	3.4	1.35
Electron mobility, $cm^2/(V \cdot s)$	1350	8500	700	2000	10,000
Charge-drift velocity, $*10^7$ cm/s	1.0	2.0	2.0	2.5	2.3
Concentration of electrons in the region of 2D electron gas, cm^{-2}	–	$3*10^{12}$	–	$(1–2)*10^{13}$	$4*10^{12}$
Critical strength of the electrical field, MW/cm	0.3	0.4	2.0	3.3	0.5
Thermal conductivity, W/cm·K	1.5	0.5	4.5	1.3	0.7

Table 6.5 Basic parameters of first serial GaN-transistors [20]

Manufacturer, series	P_{out}, W	F_{max}, GHz	G_{ss}, dB	Deff, %	V_{ds}, V
Eudyna EGNBxx	12–120	0.9–3.5	13–18	60	50
Cree Inc. CGHxx	10–120	1.3–5	16–19	60–70	28
Nitronex NPTBxx	5–180	1–6	15–20	65	48
RFMD RF393x	10–120	0.9–2.7	15–23	60–70	48
OKI KGF72xx	50	–	15	–	50
TriQuint TGA2023xx	6–100	20	8–15	55	28–40

world companies associated with production of GaAs components in one way or another start investing their funds in the technology of GaN devices. These investments bring their result, and the first commercial GaN products appear in the market in 2006–2007: packaged high-power transistors in the frequency range up to 2–4 GHz with output power of 5–50 W (slightly later – up to 120–180 W). The pioneers of the commercial market were Eudyna, Nitronex, Cree and RFHIC, quickly followed by Toshiba, RFMD, TriQuint, OKI, NXP and a number of other companies. In 2008, the first commercial MIC were first produced (wideband power amplifiers, up to 6 GHz) by Cree; in 2009, wideband 10 W MIC amplifiers with the band of 2–17 GHz were invented by TriQuint.

Main parameters of multi-purpose (without integrated wide-band matching circuits) packaged GaN transistors are given in Table 6.5.

It can be see that the basic functional compositions (5–8 types, 10–120 W) and parameters of transistors by all manufacturers are similar, except for transistors of the TGF2023 series by TriQuint supplied as crystals and serviceable at frequencies up to 20 GHz and more. Multi-purpose packaged transistors are supplied in small-sized metal-ceramic flanged or SMD packages with relatively low parasite capacities and ensure the operating frequency band from 30% to an octave and more depending to power and frequency range.

Table 6.6 Basic parameters of serial GaN transistors for communication systems of the W-CDMA standard [20]

Parameters of GaN transistors	Technology designation, transistor type, company		
	Si LDMOS Freezcale MRF21120R6	GaAs MESFET Fujitsu FLL1200IU-2	GaN HEMT Cree CGH21120F
P_{out}(CW,-IdB), W	120	100	50–60
P_{out}(max), W	120	120	115
G_{ss}, dB	11	11	15
ΔF(-IdB), MHz	150	90	350
Deff (@P_{max}), %	35	45	60–70
Deff (@W-CDMA), %	20	20–25	35
V_{ds}, V	28	12	28
$T_{j\ max}$, °C	200	175	225
R_t, °C/W	0.45	0.8	1.5
Dimensions	41x10 mm (push-pull)	34x17.4 mm (push-pull)	20x10 mm (single)

Note: W-CDMA: $P_{out} = 20$ W, ACRL<-35 dB

Properties of high-power internally matched transistors based on different technologies can be illustrated by the data of Table 6.6, which contains parameters of serially produced devices of the power level of 120 W applied in communication systems of the W-CDMA standard within 2 GHz range. This range is selected as the threshold between fields of active application of silicon and A_3B_5 devices.

Obvious advantages of GaN instrument in comparison with other types in this application include significantly (2–4 times) wider frequency band and high drain frequency both in maximum power mode and during amplification of complex signal. Moreover, the indicated parameters are implemented in a single transistor stage, while Si- and GaAs-based transistors are double-transistor assemblies (couples) requiring application of paraphase addition networks, which significantly complicates the amplifier circuit and increases its dimension. Disadvantages include stretched dynamical characteristic (gain compression is observed at power 2–3 times lower than the maximum) and currently high cost of the device per 1 W of output power.

In order to compare the possibilities of using GaN and GaAs transistors in circuits of wideband power amplifiers, let us perform a simple analysis of their specific (i.e., relative to 1 mm of the transistor gate width) parameters. Let us use known estimates for the class A amplifier with the maximum output power of P_{max} and optimal (for achieving this power) transistor load resistance R_{opt}:

$$P_{max} = V_{ds} * I_{max}/8;$$
$$R_{opt} = 2 * V_{ds}/I_{max};$$

where V_{ds} is the source supply voltage, and I_{max} is the maximum current of the open transistor channel.

Table 6.7 Comparative characteristics of parameters of HEMT transistors for GaAs and GaN technologies [20]

Parameters of transistors	GaAs\pHEMT		GaN\HEMT	
	Typical values	TGF2021 (1 mm)	Typical	TGF2023 (1.25 mm)
Specific gate-source capacity (C_{gix}), pF/mm	1.8–3	2.74	1.1–2	1.2
Specific steepness of transient response (G_{mx}), ms/mm	200–400	303	100–300	110
Specific source-drain capacity (C_{dix}), pF/mm	0.15–0.3	0.199	0.2–0.4	0.2
Specific output power (P_x), W/mm	0.7	1.0	5	5
Source-drain supply voltage (V_{ds}), V	9	10	28	32
Specific optimal load resistance (R_x), ohm/mm	29	26.6	39	54
Optimal (estimated) load resistance for output power of 10 W (R10), ohm	2	–	19	–

The presented expressions can be easily used to obtain the formula for the new parameter suggested in [20] – specific optimal load resistance (R_x):

$$R_x = {V_{ds}}^2/4 * P_x,$$

where P_x is the specific output power of the transistor – a parameter widely used in literature.

Typical specific parameters of GaN and GaAs HEMT transistors obtained from the analysis of linear equivalent circuits of transistors given in literature and reference materials of manufacturers, as well as the above R_x parameter, are summarized in Table 6.7.

Also provided are the values of parameters of specific serially produced devices (TGF2021 and TGF2023).

The following conclusions can be drawn from the analysis of the provided data:

- specific gate-source capacity and steepness of GaN transistors is 1.5–2 times lower than in GaAs transistors, which is more of an advantage for the first category from the point of view of wideband matching, as it requires lower transformation coefficients in matching circuits;
- specific drain-source capacity, which bridges the optimal load of the transistor and complicates building of an output wideband matching circuit at frequencies above certain threshold frequency is approximately equal for both classes of transistors;
- specific optimal transistor loads (R_x) are also close (slightly higher for GaN transistors).

Presented considerations allow us to make a grounded conclusion that many projects and technical solutions related to circuits and structures of matching chains designed for GaAs-based transistors and MICs can be (with minimum changes) applied to GaN transistors with equal or 20–50% greater gate width; in this case, with similar length of gates of both types of active structures, the same band, gain,

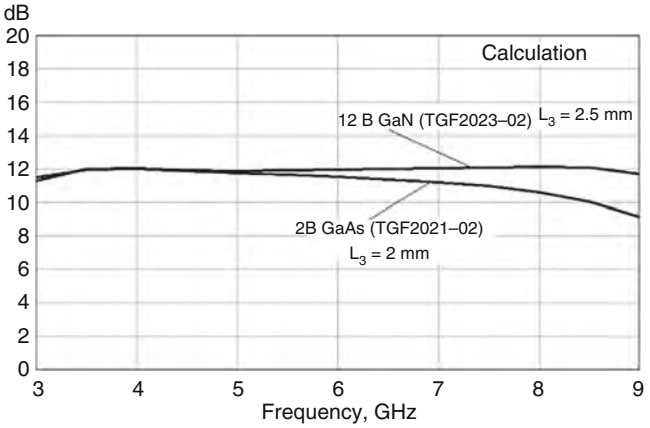

Fig. 6.13 AFC of 4–8 GHz test circuits with models of GaN and GaAs transistors

weight and dimensions will be achieved, but the output power will be several times higher. This is also confirmed by experimental results [20]. To illustrate the possibility of migration of technical solutions, Fig. 6.13 shows design AFC of the wideband amplifying stage for the 4–8 GHz range designed on GaN transistor of the TGF2023–02 type by TriQuint with the gate width of 2.5 mm and output power of 12 W, which optionally includes the TGF2021–02 GaAs transistor of the same manufacturer with the gate width of 2 mm and output power of 2 W. Similar AFCs were obtained simply by adjusting equivalent inductance of transistor gate electrode connection by 50%.

Commercially available GaN-based monolithic amplifiers designed as crystals or in metal-ceramic packages are produced by Cree, MwT, TriQuint, RFMD, etc.

Parameters and dimensions of certain MIC types, both commercially available and described in publication, illustrating main classes of amplifiers and ranges of application frequencies are listed in Table 6.8.

In comparison with serially produced GaAs MICs, new devices have 2–10 times greater output power and commensurate or greater efficiency with the same or smaller crystal dimensions. The list of produced GaN-based amplifying MICs is currently dozens (if not hundreds) times shorter than the list of GaAs MICs. To illustrate (Fig. 6.14) the rates of improvement of GaN MIC parameters, it is possible to present the chronology of development of GaN MICs of output amplifiers of the X-band for radar systems with phased antenna arrays, great attention to which is paid by military specialists due to the fact that parameters of such MICs (first of all, efficiency and output power) determine the most important tactical and technical parameters of such radars. The following references are presented here: 1 – R. Behtash et al. Coplanar AlGaN/GaN HEMT power amplifier MMIC at X-band //// 2007 IEEE MTT Symposium Digest, p.p. 1657—1659 [21]; 2 – D. M. Fanning et al. 25 W X-band GaN on Si MMIC // GaAs Mantech Conference Proceedings, 2005 [22]; 3 – H. Klockenhoff et al. A Compact 16 Watt X-Band GaN-MMIC Power

Table 6.8 Main classes of amplifiers and ranges of application frequencies [20]

Type	ΔF, GHz	P-3 dB, W	G_{SS}, dB	PAE, %	Design
CMPA2560025F Cree Inc.	2.5–6.0	25–37	23–27	>30	MSL package 13x13 mm
MGA-495940-02 MwT	4.9–5.9	10	12	–	QFN package
HRL lab.	75–92	>0.5	11–14	>17	Crystal 3.4x1.3 mm
BAE systems	4–18	3.2–4.4	10	16	Crystal 4.2x4.9 mm
ALCATEL, THALES, UNC, QinetiQ, XLIM	8–10	>30 (58 max)	13–16	>33 (38 max)	Crystal 4.5x4.0 mm
TriQuint	0.03–3	8–10	–	38	MSL package 17x12 mm
TriQuint	2–17	8–12	–	20	Crystal

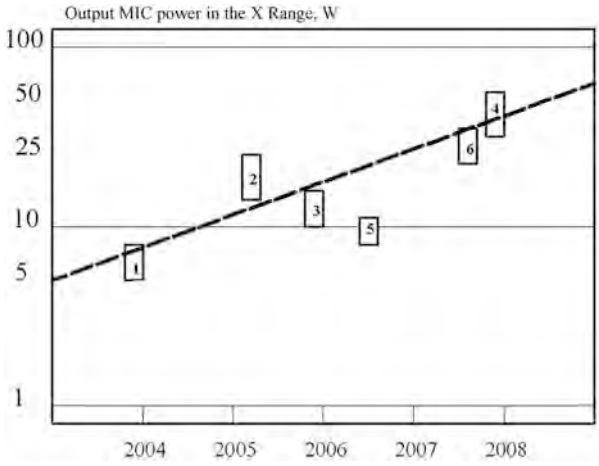

Fig. 6.14 Parameters of GaN MIC of the X range

Amplifier // IEEE MTT-S Digest, 2006, p.p.1846–1849 [23]; 4 – S. Piotrowicz et al. State of the Art 58 W, 38% PAE X-Band AlGaN/GaN HEMTs microstrip MMIC Amplifiers // IEEE Com- pound Semiconductor IC Symposium, 2008 [24]; 5 – T. Chen et al. X-Band 11 W AlGaN/GaN HEMT Power MMICs // EwMIC Conference Proceedings, 2007, p.p. 162 — 164 [25]; 6 – C. Costrini et al. A 20 Watt Micro-strip X-Band AlGaN/GaN HPA MMIC for Advanced Radar Applications // EwMIC Con- ference Proceedings, 2008, p.p. 1433 — 1436 [26].

Figure 6.15 shows structures of crystals of the 40 W GaN MIC amplifier of the X band and high-power industrial GaAs amplifier of the MAAPGM0079 type by M/A Com (proportions of crystal dimensions have been preserved) [20].

It can be seen that the design of the GaN amplifier is significantly simpler and 2.3 times smaller; moreover, there is a possibility of further increase of the output power of GaN MIC in the X range.

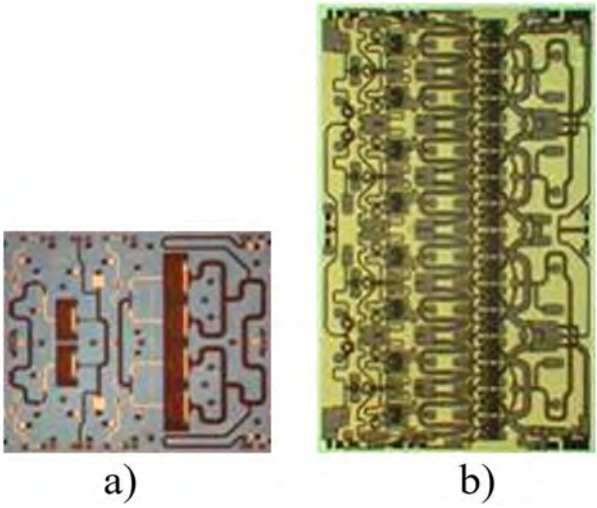

Fig. 6.15 Examples of layout solutions of designs of GaN MIC amplifiers: (**a**) GaN 10 GHz / 40 W (18 mm^2) [24]; (**b**) GaAs 10 GHz / 20 W (41 mm^2)

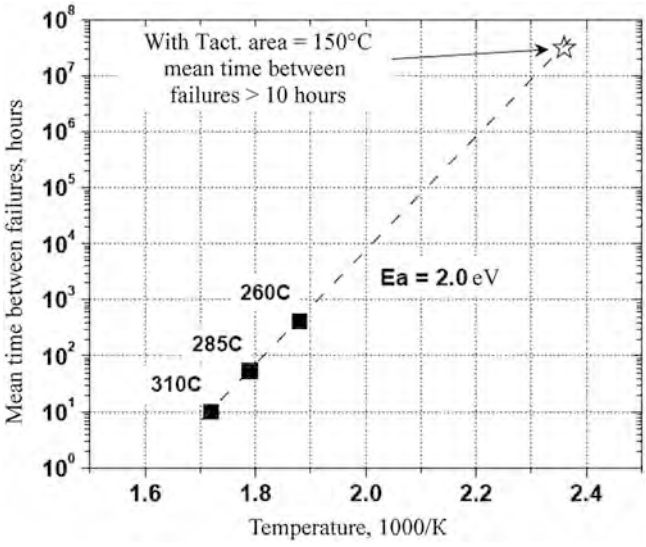

Fig. 6.16 Arrhenius curve of a GaN transistor [20, 27]

The studies of temporal stability of parameters and reliability of GaN transistors performed during development of industrial technologies have lead to acceptable reliability parameters of serial devices. Figure 6.16 shows the Arrhenius curve for power GaN transistors on silicon substrate by Nitronex as an example [20]. It is demonstrated that with temperature of the active zone of the crystal equal to 150 °C, mean time between failures exceeds 10^7 hours, and the activation energy E_a is 2.0. With the permissible operating temperature of the crystal $T_j = 200$ °C, mean time

Table 6.9 Parameters of serial devices [20]

Type	ΔF, GHz	P-3 dB, W	G_{SS}, dB	PAE, %	V_{dc}, V
Aethercomm SSPA 0.5–3.0-50	0.5–3.0	70–100	31	13–19	50
Aethercomm SSPA 0.8–2.5-200	0.8–2.5	100–200	47	11–22	50
EMPower BBM3T6AMQ	0.96–3.0	>160	56	23	28
Stealth Microwave SM2560-47GN	2.5–6.0	50	48	25	28

between failures is 10^5 hours. Also demonstrated was the immunity of devices to load mismatch of up to VSWR = 10 in high signal mode. Quick (several hours long) destruction occurs in modern GaN transistors with the active zone temperatures around 320–350 °C.

The achieved parameters are currently inferior to reliability indicators of mass-produced pHEMT transistors (MTBF at T_j = 200 °C is 10^6 hours, destruction temperature – 370-390 °C [28]), but further quick development of the technology of GaN devices shall compensate for this lag. Suggested maximum operating temperature for GaN transistors can be 350–400 °C [29]. Operating parameters of GaN transistors with gate width of 2.8 mm (output power 10 W) on SiC substrate with the crystal temperature increased to 300 °C are examined in [30]. Low-signal gain factor is reduced by 6 dB, output saturation power – by 1.5 dB, maximum channel current and steepness – approximately two times with temperature change from 50 to 300 °C.

Significant advantages of GaN transistors consists in simplified design and increased output power of ultra-wideband (with frequency coverage of more than an octave) power amplifiers. Parameters of several types of such serial devices are listed in Table 6.9.

Weight and dimensional characteristics of wideband amplifiers with GaN transistors are significantly better than in GaAs amplifiers. With equal output power and amplification, dimensions and weight (without cooling radiator) of a GaN amplifier are 2–4 times smaller than dimensions and weight of a similar GaAs amplifier.

One of the directions of using GaN transistors is the improvement of characteristics of pulse solid-state radars in L-, S- and X-ranges. The work [31] describes output wideband AESA transceiver module operating within the frequency range from 8.7 to 11.5 GHz including four GaN MICs: low noise input amplifier with noise factor of 1.8 dB and resistance to continuous input signal of 4 W, preamplifier with output linear power of 4–5 W and two output amplifiers with output power of 14–20 W each. The module in general (at the output of the circulator) provides output power of 20 W in the transmission mode and noise factor of 3 dB in the reception mode.

Specialists of the NEDI institute (Nanking, PRC) have demonstrated a four-crystal internally matched transistor of the X band with output power in the continuous mode of 100 W and efficiency of 38% [32]. In the S-band (2.9–3.3 GHz), the level of pulse output power of GaN transistor approaches 1000 W at efficiency of more than 50% [33] for pulsed mode with duty ratio of 10 and pulse duration of 200 μs. Pulse-top tilt per 200 μs amounted to 0.31 dB, phase drift – to less than 4 degrees.

Developers of GaN devices are greatly interested in wideband communication systems, first of all – in application of GaN transistors in base stations of W-CDMA, UMTS and WiMAX standards.

Development of this direction depends both on improvement of parameters of GaN transistors themselves [34] (increase in output power and efficiency, suppression of memory effects) and application of the known methods of increasing efficiency of base station amplifiers – the use of Doherty circuits [35], application of various modes of high-efficiency amplification (modes of class E [36], F [37] and so on). Commercial success of GaN transistors, achieved despite their fairly high cost, is linked to such advantages on the system level as:

- simplicity and cheapness of circuit-based implementation of high-power amplifiers;
- simplicity of obtaining wide amplification bands, coverage of several sub-bands of the station by one high-power amplifier;
- reduction in energy consumption by the basic station and associated costs;
- reduction of complexity and cost of cooling systems.

Ranges of 2.1 GHz, 3.5 GHz and 5–6 GHz are actively explored by GaN devices. With amplifier power of the 10 W level, efficiency values of more than 70–80% were demonstrated in the 2 GHz range; at the level of 100 W, efficiency values of 55–65% were achieved.

One of the obvious advantages of GaN-based transistors and MICs consists in the use of systems of radio countermeasures, which traditionally cover multi-octave frequency bands in the decimeter and centimeter ranges. One of the target problems of the American WBGSTI program, for example, was the development of the MIC amplifier for the range of 2–10 GHz with output power of 15 W and amplifier module with output power of 100 W based on it [38]. TriQuint developed a monolithic amplifier with the band of 2–17 GHz and the output power of 8–12 W [39]. Let us note that modern serial GaAs MICs in this range have output power of more than 1 W.

In Russia, studies and developments of epitaxial structures of gallium nitride and transistors based on these structures are performed by a number of companies and scientific institutions. They include RAS A.F. Ioffe PTI, JSC “Svetlana-Rost”, FSUE “NPP Pulsar”, FSUE “NPP Istok”, CJSC “Elma-Malakhit”, RAS Institute of Super High Frequency Semiconductor Electronics, FSUE “Giredment”, RAS IAP and a number of other organizations [40]. Developed are samples of high-power and low-noise GaN transistors, which are currently in the stage of laboratory tests. In

terms of commercialization of the devices, the Russian companies are, unfortunately, still far behind the leading foreign companies.

The main production and technological problems, which prevented GaN transistors and monolithic integrated microwave circuits from entering the commercial market, were solved in 2006–2007. This moment marked the beginning of active introduction of gallium nitride technology into military and commercial industry. The rates of industrial exploration of the new technology significantly (2–3 times) exceed the former rates of development of Si- and GaAs-based devices. In the next decade, the frequency range of 1–50 GHz will become the battlefield for serious struggle between two industrial technologies of high-power solid-state integrated circuits, practically equal in their frequency and amplification properties, one of which has serious advantages in parameters (GaAs), and the other wins in terms of cost and level of exploration in mass production.

6.6 Wideband Transistor Power Amplifiers of the Microwave Range

SHF power amplifiers based on transistors and monolithic integrated circuits (MIC) in many radio-technical systems determine critical tactical and technical parameters of the system, such as radiated and consumed power, operating frequency bandwidth, dimensions, weight, reliability and cost. Solid-state SHF power amplifiers in general and wideband devices in particular are often critical links of equipment. Let us consider the world level and directions of development of a specific group of microwave amplifiers – wideband transistor power amplifiers of continuous mode.

The category of wideband amplifiers includes devices with relative width of operating frequencies more than 40% (frequency coverage – ratio of upper and lower limits of the range from 1.4:1 and more, up to several decades). The main difference between wideband devices and their more narrowband relatives consists in the following structural features:

- complex design of the output stage. The possibilities of wideband matching of an active element (transistor) deteriorate significantly with a decrease in its output power and subsequent deterioration of the gate width and capacities of the active structure, which often leads to the need to use multi-channel power adders, complicating the design and inserting additional losses.
- the use of transistors with low additional reactances as active transistor elements (crystals of discrete transistors and MICs in the middle and upper part of the centimeter range and MICs in the millimeter range, as well as packaged transistors in the decimeter range and the lower part of the centimeter range).
- the need to use additional circuitry-based measures of suppressing reflected waves. Wide-band matching does not provide the possibility to obtain low power of the wave reflected from the transistor input by using reactive matching circuits (MC); therefore, excess circuitry features are used in the form of reactive-

dissipative MCs reducing stage amplification, as well as additional feedback links reducing amplification, output power and efficiency of the stage, quadrature addition circuits increasing dimensions and complicating design of the devices and additional circuits of distributed amplification affecting the efficiency.

Due to the above features, electrical parameters of wideband devices are significantly lower than those of wideband amplifiers, while their dimensions and costs are significantly (sometimes several times) higher.

However, there are many systems in which the use of wideband amplifiers is necessary. They include systems of radioelectronic suppression, ultra-wideband location equipment for electromagnetic compatibility testing, special systems of data transmission and measuring instrument.

Due to their complexity, wideband power amplifiers serve as the engine of semiconductor microwave technologies in the attempts of creating more and more powerful and wideband basic integrated elements for building of these devices [41].

Of the available wide spectrum of modern semiconductor technologies and materials [42, 43], in mass production of high-power microwave discrete and monolithic components of the continuous mode suitable for use in wideband amplifiers, the following ones are most commonly used (Table 6.10):

Table 6.10 contains no data on output power values of internally matched transistors containing internal matching circuits for a certain specific section of the frequency range and unsuitable for building wideband power amplifiers, as well as devices based on indium phosphide, which currently cannot be considered high-power devices. Let us consider the state of these technologies in detail.

Silicon Lateral Double-Diffused MOS Transistors (Si LDMOS) have firmly occupied the niche of basic elements in wideband amplifiers with frequencies up to 1000 MHz. Devices based on this technology are produced by Freescale Semiconductor, Sirenza Microdevices, PolyFET, NXP and other companies. They are distinguished by low cost of mass production, high efficiency and permissible operating temperature of the crystal (200°C). At the same time, they have low threshold operating frequencies (below 3.5 GHz) and significantly higher (by an order of magnitude or more) specific capacities of the active structures than devices based on other technologies, which creates significant difficulties for their wideband matching.

Gallium Arsenide Metal-Semiconductor Field-Effect Transistors (GaAs MESFET), which were the most commonly used construction material of wideband microwave amplifiers in the previous century, gradually lost their positions and were pushed out by Gallium Arsenide Pseudomorphic High Electron Mobility Transistors (GaAs pHEMT). Crystals of discrete MESFET transistors are currently produced by Sumitomo Electric (traditional series FLC, FLX, FLK by Fujitsu), Excelics; still in production are several series of packaged transistors of the lower part of centimeter range (e.g. popular models MGF0910A, MGF0911A by Mitsubishi Electric); wide range of MICs of powerful wideband amplifiers previously produced by M/A Com (MAAPGM-xxx series) was withdrawn from production due to liquidation of the

Table 6.10 Industrial Technologies of Powerful SHF Transistors and MICs

Technology	Types of electronic SHF components	Frequency range, GHz	Output frequency range, W	Typical transistor efficiency, %	Supply voltage, V
Si LDMOS	Multi-purpose packaged transistors	0 – 2	5 – 15	60	28
GaAs MESFET	Multi-purpose packaged transistors	0 – 14	Up to 14.5	40	8–10
GaAs HiFET	Multi-purpose packaged transistors	0 – 2.5	1 – 8	35	14 – 28
GaAs HFET	Transistors in the form of crystals and in SMD packages	Up to 10.5	Up to 10	50	8
GaAs pHEMT	Multi-purpose packaged transistors, transistors in the form of crystals and in SMD packages, MICs in the form of crystals and in different packages	0 – 50	Up to 15	55	8–10
GaInP HBT	Multi-purpose packaged transistors and MICs of the X band	Up to 10.5	Up to 10	40	9
SiC MESFET	Multi-purpose packaged transistors, transistors in the form of crystals	0 – 4	Up to 60	40	48
GaN HEMT	Multi-purpose packaged transistors, transistors in the form of crystals and in SMD packages, MICs in the form of crystals and in different packages	0 – 20	Up to 100	60	28 – 50

production itself. They are distinguished by high reliability and high linearity of the transmission characteristics, but are inferior to pHEMT transistors in terms of frequency range, efficiency and gain. They are characterized by operating crystal temperature up to 175°C and specific output power of 0.4–0.6 W/mm. High-power transistors and MICs with this technology are also produced by a number of other manufacturers (FSUE "NPP Pulsar", FSUE "NPP Istok", JSC "Oktava").

A separate branch of the formerly powerful tree of the MESFET technology is the fairly rare technology of ***high-voltage gallium arsenide MESFET field transistors***; AMCOM Communications is the largest manufacturer of these devices. Due to high voltage and small capacities of the active structure, they are suitable for use in wideband amplifiers; however, the frequency range is limited by values of 2.5–3 GHz.

Until the middle of this decade, GaAs pHEMT transistors were the most widely used material in the class of wideband devices. Significant reduction in the cost of

devices produced with the help of this technology with gate dimensions of 0.1–0.25 μm, which resulted from industrial development of processing of plates with diameters up to 150 mm [44] and achievement of high percentage yield of circuits helped these devices spread into nearly every sector of application, from mobile phones and base stations to radars, ECM systems and communication systems of the millimeter range. This technology has become standard and is currently provided by nearly all microwave MIC foundries. The use of this technology made it possible to launch serial production of monolithic amplifiers in the ranges of up to 32 GHz with power up to 4–10 W. The leading companies (TriQuint Semiconductor, Excelics, Agilent Technologies, Hittite Microwave, Sumitomo Electric, RFMD, Mimix Broadband, UMS, Transcom and a number of others) produce hundreds of types of powerful transistors and MICs of centimeter and millimeter ranges, which are used today as the basic brick for building wideband power amplifiers for frequencies above 2 GHz. They have high gain, efficiency and boundary frequencies and are suitable for operation in the AB class. Operating crystal temperature is up to 150°C; specific output power is up to 1 W/mm.

Indium-Gallium Phosphor Heterobiopolar Transistors (GaInP HBT) complete the picture of industrial technologies of power devices. United Monolithic Semiconductors (UMS) manufactures two types of specialized MIC 10 W amplifiers of the 8.5–11 GHz range for the centimeter range for radars with active antenna arrays (CHA7010 and CHA8100); the remaining presence of this technology focuses on multi-purpose path amplifiers (gain-blocks) of the range up to 6 GHz with power levels below 1 W.

A revolutionary direction in the development of power microwave components, which originated in the previous decade and entered the phase of mass production in the middle of this decade, was the direction of wide-gap semiconductor materials (***silicon carbide SiC and gallium nitride GaN***) and devices based on these technologies [45–46, 38]. Physical basics of these technologies and their features will be detailed in further sections of this chapter; for now, let us focus on industrial aspects of their use.

Silicon Carbide Metal-Semiconductor Field-Effect Transistors (SiC MESFET) in terms of frequency band are between Si LDMOS devices and devices based on gallium arsenide and gallium nitride. Their main advantages include high crystal temperature (up to 255°C), high operating voltage and extremely low specific capacities of the active structure. Specific output power is 2–3 W/mm. Disadvantages ιν χλυδε relatively low efficiency, low limit frequencies due to low mobility of electrons in the channel and high cost. They are produced in lots by only a few companies, in particular – CREE Inc. (CRF24-xxx series) in the form of chips and in multi-purpose flanged packages. They are used for creation of wideband power amplifiers with high technical characteristics within ranges up to 2.5 GHz with output power up to 100–150 W and more designed for heavy duty conditions. Frequency characteristic of the output power of one of the amplifiers designed by

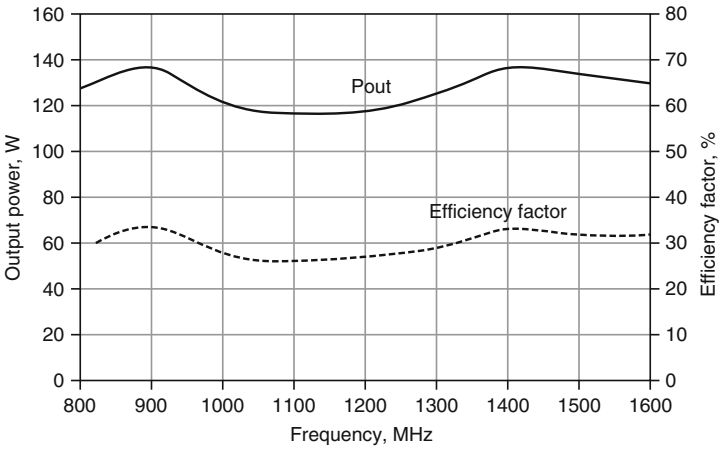

Fig. 6.17 Frequency characteristics of output power and efficiency of RM0816

Russian CJSC "Microwave Systems", with output power of more than 100 W and efficiency of more than 26% in the frequency range of 0.8–1.6 GHz [47] is shown in Fig. 6.17.

Gallium Nitride Heterostructural Field Transistors (GaN HEMT) and MICs based on these transistors, which are produced in lots by such companies as Cree Inc., TriQuint Semiconductor, Sumitomo Electric, Nitronex, RFMD have opened a new page in improvement of parameters of power wideband amplifiers of the SHF range. This technology combines the advantages important for design of modern radars and communication systems: high power supply voltage (28–50 V), high efficiency (more than 60%); possibility of operation in the AB class with low initial dissipated power; frequency range up to 20 GHz (in samples with gate width of 0.1 μm – up to 150 GHz), high gain, low capacities of the active structure and the maximum available specific output power per gate width unit (more than 5 W/mm^2). Disadvantages of mass-produced devices include stretched dynamic characteristic (reduction of the transistor gain starts at output power much lower than the maximum) and slightly higher price per power unit than in well-developed GaAs devices. Designs of MIC power amplifiers in Fig. 6.18 and 6.19 illustrate the achieved combinations of frequency bands and output power values: CMPA0060025 by Cree Inc. and TGA2570 by TriQuint Semiconductor [41]. The achieved levels of output power are at least an order of magnitude greater than the ones demonstrated by GaAs technology in these bands.

Parameters and dimensions of several types of serial MICs illustrating the main classes of amplifiers and frequency ranges of their application are given in Table 6.11.

Therefore, the is a competition between GaAs pHEMT and GaN HEMT technologies in the market of basic technologies for building of wideband power

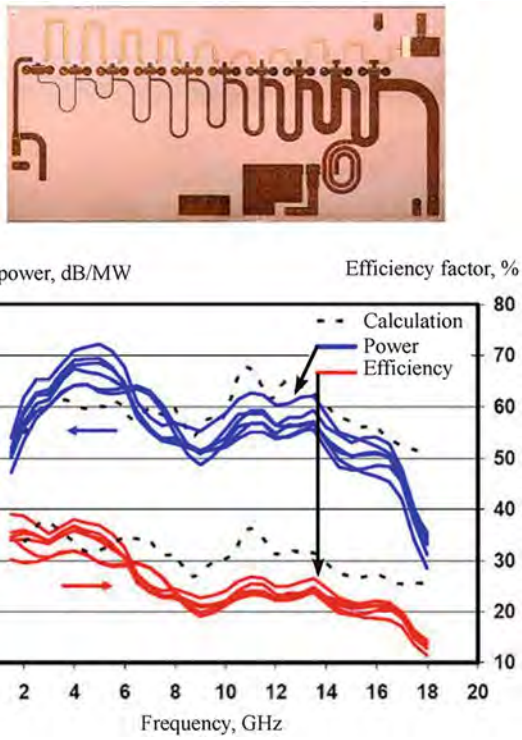

Fig. 6.18 Design and characteristics of the monolithic amplifier TGA2570

amplifiers of the centimeter range, in which technological advantages belong to the latter, and production advantages – to the former, at least for now.

The information presented above allows us to make the following conclusions:

(a) properties of GaAs and GaN transistors with equivalent gate dimensions are very close from the point of view of designing amplification blocks;
(b) many projects and technical solutions related to circuits and structures of matching chains designed for GaAs-based transistors and MIcs can be (with minimum changes) applied to GaN transistors with equal or 20–50% greater gate width; in this case, with similar length of gates of both types of active structures, the same band, gain, weight and dimensions will be achieved, but the output power and efficiency will be several times higher.

The differences become visible under more detailed observation of parameters of the second level (dynamics of harmonic levels, phase and intermodulation distortions, heat removal methods, dynamic characteristic shape, etc.). The example in Fig. 6.20 shows dynamic characteristics of two high-power amplifiers of the 2–4 GHz band with output power of 20 W and amplification of 43 dB in the linear mode – GaAs PM24-C8 amplifier produced in lots by CJSC "Microwave Systems" (curves 1) and GaN amplifier PM24-G2 designed in 2009 (curves 2).

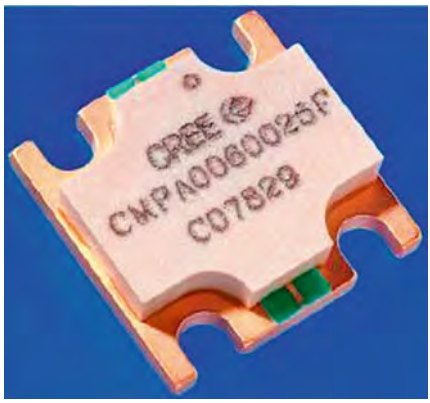

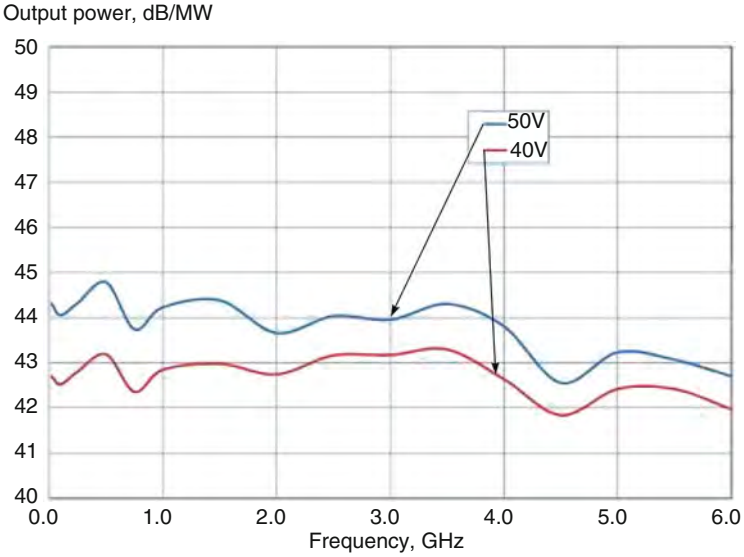

Fig. 6.19 Design and characteristics of the monolithic amplifier TGA2570

Amplifier based on GaN transistors is characterised by softer enter into the saturation mode and 5–10 dB lower level of intermodulation of the third order (IM3) at maximum output power; however, with output power 2–3 times lower than the maximum, GaAs amplifier becomes the obvious leader in terms of linearity. The amplifiers also differ in terms of character of phase-amplitude characteristics, thermal modes and a number of other parameters. Therefore, differences are manifested in system-related details of the use of devices; in general, they are mostly similar.

Complexity of MIC crystals of the microwave range has already reached a certain threshold related to limited maximum area of the crystal (25–30 mm^2), at which it (with thickness of 50–100 μm) becomes extremely complex for mounting

Table 6.11 Parameters of serial wideband monolithic amplifiers

Type	Frequency range, GHz	Output power, W	Gain factor, dB	Efficiency factor, %	Design
GaAs					
TGA2570 TriQuint semiconductor	2–18	1	16	8	Crystal
TGA2501 TriQuint semiconductor	6 – 18	2.5	24	20	Crystal
EMP216 Excelics semiconductor	6 – 18	2	20	18	Crystal
GaN					
CMPA2560025F Cree Inc.	2.5–6.0	25–37	23 – 27	> 30	Package 13 x 13 mm
CMPA0060002F **Cree Inc.**	0.02 – 6.0	4	17	25	Package 13 x 13 mm
CMPA0060025F **Cree Inc.**	0.02 – 6.0	25	16 – 21	> 30	MSL package 13 x 13 mm
TGA2540-FL TriQuint semiconductor	0.03–3	9	19	40	Package 17 x 12 mm
TGA2570 TriQuint semiconductor	2–17	8–12	10 – 14	20	Crystal
RF3826 RFMD	0,02-2,5	9	13	40	Package SMD 5x6 mm

operations, and the percentage yield during MIC mounting is reduced dramatically. Physical width of the MIC or transistor crystal (determined by the physical width of the output stage) is 4–6 mm. Maximum power taken from the crystal (having the maximum physical width in its own device class) can therefore be assessed by the values given in Table 6.12.

If we assume that the maximum physical width of the crystal is equal to 8 mm, then the maximum output power taken from the MIC crystal is structurally limited by the values provided in the last column of Table 6.12. This estimate is, of course, approximate, since the crystal arrangement density depends on the complexity of matching circuits, the length of the pin of the interdigital structure of the transistor optimal for the specific range and on the achieved specific power; however, the estimate seems to be correct.

The next step in increasing output power of transistor SHF amplifiers ισ τηε development of efficient multi-channel power adders. In order to build high-power wideband amplifiers, various adder structures are used, from traditional Lange couplers and tandem bridges to multi-channel structures based on radial adders and oversized coaxial waveguide with 24–32 channels and power addition efficiency

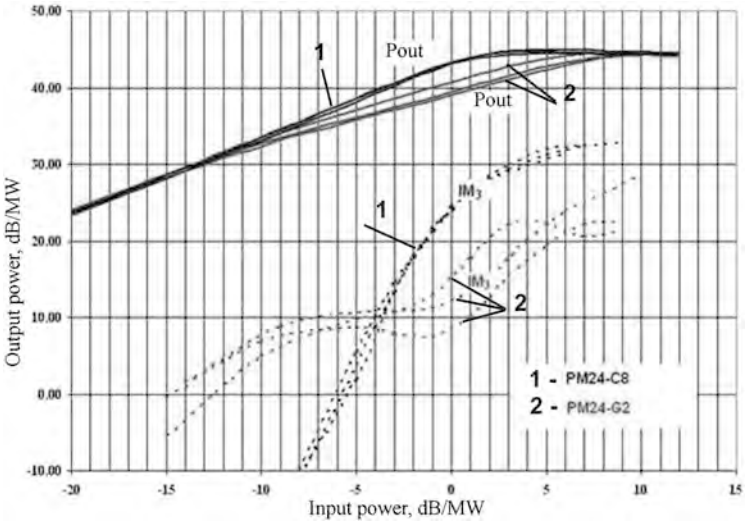

Fig. 6.20 Comparison of dynamic and intermodulation characteristics of GaAs and GaN power amplifiers of the 2–4 GHz range

Table 6.12 Maximum output power taken from MIC crystal

Technology	Transistor type (MIC)	Physical crystal width, mm	Gate with (output stage), mm	Output power, W	Maximum output power from the crystal, W (estimate)
GaAs MESFET	MAAPGM0079 M/A Com	8.15	--	20	20
GaAs HFET	TGF4260 TriQuint Semiconductor	2.4	9.6	5	
GaAs pHEMT	CHA7114 United Monolithic Semiconductor	3.31	--	8	
SiC MESFET	CRF24060D Cree Inc.	5.26	30	60	100
GaN HEMT	TGF2023-20 TriQuint Semiconductor	4.5	20	100	200

of 70–75% [41]. The latter is successfully used as SpatiumTM by CAP Wireless for building of the CHPA0618–2 amplifier with frequency band of 6–18 GHz and output power of 45 W based on GaAs monolithic blocks with power of 2 W (Fig. 6.21).

The transition from GaAs to GaN technologies observed in structures of this type on condition of solving the task of sufficient heat removal from active elements shall take wideband solid-state devices to the power level achieved by wideband vacuum

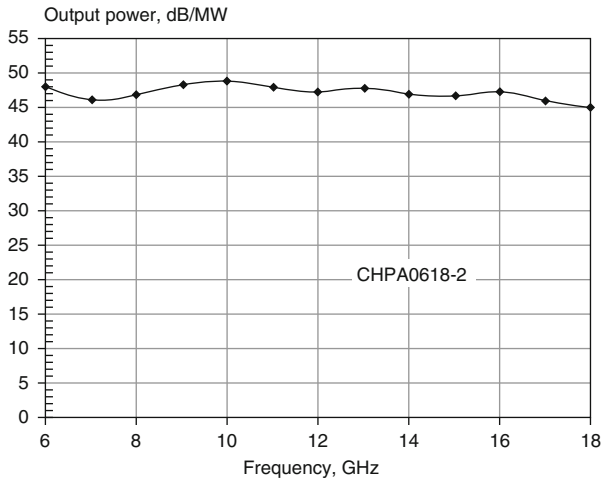

Fig. 6.21 Design and characteristics of the CHPA0618–2 amplifier based on an oversized coaxial waveguide

amplifiers based on travelling-wave tubes of the continuous mode (100–400 W), which will also be a significant moment previously unachievable by any circuitry-based tricks of developers of solid-state devices.

High-power wideband amplifiers (output power 10 W and higher) are applied in systems of radioelectronic suppression, systems of electronic compatibility testing, as well as in certain new radar location systems using wideband signals or signals with a wide range of frequency tuning. Such devices are produced abroad by companies specializing or partially specializing in amplifiers, such as Aethercomm, AML Communications, Amplifier Research, CAP Wireless, Cernex, CTT, EMPower RF Systems, Keragis, MilMega, Ophir RF, QuinStar Technology, RFCore, Stealth Microwave and some others. In Russia, the largest company specializing in development and production of such devices is CJSC "Microwave Systems" (Moscow); several types of high-power wideband amplifiers are produced by FSUE "NPP Istok" (Fryazino) and JSC "Oktava" (Novosibirsk).

Parameters of several most powerful industrially produced wideband amplifiers are given in the diagram in Fig. 6.22.

The diagram shows the data of amplifiers with various structural designs. They include traditional small-sized microwave modules, exotic structures based on 3D

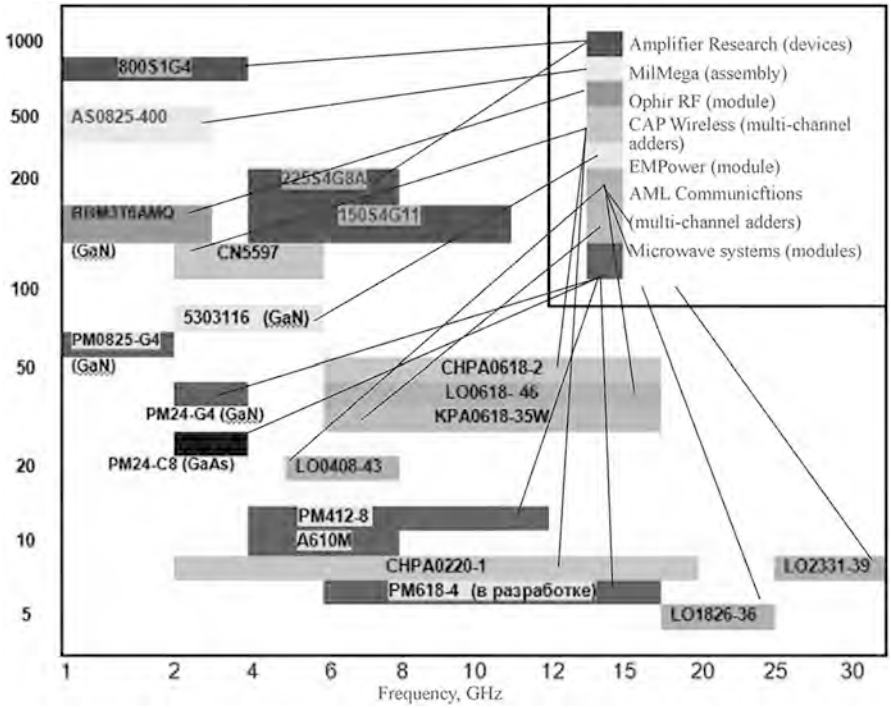

Fig. 6.22 Output power level of continuous mode of modern wideband transistor amplifiers

Fig. 6.23 Comparison between dimensions of amplifiers PM24-C8 (GaAs) and PM24-G2 (GaN)

multi-channel adders described above, and aggregates assembled in stationary units with power supply from industrial network by addition of a large number of modules.

With the development of GaAs MIC technologies, output power of UWB amplifiers of the 6–18 GHz range has grown 10–20 times over the last 10 years with simultaneous efficiency growth from 3–5% to 10–15%. Development of the GaN MIC technology in the near years will allow for another leap in the power level in this popular frequency band (3–4 times) and increase the efficiency of devices to 25% and higher. In the range of 1–4 Ghz, the use of GaN transistors already provides significant reduction in the dimensions and weight of amplifying modules; for example, the experimental GaN amplifier PM24-G2 by CJSC "Microwave Systems" has 2 times smaller dimensions and weight (Fig. 6.23), 40% lower prime cost (despite relatively high costs of GaN transistors) and 30–40% lower power consumption from the power supply source compared to similar GaAs-based amplifier PM24-C8. Other parameters of the two devices are very similar (except for "stretched" dynamics).

With the appearance of packaged GaN transistors, many manufacturers of power amplifiers (Aethercomm, EMPower RF Systems, Ophir RF) presented a wide range of models in frequency ranges of 0.8–2.5 GHz, 1–3 GHz, 0.5–2.5 GHz with output powers of 50–100 W and dimensions commensurate with older GaAs devices, which had power levels of 20–25 W in these ranges. Amplifiers for the band higher than 3 GHz entered the market immediately after Cree Inc. developed MIC of the 25 W amplifier for the frequency range of 2.5–6 GHz. After exploration of TGA2570 MICs and TGF2023 transistors, high-power wideband amplifiers were developed for the top part of the centimeter range. High rates of development of this direction can be illustrated by Fig. 6.23, which shows the dynamics of development of GaN-based MICs designed for use as output amplifiers in AESA TRMs of the 8–12 GHz range.

During 5 years of intensive developments, the power taken from the MIC crystal in this range has grown 10 times, while the output power of GaAs MICs of the same purpose produced in lots by such companies as TriQuint Semiconductor, UMS, RFMD, Mimix Broad-band remains at the level of 6–11 W, which was achieved a long time ago.

6.7 Features of Basic Process Operations of Production of GaN Device Crystals

As opposed to the traditional silicon technology, during formation of GaN structures it is nearly impossible to use such basic process operations as impurity diffusion and oxidation. The problem of diffusion alloying is associated with low diffusion coefficients of such basic impurities as aluminum, magnesium and silicon in GaN. This issue is further complicated by maximum permissible process temperature. The

problem is due to the fact that gallium starts evaporating from the GaN surface at temperatures above 900°C, while catastrophic degradation of material is observed if the temperature of 1250°C is exceeded.

Moreover, there are several limitations in the process of ion alloying of structures, since even at the maximum process temperature (1250 °C) it is impossible to achieve full activation of the implanted impurity.

Therefore, the main method of formation of alloyed GaN structures is layer-by-layer epitaxial deposition.

6.7.1 Epitaxy

Homoepitaxial growth, which is natural for other classic semiconductors (Si, Ge, GaAs) is not currently used in mass production of semiconductor devices based on nitrides, which is due to extremely high cost of bulk crystals of AlN and GaN. Therefore, a significant portion of efforts of manufacturers and researchers is aimed at developing the technology of homoepitaxial growth of low-defect nitride epitaxial structures on substrates made of other materials. Most popular materials of nitride epitaxy substrates today are sapphire (Al_2O_3), silicon carbide (SiC) and silicon (Si).

SiC has the best values of thermal conductivity and the lowest level of mismatch of permanent lattices with AlN and GaN; however, quality substrates of this material have high costs.

The main advantages of the silicon substrate are low cost, high thermal conductivity (though lower than in SiC), high crystal quality and produceability. However, the growth of quality epitaxial structures on silicon substrates is severely hindered by high value of mismatch of permanent crystalline Si lattices with GaN (17%) and AlN (19%), which causes tensile stress in the layer plane and formation of micro-cracks and mismatch dislocations.

Sapphire substrates, despite their low thermal conductivity and significant mismatch of lattices with GaN (16%) and AlN (12%), cause compression stresses in the epitaxial structure, which usually causes no micro-cracks and makes them an acceptable option for a number of applications not connected to power electronics (photo receivers, gas sensors, low-power microwave transistors).

The most popular methods of growth of GaN-based epitaxial structures are metal-organic vapor-phase epitaxy (MOVPE) and molecular beam epitaxy (MBE). The process of growth using MOVPE method is based on the reaction between trimethyl- or triethylgallium (aluminum, indium) and ammonia. The feature of the MOVPE method is relatively high pressure in the reactor (up to 1 atm) and high temperature of the substrate (1000–11,000 °C), which is required for effective ammonia decomposition. High pressure of precursor gases in the growth chamber makes it possible to perform growth at a relatively high speed (up to several μm/h). It is considered that the high temperature of growth used in MOVPE helps achieve high structural quality due to ensuring high mobility of adatoms on the growing surface.

The technology of nitride MBE is based on the growth of epitaxial structure on the substrate in flows of vaporized metal (Ga, Al, In) and nitrogen precursor. The nitrogen source can be nitrogen plasma or ammonia nitrogen, as in MOVPE. Therefore, there are methods of MBE with plasma nitrogen activation (NA) and ammonia-based MBE. NA MBE is distinguished by relatively low substrate temperature (for AlN growth, it amounts to 700–800 °C), while the ammonia-based MBE is performed at higher temperatures (1000°C and higher for AlN growth), which is determined by the need to ensure efficient decomposition of ammonia.

The feature distinguishing MBE from MOVPE is the high vacuum in the growth chamber (~10^{-4} Pa), which reduces the number of uncontrolled impurities during MBE growth and provides wider possibilities for the use of various control means during the growth process. At the same time, the possibility of nearly inertia-free (as compared with MOVPE) activation and deactivation of streams in MBE makes it possible to form a thinner layer structure, whcih is important for many instrumental appliances, such as structures with quantum wells, transistors with 2D electron gas, etc.

Isolation of Devices
is one of the first processes of structure formation, the importance of which increases together with reverse voltage. Two technologies can be used to solve this task: etching of mesa-structures and ion implantation.

Mesa-Structures ensure electrical insulation of neighboring structures on a common substrate. Their etching is usually performed by reactive ion-etching (RIE) with inductively coupled plasma (ICP) of Cl_2 or BCl_3. Addition of CH_4 to the mixture of $BCl_3/H_2/Ar$ during RIE with ICP improves anisotropy of the process and reduces erosion of the mask. The main disadvantage of insulation by means of mesa-structures consists in formation of 3D structures on the substrate, which complicates the interconnects.

Ion Implantation makes it possible to ensure isolation by planar technology methods. For this purpose, He^+, H^+ or N^+ ions are inserted in GaN surface, which improves specific resistance of the semiconductor to 10^{10} Ohm×cm. The same result is achieved by implantation of ions Zn^+ or Ar^+. Typical modes of Ar^+ implantation: energy – 150 keV, dose – 3×10^{15} cm-2, process temperature – up to 1000 °C. Effective recovery of GaN crystalline structure is aided by annealing in gaseous ammonia or nitrogen.

6.7.2 Formation of Contacts

Formation of contacts is another important process of device formation. Both ohmic and Schottky contacts are critical for functioning of the device, its characteristics and reliability.

Formation of ***ohmic contacts*** for GaN requires solution to the following problems:

- increase in the density of states at the border of the section;
- treatment of sensitive surface of the semiconductor before application of metallization;
- the need to control metal morphology at annealing temperature of more than 600 °C, including vertical diffusion of metal during annealing, lateral diffusion of contact metal to prevent surface and gate leaks, as well as recognition during electron beam lithography and photolithography. Ohmic structures for n-Gan are formed by multi-layer Ti/Al/Au, Ti/Al/Ni/Au structures, which after fast thermal annealing (FTA) at temperatures above 850 °C have contact resistance of less than 10^{-4} Ohm×cm^2. For p-GaN contacts, it is reasonable to use multi-layer Ni/Au structure, which after FTA at temperature of 600 °C has contact resistance of less than 10^{-3} Ohm×cm^2. To reduce contact resistance values, it is also possible to use ion implantation of impurities into contact windows before application of metallization. For n-GaN, this can be performed by silicon implantation with the dose of about 5×10^{14} cm^{-2} and energy of 180–250 kEv with post-implantation FTA at temperatures of 700 – 1100 °C. Additional doping of contacts for p-GaN is less efficient as compared to n-type. For these purposes, implantation of magnesium ions is used with subsequent FTA at temperature of 1100 °C. The most effective method of reducing contact resistances consists in local epitaxy of contacts by heavily doped impurity of the corresponding type. However, this method significantly complicates the structure and technology of formation of the device structure.

Formation of ***Schottky contacts*** is the most critical elements for all devices with controlling Schottky junction, since Schottky contact is what controls the process of charge transitions in the channel. The following technological problems of formation of rectifying contacts need to be solved:

- reduction of leakage currents at voltages above 300 V;
- stability at high operating temperatures;
- effects caused by formation of the Schottky gate at polar semiconductor (on Ga or N side);
- capture behavior and formation of a dipole at the boundary of the section;
- problems with adhesion of gate contacts on relatively coarse surfaces;
- mechanical stability of gates, including during processing of the back side of extremely hard materials.

Multi-layer Ni/Au-structure is the most popular material for Schottky gates, while Ir- or W-based multi-layered structures are best suited for high-temperature operations.

Treatment of surface before application of metal significantly affects reproducibility of the process and percentage yield. After opening the contact window in the passivating SiN layer, it is necessary to fully remove contamination from the semiconductor surface, preventing the surface itself from being damaged by etching.

SiN layer is etched in plasma during RIE with ICP process, which introduces minimum damages. Another critical moment before formation of the gate is the removal of resist and oxide residues. This task can be solved by removing oxide residues in NH_4OH/H_2O solution (1:10) and subsequent processing in oxygen plasma for 15 seconds. For the same purpose, it is possible to use combined processing in oxygen plasma and $HCl:H_2O$ solution (1:1).

During formation of gates, FTA at temperatures of 500 – 600 °C is also used. This procedure has the same key value as during formation of ohmic contacts, since it stabilizes parameters of device structures in time.

6.7.3 Lithography

Lithography is a basic process for any semiconductor device. Photolithography is used to form contacts of ohmic and gate contacts. Electron beam lithography is used for formation of gates with lengths under 300 nm.

6.7.4 Etching and Groove Production Processes

Etching of semiconductors is another key process, which shall conform to the following requirements:

- etching speed;
- etching selectivity;
- etching anisotropy;
- resistance to damages during etching
- surface morphology;
- etching delay.

Dry Etching of GaN structures is the main technology of pattern formation, since wet etching processes are ineffective for these purposes. The feature of RIE for nitrides of group III is the use of chloride chemistry of the process. Plasma-chemical etching can be performed in Cl_2, Cl_2/SF_6, Cl_2/Ar plasma. Etching of grooves is performed by RIE in the $Ar/Cl_2/CH_4$ system.

Wet Etching helps avoid damages to the semiconductor structure during the process. Reproducibility of wet etching is mostly controlled by the transport of reactives in the etchant and heavily depends on geometry and a number of other factors. Such acids as HCl, HNO_3 and H_2SO_4 make it impossible to achieve reasonable etching speeds. Therefore, the most common etchants for GaN are hot H_3PO_4, NaOH and KOH. Acid solutions are not used for these purposes. Alkaline solutions KOH and

NaOH (33% wt) at temperature of 50 °C are characterized by etching speed of 10–100 Å/min; they help form controlled surface of the semiconductor and are used for removal of damaged surface after dry etching.

6.7.5 Surface Formation and Device Passivation

Passivation of the device surface performs several functions, including the following:

- (during early stages) protection of open surfaces from the effect of process operations (coatings, developer solutions, plasma, environment);
- removal of surface material and supposed damages;
- modification (as a rule, reduction) of density of surface states;
- physical, mechanical and chemical stabilization of surface,
- compensation of the surface charge;
- modification of surface currents by isolating or conducting dielectrics or conducting intermediate layers.

The technology of passivation formation includes the following stages:

- surface treatment, including:
  - material removal;
  - modification of surface morphology;
- - preliminary processing of the semiconductor surface, including:
  - chemical reaction on the surface (e.g., oxidation);
  - physical conditioning (e.g., gas adsorption);
- dielectric deposition;
- formation of multi-layer structure.

Surface Treatment and cleaning conditions are extremely important throughout the entire process of structure formation. This is due to the fact that polar nature of III-N materials makes the state of surface of epitaxial layers extremely important after extraction from the growth reactor, when the structure is subjected to natural oxidation and corrosion in the air environment. To prevent it, it is recommended to grow a thin protective SiN layer in-situ on the surface of the epitaxial layer.

Before performance of PECVD processes, the surface is processed in acetone, methanol, isopropyl alcohol and water. After that, the surface is submerged into buffer oxide etchant (30:1) for 30 seconds. Surface treatment in low-energy ammonia plasma also has a positive effect on characteristics of devices. Surface treatment is the most important stage for III-N semiconductors of the p-type, for which it is recommended to perform processing in hydrogen plasma.

Deposition of Dielectrics Optimized process of passivation deposition neutralizes static and dynamic surface conditions caused by broken links on the surface, adsorbed ions and charges of residual materials, such as oxides.

Silicon Nitride is the most popular passivation material for III-N semiconductors. Typical effect of such passivation is expressed in increased output power, reduced effects of frequency dispersion and modification of leakage currents, which usually leads to reduction of the breakdown voltage. These effects ultimately result in increased service life of devices. Silicon nitride is deposited on the surface with the help of the following processes:

- plasma-chemical deposition (PECVD);
- catalytic deposition of their gas phase;
- in-situ deposition during epitaxy.

Plasma-chemical deposition is performed in the stream of monosilane with ammonia. Process temperature is 250 – 300 °C, thickness – 30-300 nm.

Oxide Passivation based on SiO_2 can be used as an alternative to nitride. SiO_2 is applied by plasma-chemical deposition at temperature of 150 °C in O_2/He plasma with monosilane. SiO_2 can also be deposited onto n-GaN surface from vapor-gas mixture of disilane and ammonia. Passivation based on MgO and Sc_2O_3 is also used.

Other Materials Many other materials were also studied, including polyimide and low-k benzocyclobutene. These materials are characterized by simplicity of application by means of centrifugation and drying at temperature of 300 °C and are similar to SiN passivation in terms of properties. Special attention shall be paid to passivation by such dielectric as AlN obtained by chemical deposition from the gas phase or by reactive magnetron sputtering; AlN passivation is characterized by good thermal conductivity and located in immediate proximity of the heat source. Moreover, this passivation significantly reduces leak currents and the effect of current collapse in HEMT.

Passivation by Epitaxial Layers is a very attractive process used to solve problems of reliability of high-voltage devices, which includes the following methods:

- heavily or moderately doped surfaces of the n-type for powerful transistors without surface passivation;
- p-type coatings of Ga/AlGaN/GaN HEMT-structures;
- deposition of AlN as passivating material;
- deposition of materials based on super-lattices;
- in-situ SiN deposition.

References

1. https://docplayer.ru/45013546-Tehnologiya-sic-v-modulyah-semikron.html
2. https://www.psma.com/sites/default/files/uploads/tech-forums-semiconductor/presentations/11-market-and-technology-trends-wbg-power-module-packaging.pdf
3. http://www.compitech.ru/html.cgi/arhiv/00_06/stat_40.htm
4. http://phg.su/basis2/X75.HTM
5. http://hightolow.ru/transistor3.php
6. https://dic.academic.ru/dic.nsf/ruwiki/1406306
7. https://en.wikipedia.org/wiki/High-electron-mobility_transistor
8. http://www.power-mag.com/pdf/issuearchive/31.pdf
9. http://www.icquest.ru/?section=4&id=35
10. https://deepblue.lib.umich.edu/bitstream/handle/2027.42/62274/sanghyun_1.pdf by Sanghyun Seo "A dissertation submitted in partial fulfillment of the requirements for the degree of Doctor of Philosophy (Electrical Engineering) in The University of Michigan 2009)».
11. https://en.wikipedia.org/wiki/Gallium_nitride
12. https://en.wikipedia.org/wiki/Silicon_carbide
13. http://www.electronics.ru/files/article_pdf/0/article_754_622.pdf
14. http://www.nanoindustry.su/files/article_pdf/1/article_1760_808.pdf
15. http://www.authorstream.com/Presentation/gourou-3038241-sic/
16. http://www.rf.unn.ru/eledep/confesem/nro_popova/2016_01_22_(53)/03.pdf
17. http://www.russianelectronics.ru/leader-r/review/doc/74228/
18. Kolpakov, A.. (2009). Technology of low-temperature sintering in power modules. *Components and Technologies*. 7. https://www.kit-e.ru/articles/powerel/2009_07_92.php
19. Kolpakov, A. (2013). SKiN-technology — Power electronics of tomorrow. *Power Electronics*. . No. 1. https://power-e.ru/pdf/2013_01_14.pdf
20. Belous, A. I., Solodukha, V. A., Shvedov, S. V. (2018). Microwave electronics in radar and communication systems. *Technical encyclopedia in 2 volumes*. 2nd ed., revised. Moscow: TEKHNOSFERA.
21. R. Behtash et al. (2007) Coplanar AlGaN/GaN HEMT power amplifier MMIC at X-band. *IEEE MTT Symposium Digest*, 1657–1659.
22. Fanning, D. M. et al. (2005). 25 W X-band GaN on Si MMIC. *GaAs Mantech Conference Proceedings*.
23. Klockenhoff, H. et al. (2006). A compact 16 watt X-band GaN-MMIC power amplifier. *IEEE MTT-S Digest*, 1846–1849.
24. Piotrowicz, S. et al. (2008). State of the art 58W, 38% PAE X-band AlGaN/GaN HEMTs microstrip MMIC amplifiers. *IEEE Compound Semiconductor IC Symposium*.
25. Chen, T. et al. (2007). X-Band 11W AlGaN/GaN HEMT power MMICs. *EwMIC Conference Proceedings*, 162–164.
26. Costrini, C. et al. (2008). A 20 watt micro-strip X-band AlGaN/GaN HPA MMIC for advanced radar applications. *EwMIC Conference Proceedings*, 1433–1436.
27. Singhal, S. et al. (2007, May 14–17). Qualification and reliability of a GaN process platform. *CS MANTECH Conference*, 83–86.
28. Leung, D. et al. (2001). High-reliability deep submicron GaAs Pseudomorphic HEMT MMIC amplifiers. *CS MANTECH Conference*.
29. Danilin, V. et al. (2004). GaN Transistor – still hardest to crack. *Electronics: NTB*, 4, 20–29.
30. Adachi, N. et al. (2005). High temperature operation of AlGaN/GaN HEMT. *IEEE MTT Symposium Digest*.
31. Schuh, P.. (2008). GaN MMIC based T/R-Module Front-End for X-Band Applications. *EwMIC Conference Proceedings*, 274–277.
32. Shi Chang Zhong et al. (2008). AlGaN/GaN HEMT with over 110 W Output Power for X-Band. *EwMIC Conference Proceedings*, 91–94.

33. Mitani, E. et al. (2007, May 14–17). An 800-W AlGaN/GaN HEMT for S-band high-power application. *CS MANTECH Conference*, 213–216.
34. Wakejima, A. et al. (2006). 370-W output power GaN-FET amplifier with low distortion for W-CDMA base stations. *IEEE MTT Symposium Digest*, 1360–1363.
35. Pelk, M. J. et al. (2008). A high-efficiency 100-W GaN three-way doherty amplifier for base-station applications. *IEEE Transactions on MTT*.
36. Lee, Y. et al. (2007). A high-efficiency Class-E GaN HEMT power amplifier for WCDMA applications. *IEEE Microwave and Wireless Components Letters*, 8, 622–624.
37. Schmelzer, D., Long, S. I.. GaN, A (2007). HEMT Class F Amplifier at 2 GHz with > 80 % PAE. *IEEE Journal of Solid-State Circuits*, № 10, 2130–2136.
38. Vikulov, I. & Kichaeva, N. (2007). GaN technology – new stage of development of SHF microcircuits. *Electronics: NTB, Business*, 4, 80–85.
39. Wilcox, G. & Andrews, M.. (2009). TriQuint delivers high power – Wideband GaN technology. *Microwave Product Digest*, №1.
40. Gallium, Indium and Aluminum Nitrides – Structures and Devices / Abstracts of the 6th All-Russian Conference, June 18-20, 2008, Saint Petersburg.
41. Kischinskiy, A. (2010). Wideband transistor power amplifiers of the microwave range – Change of generations. *Electronics: NTB*, 2.
42. Shakhnovich, I. (2005) Solid-state SHF devices and technologies. *State and Prospects / Electronics NTB*, 5, 58–64.
43. Mayskaya, V. (2004). High-frequency semiconductor devices. *Not Only Silicon and Gallium Arsenide / Electronics: NTB*, 8, 16–21.
44. O'Keefe, M. F., et al. (2003). GaAs pHEMT-based technology for microwave application in a volume MMIC production environment on 150-mm wafers. *IEEE Translation on SM, 16*(3), 376–383.
45. Pribble, W. L. et al. (2002). Application of SiC MESFETs and GaN HEMTs in power amplifier Design. *IEEE MTT-S International Microwave Symposium Digest*, 1819–1822.
46. Vasilyev, A. et al. (2007). New generation of semiconductor materials and devices. *Through GaN to Diamond / Electronics: NTB*, 4, 68–76.
47. Baranov, V. et al. (2009). *Wideband power amplifiers of decimeter range based on SiC transistors* – Proceedings of the 16th International Crimea Conference "Microwave and Telecommunication Technology" Sevastopol, Veber, pp. 55–56.

Chapter 7
Vacuum Electronics

7.1 Operating Principle, Classification and Technological Features of Vacuum Electronic Devices

As we know, vacuum electronics in the classic sense is the section of electronics including the study of interaction between the stream of free electrons with electrical and magnetic fields in vacuum, as well as methods of creating various electronic devices and units in which these interactions are used.

The main elements required to build vacuum electronic devices are:

- information signal carrier (ensemble of free electrons);
- generator of these free electrons (emitter or cathode);
- certain continual environment, the role of which is performed by vacuum (for electron-vacuum devices) or plasma (for ion devices);
- device for control of this ensemble of free electrons in continual environment;
- detector of information signals (of devices for takeoff of the electron beam energy).

Simplified schematic model of a typical vacuum electronic device (tube) is shown in Fig. 7.1 [1].

Vacuum electronics emerged in the beginning of the twentieth century; the first vacuum device was the two-electrode electronic tube (diode) invented by English scientist J. A. Fleming in 1904. Active development of vacuum electronics started in 1907, after American engineer Lee De Forest created a three-electrode tube (triode) – vacuum device with grid control of the electron stream. This lead to active development of radio communication and broadcast systems in the 1910s–1920s; appearance of electron beam devices in the 1930s determined the creation of modern television.

Exploration of the microwave region (over 500 MHz) in 1930s–1940s required development of the principles of dynamic control over electron beam, due to which

© The Editor(s) (if applicable) and The Author(s), under exclusive license to Springer Nature Switzerland AG 2021

A. Belous, *Handbook of Microwave and Radar Engineering*,
https://doi.org/10.1007/978-3-030-58699-7_7

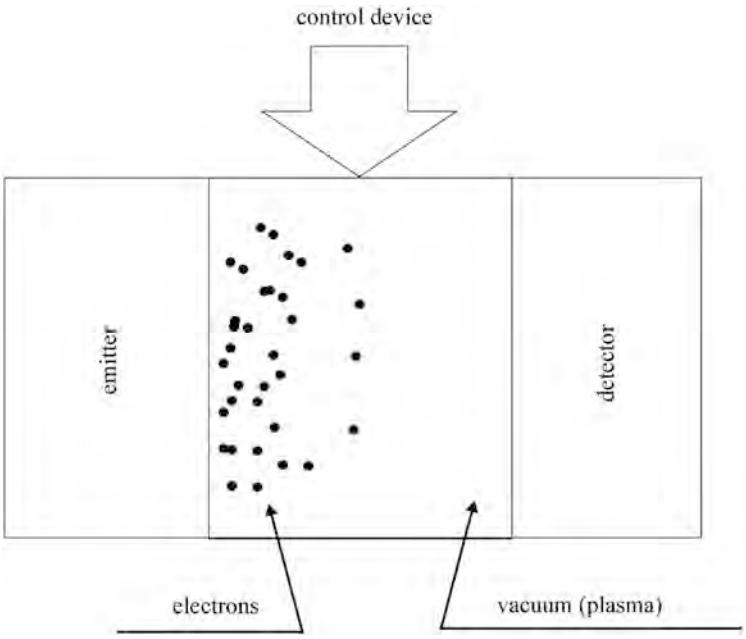

Fig. 7.1 Simplified model of a vacuum tube device

new classes of devices were created: klystrons, magnetrons, travelling-wave tubes, etc., the operation of which is based on interaction between electrons and electromagnetic microwave fields. A new direction of vacuum electronics was formed – microwave (SHF) electronics.

The relevance of tasks facing vacuum electronics in 1930s–1960s stimulated concentration of great financial and intellectual resources on this field in all developed countries, which ultimately led to creation of electronic industry. Improvement and industrial production of vacuum electronic devices became possible due to fundamental physical studies and technological developments in the following fields: solid-state physics, electronic optics, emission electronics, electrodynamics, material studies, specialized engineering, etc.

The common element of all vacuum electronic devices (tubes) is the source of free electrons – cathode, the properties of which determine basic operational and consumer characteristics of the device. There are four extremely important classes of vacuum electronic devices distinguished by physical principle of release (liberation) of electrons from the cathode. The widest class is formed by *thermoelectronic cathodes*, in which the necessary energy of electron release is transmitted due to thermal heating of the cathode. They are used both in low-power receiving and amplifying tubes in CRTs and in high-power generator tubes, which were used at the early stages of development in television and radar location. The effect *of secondary emission cathodes* is based on increasing the flow of electrons during bombardment of the cathode surface with primary electrons. The main field of application here is

formed by electronic multipliers and SHF devices. In *photocathodes*, the energy required for the release of electrons is transmitted due to interaction with radiation quanta (photons); they are used in different radiation converters, including light converters. The fourth class includes *field-emission cathodes*, operation of which is based on the principle of electron tunneling through potential barrier under the effect of strong electrical field.

Cathodes with combined types of electron emission, such as *photoelectronic cathodes*, are also being developed.

While until 1960s all electronics consisted primarily of vacuum electronics, further rapid development of related fields, especially semiconductor electronics, significantly limited the field of application of vacuum electronic devices. However, there are important technical and technological fields where these devices are still irreplaceable: radio broadcasting, television, amplification equipment, plasma technology, radar location, space communication, etc. The field of application of vacuum devices is determined by a number of features, the main of which include: low heat losses of electronic energy in the interaction space and subsequent high EFFI CIENCY of devices (up to 90% and more), as well as the possibility of intensive cooling due to dissipation of residual (not given to the electromagnetic field) energy of electron flows on electrons with large areas, which made it possible to create devices with power of up to dozens of megawatts and higher.

Depending on the operating principle and technological features, vacuum electronic devices, which make up a wide class of vacuum tube devices, are divided into *electronic tubes*, *electron beam devices*, *electrovacuum microwave devices*, *photoelectronic devices* and *X-ray tubes*. Vacuum electronic devices also include vacuum indicators, flat screens of various purpose and vacuum integrated circuits. Separate class is formed by *technological electron beam units* [2–5].

In the beginning of the twenty-first century, a brand new direction of vacuum electronics appeared – vacuum nanotechnology, which makes it possible to engineer materials and devices at the molecular level. Further development of vacuum electronics is associated both with development of newest advanced developments and devices and with modernization of traditional devices with the help of new and more efficient physical and constructive principles, the most important of which are considered in the following.

7.2 Application of Vacuum Electronics in US Military Equipment

Regardless of the fact that both vacuum and solid-state electronics equally form the basis for modern weapon systems, focal points in their developments differ significantly. In the end of the twentieth century, it was believed that vacuum electronics, which had been developed many decades ago, was becoming outdated. As a result, financing of studies and developments of vacuum devices was reduced significantly, and a number of research programs were closed.

Many US specialists in vacuum electronics, concerned by the worsening state of the industry, came out with proofs of its importance, including importance for ensuring national security and military potential of the country [7–9].

It was best expressed in the analytical report presented to the US Department of Defence (DoD) compiled based on the result of joint meeting of representatives of military departments, industry of vacuum tube devices (VTD), state laboratories and universities [8]. The report defined the existing state of the technology as well as the requirements of existing and future military systems for VTDs. Specific recommendations were given regarding investments in studies and developments necessary to maintain national technological base of vacuum electronics in the USA.

The USA was the world leader in this field of technology for many years. In the beginning of the twenty-first century, electro-vacuum industry of the USA was represented by about 20 companies. Four largest companies (Communications and Power Industries, L-3 Communications EDD, Boeing Electron Dynamic and Teledyne Electronic Technologies) accounted for about 90% of all VTD sales as of 2000.

The national laboratories supporting vacuum technology include: Naval Research Laboratory, NRL; Naval Surface Warfare Center, NSWC in Crane, Indiana; Stanford Linear Accelerator Center, SLAC; Los Alamos National Laboratory; and NASA Research Center. NRL is the main organization managing studies and developments in the field of vacuum electronics. SLAC and Los Alamos National Laboratory support developments in the interests of the Department of Energy, as well as creation of super-power SHF devices, including microwave weapons (see Chap. 9). Studies dedicated to vacuum electronics are also performed in six largest US universities: Massachusetts Institute of Technology, two institutes in California (Davis and Stanford) and three institutes in Maryland, Wisconsin and Michigan.

In 1989, sales volumes of VTDs in the USA reached 600 US $M (including power grid tubes – 130 US $M). Ten years later, by 1999, VTD sales dropped to 330 US $M (sales of power grid tubes – to 80 US $M). During the period of 1998–2000, sales stabilized at the level of 350 million dollars. It should be noted that 70–75% of the sales volume during that period were attributed to military-purpose VTDs. The share of European electro-vacuum products in the US market during this period amounted to just 10%.

The structure of VTD sales in the USA in 1999 based on tube types was as follows [1]:

VTD type	Market share, %
Helical TWTs	55
Klystrons	19
M-type devices (amplifiers with cross fields and magnetrons)	9
TWTs on coupled resonators	17

In subsequent years, a number of extensive programs were successfully implemented in the USA within the joint project of three military services. The most noteworthy are the Vacuum Electronics Initiative in 1990–1995 and complex Navy programs “Vacuum Electronic Science and Technology” (VES&T).

As is known from open sources, 272 electronic weapon systems of all US military services by the beginning of this decade included about 185 thousands of VTDs. According to specialists, these systems will be in service of the country for at least 20–30 years more, which will require replacement or modernization of a number of electrovacuum devices.

They will be supplemented with new devices necessary for fitting of newly created systems.

Speaking about specific types and services, Navy, Air Force and ground forces shall be mentioned.

For example, **US Air Force** in the period of 2000–2005, according to the data from open sources, used 46,750 VTD devices in their equipment installed on various platforms, including fighter jets (F-15, F-16), remotely piloted aircrafts (Predator), bombers (B-1B, B-2), missiles (AMRAAM), AWACS complexes and other platforms. Fault-resistant transmitter with addition of power of several TWTs on the ring-rod slowing system was developed for the air situation control station AN/TPS-75; this transmitter replaced the less reliable model based on single klystron.

During creation of the radar for the Predator RPA, the use of vacuum-semiconductor microwave power modules (MPM) based on TWTs [10] helped reduce the time of development of the system in general by 3 years. Modified wideband klystron designed for the AWACS kit replaced two separate narrowband tubes, which reduced production costs, increased reliability and simplified operation of the device. Design of the jammer JSSJ was developed in cooperation with the Navy; flight tests of the design were completed in 2008. It should be noted that two competing concepts were considered during this: wideband (2–18 GHz) powerful MPM modules by Northrop Grumman and array on high-power monolithic circuits by ITT.

US air forces are constantly declaring their interest in further development of the vacuum technology, in particular, in development of Solid State Electron Emitters based on InP/CdS/LaS for all VTD types for the purpose of achieving immediate emission of electrons with high current density (10–100 A/cm2) at low values of the modulation frequency (<20 V). Such solution helps exclude power consumption of the heater and increase service life and reliability of devices.

US ground forces widely use VTDs in the systems of detection of artillery positions (mobile radar station AN/TPQ-36 and -37 Firefinder), missile defense radars (AN/MPQ-64 Sentinel), EW systems (AN/ALQ-211 SIRFC), target seekers (PAC-I, -II, -III) and missile defense complexes (Patriot).

Ground forces of the USA have also been using the AN/TPQ-47 system (modification of the well-known Firefinder systems), which is designed as a hybrid phased array based on MPMs with air cooling, for more than 10 years. According to the information from open sources, during development of its first modification amplifiers based on SiC transistors could not compete with MPMs, since the problems of reliability of these transistors at the time were not solved to a sufficient extent.

For mobile ground terminal of hidden interference-immune satellite communication SMART-T, MPMs of the millimeter range (43.5–45.5 GHz) were also preferred

to GaAs PHEMT-based amplifiers due to higher power (>50 W). During modernization of the helicopter protection system ALQ-211 SIRFC, TWTs were replaced with MPMs, which reduced weight and dimensions and increased technical characteristics of the jammer.

TWTs on coupled resonators of the Ka band (26–40 GHz) produced in France by Thales have been used in missile target seekers of Patriot PAC-III and Medium Extended Defense System (MEADS) since 2005. In the given frequency range, TWTs are the optimal technical solution which satisfies the requirements for power (both pulsed and average) existing at the moment, as well as dimensions. Afterwards, CPI developed similar USA-made TWT with pulse power already exceeding 1 kW, which was able to work with very high pulses at high pulse duty factor in limited cooling conditions.

Since 1995, **Naval Research Laboratory (NRL)** has been using its own design of a 94 GHz klystron with pulse power of 100 kW and average power of 10 kW in the band of 600 MHz and with efficiency of 33%. In particular, this gyroklystron is used in the NRL radar station of the W-band WARLOC.

In turn, WARLOC radar is a part of the basic Haystack Ultra-wideband Satellite Imaging Radar, which operates in the X range. WARLOC radar system helps improve the resolution of the image received by the previously used Haystack radar by an order of magnitude. This complex was put into operation in 2010 [9].

It is also necessary to note development of the gyroTWT with the band of 4 GHz and power of 100 kW for radar systems of landing provision, as well as gyroTWT with pulse power of 5 kW and band of 8 GHz in the W range (96 GHz) for radars of space reconnaissance, modernization of the ship (AEGIS) station, the array of which included TWTs on connected resonators and amplifiers of M-type connected in series. Replacement of such amplifiers with multi-beam klystrons of the S band made it possible to increase radar sensitivity by 12 dB with preservation of the existing array structure. It is known that the calculation of the e-beam projector and collector of the klystron was performed using MICHELLE 3D program, calculation of the klystron in the high signal mode – in TESLA program. As a result, pulse power of the klystron in the S-band amounted to 600 kW at efficiency of 40%; current setting of the beam without SHF does not exceed 1% and amounts to 3% in saturation mode. After that, 18-beam projector and additional multi-gap resonators were used to increase efficiency and expand the band [9].

Russian experience also deserves a mention here – most multi-beam klystrons were designed in Russia. For example, “Istok” enterprise, the leader in this segment of developments, have developed and launched production of multi-beam klystrons of L-, S-, K- and Ku-bands.

US ground forces are implementing their own large-scale program of VTD development, which involves development of:

- multi-beam amplifiers for high-power low-noise radars;
- linear and wideband amplifiers as separate devices and as MPMs for EW and communication systems;

- amplifiers of the millimeter range on slow waves of Ka- and W-ranges;
- high-power gyroamplifiers of Ka- and W-ranges.
- computer modeling, including creation of the integrated software package for designing of electro-vacuum devices;
- technologies of supporting subcomponents and materials (CVD diamond, AlN ceramics), electron emitters (cathodes with current density of 10–50 A/cm 2), dielectrics, permanent magnets based on rare-earth materials, and so on.

7.3 Main Values of VTD Parameters Achieved by 2000

Dynamics of development of typical electronic microwave devices is shown in Figs. 7.2 and 7.3 [1]. As can be seen from Fig. 7.2, power density of vacuum devices during this period doubled every 2 years [7, 8]. As of 2000, the following most significant results achieved in the USA in development of VTDs could be noted [8].

In the field of TWTs:

- ultra-wideband (3–18 GHz) helical tubes with power of 125–200 W and gain of 47 dB in the center of the band and 27 dB at the edges with efficiency of 45 and 25% respectively (L-3 Communications);
- helical TWTs of the millimeter range with power of 130 W at the frequency of 44 GHz with efficiency of 40% (1995, L-3 Communications). According to the latest information, output power of such TWTs already reaches 220 W [9];
- achievement of efficiency of helical TWT for communication satellites over 73 at up to 12 GHz in the 500 MHz band. Service life of these devices is over 18 years

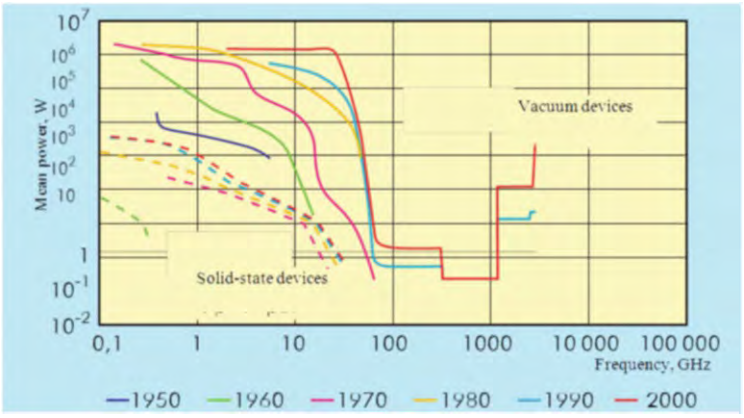

Fig. 7.2 Dynamics of changes in the power of electronic devices between 1950 and 2000: dotted lines – solid-state devices; full lines – vacuum devices

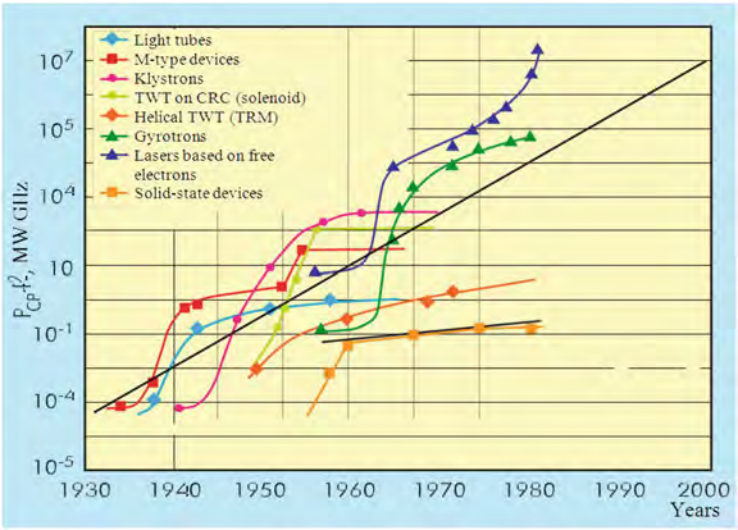

Fig. 7.3 Changes in the power determined by the product of average power by squared frequency ($P_a \cdot f^2$) of the main types of VTDs and solid-state devices over the last 70 years (1930–2000) [1]

(150 thousand hours), MTTF in orbit – over 10 mln. hours. In terms of this parameter, they are equal to or better than solid-state devices (Boeing EDD);

- TWTs on folded waveguide with power of 50–100 W within the range of 40–52 GHz. Their design can be scaled in the band of 85–100 GHz. The results of computer modeling demonstrate the possibility of achieving efficiency >30% with gradual change in the slowed wave speed and multi-stage step-down collector (L-3 Communications).
- super-linear helical TWTs for commercial communication systems. Power of a TWT with linearizer in the band of 1.8–2 GHz is 200 W with the ratio of intermodulation component of the third order and the carrier equal to −73 dB.

In the field of SHF power modules:

- wideband modules (3–18 GHz) with power over 100 W for EW systems. Further development of systems requires expansion of the band to 2–18 GHz and increase in power to 200 W (L-3 Communications and Northrop);
- microwave modules with volume under 800 cm3 with output power of 180 W within the frequency band of 4–6 GHz at efficiency of 50% and noise factor of 10 dB (Northrop);
- microwave modules of the millimeter range with continuous power of 20–50 W across the entire band of 18–40 GHz. 100 W devices are being developed for this band (L-3 Communications and Northrop).

In the field of klystrons:

- small-sized klystrons with distributed interaction, focusing by permanent magnets with pulse power of 150 W in the W band and 1.5 kW in the Ka band. The aim is to increase their mean power and band by 4–8% (CPI);
- introduction of multi-stage step-down collectors, which helped double the efficiency of klystrons for communication systems during their operation in linear mode in frequency ranges from S to Ka (CPI Company);
- small-sized klystron with pulse power of 100 kW in the W-band created with the help of German lithographic technology LIGA "Klystrino". Electronic beam diameter – 0.5 mm, channel diameter – 0.8 mm, operating voltage – 110 kV (SLAC);
- klystron with focusing by means of periodic permanent magnets with pulse power of 75 MW in the X-band – used in developments of energy weapons (SLAC);
- klystron of the L range with output pulse power of one GW at pulse repetition frequency of 5 Hz and duration of 1 μs (SLAC and Los Alamos National Laboratory).

In the field of M-type devices:

- light small-sized coaxial magnetrons for target seekers and airfield radars;
- synchronized magnetron of the S-band with pulse power of 50 MW and amplification of 13 dB, which is also used in development of energy weapons (CPI Company).

In the field of gyroscopic devices:

- gyroscopic TWT with pulse power of 100 kW and average power of 10 kW at 94 GHz with efficiency of 30%. The work was performed more than 10 years ago by CPI in cooperation with NRL, Litton and the University of Maryland and serves as a good example of successful computer design on first attempt;
- gyrotron oscillator for energy studies with continuous power of 1 MW at 100 GHz (CPI);
- gyroklystron with pulse power of 100 kW and average power of 10 kW at 94 GHz (NRL).

Unfortunately, starting from 2000, publications dedicated to military applications of SHF electronics for specific military branches nearly disappeared from open information sources.

7.4 Microwave Integrated Vacuum Electronics

At the turn of the Millenium, a number of large-scale science and technology programs aimed at priority development of new technologies was formed and launched in the USA [11]. Several projects were deployed in the field of element

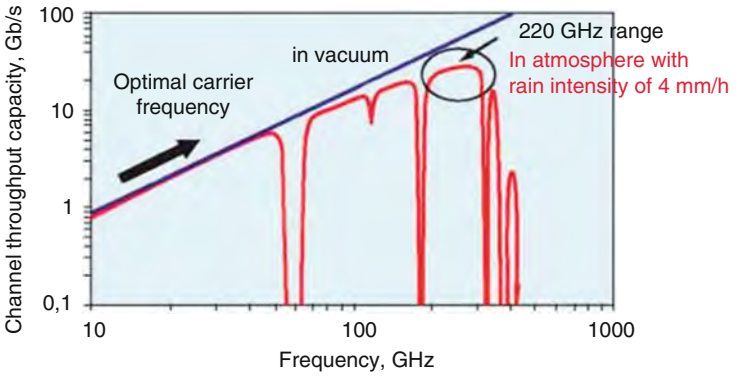

Fig. 7.4 Maximum throughput capacity of the channel in different sections of the frequency spectrum

base of microwave electronics. For example, Wide Band-Gap Semiconductor Technology Initiative (WBGSTI) has been being implemented since 2000 [12]. Implementation of the new program known as High Frequency Integrated Vacuum Electronics (HiFIVE) has commenced [13]. Similarly to WBGSTI, the program was initiated by one of structural divisions of the Defense Advanced Research Projects Agency of the USA (DARPA) – Microsystems Technology Office. Let us consider the essence of the suggested program and the tasks solved during its performance.

For example, within the framework of the HiFIVE program for SHF power transmitters precision microprocessing methods were used to create the structure of power vacuum amplifier operating in the upper part of the millimeter range (central frequency 220 GHz) with output frequency of more than 50 W and operating frequency band over 5 GHz [14]. The device includes a solid-state monolithic integrated circuit (MIC) of the millimeter band preamp, a cathode, an e-beam projector, a microstructural HF system of interaction with the electronic beam and a collector. The main parameter of the device – the product of its output power by frequency bandwidth – is not less than 500 W·GHz.

The developed technology fully complies with the requirements of serial production with the production volume that meets, first of all, military requirements.

Selection of the HF section of the millimeter range was determined by the possibility of expanding the operating frequency band, which defines throughput capacity of communication channels used for data exchange between military systems of various purposes. The section of the spectrum between 200 and 300 GHz, which is not normally used, contains a wide minimum of atmospheric attenuation of radiowaves; according to estimates, maximum throughput capacity of communication channels in conditions close to real ones can be achieved at around 220 GHz (Fig. 7.4) [15].

Today, the main impediment to using the upper section of the millimeter range is the absence of high-power wideband amplifiers for such frequencies. At lower

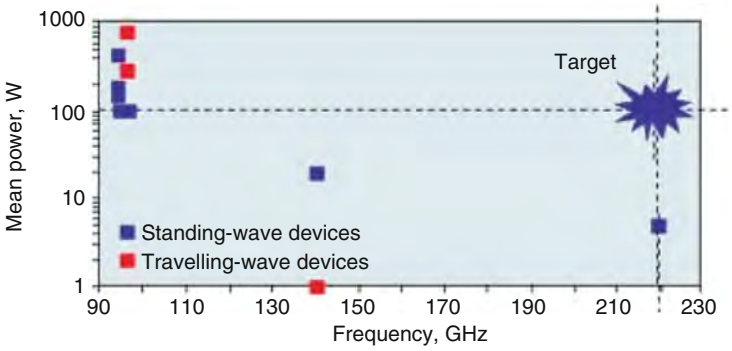

Fig. 7.5 Traditional vacuum devices of the millimeter range

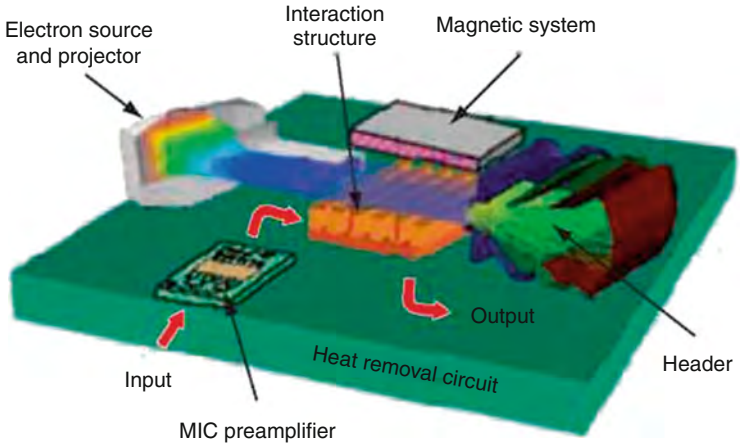

Fig. 7.6 Design of a power vacuum amplifier of the millimeter range developed using HiFIVE program [1]

frequencies of the millimeter range, traditional vacuum devices have satisfactory parameters; however, their power in the frequency domain above 200 GHz does not exceed single watts at the moment (Fig. 7.5) [1]. Moreover, their dimensions, weight and cost make them unsuitable for many military applications. Therefore, the task of creating a powerful vacuum amplifier within the range of 220 GHz was actually a relevant one. Its solution required the use of state-of-the-art technologies.

It should be noted that the invitation to participate in HiFIVE DARPA provided that only R&D proposals capable of ensuring revolutionary breakthroughs in scientific approaches, materials, instrument building and circuitry would be considered [14].

General structural diagram of the device is shown in Fig. 7.6 [16]. Before integrating all elements of the structure, it was necessary to solve complex technological tasks of creating each unit of the device.

Table 7.1 Technical possibilities during SS processing [6]

Parameters	LIGA	DRIE	MEMS
Vertical processing interval, μm	5–1000	2–400	1–80
Minimum horizontal size, μm	10	−0.5	−2–3
Beam shape factor N	100:1	100:1	−5:1
Tolerance, μm	1–2	−0.5	<1

It is known that one of the reasons of reduction in the power of vacuum tubes with transition into short millimeter range is the deterioration of slowing structures, as standard methods of their production (such as electrosparking) are too rough. Currently, there are more precise effective methods of SS production: DRIE (Deep Reactive Ion Etching), LIGA (Roentgen Lithography Galvanik Abformung – a combination of X-ray lithography, metal plating and molding), various MEMS technologies with mechanical tolerances under 1 μm (Table 7.1).

Another reason was related to the reduction in the efficiency of interaction of the electronic beam with the field of the slowing structure at short millimeter waves, since the field concentrates near its surface. Takeoff power here is measured in proportion to $Nf^{-8/3}$, where N is the beam shape factor, i.e. the ratio of the full beam width to its thickness (in case with a circular beam, N is equal to the ratio of the beam circumference length to its thickness) [15]. This effect was partially compensated by developers of SHF devices due to increase in the N value.

With an increase in the beam width (N shape factor), higher oscillation modes can occur in the slowing structure, which usually requires development of additional methods of their suppression. Other instability reasons are also possible (mismatches in SS, generation at reverse wave, etc.).

Design estimates show that in order to achieve set power of the device (50–100 W), it is necessary to implement a design with the beam shape factor of several dozen units and current density of several hundred amperes per square centimeter (Fig. 7.7) [17].

All known types of cathodes are considered as possible emission sources: cold, field-emission, on cold nanotubes, scandate, etc. (Fig. 7.8) [15, 17].

In order to obtain given current frequency (about hundreds of amperes per square centimeter) it is necessary to perform multiple (up to ten times) compression of the electron beam with the help of convergent optics, to perform its transformation along the structure of effect – ensure significant magnetic field (Fig. 7.9) [17]. Upper limit of the magnetic field based on permanent magnets is usually equal to $B_{max} = 11$ kG.

The device must include a multi-stage collector with efficiency of at least 80% (Fig. 7.10) [15, 17]. However, even with such high effectiveness of the collector, total electronic efficiency of the device does not exceed 5% (Fig. 7.11) [17].

Problems of heat removal apply both to the collector and to the slowing structure. Heat emission in the slowing structure is caused by HF losses and current interception. In this case, according to estimates, heat power on the SS surface can reach 2 kW/cm^2 (Fig. 7.12) [18]. Cooling of the structure requires special liquid cooling agent supplied via micro-channels, dimensions of which are in reverse proportion to frequency ($1/f$).

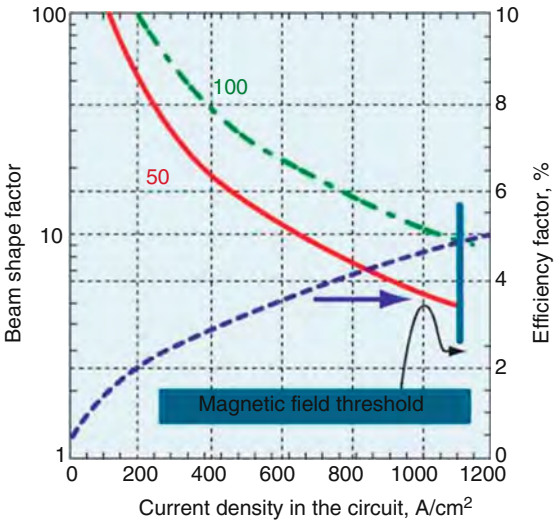

Fig. 7.7 Dependencies of the beam shape factor for different values of output power of the amplifier on SS and efficiency on current density [1]

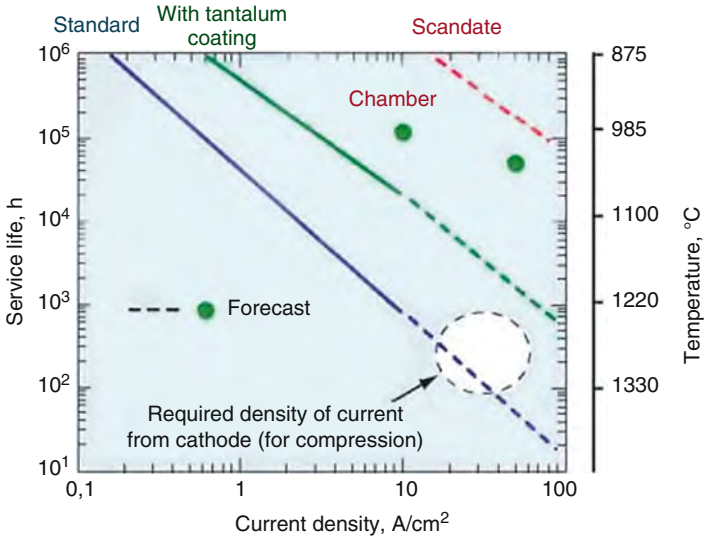

Fig. 7.8 Parameters of modern thermionic cathodes [17]

MIC technology makes it possible to achieve frequencies significantly higher than 220 GHz on condition of solving the problem of an increase in the power of MIC amplifier and reduction of losses during integration [15]. The main purpose of this monolithic amplifier is to improve the total gain factor, since the gain factor of the vacuum device itself is insufficient. Such approach was used before in development of power vacuum-semiconductor microwave modules for lower frequency ranges [19].

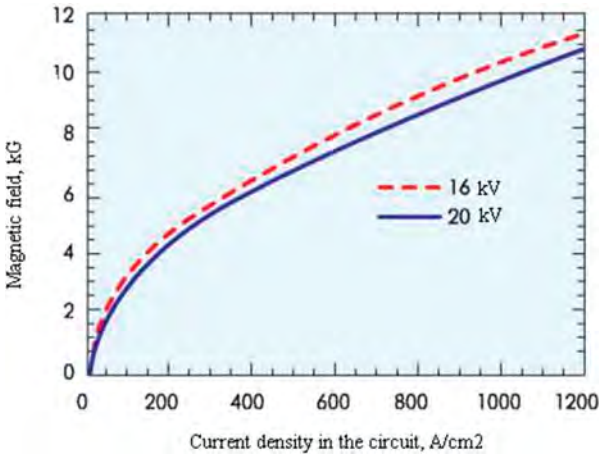

Fig. 7.9 Focusing magnetic field required for beam transportation (calculation)

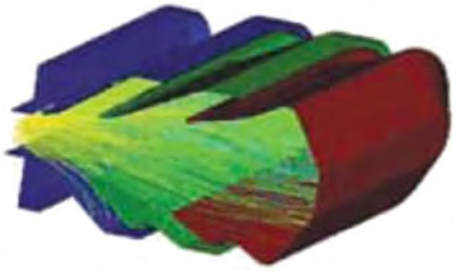

Fig. 7.10 Draft of a multi-stage collector [1]

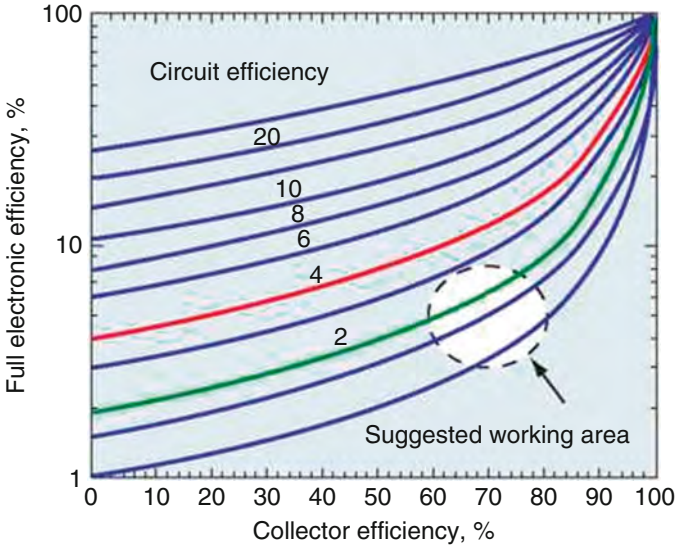

Fig. 7.11 Efficiency of the device, collector ad circuit (calculation) [1]

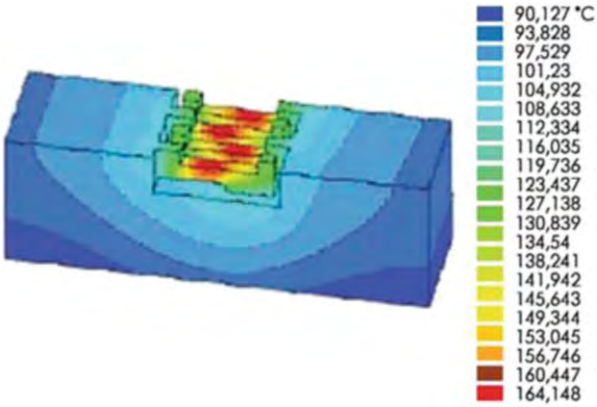

Fig. 7.12 Distribution of temperature in TWT SS with strip beam (calculation, f = 220 GHz, material – copper, SS thermal power density – 2 kW/cm^2, which corresponds to continuous output power of the device equal to 50 W at efficiency of 2.5%) [1]

Table 7.2 Table parameters of the HiFIVE program

Parameter	Phase I	Phase II	Phase III
Beam voltage, KV	20	–	–
Current density, A/cm^2	750	–	–
Beam shape factor N	25	–	–
Current passage, %	95	–	–
Central frequency setting accuracy, %	±2	–	–
Output power, W	–	50	>50
Frequency band, GHz	–	5	5
Product of power by frequency, W·GHz	–	250	500
Efficiency factor, %	–	5	5
Full current, mA	–	250	250
Additional parameters			
Parasite components during tuning of 250 kHz from carrier, dB	–	−50	−50
Output power of MIC preamplifier, mW	–	50	50

Technical assignment designed by DARPA for the HiFIVE program is briefly presented in Table 7.2 [1].

Implementation of the program is presented as a sequence of phases (stages).

Each phase of the program suggest demonstration of results achieved by the contractor and further performance of verification tests in the Naval Research Laboratory [16]. Let us briefly examine the main phases and stages of implementation of this program.

***Phase I*, Stage 1A. Electronic Beam**

The aim of this stage is to demonstrate formation and passage of hard electronic beam (shape factor 25) through the volume corresponding to future configuration of the device. Measurement of current density in the pulse mode is allowed. It is necessary to present the cathode in the final form, and its service life may differ

from the target value. Beam instability and current interception must be avoided. Magnetic support ($B_{max} < 11$ kG) shall ensure the given current passage (95%).

State Tests The system of electron beam formation or its copy with the technique and description of the testing equipment is sent to the state laboratory, where independent high-voltage tests and diagnostics of the beam are performed. The contractor provides structural dimensions of the e-beam projector and cathode, geometry of the channel and dimensions of the electromagnetic system. The state laboratory performs independent modeling of electron trajectories and comparison with the results of beam measurement.

***Phase I,* Stage 1B. Cold Tests**
This stage includes demonstration of all electromagnetic characteristics of the interaction structure produces with the help of microprocessing methods, namely: frequency characteristics of transmission/reflection, dispersion, resonances, parasite modes. The obtained data are compared to the results of 3D modeling.

State Tests After completion of cold tests, the slowing structure or its copy is transferred to the state laboratory, where independent cold tests and assessments are performed. The contractor provides the laboratory with the drawings with dimensions of the structure used to perform its modeling and comparison with the results of cold tests. The contractor also provides the lab with preliminary results of design of the vacuum power amplifier obtained with consideration of electron-wave interaction in high signal mode and parasite forms of oscillations.

***Phase II,* Stage 2A. Operational Test of the Assembled Power Amplifier**
The aim of the work is to demonstrate joint operation of all elements of the power amplifier (including MIC of the preamplifier and the collector), which shall prove the ability of the selected structure to ensure the required product of power by frequency. It is allowed for service life and other parameters of the cathode to be not in compliance with target values of the program. Heat structure of the device must ensure continuous operation of the amplifier for at least 100 h.

State Tests Specimen of the amplifier or its copy together with description of testing equipment and test methodology are delivered to the state laboratory, where high-voltage tests are performed and the absence of unwanted oscillations is confirmed. The contractor provides the laboratory with design details for all components of the amplifier. The laboratory performs independent modeling of the device in low and high signal modes, as well as thermal analysis, and compares the obtained data with measurement results.

***Phase II,* Stage 2B. Projected Cathode**
The aim of the stage is to demonstrate a cathode with very high current frequency fully compliant with the designed structure of the device as a separate component. Service life of the cathode shall exceed 1000 h at real values of the vacuum, operating voltage and full current of 250 mA measured on its surface. The cathode shall be fully prepared for inclusion into the design of a high power amplifier during the third stage of the program.

State Tests After contractor tests, the cathode or its copy is transferred to the state laboratory, which performs independent tests of its emission characteristics, temporal stability and service life, values of current and its density, as well as uniformity of emission and chemical composition of the cathode surface.

Phase III. **Integrated Structure of a Power Amplifier**
During this stage, small-sized vacuum power amplifier was demonstrated in full. During this stage, all characteristics of the amplifier are measured in continuous operation mode. All target parameters of the program are tested, including output power at 220 GHz, operating frequency band and the product of output power by operating frequency band.

After completion of the contractor tests, the final specimen or its copy with the description of hardware and methodology of testing are delivered to the state laboratory, where independent tests of volt-ampere and high-frequency characteristics of the amplifier are performed. After that, final verification of the correctness of tests is performed.

Ideologically, HiFIVE continues the aim of DARPA to promote developments of high-power small-sized wideband sources of microwave power, combining advantages of vacuum and semiconductor electronics within a single device – the so-called microwave power modules [19]. The goal of the work from the system point of view consists in significant increase in the throughput capacity of communication lines by expanding their band, which corresponds to the general trend of creating advanced weapon systems [20]. As for technological solutions required for development of integrated design of a microwave power module for the short-wave part of the millimeter range, they shall be breakthrough in nature according to the initiators of the program.

7.5 High-Power SHF Modules

Power levels between dozens and a hundred or more watts in the middle part of the centimeter band are on the border between power levels of solid-state and electrovacuum amplification devices [21–23]. At the same time, small-sized effective transmitters with such power are necessary for a number of applications, especially in military and aircraft equipment. The experience shows that neither solid-state nor vacuum technologies separately cannot ensure optimal design of the transmitter in terms of combination of such parameters as weight, dimensions, efficiency, power consumption, etc. In relatively recent time, a direction of new optimized devices combining both technologies, known as Microwave Power Modules (MPM) was developed in foreign countries. These modules occupied the intermediate region of power values between solid-state and vacuum devices and borrowed the best qualities from both groups.

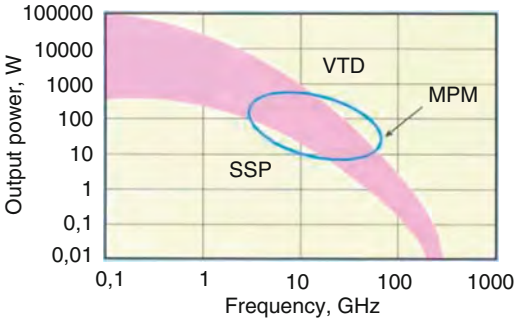

Fig. 7.13 Power levels of solid-state and electrovacuum devices [1]

Let us consider the design and features of microwave power modules.

The concept of microwave power modules was presented in 1988 in the special report of the US Ministry of Defence on vacuum microwave devices. In 1989, at the joint meeting of representatives of the government with experts in the fields of system and components, target parameters of these devices were formulated, taking into account systems in development and potential systems (Fig. 7.13) [22]:

- frequency – 6–18 GHz;
- output SHF power – 50–100 W;
- gain factor – 50 dB;
- pulse duty factor – 0–100%;
- efficiency – 33%
- spectral density of noise power – 45 dB/MHz;
- noise factor – 10 dB;
- volume – 123 cm^3;
- thickness – 0.79 cm.

Five company groups took place in the developments that began in 1991:

- Hughes EDD (currently known as Boeing EDD);
- Lockheed Sanders/Teledyne Electronic Systems (currently known as BAE Systems North America/Teledyne MEC/Teledyne Wireless);
- Northrop (currently known as Northrop Grumman);
- Raytheon (group of high-power tubes, currently a branch of L-3 Communications EDD);
- Westinghouse/Varian (currently known as Northrop Grumman/CPI).

In 1990s, most target parameters were achieved, an a new electronic microwave amplifier appeared in the market – microwave power amplifier in a light small-sized package (Figs. 7.14 and 7.15). It consisted of a miniature TWT, a solid-state preamplifier (SSA) and an integrated power source.

Solid-state amplifiers included in MPMs are standard devices produced by many companies. They are usually based on GaAs PHEMT transistors. Their purpose consists in increasing input SHF signal to the level sufficient for TWT saturation.

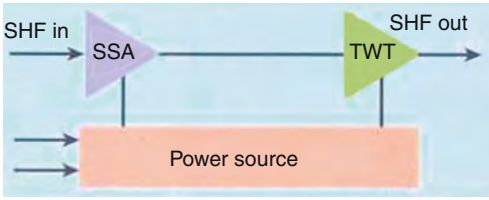

Fig. 7.14 Block diagram of a microwave power module [1]

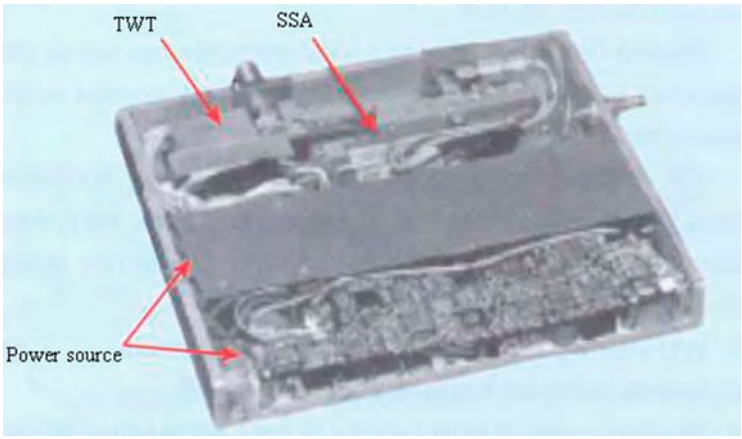

Fig. 7.15 Microwave power module [1]

Fig. 7.16 Mini-TWT used in power modules [1]

Travelling wave tube in the MPM is a helical mini-TWT with multi-stage reduction of potential of the collector (Fig. 7.16).

Uniform distribution of gain between solid-state preamplifier and high-power output power amplifier makes it possible to optimize parameters of the amplification chain in general, namely [24]:

– reduce dimensions and weight due to reduction of the gain factor and TWT length;
– increase the bandwidth due to reduction of the TWT gain;
– achieve maximum efficiency by using a multi-stage collector in the TWT;
– achieve an acceptable noise level (<10 dB) due to the use of a solid-state amplifier;

Fig. 7.17 Boards with circuits included in MPM power sources [1]

Fig. 7.18 Regular TWT with power source (left) and MPM (right) [1]

– introduce circuits of gain frequency characteristic balancing, thermal compensation and linearization into SSA;
– increase reliability at the expense of reducing high voltages in TWT with reduced gain factor.

Power source of the module converts the source voltage and produces supply voltage for TWT and SSA. The module consists of two section – low-voltage (logic and transformation circuits) and high-voltage (transformer, modulator and high-voltage circuits). The use of electronic components in surface-mount packages, new flat transformers and high-frequency switching methods made it possible to create small-sized power sources (Fig. 7.17), which ensure operation of the MPM powered by 270 V or 28 V DC or three-phase 115 V 400 Hz AC.

According to the estimate of specialists of L-3 Communications [21–23], power module of the Ku band (12–18 GHz) with the output power of 100 W is in general five times smaller and lighter than its vacuum analog (taking into account power supply and cooling) and eight times smaller than the corresponding semiconductor device (Fig. 7.18). Therefore, microwave power modules are capable of providing maximum power in a unit of volume compared to vacuum or semiconductor devices [24].

Table 7.3 Main parameters of MPMs by L-3 Communications EDD

Brand	Band of operating frequencies, GHz	Output power, W	Voltage (supply), V	Purpose
M1000	2–8	50	−90–260	Civil
M1030	14–14.5	125	−90–260	
M1125	27.5–31.5	40	−90–260	
M1221	6–18	60–100	28	Military
M1231	12.75–14.75	80	270	
M1280	18–40	20	270	
M1282	26–40	20	270	
M1340	43.5–45.5	40	−115	Space communication

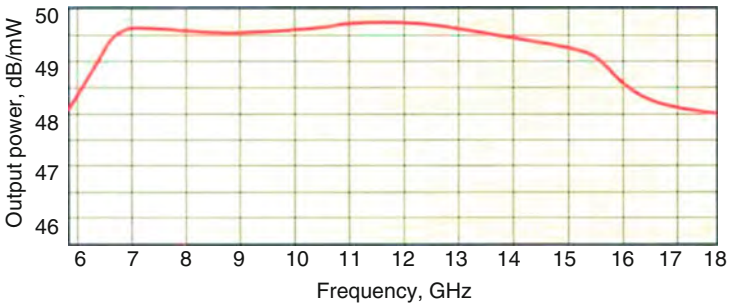

Fig. 7.19 Frequency dependence of the output power of the Ml220 module [1]

Serial production of MPMs is currently performed by a number of companies, including L-3 Communications EDD (Table 7.3), Triton, Northrop and CPI (USA), Thales (France) and NEC (Japan). The modules fully cover the range of frequencies from 2 to 40 GHz.

For example, M1221 is designed for special aerospace purposes and can operate within the temperature range of −54 . . . 85°C at altitudes over 20 km. Its dimensions are 19.9 × 16.5 × 2.5 cm, its weight – 1.8 kg [25].

Figure 7.19 [1] shows the frequency characteristic of wideband module M1220.

One of the directions of military aircraft technology is represented by remotely piloted aircrafts (RPA) used for reconnaissance, data gathering, target marking, etc. In addition to electro-optical and infrared systems, RPAs are fitted with the equipment of satellite communication of the 12–18 GHz band, where MPMs are used in transmitters. With output power of 50–100 W, one device covers a wide range of frequencies and can operate in single-band or multi-band mode. For example, such modules are installed in communication transmitters of American RPAs Predator and Global Hawk [21–23].

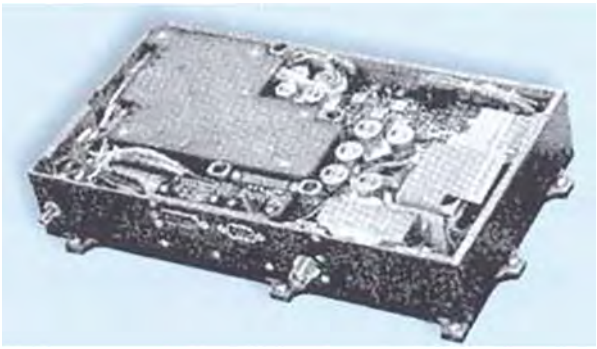

Fig. 7.20 MPM with pulse power of 1 kW [1]

In order to ensure operation in any weather conditions, developers started to include small-sized light radars with synthesized aperture in RPAs. Usually, they contain MPMs of the X-band (8–12 GHz) with output power of 100 W and pulse duty factor of 25%.

Unlike communication equipment, pulse characteristics of MPMs used in radar systems shall conform to additional requirements. In order to satisfy them, additional control circuits are included in the power source, which are used to adjust operating voltages of the TWT during the pulse period and synchronize the mode of the power source with the pulse repetition frequency. As a result, even characteristic of the operating voltage of the TWT (cathode voltage deviation <0.1%) are ensured during the pulse, and noises in the pause between pulses are minimized.

Such small-sized radars with synthesized aperture TES-AR based on MPMs are included in Predator RPAs [21–23]. For installation of long-range radars on RPAs, MPMs with pulse power 1 kW are created, with average power up to 100 W (Fig. 7.20). Special pulsed helical TWTs are used in them instead of mini TWTs. According to the latest information, MPMs of the X-band of M1270 series with such pulse power are already produced by L-3 Communications for aviation radars [26].

The following characteristics of these modules are presented:

Frequency	X-range;
Operating frequency band	2 GHz;
Input pulse microwave power	1 kW;
Gain factor in low pulse mode	55 dB;
Pulse duration	0.1–80 μs;
Level of harmonics relative to carrier frequency	−10 dB;
Operating voltage	28 V;
Operating temperature range	−40 . . . 85 °C;
Weight	4 kg;
Dimensions	28×15.2×5 cm.

The combination of parameters allows for a wide use of MPMs in electronic warfare systems, including equipment for countermeasures and deception. They can also be used in mobile satellite communication of military and civil purpose. Today, MRMs are one of the priority directions of development in foreign SHF electronics.

7.6 Vacuum SHF Devices of Centimeter, Millimeter and Terahertz Ranges

7.6.1 Vacuum SHF Devices of the Centimeter Range

According to specialists, regardless of increasingly wide use of semiconductor devices in radio-electronic systems, approximately 70% systems of military purpose still employ vacuum SHF devices [27].

Among vacuum microwave devices of these range, space TWTs are widely used, which retransmit the signal from satellites. The main developers of these TWT are Thales Electron Devices (France) and L-3 Communications Electron Technologies. Most important parameters of satellite TWTs include output power, efficiency, frequency band, service life and linearity. Since 1997, L-3 Communications has produced over 3200 TWTs for the frequency range of 2–75 GHz. In total, their operating time exceeded 140 million hours. The company recently used CHRISTI NE (for calculation of non-linear characteristics of helical TWTs based on disc model of the electron flow) and MICHELLE (for calculation of multi-stage collector) programs to modernize TWT of the X band of the 86,160 type, introducing an isolated focusing electrode into the double-anode e-beam projector. This helped improve focusing and operate in pulsed mode in addition to continuous mode. The use of cooling radiator significantly reduced heat load on the satellite. Continuous power of the tube is 160 W in the band of over 500 MHz, efficiency – 69%, weight with power source – less than 2.9 kg. According to the test, expected useful life of the tube is 15 years.

For flight tests, L-3 Communications suggests a helical TWT of the 9250H model for the range of 20.2–21.2 GHz with efficiency of 65%, capable of functioning in the orbit for over 20 years. In the saturation mode, power of the tube amounts to 150–300 W depending on the purpose without structural changes. Amplitude-phase conversion coefficient does not exceed 3.4 deg/dB.

A series of satellite TWTs for K_u and K_a bands was announced by Thales Electron Devices. Output power of the tube of the K_u range band is 150 W in the 10.7–12.75 GHz, tube of the K_a band – 170 W in the 17.3–21.2 GHz band. Company specialists are currently developing tubes of K_u- and K_a ranges with power values up to 300 and 250 W accordingly and the band of 2.9 GHz. The company is also currently modernizing TWTs of the S-range (2–4 GHz). For example, instead of TWT with output power of 250 W it offers TL2500 TWT with power of 500 W. Immediate band of the tube (150 GHz) can be tuned by 500 MHz. Thales devices are among the best in Europe; they are also used in a number of Russian satellites.

One of traditional applications of TWTs of the centimeter range is presented by electronic warfare systems. British company e2v Technologies, which specializes in this field, have developed a tube that covers the entire bottom part of the microwave band – 2–7 GHz. Output power of the tube exceeds 100 W, voltage is under 4 kW, supply power is 540 W, and dimensions are 250×50×50 mm. A while ago, the company attempted to create a TWT that would cover the entire range between

2 GHz and 18 GHz. However, due to difficulties of matching in such wide frequency band, the work was not completed. Apparently, current tasks consists in fully covering the EW range with two lines: 2–7 GHz and 6–18 GHz.

A number of developments presented in the International Conference for Vacuum Electronics in 2014 [28] belonged to the category of high-power and super-power devices. Two models of 24-beam two-cavity klystrons of the S-band with average power of 30 kW have been created and tested in the Institute of Electronics of the China Academy of Sciences. Output pulse power of the device is 500 kW, efficiency – over 35%, immediate frequency band – 10%, service life – over 3000 h.

Super high-power devices are usually designed for accelerating equipment and energy weapon systems. National Accelerator Laboratory of the USA under contract with the Ministry of Energy has developed 16-beam klystron with focusing by permanent periodic magnets with output power at 11.424 GHz of 5 MW and efficiency of over 60%. Each electronic beam of the device has its own output resonator, the energy of which is added to the energy of the other beams in the common output waveguide.

CPI developers used a four-gap distributed integration scheme in the design of super-high-power klystron of the X-band. With power of 50 MW and at the frequency of 11.994 GHz, klystron gain amounts to 48 dB, efficiency – to 40%. Duration of the HF pulse – 1.5 μs, repetition frequency – 60 GHz.

Vacuum microwave devices today are mostly developed for systems of amplification and generation of high-power radio frequency signals. The class of medium-power TWTs of the centimeter range is heavily contested by solid-state amplifiers, first of all – GaN-based models. At the same time, studies of many devices used previously in orbit performed by Boeing demonstrated that the parity of vacuum and semiconductor technologies is still preserved in the field of satellite devices [27]. The position of semiconductor devices is much stronger in transmitters of radar stations with active electronically scanned arrays (AESA), where they are, in fact, driving out power vacuum devices.

7.6.2 *Vacuum SHF Devices of Millimeter and Terahertz Ranges*

After 2000, based on the results of the HiFIVE program considered above, as well as the special program Terahertz Technology Initiative and other programs, Defense Advanced Research Projects Agency (DARPA) of the US Department of Defence focused on exploring ***millimeter and terrahertz frequency ranges*** of vacuum microwave electronics [29, 30]. The aim of DARPA was to explore the frequency range of 300 GHz-1 THz (the so-called ***terrahertz*** band, or TCHz Cap), which opens extensive possibilities for improvement of military and space equipment. The main open results in this field were reported during the International Vacuum Electronics Conference IVEC 2014 [28].

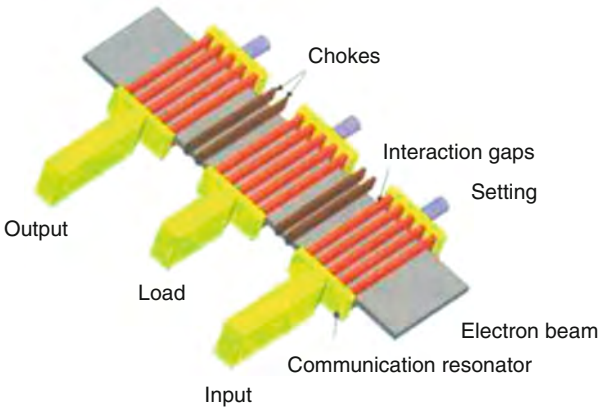

Fig. 7.21 Layout of a klystron with distributed interaction with strip e-beam [1]

Transition to short-wave ranges called for replacement of traditional designs of vacuum SHF devices with new types. Thus, many devices with regular cylindrical electron beam were replaced with devices with strip beam, which, similarly to multi-beam models, were devices with beams distributed in space (Fig. 7.21). With smaller focusing magnetic field and small-sized design, these devices ensure greater efficiency of interaction of the electron beam with electromagnetic field of the device. In the USA, Naval Research Laboratory (NRL) is the leader of works in this direction [28]. The main structural element of its devices is the specially designed e-beam projector with strip beam with dimensions of 0.3×4 mm, which produces current of 3.5–4 A at voltage of about 20 kV. Based on this projector, two devices have been created in NRL:

- narrowband three-resonator klystron with distributed interaction of the electron beam with electromagnetic field of 94 GHz, with power of 7.5 kW and gain in the saturation mode of 35 dB (Fig. 7.21);
- TWT based on the system of connected cavities with output pulse power of 10 kW at 34 GHz, gain of 15 dB and band of 5 GHz at the 3 dB level. The length of the interaction system of the lamp is less than 5 cm.

Strip beam devices are actively being development by employees of the Institute of Electronics of the China Academy of Sciences. The power of the W-band (75–110 GHz) designed by them is 30 kW at voltage of 75 kW and current of 4 A. Gain of the device is 40 dB, band – 100 MHz, efficiency – 10%. Dimensions of a flat electron beam are 10×0.5 mm.

L-3 Communications Electron Devices (USA) specializes in creation of microwave power modules (MPM) combining a TWT, a setting solid-state amplifier and a power source within a single package. The latest development of specialists of the company is M1871 NanoMPM. Continuous power of the device in the saturation mode amounts to 50 W within the range of 29–31 GHz with efficiency of 30%. Low signal amplification is 34 dB in the entire frequency band. Dimensions of the device are $11.17 \times 16.76 \times 2.54$ cm. It is designed for communication systems and radars

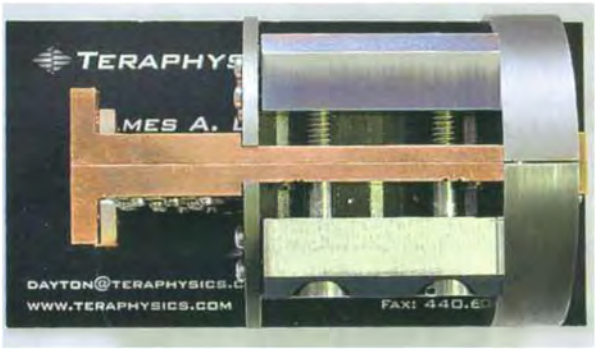

Fig. 7.22 Helical micro-TWT for 94 GHz with power of 25 W with dimensions of a business card [1]

installed on small mobile platforms (remotely piloted aircrafts, satellites, etc.). Designs of the MPM is based on a small TWT.

Creation of power sources of the K_a band (26.5–40 GHz) was also commenced by companies that had no electronic devices of their own design. For example, dB Control (subsidiary of the Electronic Technologies Group, member of the HEICO corporation, USA) offers industrial TWT amplifiers with power sources for ground and mobile radars. The design of the amplifiers is modular, with integrated air-forced heat removal. Minimum pulse power of the device – 700 W in the band of 34.5–35.5 GHz, pulse duty factor – 10%.

Vacuum Electronics National Laboratory of China has developed TWT of the Q-band (33–50 GHz) on slowing structure of the folded waveguide type. Maximum power of the device amounts to 200 W within the frequency band of 43.5–45.5 GHz. When a single-stage collector is used, the efficiency of the device exceeds 25%. Tube elements were manufactured with the help of such modern technologies as DRIE (Deep Reactive Ion Etching), LIGA, a combination of X-ray lithography, metal plating and molding, and so on.

Many works are aimed at exploration of the W range (mostly 94 GHz). Various Chinese institutes have created both narrowband (2 GHz) TWTs with pulse power of 100 W and wideband tubes (10 GHz) with continuous power of 20 W.

An interesting design of helical micro-TWT for 94 GHz with power of 25 W was suggested by Teraphisics (USA). Electron beam projector, slowing system and collector of the TWT are manufactured simultaneously using original technology with centering precision up to 2 μm. New small-sized configuration of the periodic structure of focusing by permanent magnets is also used. Dimensions of the tube are commensurate with the size of a regular business card: the length is 6.6 cm, diameter – 4.82 cm (Fig. 7.22), weight – 450 g [29].

As for frequency bands of the millimeter range, especially important is the 200–300 GHz band (C-band), which corresponds to the wide minimum of atmospheric attenuation. Interest in this band emerged during implementation of the HiFIVE program, the aim of which consisted in creating a vacuum microamplifier with output power of 50 W at the central frequency of 220 GHz [31–49]. Naval Research Laboratory and Beam Wave Research are designing a TWT with single-

stage serpentine slowing system with a length of 2.2 cm. 170 μm electron beam with current of 124 mA at voltage of 20 kV is focused by the field with magnetic inductance of 6.6 kG. The device is designed for output power of 80–90 W within the band of 231.5–235 GHz at output power of 113 mW and gain of 30 dB. If single-stage collector is used, power in the saturation mode can reach 140 V with efficiency of 23%. Diameter of the device is 14 cm, its height – 11 cm. The weight with magnetic system is about 7 kg.

Canadian department of Communications & Power Industries (CPI) continues to develop its traditional klystrons with distributed interaction of the millimeter range. Pulse amplifiers for frequency ranges of 35.5 GHz (1 and 3 kW) and 35.75 GHz (1.5 kW) are in their final stages of development. Development of two pulse klystrons for 94 GHz (1.7 kW) has been completed. The following devices have been created for higher frequency ranges, including the G range:

- amplifier for 187 GHz with continuous power of 5 W;
- tunable oscillator for 263 GHz with continuous power of 5 W;
- amplifier for 264 GHz with pulse power of 20 W.
- The weight of each device does not exceed 8 kg.

TWTs of the 220 GHz band based on folded waveguide system with the band of 5 GHz is being jointly designed by employees of the Institute of Applied Electronics and the Terahertz Research Center (China). With power of 250 mW, the band of 3.5 GHz and gain of 14 dB were achieved.

It should also be noted that Northrop Grumman Electronic Systems is the leader in development of devices of the terahertz range. It has already demonstrated vacuum amplification devices for frequencies of 0.65 and 0.67 THz (100 MW). As a result of the latest development, specialists of the company created the amplifier with output power of more than 50 MW within the range of 0.835–0.842 THz. At the frequency of 0.85 THz its power amounted to 39.4 mW, immediate band – 11 GHz in low signal mode. Single-stage step-down collector is used in the device.

References

1. Belous, A., Merdanov, M., & Shvedov, S. (2018). *Microwave electronics in radar and communication systems* (Technical Encyclopedia in 2 volumes, 2nd ed., revised, 1520 p). Moscow: Tekhnosfera.
2. Tsarev, B. M. (1967). *Calculation and engineering of electronic tubes* (3rd ed.). Moscow.
3. Lebedev, I. V. (1972). *Microwave technology and devices (Vol. 2)*: *Electrovacuum Devices*. Moscow.
4. Sobolev, N. A., & Melamid, A. E. (1974). *Photoelectronic devices*. Moscow.
5. Nikonov, B. P. (1979). *Oxide cathode*. Moscow.
6. Sheshin, E. P. https://elib.pstu.ru/vufind/EdsRecord/edseee,edseee.8745305
7. Abrams, R. H. et al. (2001, September). Vacuum electronics for the 21st century.In *IEEE Microwave Magazine* (pp. 61–72).
8. Report of Department of Defense Advisory Group on Electron Devices. (2000, December). *Special technology area review on vacuum electronics technology for RF applications*.

9. Levush, B., et al. *Vacuum electronics: Status and Trends*. www.radar2007.org
10. Vikulov, I., et al. (2007). Power SHF modules – Hybrid of vacuum and solid-state electronics. *ELECTRONICS: NTB, 2007*(7), 69–71.
11. *The National Nanotechnology Initiative: Research and development leading to a revolution in technology and industry*. www.nano.gov/NNI_08Budget.pdf
12. Vikulov, I., & Kichaeva, N. (2007). GaN technology. A new milestone in development of microwave microcircuits. *ELECTRONICS: NTB, 2007*(4), 80–85.
13. Shakhnovich, I. (2007). Strategy of development of radioectronic complex in Russia: Has the Ice Been Broken? Summary of the Nizhny Novgorod Conference. *ELECTRONICS: NTB, 2007* (7), 9–12.
14. Rosker, M. J. *High Frequency Integrated Vacuum Electronics (HiFIVE)*. http://www.darpa.mil/mto/solicitations/baa07-49/pdf/amendment2.pdf
15. Rosker, M. J. (2007, July 24). *Background, program objectives and structure*. *High frequency integrated vacuum electronics industry Day Meeting*, Arlington, 24 July 2007. http://www.darpa.mil/mto/solicitations/baa07-49/HiFIVE_Overview.pdf
16. Calame, J. *Circuit integration and circuit demonstrations*. http://www.darpa.mil/mto/solicitations/baa07-49/pdf/Integration_Demos.pdf
17. Levush, B. *High aspect ratio electron beam, high efficiency interaction structure, and high power amplifier design*. http://www.darpa.mil/mto/solicitations/baa07-49/pdf/Beam_Structure_Amplifier.pdf
18. Calame, J. *High efficiency thermal management*. http://www.darpa.mil/mto/solicitations/baa07-49/pdf/Thermal_Management.pdf
19. Vikulov, I., & Kichaeva, N. (2007). Powerful microwave modules. Hybrid of vacuum and solid-state electronics. *ELECTRONICS: NTB, 2007*(7), 69–71.
20. Wilson, J. R. (2008, January). *Avionics enter the 5th generation*. Military & Aerospace Electronics.
21. Vikulov, I., & Kichaeva, N. (2007). Microwave power modules of hybrid vacuum and solid-state electronics. *Electronics: NTB, 2007*(7), 69–71.
22. NinnisT. (2007). *Microwave power modules – Miniature microwave amplifiers for UAVs*. www.l-3com.com
23. NinnisT. (2007). *Microwave Power Modules (MPMs) – Miniature microwave amplifiers for radars*. www.l-3com.com
24. Abrams, R. H., et al. (2001, September). Vacuum electronics for the 21st century. *IEEE Microwave Magazine* (pp.61–72).
25. *Press release*. (2006, May 22). www.linkmicrotek.com
26. *L-3 electron devices introduces new 1 kW pulse microwave power amplifier*. (2007, June 25). www.l-3com.com
27. *International vacuum electronics conference*. (2013).
28. *International vacuum electronics conference*. (2014).
29. Vikulov, I. (2015). *SHF electronics today: Directions and challenges.* Electronics: NTB No.3 (00143) (pp. 64–79).
30. Vikulov, I., & Vacuum, S. H. F. (2011). Electronics in 2010. To millimeter and terahertz bands. *Electronics: NTV, 2011*(2), 108–119.
31. Vikulov, I., & Kichaeva, N. (2008). American program for microwave vacuum electronics HiFIVE. *Electronics: NTV, 2008*(5), 70–74.
32. Vikulov, I., & Kichaeva, N. (2007). Vacuum microwave electronics in the USA: State and development trends. *Electronics: NTV, 2007*(5), 66–71.
33. Vikulov, I., & Kichaeva, N. (2007). GaAs technology of monolithic SHF circuits in foreign military equipment. *Electronics: NTV, 2007*(2), 56–61.
34. Vikulov, I. (2009). WBCS-RF program, phase II. Results and targets. *Electronics: NTV, 2009* (8), 62–65.
35. Vikulov, I. (2014). GaN microcircuits to replace VTDs. *Electronics: NTV, 2014*(1), 168–174.

36. *Raytheon's GaN MMIC technology validated for space applications*. www.semiconductor-today.com/news_items/2014/DEC/raytheon_l71214.shtm
37. ADMS. *"Patriot" receives a new radar with active AESA, Military Paritet*. www.militaryparitet.com/ttp/data/ic_ttp/7701
38. Mikula, M., et al. (2014). Manga: Manufacturable GaN SiC substrates and GaN epi wafer supply chain. In *Proceedings of the 9th European microwave integrated circuits conference*, 2014 (pp. 229–232).
39. *Saab showcases fighter aircraft featuring GaN technology*. www.compoundsemiconductor.net/article
40. Joosting, J. P. (2014, November/December). *The rise of GaN on Si to take on high-power and high volume markets*. Microwave Engineering Europe (p. 15).
41. Stevenson, R. *GaN-on-Silicon gathers momentum*. www.compoundsemiconductor.net/article
42. *Peregrine expands integrated product portfolio into both ends of frequency spectrum*. www.semiconductor-today.com/news_items/2014/OCT/PEREGRINE_081014.shtml
43. *DARPA's ELASTx program demos 94 GHz fully integrated all-silicon system-on-chip transmitter*. www.semiconductor-today.com/news_items/2014/JUL/DARPA_020714.shtml
44. DARPA's mobile Hotspots Program Drives E-Band Performance Benchmarks. (2014, October 14). *Microwave Journal*. www.microwavejoumal.com/articles/23121
45. *Terahertz Triumph*. www.compoundsemiconductor.net/article/95740-terahertz-triumph.html
46. Green, D. S., et al. (2014). *The DARPA Diverse Accessible Heterogeneous Integration (DAHI) program: status and future directions*. CS MANTECH conference (pp. 343–346).
47. *US DoD launches competition for integrated photonics manufacturing institute*. www.compoundsemiconductor.net/article/integrated-photonics-manufacturing-institute.html
48. *Hybrid Hope*. www.compoundsemiconductor.net/article/95650-hybrid-hope.html
49. *«Green Light» for UK's first Compound Semicoductor Research Foundation*. www.compoundsemiconductor.net/articles/compound-semiconductor-foundation.html

Chapter 8
Semiconductor SHF Devices for Radar Sets

8.1 Element Base of TRMs for Phased Antenna Arrays

8.1.1 Attenuators for Transceiver Modules of Active Electronically Scanned Arrays

As demonstrated in Chap. 1, structure of a modern radar set is fairly similar to systems developed at the dawn of radar industry – an antenna system, a receiver, a transmitter and electronic systems of data control and processing. Development of technology in this field moved towards improvement of each component separately [1]. However, special attention was paid to development of antenna systems and gradual integration of the antenna structure with receiver and transmitter paths. In combination with improvement of the element base and transition to the use of increasingly higher frequencies for the purposes of radiolocation, phased antenna arrays are widely used, which are composed of groups of radiators with the possibility of independent control of the signal phase and generation of effective antenna radiation in general in one desired direction different from the effective radiation direction of a separate element. Therefore, it became possible to control the antenna beam by electronic means instead of mechanical.

Figure 8.1 schematically [2] demonstrates the principle of formation of the phase front and the direction of the added beam of the antenna array perpendicular to this plane of equal phases: the input signal is divided into multiple channels corresponding to the number of array elements, and the signal in each channel receives its own phase shift necessary to determine a certain position of the array beams in space.

As demonstrated in Chap. 1, there are two main types of systems on phased antenna arrays – passive and active antenna arrays. The main difference is as follows: a passive antenna array has one powerful transceiver, the signal of which is distributed among all channels, while in active electronically scanned arrays

© The Editor(s) (if applicable) and The Author(s), under exclusive license to Springer Nature Switzerland AG 2021

A. Belous, *Handbook of Microwave and Radar Engineering*,
https://doi.org/10.1007/978-3-030-58699-7_8

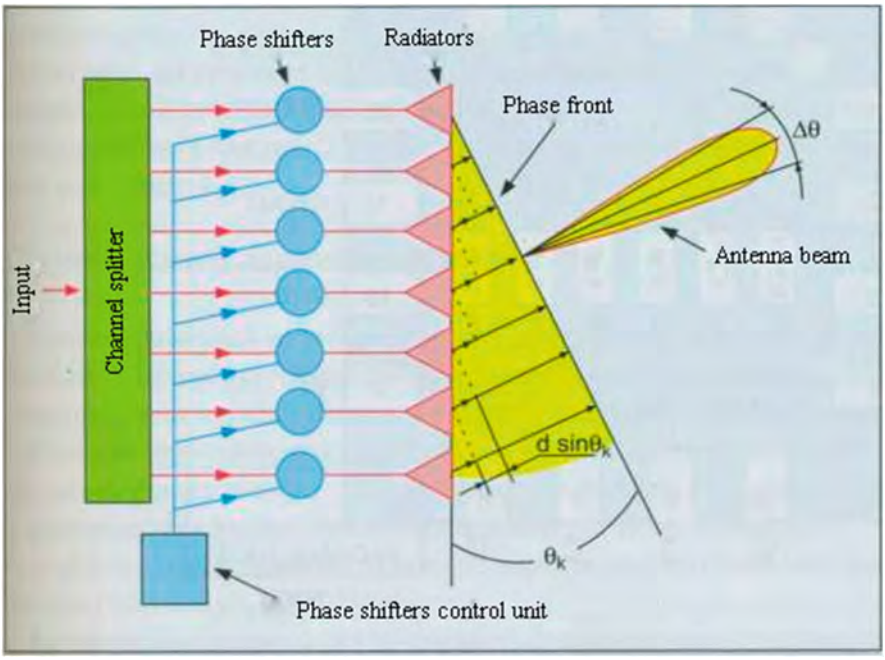

Fig. 8.1 Beam control principle in a phased antenna array

(AESA) the channel of each array element has its own transceiver. Each of the concepts has its own advantages and disadvantages: passive arrays are significantly cheaper but require the use of extremely powerful signal sources, which in turn require complex power supply and cooling circuits. Active arrays have extremely high reliability margins – failure of one or several transceivers does not cause malfunction of the entire system; however, the number of used components, difficulty of control and synchronization and the cost of the device exceed those of a passive array by orders of magnitude.

However, development of the modern base of microwave electronics allows AESA-based systems to rapidly push out passive arrays not only from the traditional positions in aviation and military equipment, but also in civil applications – sub-surface probing, radars of air traffic organization, space programs, etc.

The main element of an AESA is the transceiver module (TRM); in modern systems, the antenna of a separate array element is often a part of the TRM structure. An example of appearance of a modern TRM is shown in Fig. 8.2 [3].

In terms of architecture, design and circuity transceiver modules can be implemented by different means; however, there is a possibility of generalized presentation, as the components of such scheme are found in all such modules in one form or another. In this section, we will present a brief overview of these elements only. In order to specify the examples of TRM designs, let use determine

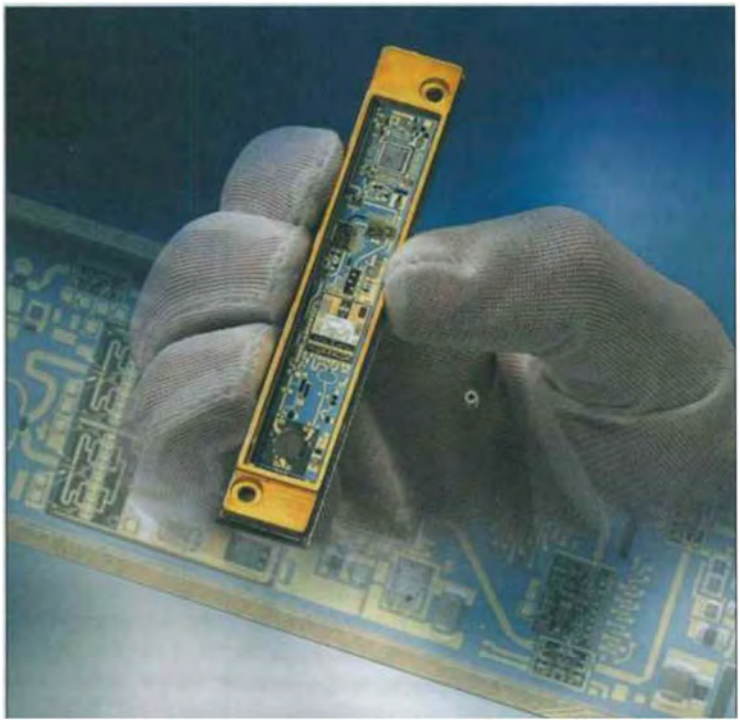

Fig. 8.2 Appearance of an AESA TRM by Cassidian

the range of components that allow to solve the task of designing AESAs in the most popular frequency ranges:

L – 1–2 GHz;
S – 2–4 GHz;
X – 8–12 GHz.

Generalized structural diagram of a TRM for AESA is shown in Fig. 8.3 [2].

The first basic element is the attenuator.

Attenuator is a common element for transmitter and receiver paths; it is designed to introduce additional variability of signals in terms of phase and amplitude and helps reduce the influence of side lobes of the diagram and eliminate mismatch between transmission coefficients of separate transceivers. As a rule, digital attenuators are used, since a controlled analog attenuator strongly depends on the quality of generation of the control signal in terms of its characteristics, which is difficult to implement in practice. In the following, we are going to consider modern solutions in the field of such components in the specific context of products of the American company Hittite Microwave – one of the leaders in production of microwave microcircuits and nearly all components of the microwave range required for building of most microwave devices.

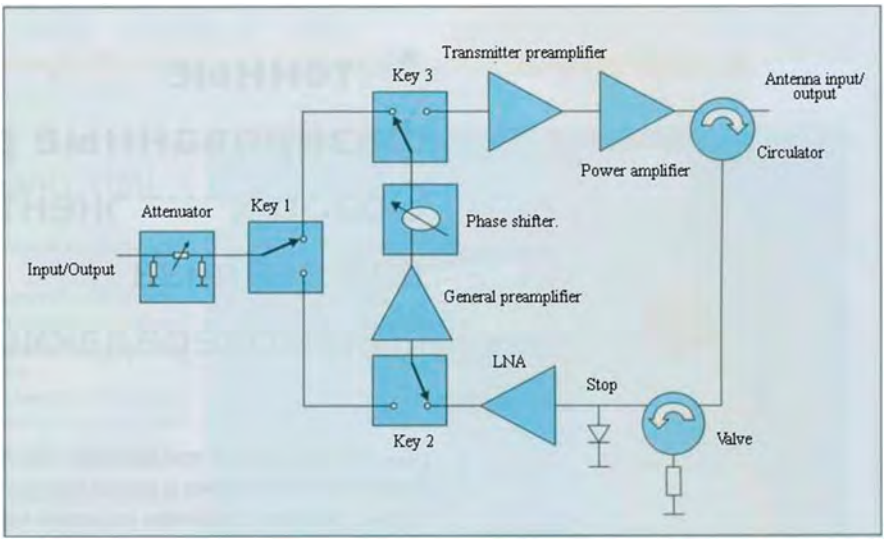

Fig. 8.3 Generalized structural diagram of a TRM [2]

In 2008–2010, a popular trend emerged for creation of wideband digital attenuators covering several frequency bands, which allowed engineers to unify their developments for various applications [3–6]. The next important step in selecting an attenuator consists in choosing its attenuation range and minimum step. Modern solutions make it possible to obtain more than 30 and 0.5 dB respectively (see Table 8.1).

As exemplified by HMC424LP3, a digital attenuator is a line of fixed attenuators with the possibility of control of each section by means of serial or parallel digital code (Fig. 8.4).

8.1.2 Two-Pole Switches for AESA

Figure 8.5 shows simplified structure of the HMC232 switch by this company. Three switches (keys) are available. Key 1 is used to split the main signal into receiver or transmitter path, the other two (key 2 and 3) are used for connection of single-directional elements (with strict input-output direction) – common preamplifier and phase shifter in the circuit of the receiver or transmitter.

Table 8.2 contains basic technical characteristics of the most interesting models by Hittite Microwave.

Selection of the switch is based, first of all, on the inserted losses and isolation between channels. Switching time shall also be taken into account. Modern switches

Table 8.1 [2] Summary table of characteristics of attenuators by Hittite Microwave

	Frequency range, GHz	Capacity bit	Intrinsic losses, dB	Range of attenuation, dB	Input intersection point of the third order, dBm	Controlling levels, V	Type of package
HMC1018LP4E	0.1–30	5	5.5	1–31	43	0/+3−5	LP4
HMC424	0–13	6	4	0.5–31.5	32	0/−5	Packageless
HMC424LP3	0–13		4	0.5–31.5	32	0/−5	LP3
HMC425	2.4–8		3.5	0.5–31.5	40	0/+5	Packageless
HMC425LP3	2.2–8		3.2	0.5–31.5	40	0/+5	LP3
HMC542BLP4E	0–4		1.2	0.5–31.5	45	0/+5	LP4
HMC624ALP4E	0–6		1.8	0.5–31.5	55	0/+5	LP4

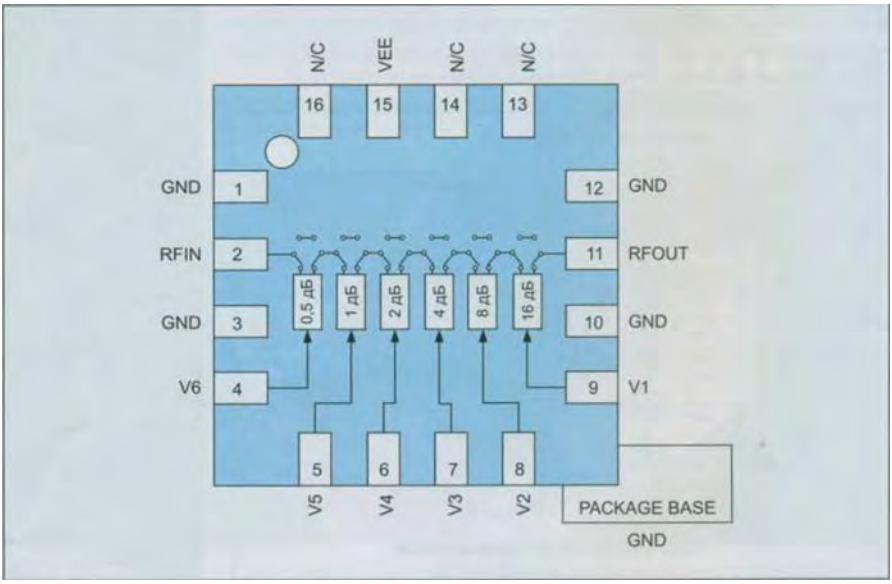

Fig. 8.4 Structure of the HMC424LP3 attenuator

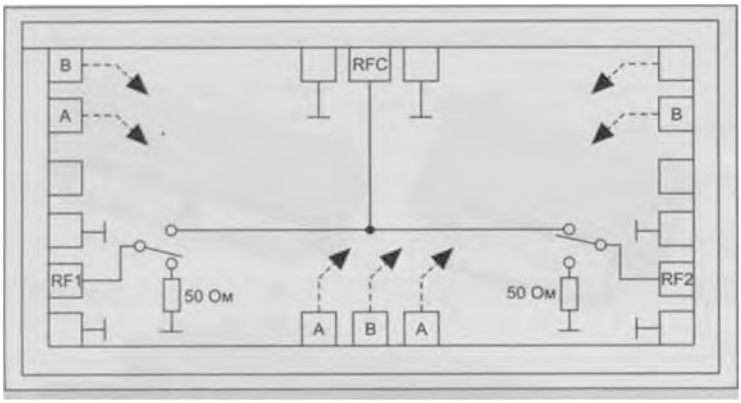

Fig. 8.5 Structure of the HMC232 switch

are capable of fully switching between transmission and reception modes in single nanoseconds, which significantly reduces the blind spot of the radar. However, it shall be noted that such switching time usually requires organization of negative control voltage. This is relatively simply to implement, but it leads to an increase in the number of components in the device circuit.

Table 8.2 [2] Summary table of characteristics of switches by Hittite Microwave

	Frequency Range, GHz	Functionality	Insertion loss, dB	Isolation, dB	Switching speed, ns	1 dB compression point, dBm	Controlling levels, V	Type of package
HMC232	0–15	SPDT	1.4	50	5	26	0/−5	Packageless
HMC232LP4	0–12		1.5	55	6	27	0/−5	LP4
HMC349LP4CE	0–4		0.9	65	150	34	0/+5	LP4C
HMC547LP3	0–20		1.8	47	6	23	0/−5	LP3
HMC607	0–15		1.7	60	5	26	0/−5	Packageless
HMC849ALP4CE	0–6		0.8	60	150	35	0/+3−5	LP4C

8.1.3 AESA Phase Shifters

Phase shifter is the main element of any AESA transceiver (Fig. 8.6), since the quality of operation of the entire system will largely depend on it. Let us consider the examples of certain phase shifter solutions by Hittite Microwave (Table 8.3).

Digital phase shifters are most commonly used due to their higher stability and noise immunity. Phase step of 5° is usually sufficient for a wide range of existing tasks; phase tuning range can reach 360°. Depending on the features of implementation of the transceiver, it is possible to select the required configuration – packaged or packageless crystal (for use in sealed volume).

Structurally (Fig. 8.6), any phase shifter is similar to the attenuator considered above: it includes a set of fixed elements of phase rotation with the possibility of control of each separate cell.

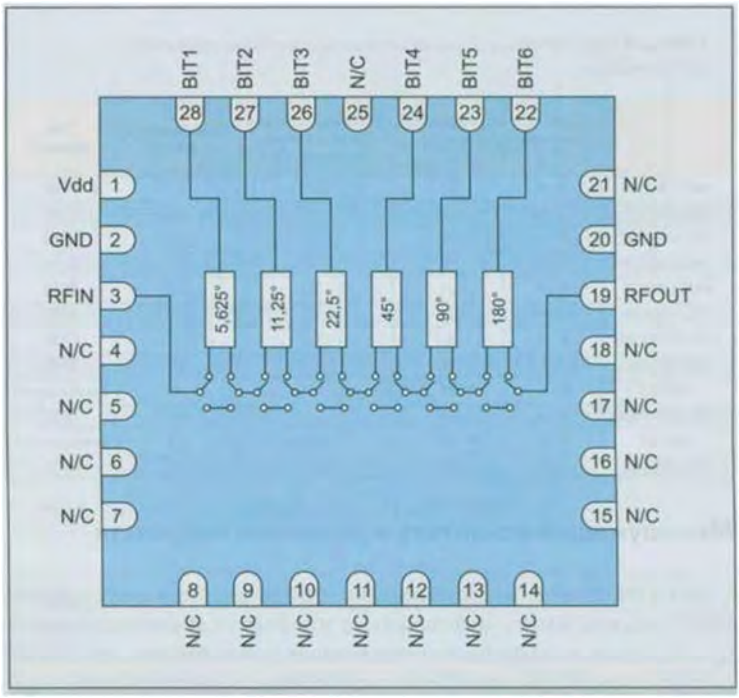

Fig. 8.6 Structure of the HMC936LP6E phase shifter

Table 8.3 [2] Summary table of characteristics of phase shifters by Hittite Microwave

	Frequency range, GHz	Capacity, bit	Insertion loss, dB	Frequency tuning range	Input intersection point of the third order, dBm	Controlling levels, V	Type of package
HMC642	9–12.5	6	6.5	5.625°–360°	41	0/+5	Packageless
HMC642LC5			7		41	0/+5	LC5
HMC643	9–12		6.5		38	0/−3	Packageless
HMC643LC5			7		38	0/−3	LC5
HMC647	2.5–3.1		4		54	0/+5	Packageless
HMC647LP6			4		54	0/+5	LP6
HMC648	2.9–3.9		4		45	0/+5	Packageless
HMC648LP6			5		45	0/+5	LP6
HMC649	3–6		6.5		44	0/+5	Packageless
HMC649LP6			8		44	0/+5	LP6
HMC936LP6E	1.2–1.4		4		45	0/+5	LP6

8.1.4 Preamplifiers of Transceivers for AESA

It is plausible to consider two elements (general preamplifier and transmitter preamplifier) together, since their parameters are quite similar. The main parameter for amplifiers is the output dynamic range and gain factor; however, noise characteristics are also important. Summary characteristics of such amplifiers by Hittite Microwave are listed in Table 8.4 [2].

As illustrated by the generalized TRM structure (Fig. 8.3), common preamplifier is used to compensate intrinsic losses of two keys (about 2–3 dB), phase shifter (about 4–8 dB) and attenuator (2–5 dB), as well as mismatch losses in the path. As a result, this amplifier shall compensate about 12–18 dB. Transmitter amplifier shall linearly enhance the signal level to the value required at the output of the end stage (stages) of the power amplifier.

8.1.5 Low Noise Amplifiers and Power Amplifiers for AESA

The structure of transceiver modules for AESA usually includes two amplifiers performing opposite tasks: LNA shall have the minimum noise coefficient at high amplification coefficient and dynamic range by input, while the power amplifier (PA) shall bring the signal to the necessary level at the antenna input with maximum amplification coefficient and minimum distortions.

The situation with low noise amplifiers is fairly simple – there is an extensive choice of the component base, and the examples are given in Table 8.5 [2].

However, selection of components for power amplifiers has recently become a difficult task. Models that are more or less attractive are subject to licensing control

Table 8.4 Summary table of characteristics of preamplifiers by Hittite Microwave

	Frequency range, GHz	Gain factor, dB	Output intersection point of the third order, dBm	Noise coefficient, dB	Package type
HMC478MP86	0–4	22	32	2	MP86
HMC636ST89	0.2–4	13	40	2.2	ST89
HMC476MP86	0–6	20	25	2.5	MP86
HMC476SC70	0–6	19	24	2.5	SC70
HMC478SC70	0–4	24	31	2.5	SC70
HMC741ST89E	0.05–3	20	42	2.5	ST89
HMC3587LP38E	4–10	14.5	25	3.5	LP38
HMC789ST89E	0.7–2.8	18	42	3.8	ST89
HMC405	0–10	16	25	4	Packageless
HMC3653LP3BE	7–15	15	28	4	LP38
HMC397	0–10	15	24	4.5	Packageless
HMC788LP2E	0–10	14	30	7	LP2

Table 8.5 Summary table of characteristics of the series of low noise amplifiers by Hittite Microwave

	Frequency range, GHz	Gain factor, dB	Output intersection point of the third order, dBm	Noise coefficient, dB	Package type
HMC374	0.3–3	15	37	1.5	SOT26
HMC516	7–17	21	20	1.8	Packageless
HMC516LC5	9–18	20	25	2	LC5
HMC565	6–20	22	20	2.3	Packageless
HMC618LP3	1.2–2.2	19	36	0.75	LP3
HMC639ST89	0.2–4	13	38	2.3	ST89
HMC667LP2	2.3–2.7	19	29.5	0.75	LP2
HMC715LP3	2.1–2.9	19	33	0.9	LP3
HMC716LP3E	3.1–3.9	18	33	1	LP3
HMC718LP4	0.6–1.4	32	40	1.5	LP4
HMC719LP4	1.3–2.9	34	39	1.8	LP4
HMC753LP4E	1–11	17	30	1.6	LP4
HMC902LP3E	5–10	19	28	1.7	LP3
HMC903	6–18	19	27	1.6	Packageless
HMC903LP3E	6–17	18	25	1.7	LP3
HMC-AL435	5–20	13	25	2.2	Packageless
HMC-AL444	2–12	17	28	1.5	Packageless

of foreign governments, and it is very difficult, if not impossible, to produce these components in Russia. Therefore, using licensed components in new developments is undesirable due to possible difficulties during the stage of serial AESA production.

It is plausible to use products by European manufacturers in relatively low-frequency ranges. This includes, in particular NXP and its line of GaN- и LDMOS-transistors (Fig. 8.7), which are not subject to licensing by US state authorities. The list of basic characteristics is given in Tables 8.6 and 8.7 [7].

Thus, there are no technical problems preventing achievement of output power of up to 350–500 W from one transistor in L and S ranges. Special attention shall be paid to the line of GaN transistors (Table 8.7) [2].

Amplifiers based on GaN transistors will be detailed below.

It is also necessary to mention such important elements of TRM design as ferrite products for signal switching and receiver protection. Antenna circulator makes it possible to redirect signal passage paths: a signal from the transmitter path is directed strictly into the antenna, and a signal from the air strictly enters the receiver path. Unlike antenna key, it has no switching delays and can work with high-power signals, which is currently unavailable to mass-produced semiconductor switches.

The valve at the receiver input included after the circulator performs the important function of protection of the transmitter output stage, as it creates the required matching for the antenna output in the transmission mode, regardless of the LNA and limiter impedances (as a rule, receiver path is disconnected from the power supply during transmission, and vice versa).

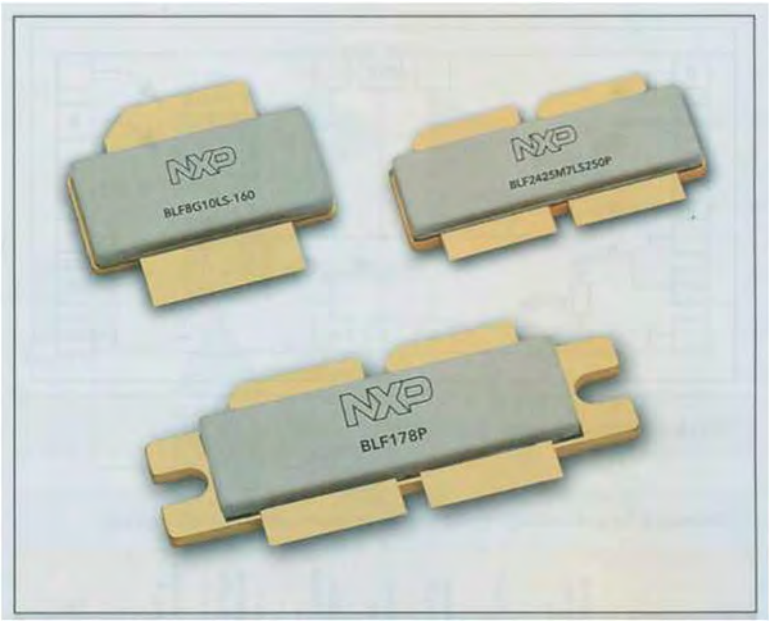

Fig. 8.7 Appearance of powerful SHF transistors by NXP

In this context, it is necessary to mention the most famous manufacturing company TRAK Microwave Ltd. (Scotland), which is capable of providing devices unique in terms of basic parameters (inserted losses and direct power) even in the standard line of products [8]. The possibilities of obtaining necessary parameters by request make it possible to solve tasks of increased complexity. Most important standard products are summarized in Table 8.8. These are valves of the Drop-In version; parameters of circulators for the same frequencies are similar. Moreover, products are manufactured in MICPuck (microstrip in protected package) configurations, in traditional microstrip, coaxial and waveguide packages (Fig. 8.8).

8.1.6 Noise-Suppressing Filters for AESA

With miniaturization of structural TRM elements, increase in the density of mounting, the level of mutual effect of radioelements and functional possibilities of radioelectronic equipment, the task of suppressing electromagnetic interferences (EMI) becomes more and more difficult. This task is one of the most important in ensuring electromagnetic compatibility (EMC) of REE. Along with technologies that help minimize the influence of noise by circuitry and structural methods during the design stage, there are also methods of direct suppression (filtration) of parasite signals with the help of noise-suppressing low pass filters (LPF). LNA is one of the

Table 8.6 Summary table of characteristics of NXP LDMOS transistors

	Minimum frequency, MHz	Maximum frequency, MHz	Output power, W	Power supply voltage, V	Gain factor, dB	Package type
BLL6H1214-500	1200	1400	500	50	17	SOT539A
BLS7G2729L-350P	2700	2900	350	32	13	SOT539A
BLS7G2729LS-350P	2700	2900	350	32	13	SOT539B
BLS7G3135L-350P	3100	3500	350	32	12	SOT539A
BLL6G1214L-250	1200	1400	250	36	15	SOT502A
BLL6H1214L-250	1200	1400	250	50	17	SOT502A
BLL6H1214P2S-250	1200	1400	250	45	27	SOT_tbd
BLS7G2933S-150	2900	3300	150	32	13.5	SOT922-1
BLS6G2731S-130	2700	3100	130	32	12	SOT922-1
BLS6G2731-120	2700	3100	120	32	13.5	SOT502A
BLS6G3135-120	3100	3500	120	32	11	SOT502A
BLS7G2325L-105	2300	2500	105	30	16.5	SOT502A

components of the AESA structure that is most exposed to EMI effect. The variants of filters examined below are designed to be used in SHF REE and ensure EMI filtration at frequencies up to 18 GHz [9–11].

Components by API Technologies/Spectrum Control of series SCI-9900/9909/9945/9980, 54-863-XXX and 54-831-XXX are most frequently used to solve EMI tasks for SHF REE.

Design of SCI-9900/9909/9945/9980 series is characterized by their air tightness, which ensures the possibility of their application in highly reliable radioelectronic equipment of military, aviation and naval purposes. The filters are glass sealed at one side and epoxy sealed at the other side (Figs. 8.9 and 8.10). Filters are manufactured in standard and reverse versions. In reverse version, glass-to-metal seal is applied to the flange side. Filters are mounted directly into the structure of the module [11, 12]. Basic characteristics of SCI-9900/9909/9945/9980 series are given in the summary Table 8.9 [2].

SCI-9900/9909/9980 series belong to the category of miniature filters and are applied in microwave modules, power supply switching and control circuits. Due to high value of maximum current (15A), filters of the SCI-9945 are mostly used in secondary power supply systems.

In some cases, EMI LPFs of 54-863-XXX and 54-831-XXX series are used as alternatives to the above series (Fig. 8.11). Filters of 54-863-XXX and

Table 8.7 Summary table of characteristics of GaN- NXP transistors

	Frequency, MHz		Output power, W	Power supply voltage, V	Gain factor, dB	Efficiency factor, %	Package type
	min	max					
CLF1G0035-100	0	3500	100	50	13.9	59.5	SOT467C
CLF1G0035S-100							SOT467B
CLF1G0035-100P				50	12.7	50.1	SOT1228A
CLF1G0035S-100P							SOT1228B
CLF1G0035-50			50	50	13	49	SOT467C
CLF1G0035S-50							SOT467B
CLF1G0060-10		6000	10	50	17	32.2	SOT1135B
CLF1G0060S-10							
CLF1G0060-30		6000	30	50	15.9		SOT1135B
CLF1G0060S-30							

Table 8.8 [2] Summary table of characteristics of TRAK Microwave gates

	Frequency range, GHz		Isolation, dB	Insertion loss, dB	Power, W		
	min	max			Peak	Forward	Reverse
T2040/DD	2	4	16	0.6	100	40	1
T800120/DI	8	12	17	0.6	100	40	1
T1214/DD	1.2	1.4	18	0.6	1000	60	1
T2123/DD	2.1	2.3	18	0.6	100	60	1
T2223/DD	2.2	2.3	20	0.5	1000	75	1
T3036/DB	3	3.6	18	0.5	100	60	1
T950105/DB	9.5	10.5	20	0.5	50	20	0.5

54-831-XXX series have metal packages with threads M3 and M4 respectively; therefore, it is possible to use standard tools (with metric pitch) for mounting. Filters are sealed by epoxy compound, which limits their use in fully sealed modules. Technical specifications of 54-863-XXX and 54-831-XXX are given in Table 8.10.

The problems of ensuring protection from electromagnetic interference and electromagnetic compatibility for radar stations and communication means will be detailed in Chap. 13.

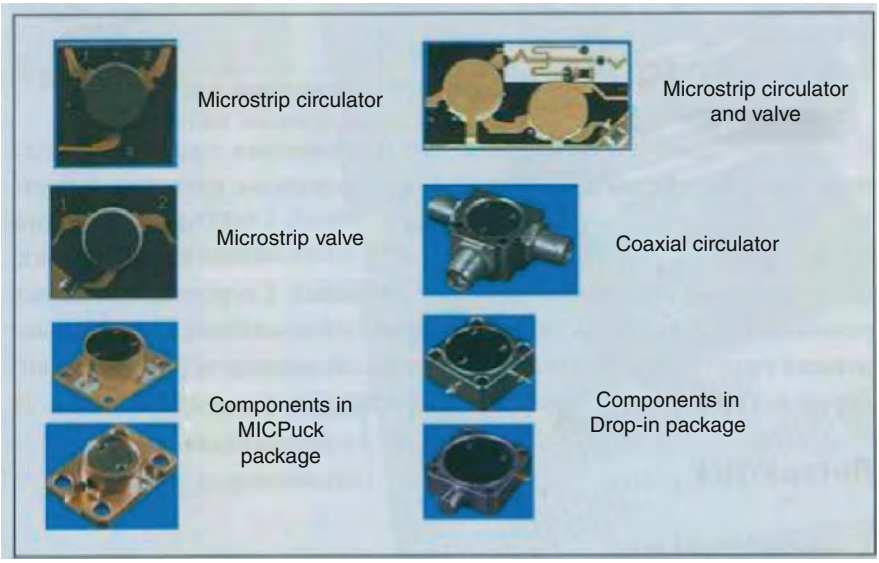

Fig. 8.8 Types of structural designs of valves and circulators

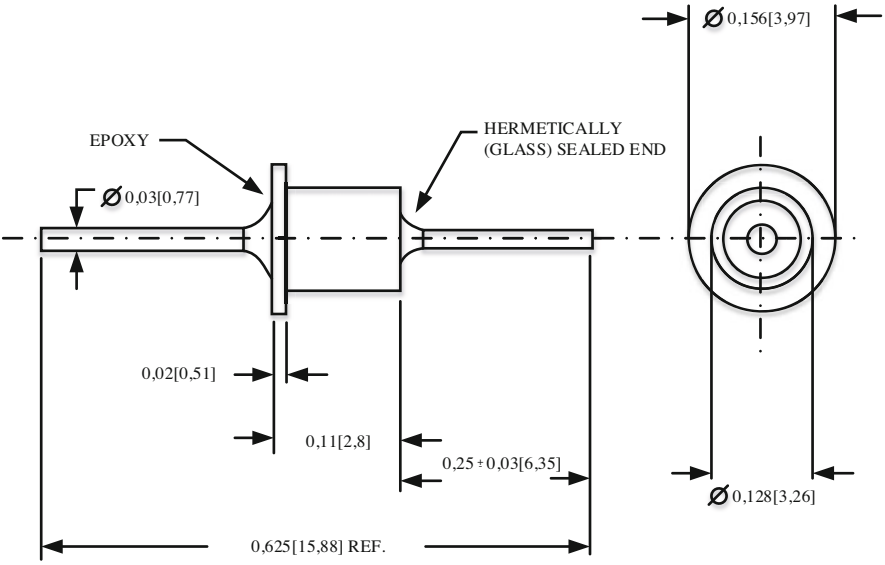

Fig. 8.9 Standard version of the filters of SCI-9900 series

Fig. 8.10 EMI Filters: (**a**) SCI-9900 series; (**b**) SCI-9909 series; (**c**) SCI-9945 series; (**d**) SCI-9980

Table 8.9 Basic technical characteristics of EMI filters of SCI-9900/9909/9945/9980 series

Parameter/Series		SCI-9900	SCI-9909	SCI-9980	SCI-9945
Filter type		C	C	LC	C
Capacitance range	min	4 pF	5 pF	10 pF	0.01 μF
	max	0.05 μF	0.027 μF	0.033 μF	1.2 μF
Voltage range, V	min	50	50	50	50
	max	200	200	200	400
Maximum current, A		5	5	5	15
Maximum inserted attenuation, dB (for reference), at	1 MHz	10	10	13	40
	100 MHz	45	42	55	50
	1 GHz	60	65	75	70
	10 GHz	60	65	75	70
Package diameter, mm		3.25 (0.128″)	3.05 (0.12″)	3.25 (0.128″)	10.16 (0.4″)

8.2 Russian Element Base of SHF Devices for Radar Sets

8.2.1 Russian Active GaAs Elements for Transceiver SHF Modules of the Centimeter Range

Especially important elements in modernization of existing and creation of new microwave equipment are field-emission transistors with Schottky barriers based on GaAs, which, due to their physical properties and design features, help solve a significant portion of tasks during designing of receiving and transmitting parts of microwave paths of communication and radiolocation systems in centimeter and millimeter wavelength ranges. Creation of the wide range of discrete transistors and introduction of the technology adapted for serial production made it possible to implement unique parameters of radiotechnical systems. GaAs transistors are used as a basis for creation of ground and in vehicle transceiver equipment of satellite communication and television systems within the frequency range of 3–18 GHz,

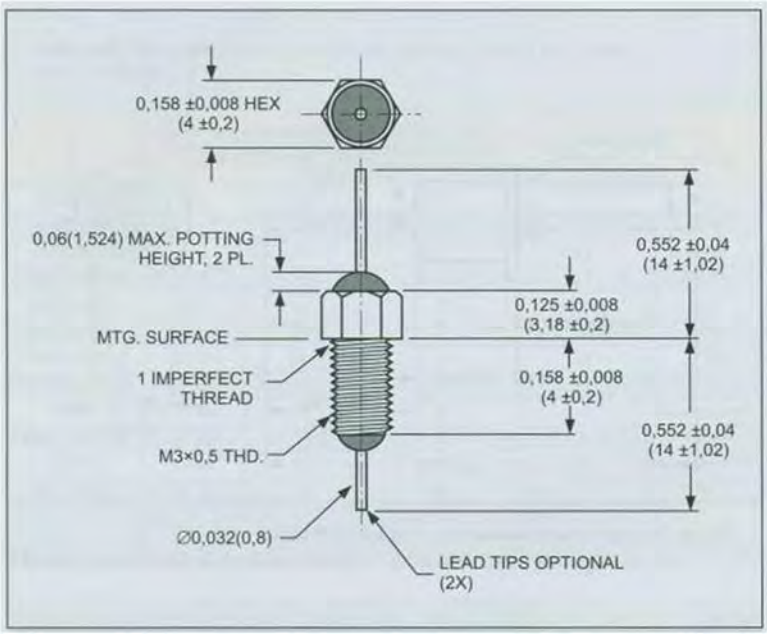

Fig. 8.11 54-863-XXX series filter

Table 8.10 General technical characteristics of EMI filters of 54-863-XXX and 54-831-XXX series

Designation	Filter type	Cmin	Voltage, V	Current, A	Thread size	Design features
54-863-004	C	0.01 μF	100	10	M3 × 0.5	Length of package (max) – 10.24 mm
54-863-005		100 pF				
54-863-007		1000 pF				
54-863-008		2000 pF				
54-863-010		4700 pF				
54-863-015		10 pF				
54-831-011	Pi	100 pF			M4 × 0.7	Length of package (max) – 15.06 mm
54-831-012		1500 pF				
54-831-013		3000 pF				
54-831-014		5500 pF				
54-831-015		0.012 μF				

radio relay communication lines of the centimeter and millimeter ranges and radiolocation systems [13–15].

The works aimed at designing microwave units of various purposes in a wide range of frequencies and achieving a high level of technology of GaAs Schottky barrier transistors and diodes made performed by the leading Russian company "Pulsar" made it possible to create monolithic integrated circuits based on the

Table 8.11 Basic characteristics of TRMs of the 3-cm range

Operating frequency band, GHz	0.5
Microwave path phase shift, deg	±180
Transmission path	
Output power, W	2–5
Gain factor, dB	25–30
Gain control range, dB	−15
Efficiency, %	15–20
Receiving path	
Noise factor (max), dB	4
Gain factor, dB	27
Gain control range, dB	−15
Dimensions, mm	30 × 8 × 120

designed microwave elements [2]. The level of subminiaturization achieved made it possible to design a microwave transceiver module (TRM) for antenna systems based on phased antenna arrays. The necessary basis was formed by the circuitry-related and structural and technological design principles formulated by developers.

For example, Table 8.11 contains basic technical characteristics of TRMs of the 3-cm range of wavelengths [13].

Final version of technical requirements for TRMs shall be specified for a definite design of antenna array. However, even the general technical characteristics presented above can be used to formulate technical requirements for TRM units and elements and select the most suitable structural scheme of a TRM (Fig. 8.12).

The presented TRM composition performs the following functions:

- provision of SHF parameters of the transmission path (TP) – amplification of the microwave signal to the set level of output power, change in phase and amplitude states of the transmission channel;
- provision of SHF parameters of the reception path (RP) – amplification of the reflected microwave signal at the set level of noise, changes in phase and amplitude states of the reception channel;
- temporal switching of receipt and transmission channels with changing state of phase and amplitude setting elements;
- protection of the receiving channel from high level of incident power;
- conversion of digital control signal into analog signal controlling SHF elements.

Designing and production of active TRM elements shall be performed during the initial stages of development of antenna arrays of radar systems. Real parameters of the element base determine the level of approximation of the properties of real module to the perfect model used by designers of systems with AESA during calculation of antenna parameters. An error in implementation of the required amplitude and phase states of the TRM antenna aperture curtain can lead to distortions of the beam pattern, errors in radiation frequency and ambient temperature changes. All this can reduce effectiveness of using radar systems with AESA.

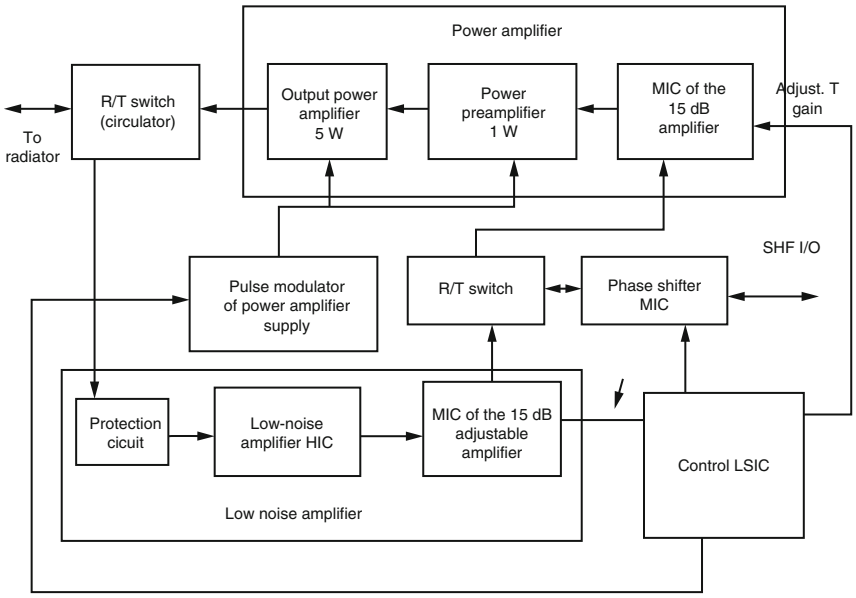

Fig. 8.12 Typical structural diagram of a transceiver module for an AESA-based radar system

Within the framework of the performed works for designing element base and TRMs for AESAs of the 3-cm range, "Pulsar" enterprise has created elements of the microwave path and tested them in test assemblies, based on GaAs Schottky barrier transistors and diodes.

During designing, the following combination of circuit-related and structural and process elements of designing SHF semiconductor devices and units was used:

- drawing up of design model of the active element (equivalent circuit, model or matrix of SHF parameters) based on theoretical and experimental materials;
- performance of primary calculation of the full circuit of the functional unit engineering model within a wide frequency range;
- testing of operational parameters in an engineering model of the unit or product;
- use of probing equipment for selection of the element base with given properties;
- adjustment of design models of active and passive elements based on measurement results and performance of final calculation of the functional unit.

Achievements in the field of computer design of hybrid and monolithic integrated circuits based on solid-state element base [13] made it possible to use computer models of active devices to perform large volume of computing works. For the purpose of checking applicability of the created program models of active elements, experimental study of microwave properties of experimental and mass-produced GaAs-based Schottky barrier FETs was performed, and hybrid and monolithic integrated circuits based on GaAs transistors and diodes were created and tested.

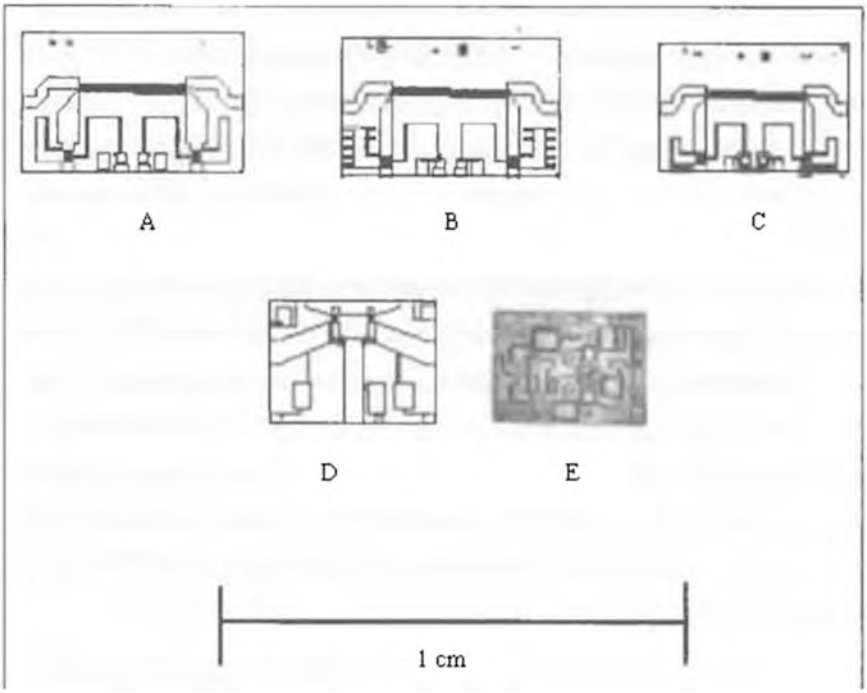

Fig. 8.13 MIC designed for use in TRMs: (**a**–c) – monolithic ICs of phase shifters for 90, 180 and 0–90°; (**d**) monolithic IC of the switch; (**e**) monolithic integrated circuit of controlled amplifier with stable phase

Figure 8.13 shows the layout of monolithic integrated circuits developed for application in TRMs of the 3 cm range.

These monolithic integrated circuits ensure performance of control functions of changing amplitude and phase states of transmission and receipt SHF paths.

Phase shifters ensure discrete phase shift of the transmission coefficient by 180 and 90° and smooth phase adjustment within 0–90°. Active elements are GaAs p-i-n diodes in discrete phase shifters and reverse-biased GaAs Schottky diodes in analog phase shifters. Phase state setting phase amounts to single nanoseconds.

Switching GaAs p-i-n-diodes are used in the two-channel switch. The time of switching of SHF signal amounts to single nanoseconds.

MIC of the controlled amplifier [14] is a two-stage GaAs amplifier with the two-gate field transistor in the second stage.

Design of the controlled amplifier helped solve the task following from the conditions of use of the AESA TRM – change in the transmission coefficient of the amplifier with its phase unchanged. Calculations and practice have demonstrated that the variants of hybrid controlled amplifiers in the required frequency band have no sufficient stability of phase of the variable transmission coefficient.

Table 8.12 [2] Results for calculation of modes with gain varied by 10 dB

	Model 1		Model 2		
Frequency, GHz	dB S21	ang S21	dB S21	ang S21	Noise coefficient, dB
8.7	12,998	15,088	23,232	15,501	4214
8.8	12,149	13,837	22,320	14,267	4096
8.9	11,448	12,790	21,568	13,226	4013
9.0	10,847	11,856	20,918	12,294	3952
9.1	10,314	10,994	20,338	11,429	3906
9.2	9829	10,180	19,805	10,612	3871
9.3	9377	94,017	19,304	98,289	3846
9.4	8947	86,503	18,825	90,730	3829
9.5	8532	79,211	18,361	83,393	3819
9.6	8127	72,107	17,906	76,250	3815
9.7	7727	65,173	17,457	69,279	3818

During calculation of SHF parameters of MIC, computer modeling methods were used. Active elements designed for matching of separation impedances and elements of SHF circuits and power supply and control circuits were selected based on the condition of practicability in MICs.

Based on the used original models, the mode of transistors in first and second stage and the width of transistor gates were selected, after which calculation of matching circuits and the entire electrical circuit was performed in MIMCAD.

Phase-stabilizing properties were determined by selection of the gate width of transistors of the first and second stages, inter-stage matching and microwave impedance connected to the control electrode. Results of calculation of modes with gain variation pitch of 10 dB are given in Table 8.12.

The last column of the table contains the noise factor, specification of which is necessary when the amplifier is used in the receipt channel.

In radiolocation systems, in the real operating conditions the input of the receiving device, in addition to useful processed signal, is subjected to the effect of signal characterized as synchronous (as a rule, intrinsic system ones with known power level and timing position) and asynchronous (external, indefinite) interferences. Level of interference power can reach the values causing temporary faults or failures of input devices of the receiving channel.

High sensitivity of receiving devices is ensured by the use of microwave LNAs at the TRM input. For LNAs, the best results in terms of noise parameters are ensured by HICs of amplifiers based on crystals of microwave GaAs FETs. Noise factor of such transistors is less than 1 dB in the 3-cm range of operating frequencies in a standard circuit of microwave LNA with amplification of 20–25 dB with operating frequency range of 10–15%. Input power dynamic range (as a rule, characterized by reduction of the amplification level relative to low signal by 1 dB) amounts to dozens and even hundreds microwatts and the permissible level of input power in case of trouble-free operation reaches 10–100 mW in continuous mode and 0.1–1 W in pulsed mode. When this power level is exceeded, input circuits of the LNA require protection.

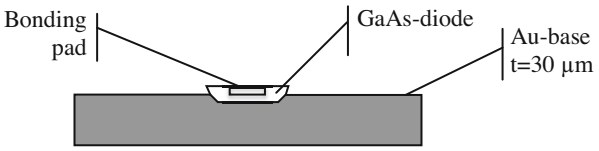

Fig. 8.14 Structure of a GaAs p-i-n-diode with integrated heat removal

It is reasonable to make limiting (for suppression of asynchronous interferences) and switching (for suppression of synchronous interferences) diodes of gallium arsenide [14]. This selection of the source material is determined by a number of its advantages, namely:

- presence of semi-insulating high-resistance material, which makes it possible to produce monolithic protective and switching devices;
- high mobility of electrons (approximately 3 times higher than in silicon), which helps count on significantly lower losses in n^- base and n^+ – regions;
- possibility of obtaining extremely sharp border between p^+- and i-regions, due to which contribution of p^+-region in the loss resistance value is close to zero;
- high operating speed (switch-off time – single nanoseconds), which is due to short lifetime of secondary carriers $\tau l = 2 \cdot 10^{-8}$ s;
- possibility of production of the p-i-n-diode structure with integrated heat removal from metal layers with high thermal conductivity (Cu, Au).

Structural design of diodes with integrated heat removal (Fig. 8.14) makes it possible to obtain values of parasite serial inductance and heat resistance several times lower than in the traditional structure with the same active area.

Losses introduced by limiting diodes designed for protection of input LNA circuits from the incident power of 5–10 W amount to 0.5 dB with the bandwidth of more than 10%.

SHF path of the receiving and transmitting channel consists (see Fig. 8.12), in addition to common elements (phase shifters and switch) of the hybrid circuit of low-noise amplifier ($K_n < 1$ dB, $K_g > 20$ dB) and controlled amplifier (see Fig. 8.13e) for the receiving channel; controlled amplifier, hybrid circuit of the power amplifier and output multi-crystal matched high-power amplifier for the transmitting channel.

In order to ensure favorable thermal mode, output stages of the power amplifier of the transmitting channel are powered by the pulse source.

Specific operations performed by the control circuit of the TRM depend on the information recorded in the transmitted message, central computer and the data stored in RAM of the control circuit. Algorithm of operation of the control circuit can be conventionally divided into TRM control and diagnosis algorithm and the algorithm of interaction with the central computer.

CC performs the following operations of TRM control and diagnostics:

- blocking of the radiated probing pulse of the transmitter;
- loss of sensitivity of the receiver;
- generation of control signals of attenuator and phase shifter.
- generation of diagnostic message about the TRM state.

All operations performed by CC are initiated by the central processor unit. The algorithm of CC operation is based on the following scheme: decoding of the command, channel type (R/T) and TRM address, performance of internal operation, change of the external CC state.

Internal operations performed by CC include:

- recording of amplitude and phase set values (initial phase shift) corresponding to various types of amplitude and phase distribution of the AESA directivity pattern in RAM;
- reading of amplitude and phase set values from RAM based on the given number of amplitude and phase distribution of the AESA directivity pattern;
- calculation of the current phase of the receiver and transmitter according to the formula:

$$P = m \cdot A + n \cdot B + j,$$

where P is the current calculated phase of the receiver (transmitter), m is the address of the TRM line, n is the address of the TRM column, j is the phase point of the set amplitude-phase distribution of the receiver (transmitter) AESA, A and B are the data characterizing the direction of the beam and supplied from the central computer;

- generation of analog and digital signals for control of amplitude and phase of the signals transmitted through the transceiver;
- generation of the diagnostic message on the state of TRM in sequential code.

Final selection of the protocol of exchange with the central computer, time characteristics and design are determined by the AESA designer.

As a result of the work performed, SHF path of receipt and transmission channel was implemented, which corresponded to the structural diagram of the TRM designed for operation in the AESA curtain. Experimental estimate of parameters of components and TRMs was obtained on local and general assemblies. Circuit of TRM parameter control based on the controlling code signal was modeled; volume of the control circuit and basic principles of its implementation were defined. Time-related characteristics of the TRM control circuit were assessed.

Masks and technology were developed; “Pulsar” State Factory produced MICs of phase shifters, controlled amplifier, limited diodes of protection circuit and switch. Hybrid integrated microwave circuits of low-noise amplifiers and power amplifiers were tested [15], which ultimately made it possible to manufacture dimensional TRM samples (Fig. 8.15).

Technological experiments in sealing the module were performed.

Tooling for probe monitoring of microwave parameters of MIC crystals and transistors was manufactured [16]. An example of the probing device for measurement of SHF parameters of MIC phase shifter is shown in Fig. 8.16.

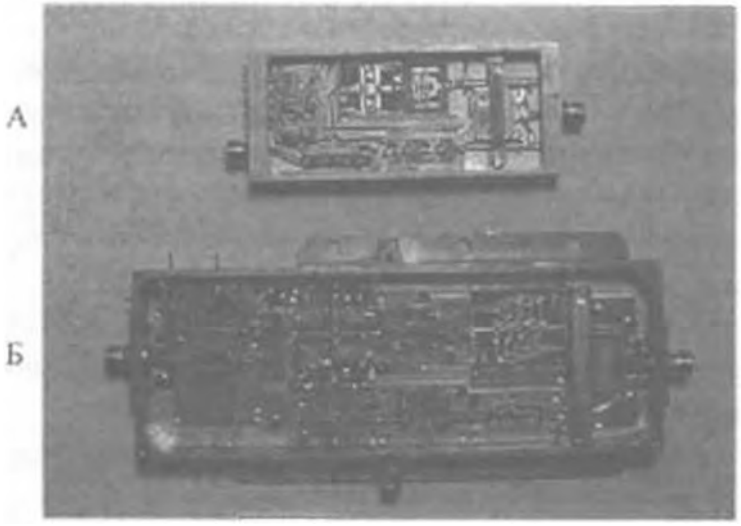

Fig. 8.15 Appearance of the TRM engineering model (**a**) and TRM sample with specified dimensions (**b**) [2]

8.2.2 SHF Devices by JSC "Microwave Systems"

8.2.2.1 Wideband Silicon Carbide-Based Power Amplifiers of the Decimeter Range

In the following we are going to consider the main results of development and experimental study of Russian wideband amplifiers of the decimeter (0.5–2.5 GHz) range with output powers of 20–200 W in continuous mode based on silicon carbide field transistors [17].

As demonstrated above, during creation of wideband power amplifiers in the decimeter range with output power over 20 W, it is preferable to use silicon carbide (SiC) field transistors due to a number of their obvious advantages. One of them is high (28–50 V) drain supply voltage, which, with the same power values supplied to load as in GaAs transistors, causes a significant (by an order of magnitude) increase in the optimal impedance of the drain load and significant simplification of matching between the transistor and load. SiC transistors are characterized by breakdown drain voltages above 100 V, high specific power (2–4 W/mm), low specific input (0.5 pF/mm) and output (0.15 pF/mm) capacities, as well as high permissible operating temperature of the crystal (up to +255 °C). Disadvantages of SiC transistors include the fact that their operating frequencies do not exceed 2.5–3.5 GHz due to low mobility of the main charge carriers, as well as high cost of the devices.

When designing powerful wideband amplifiers, specialists of JSC "Microwave Systems" used simplified non-linear models of CRF24010F and CRF24060F transistors and took a number of measures to achieve high level of output power in a

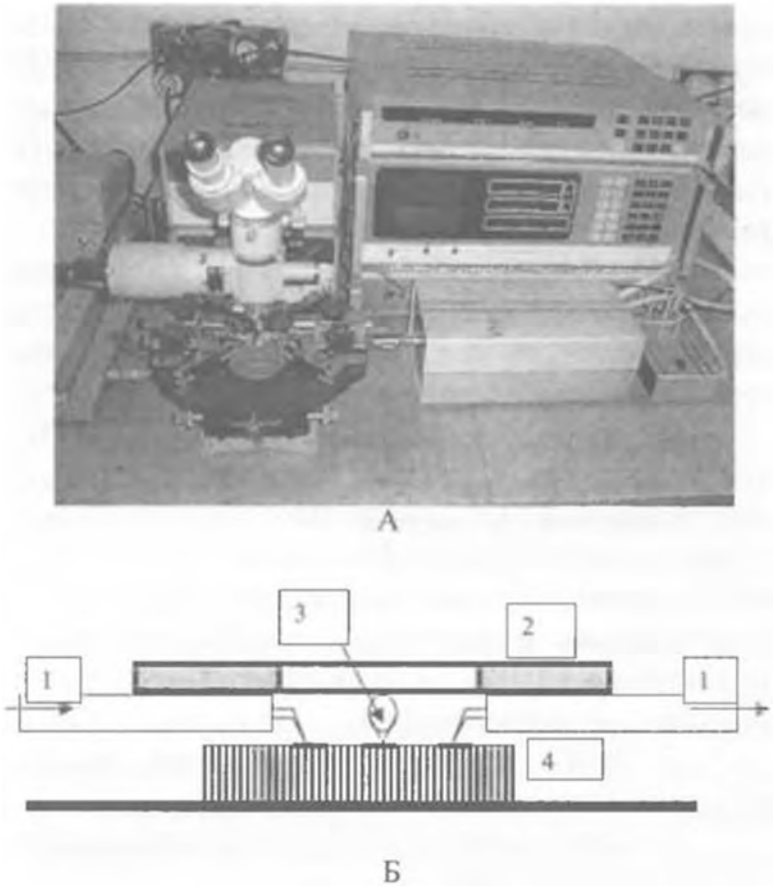

Fig. 8.16 Probing device for measurement of the noise factor of transistor and MIC chips within the range of 8–12 GHz (**a**) and design of the probing head (**b**): *1* – microaxials with probing needles; *2* – grounding washer; *3* – grounding probe; *4* – tested crystal with bonding pads [2]

wide frequency band. Ohmic losses were achieved by thickening metallization on microstrip boards. Thin-film technology based on silver-containing 20 μm thick pastes was used, as well as thin-film technology with vacuum evaporation of thick (18–25 μm) copper layers. Distributed transforming matching circuits were used in the output matching circuit, which ensured minimal losses and proper uniformity of the output saturation power (1–2 dB) in the octave bandwidth. Thermal load of the transistors was reduced by using the AB class mode with initial current equal to 20–25% of the maximum channel current, which also helped increase efficiency in the dynamic range. For better heat removal from active elements, 4 mm thick heat distributing bases were used. Arrangement of the low-frequency part of the amplifiers in the section above the high-frequency part also helped reduce thermal load due to heat removal from voltage stabilizers through the side walls.

Table 8.13 The test results of the parameters of the amplifiers [2]

Parameters	Amplifier type		
	RM051	RM0816	PM0825-1
Frequency range, GHz	0.5–1	0.8–1.6	0.8–2.5
Output power, W	182–269	117–137	21.5–27.8
Gain factor, dB	47.8–50.3	45–46.6	35.5–38.2
APC irregularity, dB	2.5	1.6	2.7
Efficiency factor, %	20–32	26–33	14–20
Supply voltage, V	+48	+48	+48
Consumption currents, A	17.4–18.8	8.45–9.35	2.9–3.2
Dimensions, mm	270 × 250.2 × 58.1	231 × 100 × 36	142.5 × 54 × 35
Weight, kg	8.8	1.31	0.45

Parameters of the studied amplifier models are given in Table 8.13.

Output amplifier stage for the frequency range of 0.5–1 GHz (RM051) is built according to four-channel balanced summation circuit based on CRF24060F transistors. Adders of the first stages are installed on polycore substrates with the thickness of 1 mm, adder of the second stage – on symmetrical strip lines with facing connection. Intrinsic power losses of the first stage amounted to 0.25–0.3 dB, in the adder of the second stage – 0.12-0.21 dB. A fragment of the structure of one of output balancing stages is shown in Fig. 8.17 [17].

Model of the RM051 amplifier was used to study the possibility of changing supply power of the output stage transistors to control output saturation power. It was determined that the reduction of output supply voltage of the drain from 48 V to 24 V has almost no effect on frequency characteristics of the amplifier. Output power at 24 V amounted to 100–130 W. The amplifier has demonstrated its workability with load VSWR increased to 6 and fault resistance in conditions of voltage breakdown.

Output stage of the amplifier in the range of 0.8–1.6 GHz (RM0816) is based on the balanced circuit with CRF24060F transistors and adder on polycore substrate. This amplifier is characterized by low levels of the second and third harmonics, which amounted to −26 dB and − 23 dB accordingly, and high efficiency (26–33%) with supply voltage of 48 V. The amplifier can also work for mismatched termination (VSWR = 2. . .5).

Figure 8.18 shows power APC and efficiency of the amplifier.

Output stage of the amplifier model in the range of 0.8–2.5 GHz (RM0825-1) is based on balanced circuit with CRF24010F transistors. Design of the stage is shown in Fig. 8.19. Matching plates and quadrature helical bridges are installed on 0.5 mm polycore substrate using the thin-film technology. Air gaps between boards and transistors are the elements of matching circuits with LPF structure.

The problem affecting parameters of SiC amplifiers is the absence of wideband transistors or monolithic integrated amplifiers with power voltage of 48 V for power levels under 10 W. The microcircuit AM012335-MM-VM with supply voltage of

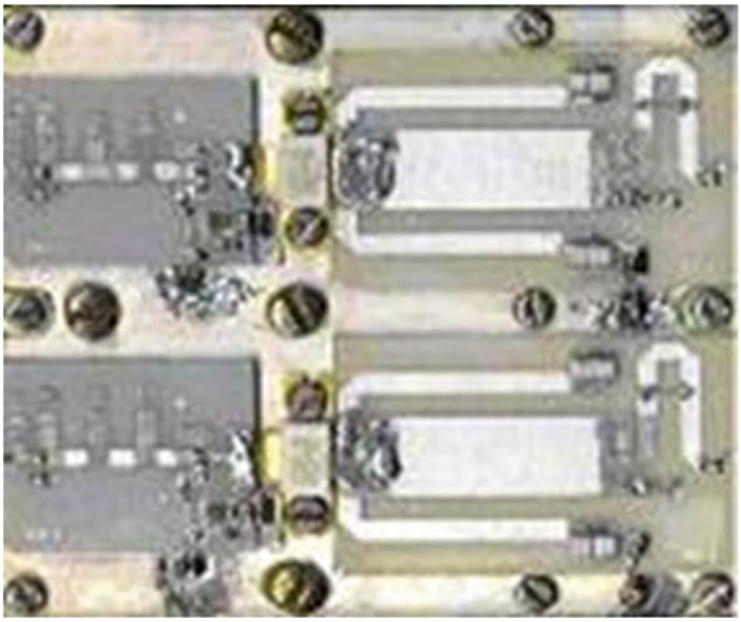

Fig. 8.17 Photo of a 0.5–1 GHz amplifying stage [2]

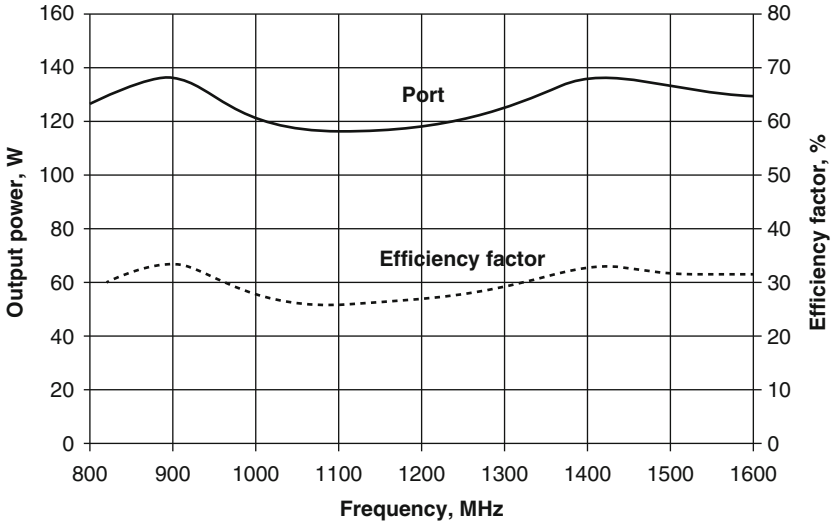

Fig. 8.18 Power APC and efficiency of RM0816 model

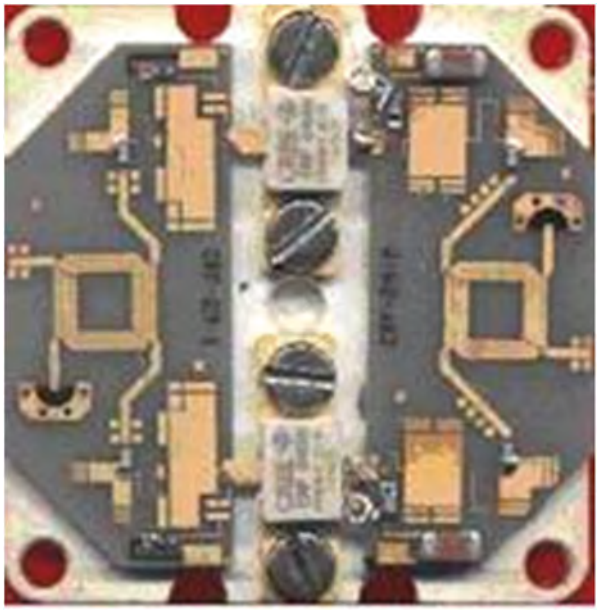

Fig. 8.19 Photo of the amplifying stage 0.8–2.5 GHz [2]

20 V and output power of 2 W was used as a preamplifier in the studied models, which significantly reduced the total efficiency, in particular – of the RM0825-1 amplifier.

Therefore, the use of modern SiC transistors and engineering approaches described in the paper makes it possible to use simple circuitry-based solutions to achieve output power values of the decimeter range amplifiers of 100–200 and more watts in continuous mode, in octave and super-octave frequency band, with efficiency of 20–30% and high AFC regularity.

8.2.2.2 Ultra-Wideband Microwave Power Amplifiers for the Range of 6–18 GHz

In this section, we will consider information about development of one of the first Russian ultra-wideband transistor amplifiers of the frequency range of 6–18 GHz and output power in linear mode of over 6 W published on the website of the "Microwave Systems" company [17]. The main problem in development of the amplifier is the creation of the powerful output stage with the width under 28 mm for its placement in the 35 mm wide amplifier package.

Output amplifying cells are based on quasi-monolithic technology. Features of the designed amplifiers are: digital 5-bit control, thermal compensation of amplification, input power detector, high-speed feed modulator (100 ns), integrated temperature sensor and input power limiter. In order to achieve output power over 6 W

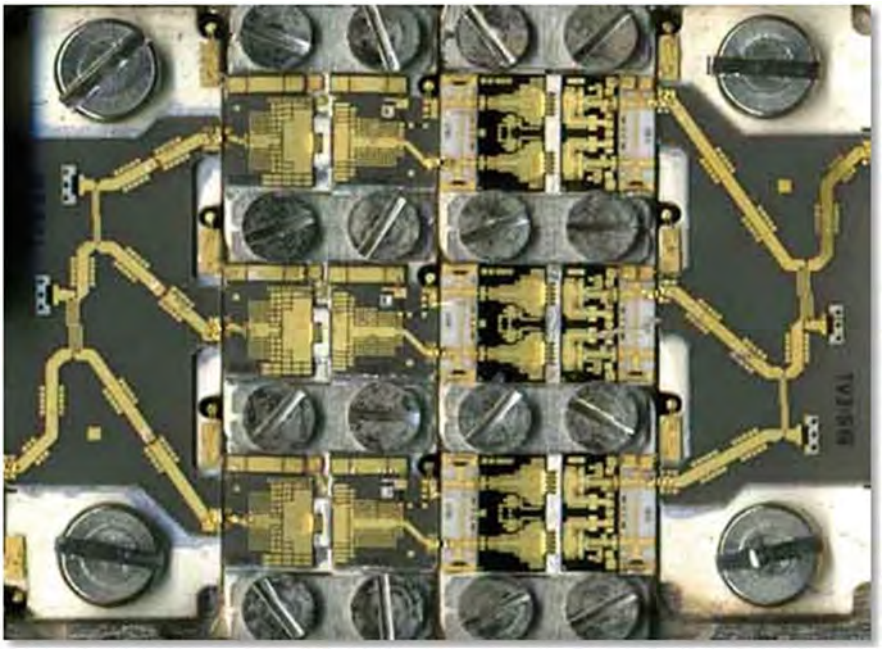

Fig. 8.20 Output amplifying stage [2]

in the 6–18 GHz, output amplifying stage was designed (Fig. 8.20), built according to the circuit of addition of three balanced amplifiers with preliminary stages ensuring power of at least 2.2 W in linear mode.

Power addition was ensured by specially designed three-channel chain power adder/splitter on Lange couplers, phase shift between the arms of which compensates the reflected signals to the maximum extent and corresponds to 60 degrees in the middle of the range.

Balanced circuits included quadrature Lange bridges made on separate substrates of polycore with thickness of 250 μm, gap width of 12 μm and metallization thickness of 5 μm. For facilitation of mounting, bridges are installed with integrated bridges [17] with underlying dielectric (polymide) layer ensuring effective protection from short circuits and mechanical impacts (Fig. 8.21).

Figure 8.22 shows the structural diagram of the developed amplifier, which includes:

- input low-noise amplification (LNA) stage; balanced electrically controlled attenuator on p-i-n diodes for smooth compensation of temperature drift of the gain factor in the frequency range of −60 – +75 °C and digital 5-bit attenuator (AT);
- power preamplifier, adjuster of AFC and PFC of the amplifying path (PP);
- preliminary amplifying stage (HIS-120) built according to quasi-monolithic technology with the use of GaAs p-HEMT transistors with 0.3 × 1200 μm

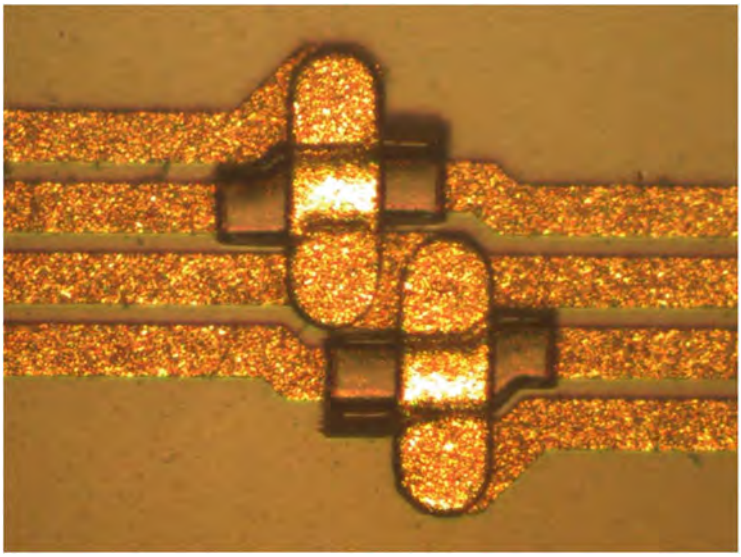

Fig. 8.21 Integrated bridges of Lange couplers with protective dielectric [2]

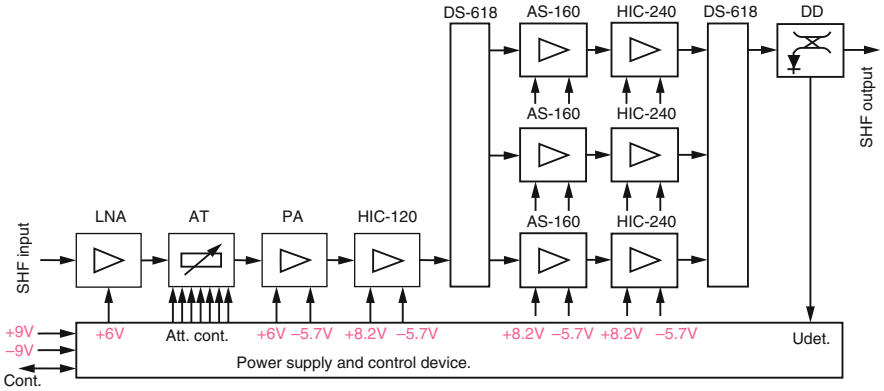

Fig. 8.22 Structural diagram of the amplifier

gates ensuring output power in the linear mode of at least 1 W and amplification of about 7–8 dB;

– three-channel chain power adder/splitter on Lange couplers (DS-618) with minimum gap between conductors of 13 μm;
– pre-output amplifying stage (UK-160) built according to hybrid technology with the use of one GaAs p-HEMT transistor with 0.3 × 1600 μm gates ensuring output power in the linear mode of at least 1 W and amplification of about 7–8 dB;

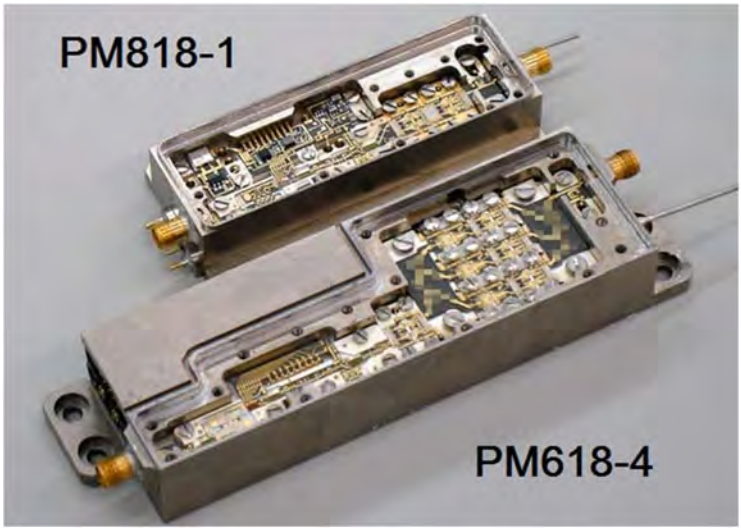

Fig. 8.23 Amplifiers RM618-4 and RM818-1 [2]

- output quasi-monolithic balanced stage (HIS-240) on two GaAs p-HEMT transistors with 0.3 × 2400 μm;
- directional detector (DD) of output power;
- power stabilizers, high-speed power modulator, buffer TTL logic elements of digital attenuator control, thermal compensation attenuator control circuit, temperature sensor, protection device (Power supply and control device).

Photograph of the structure of the designed amplifier, as well as 2 W power amplifier for the 8–18 GHz range for comparison of dimensions, is shown in Fig. 8.23.

During research works, tests of output power of the RM618-4 amplifier with GaAs p-HEMT with gate size of 0.3 × 2400 μm of the company's own design were performed, which demonstrated a significant increase in linear power (about 1 W across the entire band). Figure 8.24 shows results of measurement of power and maximum consumption current for RM618-4 sample No.1 on transistors of the company design and sample No.2 on Exelics transistors.

Figure 8.25 shows typical AFCs of three RM618-4 amplifiers.
Temperature drift of AFCs in the temperature range of −60 °C – +75 °C is not more than 4 dB.

The amplifier has dimensions of 35 × 118 × 21 mm and weight under 200 g.

Gain factor within the frequency band of 6–18 GHz is 39–47 dB at irregularity of not more than 5 dB. Current consumption in +9 V circuit is less than 6 A; mismatch – not more than ±25°, efficiency – 14–20%.

This ultra-wideband transistor amplifier RM618-4 of the 6–18 GHz range with output power of more than 6 W based on individually designed transistors can be used as channel power amplifier of an active PAA.

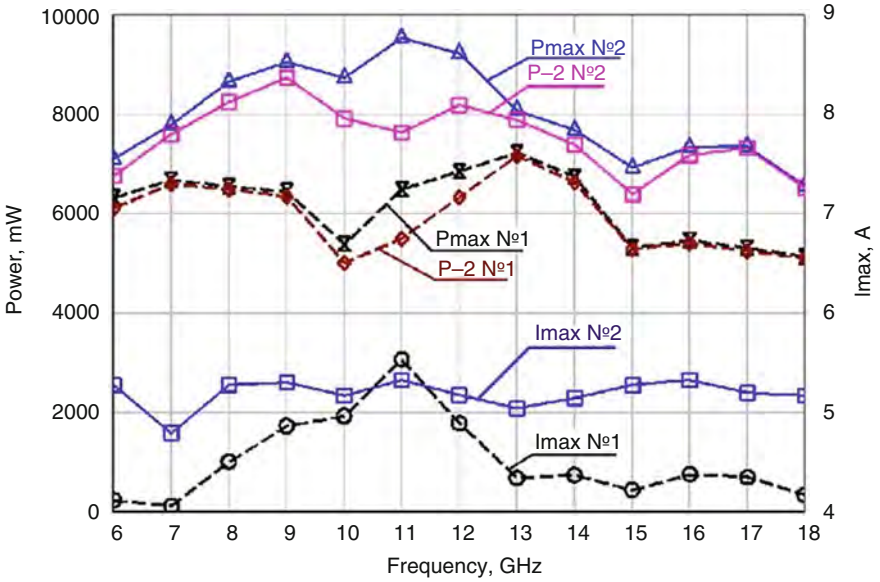

Fig. 8.24 Output power and maximum current consumption of RM618-4 amplifiers

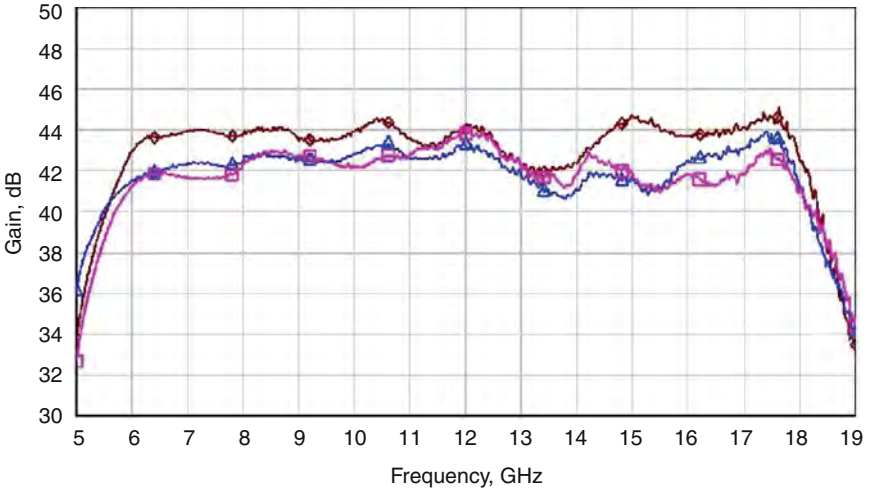

Fig. 8.25 APCs of RM618-4 amplifiers [2]

8.2.2.3 Technical Parameters of the Series of High and Low Power SHF Amplifiers by Microwave Systems

In addition to the types of SHF devices examined above, the company supplies a wide range of other high and low power SHF amplifiers to the customers.

For example, Table 8.14 contains functional features and main technical parameters of the series of high power wideband SHF amplifiers [17].

Table 8.15 presents functional features and numerical typical values of basic technical parameters of the series of low-noise wideband microwave amplifiers.

8.3 Russian GaAs Based Microwave Components by "Planeta-Argall"

"Planeta-Argall" is a rare Russian company that not only performs new developments of components (microwave transistors, amplifiers, protective devices), but also carries out mass production of these components based on approved technical specifications in the interests of equipment developers.

8.3.1 Transistor Amplifiers

In the field of transistor amplifiers, microwave products of "Planeta-Argall" [18] are represented by low-noise solid-state quasi-monolithic microwave modules [19] based on gallium arsenide. FET and p-HEMT transistors of serial transistors and their modifications of company's own design are used as active amplifying elements.

The company manufactures amplifiers in ceramic small-size non-sealed packages with microstrip or lug terminals with internal matching and displacement circuits ensuring direct installation into microstrip consumer boards with subsequent sealing.

Characteristics of amplifiers are presented in Tables 8.16, 8.17, 8.18, 8.19 and 8.20. [2]. Figure 8.26 shows the module M 421301 (APNT.434810.058 TC). Package dimensions – 7.5 × 7.5 × 1.9 mm. Figure 8.27 shows the module M 52125 (APNT.434810.078 TC). permissible input continuous power – 50 MW max. Figure 8.28 shows the module M 52127 (APNT.434810.094 TC). permissible input continuous power – 10 MW max. Figure 8.29 shows the module M 52126 (APNT.434810.093 TC). permissible input continuous power – 12 MW max. Figure 8.30 shows the module M 53214 (APNT.434840.022 TC). permissible input continuous power – 15 MW max. Figure 8.31 shows the module M 52102 (SFEK.434810.002 TC GK): permissible input continuous power – 2 W max.

Table 8.14 High power wideband SHF amplifiers

Name	Functional features	Δ F, GHz	Fg, dB, std.	Δ Fg, db, max	P_{-1} W, typ.	Psat, W, typ.	VSWR, I/O, max	Vsupp, V, stand.	Icon, A, max	Reception type	Note
A610M	Integrated power supply stabilizers	4–8	36	3	10	12	2	+10	4	TCD	Noise factor (max) – 7 dB
	Thermal gain compensation							−5	0.2		
	Integrated output power detector										
MSPA-1020-26	Integrated power supply stabilizers	1–2	39	3	0.5	0.7	2	+9	0.9	TCD	
	Thermal gain compensation							−5	0.06		
	Integrated output power detector										
MSPA-1040-28	Integrated power supply stabilizers	1–4	36	3	1.3	1.8	2	+9	1.2	TCD	
	Thermal gain compensation							−5	0.1		
	Integrated output power detector										
MSPA-2040-29	Integrated power supply stabilizers	2–4	36	3	1.3	1.8	2	+9	1,2	TCD	
	Thermal gain compensation							−5	0,06		
	Integrated output power detector										
PM12 - C8	2 in-phase outputs	1–2	42	3	2 × 10	2 × 12	2	+9	14	TCD	2-channel output. Regulated PFC.
	Integrated power supply stabilizers							−5	0.3		
	Possibility of modulation of output power and current										
	Thermal gain compensation										

	Integrated output power detector										
PM12 - C8 - 1	Integrated power supply stabilizers	1–2	47	3	18	24	2	+9	14	TCD	Regulated PFC.
	Possibility of modulation of output power and current							−5	0.3		
	Thermal gain compensation										
	Integrated output power detector										
PM24-C8	Integrated power supply stabilizers	2–4	40	3	20	25	2	+9	15	TCD	Regulated PFC.
	Possibility of modulation of output power and current							−5	0.3		
	Thermal gain compensation										
	Integrated output power detector										
PM412-8B	Integrated power supply stabilizers	4–12	>39	5	$P_{-2} > 8$	>10	2.5	+9	11	TCD	Regulated PFC
	Possibility of quick (300 ns) modulation of output power and current							−9	0.2		
	Thermal gain compensation										
	Integrated output power detector										
	5-bit digital gain control										
PM48-1	Integrated power supply stabilizers	4–8	42	4	$P_{-2} = 2.2$	2.5	2	+9	1.9	TCD	Regulated PFC.
								−6	0.2		

(continued)

Table 8.14 (continued)

Name	Functional features	Δ F, GHz	Fg, dB, std.	Δ Fg, db, max	P_{-1} W, typ.	Psat, W, typ.	VSWR, I/O, max	Vsupp, V, stand.	Icon, A, max	Reception type	Note
	Possibility of quick (300 ns) modulation of output power and current										
	Thermal gain compensation										
	Integrated output power detector										
	4-bit digital gain control										
PM618-4B	Integrated power supply stabilizers	6–18	>39	5	$P_{-2} > 4$	>5	2.5	+9	6	TCD	Regulated PFC
	Possibility of quick (300 ns) modulation of output power and current							−9	0.2		
	Thermal gain compensation										
	Integrated output power detector										
	5-bit digital gain control										
PM818-1	Integrated power supply stabilizers	8–18	36	6	$P_{-2} = 1.8$	2	2.5	+9	2.2	TCD	Regulated PFC.
	Possibility of quick (300 ns) modulation of output power and current							−6	0.2		
	Thermal gain compensation										
	Integrated output power detector										
	4-bit digital gain control										

Table 8.15 Low noise wideband SHF amplifiers [2]

Name	Functional features	Δ F, GHz	Fg, dB, std.	Δ Fg, db, max	P_{-1}/ Psat, mW, typ.	Fn, dB, typ.	VSWR, I/O, max	Vsupp, V, stand.	Icon, mA, max	Reception type	Note
MSLA-20180-4.0	Integrated power supply stabilizer	2–18	13	2	10/20	<4	2.5	7.5	90	TCD	
MSLA-20180-4.0G	Packageless	2–18	13	2	10/20	<4	2.5	7.5	90	TCD	Configuration – HIC (G). Supplied in batches from 10 pcs.
MSLA2-20180-4.0	Integrated power supply stabilizer	2–18	26	4	10/20	<4	2.5	7.5	180	TCD	
MSLA2-20180-4.0M	Integrated power supply stabilizer	2–18	26	4	10/20	<4.5	2.5	7.5	180	TCD	
	Possibility of modulation of output power and current (M)										
UVA-51A2MC	Thermal gain compensation	2–18	37	4	50/100	5	2.0	8.0	350	TCD	
	Integrated power supply stabilizer										

Table 8.16 Low-noise amplifiers of decimeter and centimeter ranges

Product name	Δf_d, GHz	Fn, dB (max)	K_l, dB (min)	ΔK_l, dB (max)	P_{out} -1 dB, MW (min)	$_{VSWR}$(I/O)	Usup./ Icons., V/mA
M42130A	1.5–3.5	1.5	18	3	5	2/2.5	6/60
M421301B	1.5–3.5	4	18	3	50	2/2.5	9/100
M421301V	3–8	2.5	16	3	5	2/2.5	6/60
M421301G	33–8	4.0	16	3	30	2/2.5	9/100
M421301D	3–5	2.5	20	3	5	2/2.5	6/600
M25125	0.8–3.5	3.5	16	4	50	2.5/2.5	9/150

Table 8.17 Low-noise amplifier of the millimeter range

Product name	Δf_d, GHz	Fn, dB (max)	K_l, dB (min)	ΔK_l, dB (max)	P_{out} -1 dB, MW (min)	$_{VSWR}$(I/O)	Usup./ Icons., V/mA
M52127	33–37	4	20	3	5	2/2	+5/75
							−5/28

Table 8.18 Power amplifier of the millimeter range

Product name	Δf_d, GHz	Fn, dB (max)	K_l, dB (min)	ΔK_l, dB (max)	P_{out} -1 dB, MW (min)	$_{VSWR}$(I/O)	Usup./ Icons., V/mA
M52126	33–37	–	13	3	150	2/2	+5/340
							−5/38

Table 8.19 Frequency converter

Product name	Δf_w, MHz	F = 33–37 GHz				V_{SWR} (I/O)/ $KstU_G$	Usup./ Icons., V/mA
		P_{het}, mW	K_{tr}, dB (min)	ΔK_l, dB (max)	P_{out} dB, mW (min)		
M53214A	74–200	10–30	13	3	8	2/2.5	9/95

8.3.2 *Protective Devices*

In addition to transistor SHF amplifiers, this company provides its customers with autonomous protective devices that require no power supply or external matching. These devices are monolithic currents of several back-to-back GaAs Schottky diodes, which ensures their resistance to high level of input microwave power, high operation speed and low power leakage [20].

Table 8.20 Low noise amplifiers with integrated protection from input continuous SHF power up to 2 W

Product name	Δf_d, GHz	Fn, dB (max)	K_l, dB (min)	ΔK_l, dB (max)	P_{out} -1 dB, MW (min)	$_{VSWR}$(I/O)	Usup./ Icons., V/mA
M5212A	1.5–3.5	1.5	17	3	5	2/2.5	6/70
M52102B	1.5–3–5	4	17	3	50	2/2.5	9/120
M52102V	3–8	2.5	15	3	5	2/2.5	6/70
M52102G	3–8	4	15	3	30	2/2.5	9/120
M52102D	3–5	2.5	19	3	5	2/2.5	6/70

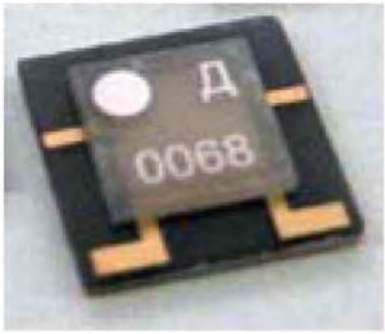

Fig. 8.26 External view of the module M 421301

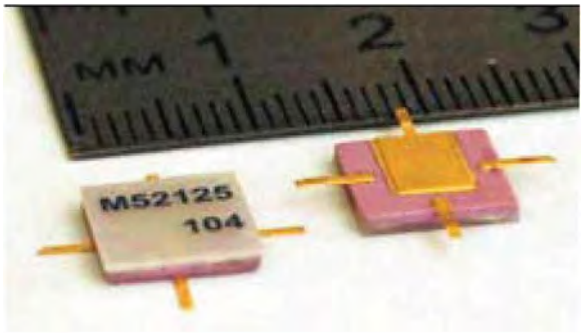

Fig. 8.27 External view of the module M 52125

Protective devices can be supplied in non-sealed ceramic packages and as separate crystals with contact pads for external connections. Back side of the crystal has galvanic gold plating for mounting of crystals into consumer circuit on conductive compound.

Characteristics of the protective devices are shown in Table 8.21; appearance is shown in Figs. 8.32 and 8.33 [2].

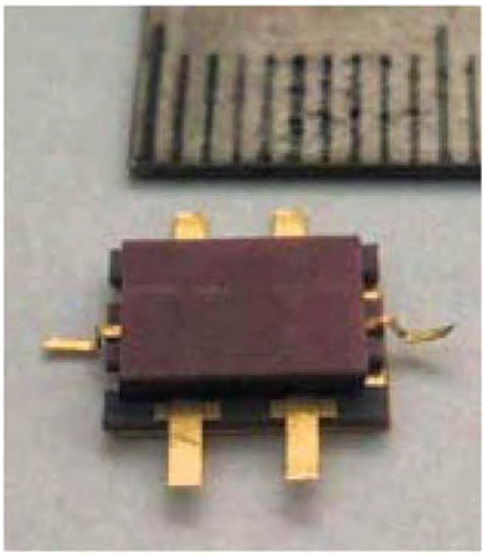

Fig. 8.28 External view of the module M 52127

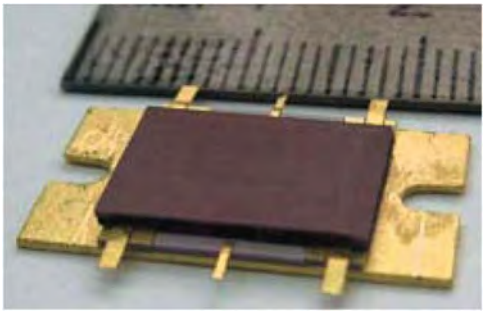

Fig. 8.29 External view of the module M 52126

Module M 54404 (APNT.434820.010 TC) is structurally designed in package for surface mounting and characterized by the operating frequency range of 0.1–6 GHz and permissible continuous input power up to 10 W.

The module M 54405 (APNT.434820.009 TC) uses three bands to cover the frequency range of 0.1–12.5 GHz at permissible input pulse power of 10 W and continuous power of up to 1.7 W.

8.3.3 Microwave Transistors

Since 2007, the list of produced low-noise GaAs-based transistors has also been expanded. Russian serial production includes transistors with expanded dynamic range – 3P618 and 3P397. Level of output power with specified value of input power is:

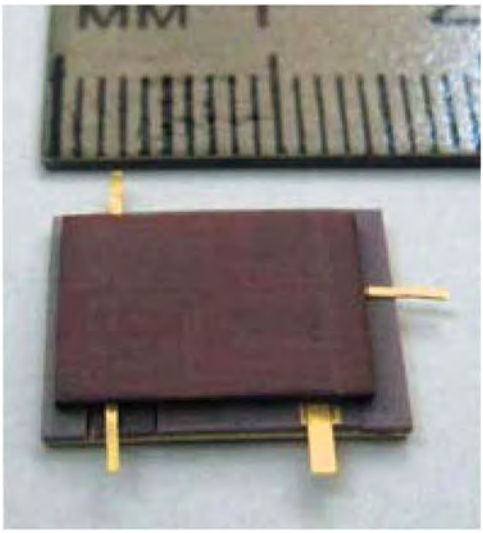

Fig. 8.30 External view of the module M 53214

Fig. 8.31 External view of the module M 52102

- 500 MW at f = 1.0 GHz – 3P618A;
- 250 MW at f = 2.0 GHz – 3P618B;
- 150 MW at f = 4.0 GHz – 3P618C;
- 100 MW at f = 8.0 GHz – 3P618C;
- 30 MW at f = 6.0 GHz – 3P397A.

Table 8.21 Protective devices

Product name	Δf_d, GHz	a_{tr}, dB (max)	P_{in}, W	$P_{out\ p}$, W	P_{leak} max, mW	P_{leak}, mW (max)	t_{rec}, ns (max)
M54404	0.1–4	0.7	10	–	50	–	50
	4–6	1.5					
M54405-1	0.1–6	0.7	1.7	10	–	20	
M54405-2	0.1–12.5	1					
	9.4–10.6	0.7					
M54405-3	0.1–12.5	1.5					

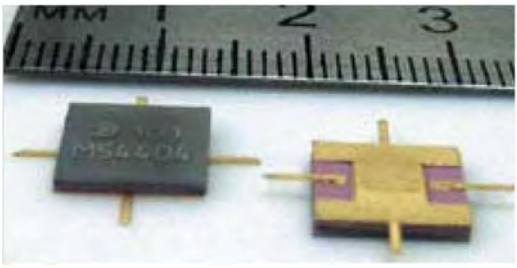

Fig. 8.32 External view of the module M 54404

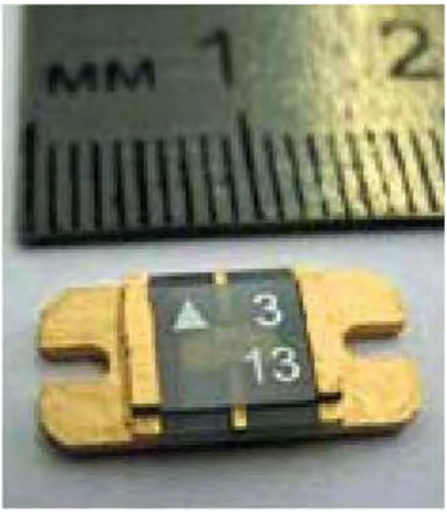

Fig. 8.33 External view of the module M 54405

Also produced are low-noise p-HEMT transistors ZP398 using four bands to cover the frequency range of 4–35 GHz.

The list of transistors includes the mass-produced two-gate transistor AP390A with NF = 2 dB at 8 GHz and NF = 3 dB at 12 GHz.

Transistor parameters are presented in Tables 8.22, 8.23 and 8.24 [2].

Table 8.22 Low-noise double-purpose microwave transistors

Name of the product	Δf_d, GHz	F_{meas}, GHz	Values of electrical parameters (T = 25 ± 10 °C)					Package
			$K_{N\ min}$, dB (max)	$K_{N\ opt}$, dB (min)	S, mA/V (min)	P_{out}, mW (min)	P (dispersion), mW	
ZP398A-2	4–18	8	0.4 (typ.)	$K_{L\ max}$ 12.9	60	–	50	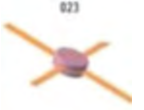
ZP398B-2	4–18	12	0.45 (typ.)	$K_{L\ max}$ 12.9	30	–	50	
ZP373A-2	1–8	4	0.4	11.5	30	–	100	
ZP373B-2			0.5	11				
ZP373V-2			0.6	10				
ZP374A-2	4–18	12	0.85	9	15	–	35	
ZP374B-2			1	10				
ZP374V-2			1.2	8.5				
ZP397A-2	0.1–6	0.1–6	0.3	16	30	30	200	
ZP398B-2	12–25	18	0.95 (typ.)	$K_{L\ max}$ 11.3	24		50	
ZP385A-2	12–25	18	0.8	9.5	15	–	35	
ZP385B-2			1	10				
ZP385V-2			1.2	8.5				
ZP618A-2	0.5–4	0.5–1	0.3	18	60	500	1000	
ZP618B-2		2	0.5	15		250	500	
ZP386A-2	18–30	25	1.05	8	10	5	30	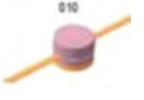
ZP386B-2			1.25	7.5				
ZP386V-2			1.5	7				
ZP398G-2	25–35	30	0.8 (typ.)	$K_{L\ max}$ 9.3	20	–	30	
ZP618V-2	1–10	4	0.7	12	60	150	300	
		8	1.5	6		100		
ZP389A-2	25–40	37	2.5	6	5	–	20	
ZP389A-5			2	6.5				

Table 8.23 Low-noise microwave transistors

Name of the product	Δf_d, GHz	fmeas, GHz	Values of electrical parameters (T = 25 ± 10 °C)					Package
			$K_{N\ min}$, dB (max)	$K_{N\ opt}$, dB (min)	S, mA/V (min)	P_{out}, mW (min)	P (dispersion), mW	
AP605A-2	0.3–8	8	3.5	5	30	75	450	
AP605A1-2			2	6	40	100		
AP605A2-2			1.5	7	50	150		
AP331A-2	1–14	10	2.5	8	15	30	250	
AP331A1-2			2	8	30	40		
AP331A2-2			1.5	8	30	30		
AP339A-2	1–18	10	2.4	10	7	25	250	
		18	4	5		15		
AP390A-2 (two-gate)	1–12	8	2	13	20		50	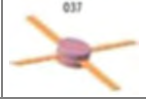
		12	3	11				

Table 8.24 Designation of technical conditions for transistors

Type of device	TC designation
ZP373A, B, V	AEYaR.432150.123 TC (D1)
ZP374A, B, V	AEYaR.432150.124 TC (D1)
ZP385A, B, V	AEYaR.432150.166 TC (D1)
ZP386A, B, V	AEYaR.432150.218 TC
ZP389A	AEYaR.432150.359 TC
ZP397A	AEYaR.432140.498 TC
ZP398A, B, V, G	AEYaR.432140.520 TC
ZP618A, B, V	AEYaR.432140.301 TC
AP331A	aAO.336.696 TC
AP338A	ADBK.432140.048 TC
AP390A	ADKB.432140.373 TC
AP605A	ADBK.432140.078 TC

Transistors are produced in lots and supplied in unsealed metal-ceramic packages (Tables 8.22 and 8.23) and as separate chips (5th modification).

Small gate length (0.25–0.3 μm), wide range of standard sizes with different packages and values of the structural parameter of gate width, which varies within 40–2000 μm, allows the consumer to select transistors with the best characteristics for the required operating frequency range.

8.4 Features of Designing SAW Frequency Selective Microcircuits

Normally the task of creating miniature stable microwave oscillators is solved by using high-quality solid-state microwave resonators in the operating frequency range of the oscillator, technologically compatible with hybrid integrated circuits. Such devices with operating frequencies of 0.3–1.5 GHz shall ensure a loaded Q-factor of the resonator of at least 3 • 103 in the upper part of the range and over 5103 in the lower one, as well as good temperature stability and long-term frequency stability. This allows to create a microwave oscillator with operating frequency of 800 MHz, having phase noise level below minus 80 dB/Hz at frequency of 100 Hz.

One of the directions of microwave oscillator development is the use of surface acoustic wave (SAW) devices [21]. In the USSR, at the end of the 1970s, the Pulsar Research and Development Institute began to solve the problem of creating mass-produced frequency-selective SAW devices and microwave oscillators based on them.

Let us briefly consider the special aspects of development of this class of chips on the example of experience in the Pulsar Research and Development Institute.

In development of frequency-selective microcircuits of the 321FEhh series, the following basic tasks had to be solved: select the design of the SAW resonator,

develop the technology of their production and methods for central frequency tuning, design the microcircuit package, process control methods and methods of measurement of microcircuit parameters.

The designs of SAW resonators can be divided into two main types: *resonators with reflective gratings and resonators in which the delay line (DL) is an element of frequency stabilization.*

DLs can be used to built resonators of higher frequency, but they have greater inserted losses (IL) than resonators with reflecting arrays (RA), and it is more difficult in such lines to ensure single-frequency operating mode. High steepness of the phase-frequency characteristic obtained in long SAW DL (in principle, it reduces noises of the microwave generator) is accompanied by high inserted losses, which ultimately increase the noise level. The calculations showed that, in the ideal case, the noise of the microwave oscillator using a SAW DL will be determined by the same amount of SAW propagation loss as in the case of SAW resonators with reflecting gratings (RG).

The maximum achievable quality factor of the SAW resonators with RG (this value, in particular, determines the minimum achievable noise level) is expressed by the following formula:

$$Q_m = \pi \cdot 1000 \cdot 20 \cdot \lg(e)/(al + a2 \cdot F) \approx 27,300/(al + a2 \cdot F),$$

where e is the base of natural logarithms; al and a2 are SAW attenuation coefficients due to the external atmosphere and SAW absorption into the substrate, respectively; F – frequency in gigahertz. For ST quartz, X-cut, and under air load, these coefficients, found experimentally, are: al = 0.47 dB/cm and a2 = 2.62 dB/cm/GHz. From the formula it follows that $Q_m = 8800$ for F = 1 GHz. A chart of Q_m as a function of F is given in [22]. Naturally, the additional losses in the SAW resonator reduce the unloaded Q-factor. These additional losses are associated with the resistance of the electrodes of the interdigital transducer (IDT), with the conversion of SAW into bulk acoustic waves (BAW), with SAW leakage from the resonant cavity formed by RG, with SAW absorption by the metal film forming the IDT electrodes, etc. At the same time, reducing losses increases the quality factor, so at a frequency F = 0.5 GHz with an air load $Q_m = 15{,}300$, and for an vacuumed device (al = 0) – $Q_m = 20{,}800$.

A big advantage when creating miniature stable microwave oscillators on SAW resonators with RG is the small size of this device, because the reflecting gratings form a resonant cavity for SAWs. The IDT, which excites SAWs, is located in this resonant cavity between two RGs. The input electrical resistance of the IDT decreases, and the devices have small losses when working without matching in the 50-ohm path even for such a weak piezodielectric as quartz ST, X-cut. Substrates from this material are suitable in terms of temperature and technological parameters for creating surfactant resonators (for example, these substrates are acoustically and technologically in good agreement with aluminium films used as electrodes of the microcircuit).

RG resonators can also be divided into two types: *single input and double input.* In a single-input resonator there is only one IDT, it is described as a two-port

network and is a functional analogue of a widely used resonator based on bulk acoustic waves (BAW). In the meter range of wavelengths for self-oscillators on single-pass resonators, well-known circuit solutions developed for quartz oscillators are used, as a rule. The advantages of this type of RG resonators is a simpler design. In particular, in this design it is easier to ensure low input electrical resistance of the device for operation without coordination in the 50-Ohm path, since only one IDT should be placed in the resonant cavity. Consequently, it can be made with a larger number of electrodes than a two-input resonator, in which there are two IDTs – an input and an output, and which is a four-port network. According to Hewlett-Packard, in 1981, this type of resonator became the world's first commercially available SAW resonator its center frequency was 280 MHz.

When using a single-input resonator in an self-oscillator, the main disadvantage is the relatively large amount of the static capacity of the device passing through, mainly due to the capacity of the IDT. With an increase in the operating frequency of the oscillator, the use of a single-input resonator in the microwave range becomes difficult, since inductance is required to compensate for the static capacitance, and this complicates the design and tuning of the oscillator circuit.

A SAW device that is free from the drawbacks of a single-input resonator and delay line is a two-input resonator. In the traditional design of a two-input resonator, two IDTs are used in the resonant cavity located near the reflective gratings [23], made in the form of shallow grooves. The first prototypes of such resonators at frequencies of ~1.2 GHz were fabricated using electron-beam lithography. However, this technology in the manufacture of serial samples had to be abandoned due to high percentage of rejected devices. There are two reasons for the high reject percentage: poor alignment of the image fields by the electron beam, which leads to distortion of the characteristics of the SAW resonator; the second is a large technological variation in the size of submicron elements, which led to a large variation in the center frequency of the instruments.

Serial models of frequency-selective microcircuits 321FE1h manufactured since 1983 were produced with central frequency within the range of 300–900 MHz. Photomasks for them were produced with multifold reduction of separate parts of the device topology with subsequent assembly of the final mask by projection photolithography. Contact lithography was used to transfer the image from the mask to the substrate. During layout calculations (in order to get as close as possible to the central frequency), the step of the phototypesetting machine used for production of the original layout parts and the subsequent minimized images were taken into account [24].

Layout elements on the substrate were made with the help of lift-off photolithography. One of the main problems that occurred during production of SAW resonator crystals for high frequencies with micron element sizes consisted in bad adhesion of photoresist to the substrate. To solve this problem, it was suggested to treat the surface by ion-chemical etching to the depth of 80–120 nm with freon CF_4 before application of photoresist [25].

However, the traditional topology of a two-input SAW resonator with an RG used in the 321FE1h chip did not allow to obtain small insertion losses without

matching at a load of 50 Ohm (path impedance). To obtain small insertion losses (~ 6 dB) without coordination, a 321Exxx chip was developed, the topology of which had 3 IDTs.

Low insertion loss and a large number of IDT electrodes, in the above-described design, led to a significant influence of reflections from IDT (both electrical and mechanical) on the parameters of the resonator. For consideration of these dependencies, they were tested, in particular, by the method of multi-channel resonator [26, 27]. In addition, theoretical model of IDT operation taking into account reflections was development, modification of which was later used for development of cavity filters [28]. This model presented good description of SAW resonators, which made it possible to develop layouts of 321FEEh microcircuits with various parameters (in particular, central frequency and inserted losses) without further adjustments of the layout. Several stages of resonator frequency tuning were developed. In particular, microcircuit layout included deepening of the region of reflector arrays – the so-called step [29]. It fitted well into the microcircuit production process, improved parameters of devices (in particular, allowed for using much thicker IDT electrodes for reduction of their resistance without significant increase in mechanical reflections, as well as carry out the first stage of tuning the central frequency of 321FEhh microcircuits [30].

Below are typical parameters of SAW resonators made on ST- and X-cut quartz. The electrical parameters of the devices were measured in the 50-ohm path without coordination (see Table 8.25).

Experimental studies of fluctuation characteristics of self-excited oscillators are mostly aimed at optimization of parameters of self-excited oscillators in terms of minimum spectral power density of the phase noise [31]. Optimization was performed both from the parameters of the used transistor and from the parameters of the generator matched in the circuit, SAW resonator.

A wide range of microwave transistors produced by the Pulsar plant made it possible to analyze the dependence of the spectral power density of the phase-noise self-oscillators using a large sample of devices (Fig. 8.34).

Studies have shown that self-oscillators on silicon bipolar devices (KT640, KT642, KTZ115, KTZ132) have a noise level 15–20 dB lower than self-oscillators on gallium-arsenide FETs with Schottky barrier (AP604, AP602, AP307). Similar dependences were observed by Shea, Sullivan, and Kindell from Sawtek when studying microwave oscillators with SAW resonators at an operating frequency of 500 MHz [32]. The spectral density of phase noise at a detuning frequency of 100 Hz in their measurements was −60 dB/Hz for field GaAs transistors and − 80 dB/Hz for silicon bipolar transistors [33].

Table 8.25 Electric parameters of the resonators

Center frequency, MHz	333.33	532.00	715.00
Loaded Q-factor	5000–7000	4000–5500	3000–4000
Insertion loss, dB	5–6	5–6	7–8
Size of metal-ceramic case (height × diameter), mm	6.5 × 17.0	2.5 × 9.5	2.5 × 9.5

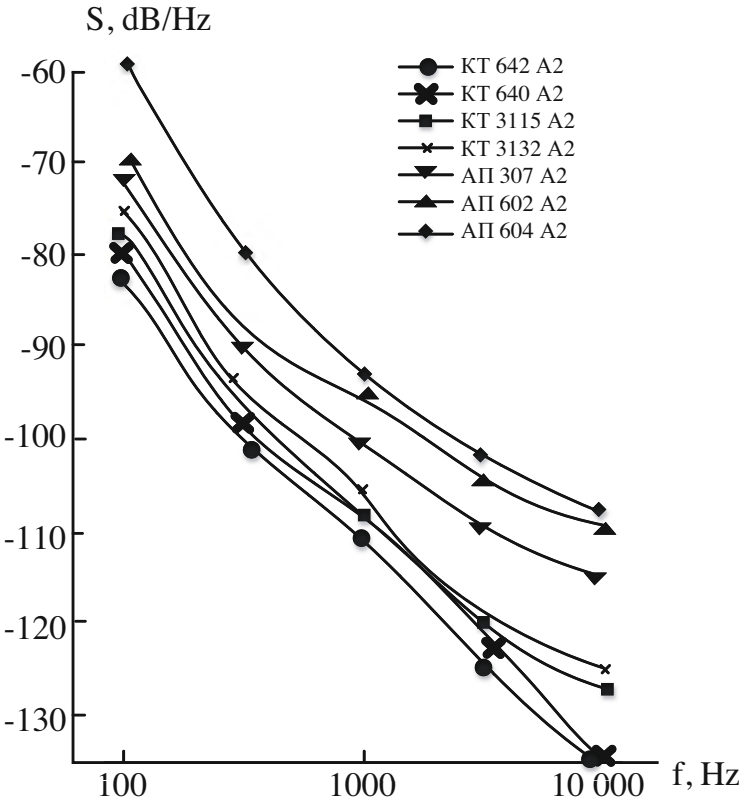

Fig. 8.34 Spectral density of phase noise of self-oscillators with SAW resonators, the amplifier stages of which are made using different transistors

The phase noise level of self-oscillators on medium power transistors (KT640, KT642) is 10–15 dB lower than the oscillators on low-noise low-power transistors (KT3 115, KT3 132), which correlates well with the spectral density of the low-frequency noise of transistors.

The minimization of phase noise spectral density of a self-oscillator can be done not only by selecting the operating mode of the transistor, but also by optimizing the coupling of the SAW resonator with the load. Optimal matching is achieved at such a coupling value of the resonator in the oscillator at which a further increase in Q-factor leads to an increase in losses in the resonator, worsening the oscillator noise. In practically relevant cases, the optimum is achieved at an instrument insertion loss of ~6 dB. Such losses can be obtained by matching for the frequency-selective chip 321FE1h or without coordination for the chip 321FEEh (as a rule, additional elements in the oscillator increase its noise and complicate the design and configuration of the microwave device).

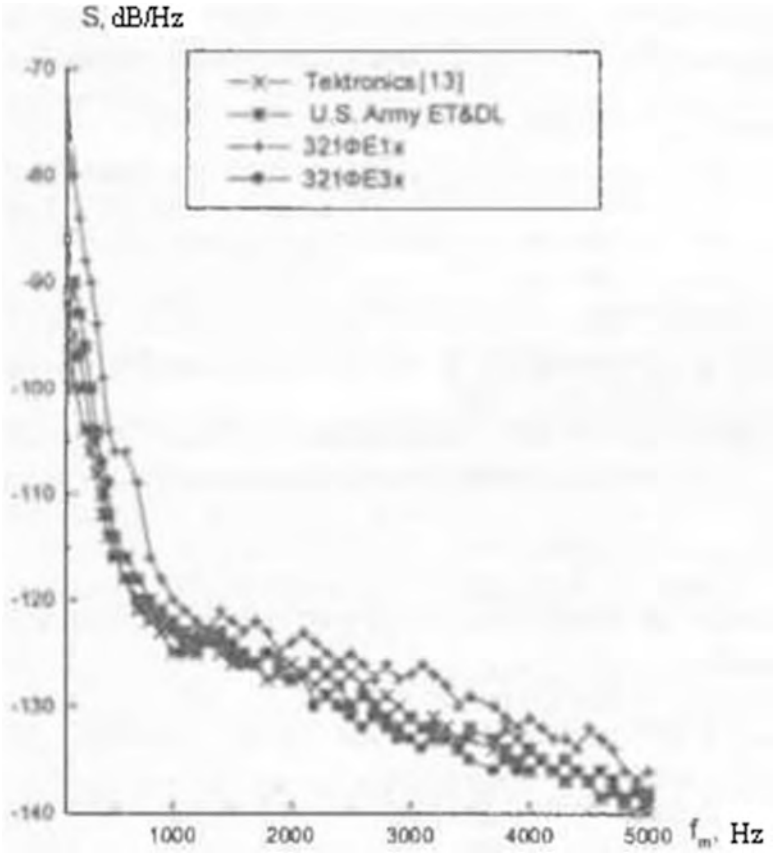

Fig. 8.35 Dependencies of spectral density of phase noise of self-excited oscillators with SAW devices

The microcircuit 321FEEx, developed in 1985, had the loaded Q-factor value in the generator equal to 5000. This helped achieve the value of phase noise spectral density of self-excited oscillators with operating frequency of 750 MHz equal to minus 90 dB/Hz with tuning frequency of 100 GHz [31], which is much better than in microcircuits 321FEx produced since 1983. The obtained results coincide with the data published at the time by specialists of Tektronix [33], U.S. Army ET & DL (Fig. 8.35).

It should be noted that the best known value of the Q-factor of a SAW device was achieved by Parker and his colleagues [34] of Raytheon Research Division in a vacuumed quartz package. This allowed them to create a microwave oscillator with operating frequency of 500 MHz, having phase noise level below minus 110 dB/Hz

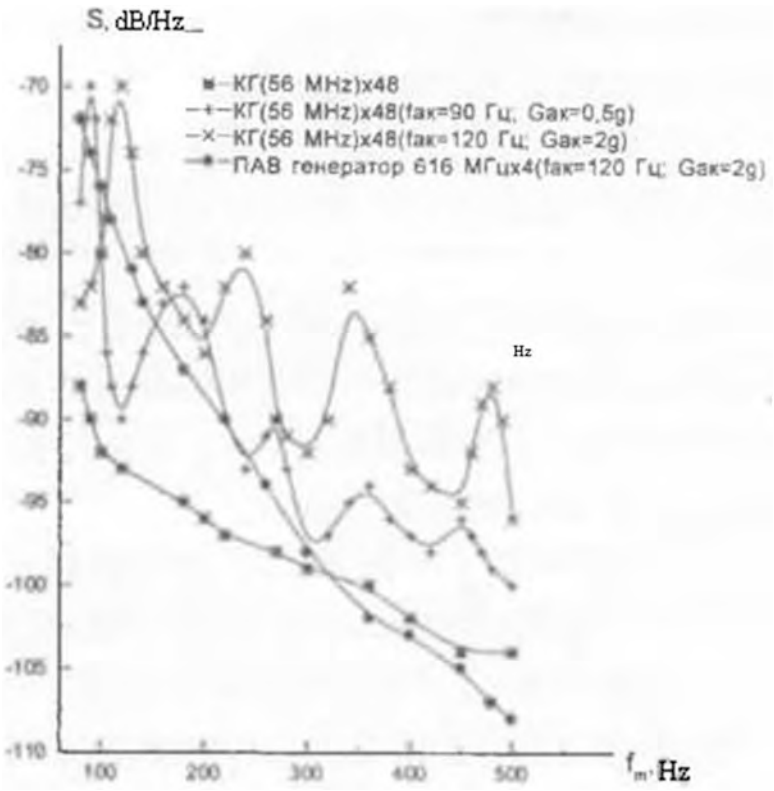

Fig. 8.36 Spectral density of phase noise of various types of microwave oscillators when affected by vibration

at tuning frequency of 100 Hz. However, such complex package and the device production process are unsuitable for mass production of SAW resonators. This makes it possible to consider 321 FE3x microcircuits to be among the best SAW devices across the world.

In terms of phase noise, microwave oscillators with SAW devices are inferior to quartz oscillators with frequency multipliers under normal conditions. However, in real equipment, self-oscillators often operate under the influence of vibrations, shocks and acoustic effects. Under these conditions, the advantages of self-oscillators with SAW resonators over quartz oscillators become obvious (Fig. 8.36).

The results of studies of microwave oscillators with an operating frequency of 2.5 GHz on various types of devices have shown that even at minor vibration loads, the parameters of quartz oscillators are significantly worsened. At vibrations with an acceleration of ~2 g, phase noise level of quartz oscillators is 10–15 dB worse than that of oscillators with SAW resonators.

8.5 Microwave Radio Receivers by RSE "Pulsar"

Main requirements for modern microwave radio receivers includes small weight and dimensions, which often determine the principal possibility of placement of modern equipment on the object.

Many microwave devices are also distinguished by toughened requirements for the operating frequency range and cyclic changes of temperatures applied to equipment placed outside the comfort area.

As early as in the 1980s, SUE "NPP Pulsar" designed and launched serial production of the series of microwave receivers of the decimeter range for airborne responder of the IFF system [35]. One of these receivers is shown in Fig. 8.37.

The following features of this device shall be noted:

At the microcircuit level – the use of the HIC technology with application of the technology of quasi-monolithic ICs available in the beginning of the 1980s (wide use of crystals of active elements, application of integrated thin-film resonators with increased permissible dissipated power).

At the level of functional devices – the use of packageless HICs for creation of functional units (with subsequent general sealing of the product).

At the level of the receiver in general:

(a) absence of special shielding cells achieved due to:

- optimal layout of the path as a whole from the point of view of minimizing the level of electromagnetic interference;
- the use of a two-stage structure of the device and carrying base as a structural element of electromagnetic isolation;
- the use of bulk-strip input microwave filters and microstrip concentrated selection filter (CSF) optimized in terms of minimum height and compatible with other units of the product;

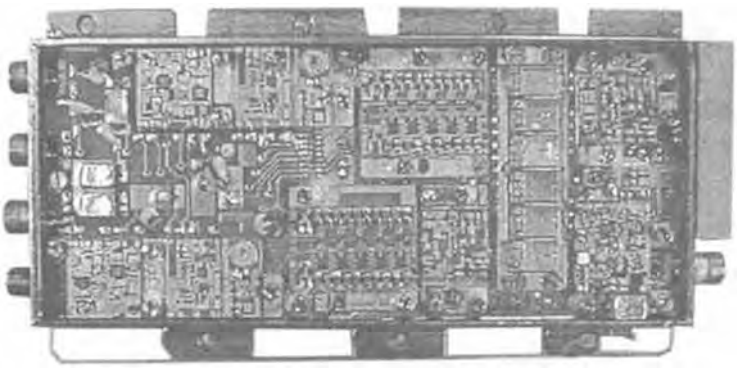

Fig. 8.37 Appearance of the microwave receiver for the airborne responder of the FFS system (1985) [2]

- the use of packages of microwave filters and CSFs (blocking the package laterally) as structural elements of electromagnetic isolation;
- the use of sealing package covers (in combination with filter packages) as locking elements of the electrically sealing cell;

(b) significant reduction of dimensions due to the use of laser sealing of the thin-wall package.

Due to the above design and technology solutions, the dimensions were decreased at least by 30 times as compared to the prototype designed with the previous generation technology. Mass production of these receivers and their operation for many years have demonstrated high level of reliability of the development. At the same time, actual reliability parameters exceeded parameters of the prototype by more than 10 times.

In the end of the 1990s, based on previous works and taking into account new technological developments, the enterprise successfully developed a wideband multi-purpose transceiver module (TRM) operating in the short part of the decimeter range. The module includes a two-channel low-noise receiving path with double frequency conversion, as well as a transmitting path with total output power of two channels around 1 W fitted with 5-digit precision phase shifter (Fig. 8.38).

Since functional saturation of this module is many times higher than in the device described above, and the requirements for weight and dimensions were defining, a number of structural and technological solutions is used here. The key solutions are:

– the use of electrically sealed micropacks containing functional units with their system of parameters ensuring minimum number of settings during module assembly to ensure intramodular EMC;
– sealing of the two-staged duralumin package with the help of the indium rope pressed through the cover by closely located screws;

As a result, such functionally saturated multi-channel transmitting and receiving device in sealed package protecting it from a wide range of climatic and mechanical impacts is implemented (with heat removal circuit elements) with extremely small

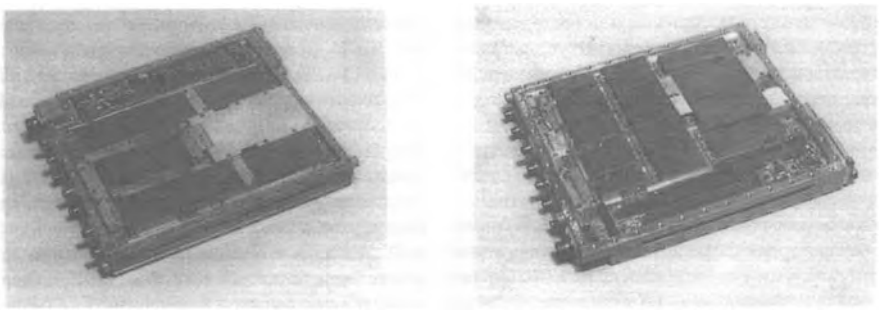

Fig. 8.38 Appearance of a multi-functional microwave transceiver module [2]

(28 × 160 × 180 mm) dimensions. The module included only Russian element base, including miniature ferrite modules of NPO "Faza" ("Phase"), as well as HF and microwave SAW filters by LLC "Butis-M". Most elements of the active element base was made in SUE "NPP Pulsar".

It should be noted that regardless of the fact that this development was performed in economic conditions that were much worse than those of earlier developments, it required less time and had significantly higher manufacturability than the receiver indicated above.

The experience of producing such TRMs (several dozens have been produced over the last year) demonstrates that their quality and manufacturability are determined by the level of the applied element base. Since only Russian element base is used in the TRMs, NPP "Pulsar" mainly focuses on development of a number of microwave electronic components that are critical for modern devices. Some of these elements are used in the created TRM.

A series of special limiting and switching GaAs-based diodes has been designed for use in the device for protection of TRM input circuits from high levels of synchronous and asynchronous interference [36]. The use of such diodes (instead of traditional silicon ones) together with the original circuitry-related solution made it possible to significantly simplify the circuit of implementation of the uncontrolled protection device, as well as reduce the losses introduced by the unit by 0.2–0.3 dB.

It is known that the level of requirements for the input protection device is largely determined by the possibilities of transistors used in input stages of the preselector. We are not necessarily talking about catastrophic failure of the device. As demonstrated by the studies, catastrophic failure is usually preceded by degradation of transistor characteristics, including, first of all, the noise coefficient. In this regard, it should be noted that the system of parameters (of both Russian and foreign) low-noise transistors does not include such crucial parameter as limit permissible level of input SHF power. Some of the data indicate that for GaAs field transistors with Schottky barrier this value is at the level of about 100 MW. For HEMT transistors, this level is 2–2.5 times lower. From the point of view of developers, the level of at least 200–500 MW is preferred.

The analysis demonstrated that creation of a low noise field SHF GaAs-based transistor (these transistors are used today in low-noise input circuits of SHF receivers) optimized in terms of the minimum noise factor as well as maximum permissible input power with the requirements desirable for the developers is a complex technological and circuitry-related task. Within the framework of solving this task, the enterprise has developed a GaAs-based low noise field microwave transistor for the decimeter wave range with low (about 0.5 dB) noise factor. Taking into account its relatively low operating current (20–30 mA), this device has no analogs in Russia. A number of technological features provided during production of this device helps calculate the increase in resistance of the transistor to the level of parasite microwave effects.

The use of Russian element base in the described device with all its advantages (first of all, in terms of well-developed quality control system) has principal downsides. They are mostly connected to the low level of integration of Russian element

base. This forces the developer to use the relatively expensive technology of thin film hybrid integrated circuits with subsequent low-performance assembly.

One of important units of the TRM described above is the small-sized precision 5-digit microwave phase shifter (PS) with the following requirements:

1. Least significant digit – 11.25°.
2. Step switching time – not more than 1 μs.
3. Accuracy of position setting, degrees, min:

- Position 11.25° – ±2;
- Position 22.5° – ±3;
- Position 45° – ±4;
- Position 90° – ±5;
- Position 180° – ±6.

The performed analysis of literature and subsequent computer design made it possible to select the type of the phase shifter circuit to implement a certain PS step.

Phase shifters with 180° and 90° steps are designed with hybrid units formed by Lange bridges used to achieve required precision of the phase shift in the given frequency range.

The option selected for creation of phase shifters with steps of 45°, 22.5° and 12.25° was based on the fact that reactivities of various nature bridging the transmission line change its electrical length differently: capacitive increases it, and inductive reduces it. Moreover, two equal reactances in the line separated by A/4 do not create a reflected wave if their specified conductances are low compared to one. Optimization of phase shifters with regard to the level of introduced attenuation is largely determined by the type of the selected p-i-n-diode. In this work, Russian diode 2A543A-5 was used to achieve acceptable losses and control currents. 1 mm thick polycore was selected as the substrate material. Figure 8.39 shows experimental characteristic of the phase shifter measured at several points of the operating frequency range. Current consumption of the designed 5-bit phase shifter (together with control circuit) does not exceed 70 mA in the +5 V circuit (in enabled state) and

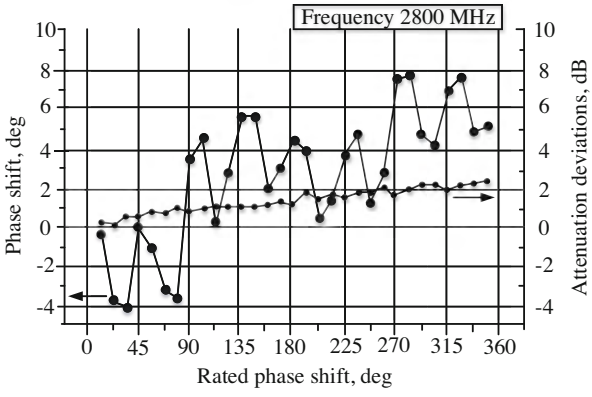

Fig. 8.39 Results of experimental study of the unit of 5-digit phase shifter at 2800 MHz [2]

20 mA in the −5 V circuit. The level of input power at which precision characteristics of the device are preserved is not less than 50 MW.

Structurally, the phase shifter is designed as a steel sealed (electrically sealed) package with integrated sealed metal-glass inputs for input and output of microwave signals, supply and control voltages. Sealing (electrical sealing) of the package is performed by means of welding thin cover with the help of roll (contact) welding. The package contains steps of the phase shifter, as well as additional amplifiers and attenuators minimizing the effect of the end VSWR – of the path on phase characteristics of the device.

The experience of production of designed phase shifters demonstrated suitability of these small-sized devices (dimensions of the package together with fixing elements, strip microwave outputs and inputs of power supply and control do not exceed 7 × 38 × 72 mm) for reproducibility.

One of the most commonly used units in microwave receivers is the switched discrete multi-bit microwave attenuator. For this purpose, "NPP Pulsar" has designed a small-sized (20 × 30 mm with the control circuit) wideband (1–3 GHz) hybrid multi-band attenuator and used it in a number of developments.

Each link of such attenuator consists of two parallel attenuators switched by p-i-n-diodes. During switching of the attenuators, the signal is reduced by the value of the difference between attenuation of two attenuators in the link. Attenuation differences in the links 0.5 dB, 1.0 dB, 2 dB, 4 dB, 8 dB and 16 dB ensures stepped change of attenuation in the path from 0.5 dB to 31.5 dB with a pitch of 0.5 dB. Implemented value of accuracy of such attenuator is not lower than ±(0.5–1) with switching speed of 0.1–0.25 μs.

The attenuator is controlled by supplying +5 V and −5 V voltage through resistors to p-i-n-diodes. Conversion of control signals with TTL levels into control voltages is performed by HIC based on specialized microcircuit of level control developed for this purpose in RPE "Pulsar", as well as GaAs-based special switching p-i-n diodes.

Concentrated selection filter for the frequency of 30–150 MHz with the usual bandwidth of 2–10 MHz is another functional unit frequently used in superheterodyne receivers. The most technologically reasonable solution for this purposes consists in the use of SAW filters. However, for a long range of applications, known disadvantages of this class of filters (high inserted losses), finite level of suppression of 2-thread and 3-thread signals, high value of signal delays, amplitude and phase pulsations in the pass band...) dictate the use of classic L- and C-filters based on concentrated elements. A well-known and technologically reasonable solution consists in using planar inductances based on thin-film technology for these purposes. In this case, capacitance connection between circuits is usually used.

In development of this variant, RPE "Pulsar" has created and used two-level design of classic (with serial communication circuit) filter based on planar inductances mentioned above. Such filter has no stretch of the high-frequency slope, which is typical of filters with capacitance connection. With bandwidth of 5 MHz, the filter has squareness ratio of 3.4 at the 30 dB level and 5.4 at the 60 dB level (provision of such level of selectivity requires staging of two SAW filters with compensating amplifier between them).

Comparison of characteristics of the examined filter with the actual results of SAW filters shows that the implemented filter, being deprived of the known disadvantages of SAW filters, excels in terms of selectivity at high tuning values, as well as in terms of inserted losses. Dimensions of the suggested filter are commensurate even with dimensions of single packaged SAW filters.

One of the key elements of multi-functional receivers determining their weight and dimensions (especially in the decimeter range of wavelengths) is the narrow-band high-Q strip microwave filter. Their development and improvement of their design are relevant problems. A wide range of such devices have been suggested over decades of work – from coaxial air filters to SAW filters and filters based on dielectric resonators. Due to mass application of technologies of hybrid and monolithic integrated circuits characterized, in particular, by small dimensions (especially height) of functional devices in modern receivers, an important problem is the task of creating filters optimized in terms of diminutiveness and height compatibility with functional units made with the help of planar technology. The paper [37] suggest narrow-band bulk-strip microwave filters on ceramics with high dielectric permittivity meeting these requirements.

The principle of operation of bulk-strip filters consists in that the end characteristic of the filter is formed in joint operation of the filtering thin-film interdigital structure and the package, the top cover of which is so close to the surface of the strip structure that the internal volume starts to directly participate in formation of the amplitude-frequency characteristic. Combined action of the above factor results in creation of an electrically efficient and extremely small (especially in terms of height) electrically sealed design, which is technologically compatible with devices of modern solid-state electronics.

The principal distinguishing feature of the suggested layout of the microstrip structure itself, which helps solve the set tasks to a significant extent, is the noticeably reduced (as compared to traditional) value of wave resistance of the used resonators. This lead to a 10–20-fold increase in their width (to 3–3.5 mm), as well as the gaps between them (to 4–5 mm). Such layout feature made it possible to create a simple, small-sized and effective system of cavity tuning and increase their Q-factor values.

PRE "Pulsar" has developed and implemented a series of original narrowband bulk-microstrip filters on ceramics with high dielectric permittivity (TL-75) in electrically sealed packages with strip outputs and setting elements. The design of filters is optimized in terms of height compatibility with functional units made using planar technology.

Main technical features of the designed bulk-strip filters are:

- small size: one of the main structural parameters – filter package height – is only 5.5 m, which makes it compatible with modern planar technology;
- reliability of fastening of the ceramic filter board in the package: the studies performed confirmed the suitability of ceramic board fastening options ensured by the design for use under mechanical and climatic effects of many different types;

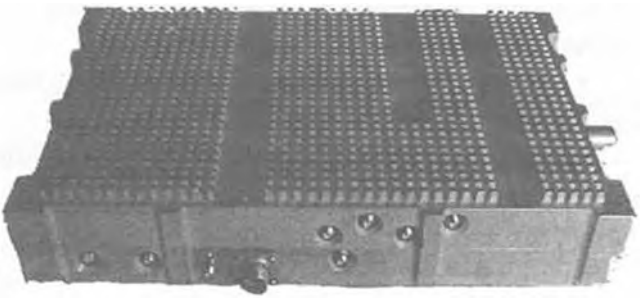

Fig. 8.40 Receiver module of the 3-cm range for the "Pechora-2M" product [2]

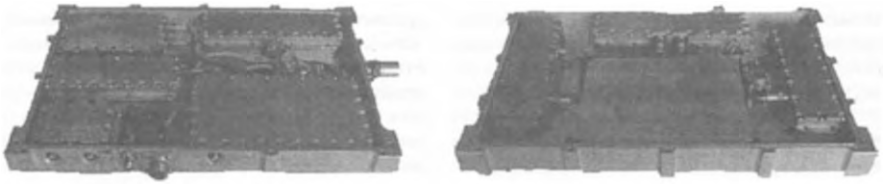

Fig. 8.41 Arrangement of receiving and frequency-setting module of the 3-cm range [2]

- internal electrical seal: despite small size, the level of electromagnetic isolation between microwave inputs of the filter exceeds 45–50 dB;
- external electrical seal: design features of the filter package make it possible to easily ensure high level of external interstage electromagnetic isolation. The use of the designed filters make it possible to create electrically sealed volumes with extremely high level of interstage electromagnetic isolation in the product naturally, without using additional walls, covers or screws;
- already supplied is the well-known radiolocation complex "Utes-M" – low-noise heterodyne module for the range of output frequencies about 1.3 GHz;
- development of a similar module for a higher frequency is almost complete;
- low-noise output microwave amplifiers with different levels of functional saturation are being produced in supplied in the interest of a long list of customers.

Significant achievements of the enterprise within the framework of modernization of one of the previously designed complexes is the successful completion of works for creation of a multi-purpose receiving and frequency-setting module of the 3-cm range (Fig. 8.40). Due to utilization of original design and circuitry-related solutions and the almost exclusive use of Russian element base (over 95% produced by "Pulsar"), the volume of equipment was reduced more than 100 times as compared to the prototype. The unit, which includes several low-noise microwave receiving devices of the 3-cm range, two-range low-noise microwave heterodyne with discrete tuning, noise generator and secondary power source (Fig. 8.41) and has volume of less than 3 l demonstrates 10–15 times higher reliability and 10 times reduced energy consumption as compared to the prototype.

SUE "NPP Pulsar" also develops microwave devices of the centimeter and decimeter ranges of wavelengths built on Russian element base:

- solid-state devices for protection from synchronous (up to 300 W) and asynchronous (up to 20 W) interferences with the inserted losses of 0.5–0.7 dB;
- low noise amplifiers with noise factor of 0.8–1 dB;
- discrete multi-bit phase shifters and attenuators;
- SHF frequency synthesizers;
- small-sized amplification-multiplication chains with SAW filters;
- microstrip and bulk-strip microwave filters of the decimeter and centimeter wavelength ranges;
- small-sized filters of concentrated selection based on planar L-C-circuits;
- various SHF amplifiers operating in continuous and pulse modes with output power up to 20 W.

8.6 High Speed Hybrid Converters for Radar Sets

As is known, it is necessary to ensure a number of additional operational requirements for modern advanced radar systems, including support of multi-purpose processing and dynamic setting modes. Many radars operate in the frequency band close to frequency spectra of other systems, in particular – communication infrastructure. This calls for development of radar systems that can be set dynamically in accordance with the requirements due to environment and operational features, which stimulates the creation of fully digital cognitive radar location systems.

The need for digital processing of the signal forces the developers to provide the possibility of signal digitalization during the initial stages of signal processing, shifting the AD converter closer to the antenna input, which creates a number of system-related problems. As an example, Fig. 8.42 [2] shows block diagram of a standard radar of the X-band, where two analog stages of frequency mixing are

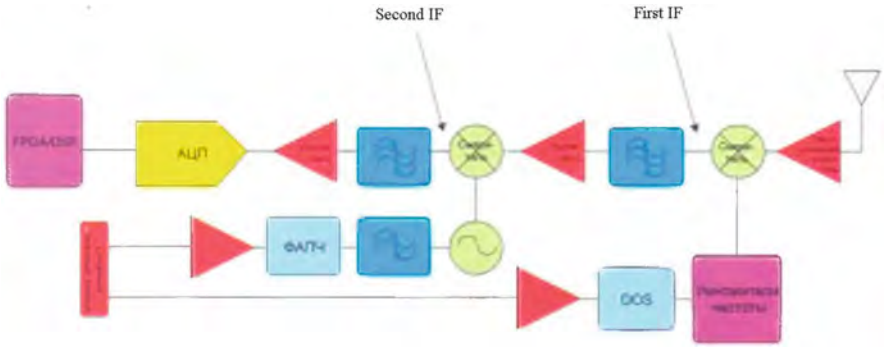

Fig. 8.42 Block diagram of the receiver path of a radar system with two intermediate frequencies

usually used. In the first stage, pulsed reflected radar signal is mixed with signal with frequency of about 1 GHz, in the second – with intermediate frequency within the range of 100...200 MHz in order to ensure signal sampling with the help of a 200 MHz/s AD converter with resolution of at least 12 bits [38].

In such architecture, the task of quick frequency tuning and signal compression can be implemented in the analog region, which calls for modification of the signal processing. It should be noted that even sampling at the frequency of 200 MHz/s is a great step forward in the field of radar data processing system; however, during the next stage of evolution it will be necessary to implement new solutions on the way to creation of fully digital radar sets.

In recent years, AD converters with sampling frequency over 1 GHz/s have appeared in the market, which makes it possible to shift digitalization of signals even closer to the antenna – after the first mixer stage. Converters with analog strip over 1.5 GHz already support digitalization of the first intermediate frequency (IF); however, linearity and spectral density of modern AD converters do not meet the system requirements.

Moreover, until recently, high-speed AD converters used mostly parallel LVDS interfaces as a means of data transmission between this converter and the platform of digital signal processing (as a rule, a FPGA or a processor). However, the use of the LVDS data bus at the AD converter output is associated with certain problems, since the LVDS bush shall operate at the frequency that significantly exceeds the permitted norms specified by the IEEE standard and cannot be acceptable for FPGA.

In order to solve this problem, system designers demultiplex output data to two or four LVDS buses to reduce data transmission speed per one bus. For example, a 10-digit ADC operating at sampling frequency of over 2 GS/s would require output demultiplexing with the coefficient of 4 for creation of a 40-digit LVDS bus. Taking into account that many radiolocation systems, especially phased antenna arrays, used multiple gigahertz AD converters, system designing becomes a difficult task, since in requires routing and matching of lengths of many lines. This is not to mention the requirement of connection of multiple FPGA outputs.

New high-speed AD converters provide solutions that not only overcome the existing problems but also help to optimize the system additionally. These converters are characterized by extremely high linearity and the analog signal pass band exceeding 3 GHz, which helps implement sub-sampling in the L-band and (partially) in the S-band. Due to this fact, direct sampling of radio frequency signal in these frequency ranges is performed. This helps reduce the number of components and the size of the system due to exclusion of one mixer. For higher-frequency systems, it makes it possible to use a higher IF, reduce the number of mixers and filters and increase flexibility of frequency distribution, since a wider spectrum of intermediate frequencies is used.

Greater linearity and lower spectral density of new converters makes it possible to use them in radar stations of the latest generation. With an increase in spectral density and expansion of the dynamic range, it is necessary to be able to control interference signals, the frequency of which is close to the frequency of the reflected radar signal. Modern AD converters can ensure parasite range without parasite

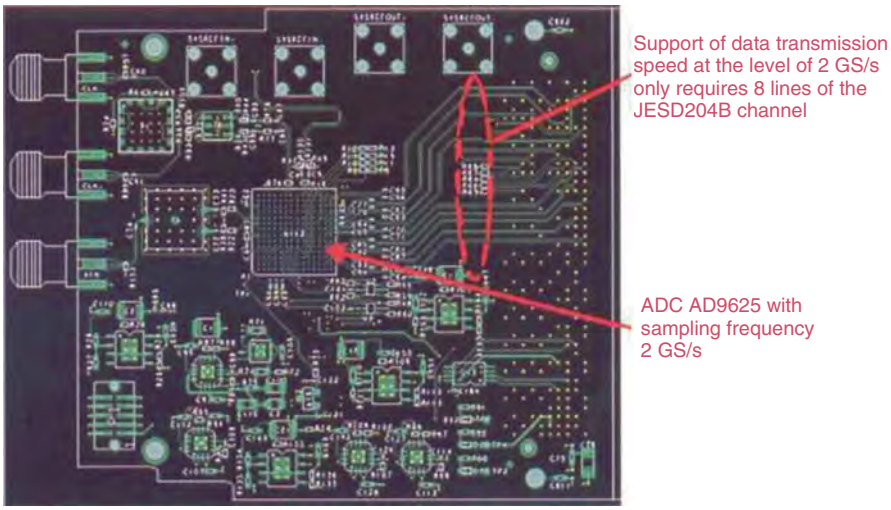

Fig. 8.43 An example of printed circuit board using data transmission channels JESD204B [2]

components of more than 75 dBs, i.e. almost 20 dBs better than in devices available during the last 10 years. This significant step is even more important than the recently introduced distribution of frequencies for communication infrastructure [38].

It would be logical to suggest that the next step of ADC manufacturers in the direction of improvement of these devices would consists in improvement of such characteristics as bandwidth, linearity and noise level. However, the next two additional functions implemented in the newest gigahertz AD converters – interface of data transmission channel of the JESD204B standard and integrated DSP functionality – provide the system developer with even more possibilities in terms of system implementation [39].

For example, data transmission channel of the JESD204B is implemented in a number of high-speed AD converters; however, it provides maximum advantages for GHz converters, in which LVDS interfaces do not meet all system requirements. JESD204B is a high-speed serial standard of data transmission between high-speed AD converters and FPGAs or other processors with the use of reduced number of differential interconnects (FPGA outputs). This protocol supports data transmission speed up to 12.5 Gbit/s.

Figure 8.43 [40] shows the board on which data transmission between 12-digit AD converter of the AD9625 type and FPGA is ensured just by 8 lines of the JESD204B standard for support of full data transmission speed at the level of 2 GS/s.

When multiple JESD204B lines are used, requirements for matching of lengths of printed board conductors are significantly reduced, since this standard requires synchronization of all lines within 920 ps, which allows for a wide variation of delays between separate JESD204B lines. The newest version B of the JESD204 standard also supports determined delay, which makes it possible to calculate the

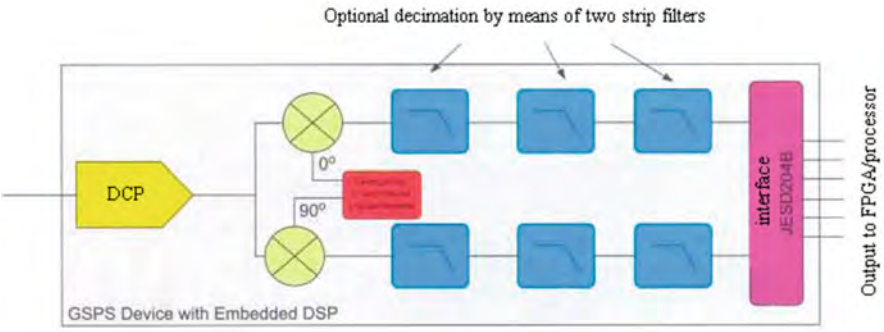

Fig. 8.44 Block diagram of a high-speed AD converter with integrated digital signal processor [2]

data transmission time from high-speed AD converter to FPGA. When the delay time is known, it can be compensated with the help of subsequent digital processing for the purpose of synchronization of data streams, i.e. performance of the key requirement for a phased antenna array and systems of generation of directivity pattern based on high-speed converters.

Data transmission channel of the JESD204B provides significant advantages for the hardware developer; however, perhaps the most important innovation of high-speed AD converters is the implementation of integrated functions of digital signal processing [41]. Latest generations of AD converters are able to support a wide range of digital signal processing operations at high data transmission speeds. It is expected that in the near future high-speed AD converters will be supported by dynamically selected digital down converters (DDC) integrated into these devices, as shown in Fig. 8.44.

Frequency band of radiolocation signals can vary significantly depending on the application; e.g., radar signals for formation of a radar image require hundreds of MHz, while target tracking radars can use signals with pass band of dozens of MHz and less. In the past, shift of a high-speed AD converter towards the antenna meant that a great number of unwanted frequencies entered FPGA or processor.

In modern FPGAs and high-speed AD converters a significant, if not the greatest, portion of the consumed power is associated with power dissipated in interfaces; therefore, unnecessary transmission of unwanted frequencies increases the power consumed by the system. In advanced multi-mode radar stations, the possibility of dynamic selection of step-down converters ensures significant advantages, relieving FPGA from performance of complex data processing tasks.

Converters with frequency reduction (digital down converters – DDC) combine a numerically controlled oscillator and decimation filters, which ensure the possibility of selecting the pass band and position of the signal within the Nyquist band of high-speed ADC and transmit only the data required by signal processing devices.

Let us consider the radar system using signals with 30 MHz band at the intermediate frequency of 800 MHz. If this signal was selected with the help of an AD converter with the speed of 2 GS/s with resolution of 12 bit, the output pass band

would be 1000 MHz, e.g. significantly exceed the signal pass band, and the speed of output data from the converter would be 3 GS/s.

If data decimation is performed with the help of a DDC with the factor of 16, it will ensure not only significant reduction of the noise level, but also reduction of the output data to 625 Mbit/s and less, which makes it possible to transmit data with the help of a single line of the JESD204B standard. This reduces general power consumption of the system significantly. Due to their ability to dynamically configure DDC, new high-speed APCs ensure the possibility of switching between different modes of power consumption and implement optimized solutions that help create cognitive radar sets.

New high-speed AD converters offer wide possibilities for creation of radar location systems due to wide pass band and high sampling speed, which helps reduce the number of system components or ensure direct sampling of the radio frequency signal. The possibility of dynamic configuration of high-speed AD converters ensures multi-purpose support and meets the advanced task of creating a fully digital cognitive radar location system.

8.7 Foreign Microcircuits for GaN-Based Transceiver Modules of Radar Systems

8.7.1 GaN-Based AESA TRMs

The use of active electronically scanned arrays (AESA) in modern systems of radiolocation and electronic warfare (EW) means is constantly expanding. A number of countries have already demonstrated unique possibilities of AESA in onboard weapon systems of airplanes F/A-18E/F (USA), Rafale (France), etc. [42–63] Similar works are conducted in the Russian Federation, where AESA is included in the radar of the fifth generation fighter jet. Main elements of AESAs of high-frequency ranges are microwave transceiver modules (TRM) based on monolithic integrated circuits. Provision of transceiver modules to radar sets with AESAs is the priority task of the international SHF industry.

Until recently, TRMs were mostly based on GaAs SHF microcircuits. Within two extensive programs for research of gallium nitride implemented in the USA and Europe (WBGSTI and KORRIGAN), intense developments of TRMs of the next generation based on this material have been completed. In the USA, in addition to demonstration and reliability tests, supplies of GaN modules for space and military equipment, including well-known radar strategic system of missile defence [65, 66], have been carried out since 2005. In order to close the gap between themselves and the USA, European companies are also taking active measures for development of their own technology of GaN microcircuits for TRMs [67–71].

Therefore, in the following we are going to consider GaN MIC components of European TRMs in detail.

Since the power of GaN-based TRMs is an order of magnitude higher than in GaAs devices, AESAs implemented on the basis of such TRMs have either wide spatial search area, or high range of target tracking, or, with other equal parameters, significantly smaller aperture [67]. At the same time, GaN transceivers are more immune to increased temperature and have higher efficiency. A TRM usually contains several MICs, including low-noise amplifiers, power preamplifiers, power output amplifiers, switches, etc. According to estimates of Thales (France), TRMs and MICs included in them make up about a half of cost of the entire AESA [69]. Let us consider relatively old GaN developments of MIC components used in TRMs by European Companies.

As noted above, GaN MIC amplifiers are key components of TRMs. In the following, we will briefly consider the main devices created by European companies in the past. This is a set of microstrip MIC amplifiers of the X band for TRMs, which included preamplifier, power amplifiers and low-noise amplifier; it was designed by joint efforts of the military electronics department of EADS Deutschland GmbH (Ulm) and the Fraunhofer Institute of Applied Solid State Physics (Freiburg), Germany [66, 68]. GaN MICs were manufactured by specialists of the Fraunhofer Institute, while design and measurement of characteristics were performed by the EADS military electronics department. AlGaN/GaN HEMT structures were produced on SiC substrates (d = 75 mm) by chemical deposition of vapor phase from metal-organic compounds (MOCVD). 0.25 mm gate and field electrode of the transistors were formed by electron beam lithography. After processing of the upper surface, SiC substrate was thinned to 100 μm, after which vias were made in its back part.

Since the number of publications on this subject in open press became severely limited after 2010, it is known from open sources that the first stage of the preamplifier forms a transistor with the gate width of 8 × 60 μm, the second stage – a transistor with the gate width of 8 × 125 μm. The amplifier is matched with 50 Ohm impedance at the input and output. Maximum output power was achieved in the saturation mode with amplification compression of 5 dB and exceeded 38 dB/MW. However, even with 1 dB compression, this output power of the amplifier was enough to power one or two high power amplifiers within the range of 8.5–14 GHz.

Transistors with equal gate width (8 × 125 μm) were installed in each of the two stages of this power preamplifier: two transistors in the first stage and four in the second. Output adder of the amplifier was amplified for maximum output power within the frequency range of 8.5–11 GHz.

During operation of such power amplifier in the AB class, its maximum output power amounted to 20 W, which conforms to the specific transistor power of 5.7 W/mm. In this case, gain factor in low signal level is 18 dB, and the efficiency is 31%. Within the frequency range of 8.5–11 GHz, gain factor in the low signal mode is not less than 15 dB. Within the entire frequency range of 8.75–11.5 GHz, measured output power of the amplifier exceeded 14 W.

Low noise amplifier (LNA) of this series was formed by two stages based on 8 × 30 μm transistors. Minimum measured noise coefficient of a low-noise AlGaN/GaN HEMT was within 0.8 dB at 10 GHz and with drain voltage (Ud) of 10 V.

Minimum noise factor of the LNA amounted to 1.45 dB, saturation power – 24 dB/MW with input power of 16 dB/MW. An important characteristic of any LNA is the maximum possible level of input power. The examined amplifier operated in a stable manner with the input power up to 4 V. However, its output power in this case was significantly reduced due to change in the shift of the first stage transistor.

TRM was assembled on the base of three specially developed GaN MIC amplifiers using the industrial technology of low-temperature cofired ceramics (LTCC). The transmitter included a preamplifier, two power amplifiers connected in series, and a circulator. Amplifiers are mounted on CuMo heat removal circuit. The receiving unit included the LNA and limiter, while GaAs switch was used to switch between channels. Multi-layered LTCC substrate also contained pulse power circuits of power GaN MICs for 30 V, LNA displacement circuits and control circuit of the switch.

The achieved results proved to foreign customers the possibility of implementing GaN-based AESA TRMs with output power of more than 20 W in the transmission mode and noise factor of the receiving channel under 3 dB.

8.7.2 Monolithic GaN Microwave Power Amplifiers

Typical representatives of this class of microwave products include GaN MIC amplifier of the X band with output power of 20 W designed by order of the military department for advanced radars with AESAs [64, 66].

This amplifier was developed by joint efforts of SELEX Sistemi Integrati and Consorzio OPTEL, as well as the University of Rome and the Polytechnic University of Turin (Italy). MIC with microstrip structure was built on GaN HEMT by SELEX Sistemi Integrati. Epitaxial GaN/AlGaN/GaN structures were grown on semi-isolating SiC substrates by MOCVD method or with the help of molecular-beam epitaxy (MBE). 0.5 μm long gate was formed with the help of the stepper photolithography method. Ohmic contacts were produced by deposition of the Ti/Al/Ni/Au structure on the GaN/AlGaN epitaxial layer with subsequent annealing at high temperature. MIC was passivated by SiN film applied by the plasma-chemical deposition method. After creation of active devices, thin-film NiCr, galvanically formed inductances, transmission lines and, if necessary, air bridges were applied. After that, the plate was thinned to 70 μm, and vias were formed at its back part with the help of dry etching by induced plasma, the surface of which was covered with the 10 μm thick gold layer with the help of galvanic metallization method.

From the point of view of circuitry, this amplifier consists of just two transistor stages. Transistor of the first stage contains four transistor cells, transistor of the second stage – eight cells. Total width of stage transistor gates is 4 and 8 mm respectively. The size of gate of a separate transistor cell – 10 × 100 μm. The amplifier was designed for the frequency range of 8.5–10.5 GHz.

Characteristics of this amplifier, which is already used in NASA's onboard equipment, were measured on a plate in pulsed mode with duty factor of 1%,

pulse duration of 10 μs and drain voltage of 20 V in the AB class mode. Output power of the amplifier within the frequency band of 8–10.5 GHz amounted to 21–28.5 W with amplification of 12.9–16.5 dB and efficiency of 29–43%. At 8.5 and 9 GHz points, power in saturation reached 30 W with efficiency of 40%.

It is also necessary to mention a number of other devices for the X band known from publications – high-power AlGaN/GaN HEMT and MIC amplifiers of L/S (1–4 GHz) and X (8–12 GHz) bands [68]. Transistors and MICs were designed by joint efforts of the Fraunhofer Institute of Applied Solid State Physics (Freiburg) and the companies United Monolithic Semiconductors (Ulm), Germany, and NXP Semiconductors (Nijmegen, Netherlands).

GaN/AlGaN were grown on SiC substrate by MOCVD method in the reactor, which made it possible to process 12 75 mm plates simultaneously. The length of MIC transistor gates is 0.25 μm. Moreover, additional optimized electrodes of field modulation are used in the structure. HEMT breakdown voltage for two electrodes exceeds 100 V.

Measurement results demonstrated that the output power of such two-stage amplifier of the X range exceed 11 W at 8.56 GHz with efficiency of 40% and gain of 17 dB with compression of 3 dB. Output power of the one-step MIC amplifier at 8.24 GHz with voltage of 20 V is 6 W, efficiency – 55%, and the linear gain – 12 dB.

Also noted shall be the results obtained within the 2 GHz range for powerful HEMT designed for military and civil systems of mobile communication. At 50 V, average specific power of the transistor amounted to 10 W/mm with efficiency of 61.3% and linear amplification of 24.4 dB. At this frequency, transistors also operated in a stable manner with elevated voltage equal to 100 V. In this case, specific power of the transistor reached 25 W/mm at efficiency $\geq$60%.

It is known that GaN amplifiers are used in the state-of-the-art systems of radioelectronic warfare. Let us consider GaN MIC amplifiers of the 2–6 GHz range for EW systems [71]. The amplifiers were developed by specialists of the Polytechnic University of Madrid, INDRA Sistemas (Madrid), Spain, SELEX Sistemi Integrati (Rome) and QinetiQ (Malvern, Great Britain).

It is interesting that two companies during the works were simultaneously designing two different designs of amplifiers: microstrip variant based on SELEX technology and coplanar structure based on QinetiQ technology. Due to the fact that GaN HEMT impedance is higher than in GaAs HEMT transistors, their matching in the wide frequency band of 2–6 GHz selected for design of amplifiers is simplified. Both amplifiers operated in the AB class mode and had two amplification stages. Required power of the output stage of each amplifier was achieved by adding output signals of four transistors with the gate width of 1 mm.

In general, frequency characteristics of the amplifier by QinetiQ corresponded to the design values except for the range of 4–6 GHz, where a small deviation (1–2 dB) of the output power (8 W) from the design value was observed. Proper correspondence was also achieved for gain factor in the mode of low signal (18 dB) and efficiency (20%) [71–73].

Another SELEX amplifier was designed for output power of 10 W at 25 V and 1.3 A. Characteristics were measured at voltage values of 20 and 25 V and current of 1.1 and 0.9 A. Measured gain factor in low signal mode in the entire band of 2–6 GHz exceeded 15 dB. Output saturation power in continuous mode reached 10 W, and the efficiency was more than 25% with 20 V voltage at the frequency of 4 GHz. At this frequency, amplifier power in the pulsed mode (pulse duration – 20 μs, duty factor – 1.1%) amounted to 17 W [71].

8.7.3 GaN-Based SHF Microcircuits of Switches

GaN MIC switches form a separate independent class of microwave ICs.

High working voltage of GaN transistors gives them significant advantages also during operation as part of switches of transceiver modules, since if GaN transistors are used, the number of transistor stages placed in series can be reduced as compared to GaAs switches [72]. In certain cases, it is even possible to exclude the circulator from the module circuits [73].

Attention shall also be paid to powerful microstrip SHF switches based on GaN HEMT for the ranges of 8–12 and 2–18 GHz [57]. The switches were jointly designed by Elettronica SpA, SELEX Sistemi Integrati, CNR-IFN and Tor Vergata University (Rome, Italy). Switches are built according to the SPDT circuit (one input, two outputs) with the help of microstrip GaN HEMT technology by SELEX. Epitaxial structures of GaN/AlGaN/GaN were grown on semi-insulating SiC substrate with the help of MOCVD or MBE methods. Both classic stepper photolithography and electron beam photolithography were used for work with masks of different layers. 0.25 μm gates were formed by means of electron beam lithography. Other process operations of creating MIC switches are the same as used for creation of MIC switches by SELEX.

Results of studies of these products demonstrate insertion losses of the switch less than 1 dB in the given frequency range (8–11 GHz) and isolation higher than 37 dB. Moreover, output matching of the switch is better than 13 dB. For measurement of characteristics, the switch was mounted into special mandrel with coaxial outputs. Tests were performed in pulsed mode (pulse duration – 100 μs, duty factor – 25%). Even with the 8 W signal supplied to the input, the switch preserved linearity of the transmission characteristic.

Within the framework of the same project, a wideband amplifier was created for the range of 2–18 GHz with inserted losses of not more than 2.2 dB, isolation greater than 25 dB and transmitted power at the 1 dB compression point of more than 5 W.

Another GaN SPDT MIC switch of the X band with working power level of more than 25 W [71–72] was designed by TNO Defence, Security and Safety (Den Haag, Netherlands) and QinetiQ (Malvern, Great Britain). Microcircuits of the switch were

built according to the coplanar GaN MIC technology by QinetiQ. The structure includes a non-alloyed 25 nm thick Al0.25Ga0.75N layer on isolating iron-alloyed 1.9 μm thick GaN layer grown on semi-insulating 4H SiC substrate with the diameter of 50 mm.

Ohmic Ti/Al/Pt/Au contacts and T-shaped Ni/Au gate with the length of 0.25 μm were formed by regular methods. The devices were passivated with multi-layered SiNx/SiO2/SiNx structure with breakdown voltage of more than 200 V, which simultaneously served as the dielectric of capacitors with metal-insulator-metal (MIM) structure. Thin-walled resistors were made on NiCr film with surface resistance of 27 Ohms per square. Inductances and coplanar lines were created in galvanic gold layer with thickness of 3 μm. Air links are formed from evaporated gold layer with the thickness of 0.8 μm.

Conductivity of transistors amounted to 230 mS/mm, current – 1030 mA/mm, threshold amplification frequency by voltage – 40 GHz, gate breakdown voltage – over 100 V. The switches were designed using the ADS Momentum program, which has been significantly improved and is now widely used in practical activities of the developers of SHF devices.

It should be noted that foreign developers managed to achieve quite high level of isolation (35 dB in the X range). Input and output reverse losses are better than 10 dB. Inserted losses are high (3.5 dB) due to relatively low isolation of transistors in the disabled state. Measurements in the pulse mode demonstrated linear dependence of the output amplifier power on the input power up to values of 25 W. Uniform isolation character is preserved across the dynamic range.

In 2008, the project of the European defence agency KORRIGAN aimed at development of GaN SHF devices and microcircuits was successfully completed [66–90]. Its main result was the creation of European infrastructure, which includes independent technological centers for creation of GaN microwave MICs for civil (base cellular communication stations) and military (AESA TRMs) applications. Development of GaN components of MIC transceiver modules was performed by European industrial companies and universities aided by departments of defence of separate countries (France, Germany, Spain).

The above results confirm the prospects of using GaN MICs in transceiver modules – both in powerful stages (preamplifiers and output amplifiers, switches) and in low-power devices (low-noise amplifiers). GaN MICs demonstrate good wideband characteristics at high output power levels. Until recently, AESA projects for onboard radars of European fighter jets were implemented by two groups of companies. One of them is headed by the Thales company, which designed an array of 1000 modules; the second is formed by the consortium of SELEX Galileo, EADS Electronics and INDRA, which successfully designed and launched mass production of the AESA complex with 1425 modules [24]. Further use of GaN transceiver modules in specific AESA models will depend on the level of readiness of the industrial technology of GaN MIC and developers of the corresponding radars.

8.7.4 Optimization of Design of GaN SHF Transistors

In order to improve characteristics of GaN-based structures used for creation of SHF transistors, process engineers have developed many new process methods.

One of such technologies is a gate recessing by plasma-chemical etching that usually is combined with a slot etching process in dielectric [91–94]. As a result, increase in transistor steepness due to decrease of gate-to-channel distance, reduction of drain source resistance –caused by absence of depletion regions of the transistor gate-source and gate-drain, minimization or even elimination of dynamic transient processes when the transistor is switched on, due to mitigation the effects of traps in the gate-drain region since the surface where they are placed can be moved away at a safe distance. Therefore, technology specialist suggest growing the passivating dielectric layer directly after growing all layers of the heterostructure [94].

Many researches aimed at search for new surface-passivating materials for transistor heterostructures based on GaN and its solid solutions have been performed in recent years. The use of new materials allows to increase more than twofold the pulse current of the transistor and its steepness, as well as significantly reduce switch-on time due to compensation of interface states [95].

Developers of GaN-based SHF technologies from Cree, TriQuint, Northrop Grumman and other companies have achieved high-frequency response characteristics of the transistor configurations that became the base for development and creation of efficient power amplifier integrated circuits operating in wide ranges. These chips outperform the integrated circuits based on gallium arsenide (GaAs) by more than 10 times in mass-dimensional parameters [91]. Mass production of power amplifiers based on GaN-heterostructures with frequencies up to 100 GHz has already started; QuinStar Technology company in cooperation with HRL company has developed transmit-receive modules for radiolocators in 94-GHz range with power output more than 5 W [94].

Thus, the main production and technology problems that prevented commercialization of transistors and monolithic ICs based on GaN were solved [96], and the active introduction of GaN-based technology into the field of SHF devices began. The rates of industrial exploration of the new technology significantly (2–3 times) exceed the former rates of development of Si- and GaAs-based devices. [97].

8.7.5 SHF Microcircuits by RFHIC

8.7.5.1 GaN-Based SHF Microcircuits by RFHIC for Wireless Communication Systems

New solutions in the area of GaN-based technology are offered by leading global producers of SHF-devices such as RFHIC company.

RFHIC (South Korea) is one of leaders in the markets of telecommunication and radar equipment. This supplier of GaN-based SHF chips has full production cycle that includes the product development and assembly during which the crystal installation on the base, cable splicing, packaging and sealing operations are performed.

RFHIC company produces a wide range of GaN-based products for SHF electronics ranging from cable TV amplifiers to power amplifiers for radiolocation. The basic specifications of products made by this company are discussed below.

First of all, it is worth noting the amplifiers made by RFHIC company for wireless communication systems, which are intended for application in modern networks using different data transmission format including LTE, CDMA, WCDMA, and WIMAX. They can be conditionally divided into groups by power and operating voltage range.

The first group includes SHF-amplifiers with a rated power of 5...10 W and operating voltage of 28 V. These amplifiers are intended for operation at the frequency range of 2...3 GHz and have a gain factor of 40 dB.

The following group includes amplifiers with a rated power of 28 W and operating voltage range of 48...50 V. These amplifiers are intended for operation at the frequency range of 0.8...3 GHz and have a gain factor of 44.5 dB.

The third group includes amplifiers with a rated power of 56 W and operating voltage of 48...50 V. These amplifiers are intended for operation at the frequency range of 0.8...3 GHz and have a gain factor of 47.5 dB.

The fourth group includes SHF-amplifiers with a rated power of 80 W and operating voltage range of 48...50 V. These amplifiers are intended for operation at the frequency range of 0.8...3 GHz and have a gain factor of 55 dB.

In addition, amplifiers for wireless communication systems include hybrid amplifiers with a power of 1...5 W and operating voltage of 28 V, as well as amplifiers based on Doherty circuit with a power of 7 W and operating voltage of 31 V. The specified amplifiers are intended for operation at the frequency range of 0.8...3 GHz and with a gain factor of 27...38 dB; as well as at the frequency range of 1.5...3 GHz and with a gain factor of 14...16 dB respectively.

The basic types and technical characteristics of SHF-amplifiers made by RFHIC company for wireless communication are listed in Tables 8.26, 8.27 and 8.28.

Since these amplifiers are GaN-based, they can operate at high values of temperature and voltage.

8.7.5.2 GaN Amplifiers for Pulse Radar Sets

Amplifiers for pulse radar stations (see Fig. 8.45) based on GaN have wide frequency ranges covering almost the entire spectral region of frequences between 135 MHz and 10 GHz, as well as high power level.

All their variety shall also be conventionally divided into several groups. The first one includes hybrid amplifiers. They cover a fairly good range of operating

Table 8.26 Basic types and technical characteristics of GaN-based amplifiers made by RFHIC company for wireless communication

Type	Frequency, MHz	Gain, dBm	Output power, dBm	Efficiency factor, %	Dimensions, mm
Amplifiers with a power of 5... 10 W (28 V)					
RTP 21005-11	2110...2170	45	37	40	
RTP 21010-11	2110...2170	45	40	40	100 × 50 × 20
RTP 26010-N1	2570...2690	40	40	38	
Amplifiers with a power of 28 W (48...50 V)					
RTP 08028-20	869...894			42	
RTP 18028-20	1805...1880	44.5	44.5	42	125 × 90 × 20
RTP 21028-20	2110...2170			42	
RTP 26028-20	2496...2690			40	
Amplifiers with a power of 56 W (48...50 V)					
RTP 08056-20	869... 894				
RTP 18056-20	1805...1880	47.5	47.5	42	150 × 90 × 20
RTP 21056-20	2110...2170				
RTP 26056-20	2620...2690				
Amplifiers with a power of 80 W (48...50 V)					
RTP 08080-20	869...894				

(continued)

Table 8.26 (continued)

Type	Frequency, MHz	Gain, dBm	Output power, dBm	Efficiency factor, %	Dimensions, mm
RTP 18080-20	1805...1880	55	49	42	170 × 100 × 20
RTP 21080-20	2110...2170				
RTP 26080-20	2620...2690				

Table 8.27 Technical characteristics of hybrid GaN-based amplifiers with a power of 1...5 W (28 V) made by RFHIC company for wireless communication

Model	Frequency, MHZ	Gain factor, dB	Output power, dBm	Efficiency factor, %	Operating voltage, V
HT0808-15A	869...894	37	33	26	28
HT1818-15A	1805...1880	33	33	25	28
HT1818-15M	1805...1880	34	33	27	5/28
HT2121-15A	2110...2170	33	33	24.5	28
HT2121-15M	2110...2170	32	33	26	5/28
HT2626-15A	2610...2690	30	34	25	28
HT2626-15M	2610...2690	30	33	25	5/28
HT2627-15A	2650...2750	27	33	31	28
HT0808-30A	869...894	38	37	28	28
HT0909-30A	925...960	36	37	27	28
HT1818-30A	1805...1880	38	37	26	28
HT1919-30A	1930...1995	38	37	26	28
HT2121-30A	2110...2170	36	37	26	28
HT2626-30A	2610...2690	32	37	28	28

Table 8.28 Technical characteristics of hybrid GaN-based Doherty amplifiers with a power of 7 W (31 V) made by RFHIC company for wireless communication

Model	Frequency, MHz	Bandwidth, MHz	Gain factor, dB
RTH18007-10	1805...1880	75	16
RTH20007-10	1930...1995	65	16
RTH21007-10	2110...2170	60	15
RTH26007-20	2620...2690	70	14

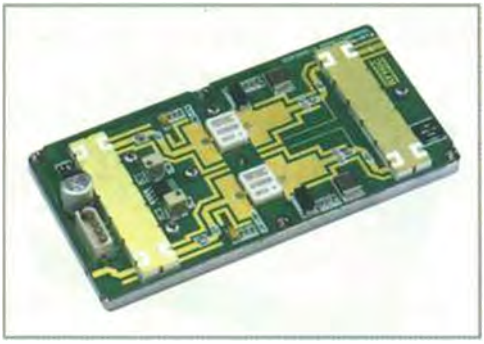

Fig. 8.45 The appearance of SHF-amplifier made by RFHIC company for pulse-modulated radar [2]

frequencies between 400–450 MHz and 9.3–9.5 GHz. Their gain factors can take values within the range of 8–33 dB. Efficiency of amplifiers of this group can reach 40–70%.

The next group includes low-noise GaN amplifiers. These amplifiers cover the range of operating frequencies from 1.2–1.4 GHz to 9.3–9.5 GHz, while the gain factor takes values within the range of 10...18 dB. Efficiency of these amplifiers reaches 18–30%.

The third group includes pallet amplifiers. They cover the frequency range between 135–460 MHz and 9.0–10.0 GHz, while their gain factor occupies the range of values of 8...39 dB. Efficiency of these amplifiers reaches 5–20%.

Power amplifiers with the output power values reaching 200 W – 2.6 kW and operating frequency ranges covering almost the entire region between 1.02–1.03 GHz and 9.30–9.50 GHz can be attributed to a separate group. The value of their gain factor lies within 20–63 dB, while their efficiency reaches 20–45%.

The main standard sizes and characteristics of GaN-based amplifiers for radar sets by RFHIC are given in Tables 8.29, 8.30, 8.31, 8.32 and 8.33.

The same category of products includes ***GaN-based transformers-rectifiers***, the main models and characteristics of which are presented in Tables 8.29, 8.30, 8.31, 8.32 and 8.33.

Another characteristic type of products by RFHIC includes multi-purpose powerful GaN amplifiers (for different application, including heavy duty conditions and

Table 8.29 Types and characteristics of hybrid amplifiers for radars based on GaN by RFHIC

Type	Frequency	Gain factor, dB	Output power, W	Efficiency factor, %	Operating voltage, V
HR2731-50A	2700...3100	26	50	50	50
HR2933-50A	2700...3500	25	50	50	50
HR2933-70A	2900...3300	24	80	50	50
HR5459-25B	5400...5900	20	25	40	50
RRC94030-10	9300...9500	17	25	40	50
HR9395-08A	9300...9500	11	8	40	50
HR9395-30A	9300...9500	9	30	40	50
RNP04006-A1	400...450	33	4	70	24

Table 8.30 Types and characteristics of low-noise amplifiers for radars based on GaN by RFHIC

Type	Frequency	Gain factor, dB	P1dB, dBm	Input power, dBm	Operating voltage, V
CL1302D-L	1200...1400	18	20	30	5
CL3102D-L	2700...3500	11.5	20	30	5
CL5602	5400...5900	15	23	18	5
CL9402	9300...9500	10	22	18	5

in particular elevated ambient temperature). These amplifiers cover relatively wide frequency ranges, approximately from 20–512 MHz to 2.0–6.0 GHz. Values of the gain factor are within 17...60 dB, while operating voltage values lie within 24...33 V. Basic models of this group and their characteristics are given in Table 8.34.

An aspect important for REE developers shall be noted: due to certain differences between Russian and foreign standards of frequency ranges and corresponding values of power of products in microwave ranges, Russian developers are often unable to find foreign components that would fully comply with Russian requirements. This problem can be solved by testing the imported amplifier within the required frequency range or modifying it to the level of compliance with Russian standards. RFHIC have implemented a number of projects with Russian companies (in particular, with ProChip) in both of these directions in 2010–2014.

Table 8.31 Types and characteristics of pallet amplifiers for radars based on GaN by RFHIC

Type	Frequency	Gain factor, dB	Output power, W	Efficiency factor, %	Operating voltage, V
RRP03250-10	135…460	31	300	20	50
RRP10350-1	1030…1090	28	350	10	50
RRP10800-10	1030…1090	27	800	10	50
RRP1214500-14	1200…1400	14	560	20	50
RRP2731080-39	2700…3100	39	100	20	50
RRP2731200-08	2700…3100	8	250	20	38
RRP2731330-09	2700…3100	9	400	20	50
RRP2731160-35	2700… 3500	35	180	20	50
RRP2735200-30	2700… 3500	32	230	20	50
RRP5257550-35	5250…5750	35	600	5	50
RRP5657500-35	5600…5700	35	550	10	50
RRP9095080-08	9000…9500	8	80	10	50
RRP9095150-18	9000…9500	18	150	10	50
RRP090100120-15	9000…10000	15	120	10	50
RRP3842075-30	3860…4140	29	75	10	50

Table 8.32 Types and characteristics of high-power amplifiers for radars based on GaN by RFHIC

Type	Frequency	Gain factor, dB	Output power, W	Efficiency factor, %	Operating voltage V
RRP102600-10	1026…1034	20	2600	40	25.5
RRP131K0-10	1200…1400	53	1000	45	12.5
RRP291K0-10	2700…3100	60	1000	35	12.5
RRM291K5-10	2700…3100	62	1500	30	12.5
RRP311K0-10	2900…3300	60	1000	35	12.5
RRM27312K0-62	2700…3100	63	2000	30	12.5
RRM52571K0-50	5250…5750	50	1000	25	12.5
RRM9395200-56	9300…9500	56	200	20	50

Thus, recent achievements in the field of technology of creating GaN-based heterostrutures and solid GaN solutions demonstrate the prospects of application of these materials in electronic and optical-electronic devices. Studies and developments in the field of SHF microelectronics associated with expanding the field of application of GaN-based wideband structure transistors to millimeter and submillimeter wavelength range open new possibilities for developers of Russian radar and communication systems.

Table 8.33 Basic characteristics of transformers-rectifiers for radars based on GaN by RFHIC

Type	Frequency, GHz	Output power, W	Gain, dB	Pulse rate, %	Pulse width, μs
RFCR91-XTRM-015SP-200A	9.0…9.2	15	42	10	100
RFCR93-XTRM-015SP-500A	9.0…9.5	15	42		100
RFMR57-CTRM-020SP-500A	5.4…5.9	20	40		50
RFMR31-STRM-200-400B	2.9…3.3	200	53		500
RFMR13-LTRM-250-100B	1.3…1.4	250	54		2000
RFMR13-LTRM-250-200B	1.2…1.4	250	52		2000

Table 8.34 Basic types and characteristics of high-power amplifiers based on GaN by RFHIC

Type	Frequency, MHz	P3dB (P1dB), dBm	Gain factor, dB	Operating voltage, V	Current, A
RWS02520-10	20…512	43	40	28	2.5
RWS02540-10	20…512	46	41	28	3.2
RWS05020-10	20…1000	43	36	28	2.3
RWP03040-10	20…520	46	42	28	3.8
RWP03040-50	20…500	46	39	28	4
RWP03160-10	20…500	52	43	28	11
RWP05020-10	20…1000	43	40	28	2.3
RWP05040-10	20…1000	46	38	28	3.5
RWP06040-10	450…880	45	40	28	3
RWP06040-60	500…1000	46	42	28	4.5
RWP15040-10	500…2500	47	38	32	5.0
RWP15080-10	700…2700	50	53	32	10.0
RWP17050-10	700…2700	47	37	32	4.5
RUP15010-10	500…2500	40	17	28	1
RUP15020-10	500…2500	43	15	28	2
RUP15020-11	500…2500	43	50	30	3.5
RUP15030-10	500…2500	45	13	28	4
RUP15050-10	500…2500	47	13	28	5.5
RUP15050-11	500…2500	47	60	30	7
RUP15050-12	500…2500	47	60	30	7
RWP15020-50	1000…2000	43	29	28	3.6
RNP19040-50	1800…1900	47.5	33	28	3.7
RWP25020-50	2000…3000	44	25	28	2.8
RNP21040-50	2100…2170	47.5	33	28	3.9
RFC042	400…800	–	23	24	0.4

(continued)

Table 8.34 (continued)

Type	Frequency, MHz	P3dB (P1dB), dBm	Gain factor, dB	Operating voltage, V	Current, A
RFC092	800...1000	(30)	23	24	0.4
RFC1G22-24	20...1000	(30)	22	24	0.4
RFC1G21H4-24	20...1000	36	21	24	0.55
RFC1G21H4-24-S	20...1000	36	21	24	0.55
RFW2500H10-28	20...2500	36	17	28	0.7
RWM03060-10	20...520	49	55	28	7
RWM03125-10	20...520	51	55	28	9
RWM03125-20	20...520	51	55	28	9
RUM15040-10	500...2500	46 (Psat)	56	28	5.5
RUM15040-20	500...2500	46 (Psat)	56	28	5.5
RWP15100-R0	500...2500	50	42	33	10
RUM43010-10	2500...6000	40 (Psat)	29	28	2.2
RUM43020-10	2000...6000	43 (Psat)	35	28	4

8.8 HF and SHF Devices by Mini-Circuits

8.8.1 Integrated Monolithic Amplifiers of the VNA Group

Mini-Circuits Laboratory specializes in production of HF and SHF devices [98, 99].

The range of products manufactured by Mini-Circuits is extremely wide and includes the following:

- amplifiers (both monolithic and hybrid) with voltage from 3 to 28 V operating within the range of up to 10 GHz;
- attenuators for 50 and 75 Ohm (two-phase, digital, fixed);
- switches for different numbers of directions (GaAs-based and TTL-controlled);
- adders, slippers with various power values with isolation up to 50 dB;
- mixers for different ranges (from 10 MHz to 10 GHz);
- passive filters (low frequency, bandpass, high frequency) for 50 and 75 Ohm, 0–2.2 GHz;
- voltage controlled oscillators (monolithic, low noise);
- frequency doublers for the range of 5 kHz – 3 GHz;
- signal limiters for the range of 10 kHZ − 900 MHz;
- resistance transformers for up to 1.5 GHz;
- modulators-demodulators, phase detectors and many other devices.

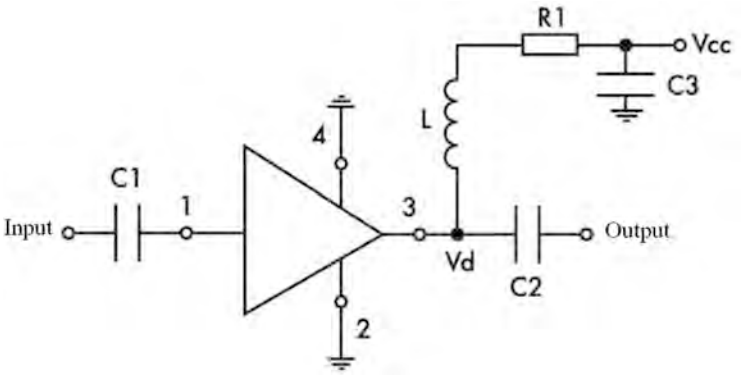

Fig. 8.46 Power supply circuit of most monolithic VHF amplifiers

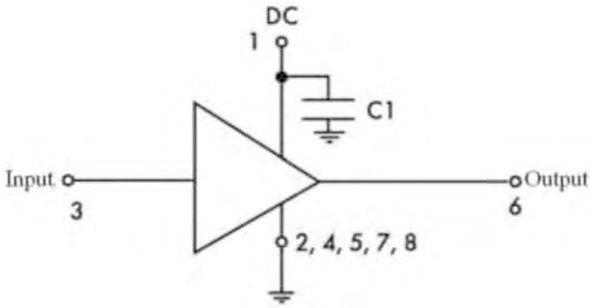

Fig. 8.47 Power supply circuit of a VHF VNA amplifier

Within this section, we will focus on brief description of the most popular Mini-Circuits products – monolithic integrated microwave amplifiers, double balanced mixers based on LTCC technology, as well as frequency mixers and attenuators.

Monolithic high-frequency amplifiers are powered by direct current source. In practice, they are modeled on the basis of a voltage source, a radio frequency choke and a resistor. Additional separating capacitors are installed at the input and output of such amplifiers. All these external elements occupy place, increase the cost and number of components.

Figure 8.46 shows power supply circuit of typical microwave amplifiers. In this case, amplifier output is used for power supply. In order to prevent reduction of the gate factor and output power, total imaginary impedance R1 and L shall be not less than 500 Ohm. Moreover, resonance frequency of the choke shall be higher than its operating frequency.

Monolithic amplifier of the VNA group has independent terminals for supply of feed voltage and frequency (Fig. 8.47). These amplifiers are mostly designed for operation with voltage sources and are not actually burdened by external components. An exception is the separating capacitor C1, capacitance of which shall be within 100 pF – 0.1 mF; upper level of capacitance ensures certain filtration of noises of the voltage source. These amplifiers have cases for surface mounting and 8 pins (Fig. 8.48).

Fig. 8.48 Appearance of a VNA amplifier

Table 8.35 Characteristics of VNA amplifiers

Model	Frequency range	Gain factor, dB	IP3, dBm	Current consumption, mA	Heat resistance, °C/W	Isolation coefficient, dB
VNA-21	0.5–2.5	12	18	33	105	34
VNA-22	0.5–2.5	13	27	80	102	30
VNA-23	0.5–2.5	18	20	32	110	33
VNA-25	0.5–2.5	16	27	85	125	40
VNA-29	0.5–2.6	20	19	35	125	40

VNA amplifiers have such high values of the isolation factor (Table 8.35) that they can be used as active insulators. An important feature of these amplifiers is the fact that they are powered with voltage sources within the range of 2.8–5 V, which makes it possible to use accumulators as power sources.

8.8.2 Double Balanced Mixers of the MCA1 Group

For frequencies under 5 GHz double balanced mixers can be implemented on ferrite basis, which makes them quite small and reliable. For higher frequencies, semiconductors are used as the mixer basis.

Double balanced mixers manufactured with the Blue Cell LTCC technology are distinguished by their low cost and small dimensions. This technology makes it possible to create a multi-level chain based on ceramic substrate strips. Conductive, dielectric and resistive pastes are applied to ceramic plates, which are then baked in a

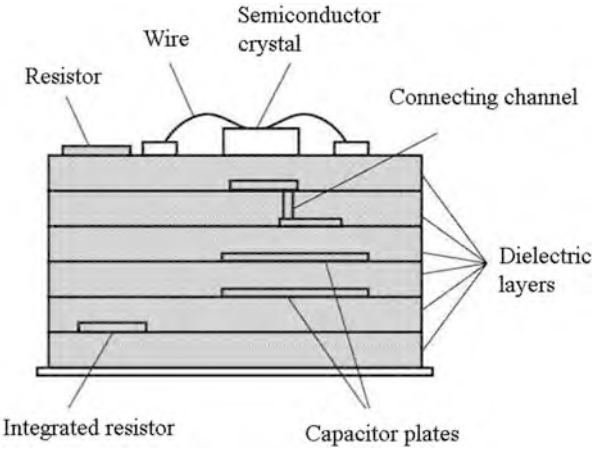

Fig. 8.49 Typical structure of Blue Cell LTCC [2]

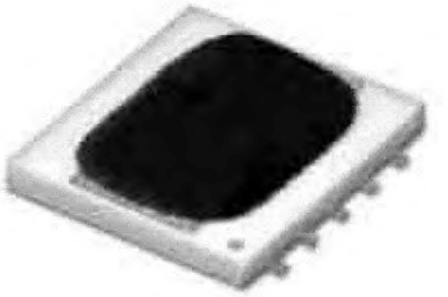

Fig. 8.50 Appearance of mixers of the MCA1 group [2]

special furnace at the temperature of +850 °C into a single multi-layered "cake", sealed and monolithic. Typical Blue Cell LTCC structure is shown in Fig. 8.49 and consists of several dielectric levels, conductors, integrated resistors and capacitors, as well as connecting channels.

High level of integration between elements of this structure helps implement the device in the surface mount package (Fig. 8.50). The height, length and width of the package are 0.065″, 0.3″ and 0.25″ respectively. Temperature stability of ceramic materials used in the Blue Cell LTCC technology significantly simplifies solution to the problem of temperature balance. Such mixers operate within the frequency range of − 55 – 100 °C and can be used in civil or military applications.

Technical characteristics of this group of mixers are given in Table 8.36.

8.8.3 Series of Multi-purpose High-Frequency Amplifiers

With thousands of ready-made and tunable models, Mini-Circuits offers the greatest choice in the world – over 10,000 devices for radio signal processing.

Table 8.36 Characteristic of MCA mixers

Model	Frequency range, MHz		Average conversion losses, dB	Isolation coefficient, dB	
	RF, HF	IF		RF–HF	RF–IF
MCA1-24	3000–2400	DC-700	6.10	40	25
MCA1-24LH	3000–2400	DC-700	6.50	40	11
MCA1-24MH	1000–4200	DC-700	6.1	40	25
MCA1-42	1000–4200	DC-150	6.10	35	20
MCA1-42LH	1000–4200	DC-1500	6.00	38	20
MCA1-42MH	1600–4200	DC-1500	6.20	35	20
MCA1-60	1600–4400	DC-2000	6.30	32	17
	4400–6000	DC-2001	6.20	23	18
MCA1-60LH	1700–4400	DC-2002	6.60	35	17
	4400–6000	DC-2003	6.00	27	21
MCA1-60M	1600–4400	DC-2004	6.90	32	17
	4400–6600	DC-2005	6.00	22	15

Most products of the company are manufactured with the help of the patented LTCC (Low Temperature Co-fired Ceramic) technology, which makes it possible to create devices that are immune to external effects, inexpensive and suitable for special use. High quality of electronic components by Mini-Circuits is confirmed by their operational reliability [99]. The company provides detailed technical information to the developers of equipment using these components.

Mini-Circuits offers HF amplifiers with various combinations of gain, noise factor, coefficients of non-linear distortions and output power, with SMD packages or with pinouts for installation into holes, as well as in the form of modular structures with coaxial connectors. There are the following variants of amplifiers: general use wideband amplifiers, low-noise, pulse amplifiers, amplifiers with wide dynamic range, double amplifiers, amplifiers with adjustable gain, as well as power amplifiers.

Mini-Circuits is distinguished by the wide range of MMIC (Microwave Monolithic Integrated Circuit) developments based on MESFET, GaAs, PHEMT and InGaP technologies. The company provides the developers with reference data and recommendations for application and publishes X-parameters of models for the most popular MMIC types. The coverage of frequency ranges is 0–21 GHz with noise factor of not more than 0.35 dB and power of up to 100 W. Amplifiers by Mini-Circuits are used in such fields as telecommunications, 4G LTE hWCDMA. Moreover, the company can create inexpensive amplifiers based on specific customer requirements.

In order to simplify selection of the amplifier compliant with technical requirements of the customer, Mini-Circuits offers engineers to use their own specialized

Table 8.37 Technical characteristics of new models of attenuators

Series name	Frequency range, GHz	Attenuation, dB	Dissipated power, W	Notes
YAT	0–18	0, 1, 2–9, 10, 12, 15, 20, 30		High precision; package 2 × 2 mm
RCAT	0–20	–	2	High precision; package 2.2 × 2.2 mm
FW	0–12	1, 2–9, 10, 12, 15, 20	1	Solid package structure
BW·Kxx2W44 +	0–40	3, 6, 10, 20	2	High precision
BW·NxxW50 +	0–18	10, 20, 30, 40	50	High precision

patented database YONI. In this program, amplifier search is based on several basic parameters: package type, frequency band, gain factor, reflection losses, noise factor, input and output isolation, output power, output signal power level in the IP3 point, supply voltage. The program will analyze many hundreds of serially produced amplifiers and quickly select a dozen of the most suitable types.

Basic technical characteristics of several new models of amplifiers are presented in Table 8.37. The appearance of amplifiers is shown in Fig. 8.51.

8.8.4 Frequency Mixers

These HF components are used in nearly every radio transmitter or receiver. Many information sources are dedicated to features of circuitry solutions and characteristics of mixers. Detailed review of the products of foreign companies is presented in [100, 101].

Mini-Circuits manufactures frequency mixers of many types: active, passive, with high IP3 value (up to 37 dBm), with suppression of the mirror channel, in sealed packages. The range of working frequencies (RF, LO) is 0.04–20 GHz. LO reference signal power – +3 − +27 dBm.

YONI search program can be used to simplify selection of the mixer. Selection of the required mixer is performed based on several basic parameters: package type; frequencies of signals of RF, LO, IF ports; LO signal power; power level of the input signal in the IP3 point; attenuation between LO-RF, LO-IF ports.

Table 8.38 contains technical characteristics of several new models of frequency mixers. Figure 8.52 shows the appearance of mixers. Table 8.39 shows basic technical characteristics of certain new amplifiers.

Fig. 8.51 Amplifiers: (**a**) CMA-162LN+; (**b**) PMA2-33LN+; (**c**) VNA-28A+; (**d**) TSS-53LNB+; (**e**) PMA4-33GLN+; (**f**) AVM-273HP+; (**g**) ZVE-2W-272+; (**h**) LZY-5+; (**i**) ZHL-100W-352+; (**k**) HPA-272+ [2]

8.8.5 Attenuators of HF and SHF Ranges

Mini-Circuits produces several types of attenuators: fixed, inclusion precision types, as well as voltage- or digital code-controlled. Fixed attenuators can have attenuation values up to 50 dB and operating frequency up to 40 GHz; voltage-controlled attenuators – attenuation values up to 47 dB and operating frequency up to 7 GHz; digitally controlled attenuators – attenuation values up to 35 dB and operating frequency up to 4 GHz.

Technical characteristics of several new models of attenuators are presented in Table 8.3. The appearance of attenuators is shown in Fig. 8.53 [2].

Table 8.38 Technical characteristics of new models of frequency mixers

Model	Frequencies RF, LO, GHz	P_{LO}, dBm	P_{IP3}, dBm	I dB LO-RF	I dB LO-IF	Package type
HJK·251·H+	0.04–0.25	+17	+32	50	45	Package 13 × 10 × 6 mm
RCIR·161LH+	0.08–0.17	+10	+17	58	48	MCS 32, dB, package 22 × 20 × 6 mm
MDB·73H+	2.2–7	+15	–	38	46	WB, DB, package 4 × 4 × 1 mm
LAVI·452VH+	3.2–4.5	+23	+33	36	32	Package 13 × 13 × 5 mm
SM·193H+	7.3–19	+17	+(17–25)	26–32	11–18	WB, DB, package 5 × 5 × 2 mm

Note. P_{L0} – reference signal power; P_{IP3} – output signal power level at IP3 point; I_P – isolation of ports (signal attenuation); DB – double-balanced; MCS – mirror channel suppression; WB – wide frequency band

In conclusion, it should be noted that products by Mini-Circuits occupies the leading positions among high-quality and inexpensive models of electronic components of the radio frequency range. The model range of these components is wide and constantly updated.

8.9 SHF Chips by Hittite Microwave

8.9.1 SHF Chips of Attenuators by Hittite Microwave

One of global leaders in the sphere of microwave electronics is American company Hittite Microwave was established for development and production of analog and superhigh-speed monolythic microwave integrated circuits and modules of radio-frequency, microwave and millimeter wave bands overlapping direct-current frequencies up to 110 GHz for military and civilian usage [102].

Monolythic and hybrid film integrated chips produced by this company using transistors of MESFET, PHEMT, MHEMT and HBT-type based on GaAs, InGaP/GaAs, InP, SiGe.

Functional parts and integrated chips are in die form or mounted in mini surface-mount cases of more than 20 uniform types made with the use of special plastics and ceramics. Some products represent pressurized modules with coaxial SMA-connectors. The corporation adheres to the modern environmental requirements for materials and technologies in accordance with RoHS directive (Restriction of Hazardous Substances Directive) of the European Union and produces RoHS-versions of many its products.

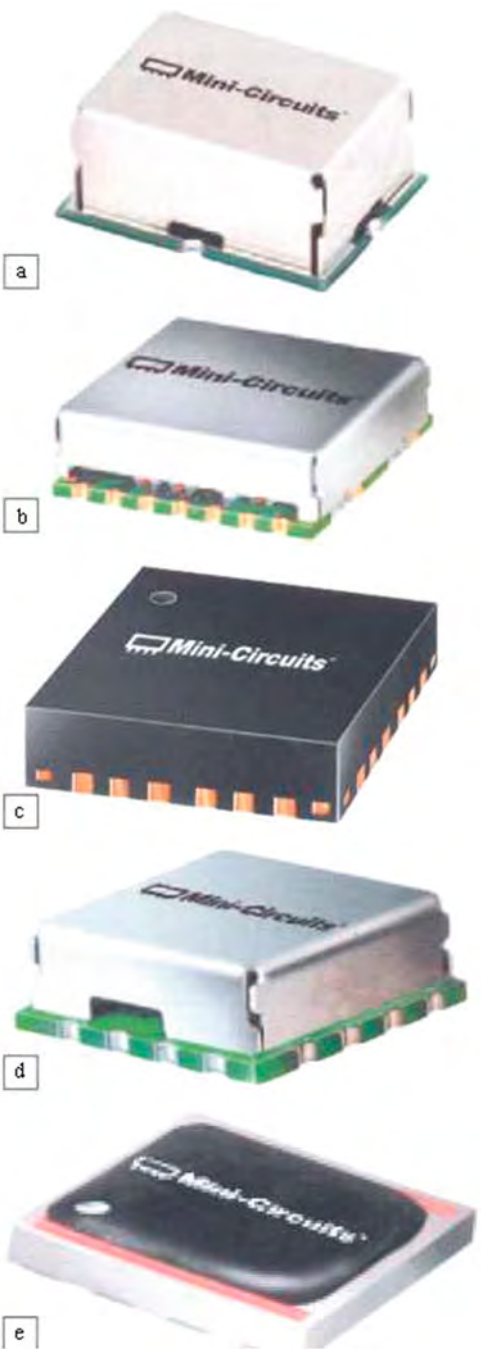

Fig. 8.52 Mixers: (**a**) HJK-251-H+; (**b**) RCIR-161LH+; (**c**) MDB-73H+; (**d**) LAVI-452VH+; (**e**) SIM-193H+ [2]

Table 8.39 Basic technical characteristics of some new amplifiers

Model	Frequency range, GHz	Gain factor, dB/Noise factor, dB	Output power $P_{out\ 1\ dB}$, dBm/Output power $P_{out\ IP3}$, dBm	Package type
CMA·162LN+	0.7–1.6	23/0.5	+20/+30	SM, WDR, LN, package 3 × 3 × 1 mm
PMA2·33LN+	0.4–3	14/0.38	+17/+38	SM, LN, OP, package 2 × 2 × 1 mm
VNA·28A+	0.5–2.5	20/3.7	+8/+18	SM, MMIC, package 6 × 5 mm
TSS·53LNB+	0.5–5	21/1.4	+21/+34	PM, LN, UWB, OP, package 3 × 3 × 1 mm
PMA4·33GLN+	0.7–3	39/0.47	+23/+40	SM, LN, OP, package 4 × 4 mm
AVM·273HP+	13–26.5	13/8.5	+27/+32	SM, UWB, package 5 × 5 mm
ZVE·ZV·272+	0.7–2.7	33/4	+33/+39	CC, IP, OP, package 62 × 50 × 19 mm
LZY·5+	0.0004–0.005	52/-	+50/+58	CC, RC, HP, OP, package 154 × 93 × 25 mm
ZHL·100W·352+	3–3.5	50/8	+50/+55	CC, HP, OP, package 230 × 153 × 30 mm
HPA·272+	0.7–2.7	48/8.5	+50/+55	CC, HP, OP, package 483 × 508 × 132 mm

Note. $P_{out1\ dB}$ – output power at which the gain is reduced by 1 dB; $P_{out\ IP3}$ – the level of output power in the IP3 point; WDR – wide dynamic range of the signal; HP – high power; RC – remote control; OP – overheating protection; CC – coaxial connectors; Mill – low-noise; SM – surface mounting; UWB – ultra-wideband; IP – increased power

A wide range of Hittite components of various purpose includes: ***amplifiers, attenuators, mixers, amplitude and phase modulators, phase-shifters, frequency multipliers and frequency dividers, voltage controlled oscillators, switches, sensors*** and other components intended for equipment of mobile, cell and satellite radio communication, fiber optic communication lines and radars.

Let's consider in more detail the SHF-chips of attenuators with fixed attenuation Resistive attenuators with fixed attenuation as well as with attenuation controlled by analog and digital signals are widely applied in radio sets and measuring instruments. Generally, these are coaxial structures based on T- and inverted-U-shaped structure. Hittite Microwave is one of the few companies of the world that produces subminiature resistive SHF-attenuators represented by integrated chips with a frequency band from direct current up to 50 GHz. In this case, the coaxial structure was abandoned in favor of microstrip structure that is more miniature and suitable for microelectronic design.

Fig. 8.53 Attenuators: (**a**) YAT; (**b**) RCAT; (**c**) FW; (**d**) BW-Kxx2W44+; (**e**) BW-NxxW50+

Developers of radar systems know that T-shaped attenuators are more suitable for building of attenuators with small fixed attenuation of gain factor up to 10 dB because they have narrower range of design resistance of the resistors than that of inverted-U-shaped attenuators. However, in case of greater attenuation, the resistance of the resistor in the vertical part of T-shaped structure becomes too small for integrated form of the attenuator. This disadvantage is easily removed by building of attenuators with two T-shaped parts.

Chips HMC650/651/652/653/654/655/656/657/658 are linear ultra-bandwidth attenuators with fixed attenuation that are based on T-shaped structure. They are designed for operation under conditions of matching with standard 50-Ohm resistance of the generator and load. They are produced with attenuation of 0, 2, 3, 4, 6, 10, 15 and 20 dB. Attenuators are delivered either in mini LP2-cases or in die form as a chip.

The basic parameters of chips of attenuators with fixed attenuation are listed in Table 8.40. Attenuators with attenuation of 10, 15 and 20 dB are implemented in two-step form.

Chips of attenuators with attenuation up to 10 dB are built as single T-shaped attenuators (Fig. 8.54a). Chips of attenuators with attenuation of 10, 15 and 20 dB are built as two-step T-shaped attenuators (Fig. 8.54b). It allows to limit the ratings of vertical resistors using permissible values.

Table 8.40 Parameters of chips of attenuators with fixed attenuation

Type of chip	Bandwidth, GHz	A of gain factor, dB	Gain factor, dB	Quantity of terminals	Dimensions, mm	Package type
HMC650	DC-50	±0.2	0.15	–	17 × 18	Chip
HMC651		±0.3		–	23 × 18	Chip
HMC652		±0.2	2	27	17 × 18	Chip
HMC652LP2E	DC-25	±0.5			–	LP2
HMC653	DC-50	±0.2	3	26	17 × 18	Chip
HMC653LP2E	DC-25	±0.5			–	LP2
HMC654	DC-50	±0.2	4	25	17 × 18	Chip
HMC654LP2E	DC-25	±0.5			–	LP2
HMC655	DC-50	±0.2	6	26	17 × 18	Chip
HMC655LP2	DC-25	±1.5		25	–	LP2
HMC656	DC-50	±0.1	10		17 × 18	Chip
HMC656LP2	DC-25	±1.5			–	LP2
HMC657	DC-50	±0.4	15		17 × 18	Chip
HMC657LP2	DC-25	±2			–	LP2
HMC658	DC-50	±0.5	20		23 × 18	Chip
HMC658LP2	DC-25	±2			–	LP2

Figure 8.55a shows the dependence of gain factor on frequency (in the range of 0 to 50 GHz) for chips with small (2, 3, 4 and 6 dB) attenuation. Figure 8.55b shows the similar dependence diagrams for chips with attenuation of 10, 15 and 20 dB with two-step attenuators.

Developers need to know the dependence of reverse losses on frequency in order to evaluate exactly the attenuator behaviour in the radar station under design. Such dependence diagrams are given in the manufacturer's descriptions of chips. For example, dependence diagrams for one-step attenuators are shown in Fig. 8.56.

Generally, chips of attenuators are designed for connection between two 50-Ohm transmission lines in the impedance matching mode. As shown in Fig. 8.57 It is technologically implemented by means of gold wires.

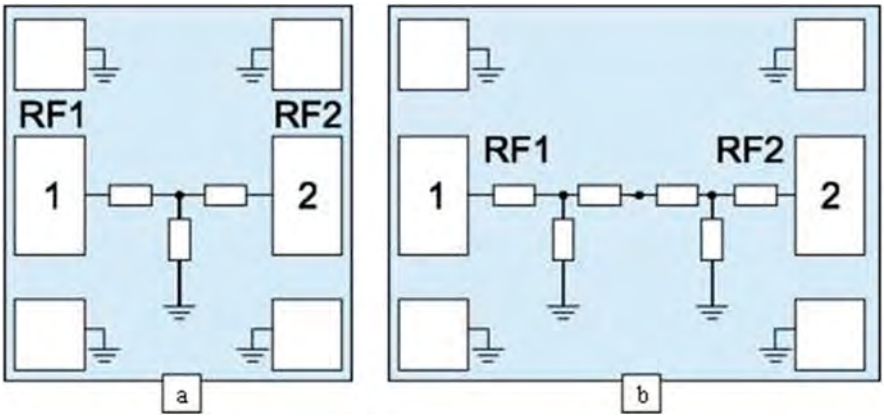

Fig. 8.54 Typical functional diagram: (**a**) microcircuits of a single T-shaped attenuator; (**b**) microcircuits with two T-shaped attenuators

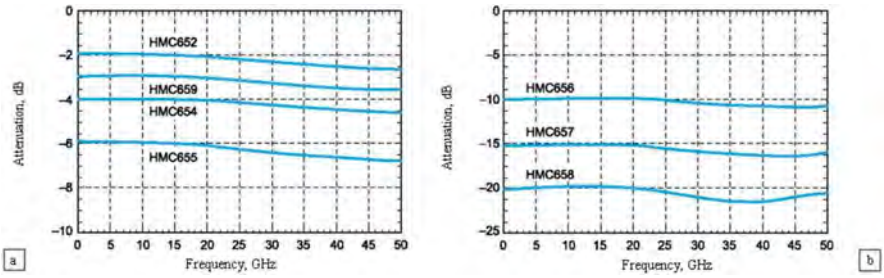

Fig. 8.55 Attenuation-frequency dependence: (**a**) one-step attenuators; (**b**) two-step attenuators

8.9.1.1 Standard Attenuator Chips with Analog Control

Hittite Microwave produces a series of attenuators with analog voltage control attenuation (Analog VVA). They are designed on inverted-U-shaped circuits with a variable horizontal resistor. Basic technical specifications of such attenuators are listed in Table 8.41 [2].

Typical mini surface-mount package of chip of attenuator with adjustable attenuation. Such package provides small parasitic inductance of terminals. Functional diagram of chip HMC346 is illustrated in Fig. 8.58. The chip contains one controlled resistor and implements U-shaped circuit of the attenuator. It should be emphasized that it is the way how most of attenuators are implemented.

Figure 8.59 shows the typical attenuation-frequency dependence for chip HMC346. Generally, these diagrams take the form of horizontal lines but in case of greater attenuations, the characteristics are no longer uniform.

Figure 8.60 shows the general view of printed circuit board with mounted in its middle the chip HMC346 of attenuator with adjustable attenuation. It should be

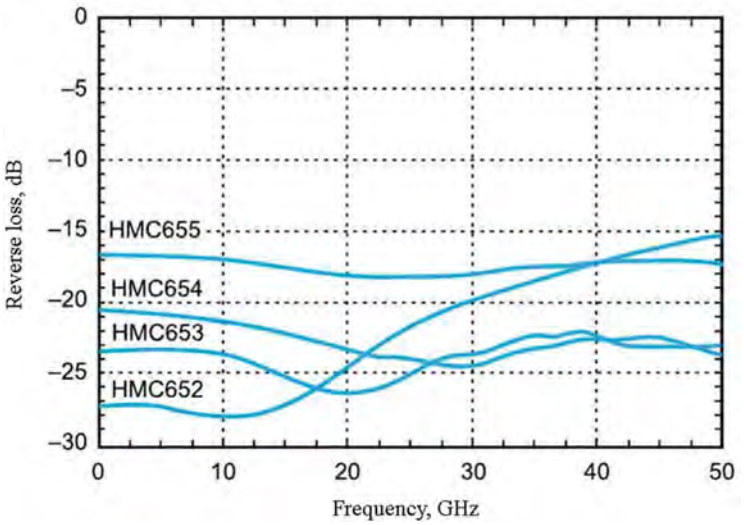

Fig. 8.56 Dependence of reverse losses of one-step attenuators on frequency

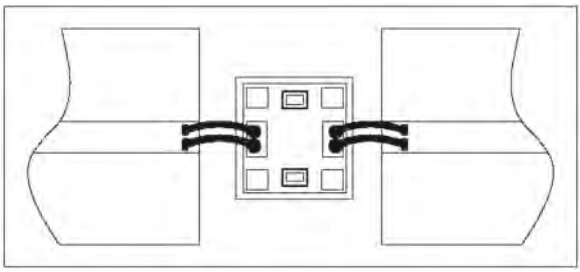

Fig. 8.57 The standard connection of attenuator chip between two 50-Ohm transmission lines

noted that the upper part of the chip contains a microstrip line segment similar to the specified line segments connecting the attenuator chip. It is used to evaluate the line attenuation without attenuator chip that is practically used during calibration of attenuator chips. Connectors J1 and J2 are mini coaxial 50-Ohm connectors of PCB type.

8.9.1.2 Attenuator Chips with Digital Control

For modern radar stations, it is necessary to use SHF-chips of controlled attenuators with digital control that represent a set of attenuators with fixed attenuation switched-over by means of special digital control circuit. Generally, the bit capacity of a control digital signal is from 1 to 7 bits. It determines the range of attenuation variation. For example, 6-bit chip HMC424 has a DC frequency bandwidth up to

Table 8.41 Basic parameters of attenuators of Analog VVA type

Chip	Bandwidth, GHz	Losses, dB	Gain factor, dB	II3, dBm	Control voltage, V	Package type
HMC-VVD102	17–27	1.5	0–22	17	−4... +4	Chip
HMC-VVD104	70–86	2	0–14	–	−5... +5	
HMC-VVD106	36–50	1.5	0–22	17	0/+4	
HMC346	DC-20	2.2	0–25	10	0. −3	
HMC346C8	DC-8	2	0–30			C8
HMC346G8						G8, H
HMC346LC3B	DC-18	1.5				LC3B
HMC346LP3	DC-14	2				LP3
HMC346MS8G	DC-8	1.5	0–32			MS8G
HMC473MS8	0.45–2.2	1.9	0–48	20	0. +3	MS8
HMC712	5–30	2.5	0–30	32	0. −3	Chip
HMC712LP3CE	5–26.5	3.5	0–28			LP3C
HMC812LC4	5–30	2	0–30	28		LC4
HMC973LP3E	0.5–6	2.5	0–26	35	0. +5	LP3
HMC985	0–50	3	0–35	33	0. −3	Chip

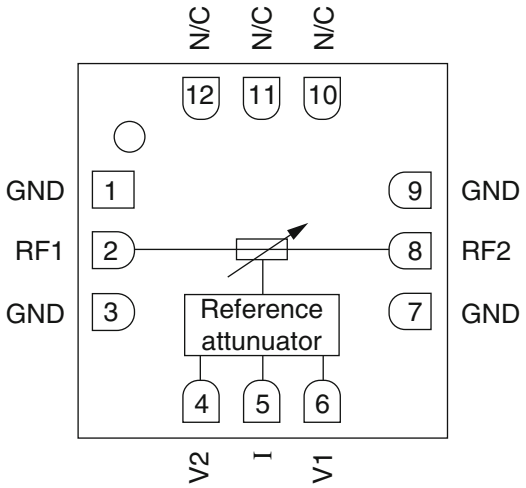

Fig. 8.58 Simplified functional diagram of chip HMC346

13 GHz, reverse losses of 4 dB and attenuation adjustment from 0.5 to 31.5 dB. The chip is in die form, power is 5 V.

Chip HMC939 is distinguished by the highest operating frequencies from 0.1 to 50 GHz. It is a 5-bit digital attenuator based on GaAs-technology. The chip contains a set of attenuators with attenuation of 1, 2, 4, 8, 16 dB, the switching of which results in attenuation up to 31 dB with resolution of 1 dB. The chip crystal is 2.36 × 1.02 × 0.1 mm in size. The functional diagram of the chip is illustrated in Fig. 8.61.

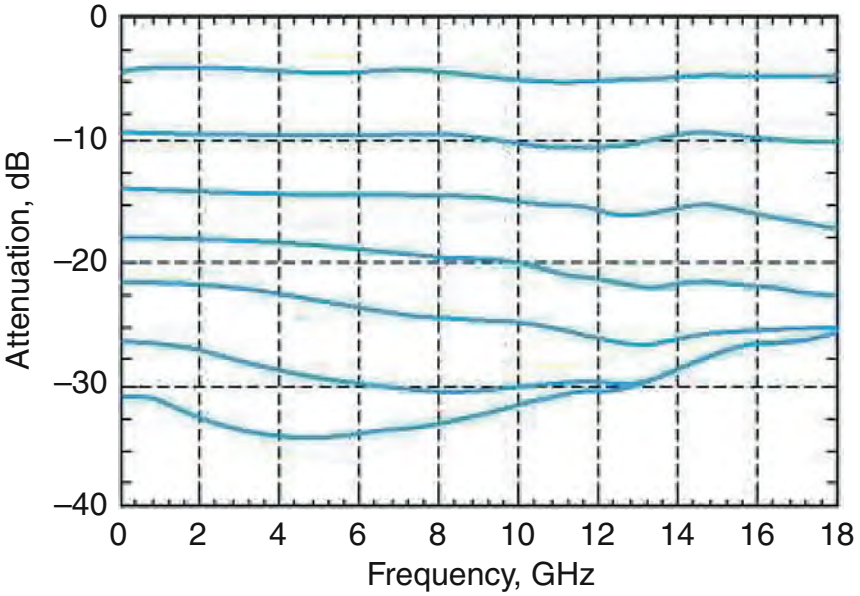

Fig. 8.59 Typical attenuation-frequency dependence for chip HMC346

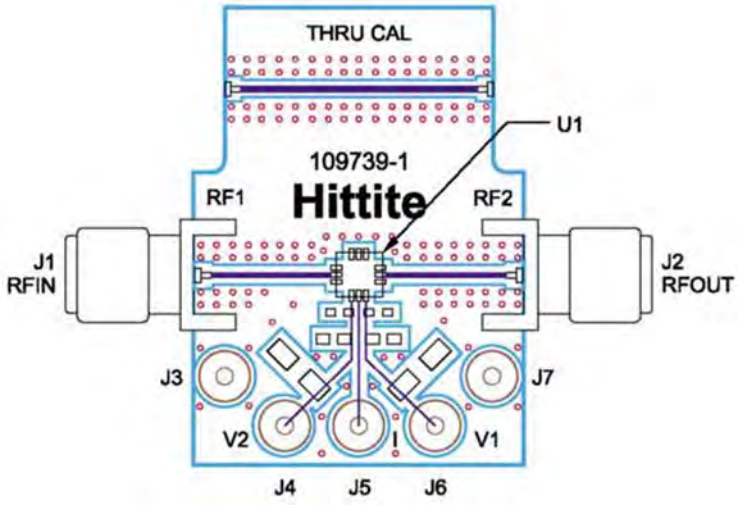

Fig. 8.60 General view of printed circuit board with mounted in its middle the chip of attenuator with adjustable attenuation [2]

Typical attenuation-frequency dependence at difference levels of digital control signal is illustrated in Fig. 8.62.

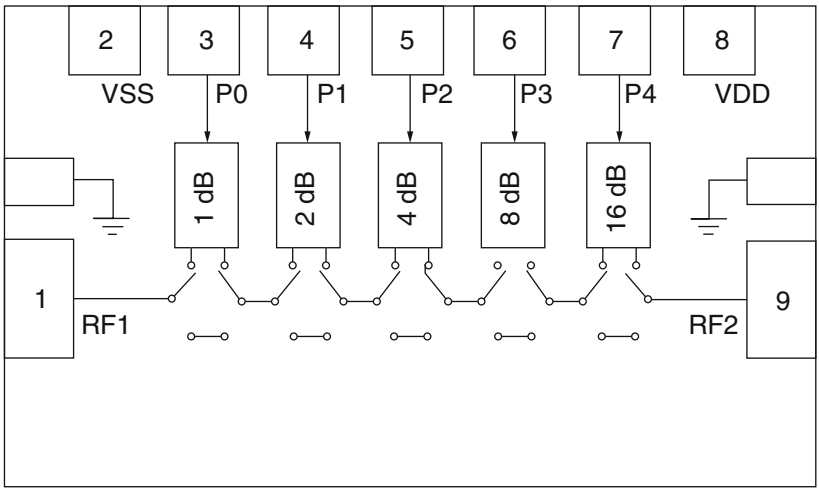

Fig. 8.61 Simplified functional diagram of chip HMC939

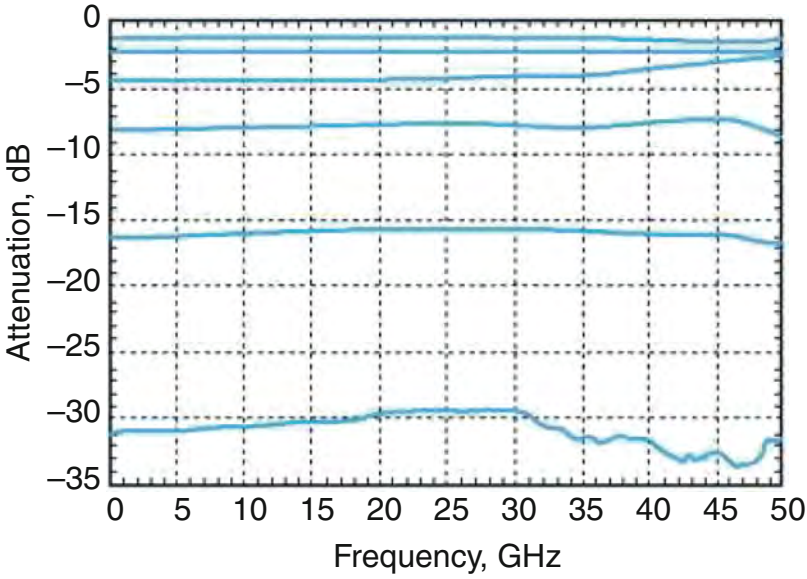

Fig. 8.62 Typical attenuation-frequency dependence at difference levels of digital control signal

1-bit chips (commutated attenuators) have a special place among digital attenuators. So, Fig. 8.63 shows the schematic circuit diagram of commutated attenuator with chip HMC800LP3E.

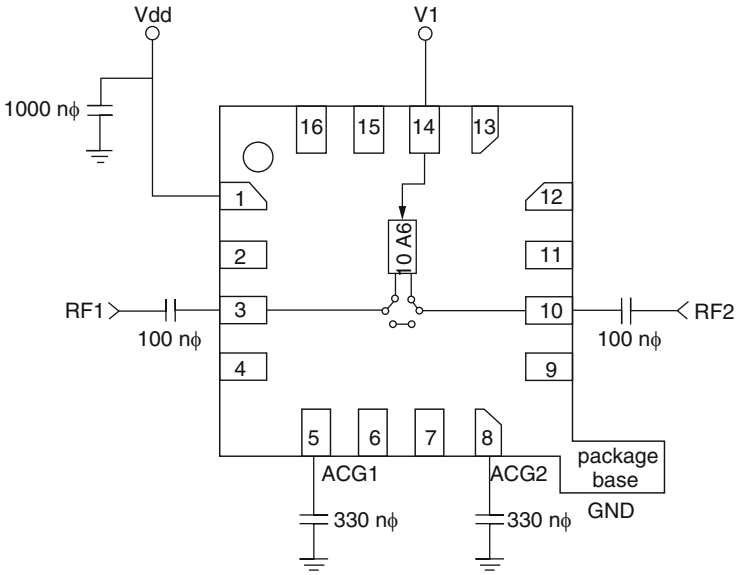

Fig. 8.63 Schematic connection circuit diagram of 1-bit digital attenuator – chip HMC800LP3E

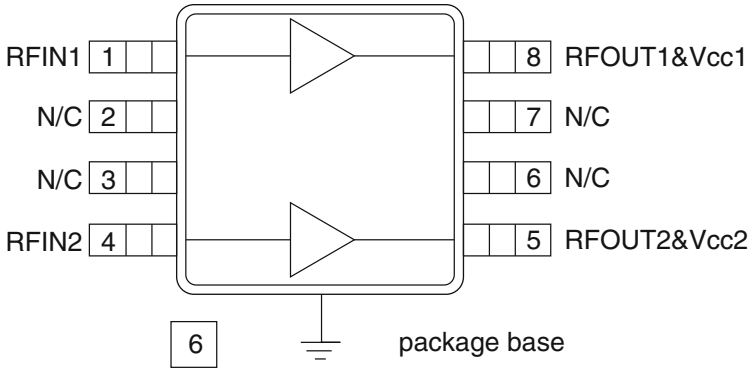

Fig. 8.64 The functional diagram of chip HMC471MS8G/HMC471MS8GE

8.9.1.3 SHF and Ultra-Wideband Amplifiers with Fixed Gain

Here, first of all, it is necessary to consider chip HMC471MS8G/HMC471MS8GE. It is a typical two-channel wideband dual amplifier based on SHF heterotransition germanium silicon transistors. The chip is placed in mini package M28G with low-inductance beam leads (Fig. 8.64). Here, each channel has a bandwidth from 0 to 5 GHz when a gain factor of 20 dB and the maximum output signal of 20 dBm. Hittite company produces a wide range of such chips with different parameters.

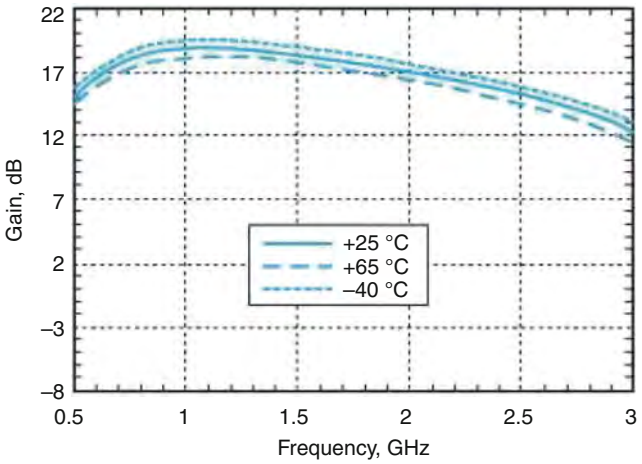

Fig. 8.65 Typical dependence of gain factor on the operating frequency and temperature of each channel of chip HMC471MS8G/HMC471MS8GE

Fig. 8.66 Typical dependence of the maximum output power in the first harmonic of sinewave on frequency and temperature for chip HMC471MS8G/HMC471MS8GE

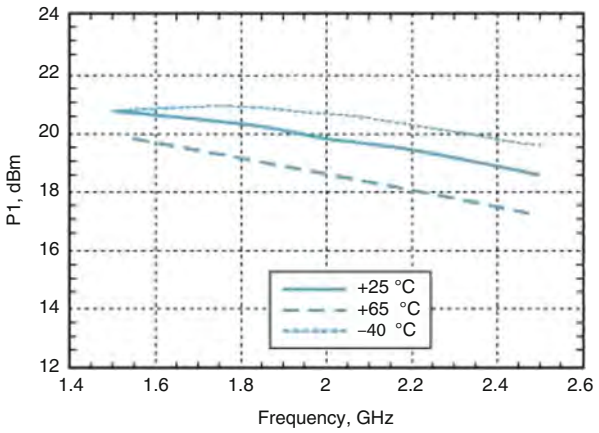

Figure 8.64 shows that amplifiers of both channels are not differential and have one input and one output. Actually, each channel of this chip represents a compound transistor with open output. Such design of a circuit provides the flattest amplitude-frequency response with zero low-frequency cutoff but there is stable offset voltage set by external circuits in input and output.

Typical dependence of this chip gain factor on the operating frequency for three values of temperature is illustrated in Fig. 8.65. It is not difficult to see that temperature stability of gain factor is rather higher that results from application of transistors on wide-band-gap semiconductive materials.

Figure 8.66 shows the dependence of the maximum output power in the first harmonic of sinewave on frequency and three values of ambient temperature.

Two channels in this chip allows to form the wideband balanced power amplifiers with lower level of the third harmonic of output signal and increased power of output signal. Typical circuit of this amplifier is illustrated in Fig. 8.67.

Figure 8.68 shows the general view of printed circuit board of balanced amplifier based on chip HMC471MS8G/HMC471MS8GE that is built on packageless components with leads in the form of thin gold wires.

The maximum output power of such amplifier depends on the power supply voltage value. The firm offers a row of amplifiers with frequencies up to 86 GHz and with a power up to 2 W.

SHF-amplifier-driver HMC-AUH256 (Fig. 8.69) has frequency band from 17.5 to 41 GHz and it is based on gallium-arsenide (GaAs) field-effect transistors with Schottky barriers as a gate. This circuit has a gain factor of 21 dB, the maximum output power of + 20 dBm, power supply voltage of +5 V, and consumption current up to 295 mA. Frequency-gain factor dependence is shown in Fig. 8.70.

Like many key producers, Hittite Microwave company produces a series of ***wideband and ultraband small-signal amplifiers with standardized noise coefficient***. There is a common pattern: the wider bandwidth of amplified frequencies, the less gain reached. Devices with reactive circuits of impedance matching (total

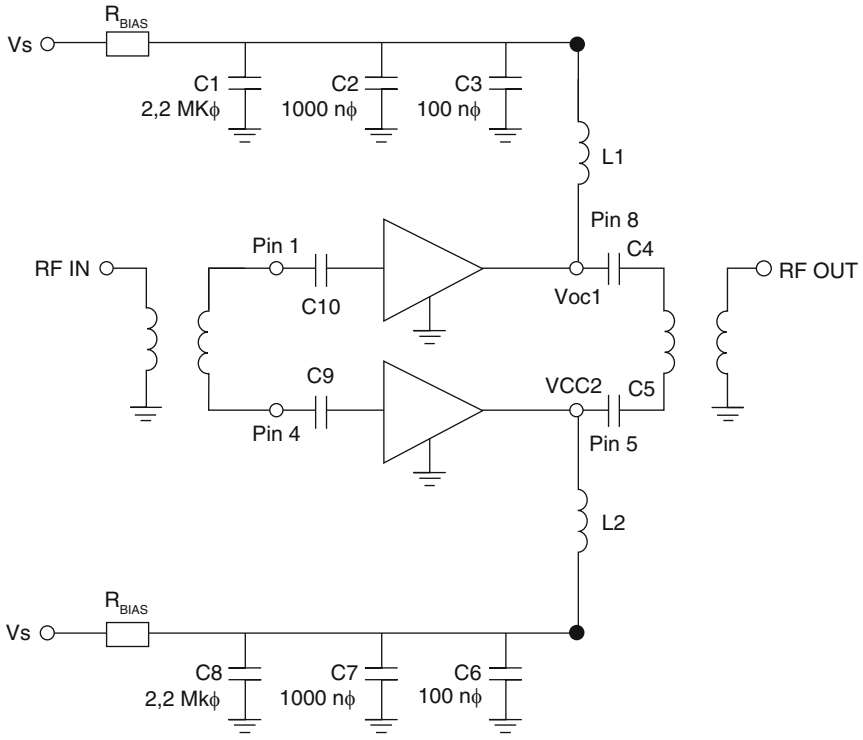

Fig. 8.67 Typical recommended circuit of balanced amplifier based on chip HMC471MS8G/HMC471MS8GE [2]

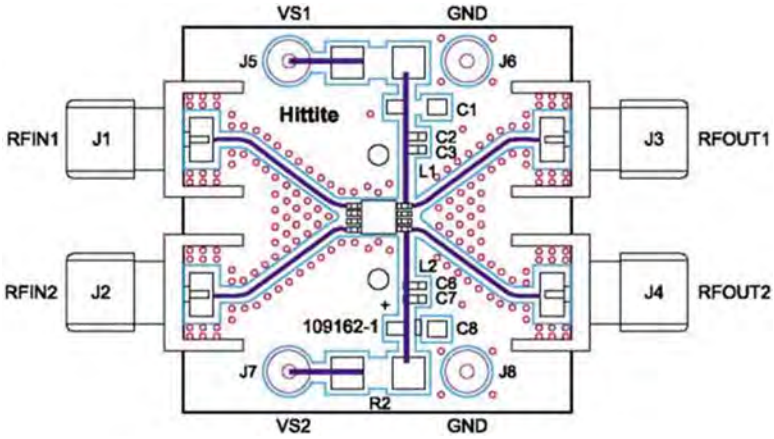

Fig. 8.68 The general view of printed circuit board of balanced amplifier based on chip HMC471MS8G/HMC471MS8GE [2]

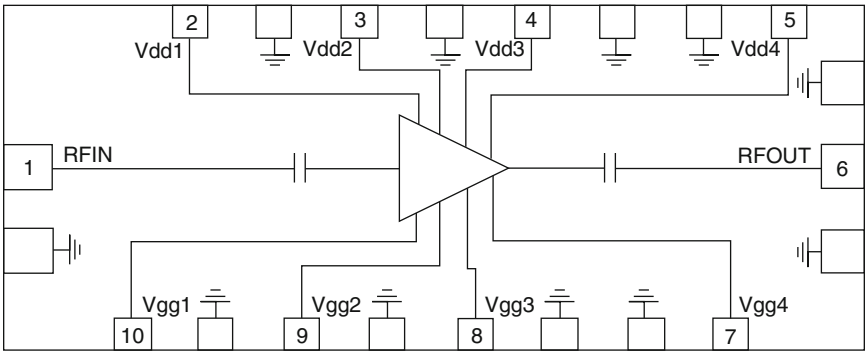

Fig. 8.69 Simplified structural diagram of SHF-amplifier-driver HMC-AUH256

resistance) of input and output with their circuits included in amplifier have the maximum gain. Developers of transmit-receive modules for radar stations attach importance to the fact that ultra-wideband amplifiers are characterized with detailed organization of connection of the chip input and output to their terminals and HF-connectors (along with band broadening). Generally, the system of s-parameters is used for description of such chips.

Figure 8.71 illustrates the functional diagram of SHF-chip HMC-AUH320 with bandwidth of amplified frequencies from 71 to 86 GHz when small-signal gain factor is 15 dB. The maximum output power of this circuit is 15 dBm.

Frequency-gain factor dependence of chip HMC-AUH320 is shown in Fig. 8.72. As we can see, non-uniformity of this dependence in this operating frequency band doesn't exceed 3 dB.

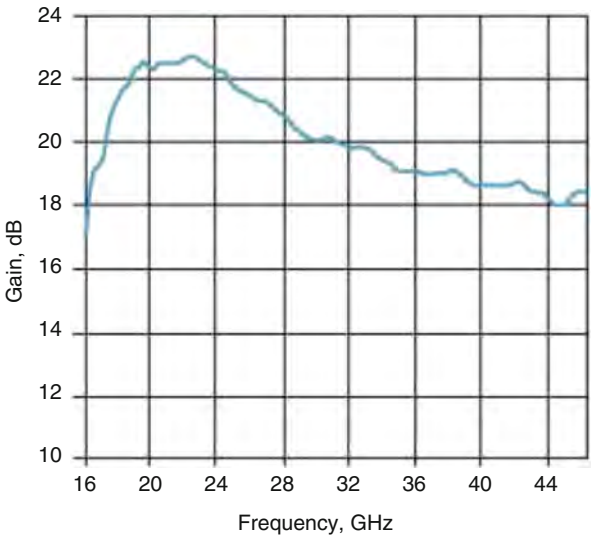

Fig. 8.70 Typical gain factor-frequency dependence of amplifier-driver HMC-AUH256

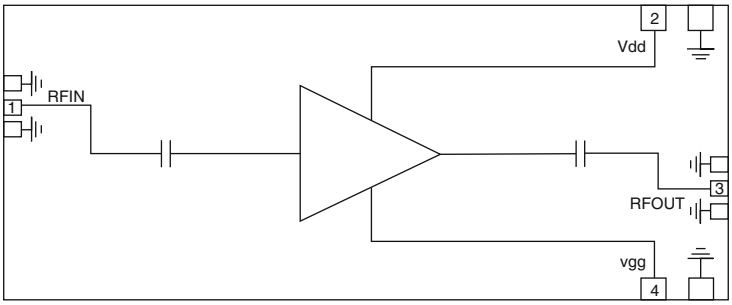

Fig. 8.71 Simplified functional diagram of SHF-chip HMC-AUH320

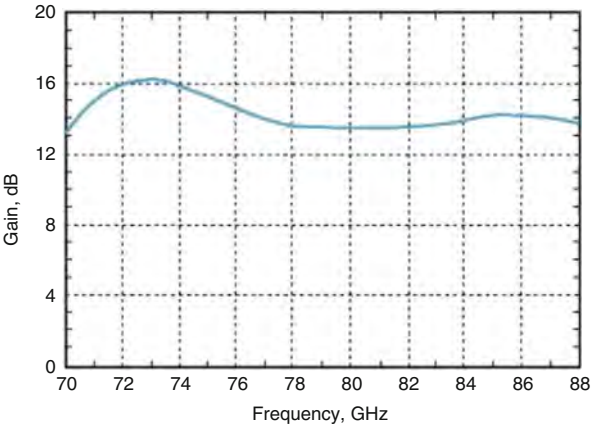

Fig. 8.72 Typical gain factor-frequency dependence of chip HMC-AUH320

The developers have to optimize accurately the structure and scratch their head over the choice of materials applied in the most of ultra-wideband amplifiers with bandwidth of a few units or dozens of GHz. Signal circuits are usually designed as matching and 50- or 75-Ohm circuits. In this case, all power-supply circuits should have blocking circuits (for example, by means of capacitors with very low inductance of leads).

One more ultra-wideband chip HMC-AUH232 (Fig. 8.73) belonging to Wideband class has very wide bandwidth of amplified frequencies (from DC voltage up to 43 GHz) when small-signal gain factor is 12 dB.

Typical amplitude-frequency response of chip AUH232 is illustrated in Fig. 8.74a; dependence of noise factor on operating frequency is shown in Fig. 8.74b.

Analysis and measurement of characteristics of above-described SHF integrated chip are the practical issues for developers. These are the so-called "eye" circuits are used for control of wideband amplifiers. Ultra-wideband digital storage oscilloscopes made by Agilent, Tektronix or LeCroy are used for building of such circuits [103, 104].

Figure 8.75 shows a typical example of circuit of ultra-wideband amplifier based on chip HMC-AUH232 that is the most widely used by developers.

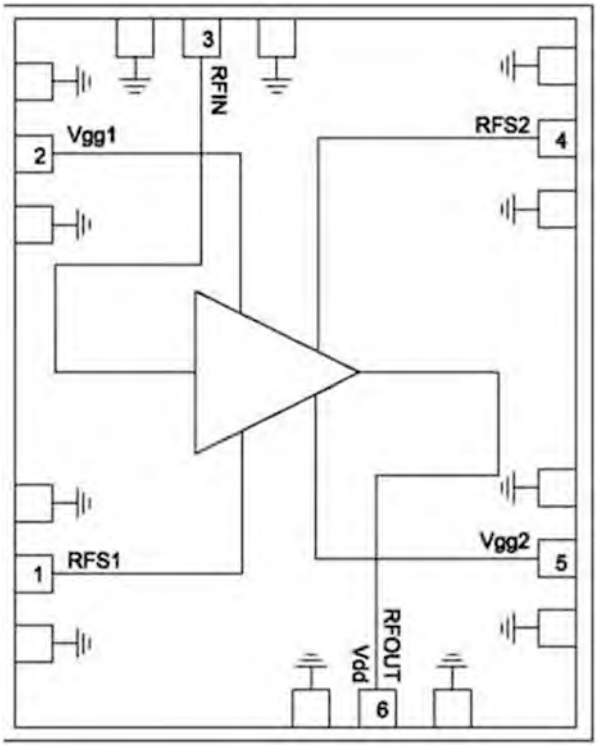

Fig. 8.73 Standard structure of ultra-wideband chip HMC-AUH23

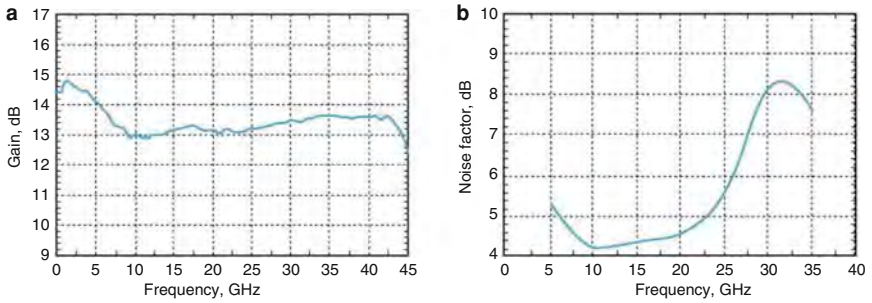

Fig. 8.74 Typical dependences for chip HMC-AUH232: (**a**) gain factor-frequency dependence; (**b**) noise factor-frequency dependence

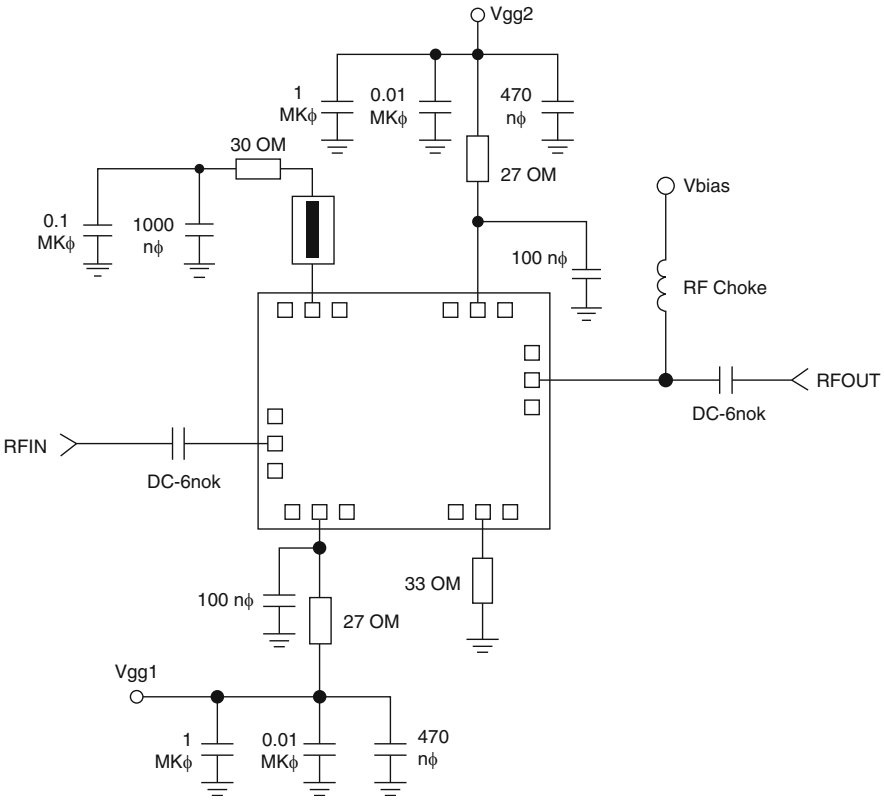

Fig. 8.75 Typical example of electric circuit of ultra-wideband amplifier based on chip HMC-AUH232

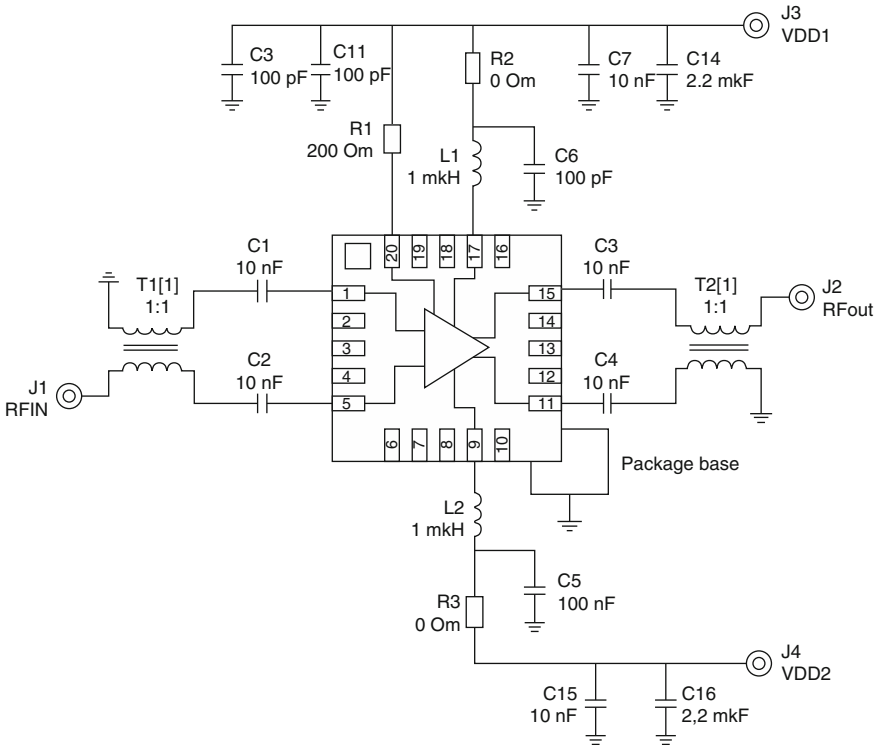

Fig. 8.76 Typical circuit of building of wideband amplifier based on chip HMC770LP4BE with differential input [2]

Compared to standard chips of operating amplifiers, the wideband and ultra-wideband chips rarely contains differential stages since they have more complex circuit and narrower width of amplified frequencies. Figure 8.76 shows a typical example of the most widely used circuit of ultra-wideband amplifier based on chip with differential input. Frequency band of this circuit is from 0.04 to 1 GHz, small-signal gain factor is 15 dB. The chip has a low noise level: noise factor NF is only 2.75 dB.

Generally, the system of s-parameters is used for more complete assessment of behavioral features of such attenuator chips, as well as other SHF-devices.

So, Fig. 8.77 shows the typical s-parameters-frequency dependence for differential amplifier chip HMC770LP4BE.

Developers of radar systems can find more details and s-parameters of chips made by Hittite Microwave corporation in Data Sheet documentation available on website of this corporation (usually in PDF-format).

It should be noted that Hittite Microwave corporation is one of global companies producing a wide range of SHF-amplifiers with a gain (transmission) factor

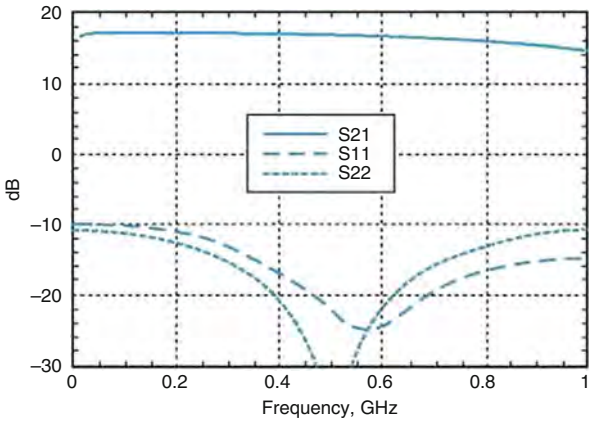

Fig. 8.77 Typical dependence of transmission factor on return losses (s-parameters) for chips of differential amplifier HMC770LP4BE

Table 8.42 Basic specifications of analogue control amplifiers

Chip	Bandwidth, GHz	Gain factor, dB	NF, dB	OIP3, dBm	P1, dBm	Power, V/mA
HMC287MS8	2.3–2.5	–9–21	2.5	7	3	3/9
HMC694	6–17	1–23	5	30	22	5/150
HMC694LP4	6–17	0–23	6	30	22	5/175
HMC972LP5E	0.5–6	–35–15	7.5	28	21	3/90

controlled by electronic means. Such amplifiers are widely used in wireless systems (WiBro, WIMAX, 4G), mobile and cellular telephony, testing and measuring instruments.

Amplifiers with adjusted gain belong to class of ICs Automatic Gain Control (for system with automatic gain control) and Variable Gain Amplifiers. The first class includes the popular model of amplifiers HMC992LP5E with relatively low frequency band: from 0.05 to 0.8 GHz. In turn, amplifiers belonging to class of Variable Gain Amplifiers are divided into amplifiers controlled by analog signal and controlled by digital signal. The basic specifications of analogue control amplifiers are listed in Table 8.42.

Chip HMC287MS8 is of particular note: it has a frequency band of 0.2 GHz and a dynamic range of gain drift of 30 dB at amplified signal medium frequency of 2.4 GHz. This chip is designed in package MS8 and has low power consumption: consumption current is only 9 mA at power-supply voltage of 3 V (see Table 8.42).

Functional circuit HMC287MS8 (Fig. 8.78) is very simple and contains only one SHF-amplifier with an adjusted gain factor and built-in coupling capacitors.

Typical gain factor-operating frequency dependence at deferent control voltage for this chip is illustrated in Fig. 8.79a. It is qualitatively different for various control voltages: when VCTRL is close to 0, the gain factor slowly drops while the frequency is increasing; and when VCTRL is more than 1 V, the gain factor becomes greater while the frequency is increasing.

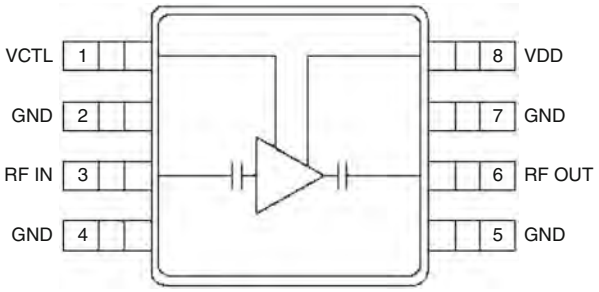

Fig. 8.78 Functional structure of chip HMC287MS8

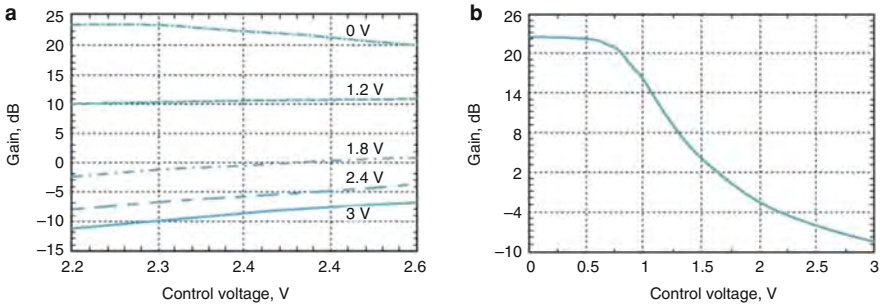

Fig. 8.79 The gain factor dependence for chip HMC287MS8: (**a**) dependence on frequency at deferent control voltage; (**b**) dependence on control voltage

Typical gain factor-operating frequency dependence at deferent control voltage for chip HMC287MS8 is illustrated in Fig. 8.79b. When VCTRL is changing from 0 to 1.2 V, the gain factor remains almost unchanged, and then it decreases according to non-linear law.

Functional circuit of more wideband chip (bandwidth from 4 to 17 GHz) is illustrated in Fig. 8.80. According to specification, it is similar to the circuit as previously described for chip HMC287MS8. Bandwidth expansion up to 6–17 GHz results in significant increase of consumed power: consumption current is 175 mA at power-supply voltage of 5 V. Parameters of chip HMC287MS8 are very similar to parameters of other chip HMC694.

Typical gain factor-frequency dependence at deferent control voltage for chip HMC694LP4 is shown in Fig. 8.81. The graphs have quite noticeable irregularity (especially at frequency lower than 7 GHz) resulted from weak resonance.

It may be noted that chip HMC972LP5E positions itself at the intersection between the chips described above in regards to bandwidth (from 0.5 to 6 GHz). Consequently, it is applicable to consumed power: power-supply voltage is 5 V at consumption current of 90 mA.

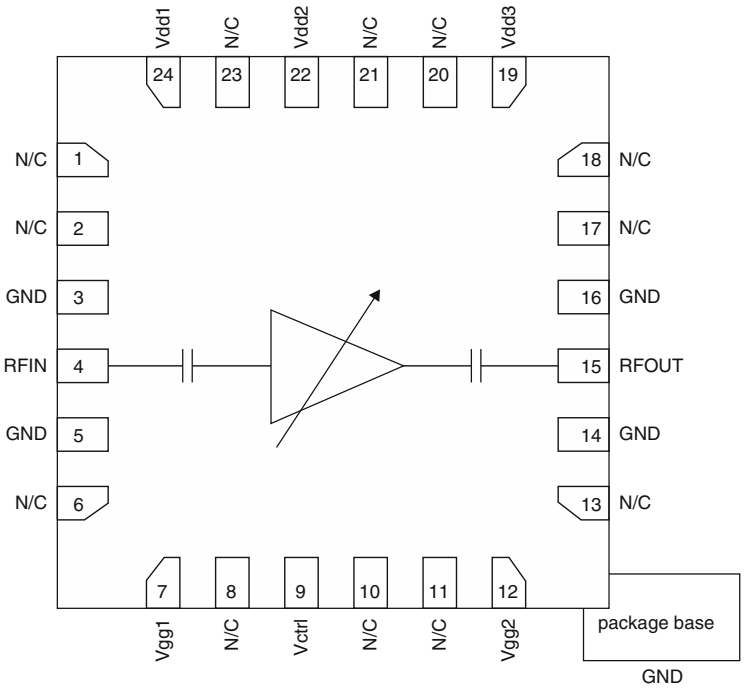

Fig. 8.80 Simplified functional diagram of SHF-chip HMC694LP4

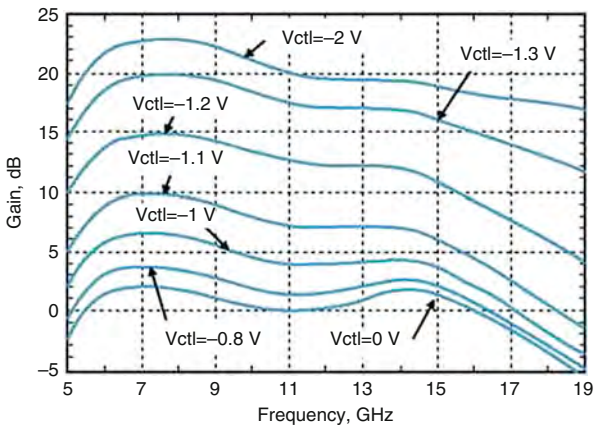

Fig. 8.81 Typical gain factor-operating frequency dependence at deferent control voltage for chip HMC694LP4

Finally, it is worth noting one more type of SHF-devices such as amplifiers with digital control of gain factor. This type of wideband SHF-amplifiers (chips with digital control of gain parameters) differs with circuit-based features, notably the control circuit is characterized by number of bits and control type (with parallel interface P and serial interface S). The rest of parameters of digitally controlled

Table 8.43 The basic parameters of digitally controlled amplifiers

Chip	Bandwidth, GHz	Gain factor, dB	NF, dB	Interface, bit/type	OIP3, dBm	P1, dBm	Power supply, V/MA
HMC625LP5	DC-6	–13.5–18		6/S, P	33	19	5/88
HMC626LP	DC-1	8.5–40		6/P	36	20	5/176
HMC694LP4	0.07-4	–19.5–12		7/S, P	33	152	5/150
HMC960LP4E	DC-1	0–40		6.3/S, P	30	13	5/70

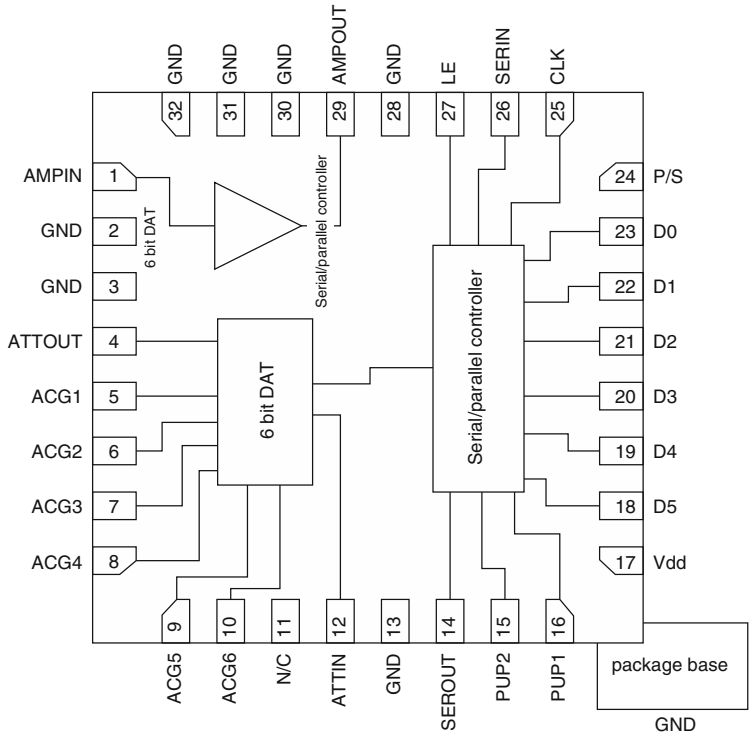

Fig. 8.82 The functional diagram of chip HMC625LP5

amplifiers are the same as parameters of analog controlled amplifiers. Table 8.43 specifies the parameters of four digitally controlled amplifiers that are most widely used:

Figure 8.82 shows the functional diagram of chip that is a digitally-controlled amplifier HMC625LP5. This ultra-wideband chip has a bandwidth of amplified DC frequencies up to 6 GHz. The gain factor-frequency dependence at deferent control voltage for chip HMC625LP5 is shown in Fig. 8.83.

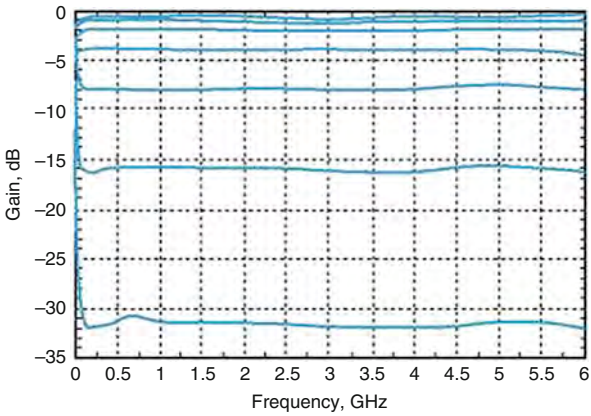

Fig. 8.83 Typical gain factor-operating frequency dependence at deferent control voltage for chip HMC625LP5

8.9.2 Monolithic SHF Microcircuits of Full Synthesizers by Hittite Microwave

8.9.2.1 Monolithic Chips PLL of SHF Synthesizers

For production of monolithic integrated chips of SHF synthesizers, the company uses the modern element base of heterotransition superhigh-speed transistors based on the wide-band gap semiconductive materials [105].

Frequency synthesizers of these devices are implemented on one-two monolithic chips of very small size with the minimum quantity of external packageless components that enables their usage not only in radar systems but also in modern devices of mobile communication.

The company produces a series of chips of quite completed synthesizers in a very high frequency range of frequencies which are one or another implementation of the main classical circuit of a synthesizer [106, 107]. The ratio of frequencies (of output and frequency reference signals) can be either integer or fractionally rational values. Let's consider in more detail the monolithic chips that allows to design the quite completed frequency synthesizers in the widest frequency range using only 2–3 chips.

The basic characteristics of chips of microwave band synthesizers (Microwave) are listed in Table 8.44 [2].

In additional to usual parameters, they are characterized by jitter (timing instability). Jitter is measured in femtoseconds and degree portions. Generally, its root-mean-square value (RMS) is given in fractionally rational mode of chip operation.

The typical example of this chip class is chip HMC807LP6CE (Fig. 8.84) with a frequency range 12.4 to 13.4 GHz. Compared to the other chips, it has the highest frequency, slightly worse phase noise and the smallest power of output signal. Nevertheless, it is quite sufficient for most part of applications. This chip has the minimum jitter.

Table 8.44 Chips of microwave band synthesizers made by Hittite Microwave company

Type of chip	Frequency, GHz	Phase noise, dBc/Hz	Pout, dBm	Jitter, fsec/
HMC764LP6CE	7.3–8.2	−101/−140	15	196/0.58
HMC765LP6CE	7.8–8.8	−101/−140	13	193/0.61
HMC783LP6CE	11.5–12.5	−99/−134	10	181/0.81
HMC807LP6CE	12.4–13.4	−98/−132	8	175/0.84

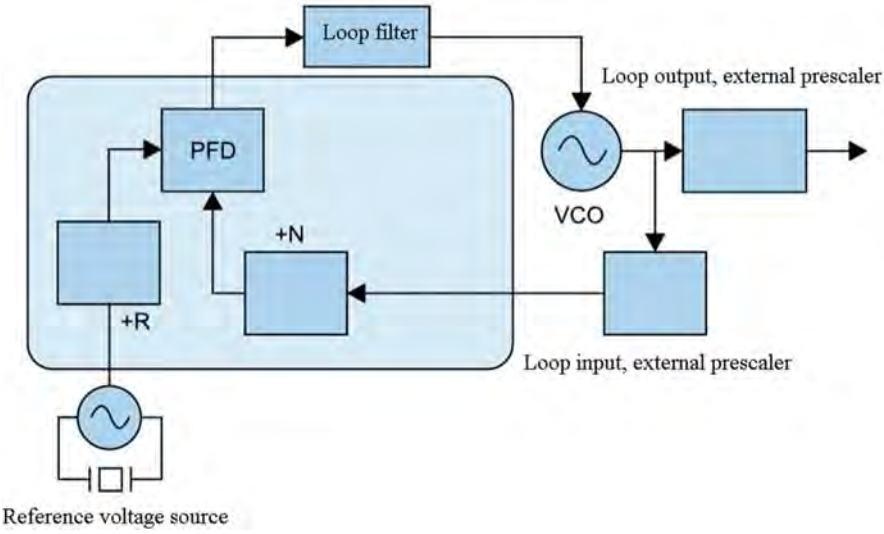

Fig. 8.84 Simplified functional diagram of SHF-chip HMC807LP6CE

The phase noise depends on the synthesizer operation mode. It is lower when one frequency divider is used (the other frequency divider is not used and that's why it doesn't make noise, its dividing ratio is taken to be equal to 1), as well as the integer mode is implemented. Figure 8.85 shows the dependence of SSB phase noise on frequency offset in relation to the central frequency in single-side band measurement mode during the integer operation of the synthesizer and at different signal frequencies. Figure 8.86 shows the dependency at different ambient temperatures (and at a frequency of 12.9 GHz).

In case of operation with two frequency dividers in fractionally rational mode, the SSB phase noise increases since two frequency dividers make noise. Figure 8.87 shows the dependence of SSB phase noise on frequency offset when signal frequency is equal to 12.902 GHz in fractionally rational mode.

Of course, such chips are characterized by many other parameters relating to the built-in VCO. Their detailed description is given in documentation that is available on the website of Hittite Microwave company [105].

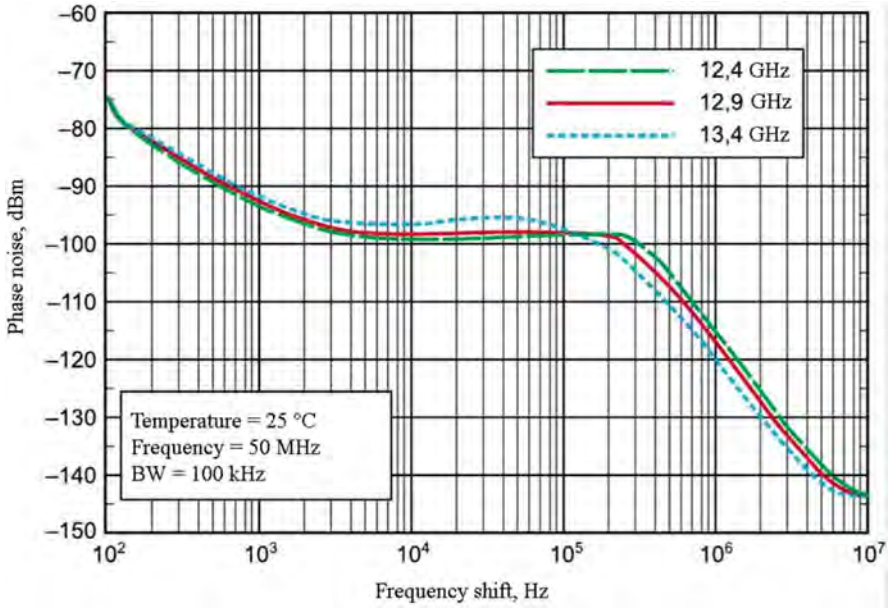

Fig. 8.85 The dependence of SSB phase noise on frequency offset in the integer mode at different signal frequencies

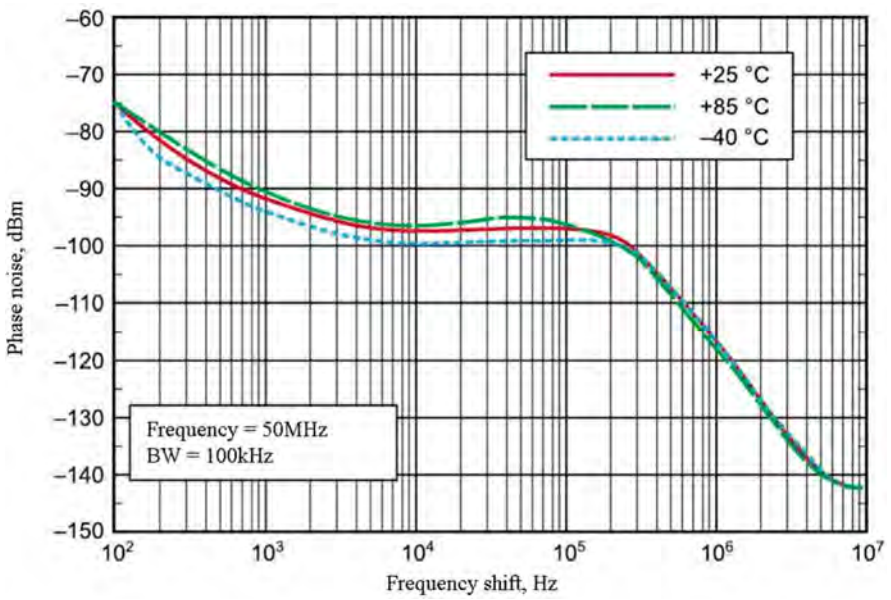

Fig. 8.86 The dependence of SSB phase noise on frequency offset in the integer mode at different ambient temperature

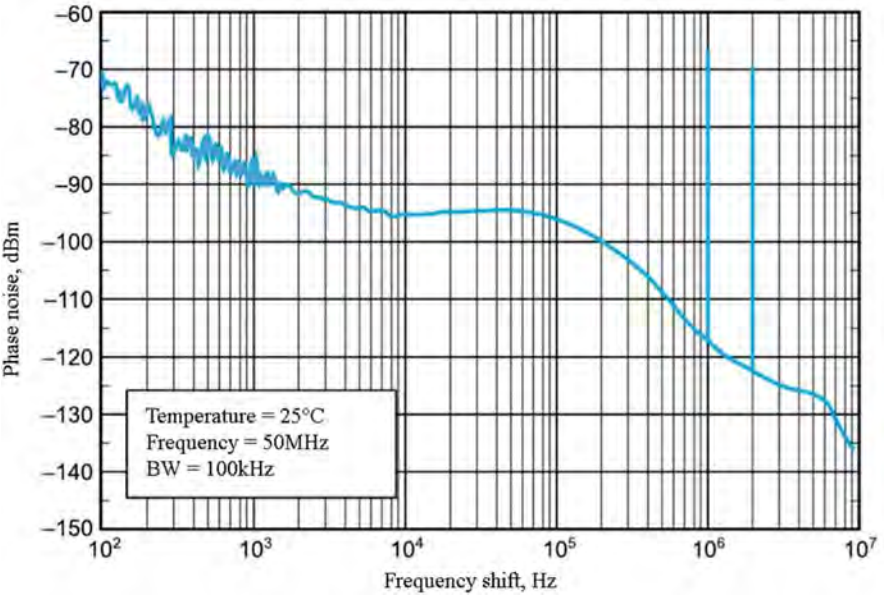

Fig. 8.87 Dependence of SSB phase noise on frequency offset when signal frequency is equal to 12.902 GHz in fractionally rational mode

8.9.2.2 Three-Band Monolithic Microcircuits of Synthesizers

Hittite Microwave company produces a series of PLL synthesizers having a built-in VCO with three frequency bands (Tri-Band RF VCO). They are characterized by the fact that the first frequency divider is replaced by the circuit generating three frequencies: $f_0/2$, f_0 and $2f_0$. Thus, three variable-frequency ranges can be reached by changing the dividing ratio of the second frequency divider (and even by making it to be a frequency multiplier). Table 8.45 [2] specifies the data of chips when using the medium frequency f_0.

The complete data of these chips are available on the company's website.

Let's consider a chip HMC840LP6CE as an example of the most high-frequency three-band synthesizer. It has a built-in VCO and three frequency bands: 1310–1415, 2620–2830 and 5240–5660 MHz, as well as a built-in testing program that carries out tests and calibrations. The chip is designed in 40-pin package LP6CE, 6 × 6 mm in size and 36 mm^2 in area.

Functional diagram of chip of three-band synthesizer HMC840LP6CE is shown in Fig. 8.88. Its design and operation are clear and described above. Figure 8.89 illustrates the level of phase noise of the chip. The level of phase noise in fractionally rational mode is a bit higher than in the integer mode. The reasons of this have already been explained.

Figure 8.90 shows the typical adjustment curves of synthesizer HMC840LP6CE. They cover all the frequency range of this synthesizer.

Table 8.45 Chips of wide-band synthesizers Hittite Microwave (the data are specified for the medium frequency range)

Type of chip	Frequency, GHz	Phase noise, dBc/Hz	Pout, dBm	Jitter, f_{sec}/*
HMC828LP6CE	1285–1415	−112/−143	10	180/0.09
HMC822LP6CE	1330–1650	−112/−142	6.5	180/0.11
HMC838LP6CE	1590–1890	−118/−143	7.5	180/0.12
HMC821LP6CE	1720–2080	−112/−141	6.5	180/0.13
HMC837LP6CE	2050–2300	−117/−141	10.5	180/0.15
HMC839LP6CE	2100–2410	−115/−140	7.5	180/0.16
HMC820LP6CE	2190–2550	−112/−141	6.5	180/0.17
HMC840LP6CE	2620–2830	−118/−139	9	180/0.1

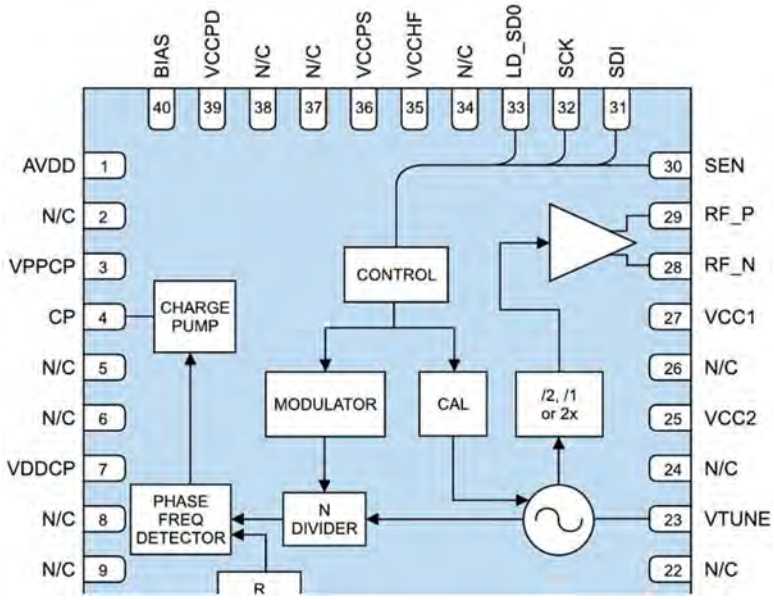

Fig. 8.88 Functional diagram of chip of three-band synthesizer HMC840LP6CE

8.9.2.3 Wide-Band Monolithic Microcircuits of Synthesizers

Hittite Microwave also produces wide-band chips of Wideband RF VCO class having wider frequency range than that of chips previously described. One of such chips is HMC829LP6GE (Fig. 8.91) has three extended frequency ranges: 45–1050, 1400–2100 and 2800–4200 Mhz. The low frequency limit of the first range is up to 45 MHz, the frequency ratio is equal to 2 at other ranges. Package of SMT type with 40 pins, its dimensions are 6 × 6 mm. The chip is powered from the constant-voltage source of 3.3 and 5 V.

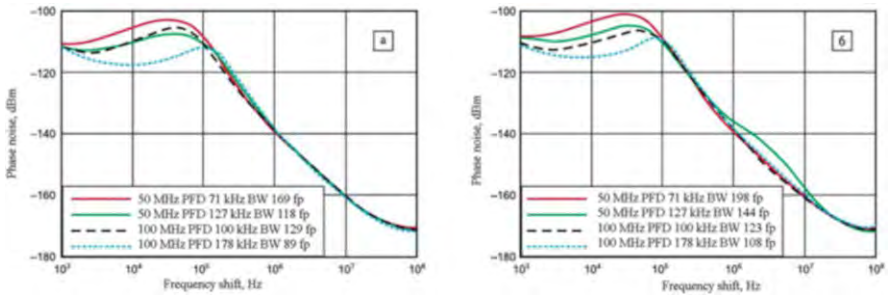

Fig. 8.89 The phase noise in the integer mode (**a**) and fractionally rational mode (**b**) at a frequency of 2.6 GHz for chip HMC840LP6CE

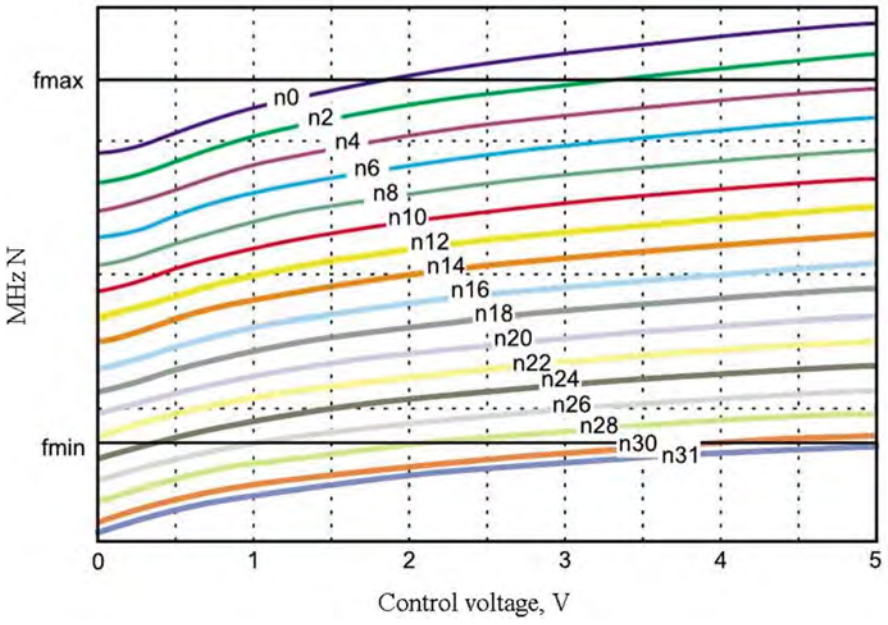

Fig. 8.90 The typical adjustment curves of chip HMC840LP6CE

The chip phase-lock detector provides the capture area of 100 MHz. The chip provides the phase noise of −110 dBc/Hz when frequency offset is 100 kHz.

24-bit capacity provides frequency resolution up to 3 Hz. There is possibility to carry out digital test of chip operation and its calibration. Figures 8.92 and 8.93 show the phase noise of chip HMC829LP6GE in the integer mode and fractionally rational mode. In general, it's very low and ensures high frequency stability of synthesizers based on this chip.

Figure 8.94 shows the dependency of output signal power on frequency. Power change within each frequency sub-band is small.

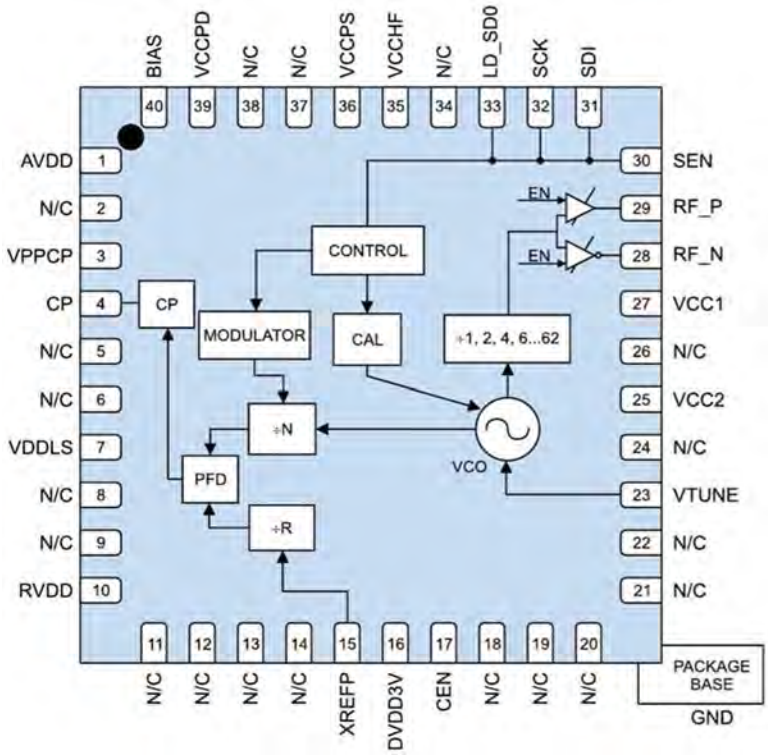

Fig. 8.91 The functional diagram of chip HMC829LP6GE

Figure 8.95 shows the assembly of chip HMC829LP6GE on printed circuit board. Packageless resistors and capacitors are used. Data Sheet for this chip provides a detailed specification of the circuit board elements.

Another chip produced is HMC830LP6GE. It provides a frequency range from 25 MHz to 3 GHz. The lower limit of frequency range is up to 25 MHz and covers the short-wave region of output signal. Frequency resolution of 3 Hz is provided. The functional diagram of this chip is similar to the diagram shown in Fig. 8.91. The specified frequency range is provided by the choice of the range of fundamental generator frequencies from 1500 to 3000 MHz.

Figure 8.96 shows the dependency of output power HMC830LP6GE on output frequency at three values of temperature The feature of this chip is a jump-over of power value at a frequency of 1500 MHz.

The detail characteristics of this chip and the user guide can be found in [105].

The cascade circuit can be used to ensure the quartz crystal control and to increase the reference frequency of synthesizers. Its example is shown in Fig. 8.97. The synthesizer in such circuit acts as a frequency multiplier.

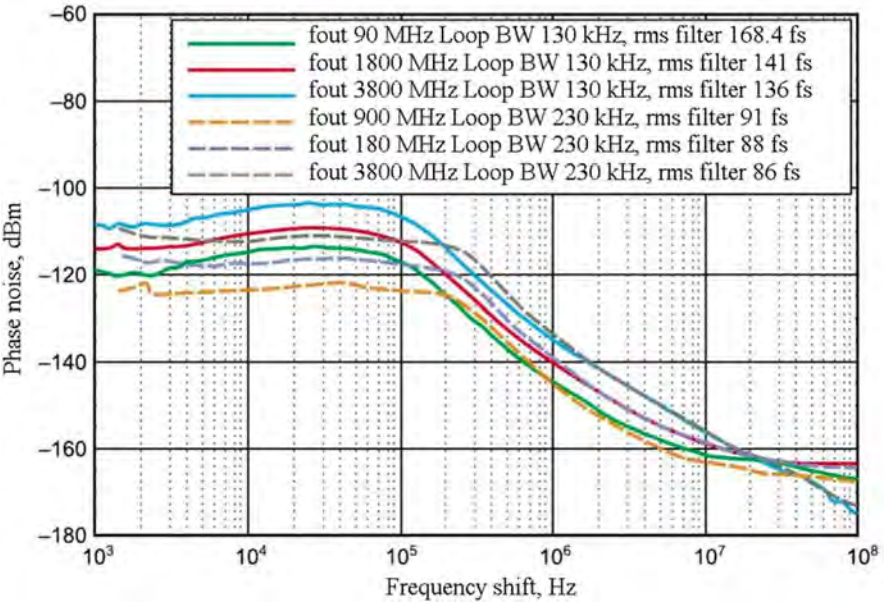

Fig. 8.92 The phase noise of chip HMC829LP6GE in the integer mode

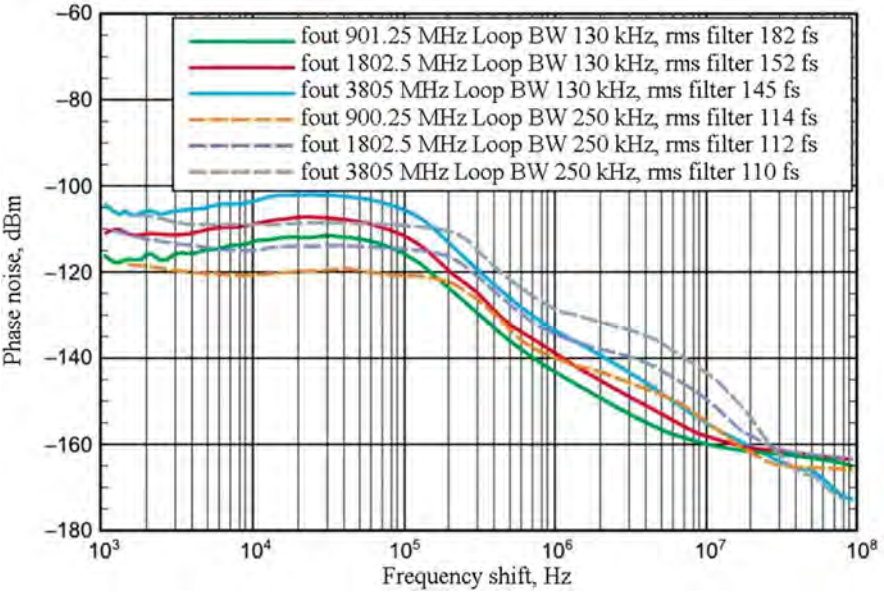

Fig. 8.93 The phase noise of chip HMC829LP6GE in the fractionally rational mode

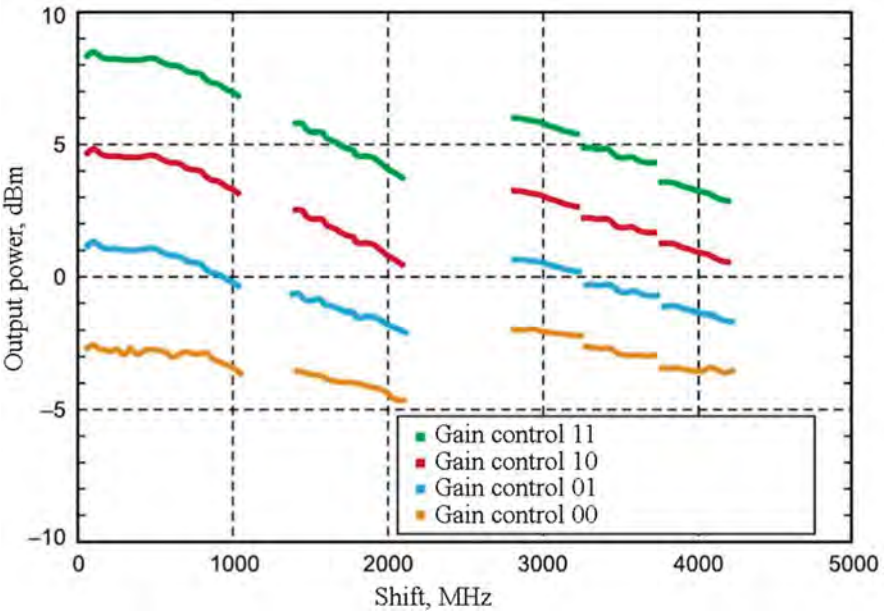

Fig. 8.94 Typical dependence of output signal power on frequency

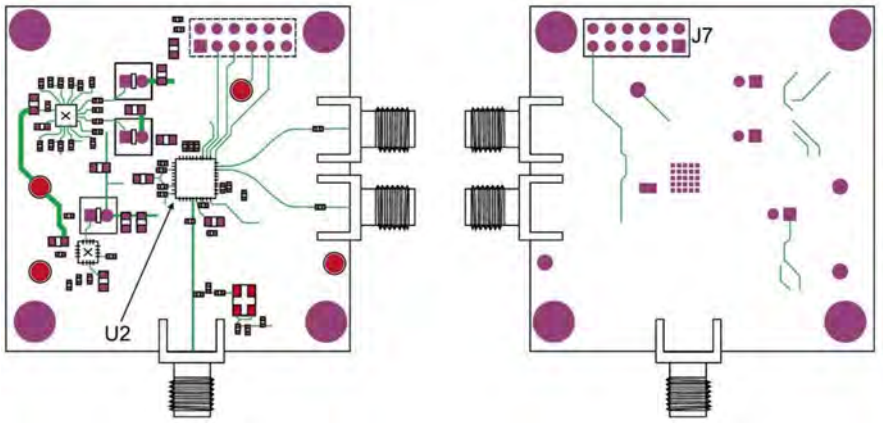

Fig. 8.95 Assembly of chip HMC829LP6GE on printed circuit board [2]

8.9.2.4 Chips HMC983 and HMC984 Are for Building of Ultra-Wideband Synthesizers

Hittite Microwave produces a special-purpose pair of chips for phase-locked loop. These are chips HMC983 and HMC984 with a bandwidth from 0 (DC) to 7 GHz. The feature of these chips is the lowest zero cut-off frequency that allows to create

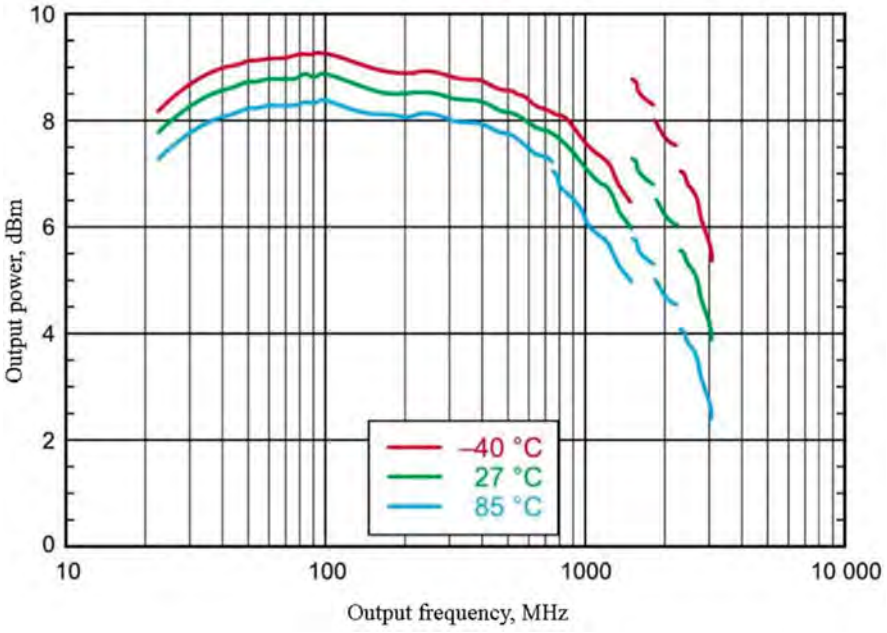

Fig. 8.96 Dependency of output power on output frequency for chip HMC830LP6GE at different values of temperature

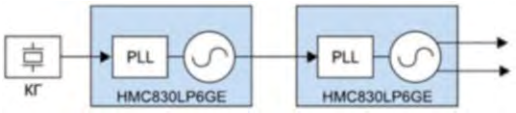

Fig. 8.97 Connection of quartz crystal-controlled generator to synthesizers

synthesizers which low cut-off frequency captures the ranges of audio and infrasonic frequencies. Perhaps the main scope of application of such synthesizers is measuring instruments: currently, many series sinusoidal wave generators and spectrum analysers produced by global leading companies have the frequency range that is typical for these chips.

Chip HMC983LP5E is a wideband synthesizer with improved parameters. The chip has 32-pin package LP5, 5 × 5 mm in size.

Supply voltage is 3.3 and 5 V; the values of the consumed current depend on a chip condition; they can be found in Data Sheet.

The chip contains the 20-bit frequency divider. The maximum reference frequency of the chip is 350 MHz, the maximum frequency of the phase detector PFD is150 MHz. The frequency resolution is 0.18 μHz when the reference signal frequency is 50 MHz. The chip contains 38-bit 100-Hz ΔΣ-modulator (DSM). The functional diagram of chip HMC983LP5E is shown in Fig. 8.98.

This chip is characterized by low level of phase noise reaching the record value: −160 dBc/Hz when the reference signal is 100 Hz. Figure 8.99 shows the

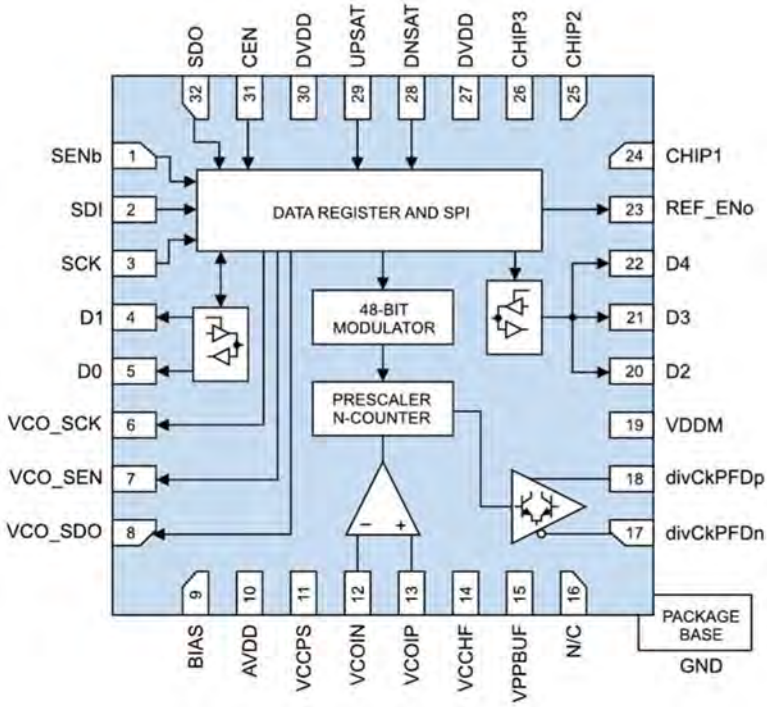

Fig. 8.98 The functional diagram of chip HMC983LP5E

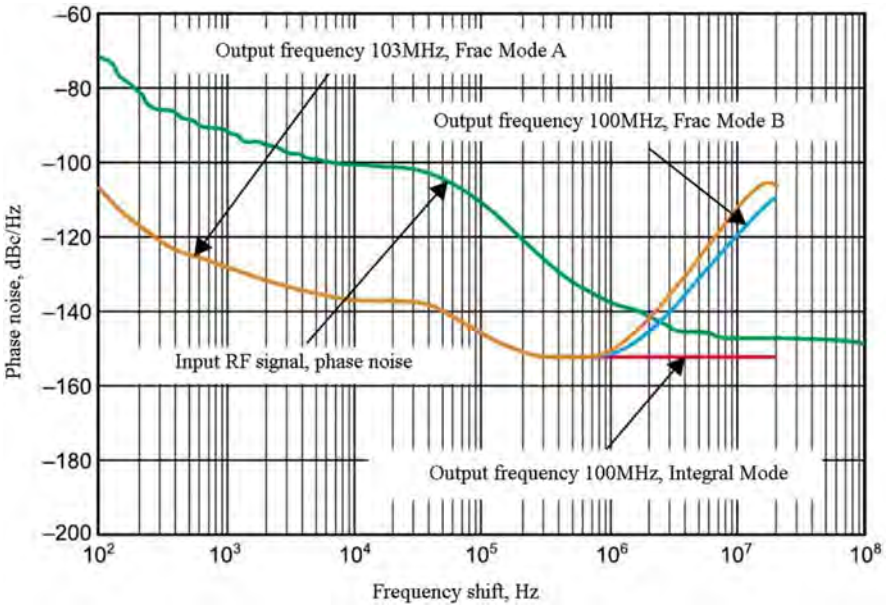

Fig. 8.99 Phase noise of chip HMC983LP5E with reference signal of 100 MHz

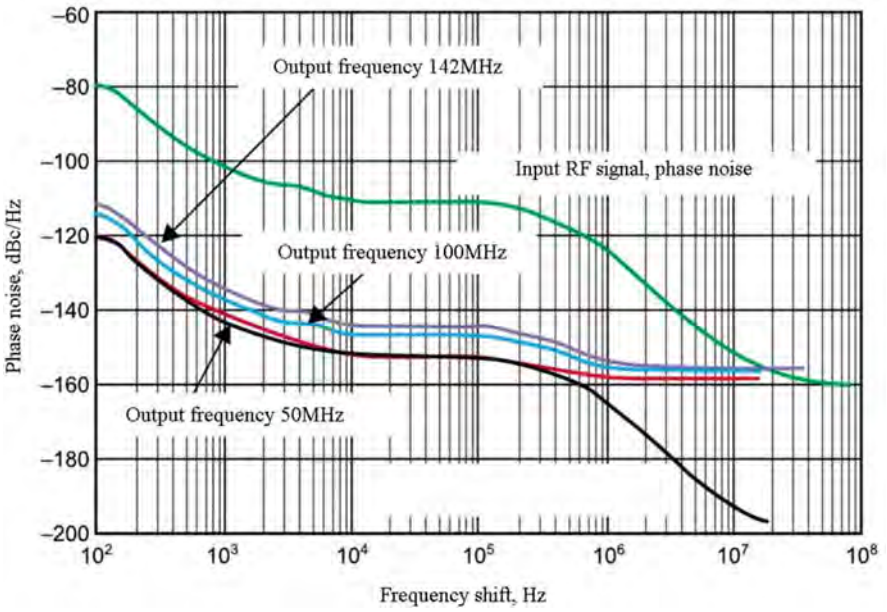

Fig. 8.100 The phase noise of chip HMC983LP5E when the reference signal is with a frequency of 50, 100, and 142 MHz

dependence of phase noise in the synthesizer output on frequency offset at the central frequency of 6 GHz. Figure 8.100 shows the same dependence at different frequency of reference signal input.

Figure 8.101 shows the oscillograph records of the frequency divider (reference frequency is 66 MHz, synthesis frequency is 6.5 GHz).

The chip contains a digital frequency sweeper that ensures the linear law of frequency rise and fall with automatic and manual start. Actually, a sweeping signal received during digital synthesis is multiple-step but as you can see in the Fig. 8.102, the step amplitude is so small that oscillograms shows a signal as analog one. There are two sweeping modes: double-sided and one-sided. Its essence is clear (Fig. 8.102).

Chip HMC984 represents a part of synthesizer (Fig. 8.103). Its second part is based on chip HMC984.

This chip contains a digital phase-lock detector and 14-bit reference frequency divider.

The special chip is built for testing of synthesizers on chips HMC983, HMC984 and HMC507. Its functional circuit is illustrated in Fig. 8.104. The appearance of printed circuit board is shown in Fig. 8.105.

Data Sheet for this chip provides a detailed specification of elements of the printed circuit board.

Figure 8.106 shows the functional circuit of wideband synthesizer based on chips HMC983 and HMC984.

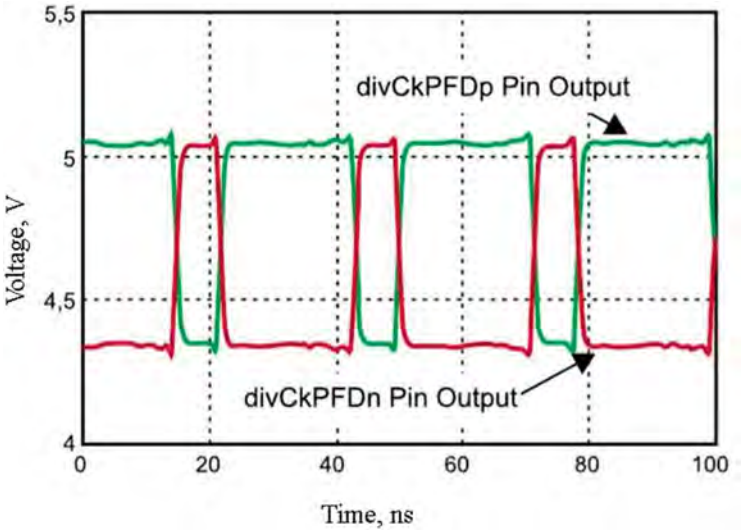

Fig. 8.101 Oscillograph records of the frequency divider of HMC983LP5E

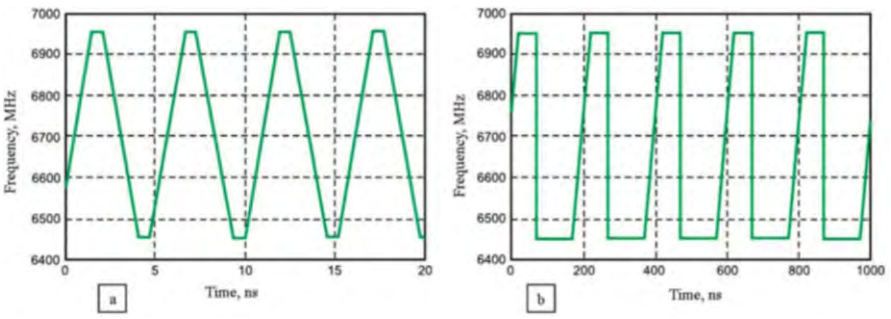

Fig. 8.102 Frequency-time dependency in two sweeping modes: (**a**) double-sided; (**b**) one-sided

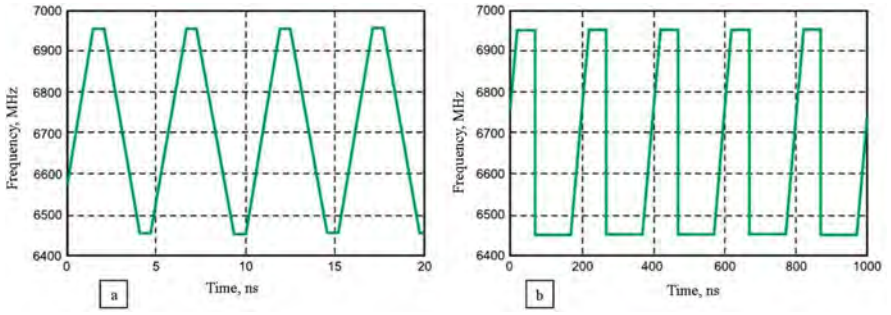

Fig. 8.103 The functional diagram of chip HMC984

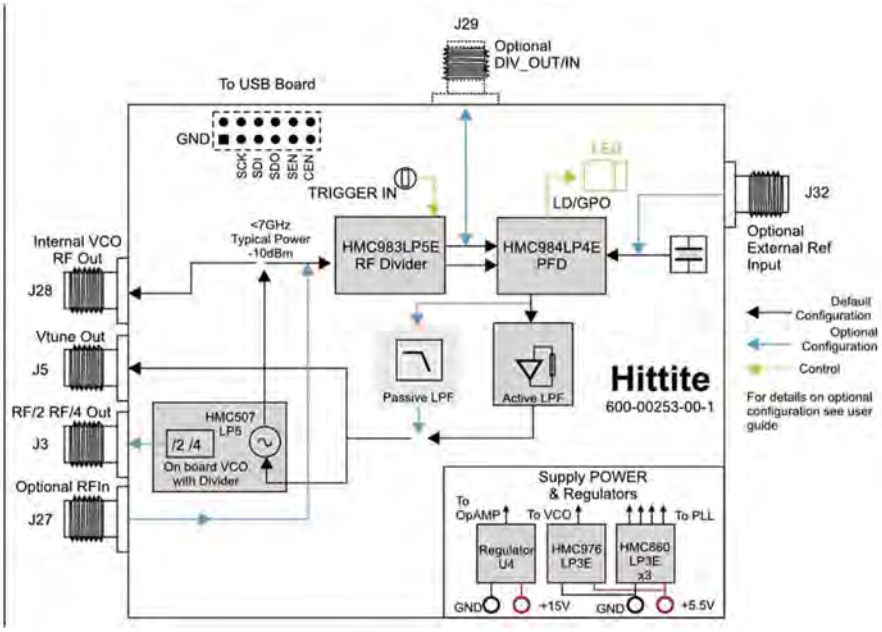

Fig. 8.104 Functional diagram of board circuit for testing of chips HMC983 and HMC984 [2]

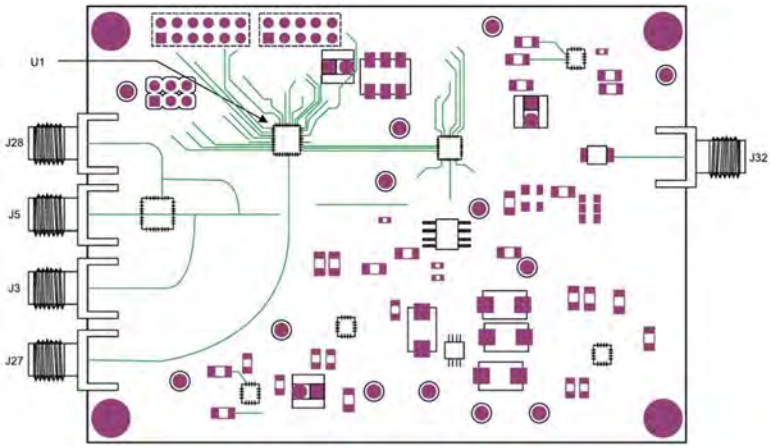

Fig. 8.105 Printed circuit board for testing of chips HMC983 and HMC984 [2]

As mentioned above, chip HMC507 can be used as a voltage-controlled oscillator. Thus, the full synthesizer is implementer on three monolithic chips.

Board (Figs. 8.105 and 8.106) is used as a part of the computerized testing system shown in Fig. 8.107. The system allows to receive all characteristics of synthesizers

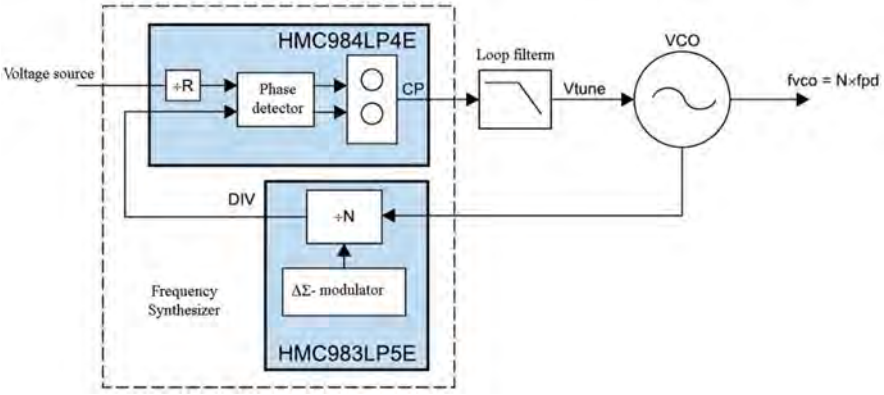

Fig. 8.106 The use of chips HMC983 and HMC984 for building of wide-band frequency synthesizers [2]

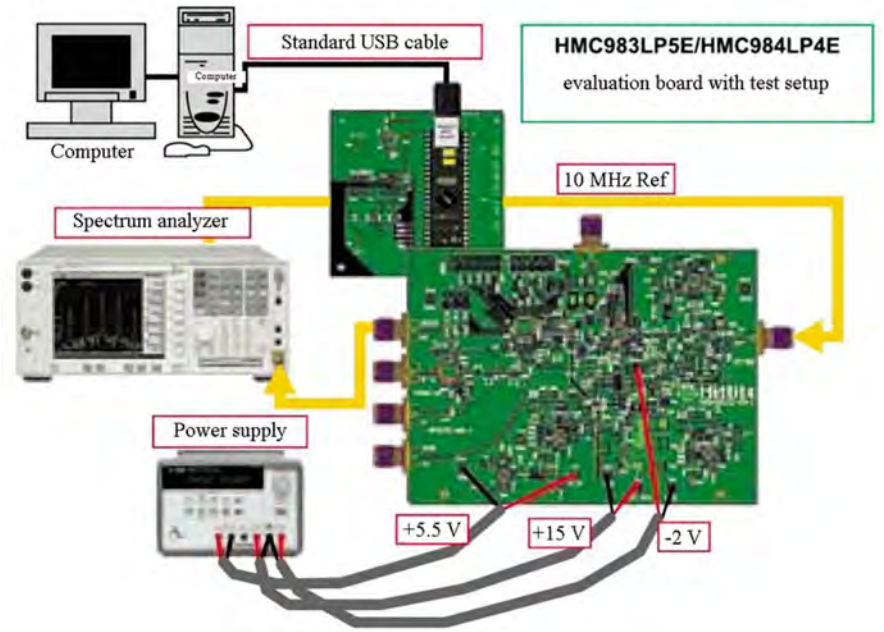

Fig. 8.107 Computerized testing system of HMC983 and HMC984 [2]

that are described above, as well as many others. It is required for design of synthesizers of different types based on the described integrated chips.

Description of the system interface and user's manual are available on the company's website [105].

8.9.2.5 Monolithic Chips of Wide-Band Frequency Synthesizers HMC701/702/703

Hittite Microwave company produces a series of monolithic chips for wide-band frequency synthesizers. One chip of such synthesizer includes all nodes for external control VCO (two frequency dividers, phase-lock detector, frequency sweeper of program control).

The basic parameters of such chips are listed in Table 8.46 [2].

This table specifies the frequency range, maximum frequency of the phase detector Fpfd max, phase noise, frequency resolution, supply voltage and current.

Two of these chips have the lower limit of frequency range 10 kHz, so they cover even the part of audio frequency range. Such cut-off frequency relieve from the necessity to use coupling capacitors of high capacity in the synthesizer.

Functional diagram of chip HMC702LP6CE is illustrated in Fig. 8.108. The chip has the maximum frequency of the phase detector being equal to 75 MHz and frequency resolution of 3 Hz. 16-bit reference signal divider.

The phase noise is equal to −98/103 dBc/Hz (in the integer and fractionally rational modes) when frequency offset is 20 kHz. The mentioned phase noise [105] is specified in Table 8.46. Figure 8.109 shows the dependence of phase noise on frequency offset in relation to the central frequency for integer (at a frequency of 13 GHz) and fractionally rational (at a frequency of 12 GHz) mode of synthesizer operation.

Comparative analysis of phase noise for a few chips at different frequency of output signal is shown in Fig. 8.110.

Synthesizers with phase-locked loop are inertial devices. Figure 8.111 shows the cycle of time change of frequency for synthesizers with phase-locked loop of voltage-controlled generator. It's clear that transient period can reach tens of microseconds.

Chip HMC703LP4E is an ultra-wideband synthesizer with a frequency band from direct current up to 8 GHz. Its functional diagram is illustrated in Fig. 8.112. The chip is designed in mini package LP4E 4x4 mm in size with 24 pins. It includes

Table 8.46 The basic parameters of monolithic chips for terminated wide-band frequency synthesizers

Type of chip	Range of frequencies	Fpfd max, MHz	Phase noise, dBc/Hz	Resolution, Hz	Power supply
HMC701LP6CE	10 kHz. . . .8 GHz	75	−221/ −227	3	+5 V at 37 mA, +3.3 V at 90 mA
HMC702LP6CE	10 kHz. . . .4 GHz	100	−221/ −227	6	+5 V at 37 mA, +3.3 V at 136 mA
HMC703LP4E	DC. . . .8 GHz	100	−230/ −233	3	+5 V at 6 mA, +3.3 V at 52 mA

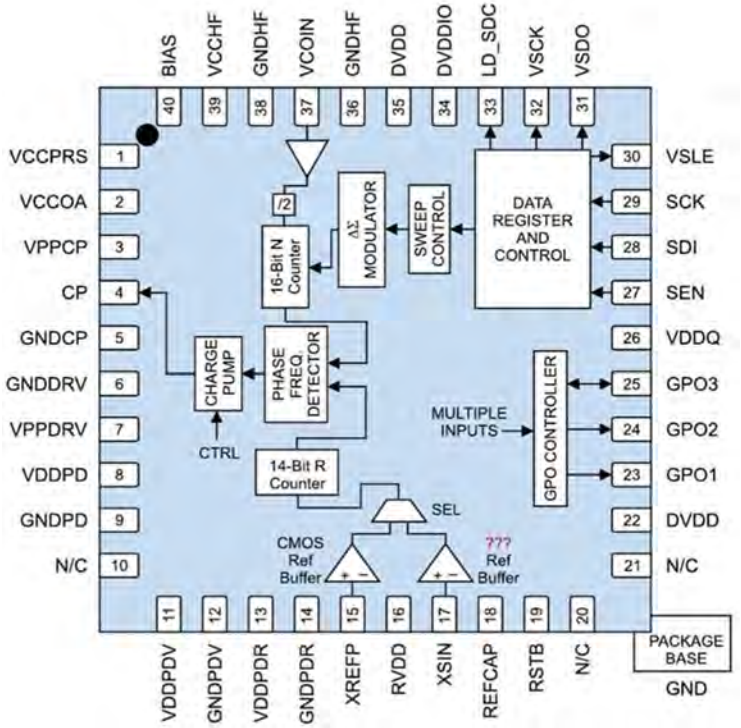

Fig. 8.108 The functional diagram of chip HMC702LP6CE [2]

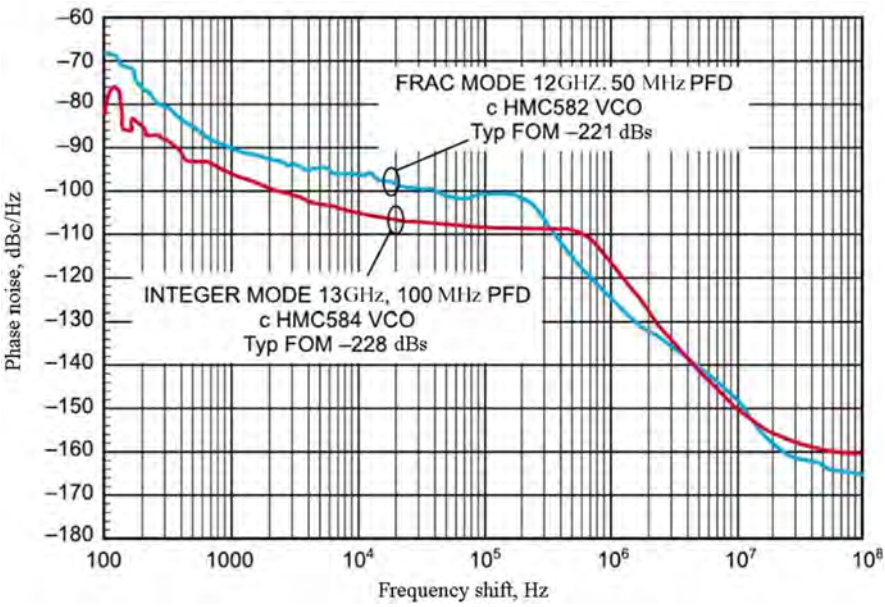

Fig. 8.109 The phase noise of chip HMC702

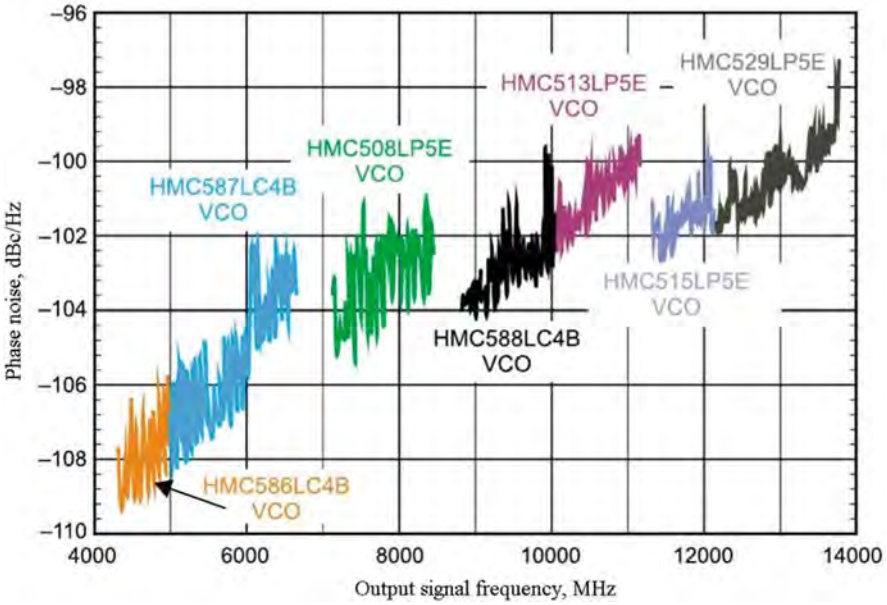

Fig. 8.110 Phase noise of different chips of synthesizers

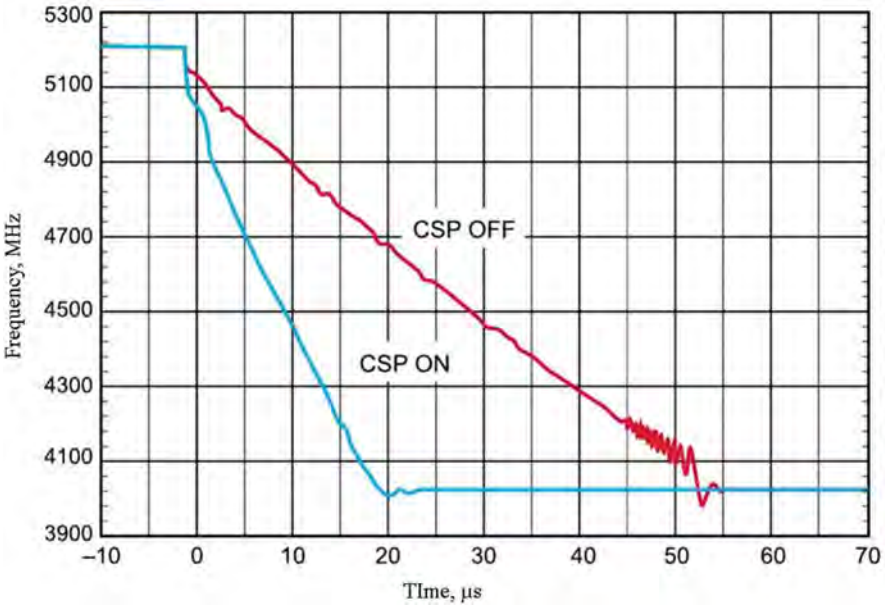

Fig. 8.111 Frequency change cycle of synthesizer based on chips HMC983 and HMC984 from 5200 to 3950 MHz

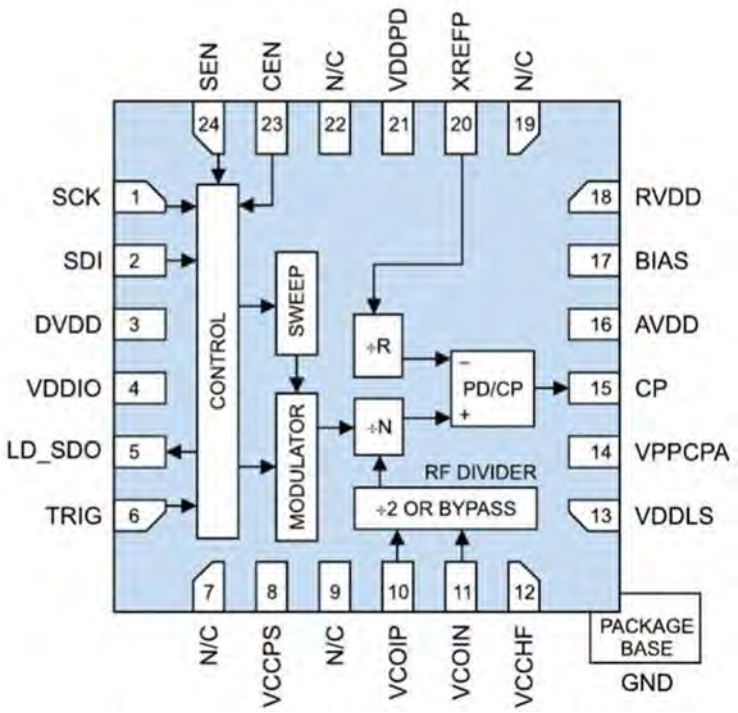

Fig. 8.112 The functional diagram of chip HMC703LP4E

frequency and phase modulators, control system with internal and external start-up, frequency sweeper and phase-lock detector.

The level of chip phase noise is equal to −112 dBc/Hz in fractionally rational mode at a frequency of 8 GHz when frequency offset is 50 kHz. The specified phase noise is equal to −230 dBc/Hz in fractionally rational mode and to −233 dBc/Hz in integer mode.

The maximum frequency of the reference-frequency generator is 100 MHz, jitter is less than 50 f_c (RMS).

Typical functional circuit of wideband synthesizer based on chip HMC703LP4E with external VCO is illustrated in Fig. 8.113.

Figure 8.114 shows the functional diagram of board circuit for testing of synthesizer chips HMC703 with controlled generator circuit HMC508.

The board represents a completely built-up synthesizer on the specified chips.

Testing board topology is shown in Fig. 8.115 The complete specification of its components can be found in documentation available on the website [105].

The dynamic properties of the synthesizer can be optimized by improvement of the filter installed in output of phase detector. In particular, the active filter based on the integrated operational amplifier can be installed instead of usual filter. Functional circuit of such synthesizer is illustrated in Fig. 8.116.

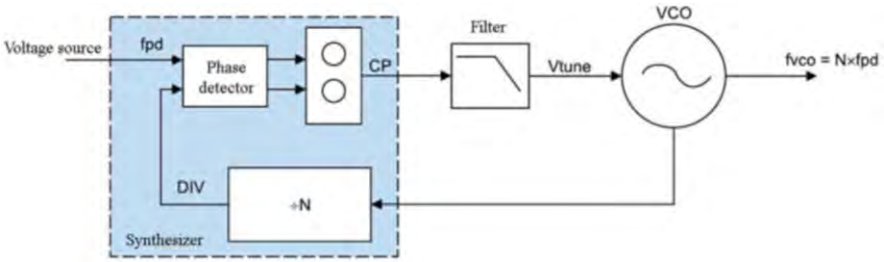

Fig. 8.113 Functional diagram of full synthesizer based on chip HMC703LP4E with external VCO

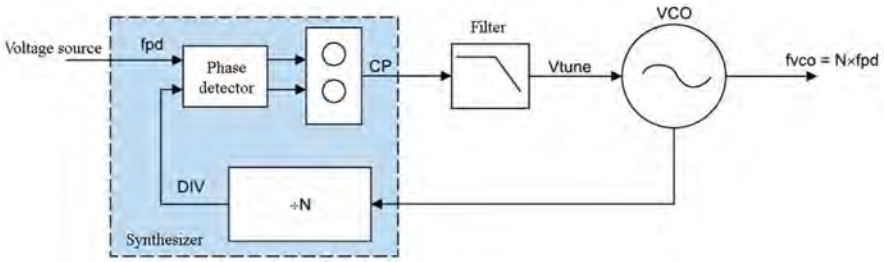

Fig. 8.114 Functional diagram of chip testing board [2]

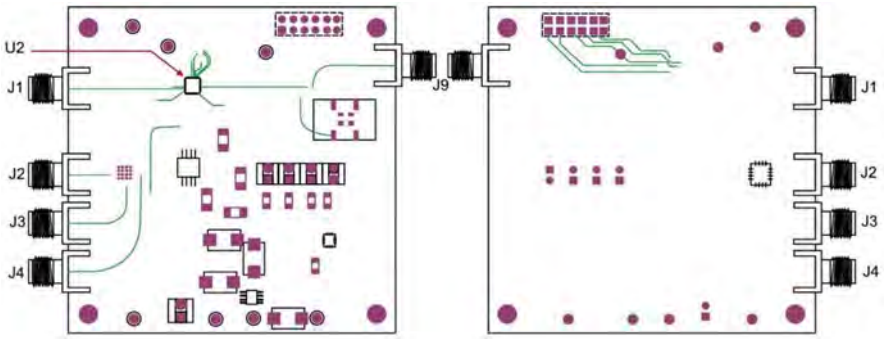

Fig. 8.115 Test board layout [2]

8.9.2.6 Software for Monolithic Chips of Synthesizers

For ensuring proper operation of frequency synthesizers based on monolithic chips, Hittite Microwave company produces software and firmware in addition to testing boards (for example, that are shown in Figs. 8.114 and 8.115). Installation of type shown in Fig. 8.117 is used for firmware adding to storage of monolithic chips of frequency synthesizers.

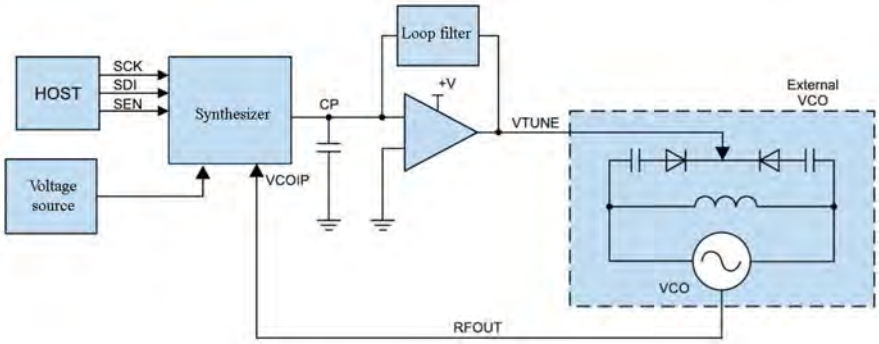

Fig. 8.116 Functional diagram of synthesizer with active filter in output of phase detector

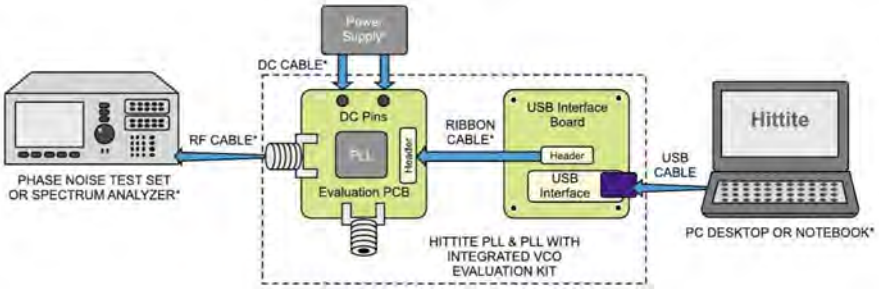

Fig. 8.117 Installation for firmware adding to storage of monolithic chips of frequency synthesizers [2]

Software for synthesizer control is implemented with graphic user interface (GUI). Its operation can be started with setting-up the synthesizer type in window shown in Fig. 8.118.

Window view for different synthesizers can have significant but not fundamental distinctions. Figure 8.119 shows the window of operation with PLL synthesizers.

GUI window of parameter setup and testing of various models of frequency synthesizers with enhanced capabilities is shown in Fig. 8.120. Detailed description of synthesizer programming and peculiarities of their testing are given in User Manual that is available on the website [105]. It describes some features of one or another circuit of the synthesizer [108].

Thus, scope of application of the above-considered monolithic chips of frequency synthesizers and frequency-stable signal generators is very diverse. Scope of application includes microwave radio transmitters and radio receivers, base stations of mobile communication systems (GSM, PCS, DCS, CDMA, WCDMA), wireless communication lines (Wireless LANs, WIMAX), high speed measuring and testing equipment (including in microelectronics and nanotechnologies), cable television, sensor systems, phase arrays AESA, SHF-jammers, FMCW radar systems, and etc.

Fig. 8.118 Window of synthesizer type selection

Fig. 8.119 GUI window for PLL synthesizer parameter control

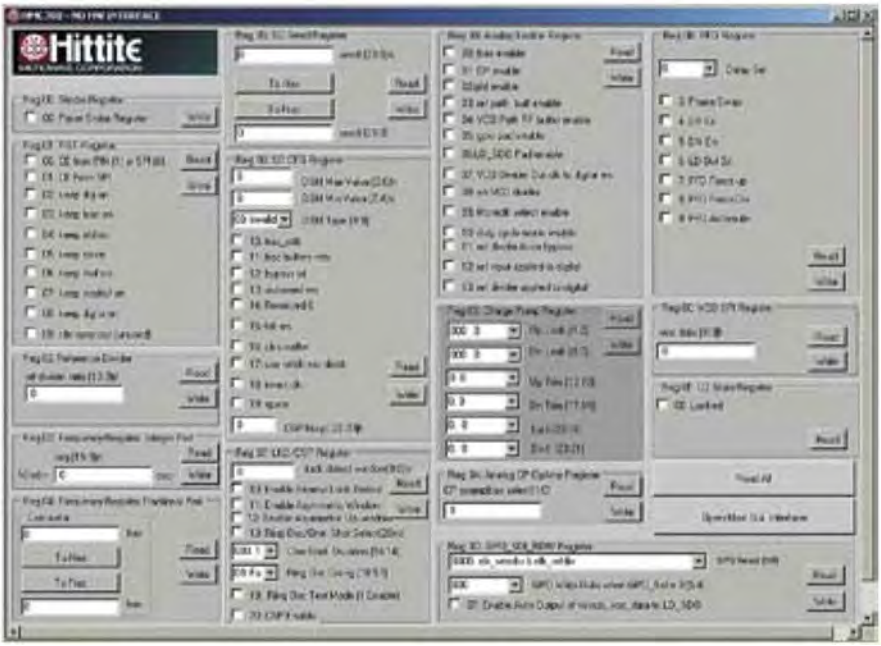

Fig. 8.120 Window of parameter setup and testing of various models of frequency synthesizers with enhanced capabilities

Small overall dimensions and weight of monolithic chips made by Hittite Microwave company, as well as their high (record) frequency rates allow to apply these chips in the modern communication systems, radio technical apparatus, electronic and measuring equipment.

8.10 Specifics of Selecting Element Base for Secondary Power Supply Systems of AESA Transceiver Modules

8.10.1 Principles of Building Power Supply Systems for AESA TRMs

Let us consider the possible options of organizing power supply system for radar sets using active electronically scanned arrays (AESA), as well as the element base by SynQor, which can be used as the basis for building such systems.

At the moment, radar stations of the new generation with active electronically scanned arrays are more and more widely used in such critical spheres as complexes of aerospace defence, navigation systems, remotely piloted aircrafts, etc. [109].

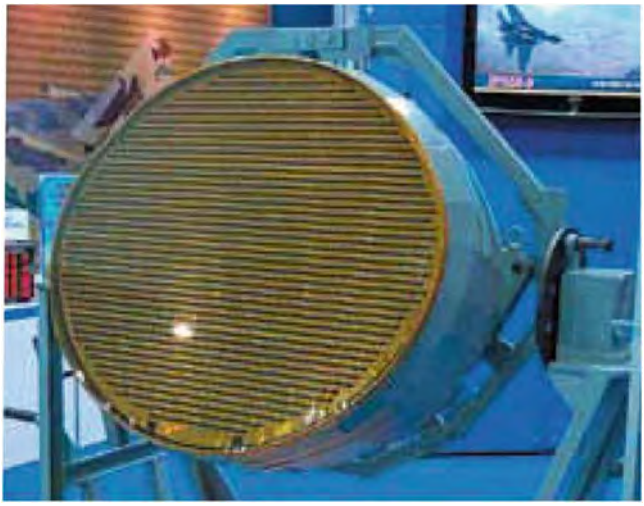

Fig. 8.121 AESA of a plane radar [3]

The main difference between radars with AESAs from stations of past generations where mirror antennas and slotted antennas as well as passive phased antenna arrays is the fact that transceiver modules, each of which operates with an individual radio signal emitter, are installed on the antenna device array curtain (Fig. 8.121).

This feature imposes strict requirements in terms of weight and dimensions, efficiency and reliability of the power supply system; at the same time, the number of power supply channels is determined by the number of TRMs and increases by several orders of magnitude as compared to radars with passive PAAs.

For a power supply system, radio signal emitter is an active linear low-voltage load with high requirements for stability of voltage of the energy-storage capacitor [110]. Non-compliance with such requirements can affect such important parameter as amplitude-phase stability of SHF radio pulses of the transmitter channel, which will ultimately impair selection of moving objects by the radar set [111].

This imposes certain requirements on the selection of the power supply circuit of AESA TRMs, as well as on the selection of the relevant element base.

Power supply system of TRMs with AESAs is one of the most power-consuming in the entire radar set (on the average, up to 35% of the entire station power) [112–114]. In this case, power supply system of the antenna curtain greatly contributes to weight and dimensions of the station and has a more complex structure that the power supply system of other units. As a result, selection of the power supply organization option is one of the crucial stages of building the entire complex.

Today, developers of such systems are facing a number of tasks: ensuring the necessary line of output voltages and minimum electrical losses, organization of galvanic isolation of transceiver equipment modules, as well as minimization of financial costs, if possible.

Due to this fact, it is necessary to pay special attention to the issues of organizing the power supply system by selecting its proper architecture.

The following basic requirements for the electric power supply system can be identified [113]:

- minimum weight and dimensions;
- maximum reliability of the system;
- maximum efficiency;
- serviceability.

Power supply system can be built using different circuits; however, centralized or decentralized circuits or their modifications are used as a basis.

Centralized Circuit

All modules are powered by several high-power voltage controllers, which provide the system with all necessary current and voltage ratings (Fig. 8.122). Average efficiency of such circuit is 80–85%.

The advantage of centralized power supply system is the convenience in its maintenance and operation; disadvantages include high losses during transmission of high currents and low reliability [113], which leads to the necessity of redundancy of units.

Decentralized Circuit

In this case, each module is powered by its own low or medium power supply source (Fig. 8.123).

An individual galvanically isolated power source can be used for each standard voltage rating.

Average efficiency of such circuit is 85–92%. Advantages include high reliability and efficiency, disadvantages – large weight and dimensions and relative inconvenience in maintenance.

It is also necessary to take into account the following circumstance while selecting the architecture. As a rule, TRM packages are connected to the package of antenna array of the station. Therefore, in case of any organization of the power

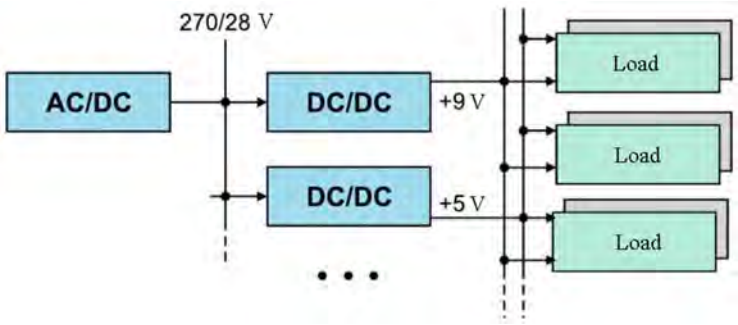

Fig. 8.122 Centralized power supply circuit

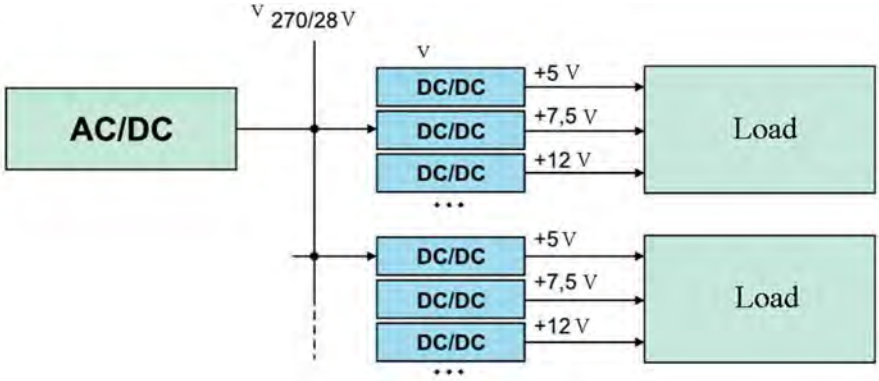

Fig. 8.123 Decentralized power supply circuit

supply system, it is necessary to ensure galvanic isolation between output terminals of secondary power sources and the airplane bus of the station. Today, decentralized architecture or its modifications are mostly used for building power systems of AESA TRMs [113–115]. However, in order to build an effective and balanced system, it is necessary to take into account such factors as selection of the best place for secondary power sources and their type.

Selection of the optimum element base is one of important tasks during development of any power supply system. Modules based on hybrid technology are often used in critical applications to solve these problems. Products of such well-known manufacturers as International Rectifier (IR), VPT, MDI, etc. can be used as examples.

Today, manufacturers of power supply modules offer solutions based on packaged radioelectronic components (SMD) by Mil-Cots and Military, which can be a good alternative to hybrid power sources in a number of cases.

Both hybrid and surface-mount element bases have their advantages and disadvantages.

8.10.2 Technological Features of Production of DC/DC Converters

Hybrid Technology

DC/DC converters produced using the hybrid technology are gas-filled sealed metal packages containing semiconductor chips and passive electronic components installed on ceramic substrate (Fig. 8.124) [116]. The use of ceramic substrate with high thermal conductivity makes it possible to nearly eliminate the problem

Fig. 8.124 Power supply module manufactured using the hybrid technology [2]

Fig. 8.125 Contact unit of a hybrid power supply module [2]

of local overheating of separate components of the DC/DC converter. As a result, this production technology allows the converter to be immune to high temperatures up to +185 °C (more often – to +125 °C).

However, this production technology has a certain disadvantage – possible loss of air tightness. Inner cavity of the converter is filled with inert gas, while sealing and electrical insulation of the package in the pin region is ensured by melting of glass insulators located directly at each output contact (Fig. 8.125). Therefore, mechanical damages caused to pins during installation or vibratory loads can lead to cracking of glass insulators and further depressurization of the entire module. Therefore, if the weight and dimensions are significant, the manufacturer often abandons the use of vertically installed pinouts. This indicates the need to introduce additional process operations and increase the area of the installation location [117].

The circuitry used in hybrid converters usually suggest minimum number of passive components placed inside the converter package, which calls for installation of external components [116]. This fact increases the size of the end product.

Advantages of DC/DC converters manufactured using the hybrid technology include the wide range of working temperatures, small weight and dimensions, full galvanic insulation of output circuits (as a rule) and the potential possibility of ensuring immunity to the effects of ionizing radiation.

The latter aspect often requires additional licensing and certification during procurement. Disadvantages in certain cases include the need to install external passive components, as well as introduction of manual mounting operations (if the pins are positioned horizontally).

Another important downside is high cost due to complex technological process of production.

Surface-Mount Technology (SMT)

DC/DC converters manufactured according to SMT technology are the modules with printed circuit boards with installed electronic components in sealed SMD packages (Fig. 8.126). Installation of SMD components is performed within a single process cycle, which helps increase the production volume and reduce costs as compared to the hybrid technology [117].

In addition to financial attractiveness, SMT converters are immune to vibration loads and mechanical damages of output contacts. For example, if one of the contacts is bent, this will not disrupt workability of the source in general.

However, DC/DC converters made using SMT technology have a certain disadvantage – local overheating due to low thermal conductivity of the material used for production of the printed circuit board of the source. One of the solutions to this problem consists in adding new metal layers to the printed circuit board, which ensures redistribution of heat energy by preventing deformation and local overheating at temperatures of up to +125 °C [117]. In turn, for the purpose of removal of excess heat SMT converters are sealed by filling internal cavity of the source with heat-conductive compound.

As noted above, one of the advantages of hybrid converters are their small weight and dimensions; however, it shall be noted that when SMT technology is used, manufacturers place nearly all necessary passive components used in input/output filters inside the DC/DC converter and implement multiple additional functions.

Technological solutions used during production of DC/DC converters according to the SMT technology make it possible to apply the module in a number of most critical tasks, in particular, during organization of the AESA TRM power supply system. At the same time, SMT converters will be more advantageous than hybrid sources in terms of such parameters as resistance to vibratory loads, the need to use additional passive components and total cost.

SynQor products of the Hi-Rel subgroup (Fig. 8.128) can be used as a basis for building the power supply system for AESA TRMs. DC/DC converters of this

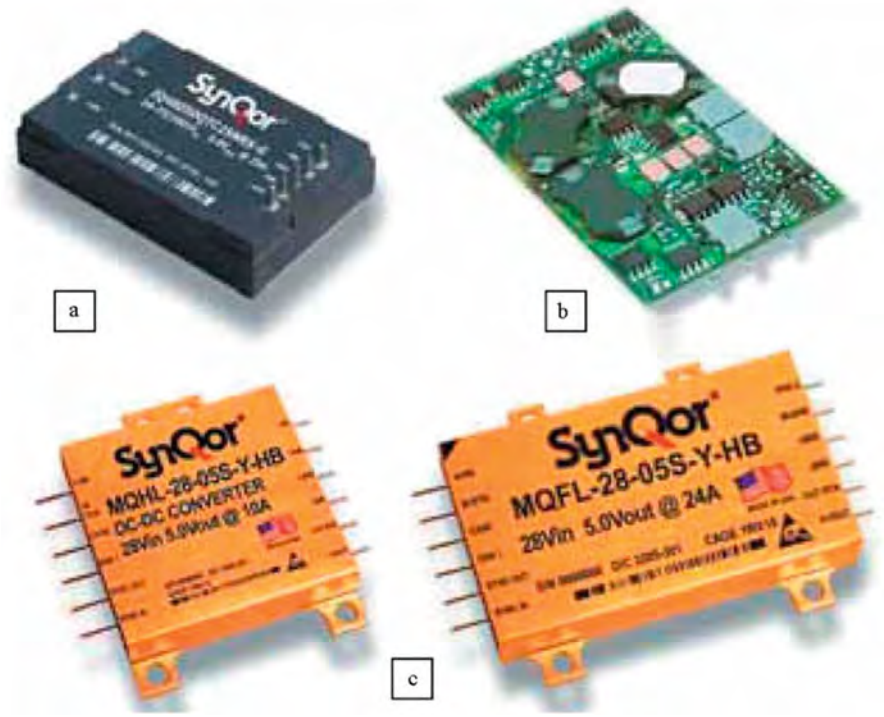

Fig. 8.126 SynQor power supply modules manufactured using SMT technology: (**a**) InQor group (industrial applications); (**b**) PowerQor group (telecommunication applications); (**c**) Hi-Rel group (highly reliable applications)

sub-group are adapted for basic levels of input voltage equal to 28 V (MQFL/MQFL/MQBL series) and 270 V (MQFL-270 series) (Table. 8.47) and designed for use in the most extreme operating conditions, including military equipment.

8.10.3 Features of SynQor Converters of the Hi-Rel Series

SynQor DC/DC converters are distinguished by the two-step conversion circuit (Fig. 8.127) built according to the following principle: at the first step, input voltage is reduced to a certain base level; at the second step, base level is increased or reduced to the required value, and galvanic isolation of output power circuits is ensured. This conversion circuit helps achieve efficiency up to 91% [116].

Features of Hi-Rel converters also include:

Table 8.47 Basic technical parameters of SynQor converters of the Hi-Rel subgroup

Series	Range of input voltage, V		Maximum output power, W	Coefficient of efficiency, %
MQFL-28	Operating	16–40	60–120	91
	Maximum	16–50		
MQFL-28E	Operating	16–70		90
	Maximum	16–80		
MQFL-28VE	Operating	16–40		90
	Maximum	5.5–50		
MQFL-270	Operating	16–70		90
	Maximum	5.5–80		
MQFL-270L	Operating	155–400		88
	Maximum	155–475		
MQHL-28	Operating	65–350	60–75	86
	Maximum	65–475		
MQHL-28	Operating	16–40	30–50	91
	Maximum	16–50		
MQHL-28E	Operating	16–70		90
	Maximum	16–80		
MQHR-28	Operating	16–40	15–25	91
	Maximum	16–50		
MQHR-28E	Operating	16–70		90
	Maximum	16–80		
MQBL-28	Operating	16–40	12–20	91
	Maximum	16–50		
MQBL-28E	Operating	16–70		90

Note. The following parameters are the same for all models:
– range of output voltages (1.5/1.8/2.5/3.3/5/6/7.5/9/12/15/28/±5/±12/±15 V);
– conversion frequency (500–600 kHz);
– operating temperature range (−55. . . + 125 °C)

- galvanic insulation of all power and signal circuits;
- protection of short circuit, overloads and overheating with automatic recovery of work;
- function of parallel activation with uniform distribution of current load between converters;
- voltage control at the load with automatic correction of losses at conductors of the supply chain;
- fixed conversion frequency of 500–600 kHz;
- possibility of adjustment of output voltage.

Wide operating temperature range of SynQor Hi-Rel converters shall be noted: −55. . . + 125 °C. These values were achieved by using a number of circuit-related solutions, as well as innovative packaging technology QorSeal.

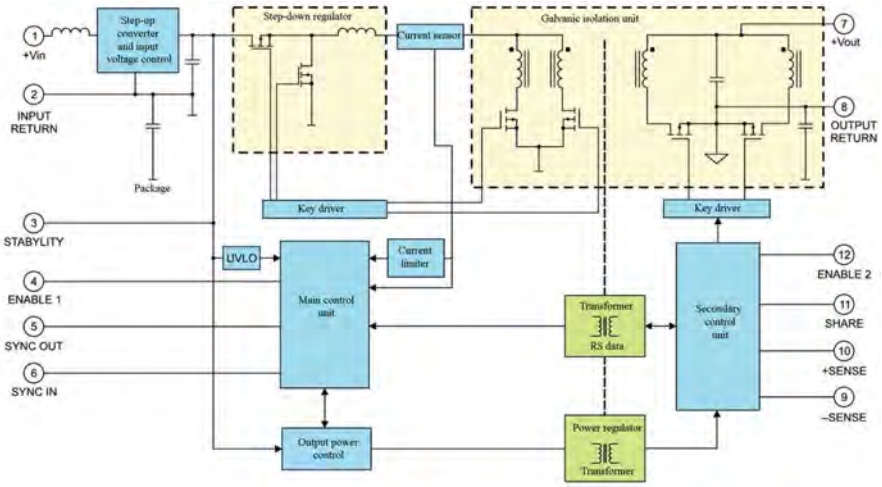

Fig. 8.127 Structural diagram of the SynQor power module of the Hi-Rel subgroup [2]

QorSeal Packaging Technology

Design of a Hi-Rel converter with QorSeal technology (Fig. 8.128) is based on a full metal aluminum package with protective nickel coating, to which a layer of gold is galvanically applied [117].

Source design is distinguished by the fact that the printed board of the Hi-Rel converter has no direct contact with the package due to the fact that its fixture is ensured by side bars made of polymeric material.

Sealing is performed by filling internal cavity with heat-conductive compound. Compound is supplied under low pressure through process holes in the package, ensuring sealing and heat removal from components.

The printed circuit board used in Hi-Rel converters deserves a special mention. As noted above, metallized layers were added to the structure of the printed board in order to solve the problem of local overheating and better heat redistribution. This made it possible to use power semiconductor components, which are produced in small-sized packages exclusively. SynQor specialists also fully abandoned electrolytic capacitors and only used ceramic ones. All these measures together helped reduce weight and dimensions of converters and ensure stable operation within a wide frequency range.

8.10.4 Electromagnetic Processes in the Power Supply System of AESA Transceivers

AESA power supply system shall ensure power supply to all TRMs of the antenna array curtain, the current consumption of which is usually pulsed; this requires

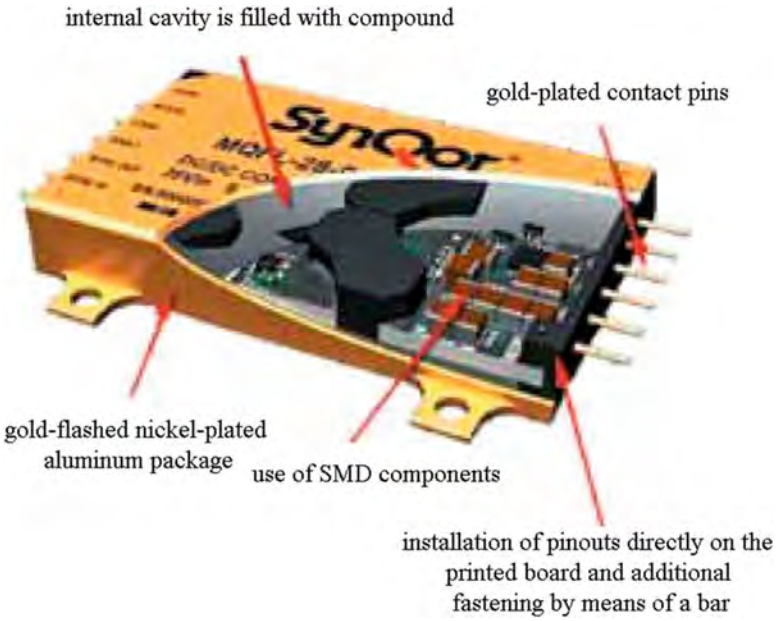

Fig. 8.128 Design of the SynQor power supply module of the Hi-Rel subgroup with the QorSeal packaging technology [2]

inclusion of energy storage devices into the power supply system. Dimensions of the antenna curtain of a radar can reach several dozen meters, while the quantity of TRMs can reach several dozens or even hundreds [117].

In order to increase the level of electromagnetic compatibility of the AESA power supply system with the supply network, it is recommended to use additional EMI filters (Fig. 8.129).

One of the options of such element base can consist of SynQor EMI power filters of the Hi-Rel subgroup [118] (Table 8.48).

The range of SynQor EMI filters includes three classes:

- Passive Filters;
- Reverse Polarity Protection Filters;
- Transient Suppression Filters.

Especially interesting are Transient Suppression Filters (Fig. 8.130). They provide additional protection from overloads, input voltage drop, short circuits and polarity reversal and support functions of soft-start, standby (disconnection of active components of the EMI filter for reduction of power consumption with load disabled), Enable Load (function of relay of the load enable/disable control signal).

Hi-Rel EMI filters, similarly to power sources of this subgroup, are manufactured using multi-layer printed circuit board with metallized layers and packaged using the QorSeal technology [115] (Fig. 8.128).

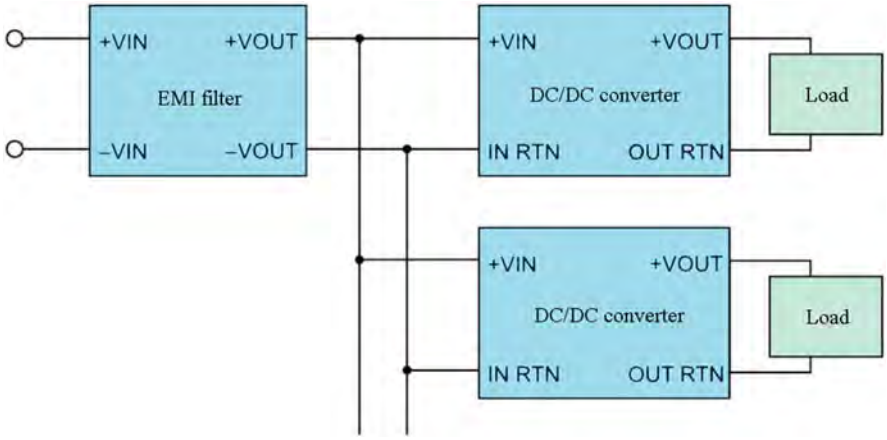

Fig. 8.129 Typical wiring diagram of an EMI filter SynQor [3]

Table 8.48 Basic technical parameters of SynQor EMI filters of the Hi-Rel subgroup

Name	Current, A	Input voltage, V		Suppression of interferences, dB	
		Nominal	Limit (<100 ms)	Differential (at 500 kHz)	General type (at 500 kHz)
MQME-28-P	20	±40	±50	>80	>60
MQME-28-T		±40	+110, −50		
MQME-28E-P		±70	±100		
MQME-28E-T		±70,	+110, −70		
MQME-28E-T6		40	+210, −70		
MQME-270-P	2	±400	±500		
MQME-270-R					
MQHE-28-P	10	±40	±50		
MQHE-28E-P		±70	±100		
MQHE-270-P	1	±400	±500	>50	

Note. Insulation voltage for all models amounts to 500 V

Organization of the secondary power supply system of AESA TRMs is one of important stages of building the entire radar set complex. The developers need to solve the problem of selecting the power supply system circuit, as well as the

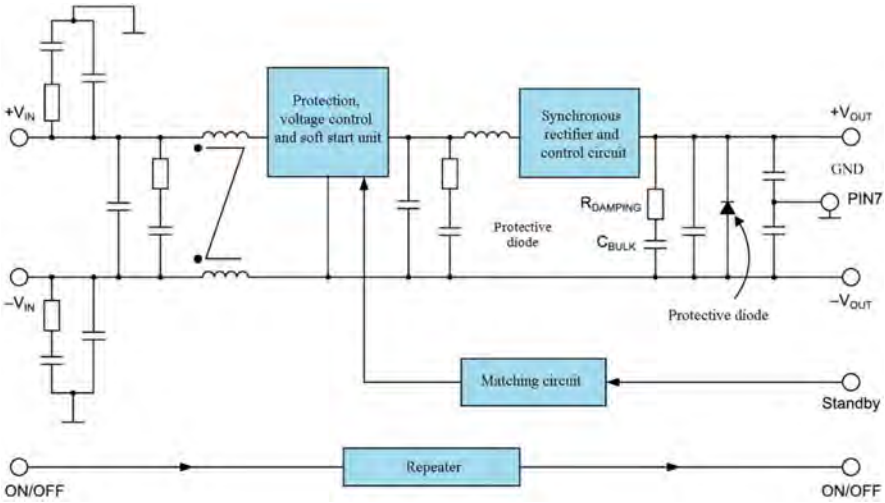

Fig. 8.130 Generalized structural diagram of the EMI filter SynQor MQME-28E-T (Transient Suppression Filter)

element base on which this circuit will be implemented. SynQor products of the Hi-Rel subgroup can be used as this element base. This subgroup includes DC/DC converters and EMI filters adapted for basic levels of input voltage equal to 28 and 270 V. Technological solutions used during production of Hi-Rel power supply modules by SynQor (packaging technology – QorSeal) make it possible to ensure stable temperature within the range of working temperatures of 55... + 125 °C, as well as high immunity to vibration loads. At the same time, the price of modules is in the lower price category (as compared to hybrid converters). In order to ensure electromagnetic compatibility of the power supply system with power supply modules, it is reasonable to use EMI filters (Passive Filter, Reverse Polarity Protection Filter, Transient Suppression Filter).

These features make it possible to use SynQor in heavy duty conditions, including in highly reliable military equipment.

References

1. Belous, A., Saladukha, V., & Shvedau, S. (2017). *Space microelectronics. Volume 2: Integrated circuit design for space applications* (605 p). Artech House.
2. Belous, A., Merdanov, M., & Shvedov, S. (2018). *Microwave electronics in radar and communication systems* (Technical Encyclopedia in 2 Volumes, 2nd ed., rev., 1520 pages) Moscow: Tekhnosfera.
3. Pavlov, S., & Filippov, A. (2014). Phased antenna arrays. A review of component base for implementation of transceiver modules. *Components and Technologies*, *7*.
4. www.radartutorial.eu
5. www.radiosounding.ru/

6. www.hittite.com
7. www.nxp.com
8. www.trakeurope.com
9. www.chainhomehigh.wordpress.com
10. www.apitech.com
11. Low Pass EMI Filter Catalog API Technologies/Spectrum Control. (2012).
12. Filippov, A. B. (2011). Spectrum advanced specialty products – Components and solutions for ensuring EMC of radio equipment. *Components and Technologies, 9–10*.
13. Dedinets, V. E., Zubkov, A. M., Abolduev, I. M., & Ionov, V. E. (1996). *Monolithic gallium-arsenide amplifier of the 3 cm range with phase-stable amplification adjustment*. In 6th international Crimean microwave conference. Ukraine, Sevastopol.
14. Abolduev, I. M., Vald-Perlov, V. M., & Minnebaev, V. M. (1999). *Design of low-noise amplifiers with protection from high level of input power*. In 9th international Crimean microwave conference. Ukraine, Sevastopol.
15. Abolduev, I. M., Zubkov, A. M., & Minnebaev, V. M. (1998). *Power amplifier of the X-band for AESA*. In 3rd international conference and exhibition "Satellite communication". Moscow.
16. Ionov, V. E., Abolduev, I. M., Zubkov, A. M., & Dedinets, V. E. (1996). *Multi-purpose probe devices for measurement of parameters of monolithic circuits and GaAs transistors in the frequency range up to 20 GHz*. In 6th international Crimean microwave conference. Ukraine, Sevastopol.
17. http://www.mwsystems.ru/
18. Karpov, Y. (2007). Russian transistor SHF amplifiers. *Components and Technologies, 1*.
19. www.argall.ru
20. Myakishev, Y., Gulyaev, V., Zhuravlev, K., & Quasi-Monolithic Integrated SHF. (2006). Circuits: Technology and devices. *Electronics: NTB, 6*.
21. Bell, D. L. T., & Li, R. C. M. (1976). Surface acoustic wave resonators. *TIIER, 64*(5), 171–183.
22. Joseph, T. R. (1977). *SAW oscillators for phase locked applications*. IEEE. – 31st annual symposium of frequency control.
23. Tanski, W. J., Cyr, R. A., Dragonetti, P. C., & Kosco, E. G. (1981). A radar system application of an 840 MHz SAW resonator stabilized oscillator. *IEEE Transactions on Microwave Theory and Techniques, v.MTT-29*(5), 424.
24. Sobolev, V. D., & Fedosov, V. I. (1988). AC USSR No. 1436830. Method of producing resonator masks on surface acoustic waves. Priority dated October 30, 1986.
25. Kislyakova, O. V., Kondratiev, Y. P., Timashev, V. V., Fedorets, V. N., & Fedosov, V. I. (1993). RF Patent No. 1762727. Method of manufacturing resonators on surface acoustic waves. Priority dated March 11, 1990.
26. Bray, R. C. (1988). Application s of SAW resonators in high- performance instrumentation. *IEEE Trans, on Ultrasonics, Ferroelectrics and Frequency Control, 35*(3), 331–341.
27. Anisimkin, V. I., Magomedov, M. A., & Fedosov, V. I. (1985). Resonator on surface acoustic waves. *Letters to TPJ, 11*(1), 56–61.
28. Fedosov, V. I. (1998). *A «non-local» equivalent circuit for reflective SAW transducers*. In Proceedings of 1998 international symposium on Surface Waves in Solids and Layered Structures. June 7–12, 1998, St. Petersburg- Moscow, Russia, pp. 163–167.
29. Kislyakova, O. V., Kondratiev, Y. P., Timashev, V. V., Fedorets, V. N., & Fedosov, V. I. (1993). RF Patent No. 1313317. Resonator on surface acoustic waves. Priority dated June 21, 1985.
30. Kislyakova, O. V., Kondratiev, Y. P., Timashev, V. V., Fedorets, V. N., Fedosov, V. I. (1993). RF Patent No. 13351 10. Method of manufacturing resonators on surface acoustic waves. Priority dated August 9, 1985.
31. Dokuchaev, Y. P., Kamenetskiy, Y. A., Kolkovskiy, Y. V., & Fedosov, V. I. (1983). *Studies of noises of self-excited oscillators with SAW resonators*. In Proceedings of the scientific session "Radio measurements" (Vol. 2, p. 224). Kaunas.

32. O'Shea, T., Sullivan, V., & Kindell, R. (1983). *Precision L-band SAW oscillator for satellite application*. IEEE. –37st annual symposium of frequency control.
33. Sang, E., Beckman, R., Show, Ph., & Wright J. (1986). *Design and manufacture of SAW resonators for low phase noise and low vibration sensitivity applications*. IEEE ultrasonics symposium.
34. Montress, G. K., Parker, T. E., Loboda, M. J., & Greer, J. A. (1988). Extremely low-phase-noise SAW resonators and oscillators: design and performance. *IEEE Transactions on Ultrasonics, Ferroelectrics and Frequency Control, 35*(6).
35. Senderuk, Y. S. (2000). *Studies and development of a set of solid-state micro-miniature integrated circuits for modern special-purpose receivers*. Ph.D. thesis in Engineering Science. Moscow.
36. Abolduev, I. M., Vald-Perlov, V. M., & Zubkov, A. M. *GaAs – Active elements in transceiver modules of the centimeter range* (p. 85). See Present Publication.
37. Zubkov, A. M., & Polyanov, A. B. *Wideband gallium-arsenide integrated circuits* (p. 91). See Present Publication.
38. Volin, D. (2014). On the way to fully digital radars: New solutions for high-speed ACCs. *Electronic Components, 8*, 38–40.
39. Bosworth, D. Demand for digital: Challenges and solutions for high-speed ADCs and RADAR systems. www.edn.com
40. Frenzel, L. New JESD204B interface speeds and simplifies ADC to FPGA interconnection. electronicdesign.com
41. Harris, J. What is JESD204 and why should we pay attention to it? www.eetimes.com
42. SHF semiconductor devices and their use. Moscow (1972).
43. Powerful electrovacuum SHF devices. Moscow (1974).
44. Semiconductor devices in SHF circuits. Moscow (1979).
45. http://vlad-gluh.livejournal/com/420211.html
46. http://blog/i.ua/user/2663242/940249/
47. http://armsdata.net/nuclear/116.html
48. http://rnns/ru/14834-udarnaja-sila-poslednee-preduprezhdenie.html
49. http://ss-op.ru/reviews/view/55
50. Gurtov, V. A. (2005). *Solid-state electronics*. Moscow.
51. Belous, A. I., Blinkov, O. V., & Silin, A. V. (1990). Bipolar microcircuits in interfaces of automatic control systems. *Moscow, Radio and Communication*.
52. http://www.twirpx/com/file/400874/
53. http://dxdt/ru/2007/11/26/836/
54. Scarpulla, J. R. (2004). *Reliability and qualification challenges for RF devices*. Los Angeles: The Aerospace Corporation.
55. Horowitz, P., & Hill, W. (1984). *The art of electronics*: Transl. from Eng. in 3 volumes. Moscow: Mir.
56. Belous, A. I., Yemelyanov, V. A., & Turtsevich, A. S. (2012). *Basics of circuitry of microelectronic devices* (472 p). Moscow: Tekhnosfera.
57. Kayali, S., Ponchak, G., & Shaw, R. (1996). *GaAs MMIC reliability assurance guideline for space applications*. NASA Lewis Research Center.
58. http://www.pvsm/ru/radiosvyaz/20389
59. Brookner, E. (2008). Phased-array radars: Past, astounding breakthroughs and future trends. *Microwave Journal, 51*(1), 30.
60. Mancuso, Y. (2008). *Thales components and technologies for T/R modules*. In Proceedings of the 3rd European microwave integrated circuits conference. Amsterdam, October, p. 270.
61. www.RG.RU, 2008, No. 227, p. 14.
62. Growing market for Active Electronically Scanned Arrays (AESA). *Microwave Journal, 52* (7), 47 (2009).
63. Raytheon demonstrates gallium nitride advantages in radar components. *Microwave Journal,* 51(6), 48 (2008).

64. *Microwave Journal, 51*(10), 62 (2008).
65. Mumford, R. (2008). Microwaves in Europe: Historical milestones and industry update. *Microwave Journal, 51*(10, Part II), 88.
66. Vikulov, I., & Kichaeva, N. (2007). GaN technology: A new milestone in development of microwave microcircuits. *Electronics: NTB, 4*, 80–85.
67. Russel, M. E. (2007). *Future of the RF technology and radars*. In Proceedings of the IEEE radar conference, p. 11.
68. Schuh, P., et al. (2008). *GaN MMIC based T/R-module front-end for X-band applications*. In Proceedings of the 3rd European microwave integrated circuits conference. Amsterdam, October, pp. 274–277.
69. Costrini, C., et al. (2008). A *20 Watt micro-strip X-band AlGaN/GaN HPA MMIC for advanced radar applications*. In Proceedings of the 38th European microwave conference. Amsterdam, October, p. 1433.
70. Quay, R., et al. (2008). *Efficient AlGaN/GaN HEMT power amplifiers*. In Proceedings of the 3rd European microwave integrated circuits conference. Amsterdam, October, p. 87.
71. Gonzalez-Garrido, M., et al. (2008). *2–6 GHz GaN MMIC power amplifiers for electronic warfare applications*. In Proceedings of the 3rd European microwave integrated circuits conference. Amsterdam, October, pp. 83–86.
72. Alleva, V., et al. (2008). *High power microstrip GaN-HEMT switches for microwave applications*. In Proceedings of the 3rd European microwave integrated circuits conference. Amsterdam, October, pp. 194–197.
73. Jansen, J., et al. (2008). *X-band GaN SPDT MMIC with over 25 W linear power handling*. In Proceedings of the 3rd European microwave integrated circuits conference. Amsterdam, October, pp. 190–193.
74. *Microwave Journal, 49*(6), 22 (2006).
75. www.raytheon.com
76. Compound Semiconductor, July 2005.
77. www.northropgrumman.com
78. Compound Semiconductor, March 2005.
79. en.wikipedia.org
80. Proceedings of the 35th European microwave conference, 2005, pp. 809–812.
81. http://www.chipnevs.ru/html.cgi/arhiv_i99_04/stat-56
82. http://www.kit-e/ru/articies/svch/2005_9_174.php
83. Aerospace Defense, 2005, N2 (21).
84. Aviation Week and Space Technology, 2005, N 8.
85. Military Microwaves Supplement, June 2006.
86. *Microwave Journal, 49*(1), 24 (2005).
87. Electronics EEXPRESS, March 2006.
88. GaAs Mantech Digest, 2004; 2005.
89. Compound Semiconductor, May 2005.
90. 13th GaAs symposium, Paris, 2005, pp. 361–363.
91. Turkin, A. N. (2011). Gallium nitride as one of advanced materials in modern optical electronics. *Components and Technologies, 5*, 6–10.
92. Yunovich, A. E. (1996). Light-emitting diodes based on GaN heterostructures and its solid solutions. *Lighting Engineering, 5/6*, 2–7.
93. Zalina, K. G., Kudryashov, V. E., Turkin, A. N., & Yunovich, A. Z. (1997). Luminescence spectra of blue and green light-emitting diodes based on multi-layered InGaN/AlGaN/GaN heterostructures with quantum wells. *FTP, 31*(9), 1055–1061.
94. Fedorov, Y. (2011). Wide-band heterostructures (Al,Ga,In)N and devices based on them for millimeter range of wavelengths. *NTB Electronics, 2*, 92–107.
95. Turkin, A. N., & Yunovich, A. E. (2014). Nobel prize laureates: in physics – I. Akasaki, H. Amano, S. Nakamura. *Nature, 2015*(1), 75–81.

96. Kischinskiy, A. A. (2009). *Solid-state SHF gallium nitride-based amplifiers – State and prospects of development*. In Proceedings of the 19th international Crimea conference "Microwave and telecommunication technology". Sevastopol. Veber.
97. Fedorov, Y. V., Gnatiuk, D. D., Galiev, R. R., Scherbakova, M. Y., Sveshnikov, Y. N., & Tsyplenkov, I. N. (2010). *Power amplifiers of the EHF range on heterostructures of AlGaN/AlN/GaN/sapphire*. In Proceedings of the 9th science and technology conference "Solid-state electronics, complex functional units of radioelectronic equipment". Zvenigorod. December 1–3, pp. 44–46.
98. Belov, L. (2004). Frequency converters. Modern HF components. *Electronics: NTB, 2*.
99. Belov, L. (2005). Mini-circuits – A reliable supplier of microwave components. Corporation profile. *Electronics: NTB, 6*.
100. Belov, L. (2006). Low and medium power solid-state amplifiers. *Electronics: NTB, 5*.
101. Gudin, M. (2003). HF and SHF devices by mini-circuits. Part 1. *Components and Technologies, 2*.
102. Diakonov, V. (2011). Monolithic SHF microcircuits of attenuators and Amplifiers by Hittite Microwave. *Components and Technologies, 10*, 14–22.
103. www.hittite.com
104. Afonskiy, V. P., & Diakonov, V. P. (2011). *Electronic measurements in nanotechnologies and microelectronics*. Moscow: DMK-Press.
105. www.hittite.com
106. Dyakonov, V. P. (2011). Picosecond digital monolithic microcircuits by Hittite Microwave. *Components and Technologies, 9*.
107. Afonskiy, V. P., & Diakonov, V. P. (2011). *Electronic measurements in nanotechnologies and microelectronics*. Moscow: DMK-Press.
108. Mihkhalev, P. (2006). PPL microcircuits and synthesizers based on them by Analog Devices. *Components and Technologies, 4*.
109. Vorobyev, S. (2014). Selection of element base for secondary power supply systems of AESA transceiver modules. *Components and Technologies, 10*, 36–40.
110. Pavlov, S., & Filippov, A. (2014). Phased antenna arrays. A review of component base for implementation of transceiver modules. *Components and Technologies, 7*.
111. Efremov, V. (2014). Component base for AESA: High-frequency connectors. *Components and Technologies, 9*.
112. Kirienko, V. P. (2008). Adjustable converters of systems of pulsed power supply/ I. N. Ulyanov ChSU.
113. Kushnerev, N. A., & Shumov, M. A. (2007). Power supply systems of active phased antenna arrays. *Radio Technology, 12*.
114. Dominiuk, Y. V., & Levitan, B. A. (2012). Power system of pulse active electronically scanned array. *Radiotechnics, 11*.
115. Nikitin, M. (2011). Small-sized EMI filters SynQor for civil and military applications. *Electronic Components, 8*.
116. Nikitin, M. (2011). High-reliability DC/DC-converters for application in military and transport equipment. *Components and Technologies, 1*.
117. Nikitin, M. (2011). Mil-COTS DC/DC-converters by SynQor – A good replacement for hybrid DC/DC-converters in critical applications with limited budget. *Components and Technologies, 5*.
118. Khvatov, S. V. (2011). *Electromagnetic processes in the power supply system of radar transmitters*. R.E. Alekseev NSTU.

Chapter 9
HF and SHF Components for Radar Sets

In addition to microcircuits, phase shifters, receivers and transmitter, a wide range of other HF and microwave components is used during development of modern radars, from basic resistors, capacitors and microwave filters to various microwave cables and high-frequency connectors (plugs, sockets, sealed adapters).

Of all the variety of HF and SHF components for radars, we will only consider the most characteristic technical solutions of SHF filters, SHF resistors and high-frequency connectors [1–4].

9.1 Microstrip Filters for SHF Systems

As is known [1], frequency band of 3.1. . .10.6 GHz is allocated for ultra-wideband communication. It is used at high-speed data transmission systems, in precision radars and equipment of different types. Due to the wide frequency range, the interference between signals, including narrowband signals, is very strong, and it is always necessary to take special measures to eliminate or at least reduce it.

Filters are an integral part of any ultra-wideband system. Until recently, developers of microwave systems widely used filters on resonators with discrete impedance. However, they have one extremely significant disadvantage: they cannot have a single pass band, and the production of filters of this type with double band is extremely expensive; moreover, they cannot be used in combination with the existing SHF ICs. Other known solutions also proved impractical due to low efficiency of suppression of unwanted signals.

Below we will consider on the of the most effective technical solutions – small-sized circuit of the filter with two operating ranges and high selectivity shown in Fig. 9.1 [1]. Here, the multi-more resonator (MMR) forms a pair of zeros in the upper and lower stop bands. Two parallel U-shaped USS cuts provide two stop bands,

© The Editor(s) (if applicable) and The Author(s), under exclusive license to Springer Nature Switzerland AG 2021

A. Belous, *Handbook of Microwave and Radar Engineering*,
https://doi.org/10.1007/978-3-030-58699-7_9

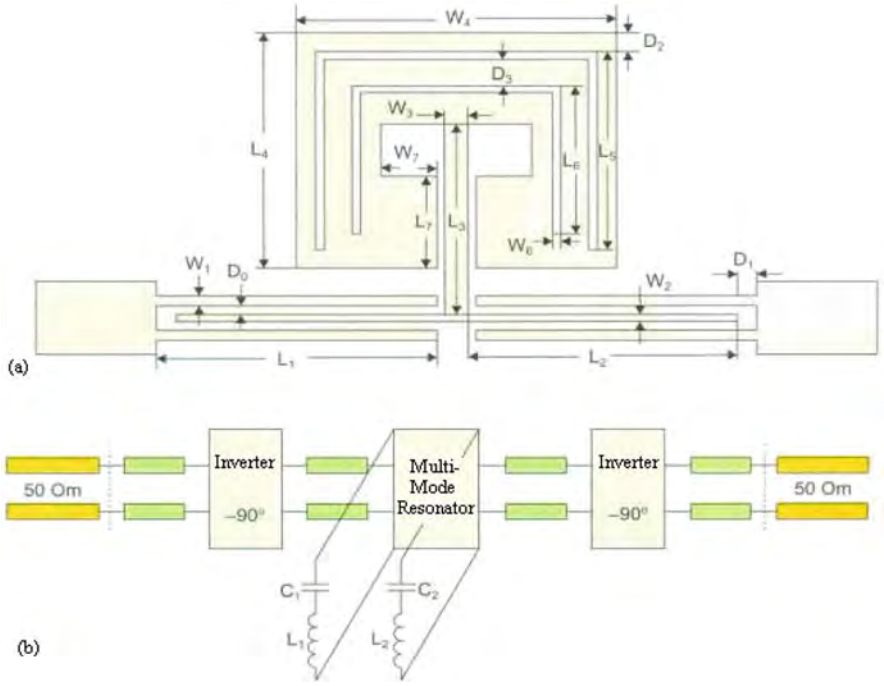

Fig. 9.1 Filter configuration and its equivalent diagram

which can be adjusted by the developer of the system without changing the size of the filter. Central frequencies of stop bands of such filters are 5.8 GHz and 8.0 GHz.

Such interdigital structure ensures high coherence inside the pass band. In the equivalent circuit (Fig. 9.1), the cuts are presented as two bypass resonance contours. It can be seen that two separate transmission lines separated by the inverter J can be achieved. The length of the cut is approximately equal to half of the wavelength. Threshold frequencies of the stop band are determined by the expressions [1]:

$$f_{notch-lower} = c/\left[\lambda_{notch-even}\left(\varepsilon_{eff}\right)^{0,5}\right] = c/\left[(2W5 + 4L5)\left(\varepsilon_{eff}\right)^{0,5}\right], \quad (9.1)$$

$$f_{notch-upper} = c/\left[\lambda_{notch-even}\left(\varepsilon_{eff}\right)^{0,5}\right] = c/\left[(2W6 + 4L6)\left(\varepsilon_{eff}\right)^{0,5}\right], \quad (9.2)$$

where $f_{\text{notch-lower}}$ ισ τηε lower threshold frequency; $f_{\text{notch-upper}}$ ισ τηε upper threshold frequency; $\lambda_{\text{notch-even}}$ ισ τηε corresponding wavelength; ε_{eff} ισ τηε dielectric constant; c ισ τηε speed of light in vacuum.

Results of modeling of frequency characteristics of cuts in the High Frequency Structure Simulator 11 (HSFF) Ansoft/ANSYS software are shown in Fig. 9.2. When the outer cut (L5 in Fig. 9.2a) is extended, lower threshold frequency is

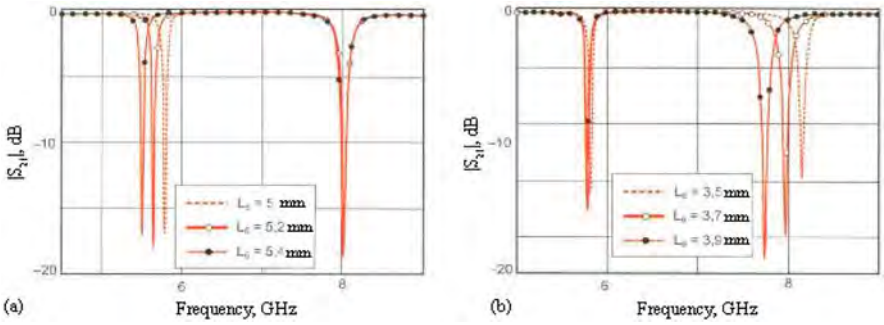

Fig. 9.2 Filter AFC during variation of cut parameters

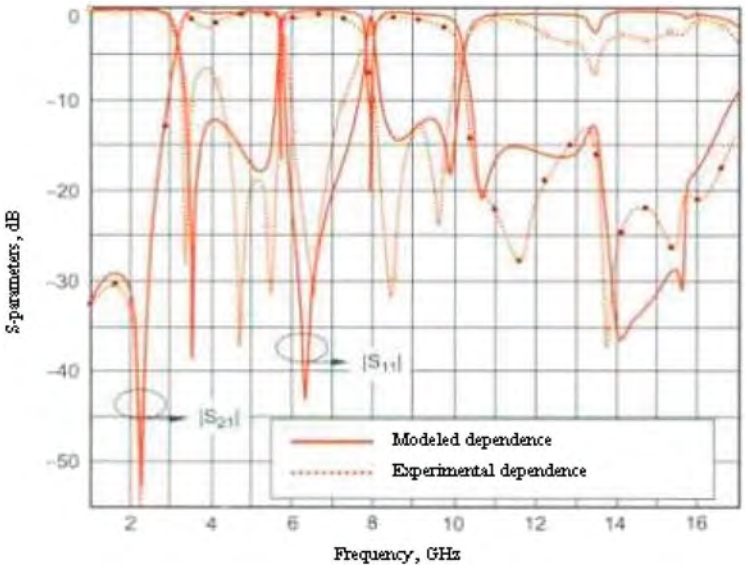

Fig. 9.3 Comparison of experimental and modeled dependencies

reduced. When the inner cut (L6 in Fig. 9.2b) is extended, upper threshold frequency is reduced.

This filter is manufactured using a printed duroid board (RT/5880) 0.813 mm thick. Relative dielectric constant of the substrate is 2.20 along the Z axis at 10 GHz; loss tangent is 0.0027. Optimal dimensions of the structure: L1 = 7.0 mm; L2 = 6.7 mm; L3 = 5.0 mm; L4 = 6.2 mm; L5 = 5.1 mm; L6 = 3.8 mm; L7 = 2.4 mm; W1 = 0.3 mm; W2 = 0.2 mm; W3 = 0.6 mm; W4 = 8.0 mm; W5 = 7.0 mm; W6 = 4.8 mm; W7 = 1.4 mm; D0 = 0.1 mm; D1 = 0.5 mm; D3 = 0.6 mm; D4 = 0.1 mm.

Figure 9.3 [1] shows experimentally obtained and modeled results; as can be seen, measurement and modeling results are almost identical.

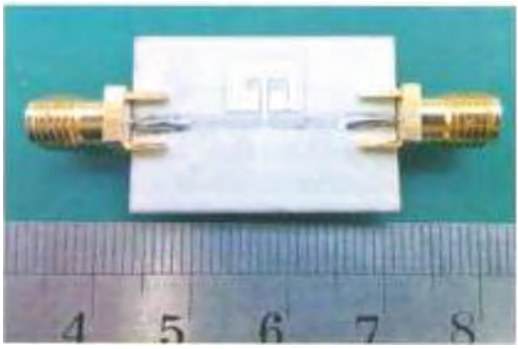

Fig. 9.4 Appearance of the filter

Reverse loss factor of such filter is usually not worse than 15 dB in most part of the pass band. Inserted loss ratio on both stop bands exceeds 15 dB. As indicated by developers [1], measurements were performed at frequencies of 5.8 GHz and 8.0 GHz. 3 dB losses amount to 1.1% at 5.8 GHz and to 1.2% at 8.0 GHz. Zeros are at 2.3 GHz and 11.6 GHz. Small discrepancy between modeling and experimental measurement results is due to such factor as reflection from connectors or end coefficient of losses in the substrate. Figure 9.4 shows the appearance of this filter. Overall dimensions of this device are 20 × 27 mm.

9.2 Features of Using Acoustic Wave-Based Microwave Filters

Features of application of surface-acoustic-wave SHF filters for wireless devices are detailed in [2, 3].

As is known to specialists, frequency spectrum within the range of 400 MHz. . .6 GHz is occupied by a large number of wideband wireless and telecommunication signals. In particular, LTE, GSM, CDMA, WiFi and Bluetooth devices operate within this spectrum. For example, frequencies near 60 GHz are allocated for WiGig wireless transmission. 60 GHz radiation is absorbed by atmosphere and radiation, and therefore WiGig devices can operate at distances of not more than 10 m at low signal power. Thus, they do not require powerful filter.

The following structural filtration methods are usually applied for WiGig devices: waveguides integrated into substrate, cavities on reversed integrated circuits, as well as the use of MEMS technologies and foiled non-radiating dielectric waveguides.

Frequency spectrum that is not supported by the device shall be filtered out in order to avoid interference. Due to the fact that the size is an important parameter for wireless devices, various “tricky” filtration circuits, which ensure matching of impedances and small size, are used.

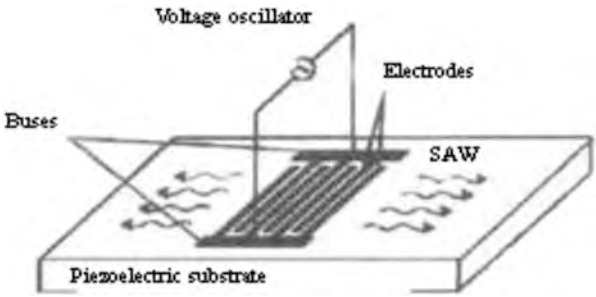

Fig. 9.5 Structure of a surface-acoustic-wave filter

When designing such filter, it is necessary to take into account many parameters: inserted losses, selectivity, reverse loss factor, linearity, power and thermal stability. Small size is an important factor for most modern devices; moreover, the height is as important as the area of the component or board.

Latest achievements in the field of acoustic filters make it possible to manufacture small-sized and precise filters. Surface (SAW) and Bulk (BAW) Acoustic Wave-based filters are successfully used for HF and SHF ranges.

SAW filters are usually made on piezoelectric substrate, the ends of which contain converters of the acoustic signal into electrical signal. The body of such filter consists of an array of electrons of alternating polarity. When electromagnetic field is applied, the structure generates surface wave (Fig. 9.5).

SAW filters are commercially applied at frequencies of 30 MHz. . .3 GHz. At low frequencies, filter dimensions become too large, and SAW filters are therefore usually replaced with monolithic bulk acoustic wave filters, other sides of which are made of piezoelectric ceramics. At frequencies above 3 GHz, resolution of the photolithographic process cannot provide high percentage yield, and the price of such filters cannot compete to other solutions, except for special applications (military equipment, weapon systems, space instrument engineering, etc.).

Figure 9.6 shows the basic LC circuit connected to power source with internal resistance $R[1]_s$:

$$V_{out} = X_t \cdot V_{in}/(X_t + R_s) \tag{9.3}$$

where $X_t = X_L X_C/(X_L + X_C)$; $X_C = 1/jwC$; $X_L = jwL$. Formula (9.3) can be rewritten as:

$$\frac{V_{out}}{V_{in}} = 20\text{lg}, mag\left[\frac{jwL}{R_s - w^2 R_s LC + jwL}\right] \tag{9.4}$$

$$Q = \frac{f_c}{f_b - f_a} \tag{9.5}$$

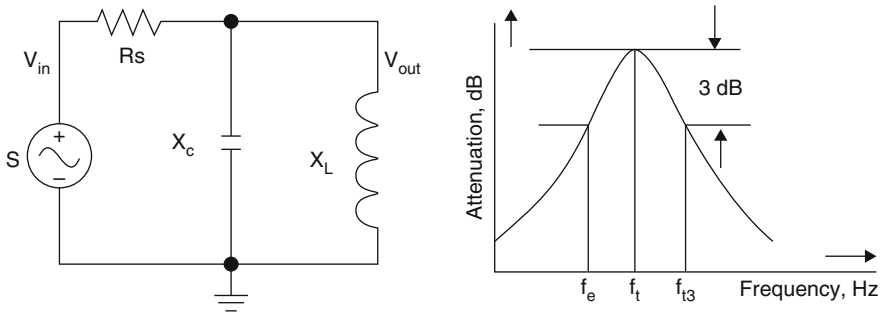

Fig. 9.6 Resonant LC circuit and output characteristic of SAW filter

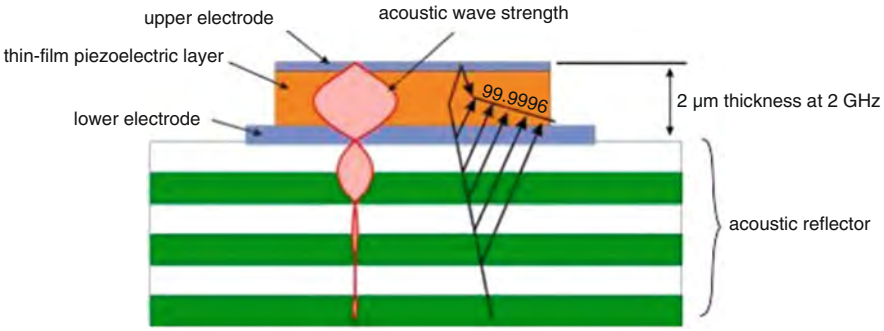

Fig. 9.7 Structure of a bulk-acoustic-wave filter

The other type of filters is represented by bulk acoustic wave filters (BAW).

Surface-acoustic-wave filter is a crystal resonator with metal electrodes at the top and bottom. Under the effect of the electrical system, the crystal resonator generates acoustic waves that create the standing wave inside the device (Fig. 9.7). Acoustic energy propagates in vertical plane. In order for the resonance to occur at high frequency, the thickness of the substrate shall be equal to several micrometers. As compared to other devices of the same size, BAW filters are characterized by lower coefficient of inserted losses and higher Q-factor in the SHF range.

The type of the adjustable filters used is also very important for the developer.

Filter characteristics are adjusted by changing capacity of the varactor by supplying control voltage.

Figure 9.8 shows one of possible circuitry configurations. The circuit consists of two resonators connected by inductive coupling.

$$L_C = L_Q, \tag{9.6}$$

where L ισ the inductance of the resonance circuit; Q is τηε loaded Q-factor of a single resonator.

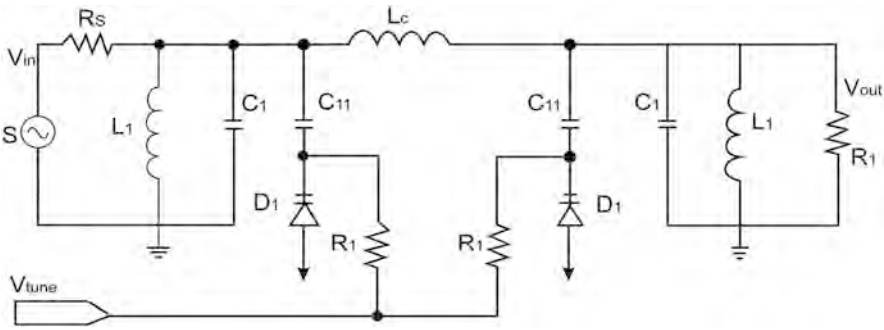

Fig. 9.8 Adjustable filter with two resonators

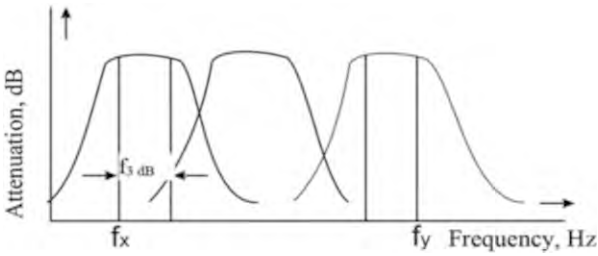

Fig. 9.9 Output characteristic of the filter

Inductive coupling is used during work at higher frequencies. Total capacity of the resonator is determined by the following relation:

$$C = C_1 + C_{11} \| C_V,$$

where C_V is the varactor capacity.

Both varactors are controlled by the V_{tune} signal.

Let us assume that the filter must be switched from frequency f_x to frequency f_y, and the frequency band of 3 dB equal to $f_{3\text{ dB}}$ is set (Fig. 9.9). The first necessary step is to determine values of L and C ensuring resonance at the required frequency. It should be noted that Q-factor of the circuit is higher in case of lower inductance and greater capacity.

For the selected L value at angular frequencies f_x and f_y the capacitance of capacitors C_{fx} and C_{fy} is calculated. To switch the filter from the frequency of f_x to f_y, capacitance C_{fx} shall be replaced with capacitance C_{fy}. This is performed by changing the control signal on the varactor. Typical output characteristic of the varactor is shown in Fig. 9.10.

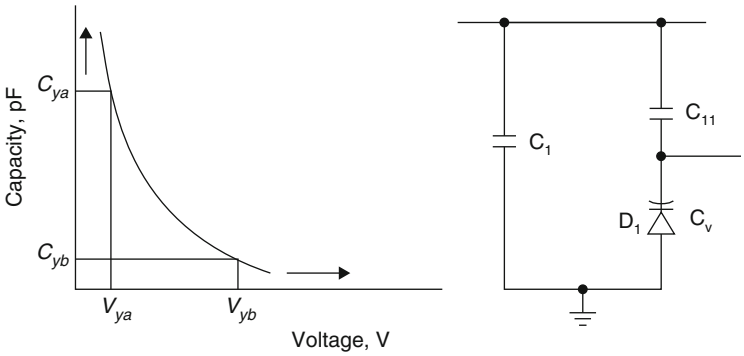

Fig. 9.10 Adjustable varactor-based circuit

The range of the varactor capacity is limited by values C_{ya} and C_{yb}. Let us calculate the capacities C_1 and C_{11}. If C_{11}»C_{yb}, the following relations are true:

$$C_{\min} = C_{f1} = C_1 + C_{yb},$$

$$C_{\max} = C_{f2} = C_1 + C_{11} \| C_{ya}.$$

After that, Eqs. (9.4) and (9.5) are used to calculate values C_1 and C_{11} for given values of C_{ya} and C_{yb}. Inductance of the connecting choke is calculated according to the formula (9.6).

As wireless technologies are constantly evolving, the problem of isolation of signals from each other becomes more and more complicated. Therefore, developers are more and more actively using acoustic wave-based filters and adjustable filters for separation of signals [2, 3].

9.3 Features of Using Special Design Solutions of Cable Sealing Glands for SHF Devices

As is know, absolute majority of radar sets and other SHF devices are designed for operation in heavy duty conditions. Therefore, developers of radar sets are forced to use corresponding technical solutions with regards both to packages of the designed products and to selection of the SHF element base, including corresponding connectors, wires and cables for structural design of different units and nodes of radar sets. All these structural elements are actually important and influence a lot of parameters. Selection of connectors is based on the contact current value, required mechanical engaging force and mounting method. Design of wires and cables must take into account their operation possibility in the conditions of the given

environment. The package of an electronic unit is also produced based on the required mechanical and climate protection.

However, there is one problem point, neglect of which can negate all adopted effective design solutions: this is the cable I/O point. Here, it is necessary to ensure the given high level of protection from dust, dirt and moisture, as well as mechanical protection of the cable. It is possible to use a reliable connector with additional mechanical fixation and sufficient engaging force; however, if its disengagement is problematic, then the wires can be easily torn out of it during maintenance of the unit. The same applies to possible breakage of conductors under the effect of vibration and impacts. Therefore, product developer shall not only to take measures for sealing of the input, but also ensure proper fixture of the cable. Moreover, it is necessary to remember that the cable I/O point can receive or emit radiation of electromagnetic interference. Traditional rubber seal or plastic holder in this case cannot ensure proper shielding, as their installation requires a hole with the diameter much greater than the diameter of the shielded cable itself.

As is known, these problems in the past were solved with the help of rubber seals, by processing inputs with sealants or glues, while mechanical strength was ensured by brackets or special clamps. However, the clamps often crushed the cable during operation, since it was bent and compressed for reliable fixation. Today, such solutions can only be used for single-time and non-critical applications. Rubber seals degrade over time; their fillers migrate into the cable shell and reduce its reliability. Moreover, they do not guarantee proper fixture. Mechanical brackets cannot ensure protection from dust and moisture, while plastic holders can damage the cable. Additional sealing with special compounds affects repairability of the device. Therefore, shielding of inputs is always very important. It is often performed by soldering the cable shield to the enclosure at the point of cable input; however, repairability in this case is not provided at all.

Specially designed inexpensive sealing glands are the best reasonable solutions. Today, many types of these seemingly insignificant structural elements are produced. The use of such sealing glands will help developer of the equipment, as well as consumers and maintenance personnel, avoid multiple problems. Thus, it is possible to significantly reduce the effects of vibration, mechanical impacts, dust and dust, which impair quality and reliability of equipment (Fig. 9.11).

This sealing gland eliminates the need to care about the state of the cable input, e.g. in cable boxes. The cable is reliably fixed by rubber seal, which ensures sufficient sealing of the input and prevents the cable from movement and deformation. At the same time, internal parts of the device are properly isolated from environmental effects. The cable can be easily moved, laid anew and fixed in the required position once again due to the original collet-type clamp. The cable is secured with the help of a cap nut. All this simplifies the assembly and improves maintainability of the end product. Appearance of the design of such sealing gland is shown in Fig. 9.12.

The simplicity of the solution is due to the fact that the gland performs the function of holding clamp of the external plastic coating of the cable or wires by means of cylindrical coupling. It is made of special elastic rubber preventing

Fig. 9.11 Typical collet-type sealing gland ORTAC (PG11) [4]

Fig. 9.12 Structural elements of a typical collet-type sealing gland

migration of its filler into the cable coating. Appearance of the cable is not impaired: there is no dark blurry band, which is typical of rubber seals of the old type. Cap nut not only fastens the cable, but also ensures the required clamping strength. Due to this fact, it is fully protected from damages during attachment.

Collet-type sealing glands can be made not only of plastic. Their metal modifications can be used for special applications requiring proper shielding if the cable I/O point. These sealing glands operate reliably in the most extreme conditions and ensure immunity of equipment to electromagnetic effects, as well as the minimum level of emitted radio interference. Examples of such sealing gland installed on the cable are shown in Figs. 9.13 and 9.14.

There are many types of sealing glands, which differ in therms of materials and dimensions depending on the field of application. For convenient selection of the specific type, it is enough to know the diameter of the opening in the device where the sealing gland is to be installed. The range of diameters of sealing glands is given in Table 9.1 [4].

Sealing gland packages are usually made of polyamides or brass and coated with nickel. They are distinguished by different ranges of operating temperatures and fire resistance and ensure the protection class IP65, IP67 or IP68 (Table 9.2).

One of the directions in further development of collet-type sealing glands consisted in modernization of their structure by introducing additional elements increasing their reliability and facilitating their use in specific applications. For

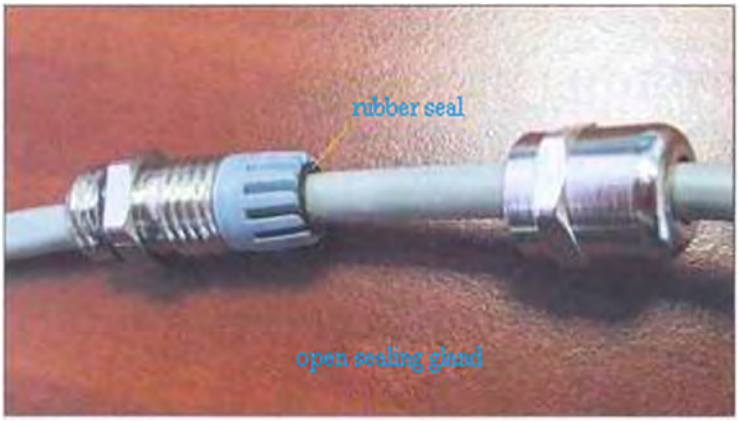

Fig. 9.13 Open metal sealing gland of collet type installed on cable [4]

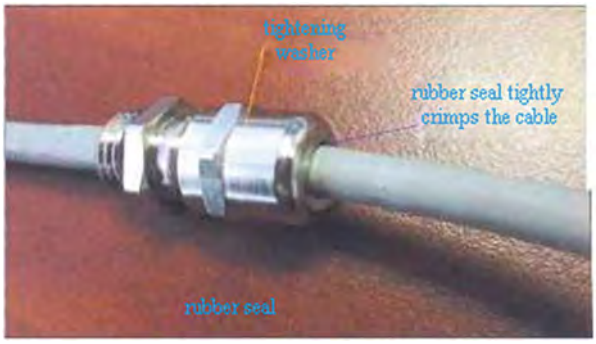

Fig. 9.14 Metal sealing input of the collet type installed on cable [4]

Table 9.1 Standard range of values of sealing gland diameters

Thread type	Diameter
Inch	PG7, PG9, PG11, PG13.5, PG16, PG21, PG29, PG36, PG42, PG48
Metric	M16x1.5, M20x1.5, M25x1.5, M32x1.5, M40x1.5, M50x1.5, M63x1.5

Table 9.2 Operating temperature range

Sealing gland package material	Operating temperature range, °C	Permitted short-term temperature excess, °C
Polyamide	−30... + 80	+150
Nickel-plated brass	−40... + 100	
Polyamide U0-UL94	−40... + 100	

example, a combination of sealing gland and flexible input was created. This reduces the load on the cable in case of its bending at the fixture point. As is known, this place is the most vulnerable in designs with moving cables. Such significant addition is found in sealing glands of series OMRG, OMRL, OMRB and ORG, ORL, ORB (Fig. 9.15). They are also produced with different dimensions, which makes it easier for designers to select them for specific design of the cable I/O point.

Sealing glands with cylindrical sleeve of heat-resistant silicon rubber are designed for operation in elevated temperature conditions (Fig. 9.16): they can be operated at temperatures within −40 – +200°C. They are represented by MBSG and PBSG series with metric and inch ranges of sizes.

In addition, there are sealing glands of OKMR and OKRP series with improved cable fixture (Fig. 9.17). Their feature consists in the cable strain relief.

Fig. 9.15 Sealing gland with flexible input reducing cable bend load

Fig. 9.16 ORTAC sealing gland

Fig. 9.17 Sealing gland with reinforced cable fixture

Therefore, a wide selection of sealing glands is currently offered to developers of SHF systems. This helps solve the problems related to inclusion of cables into devices requiring special protection from the environment. The use of sealing glands makes it possible to ensure reliability and operating characteristics of the products due to guaranteed elimination of negative environmental effects on internal elements of their control units, as well as ensure reliable mounting and fixture of cables.

9.4 Russian Powerful Stripline SHF Resistors

Telecommunication systems, first of all means of communication, navigation and radar location are the main motive force of development of SHF electronics.

The most visible progress over the last 20 years occurred in the field of strip microwave electronics; Russian developers – JSC "NPO ERKON" and JSC "KB Ikar" – fairly successfully compete with foreign companies.

First Soviet strip SHF resistors (S6–9, R1–8) were developed in the 1970s for hybrid SHF microcircuits and modules. Chromium silicide-based alloys were used as materials of the resistive layer (PC3710, 5402, etc.). These materials ensure acceptable values of stability under electrical load and TRC within ±150 ppm/deg.

The main trend in the development of resistor SHF component base in the subsequent years was the increase in power and operating frequencies of products with simultaneous reduction of their overall dimensions. The works of Russian manufacturers in this direction resulted in a series of high-power microwave resistors for strip lines: R1–2, R1–3, R1–5, R1–9, R1–17. Structurally, these resistors are usually designed as flat chips with planar contacts and metallized reverse side; they are installed directly on the heat removal path with the help of soldering or on the intermediate fixture element – screw or flange.

Resistors R1–2 and R1–5 failed to gain widespread mostly due to their relatively low dissipation power (up to 5W), while resistors R1–3, R1–9 and R1–17 are actively used in a wide range of SHF equipment. According to specialists, resistors R1–17 are the most advanced of the group in terms of their characteristics. These resistors are considered in detail in the following.

This type of resistor is designed for operation with heat removal in wideband units of high-frequency equipment as end loads, in power division and addition circuits, at direct and alternating current within the frequency range of 0–3000 MHz. Operating temperature range: −60... + 125°C. Main parameters of these resistors are given in Table 9.3 [5, 6].

The main design variants of resistors are shown in Fig. 9.18.

Production of R1–17 resistors was launched in 1996. At first, the resistor with power of 100/150 W was developed; in 2006, the range was extended by the R1–17 product with the power of 400 W, and in 2007, the device with the power of 250 W was invented; this range of resistors was significantly extended in the following years in terms of power.

Table 9.3 Main parameters of powerful stripline SHF resistors of the R1–17 series

Resistor type	Nominal dissipation power, W	Nominal resistance, Ohm	Permitted resistance deviation, %	Operating frequency range, GHz	Running hours, h	Weight, max, g
R1-17-100	100	12,5; 25; 50; 75; 100	±1; ±5	4.3	20,000	4.0
R1-17-150	150			4.3	15,000	4.0
R1-17-250	250	12,5; 25; 50; 75; 100	±5	6.5	15,000	7.0
R1-17-400	400	12,5; 25; 50; 75; 100	±5	12.4	15,000	11
R1-17-100-1	100	12,5; 25; 50; 75; 100	±1; ±5	4.3	20,000	1.5
R1-17-150-1	150			4.3	15,000	1.5
R1-17-A[a]	150	12,5; 25; 50; 75; 100; 150	±1; ±5	(0 to 1.0)	15,000	3.5
R1-17-B[a]	150			(0 to 1.0)	15,000	5.0
R1-17-250-2[a]	250	12,5; 25; 50; 75; 100	±5	(0 to 0.8)	15,000	10.5
R1-17-400-2[a]	400	50	±5	(0 to 0.4)	15,000	10.5
R1-17-400-2.1[a]	400	50	±5	(0 to 0.5)	15,000	10.5

Note: [a]The resistor can be used as terminal load

Fig. 9.18 Design variants of R1–17 resistors

Similar foreign devices are also found in the Russian market. According to expert estimates, the ratio of the shares of imported/Russian products in the market can be presented as 50/50 [5, 6].

Most popular foreign analogs are the resistors produced by American companies Anaren (models RFP-250-50 RM, RFP-400-50T) and ATC (models CR13725T0100J, CR13737T0100J, FR10870N0100JBK, FR10975N0100JBK), which make up 80–90% of the market volume of foreign analogs of R1–17. Moreover, products of American companies Aeroflex (KDI-Resistor Products) and Barry (Barry Industries, Inc) are available.

It should be noted that most foreign manufacturers use beryllium oxide-based substrate (BeO) in their products instead of aluminum nitride-based (AlN) ceramics, which is traditionally used for powerful resistors. This helps achieve better heat

dissipation, but negatively affects environmental safety, as beryllium compounds are extremely toxic, especially in the form of dust and gas, have allergic and cancer-inducing effects and irritate skin and mucous membranes.

9.5 High Frequency Connections for Active Phased Antenna Arrays

The aim of this section ισ τo consider structural features and operational characteristics of the most widely used high-frequency connectors for radar equipment manufactured by Russian and foreign companies (A. I. Shokin Enterprise "Istok", "Radiant-Elcom", Irkutsk Relay Plant, Carlisle, Glenali, Amphenol) [7].

The main directions in APAA building is increasing the number and density of transceivers and reduction of the product cost due to high integration of transceivers in a single module. Therefore, one of the most difficult tasks in designing new APAA is the problem of ensuring heat removal from transceivers and selection of high-frequency connectors for connection of these transceivers to antenna elements and APAA control system.

For the purpose of convenient presentation of material, let us use the simplified AESA design shown in Fig. 9.19. Fixed number of antenna elements (1) are individually connected to the corresponding number of transceivers (2) (one transceiver per one antenna element), heat removal from which is ensured by the cooling system (3). Control system (4) is connected to the rear part of transceiver modules; cooling system is also connected to it. The system (5) of adaptive processing and generation of the monopulse signal is located behind the control system.

Switching of high-frequency AESA path is performed by means of small-sized high-frequency connectors with SMP latches.

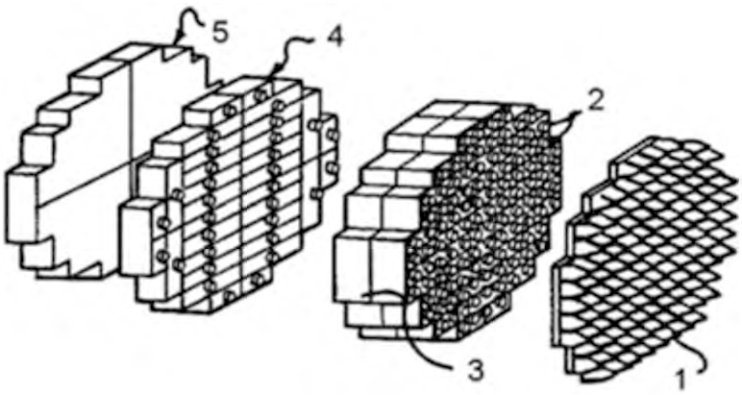

Fig. 9.19 Simplified variant of presentation of the APAA structure

Connectors used in AESA designs shall conform to the following basic requirements:

- upper application frequency: 40 GHz;
- latching junction mechanism;
- small overall dimensions, possibility of connection with center-to-center distance between connectors equal to 4.8 mm;
- possibility of surface mounting on the printed board;
- strong structure ensuring vibratory loads of at least 10 g and impact loads of at least 100 g;
- presence of golden coating to ensure good shielding properties.

These requirements are met to the fullest extent by SMP connectors included in the 94007/94008 DESC standard and represented in Russia by Rosenberger, Radiall and Carlisle.

Connectors by Irkutsk Relay Plant

Of the range of Russian manufacturers, we will consider one of the leading companies in this class.

The plant has developed Russian analogs of imported connectors of the SMP series [8, 9]. The following specifics shall be considered: production of connectors with QCD acceptance is performed by A.I. Shokin JSC "NPP Istok" [8], while serial production of connectors with the quality category "VP" is carried out at Irkutsk Relay Plant [9].

Main characteristics of connectors by JSC "Irkutsk Relay Plant" are given in Table 9.4. Figure 9.20 shows the appearance of connectors, Fig. 9.21 – their design.

The following types of connectors are produced: straight/angular cable socket for soldering on cable RK50-1.2-22, RK50-1-23, PK50-1-24, sealed appliance inlet, sealed plug-to-plug connector, socket-to-socket connector. It is necessary to specifically note the socket-to-socket adapter, the so-called Bullet, one of the task of which is the transmission of signal between two printed boards parallel to each other. Production of adapters with individual package length is possible by orders of radar set developers, which allows the APAA developer to ensure the necessary distance between printed circuit boards.

These connectors are characterized by relatively high mechanical strength, which helps ensure their operation in various AESAs of military aircrafts and space vehicles. Permissible sinewave vibratory loads usually amount to 10 g in the frequency range of 50–2000 GHz, while permissible impact loads reach 40 g. Packages of unsealed connectors of this series are made of BrB2 bronze (according to GOST 15834) packages are gold-plated in order to improve shielding properties. Cases of sealed connectors are made of 29 NK alloy (according to GOST 10994). The connector is sealed by means of glass-to-metal seal with helium leakage rate of 1.3×10^{-11} m3·Pa/s (1×10^{-7} l·μm Hg/s).

One of the main tasks within the framework of designing of Russian analogs of SMP connectors was the creation of small-sized high-frequency connectors for application in radar equipment with high component density, necessary operational characteristics and high reliability.

Table 9.4 Basic characteristics of connectors

Connector name	Connector designation	Limit operating frequency, GHz	Voltage standing-wave ratio (VSWR), max	Direct losses, dB, max	Shield attenuation, dB at least
Direct cable outlet	SR-50-969VF-00	26.5	1.6	0.55	−65
Direct cable outlet	SR-50-969VF-01				
Direct cable outlet	SR-50-969VF-02				
Angular cable outlet	SR-50-970VF-00	26.5	1.5	0.5	−65
Angular cable outlet	SR-50-970VF-01				
Angular cable outlet	SR-50-970VF-02				
Direct cable outlet	SR-50-971VF-00	40	1.6	0.55	−65
Direct cable outlet	SR-50-971VF-01				
Direct cable outlet	SR-50-971VF-02				
Sealed appliance inlet	SRG-50-972V	18	1.35	0.35	−65
Inter-board connection socket	SR-50-968FV	18	1.6	0.6	−65
Sealed adapter	SRG-50-974V	18	1.35	0.35	−65

Fig. 9.20 Appearance of connectors. Here: (**a**) SR-50-968FV socket-to-socket connector; (**b**) SR-50-969FV-00, SR-50-969FV-01, SR-50-969FV-02 straight cable socket; (**c**) SR-50-970FV-00, SR-50-970FV-01, SR-50-970FV-02 angular cable socket; (**d**) SR-50-971FV-00, SR-50-971FV-01, SR-50-971FV-02 straight cable socket; (**e**) SRG-50-972V sealed appliance inlet; (**f**) SRG-50-974V sealed adapter

All these connectors have successfully passed strict control for conformity to the requirements of reliability by short-term and long-term tests for failsafe operation and preservation in accordance with GOST RV 20.57.414. Rated service life of connectors amounts to 25 years; they are capable of withstanding 5000 hours of effect of +155 °C temperature. The number of junction cycles reaches 100.

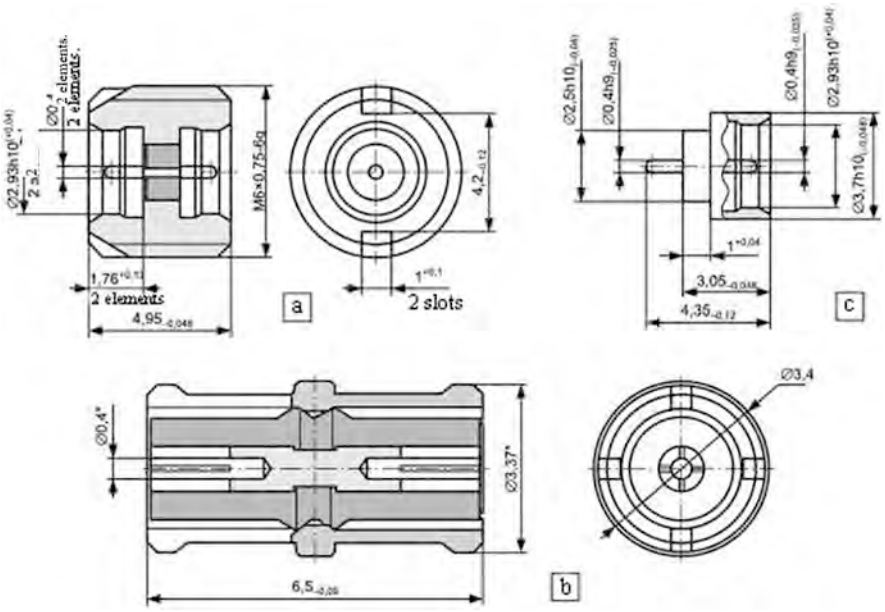

Fig. 9.21 Typical design of Carlisle connectors. Here: (**a**) straight cable socket KAPD.434511.020; (**b**) sealed connector (adapter) KAPD.434511.021; (**c**) socket-to-socket connector KAPD.434511.023

Carlisle company is one of the largest manufacturers of radio frequency cables.

Connectors for mounting on cable always ensure certain flexibility in selection of cable products; they support mounting on Russian cables, as well as on foreign semi-rigid coaxial cables with diameters of 0.047“ and 0.086”.

Cables are manufactured according to the Semi-Flex technology; i.e., the cable retains its shale when bended manually. This feature of Carlisle cables presents an advantage in comparison with other semi-rigid coaxial cables, bending and shaping of which requires a special tool. External cable conductor consists of braid with copper strand and tin coating. In addition to the specific design of the external conductor, inner layers of copper foil, central conductor and dielectric with semi-rigid structure ensure high operational characteristics and radio sealing of Carlisle products, which set them apart from competing products. Basic technical characteristics of semi-rigid coaxial Carlisle cables are given in Table 9.5.

Appearance of the Semi-Flex cable reinforced with connectors is shown in Fig. 9.22 [1].

In conclusion of this section, we will provide a brief overview of miniature combined connectors with power contacts of the MicroD series, parameters of which are regulated by the MIL-DTL-83513 standard (appearance of the MicroD series connectors is shown in Fig. 9.23). These connectors are widely used in onboard radars due to their small dimensions and high component density (contact

Table 9.5 Characteristics of Carlisle cables

Cable type	Series	Insulation type	Maximum operating frequency, GHz	VSWR at maximum frequency	Supported series of connectors
.047Semi-flex	604	No[a]	20	1.50:1	SMP, SSMP, SMA, MMCX
.086Semi-flex	600	No[a]	40	1,38:1	SMP, SSMP, SMA, K, MCX, TNC, N, BMA
	620	Polyurethane	26.5	1.17:1	
	650	Fluorinated ethylene propylene (FEP)	18	1.17:1	

Note: [a]Only external conductor with tin-plated copper braiding

Fig. 9.22 General view of Carlisle Semi-Flex based cable assembly

Fig. 9.23 Appearance of MicroD connectors

Fig. 9.24 Appearance of TwistPin contact

Table 9.6 Characteristics of connectors of the MicroD series

Parameter	Value
Operating current load on contact (at −50... + 150°C)	3 and 13 A
Operating voltage	600 V at the sea level, 150 V at 21 km
Insulator resistance	Min 5000 Ohm
Contact resistance	Max 8 mOhm
Operating temperature range	−50... + 150°C
Immunity to saline solution	48 h
Mechanical impact	50 g
Sinusoidal vibration	20 g
Number of engagement cycles	500
Engaging force	2.8 N per contact
Shielding efficiency	Min 65 dB

pitch 1.27 mm). In Russia, connectors of this series are represented by products of Glenair and Amphenol. MicroD connectors have rectangular form factor, which ensures dense arrangement, and are equipped with milled packages made of aluminum or stainless steel.

In connectors of the MicroD series by Glenair, pin contacts of the unique TwistPin design are used, which are characterized by low electrical resistance due to large area of contact between the pin and the socket and high vibratory resistance. The image of TwistPin contact is shown in Fig. 9.24. High operational characteristics of the contact are achieved due to the features of its design, formed by intertwined gold-plated beryllium copper wires with a thicker section in the central part creating the spring effect when coupled with the socket. Parameters of MicroD connectors are presented in Table 9.6.

9.6 HF and SHF Components of Spectrum Advanced Specialty Products

Spectrum Control, Inc. (USA), founded in 1968, is one of the leaders of the world market in the segment of HF and SHF components.

In this section, we will present a brief overview of development of the line of these components and their most popular series.

Products of Spectrum Advanced Specialty Products (SASP), member of Spectrum Control.

The company develops 4 fields of HF and SHF components:

- Coaxial Filters&Interconnects;
- Advanced Ceramic Components;
- Power Filters & Film Capacitors;
- Specialty Connectors & Cabling.

It is necessary to note that SASP applies the principles of uniting components into groups that are different from the ones traditionally used in Russia. For convenient navigation of the reader through the company website [10–15] and possibility of comparison with catalogs and technical documentation, classification of the manufacturer will be saved below.

The group "Coaxial filters and intercomponent connections" includes the following products:

- surface mount filters;
- terminals;
- filter assemblies;
- low frequency filters;
- rectangular connectors with integrated filters.

Surface mount filters produced by SASP make it possible to increase the mounting density and achieve subminiaturization of modern radio equipment with the help of automated component mounting means.

The line of surface mount filters includes the following series:

– SF (Fig. 9.25) 3-pin feed-through capacitors (4 standard sizes: 0603/0805/1205/1806), with a wide range of capacities: COG (NPO), 22–470 pF, X7R, 470 pF – 0.047 μF, Y5V 0.1 and 0.22 μF. Voltage – 25/50/100 V, current – 0.3-2 A, temperature range – −55. . . + 125 °C.
– LC/LZ filters of the LC type with the cutoff frequency of 10–220 MHz for the LC series and of 10 MHz – 2 GHz for the LZ series. Operating voltage – 25V, current – 50–100 mA (earlier versions of this series had the current of 10 mA).
– MSM/RSM/SSM/PSM – the family of filters of the Power Filters category designed for application in telecommunication equipment.

Fig. 9.25 Appearance of SF series SMD filters by SASP

Table 9.7 Technical characteristics of Power SMD filters

MSM	RSM	SSM	PSM
10 A – C-filter	10 A – Pi-filter		20 A – C-filter 10 A – Pi-filter
47, 150, 270, 1000 pF	100, 500, 1500, 2000, 4000 pF		68 pF – 0.01 μF
100 V	100 V		200 V

They are designed for maximum current of 10A (for series SSM/RSM/MSM) and 20A (for PSM).

Basic characteristics of Power SMD filters are given in Table 9.7.

It should be noted that the line of SMD components by Spectrum Advanced Specialty Products is fairly well optimized for potential consumers in terms of the scale of capacities (nomenclature redundancy has been minimized). Here, each standard size has 4–5 capacitance values (except for SF 8–10 series – 10 capacitances) with voltage scale of 25/50/100/200 V, which allows developers and manufacturers to solve their problems without resorting to significant extension of the applied list of products.

Terminals are a small problem, which is nevertheless important for developers of microwave radar equipment.

The line of products of SASP includes two type of terminal blocks with integrated filters:

– PCB mount for mounting on printed circuit boards. Manufactured with integrated 2500 pF integrated filter for voltage of 100 V and maximum current of 12 A. There are two different pin pitches: 5.08 mm (American standard) and 5 mm (European standard). Number of terminals: 2–12.

Typical values of introduced attenuation – 10.4 dB at 10 MHz, 29.9 dB at 100 MHz and 49.9 dB at 1000 MHz.

– Filtered Terminal Blocks – for suspended mounting. Each terminal contains an integrated Pi filter with capacity of 2500–5200 pF for voltage of 100V and current of up to 20A. The number of terminals in the unit: 2–6. Typical values of introduced attenuation – 22 dB at 30 MHz, 48 dB at 100 MHz and 75 dB at 1000 MHz.

Terminal blocks are designed for application in HF and SHF telecommunication and measurement equipment and power supply systems of SHF units.

In addition to single filters, the company produces **filter assemblies.**

SASP production program includes 3 families of filter assemblies:

– Easy Mate Filter Plates 52-898-XXX-XXX и 52-960-XXX-XXX;
– Easy Mate Jr. Filter Plates 52-978-XXX-XXX and 52-979-XXX-XXX;
– Bolt-in Style Filter Plates 52-970-XXX-XXX and 52-971-XXX-XXX.

Table 9.8 Basic characteristics of Filter Plates

Series	Designation SASP	Center-to-center distance[a], mm	Number of rows in the plate	Max qty. of filters in a row, pcs. (A-B-C-D plate)	Standard plate side
Easy mate filter plates	52-898-XXX-XXX	2.54	1 or 2	6 (A) or 13 (B)	A = 27.74 mm B = 46.02 mm
	52-960-XXX-XXX	2		7 (A) or 16 (B)	
Easy mate Jr. filter plates	52-978-XXX-XXX	2.54	1	7 (A) or 10 (B)	A = 25.15 mm B = 31.49 mm
	52-979-XXX-XXX	2	1	7 (A) or 10 (B)	
Bolt-in style filter plates	52-970-XXX-XXX	2.54	1 or 2	5 (A), 10 (B), 20 (C), 30 (D)	A = 26.92 mm B = 39.62 mm C = 65.02 mm D = 90.42 mm
	52-971-XXX-XXX	2		6 (A), 12 (B), 25 (C), 37 (D)	

Note. [a]2.54 mm – standard density, 2 mm – high density

Filter Plates – filter assemblies (sometimes referred to as filtering boards or plates). Filter plate is one of the most in-demand and popular components of the SASP nomenclature, which is applied in data transmission and processing devices, security systems, telephone communications, control circuits and other fields requiring protection of the processed signals from distortions due to HF interferences. Filter assemblies are sets of filters of a certain configuration (C- or Pi-type, 20 options total) soldered into the plate of standard size.

This makes it possible to install groups of filters in radio equipment. Main characteristics of Filter Plates are given in Table 9.8.

All three series have similar parameters but differ in terms of design and mounting technique. Electrical characteristics of filters used in the assemblies are given in Table 9.9.

Certain common parameters for all three series of Filter Plates can be presented:

- Maximum current – 5 A for standard density of arrangement of filters (with center-to-center distance of 2.54 mm) and 3 A for high density (with center-to-center distance of 2 mm).
- Diameter of pins is 0.64 mm for standard density and 0.51 mm for configuration with high density of filters.
- 4 options of pin configuration:

  (a) straight;
  (b) bent at 90° at both sides;
  (c) bent at 90° at one side (left or right position relative to the marking surface), straight at the other side (Fig. 9.26).

Table 9.9 Characteristics of filters applied in Filter Plates assemblies

Filter code	Type of the filter	Capacity of the filter	Capacity deviation	Cut-off frequency (at the level of 3 dB) MHz	Voltage, V	Minimum attenuation value, dB							
						5 MHz	10 MHz	20 MHz	50 MHz	100 MHz	200 MHz	500 MHz	1 GHz
A	C	68 pF	±20%	77	100	–	–	–	–	–	3	10	16
B		100 pF	±20%	53	100	–	–	–	–	1	6	14	19
C		135 pF	+100/−0%	23	100	–	–	–	1	5	10	16	20
D		470 pF	±20%	11	100	–	–	2	7	13	19	25	27
E		820 pF	±20%	6	100	–	2	6	12	18	24	30	33
F		1000 pF	±20%	5	100	–	3	7	14	20	26	32	35
G		1500 pF	±20%	3.5	100	1	4	10	16	22	29	36	37
H		2500 pF	+100/−0%	1.3	100	5	11	17	23	29	35	38	40
I		4000 pF	+100/−0%	0.8	100	9	15	21	27	34	38	42	46
J	Isolated	10 pF	Max	635	100	–	–	–	–	–	–	–	–
K	Grounded insert		–			–	–	–	–	–	–	–	–

L	Pi	68 pF	±20%	65	100	–	–	–	–	1	6	17	23
M		100 pF	±20%	46	100	–	–	–	–	2	9	22	28
N		135 pF	+100/−0%	25	100	–	–	–	1	6	17	26	34
O		470 pF	±20%	11	100	–	–	–	9	18	22	36	43
P		820 pF	±20%	6	100	–	–	4	13	23	31	45	52
Q		1000 pF	±20%	5	100	–	2	7	16	24	36	51	59
R		1700 pF	+100/−0%	1.9	100	1	6	14	28	35	49	64	69
S		2500 pF	+100/−0%	1.3	50	4	9	16	28	41	54	70	70
T		5000 pF	+100/−0%	0.7	100	9	15	28	41	53	66	70	70

Fig. 9.26 Appearance of terminals

Fig. 9.27 Easy Mate Filter Plates assembly

Part number for the order is formed as follows (let us consider the example of the 52-971-206-IA0 assembly):

- 52 – designation of the Filter Plates group;
- 971 – high-density Bolt-in Style series;
- 206: 2 – number of filter rows, 06 – number of filters in a row
- IA0: I – filter code (Pi – 4000 pF (Table 9.9)); A – plate size (26.92 mm); 0 – configuration of pins (straight).

Filter assemblies have the following differences in terms of configuration of plates and mounting technique:

– Easy Mate Filter Plates (Fig. 9.27) are produced with two sizes of mounting plates (27.74 × 15.8 and 46.02 × 15.8 mm) with single-row and double-row arrangement of filters. Mounting in REE is performed by installation into the partition between units; fixation in the partition is ensured by slots of mounting plate.

Fig. 9.28 Easy Mate Jr. assembly Filter Plates

Fig. 9.29 Bolt-in Style Filter Plates assembly

– Easy Mate Jr. Filter Plates (Fig. 9.28) have two standard plates sizes (25.15 × 6.6 and 31.49 × 6.6 mm) with single-row arrangement of filters. This is a low-profile development of the previous series.
– Bolt-in Style Filter Plates (Fig. 9.29) – 4 standard sizes of plates: length: 26.92; 39.62; 65.02; 90.42 mm; height – 12.7 mm. Filters are arranged in one or two rows (with standard or high density). Installation in REE: with threaded fastening element, into external or internal panel of the device.

As an example, Fig. 9.30 shows standard method of mounting devices of Easy Mate Filter Plates series. This family of components has a number of advantages as compared to single filters:

- Ensures filtration of interference during transmission of signals between internal system modules.
- Helps reduce labor costs during mounting of multi-channel lines, including during mounting in partitions between equipment sections.
- Higher filtration performance as compared to SMD components at frequencies above 50 MHz.
- Reduced risk of damaging filtering elements during mounting (thermal shock during soldering), since there is no direct contact between the soldering tool and the ceramic filter.

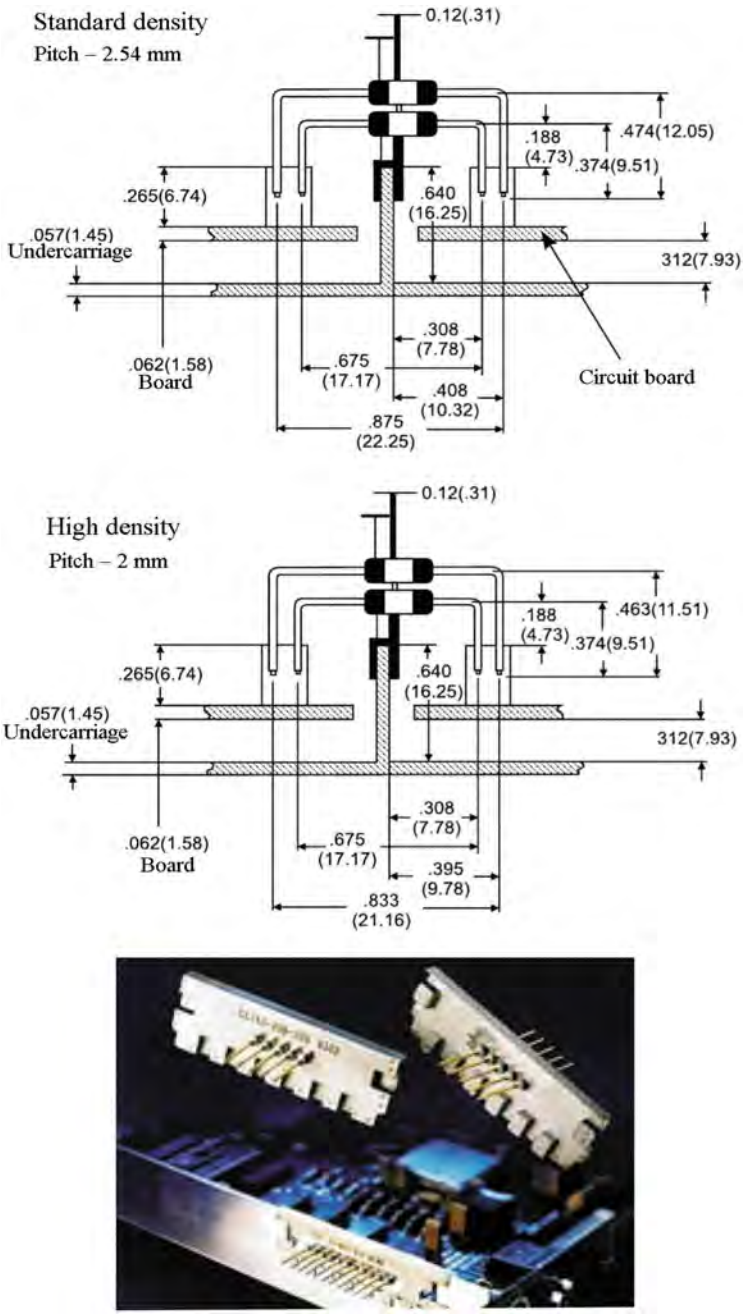

Fig. 9.30 Drafts and typical examples of mounting of the Easy Mate Filter Plates assembly (printed board)

- High reliability of the assembly: 100% testing of filters before mounting in the plate and after assembly.
- Possibility of implementation of the required (non-standard) assembly configuration. Individual solutions for the customer – combination of different filter types on one board.

Low Pass Filters (LPF) make up the basic list of components applied in microwave radioelectronic equipment – mostly for suppression of parasite electromagnetic interferences. Theoretical basics of this class of components, principle of operation and electrical circuits are detailed in [16]. Spectrum Advanced Specialty Products produces a wide range of commercial and military LPFs in accordance with the requirements of MIL-PRF-28861, MIL-PRF-15733 and DSCC 84084 designed according to C-, LC-, Pi- and T-circuits.

The range of filters is divided into 4 groups:

– Solder-in Filters – unsealed (unprotected) and compound-sealed, designed for soldering directly into the device package or on the printed board.
– Miniature Filters – small-sized, compound-sealed filters designed for soldering, pressing into the device package or mounting into a threaded channel.
– Resin Sealed Bolt-in Filters – compound-sealed, in threaded package.
– Hermetically Sealed Threaded Case Filters.

Let us briefly consider characteristics of each of these LPF groups.

Solder-in Filters (non-sealed filters)
Appearance of unsealed unprotected filters is shown in Fig. 9.31.

The range of this category includes 29 Pi-filters of 7 standard sizes with the bushing diameter of 2.79–5.94 mm. Capacitance range – 1300 pF – 0.022 μF; operating voltage – 50-500 V; maximum current – 10–25 A.

The most popular types of this group: 1223-012 (3000 pF), 1251-001 (1500 pF), 51-750-313 (0.022 μF), 51-713-002 (1500 pF).

They ensure the level of inserted losses of 65–70 dB at 1 GHz. Operating temperature range: 55... + 125 °C. SASP uses tubular two-section capacitors of its own design for production of filters of this category.

Fig. 9.31 Appearance of non-sealed filters

Filters of these category are widely used in data transmission systems as elements of filter assemblies of the required configuration.

Solder-in Filters (sealed filters) group is supplemented by a series of high-temperature inline filters of large diameter sealed with compound, SCI-9945 (Large Diameter Solder-in High Temp Filters). SCI-9945 is the development and continuation of the SCI-9900 series in the direction of increasing filter capacitance to 1.2 μF and maximum current to 15 A. This series is distinguished by high tolerable soldering temperature during mounting: up to +300 °C. Basic characteristics of SCI-9945 are given in Table 9.10, while appearance is shown in Fig. 9.32.

Filter design can be described as follows: inline multi-layered disc capacitor installed in flanged metal package. On the flange side, the filter is sealed with epoxy compound, on the other side – with glass-to-metal seal. There is also a reverse version, in which with glass-to-metal seal The filter is designed for use in circuits with low and medium impedance levels.

Mass series: **Miniature Filters** SCI-9900 (Miniature Solder-in Filters) and SCI-9925 (Spec Spin Filters) are widely known in Russia and used mostly in SHF modules and units due to their small size (package diameter 3.25 mm). SCI-9900 are soldered directly into the REE package; SCI-9925 is equipped with knurled filter package and pressed with the help of the SCI-9925-200 tool. These series belong to the category of low-capacity and are applied in circuits with low impedance. The range of capacitances (4 pF – 0.030 μF) is free from excess: SCI-9900 includes 8 types, while SCI-9925 includes only 7 of them, which is absolutely enough for solving tasks of EMC of radioelectronic equipment.

The group also includes the modified series of LC filters SCI-9980. Basic characteristics of the group are given in Table 9.11. Filters of this series are used in HF/SHF equipment of the 500 kHz – 10 GHz range in application where there is a difference between source and load impedances. Overall dimensions: package diameter – 3.25 mm, length – 5.08 mm, pin diameter – 0.76 mm. Package drawing is shown in Fig. 9.33; appearance of the filters is shown in Fig. 9.34.

Resin Sealed Bolt-in Filters group includes threaded filters in metal packages sealed with special compounds. SASP produces a wide range of C-, Pi- and LC-filters with thread of inch sizes #2–56, #4–40, #6–32, #6–40, #8–32, #10–32, etc. Wide ranges of capacitances (65 pF – 1.0 μF) and voltages (35–2500 V) are available. Maximum current – up to 100 A.

The appearance of threaded filters is shown in Fig. 9.35.

Two series of small-size threaded filters in metal package with metric thread are also produces. More specifically, these are series 54-863-XXX (C-filter, M3x0.5 thread) and 54-831-XXX (Pi-filter, M4 × 0.7 thread). Basic technical characteristics are presented Table 9.12.

Filters of the 54-874-XXX series (Spec Spin Filters) belong to the category of miniature threaded filters (Fig. 9.36). Mounting method: into prepared threaded hole (thread #2-56) into elements of the chassis or package of the REE with the help of the 54-874-200 tool.

Electrical characteristics: C-filter, capacitance: 10 pF – 0.01 μF, voltage: 50 V, current: 5 A. Package and pins are gold-plated. Due to small package diameter

Table 9.10 Basic characteristics of filters of series SCI-9945

Designation[a]	Type of the filter	Voltage, V	Current, A	C(min)	Minimum attenuation value, dB					
					500 kHz	1 MHz	10 MHz	100 Hz	1 GHz	10 GHz
SCI-9945-125H	C	50	15	1.2 μF	33	37	52	70	70	70
SCI-9945-504H	C	100	15	0.5 μF	26	34	42	58	70	70
SCI-9945-754H	C	100	15	0.75 μF	31	37	43	62	70	70
SCI-9945-105H	C	100	15	1 μF	31	40	48	64	70	70
SCI-9945-503HAC	C	200[b]	15	0.05 μF	7	15	34	42	70	70
SCI-9945-154HAC	C	200[b]	15	0.15 μF	17	24	38	50	70	70
SCI-9945-103H	C	400	15	0.01 μF	–	4	20	34	50	60
SCI-9945-503H	C	400	15	0.05 μF	7	15	34	44	70	70

Notes:
[a]Reverse version is available. Part order number – SCI-9945 R-XXXH
[b]200 V DC or 125 V AC/400 Hz

Fig. 9.32 Appearance of SCI-9945

(2.79 mm), the use of this component makes it possible to form filtering assemblies of the required configuration with minimum geometrical dimensions.

Finally, the **group of Hermetically Sealed Threaded Case Filters** includes filters in metal threaded package with glass-to-metal seals. Filters of this category are produced in three standard sizes with the package diameters of 9.78, 10.41 and 17.45 mm. Thread size 1/4-28 Unf-2A and 5/16-24 Unf-2A. Applied LPF circuits: C-, LC-, Pi-, T- and double T. The filters have high values of capacity between 0.03 and 5.2 μF, which ensures suppression of electromagnetic interference up to 80 dB within the frequency range of 10 kHz – 1 GHz and higher, maximum current up to 25 A and voltage of 50-400 V (Fig. 9.37). Filters of this category are mostly used in power sources of telecommunication equipment, industrial and medical equipment and control devices of electrical equipment of SHF devices and systems. Part of the range of low pass filters (about 40%) is formed by military-purpose components (MIL-PRF-28861, MIL-PRF-15733 and DSCC 84084).

In addition to the information presented in Sect. 9.3, developers of SHF devices shall also know about the connectors produced by this company.

Provision of EMC of radio equipment and the necessity of protection from the effects of external and internal electromagnetic interferences determines the use of different solutions. **Rectangular connectors are** one of the directions. They include not only filters, but also other more complex systems, such as ***connectors with integrated filters***.

The line of rectangular connectors by Spectrum Advanced Specialty Products also includes several groups, namely:

- D-Sub with integrated filters, including Low Profile, Combo, High Density, Micro D.
- Modular Jack RJ45 with integrated EMI filters or ESD protection, single or assemblies up to 8 connectors.
- Mini Din with EMI filters, single or assemblies of up to 6 connectors.
- USB with integrated EMI filters or ESD protection.
- The company produces several series of D-Sub connectors, which differ in terms of the type of applied filters and modifications:

Table 9.11 Basic characteristics of LC filters of series SCI-9980

Designation[a]	Voltage, V	Current, A	C(min)	Minimum attenuation value, dB					Labeling (point-color)
				1 MHz	10 Hz	100 Hz	1 GHz	10 GHz	
SCI-9980-100	200	10	10 pF	–	–	–	7	20	1-purple
SCI-9980-101	200	10	100 pF	–	–	5	22	35	1-green
SCI-9980-102	200	10	1000 pF	–	8	25	40	42	1-white
SCI-9980-103	200	10	0.01 μF	8	27	48	65	65	2-white
SCI-9980-122	200	10	1200 pF	–	8	28	42	50	1-white
SCI-9980-152	200	10	1500 pF	–	10	28	43	53	1-white
SCI-9980-153	200	10	0.015 μF	10	28	50	65	65	2-white
SCI-9980-250	200	10	25 pF	–	–	–	13	25	1-blue
SCI-9980-272	200	10	2700 pF	8	13	32	45	55	1-red
SCI-9980-273	200	10	0.027 μF	13	33	53	75	75	2-red
SCI-9980-333	200	10	0.033 μF	13	35	55	75	75	2-red
SCI-9980-501	200	10	500 pF	–	–	18	37	38	1-brown
SCI-9980-502	200	10	5000 pF	8	17	35	47	55	1-yellow

Note. [a]All filters are available in reverse version. Part order number – SCI-9980-XXXR

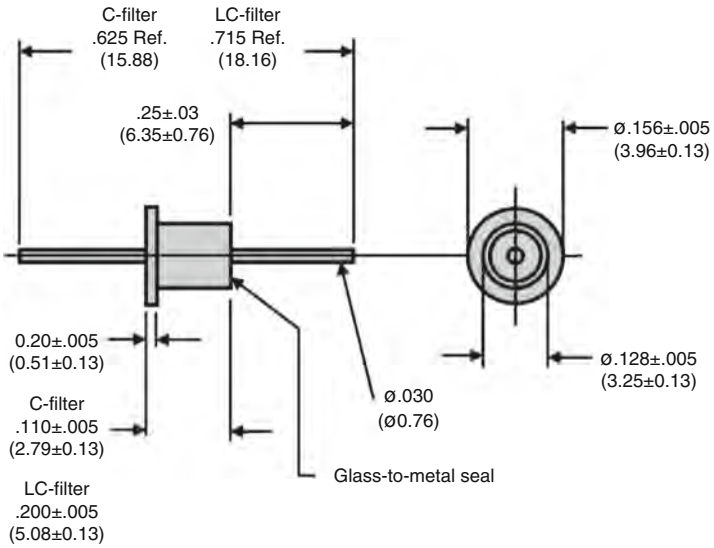

Fig. 9.33 Drawings of packages of SCI-9900 and SCI-9980 series

Fig. 9.34 Appearance of SCI-9980

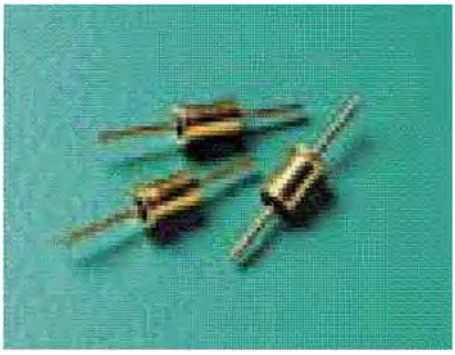

Fig. 9.35 Appearance of threaded filters

Table 9.12 Basic characteristics of filters

Designation	Filter type	C(min)	Voltage, V	Current, A	Thread size	Design features
54-863-004	C	0.01 μF	100	10	M3 × 0.5	Package length (max)-10.24 mm
54-863-005		100 pF				
54-863-007		1000 pF				
54-863-008		2000 pF				
54-863-010		4700 pF				
54-831-011	Pi	100 pF			M4 × 0.7	Package length (max)-15.06 mm
54-831-012		1500 pF				
54-831-013		3000 pF				
54-831-014		5500 pF				
54-831-015		0.012 μF				

Fig. 9.36 54-874-XXX series filters

Fig. 9.37 Example of design solutions of sealed filters

– 100 series: number of contacts – 9, 15, 25, 37. Leadless ceramic capacitors with capacitances of 50, 100, 180, 220, 470, 820, 1000, 1500, 2200, 5600 pF and 0.047 μF (customer configuration is possible) are used as filters (Fig. 9.38). Operating voltage – 200 V, current – 5 A, resistance of contacts – <8 mOhm. Operating temperature range − 55. . . + 85 °C. Mounted on printed circuit board or device panel.

Fig. 9.38 Appearance of D-Sub devices of the 100 series

Fig. 9.39 Appearance of D-Sub devices of the 700 series

Due to application of low-profile filters, overall dimensions of the connectors of this series are the same as in standard D-Sub. This makes it possible to modernize radio equipment without changing the design (replacing regular D-Subs with filtered ones).

– 700 series: number of contacts – 9, 15, 25, 37, 50. C- and Pi-type filters made of tubular capacitors (Fig. 9.39).

Electrical characteristics of the filters used in D-Sub connectors of the 700 series are listed in Table 9.13. Operating temperatures range is −55. . . + 125 °C. The series also includes D-Sub adapters (sometimes referred to as savers). The adapter is a two-sided D-Sub connector (plug) with integrated filters (Fig. 9.40). Each adapter has two flanges for mounting on REE panel. The use of the filtered adapter helps perform quick modernization, adjustment or change of the parameters of radioelectronic equipment and connection of cable assembles, at the same time ensuring protection from the effect of electromagnetic interference.

The most popular adapters are collected in the engineering kit 56-700-002 (Adapter Test Kit).

Combined D-subs (Filtered Combo D-Sub) (Fig. 9.41) are widely used in telecommunication and computer equipment, power sources of base stations and industrial equipment. 3 types of contacts are used in different combinations in this series:

- high-power – maximum current 20 and 40 A;
- coaxial – 50 and 75 Ohm;
- signal – maximum current 5 A.

Table 9.13 Characteristics of filters used in D-Subs of the 700 series [1]

Code of the filter	Type of the filter	Filter capacity	Capacity deviation	Cut-off frequency (by level) 3 dB, MHz	Voltage, V	Minimum attenuation value, dB									
						5 MHz	10 MHz	20 MHz	50 MHz	100 MHz	200 MHz	500 MHz	1 GHz	2 GHz	5 GHz
J	Pi	100 pF	+100/−0%	32	100	–	–	–	2	6	11	27	40	43	40
A		310 pF	±20%	1.1	100	–		3	1	13	21	36	43	50	45
C		1000 pF	+100/−0%	3.2	100	–	5	9	19	30	43	62	70	68	63
K		2500 pF	+100/−0%	1.3	50	8	13	18	33	45	58	73	78	70	65
E		4000 pF	+100/−0%	0.8	50	8	13	20	35	48	61	76	80	70	65
N	C	375 pF	±20%	14	200	–	–	2	1	13	20	29	35	30	29
L		500 pF	±20%	10.6	200	–	–	3	10	15	22	31	37	33	31
F		830 pF	±20%	6.4	200	–	4	9	16	22	28	35	39	38	36
B		1000 pF	+100/−0%	3.2	200	–	5	10	17	23	30	37	43	44	42
D		5000 pF	+100/−0%	0.61	100	10	16	22	30	35	41	50	52	52	50

Fig. 9.40 D-Sub adapter

Fig. 9.41 Combo D-Sub series

Integrated filters of the C-type, in-line, with capacity of 470, 820, 1000, 1500 and 4000 pF. They ensure filtration of electromagnetic interferences. Most popular configurations:

- 3W3 3 power (or coaxial) contacts;
- 5W5 5 power (or coaxial) contacts;
- 9W4 4 power (or coaxial) contacts and 5 signal contacts;
- 24W7 7 power (or coaxial) contacts and 17 signal contacts.

Configuration of outputs makes it possible to mount Combo D-Sub connectors directly on the PCB or in the device panel.

Micro D-Sub series is a relatively new one in the production program of Spectrum Advanced Specialty Products. It is manufactured in accordance with the requirements of MIL-DTL-83513 for 9, 15, 21, 25, 31 and 37 contacts (Fig. 9.42). The basis of the line of integrated filters is formed by inline filters with capacity of 100, 470, 820, 1500 and 4700 pF. Operating frequency – 100 V, maximum current – 3 A. Minimum inserted attenuation (for the 4700 pF filter) – 34 dB at 100 MHz and 54 dB at 1 GHz.

In addition to the above types of connectors, filtered series are produced: 500 Low Profile, 600 Hi-Density (15, 26, 44, 62, 78 contacts), RJ45 (single and assemblies of up to 8 pcs), mini-DIN, USB1.1 and 2.0.

The overview of the range of coaxial filters, filter assemblies and connectors with integrated filters would be incomplete without familiarization of the main elements of these components – special ceramic capacitors, tubular and disc.

Fig. 9.42 Micro D-Sub appearance

Spectrum Advanced Specialty Products (SASP) has its own scientific and manufacturing base for development and production of these components.

9.7 Ceramic SHF Components for Radar Sets

9.7.1 Ceramic Capacitors

Let us consider features of this class of SHF components in the specific context of products by Advanced Ceramic Components – one of the leaders in this field of the world market. Depending on structural design, tubular and disc ceramic SHF capacitors are distinguished.

Tubular condenser is a ceramic pipe with applied external and internal electrodes (C inline type) or a two-sectional structure – one external and two internal electrodes (Pi-circuit). Electrodes are usually made of silver with nickel-barrier sub-layer; the material of ceramic tubes – NP0, X7R, Y5V. These capacitors are designed for voltage of 50, 100 and 200 V. The range of capacitances is fairly wide – from 10 pF to 0.015 μF.

Structurally, these are 7 standard tube sizes with inner diameter of 2.06–3.10 mm, inner diameter of 1.27–2.08 mm and length of 4.39–8 mm, with permissible deviation of geometrical dimensions of ±0.05 mm for tube with inner diameter of 2.06 mm and ± 0.1 mm for tube with diameter of 3.10 mm (Fig. 9.43). Tubular ceramic condensers are used for production of Solder-in filters (unsealed), as well as elements of filter assemblies Filter Plates, filter contacts for D-sub connectors of series 700, D-3899 and terminals (Filtered Terminal Blocks).

Disc multi-layer ***capacitors*** have higher values of capacity and voltage as compared to tubular ones. The range of capacitances – from 33 pF to 15 μF; voltage – 50, 100, 200 and 500 V. Applied ceramic materials include NP0, X7R, and Z5U. ACC produces 7 standard sizes with outer diameters of 2.03–15.11 mm, inner diameters of 0.76–2.41 mm and thickness of 1.14–3.18 mm, with permissible tolerance of geometrical dimensions of ±0.13/±0.25 mm (Fig. 9.44). Disc capacitors are used in production of hermetically sealed threaded case filters.

Fig. 9.43 General view of tubular ceramic condensers

Fig. 9.44 General view of disc ceramic condensers

Field of application of tubular and disc capacitors is not limited by the needs of radar equipment manufacturers. Manufacturers of radio equipment for commercial and industrial applications widely use these components in their circuits as integrated elements of printed circuit boards and modules where EMC tasks need to be solved.

Another direction of development of capacitors is represented by SMPS (***Switch Mode Power Supply***) sources (Fig. 9.45). The component is an assembly of multilayer ceramic capacitors with high capacitance (Cmax = 47 μF at 50 V) with configuration of pins for three-dimensional or surface mounting. SMPSs have the following advantages compared to tantalum capacitors: lower values of ESR and ESL and low level of voltage pulses. Typical dependence of ESR on frequency for tantalum and SMPS capacitors is shown in Fig. 9.46.

The industry produces three standard sizes of capacitor assemblies SMP-3, 4, 5, and their range is constantly being expanded. The range of capacitances – from 0.01 μF to 47 μF; voltage – 50, 100, 200 and 500 V. TCC groups – BP, BX, BR and BQ. SMPS series is certified for use in military equipment according to MIL-PRF-49470 and DSCC 87106.

Fig. 9.45 General appearance of SMPS capacitors

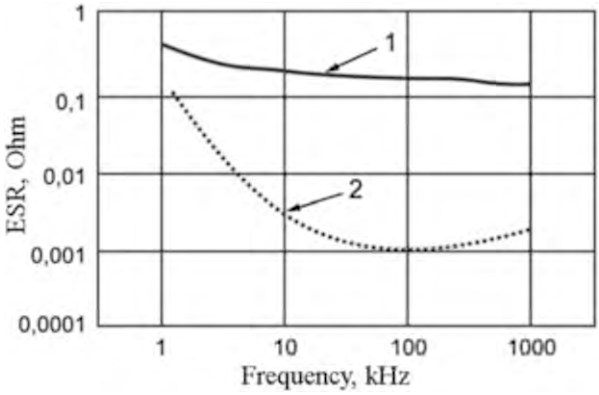

Fig. 9.46 Typical frequency dependence of ESR tantalum and SMPS capacitors 1- typical dependence of tantalum capacitors, 2 – typical dependence of 30 μF capacitor X7R.

9.8 Line Filters and Film Capacitors for Radar Sets

Condenser devices of this type are designed for application in radar sets, as well as electrical equipment, telecommunications, power industry, industrial and medical equipment, computer equipment and direct and alternating current with frequency of 50/60 Hz.

The field of **Power Filters & Film Capacitors** usually includes several basic groups:

- Single Line Filters;
- Power Entry Modules;
- Power Line Filters, single-phase and three-phase;
- Film Capacitors.

Let us consider the main features of these devices in the specific context of the SASP company. The line of **single line filters** has the common designation 52-226-XXX-XXX or 52F226-XXX-XXX for RoHS version (Fig. 9.47). The

Fig. 9.47 Single line filters

Fig. 9.48 Input network modules

main purpose of this class of filters is suppression of electromagnetic interferences in power lines of devices. Filters with two main circuit types are used, C- and Pi-type, with the use of protective capacitors of the Y2/Y4 type.

Y2 class filters are used in alternating current circuits with voltage up to 250V and have the following characteristics: capacitance range from 2200 pF to 1 μF, maximum current up to 300 A. Y4 class filters are used in direct current circuits with voltage up to 130V. Capacitance range from 0.01 to 4.7 μF, maximum current up to 300 A. Operating temperature range – −40. . . + 85 °C. Filters ensure suppression of EMI up to 90 dB at the frequency of 1 GHz with filter capacity of 4.7 μF.

Input network modules are designed for connection of power supply to the device and provision of protection from the EMI effect. Input network module is a connector (plug), which can have various configurations: single, with integrated fuse and combined with switch (with or without fuse) (Fig. 9.48).

All network modules contain integrated noise suppression filters designed according to the typical circuit (Fig. 9.49). Maximum current: up to 15A at voltage of up to 250V. Design of the modules makes it possible to mount them into device panel or on printed circuit board.

Another group of products is presented ***by network single-phase and three-phase filters***, which are finished off-the-shelf modules, which, if necessary, can be quickly installed on the device package or directly into it (Fig. 9.50). Connection is possible by means of standard terminals, as well as with the help of threaded connection. Filters are built according to single-stage or two-stage circuits and have low values of leakage current (0.35–3 mA max.). Maximum current: up to 120A (single-phase version) and up to 200A (three-phase version). Fields of application, in addition to radar equipment, include computers and peripheral devices, as well as UPS.

Film capacitors by SASP (Fig. 9.51) in the past were mostly used for production of powerful custom filters. Due to the development of the markets of alternative electricity sources and power electronics, this class of components was significantly

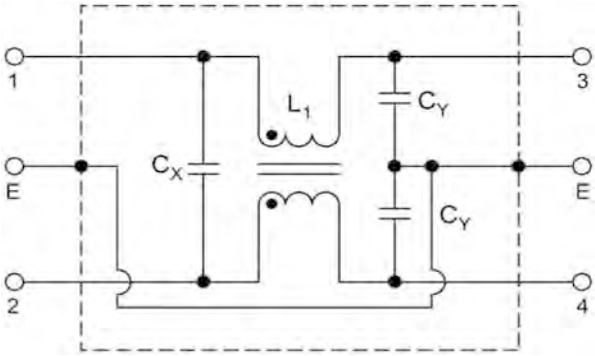

Fig. 9.49 Typical filter diagram

Fig. 9.50 Single-phase and three-phase line filters

Fig. 9.51 SASP film capacitors

expanded by consumers. Film capacitors are considered as an alternative to aluminum electrolytic condensers due to their lower values of ESR, ESL and ripple current. The line includes three basic series.

55DC Link – metallized polypropylene capacitors with capacitance of up to 680 μF and voltage of 900–1300 V. Their working temperature range is 55… + 85 °C (standard version), which can be expanded to −55… + 105 °C (Fig. 9.52). The main fields of use are inverters of wind generators and solar power plants, as well as electrical drive control systems.

Fig. 9.52 55DC series capacitors

55HV high-voltage polyester models with voltage of up to 20 kV, as well as 55PP high-power polypropylene models with voltage of up to 2 kV and capacitance of up to 100 μF. Application: alternative power sources, charging devices, electrical equipment of aircrafts, power sources of radar and laser equipment, electrical drive control, medical equipment.

9.9 Special Connectors and Cable Assemblies

The basis for this direction **(Specialty Connectors & Cabling)** is formed by filtered and non-filtered cylindrical connectors compliant with standards MIL-DTL-38999/83723/26482/55116 (Fig. 9.53), as well as connectors of the Rapid Mate family. The use of this class of connectors allows for complex solution to EMC (noise suppression) directly at the input/output of microwave radioelectronic devices or in connections between units, thus eliminating the need to apply separate filters (where possible) [3, 17–20].

Cylindrical connectors are manufactured with integrated filters of C-, LC-, Pi-types, which are based on tubular condensers or planar condenser assemblies (Fig. 9.54). Table 9.14 contains the list of the most popular and widely used configurations of C-filters and their electrical characteristics, provided as an example.

The capacitors can include filters of the same type or different types – specific solutions depend on the customer requirements. Main recommendations and features of application of this group of connectors are given in [20]. First of all, these cylindrical connectors are designed for military equipment, which often demands non-standard configurations and special solutions, as well as for onboard aviation electronics.

Fig. 9.53 SASP cylindrical connectors

Fig. 9.54 Planar filters

One of the latest inventions is the Mini-MIL-38999 series, which includes small-sized equivalents of cylindric connectors MIL-DTL-38999. The use of the new series makes it possible to minimize weight and dimensions of the radioelectronic equipment and simultaneously provide protection from interference. Mini-MIL-38999 are produced in configurations with 1–55 contacts; the size of contacts is #23 – #9. Integrated filters (C or Pi) ensure suppression of electromagnetic interference up to 70 dB (for Pi-filter with electrical capacity of 0.02 μF) within the frequency band of 1 MHz – 1 GHz.

In addition to filtered connections, there are also series without filters in the market: MIL-DTL-38999/83723/26482/55116 and Mini-MIL-38999.

Rapid Mate is the new series of special connectors, which can be supplied with or without filters (Fig. 9.55). Components applied in filtering assemblies (Filter Plates, Table 9.9) are used as filters, which ensures high level of protection from HF interference. Rapid Mate ensure quick (non-fixed) connection of mobile devices, such as portable radio stations, to chargers, or scanners for quick reading of information from the device.

Cable assemblies are non-standard devices produced according to individual orders with SASP connectors. As a rule, these devices are ordered by manufacturers of aviation equipment, aircrafts, weapons, oil and gas, industrial and medical equipment.

Table 9.14 Characteristics of C-filters applied in cylindrical connectors

Maximum electrical capacity of the filter, pF	Operating voltage, V		Filter cutoff frequency, MHz	Minimum attenuation value, dB				
	DC (+85 °C)	AC (+85 °C)		1 MHz	10 MHz	100 MHz	500 MHz	1 GHz
1000	200	115	5	–	4	21	34	39
2000	200	115	1	–	9	26	39	44
3000	200	115	1	–	12	30	43	48
5000	200	115	1	1	16	34	46	52
7000	200	115	1	3	19	37	49	55
10,000	200	115	1	4	21	39	52	57
20,000	100	–	0.5	9	26	44	57	62

Fig. 9.55 Rapid Mate series

9.10 Evolution of Packages for Devices and Units of Radioelectronic Equipment

For many years, packages were used solely as protective cases for electronic components in industrial and military electronic systems. Available packages were usually limited by simple box design. Limited range of dimensions significantly reduced the possibilities of radio equipment developers in selection of electronic SHF components. Connectors of the designed device were usually selected regardless of the package. Therefore, it was very difficult to combine all necessary element connections in a single package. Cost-effective solutions with extensive functionality were rare in such conditions [21].

Following the example of consumer electronics, manufacturers of military and industrial electronics have recently started reacting to the changing requirements for products. In particular, multi-purpose transforming packaged systems were invented, which can be easily modified depending on specific applications. Manufacturers of modern packages offer multiple solutions to these tasks. For example, Fig. 9.56 presents the range of packages by Phoenix Contact.

As is known, the performance of an electronic device is significantly influenced not only by the package itself, but by connection technologies as well. Ideally, packages shall not limit selection of the connection technology. For example, Phoenix Contact offers connections to the printed circuit board with the help of terminals as well as quick connectors in its series of packages ME and ME MAX. Device developers can additionally select connectors for different cross-sections of conductors 1.5 mm^2 and 2.5 mm^2. This means that the quantity of contacts can be varied within a wide range without changing the size of the board.

In the course of the last few years, increasing complexity of radioelectronic equipment and number of connections have made organization of electrical wiring a more complex task. Therefore, REE design specialists, especially in the field of microwave systems, mostly use the so called Plug and Play technology, which offers a system of packaged with connectible independent modules.

Fig. 9.56 Minimum range of electronic device packages by Phoenix Contact [1]

According to this technology, special connectors are simply inserted into the DIN rail and combined into a system. In order to ensure sufficient flexibility, the number of contacts can be changed. The widely used package ME PLC, for example, supports connection of up to 50 contacts. This makes it possible to create modular structured control systems for field and top levels of the automation system. Replacement of devices (e.g., for maintenance) is easily implemented, since separate modules can be removed from the group without interrupting operation.

Without this combined solution between the package and connectors for PCB connection, it would be impossible to design multi-functional systems necessary to satisfy modern production requirements.

Due to the fact that the space in the control cabinet of any radio equipment is usually very limited, many manufacturers use packages for electronic devices with connections in the easily accessible front part of the device. An example of such package, ME PLC, was created by Phoenix Contact according to these requirements. Red extractor is used to ensure reliable connection between connectors and convenient extraction of connectors from the package. The cover of the package already contains Push-in connectors to simplify the connection procedure. Conductors are attached to them with the help of a simple technology without using additional tools.

Dimensions and features of Phoenix Contact packages are determined by the number and arrangement of printed circuit boards, as well as overall dimensions of electronic components. Type and number of connection points also have significant influence on the package itself. Modular design devices are mostly used in the field of applications for measurement and control. Modular design principle turned out to be perfect for HF and SHF applications. Designers of innovative packages also offer configurable solutions for design of the package itself, and the device developer can create a custom consumer-specific package design. For example, the package BC 161.6 by Phoenix Contact allows for very flexible approach to device development (Fig. 9.57). Configuration of the package can allow the engineer to freely allocate mounting space for connectors to the printed circuit board. Moreover, orders for additional modification are possible if required by the developer.

Fig. 9.57 General appearance of the BC 161.6 package by Phoenix Contact [1]

Clearly, design and service of packages of electronic images are also very important for modern radio equipment. Modern and functional design of the package visually demonstrates quality of the product and professional level of the manufacturer.

Modern device manufacturers are interested in a much wider functionality of packages than simple protection of electronic components; packages shall be easily adapted to all customer requirements. Convenience and number of connections to PCB play the leading role in selecting the packaged system. Moreover, end design of the device is very important for many manufacturers; since the package is the "face" of any device, the manufacturer shall ensure the corresponding quality of packages, since the design of devices is a part of the company's image.

References

1. Belous, A., Merdanov, M., & Shvedov, S. (2018). *Microwave electronics in radar and communication systems* (Technical encyclopedia in 2 volumes, 2nd ed., revised, Vol. 1520, p. 2). Moscow: Tekhnosfera.
2. Belous, A., & Saladukha, V. (2019). *High speed electronics system design. Art, science, experience*. Cham: Springer.
3. Peng, H., Luo, Y., & Zhao, J. (2014). Small-sized filter for ultra-wideband systems. *Electronic Components, 11*.
4. Belous, A., Saladukha, V., & Shvedau, S. (2017). *Space microelectronics volume 2 integrated circuit design for space applications* (p. 605). Boston: Artech House.
5. Kosolapov, A. (2014). Sealing glands- an integral element of mechanical protection. *Components and Technologies, 6*, 174–175.
6. Simakov, S. V., Zudin, N. N., Suraleva, T. A., Podmogaev, V. E., & Pratusevich, N. Y. (2008). HF and SHF Resistors and Absorbers. In *Passive electronic components-2008: Proceedings of international science and technology conference*. Nizhny Novgorod.
7. Efremov, V. (2014). Component base for AESA: High-frequency connectors. *Components and Technologies, 9*, 22–24.

8. www.radiant.su
9. Dzhurinskiy, K. B. (2006). *Miniature coaxial radio components for microwave microelectronics. Connectors, coaxial-microstrip transitions, adapters, microwave inputs, low-frequency inputs, isolation stands, interference filters*. Moscow: Tekhnosfera.
10. Patent EP 0 621 654 A2 by Conrad, John C., Tomanek, Robert L., Boland, Timothy L.
11. www.glenair.com
12. www.carlisleit.com
13. Pavlov, S., & Filippov, A. (2014). Phased antenna arrays. A review of component base for implementation of transceiver modules. *Components and Technologies, 7*.
14. EMI Filters and Filterd Interconnects: Spectrum Control Inc. Catalog 27-0027-0048. (2002).
15. www.specemc.com
16. Dzhurinskiy, K. (2006). *Miniature coaxial radio components for microwave microelectronics*. Moscow: Tekhnosfera.
17. Easy Mate EMI Filter Plates: Design Guide. (2006).
18. EMI Filtered D-Sub Connectors: Design Guide. (2006).
19. Dzhurinskiy, K. B., & Filippov, A. V. (2007). Spectrum control products for suppression of electromagnetic interferences. *Components and Technologies, 7*.
20. Specialty Connectors & Harnessing: Design Guide. (2010).
21. Beck, A. (2014). Evolution of packages for electronic devices. *Electronic Components, 10*.

Chapter 10
Methods and Means of Ensuring Reliability of Radar and Communication Systems

10.1 Electromagnetic Compatibility: Terms, Definitions, Classification

10.1.1 The Nature of Electromagnetic Interference

In general, the term "Electro-Magnetic Compatibility (EMC)" refers to the ability of equipment to work correctly in its electromagnetic environment without affecting this environment, to which other electric devices also belong, in an unacceptable manner [1].

Currently, strong emphasis is being put on the issues of ensuring electromagnetic compatibility (EMC) of high-speed electronic devices and modules with their individual assemblies and components. There is an increase in requirements for further improvement of EMC characteristics due to constant widening of scope of electronic device application. System solutions based on microelectronics and semiconductor electronics are used in all industries, household and transport. Currently, the evaluation of products regarding to EMC is needed even more than at earlier stages of electronics development. The basic concepts of electromagnetic compatibility consider the effects of both radiated and conductive interferences (so-called crosstalks) propagated through conductors (for example, crosstalk on power supply circuits), as well as the sensitivity of electrical equipment to the effects of interference (immunity). In this case, the electromagnetic compatibility characteristics can be determined in the frequency range 0. . .400 GHz. Interrelation of basic electromagnetic compatibility concepts is given in Fig. 10.1.

Electromagnetic interferences arise from natural phenomena or as a result of technical processes. Examples of natural interferences include atmospheric disturbances (electromagnetic impulses are generated during lightning strike) or electrostatic discharges (ESD). The latter are particularly important for semiconductor electronics. In industrial equipment and radar system units, the main interference

© The Editor(s) (if applicable) and The Author(s), under exclusive license to Springer Nature Switzerland AG 2021

A. Belous, *Handbook of Microwave and Radar Engineering*,
https://doi.org/10.1007/978-3-030-58699-7_10

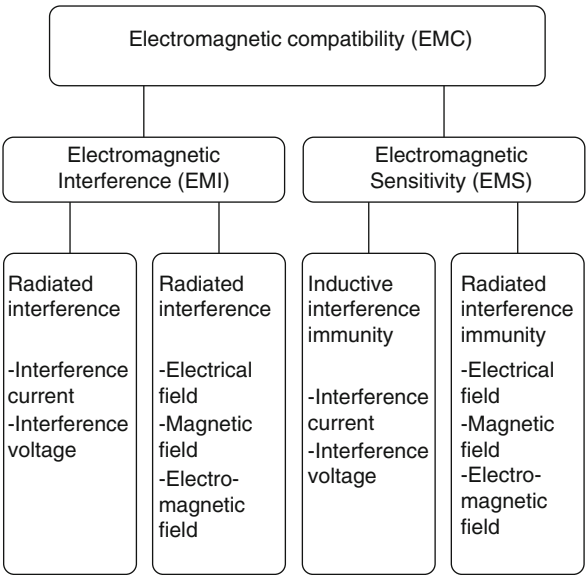

Fig. 10.1 Various aspects of electromagnetic compatibility [1]

source is a switch-over process in electric circuit related to very fast change in current and voltage that in its turn, leads to appearing of electromagnetic interferences which can be either periodic or random ones. The effects of these interferences can be of conductive nature (as current or voltage crosstalks in conductors) or of radiative nature (under influence of alternating magnetic field).

Type of conducted interference is called a symmetric or differential mode interference when the current induced in conductors has a sign, i.e. it flows with the same amplitude both in forward and backward directions. If the interference current is grounded or it flows in one direction, then such interference is called the asymmetric or common-mode interference.

Electromagnetic coupling between interference source and receiver can result from:

- galvanic coupling (the most commonly encountered case) that creates differential mode interferences;
- capacitive coupling
  that is caused by alternating electric field exposure to capacitive parasitics;
- inductive coupling caused by presence of conductor through which the current is flowing, in the alternating electric field;
- electromagnetic coupling that can be of conductive nature (occurs as crosstalk between conductors inside cable bundles or between conducting tracks of the printed circuit board); or it is propagated by radiation (if the gap width between the interference source and receiver exceeds 0,1 of radiation wavelength λ).

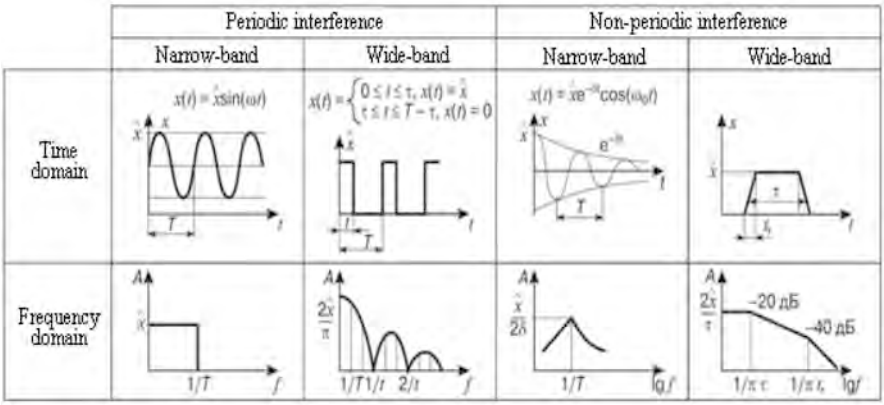

Fig. 10.2 Illustrations of different interference signals in the frequency and time domains

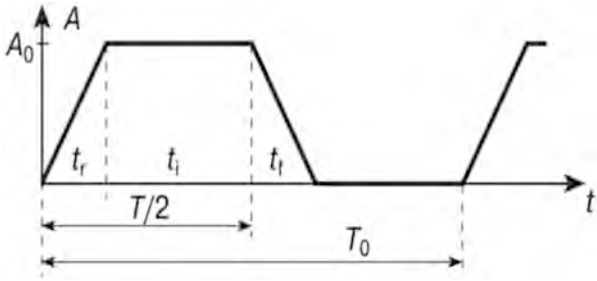

Fig. 10.3 Illustration of signal switch-over process as a trapezoidal function

Interference Signal Representation Forms

Interferences that are of periodic or random nature in certain time interval, can be mathematically represented as overlapping of sinusoidal and cosinusoidal signals of different frequency and amplitude. Figure 10.2 shows typical signals and interferences and their spectral representations.

Semiconductor switch contacts, logical integrated circuits, microcontrollers are the sources of broadband interferences caused by internal processes in these devices and by operation of clock-pulse generators. Signals of the specified interferences are of periodic nature and they can be decomposed in frequency spectrum using Fourier transformation. Approximating expressions that can be used when calculating the amplitudes and break frequencies of trapezoidal waveforms are given below in this section. An example of waveform is shown in Fig. 10.3; its relevant approximating spectrum envelope is shown in Fig. 10.4. Graph of spectral dependence of signal amplitude on frequency parallels the frequency axis from the base frequency of a signal to the first break frequency f_{g1}. The amplitude decreases with a slope of 20 dB/decade in the spectral region between the first and second (f_{g2}) break frequencies; and with a slope of 40 dB/decade in the last region.

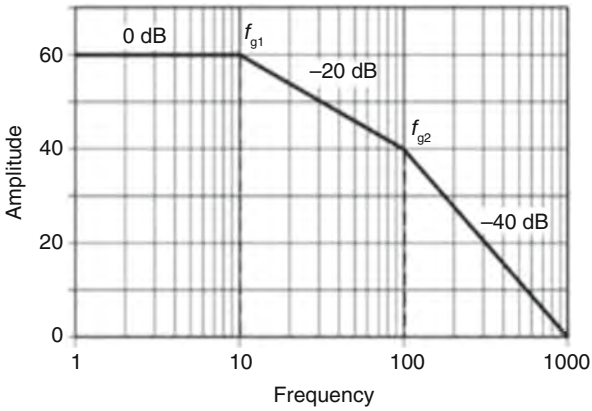

Fig. 10.4 Spectral characteristic envelope shape

The following notations are used in formulae below:

A_0 – original signal amplitude;
A_n – amplitude of$n$-th harmonics;
T_0 – period of the signal fundamental frequency;
t_i – pulse length;
t_S – switch-over time ($t_r = t_f$);
n – harmonic number of the fundamental frequency;
n_{g1} – number of harmonics of the first break frequency;
n_{g2} – harmonic number of the second break frequency;
f_0 – fundamental frequency;
f_{g1} – the first break frequency;
f_{g2} – the second break frequency.

The signal amplitude doesn't depend on the frequency [1] in the first spectral region within the frequency range $f_0 \ldots f_{g1}$:

$$A_n \approx \frac{2 \cdot A_0 \cdot t_i}{T_0}. \tag{10.1}$$

In the second spectral region within the frequency range $f_{g1} \ldots f_{g2}$, the signal amplitude falls with a slope of 20 dB on the decade:

$$f_{g1} = \frac{1}{\pi \cdot t_i}, \tag{10.2}$$

$$A_n \approx A_0 \cdot \frac{2}{\pi} \cdot \frac{1}{n}. \tag{10.3}$$

In the third spectral region (frequency is higher than f_{g2}), the signal amplitude falls with a slope of 40 dB on the decade:

$$f_{g2} = \frac{1}{\pi \cdot t_S}, \tag{10.4}$$

$$A_n \approx A_0 \cdot \frac{2}{\pi^2} \cdot \frac{1}{n^2} \cdot \frac{T_0}{t_S}. \tag{10.5}$$

Measurement of Electromagnetic Radiation

Measurements of electromagnetic radiation are performed in the frequency domain using a test pattern receiver or spectrum analyser. These devices allow for evaluation of various interference characteristics by measuring their peak, quasi-peak, average or effective values. In this case, measurements are performed in relation to the defined level providing for appropriate indication when measuring physical values from μV to V. The device readings correspond to logarithmic ratio of signal amplitude to reference value (this reference value is commonly referred in communication engineering to as effective power or interference power). The power level is determined as common logarithm of the measured signal power to actual power ratio multiplied by ten. It is measured in decibels [1]:

$$p = 10 \cdot \log_{10} \frac{P_x}{P_0}, \text{dB}. \tag{10.6}$$

In communication engineering, it is accepted that the reference (effective) power P_0 is 1 mW. For making emphasis on this, letter "m" is added to the unit of power level measurement (dBm, i.e. decibels are counted with respect to level of 1 mW). The level of voltage or field strength received during measurement of electromagnetic radiation has dimension dBμV or dBμV/m respectively, and the formula for it can be determined from the expression for power level. The reference value of 1 μV corresponds to the value of 0 dBμV. Therefore, the measured power level value of 0 dBm corresponds to the voltage level of 107 dBμV for systems with 50-Ohm wave impedance.

Voltage level formula [1]:

$$p = 20 \cdot \log \frac{U_x}{U_0}, \text{dB}\mu\text{V}. \tag{10.7}$$

The sensitivity of test receivers of electromagnetic interferences depends on the operating frequency which is determined according to the requirements of CISPR16 standard. The choice of frequency is made by means of different bandpass filters, depending on the required range of operating frequencies as it is specified in Table 10.1. [1]

Table 10.1 Choice of transition band of measuring bandpass filters according to the operating frequency range

Bandwidth (BW)	200 Hz	9 kHz	120 kHz
Frequency range	0.01…0.15 MHz	0.15…30 MHz	30…1000 MHz

If the reception channel of the receiver "captures" only one harmonic of interference signal, then the measured value doesn't depend on the transmission bandwidth (B_W) and the indicator characteristics. Such interference is called narrow-band. On the contrary, the broad-band interference occurs when the signal fundamental frequency is low; therefore, there are several signal harmonics at once in the frequency band of the test receiver, and the measured value depends on the receiver transmission bandwidth (B_W) and quality of signal harmonic analysis. In this situation, the "integrated" procedure for signal measurement is inapplicable since it doesn't reflect its actual amplitude-frequency characteristic (AFC). Such interference occurs when measuring the broadband signals at the boundaries between operating frequency ranges of the test receiver (0.15 MHz and 30 MHz) where step changes of their amplitude happen.

10.1.2 EMC Terms, Definitions and Classification

Electromagnetic compatibility of radio electronic systems (RES) is the ability of these devices to operate simultaneously under actual operating conditions, when exposed to spontaneous electromagnetic interference (SEI), without generating any intolerable electromagnetic interference (IEI) for other devices.

The scope of EMC issues under consideration includes almost all the radio frequency resource (RFR) that is divided into the following bands according to the standards of International Radio Consultative Committee [1]:

- 9–535 kHz;
- 535–1605 kHz;
- 1605–4000 kHz;
- 4–29.7 MHz;
- 29.7–100 MHz;
- 100–470 MHz;
- 470–2450 MHz;
- 2450–10,500 MHz;
- 10,500–40,000 MHz;
- 40000–275000 MHz;

Technical characteristics of any RES can be divided into two large groups:

- **Functional characteristics** such as radio-transmitted power and receiver sensitivity;
- **The characteristics influencing on the EMC level**. For example, the extraneous emission power and the receiver susceptiveness on the side channel.

Specialists distinguish the following EMC levels:

- Intra-hardware EMC (inside the unit, node, and etc.);
- Intrasystem EMC (inside the radioelectronic complex);
- Intersystem EMC (between different systems and complexes).

Practically, RES developers often use the term **"electromagnetic environment (EME)"**, meaning determination of real conditions under which the specific product operates or will operate with or without the desired signal in input during SEI action through this input or apart from it. According to three above-said EMC levels, three types of EME are determined respectively.

Methods and ways of ensuring EMC are divided into the following groups:

- **Organizational** measures generally belong to the level of intersystem EMC and include the rational choice of radio channel frequencies for different radio services, as well as determination of location for devices, and etc.
- **Technical** measures are divided into design-engineering and circuit-based ones. Design-engineering measures are implemented mainly at intra-system and intra-hardware levels of EMC ensuring. EMC ensuring requirements should be included in the design specification and in the subsequent production specifications during production and operation.

For deeper understanding of the essence of the material stated in this chapter, it is necessary to give a few terms and definitions from this technical field.

Electromagnetic interference is an electromagnetic, electric or magnetic process generated by any source in space or by conducting medium and influencing on operations with a desired signal in radioelectronic equipment.

Intolerable electromagnetic interference (IEI) generated in space is called a **radiated** interference; and IEI generated in conducting medium is called **conductive** (or inductive) interference.

Spontaneous electromagnetic interferences (SEI) is caused by random processes occurring in the interference sources; that's why they are of probabilistic nature and described by statistical tools.

Receptor is any engineering device reacting to an electromagnetic desired signal or to IEI.

Electromagnetic environment (EME) is the totality of electromagnetic, electric, magnetic fields, currents, interference voltages and signals in the defined region of space which influences or can influence on the receptor operation.

EME is quantitatively defined by EMC characteristics of the receptor.

Radio frequency resource is the totality of radio electromagnetic fields that is possible to use for data communication or energy transmit and receive.

Receptor sensibility is a metric for reaction to the external IEI with or without desired signal.

Sensibility threshold is the maximum allowed SEI level when the receptor works correctly.

Receptor immunity is a feature to resist to external and internal EMI due to the choice of the desired signal structure and receptor design concept.

Interference immunity of the receptor is a feature to resist to external and internal EMI due to circuit and design means which are not impairing the selected structure of the desired signal and receptor design concept.

Shield is a structural element of radioelectronic equipment in the form of metal grounded cover with high electrical or magnetic conductivity. It serves for attenuation of EMI in certain region of space within the wide range of frequencies.

Shielding is a way of EMI attenuation using metal cover (shield) with high electrical or magnetic conductivity.

Filtration is attenuation of voltage and interference current by using an electric circuit (filter) damping in the specified ranges and in the specified frequency bands.

Grounding is an electric circuit that possess the property of preserving the minimum (ground) potential.

There are two levels of a hierarchy in the EMI classification: EMI classification by type and by kind. Figure – shows the EMI classification by type: radiostation, industrial and natural interferences. In its turn, each of this types has its own "subclasses", first of all "radiated" and "conductive", etc.

The following terms are accepted in communication engineering for the most commonly occurring EMI:

So, **radiostation** interferences are generated by antenna of radio transmitting center.

Industrial interferences are generated by electrotechnical, electronic and radioelectronic household appliances, industrial, medical and scientific devices and equipment, etc.

In view of the diversity of interference sources, the industrial interferences are the most common type; it covers a wide range of frequencies (from tens of Hertz to a few gigahertz).

Natural interferences are caused by natural physical processes such as electromagnetic radiation (space and atmospheric noise, relict radiation, solar radio emission, atmospherics, electrostatic fields of different atmospheric formations, aircrafts, and etc.).

Contact interferences are caused by re-emission from current-carrying mechanical contacts with non-linear current conductivity when these contacts are exposed to radiation from rather high-power radio transmitter.

These interferences are typical for moving objects (ships, tanks, airplanes, cars, and etc.), and the level of such interferences grows with speeding-up of the object.

Figure 10.5 shows the conventional EMI classification by type.

Figure 10.6 shows the conventional classification of the second-level EMI by their kind: for example, interferences differ in frequency and spectrum (H4, B4, CB4, sinusoidal, impulse, modulated, noise, impulse-noise interferences), in time

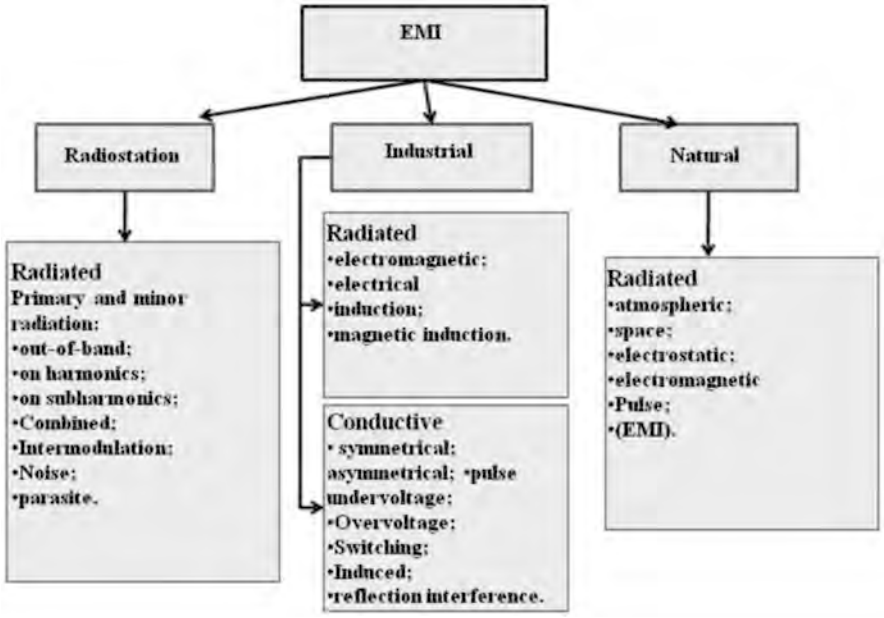

Fig. 10.5 EMI classification by type [1]

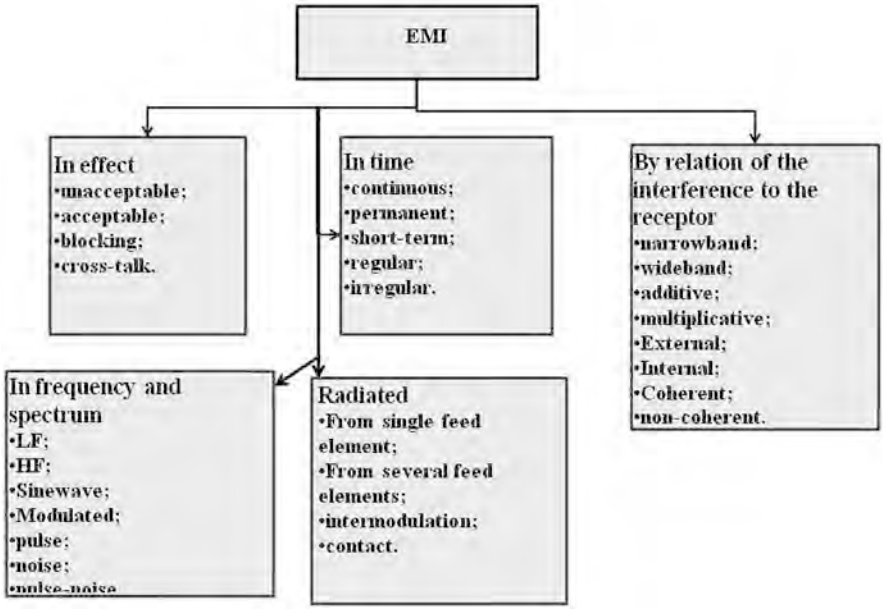

Fig. 10.6 EMI classification by kind [1]

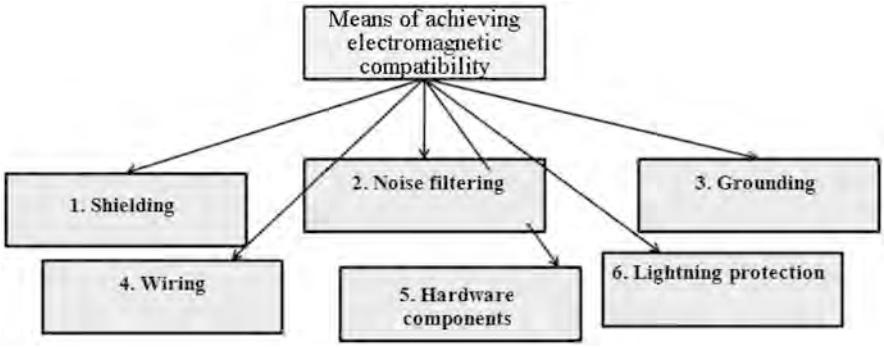

Fig. 10.7 Methods of ensuring EMC [1]

(constant, continuous, short, regular interferences), in effect level (permissible, intolerable, cross-talk, blocking interferences) in interference relation to the receptor (narrowband, wideband, additive, multiplicative, external, internal, coherent, non-coherent interferences), radiated (from one source, a few sources, contact, intermodulation interferences).

Figure 10.7 shows the basic methods (means) of ensuring EMC. These methods include shielding, filtering of interferences, electrical grounding, choice of special wired-logic connections and relevant element-component base, lightning protection (high-power electromagnetic pulse). Methods and means of RES protection against SHF-emissions and EMI are detailed below.

10.1.3 Regulations and Standards for Electromagnetic Compatibility

There are many regulations and requirements for ensuring electromagnetic compatibility of equipment. They are divided into standards regulating the measuring equipment specifications, test system parameters and measurement procedure for interferences of different nature. Defining a procedure to test the electric devices for electromagnetic compatibility, these regulations prescribe the criteria which can provide the grounds for conclusion that the tested devices meet EMC requirements.

Work on standardization of requirements for electromagnetic compatibility is carried out at the international, European and national levels. ISO (International Organization for Standardization), IEC (International Electrotechnical Commission) and CISPR (International Special Committee on Radio Interference) share the bulk of the burden at the global level. At the European level, this work is performed by CEN (European Committee for Standardization) and CENELEC (European Committee for Electrical Standardization) and ETSI (European Telecommunication Standards Institute).

Semiconductor integrated chips are relatively new object of EMC-standardization that requires adoption of special regulations applicable only to these devices. Electromagnetic compatibility requirements for them are almost identical to that for other devices and components; however separate IC components are rarely used only in one area of application. The IEC developed two groups of regulations which standardize the procedures for measurement of electromagnetic emissions (standard IEC 61967) and of IC immunity (standard IEC 62132).

The peculiarity of EMC is an unintentional nature of generated and analyzed interferences. In addition, characteristics of interferences and effects are prescribed for strictly specified conditions of operation of vehicles. For these reasons domestic and international practice in this field is characterized by a high level of regulation of interference measurement techniques and immunity testing. The introduction of Technical Regulations of the Customs Union TP TC 020/2011 "Electromagnetic Compatibility of Technical Equipment" in 2013 eloquently emphasizes the importance of such regulation, as well as of achieving EMC in a modern environment saturated with electric, electronic devices and radio aids. The Regulations apply to civilian products. Naturally, the described interference and immunity criteria of the Customs Union, as well as the assessment methods included in the Regulations are similar for products of defense and may other industries, such as aviation and automotive industries and communications industry. It is obvious that having own specific additional EMC requirements, the military standards will be stricter than regulations applied to the equipment of non-military nature (Tables 10.2, 10.3 and 10.4)

Trend analysis of changes in national defence industry standards shows that they are mainly based on similar foreign standards and often function as their analogues. Such situation has led to the fact that almost in every field, the current national standard is the second to latest version of a similar foreign standard. That's why for assessment of current requirements for national defence products, it is necessary to consider and rely on the relevant foreign standards.

Here, the governing standard is MIL STD 461 and MIL STD 462 partially. Despite the fact that standard MIL STD 461 was adopted in the interests of the US Department of Defense, it is applied in different spheres, especially in the area of development of management systems, computing systems, components of aviation and automobile equipment. This is due to the fact that the requirements of the specified document are tougher than that of civil standards; the compliance of vehicles to the requirements of MIL STD 461 is regarded as meeting the requirements of national standards. In addition, compliance with the requirements of the standard ensures the use of vehicles in the defence industry, increasing competitive ability and market share of the product. Nevertheless, it would be beneficial to consider the standards for aviation products (D0-160), as well as the relevant automotive standards specified in UNECE Regulation No. 10. This is due to the fact that dual-use devices often become subject matter of these standards, making the requirements specified therein important for defense industry products in general.

Trend analysis of changes of the basic requirements in these standards is given in Tables 10.2, 10.3 and 10.4. The analysis revealed the considerable similarity of

Table 10.2 Trends of changes in the requirements of standards of series MIL STD 461 (designations in the frequency ranges: U – voltage, I – current, E – electric-field strength, H – magnetic-field strength; frequency without units of measurement is expressed in Hz) [1]

Test	Test description	MIL STD, version/year					
		461 A	461 B	461C	461D	461E	461F
		1968	1980	1986	1993	1999	2007
CE101	Power supply lines, conductive interferences	I:0.03 – 20 kHz	CE101 I:30 Hz -15 kHz		I:30 – 10 kHz		
CE102	Signal cables, conductive interferences	I:30 – 20 kHz			Power supply lines: U: 10 kHz – 10 MHz		
CE103	Power supply lines, conductive interferences	I:20 kHz – 50 MHz	CE103 I:15 kHz -50 MHz				
CE104	Signal cables, conductive interferences	I:20 kHz – 50 MHz					
CE105	Inverse filter method	I:30 -50 MHz					
CE106	Antenna inputs	10 kHz – 12.4 GHz	10 kHz – 26 GHz		10 kHz – 40 GHz		
CE107	Power supply lines, pulses, time domain		CE07				
CS101	Power supply lines, conductive LF-interferences	30 – 50 kHz				U:30 –150 kHz	
CS102	Power supply lines	50 kHz – 400 MHz					
CS103	Antenna ports, intermodulation	30 – 10 GHz	15 kHz – 10 GHz				
CS104	Antenna ports, undesired signals (2)	30 – 10 GHz	30 – 20 GHz				
CS105	Antenna ports, cross-modulation	30 – 10 GHz	30 – 20 GHz				
CS106	Impulse interferences, power supply lines	100/10	200/10;0,5				400/5
CS107	Switching interferences	CS107					
CS108	Antenna ports, undesired signals (1)	30 – 10 GHz					
CS109	Structural currents		60 – 100 GHz				

(continued)

Table 10.2 (continued)

Test	Test description	MIL STD, version/year					
		461 A	461 B	461C	461D	461E	461F
		1968	1980	1986	1993	1999	2007
CS110	Damped sinusoids, contacts 10 kHz – 100 MHz			CS10			
CS111	Damped oscillating interferences, cables			CS11			
CS114	Conductive high-frequency interferences, current				I:10 kHz -400 MHz	I:10 kHz – 200 MHz	
CS115	Conductive pulse interferences, front				2/30 ns, 5 A		
CS116	Damped oscillating interferences, cables				10 kHz – 100 MHz (6 frequencies)		
RE101	Magnetic field, emission	30 Hz – 30 kHz	30–50 kHz		H:30-100 kHz		
RE102	Electric field, emission	14 kHz – 10 GHz			E:10 kHz -18 GHz (per 1 m)		
RE103	Harmonic and parasite signals, antennas	10 kHz – 40 GHz					
RE104	Magnetic field, emission	20–50 kHz					
RE105	Automobiles, motors, emission	E:150 kHz -1 GHz					
RE106	Overload of power supply lines	E:14 kHz -1 GHz					
RS101	Magnetic field, stability	30 Hz – 30 kHz	30–50 kHz		30–100 kHz		
RS102	Electric/magnetic-field crosstalk	Power frequency magnetic field and impulse		Magnetic field/ Electric field			
RS103	Electric field, stability	14 kHz – 10 GHz		14 kHz – 10 GHz (40 GHz)	10 kHz – 40 GHz		2 MHz – 40 GHz
RS104	Harmonic magnetic field crosstalk	14 kHz – 30 MHz					
RS105	Pulsing electromagnetic field			RS05	RS105, 50 kV/m, front 75 ns		

Table 10.3 Principal differences of the last version of document DQ-160D (by chapters DO 160D) [1]

Chapter No.	Test	Purpose and special aspects	Basic amendments to the version
15	Magnetic field	Assessment of influence of the test object on readings of compass or on readings of magnetic-field sensor	Detailed figure illustrates the test set and test methods
16	Input power supply	Immunity to power supply change under normal and emergency condition of the aircraft, as well as distortions and effects on the aircraft power-supply system	Requirement for testing the resistance to instant power interruptions and characteristics of interruptions. Emergency test of resistance to impulse interference for each AC phase.
17	Voltage impulses	Impulse voltage-resistance in AC/DC supply lines, analogue CS 106 MIL STD 46 1F	At least 50 impulses of positive and negative polarity are required
18	Conductive low-frequency interferences of audiofrequencies	Interference immunity in supply lines, test is almost identical to CS 101 MIL STD 46 1F with small differences in level and frequency	100-W limitation of the maximum tolerable consumed power was replaced with 36-A limitation of the maximum consumed current at the peak-to-peak level. Specification of 0.6-Ohm impedance for oscillating transformer was deleted.
19	Inductive interferences of low-frequency field	Resistance to interferences induced by low-frequency magnetic and electric fields and transient voltage impulses.	Note on test inapplicability to the input power supply lines; test of resistance to inductive electrical fields was added
20	Radio frequency interferences (conductive and radiated interferences)	Resistance to conductive and radiated interferences with amplitude and impulse modulation. Tests are respectively similar to method MIL STD 46F CS114 for frequencies of 10 kHz -400 MHz using a current probe, and to method MIL STD 46 1F RS103 for frequencies of 100 MHz-18 GHz using semi-anechoic or reverberation chamber	The wording and terms were revised to match the content of section with the requirements of other standards. Requirement regarding to the exposure of all front surfaces to radiation. Reference to equality of the distance to antennas during calibration and tests. Method in the reverberation chamber was changed from continuous rotation mode to discrete rotation of the mixer; new relevant techniques were adopted.
21	Emission of radio frequency interferences (conductive and radiated interferences)	Emission of conductive interferences in the connecting cables and power supply lines and of radiated interferences.	New limit of interferences for high-frequency and navigation receivers was added. The frequency was changed from 1 GHz to 960 MHz

(continued)

Table 10.3 (continued)

Chapter No.	Test	Purpose and special aspects	Basic amendments to the version
		Conductive interferences are measured within the range of 150 kHz-152 MHz using a current collector; radiated interferences are measured within the range of 100 MHz-6 GHz in echo-free or reverberation chamber	at which the transmission band ranges from 100 kHz to 1 MHz. The option to use a 10-kHz transmission band at frequency points higher than 960 MHz was deleted; and it was noted that the pre-amplifier could be used.
22	Impulse interferences induced by lightning	Resistance to impulses induced by lightning in the contact connectors, connecting cables and supply lines. The contact entry (for damage stability) or cable entry (for disruption stability). The section considers the following possible impulses: simple impact, multiple impact and multiple flash	The method of resistor to determine the source impedance for contact entry was excluded. Impulse form 6 for cable entry was added only for multiple flash tests
23	Direct lightning effects	Resistance of the external electrical and electronic equipment to the direct lightning effects. Since these tests result usually in breakage, then the object isn't powered. High voltage is required up to levels of thousands of kilovolts and/or hundreds of amperes	There are no changes in comparison with the previous version
24	Electrostatic discharge	Equipment resistance to air electrostatic discharge. This test is intended to determine whether this object can function during or after air electrostatic discharge. Action of 10 impulses of positive and negative polarity of 15 kV	Amendments includes the explanation of possibility to use test points, in particular, confirmation that connector contacts are not checked.

Table 10.4 Difference in EMC requirements specified in national and foreign standard for vehicles [1]

Tests	Requirements for parts	
	GOST R 41.10-99 (Rules No.10, 1997)	UNECE Rules No.10, 2012
Emission of interferences from vehicle and electronic component assemblies	30–1000 MHz	30–1000 MHz
Vehicle resistance to the radiated interferences	Frequency range 30–1000 MHz Level of 24 V/m in 90% frequency points, including not less than 20 V/m within the full range of frequencies.	Frequency range 20–2000 MHz Level of 30 V/m in 90% frequency points, including not less than 25 V/m within the full range of frequencies.
Resistance of electronic component assemblies to the radiated interferences	48 V/m in 150-mm strip line; 12 V/m in 800-mm strip line; 60 V/m in TEM-cell; 48-mA interference current by BCI method	60 V/m in 150-mm strip line; 15 V/m in 800-mm strip line; 75 V/m in TEM-cell; 60-mA interference current by BCI method
Resistance of electronic component assemblies to the impulse interferences in supply lines	Absent, the relevant tests are specified in GOST	Impulses 1,2a/2b, 3a/3b, 4 (3-rd level of rigidity) according to ISO 7637-2 (2004)
Emission of impulse interferences to the power supply lines	–	Section based on ISO 7637-2 (2004) is included
Electrostatic discharge	–	Reference to ISO 10605 is included
Tests specific for hybrid cars	–	Tests for resistance to impulse microsecond, nanosecond interferences, distortions of supply line, etc.

physical nature of tests by showing the possibility to bring together the test methods specified in different regulatory documents. To make the point stronger, MIL STD 461 (version C) will be introduced any time soon. It is assumed that the new version of the standard will include new tests, in particular CS117, RS106, RS108, which are very similar to the tests specified in DO-160. Thus, CS117 test will be similar to the test described in Section 22 of DO-160 with some changes:

- it is assumed that immunity testing will be performed only with regard to repeated impact and repeated flash;
- interference cable entry should be the only test method;
- limit the application of this test to airborne electrical equipment.

The RS106 and RS108 tests will be similar to the RS105 tests and Section 23 of RTCA/DO-160, respectively.

The main trends in requirements for EMC of defence products are as follows:

- frequency extension for evaluation of emission up to 18 GHz and stability up to 40 GHz;
- increase in toughness of tests for immunity to radiated interferences up to 200 V/m for narrowband interferences and up to 7 W/m for impulse interferences and some vehicles.

No significant changes in other tests.

It can be said that three specified standards fully cover the entire list of regulations and methods for estimation of EMC values; and vehicle compliance to the regulations specified in these standards makes it fully satisfying the EMC requirements. The standards offer the alternative methods of estimation that is convenient for manufacturers and crash testers of vehicles.

The most of EMC requirements don't raise any difficulties if the required tools are available. Many products manufactured by different foreign companies (such as SOLAR, AMETEK, TESEQ, Keysight and others) are currently available in the market. They include universal automatic test oscillators, impulse-noise generators, various interference input devices, measuring antennas, as well as measuring receivers, measuring sensors or current collectors. Special attention is paid to tests for resistance to high-power interferences which require to install high-power amplifiers and anechoic shielded chambers in conventional configuration that makes them extremely expensive. At the same time, reverberation chambers and field generators (for instance, GTEM cells) are widely used abroad to abandon the use of anechoic chambers and high-power amplifiers. So, primary qualification of reverberation chamber TESEQ showed that only 1 W of input power is required for field of 200 V/m in the frequency range up to 18 GHz. Thus, there is an opportunity for significant reduction in cost of estimation of resistance to the radiated interferences (Fig. 10.8).

One more tendency of development of technical means in the EMC area is a natural desire of manufacturers and test engineers to have available complex systems which allow to carry out tests according to several standards simultaneously in one assembly. Since when testing of EMC characteristics, the check for resistance is more expensive, this is an area where complexation of test is considered.

Tables 10.5 and 10.6 [1] specify the results of comparison of test characteristics by three test groups such as resistance to conductive low-frequency interferences, resistance to conductive high-frequency RF interferences, resistance to radiated RF interferences. Closeness of frequency ranges and test toughness is obvious. Noticeable similarity of test characteristics are used to form the complex test systems which provide for requirements to perform checks according to several standards simultaneously. The tables specify an approximate combination of suggested assemblies using the example of equipment of famous and popular manufacturers such as TESEQ, Keysight and others (Fig. 10.9).

Figures 10.7, 10.8 and 10.10 show the technical configurations of suggested unified test units.

Figure 10.10 show the configuration of test unit based on three amplifiers and two radiating antennas. It is clear that the quantity of amplifiers can be increased

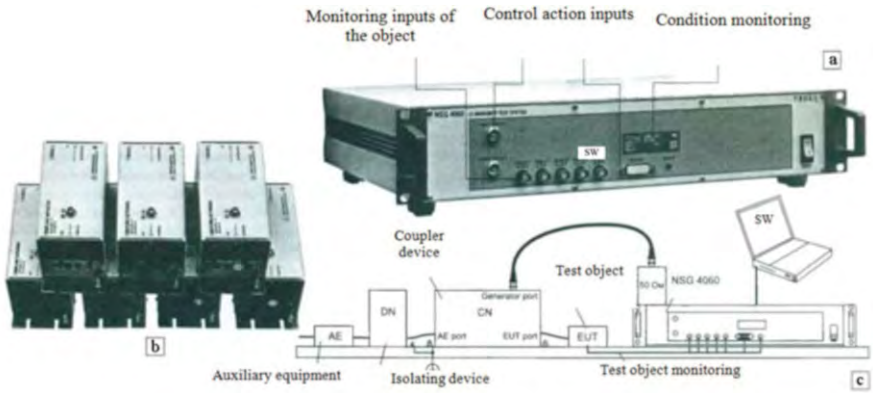

Fig. 10.8 Technical means and configuration of assembly for checking the resistance to conductive low-frequency RF interferences (**a**) generator NSG 4060; (**b**) coupling-decoupling networks; (**c**) test configuration [1]

Table 10.5 Tests for resistance to conductive RF interferences [1]

Documents	Effects (level, range, signal)	Equipment
Low-frequency RF conducted interference immunity		
GOST R 51317.4.16	Up to 30 V, in the range of 15–150 kHz narrowband	NSG 4060 (TESEO) is a dedicated test system that consists of a generator 15–150 kHz, power amplifier up to 200 W, monitoring unit. Coupling-decoupling networks at option (TESEQ). Additional modules (TESEQ) for high-current supply lines
MIL STD 461F, CS101	Up to 6 V, in the range of 30 Hz – 150 kHz or from the second harmonic of power supply frequency.	
DO-160, section 18	Up to 4 V, in the range of 700 Hz – 32 kHz for AC supply, in the range of 10 Hz – 200 kHz for DC supply	
UNECE Rules No.10	Absent	
High-frequency RF conducted interference immunity		
GOST R 51317.4.6	Up to 10 V, in the range of 150 kHz – 80 MHz, with AM and increase of maxima	NSG 4070, TESEO is a dedicated test system that consists of a generator 9 kHz – 1 GHz, monitoring unit; three-channel power meter with optionally build-in power amplifier up to 75 W within the full range or in 150 kHz – 230 MHz. Power amplifier (TESEQ), 100 W. Coupling-decoupling networks (TESEQ) at option depending on type of lines (with line interruption). Current probe (TESEQ) for input of interferences of symmetric or asymmetric currents (without line interruption). Matching attenuator (TESEQ). Accessories and software.
MIL STD 461F, CS114	Up to 109 dBμA (300 mA), in the range of 10 kHz – 200 MHz, meander and impulse modulation with preserving maxima	
DO-160, section 20 (n. 1)	Up to 300 mA, in the range of 10 kHz – 400 MHz, meander and impulse modulation with preserving maxima	
UNECE Rules No.10, ISO 11452-4	Up to 60 (100) mA, in the frequency range of 1–400 MHz, AM with preserving maxima	

Table 10.6 Tests for resistance to radiated high-frequency interferences (the unit case) [1]

Documents	Effects	Equipment
GOST R 51317.4.3	Up to 10 V/m, in the frequency range of 0.08-6 GHz, AM with increasing maxima	ITS 6006 (TESEO) – is a dedicated test system that consists of a generator 80–6000 MHz, monitoring unit; three-channel power meter, commutator and switching device. Power amplifiers up to 6 GHz (TESEQ with power output up to 100 W). Radiating antennas (0.08–6 GHz), GTEM-cells (TESEQ, 10 kHz – 20 GHz), reverberation chambers (TESEQ, ranging 0.5–18 GHz). Accessories (commutators, couplers, power meters – at option). Software applications (general and dedicated- for certain requirements and configurations)
UNECE Rules No.10	Up to 30 V/m (75 V/m for device), in the frequency range of 0.02-2 GHz (1 kHz, 80%), with preserving maxima	
DO-160, section 20 (clause 2)	Up to 200 (300) V/m, in the range of 100 MHz – 18 GHz, meander and impulse modulation with preserving maxima	Generator (for example, Keysight N5183A with options up to 20 Hz and modulation). Power amplifiers up to 3 GHz (TESEQ with power output up to 1kW). up to 18 GHz (IPI, with power output up to 100 W in a range up to 18 (40) GHz). Radiating antennas (0.03–40 GHz), GTEM-cells (TESEQ, 10 kHz – 20 GHz), reverberation chambers (TESEQ, ranging 0.5–18 GHz). Accessories (commutators, couplers, power meters – at option). Software applications (general and dedicated- for certain requirements and configurations)
MIL STD 461F, RS103	Up to 200 V/m, in the range of 2 MHz – 18 (40) GHz, meander and impulse modulation with preserving maxima	

depending on the required frequency range of tests and characteristics of antennas. As well, instead of antennas, field generator as GTEM-cells or reverberation chambers can be connected. As the result, the configuration universality is observed. Each of illustrated test units is a test system, so it is subjected to validation as test equipment. Validation processes, including calibration techniques are described in detail in the relevant standards; and they don't raise any technical problems during their implementation.

Trend analysis of requirements in the EMC area shows their similarity in relation to stipulation of regulations and test techniques. So, the complex unified systems for

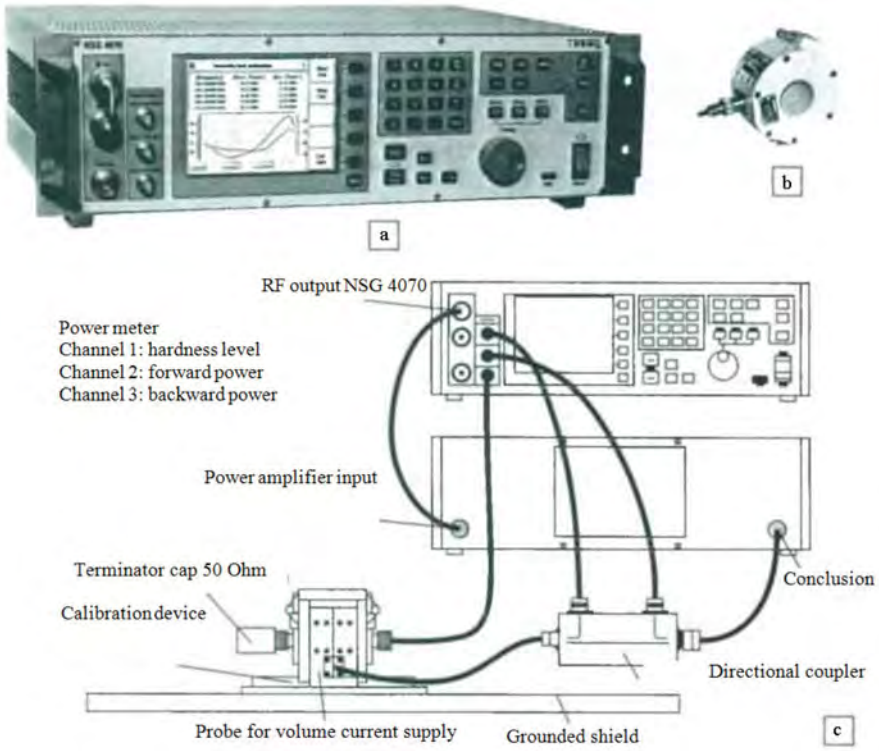

Fig. 10.9 Technical means and configuration of assembly for checking the resistance to conductive high-frequency RF interferences (**a**) generator NSG 4070; (**b**) probe; (**c**) assembly configuration [1]

EMC tests can be created. The research of available technical means shows the practical opportunity to implement the complex test systems. This factor is useful to have in mind when organizing and making up a set of test laboratories intended for testing the defense products and technical means of general purpose. As a result, laboratories with a fairly wide scope of accreditation are established.

10.2 Ensuring Electromagnetic Compatibility of Microprocessor Control Units of Electronic Devices

10.2.1 Design Features of Printed Circuit Boards Optimized in Terms of Electromagnetic Compatibility

Thus, HF electromagnetic interference should be suppressed in its source (at the level of a semiconductor element), otherwise it will be necessary to take measures on their attenuation either at the circuit level or in the terminal device affected by such

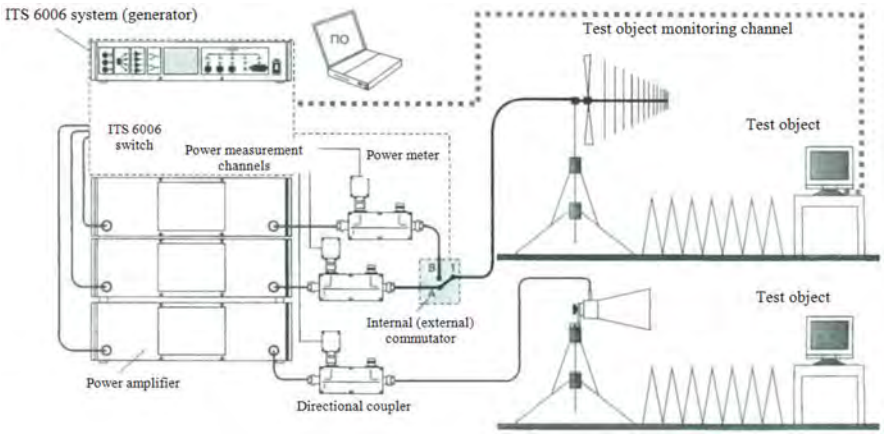

Fig. 10.10 Technical means and configuration of assembly for checking the resistance to radiated RF interferences (when using the radiating antennas) [1]

interference. Only it will cost much more. Although the IC design with due regard to the known concept of on-chip interference suppression [1] requires some spending, this solution is much more efficient than any emergency measures on protection of external devices against interference. EMC parameter optimization for systems based on microcontrollers should be performed at the chip level, as well as at the level of printed circuit board.

Before proceeding with the EMC parameter optimization for electronic systems, a number of tests should be performed at the level of certain IC, separate modules and systems of the devices under development, taking into account the following factors:

- level of electromagnetic interferences generated by the integrated circuits;
- interference immunity at the component level (of integrated circuits);
- level of interferences generated by separate systems and devices;
- interference immunity at the system level;
- level of interferences generated during operation of electronics;
- interference immunity of all equipment in whole.

The modern microcontroller architectures apply a synchronous timing. It means that the active pulse edge of system clock frequency with respect to which the microcontroller logic circuits are switched-over, should arrive simultaneously (as far as it is possible) at all points of the printed circuit board. That's why there are very short and steep current impulses with high rate of rise *di/dt* reaching 100 mA/ns in the system. High currents of overcharge are required for generation of clock frequency impulses rectangular in shape (in practice, these impulses have trapezoidal shape with maximum steep rising and falling edges). The specified requirement is applied to the all transistors which must be switched over simultaneously. Due to flow of high switching currents, high-frequency electromagnetic radiation is generated; and the higher radiation is, the more energy is consumed by

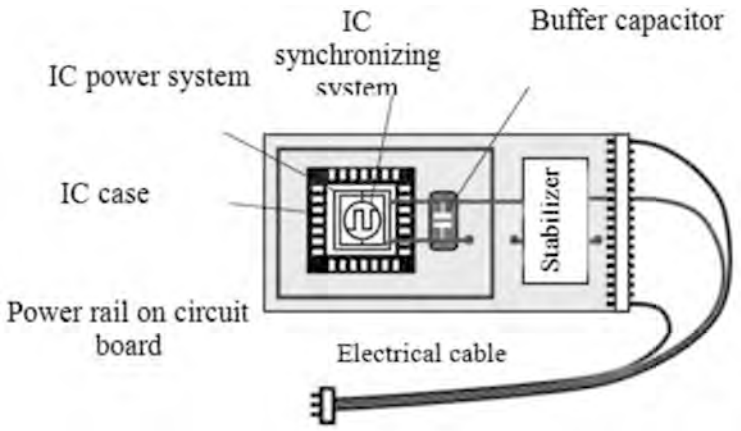

Fig. 10.11 Interference propagation path in the clocked systems [1]

the system from the external power supply. It should be recalled that the high-frequency component of this energy dissipates in the environment; in this case, conductive paths and other elements of printed circuit board act as transmitting antennas. That's why it is very important that the source of high charging current that can ensure the required switching rate of clock frequency impulses of the microcontroller, is located as close as possible to the radiation source, i.e. to the microcontroller. Then, energy radiated by structural elements of the printed circuit board will be lower than in the situation when the "switching" energy source is a constant-voltage regulator located at a certain distance from the microcontroller. In the latter case, HF-interference propagates on the following path: IC internal power bus – IC package – power bus on the printed circuit board (Fig. 10.11).

Because of this, a large number of buffer capacitors ensuring the current required for switching are located on the printed circuit board between the power and ground buses in close proximity to the microcontroller. The capacitors are charged in the period of time between two active edges of clock pulses. Unfortunately, the use of discrete capacitors on the printed circuit board fail in that they have non-zero contact inductance (ESL is equivalent series inductance) and contact resistance (ESR is equivalent series resistance). Their values (of about 2 nH and 30 mOhm) are rather high to make capacitor lose its capacitance properties at the highest frequencies. On the contrary, the contact inductance of built-in capacitor located in close proximity to the internal IC power bus is negligible. Therefore, the more quantity of such internal capacitors can be integrated directly in the chip, the higher effect of HF radiation suppression is.

The level of electromagnetic radiated interferences can be reduced by using of the appropriate circuit-based and engineering solutions when developing the printed circuit board. They include: the use of inductive filters (for example, chokes and ferrite beads) operating as low-pass filters; building of the printed circuit board with

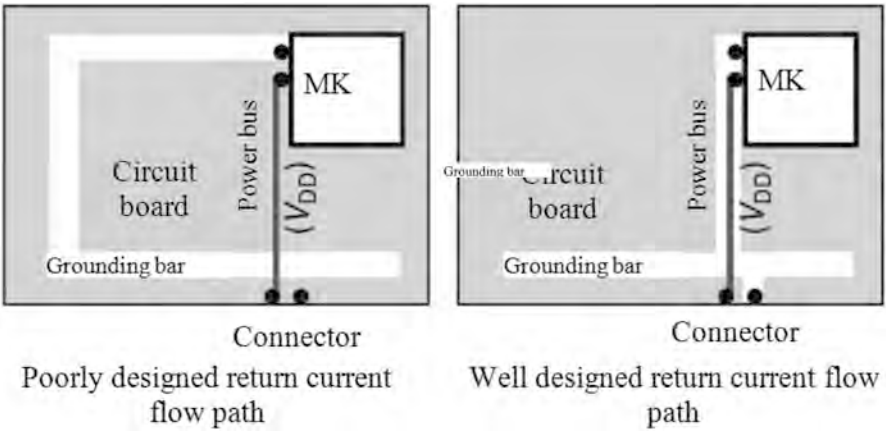

Fig. 10.12 Power wiring on double-layer printed circuit board [1]

an additional grounded layer without through-holes in it; wiring of connections for HF signals as strip lines; the use of additional capacitors and electromagnetic shields. However, all these additional elements increase cost of electronic devices that is critically important in the mass production.

If for economy reasons, it is decided to use the printed circuit board only with two layers, then one of these layers should be dedicated to grounding (GND и V_{SS}) as much as practical. If it isn't practical, than the buses of positive supply voltage (V_{DD}) and V_{SS} should be located as close to each other as possible or one above the other in order to minimize the path of return current flow and, consequently, to reduce the level of common-mode interferences (Fig. 10.12).

When designing the multi-layer printed circuit boards, it should be provided two separate layers dedicated only to supply voltage buses (V_{DD} and V_{SS}). Any other supply voltage in the circuit should be connected to "islands" located just below those modules that use these supply voltages. It is desirable to ensure the maximum parasitic capacitance between supply layers in order to minimize the level of electromagnetic radiated high-frequency interferences. It can be achieved by placing the internal layers of the printed circuit board just one above the other (Fig. 10.13).

For example, the second layer can be dedicated to signal ground in the 6-layer printed circuit board that ensures the preset value of impedance with respect to high-frequency data signal. Here, similar to wiring of power buses, special attention should be paid to that the return current flow paths are as short as possible. It is particularly important to avoid the electric contact of ground layer to adjoining layers via through-holes (Fig. 10.14).

The highest priority should be given to location of a few IC on the printed circuit board First of all, it is necessary to lay the power buses from the constant-voltage regulator. Voltage should be supplied separately to high-speed logic circuits, "low" logic circuits and sensitive analog cascades in order to minimize the cross-effect of

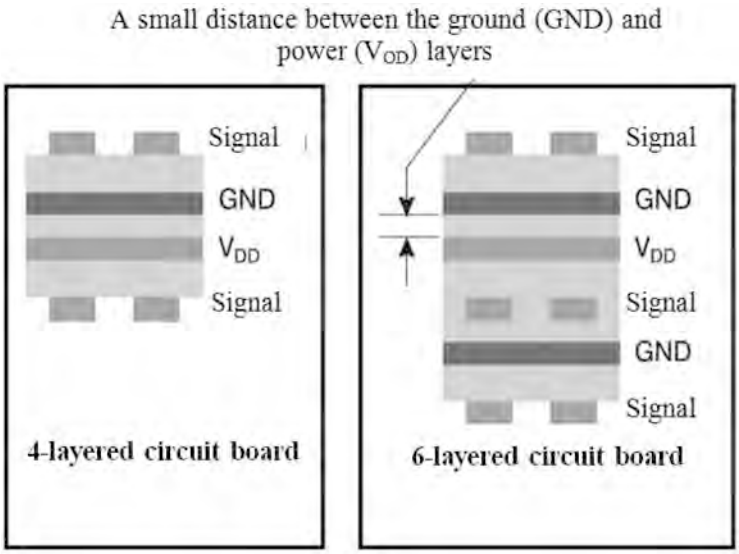

Fig. 10.13 Distribution of layers in the multi-layer printed circuit board [1]

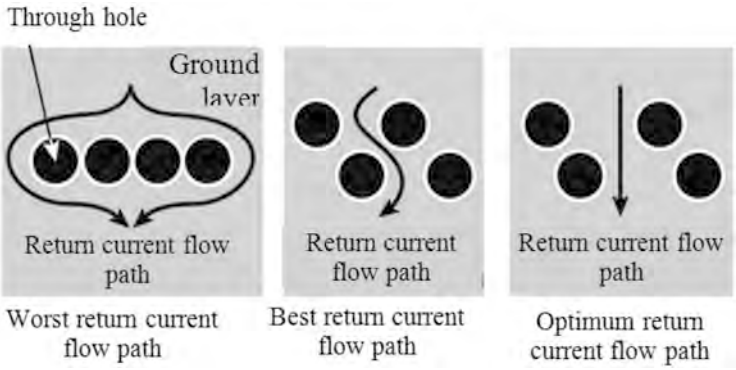

Fig. 10.14 Optimization of return current flow paths for HF signals on the printed circuit board [1]

these circuits. The relevant power lines (paths) should be connected according to "star" schema at one point in the constant-voltage regulator (Fig. 10.15).

When using buffer capacitors, they should be located on the printed circuit board in such a way that switching current is supplied to IC on the shortest path. In this case, current from the power source flows through the capacitor to IC (using buses V_{DD} or V_{SS} depending on the IC connection diagram). It is illustrated in Fig. 10.16 which shows examples of correct and wrong connection of buffer capacitors to the power terminals of the microcontroller. Two upper schemes in Fig. 10.16 belong to the situation when components are located on one side of the board; and two lower

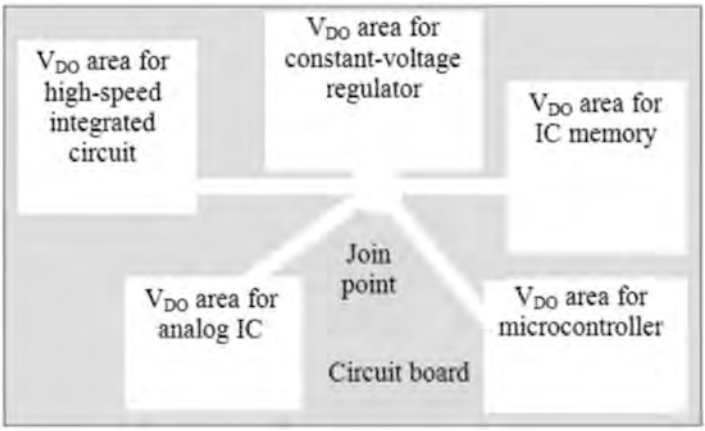

Fig. 10.15 Wiring of iC power buses of different types according to "star" schema

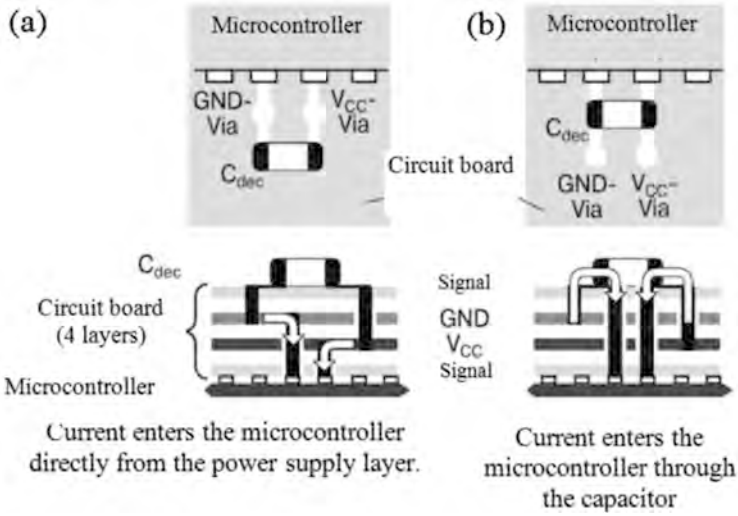

Fig. 10.16 Incorrect (**a**) and correct (**b**) location of buffer capacitor [1]

schemes belong to the situation when microcontroller and capacitor are located on the face and back sides of 4-layer printed circuit board (PCB).

When connecting to the ceramic- or quartz-crystal resonator oscillator that is built in the microcontroller, special attention should be paid to that a conductive area ("island") connected to the microcontroller terminal V_{SS} (ground) is formed just under the location of the main terminal of the resonator on the printed circuit board. It is the only way to avoid the return current flow on the surface of ground layer of the printed circuit board.

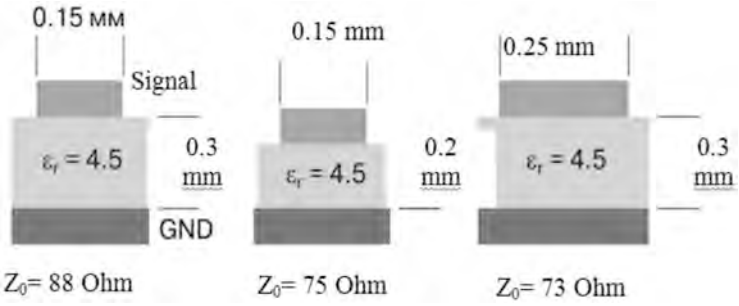

Fig. 10.17 Typical signal impedances of microstrip lines [1]

In addition to the buffer capacitor concept, in terms of reduction of the HF radiation level and ensuring the desired signal integrity, "canalization" is of paramount importance during transmission of HF desired signals using data buses. Radiation or HF interference entry in the power-supply circuit can be efficiently avoided by shielding of signal tracks. In this case, a microstrip line (when using single-layer shielding) or full strip line (when using double-layer shielding) is formed. In both cases, strip lines can be designed with the preset impedance in order to match them with output impedance of the driver of signals. Figure 10.17 shows the examples of such lines with different impedances.

The line and driver impedance matching is aimed at improving signal integrity during its transmission over the line, while reducing the level of radiated interferences. On the contrary, mismatch between impedances leads to the signal reflection from line to driver which causes the signal rise-time distortions (signal bursts) or even generation of parasitic HF oscillations ("ringing effect") at the moment of their switching over. This effect is considered in more detail in 10.2.3.

Computer Modelling and Simulation of EMC Characteristics

Computer simulation can be performed in the time or frequency domain. The picture obtained in the time domain serves to assess signal integrity, i.e. edge steepness, signal bursts/undershoots or "ringing" during signal transmission. The results of computer modelling help to identify "oversize" drivers, extremely long connecting wires and impedance mismatching. To ensure technical support of their products, the IC manufacturers provide so-called computer IBIS-model (specifications of input/output buffer) for digital switching circuits that describe switching characteristics for all drivers included in this IC. Structural elements of the printed circuit board can be described within the so-called Transmission Line Model (TLM) or using 2D/3D standard elements (depending on the PCB type) in order to simulate different geometric forms. The more unsuccessful design of the printed circuit board, the more thoroughly the modelling process of this PCB and its surrounding elements should be performed, the more data volume is processed and the more computational resources are required. Simulated parameters are recorded as complex RLCG arrays,

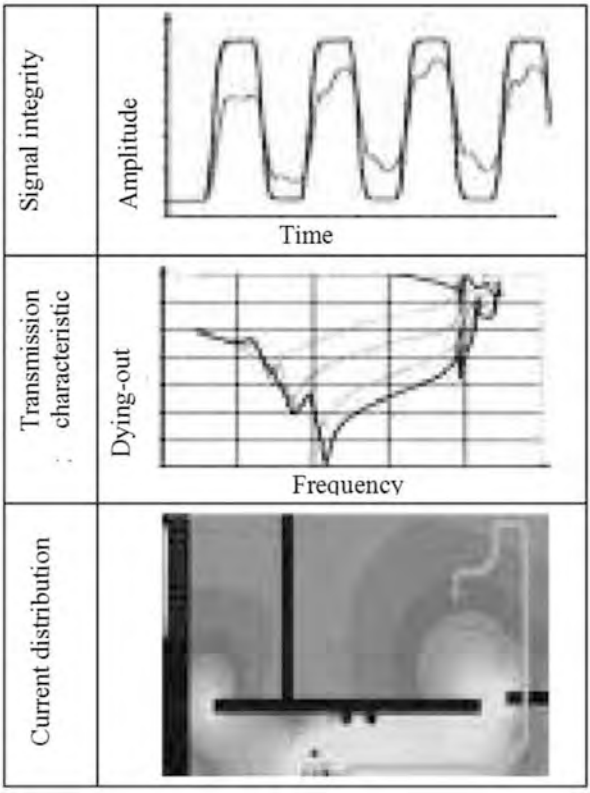

Fig. 10.18 Computer analysis of signal integrity in the time domain (the top graph), transmission factor S21 in the frequency domain (the central graph) and local current distribution on the printed circuit board (the bottom graph) [1]

which are solved using electromagnetic field solver programs. Using these programs, it is possible to make calculations at the conductor level, as well as at the field level. Figure 10.18 shows the examples of such analysis in the time or frequency domain.

10.2.2 Measurement of the Level of Interference Emitted by Microcontrollers

In assessing the level of interference radiated by microcontrollers, the measurement technique conforming to standard IEC 61967 is applied. This standard describes 5 different methods of measurement of conductive (IEC 61967-4, the former standard VDE 767.13) and radiated (IEC 61967-2, the former standard SAE 1752/3) interferences. Besides, the national standards include additionally various measuring techniques which were offered by national omissions on EMC issues and currently co-exist with standard IEC 61967. Detailed description of interference measuring techniques standardized in accordance with IEC 61967 is given above.

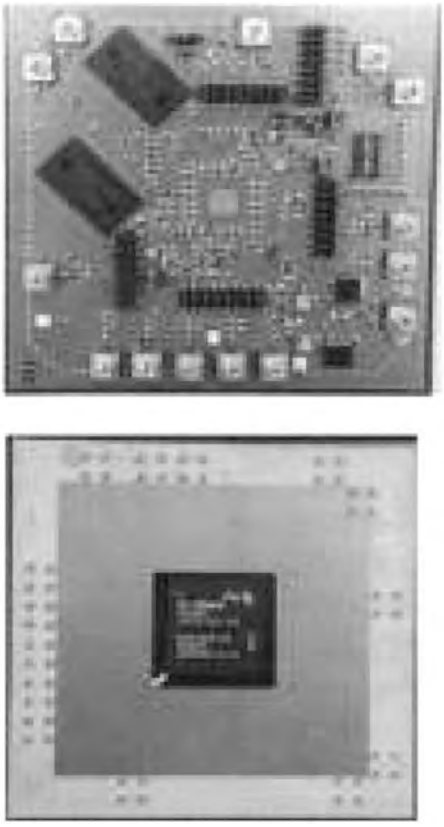

Fig. 10.19 The test board for measurement of the level of interferences emitted by microcontroller. At the top – the upper side of the board; at the bottom – the lower side of the board with IC under test [1]

Two of these measuring techniques can be implemented with the use of one test board (Fig. 10.19). Structurally, the universal test board for measurements by TEM-chamber method is a square 4 inches on side (10.14 cm). The microcontroller IC under test is located on the shielded back side of the printed circuit board, and peripheral items (memory, clock-pulse generator, external input/output ports) on the face side. The same board together with a near-field scanner can be used when measuring the electromagnetic field distribution along the surface of IC under test. Such test is useful to determine the microcontroller terminals which are critical in terms of radiated interferences.

In a typical spectrum, the interferences radiated by the microcontroller, stand out sharply by harmonic amplitude of the system clock frequency. When comparing the levels of radiated interferences obtained at different stages of IC design, the signal spectrum envelope is used. Figure 10.20 shows a typical spectrum of such interferences emitted by microcontroller that operates with a clock frequency of 40 MHz.

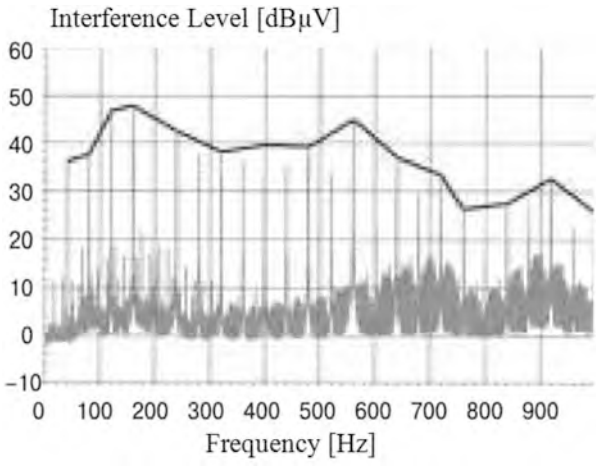

Fig. 10.20 Spectrum of interferences emitted by microcontroller which was obtained during measurement by TEM-chamber method in accordance with IEC standard 61967-2. 40-MHz clock frequency of microcontroller [1]

Sources of Interferences and Their Propagation Paths

The microcontroller consists of many functional modules (Fig. 10.21). First of all, there is a central processing unit (CPU) responsible for calculations and data transfer process control.

Peripheral modules or simpler "peripherals" of the microcontroller include memory modules (random-access memory, programmable read-only memory, electrically alterable read-only memory, flash memory), timers (for example, timers of capture/comparison), series and parallel data transfer interface (ASC, SSC, SPI, parallel port), special modems (CAN, J1850), interruption controllers, and external memory interface (EBU is an external bus unit). For ensuring the maximum computational power of the microcontroller, data buses should have the maximum transmission capacity and operate at the highest possible clock frequency. The high clock frequency of data transmission means that the microcontroller has little time for data processing, that's why the duration of latent phase of data transmission cycle should be set as much as possible. Consequently, it is necessary to provide the extremely steep edge of clock frequency signals; moreover, these signals should arrive synchronously within the whole system.

Since during switching process all microcontroller transistors consume current flowing in the inner power bus, it is the main HF-interference propagation path (it is counted that up to 60% of HF-interferences penetrate the surrounding systems using the power-supply circuit of the microcontroller). Around another 30% of interferences propagate through input/output ports; and only the rest of 10% are emitted directly in the environment. Those high-frequency interferences which aren't suppressed by circuit-based techniques at the chip level (for example, due to the use of decoupling capacitors integrated in the crystal) penetrate the systems surrounding the microcontroller through the contact pads of the power buses. The external systems exposed to impact of interferences include a printed circuit board where the microcontroller is located. This HF-interference can be partially attenuated by discrete decoupling capacitors which should be located as close to the power

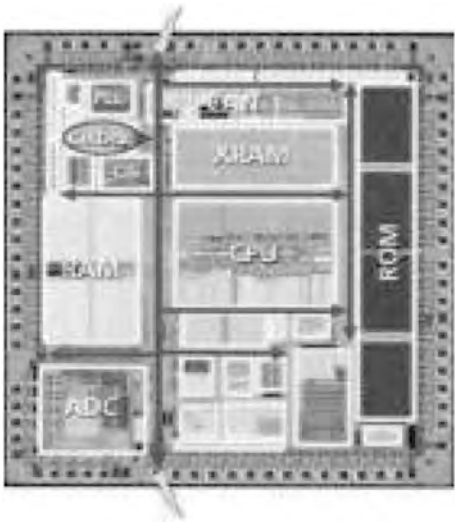

Fig. 10.21 Location of functional modules in the package of microcontroller using the system of centralized clock pulse synchronization [1]

terminals of the microcontroller as possible. These capacitors can efficiently suppress the interferences at rather lower frequencies up to 10 MHz because they have non-optimal characteristics of contact inductance (ESL is equivalent series inductance being equal to about 2 nH) and contact resistance (ESR is equivalent series resistance being equal to about 30 mOhm). Then, high-frequency interferences aren't attenuated. In this case, it is necessary to ensure the suppression of electromagnetic HF interferences inside the chip by minimizing their sources and propagation paths.

The clock pulse synchronizing system is the main source of narrowband high-frequency electromagnetic interferences. They are overlapped with secondary clock impulses and aperiodic signals which cause the emergence of interferences of wideband component in the spectrum (Fig. 10.20). Modern complex and high-performance microcontroller system use impulse synchronization for control of all logic circuits, i.e. clock impulse signals should simultaneously arrive at all points of the system. Current impulses of very large amplitude (about a few amperes) are generated during simultaneous switching of hundreds of thousands of transistors in the power supply system of the microcontroller. Ideally, the bus has low impedance for avoiding of large voltage drops on it, that's why the major contribution to the HF-interference generation is made by the current flowing in the power supply circuit. Depending on organization of synchronization of internal logic circuits, current impulses emerge one or two times over a period of clock frequency. They are characterized by very steep edge, also they gradually damp while signal is passing through different stages of logic circuits (Fig. 10.22).

Switching currents of logic circuits which are located on the semiconductor crystal of the microcontroller, are supplied from the external power source in normal operating mode. However, Simultaneously Switching Noises (SSN) are generated

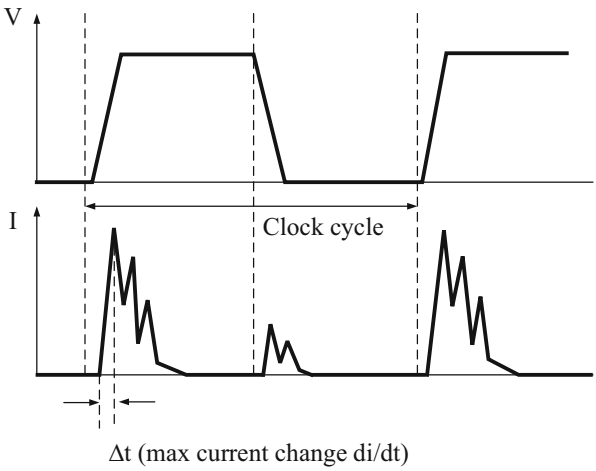

Fig. 10.22 Current and voltage waveform for clock signal

due to high steepness of current pulses (great value *di/dt*) and the presence of resistance parasitics and inductances in the power-supply circuits. High-frequency component of these noises penetrates the near electronic systems or it is radiated in the environment. That's why the power supply system of microcontrollers includes decoupling (buffer) capacitors which are located as close to the current consumers, i.e. integrated circuits, as possible. Ideally, it means that each microcontroller is supplemented by capacitor located directly on its power terminals. It is practical to use these capacitors from two points of view:

– First, they serve as local current sources at the moment of switching of clock frequency impulses;
– Secondly, they limit on some extent the high-frequency interference propagation from the microcontroller to the constant-voltage regulator or vehicle accumulators.

Circuit-Based Methods of Preventing Interference Radiation from Microcontrollers

The closer to the EMI sources the elements intended for interference suppression are located, the higher their efficiency. EMC characteristics of electronic devices can be improved by the following measures: limit of pulse steepness during switch of transistors and logic circuits (elements), as well as location of additional charge sources (capacitors) in close proximity to the switched logic circuits. It is allowed to reduce the steepness of clock pulse edges only if it doesn't contradict to requirements for the microcontroller performance. Simultaneous working transistors and logic elements should not generate impulses with extremely steep edges. In the world today, circuit synthesis methods have become widespread in which the appropriate circuit components are chosen with the use of software tools.

Most manufacturers of microcontrollers integrate capacitors in chips which are intended for current impulse limiting during switch. In combination with its series

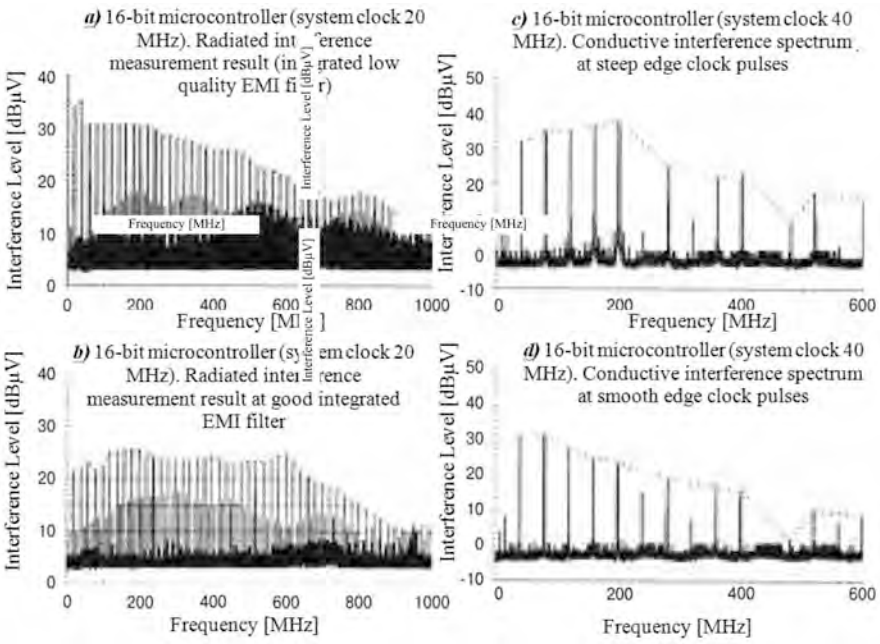

Fig. 10.23 Reduction of the level of electromagnetic interferences radiated by microcontroller using circuit-based (on-chip) methods. Left – the spectrum of radiated interferences without (**a**) and with (**b**) decoupling capacitor. Right – the spectrum of conductive interferences in output of input/output port driver during steep (в) and smooth (г) edges of clock signals [1]

low-resistance series, such capacitor forms a low-pass RC-filter. Thus, the high-frequency component of switching current is attenuated inside the chip and it isn't allowed to pass through to the outside. The use of series inductance would be more efficient (since they have lower series resistance) but too large surface area of semiconductor crystal is required to implement the integrated inductance of about 100 nH. Systematic studies dedicated to the operation of microcontrollers have demonstrated that their design with due regard to the implementation of similar RC structures can significantly reduce the level of radiated interference. Figure 10.23 a,b gives a graphic presentation of results of two measurements of the level of electromagnetic interferences radiated by 16-bit microcontroller.

In the first case, no any measures aimed at improvement of EMC-characteristics are provided in the microcontroller; in the second case, the microcontroller is designed using the concept of built-in decoupling capacitors. It is clear that the interference level in critical (used for FM-Broadcast) frequency range of 100 MHz can be reduced by 10 dB.

Interferences appearing during signal switching in output of input/output port driver of the microcontroller contribute to the total level of interferences generated by the microcontroller. Signal lines on the printed circuit board connected to the port terminals are very effective antennas up to a few centimetres in length (similar to the

power buses above-considered). Some circuit-based measures should be taken to minimize the interferences generated by output stages (drivers) of input/output ports. The most commonly used method is reduction in the output power of the driver or leading edge smoothing (control of signal rise rate). Since the parameters of driver output transistors are usually chosen with something to spare (with a view to the worst operating conditions), as a rule, it is possible to use impulses with less steep edges. It is particularly applicable to the cases when the driver operates at low clock frequency or with low capacitive load. Figure 10.23 c, d shows in a spectral view the results of measurements of conductive interference generated by 16-bit microcontroller in output of input/output port driver. In the first case, edges of clock impulse signals have more steepness, and in the second case, their steepness is reduced. The use of similar method allows to reduce the interference level in FM-range (100 MHz) approximately by 6 dB.

Another circuit-based method for improvement of EMC-characteristics of the microcontroller systems is the use of generators of frequency-modulated clock signals collectively known as a "generator with distributed spectrum". Even with very limited level of modulation (0.5...1%), it becomes possible to considerably reduce the amplitude of narrowband interferences which are harmonics of clock frequency. At the same time, the interference level is slightly increased in the sideband. Although such method does not reduce the total radiated energy, its distribution over the spectrum is more uniform, making it possible to limit the maximum amplitude of electromagnetic interference.

The level of interferences generated by the microcontroller can be reduced by improvement of its packaging and terminal layout diagram. Currently, the IC packages based on leadframe are widely used (Fig. 10.24a). In such packages, the signal lines and power buses connecting the IC semiconductor crystal to its terminals are laid as "spidery legs". Packages of DIL, PLCC, M-QFP and T-QFP types are designed according to such technology. The more distance is between the crystal semiconductor substrate and external terminal of the package, the higher contact inductance of this connection is. It consists of leadframe inductance and inductance of wire connection which ensures the electric contact between the crystal and leadframe. When designing the microcontroller terminal layout diagram, special attention should be paid to wiring of power terminals that should be coupled and located as close to the center of the relevant package side as possible. Such location can minimize the inductance of internal connections and create the optimal conditions for blocking of interferences.

While the signal line wiring layout is set in advance and it can't be changed in the packages with leadframe, the use of packages performed on BGA technology (ball grid arrays, Fig. 10.24b) allows to optimize the critical regarding to EMC signal connections and supply lines by developing the appropriate templates. Here, terminals are performed on the lower part of the package as small balls which are welded to the contact pads of the printed circuit board by pinpoint soldering method. The electric contact between the IC semiconductor crystal and the relevant paths of the support plate is performed either using wire connections or directly through bumps in the variant of "face-down" crystal.

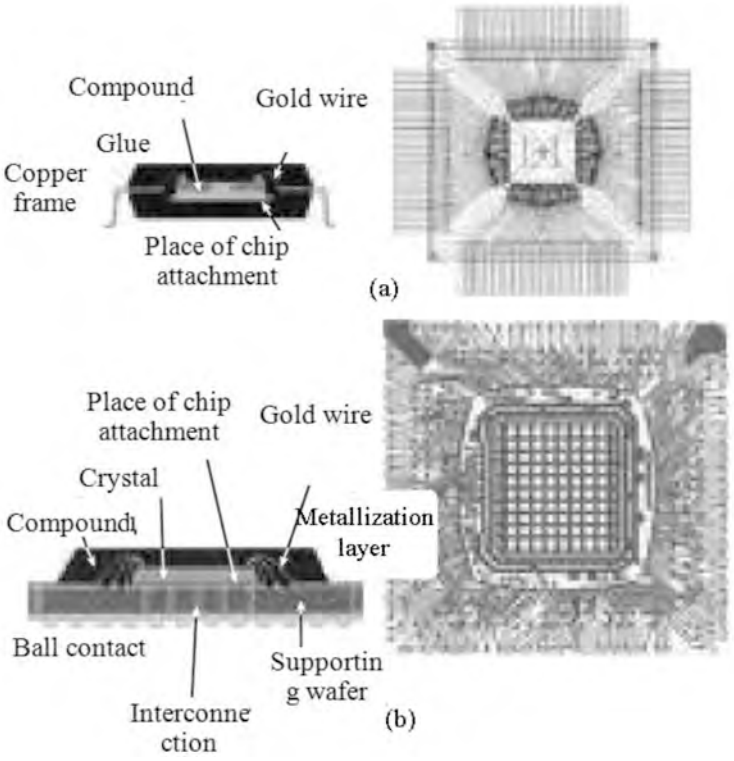

Fig. 10.24 Top view and cross-sectional image of packages with lead frame (**a**) and of BGA type (**b**) [1]

Computer Modelling and Simulation of EMC Characteristics

If during design of the printed circuit boards, computer simulation of their EMC characteristics have been widely used for quite a while, then the technique of modelling and software-based simulation of EMC characteristics of microcomputers is still at the initial stage of its development. The main reason of this is the great complexity of microcontroller. The software-based simulation of its operation at the transistor level requires extremely large data arrays and takes much time. The more practical solution is the software-based generation of equivalent current sources which simulate the microcontroller "behaviour" in whole or its separate modules when switching the currents.

Various standard program models have been developed for carrying out the system-oriented computer simulations of EMC-parameters of the microcontroller. For example, IBIS-model describes only characteristics of input/output ports. So-called Integrated Circuits Electromagnetic Emission Model (ICEM) determines

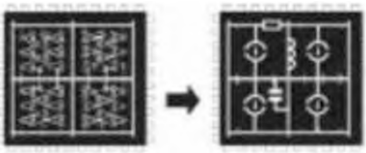

Fig. 10.25 Modelling of complex IC using equivalent current sources and extraction of RLC-loops [1]

the equivalent current sources connected to the IC power terminals. Although the interference level at these terminals of the microcontroller is essential and it needs to be primarily evaluated, the simulation model should contain the data on package type and PCB layout in close proximity to the IC (for example, taking into account so-called "blocking concept"). At the crystal level, such model should describe the equivalent current sources relevant to the functional modules of the microcontroller and include a precision RLC-model of the voltage power source (Fig. 10.25).

The quality of a computer model depends directly on its ability to correctly calculate dynamic switching currents and accurately extract parasitic RLCs. If the model is used only for qualitative assessment of EMC characteristics, for example, during modernization of the device, then its quantitative accuracy may be compromised to some extent.

Up until now, the issue on the microcontroller interference immunity hasn't gained much attention since the power-supply voltages of 3.3...5 V exceed by many times the level of external electromagnetic interferences; this issue becomes relevant when the supply voltage is reduced down to 1.5 V. Assessment of the microcontroller interference immunity by using the appropriate measurement techniques (for example, error ratio measurement during signal transmission) is extremely expensive since prior identification is required for those circuit elements which perhaps, improperly operate under the influence of interferences, and develop a specialized (custom) program to control the process of measurements. Since methods for testing the printed circuit boards were developed, some efforts have been made to standardize the IC immunity measuring techniques at the international level. They refer mainly to radiated HF fields and induced HF currents.

Currently, work is under way on implementing the units for testing IC immunity to the action of impulse interferences. The microcontroller immunity to the action of electrostatic discharge (ESD) is important. In this regard, it is worth noting that none of microcontroller terminals (not including the power terminals) is connected directly to connectors which are intended for external connections, that's why the requirements for protection of the microcontroller against external electrostatic impulses are not so strict as for other IC or the whole system.

The greatest impact on the microcontroller immunity is due to interferences occurring in the power-supply circuit during flow of high switching impulse currents in it (so-called SSN-noises). These interferences are caused by processes inside the microcontroller and by influences of external devices, especially by high-power semiconductor elements; and they can significantly impair the signal-to-noise ratio.

10.2.3 Ensuring Electromagnetic Compatibility in Wired Communication Systems

The term "wired communication systems" can refer to a wide range of devices and technologies. It includes elements of telecommunication networks, switching centers and LAN routers, as well as subscriber devices for private use, for example, telephones, personal computers and network termination devices [1].

However, the requirements for EMC ensuring in the area of communication systems refer to the entire systems but not to their separate components. Consequently, the electromagnetic compatibility tests should be mainly carried out at the level of external interfaces of:

– signal lines (check of HF voltage values and current levels);
– supply lines (check of HF voltage values);
– packages (check of electric and magnetic field strength).

Data-transmission rates in the communication systems become higher and higher. Therefore, there is an increase in the width of analog signal transmission band dedicated to provision of various services. So, for example, now the ADSL and VDSL services use the same frequency range as wired radio does that should be protected by the appropriate EMC regulations. The frequency ranges used by various services of wired communication are illustrated in Fig. 10.26.

It is rather difficult to meet the EMC requirements when operating in this frequency range. One does not just add a filter to interface since in this case, the desired signal transmitted over a communication channel can be impaired too. Figure 10.27 shows the typical signal spectrum on ADSL line. Common-mode voltage was measured by EMI receiver using standard coupling circuit for telecommunication lines.

ADSL signal spectrum ranges from 30 kHz to 1.1 MHz. Figure 10.27 shows two graphs. The first graph shows measured peak values (Pk), the second graph shows average values (Avg) of a signal. It conforms to a standard defining the different limit values for each type of measurements.

But now remember that DSL-protocol is symmetrical with respect to ground, that's why a signal shouldn't appear when measuring in the common mode. The

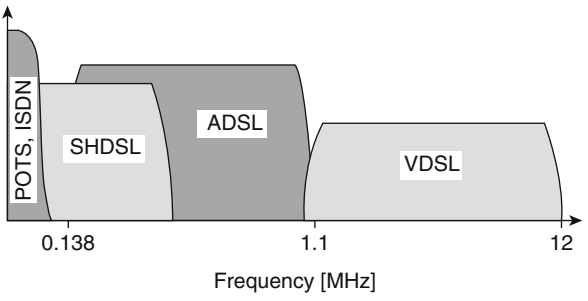

Fig. 10.26 The frequency ranges dedicated to provision of wideband services in the wired communication systems [1]

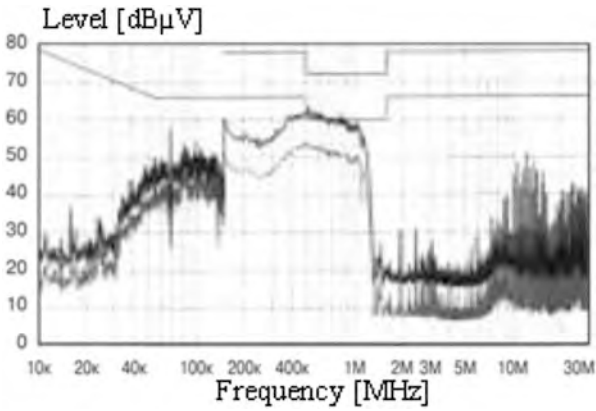

Fig. 10.27 Signal spectrum on ADSL line

reason for its presence in the graph is certain asymmetry of the test circuit. There is a narrowband interference in the signal spectrum. Its source is a voltage converter on the system board or clock frequency impulses and their harmonics. These interferences from the system board must never be allowed to penetrate ADSL line.

It is clear that the presence of such "mixture" of the desired signal and interference raises some difficulties when choosing the best strategy to reach the required level of EMC. Sooner or later, it becomes clear that the best way to solve this issue is a circuit-based improvement of the system itself both at the level of its printed circuit board, and at the component level.

A few ideas to arrange the signal passage inside the system are considered below.

Systems, Components and Basic Concepts

Telecommunication devices generally contain the following components:

- Power source;
- Digital Front-Ends (DFE) such as digital signal processor (DSP) and microcontroller;
- Analog Front-Ends (AFE) such as analog-to-digital converters (ADC) and digital-to-analog converters (DAC);
- amplifiers – transmitter amplifier (line driver) or receiver amplifier.

Typical block diagram of very simple communication system is shown in Fig. 10.28.

Each communication system should meet the certain EMC requirements, moreover, these requirements should be specified at the system design stage. Here, the key points are as follows:

- determination of EMC characteristics for new products;
- system design: breaking down the system into small functional units (modules) if EMC calculation at the system level is difficult to be performed;

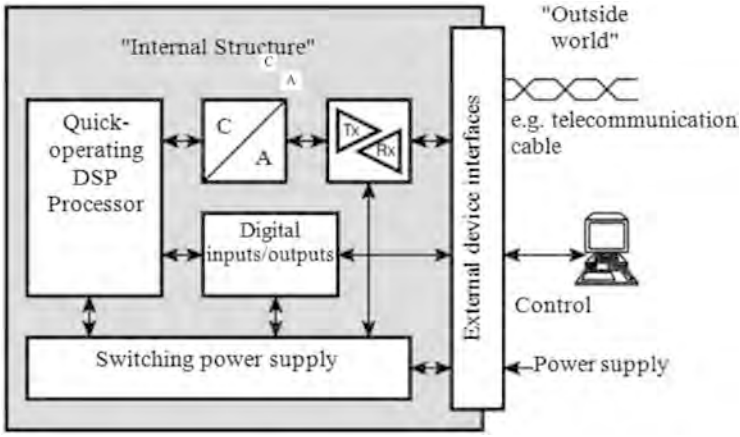

Fig. 10.28 Typical block diagram of wired communication system

– modular design: prior to start designing the system in whole, EMC characteristics of separate modules should be determined using the computer simulation, software emulation or by testing the ready prototypes;
– check for compliance of EMC characteristics of products under development to the established regulations for all possible scopes of application;
– consideration of EMC-parameters in quality assessment (QA).

EMC characteristics are influenced by any changes in module such as replacement of components or connecting cables. EMC characteristics can be changed even as a result of error correction in the software;

– distribution of products (developed system) only at that market for which they were intended;
– receiving of reports on faults related to the EMC issues; organization of feedback with users that contributes to the process of improvement of products both ready and under development.

10.2.4 Design of Printed Circuit Boards for High-Speed Communication Systems

As you can see in Fig. 10.28, the digital signal processor (DSP) with a clock frequency cycle duration of 10 ns and less carries the main burden of signal processing in the system. But is it possible to talk about the fact that these 10 nanoseconds is a criteria of really high rate of operation?

The meaning of term "high-speed" depends on the context where it is used. However, since it is about the design of printed circuit boards, this term can be rather clearly defined using formal signal characteristics. The following notations will be used below: rise time t_r, fall time t_f, pulse time t_p during which the signal is in HIGH logical state. Frequency spectrum of such signal can be easily calculated using Fourier transformation:

$$\lambda = \frac{c \cdot \pi \cdot t_{fr}}{\sqrt{\varepsilon_r}}, \tag{10.8}$$

$$f_{\text{highspeed}} = \frac{1}{\pi \cdot t_{fr}}, \tag{10.9}$$

where $t_{fr} = \min(t_r, t_f)$; c – speed of light in vacuum, ε – specific inductive capacitance of the printed circuit board.

If length of conducting track of the printed circuit board l_{track} is consistent with signal wavelength λ (for example, it exceeds the value λ/20), then the signal is high-speed. In this regard, it is worth noting that spectrum of digital signals with high steepness of edges includes components of very high frequency even at low frequency of a clock signal. It means that the impulse signal characterized by a rise time of 500 ps should be considered as high-speed if the length of relevant conducting track of the printed circuit board exceeds 11.75 mm. On one side, that's good: It is enough to make the track shorter than 11,75 mm and the signal passing through it, is no longer a high-speed signal. But, unfortunately, there is a flip side of the coin when designing the printed circuit board: it isn't always possible to "keep" the desired length of all tracks. In this case, it is especially important to take into account the requirements for EMC and ensure signal integrity.

What exactly is "signal integrity"? The following definition of this term can be found on the website of Signal Consulting Inc. (http://signalintegrity.com): "... it is a research area occupying the intermediate position between digital design and analog circuit building theory. Here, parasitic damped oscillations ("ringing"), crosstalk noises, ground instability and power source interferences are considered. Here it is studied how to build actually high-speed digital equipment that really works. Here, practical real-life solutions are developed for designing the high-speed systems". The signal integrity refers to ensuring "... the maximum performance and minimum cost of interconnection technologies used in the high-speed digital devices".

Thus, the term "signal integrity" refers to small but important area of EMC, particularly, to the internal structure of the system under design (Fig. 10.28). In a sense, this is more abstract term that laws of electrodynamics. With an increase in high-speed performance of IC, engineers have to pay more and more attention to the issues of electromagnetic compatibility. However, developers of digital devices aren't usually well-grounded in analog or high-frequency technologies; as a rule, they don't want bother with studying the basic laws of electrodynamics.

To ensure signal integrity, special attention should be paid to the following factors:

– Crosstalk;
– Parasitic damped oscillations (“ringing”);
– Ground instability;
– Power source interferences.

This section describes below in more detail how to ensure good signal integrity during development which is basis for good EMC.

Crosstalk

Crosstalk is an electromagnetic interconnection of signal tracks located inside the semiconductor circuits, on the printed circuit board or in the multicore telephone cables.

In electrotechnics, crosstalk is considered as an undesirable, but inevitable phenomenon. However, it can be kept within certain limits to prevent its impact on the system performance.

Conducting tracks of the printed circuit board or telephone lines are so-called shared circuit elements; and their characteristics can’t be determined by formulae intended for description of elements with lumped parameters (of resistors, capacitors, impedance coils and transformers). However, in electrical engineering, a method is used whereby circuits of elements with lumped parameters are used to represent distributed elements. Such approach is acceptable only because a conducting track in length l_{track} and a chain of n conductors each in length$dz = l_{\text{track}}/n$ can be considered as identical to each other. If the length Δz of conductor strand is rather small, then as mentioned above, signal that passes through it, can’t be considered as high-speed one. The conductor strand dzcan be expressed as its equivalent elements with lumped parameters (of resistors, capacitors, chokes and transformers).

Similar model is shown in Fig. 10.29 where two loss-free conductors are illustrated. The chain c_1–l_1 is used as a model of the first loss-free conductor, and the chain c_2–$l_2$is used as a model of the second one. The elements c_{m} (capacitive coupling) и l_{m} (inductive coupling) are used to show the interconnection of conductors.

Solution of simultaneous partial differential equations for this model describes a wave which is propagated in forward and backward directions [1]:

$$u_i(z,t) = A_i u_i(z + v_i t) + B_i u_i(z - v_i t) \quad \text{для} \quad i = 1,\ 2. \tag{10.10}$$

This solution can be obtained by linear algebra methods using a diagonalizing matrix. Types of crosstalk are shown separately in schemes below in order to simplify their explanations.

Inductive Crosstalk

Figure 10.30, explaining the effect of forward crosstalk and backward crosstalk, shows a conductor conventionally “broken” into n unit cells. Each of them can be

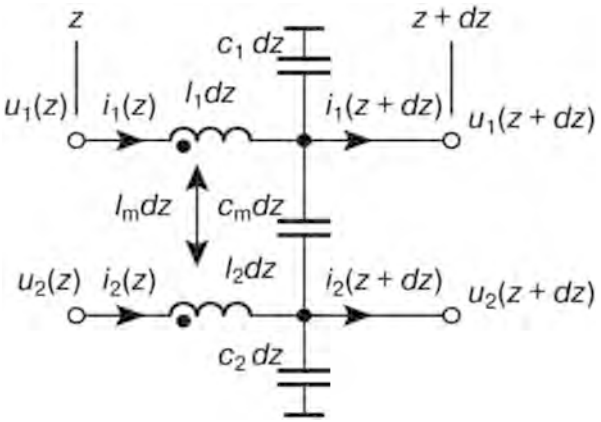

Fig. 10.29 Simple model of crosstalk with the use of two loss-free conductors (conductor length is *dz*)[1]

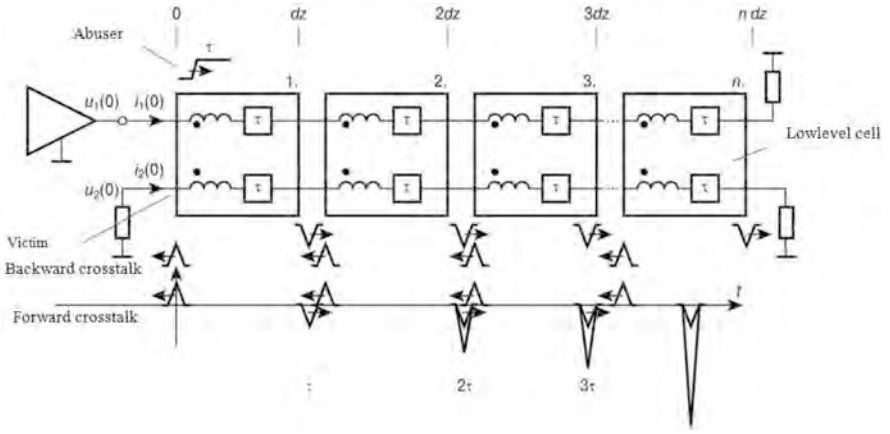

Fig. 10.30 Inductive crosstalk [1]

shown as a transformer and time-delay element $\tau = dz/v$. This discrete model simplifies the description of crosstalk which is divided into forward and backward crosstalk.

The amplitude of forward crosstalk impulse increases while increasing the parameter z and these impulses are inverted with regard to the "aggressor" conductor. Let's assume that measurements in the "victim" conductor are performed at point $z = 1 \cdot dz$. The result of measurements corresponding to time point $t = 1 \cdot \tau$ will be a short negative pulse.

However, measurement at point e $z = 2 \cdot dz$ will show an impulse of double amplitude that is relevant to time point $t = 2 \cdot \tau$. This doubling is related to pileup of a pulse converted in unit cell No.2 and a pulse which is propagated through "victim" conductor from point $z = 1 \cdot dz$ to point $z = n \cdot dz$.

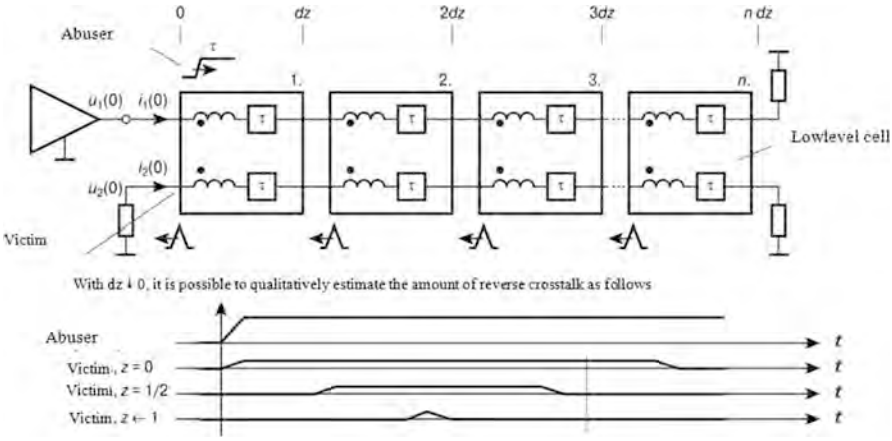

Fig. 10.31 Inductive crosstalk [1]

Backward crosstalk pulse duration (width) increases as parameter z is reduced but the impulse amplitude remains unchanged; and this impulse isn't inverted with regard to the "aggressor" conductor. Let us assume again that signal measurements are performed at different points along the conductor. Measurement at point $z = (n - 1)\cdot dz$ shows a small positive single impulse which is generated at time point $t = (n - 1)\cdot\tau$ and backward propagated through the conductor towards point $z = 0$. Two impulses will be marked at point $z = (n - 2)\cdot dz$: the first impulse is at time point $t = (n - 2)\cdot\tau$ and the second one is at time point $t = n\cdot\tau$. This additional impulse is a backward-moving impulse which appears at point $z = (n - 1)\cdot dz$ and it "arrives" at point $z = (n - 2)\cdot dz$ after delay time τ. n impulses will be marked at point $z = 0$. Each of these impulses will have delay time $2\cdot\tau$ due to delays both in the "aggressor" conductor and in the "victim" conductor. When $dz \rightarrow 0$, impulses become inseparable between each other and combine in one long impulse with small amplitude.

Figure 10.31 shows qualitative dependences of crosstalk values at different points of the conductor (parameter z) on time t.

Capacitive Crosstalk

The model shown in Fig. 10.32 is very similar to the above-considered model for inductive crosstalk but in this case, the inductive transformer is replaced with a capacitor transformer (i.e. capacity coupling between conductors is implemented).

The amplitude of forward crosstalk impulse increases while increasing the parameter z and these impulses aren't inverted with regard to the "aggressor" conductor. Let's assume that measurements in the "victim" conductor are performed at point $z = 1\cdot dz$. The result of measurement relevant to time point $t = 1\cdot\tau$ will be a small positive pulse. However, measurement at point $z = 2\cdot dz$ will show an impulse of double amplitude which appears at time point $t = 2\cdot\tau$. This doubling is related to pileup of a pulse converted by capacitor transformer in unit cell No.2 and a pulse which is propagated along the "victim" conductor from point $z = 1\cdot dz$to point $z = n\cdot dz$.

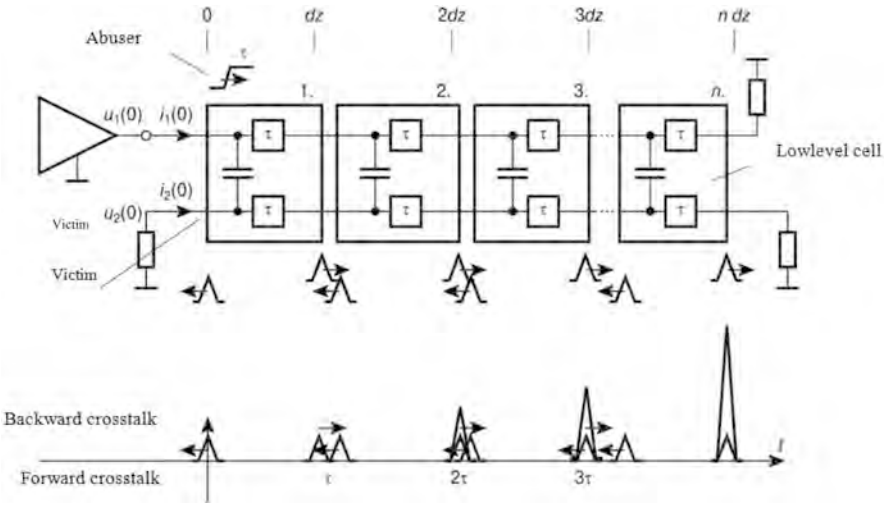

Fig. 10.32 Capacitive crosstalk [1]

Backward crosstalk pulse duration (width) increases as parameter z is reduced but the impulse amplitude remains unchanged; and this impulse isn't inverted with regard to the "aggressor" conductor. Let us assume again that signal measurements are performed at different points along the conductor. Measurement at point $z = (n - 1)\cdot dz$ shows a small positive single impulse which is generated at time point $t = (n - 1)\cdot\tau$ and backward propagated along the conductor towards point $z = 0$. Two impulses will be marked at point $z = (n - 2)\cdot dz$: the first pulse – at time point $t = (n - 2)\cdot\tau$; the second one – at time point $t = n\cdot\tau$. This additional impulse is a backward-moving impulse which appears at point $z = (n - 1)\cdot dz$ and it "arrives" at point $z = (n - 2)\cdot dz$ after delay time τ. n impulses will be marked at point $z = 0$. Each of these impulses will have delay time $2\cdot\tau$ due to delays both in the "aggressor" conductor and in the "victim" conductor. When $dz \rightarrow 0$, impulses become inseparable between each other and combine in one long impulse with small amplitude.

Combination of Inductive and Capacitive Crosstalk

If inductive and capacitive crosstalk are well-balanced as is the case when signal conductors on the printed circuit board are shielded by power or ground layers (i.e. they are performed as "full" strip line), then the forward crosstalk value is close to zero. If conducting tracks of the external signal layers of the printed circuit board are shielded by the ground layer only from one lower side (i.e. they are microstrip lines), the capacitive coupling is weaker than inductive one; and there is a forward crosstalk inverted with regard to the "aggressor" conductor in the "victim" conductor. The reason of capacitive coupling attenuation lies in the fact that most electric-field lines are completed through air but not through dielectric material of which the printed circuit board is made.

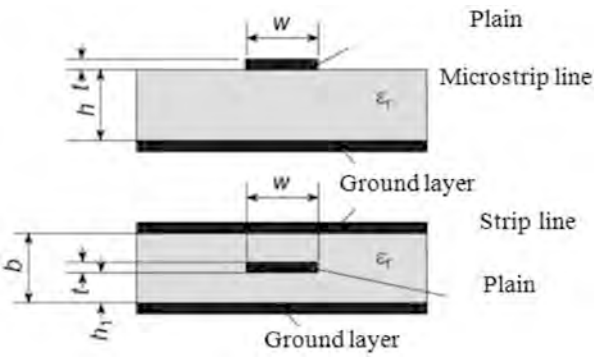

Fig. 10.33 Comparison of designs of microstrip line and "full" strip line [1]

Inductive backward crosstalk is always non-inverted with regard to the "aggressor" conductor and its value depends on the geometrical pattern according to which the signal conductors of the printed circuit board are performed as microstrip (asymmetric) lines or strip line. Figure 10.33 shows the difference between these two options.

On the basis of all the above-stated, it is possible to define the following rules by which it should be guided to reduce the crosstalk level.

- Limit the steepness of signal impulse edges (i.e. rise/fall time should be increased; and value *dv/dt* should be reduced).
- Properly perform the wiring layout of the printed circuit board (special attention should be paid to the geometrical pattern of the conducting tracks):
  - Use the tracks of the minimum possible length;
  - Provide as much track spacing as possible;
  - Don't lay the transmission lines which are sensitive to signal crosstalk, in parallel to tracks in which signals are characterized by high steepness of edges;
  - Differential signal transmission lines should be placed in parallel to each other with as small a gap as possible; It should be done in order that each conductor of the differential line is influenced by the same interference that ensures their pulse-to-pulse cancellation in the differential signal.
- The ground layers should be added in such a way as to avoid of forming the ground islands. Use the ground islands only when you are sure that tracks dedicated to high-speed signal transmission don't cross the ground islands.
- The ground island located under the conducting track on which the high-speed signal is transmitted, doesn't allow the return current to flow on the shortest way, i.e. value l_m will be increased anyway.
- The external signal layers are worse than internal ones in terms of interference immunity:
  - strip lines are more efficient than microstrip lines;
  - when using the strip lines, values c_m and l_m are balanced that's why the forward crosstalk is very small;

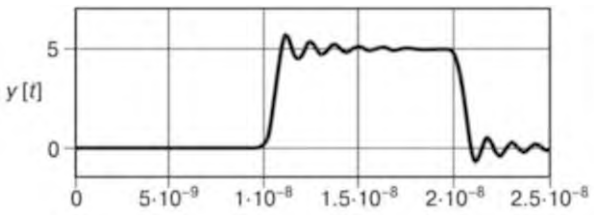

Fig. 10.34 The example of relaxation oscillation (ringing) occurring during transmission of digital high-speed signals

– when using microstrip lines, electric-field lines pass mainly through the air but not through dielectric material (unlike the strip line), that's why the capacitive coupling is weaker than inductive one.

The crosstalk level increases when signal is reflected at the leads of conductor. The ways to reduce these reflections are considered below.

Relaxation Oscillation (Ringing)

So-called ringing, the example of which is shown in Fig. 10.34, is parasitic oscillations which occur during transmission of digital high-speed signals.

The reason of these oscillations is the impedance mismatching of signal source and receiver. Due to this, a part of signal energy (or even all this energy) is reflected back to the line. The ringing amplitude is determined by reflection coefficient, and the frequency of these parasitic oscillations depends on the conductor length l_{track} (Fig. 10.35).

Here, the following expressions are used. The frequency of parasitic oscillations is calculated by formula:

$$f_{\text{ring}} = \frac{c}{2 \cdot \sqrt{\varepsilon_r} \cdot l_{\text{track}}}, \tag{10.11}$$

coefficient of reflection from the signal source side

$$\rho_S = \frac{Z_S - Z_0}{Z_S + Z_0}, \tag{10.12}$$

coefficient of reflection from the signal receiver side

$$\rho_L = \frac{Z_L - Z_0}{Z_L + Z_0}. \tag{10.13}$$

Since the width of digital high-speed signal transmission band should be rather wide, it is not possible to decrease the reflection coefficient down to zero. However, there are some other ways to reduce the parasitic oscillations down to the level that meets the system requirements (Fig. 10.36).

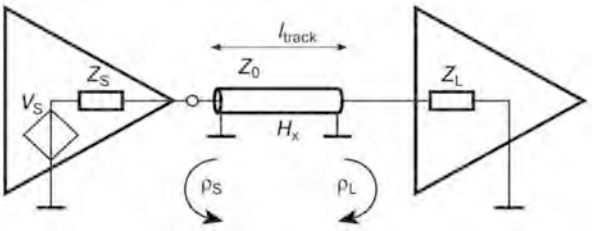

Fig. 10.35 Reflection signal model

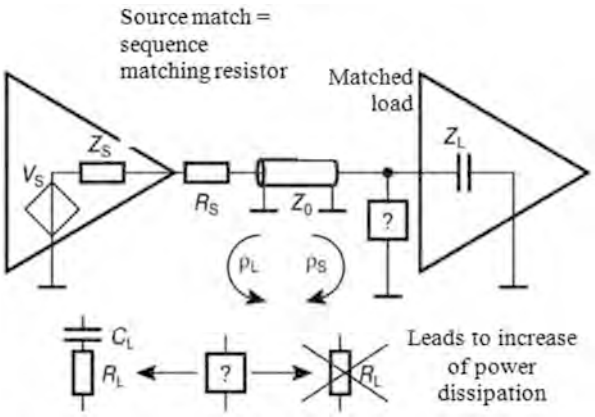

Fig. 10.36 The recommended connection scheme of tracking resistor during transmission of digital signals [1]

It is recommended to calculate the values of relevant resistors and capacitors using the following formulae:

$$R_S = |Z_0| - |Z_0| (\text{usually } |Z_0| > |Z_0|); \tag{10.14}$$

$$R_L = |Z_0|; \tag{10.15}$$

$$|\rho C_L| >> \left|Z_0^{-1}\right|, \text{where } \rho = j \cdot 2\pi \cdot f_{fr}; \tag{10.16}$$

$$C_L \approx 10 \cdot \frac{1}{2\pi \cdot f_{fr} |Z_0|} = 5 \cdot \frac{t_{fr}}{|Z_0|}, \tag{10.17}$$

where $t_{fr} = \min(t_f, t_r)$, i.e. corresponds to the value of critical edge pulse time.

Taking into account these boundary conditions, the "ringing" level can be reduced using the following rules:

- Find the critical (i.e. the most high-speed) signal in the system.
- The length of the PCB conducting tracks intended for high-speed signal transmission should be the minimum one (shorter than λ/20 for cut-off frequency relevant to the steepest pulse edges).
- The conducting track impedances should be matched.
- Use the continuous layers of ground (but not separate ground "islands").
- Place the series termination resistor as close to the signal source as possible (i.e. to the line driver).
- Place the load tracking resistor as close to the signal receiver (to load) as possible.
- The matching load is intended for AC matching of impedances, i.e. DC current shouldn't flow through it (otherwise, it results in increased power looses during signal transmission).

Crosstalk and parasitic oscillations ("ringing") have a direct impact on the transmitted signals. However, when designing the systems,it is necessary to take into account other aspects of EMC related to organization of appropriate ground layers or to proper choice of the system power source.

Ground Instability

Ground instability is undesired voltage drop of a signal in the conductors connected to the ground. This phenomenon can appear at the level of the printed circuit board, as well as inside the chip (Fig. 10.37). As a rule, di/dt ratio is very high in digital high-speed system that is related to very small values dt (time of signal switching from HIGH level to LOW level and conversely). Here, the most critical factor is the parasitic inductance value of the conductor connecting the chip with ground. Due to high speed of signal switching, the inductive component of the complex impedance of the conductor exceeds its resistive component significantly. It means that the current amplitude in the conductor isn't very large.

To reduce the effect of ground instability, the following rules should be observed:

- Decrease the steepness of signal edges (i.e. increase the impulse rise/fall time).
- Use the connecting wires of low-inductance types as grounding wires. The entire conducting layer (or layers) of the printed circuit board should be used as ground but not separate regions or areas on any layer (since the return current tends to flow on the path with the lowest impedance).
- Use a great number of additional decoupling capacitors; each of them should be located in close proximity to the relevant power or ground terminals of IC.
- Apply the method of parallel connection of a few capacitors with different capacity ratings (for example, 10 pF, 1 nF and 100 nF) in order to reliably "overlap" the entire range of switching frequencies which can be used in the system. Pay attention that in real conditions, the capacitor with the highest rated capacitance value has the worst capacitance parameters at the high frequencies and even it can behave similar to inductor.
- The IC developers are recommended to implement the read buses inside them for internal use; since the current flowing through these lines is very small, the addition of them won't lead to the increase in the ground instability effect.

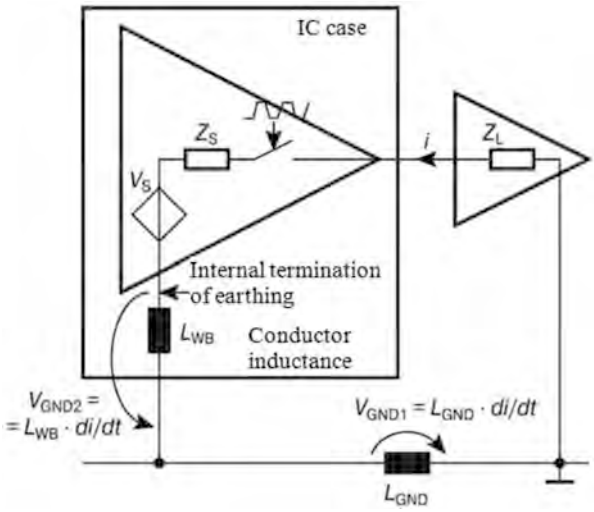

Fig. 10.37 Scheme explaining the effect of ground instability [1]

Many internal ground terminals should be located along the perimeter of the IC semiconductor crystal.

Power Source Interferences

The system power source interferences can occur for several reasons: due to current switching processes in its different components and as a result of penetration of interferences from DC/DC-converter operating in the key mode in the power supply circuit. During the operation of DC/DC-converters, impulses of large amplitude and with high rate of rise (*di/dt*) are always generated. The main problem is that interferences which are propagated along the power-supply circuit, impair the efficiency of operation of analog circuits (for example, ADC, DAC or operating amplifiers) since the value of power supply rejection ratio (PSRR) of these circuits can't be indefinitely great. Therefore, interferences penetrating the power source circuit cause the emergence of interferences in IC outputs; attenuation degree of these interferences depends on PSRR value.

Interferences of similar type can be reduced by using the following methods:

- Use the conducting tracks with low impedance for power buses (for example, conducting tracks can be widened; or a ground layer can be used, that's even better). It can minimize voltage drop in the power bus.
- Use ferrite beads or resistors for reduction of interferences in the power buses. Choose parameters (I_{max}, f_{20dB}, R_{DC}, and etc.) in accordance with the specified operating range. Of course, it is necessary to use local energy storage units (capacitors) which should be located as close to the components consuming high current as possible.
- Decoupling capacitors should be located in close proximity to the power or ground terminals of IC.

  - It is necessary to take into account the fact that real capacitors contain parasitic elements such as equivalent series inductance (ESL) and equivalent series resistance (ESR). These elements have strong impact on the operational efficiency of the decoupling capacitor.

- Carefully select the parameters of the power source, i.e. such operating frequency of DC/DC converter, which makes it possible to:
  - meet the requirements for performance and noise level of IC (it should be noted that PSRR value is reduced with an increase in operating frequency), or
  - selected operating frequency of DC/DC converter were out of frequency range used by the system for data communication, or
  - if possible, use the linear power supply.

Many recommendations on optimal design of printed circuit boards in terms of ensuring the EMC and signal integrity, are applicable for IC design at the crystal level. They concern not only "solid-state circuit engineering" but also take into account the application aspects (for example, how to dedicate the IC terminals correctly, chose the timing parameters, and etc.). Development of chips meeting the requirements for functionality and EMC is not the sufficient condition for development of the entire systems which satisfy these requirements. The solution of this task supposes close cooperation among IC developers, system developers and users. Taking into account all of the above, the following recommendations on system development can be offered:

- The conducting tracks on the printed circuit board should be done as short as possible (first of all, it concerns the high-speed signals).
- Use separate layers of multilayer printed circuit board for wiring the power and ground buses; insulation regions on these layers should be avoided.
- The adjacent layers should be used for wiring the power and ground buses since together they form a shared circuit capacitor.
- Decoupling capacitors should be located in close proximity to the power or ground terminals of IC.
- Check of the reference data of decoupling capacitors. Their parasitic parameters (ESR, ESL, resonance frequency) should be taken into account when designing the high-speed systems.
- The relevant impedances should be matched to minimize the signal reflection.
- Use the properly selected resistors for load matching of the high-speed signal lines (of the PCB conducting tracks).
- Make sure that path of return current flowing is minimal. The level of return HF current is much lower than the current level in the signal line (the loop with the lowest impedance has the smallest inductance at high frequencies).
- The length of loops in which the impulse currents flow with high rate of rise (di/dt) should be as short as possible. In such a way, it is possible to reduce the crosstalk level, as well as electromagnetic emissions and other interferences related to EMC.

- When designing the printed circuit board, the tracks of high-speed digital signals should be located away from the tracks on which signals of sensitive analog devices pass.
- Parallel location of the printed circuit board tracks can have both positive and negative effect:
  - avoid of parallel location of tracks if it is necessary to have the minimum level of crosstalk;
  - otherwise, for differential signal transmission, it is necessary to use parallel tracks which are located as close to each other as possible.
- Increase the spacing between those tracks where cross impact of signals is undesirable.
- Wiring of trucks for the most high-speed signals should be performed on internal layers of multilayer printed circuit board.
- Work on system design should be performed in close cooperation among IC design engineers, system developers and developers of printed circuit boards.

10.3 Protective SHF Devices for Radar Stations and Communication Systems

10.3.1 Classification and Features of Creation of Protective SHF Devices for Radar Location and Communication

Currently, the protective SHF devices are widely used both in military and in civil radar location, communication and navigational complexes. They are intended to protect ingress paths of radar station receivers against high levels of SHF power of own and "strange" transmitters.

Previously, the protective devices were used only in the ground, mobile, fixed, marine and airborne radar sets. Most often, the locator had one common antenna for transmission of a large signal and reception of the same target-reflected signal. That's why one of master nodes of antenna-feeder devices (AFD) is an antenna switch with protective device.

In communication and navigational systems, a probing or transmitted signal arrives at the retranslator on the satellite which as a rule, forms a backward signal at other frequency. The issue of protection of the receiver against its own transmitter is solved by the presence of diplexer in AFD. That's why the protective device isn't usually installed in the synchronous satellite communications and navigational systems. However, the protective device is required for communication and radar location systems when intended interferences are generated. Marine radio communication and location systems are the most vulnerable because the breaking signal

sources can approach the ship at rather short distance. It is possible to imagine such situation in the air when using the modern means of electronic countermeasure.

The protective devices which protect the receiver input against its own transmitter, can be controlled by supplying to them a control signal synchronized with a transmitter signal. The protective devices intended for protection of receivers against "strange" signals are commonly referred to as limiters; limiters which are not required the power voltage supply for their operation are commonly referred to as stand-alone limiters [3, 4, 5]. Implementation of stand-alone protective devices is more difficult than controlled protective devices because they have to operate under action of SHF signal, for which the thinner structure (for example, solid-state structure) is required. When possible, the stand-alone protective devices are used instead of controlled ones because in this case, the protection reliability increases. The stand-alone protective devices will be considered in this section.

Developers of transmit equipment have been dealing with the issues of transmit equipment creation and improvement since it first emerged to the present [3–5]. Over the decades, as improvements are introduced into receivers and high-capacity power supply sources, the requirements for protective devices become more and more difficult to implement.

Due to emergence of modern technology of semiconductor transistors used in the receiver stage, it became possible to reduce distances between their electrodes that is required for implementation of low gain-to-noise-temperature. However, this reduces the permissible level of SHF power supplied to the receiver input stage; so currently, it is equal to the very few mW. From the other side, the presence of superpower pulse generators which can be used as breaking signal sources, causes the necessity to build the protective devices which are capable of resisting the action of impulse SHF power reaching units of kW and continuous SHF power reaching hundreds of W.

The mentioned requirements become difficult to implement especially in the upper part of the frequency range where communication and radar location systems operate; currently, it is cm- and mm-range but in perspective, it will be submillimeter-wave range. In this case, it is necessary to ensure low inserted losses of the protective device; otherwise, it is not practical to reduce the receiver noise due to the use of very vulnerable transistor in its input. Typical required losses of the protective device don't exceed 0.5+2.5 dB depending on the value of average operating frequency.

The protective device parameter set wouldn't be complete without consideration of spike leakage energy limitation and time of protective device recovery once the SHF-power action on it is over. Spike leakage energy can deactivate the receiver input transistor because of breakdown of its interelectrode spacings. The permissible values of spike leakage energy are within 10–20 nJ. Recovery time defining the dead zone location distance is tens and hundreds of nanoseconds (when the recovery time is 1 μ, the dead zone location distance is 150 m).

For specific applications, there is a variety of additional requirements complicating the implementation of protective device: capability to withstand severe mechanical and climatic effects; small dimensions, and etc.

Despite the significance of protective device for operation of complex hardware, this class of SHF-devices has not been given sufficient attention throughout its historical development. It was reflected in explanation of physics of processes which occur in semiconductor protective devices. The well-grounded monographes on transistor amplifiers were written [6, 7], but only recently, certain publications of polemical character have begun to appear [6]; and prior to this, the protective devices had been analyzed generally from the perspective of equivalent-circuit concept [9]. Other examples could be mentioned to explain the lack of consideration for protective devices. Semiconductor transistors intended for input amplifiers and power amplifiers are implemented on multilayer structures based on different materials (silicon, gallium arsenide, indium phosphide, and etc.). Precision process equipment was specially developed for production of semiconductor substrates and application of electrodes. So it should seem that this equipment could become the basis for improvement of semiconductor diodes used in the protective devices but this has not yet happened. The industry continues manufacturing the diodes developed 10 and more years ago.

Work [3] attempts to trace the major milestones of protective device development, to find deterrents to their development, as well as discuss the prospects for their improvement.

Among many SHF-protective devices, it is possible to highlight three of the most widely used types: Gas discharge, semiconductor protective devices, their combinations and vacuum protective devices. They are the focus of further consideration in this section.

10.3.2 Gas Discharge Protective Devices

Gas discharge protective devices had appeared prior to others and still occupy their rightful place as a stand-alone protective section which is capable of withstanding the impact of high power [3, 4]. There are coaxial and waveguide protective devices. The most commonly used type of waveguide gas discharge protective devices is shown in Fig. 10.38. In one of the first variants, the containment area is formed in the wave-guide duct (Fig. 10.38a). In general case, it contains a resonator with a gas discharge spacing or a resonator system with a few discharge spacings. The pressurized volume is filled with gas under certain pressure. At the low level of power, gas isn't ionized; and the total SHF-power passes through the discharger; at the high level of power, discharge occurs due to gas ionization in the discharge gap; current flowing in it make the discharge gap shorter that leads to off-resonance cavity, as well as the forward SHF-power bounces off it. Gas discharge protective devices shown in Fig. 10.38a are an optimal solution for use in mm-range of wave length.

The gas dischargers have gone through many phases of improvement. Among them it's worth noting a move towards the use of inserted, in particular, capillary dischargers in which only zone of discharge gap is filled with gas instead of filling the total volume (Fig. 10.38b, c). It makes possible to significantly increase in high-

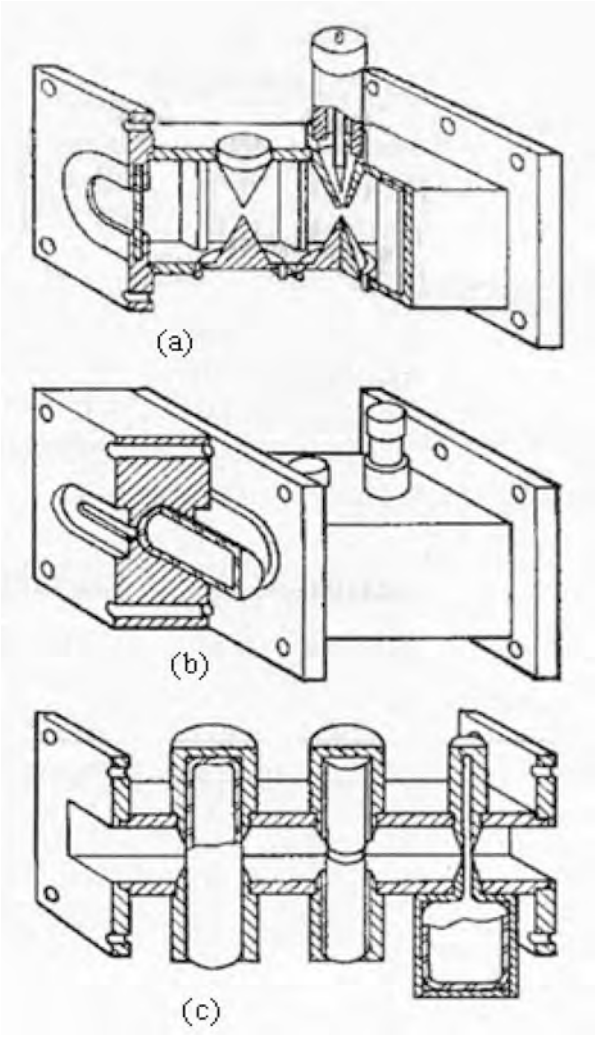

Fig. 10.38 Gas discharge protective devices: (**a**) with pressure-tight resonators; (**b**, **c**) with inserted resonators [1]

speed performance of gas discharge protective devices reaching the fractions of μs. The inserted discharger contains the quartz envelope filled with chemically-active chlorine [10]. The inserted dischargers are used in dm- and cm-ranges of wavelength.

The largest jump in gas discharger development can be attributed to introduction of radioactive elements (for example, tritiated titanium film) in zone filled with gas to ensure automatic ignition of gas discharge [11]. Previously, for ignition, it was necessary to supply high external voltage (up to hundreds of Volts) through special electrode that was rather inconvenient, particularly for protection of disconnected equipment.

The gas dischargers are produced in many options and can differ in allowable input power and in leakage power. Depending on this, there are dischargers of preliminary and final protection of the receiver.

The main disadvantage of gas discharge protective devices is their slow speed of response. Both gas discharge and semiconductor protective devices are characterized by discrepancy between the response time and forward SHF-power. The recovery time is a limitation parameter determined by plasma-discharge time since the end of the transmitter impulse. Another disadvantage is high power consumption due to insufficiently high conductivity of gas discharge. Currently, the pace of improvement of gas discharge protective devices has decreased significantly; the great leap in their development could hardly be expected. The primary focus is on other types of protective devices.

With the advent of semiconductor protective devices it became possible to add stages of semiconductor protective devices to stages of gas discharge protective devices. In these additional stages, the spike leakage energy can be reduced due to their increased high-speed performance. Now, such combined protective devices are the main type of protective devices.

10.3.3 Semiconductor Protective Devices

Semiconductor protective devices have the greatest potential for improvement thanks to their high reliability (at least, it is no lower than reliability of quiet transistors located behind them). First of all it concerns the creation of rational electrodynamic systems in which the properties of semiconductor structure are used to the fullest extent possible. The waveguide protective devices are commonly used because low-noise amplifier in waveguide design works better than coaxial (or strip-line) low-noise amplifier thanks to filtering properties of waveguide duct itself. Besides, being waveguide structure, the waveguide duct itself is less sensitive to impact of high SHF-power and it has lower losses than coaxial and strip-line amplifiers.

For building the semiconductor protective devices, the waveguide has one more advantage: it easily houses an assembly of many semiconductor structures that enables a proportional reduction in electrical load on each structure and increase in permissible input SHF-power.

The following milestones can be distinguished in the history of development of semiconductor protective devices. One of them is “make-up” of switching diodes. One path houses a semiconductor limiting pin-diode VD1 with rather thick base which functions as main switching link, and a low-power “makeup” pn-diode VD2 which is loosely connected to the path and electrically connected to the current circuit of pin-diode [12] (Fig. 10.39). The current circuit includes resistors R_1 R_2 and chokes $L_{др}$ which ratings are selected depending on duration of SHF-power pulses $P_{пад}$. It ensures a few advantages in comparison with usual version of semiconductor protective devices. First, the use of rather “thick” pin-structures ensures an increase

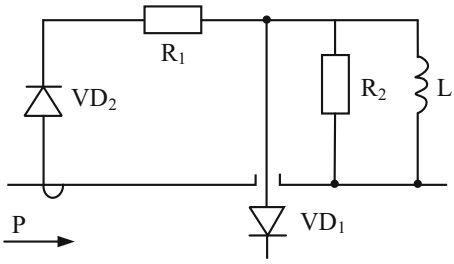

Fig. 10.39 Equivalent circuit of limiter with "make-up"

of protective device power; secondly, these pin-structures can be used at higher frequency in the stand-alone operation mode. With the advent of "makeup" in the semiconductor protective devices, it became possible to create combined gas discharge-semiconductor protective devices in which the specific weight of semiconductor stages were more significant.

Another way to improve the protective devices is search for such solutions which can boost the permissible input SHF-power without sacrificing other important parameters of the protective devices (first of all, such parameters as high-speed performance and inserted losses in working band). Over the past three decades, a variety of original solutions has appeared. These solutions provide for parallel, serial and parallel-serial SHF-current connection of a few diode structures in cross-section and longitudinal section of the waveguide.

Figure 10.40 schematically shows the options of such solutions. The diodes and their connecting conductors are located in cross section of the rectangular waveguide.

In case of serial SHF-current connection of diodes (Fig. 10.39 [13, 14]), it is possible to increase the diode capacitance in proportion to the quantity of diodes in the series circuit without any change in the diode structure. In this case, the total impedance of diode assembly is equal to the impedance of one diode; and permissible power can be increased in proportion to the quantity of diodes. However, this advantage of series circuit couldn't be implemented because it was difficult to provide appropriate heat removal from all diodes if there are more than two diodes.

Parallel connection of diode structures (Fig. 10.41a, b [15, 16]) is unprofitable especially while attempting to reach mm-range of wavelength, because of reduction in impedance of the assembly of a few diodes. Indeed, to keep the impedance being equal to the impedance of a single-diode protective device, it is required to reduce the capacity of each diode in proportion to the quantity of diodes. In this case, SHF-current flowing through each diode is reduced by the same number of times. As a result, the permissible power of the protective device with parallel-connected diodes is similar to that of a single-diode protective device.

That's why the solution schematically shown in Fig. 10.39, 10.40 can be considered as a prototype of rational resonant circuits with parallel-serial switching of diode structures on SHF-current which are shown in Fig. 10.42a, b, c, d [17, 18, 19]. Series-parallel switching enables distribution of SHF-power absorbed in protective mode between many diode structures while keeping unchanged the

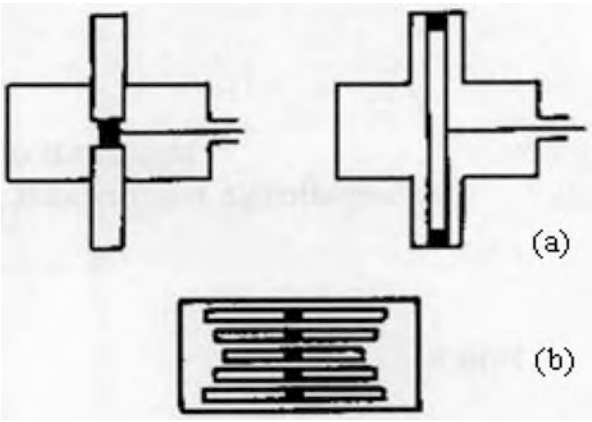

Fig. 10.40 Serial connection of diodes in the limiters: (**a**) diodes with rods; (**b**) nipin – diodes

impedance properties of a single-diode protective device. Options [17, 18], known as "resonant arrays" (Fig. 10.43b, c) have worked well as stages immediately behind the gas discharge protective devices. Proper heat removal from diode structures installed on the side walls which are exposed to the waveguide, and equal current distribution between them ensure the increase in permissible forward power to the first approximation in proportion to the quantity of diodes.

Competitive solution of protective devices based on pin-diodes is shown in Fig. 10.42d [19]. A series-parallel connection of pin diodes is also applicable. Their location in the entire cross section area enables an increase in the quantity of diodes in comparison with the design illustrated in Fig. 10.42b, c, but there is worse heat removal from each pin-structure. As a result, advantage of such design in forward power is minor.

The search for successful solutions for semiconductor protective devices is still under way, although there is a sense of some saturation in this direction.

In large series of resonant arrays, some variants of which are shown in Fig. 10.42, 6 [17, 18], attention should be drawn to one solution [20, 21] concerning creation of "semi-array" (Fig. 10.43). Although, in this case, the purpose was to connect in-series "makeup" and switching diodes but not identical diode structures, it should be noted that this solution can get a definite development. Both in resonant array [17, 18] and in semi-array, the circuit consisting of in-series SHF-current-switched diodes, have good heat removal from the diode structures included in it. It can be useful to build the protective devices with many in-series structures.

Possible increase in the quantity of diode pin-structures between which SHF-power is evenly distributed in case of proper building, created an illusion about removal of gas discharge stages in the protective devices and about an increase of much-needed high-speed performance.

However, along with indisputable advantages of many-diode protective devices, there are some disadvantages which haven't been overcome by now, and coping with which is actually problematic.

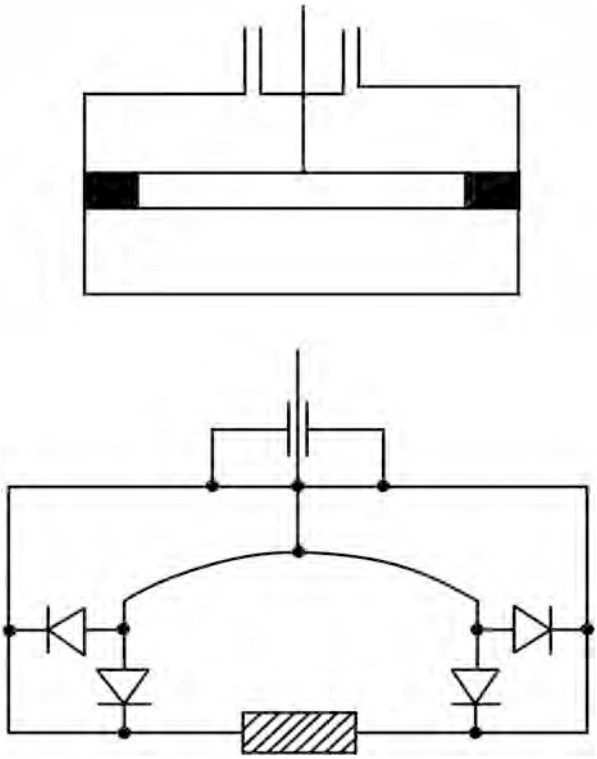

Fig. 10.41 Parallel connection of diodes in the limiters

First, it is difficult to place a great number of diodes with equally good heat removal in the waveguide. Because of this, some groups of diodes will be in the worst conditions, so the efficiency of an increase in their quantity decreases.

Secondly, in any sequence of diode switching, the failure of one diode leads to uneven distribution of the SHF-power absorbed by other diodes, thereby beginning a snowballing process of destruction of the entire protective device.

Thirdly, non-identity of diode parameters is the reason of failure of one of the many diodes, especially if they aren't produced in unified process cycle similar to large matrix crystal.

The possibilities to overcome the specified disadvantages of many-diode versions of protective devices can be found in the following directions. It should be noted the possibility to increase the permissible input power of single lumped or quasi-lumped element of the protective device. In this case it can include many diode structures and even a few types of interconnected diode structures. Monolithic form of such assembly ensures its dimensions much less than operating wave length. At the same time, the identity of all single elements included in such monolithic device is ensured. The similar conditions of heat removal from each diode are automatically provided.

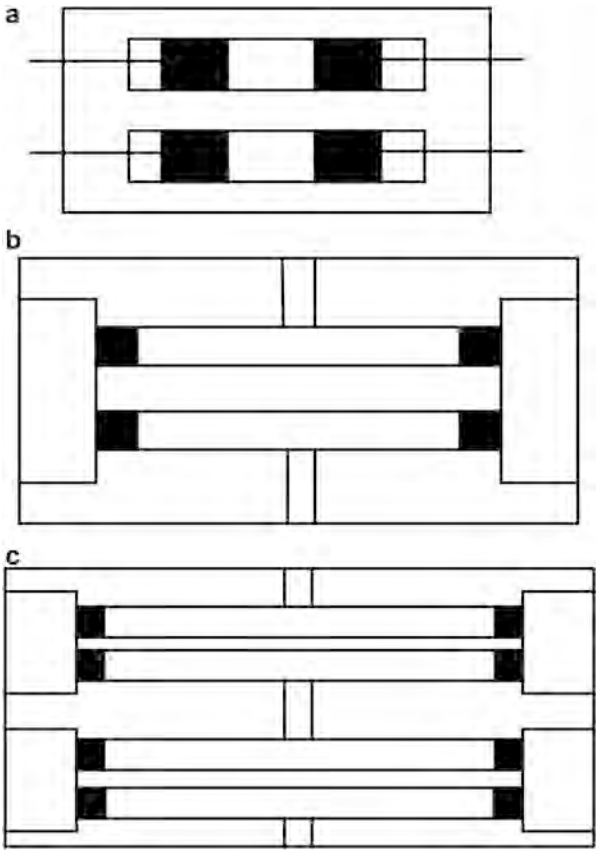

Fig. 10.42 Parallel-serial connection of diodes in the limiters: (**a**) nipin – diodes; (**b**, **c**) resonant arrays; (**d**) waveguide window [1]

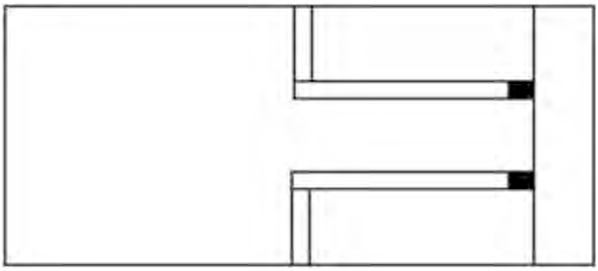

Fig. 10.43 Resonance principle of building of "semi-array"

The matching circuits of lumped design can be used in these monolithic devices, if needed. Similar solutions are known in the semiconductor electronics. The most impressive results belong to the use of the integrated diamond heat removal in generators [22] and creation of high-power transistor amplifiers of continuous power for tens and hundreds of W.

For example, taking into account that at least 50% of delivered power dissipate on the transistor structure itself in the transistor amplifier, and not more than 20–25% of delivered power dissipate in the diode protective devices, it should be expected that the permissible input power of single-element (monolithic) protective devices can exceed the power of transistor power amplifiers by 2 times at least.

It would seem advisable to combine functions of "makeup" and switching diodes in one element [20, 21, 23]. During researches which were significant in their duration and scope, the favorable ratio between capacities of main and makeup diodes was found; and this principle was implemented in practice using low-frequency models.

Development of semiconductor protective devices isn't satisfied by creation of high-power and superpower stages which could replace "slow" gas discharge protective devices. The frequency barrier of semiconductor protective devices, especially stand-alone devices is one of the most important problem that hasn't been completely solved yet. Actually, as operating frequency increases, it is necessary to reduce thickness of the base of the conventional pin-diode and simultaneously to reduce its capacity, as a result of which the protective device can't perform its protective functions because of too low value of permissible operating power. The specified combination of functions of makeup pin-diode and switching pin-diode in one diode structure partially solves the task to reach short wave band. Even greater opportunities in this direction are offered by creation of diodes with compound section of lifetime-killer doping. [22] offers five-layer structures; and [8] shows the principle of their operation. Figure 10.44 schematically shows the five-layer diode structure.

Compared to a conventional pin-diode designed as layers 1, 4, 5, layers 2, 3 were introduced in the five-layer structure which perform function of hole injector, and they are located between base 4 and the first doped layer; the lifetime-killer doping of these areas is performed in steps. (N_4«N3; N_2<N_3 where N is a doping concentration). Thanks to the presence of layers 2,3, it is possible to limit the time of transit through injecting area, enable passage of the minority carrier, and maintain the constant capacitance value at which such voltage can be generated that opens the diode structure under the impact of input SHF-signal.

Work [8] explains the principles for behaviour of various types of diodes operating in SHF-range; as well as it shows the equivalent circuit of diode structure which contains not one parallel connection of capacity and resistance but series connection of two such circuits, as shown in Fig. 10.45. In addition, this work describes a mechanism of changing of all elements of the equivalent circuit under action of applied SHF-field, also it shows the dependence of their value on the selected diode structure in the total frequency range. This model can explain a variety of interesting processes in diodes used in the protective devices, in particular, "hysteresis" in the amplitude characteristics. It is hoped that the suggested representation of diode operation at SHF provides new opportunities for synthesis of promising diode structures not only for protective devices but also for other types of SHF-devices.

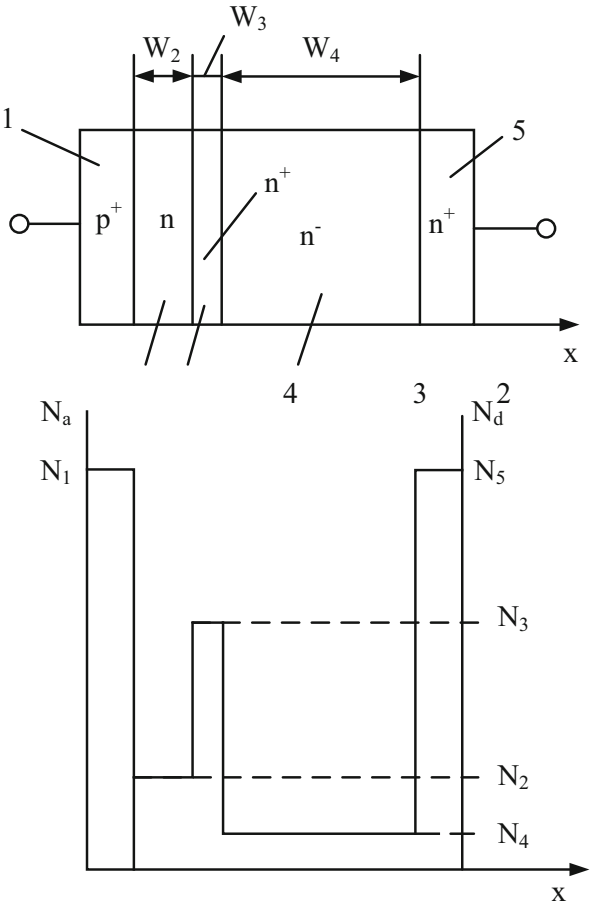

Fig. 10.44 Section and concentration distribution of carriers in the five-layer limiting structure

Attempts to improve parameters of semiconductor limiters using available technological capabilities stimulate the use of FET gate-to-drain junctions instead of pn- and pin- structures [24, 25]. These gate-to-drain junctions are based on GaAs and they have higher performance than commercial silicon diodes.

Obviously, it confirms the lack of consideration for developments of protective devices, since transistors which being more diverse and advanced in terms of technology are used because there is no appropriate choice of pin- and pn-diodes. Moreover, part of these devices are not used that's unreasonable.

Currently, there are prerequisites to consider the behaviour of complex structural synthesis of semiconductor diodes to be progressive for limiters.

Semiconductor protective devices have wide prospects for further development. The key to this is a wide range of ideas for their improvement, appearing recently. These ideas include the use of "trigger" properties of two-diode semiconductor chains. [26–28]. The development of the principle of contactless protective devices, made in the form of waveguide inserts of dielectric plates on which diodes are placed

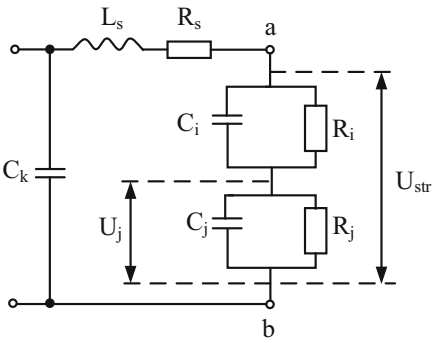

Fig. 10.45 Equivalent circuit of limiting diode at SHF

that are not conductively connected to the walls of the waveguide is of interest [29]. In this case, the insertion loss of the protective devices decreases, which is important for the formation of the last relatively low-power cascades most sensitive to this parameter.

The implementation of promising ideas at the level of R&D and subsequent serial production, apparently, will be determined by the peculiarities of the political and economic situation in the country, affecting the relevance of complexes containing protective devices.

10.3.4 Vacuum Protective Devices

The idea of the emergence of vacuum protective devices was dictated by the need to create ultra-high-speed protective devices capable of responding to superpulse impulses with nanosecond pulse fronts. The first vacuum protective devices appeared in the 60s [27] and were called "protective devices based on secondary electron resonance (SER). The principle of operation of these devices lies in the fact that in a SHF-resonator, pumped off to extreme vacuum and containing in the microwave field a source of electrons with secondary emission, an electron beam arises under the influence of an external microwave field. This beam increases if the secondary emission coefficient is greater than 1 and the condition of equality of the time of flight of electrons between the electrodes of the resonator for the half-period of the microwave field oscillations is satisfied. In this case, the resonator is detuned, and the main part of the microwave power is reflected from the resonator [2]. Recent attempts to improve the SER protective devices relate to the 70s. With their indisputable advantage – high speed (less than 15 not in 3-cm wavelength range), they have disadvantages that were too difficult to overcome – narrowband, high consumption of microwave power, heating of resonators and difficulty of maintaining secondary emission at high density of microwave current.

It is possible that SER protective devices will develop a "second wind" in the future with the development of field emission technology and technology for

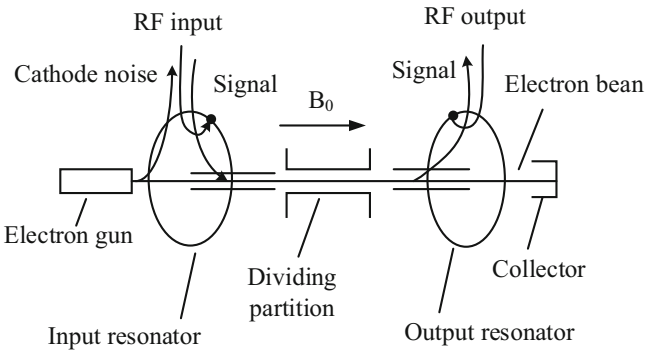

Fig. 10.46 Equivalent circuit of cyclotron protective device

building wideband resonators, but at present they have been superseded by relatively new vacuum protective devices, known as cyclotron protective devices [30–32].

The principle of operation of the cyclotron protective device is illustrated in Figure 10.46 [32]. The tape electron flow formed by the electron gun passes through the input resonator, the separation section, the output resonator and settles in the collector. An extensive capacitive gap is made in each of the resonators. When a longitudinal magnetic field B_0 and a small microwave signal (or absence thereof) are applied the conditions for the passage of a tape electron beam and the transmission of the microwave signal from the input resonator to the output one are created. Starting from the threshold microwave signal and further as it increases, the electron beam is deflected and settles in the capacitive gap of the input resonator. In this case, the input resonator is not consistent and most of the input microwave power (up to 90%) is reflected from it.

Cyclotron protective devices are produced by the industry complete with solid-state low-noise amplifiers. The protective device speed does not exceed 20 ns. In the 3–4 cm wavelength range, the maximum permissible power per pulse is at least 10 kW with an average power of 300 W.

It may be desired that this relatively young type of vacuum protective devices continues to improve at a faster rate. It is necessary to overcome the traditional disadvantages for resonant vacuum devices that use a magnetic field – narrowband and high weight. The hope of success in this direction is instilled by a good theoretical analysis of the passage of an electron beam through a cyclotron protective device with a non-uniform magnetic field applied [33].

Thus, microwave protective devices, being an important node of many location and communication complexes, have a history rich in inventions and stages of technological improvement. A great contribution to this fruitful process was made by our scientists and developers: I.V. Lebedev, S.I. Rebrov,. D. Ya. Ashkenazi, A. M. Starik, K. K. Shutov, O.S. Orlov L. M. Yakuben et al.

10.4 Features of Assessment of the Resource of SHF Devices Considering the Reliability of Mechanical Components

As shown above, SHF-devices have a wide scope of application: from simple household appliances to complicated devices of military and space technology, since the reliability of all such devices is extremely important, you need to be able to most accurately assess both the probability of uptime, operating time, and resource. In particular, this is due to the fact that the entire space technology is by definition non-recoverable and after the onset of a limiting state (i.e. exhaustion of the resource) the probability of failure starts to increase very quickly.

According to [34, 35], resource is the total operating time of the object from the start of its operation or its resumption after repair to the transition to the limiting state, the gamma percentage resource is the total time during which the object does not reach its limiting state with probability γ expressed as a percentage, and the average resource is the expectancy of a resource. The limiting state is the state of the object in which its further operation is unacceptable or impractical or the restoration of its operational state is impossible or impractical [37, 38].

Another important point in determining the value of the resource of electronic devices, including microwave devices, is the consideration of mechanical components. It is worth noting that failures can be interconnected: malfunctions of mechanical parts lead to the failure of the electronic component, and vice versa. Structural damage, deformations can lead to signal distortion, and electrical disturbances due to the failure of the ECB can lead to unsoldering of wires from the contact pads, temperature increase, etc. Thus, neglecting the failures of mechanical components, the developer involuntarily overestimates the resulting values of the reliability and durability indicators of the designed SHF-devices.

Resource assessment methods are clearly regulated by OST [37], resource values for limiting and lite operating conditions are given in the Technical Conditions for domestic development. However, they do not describe the transition from these values to those specified for the product, i.e. the developers are forced to evaluate the product resource at the lower boundary, since space technology operates in the conditions different from the limiting and lite conditions. Also, the time schedule of the product is usually not taken into account when the product undergoes various checks on the ground before being directly launched into space, is transported to the launch site, stored, etc. Detailed coverage of these issues is presented in one of the first works [34] of the team of authors of the Moscow Institute of Electronics and Mathematics of the National Research University Higher School of Economics (Moscow). It is shown here how to estimate the resource of a product functioning in certain conditions, and how to take into account the uneven use of the resource from the moment of commissioning.

Below the text of its active positions is provided as close as possible. So, in order to take into account the uneven consumption of a resource, it is necessary to normalize values for different groups of equipment with respect to one, arbitrarily chosen (for definiteness, let us call it "resource under normal conditions" – $T_{\text{r.n.c.}}$).

As a result, we obtain the proportionality coefficient for the use of the resource K (T_p): for $T_{\text{r.n.c.}}$, it will be equal to one, for lite operating conditions, the coefficient will be strictly greater than one, for more severe conditions, the coefficient will be strictly less than one. Indeed, if we turn to the Technical Conditions, then for lite conditions, the resource is greater than for the limiting ones, and hence the result of normalization with respect to $T_{\text{r.n.c.}}$:

$$K(T_{\text{p}}) = \begin{cases} > 1, & \text{при } T_{\text{p}} > T_{\text{р.н.у.}} \\ 1, & \text{при } T_{\text{p}} = T_{\text{р.н.у.}} \\ < 1, & \text{при } T_{\text{p}} < T_{\text{р.н.у.}} \end{cases}. \tag{10.18}$$

Then, using this coefficient, the consumed resource is calculated during the operation of the product under the conditions of each group of equipment, i.e. for "normal conditions", the amount of consumed resource is equal to the time of operation under these conditions, and, for example, for more severe conditions, more resource is used up for the same time. For periods of operation in the conditions of each group of equipment, the difference between the actual value of the resource and the normal one is determined and subtracted from the $T_{\text{r.n.c}}$. Then the true value of the resource T_{r} of the product in the given conditions of groups of equipment can be determined from the following expression:

$$T_{\text{p}} = T_{\text{р.н.у.}} - \sum_{i=1}^{n} t^{(i)} \cdot \left(\frac{1}{K_i(T_{\text{p}})} - 1 \right), \tag{10.19}$$

where $T_{\text{r.n.c.}}$ is the value of the resource for the selected "normal" operating conditions; n is the number of groups of equipment operating conditions (excluding "normal"); $t^{(i)}$ is the operation time in the conditions of the i-th group of equipment; $K_{\text{i}}(T_{\text{p}})$ is the proportionality factor of resource consumption for the conditions of the i-th group of equipment.

The method of calculating the resource for certain conditions of groups of equipment is given in [36]. In domestic Technical Conditions, resource values for limiting and lite operating conditions are usually given, while article [34] discusses how to switch from the values specified in the Technical Conditions to real ones:

$$T_{\text{p}} = \frac{T_{\text{p}}(\text{ПУ})}{K_{\text{И}} \cdot K_{\text{Н}}}, \tag{10.20}$$

where T_{r} (LS) is the resource value specified in the Technical Conditions for the limiting conditions of operation; U_{F} – utilization factor; L_{F} – load factor (critical parameter).

In Eq. (10.20) U_F is determined according to formula (10.21), and L_F is determined according to formula (10.22):

$$K_И = \frac{t_{\Sigma pp}}{t_{\Sigma pp} + t_{\Sigma ож}}, \tag{10.21}$$

where $t_{\sum dc}$, $t_{\sum st}$ – the total time spent in the duty cycle and standby for the period of operation:

$$K_H = \frac{\Psi_{pp}}{\Psi_{ном}} \tag{10.22}$$

where Ψ_{dc} is the critical parameter value in the duty cycle; Ψ_{nom} is the nominal value of the critical parameter according to the Technical Specification.

The authors [34] consider a typical product of onboard electronic equipment for space technology – a microwave switch as an example. During operation, the switch is exposed to various external influencing factors (EIF). First, the product is stored indoors (in the warehouse) for one year (8760 h), which corresponds to group 1.1 [44], and is further transported by any type of transport (group 1.3 for automotive, 3.1 for aviation, 1.9 for railway) to the launch site of the carrier rocket for five days (120 h), after which the rocket is launched and placed into orbit (group 4.1) for two days (48 h) and, finally, performs its main functions (reception and transmission in the microwave range) until the end of the active shelf life (ASL) in the conditions of group 5.3 (Fig. 10.47). According to the Technical Conditions and article [37], the product resource for each of the equipment groups will be different. Taking into account the above information about storage, transportation and direct operation of the product, we conclude that the resource is spent unevenly.

After analyzing the technical documentation data on the switch, a failure tree was built (Fig. 10.48) [41, 42], where the following events are marked with numbers: *1* – the product is inoperable; *2* – product failure; *3* – no signal processing; *4* – violation of fastening and sealing; *5* – failure of the electronic part; *6* – no signal in the input of the circuit; *7* – no signal processing in the boards; *8* – no output signal; *9* – failure of input cascades; *10* – no signal in input 1; *11* – no signal in input 2; *12* – failure of the elements of input No. 1; *13* – failure of W1; *14* – failure of XW1; *15* – burnout of the valve W1; *16* – burnout of the connector XW1; *17* – failure of the elements of input No. 2; *18* – failure of W2; *19* – failure of XW2; *20* – burnout of valve W2; *21* – burnout of connector XW2; *22* – board failure; *23* – lack of power to the diode of the XN1 board; *24* – lack of power to the diode of the XN2 board; *25* – failure of one of the diodes VD1-VD8; *26* – failure of one of the diodes VD1-VD8; *27* – output cascade failure; *28* – no signal on bridges XN8, XN9; *29* – failure of the outputs of the product; *30* – failure of the bridges XN8, XN9; *31* – no signal of bridge XN8; *32* – no signal of bridge XN9; *33* – damage to the conductive paths of the bridge

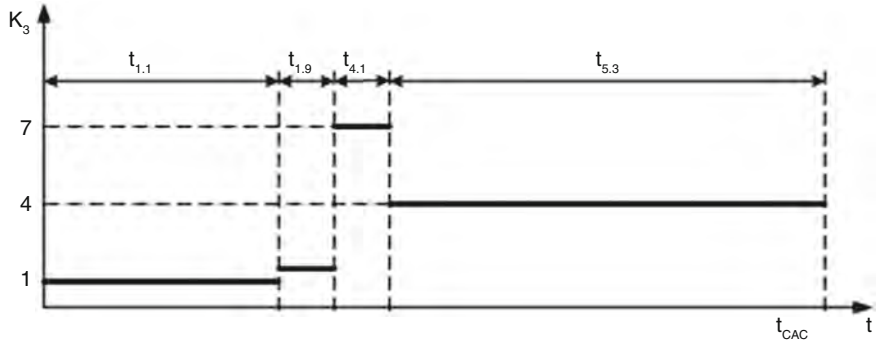

Fig. 10.47 Time schedule of commutator operation

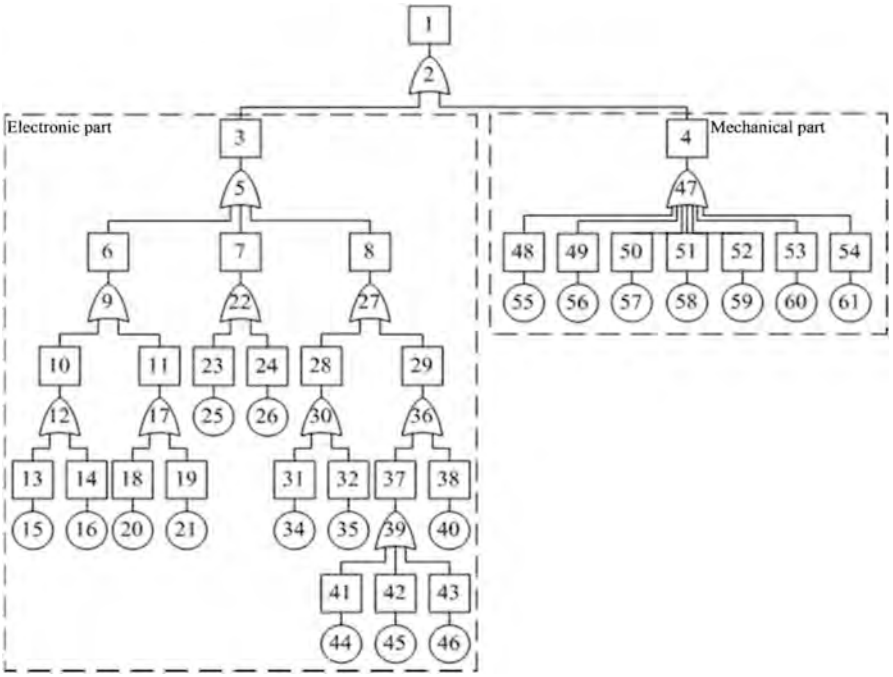

Fig. 10.48 Commutator failure tree

XN8; *34* – damage to the conductive paths of the bridge XN9; *36* – no signal in the output channels; *37* – failure of output connectors XW3-XW5; *38* – failure of the circulator W3; *39* – no signal on connectors XW3-XW5; *40* – burnout of the circulator W3; *41* – failure of the connector XW3; *42* – failure of the connector XW4; *43* – failure of the connector XW5; *44* – burnout of the connector XW3; *45* – burnout of the connector XW4; *46* – burnout of the connector XW5; *47* – destruction

Table 10.7 The results of the calculation of the reliability of the switch

Name of the component	Operational failure rate, 1/h	The failure rate in standby mode, 1/h	Gamma percentage resource, h
Electronic part	7.27e-07	5.56e-08	23400
Mechanical part	9.92e-07	7.26e-08	26200
Switch	1.71806079201876E-6	1.281957368E-7	23400

of welded, brazed and glued joints and depressurization of plugs and gaskets; *48* – failure of screws fastening valves W1, W2; *49* – solder connection failure of jumpers on the XN1, XN2 boards; *50* – failure of the welded connection of jumpers of XN5, XN6 boards; *51* – stub failure; *52* – failure of adhesive bonding of boards XN4, XN6; *53* – cover screws failure; *54* – cover gasket failure; *55* – loosening of the fastening of valves W1, W2; *56* – destruction of the solder connection of the jumpers of the XN1, XN2 boards; *57* – destruction/failure of the welded joint of jumpers of the XN5, XN6 boards; *58* – deformation of the plug; *59* – peeling of the adhesive film in the connection boards XN4, XN6; *60* – loosening of the cover; *61* – deformation of the gasket cover. As you can see, the failure of the product is equally dependent on the failure of electronic and mechanical parts.

The results of the calculation of reliability indicators carried out in accordance with the constructed tree are given in Table. 10.7 [1], and the Figure 10.49 [1] shows the contribution to the overall reliability of the electronic and mechanical components of the switch. The calculation of the electronic part was carried out on the basis of the data given in [39], the mechanical part – on the basis of [40].

As can be seen from the figure, the reliability of the "mechanical" part is comparable to the "electronic" part and, neglecting it, we unwittingly "improve" the reliability by 2 times. In other words, it is quite obvious that mechanical components should be taken into account when calculating the reliability and durability of microwave devices. The Table 10.7 presents the obtained values of reliability indicators, and the resource is calculated taking into account non-stationary conditions of operation using the expression (10.19).

When calculating the final resource from Table 10.8 using expression 10.19, the conditions for group 5.3 were taken as "normal" conditions and, as can be seen, the total value is higher than for group 5.3 on average by 4000 h (a little less than six months).

The calculation carried out by the authors [34] confirmed the need to take into account the functioning in the conditions of various groups of equipment when assessing the resource. In connection with the tightening of requirements for equipment, it is not always possible to afford the luxury of estimating the lower boundary (the worst case), since such requirements imply accurate calculations. The proposed method of calculating the resource takes a step towards increasing the accuracy of the resource calculations. Another important fact is visual demonstration of the influence of mechanical components of microwave devices on reliability (Figure 10.49). It is noteworthy that taking into account the mechanical components impairs the resulting values of reliability indicators to the same extent as electronic

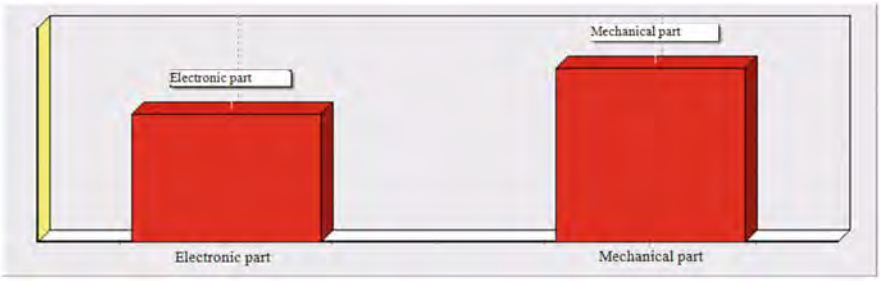

Fig. 10.49 Contribution to electronic and mechanical switch reliability

ones [43–45]. Thus, all the proposed measures for more accurate calculations confirm the need to develop methods for accurate calculations with stricter requirements for SHF-devices.

Summarizing this section, we can draw the following conclusions:

- when assessing reliability, in particular durability, it is necessary to take into account the mechanical components of SHF-devices;
- the numerical value of the resource depends on the specific group of equipment, i.e. from the set of EIF, and in assessing the durability indicators it is necessary to take into account the nonstationarity of the operating conditions of the SHF-device.

10.5 Features of Organizing Electric Power Supply Circuits of Radar Set Microwave Devices

As developers of radioelectronic equipment are all aware, noise generated in the electric circuits impairs the reliability parameters of any electronic system. For designing a highly-reliable system, it should be fully understood how noise is generated and propagated in the power distribution network. Noise is minimal if the signal source, wiring and load are electrically matched with each other [46].

The output resistance of signal generators, oscilloscopes, spectrum analysers and vector network analyzers is often equal to 50 Ohm. This equipment is connected to other units by means of 50-Ohm coaxial cables and 50-Ohm connectors.

Other standard levels of impedance are used in practice. For example, the value of 100 Ohm is often used in the wiring on the digital circuit boards; and the value of 75 Ohm is often used in closed-circuit television systems. It is strictly required to use only matched wiring layouts in all this equipment that improves the performance capabilities of applications and minimizes the noise. The same requirement is applicable to the design of common power distribution network of SHF-devices.

Table 10.8 Microwave switch reliability indicators

Type of device	Operational failure rate	Failure rate in standby mode	Resource				
			1.1	1.9	4.1	5.3	Total
Electronic part							
FPVN2-88	7.30e-08	8.76e-10	120000	80000	21800	60000	64300
FTsP2-13	1.90e-07	8.93e-10	120000	80000	21800	60000	64300
SRG-50 (VR0.364.026TC)	5.49e-09	7.69e-09	200000	133000	53300	100000	104000
EEE-wave soldering	6.90e-10	6.90e-12	131400	87600	35000	65700	70000
2A517A-2N, B-2N	4.50e-08	1.68e-09	50000	47600	10000	17800	23400
Printed circuitry	3.40e-11	3.40e-13	500000	230800	95200	178600	184000
Mechanical part							
Valve mounting screw	1.00e-09	1.00e-11	876000	584500	233600	438000	442400
Jumpers soldering	1.20e-09	1.20e-11	131400	87600	35000	65700	70000
Welding wires to contact pads	2.40e-10	2.40e-12	87600	58400	23300	43800	48100
Fluoroplastic connector plug F-4 (or F5)	3.60e-07	3.60e-08	175200	116800	46700	87600	91970
Glued board connection	2.40e-08	2.40e-09	61300	40800	16300	30600	34900
Cover mounting screw	6.00e-09	6.00e-11	876000	584500	233600	438000	442400
Cover gasket	2.88e-07	2.88e-08	43800	29200	11600	21900	26200
Cover soldering and sealing	2.40e-07	2.40e-09	131400	87600	35000	65700	70000

The brief analysis of typical power distribution network of SHF-system was performed.

Power distribution network (PDN) includes a voltage regulator module (VRM), interconnected layers of printed circuit board, connecting wires and loads to which power is supplied. Figure 10.50 shows a typical dependence of impedance of the well-balanced power distribution network on frequency. The impedance of this PDN is 3,3 Ohm. Here, the output impedance of the voltage regulator is equal to 3.3 Ohm and the load impedance (ZPCB) is 3.3 Ohm that ensures perfectly even characteristic of power distribution network (PDN).

If connections between the voltage regulator module and power distribution network are mismatched in any direction, they become sensitive to noise that impairs the system operating parameters. Figure 10.51 [1] shows the impedance-frequency characteristic of power distribution network in three cases when the voltage regulator

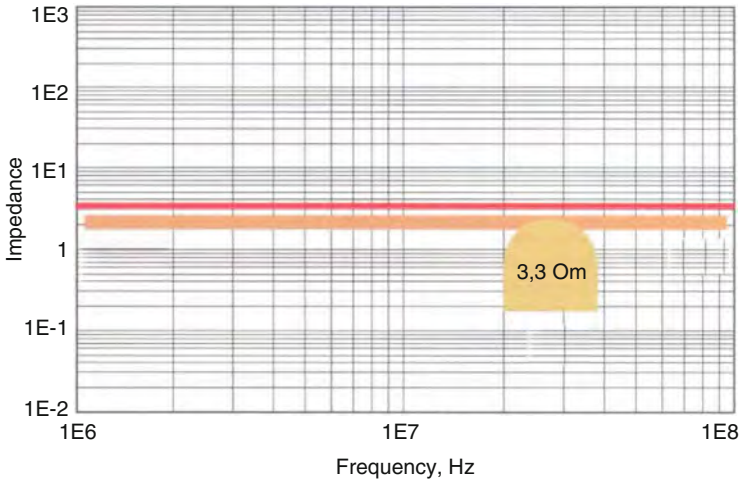

Fig. 10.50 In the well-balanced power distribution network, impedances of voltage regulator, printed circuit board and load are matched within the full range of frequencies below the specified one [1]

impedance is more, less than or equal to the impedance of the printed circuit board and load (Fig. 10.52).

If the voltage regulator impedance is too high, the resultant impedance of power distribution network is mainly capacitive in effect at frequencies lower than resonance frequency of the printed circuit board, and it is reduced at a rate of 20 dB/decade. If the voltage regulator impedance is too low, the resultant impedance of power distribution network becomes inductive in effect at frequencies lower than resonance frequency of the printed circuit board, and it is increased at a rate of 20 dB/decade.

As shown in Fig. 10.53, addition of a decoupling capacitor with high Q-factor allows to eliminate the first maximum; but at low and high frequencies, the peak values of impedance remain and exceed by far the impedance of the printed circuit board

As the signal passes through the transmission line, the PCB impedance has a sharp peak near the load at a frequency which is twice as much as a resonance frequency of this board. In case of resultant inductive impedance of the power bus, the amplitude of this peak has a positive value; and in case of capacitive impedance, the amplitude has a negative value.

Figure 10.54 shows that even if close to the load, there is a decoupling capacitor having ESR equal to PCB impedance and ESL lower than PCB impedance, the characteristic can't be considered optimal because of the presence of negative peaks in the range of high frequencies.

Figure 10.54 shows the frequency characteristics for three cases under consideration with different impedances of the voltage regulator. These curves are characteristics of transmission lines with cyclic-repeated positive and negative peaks. At

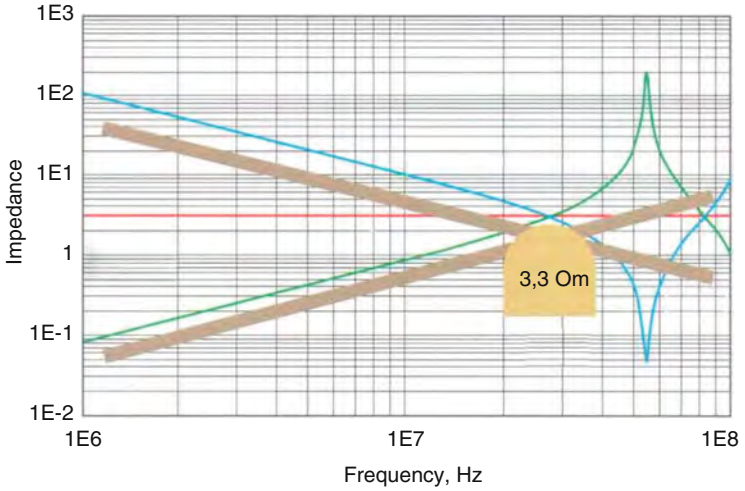

Fig. 10.51 Impedance-frequency characteristic of typical SHF-device board [1]

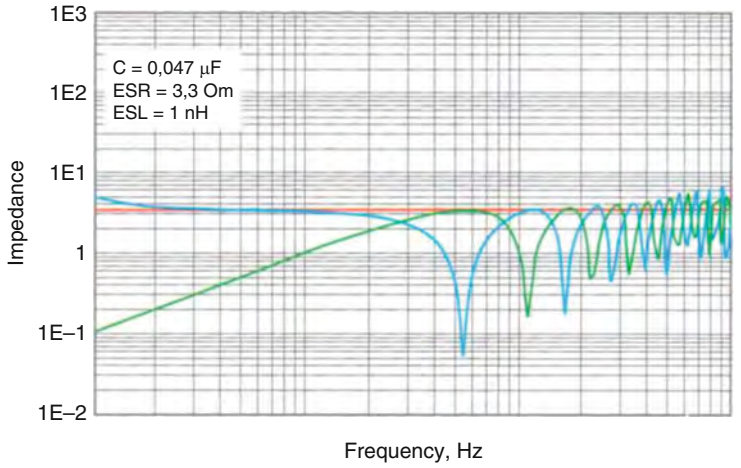

Fig. 10.52 If the voltage regulator impedance is higher or lower than impedance of the printed circuit board (PCB), the peak values of the voltage regulator impedance are much higher than PCB impedance [1]

higher frequencies, the characteristics of the board with resultant capacitive impedance has a negative peak followed by a positive peak, then these peaks cyclically revolve. At higher frequencies, the characteristics of the board with inductive impedance has a positive peak followed by a negative peak; by alternating, these peaks form similar cyclic-repeated sequence. In both cases, the maximum peaks of voltage regulator exceed by far the impedances of the load and printed circuit board;

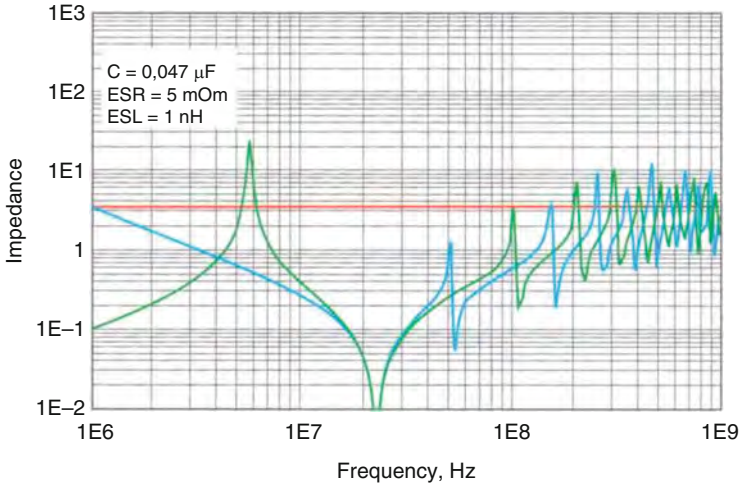

Fig. 10.53 Impedance-frequency characteristic of the board with decoupling capacitor [1]

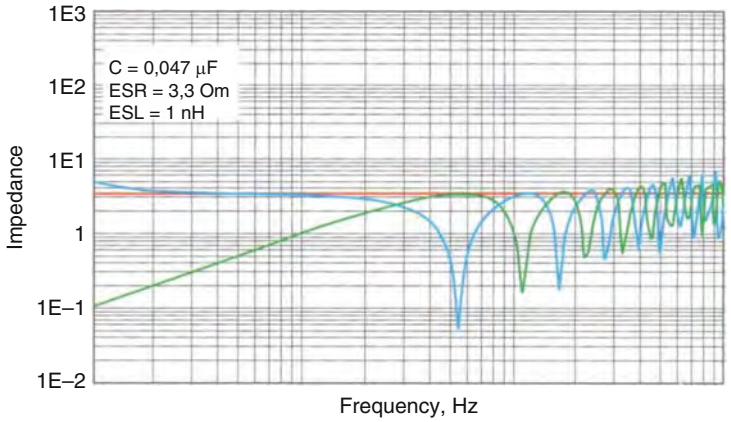

Fig. 10.54 The presence of negative peaks in the range of high operating frequencies [1]

and the negative peaks are much lower than impedances of the load and printed circuit board.

Generally, a decoupling capacitor is added to the load in order to smooth the characteristics of resultant impedance of power distribution network and improve the system operating parameters. Figure 10.55 shows the results of use of the ceramic capacitor with a capacity of 0.47 μF.

Addition of the ceramic capacitor reduces LF-impedance down to the value of PCB impedance; however, in this case, the peak inductive impedance at lower frequency with smaller amplitude exceeds by far the PCB impedance. At higher

frequencies, the output impedance of the regulator is increased again and it exceeds the PCB impedance.

In order that the peak impedance remains below the PCB impedance, the equivalent series resistance (ESR) of the ceramic decoupling capacitor should be equal to the PCB impedance within the full range of frequencies higher than the first resonance frequency; and the equivalent series inductance (ESL) of this capacitor should be equal to the PCB impedance at the highest frequency of the range under consideration. In this case, the capacitor ESR is equal to 3.3 Ohm, and its ESL should be less than 1 nH (Fig. 10.54).

Negative peak values being much lower than impedance of the printed circuit board continue to impair the system performance. The impedance close to the load is an internal impedance of the power source for the next circuit. This impedance should be equal to the resultant impedance of the board in order to minimize the peaks in characteristics of the next circuit (Fig. 10.55).

As shown in Fig. 10.56, the tantalum capacitor with low ESR is installed in the top power distribution network close to the voltage regulator. The bottom power distribution network provides the maximum flat frequency characteristic

Here we will list some core capabilities to use these principles in practice in order to reduce the cost of project under development while improving the system performance.

Of course, the voltage regulator with lower impedance and better regulating characteristic costs more. If impedance of this device is lower than characteristic impedance of the printed circuit board, then under load the peaks can appear on the frequency characteristic of the impedance.

PDN on the printed circuit board should not be too complicated. To reduce its impedance, it is necessary to expand the board area that leads to unreasonable increase in the number of levels and, consequently, to the rise in the product cost.

When using the tantalum capacitors with low ESR, there is an increase in the system production cost. To provide impedance matching on the power distribution, a capacitor with a higher ESR value is required, which allows relatively inexpensive tantalum or aluminum capacitors to be used. Often this is also the case when parallel decoupling capacitors are installed in parallel with large-capacity capacitors. To obtain equality with impedance of power distribution it is required to use high capacity capacitors with a higher ESR value. In some cases an external resistor is installed in series with the capacitor for this purpose. This solution is the least expensive.

As seen in Fig. 10.57, the characteristic with maximum linearity in almost the entire frequency range is shown by curve 1. Curve 2 illustrates the characteristics of the power distribution network which includes a tantalum capacitor with low ESR.

In cases where the regulator is linear, it does not need capacitors – they need to be installed only at the load.

The output impedance of all voltage regulators allows you to determine the stability – a critical parameter of any application. In addition, it is used to establish peak impedance values caused by a small margin of stability. Of course, it can be

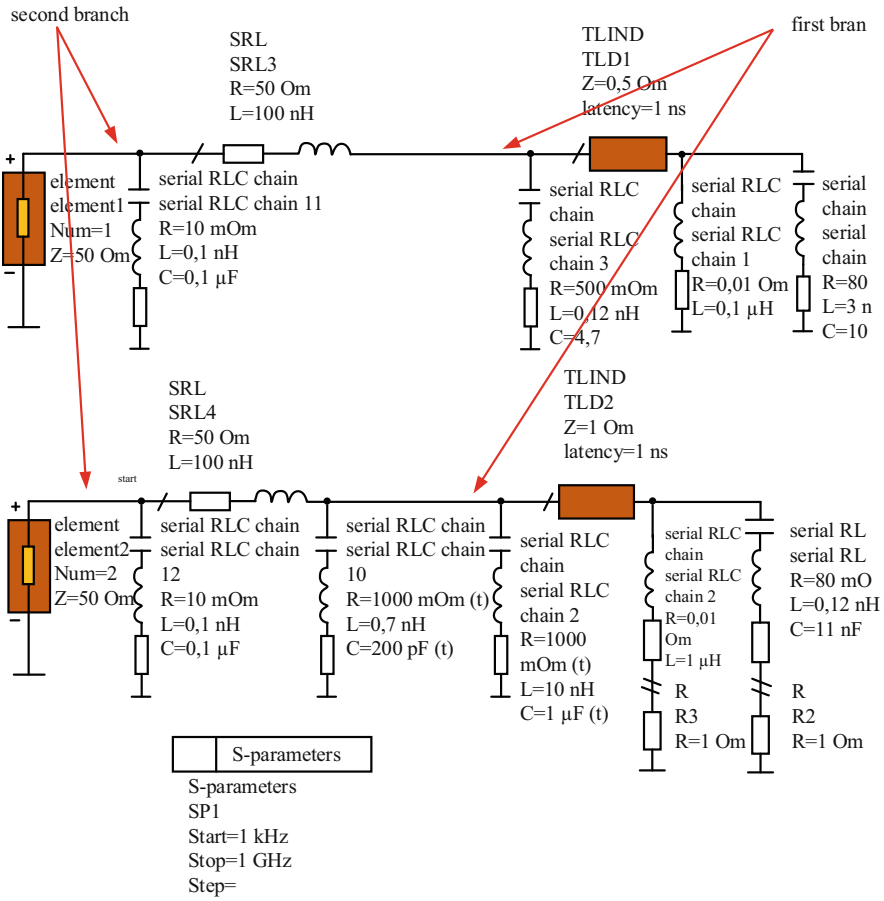

Fig. 10.55 Equivalent electrical power distribution network with a series-connected 1-Ohm circuit [1]

increased by changing the value of the compensating resistance or capacitor, it will be much cheaper than using smoothing filters.

For cascaded circuits, impedances should be equal. For example, if a circuit with a low impedance is followed by a circuit with a large impedance, the power distribution circuit can become inductive, which is difficult to correct, then, as with equal impedances, balance is maintained.

The noise is minimal in the system with matched impedances of the voltage regulator, printed circuit board and load. Paradoxically, the series-connected resistor between the voltage regulator module and the printed circuit board reduces the range of voltage fluctuations near the load.

As shown in Fig. 10.58, more expensive PDN doesn't provide the required damping that results in the presence of a sharp peak on the impedance-frequency

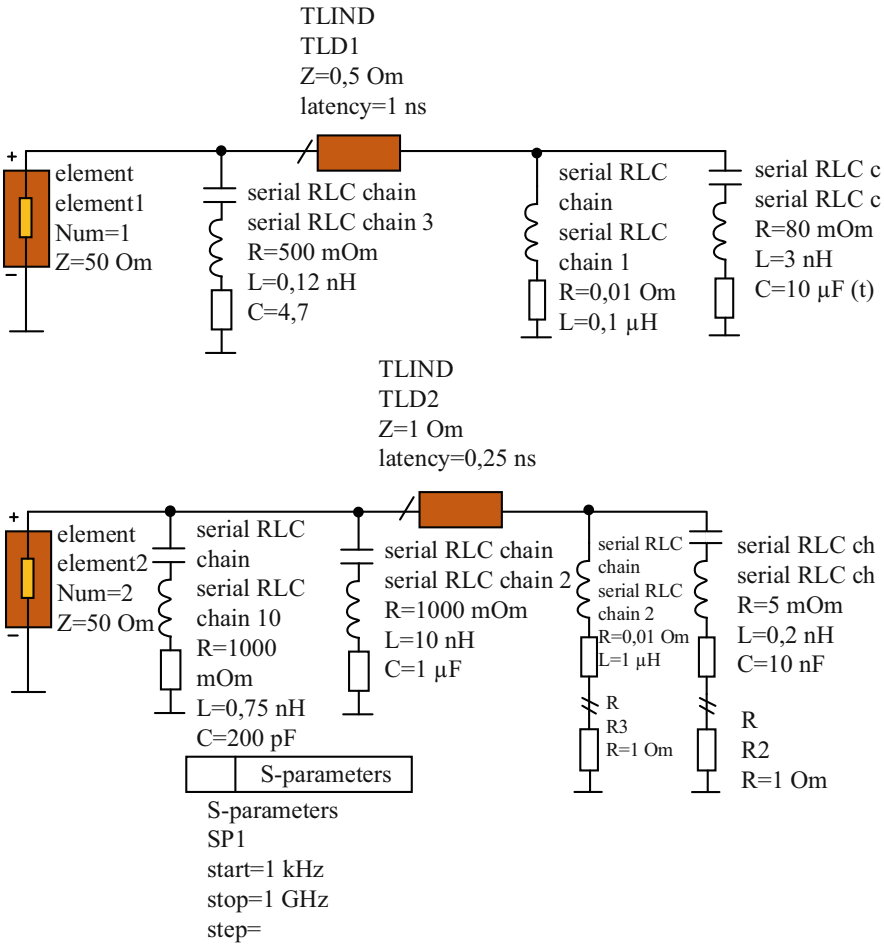

Fig. 10.56 Equivalent electrical power distribution network with a tantalum capacitor [1]

characteristics which impairs the system performance and requires an additional damping circuit [46].

According to Fig. 10.58, the power distribution network (PDN) operating in the frequency range of 0–1 GHz with the maximum impedance of 2 Ohm, includes a linear voltage regulator with inductance of 1 µH and series resistance of 10 mOhm. These typical values for linear voltage regulator operating at current of 100 mA can be easily measured. When designing this PDN, two approaches are used (Fig. 10.56). The first approach provides the maximum linearity; the second approach is a typical solution in which along with a regulator, a capacitor with low ESR is installed that increases the dimensions of the printed circuit board.

Figure 10.57 shows the results of simulating impedance from the load. The comparative cost of a solution that uses a larger printed circuit board and a capacitor

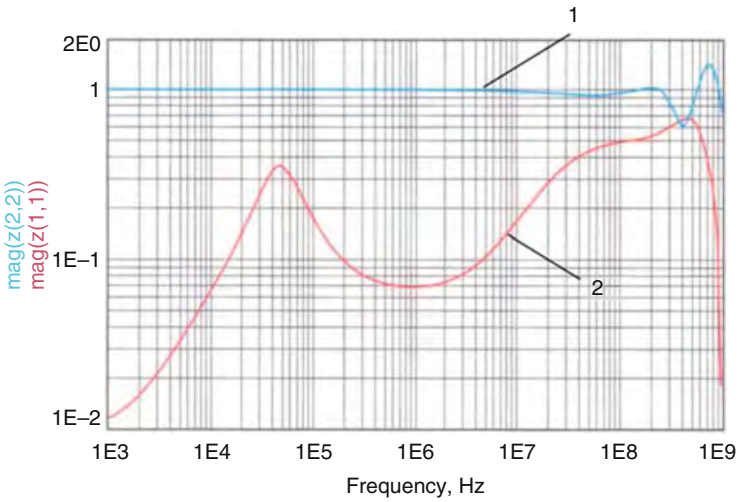

Fig. 10.57 Frequency response of a board with a tantalum capacitor with a low ESR [1]

with a small ESR is slightly lower, but it provides a lower impedance (albeit with a non-linear characteristic).

It should be noted that a more expensive solution may cause problems to other individual power supply circuits connected to this node due to insufficient damping below 1 kHz and in the range of 100 kHz ... 10 MHz. An additional 1-Ohm circuit consisting of inductance per 100 nH and a capacitor per 100 nF is connected to this node (Fig. 10.55). Figure 10.58 shows the results of simulation of the impedance characteristics on the side of the second circuit. Further improvement in performance is provided by using a 1-Ohm resistor, which is connected in series to 0.1 μF capacitors in the second circuit, if the impedance of the load connected to this node of the power distribution circuit does not reach 1 Ohm.

The exact matching of impedances of the voltage regulator module, printed circuit board levels and load circuits with each other, as well as their conformity to the specified value enable to create the straight-line characteristic and minimize the area of the wire-circuit board. This optimization also reduces the use of expensive low ESR capacitors and low impedance voltage regulators.

10.6 HF and SHF Components for Suppression of Electromagnetic Interference

One of the main technical solutions to the problem of ensuring electromagnetic compatibility (EMC) of SHF-devices is the suppression of electromagnetic interferences.

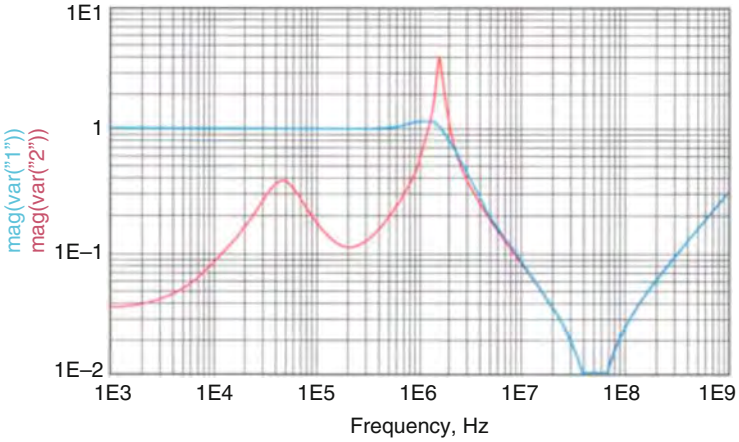

Fig. 10.58 Example of frequency characteristics of power distribution network [1]

For this purpose, various low-pass filters, filter connectors and assemblies, filters for surface mounting, etc., which are widely used in SHF-system, communication and telecommunication systems, in aerospace equipment, in industrial electronics, medical equipment, are used.

A brief look at the main technical characteristics of these components on the example of the nomenclature of products of the company Spectrum Control already mentioned above, which is one of the major global manufacturers of this type of components [47].

The main types of Spectrum Control products are shown in Fig. 10.59.

Ceramic Capacitors

Spectrum Control uses two types of capacitors in its production: tubular and disk multilayered. They are the main elements of noise suppressing low-pass filters and are intended for shunting electromagnetic interference to the ground. The main parameters of the capacitors are presented in Table 10.9

Spectrum Control produces 55 sizes of tubular capacitors: 31 – C-type, including multilayer, 24 Pi-type, as well as 35 sizes of multilayer disk capacitors. The advantage of these capacitors in comparison with standard capacitors with wire leads is a small amount of their own inductance.

The simplest C-type capacitor is a tube with metallized wafers of one of the ceramic materials (NPO, X7R, BX, Z5U, etc.) with different dielectric constant. Coating of capacitor plates is made of wear-resistant silver nickel barrier layer. Pi-type tubular capacitors are a combination of two capacitors connected in parallel.

Disk multilayer capacitors have a higher level of electrical capacitance (up to 10 μF) compared with single-layer capacitors. They are used in the construction of noise suppressing filters with an operating voltage of up to 400 V and with a small transition area of the frequency dependence of the insertion loss. It should be noted that the creation of multilayer ceramics made it possible to develop not only

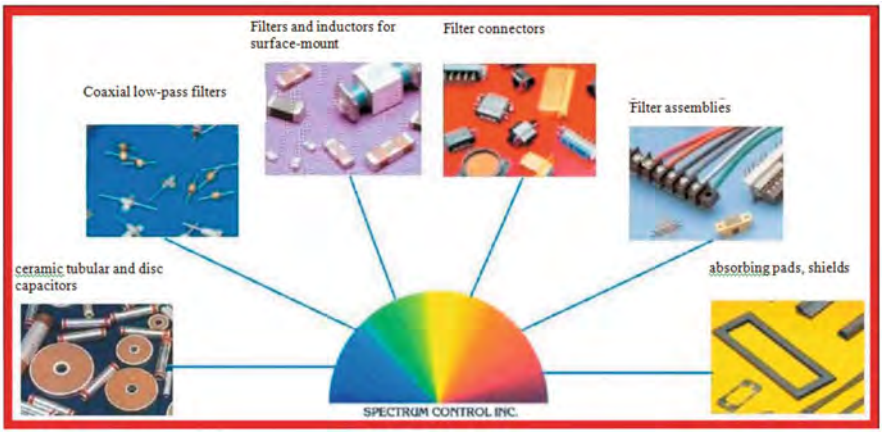

Fig. 10.59 Spectrum Control products

Table 10.9 The main parameters of ceramic capacitors

Capacitor type	Dimensions, mm			Electrical capacity	Operating voltage, V
	Outer diameter	Inner diameter	Length (thickness)		
Tubular C-type	1.6; 1.83; 2.06; 2.11 2.41; 2.67; and 3.79	0.94; 1.14 1.19; and 1.75	4.39; 8.38; 10.01; 10.8; and 11.43	from 270 pF to 0.82 μF	500, 100 and 200
Tubular Pi-type	1.55; 1.6; 1.85; 1.91; 2.49; 3.18 and 3.86	0.51; 0.66; 0.81 0.86; 1.14 and 1.73	7.62; 7.75; 2.57; 9.4; 10.8 and 11.3	from 4700 to 30000 pF	
Multi-layer disc C-type	2.54; 3.35; 4.95; 6.3; 8.58; 11.04 and 15.04	2.01; 2.4; 1.57 1.93 and 2.41	1.0; 1.5; 1.78; 2.9; 2.79; 3.05 and 3.81	from 50 pF to 3.8 μF	50, 100,150, 200, 300, 400

capacitors, but also inductors, chokes, ceramics with a low sintering temperature, microstrip microwave outputs and other components with a high level of parameters.

The operating range of capacitors of all types is from –55 to + 125 °C.

Coaxial Low-Pass Filters

The design, principle of operation, electrical circuits of coaxial low-pass filters are considered in [48, 49]. Spectrum Control produces several hundred sizes of pass-through noise suppression filters with C-, L-C-, Pi- and T-electric circuits (Fig. 10.60).

By design, these filters can be attributed to one of four typical groups:

1. Miniature, sealed with metal-glass joints, nonthreaded, soldered into the device housings filters (Miniature Solder-in Filters);
2. Sealed with compound, nonthreaded, soldered into the device housings (Solder-in Filters);

Fig. 10.60 Noise suppression filters made by Spectrum Control

3. Sealed with compound, threaded, including for chains with high voltages and currents (Resin Sealed Bolt-in Filters);
4. Sealed with metal-glass joints, threaded (Bolt-in Style Hermetic Filters or Glass Seal Filters).

Filters of all types are available for both civil and military use (in accordance with the standards MIL-F-15733 and MIL-F-28861). The main parameters of the filters of all groups are given in Table 10.10.

The filters of the first group are a capacitor placed in a metal sleeve with a flange, sealed at one of the ends with the metal-glass joint. The opposite end of the sleeve is sealed with epoxy compound. The designation of filters in which the joint is located on the side of the flange is supplemented with the letter "R" at the end (Reverse).

To indicate the capacity of filters, the color marking is applied . The red color of the compound corresponds to the capacity of 2700 pF, white 1200 pF, brown 500 pF, and etc. The metal surfaces of the filters are gold plated. Filters of this group have increased reliability and withstand heating to a temperature of 260°C when soldered into the housing of products.

A new series of SCI-9925 C-type filters, mounted in the housing of products by pressing, has also been developed. The flange sleeve of such filters is knurled, and the metal-glass junction is made on the side opposite to the flange. Filters are pressed into holes with a diameter of 3.5–3.8 mm in the housing of the product using a special tool SCI-9925-200.

C-type filters are used in high impedance circuits, unless a very large amount of electrical capacity is required.

The second large group of filters are compound-sealed nonthreaded filters of various designs. They have found application in devices with a dense arrangement of components, in which the possibility of using a tool for mounting filters is limited.

The third, largest group includes threaded filters, sealed with compound. It includes threaded filters on the 4-40 UNC-2A, 6-32 UNC-2A, 6-40 UNF-2A, 8-32 UNC-2A, 10-32 UNF-2A, 12-28 UNF-2A, 12-32 UNEF-2A, 5 / 16-24 UNEF-2A housings, etc., as well as filters for high currents and voltages. Spectrum Control manufactures threaded filters with C-, L-C- and Pi-electric circuits. The threaded filters are either screwed in and then soldered into the housing of the product, or passed into a smooth hole in the wall of the housing and secured on the reverse side with a nut and a lock washer.

Table 10.10 The main parameters of the filters

Filter series number	Number of typical sizes / design variants	Electrical capacity	Electrical capacity	Operating voltage, V	Operational	Design features
I. Miniature enclosed threadless filters						
SCI-9900, SCI-9910, SCI-9920	16/2	C	10 – 30000 nΦ	50; 100; 200	5	Tube diameter: 3.25 mm. Center conductor diameter is 0.76 mm. The length of the sleeve is 2.79 mm.
SCI-9925 (new)	7/1					Same, thread length: 1.02 mm
II. Compound sealed ncnthreaded filters						
54803004X5R 54–785, 54–786 ⇒ Ap.	12/5	C	100 nΦ – 0,3 mkΦ	10; 25	50; 100; 250; 750	Tube diameter: 3.18; 3.96; 4.83 and 5.59 mm. Central conductor diameter: 0.81; 1.02; 1.12 and 1.59 mm.
51–703, 51–704, 51–713, 51–723, 51–750 ⇓ Ap.	29/8	P_i	1300 nΦ – 0,022 mkΦ	10; 15; 25	50; 70; 200; 500	Tube diameter: 3.56; 3.97; 4.95 and 5.94 mm. Central conductor diameter: 0.81 and 1.02 mm
III. Compound sealed threaded filters						
SCI-9110, SCI-9112, SCI-9120, SCI-9122 ⇓ Ap.	31/4	C	10 nΦ – 0,056 mkΦ	50; 100; 200	3; 10	Thread 4-40 UNC-2A. Thread length: 3.56 and 5.59 mm. Central conductor diameter: 0.41; 0.46; 0.51; 0.64 and 0.81 mm.
SCI-3102, SCI-3112, SCI-3122 ⇓ Ap.	16/1	L-C, P_i	1500 nΦ – 0,075 mk Φ		3; 5; 10	Thread 4-40 UNC-2A. Thread length is 5.59 mm. Central conductor diameter: 0.41; 0.46 and 0.64mm.
54–874 (new)	18/2	C	10–10000 nΦ	50	5	Thread 2-56 UNC-2A. Non-threaded part of tube: 2.67 mm, length

(continued)

Table 10.10 (continued)

Filter series number	Number of typical sizes / design variants	Electrical capacity	Electrical capacity	Operating voltage, V	Operational	Design features
						of tube: 5.63 mm. Cents conductor diameter is 0,61 mm.
51–726,54–779 ⇓ Ap.	14/3	C, L-C, P_i	10 nФ – 0,05 мкФ	50; 100; 200	3; 10	Thread 6-32 UNC-2A, 6-40 UNF-2A. Thread length: 5.59 and 5.72mm. Central conductor diameter: 0.46 and 0.81mm
SCI-9210, SCI-9220 ⇓ Ap.	17/4	C	80 nФ – 0,21 мкФ	50; 70; 100; 150; 200	10	Thread 8-32 UNC-2A. Thread length: 5.94 and 6.77mm. Central conductor diameter: 0.81; 1.02 and 1.3 mm.
51-712, 1250 ⇓ Ap.	22/6	L-C, P_i	65 nФ – 0,031 мкФ	50; 70; 100; 125; 200	10:15; 20	Thread 8-32 UNC-2A. Thread length: 4.15; 6.17; 6.77 and 8.0mm Central conducts diameter: 0.81 and 1.02 mm
54-761, 54-786 ⇓ Ap.	6/2	C, P_i	0,01 – 0,8 мкФ	50; 100; 200	10	Thread 10-32 UNF-2A. Thread length: 5.94 and 8.33mm. Central conductor diameter: 0.81 and 1.02mm
9910-381, 54804002X5R	8/4	C	100 nФ – 1 мкФ	35; 50; 100; 250	10; 15	Thread 12–28 UNF-2A; 12–32 UNEF-2A. Thread length 5.54; 7.14; 7.9 and 10.31mm. Central conductor diameter: 0.81; 1.02 and 1.3 mm.
51–714, 51–719 ⇓ Ap.	33/6	P_i	1300 nФ – 0,15 мкФ	50; 70; 100; 200; 300 ⇓ 350	10	
SCI-9550, 51–702 ⇓ Ap.	12/3	C, P_i	1000 nФ – 0,1 мкФ	100; 200; 400; 500 ⇓ 700	25	Thread 5/16-24 UNC-2A; 5/16-32 UNC-2A; 5/16-32 UNEF-2A. Cents conductor diameter is 1,45 mm.

(continued)

Table 10.10 (continued)

Filter series number	Number of typical sizes / design variants	Electrical capacity	Electrical capacity	Operating voltage, V	Operational	Design features
54–844, 54–763, 54–853 ⇓ Ap.	9/5	C	1000 nΦ – 0,22 мкΦ	60; 200; 600; 750 ⇓ 1250	25; 50; 100	Filters for high voltages and currents. Thread 7/16-28 UNEF-2A; 5/8-24 UNEF-2A; 5/16-24 UNEF-2A etc. Central conductor diameter: 1.3; 1,45 and 1.58 mm.
1280–060	1/1	P_i	1500 nΦ	2500	25	Thread 3/8-32 UNEF-2A. Thread length is 9.53 mm.
IY. Sealed threaded filters						
51–359	96/2	L-C	0,15 – 1,4 мкΦ	80; 100; 150; 200; 250 ⇓ 300	0,06; 0,15; 0,45; 0,5; 1; 2; 5; 10; 15 ⇓ 25	Filter package thread: 1 /4-28 UNEF-2A

To date, a huge range of filters of this group is developed and produced. The new series 54–874 of miniature filters with 2–56 UNC-2A thread without hex head attracts attention. These filters are screwed into the housing of the product like a corkscrew (Spec Spin Filters) using a special screwdriver 54-874-020.

Filters are convenient for products that require simultaneous installation and quick replacement of many filters located close to each other.

In addition, Spectrum Control produces a numerous series of filters designed for high currents (up to 100 A) and voltages (up to 2.5 kV).

Threaded filters of this group are widely used in microwave technique, telecommunications equipment, control devices.

The last, fourth, group includes threaded filters, sealed with metal-glass junction. They are designed for large currents and voltages, have high electrical capacity and provide for the suppression of electromagnetic interference at frequencies ranging from units of kilohertz.

Filters are produced in versions with C-, L-C-, Pi- and T-electric circuit. Their nomenclature is extremely diverse with over 250 items. Typical filter housing diameters are 9.78 mm (0.375′∅ group) and 17.45 mm (0.690′∅ group). As an example, Table 10.3 shows the parameters of the L-C-filters of the most numerous 0.375′∅ group. The magnitude of the attenuation of these filters at frequencies above 1 GHz exceeds 70 dB.

Filters of this group are used in power supplies, ignition systems, equipment for the coal and oil industry, in medical technology.

Surface Mount Filters

The accelerated development of mobile, wireless and telecommunications systems, computers, peripherals, aerospace systems and other areas of technology has led to microminiaturization, high-density mounting of microelectronic microwave devices and the introduction of high-performance surface-mount technology. Such mounting involves group methods of automated assembly and soldering of device components.

But for this reason it was necessary to create the appropriate radio components, including noise suppression filters in a chip-performance.

Spectrum Control has developed and produces ceramic three-pin chips filters of C, L-C and Pi types (Fig. 10.14).

They have the shape of parallelepipeds of length L, width W, height T with a width of pins at the ends of LE and with a width of central pin LM. C-type chips are available in the following groups: SF 0805, SF 1205 and SF1806 and L-C-type of the group LC 0805 and LC1206.

The group number is formed by a combination of the length and width of the chips, measured in inches. The sizes and nominal capacity of filters are given in Table 10.11.

Spectrum Control produces 8 chips of the SF 0805 group, 9 SF 1205 and 10 SF 1806. You can select chips with a nominal capacity from 22 to 220,000 pF.

The filters of the first two groups are designed for a working voltage of 50 V and a current of 0.3; 0.4 and 1.0 A, the third group, respectively, is designed for 100 V and

Table 10.11 Parameters of chip filters of C and LLCC types

Chip group	Dimensions, mm					Rated capacitance, pF
	L	W	T	LE	LM	
C-type						
SF 0805	2 ±0.2	1.25 ±0.2	0.8 ±0.2	0.3 ±0.2	0.6 ±0.2	22–22000
SF 1205	3.2 ±0.2		0.7 ±0.2	0.4 ±0.3	1.1 ±0.3	22–47000
SF 1806	4.5 ±0.3	1.6 ±0.3	1.0 ±0.3	0.5 ±0.3	1.4 ±0.3	22–220000
L-C-type						
LC 0805	2 ±0.2	1.25 ±0.2	0.8 ±0.2	0.3 ±0.2	0.6 ±0.2	–
LC 1206	3.2 ±0.2	1.6 ±0.3	1.0 ±0.3	0.4 ±0.3	1.1 ±0.3	–

0.3 A. Filters operate in a temperature range from −55 to 125 °C. The level of attenuation of all filters increases with increasing of their capacity. At a frequency of 1 GHz for filters with a capacity of more than 220 pF, the value of the insertion attenuation is approximately 40 dB.

L-C-type filters for surface mounting, depending on the values of capacity and inductance, have a cutoff frequency (the frequency at which the insertion loss is 3 dB) from 10 to 220 MHz with a tolerance of 20%. These filters are rated for 25 V operating voltage and 10 mA operating current.

All chips are mounted on the board by soldering at a temperature of 220–240 °C. After soldering, ultrasonic cleaning of flux residues is necessary: oscillation frequency is not more than 28 kHz, time is not more than 5 minutes.

In addition, Spectrum Control produces two series of high-power surface-mounted filters: PSM and SSM, designed for operating currents of 10 and 20 A. Filters are used in power amplifiers, power supplies, motor control devices. The appearance of filters is shown in Fig. 10.15 (Figs. 10.61 and 10.62).

The PSM (Power Surface Mount) series filters can have a C or Pi-electric circuit.

The rated operating current of the capacitive filters is 20 A, 10 A for Pi-filters, the nominal DC voltage is respectively 200 and 100 V. The capacity of PSM filters can be selected in the following row: 68, 100, 130, 470, 820, 1000, 1500, 2500, 4000 for the Pi circuit and 10,000 pF in addition to the indicated capacities for circuit C.

The SSM (Square Surface Mount) series filters have only a Pi-electric circuit, they are designed for an operating current of 10 A and a DC voltage of 100 V. Their electrical capacity can be 100, 500, 1500, 2000 and 4000 pF.

Chip filters of all types are supplied usually packed in plastic tape for automated installation. Finally, Spectrum Control continues to produce high-frequency three-lead ceramic filters for mounting on PCB-based board. Filters provide an insertion attenuation of 20 dB at frequencies from 100 MHz to 1 GHz and have a cut-off frequency of 8 MHz. The minimum electrical capacity of the filters is 800 pF, the maximum operating current is 10 A, and the voltage is 50 V.

In addition to the above components, other products should be noted – filter connectors and multi-lead assemblies, the range of which is huge, a large group of filter pads of different profiles, sections and protective shields.

Fig. 10.61 Three-pin ceramic filters

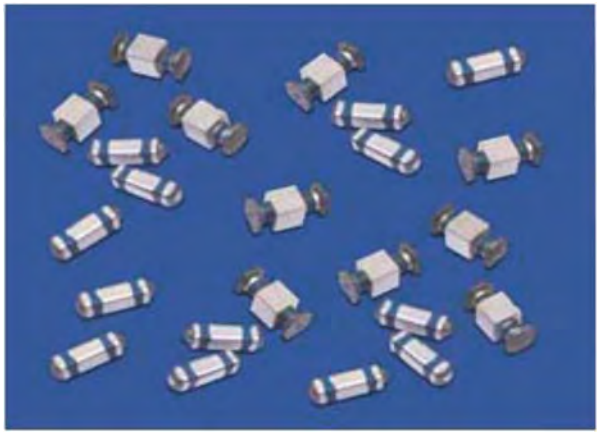

Fig. 10.62 PSM and SSM Series Filters

10.7 Assessment of Resistance of Microcircuits to the Effect of Electromagnetic Interference

The issues of protecting communications electronics equipment against the impact of HF and SHF electromagnetic interference (EMI) are especially relevant due to rapid expansion of fields and areas of application of radioelectronic devices with semiconductor devices (SD) and microelectronic integrated circuit (MIC) as their main components. The main factors provoking a keen interest in this issue, are as follows [50, 51]:

– constant increase in power levels of modern radio transmitters up to hundreds of kilowatts in the continuous-wave mode, and up to tens of megawatts in the pulsed

mode. In this regard, many radioelectronic devices have to operate in the electromagnetic fields, the power flow density of which reaches a few tens of kW/m^2 in the decimetric and centimetric wave bands (Fig. 10.63);
– increase in the integration level of modern integrated chips. In this case, there is a reduction in levels of voltages and currents consumed. The desired signal energy of microelectronic devices is relatively similar, and sometimes it is even lower than energy of EMI. Furthermore, due to improvement of high-speed performance of modern digital systems and a decrease in operating signal duration down to units and even fractions of nanoseconds, the computing devices themselves can generate HF interferences, the level of which is sufficient for failures to occur.
– constant complication of radio electronic systems (RES). The developers are often faced with the task to saturate a small-sized unit with radioelectronic equipment of various functional purpose. Inevitable close spacing leads to crosstalk and aggravates a problem of electromagnetic compatibility (EMC);
– enhancement of capabilities of electronic warfare devices. The presence of superpower SHF-signal sources based on gyrotrons, klystrons, magnetrons, lasers, beam-plasma oscillators enables remote target impact on radio equipment in order to put it out of order by damaging its sensitive element base.

Traditional methods of improvement of RES interference immunity are conditionally divided into design-technological, circuit-based and systematic ones. It's a common practice to start considering carefully the issues on equipment protection against interference attack only at the stage of engineering study of the product. That's why the simplest engineering methods are the most commonly used. Here, various shields are most frequently used for protection against interferences. In theory, by the use of ideal continuous shields, it is possible to reach the shielding efficiency of 100 dB and higher. However, in practice, such attenuation is difficult to be obtained, as it was shown above. The presence of various irregularities (holes and cracks for ventilation and indication, leads, joints, covers, and etc.) creates additional channels for penetration of electromagnetic fields in the shielded area. The more effective shields are those of special design with holes for leads, ventilation and indication as below-cutoff waveguide; however in this case, the cost, dimensions and weight of the device increase significantly. The known circuit-based methods involve the use of various additional components such as filters, chokes, transformers, excess-voltage suppressors, optoelectronic elements to reduce the levels of interferences.

Effective means for immunity improvement are system methods related to the use of various error control codes for correction of system and group errors. However, when interference has impact not only on the communication line but also on all controlling electronic devices, all processing equipment and information containing in it, they don't show the intended effect.

Therefore, one of resources for improvement of RES interference immunity is identification and consideration of susceptibility to the EMI impact of the element base, in particular, semiconductor devices (SD) and integrated chips (IC). The

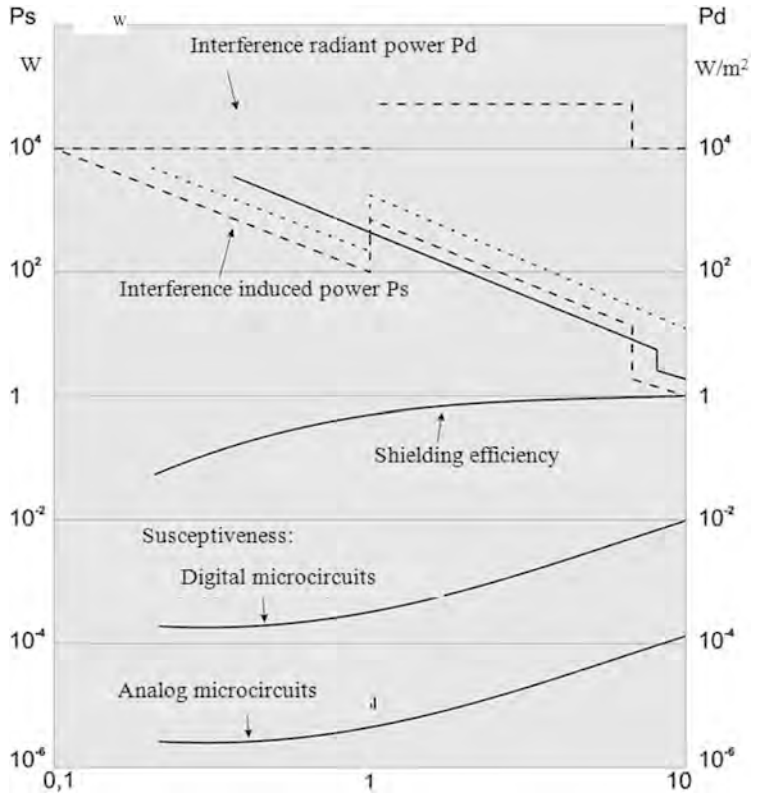

Fig. 10.63 Analysis of electromagnetic environment within the operating area of radioactive equipment [1]

system approach to design of radioactive equipment assumes the consideration of issues concerning an increase in operational reliability, already at the bottom step of hierarchy when choosing the element base and designing the printed circuit boards. Since the induced interference signals finally penetrate the circuits of radio electronic systems and impact on their elements, the immunity of communication systems, remote control stations, and data processing systems is mainly defined by the susceptibility of the element base, in particular, semiconductor devices and integrated chips. The results of researches performed by national and foreign scientists show that in some cases, the choice of the element base which is less susceptible to the interference attack, allows to reduce the material and financial expenses on the EMC immunity by tens and hundreds of times at the stage of equipment operation (Fig. 10.64).

Susceptibility of discrete semiconductors and microelectronic integrated circuits to interference was studied as early as in the 1970s, due to problems encountered during operation of special equipment. The results of the first studies of radio

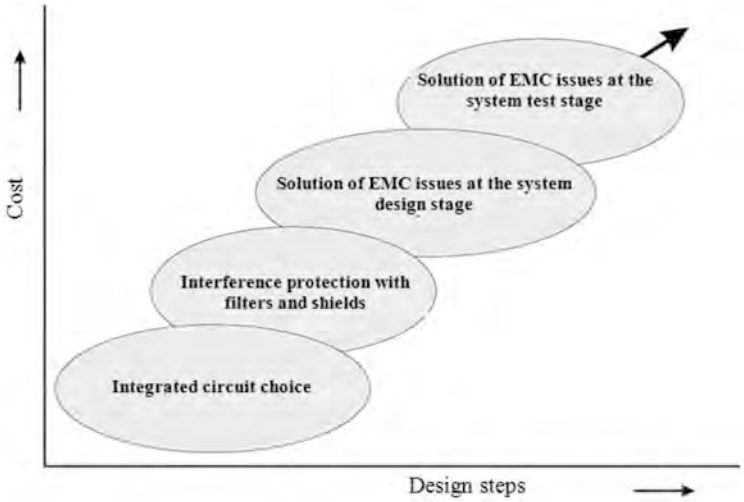

Fig. 10.64 Dependence of EMC ensuring costs on design stage [1]

frequency interference impact on the characteristics and parameters of SD and IC are detailed in [51, 52]. Nowadays, these studies were given a new impetus [53] due to further development of special electronic-countermeasures receivers, as well as due to requirements for safe operation of industrial equipment, transport, communication systems, and household appliances.

When choosing a method to study the susceptibility of semiconductor devices and integrated chips to the EMI impact, one should be guided by the following basic criteria: receiving the maximum information on change of discrete semiconductors and microelectronic integrated circuits characteristics and parameters under the influence of interferences; the accuracy of determination of the interference signal levels and values of monitored parameters; minimization of costs on research practice; making the experimental conditions similar to the actual interference environment.

When evaluating the susceptibility of radio electronic systems and units, the radiation method is used for EMI impact simulation. An interfering signal is supplied to the antenna that transmits it in the direction of the item under study. Generally the latter is located at a distance of 1 m from the feeding antenna. Such method was used when testing the semiconductor devices and integrated chips for immunity [51, 54, 55]. The evaluation criterion was taken as the level of exposure which leads to the irreversible failure, i.e. breakdown of the element. The studies demonstrated [54, 55] that most often, degradation changes occurred in the parameters of IC circuits either having longer leads or being oriented perpendicular to the electromagnetic field vector. Degradation changes accumulated when exposed to series of SHF-impulses. Most often, the failure reason was breakdown of Schottky input diodes and p-n-junctions of transistors of Schottky transistor-transistor logic elements. However, when using such method, it is very difficult to exactly determine the interfering

signal energy absorbed by transistor, IC or p-n-junction; when calculating the levels of EMI crosstalk at terminals of SD and IC and their external circuits, many assumptions have to be made due to uncertain positioning of conductors of various designs of test specimens with reference to the direction of the interference field vector. Furthermore, such tests are expensive. Therefore, in this case, the radiation method which is effective for testing of separate nodes and units, should be replaced with a conductive method of EMI supply to the terminals of SD and IC. By supplying the radio-interference through separating capacitance directly to the terminal of element under test, the interfering signal energy absorbed can be quite exactly determined by known methods. However, when supplying EMI to one of terminals, it isn't possible to prevent its impact on others. It is difficult to take into account the degree of relation between them, especially for IC of high integration level. It depends on chip package design, its connection to the circuit. In consequence, there is uncertainty of the experiment. But it is almost completely eliminated if the worst-case scenario is simulated to which the condition of full (almost full) of input EMI power absorption in the circuit of the terminal under test corresponds. By analyzing the changes in SD and IC parameters during sequential supply of radio-interferences to all terminals, it is possible to determine the most susceptible of them. The testing technique is much cheaper, the test results provide more information to the equipment developers.

At the first study phase, the authors [49, 50] paid attention to studying the susceptibility of bipolar and field-effect transistors, primitive logic gate (LE) Not-AND, elementary operating amplifier (OA). The testing technique involved the analysis of changes in voltage-current characteristics of diodes [56] (Fig. 10.65) and transistors [57], voltage-transfer characteristics of logic element (Fig. 10.66) and operating amplifier. The sensibility criteria (threshold) was taken as EMI level leading to the circuit failure or to certain change of static parameters SD and IC.

During tests of integrated chips, it was found that it was more appropriate to evaluate their sensibility in the dynamic mode when supplying test operating signals to input [58]. During studies conducted at the Belarusian State University of Informatics and Radioelectronics (BSUIR Minsk), several prototypes of monitoring and metering instruments (protected by copyright certificates and a patent [59]) were designed and manufactured to determine susceptibility thresholds in both simple and complex microelectronic integrated circuits. The integrated circuit under study is placed in the measurement chamber; impact of interference on other circuits of the device is prevented by means of decoupling filters. Change in parameters of the integrated circuit under study is monitored by comparison of their parameters with parameters of the identical chip of reference. The sensibility analyzers can work both in manual and automatic mode.

Depending on the frequency range for measurement of exposing EMI level, the selective HF-voltmeter, oscillograph or absorbed SHF-power meter can be used. The display processing units are designed in such a way that enable to study the sensibility using a "certain failure" criteria related to change in the output state of the integrated circuit, as well as a "possible failure" criteria that is a deviation of one

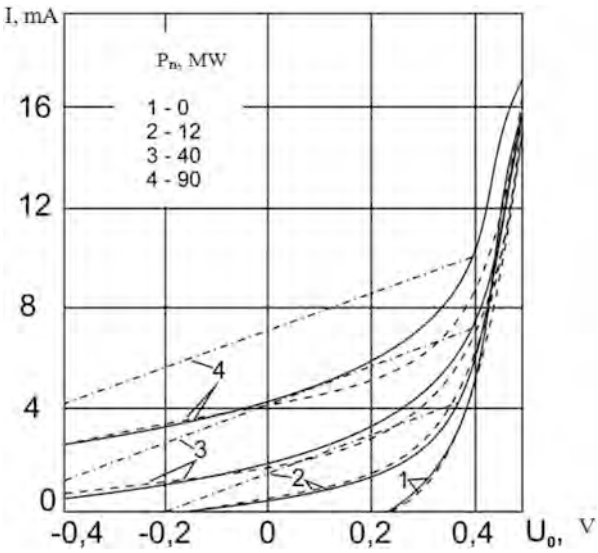

Fig. 10.65 Experimental and rated changes in characteristics of diode D9A when exposed to EMI at a frequency of 400 MHz

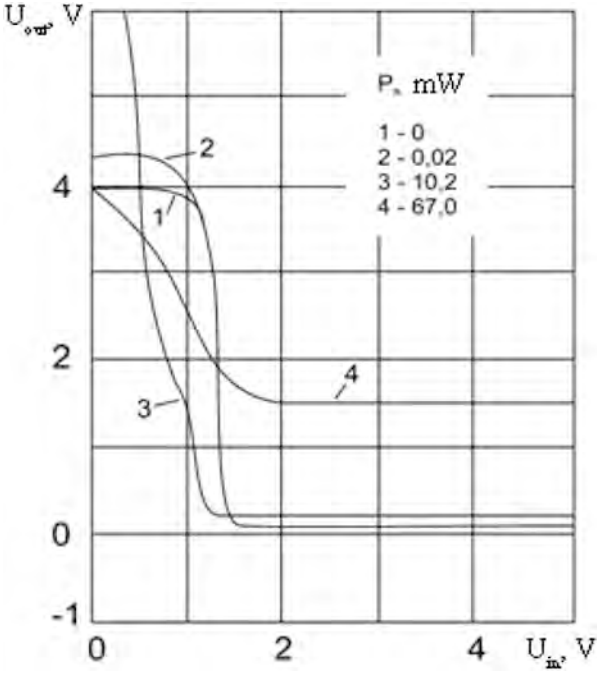

Fig. 10.66 Change in transfer characteristic Of IC K155LAZ when its output exposed to EMI at a frequency of 95 MHz

or a few parameters from the permissible limits. It is possible to carry out monitoring simultaneously by a few outputs of the integrated chip under study.

Figures 10.67 and 10.68 show the experimental and rated dependencies of some transistors and digital chips. The test results were used in special handbooks for

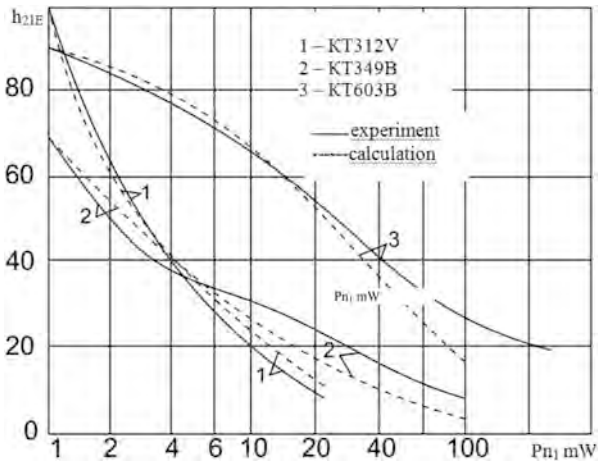

Fig. 10.67 Experimental and rated dependences of a change in the transmission factor of a 450 MHz interfering signal using bipolar transistor current flow from the absorbed power level with impact on the base circuit

developers of radio equipment operating in the high interference signaling environment.

Studies of different types of diodes, transistors and IC [56–58, 60] demonstrated that:

- susceptibility of SD and IC to interference decreases with increasing frequency of interfering signals. Sharp increases or decreases of the sensibility threshold can be observed at some frequencies. This is due to influence of parasitic inductance and capacitance of packages, and distinctive features of IC connection;
- with increasing level of integration of IC, i.e. with a decrease in the size of components and an increase in the density of their arrangement, the susceptibility to interference is higher. So, during tests of bipolar transistors, it was found that devices with large emitter perimeter, i.e. having interdigitation of the emitter-to-base junction, are less sensitive;
- sensitive circuits of operating amplifiers, low-power bipolar transistors, high-speed digital microelectronic integrated circuits are very susceptible to radio interference. Field-effect transistors, CMOS IC, chips with increased load-carrying capacity have better interference immunity;
- in microcircuits of various series, the dynamics of changes in parameters with an increase of interfering signal is not uniform. So, in the metric wave band of EMI, most often LE AND-NOT of 155 (TTL), 531 and 555 (TTLS) series have unacceptable changes in dynamic parameters such as turn-off delay; when exposed to interferences, elements of 1533 (TTLS) series have the most critical changes in static parameters: logic-0 level and logic-1 level.

The developed technique of SD and IC testing can serve as a basis for experiments on sensibility evaluation of separate units and the entire devices [60]. Test results classification allows using them not only as handbooks for developers of modern radio equipment but also as tutorials for training specialists in EMC.

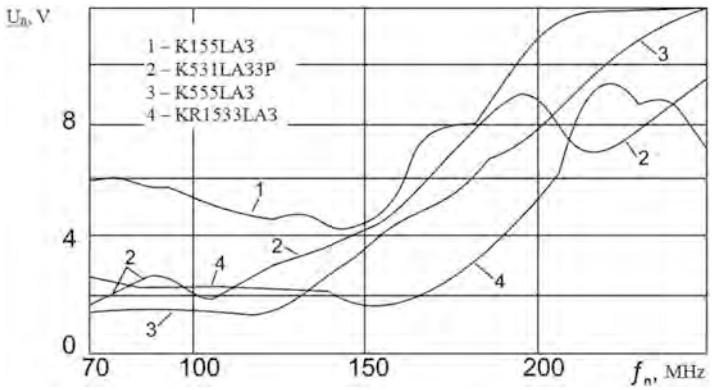

Fig. 10.68 Dependence of sensibility threshold of transistor-transistor logic and Schottky transistor-transistor logic elements on frequency of radio interference having impact on the input

Fig. 10.69 Test using a bioman

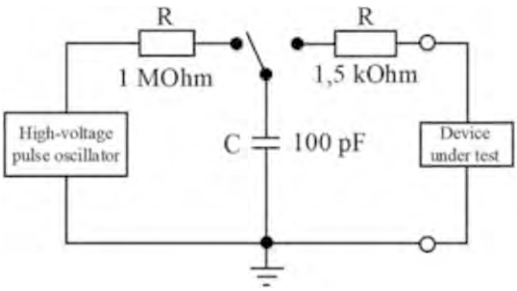

10.8 Standard Methods of Testing SHF Devices for Resistance to Electrostatic Discharges

In order to satisfy a wide range of technical requirements for applications of various industrial segments, multiple test standards have been created. In the following, we will briefly consider the main standards of testing for resistance to electrostatic discharge and certain features and differences between tests at the levels of separate devices and system in general.

There are multiple different standards of testing of electrostatic discharge, and selection of the specific one depends on the application. Electrostatic discharge is determined as sudden and momentary flow of electrical current between two objects with different electrical potentials, which causes malfunction of equipment and, ultimately, production losses worth billions of dollars every year. Therefore, all manufacturers of electronic devices shall take the possibility of electrostatic discharge when designing the system.

Protection from electrostatic discharge is based on a wide range of circuits and models. However, regardless of the protection circuit selected by developers, the entire system passes tests for protection of electromagnetic interference.

10.8.1 Standards of Tests at the Device Level

10.8.1.1 Bioman

The test at the device level based on bioman is the most popular test for resistance to electrostatic discharge. It diagnoses the ability of electronic components to be damaged as a result of electrostatic discharge. This test imitates the discharge that occurs during contact of the electronic device with a hand. Failures during bioman tests of microcircuits are usually manifested in destruction of the p-n-junction, penetration of metal, melting of metal layers, lobing on bonding pads and destruction of the gate oxide layer [61–63].

The test procedure consists in supplying high voltage to 1 MOhm resistor and 100 pF capacitor (Fig. 10.69). After the capacitor is fully charged, the circuit switches, and the capacitor appears in the same circuit with the 1.5 kOhm resistor and the tested device, to which the accumulated charge is supplied. High voltage value varies within the range of 0.5–15 kV depending on the requirements.

Figure 10.70 shows a typical oscillogram, which demonstrates that the current emission reaches 1.4–1.5 A at the moment of capacitor discharge, after which the curve asymptotically approaches zero after 500 ns. Therefore, power of 22.5 kW passes through the tested device.

10.8.1.2 Machine Model

Tests at the device level based on the machine model, which was popular in the 1990s, is not currently used. After connection to the power supply network, industrial equipment accumulates the electrical charge, which can damage electronic components. Machine model makes it possible to test devices for protection from discharge that can melt metal layers, destroy p-n-junction and damage the oxide layer of the gate.

The procedure of testing using the machine model consists in supplying high voltage to the resistor connected to the 200-pF capacitor in series (Fig. 10.71). When the capacitor is fully charged, it will connect to the choke with inductance of 0.5 μH and then to the tested device. As a rule, the voltage supplied to the capacitor is 50–400 V.

Analysis of the current oscillogram (Fig. 10.72) shows that an oscillation transient takes place in the R-L-C current, in which the current value reaches ±3, which is four times higher than the current swing in the bioman test model. Therefore, power dissipation in the second model takes more time. It can also be seen that the

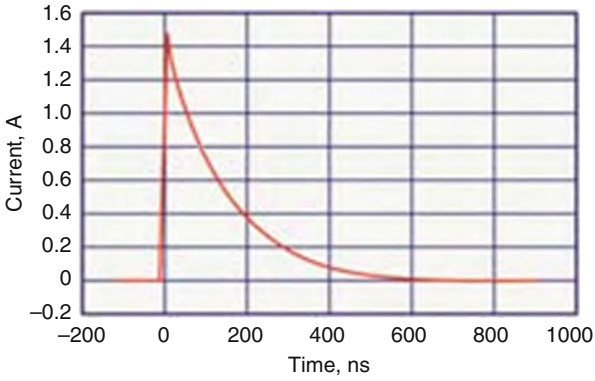

Fig. 10.70 Electrostatic discharge current during bioman testing

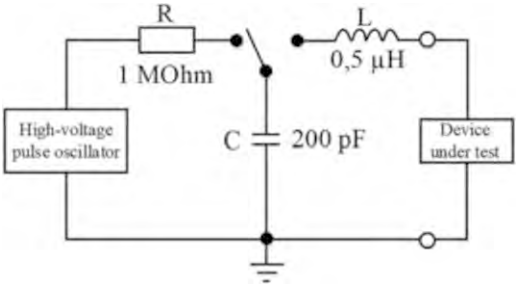

Fig. 10.71 Machine test model

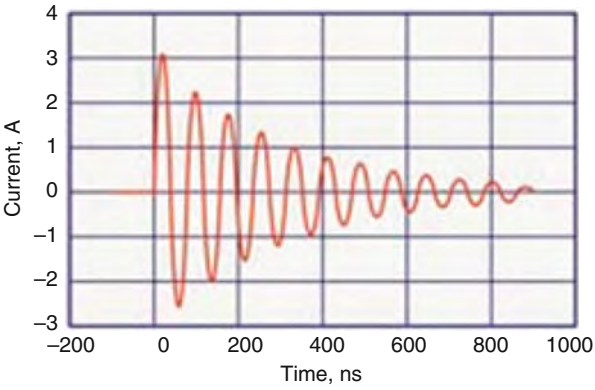

Fig. 10.72 Electrostatic discharge current in the machine testing model

current curve starts to asymptotically approach zero after 900 ns. Maximum dissipated power on the tested device in this case amounts to about 1.2 kW.

It should be noted that each pin of the tested device in the machine model must be tested for conformity to the standard. The crystal is installed on specially designed board equipped with interface for connection to automated measuring device. Each pin of the device under test is tested separately, while the rest of the pins are grounded on the board. This procedure is performed untill all pins are tested.

10.8.1.3 Charged Device Model

Testing procedure at the device level with the help of the charged device model imitates the situation that often happens to equipment in automated production. It is known that microcircuits of running equipment accumulate electrical charge. When these ICs touch a grounded conductor, internal circuit capacities are discharged. In charged device model test, the tested device is placed on the board with its base facing upwards.

Metal plate and tested device are divided by insulating material. This plate is connected to a high-voltage power source. The required voltage level is set on it. This test is repeated for each pin; three discharge pulses with negative and positive polarities are supplied to all pins (Fig. 10.73).

Figure 10.74 shows oscillogram of the discharge obtained during device testing with the help of charged device model. It can be seen that the transient takes a very short period (not more than 2 ns), which complicates modeling in practice. The oscillogram also shows that the current of 5–6 A flows faster than during 1 ns. As a result of such electrostatic discharge, oxide layer of the gate is destroyed, the charge is intercepted, and the p-n-junction is damaged.

10.8.2 Comparison of Test Methods at the Device Level

Methods of electrostatic discharge modeling with the help of bioman, machine model and charged device model are the most well-known procedure of electronic component testing at the device level. These models are compared in Table 10.12.

10.8.3 Standards of Tests at the System Level

10.8.3.1 Electrostatic Discharge Immunity

Electrostatic immunity discharge test (Fig. 10.75) is a test at the system level, which imitates the electrostatic charge between a person and an electronic component. This charge is accumulated on human body in clothes made of synthetic fibers, as well as in conditions of low relative humidity in rooms with carpets. To imitate the discharge, pulses are supplied to the tested device from the generator in two ways. In the first way, physical contact with this device is implemented. In the second, the discharge occurs through air. This test is defined by the specification IEC61000-4-2 ofo the International Electrotechnical Commission.

In this test, pulse rise time shall be less than 10 ns, its duration – 100 ns. During electrostatic discharge immunity test, it is necessary to ensure at least 10 discharges of different polarity with an interval of 1 s. In accordance with specification, the device is tested at least 20 times (Fig. 10.75).

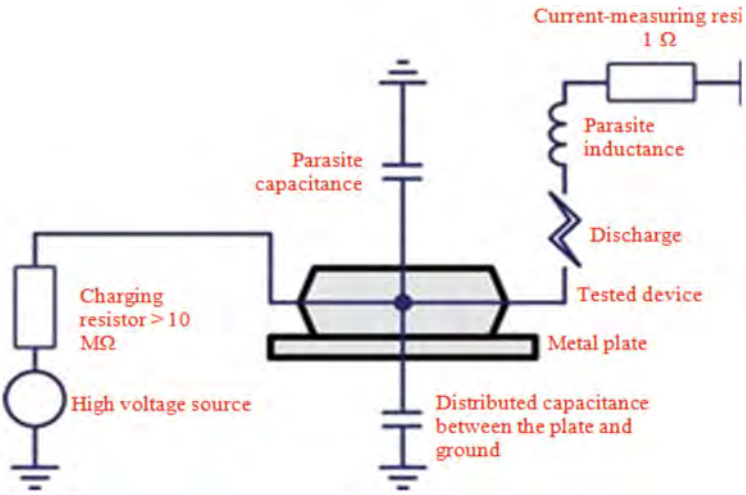

Fig. 10.73 Charged Device Model

Fig. 10.74 Discharge current during charged device model tests

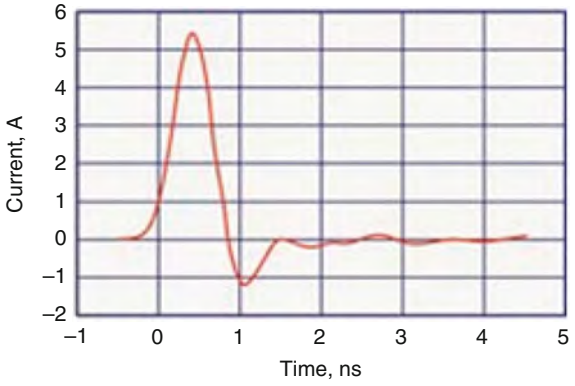

Figure 10.76 illustrates the difference between test standards at the levels of device and system. In the IEC standard, which is often referred to as gold standard of component testing, test voltage is 8 times higher than in charged device model tests and 20 times higher than in bioman tests.

10.8.3.2 High-Speed Transient Immunity

Standard IEC61000-4-4 for system level test is known as high-speed transient (HST) immunity test (Fig. 10.77). This test involves simulation of transients, which occur in normal operating conditions during deactivation of inductance loads, relay contact

Table 10.12 Testing methods at the device level [1]

Model	Bioman	MM	CDM
Test levels, V	2000, 4000, 8000, 15000	100, 150, 200	250, 500, 750, 1000
Max. current, A	1.5	±3	5–6
Pulse width, ns	~ 150	~ 80	~ 1
Rise time	2–10 ns	~ several ns	< 400 ps
Typical failures	destruction of p-n-junction; metal penetration; melting of metal layers; lobing on bonding pads; destruction of oxide layer of the gate	destruction of p-n-junction; melting of metal layers; destruction of oxide layer of the gate	destruction of oxide layer of the gate; charge interception; destruction of p-n-junction

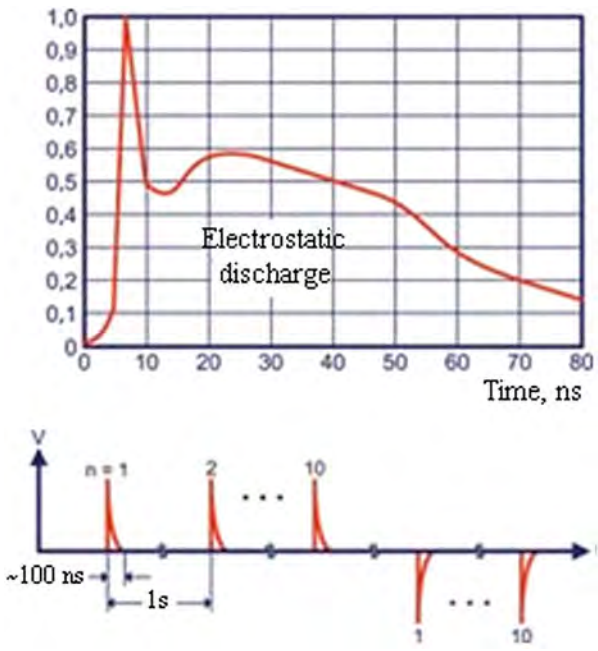

Fig. 10.75 Protection from electrostatic discharge in accordance with IEC61000-4-2

bounce and functioning of multi-purpose electrical motors. The test is performed at all power, signal and ground outputs.

It is also known as surge immunity test; surges are defined as sequences of pulses of finite duration. During this test, the generator creates pulse bursts, the amplitude of which is reduced twice relative to the maximum value over less than 100 ns. Duration of each subsequent pulse is usually 1 μs greater. Typical duration of a

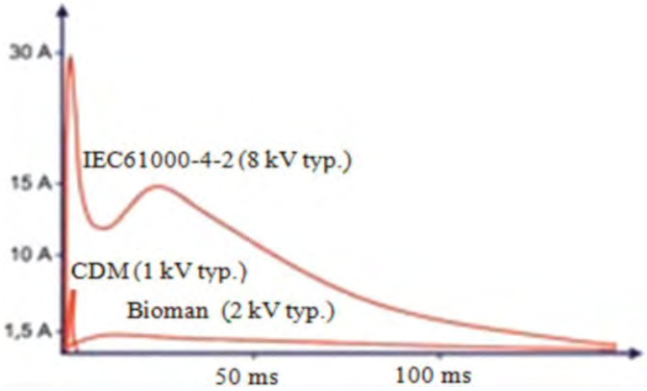

Fig. 10.76 Generalized between tests at the levels of device and system

pulse is 15 ns. The interval between two consecutive pulses is 300 ms. This cycle is repeated for 10 s, after which a pause is set.

Such pulse sequences are repeated for 6 times during 110 s. In this test, pulse rise time is very short, repetition frequency is high, and power is low.

While this test is similar to other ones in terms of pulse rise rate and low energy consumption, its difference lies in the number of pulses per one test cycle. If the interval between two neighboring fronts amounts to 1 μs, in the HST immunity test a 15 ms sequence contains 15,000 pulses. Multiplying this number by the number of bursts contained in a 10 s interval, i.e. by 10 s/300 ms, we get 500,000 pulses. Therefore, six 10s intervals with 10 s pauses between them contain 3 million pulses.

Since the contact during HST immunity test occurs through capacitance, industrial internally shielded cable can significantly simplify connection to the tested device due to noticeable attenuation in the energy of the pulses supplied into conductors through the capacitive isolation between them and the cable shield.

10.8.3.3 Surge Immunity

Surge immunity test, IEC61000-4-5 (Fig. 10.78) is the strictest test for immunity to transient voltage based on such parameters as current and pulse duration. However, the use of this method is often limited by the length of power and signal lines ($L > 30$ m). Surge immunity test is known as the lightning test, since it imitates transients caused by lightning charge (direct stroke or voltages and currents caused by indirect stroke), or transients during switching of power sources, including load variations and short circuits.

Output signals of the pulse generator are set for conditions of the idle run and short circuit. The ratio of peak voltage of the idle run to the peak current of short circuit is the output impedance of the oscillator. This test is characterized by high current due to low impedance of the generator and great duration of pulses

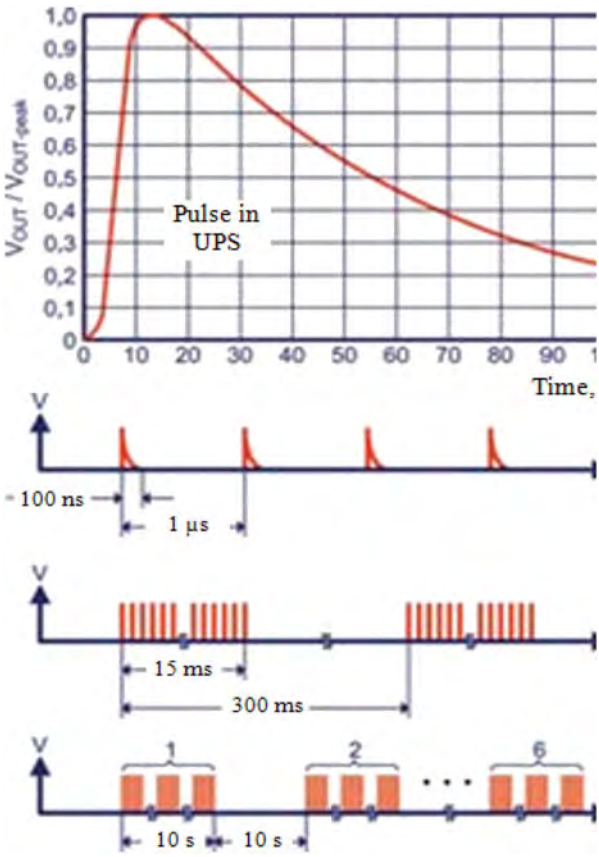

Fig. 10.77 HST immunity testing in accordance with IEC61000-4-4

(approximately 1000 times higher than during electrostatic discharge and HST immunity tests).

In this test, five pulses of positive and negative polarity are generated. The interval between two consecutive pulses is less than 1 minute. With the reduction of this pause to 12 s, the total testing time is reduced to 2 min.

Let us present the results of summarized comparison of system-level tests

System-level test standards are listed in the specification IEC61000-4. Of 25 tests standards of this family of specifications, ESD (IEC61000-4-2), EFT/Burst (IEC61000-4-4) и Surge/Lightning (IEC61000-4-5) are the ones that belong to the unstable voltage immunity tests. Table 10.13 helps compare these standards.

It should be noted that due to toughening of requirements for tests at the system level, such tests at the device level as machine model tests, charged device model tests and bioman tests cannot be considered fully suitable at low values of voltage and current.

It is necessary to take into account the great difference between electrostatic discharge immunity tests, as well as surge tests at the level of industrial equipment

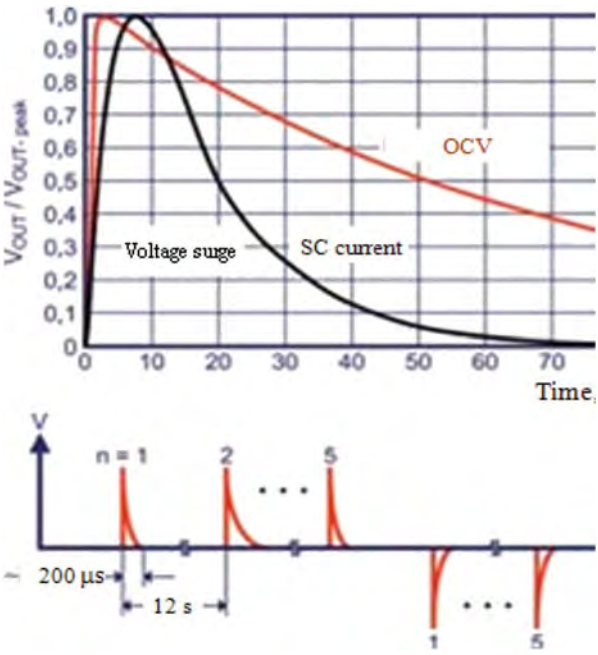

Fig. 10.78 Surge immunity testing in accordance with IEC61000-4-5

Table 10.13 Comparison of pulses at the system level [1]

Test	Standard	Tested lines	Voltage, kW
ESD (electrostatic discharge immunity)	IEC61000-4-2 Air-Gap	Power, signal	± 15
	IEC61000-4-2 Contact	Power, signal	± 8
EFT/Burst (HST immunity)	IEC61000-4-4	Power	± 4
		Signal	± 2
Surge/Lightning (power surge immunity)	IEC61000-4-5 (8/20 µs) 42 Ohm – 0.5 µF	Signal	± 0,5
	IEC61000-4-5 (8/20 µs) 2 Ohm – 18 µF	Power	± 1

and consumer products. In development of customer electronics, electrostatic discharge immunity test has high priority due to high probability of the contact between human and electronic components through cable connectors.

Developers of special and industrial equipment, on the other hand, value the results of surge tests higher than the results of electrostatic discharge immunity tests, since in industrial equipment, for example, transients related to switching of electrical motors and other inductance loads are much more dangerous for the system than

electromagnetic effects, since humans only come in contact with industrial equipment during its installation and repair.

10.9 Passive Intermodulation in SHF Circuits

Intermodulation distortion level (IDL) of broadband microwave signals is a critical parameter influencing on characteristics of communication systems and on possibility of their compliance to EMC standards [64]. A specific type of IDL is passive intermodulation (PIM) occurring in nodes and structures traditionally considered to be linear ones: in substrates of printed circuit boards, microstrip lines, radio-frequency cables and connectors, in antenna structures and items surrounding the antenna. An increase in signal power, frequency-division multiplex, increase in space density of equipment location at mobile base stations and other factors [65] impose very tough requirements on the level of PIM. The PIM causes, measurement techniques and reduction methods are considered in detail in work [64].

10.9.1 Mechanisms of the Occurrence of Passive Intermodulation

The intermodulation phenomena occur in electric circuits during nonlinear conversion of the amount of fluctuations of a few frequencies or one signal with continuous frequency spectrum [1]. In addition to distortions within the range of input signal frequencies, the out-of-band interfering intermodulation components with frequencies that were absent in input, occur in the output circuit of such node. PIM products can get in the transmission band of the receiver of this communication system or in the frequency bands of other communication systems, thus violating the EMC requirements. For users of telecommunication systems, it means that the signal-noise-rate is impaired and the information reception quality is decreased [66].

If two sinewave oscillations with frequencies of f_1 and f_2 are supplied to input of the electronic assembly, then components with combination frequencies $f_K = \pm nf_1 \pm mf_2$, where n и m are positive whole numbers 0,1, 2,.... are generated in output. If one or both transmitted signal components (Tx) has continuous spectrum with emission frequency band Δ (Fig. 10.79), then receiver interferences (Rx) have a structure of third-order intermodulation band IM3 based on combinations of the form $2f_1$-f_2 and $2f_2$-f_1, of fifth-order intermodulation band IM5 based on combinations of the form $3f_1$–$2f_2$ and $3f_2$–$2f_1$, as well as intermodulation bands of higher odd order.

The levels of components with frequencies higher or lower than transmission band (IM^+ and IM^- respectively as shown in Fig, 10.78) are identical if non-linearity is inertia-free; they can differ if memory effect caused by amplitude-phase

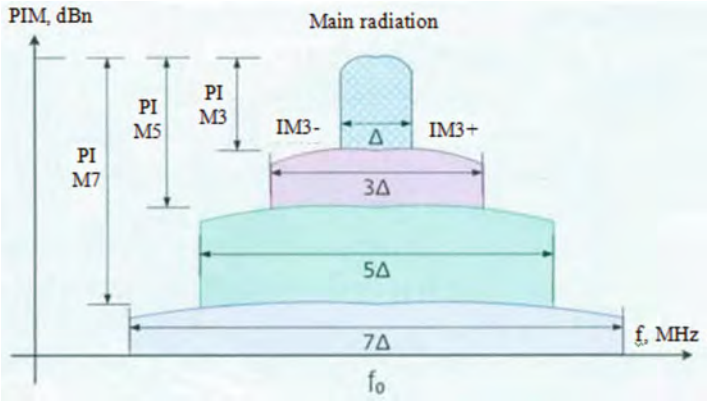

Fig. 10.79 Intermodulation products in output of non-linear node close to the operating frequency band. f_0 is the signal central frequency [1]

conversion appears in the inertial non-linear element. The ratio between the levels of intermodulation products of the third, fifth and higher orders varies as the input signal power $P_{вх}$ increases at frequencies f_1 and f_2: power of IM3 increases at the rate of 3 dB/dB, power of IM5 increases at the rate of 5 dB/dB, and so on.

Under the conditions of severe deficiencies in frequency resource, IMI components can penetrate the assigned bands of the low-noise receiver of its or adjacent frequency standard and can impair its operation [67]. For example, receive/transmit bands (890–915)/(925–960) MHz are assigned to the communication network of GSM-900 standard. For transmission frequency values of 930 and 955 MHz, the third-order intermodulation component with a frequency of $2\times930-955 = 905$ MHz penetrates the band for reception of this standard. For standard 3G-UMTS with frequencies of (1920–1980)/(2110–2170) MHz, the seventh-order intermodulation component with a frequency of $4f_1–3f_2$ penetrates the band for its reception.

The situation becomes more difficult when antennas of different standards are located in one cell tower [68]. For example, the second-order intermodulation products of GSM-900 system penetrate the band for GSM-1800 reception; the fourth-order intermodulation products of GSM-900 system and the third-order intermodulation products of GSM-1800 system interfere the reception of signals of UMTS standard. With the further development of wideband 4G system with frequency bands from (832–839,5)/(791–798,5) MHz to (2530–2540)/(2650–2660) MHz and digital TV in Russia, there is an increase in risk of inadmissible exposure of interfering intermodulation products. Widespread application [69] of co-siting services (shared use of equipment by different operators and for different communication standards) results in that radiation caused by the passive intermodulation pollutes the frequency bands of the network base stations.

10.9.2 Causes of the Passive Intermodulation and Methods for Reducing its Level in RF Connectors

In coaxial connectors [70, 71], non-linear phenomena causing PIM can appear due to insufficiently tight contact in the current-carrying connections "metal-metal", as well as due to impact of non-linear processes in the connector housing or in its surface coverage.

Cavities, irregularities, microcracks and dirt accumulation can appear on the metal surface at the contact area along the center conductor or on the internal surface of the coaxial line due to coaxial connector design features or manufacturing technology, insufficient force at the contact area, deficiencies in cable-end sealing. In this case, the conductive path becomes longer, the potential voltage barrier appears; microscopic sparking can occur with generation of intermodulation products. Surface metallic oxides act as metal-oxide detectors with non-linear characteristic ("diode effect"). The metal surface accumulates moisture, dust, organic impurities and residues of various metal salts after operations of chemical etching and coating deposition. They also have non-linear voltage-current characteristic (VAC) causing PIM. The sealing contact is required to avoid corrosion from exposure to ambient oxygen since the oxide layer of even small thickness has non-linear voltage-current characteristic.

The resistive and magnetic-resistive effects in dissimilar conductors inside connector cause a local resistance change at the contact area. Steel (including stainless steel), iron, nickel have ferromagnetic properties with possible effects of hysteresis causing the non-linear phenomena and PIM. Therefore, the connectors of high quality should be made of expensive but nonmagnetic materials such as brass, beryllium and phosphorous bronze. If the corrosion-resistant coating is applied to the material having magnetic properties (for example, as a result of silver-plating or gold plating), it is necessary to take into account the skin layer depth for HF-currents passing through contacts. In case of insufficient thickness or unevenness in coating, the currents penetrating the basic material cause PIM. If there are strict requirements for PIM, it is inadmissible to use electrodeposited nickel as a corrosion-resistant coating of the connector. The connector housing made of aluminium alloys reduces the product weight but the oxide film on the surface of this material can generate an inadmissible level of PIM.

"White bronze" (non-magnetic corrosion-resistant wear-resistant alloy of copper, tin and zinc) and silver are widely used for coating the connectors optimized by PIM level. Level IM3 in the top-quality connectors, the housing of which is coated with "white bronze", and the central contact is coated with silver, doesn't exceed −155 dBc when testing by a dual-frequency signal with a power of 2x43 dB/mW. The measurements of IM3 level for typical coaxial connectors using a test signal with a power of 2x43 dB/mW at frequencies of 463 and 468 showed that the level of self-interference IM3 for connectors of SMA type was 108 dBc, for connectors of BNC type was 118 dBc, for connectors of "standard" type was 123 dBc, for connectors of

"coated with silver N" was 163 dBc, for connectors of DIN 7–16 type was not worse than 175 dBc. It was found that direct connectors have lower level of PIM than right-angle connectors.

It is difficult to detect the low-quality preparation and cable sealing in the coaxial connector when inspecting with the naked eye. The connector quality by PIM parameter decreases as quantity of connect-disconnect cycles growths due to wear and tear, microcracking, and force weakening in connections "metal-metal".

10.9.3 Passive Intermodulation in the Printed Circuit Board Material

The substrate material and manufacturing technique of the printed circuit board are essential to reduce the level of PIM. Leading manufacturers of clad dielectric materials (laminated plastics) for SHF-board substrates optimize the properties of their products by decreasing the level of dielectric losses, matching of the dielectrics coefficient of thermal expansion in different directions with thermal-expansion coefficient of metal coatings [72]. For example, special-purpose PIM-laminated material of DiClad 880-PIM type made by Arlon-MED Company on the basis of multilayer glass-fabric-reinforced foiled PTFE has a dielectric permittivity of ε_f=2.20 at a frequency of 10 GHz with a thermal factor of $TK_\varepsilon = -160$ ppm/°C and low attenuation of $tg\delta = 0.0009$. The laminated material has high-thermal conductivity $\lambda = 0.261$ W/mK within the temperature range −40 to 150 °C. The products made of this material are tested by a dual-frequency signal with a power of 2x20 dB/mW in the range of 1.9 GHz. The test results show that the relative level of IM3 doesn't exceed −155 dBc.

10.9.4 PIM in Band, Coaxial and Waveguide Transmission Lines

The PIM level in transmission lines is increased due to cold welding, twisting, tie wrap, impurities on the dielectric plate, cracks in the semi-rigid cable sheath, ambient temperature fluctuations, heating of conductors from flowing direct and high-frequency current.

In the microstrip transmission lines [73], the PIM level can increase due to the following reasons: the use of PCB dielectric of insufficiently high quality; the use of coating interlayers made of nickel having ferromagnetic properties; occurrence of temperature distribution gradients in the board material caused by heating of printed conductor.

It was found that when testing by a dual-frequency signal with a power of 40 dB/mW (10 W) in the range of 1.8 GHz, the level IM3 is −78 dB/mW in the models of coaxial cables which aren't designed for reduction of PIM level; when using cables and connectors of DIN 7–16 type certified by this parameter, the level of such interferences is reduced by 30 dB and it doesn't exceed −125 dB/mW.

The fluctuations in ambient temperature caused by differences in thermal-expansion coefficients for substrate, coatings and metallization lead to a decrease in tightness of joint and to formation of local zones with oxides having non-linear voltage-current characteristic. Heating of the printed conductor from the current flowing in the transmission line [74] causes different thermal expansion of substrate and coating dielectric.

The specific PIM source – multipactor effect – is typical for passive transmission lines included in satellite repeaters operating in vacuum, for presence of electrojet current causing the secondary electron emission.

10.9.5 PIM in Directional Couplers, Frequency Duplexers and Transformers

In the directional couplers, valves and circulators containing ferrite materials [75], the non-linear effects are caused by hysteresis nature of their magnetic properties. With the increasing power of an input signal, the magnetic-flux density increases that leads to the saturation mode as a result of which the PIM level becomes higher.

In addition to non-linearity caused by ferrite metal, the increased level of PIM in the transformers with ferrite cores is due to magnetic reluctance of the core. The manganese-zinc cores of low resistance are used for typical passive components. They are usually coated with insulating material to prevent short circuit. Winding wires are insulated to prevent short circuit between winding turns. It was found that during standard assembly operations, it is possible to damage the insulation of wires and core that leads to local short circuits and, as a result, the PIM level increases [76]. The use of special materials and insulation quality control in the structures optimized by PIM level reduce the probability of such effects.

The architecture, materials and manufacturing technique of the frequency-splitting filters-diplexers play an important role in reducing the impact of PIM on operation of data-transmission system. The high-order resonant circuits with accurate adjustment should be used for ensuring the squareness of amplitude-frequency characteristics in the transition zone between bands *T*x and *R*x. The use of tuning elements in the form of steel screws with insufficiently dense silver coating can significantly increase the PIM level due to metal oxides in the threaded joints, and lead to the dynamic changes in the PIM level under influence of mechanical vibration.

10.9.6 External PIM Sources

The PIM sources being external in relation to transmitting device and antenna path [77] are structural components of the antenna assembly, cell towers and items and facilities surrounding the antenna. They include steel bolts, couplings, contact joints having non-linear voltage-current characteristics and being capable of re-emitting the power of incident SHF-signal in different directions at different combination frequencies. As a result, the signal in artificial antenna can have the permissible level of PIM, but in the far-field region, the PIM level increases up to impermissible values. This phenomenon known as "rusted bolt effect" is typical for antennas and structures which are inadequately protected against impact of aggressive environment. During operation of 3C/4G network base stations in common band, the PIM from external sources leads to loss of operational efficiency and reduction of coverage area (Fig. 10.80) [77].

Modern antennas are complex electrical and mechanical structures which support a few bands and polarisations, as well as they have a remote-controlled directional diagram. Consequently, there is a strong possibility that mechanical failures occur during signal transmission. The antenna is usually checked for PIM level prior to installation. For exact measurement of antenna characteristics under operating conditions, its location needs to be taken into account since there is a potential for PIM occurrence from external sources. Ideally, the antenna should be located on the metal structure not less than 0.5 m in height above ground, and its main beam should be pointed to the open space. The place around the antenna should be free of any metal structures (fences, elevators and towers) which can cause PIM. The airports, sports facilities and long tunnels can use the distributed antenna systems where signals from base stations of all operators are combined and use the common antenna and distributing system [69]. In such cases, PIM prevention is a critical task which cannot be solved even with a filtration of high quality.

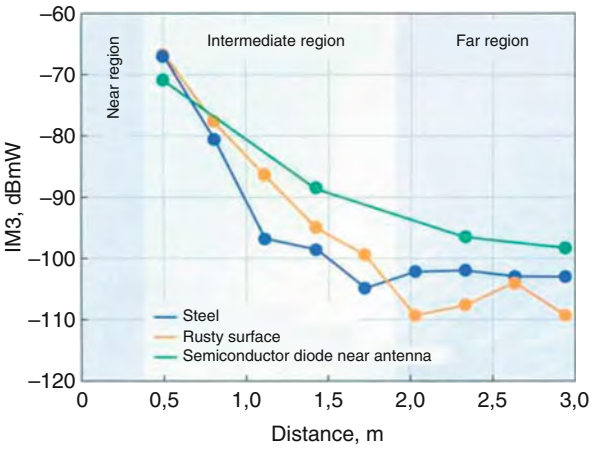

Fig. 10.80 Change in PIM level depending on the distance between the reflecting object and antenna (anechoic chamber, test 2×20 W) [1]

For search and minimization of interferences from external PIM sources, azimuth of main beam direction and angle of directional diagram elevation are used; it is required to remove non-linear units re-radiating IM-components, for example, metal beams where iron oxides can appear.

The frequency duplexers (splitters of incident and reflected waves of close frequency bands) with increased squareness of amplitude-frequency characteristics in the boundaries of frequency bands, as well as structures containing materials and components that may lead to nonlinear conversions of transmitted signals are used to decrease the PIM level. Measures are taken to reduce the peak-factor of the sum signal power of different frequency bands in common parts of antenna path; and the type of polarization of transmitting and receiving antennas is changed. Recommendations have been developed for location of antennas of different standards and frequency bands in one tower in order to minimize their interrelation and impact, as well as for design and location of indoor antennas taken into account the design features of building and equipment.

10.9.7 PIM Level Evaluation Methods

In literature and in practice, great attention is paid to evaluation of the IDL level and to measures on their reduction for improvement of energy performance of the power amplifiers [76]. Recommendations of International Electrotechnical Commission (IEC) 62037 (committee 46, work group 6) [78] determine the procedure for measurement of PIN level by testing the circuit or component using a signal in the form of a sum of two sinewave oscillations of offset frequencies f_1 and f_2 having the same power of 2×10 W, 2×20 W or 2×30 W, as well as measurement of spectral component level at one of frequencies IM3 – $2f_1$–f_2 or $2f_2$–f_1.

The PIM level can be measured by two methods: “at reflection” (Fig. 10.81a) and “at transmission” (Fig. 10.81b) The cable assemblies, filters, mixers, and antennas can be used as units under test. The spectrum analyser acts as a receiver.

When measuring the low-level PIM, measures should be taken to properly weaken coupling between the test signal synthesizers using bridge adder; to ensure the low level of own PIM-components occurring in cables, connectors, frequency filters, in high-power matched load of the measuring circuit (not more than 170 dB/mW for test signal of 2×43dB/mW).

As a characteristic of PIM level of measured component [78], it is recommended to use absolute power of a signal at a frequency of IM3 in the logarithmic scale [dB/mW] with respect to power of 1 mW or its power value with respect to power of each test signal source in the scale [dBc] with obligatory reference to the power of test signal. Therefore, evaluations of PIM −110 dB/mW and −153 dBc are of equal value when the test signal is 2×43 dB/mW.

Since the PIM level can change within very wide ranges, for detection of serious failures in the radio-frequency path, the test signals of lower power, for example, of

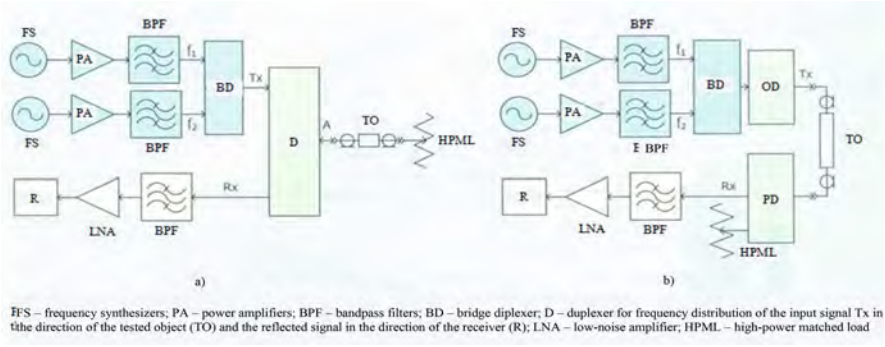

Fig. 10.81 PIM level measuring diagram by methods "at reflection" (**a**) and "at transmission" (**b**) [1]

2×2 W is used; and for fine measurements and detection of additional sources, the test signal power is increased up to 2×4 W and more.

In case of increased operating power of radio transmitting equipment, the greatest interferences for the receive path can be generated by intermodulation components of higher odd order such as IM5, IM7, and etc., the power of which is increased much faster as the test signal power increases (Fig. 10.82).

In systems with many carrier frequencies, it is necessary to control the level of operating signal power peak factor for adjusting the test source power in accordance with it. When using the transmission technology with extended spectrum, the PIM-interference is wideband too that should be taken into account when adjusting the receiver.

The method "at reflection" has higher sensitivity; it is used for items with one and two ports. In [78] it is recommended that the residual level of own intermodulation products and other elements of measuring circuit was by 10 dB lower than the level of products of the device under test and doesn't exceed −170 dBc. It is suggested to carry out a dynamic test (Fig. 10.83) during which the mechanical integrity and structural stability are checked. For this purpose, the tapping of components and junctions, filters, backboards, antennas, cable bending is performed. Tapping is used to identify defects of contact connections, which can increase the PIM level when exposed to heat, cold, wind, vibration, fluctuating loads.

The primary test of the PIM level is performed by method "at transmission", then method "at reflection" is used; in this case, the nearest point with significant level of PIM is determined. Each time when the source is found, the search precision is increased in terms of the value of the PIM source. Tests will be repeated until all considerable dynamic effects of PIM are eliminated.

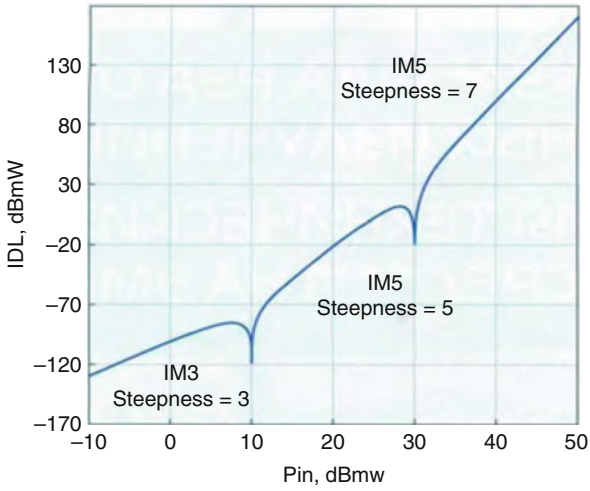

Fig. 10.82 The total power of combination interferences depending on the power of double-frequency test signal [1]

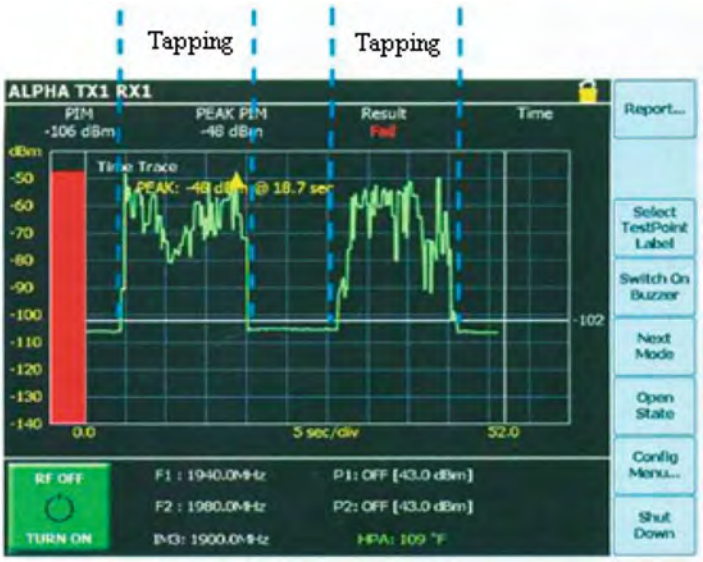

Fig. 10.83 Dynamic PIM-test during component tapping with test signal

10.9.8 Specialized Equipment for PIM Testing

Special-purpose equipment to test the circuits, devices and systems for the PIM level is produced by such companies as Kaelus, Agilent, Rosenberger, Wireless Telecom Group, AWT Global, Anritsu, and etc.

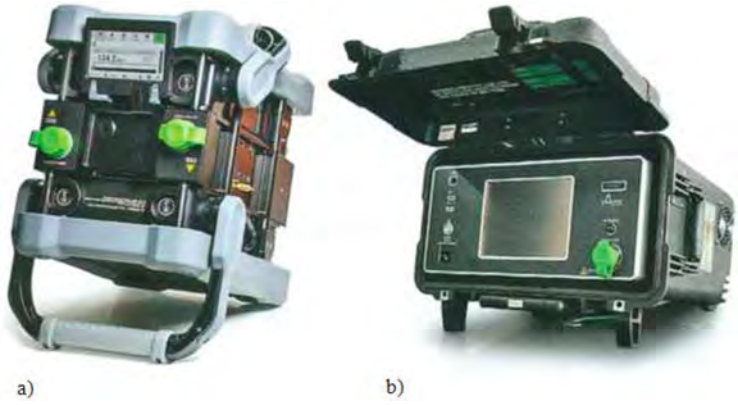

Fig. 10.84 PIM level meters by Kaelus: (**a**) battery-powered tester of iTA series; (**b**) portable analyzer of iOA series [1]

Kaelus company (department of Smiths Interconnect company) is a successor of Summitek Instruments, a well-known manufacturer of equipment for testing the PIM-parameters of the network base stations. The portable battery-powered passive intermodulation analyzer of iTA series made by this company (Fig. 10.84a) combines two frequency ranges. It is designed for operation at the top or at the bottom of the antenna pole, on the roof, in the building with phased-array multiple DAS-systems. Series iTA includes model for standards LTE-800, GSM-900, DCS- 1800, LTE-2600, AWS, and etc. equipped with built-in modes of monitoring for spectrum, frequency sweeping and of tracking the PIM changes by time during dynamic test according to standard IEC 62037. Their self-generated PIM level is not more than −168 dBc during test 2×20 W. The receiver sensitivity enables measuring the PIM-components with the power level from −50 to −128 dB/mW. The input power of two test sources is set within the range 20–43 dB/mW in increments of 1 dB. The IM-components of the third-, fifth-, optional seventh- and ninth- orders are checked. The weight of tester iTA is 22 kg; the shock resistance is 40 G. Being powered by integrated batteries, the device operates up to 2 h at a temperature −10 to 45 °C. Range- to-Fault and Distance-to-PIM Modules promptly determine distances to the irregularities in the path and to a few PIM-sources, respectively.

The analyzers of iQA series (Fig. 10.85) enable monitoring of intermodulation components of odd order from IM3 to IM11. They have the test signal power from 33 to 43 dB/mW. They are powered by the mains and operate within the ranges Tx/Rx from the lowest band of standard 700 NHz – (728–746)/(698–716) NHz to the frequencies of standard UMTS – (2110–2170)/(1920–2080) MHz.

Laboratory analyzer of S1L series made by AWT Global Company (Fig. 10.85a) is intended for diagnostics of PIM-phenomena at frequencies from 730 to 2690 MHz. Sensitivity to PIM-components in the analyzer S1L is −172 dBc during test 2x43 dB/mW; the power of test signal sources is set within 15–46 dB/mW. The device enables measuring of intermodulation components of odd order from IM3 to

Fig. 10.85 Laboratory PIM-analyzers: (**a**) of S1L series made by AWT Global Company; (**b**) of Portable Type series made by Rosenberger Company;

IM25; it has 96 dB; it records the results; it is equipped with Distance-to-PIM and Distance-to-Fault measurement modes. The device is equipped with cables, matched loads, connectors and adapters with low PIM level, test distorted signal source PIMGEN with the PIM level up to −80 dB/mW.

The PIM level analyzers produced by Rosenberger company in portable (Fig. 10.85b) and rack-mounted design. They are intended for operation with standards AMPS, EGSM, DCS, PCS, UMTS, WiMAX in bands (3500–3600)/(3400–3500) MHz. They check the IM-components of the third to ninth order using double-frequency test signal with a power of 37 to 46 dB/mW. Their self-generated PIM level is not more than −168 dBc.

Tester MW82119A of PIM Master series made by Anritsu company [77] (Fig. 10.86) was developed for calibration of PIM level in the frequency band of 900 MHz in networks GSM, UMTS-900 and LTE. It is characterized by high-precision measurements and equipped with Distance-to-PIM mode to determine the distance to the non-linearity source and PIM vs. Time mode for dynamic testing. The GPS-receiver is optionally available. It allows to provide the recorded information with exact coordinates of measuring point. In addition to standard power 2×20 W, this device has an option to test using a signal with an increased power of 2×40 W for more precise determination of problems which may go undetected when tested by a signal of standard power.

It should be noted that modern telecommunication systems depend more than ever before on the characteristics of radio-frequency infrastructure, the implementation of which is directly related to the design of components and quality of their couplings. PIM-testing has become an integral part of creation of new telecommunication systems and technologies. The archive of test results can be used for network monitoring in case of degradation of communication quality and call blocking.

Problems arising from the increased level of PIM and violation of system internal requirements for EMC should be approached in their entirety: measures should be taken to optimize the linearity of materials and components within the intervals of

Fig. 10.86 PIM-level analyzer MW82119A of PIM Master series made by Anritsu company

changes in the environmental parameters; frequency bands, architecture and manufacturing technique of frequency-splitting circuits, as well as design and layout of antennas should be selected taking into account the requirements for PIM.

References

1. Belous, A. I., Merdanov, K. M., & Shvedov, S. V. (2018). *SHF electronics in radar and communication systems* (Technical Encyclopedia in 2 volumes. 2nd edn, revised, 1520 pages). Moscow: Tekhnosfera.
2. Semiconductors. Technical information, technologies and characteristics. Infineon Technologies. http://www.symmetron.ru/suppliers/infineon/book-semiconductors.shtml
3. Alybin, V. G. (2002). Problems of creating SHF protective devices for radar location and communication. In *12th international crimean conference "Microwave equipment and telecommunication technologies"*. Conference materials [Sevastopol, September 9–13, 2002]. Sevastopol, "Veber", 2002.
4. Ashkenazia D. Y., Belyaev V. P., Brodulenko G. I., Lagovier B. B., Lebedev I. V., Mandelshtam M. Y., Perets R. I., Rebrov S. I., & Starik A. M. (1976). *Resonant arresters of antenna switches* (I. V. Lebedev, Ed.) (274 p.). Moscow: Soviet Radio.
5. Ropiy A. I., Starik A. M., & Shutov K. K. (1993). *SHF protective devices*. (128 p). Moscow: Radio and Communication.
6. Sze, S. (1984). *Physics of semiconductor devices in 2 volumes* (Transl. from Eng. M. Shur. Modern Gallium Arsenide-Based Devices. Transl. from Eng., ed. by R.A. Suris – M: Mir, 1984, 456 and 456 p).

7. Shur, M. (1991). *Modern GaN-based devices* (Transl. from Eng., ed. by M.E. Levinshtein and V. E. Chelnokov, 632 p). Moscow: Mir.
8. Lebedev, I. V. (1995). New look at impedance characteristics of semiconductor SHF devices. *MPEI Bulletin*, No. 2, pp 19–29.
9. Lebedev, I. V., & Alybin, V. G. (1978). Resonant array and its use for creation of microwave devices. *News of Higher Educational Institutions of the USSR – Radioelectronics, XXI*(10), 24–31.
10. Soushworth, G. C. (1950). Wave guide system. US Patent no. 2514678.
11. Goldie, H. (1972). Radioactive (tritium) ignitor for plasma limiters. *IEEE Transactions, ED-19* (8), 917–928.
12. Gawronsri, M., & Goldie, J. (1977). 20WMIC L-band receiver protector. *Microwave Journal, 5*, 43–46.
13. Butson, P. S., & Thompson, G. T. (1964). Useful microwave hybrid circuit. *Proceedings of the IEEE, 111*(7), 1281–1282.
14. Liberman, L. S., Sestroretskiy, B. V., Shpirt, V. A., & Yakuben, L. M. (1972). Semiconductor diodes for control of SHF power. *Radiotechnics, 27*(5), 9–24.
15. Kirillov, A. V., & Karchevskiy, E. V. (1982). AC No. 1 042110 (USSR) cl. H01P1/15.
16. Ramay, R. L. (1972). US Patent No. 3649935. Active irises and windows.
17. Lebedev, I. V., & Alybin, V. G. (1977). A. C. 566297 (USSR). Devices for addition of power values of SHF devices. Publ. in 1977, Bull. No. 27.
18. Lebedev, I. V., & Alybin, V. G. (1978). Resonant array and its use for creation of microwave devices. *News of Higher Educational Institutions of the USSR – Radioelectronics, 21*(10), 24–31.
19. Bakeman, P. E., & Armstrong A. L. (1976). Fast high power octave band width X-band waveguide microwave switch. In *IEEE MTT-S International microwave symposium*, Cherry Hill, Digest of technical papers, pp. 154–156.
20. Lebedev, I. V., Ugnichev, L. V., Skorobogatov, D.V., et al. (1992). A. C 1737571 (USSR) IPC H01P1/15. Microwave power limiter. Discoveries. Inventions, 1992, No. 20.
21. Prokhorov, R. A., Lebedev, I. V., & Skorobogatov, D. V. (1993). [Patent 1827041 (USSR), IPC H01P1/15, H01P1/22. Microwave power limiter. Discoveries. Inventions, 1993, No. 25.
22. Rucken, C. T., Wamoss, J. W., Hill, C. N., & Cox, N. W. (1977). Series-connected GaAsSi IMPATT-diodes chips. *Electron Letters, 13*, 331–332.
23. Lebedev, I. V., Shnitnikov, A. S., Ugnichev, D. V., & Rebrov, A. S. (1989). A. C. 1483518 (USSR), IPC H01P1/15 Limiting Device. Inventions. Discoveries. 1989, No. 20.
24. Lazunin, Y. A., & Fefelov, A. G. (1990). Field transistor-based resonant limiter of SHF power. *News of Higher Educational Institutions of the USSR – Radioelectronics, 33*(5), 83–84.
25. Krutov, A. V., Mitlin, V. A., & Rebrov, A. S. (2002). Low-power protective device. In *12th international crimean conference "Microwave equipment and telecommunication technologies"*. Conference materials [Sevastopol, September 9–13, 2002]. Sevastopol, "Veber".
26. Lebedev, I. V., & Shnitnikov, A. S (1993). RF Patent 2003 208 C1, IPC H0129/06. Semiconductor limiting diode. Inventions. Discoveries. 1993, No. 41–42.
27. Lebedev, I. V., Schnitnikov, A. S., & Dyakov, I. V. (1997). Diode-based control SHF devices of the trigger type. *Radiotechnics*, No. 1.
28. Lebedev, I. V., & Dyakov, I. V. (1997). Trigger properties of two-diode chains at high and super-high frequencies. *Radiotechnics*, No. 9, pp. 54–60.
29. Lebedev, I. V., Schnitnikov, A. S., Drozdovskiy, N. V., & Drozdovskaya, L. M. (1995). Patent Application 94011538 (RF), IPC H01P1/15 Microwave limiting device. Decision on Patent Issuance, 1995.
30. Forrez, M., & Milazzo, C. (1962). Duplexing and switching with multi- pactor discharge. *Proceeding of IRE*, № 4, pp. 442–451.
31. Budzinskiy, Y. A., Bykovskiy, S. V., Kantuk, S. P., & Mastrukov, M. A. (1999). Electronic microwave devices on quick cyclotron wave of electron beam. *Radiotechnics*, No. 4, p. 32.

32. Budzinskiy, Y. A., Bykovskiy, S. V., Vildanov, S. A. et al. (2001). Packaged amplifiers with cyclotron protection for radar receivers. In *11th international crimean conference "Microwave equipment and telecommunication technologies"*. Conference Proceedings, September 10–14, 2001, Sevastopol, pp. 190–191.
33. Golenitskiy, I. I., Dukhanin, N. D., Budzinskiy, Y. A., & Bykovskiy, S. V. (2001). Modeling of a 3D electronic-optical system of a cyclotrone protective device. In *11th international crimean conference "Microwave equipment and telecommunication technologies"*. Conference Proceedings, September 10–14, 2001, Sevastopol, pp. 216–217.
34. Karapuzov, M. A., Polesskiy, S. N., & Zhadnove, V. V. (2014). Influence of external perturbing factors on service life of SHF devices. *Reliability and Quality of Complex Systems, 2*(6), 14–20.
35. GOST 27.002-89. Reliability in technology. Basic concepts. Terms and definitions.
36. Zhadnov, V. V. (2013). Design estimate of service life of electronic means of space vehicles and systems. *Reliability and Quality of Complex Systems*. No. 2, pp. 65–73.
37. OST 4G0.012.013-84. Radioelectronic equipment. Determination of lifespan indicators.
38. GOST 27.003-89. Reliability in technology. Composition and general rules of setting reliability requirements.
39. Reliability of radioelectronic devices: Reference book. URL: http://www.twirpx.com/file/1062157/
40. NSWC-11. Handbook of reliability prediction procedure for mechanical equipment.
41. GOST R 27.302-2009. Reliability in technology. Analysis of the tree of failures.
42. GOST RV 20.39.304-98. Complex system of general technical requirements. Requirements for immunity to external factors.
43. Zatylkin, A. V. (2012). *Adaptive testing system based on fuzzy inference* (Reliability and quality: pr. of international symposium: in 2 volumes, N. K. Yurkov, Ed., Vol. 2, pp. 133–135). Penza: PSU Publishing House.
44. Litvinov, A. N., & Yurkov, N. K. (2013). Modeling of strain-stress state in layered RES structures during process and operational effects. *Reliability and Quality of Complex Systems*. No. 3. pp. 16–22.
45. Goryachev, N. V., Lysenko, A. V., Grab, I. D., & Yurkov, N. K. (2012). *Program for engineering calculation of overheating temperature of an electronic radiocomponent crystal and its heat removal* (Reliability and Quality: pr. of International Symposium: in 2 volumes, N. K. Yurkov, Ed., Vol. 1, pp. 340–340). Penza: PSU Publishing House.
46. How to improve parameters of a system and reduce its cost. *Electronic Components*, 2012, No.1, pp. 18–21.
47. Dzhurinskiy, K., & Filippov, A. (2007). Spectrum control products for suppression of electromagnetic interferences. *Components and Technologies*, No.7, pp. 100–103.
48. Dzhurinskiy, K. (2006). *Miniature coaxial radio components for microwave microelectronics*. Tekhnosfera: Moscow.
49. EMI filters and filtered interconnects: Spectrum Control Inc. Catalog 10/02 20. Moscow, 2002.
50. Titovich, N. A., & Polzunov, V. V. (2015). Studies of susceptibility of semiconductor devices to the effect of electromagnetic interference. *BSUIR Reports, 2*(88), 114–118.
51. Brigadan, A. M., Titovich, N. A., Kirshchov, V. M., et al. (1992). II Electronic Equipment. Issue 1 (148), pp. 3–13.
52. Mardiguian, M. (1988). *A handbook series on electromagnetic interference and compatibility*. Vol. 5. Electromagnetic Control in Components and Devices. Virginia.
53. Avdeev, V. B., Avdeeva, D. B., & Berdyshev, A. V. (2011). Information countermeasures against terrorist threats: Technological Institute of the Federal State Higher Professional Educational Institution "Southern Federal University". No. 16, pp. 11–16.
54. Titovich, N. A. (1995). Abstracts of science and technology conference "Modern problems of radio technology, electronics and communication". *Minsk*, pp. 189–191.
55. Titovich, N. A., Polzunov, V. V., & Murashkina, Z. N. (2011). Proceedings of the 15th international science and technology conference "Modern communication means". Minsk, September 27–29, 2011.

56. Titovich, N. A., & Brigidin, A. M. (1992). Radiotechnics and Electronics. Issue 21. pp. 157–160.
57. Titovich, N. A. II (1993). Int. symposium on EMC: Collection of Scientific Reports. Saint Petersburg, pp. 171–175.
58. Titovich, N. A. II (1991). Radio Technology and Electronics. Issue 20, pp. 84–87.
59. Titovich, N. A., & Buevich, E. A. Device for control of parameters of digital integrated circuits under the effect of electromagnetic interference. RF Patent 2069865.
60. Titovich, N. A., & Polzunov, V. V. (2009). Proceedings of the Intern. STC dedicated to 45th anniversary of MRTI-BSUIR. Minsk, March 19, pp. 73–74.
61. Berd, D., & Kugelstadt, T. (2012). Electrostatic Discharge Test Standards. Electronic Components, 2012, No.1, pp. 18–21.
62. http://www.russianelectronics.ru/developer-r/review/2327/doc/58197/
63. Byrd, D., & Kugelstadt, T. Electrostatic discharge testing standards understanding & comparing the differences//www.eetimes.com.
64. Belov, L., Kochemasov, V., & Stroganova, E. (2015). Passive Interpolation in SHF Circuits: Occurrence Mechanisms. *Measurement Methods and Reduction Means / Electronics: NTB. No., 3*(00143), 80–91.
65. Hartman, R. (2011, May 11). Passive Intermodulation (PIM) Testing Moves to the Base Station. *Microwave Journal*.
66. Cannon, N. (2011, October 7). PIM testing crowing in importance as 4C rolls out in Europe. *Microwave Journal*.
67. Strigin, I. (2013). Passive intermodulation interferences in mobile communication means. *Communication Means and Technologies* No. 2, pp. 39–40.
68. Stroganova, E. P. (2008). Intellectual antennas for 3G networks. *Communication Technologies and Means*, No. 6, pp. 42–45.
69. Stroganova, E. P. (2008). Cositing: Pros and Cons. *Communication Technologies and Means*, No. 4, pp. 68–70.
70. Dzhurinskiy, K. (2006). *Small-sized coaxial radiocomponents for microelectronics* (2nd ed.). Moscow: Tekhnosfera.
71. Jargon, J. A., & DeGroot, D. C. (1999, October). Comparison of passive intermodulation measurements for the u.s. wireless industries (NIST Technical Note 1515).
72. Bogdanov, Y., Kochemasov, V., & Khasianova, E. (2013). Foiled dielectrics – selection of the best option for printed circuit boards of HF/SHF ranges – print mounting, 2013, p. 1 – No.2 (0043), pp. 156–168, p. 2 – No. 3 (0044), pp. 142–147.
73. Wilkerson, J. R., Lam, P. C., Card, K. C., & Steer, M. B. (2011, May). Distributed passive intermodulation distortion on transmission lines. *IEEE Transactions on Microwave Theory and Techniques, 59*(5), 1190–1205.
74. Rocas, E., Collado, C., Orloff, N. D., Mateu, J., Padilla, A., O'Callaghan, J. M., & Booth, J. C. (2011, February). Passive intermodulation due to self-heating in printed transmission lines. *IEEE Transactions on Microwave Theory and Techniques, 59*(2), 311–322.
75. Collins, S., & Flynn, K. (1999, November 1). Intermodulation characteristics of ferrite-based directional couplers. *Microwave Journal.*
76. Belov, L. A., Kondratov, A.S., Rozhkov, V. M., & Romaschenko, K. V. (2012). Increasing linearity and energy efficiency of power amplifiers of wideband microwave signals. *Electrocommunication*, No. 5, pp. 23–25.
77. Bell T. Mitigating external sources of passive intermodulation. Anritsu Company, 2013-9, № 11410-0756, Rev. A.
78. IEC Standards for PIM Measurements. IEC 62037: Passive RF and Microwave Devices, Intermodulation Level Measurement, parts 1...8, IEC 62037-2 Ed. 1.0 b:2013 RF Connectors, connector-cable assemblies and cables. Intermodulation Level Measurement.

Chapter 11
Radiophotonics in Telecommunication and Radar Location Systems

11.1 Photonic Devices Based on Surface-Emitting Lasers with Vertical Resonators

Photonics in the general sense [1, 2] studies various phenomena, devices and systems related to optical radiation (photons). EU has recognized photonics as one of the five most efficient and environmentally friendly technologies, which ensure significant improvement of the quality of life [3]. One of the most important spheres of application of radiophotonics is represented by telecommunication optic fiber (TCOF) systems, which occupied the leading position in the international infrastructure of communication networks in the twenty-first century. Their general principle of operation consists in electro-optical transformation of the information signal, transmission of the modulated optical signal via optic fiber waveguide and reverse optical-electrical conversion to the range of modulating frequencies.

Semiconductor laser emitters (SLE), are widely used for electro-optical conversion in TCOF systems; the only example of these emitters since the beginning of development of TCOF systems was the edge-emitting SLE with *horizontal cavity* [4]. However, another SLE [5] was invented in Japan in the beginning of the 1990s, which was distinguished by surface emission from *vertical micro-cavity*. This type of laser also became known as VCSEL (Vertical-cavity surface-emitting laser). Due to advantages of the VCSEL technology, there are so many various developments of photonic structures based on this structure [6] that it is possible to speak about formation of a specific branch of photonics – vicselonics.

The term "vicselonics"introduced by the authors of the fundamental Russian review article [1], which formed the basis for this paragraph, is an amalgam of two terms – VCSEL and photonics.

© The Editor(s) (if applicable) and The Author(s), under exclusive license to Springer Nature Switzerland AG 2021

A. Belous, *Handbook of Microwave and Radar Engineering*,
https://doi.org/10.1007/978-3-030-58699-7_11

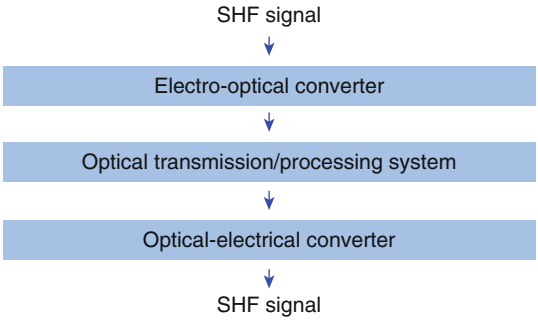

Fig. 11.1 Radiophotonic radar building principle

We will analyze the main directions of using VCSEL technology in photonics, in particular – in its new scientific and technical direction, radiophotonics, which is considered very promising for both civilian and military applications [7].

In the second half of the previous century, a new scientific and technical direction emerged at the junction of photonics and traditional electronics – optoelectronics, which has reached industrial maturity but still remains one of the most relevant fields. This is confirmed by its continuous development with identification of independent interdisciplinary directions, one of which is microwave photonics – the result of integration between optoelectronics and microwave radioelectronics [8]. In recent years, the term "microwave electronics" in Russian scientific and technical periodic publications has been mostly replaced with the more general term "radiophotonics" [9], which we will use in the following.

The basic principle of radiophotonic principle of building radioelectronic equipment (REE) [10] is shown in Fig. 11.1: input signal of the SHF range is converted to the optical range by means of electro-optical converter. Modulated optic signal with the help of optic fiber (or integrated optic) units and devices is processed or simply transmitted to a remote equipment point, where inverse optical-electrical conversion to the microwave range is performed.

As compared to TCOF systems, radiophotonic equipment, in addition to transmission in the optical range, requires direct processing of optical radiation carrying the signal. As is known, in traditional radioelectronic equipment similar data processing is performed with the help of *functional microelectronic components of the radio frequency range*. Transfer of the processing operation to the optical range significantly simplifies REE architecture and increases its basic technical parameters, such as speed of operation, operating frequency band, weight and dimensions, dynamic range, electromagnetic compatibility, etc. [11] Unlike TCOF systems, in radiophotonic devices it is usually not necessary to use laser radiation with significant power. Lower power as compared to traditional SRLs is what limits application of VCSEL in telecommunication optic fiber systems, where they are used in relatively short distributing lines [12].

On the contrary, in radiophotonic units of signal processing, VCSEL provides the main advantages based on its own advantages in comparison with an edge-emission laser [6, 13]:

- small size of the structure (resonator length is smaller almost by two orders of magnitude);
- low threshold generation current (0.5–2 mA as compared to 10–15 mA);
- low power consumption (5–10 times lower);
- better efficiency of fiber penetration due to spatial symmetry and relatively low divergence of the output beam (10–12° against 30–40°);
- significantly lower temperature dependence of threshold current and energy characteristic;
- relative simplicity of ensuring single-frequency mode;
- relatively wide band of continuous wavelength tuning (5–7 nm);
- simplicity of formation of a two-dimensional laser array on a single substrate;
- higher produceability of the end product due to the possibility of testing during production process directly on the plate.

Modern semiconductor technologies using surface-emitting lasers offer the possibility of creating small-sized and very efficient devices. Development of VCSEL in the beginning was based on two laser systems [5]. The first includes AlCaAs/CaAs-based lasers operating in the first transmission window of the crystal waveguide near 0.85 μm – so-called short-wave VCSEL. Devices based on such lasers are widely applied in cost-efficient TCOF systems for local data transmission networks, computer reflecting interfaces of the active cable type and computer optical mouses [13].

In lasers of the second type, the so-called long-wave VCSELs, InP-based semiconductor materials are used, due to which they can operate in the second (wavelength about 1.3 μm) and third (wavelength about 1.55 μm) transmission windows (spectral ranges O, S (second window) and C, L (third window) according to the conventions of the International Telecommunication Union), which are more promising for telecommunication systems. However, this type of lasers is introduced relatively slowly due to process difficulties. Moreover, another important problem is ensuring reliable operation of VCSEL at elevated ambient air temperatures, which are usually required for radioelectronic equipment. Analysis of different laser heterostructures shows that during development of long-wave VCSELs, systems with InAlCaAs-based active region are mostly used in the second window, while systems with InCaAsP-based active region are generally applied for the third transmission window [12].

In turn, modern laser structures for the longwave range are manufactured according to planar-epitaxial technology using two structures: fully *epitaxial*, where active region and mirrors are formed by means of the same materials, and *alloyed* with separately manufactured Bragg mirrors based on AlGaAs/GaAs and their subsequent alloying with the heterostructure of the active region at specific

temperatures and under specific pressure [14]. While the benefit of the first method consists in relative simplicity of the technological process, its significant downside is the reduced heat removal from the active region due to relatively low thermal conductivity factor of the quaternary solid solution used in this case to form a multi-layer reflector. This disadvantage is partially eliminated by means of fused structure due to the fact that the mirrors here are formed by alternating AlGaAs/GaAs layers, like in shortwave VCSEL. However, this technological technique increases the number of operations and, subsequently, the cost of production.

However, alloyed long-wave VCSEL is considered to be the key component of equipment of modern and future local telecommunication networks [15] and units of radiophotonic processing in REE [16]. Modern state and potential of using VCSELs of this design in radiophotonic units of microwave REE are studied in detail in a number of works [16]; thus, in the following we will only present a brief overview of design features and main technical parameters of this device as a basic element of the component base of radiophotonics.

11.2 Design of a Long-Wave Alloyed Surface-Emitting Laser

The main elements of the structure of a long-wave alloyed VCSEL [1, 15] are (Fig. 11.2): heterostructure containing doped n-layers based on InP and multi-quantum-dimensional InP/InAlCaAs-based active region, as well as two GaAs/AlGaAs-based Bragg reflectors. These elements during production are alloyed in two planes. Tunnel junction is used for current and optical limitation.

The distinguishing feature consists in the fact that, unlike a classic edge-emitting laser, radiation channel of a VCSEL is arranged vertically (Fig. 11.3).

In order to ensure conditions of laser generation, the active region here, like in a traditional laser, is located between two mirrors, which in this case are designed as two distributed Bragg reflectors (DBR). However, the length of the VCSEL cavity here is smaller almost by two orders of magnitude and approximately corresponds to the working wavelength; therefore, in order to create effective laser generation, the developer has to meet two conditions: increase optical amplification in the active region and ensure high (close to 1) mirror reflection coefficient. The first condition is relatively easy to meet by using quantum-dimensional structure of the active region (up to 10 nanolayers with thicknesses of several nanometers) based on quantum wells or quantum dots are used. The second requirement is provided by using multi-layered (over 30 layers) mirror structure. As in this case the total number of epitaxial layers in the structure exceeds 100, it creates significant difficulties for the developer in physical modeling of this design.

It should be noted that the current (as of 2015) experience in development of radiophotonic devices helped identify the following additional advantages of long-wave VCSELs: *possibility* of significant improvement of dynamic characteristics of

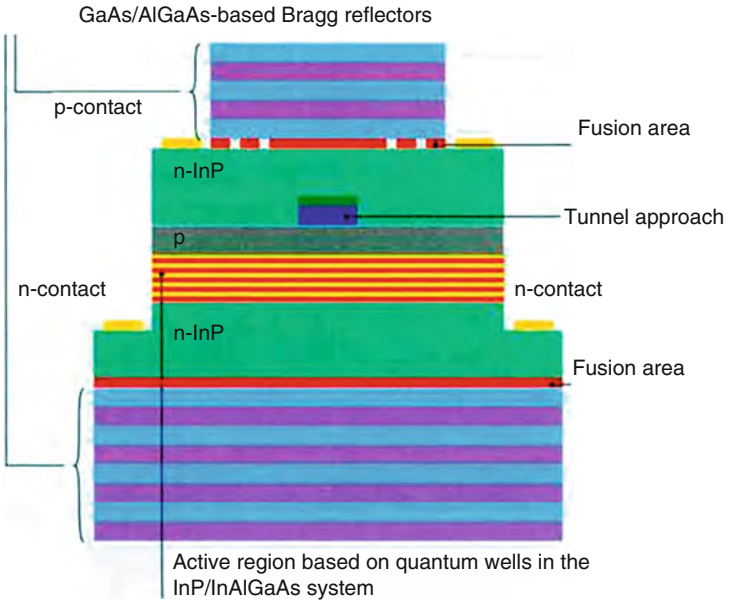

Fig. 11.2 Draft of the cross-section of vertical structure of an alloyed VCSEL [1]

Fig. 11.3 Draft of the crystal of a long-wave VCSEL [1]

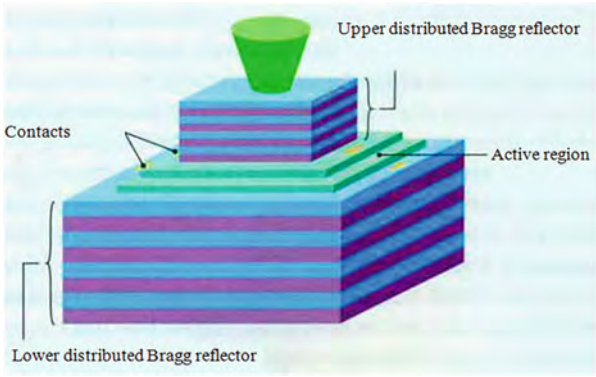

these devices due to the so-called optical injection synchronization [17], as well as (which is important from the technical-economic) point of view, compatibility with the mass-produced silicon integrated optical technology [18].

In order to perform specific assessment of the considered VCSEL as a basic element of the component base of vicselonics, it is necessary to present the achieved values of main static and dynamic parameters of the alloyed long-wave VCSELs, in particular – the device developed in the Laboratory of Physics of Nanostructures (LPN) of the École Polytechnique Fédérale de Lausanne (EPFL) – www.epfl.ch presented in one of the most informative papers on the subject [1].

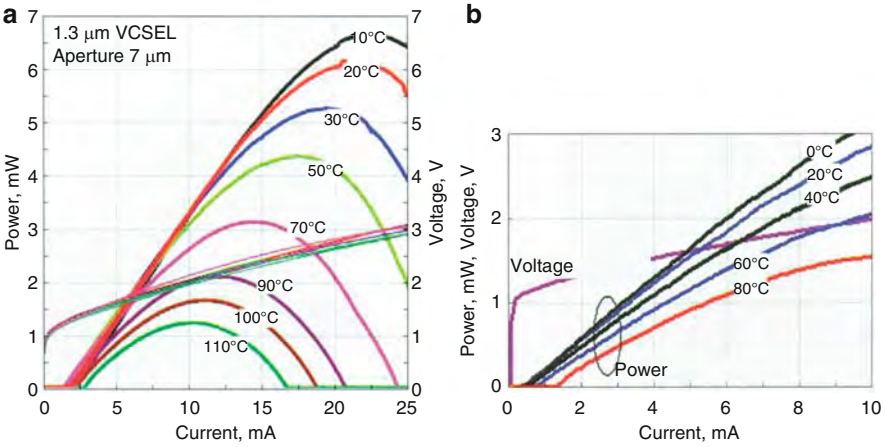

Fig. 11.4 Measured volt-ampere and watt-ampere characteristics of a single-frequency VCSEL; (**a**) in the O-band; (**b**) in the C-band [1]

11.3 Basic Technical Characteristics of a Long-Wave Alloyed Surface-Emitting Laser

11.3.1 Electrical and Power Characteristics

As can be seen from Fig. 11.4, the following actual results were obtained at room temperature: threshold current was 2 mA in the O-band and less than 1 mA in the C-band; maximum radiation power in continuous mode amounted to 5–6 mW; power consumption in quasi-linear transformation mode – 20 mW in the O-band and 8 mW in the C-band. Moreover, continuous radiation power of 1.5 mW at temperatures of 100 °C in the O-band and 80 °C in the C-band was achieved at operating current of 9 mA. It is clear that the achieved results are constantly improving, and the record value of radiation power in continuous single-frequency mode for any VCSEL type has been achieved and amounts to 8 mW at room temperature [19–21].

11.3.2 Low-Signal Frequency-Modulation Characteristics

As follows from Fig. 11.5, the band of direct modulation at the −3 dB level exceeds 7 GHz with displacement current equal to 10 mA. Measures for improvement of the laser structure used by developers of the leading world companies have lead to extension of the modulation band to 11 GHz [22, 23]; there are also ways to further extension of the band - to 15 GHz and higher.

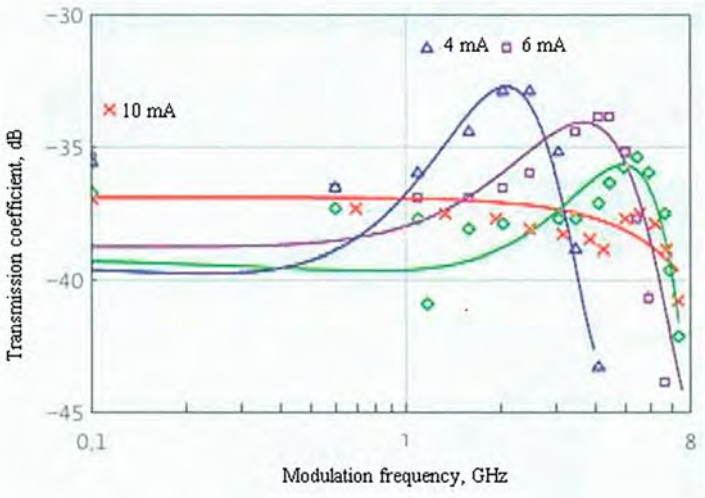

Fig. 11.5 Typical low-signal frequency-modulation characteristics at different displacement currents [1]

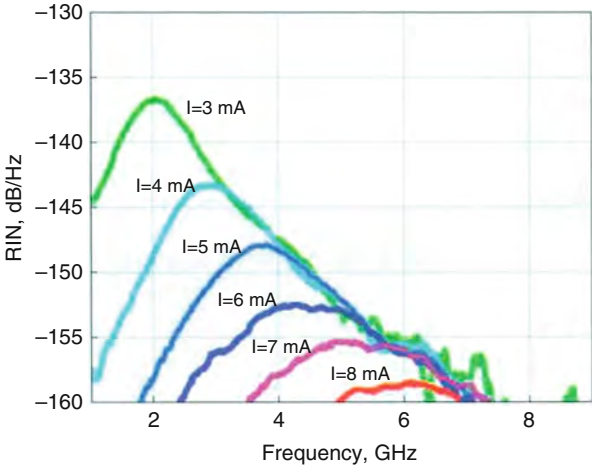

Fig. 11.6 Typical noise characteristics (RIN) of the O-range laser at different displacement current values (ambient temperature – 20 °C) [1]

11.3.3 Noise Characteristics

Figure 11.6 shows that values of Related Intensity Noise (RIN) are reduced with an increase in the displacement current and increased with an increase in the modulation frequency, which corresponds to other data known form literature. At room

temperature, RIN value at the modulation frequency of 1.5 GHz amounts only to 160 dB/GHz (minimum threshold of the testing station) with the displacement current as low as 5 mA [23].

11.3.4 Linearity in High Signal Mode

As is known, the most illustrative way of assessing linear properties of any active device (in this case – semiconductor laser) consists in finding its input intersection point (IIP) [24, 25]. As is known from literary sources, simplified assessment of IIPs of the third and fifth orders (IIP3 and IIP5) can be performed using the following formulas [26]:

$$\mathrm{IIP3} = \mathrm{P_i} + \mathrm{IMD3}/2,$$

$$\mathrm{IIP5} = \mathrm{P_i} + \mathrm{IMD5}/4.$$

Here, IMD3 and IMD5 are intermodulation distortions of the third and fifth order respectively, which are measured with the help of a standard photodetector in the microwave range and a basic radio frequency spectrum analyzer; Pi is the power of the modulating signal.

These formulas and measurement results were used to obtain values of IIP3 and IIP5 for VCSEL of the O-band [27] in frequency domains of modulating signals near 1 and 6 GHz (Table 11.1).

As follows from Table 11.1, the achieved level of IIP3 and the linearity of the studied VCSEL is reduced as the modulation frequency increases, which conforms to other known experimental information [28]. Comparison with similar results presented in other publications shows that the IIP of the third order of the long-wave alloyed VCSEL with intracavity arrangement of contacts considered in this section is approximately 10 dB higher than in a long-wave VCSEL with a different design [28] and at the level of the best results for a short-wave VCSEL with oxide aperture [29].

11.3.5 Spectral and Tuning Characteristics

The following parameters were experimentally determined for VCSEL of the C-band in [21]: coefficient of suppression of spurious modes within the entire

Table 11.1 Input intersection points for different frequencies

Frequency domain, GHz	IIP3, dB	IIP5, dB
1	26	20
6	19	17

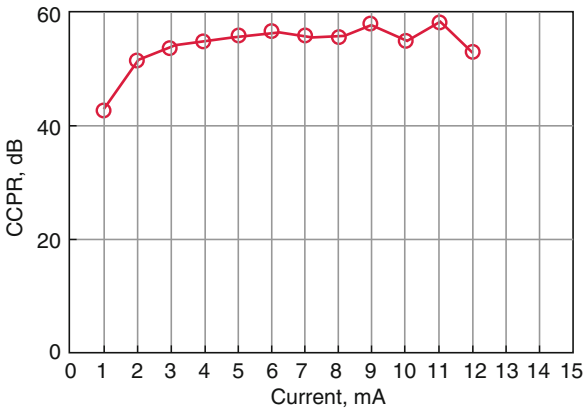

Fig. 11.7 Dependence of the coefficient of suppression of spurious modes on displacement current value

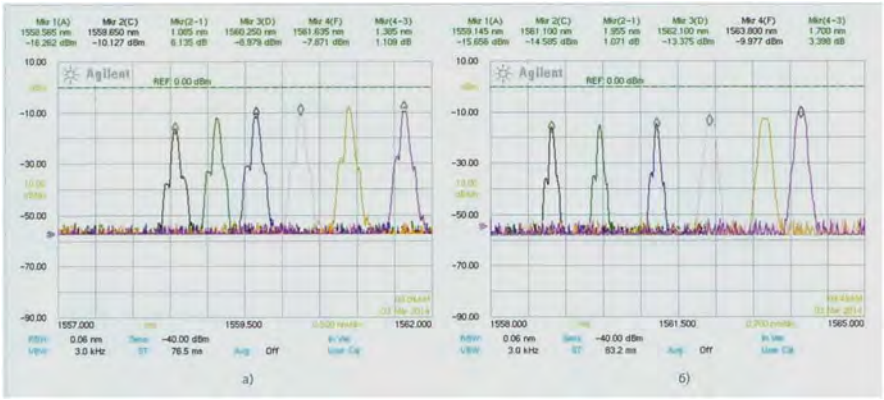

Fig. 11.8 Characteristics of radiation wavelength tuning: (**a**) by displacement current; (**b**) by temperature

range of operating currents (Fig. 11.7), spectral characteristics during tuning by displacement current within the range of 3–13 mA with a pitch of 2 mA (Fig. 11.8a) and during tuning by temperature within the range of 25–50 °C with a pitch of 5 °C (Fig. 11.8b) [16], as well as the width of the spectral line of the laser [21] (Fig. 11.9).

As can be seen from these figures, this laser operates in single-frequency mode with minimum suppression of spurious modes of more than 40 dB; average steepness of tuning of the radiation wavelength by temperature is equal to 0.18 nm/°C, by displacement current – 0.3 nm/mA; minimum width of the generation line is about 4 MHz.

Specific properties of VCSEL described above allowed the developers to create a number of more effective structural modifications on its basis. Of all their multitude, the most important representatives of this sphere will be considered in the following, taking into account limited volume of this technical encyclopedia: VECSEL, MEMS-VCSEL, LICSEL, MIXSEL operating in O-, S- and C-ranges. With respect

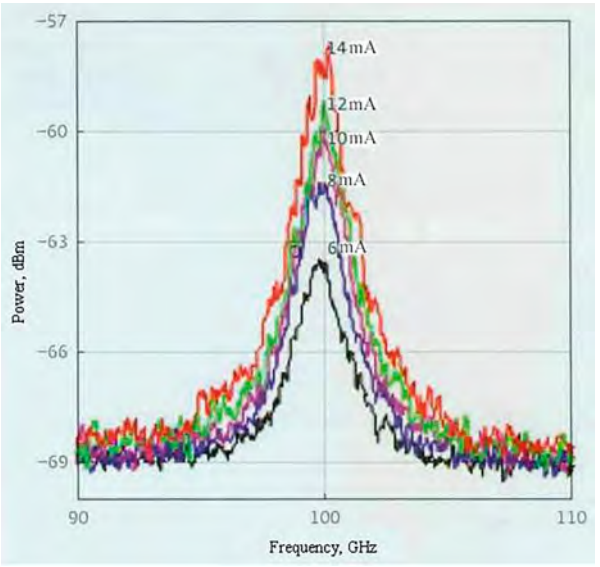

Fig. 11.9 Width of the radiation line in the C-range at different displacement currents

to presentation of the material, the authors have adopted the approach described in [1], which consists in successive description of distinguishing features, building principles, circuits and structures, basic parameters and characteristics achieved at the modern level of scientific and technical development of radiophotonics.

11.4 Continuous Generation Lasers: VECSEL, MEMS-VCSEL, LICSEL

Vertical External Cavity Surface-Emitting Laser (VECSEL) [1] is the most advanced and actively developed element of the component base of radiophotonics, which successfully combines functioning of semiconductor lasers within a wide frequency range and the tried and tested technology of organization of external pumping and effective heat removal of disc solid-state lasers. Its creation was determined by rapid development of photonic technologies, during which certain limitations of VCSEL fields of application were identified, mostly connected to insufficiently high output power (Fig. 11.4) and insufficiently narrow radiation line (Fig. 11.9). Basic VECSEL elements (Fig. 11.10) – amplifying semiconductor crystal (ASC), which is a VCSEL with the upper mirror removed (Fig. 11.2), and external spatial optical resonator formed by a Bragg ACS reflector at one side and a semi-transparent spherical mirror at the other side [30].

Such output mirror ensures the required focusing of the intracavity beam to the ASC surface and generation of a diffraction-limited symmetrical output beam, the

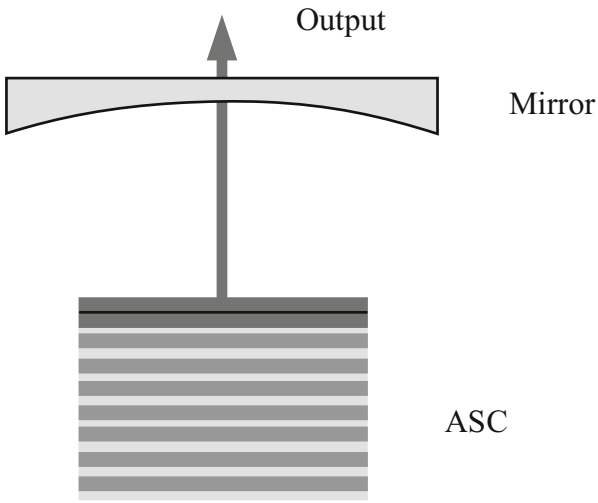

Fig. 11.10 Generalized VECSEL structure

quality of which is commensurate with that of gas and solid-state lasers. It should be noted that efficient and reliable operation of a real laser of this type may require certain additional elements not shown in Fig. 11.10, such as optical pumping source and cooling device of the amplifying crystal, which will additionally complicate its circuit.

In the C-band (wavelength range of 1530–1565 nm), which is the most important to radiophotonics according to the EU classification, amplifying semiconductor crystal is designed on the indium phosphide substrate with InCaAsP or InGaAlAs with quantum-dimensional active structure, like in VCSELs. However, with formation of Bragg reflectors based on these semiconductor structures, relatively weak contrast of the refraction index usually calls for an increase in the number of lattice layers (with subsequently increasing losses of the optical signal). The best option consists in using a mirror based on alternating AlGaAs/GaAs layers (or dielectric layers) with their subsequent alloying directly before the amplifying structure [31, 32]. Moreover, the use of a high-Q spatial optical resonator, in addition to the obvious possibility to increase power and significantly narrow the generation line, makes it possible to integrate various optical elements, which create significant additional advantages. In particular, insertion of Fabry-Perot filters ensures implementation of the single-frequency coherent operating mode.

There are two basic variants of building this laser known today: with electrical pumping (EP-VECSEL) and with optical pumping (OP-VECSEL). The first option is more cost-effective, since it does not require presence of the special pumping laser and preserves the small size typical of VCSEL. EP-VECSEL circuits in hybrid (with spatial resonator) [33] (Fig. 11.11) and monolithic [34] (Fig. 11.12) versions have already been created. OP-VECSEL, which ensures critically high output power, can also be based on a hybrid (with a separate pumping source) [35] (Fig. 11.13) or a

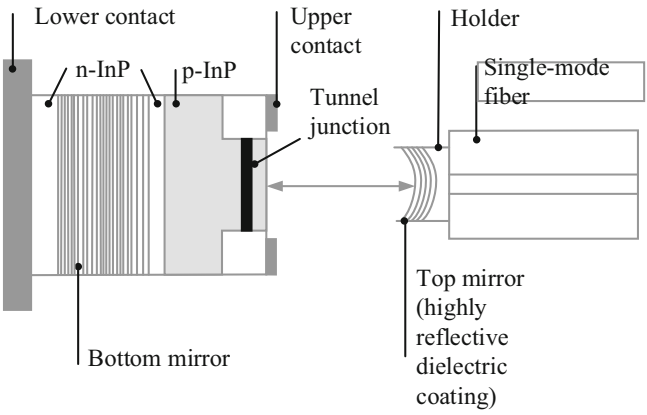

Fig. 11.11 Draft of the EP-VECSEL structure in hybrid configuration

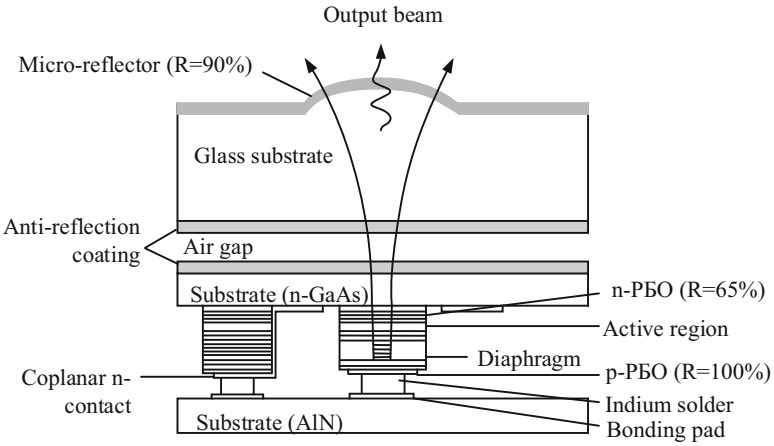

Fig. 11.12 Draft of the EP-VECSEL structure in monolithic configuration

monolithic (with integrated power source) [36] (Fig. 11.14) system. Hybrid version of OP-VECSEL has already been practically implemented in the form of two circuits [35]: linear (Fig. 11.13a) with single-frequency output signal and T-shaped (Fig. 11.13b) (ASC1 and ASC2 pumping circuits are not shown) with two output signals of orthogonal polarization.

After comparing the diagrams in Figs. 11.11, 11.12, 11.13 and 11.14 [1], the reader can conclude that the critical component of all these circuits is the ASC mentioned above, which is implemented as a separate structural element in the hybrid VECSEL circuit or is included into a monolithic structure. In both cases the condition for its reliable operation in VECSEL, which determines longevity of the device in general, consists in the presence of effective heat removal, which prevents overheating of the semiconductor structure with dissipated power up to

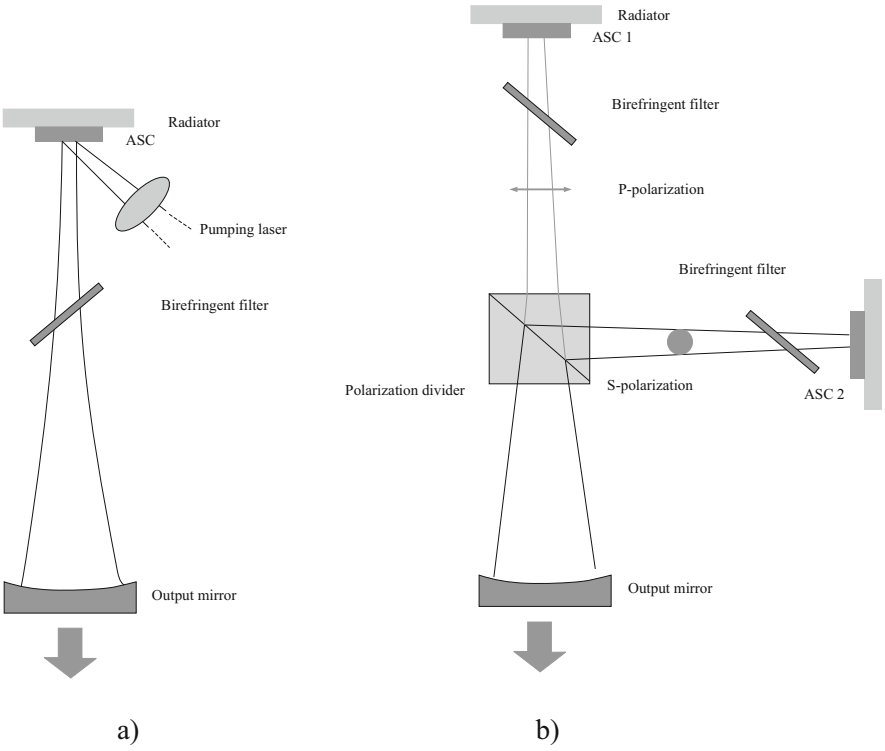

Fig. 11.13 Principles of building hybrid OP-VECSEL circuits: (**a**) linear; (**b**) T-shaped

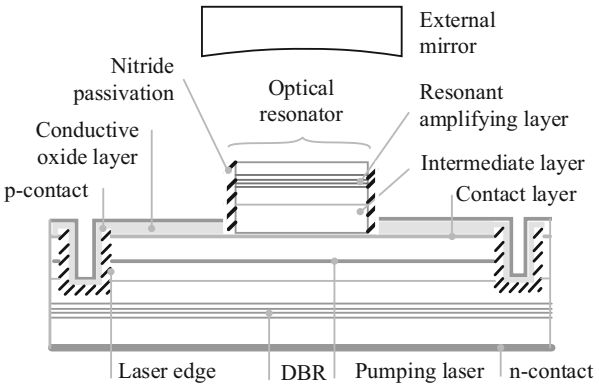

Fig. 11.14 Diagram of an OP-VECSEL with integrated pumping source

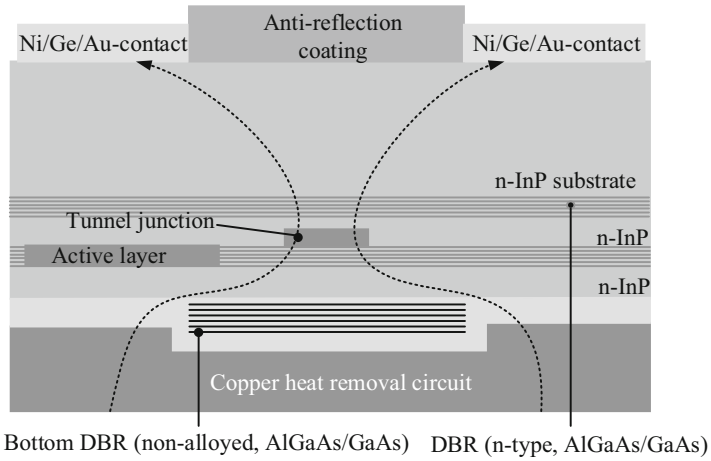

Fig. 11.15 Draft of cross-section of the alloyed EP-VECSEL ASC

dozens of watts. Of course, this requirement is significantly toughened for longwave VECSELs operating in radiophotonic devices due to lower heat conductivity of semiconductor compounds applied in the C-range. Promising solution to this problem here, similarly to the case with VCSEL, is ensured by alloyed structure of the active region and mirror with integrated diamond radiator installed on copper base [37, 38]. Another important difference of an alloyed ASC consists in the introduction of the region ensuring expansion of the carrier charge to the top ring electrode between the quantum-dimensional amplifying layer and the upper reflector (Fig. 11.15) [39], which is required to increase quantum efficiency of the laser. In order to increase uniformity of current distribution over the volume of the region, tunnel junction is used (similarly to the one used in VCSEL), cross dimensions of which are matched with the thickness of the current expansion region. Dotted lines are used to indicate trajectories of the injection current flowing between the top and bottom disc electrodes. Intermediate semi-transparent (70%) Bragg reflector based on AlGaAs/GaAs layers of the n-type is designed for compensation of absorption losses in alloyed regions of the ASC. Deposition of galvanic copper coating on the lower electrode ensures efficient heat removal with thermal resistance within 13–25 K/W throughout the entire range of operating temperatures of the device.

As follows from the analysis of multiple literary sources [1], there are two approaches to building high-power VECSELs, which can be used as setting generators of multi-element radiophotonic antenna arrays of the microwave range, as well as pumping sources (1450–1480) of fiber erbium and Raman amplifiers: the use of a thermoelectric micro-cooler (TEMC) [39] for devices with electrical pumping (Fig. 11.16a) and water or air cooling [40] for devices with optical pumping (Fig. 11.16b). Electrical and power characteristics were obtained by studying these circuits (Fig. 11.17). They allow us to conclude that during operation of a long-wave VECSEL with electrical pumping in continuous single-frequency mode, it is

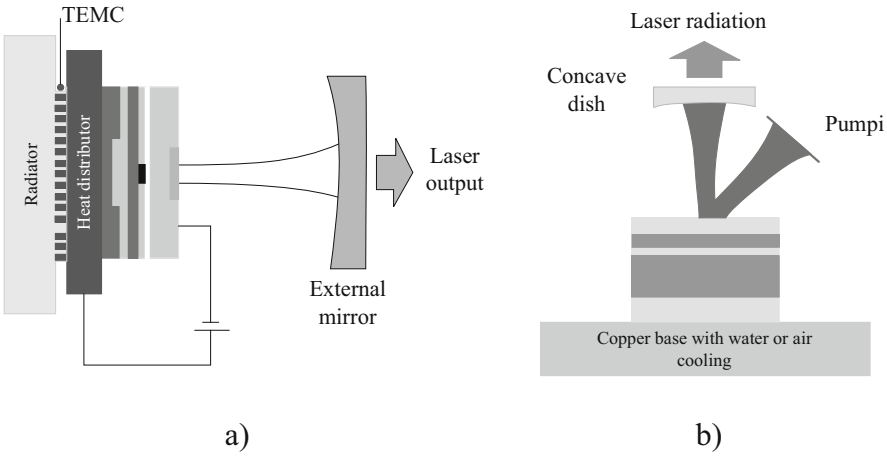

Fig. 11.16 Design draft of advanced circuits of a high-power VECSEL: (**a**) for EP-VECSEL; (**b**) for OP-VECSEL

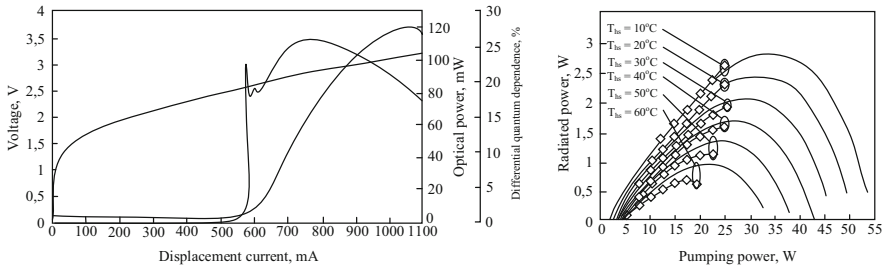

Fig. 11.17 Electrical and power characteristics of high-power VECSELs: (**a**) EP-VECSEL (heat removal temperature 3 °C); (**b**) OP-VECSEL (T_{hs} – heat removal temperature; full lines are used to indicate the modeling results)

possible to achieve output power of 100 mW, which is 40 times greater than the output power of VCSELs of the same spectral range (Fig. 11.4). The use of optical pumping in lasers of S- and C- ranges makes it possible to increase it to 1–3 W with heat removal temperature up to 50 °C.

As is know, quality of operation of a generator of any frequency range, in addition to its output power, is characterized by noise characteristics, which for lasers are usually determined [4] as relative intensity noise (RIN) and the width of the radiation line at the half level. OP-VECSEL intensity noise in the C-band amounts to less than −160 dB/Hz near the carrier and reaches the threshold of the test unit (−170 dB/Hz) at frequencies of more than 500 MHz (Fig. 11.18) [41], which is significantly lower than the same parameter both for VCSEL and for edge-emitting laser [4]. Fundamental reason for this consists in longer lifespans of photons in the resonator and carriers in the ASC. Another advantage of VECSEL consists in fundamental

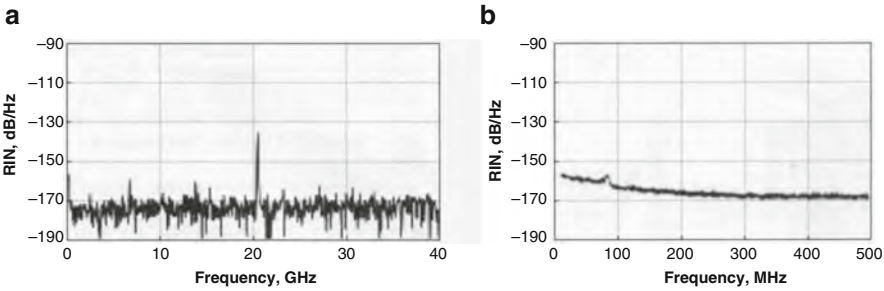

Fig. 11.18 Noise characteristics of a 100 mW VECSEL (at room temperature): (**a**) in the wide frequency band of 0.1–40 GHz (the peak near 20 GHz is associated with the effect of the external optical resonator); (**b**) in the frequency band of 10–500 MHz close to the carrier

narrowing of the radiation line, since its width is in reverse proportion to the resonator length [4]. In a long-wave OP-VECSEL, it is possible to ensure single-mode operating mode with suppression of spurious modes over 60 dB and radiation line with the width of dozens kHz (Fig. 11.19) [42], narrower than the so-called Lorentz line (dotted line in Fig. 11.19a). It should be noted that the above data are much better than the measurement results of VCSEL spectral characteristics (Figs. 11.7 and 11.9).

Another significant disadvantage of continuous-mode VCSELs discovered during development of photonic technology consists in insufficient width of the generation line tuning band. For example, according to Fig. 11.8, in case of the most basic control of displacement current and temperature, it does not exceed several nanometers, while effective functioning of certain radiophotonic devices, such as diagram-forming device, tuning at least in the entire C-band (35 nm) is required. Two approaches have been suggested to solve the problem, which use adjustment of physical or optical length of the VCSEL resonator; this length, as mentioned above, is commensurate with the radiation wavelength. The laser in which the first approach is implemented is known as MEMS-VCSEL (Micro Electro- Mechanical System-VCSEL); the most common name of the laser based on the second approach is LICSEL (Liquid Crystal Surface Emitting Laser). These structures have been actively studied by various university science groups over *the last 10 years*. Vast volume of results have been obtained during works; therefore, only the most important ones are considered in [1].

It can be said that the general principle of building of a modern MEMS-VCSEL of the C-band [43] consists in formation of an upper Bragg mirror (Fig. 11.2) in the form of a mobile microelectromechanical membrane (Fig. 11.20). Continuous tuning band for this device is 102 nm (Fig. 11.21), which is 25 times wider than the tuning band of a standard VCSEL (Fig. 11.8). Obvious disadvantage of the considered MEMS-VCSEL structure from the point of view of operation in a practical device is the dependence of power and especially wavelength on the ambient temperature, which corresponds to a standard VCSEL (Fig. 11.8) [1].

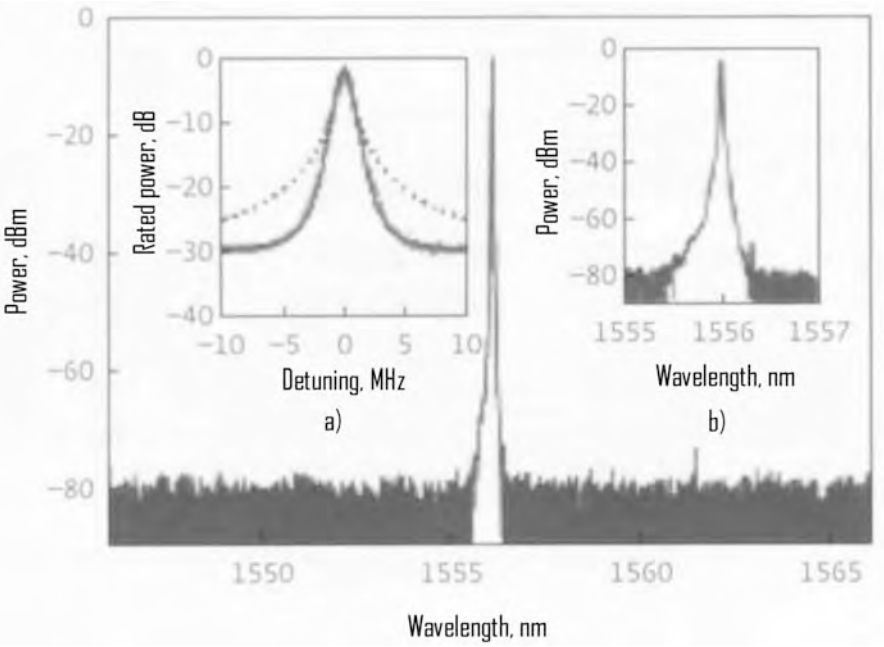

Fig. 11.19 Measured spectral characteristics of OP-VECSEL of the C-band with power of 77 mW (at room temperature): (**a**) measurements by autoheterodyne method with the help of radiotechnical spectrum analyzer; (**b**) measurements with the help of optical spectrum analyzer in wide band near the carrier

Specific MEMS-VCSEL [44] structure has been suggested for compensation of thermal sensitivity of the wavelength, in which the upper mirror is installed on a microcantilever with the length of about 100 μm (Fig. 11.22). According to the experimental studies performed, minimum thermal sensitivity of the wavelength in the C-band was at the level of 0.0016 nm/°C. This result corresponds to an approximately 100-fold reduction of sensitivity as compared to standard VCSEL and allows us to assume that the considered structure operates in athermal mode, i.e. does not require presence of a temperature control unit with power consumption of several watts, which is usually used in semiconductor lasers.

A more cost-effective solution to the problem of expanding VCSEL wavelength tuning band consists in adding a transparent liquid crystal layer inside the cavity, the refraction factor of which changes under the effect of external electrical voltage V_{LC}, which makes it possible to adjust optical length of the laser resonator. The main difference between such laser (LICSEL) and standard VCSEL (Fig. 11.2) consists in the intracavity layer based on nematic liquid crystal structure (Fig. 11.23) [45]. Typical tuning characteristic of LICSEL at fixed displacement current and temperature stabilized at the level of 20°C (Fig. 11.24) demonstrates that the continuous frequency tuning in the range of variation $V_{LC} = 0.2–4$ V is 34 nm. This is almost

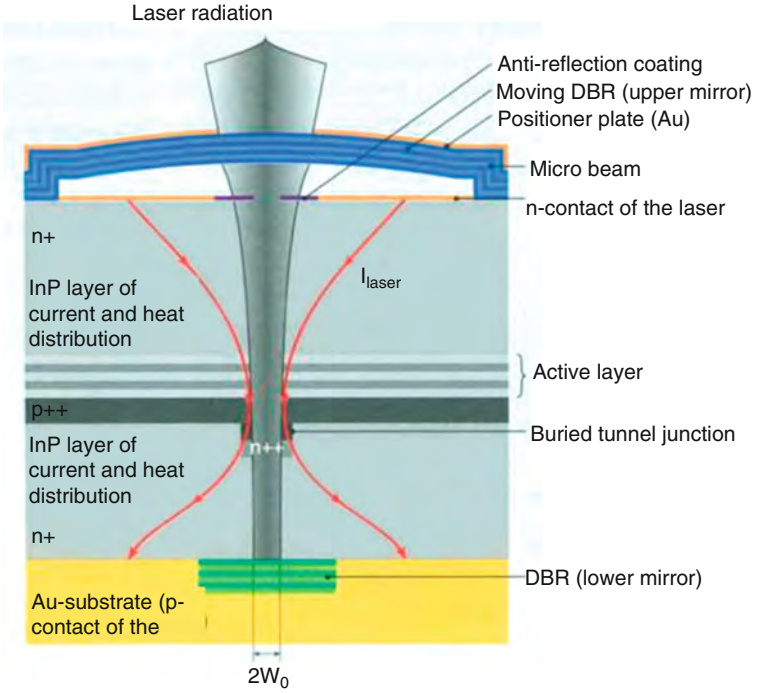

Fig. 11.20 Cross structure of MEMS-VCSEL. W_0 – laser beam aperture, l_{laser} – laser current [1]

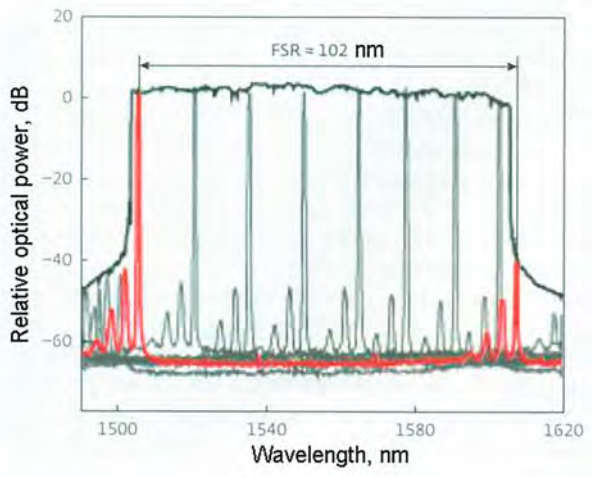

Fig. 11.21 Characteristics of MEMS-VCSEL radiation frequency tuning (fixed displacement current, crystal temperature 20 °C). FSR (free spectral range)

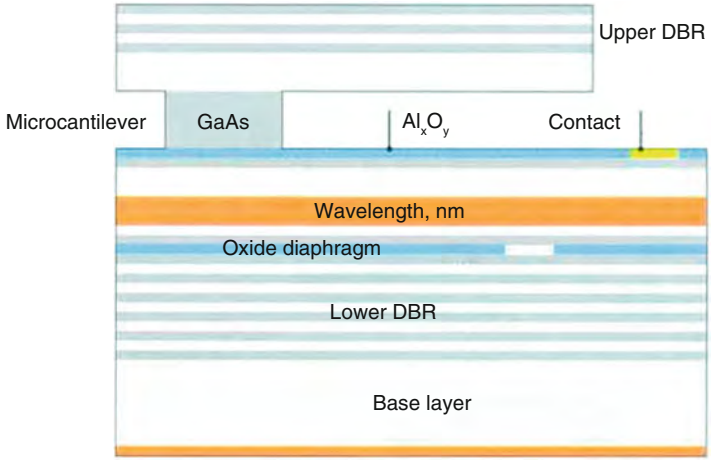

Fig. 11.22 Structure of an athermal MEMS-VCSEL

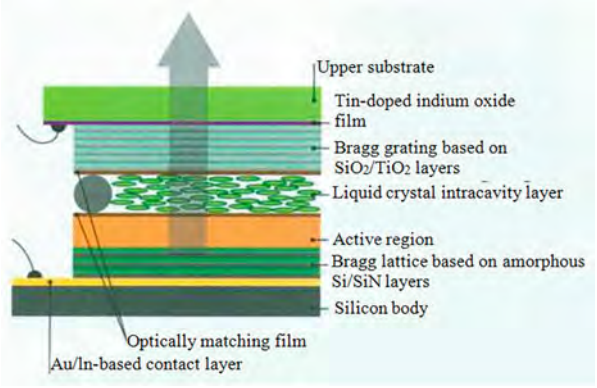

Fig. 11.23 Draft of the cross structure of a long-wave LICSEL

10 times wider than the tuning band of a standard VCSEL (Fig. 11.8) and in most practical cases conforms to requirements for radiophotonic devices.

It should be noted that introduction of an athermal MEMS-VCSEL or a simpler functional analog (LICSEL) opens the road to effective use of radiophotonic technologies in onboard radio equipment with strict requirements for energy consumption. In this case, thermal stabilization of the radiation spectrum with power consumption of several watts, which is required for operation of any semiconductor laser, can be replaced with frequency stabilization with consumption close to zero, which operates similarly to the radiotechnical automatic frequency tuning scheme.

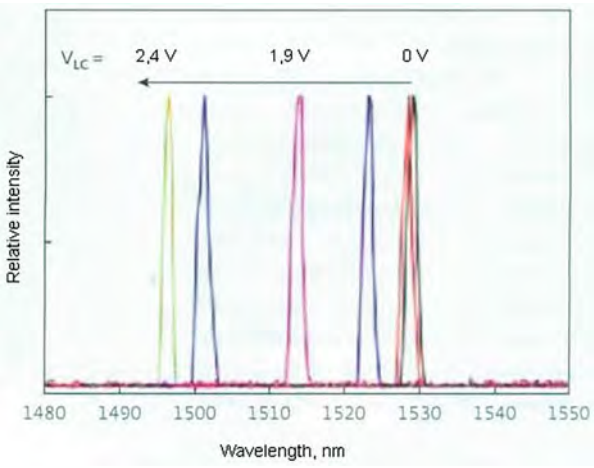

Fig. 11.24 LICSEL tuning characteristics

11.5 Pulse Generation Lasers: VECSEL-SESAM, MIXSEL

Development of the component base of radiophotonics is associated not only with continuous generation lasers described above, but also with pulse lasers [1]. An important feature of photonic technologies in this direction is the possibility of simple generation of sequential coherent VHF optical pulses with the help of so-called passive mode synchronization lasers (PMS). Such lasers are widely used in TCOF systems, spectrology, material studies, etc. The prospects of their use in radiophotonic devices consist, for example, in creating multiwave precision generators of optical pulses for beam-forming devices and radiophotonic analog-digital converters.

PMS equipment for several years have been developing on the basis of solid-sate and semiconductor lasers, mostly in the short-wave (about 1 μm) spectral range. The advantage received a boost with the emergence of the VECSEL technology, which, as noted above, combines advantages of solid-state and semiconductor lasers. Traditional PSM circuit contains two principal elements: active laser structure and saturating absorber, in which the cavity losses are modulated. In practical devices, this operation is usually implemented with the help of a mirror based on a semiconductor saturable absorber, known as SESAM (Semiconductor Saturable Absorber Mirror). SESAM contains a semiconductor DBR with inserted quantum-dimensional absorber layers.

Two main schemes of building pulse generation VECSELs are known today [1, 46, 47]: with separate ASCs and SESAMs (Fig. 11.25a), known as VECSEL-SESAM, and with integrated ASCs and SESAMs (Fig. 11.25b), known as MIXSEL (Mode-locked Integrated eXternal-cavity Surface Emitting Laser). Optical pumping is used for operation of both circuits, which is introduced according to Fig. 11.16b. Monolithic structure of the MIXSEL laser is usually grown by means of molecular-beam epitaxy and contains five sections (Fig. 11.25b): highly reflective AlAs/GaAs-based DBR; absorber based on the layer of self-organizing InAs quantum dots

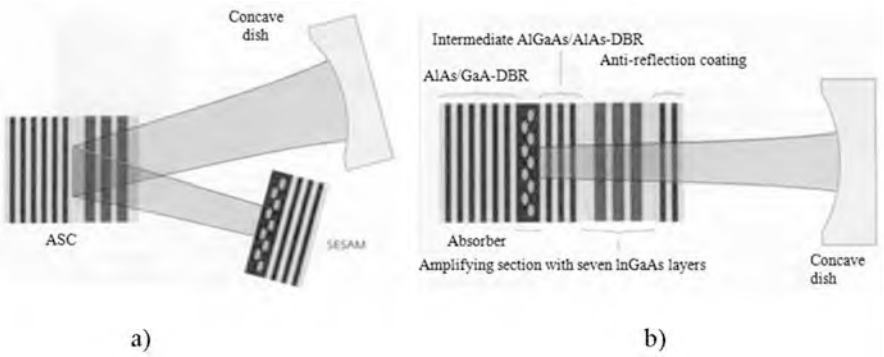

Fig. 11.25 Operating principles of the passive generation VECSEL circuit with passive mode synchronization: (**a**) VECSEL- SESAM; (**b**) MIXSEL

inserted in low-temperature GaAs layers; intermediate AlGaAs/AlAs-based DBR preventing absorption of the pumping signal in the absorption section; amplifying section with seven quantum-dimensional InGaAs layers; anti-reflecting coating, which ensures optimal distribution of the fields of amplification and absorption section fields.

Studies and developments of VECSEL-SESAM and MIXSEL in recent years mostly have taken place in the directions of finding ways of increasing mean radiation power, reducing the duration of the optical pulse and advancement of repetition frequency into the microwave range, which is a necessary condition for the use of these lasers in radiophotonic devices. In circuit 11.25, a, the effect of application of epitaxial layers based on quantum wells (QW) and quantum dots (QD) in VECSEL structures (in ASCs) and in SESAM structures was studied. Results of measurement at repetition frequencies from 2 to 50 GHz [46, 48] (Fig. 11.26) make it possible to draw the following conclusions. MIXSEL ensured the highest average radiation power (up to 6.4 W), but the pulse duration exceeds 20 ps, which is unsuitable for most radiophotonic devices. Pulses with duration under 200 fs at average power of about 20 mW is ensured by using QW layers in both elements of the laser with ASC. Parameters optimal for use in radiophotonics (pulse duration under 1 ps, average power of 100 mW – 1 W) is achieved by implementing both elements on the base of QD layers. However, further improvement of operation of the MIXCEL circuit made it possible to achieve even more advanced results [49]: duration of pulses of 570 fs in the repetition frequency range of 5–101 GHz at average power of 127 mW.

All the above experimental data were obtained for short-wave lasers, the studies of which are most extensive. There are much less publications dedicated to longwave MIXSELs, and the results described in them are significantly more modest. From the technological point of view, alloyed structure is considered promising here, like in VCSEL (Figs. 11.2, and 11.3) and in ASC of high-power continuous-generation VECSEL (Fig. 11.15) [50]. An example of such laser is the longwave VECSEL-SESAM of the Z-shaped configuration using optical pumping [50] (Fig. 11.27a). For

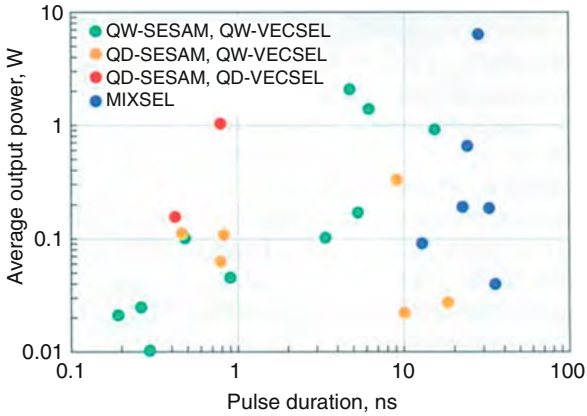

Fig. 11.26 Results of experimental study of shortwave VECSEL-SESAM and MIXSEL [1]

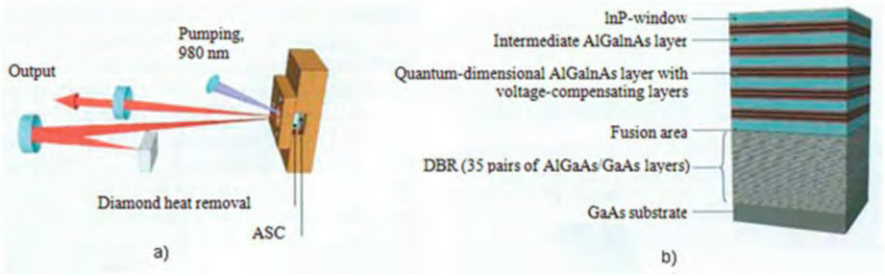

Fig. 11.27 Draft of a longwave VECSEL-SESAM: (**a**) Z-shaped configuration with the use of optical pumping; (**b**) ASC design [1]

this VECSEL-SESAM, a special ASC was designed (Fig. 11.27b), in which the active region grown on InP substrate with the help of the unit for metal-organic vapor-phase epitaxy is alloyed with the DBR grown on GaAs substrate with the help of molecular beam epitaxy unit. During the experimental study, ASC temperature was maintained at the level of 15 °C by means of water cooling; SESAM temperature – at the level of 21 °C by means of TEMC. The following results were obtained by measurements: pulse duration – 6.4 ps at average radiation power of about 100 mW and pumping power of about 9 W. Repetition frequency determined by total cavity length (Fig. 11.27a) amounted to 950 MHz. Higher repetition frequency was achieved during experiments with C-range MIXSELs [51] (Fig. 11.28). The circuit includes ASC with hybrid metamorphic mirror optimized for high radiation power at room temperature and quick SESAM based on InCaAsN/GaAsN, which helped avoid the need to use water cooling. As follows from the experimental data, duration of the pulse was at the level of 1.7 ps, which conforms to general width of the MIXSEL signal spectrum equal to 2.29 nm (about 300 GHz), pulse repetition frequency is 2 GHz, and the width of the generation line characterizing noise properties of the device does not exceed 1 kHz.

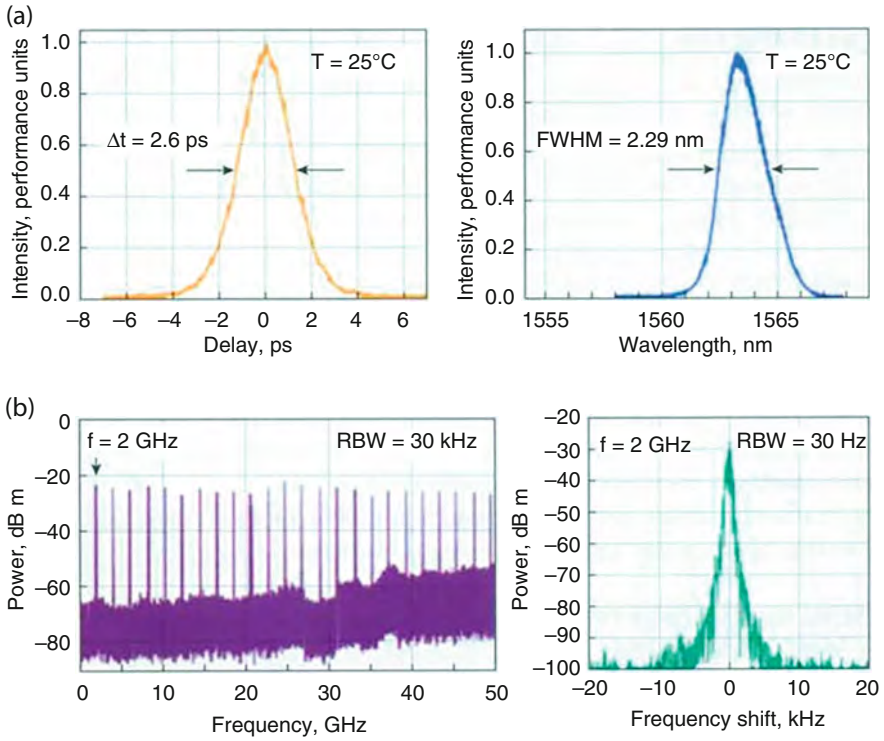

Fig. 11.28 Results of experimental study of C-range MIXSELs: (**a**) autocorrelation function (left), Fourier spectrogram (right); (**b**) radio frequency spectrum of pulse sequence (left), first harmonic spectrum (right). FWHM – half-level spectrum width; RBW- pass band resolution

Therefore, there are many VCSEL-based devices that are widely applied in optic fiber and radioelectronic equipment.

11.6 Main Directions of Fundamental Studies in the Field of Component Base of Radiophotonics and Functional Devices Based on It

Development of radiophotonics is one of the most important scientific and technological priorities in development of electronic and radioelectronic industry. However, implementation of practical requirements of this priority direction requires performance of complex fundamental theoretical and experimental studies aimed both at modernization of the existing national component base of photonics and at creation of the specialized optical component base of radiophotonics. Especially interesting is the so-called standard range (C-range) with wavelengths of

1530–1565 nm, which corresponds to one of transmission windows of optical fibers. This field is developing more and more actively as a separate interdisciplinary scientific, technical and technological area, which is confirmed by the rapid increase in the number of publications (over 100,000 during the last 5 years according to IEEE Xplore Digital Library).

Performance of fundamental studies will provide a basis for creation of new systems of radiophotonics and their introduction into such fields of industry as telecommunications, radar location and electronics, which are important for increasing technological independence of safety of any state.

The *main directions* of these studies shall be presented:

1. Mathematical modeling and experimental verification of advanced radiophotonic devices: low-noise optoelectronic generators of microwave signals tunable in a wide band; optoelectronic mixers and frequency converters of the microwave range; optical filters with modulation band in the microwave range;
2. Fundamentals of creating edge-emitting and surface-emitting lasers with wavelengths of 1530–1565 nm and functional devices based on these lasers;
3. Highly effective, highly stable, tunable, highly coherent laser structures, radiators and models with the modulation band in the microwave range (including the ones with injection synchronization);
4. Highly stable small-sized laser generators of super-short pulses with repetition frequency in the microwave range;
5. Modeling and verification of photo detectors in the C-band with forward, reverse and side flashes and functional devices based on these photo detectors: spectral-selective, highly-linear photo-detection structures and modules with the pass band in the microwave range;
6. Physical basics of creating the new generation of ultra-high-speed optical switches and modulators at the wavelengths of the C-band of interferometric and absorption types in integrated version: ultra-high-speed optical switches; optical modulators of radiation intensity with the modulation band in the microwave range and low half-wave voltage; phase and vector optical modulators with the modulation band in the microwave range; optical modulators based on new materials and structures, including polymeric and plasma modulators;
7. New methods of creation and diagnostics of the optic fiber component base in the C-range and functional devices based on it: high-dispersion and multi-core fiber; aniso-periodic fiber Bragg lattices; high-efficiency fiber amplifiers; low-noise fiber laser generators.

11.7 Examples of Use of Radiophotonic Devices in Radar Location

Radiophotonics, which studies interaction between optical and microwave signals, helps create electronic devices with parameters that cannot be achieved by traditional means. Ultra-wideband analog optic fiber communication lines, delay lines, as well

as elements of radiophotonics, filters, generators and other microwave devices with radiophotonic elements are applied in systems of electronic warfare and countermeasures and in radar stations [1]. For example, the article [52] examines practical experience of development of a number of radiophotonic devices to be used in radar equipment.

Let us list the main advantage of radiophotonic devices once again:

- Extremely low losses and dispersion of the optic fiber (less than 0.2 dB/km at 1550 nm, optical carrier ~200 THz).
- Ultra-wide band (available frequency band of optic fiber ~50 THz, frequency band of modern photodiodes and modulators – 100 GHz and higher).
- Low level of phase noise (the process of direct optical detection with the help of a photodiode is immune to the phase of optical radiation – phase and phase noises of the optical carrier).
- High phase stability of optic fiber. Resistance to electromagnetic interference; no interferences introduced.
- Galvanic isolation of photonic circuits.
- Small weight and dimensions of optical fiber.
- Mechanical flexibility of the optic fiber (simplifies the structural design).
- Main problems of radiophotonic devices:
- Amplitude noise and attenuation introduced by modulation-demodulation of the optical signal (noise factor of the channel usually amounts to 10–30 dB, attenuation – up to 30 dB, which calls for the use of low-noise amplifiers at the input and linear amplifiers at the output with all their disadvantages).
- Limited dynamic range caused by non-linearity of optical modulators and direct current modulation of semiconductor lasers.
- Let us consider examples of practical implementation of certain radiophotonic devices [1, 52].

11.7.1 Active Delay Lines

An active delay line includes: an optical radiation source (semiconductor laser), radiation of which is modulated by the HF signal, an optic fiber coil of the required length and a photo receiver detecting the delayed optical signal. In case of necessity to compensate attenuation of the signal introduced by modulation/demodulation of the optical signal and attenuation in the fiber, transistor amplifiers for the required frequency band are added in the path.

Characteristics of a switched delay line for 16 positions [52] can be presented as an example.

Main characteristics:

- Quantity of optical delay lines: 16.
- Signal delay value – 26.7 ns – 9.9867 μs.
- Frequency band: 0.01 ÷ 14 GHz.

– Input microwave signal power: up to 5 MW.
– Attenuation of the SHF signal between input and output: 40 dB max
– Irregularity of the SHF signal transmission coefficient in the working frequency band: 5 dB max.
– Error of microwave signal delay: ±2.5 nm.
– Temperature coefficient of delay time change: not more than 5×10^{-6}/°C.
– Delay time control: manual or by binary code of TTL levels.
– Switching time of delay lines: under 10 ms.
– Power consumption of the supply circuit: 30 W max.
– Overall dimensions: 368 × 200 × 150 mm.
– Operating temperatures range: 10–35 °C.

Figure 11.29 shows frequency characteristics measured during switching of the delay from zero (initial) to 9.9867 μs; Fig. 11.30 – its photographs.

Since this device was designed for metrology tasks only, amplifiers were not used in its path, and the operating frequency band was limited by characteristics of analog optoelectronic modules.

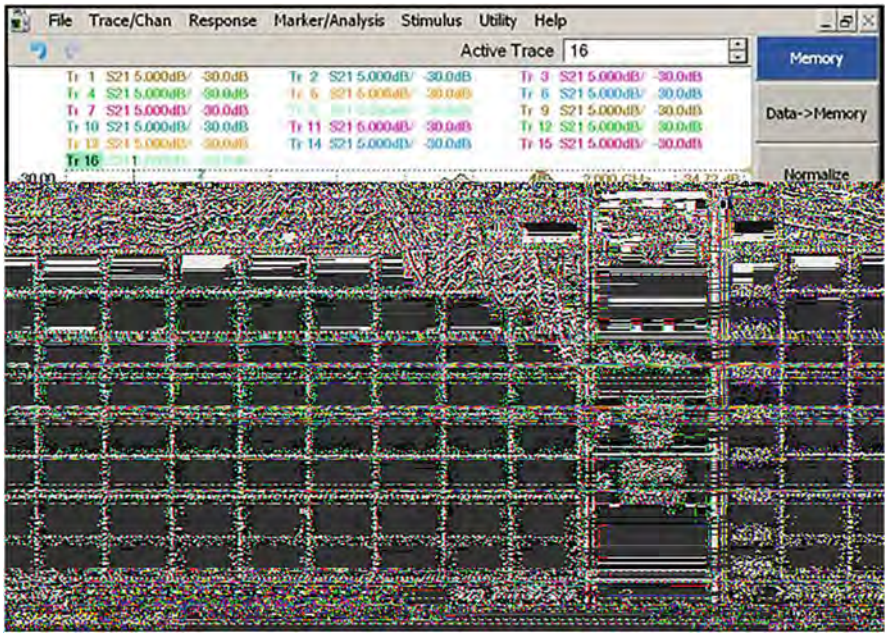

Fig. 11.29 Frequency characteristics of the switched delay line [52]

Fig. 11.30 Photographs of the switched delay line: general appearance and with cover removed [52]

11.7.2 Channels for Long-Distance Transmission of Microwave Signals

Figure 11.31 [1] shows structural diagram of the optic fiber path for transmission of X-band analog signals for 50 km (Figs. 11.32 and 11.33).

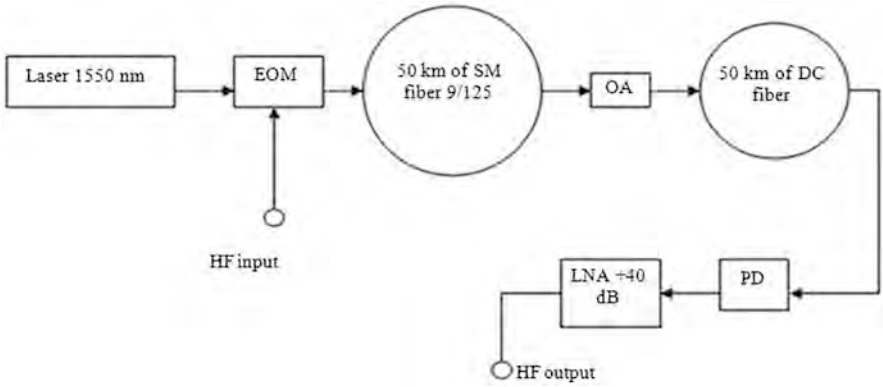

Fig. 11.31 Structural diagram of the path of transmission of X-band analog signals for 50 km: *EOM* electro-optical modulator, *SM* single-mode fiber, *OA* optical amplifier, *DC* dispersion-correcting fiber, *PD* photo detector, *LNA* low-noise microwave amplifier [52]

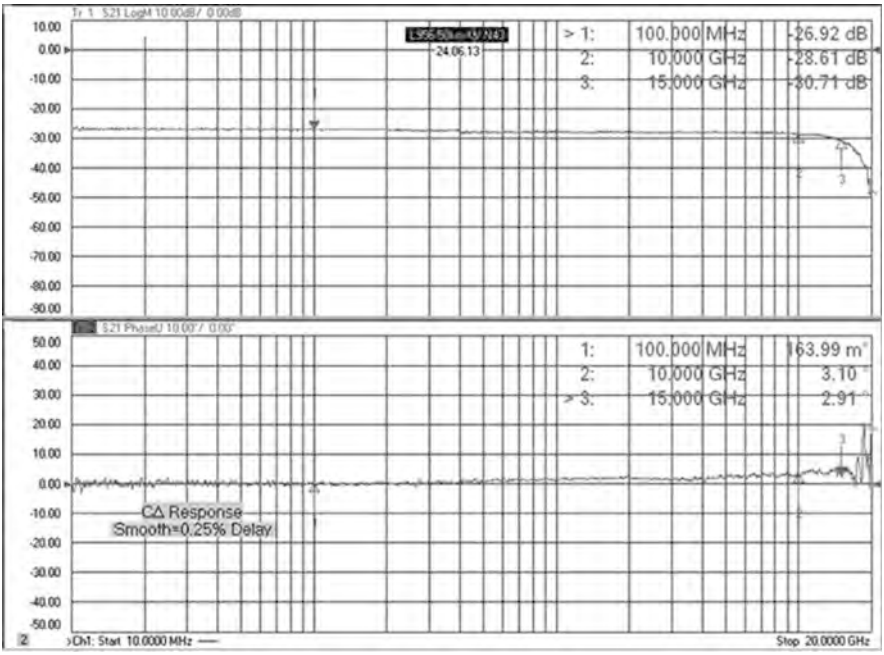

Fig. 11.32 AFCs and PFCs of the analog path with dispersion compensation in a wide frequency range with wide-band photo receiver (without LNA) [52]

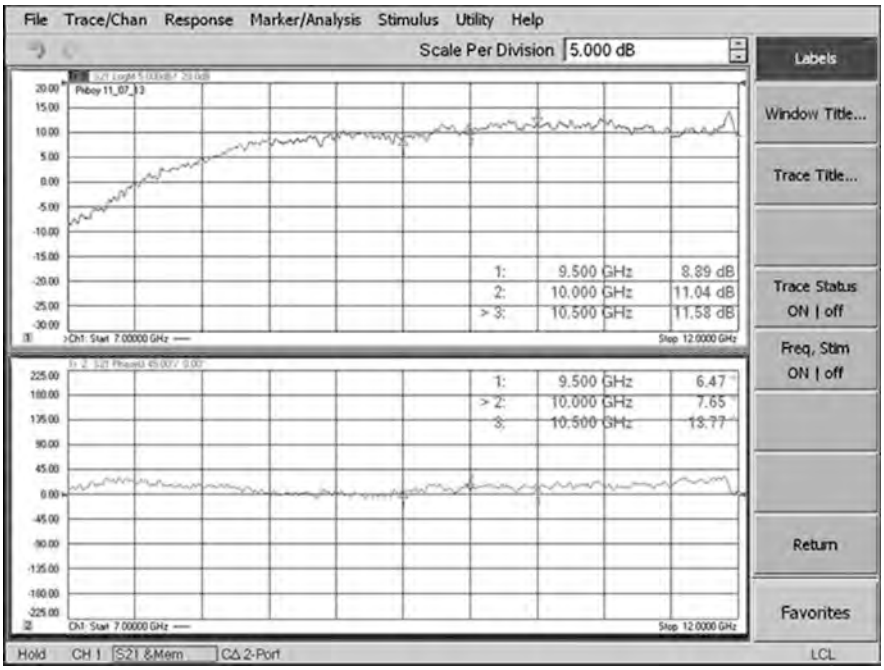

Fig. 11.33 Measurements of AFCs and PFCs of the full analog path in the frequency band of 9.5 ÷ 10.5 GHz (with LNA) [52]

11.7.3 Systems of Distribution of Radio Signals over Radar AESA Curtain (Figs. 11.34, 11.35, 11.36, and 11.37)

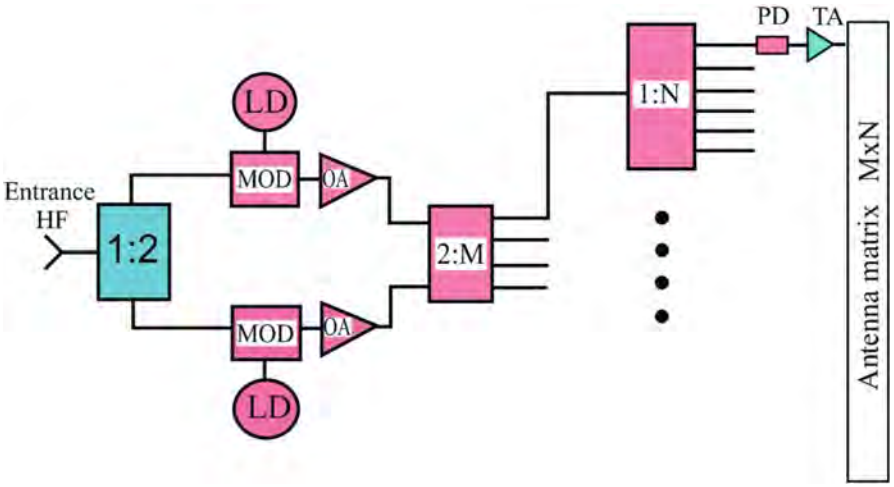

Fig. 11.34 Structural diagram of the system for distribution of radio signals across the radar antenna curtain: 1:2 – HF splitter for main and backup channels; *LD* laser diode, *MOD* optical modulator, *OA* optical amplifier, *2:M* optical splitter for M outputs, *1:N* optical splitter for N outputs, *PD* photodiode, *TA* transistor amplifier [52]

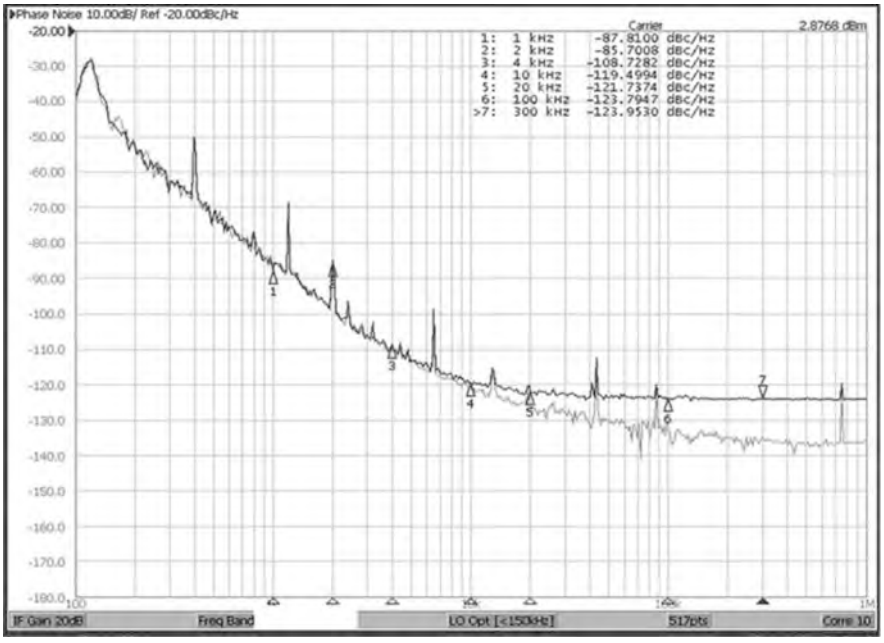

Fig. 11.35 Phase noises of a radar transmitter: lower curve – at the input of the distribution system, upper curve – at the output of the distribution system (MxN = 128) [52]

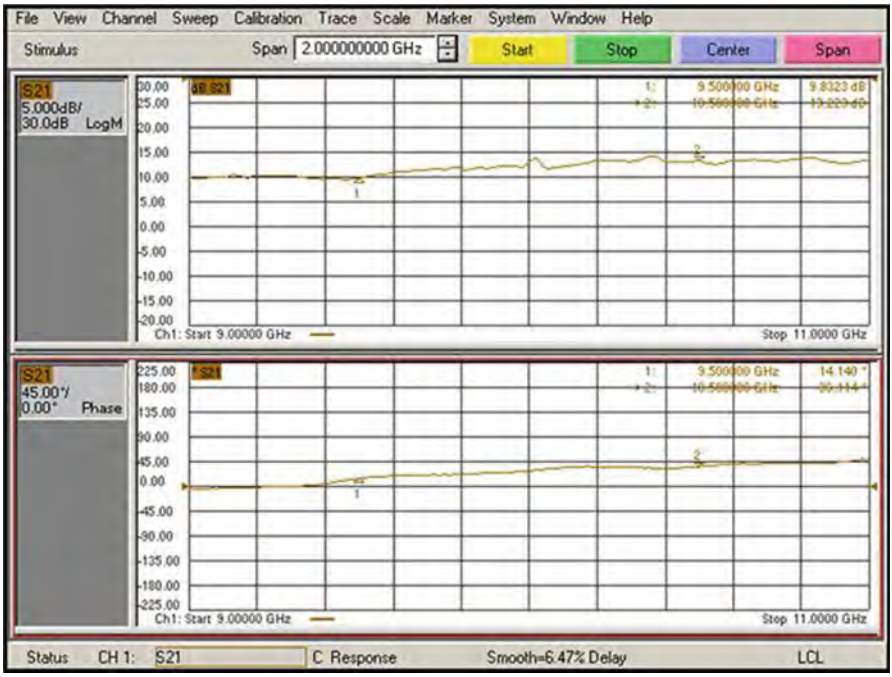

Fig. 11.36 AFCs and PFCs of the system of distribution of the X-range for 128 outputs [52]

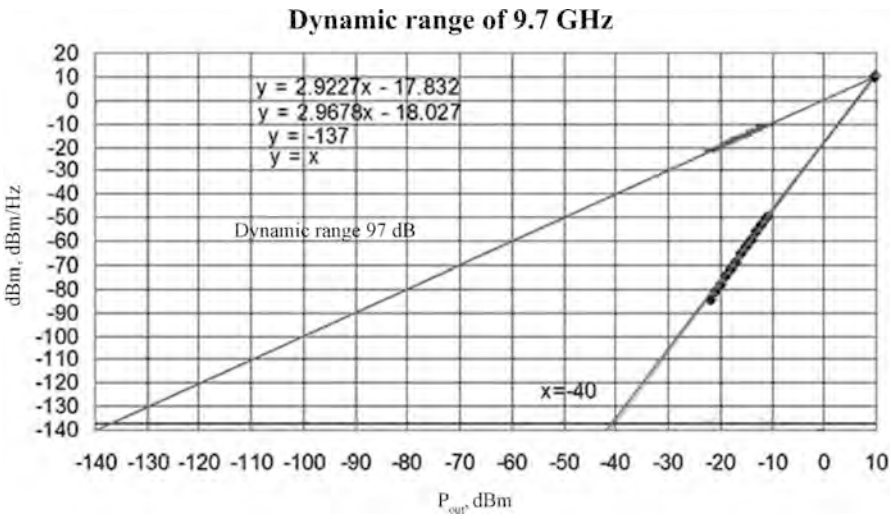

Fig. 11.37 Dynamic range of the system of signal distribution across PAA of the X-band free from products of the third order in the 1 GHz band [52]

11.7.4 Measurement and Calibration Means for Radar Sets

In this section, it is necessary to mention specialized measurement and calibration means for radar equipment [1].

An example of implementation is the engineering prototype of the stand for measurement of radar parameters without airing in field or workshop conditions. This stand makes it possible to significantly simplify and reduce cost of setting, inspection and attestation of the radar [1, 52]. Structure of the stand is shown in Fig. 11.38.

Basic technical specifications of the stand:

– Frequency band of the SHF signal	9–11 GHz;
– Microwave signal delay time	67.765 μs;
– AFC irregularity in the band of в 9÷11 GHz	not more than 5 dB;
– PFC non-linearity in the band of 9÷11 GHz	±10 deg.;
– VSWR at the modulator input	2.3 max;
– VSWR at the modulator output	1.5 max;
– Transmission coefficient	not more than −10 dB;
– Maximum permissible level of the input signal	100 mW;
– Supply voltage	21÷29 V DC;
– Current consumption	1.5 A max;
– Length of optical cable on the coil	160 m;
– Readiness time (from the moment of power supply)	15 s;
– Operating frequency range	–30 to +50 °C.
– Dynamic range free from products of intermodulation of the third order	
– 1 dB cut of the transmission coefficient corresponds to the input signal level of at least	100 mW.

Figure 11.39 shows frequency characteristics of the stand, Fig. 11.40 – photographs of its main units: optical receiver unit, optical transmitter unit with delay line, optic fiber coil.

The presented examples demonstrate that, despite extremely limited range of photonic element in the Russian market, many tasks of radar location equipment can already be successfully solved by methods of radiophotonics.

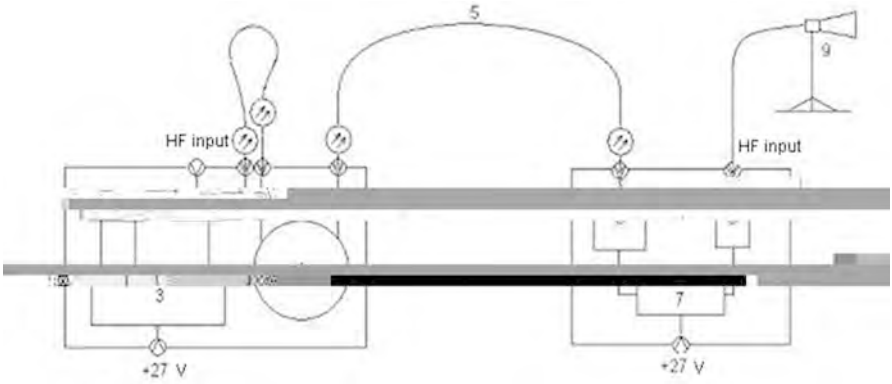

Fig. 11.38 Structural diagram of the stand: 1 – laser; 2 – modulator; 3 – circuit of stabilization of laser and modulator modes; 4 – optic fiber delay line for 67.765 μs; 5 – optical cable, 160 m; 6 – photo receiver; 7 – amplifier; 8 – ferrite isolator; 9 – horn antenna

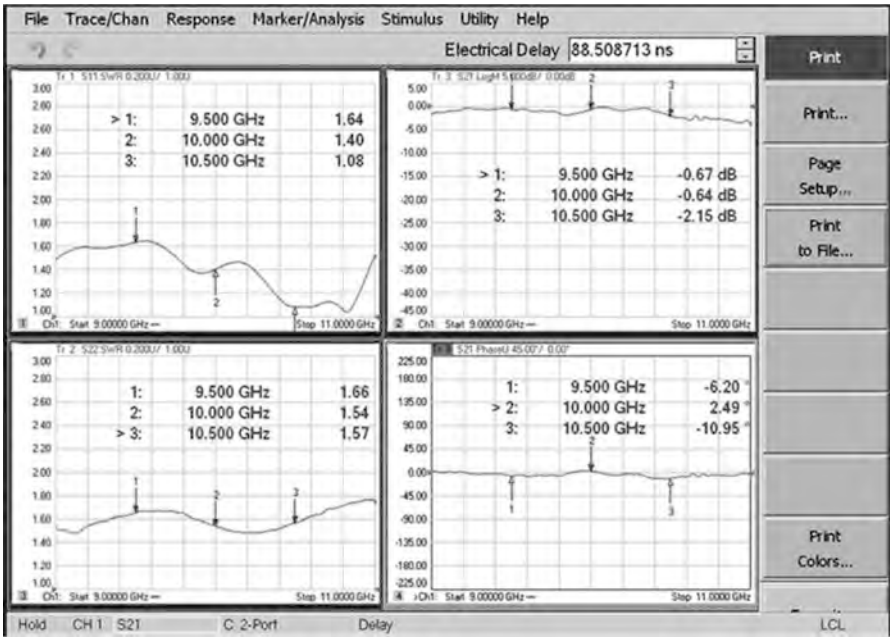

Fig. 11.39 Frequency characteristics of the analog path of the measuring stand [1]

Fig. 11.40 Photo of stand units: optical receiver unit; optical transmitter unit with delay line; optic fiber coil (tripod with horn antenna is not shown) [1]

11.8 Microwave Photodetectors for Radiophotonics, Radar Location and Optic Fiber Communication Systems

11.8.1 Physical Principles of Operation of Microwave P-I-N Photoelectric Detectors

As noted in the beginning of this chapter, a new field of science and technology, known as microwave photonics (radiophotonics) was created in recent years [53]. Synthesis of optoelectronic technologies of data processing and transmission with the possibilities of microwave electronics helped achieve brand new possibilities for processing and conversion of SHF signals in communication devices and radar systems with active electronically scanned arrays [54–57]. Building of devices using radiophotonics technologies requires laser emitters, optical modulators, phase shifters, splitters and duplexers, diffraction elements and powerful high-speed photodetectors.

In such system, the transmitter coverts the electric signal into optical signal, which is later processed by optoelectronic circuits and sent via optic fiber cable to the photoreceiver at the end point, which converts the optic signal into electric signal.

Greatest attenuation of the optic signal in modern optic fiber cables is observed near the wavelength of 1.55 μm, which determines the use of lasers with radiation waves of this length and optic signal receivers based on high-quality semiconductor materials with high absorption coefficient near 1.55 μm [58].

In radiophotonic systems based on optic fiber amplifiers, the power of optical radiation incident on the photosensor is higher than in regular optic fiber

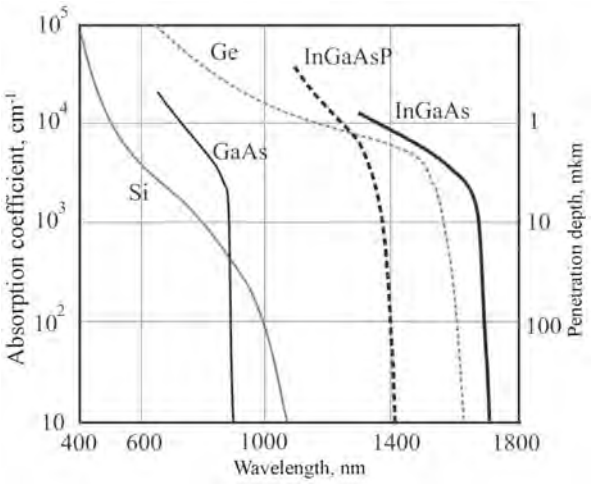

Fig. 11.41 Absorption coefficients of semiconductor materials based on [59]

communication systems by two or more orders of magnitude, which requires significant expansion of the linear range of photosensors (increase in the saturation photocurrent). Photosensors with high saturation current (high-power photosensors) are capable of producing electrical microwave signal with the amplitude of about 1 V at frequencies of 10–100 GHz, which is sufficient for direct control (without microwave amplifiers) of the downstream microwave circuit. The use of photosensors with high saturation photocurrent expands the dynamic range, reduces losses and noise factor of analog waveguide-optical transmission lines of microwave signals.

High-power photodetectors can also be used as frequency-tuned SHF oscillators. In this regard, determination of the main physical regularities and characteristic process features determining the possibility of creating high-power microwave photodetectors is a relevant and important task.

Figure 11.41 shows spectral absorption values for semiconductor materials ensuring absorption of infrared radiation with wavelengths up to 1.7 μm. The figure shows that germanium and solid InGaAs solutions have high absorption values near 1.55 μm. Direct-band solid $In_xGa_{1-x}As$ solution with indium contents of $x = 0.53$ has higher absorption coefficient ($\alpha = 0.705\ \mu m^{-1}$) at wavelength of 1.55 μm and lower individual concentration of charge carriers than indirect-band germanium ($\alpha = 0.4\ \mu m^{-1}$). Therefore, most popular are photo detectors based on solid $In_{0.53}Ga_{0.47}As$ solutions matched in terms of constant of the crystalline lattice with InP structure, which is important for epitaxial growth of fault-free heterostructures ensuring low dark currents of the photo receiver at high breakdown voltages [59].

As a rule, developers of microwave systems use photodiodes (PD) as microwave photodetectors; in these diodes, carriers photogenerated in the absorption region are separated under the effect of strong magnetic field, and signal current or voltage is produced in the external circuit as a result. The following types of photodiodes are most popular: p-n-PD, p-i-n-PD, PD with Schottky barrier and avalanche

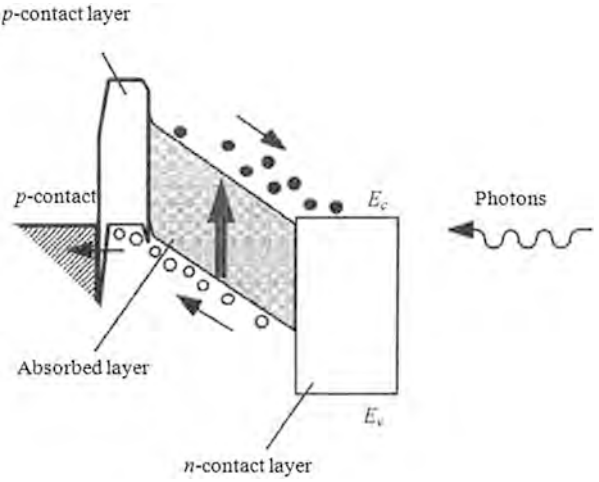

Fig. 11.42 Power diagram of a traditional p-i-n-photodiode [1]

PD. Currently, p-i-n-PDs and their modifications are most widely used in analog optic fiber lines.

The aim of this section is to describe basic physical principles of operation of microwave SHF p-i-n PDs, analyze physical phenomena limiting characteristics of these devices and review the latest achievements in the field of InGaAs-based p-i-n PDs structures used in analog optic fiber communication lines.

Energy diagram of a traditional p-i-n-PD based on double heterostructure at reverse displacement is shown in Fig. 11.42. The photodiode consists of heavily doped contact p + − and n + regions of wide-gap material (InP) and narrow-gap non-doped absorbing layer (i-InGaAs). Usually, reverse voltage is supplied to PD, which ensures full depletion of the absorbing layer. Under excitation by light with wavelength of 1.55 μm, electron-hole pairs are generated in the absorbing layer, which are divided by the electrical field and form the photocurrent I_{Ph} defined as [60]:

$$I_{ph} = \frac{\eta q}{h\nu} P_{opt}. \tag{11.1}$$

where η ισ τηε quantum efficiency, q ισ τηε electron charge, h ισ τηε Planck's constant, v ισ τηε frequency of light, P_{opt} ισ τηε incident optical power. Quantum efficiency, in turn, can be expressed as follows:

$$\eta = (1 - R)\left(1 - e^{-\alpha d}\right), \tag{11.2}$$

where R ισ τηε reflection coefficient, α ισ τηε light absorption coefficient, d ισ τηε thickness of the depleted region.

It is generally accepted that the threshold frequency of the photo receiver is determined by 3 dB reduction in the amplitude-phase characteristic. Regardless of

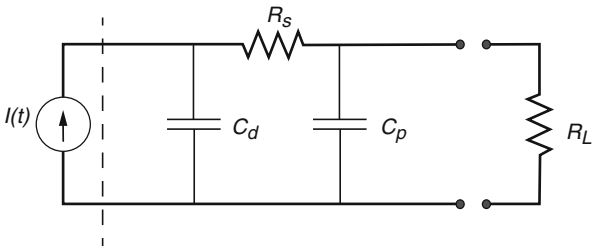

Fig. 11.43 Simplified equivalent circuit of a p-i-n-PD

the p-i-n PD material, there are several basic factors that limit the speed of its operation. They include the time of flight of charge carriers in the depleted region, time constant τ_{RC}, diffusion current and concentration of charge carriers accumulated at the boundaries of hetero junctions forming the barriers [61]. Time of flight of charge carriers is set by the drift time of charge carriers through the absorbing layer, mostly by the drift time of holes, since their drift speed is usually lower than the drift speed of electrons. Time constant τ_{RC} is determined by the parameters of the equivalent *RC*-circuit of the photodiode (Fig. 11.43), which include serial resistance R_s, enabling resistance of contacts, load resistance R_L, diode capacity C_d and parasite capacity C_p. Diffusion current shall be taken into account in homo-transitional structures, when charge carriers generated during light absorption in p + − and n + −contact regions diffuse into the absorbing layer for the value of diffusion length and contribute to the general photocurrent of the photodiode. The criterion of domination of drift transfer as compared to diffusion transfer is [61].

$$E >> \frac{kT}{q} L_e,$$

where E ισ τηε electrical field in the absorbing layer, k ισ τηε Boltzmann factor, L_e ισ τηε diffusion length of electrons. In p-i-n-PDs based on homo junction structures, the diffusion current component is lower that the drift component and introduces certain stretching in the time of pulse response of the photodiode. In case with p-i-n-PD based on double InP-InGaAs-InP heterostructure, diffusion current can also be disregarded, since there is no absorption in the wide-gap contact region n + -InP. On the other hand, presence of barriers at the borders of heterostructure can lead to accumulation of charge, which reduces electrical field in the absorbing layer and subsequently reduces the speed of operation of the photodetector. This problem can be solved by growing layers or super-lattices with gradient composition [62].

If the time of flight of charge carriers and the time constant τ_{RC} do not depend on each other, and diffusion current and charge accumulation of hetero-barriers can be disregarded, then the boundary frequency f_{3dB} can be expressed as follows [1, 63–65]:

$$\frac{1}{f_{3dB}^2} = \frac{1}{f_t^2} + \frac{1}{f_{RC}^2}, \tag{11.3}$$

where frequency f_t is determined by the time of flight, f_{RC} – by the time constant τ_{RC}. In turn, f_t can be recorded as [65]:

$$f_t = \frac{3,5\nu}{2\pi d}, \tag{11.4}$$

where v is determined as:

$$\frac{1}{\nu^4} = \frac{1}{2}\left(\frac{1}{\nu_e^4} + \frac{1}{\nu_h^4}\right), \tag{11.5}$$

where v_e and v_h are drift speeds of electrones and holes respectively. For InGaAs, typical values close to saturation are $v_e = 6.5 \times 10^6$ cm/s and $v_h = 4{,}8 \times 10^6$ cm/s [65]. Since mobility of holes is lower than mobility of electons, their drift speed is what limits frequency properties of a p-i-n-PD.

If we disregard the parasite capacity C_p (Fig. 11.43), then the component of the boundary frequency related to the time constant τ_{RC} can be recorded as:

$$f_{RC} = \frac{1}{2\pi(R_L + R_S)\, C_d}, \tag{11.6}$$

here, diode capacity $C_d = \varepsilon A/d$ is determined by parameters of the material (ε – dielectric permittivity, d – thickness of the depleted region of the absorbing layer) and A – area of the photo receiver. Load resistance R_L usually amounts to 50 Ohm; serial resistance R_s shall be much lower than R_L.

The contribution of the time of flight and time constant τ_{RC} in the boundary frequency of an InGaAs-p-i-n-PD was calculated in [66]. Figure 11.44 taken from this paper demonstrates dependencies of the boundary frequency on the thickness of depleted (absorbing) region at different values of the PD window radius, i.e. capacity of the devices. In the calculation, it was suggested that $R_L = 50$ Ohm, $R_s = 10$ Ohm, radius of the photodiode window varies within the range of $r = 10$–80 μm, and the thickness of the absorbing layer d varies within 0.1–3.5 μm. According to these calculations, in order to achieve high speed of a PD, it is necessary to reduce thickness of the absorbing layer and the area of the window. Thus, the value of thickness of the absorbing layer is a certain compromise between thickness ensuring high quantum efficiency and thickness that allows to achieve high boundary frequency of the PD. As a rule, boundary frequency of a p-i-n-PD with traditional design is $f_{3dB} = 20$ GHz [66].

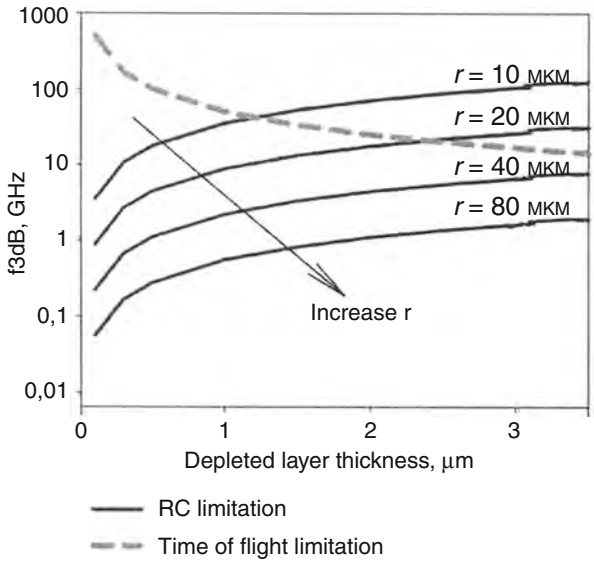

Fig. 11.44 Contribution of the time of flight and the time constant τ_{RC} to boundary frequency in case of variation of the window radius (r) in InGaAs p-i-n-PD [66]

11.8.2 Physical Mechanisms of Limiting Photocurrent of a P-I-N-Photodiode

There are two main reasons limiting photocurrent of p-i-n-PDs with an increase in the optical signal power: (a) spatial charge effect causing saturation of photocurrent and caused by the effect of photogenerated charge carriers on spatial distribution of the electrical filed in the absorbing layer [67–71], and (b) self-heating effect caused by PD heating due to the flow of high density of photocurrent [71–76].

With low density of optical radiation, concentration of photogenerated mobile charge carriers is much lower than the concentration of background impurity atoms, which is distributed in the absorbing layer in a fairly uniform manner. Therefore, electrical field in the absorbing layer is uniform and determined by concentration of ionized impurity atoms. As the optical power increases, concentration of photogenerated charge carriers becomes greater than the concentration of impurity. Due to the differences in the drift speeds of electrons and holes, they are distributed unevenly in the absorbing layer and sihled the original electrical field, distorting its distribution. In [71], K. Kato calculated charge density in the absorbed layer for holes and electrons (Fig. 11.45). The following data were taken for calculation: thickness of the absorbing layer was $d = 0.2$ μm, applied voltage $U = 1.5$ V, background doping level $N_i = 10^{15}$ cm^{-3}, drift speeds of electrons and holes close to saturation $v_e = 6.5 \times 10^6$ and $v_p = 4.8 \times 10^6$ cm/s, respectively.

As can be seen from Fig. 11.45, concentration of holes near p + region is higher than concentration of electrons near n + region due to the drift speed of holes being lower than the drift speed of electrons. As a result, total current density is not

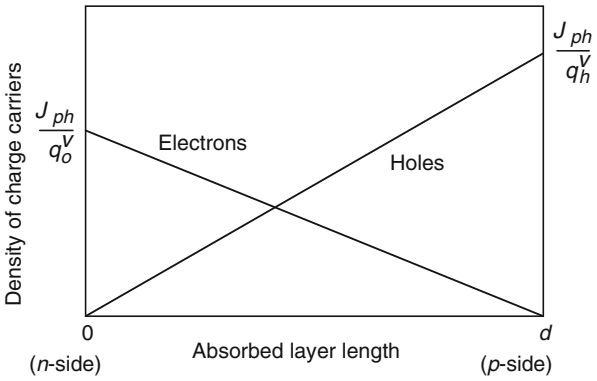

Fig. 11.45 Density of charge carriers in the absorbed layer of a p-i-n-PD at high optical power

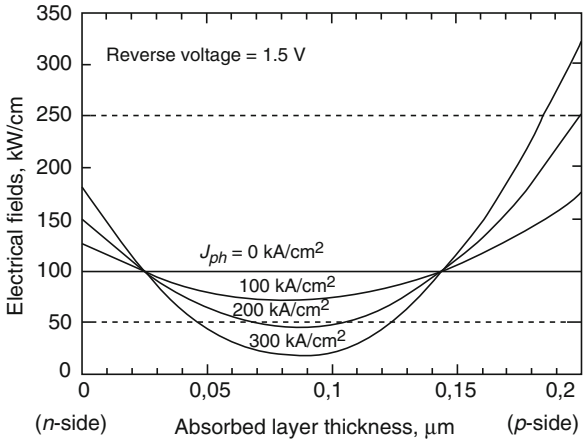

Fig. 11.46 Electrical field profile at different densities of photocurrent in a p-i-n-photodiode [1]

constant at each point of the absorbing layer and higher near the p + − region, which leads to a distortion in the electrical field profile.

Distribution of electrical field in the absorbing layer for different photocurrent densities is shown in Fig. 11.46 [71]. It can be seen that irregularity in the electrical field strength increases together with photocurrent density. Electrical field strength is reduced near the middle of the absorbing layer, which reduces drift speeds of holes and electrons and, as a result, causes reduction in the boundary frequency of the PD.

In order to calculate the maximum permissible optical power (max P_{opt}) or maximum value of photocurrent (max I_{ph}) at which linearity of the photo response is preserved, it is necessary to solve a system of non-linear equations of continuity and full current and Poisson's equations [77]. The paper [78] suggests a simple method of assessing the value max I_{ph} based on the order of magnitude:

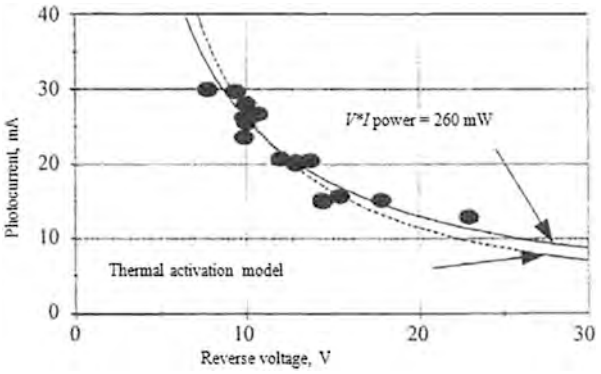

Fig. 11.47 Measured values of photocurrent of a p-i-n-PD on voltage during permanent flashing; dots are used to indicate photocurrent values during thermal breakdown [75]

$$\max j_{ph} = \mu_n \frac{\varepsilon V^2}{d^3} = \mu_n \frac{C_{d0}^3 V^2}{\varepsilon^2} \tag{11.7}$$

where max j_{ph} = max I_{ph}/A and C_{d0} = C_{d}/A = ε/d αρε maximum density of photocurrent and specific capacity of the p-i-n-PD respectively, A ισ τηε photodiode area, s ισ τηε dielectric permittivity of the semiconductor. Saturation of real p-i-n-PDs at the frequency of 20 GHz usually occurs at the photocurrent level max j_{p} = 10–20 mA [67].

If the applied voltage is equal to zero, the effect of space charge is maximum [70]. Due to this reason, displacement voltage shall be selected based on the condition of full depletion of the absorbing layer. With an increase in the applied reverse voltage, the effect of space charge is slightly weakened, but there is a possibility of electrical breakdown (collision ionization) due to high strength of the electric field in the depleted area [71] or thermal breakdown due to self-heating [74, 75].

Joule heating is determined by serial connection of contacts and density of photocurrent and is limited by thermal conductivity of the material and its geometry [72]. Papers [71–73] present numerical modeling of dissipation of thermal power of p-i-n-PDs at high values of optical radiation. Increased temperature can cause failure of the p-i-n diode (thermal breakdown) due to thermal activation of dark current. In [75], simple model of thermal dependence of dark current was used, and thermal displacement was associated with diode heating power IxV during reverse displacement. General PD current in case of temperature variation was recorded as [1]:

$$I = I_{ph} + I_0 \exp\left(\frac{-\Delta E}{k(T_0 + VIR_{Total})}\right), \tag{11.8}$$

where ΔE ισ τηε is the energy of the In-GaAs gap width, R_{Total} ισ τηε thermal resistance measured in deg./W. Figure 11.47 shows the experimentally measured dependence of photocurrent on voltage of different p-i-n-PDs, where dots are used to

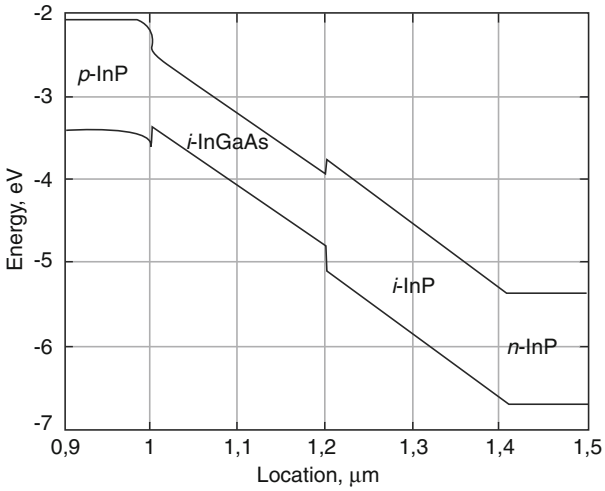

Fig. 11.48 Energy diagram of a DDR PD

indicate photocurrent values during thermal breakdown; full curve is built in accordance with the expression (11.8).

More effective heat removal from the depleted region of the p-i-n-PD leads to an increase in the maximum photocurrent [76]. For example, if epitaxial layers of InGaAs/InP are grown directly on silicon substrate with high thermal conductivity, such heterostructure will make it possible to improve heat removal from the active PD region [79]. Another approach – PD mounting by flip-chip method on thermally conductive AlN substrate, which also reduces thermal resistance of the PD significantly [80].

Therefore, the most advanced designs of p-i-n-PD providing low inertia and expanded dynamic range of photoresponse, shall ensure equal time of flight of charge carriers in the absorption region or transmission of the signal by one type of charge carriers with high mobility (usually by electrons) and efficient heat removal.

11.8.3 Design Features of Photodiodes

11.8.3.1 Double Depletion Region Photodiode

In this structure of the p-i-n-PD suggested by Effenberger и Joshi [81], depleted layer consists of two parts (Double Depletion Region): absorbing and drift InGaAs layer and additional dirft wide-gap InP layer (Fig. 11.48). Photogenerated holes move only in the InGaAs layer; photogenerated electrons pass two layers – InGaAs and InP. Since the drift speed of electrons is higher than drift speed of holes, in order

to balance the times of flight of electrons and holes and reduce the effect of spatial charge, it is necessary to increase the span of electrons, i.e. the thickness of the InP layer. In [82], boundary frequency $f_{3dB} = 65$ GHz was achieved at DDR p-i-n-PD with the diameter of photosensitive area of 10 μm; with the diameter of 30 μm, high sensitivity (0.67 A/W) was achieved with boundary frequency $f_{3dB} = 12$ GHz in conditions of high linearity of photocurrent from the optical radiation power [83, 84]. The paper [85] presents numerical modeling of frequency characteristics of the heterostructure for DDR p-i-n-PD and defines the best thickness values of absorbing (0.42 μm) and drift (0.58 μm) layers for boundary frequency of 25 GHz.

11.8.3.2 Photodiode with Partially Depleted Absorber (PDA)

In heterostructures with partially depleted absorbers, the energy diagram of which is shown in Fig. 11.49, spatial charge effect is diminished by reducing thickness of the i-InGaAs drift layer and balancing of electron and hole streams in this layer. For this purpose, additional absorbing layers InGaAs of p-type and n-type conductivity are included in the heterostructure [86]. When PDA p-i-n PD is illuminated, photogenerated electrons and photogenerated holes are injected from the absorbing p-InGaAs layer into i-InGaAs and n-InGaAs layers respectively. With the thickness of the n-InGaAs greater than the thickness of the p-InGaAs layer, the flow of electrons is greater than the flow of holes [87]. Advantages of PDA p-i-n-PDs consist in the fact that at low reverse voltages it is possible to achieve high quantum efficiency, high photocurrent and speed values and low thermal resistance due to minimization of the spatial charge accumulation effect, short flight time and smaller thickness of the drift region [86–88].

At PDA p-i-n-PD, photocurrent values of 55.7 and 111.7 mA were achieved at 10 GHz and 300 MHz respectively [86]. In [89], maximum photocurrent values of 430 mA at 300 MHz, 199 mA at 1 GHz and 24 mA at 50 GHz were achieved. Sensitivity of 0.8 A/W was obtained for the PDA p-i-n-PD with the area of 5×20 μm radiated through the optic fiber cable with diameter of 6 μm.

11.8.3.3 Unipolar Heterojunction Photodiode (UTC)

In 1997, employees of NTT System Electrons Laboratories suggested the design of a p-i-n-PD in which the drift of charge carriers was performed solely by electrons [90]. This helped neutralize the effect of space charge and obtain a uniform field in the drift layer. Power diagram of the UTC (UniTraveling Carrier) heterostructure of the p-i-n-PD is shown in Fig. 11.50. Unlike the structures of traditional DDR and PDA p-i-n-PDs considered above, in UTC p-i-n-PDs absorbed and drift layers are separated. Key parts of the infrastructure for an UTC p-i-n-PD include doped absorbing InGaAs layer of p-type conductivity with concentration of acceptors of 10^{17}–10^{18} cm^{-3} and thickness of 75–300 nm and lightly doped wide-gap drift InP layer with n-type conductivity with concentration of donors of less than 10^{15} cm^{-3}

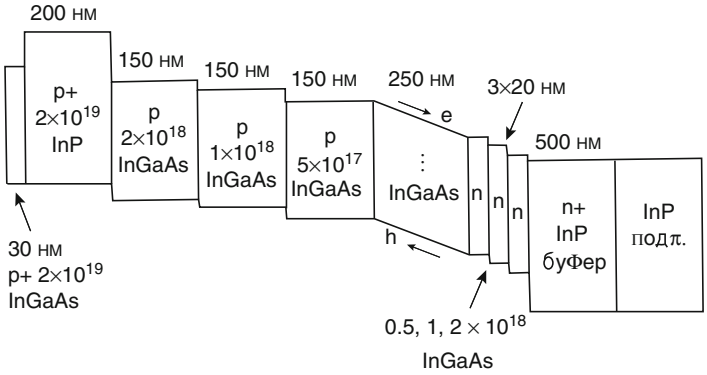

Fig. 11.49 Energy diagram, doping levels and thicknesses of layers of the heterostructure with partially depleted absorbing layer for PDA PD [86]

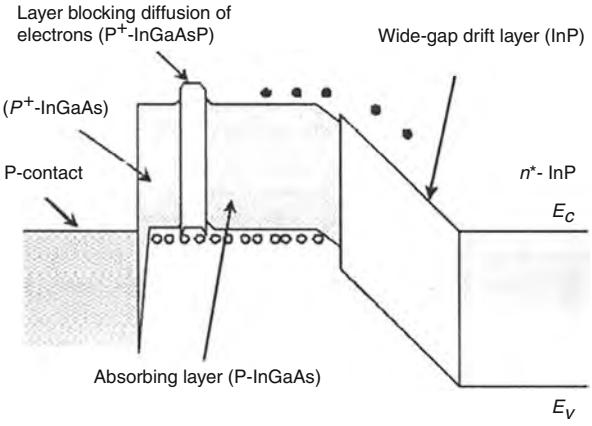

Fig. 11.50 Energy diagram of the heterostructure of a UTC PD

and thickness of 75–300 nm. In order to block diffusion of electrons into the p + −contact, wide-gap heavily doped InGaAsP layer (with the gap width Eg about 1 eV) or InAlAs layer (($Eg = 0.97$ eV) with p-type conductivity and thickness of 20–30 nm is grown on top of the absorption layer. During supply of reverse displacement, the absorbing layer is in electrically neutral condition (due to high concentration of acceptor inclusions), while strong electrical field is created in the wide-gap drift InP layer. Photogenerated electrons from the absorbing InGaAs layer diffuse into the drift InP layer; in the direction of the p + −contact, diffusion of electrons is blocked by the barrier of the wide-gap InGaAsP layer. Excess quantity of photogenerated holes in the absorbing layer relax over the dielectric relaxation time τ_R(1/2- $\tau_R = 1.2$ THz for InGaAs with the concentration of holes $p = 4{\cdot}10^{17}$ cm^{-3}).

Movement of electrons in the absorbing layer is due to their diffusion with effective speed $3D_n/d_a$ [91], where D_n ισ τηε electron diffusion coefficient, d_a ισ τηε thickness of the absorbed layer, and then in the drift layer [91]. Due to the high

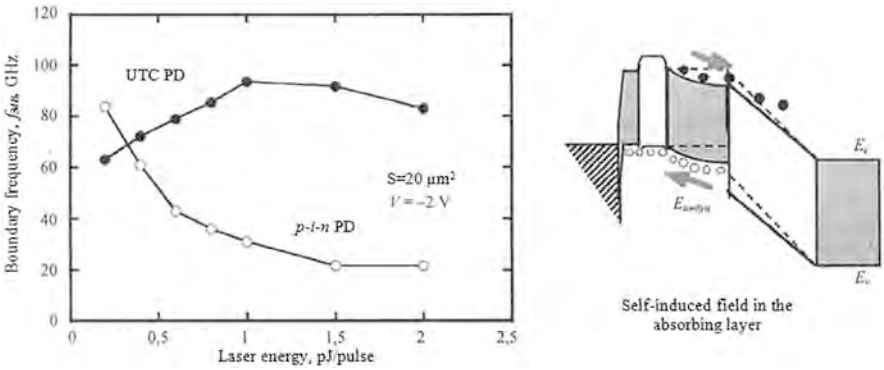

Fig. 11.51 Boundary frequency depending on the power of incident radiation for UTC PD and traditional p-i-n-PD [93]

value of electron mobility in InGaAs (9700 $cm^2/V{\cdot}s$ at room temperature [92]), electrons quickly reach the drift (depleted) layer. Since the drift of charge carriers is performed by electrons only, there is no effect of space charge even with high power of the recorded light emission. Simple estimate shows that in a UTC p-i-n-PD wit the thickness of the absorbing layer equal to 75–450 nm, diffusion time τ_D varies within the following limits.

$$\tau_D = \frac{d_a^2}{3D_n} = \frac{\left(75 \div 300 \cdot 10^{-7}\text{см}\right)^2}{3 \cdot 250\ \text{см}^2/\text{с}} (0.075 \tilde{\div} 1.2) \cdot 10^{-12}\ \text{s}.$$

Time of flight through the 300–400 nm thick drift InP layer of electrons with the speed of up to $4–10^7$ cm/s in electrical field with moderate strength also amounts to single picoseconds. Thus, boundary frequency of a UTC-p-i-n-PD estimated based on the time of transport in heterostructure and without taking into account the time constant τ_{RC} is higher than in a traditional p-i-n-PD, since it is determined by diffusion and drift of quick electrons instead of slow holes. Moreover, operation speed of a UTC p-i-n-PD increases together with the power of registered radiation due to acceleration of transport of electrons in the absorbing layer. This is caused by emergence of self-induced electric field in the absorbing layer, which is due to flow of holes into the contact region. This current becomes significant at sufficient concentration of photogenerated holes. As can be seen from Fig. 11.51, self-induced electrical field stimulates movement of electrons in the opposite direction [93, 94].

Unfortunately, the use of thin absorbing layers for expansion of the dynamic range of UTC p-i-n-PDs does not allow to achieve high current sensitivity. Typical values for a vertically illuminated PD presented in literature are about 0.1 A/W. In order to improve quantum efficiency and current sensitivity, registered radiation is entered into the heterostructure of the UTC-p-i-n diode not vertically but along the absorbing layer, which helps increase ampere-watt sensitivity of the device [95, 96].

By now, various modified versions of UTC p-i-n-PDs (Modified UTC) have been suggested [97–103]. First, in order to accelerate movement of electrons in the absorbing layer, gradient or step-wise doping is implemented in the absorbing layer, which induces the integrated electrical field. Second, in order to ensure free entrance of electrons into the drift layer, barrier height in the conductivity zone at the heteroboundary of InGaAs-InP is reduced. For this purpose, thin layers of InGaAsP with alternating compositions are placed between absorbing and drift layers. In [100], sensitivity of UTC p-i-n-PDs with various thickness values of absorbing layers amounted to 0.69–0.84 A/W at maximum photocurrent of 134–144 mA and frequency of 24 GHz. In [103], the most impressive parameters were achieved at modified UTC p-i-n-PDs in terms of boundary frequency 250 GHz and photocurrent of 17 mA at 50 Ohm load, which was close to the theoretical limit.

Certain applications, in particular radar antenna systems [104], require SHF PDs operating at zero displacement. The paper [105] contains comparative studies of traditional and waveguide p-i-n-photodiodes. For UTC PD with current sensitivity of 0.2 A/W, boundary frequency amounted to 13 GHz at zero displacement and 32 GHz at displacement of −1 V. For traditional p-i-n PD, the value of the cutoff frequency amounted only to 4 and 18 GHz in the same conditions.

In conclusion, it should be noted that the most active development of microwave PDs for analog optic fiber communication in the last 20 years has been carried out by scientific groups from the USA, Japan and Taiwan. When designing microwave PDs, it is necessary to clearly define tasks and conditions of applications in which the specific device type will be used. Most commonly used and in-demand microwave PDs are structures based on PDA PDA p-i-n-PDs and modified UTC p-i-n-PDs, which meet the parameters of the speed of operation and dynamic range in terms of input power of light radiation. Further tasks in development of SHF PDs include improvement of the heterostructure production technology and optimization of design of photodetectors.

References

1. Belous, A., Merdanov, M., & Shvedov, S (2018). *Microwave electronics in radar and communication systems* (Technical encyclopedia in 2 volumes, 2nd ed., revised, 1520 pages). Moscow: Tekhnosfera.
2. Wikipedia.: http://ru.wikipedia.org/wiki
3. Svanberg, K. (2011). President's letter. Solutions are green. *SPIE Professional, 6*(3), 3.
4. Physics of Semiconductor Lasers: Transl. from Jap. / Ed. by H. Takuma. Moscow: Mir (1989), 310 p.
5. Iga, K. (2000). Surface-emitting laser – its birth and generation of new optoelectronics field. *IEEE Journal on Selected Topics in Quantum Electronics, 6*(6), 1201–1215.
6. Koyama, F. (2009). VCSEL photonics – advances and new challenges. *IEICE Electronics Express, 6*(11), 651–672.
7. Ridgway, R. W., Dohrman, C. L., & Conway, J. A. (2014). Microwave photonics programs at DARPA. *IEEE Journal of Lightwave Technology, 32*(20), 3428–3439.

8. Belkin, M. E., & Sigov, A. S. (2009). New direction in photonics – microwave optoelectronics. *Radio-Electronics, 54*(8), 901–914.
9. Shulunov A. N. (2014). The Use of Radiophotonics nd Radar Location. In *24th International crimea conference "Microwave and Telecommunication Technology" (CriMiCo'2014)*, September 7–13, Sevastopol, Crimea, Russia. Vol. 1, p. 2–5.
10. Iezekiel, S. (Ed.). (2009). *Microwave photonics: Devices and applications* (p. 342). Hoboken: Wiley.
11. Herczfeld P. R. (1996). The past, present and future of microwave photonics. In *International topical meeting on microwave photonics technical digest*, 3–5 Dec. 1996, TU2–1, p. 25–28.
12. Gamage P.A., Nirmalathas A., Lim C., et al. (2008). Multi- services distribution using power-efficient low-cost VCSELs. In *International topical meeting on microwave photonics technical digest*, MPW', pp. 169–172.
13. Koyama, F. (2006). Recent advances of VCSEL photonics. *IEEE Journal of Lightwave Technology, 24*(12), 4502–4513.
14. Black, A., Hawkins, A. R., Margalit, N. M., et al. (1997). Wafer fusion: Materials issues and device results. *IEEE Journal on Selected Topics in Quantum Electronics, 3*(3), 943–951.
15. Kapon, E., & Sirbu, A. (2009). Long-wavelength VCSELs: Power- efficient answer. *Nature Photonics, 3*(1), 27–29.
16. Belkin, M. E., & Yakovlev, V. P. (2014). Nanostructured vertical cavity surface-emitting laser of spectral O- and C-ranges as a key element of microwave photonics devices. *Nanomaterials and Nanostructures, 5*(3), 37–49.
17. Chrostowski, L., Chang, C.-H., & Chang-Hasnain, C. J. (2003). Enhancement of dynamic range in 1.55-um VCSELs using injection locking. *IEEE Photonics Technology Letters, 15*(4), 498–500.
18. Belkin, M. E., & Sigov, A. S. (2012). A study of the problems of creation of optical interconnections. *Nano, 2*(32), 18–28.
19. Mircea, A., Caliman, A., Iakovlev, V., et al. (2007). Cavity mode – Cain peak tradeoff for 1320-nm wafer-fused VCSELs with 3-mW single-mode emission power and 10-Cb/s modulation speed up to 70°C. *IEEE Photonics Technology Letters, 19*, 121–123.
20. Mereuta, A., Sirbu, A., Iakovlev, V., et al. (2004). 1.5 pm VCSEL structure optimization for high-power and high temperature operation. *Journal of Crystal Growth, 27*, 520–525.
21. Caliman, A., Iakovlev, V., Mereuta, A., et al. (2011). 8 mW fundamental mode output of wafer-fused VCSELs emitting in the 1550-nm band. *Optics Express, 19*, 16996–17001.
22. Belkin, M., Belkin, L., Sigov, A., et al. (2011). Performances of microwave-band analog signal transmission using wafer-fused long wavelength VCSELs. *IEEE Photonics Technology Letters, 23*(20), 1463–1465.
23. Belkin, M., Sigov, A., Ellafi, D., Iakovlev, V., & Kapon, E. (2014). Nano-engineering in long wavelength wafer-fused VCSEL fabrication for microwave photonics. *Nanomaterials and nanostructures, 5*(2), 33.
24. Civis, S., Zelinger, Z., Nevrly, V., et al. (2014). Near-infrared wafer-fused vertical-cavity surface-emitting lasers for HF detection. *Journal of Quantitative Spectroscopy & Radiative Transfer, 147*, 53–59.
25. Belkin, M. E. (2006). Method for calculation of the number of transmitted channels in multi-channel optic fiber system with HF and SHF sub-carriers. *Radiotechnics, 12*, 88–91.
26. Belkin, M. E., & Belkin, L. M. (2009). Study of efficiency of using a semiconductor laser radiator for transmission of multi-channel analog signals of the microwave range. *Nano- and Microsystem Equipment, 11*, 32–37.
27. Belkin, L. M., & Belkin, M. E. (2011). Structureless model of a surface-emitting laser with modulation band in the microwave range. *Nano- and Microsystem Equipment, 10*, 9–17.
28. Qian, X., Hartmann, P., Ingham, J. D., Penty, R. V., & White, I. H. (2005). Directly-modulated photonic devices for microwave applications. *IEEE MTTS International Microwave Symposium Digest, 44*, 909–912.

29. Carlsson, C., Larsson, A., & Alping, A. (2004). RF transmission over multimode fibers using VCSELs – comparing standard and high-bandwidth multimode fibers. *IEEE Journal of Lightwave Technology, 22*(7), 1694–1700.
30. http://www.rp-photonics.com/vertical_external_cavity_surface_emitting_lasers.html
31. Sirbu, A., Okhotnikov, O., & Kapon, E. (2013). Wafer- fused 1300 and 1550 nm-waveband vertical external cavity lasers. *In SPIE Newsroom*. https://doi.org/10.1117/2.1201307.004905.
32. Rantamaki, A., Sirbu, A., Saarinen, E. J., Lyytikainen, J., Mereuta, A., et al. (2014). High-power flip- chip semiconductor disk laser in the 1.3 fim wavelength band. *Optics Letters, 39* (16), 4855.
33. Bousseksou, A., Kurdi, M. E., Bouchoule, S., Salik, M. D., & Sagnes, I. (2004). Tunable InP-based EP-VECSEL operatingat room temperature and in CW for 1.55 jim wavelength. *The 17th Annual Meeting of the IEEE Lasers and Electro-Optics Society, LEOS, 1*, 408–409.
34. Keeler, G. A., Serkland, D. K., Geib, K. M., Peake, G. M., & Mar, A. (2005). Single transverse mode operation of electrically pumped vertical-external-cavity surface- emitting lasers with micromirrors. *IEEE Photonics Technology Letters, 17*(3), 522–524.
35. Lukowski, M., Hessenius, C., & Fallahi, M. (2015). Widely tunable high-power two-color VECSELs for new wavelength generation. *IEEE Journal of Selected Topics in Quantum Electronics, 21*(1).
36. Illek, S., Brick, P., Diehl, W., Furitsch, M., Lindberg, H., & Pietzonka, I. (2008). Monolithic integration of pump lasers and a vertical external cavity surface emitting laser (VECSEL). *CLEO/QELS conference proceedings*, CWD2.
37. Rantamaki, A., Rautiainen, J., Sirbu, A., Mereuta, A., Kapon, E., & Okhotnikov, O. G. (2013). 1.56 µm 1 watt single frequency semiconductor disk laser. *Optics Express, 21*(2), 2355–2360.
38. Iakovlev, V., Walczak, J., Gebski, M., et al. (2014). Doublediamond high contrast-gratings vertical external cavity surface emitting laser. *Journal of Physics D: Applied Physics, 47* (065104), 1–8.
39. Caliman, A., Sirbu, A., Mereuta, A., Pierscinski, K., Iakovlev, V., et al. (2013). 14XX nm-wavelength electrically- pumped VECSELs fabricated by wafer fusion. *Optics Express, 21*(11), 13668–13674.
40. Zhao, Z., Bouchoule, S., Ferlazzo, L., Sirbu, A., et al. (2012). Cost-effective thermally-managed 1.55-µm VECSEL with hybrid mirror on copper substrate. *IEEE Journal of Quantum Electronics, 48*(5), 643–650.
41. Baili, C., Morvan, L., Pillet, G., et al. (2014). Ultralow noise and high-power VECSEL for high dynamic range and broadband RF/optical links. *IEEE Journal of Lightwave Technology, 32*(20), 3489–3494.
42. Tourrenc J.P., Bouchoule S., Khadour A., et al. (2007). High-Power Single-LongitudinabMode VECSEL at 1.55lim with a Hybrid Metal-Metamorphic Bragg Mirror. In *The 20th Annual Meeting of the IEEE Lasers and Electro-Optics Society*, LEOS, pp. 256–257.
43. Gierl, C., Gruendl, T., Debernardi, P., et al. (2011). Surface micromachined tunable 1.55 lim-VCSEL with 102 nm continuous single mode tuning. *Optics Express, 19*(18), 17336–17343.
44. Koyama, F. (2008). New functions of VCSEL-based optical devices. *Chinese Optics Letters, 6* (10), 755–762.
45. Castany O., Paranthoen C., Levallois C., et al. (2011). Demonstration of a 34 nm monolithic continuously tunable VCSEL at 1.55 µm combined with liquid crystal. In *23rd International Conference on Indium Phosphide and Related Materials – IPRM 2011*, pp. 1–4.
46. Sudmeyer, T., Wittwer, V. J., Hoffmann, M., et al. (2011). Ultrafast VECSELs and MIXSELs: Gigahertz semiconductor lasers with multiwatt average power. *IEEE Photonics Conference (PHO)*, 209–210.
47. Maas D. J. H. C., Bellancourt A.-R., Rudin B., et al. (2007). MIXSELs – a new class of ultrafast semiconductor lasers. In *European Conference on Lasers and Electro- Optics, and the International Quantum Electronics Conference*. CLEOE-IQEC, CWI1, 1 p.

48. Wittwer, V. J., Sieber, O. D., Mangold, M., et al. (2012). First MIXSEL with a quantum well saturable absorber: Shorter pulse durations and higher repetition rates. In *Conference on Lasers and Electro-Optics (CLEO)*. CW1N.2, 2 p.
49. Mangold, M., Zaugg, C. A., Link, S. M., et al. (2014). Recent advances in ultrafast MIXSELs. In *Conference on Lasers and Electro-Optics (CLEO)*. SF2G.3, 2 p.
50. Rautiainen, J., Lyytikainen, J., Toikkanen, L., Nikkinen, J., Sirbu, A., et al. (2010). 1.3-μm mode-locked disk laser with wafer fused gain and SESAM structures. *IEEE Photonics Technology Letters, 22*(11), 748–750.
51. Khadour, A., Zhao, Z., Bouchoule, S., et al. (2010). Generation 1.7-ps mode-locked pulse with low RF linewidth from a 1.55 μm VECSEL operating at 25°C. In *23rd Annual meeting of the IEEE photonics society* (pp. 295–296).
52. On Practice of Using Radiophotonic Devices in Radiolocation / Report at 2nd All-Russian Science and Technology Conference Prospects of Development of Long-Range Detection Radars and Integrates Systems and Complexes of Informational Provision of Aerospace Defense. Moscow (2014). http://www.centervospi.ru/articles/272
53. Chistokhin, I. B., & Zhuravlev, K. S. (2015). Microwave photodetectors for analog optic fiber communication / achievements of applied physics. *Physical Equipment and Its Elements, 3*(1), 85–94.
54. Minasian, R. A. I. (2000). *Optical Fiber Technology, 6*, 91.
55. Seeds, A. J., & Williams, K. J. (2006). *II Journal of Lightwave Technology, 24*, 4628.
56. Berceli, T., & Herczfeld, P. (2010). *IEEE Transactions on Microwave Theory and Techniques, 58*, 2992.
57. Mali, B., & Xie, Y. M. (1995). *II Optics Letters, 20*, 1901.
58. Urick, V. J., Hastings, A. S., McKinney, J. D., et al. (2008). *II IEEE International Topical Meeting on Microwave Photonics*, 86.
59. Adachi, S. (1992). *Physical properties of III-V semiconductor compounds*. New York: Wiley.
60. Shur, M. (1990). *Physics of semiconductor devices*. Englewood Cliffs: Prentice-Hall.
61. Bowers, J. E., & Wey, Y. G. (1995). High-speed photodetectors. In M. Bass (Ed.), *Handbook of optics: fundamentals, techniques and design* (2nd ed.). McGraw-Hill Inc.
62. Wey, Y. G., Giboney, K. S., Bowers, J. E., et al. (1993). *II IEEE Photonics Technology Letters*.
63. Simons, R. (1990). *Optical control of microwave devices*. Boston: Artech House.
64. Drigger, R. G. (2003). *Encyclopedia of optical engineering* (Vol. 2). New York: Marcel Dekker.
65. Kato, K., Hata, S., Kawano, K., et al. (1993). *IIIEICE Transactions on Electronics, E76-C*, 214.
66. Shiyu, X. (2012). *Doctor of philosophy*. The University of Sheffield.
67. Beling, A., & Campbell, J. C. (2009). *Journal of Lightwave Technology, 27*, 343.
68. Liu, P.-L., Williams, K. J., Frankel, M. Y., et al. (1999). *II IEEE Trans. Microw. Theory Tech, 47*, 1297.
69. Williams, K. J., Esman, R. D., Wilson, R. B., et al. (1998). *II IEEE Photonics Technology Letters, 10*, 132.
70. Malyshev, S., Chizh, A., & Andrievski, V. (2004). In *Proc. 12th Eur. Gallium Arsenide Other Compound Semicond. Appl. Symp*., p. 283.
71. Kato, K. (1999). *II IEEE Transactions on Microwave Theory and Techniques, 47*, 1265.
72. Williams, K. J., & Esman, R. D. (1999). *II Journal of Lightwave Technology, 17*, 1443.
73. Malyshev, S. A., Chizh, A. L., & Vasileuski, Y. G. (2008). *II Journal of Lightwave Technology, 26*, 2732.
74. Li, X., Li, N., Zheng, X., et al. (2003). *II IEEE Photonics Technology Letters, 15*, 1276.
75. Paslaski, J., Chen, P. C., Chen, J. S., et al. (1996). *II Proceedings of SPIE, Photonics and Radio Frequency, 2844*, 110.
76. Williams, K. J., Tulchinsky, D. A., & Campbell, J. C. (2007). *II IEEE International Topical Meeting on Microwave Photonics*, 9.

77. Ghione, G. (2009). *Semiconductor devices for high-speed optoelectronics*. Cambridge: Cambridge University Press.
78. Filachev A.M Tabukin I. // Trishenkov M.A. Soild-state photoelectronics, photodiodes. – Moscow: Fizmatkniga, 2011.
79. Pauchard, A., Bitter, M., Pan, Z., et al. (2004). *II IEEE Photonics Technology Letters, 16*, 2544.
80. Itakura, S., Sakai, K., Nagatsuka, T., et al. (2009). *II IEEE International Topical Meeting on Microwave Photonics (MWP)*, 4.
81. Effenberger, & Joshi, A. (1996). *Journal of Lightwave Technology, 14*, 1859.
82. Joshi, A. M. (2000). *Materials Research Society Symposium Proceedings, 607*, 115.
83. Datta, S., Joshi, A., & Becker, D. (2009). *II Proceeding of SPIE, 7339*, 733905-1-10.
84. Joshi, A., Heine, F., & Feifel. (2006). *Proceedings of SPIE, 6220*, 62203-1-14.
85. Fernandes, C. C., & Pereira, J. T. (2011). *Proc. Portuguese- Spanish Conf. in Electrical Engineering, Portugal, 1*, 1.
86. Li, X., Li, N., Zheng, et al. (2003). *II IEEE Photonics Technology Letters, 15*, 1276.
87. Tulchinsky, D. A., & Williams, K. J. (2005). *II Optical Sciences NRL Review*, 195
88. Malyshev, S. A., Chizh, A. L., & Vasileuski, Y. G. (2008). *II Journal of Lightwave Technology, 26*, 2732.
89. Tulchinsky, D. A., Li, X., Li, N., et al. (2004). *IEEE Journal of Selected Topics in Quantum Electronics, 10*, 702.
90. Ishibashi, T., Kodama, S., Shimizu, N., et al. (1997). *II Japanese Journal of Applied Physics, 36*, 6263.
91. Ishibashi, T., Furuta, T., Fushimi, et al. (2000). *II IEICE Transactions on Electronics, E83-C*, 938.
92. Datta, S., Roenker, K. P., Cahay, M. M., et al. (1999). *II Solid State Electronics, 43*, 73.
93. Ishibashi, T., Furuta, T., Fushimi, H., et al. (2001). *II Proceedings of SPIE, 4283*, 469.
94. Shimizu, N., Watanabe, N., Furuta, T., et al. (1997). *II Japanese Journal of Applied Physics, 37*, 1424.
95. Fukano, H., Muramoto, Y., & Matsuoka, Y. (2000). *II Japanese Journal of Applied Physics, 39*, 2360.
96. Hirota, Y., Ishibashi, T., & Ito, H. (2001). *II Journal of Lightwave Technology, 19*, 1751.
97. Jun, D.-H., Jang, J.-H., Adesida, et al. (2006). *II Japanese Journal of Applied Physics, 45*, 3475.
98. Wang, X., Duan, N., Chen, H., et al. (2007). *II IEEE Photonics Technology Letters, 19*, 1272.
99. Guo, L., Huang, Y., Duan, X., et al. (2012). *Chinese Optics Letters, 10*, S12301–S12304.
100. Li, Z., Pan, H., Chen, H., et al. (2010). *II IEEE Journal of Quantum Electronics, 46*, 626.
101. Rouvalis, E., Baynes, F., Xie, X., et al. (2014). *II Journal of Lightwave Technology, 32*, 3810.
102. Ishibashi, T., Muramoto, Y., Yoshimatsu, T., et al. (2014). *II IEEE Journal of Selected Topics in Quantum Electronics, 20*, 3804210.
103. Shi, J., Kuo, F., & Bowers, J. *II IEEE Photonics Technology Letters, 24*, 533.
104. Godinez, M. E., McDermitt, C. S., Hastings, A. S., et al. (2008). *II Journal of Lightwave Technology, 26*, 3829.
105. Yang, H., M. Daunt, C. L. L., Gity, F., et al. (2010). *II Proceedings of SPIE, 7847*, 784705-1-8.

Chapter 12
Measurement of Electrophysical Parameters of Dielectric and Semiconductor Materials and Structures of Microwave Electronics

12.1 Analysis of the Modern State of Studies in the Field of Technologies of Parameter Control of Dielectric and Conductive Materials at SHF

12.1.1 Features of Using Microwave Measurement Methods in Semiconductor Microwave Electronics

Level of development of technology of manufacturing layers of different materials with thicknesses from several nanometers to dozens of micrometers largely determines the effectiveness of production of the existing and successful creation of new devices of solid-state microelectronics and nanoelectronics [1, 2]. In order to achieve high level of perfection of layered structures, in particular, structures based on nanometer films, it is necessary to use high-precision methods of measurements of electrophysical parameters of dielectric and semiconductor materials and structures, as well as metal films.

During measurement, contact methods are used most often, i.e. parameters of semiconductor and dielectric materials and metal films are measured at direct or low frequency current [3–5]. Measurements with the help of such methods are performed in case of presence of the probe with the sample. This often results in destruction of the tested material. The use of such methods can cause their characteristic unwanted effects, such as injection of charge carriers into the material caused by contact, emergence of contact difference of potentials, thermal voltages, which cause persistent measurement errors; moreover, the influence of these effects may vary depending on the temperature, which causes difficulties during measurements in a wide range of temperatures. Probing methods are also difficult to use for measurement of small-area samples with aribtrary geometry.

© The Editor(s) (if applicable) and The Author(s), under exclusive license to Springer Nature Switzerland AG 2021

A. Belous, *Handbook of Microwave and Radar Engineering*,
https://doi.org/10.1007/978-3-030-58699-7_12

One of the advantages of non-contact methods, which include, among others, SHF methods, is the possibility of performing measurements without destroying the material or altering its properties [6–31].

An advantage of SHF measurements is the possibility to use one test unit and one sample to determine several parameters, measurement of which by contact methods requires creation of various stations and the use of several samples of the same type. Absence of contact allows for placing measurement instruments outside the field of temperature effect on the semiconductor and subsequent measurement of semiconductor properties within a wide range of temperatures. The use of microwaves for measurement makes it possible to study dependencies of certain parameters on frequency. Contactless nature of methods opens up new possibilities for the study of anisotropic effects. Due to possibility of application of strong electrical fields without using contacts, SHF methods can be applied to study kinetics of carrier heating in the electrical field, as the absence of contact prevents injection. These methods make it possible to perform express measurements, testing and culling of semiconductor semi-finished parts for devices, as well as control parameters during heat treatment. Tests using microwaves are very important to determine parameters of film structures due to the fact that microwave methods of film testing make it possible to perform various measurements without destroying the film and use the tested samples for production of instruments.

It should be noted that SHF methods are the best option if the tested materials and structures are used in semiconductor SHF electronic devices, since the studies with the use of probe methods, for example, can provide insufficient information for designing SHF devices with given characteristics. Advantages of semiconductor microwave devices compared to their vacuum analogs make development of new methods of determining semiconductor parameters a relevant task.

SHF measurement methods differ in term of physical effects on which they are based, type of the used measurement scheme, and the character of mutual location of the sample and electrodynamical system. Classification of microwave methods according to their underlying physical principles is based on: effect on suppression of electromagnetic energy by charge carriers, delayed action of carriers in microwave field, rotation of the wave polarization plane during curving of trajectory of charge carriers and resonances. Based on the used circuit, microwave methods are divided into waveguide, bridge, cavity (resonator) and microstrip methods. In terms of mutual positions of the tested sample and electrodynamical system, microwave methods are subdivided into measurements by passing methods, when the sample is placed inside the system, and methods of measurement by applied systems, when the sample is applied to the open end of the microwave path or hole in the cavity, or designed as a part of their walls.

The most popular methods are waveguide and resonator ones. During the use of waveguide methods, interaction of SHF wave propagating in the waveguide with the sample placed in the waveguide is considered, and the intensity of transmitted and reflected waves is measured. During resonator measurements, the circuit is set to resonance by changing dimensions of the electrodynamical system or generator frequency. These methods are based on absorption of electromagnetic energy by

free charge carriers and change in the equivalent dimensions of the resonator with the semiconductor placed inside. Determination of the change in resonator characteristics can be used to determine dielectric permittivity and conductivity of the material, change in the conductivity caused by superposition of magnetic field, illumination of the sample, etc. If the dependence between electrical conductivity change and absorption in the sample is linear, it is possible to find the value of the setting time of unbalanced processes in semiconductors, such as bulk life of additional charge carriers and speed of surface recombination. Introduction of the tested sample in the testing cavity system leads to a shift in the resonant frequency and change in the Q-factor of the cavity, the variation of which is used to calculate the sample parameters.

During development of the technology for creation of layered structures based on nanometer metal films used in microelectronics, acoustic and optical electronics, it is important to measure exact thickness of the metal layer and its conductivity upon completion of the process cycle. Such measurements should be preferably performed without destroying the structure, e.g. with the help of microwave radiation [6–8, 11, 32].

In order to determine thickness and conductivity of nanometer metal films in layered structures, it is possible to use the results of measurement of transmission and reflection spectra of the microwave radiation interacting with them, if their theoretical description is known [33–50]. Determination of electrophysical parameters of layered structures based on transmission and reflection spectra of the electromagnetic wave is associated with the need to solve the reverse task [37].

Layered structures, completely filling cross-section of the waveguide and designed as alternating layers of dielectrics with different thickness and permittivity values, forming the structure periodical along the distance of propagation of the electromagnetic wave with the thicknesses of the structure layers comparable to the wavelength of propagating radiation, are one-dimensional photonic crystals in the SHF range. Photonic crystals containing conductive layers, including nanometer metal films, have pronounced resonant characteristics.

Transmission spectrum of such structure contains the frequency domain unavailable for propagation of electromagnetic wave – analog of the gap in crystals [51]. In case of irregularities of the layered structure, narrow transmission windows can occur in the gap of the photonic crystal [52].

One-dimensional photonic crystal in the SHF range can be implemented both with the help of waveguides with dielectric filling [53] and with the help of planar transmission lines with periodically changing structure [54–60].

The use of the photonic crystal changes the reflection coefficient from values close to zero to values close to one within the measured frequency range, which expands the range of measured thicknesses and the class of tested materials, and at the same time ensures the possibility of measurements in the selected frequency range and creation of functional SHF electronic devices based on the results of these measurements [52, 53, 61–70].

In this connection, it is relevant to study specific features of interaction of electromagnetic radiation of the microwave range with one-dimensional waveguide

photonic crystals, determination of the possibility of expanding the range and increasing reliability of measurement of electrophysical parameters and thicknesses of thin nanometer metal films, layers of dielectric and semiconductor materials included in the composition of one-dimensional waveguide photonic crystals as irregularities, based on reflection and transmission spectra of interacting radiation of the microwave range of wavelengths.

12.1.2 Measurement of Electrophysical Parameters of Materials by Waveguide Methods

Solutions to problems of describing interaction of a SHF wave propagating in the waveguide containing a dielectric or conductive material, have been known for a long time and presented in multiple articles reviewed by authors of [8]. As a rule, waveguide methods are based on measuring the complex reflection R or transmission T coefficient of the waveguide section containing the sample and determination of electrophysical parameters of the sample according to formulas linking them to R and T. Expressions linking R and T to electrophysical parameters of the material depend to a great extend on the method of placement of the sample in the waveguide, shape of its cross-section and dimensions.

Depending on the shape of the sample and its position in the waveguide, waveguide-based measurement methods can be divided into three main groups [8]: first – the sample completely fills cross-section of the waveguide; second – sample in the form of a plate is placed in the center of the rectangular waveguide parallel to the narrow wall; third – sample in the form of a bar with round or square cross-section is placed in the center of the waveguide and perpendicular to the wide wall.

For example, first tests of semiconductor parameters at SHF were performed by waveguide methods using samples completely filling cross-section of the waveguide [71].

The output of relations linking electrophysical parameters of the semiconductor with characteristics of the wave propagating in the waveguide (i.e., propagation constant) is based on solving a system of Maxwell equations in corresponding boundary conditions. When thin high-Ohm samples are placed in the waveguide, it can be considered that the field in the waveguide containing the sample has no significant differences from the field in the empty waveguide. Methods of perturbation theory are efficient for determination of the propagation constant of an electromagnetic wave [72].

Waveguide methods of measurement of electrophysical semiconductor parameters based on rotation of the electromagnetic wave polarization plane in the semiconductor material, as well as on conversion of linear polarization into elliptical polarization due to anisotropy of electrical conductivity of the semiconductor sample in the magnetic field B can be used for contactless determination of mobility of free charge carriers.

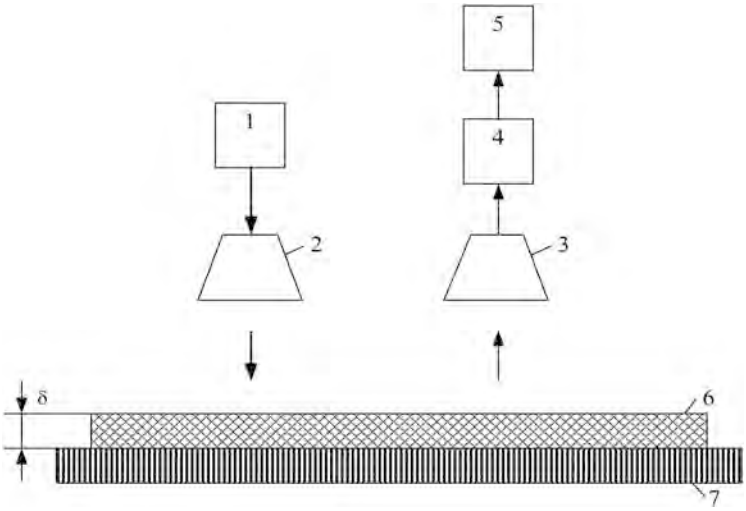

Fig. 12.1 Device implementing the task of measurement of dielectric surface applied to dielectric base: 1 – microwave oscillator, 2 – emitter of electromagnetic oscillations, 3 – receiver of reflected electromagnetic oscillations, 4 – detector, 5– indicator, 6 – dielectric coating, 7 – dielectric base

For determination of thickness of dielectric coating with known reflection coefficient of the material applied to dielectric base, the author of the RF patent [73] suggest the method that consists in probing of the dielectric layer applied to dielectric base with electromagnetic radiation at fixed frequency and reception of the reflected signal at the distance significantly exceeding wavelength of the probing radiation (Fig. 12.1). Surface thickness δ is calculated using the expression:

$$\delta = \frac{E \cdot R - k\sqrt{30 \cdot P \cdot G}}{E}, \tag{12.1}$$

where R *is the* distance between the radiator and the surface of the dielectric base, P is the radiator power, G is the directivity of the radiator, k is the reflection coefficient.

The RF patent [74] describes the method of determining complex dielectric and magnetic permittivity of a thin radar-absorbent material based on the result of measurement of complex reflection R and transmission T coefficients of the electromagnetic wave in the section of coaxial line with measured material.

In order to determine complex dielectric permittivity and thickness dielectric coatings on metal, the authors of the RF patent [75] suggest excitation of electromagnetic oscillations at different but close wavelengths in the volume of the dielectric coating. Measured values of distribution of amplitudes of these waves along the surface of the dielectric layer are used to calculate attenuation coefficients of the field of each wave along their propagation direction and determine the value of

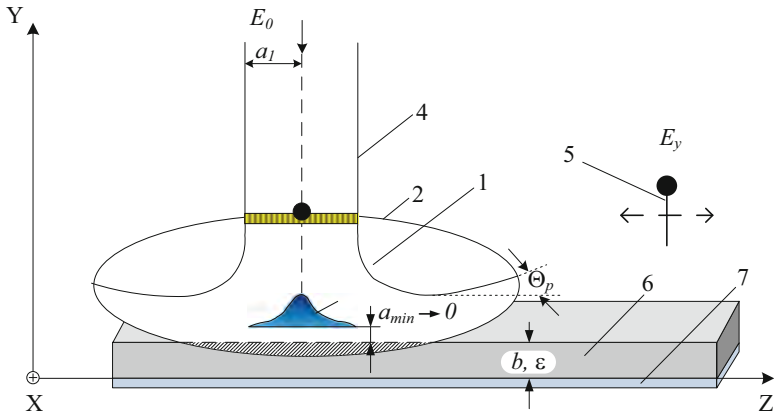

Fig. 12.2 Diagram of the device for determination of thickness and complex dielectric permittivity of dielectric coatings: 1 – device for excitation of slow surface waves; 2 – upper dish of the aperture, lower part of the aperture – underlying metal surface; 3 – matching cone; 4 – round waveguide; 5 – receiving vibrator; 6 – surface layer of dielectric coating; 7 – metal substrate

specific conductivity of the dielectric coating, real and imaginary parts of complex dielectric permittivity, as well as thickness of the dielectric coating (Fig. 12.2).

Device for measurement of high values of complex dielectric permittivity of heavily absorbing materials at SHF [76] contains a metal waveguide, short-circuited at the end, while the side wall contains a long longitudinal cut with matching skews, which is covered by reference short-circuiting device or tested sample during the measurement process.

The measuring cell [77] designed for control of microwave parameters of dielectric materials contains the section of evanescent waveguide, which in turn contains the composite insert made of the tested dielectric sample and two mobile dielectric elements; the insert is resonant at the operating frequency. Mobile dielectric elements are made with stepped protrusions. The gap width between protruding parts of dielectric elements ensures frequency compensation in the measuring cell when the tested sample width is changed.

The device for measurement of high values of complex dielectric permittivity of heavily absorbing materials at SHF suggested in [78] contains a U-shaped waveguide, which is short-circuited at the end. The side wall opposite to the crest contains a long longitudinal slot parallel to the U-waveguide axis and equipped with matching skews. The width of the cut, which extends over the entire wall of the U-waveguide during measurement, is covered by reference short-circuiting device or the tested sample. Similarly, the device [79] contains an H-shaped waveguide short-circuited at the end. One of the walls of its crest contains a long longitudinal slot parallel to the H-waveguide axis. The slot is equipped with matching skews; the width of the slot coincides with the width of the corresponding crest of the H-waveguide shape and is closed by reference short-circuiting device during measurement.

12.1.3 Measurement of Semiconductor Parameters by Bridge Methods

Accuracy of measurement of semiconductor parameters can be increased by using bridge circuits instead of waveguide methods described above for SHF measurements. Waveguide Ts are used as microwave bridges (Fig. 12.3). Waveguide Ts are junctions between two one-wave waveguides at straight angles – T-shaped joints. There are T-shaped connections in the plane of the E wave H_{10}, or E-junctions (Fig. 12.3b), and in the H plane, or H-junctions (Fig. 12.3a).

In the presence of matched loads in arms 2 and 3, as follows from the field distribution pattern in Fig. 12.3, waves in the E-joint propagate in the opposite directions with equal (at equal distances from the branching) magnitudes and out-of-phase cross electrical components and equal in-phase cross magnetic components; waves in the H-joint propagate with equal and in-phase cross electrical components and equal out-of-phase cross magnetic components.

Connection of E- and H-joints in one unit is known as double waveguide T-joint (Fig. 12.4). Arms E and H of the double T-joint are isolated from each other, i.e. when the wave H_{10} is supplied into the E arm, this wave does not enter the H arm; similarly the wave does not enter the E arm when supplied into the H arm. In the presence of matching loads in arms 1 and 2, arms 4 and 3 of the double T-joint are isolated from each other, i.e. when the wave H_{10} is supplied to the arm 3, it does not enter the arm 4, and vice versa. The wave starts passing from arm 3 to arm 4 in the presence of reflected waves with different phases in arms 1 and 2.

The use of bridging measurement methods can be exemplified by measurement of electrical conductivity and dielectric permittivity of silicon of the n-type and

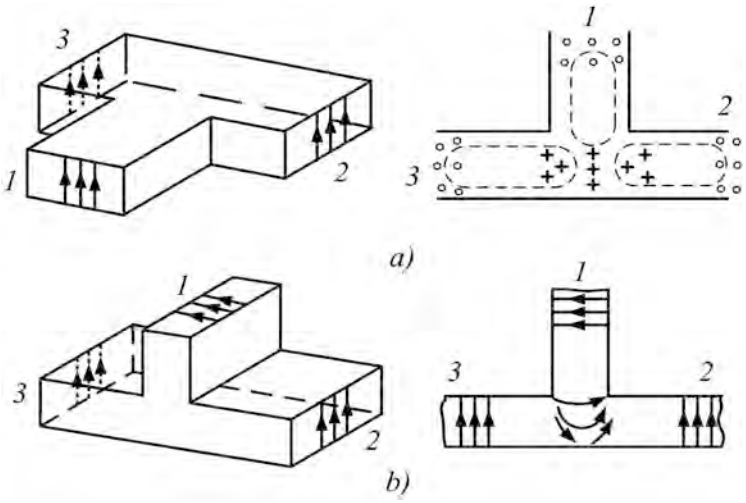

Fig. 12.3 Waveguide Ts

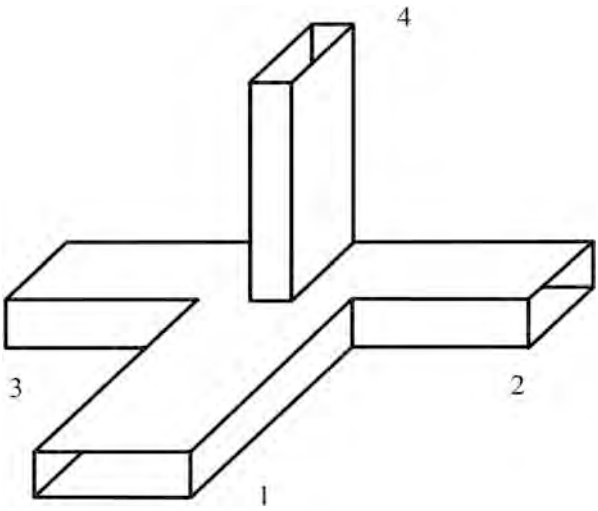

Fig. 12.4 Double waveguide T

germanium of the *p*-type within the temperature range of 77–330 K at the frequency of 24 GHz with the help of double waveguide T-joint described in [80].

The measurement scheme is shown in Fig. 12.5. With short-circuited lower arm, precision attenuator and short-circuiting device in the upper arm are used to set the circuit based on indications of the zero indicator for the absence of oscillations in the -arm of the T-junction during their supply into the *H*-arm. After that, reference short-circuiting sections is replaced with similar structure containing semiconductor, and balance is achieved once again. Measured ratio of reflection coefficients $\frac{R_2}{R_1}$ is used to determine the attenuation constant and phase constant of the waveguide section with semiconductor and subsequently electrical conductivity and dielectric permittivity.

Limitedness of bridge methods can be due to asymmetry of the used waveguide Ts and the need to use samples of the specific shape.

12.1.4 Measurement of Semiconductor Parameters by Cavity Methods

Cavity methods are used for measurement of electrophysical parameters and study of properties of semiconductor materials in the SHF ranges.

Basic characteristics of a cavity largely depend on the parameters of the medium filling it. For example, an increase in permittivity causes the wave propagation speed to reduce, thus increasing equivalent dimensions of the cavity and resonant wavelengths and reducing resonant frequencies. Change in the conductivity of the environment causes changes of losses and, accordingly, change in the Q-factor of the cavity itself. Determination of change in the resonant frequency and Q-factor of

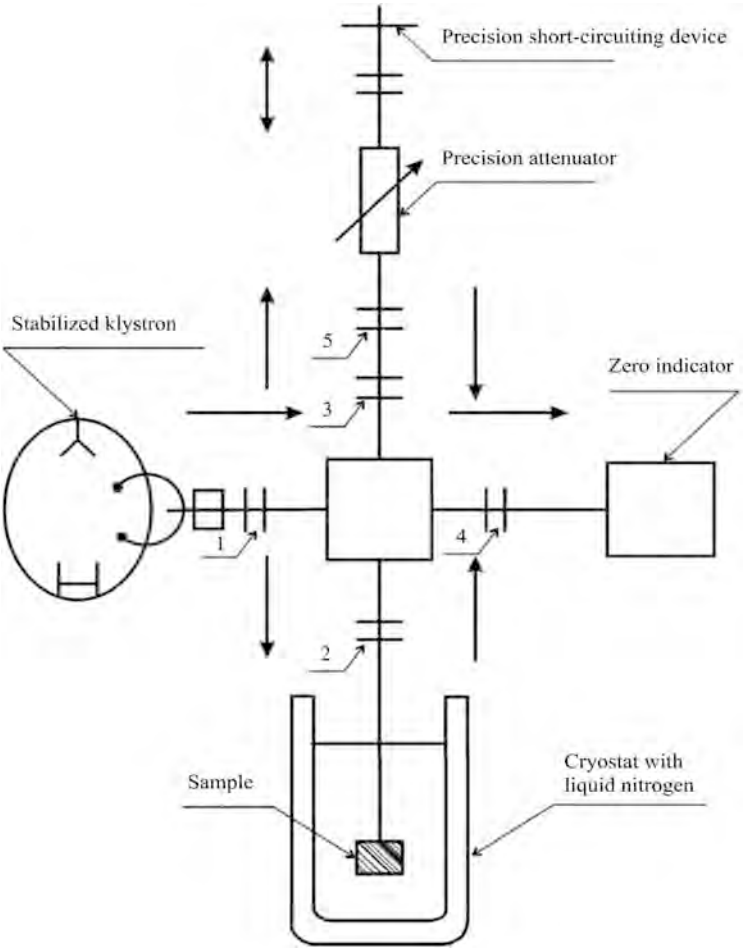

Fig. 12.5 Diagram of measurement with the help of double waveguide T-joint

the cavity with placement of the tested sample inside it forms the basis for resonant methods of measurement of semiconductor parameters [6, 27].

Quantitative assessment of changes in resonant frequency and Q-factor in case of insertion of a semiconductor sample into the cavity can be performed using the perturbation theory.

Cylindrical resonator (cavity) is one of the types of resonators widely used in measurement of parameters of semiconductor and dielectric materials [6, 27, 81]. Tested samples in this case are designed as round bars and placed along the axis of symmetry of the cavity, completely or partially filling its length, or in the form of a disc with the radius equal to or less than the radius of the cavity. The type of oscillations excited in the cavity is selected in accordance with the geometry of the sample. For bar-shaped samples (Fig. 12.6), it is convenient to use oscillations with

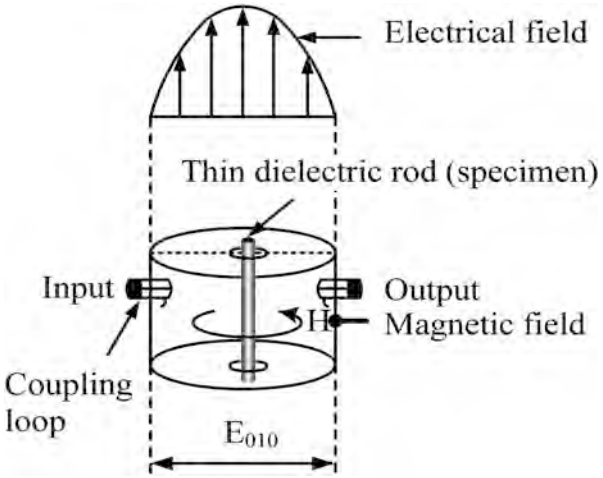

Fig. 12.6 Cavity of type E_{010}, used for measurements at frequencies up to 10 GHz

the lowest resonance frequency of the type E_{010} [82–86]. Electrical field in this case has only the longitudinal component E_Z and does not depend on the resonator length. In this case, in order to ensure low distortion of the field, values permittivity, conductivity and radius of the sample shall be low.

Moreover, in case of partial filling of the cavity length, bound charges occur in longitudinal electrical field at the edges of the specimen, which can significantly distort the field in the resonator.

Measurement of dielectric permittivity and conductivity of samples with high values ε_L and σ characteristic of semiconductor materials are performed in the frequency range of 8–40 GHz using oscillations of the H_{0nq} type [87–88]. An important advantage of the cavity operating at frequencies of these types is the possibility of its tuning with the help of a displaceable piston. The use of piston is due to the fact that in this case the electrical field only has cross-components; therefore, there are no currents flowing from end surfaces of the resonator, and the defects of the piston contact will have no effect on the Q-factor of the cavity, while in the resonator with oscillations of the E_{010} type bad contact of the piston with the lateral surface of the cavity will increase losses in the cavity walls and cause a significant change in the Q-factor. Moreover, the absence of the current flowing through the piston to the cavity walls makes it possible to use the type of the piston that has no direct contact with resonator walls, which increases the reliability of the cavity even more and ensures stability of the Q-factor. The use of a tunable cavity makes it possible to apply an oscillator operating at fixed frequency, which in turn ensures the possibility of frequency stabilization of the generator and therefore helps obtain higher accuracy of measurements. It should be noted that bound charges distorting field in the cavity do not occur at edge surfaces of the specimen due to absence of the longitudinal field component.

When the tested sample is placed in the cavity, its permittivity is determined based on the value of change in the resonant frequency, and its conductivity is determined from the value of change in the Q-factor of the cavity. Such unambiguous connection between dielectric permittivity with the change in the resonator frequency and electrical conductivity with the change in the Q-factor exists if only one type of oscillations is excited in the cavity. Otherwise, it is necessary to consider adjustments of a higher order in the excitation theory [89]. It follows from the expression for frequency shift and change in Q-factor in the second approximation of the perturbation theory taking into account excitation of several oscillation types in the cavity with insertion of semiconductor that the frequency shift is determined not only by dielectric permittivity of the semiconductor but also by its conductivity, while the Q-factor value depends on dielectric permittivity as well as on conductivity. Therefore, widely used working ratios for cavity measurement methods obtained in the first approximation of the excitation theory can only be applied if oscillations of a single type exist in the cavity.

Cavity methods of measurement of material parameters based on the measurement in the frequency shift and change in the Q-factor with the sample placed inside the cavity have a number of disadvantages. In particular, these methods are destructive, as their use requires production of samples of specific shape. Moreover, tested parameters of the material are averaged across the entire volume of the sample located inside the cavity, which makes it impossible to study the possibility of variation of parameters across its area or volume. In order to perform such measurements, it is necessary to reduce the material volume used for averaging, i.e. increase the locality of measurements.

There are methods based on the use of the so-called hybrid mode resonator, which is an oversized cavity with heavily reflecting walls; inside the cavity, isotropic radiating field is maintained due to the effect of an arm agitator. Unlike standard cavities of discrete oscillation types, response from cavities of mixed oscillation type to injected electromagnetic field is only weakly connected to frequency. Therefore, such cavities can be used for wideband measurement at SHF and millimeter wave range frequencies [90–94].

There is a class of cavity methods that help increase locality of measurements and test samples without shaping them in advance [29, 95, 96]. These methods are based on the fact that resonant frequencies and Q-factor of the cavity are determined not only by the parameters of the medium filling it, but also by the conditions applied to the limiting surface. For example, if a part of the cavity wall is replaced with the tested sample, it will cause changes in the resonant frequency and Q-factor of the cavity.

A simple example of measuring cavity of such type is the coaxial cavity with the opening in the end wall (Fig. 12.7). Concentration of the field in the gap between the central coaxial rod and the end wall ensures sufficiently strong interaction of the electromagnetic field of the cavity with the tested sample applied externally even with small dimensions of the opening. Thus, locality of measurements is increased,

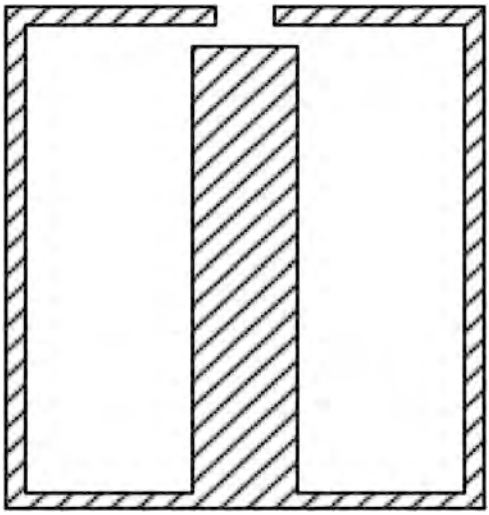

Fig. 12.7 Section of a holed coaxial resonator

and part of requirements for the shape of the sample are abandoned. However, in this case it becomes difficult to achieve sufficiently strict mathematical relations linking material parameters with the change in the parameters of the resonator. Therefore, such methods are no longer absolute, and measurement of unknown parameters is performed with reference specimens and calibration curves, nomographic charts or tables based on them, which can lead to a significant decrease in the accuracy of measurements. Moreover, the impossibility to separate the effect of different parameters of the tested material on cavity characteristics determines the need to use fixed parameters, except for one measured parameter.

Such limitations of calibration methods reduce their value; however, they find their use for determination of variation of a certain parameter relative to its average value. Simplicity of measurement and absence of special requirements with regard to the shape of the sample make it possible to widely use calibration cavity methods for 100% control of products during process operations of their production.

The latest developments in the field of cavity testing methods include papers [97–105].

The authors of patents [97, 98] suggest performing measurements with the help of a waveguide standing-wave resonator. The value of complex dielectric permittivity is determined based on measured values of resonant frequency, attenuation and Q-factor.

Patent [99] suggests using a cavity with plane-parallel mirrors, one of which is formed by the tested material. The coefficient of signal transmission through the cavity is calculated, after which the form of the transmission coefficient curve taking is recovered taking into account various losses, and target electrophysical parameter are calculated. The device for implementation of this method is also suggested.

Device suggested in [100] for determination of relative dielectric permittivity and dielectric loss tangent of low-impedance materials consists of a microwave oscillator, a measuring device for complex reflection factor, a frequency meter, a coaxial resonator and a sample of tested material. Coaxial resonator is short-circuited at the end, and the central conductor is made of measured low-impedance material; the central metal conductor is used as reference.

The device [101] for measurement of electrophysical parameters of dielectric materials contains a coaxial resonator with measuring opening at the end and a press; it is equipped with an evanescent waveguide with round cross-section coaxial to the measuring opening and with the inner radius exceeding the radius of the measuring opening at least three times, while the face end area of the cavity exceeds the cross-section area of the evanescent waveguide; a flange is installed on the outer side of the evanescent waveguide near one of its ends, which contains an elastic ring; the other end of the evanescent waveguide is limited by the end wall, and the evanescent waveguide is placed inside a cylindrical hole in the press and connected to the press via the elastic ring. It can be used for non-destructive local determination of permittivity and tangent of the angle of loss of dielectric materials for microelectronics.

The device [102] is designed for control of thickness, permittivity and other parameters of film and sheet dielectric materials; it contains the open SHF cavity and the device for measurement of its resonant frequency. In order to improve testing accuracy in the conditions of temperature instability and mechanical vibration of the resonator, the device contains an inductance coil attached to the first resonator mirror, and inductance meter and two differential amplifiers connected to the coil in series, and a reference voltage source. In order to further increase testing accuracy, at least a part of the second mirror of the open resonator is made of a ferromagnetic material.

The device [103] for measurement of electrical conductivity of elementary granules of conductive powder includes an open microwave resonator separated by two spherical mirrors. The sample holder is located in the center. The resonator is excited by signals delivered from the synthesizer with slow deployment through linear polarizer. The receiving antenna, which senses the resulting electromagnetic field, is connected to the spectrum analyzer. The entire system is controlled by the computer. Electrical conductivity of individual granules is determined based on resonance characteristics in vacuum and in the presence of tested dispersion of the powder granules. Resonance is achieved at the TEM 00q mode, where q is an odd integer.

Measurement of complex dielectric permittivity of low-impedance materials with rough surfaces by cavity method [105] consists in the following: reference short-circuiting device and two additional reference short-circuiting devices (with rough and smooth surfaces) are used to perform measurement of resonance frequency and Q-factor of the cavity with reference short-circuiting devices and the sample of the tested material, after which the obtained results are used to calculate values of complex dielectric permittivity.

12.1.5 Measurement of Material Parameters by Waveguide Dielectric Resonance Method

Traditional cavity testing methods are based on using metal resonant cavities of various types [106]. Determination of dielectric permittivity ε and conductivity σ of the material in this case, as noted above, is performed based on measured values of changes in the resonant frequency and Q-factor of the resonator with the tested material placed inside the cavity, or in case of contact of the material with the communication element, e.g. the opening in the cavity wall, when application methods are used [6]. It should be noted that when a sample with high ε value with the order of value unknown in advance is inserted into the cavity, there can be ambiguity in determination of dielectric permittivity due to the fact that the change in the electrical length of the cavity in this case can exceed half of the wave length. In this case, tests shall be performed with samples of the tested material with various thickness values. This feature is also typical of waveguide methods and determined by periodicity of trigonometric functions used for description of wave and oscillation processes. Practical use of traditional cavity methods is associated with high requirements for the quality of mechanical treatment of surfaces during production of metal resonant cavities. Moreover, due to fairly high thermal expansion ratios of metals, characteristics of metal resonant cavities are quite critical to changes in the ambient temperature.

A separate class is formed by cavity methods based on the effects of dielectric and waveguide-dielectric resonances [107–110]. These methods are distinguished by the fact that their implementation does not require production of special metal resonant cavities, since their underlying resonant phenomena are observed in common transmission lines when a dielectric or a semiconductor is placed in such line.

Occurrence of the examined resonance phenomena is due to the difference between permittivity values of the medium filling the waveguide system and the tested sample placed inside, dielectric permittivity of which is a complex value.

Measurement of material parameters using the dielectric resonance method is performed as follows. The cavity is made from tested material and placed in the transmission line, after which its resonant frequency and Q-factor are determined. These measured values are then used to calculate permittivity and conductivity of the tested material. However, this measurement method in most cases requires production of samples of special shape, i.e. is actually destructive.

At low values of ε ($\varepsilon < 20$) or high values of ε, but on condition of proximity of one of cross-sectional dimensions of the sample, waveguide-dielectric resonance is observed due to high effect of the waveguide walls on the structure of the field in the filled area. Regardless of the variety of methods of waveguide filling that cause waveguide dielectric resonance, the mandatory condition for its surveillance, with rare exceptions, is the existence of the type of oscillations for which the empty waveguide is beyond cutoff at the section of waveguide containing the sample.

Insertion of the tested sample in the waveguide reduces critical frequencies of all types of waves, therefore, starting from certain frequency, which is inversely

proportional to ε and filling level; at the same time, propagation of waves of higher types becomes possible in the section of filled waveguide in the operating frequency band.

Since the sections of the free waveguide before and after the sample (relative to the wave propagation direction) are evanescent for higher types of waves, they experience multifold reflections at the border of empty and filled waveguides, being locked in the waveguide section containing the tested sample.

Each wave existing in this section in turn excites the full set of waves of the H_{S0} type, including the wave of the main type H_{10}, which is the only one capable of propagating outside this region. Therefore, there are several waves of the type H_{S0} in the section of the filled waveguide. It should be noted that amplitudes and phases of these waves differ from each other and have different frequency dependencies.

Waveguide-dielectric resonance, which is manifested in sharp attenuation of the transmitted wave and an increase in the amplitude of the reflected wave, is the result of interference attenuation of these waves in the waveguide section after inclusion of the sample and addition in the section before inclusion of the sample. Such interference process occurs at certain phase and amplitude relations at resonant frequency.

Determination of permittivity for the sample of the given size placed inside the waveguide is performed based on the measured value of the resonance frequency using nomographic charts based on the results of numerical solution of the corresponding electrodynamical problem of interaction of the electromagnetic wave with irregularities in the waveguide [84]. The possibility of determining conductivity of the sample occurs due to its effect on Q-factor of the resonance, as well as on the value of attenuation introduced at resonant frequency.

12.1.6 Measurement of Parameters of Materials and Structures by Autodyne Methods

Parameters of semiconductor and dielectric materials can be measured using the effect of autodyne detection in semiconductor microwave oscillators [111]. The possibility of using Gunn-diode based autodyne frequency converter for measurement of permittivity or thickness of dielectric materials is demonstrated in [112]. The use of Gunn diodes for creation of autodyne frequency converters was researched by many authors [112–118]. Permittivity or thickness of the dielectric layer can be determine based on the shift of intermediate frequency with the dielectric introduced into the oscillator circuit. The use of Gunn diodes in autodyne oscillators as compared to oscillators using other semiconductor elements makes it possible to ensure advantages in terms of combination of such parameters as maximum operating frequency, output power, frequency stability and power consumption.

The use of the effect of autodyne detection in semiconductor SHF generators [119–126] for control of material parameters is based on determining dependencies

of the value of the detected signal on parameters of tested layers, such as thickness and permittivity [9, 127–138].

The most popular device in practice of the ones based on autodyne detection principle is the SHF thickness gauge of the SIT-40 type [139–151].

Disadvantages of autodyne measuring devices include the need to use a number of calibration dependencies.

12.1.7 *Measurement of Material Parameters Using Synchronized Oscillators*

The works [152–162] studied the possibility of increasing sensitivity of SHF methods of measuring mobility of free carriers, electrical conductivity and thickness of the epitaxial layer of semiconductor structures with the use of the mode of subtraction of coherent signals: clock signal and signal from the Gunn-diode based synchronized generator. The use of the synchronization phenomenon makes it possible to change the phase difference between output signal of the self-excited oscillator and the clock signal by adjusting frequency of the clock signal and thus achieve the given value of output signal power at general load in comparison circuits or, in case of nearly complete attenuation of signal, greatly increase phase sensitivity of the comparison circuit (Fig. 12.8).

This circuit of semiconductor synchronized SHF oscillator operating in the mode of subtraction of coherent signals: clock signal and the output signal of the synchronized oscillator can be used to determine the value of change in the power of the output microwave signal, e.g. in case of change in thickness and electrical conductivity of the epitaxial layer of the semiconductor structure placed in the waveguide path. However, the use of the proposed measurement technique suggest fairly high requirements for stability of output parameters of synchronized oscillators and the quality of connections of functional units in the measuring system.

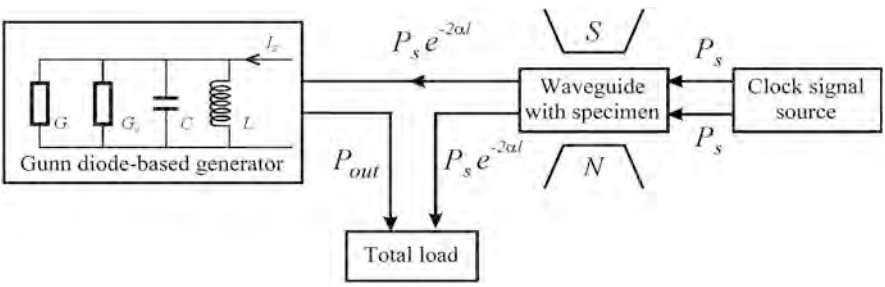

Fig. 12.8 Flow diagram of the installation, equivalent diagram of single-circuit diode semiconductor synchronized generator with resistive active semiconductor element

12.1.8 Near-Field SHF Microscopy of Material Properties

Near-field microwave (SHF) microscopy has led to the possibility of performing a new class of electrodynamical experiments for material testing. Such experiments, which are free from limitation of traditional microwave optics, can be performed at high space resolution within a wide frequency range. Moreover, measurements can be performed quantitatively, which makes it possible to create patterns of microwave properties of materials [32]. Synge, who noted the possibility of near-field microscopy in his fundamental article in 1928 [163], was the originator of the interest in this form of microscopy. Early attempts to implement quantitative microwave measurements with high resolution, following the works of Frait [164, 165] and later Soohoo [166], were most likely performed by science groups engaged in the study of ferromagnetic resonance.

Figure 12.9 shows the main types of probe-sample systems used in near-field SHF microscopy.

Figure 12.9*a* shows a traditional bulk microwave resonator with a small hole in the wall. The sample (specimen) is placed close to this wall; a small region of the sample determines the resonance frequency (causing its shift by Δf) and Q-factor of the resonator. Since the hole is small (d = 0.5 mm according to Frait [164, 165], and the sample introduces very small perturbations in the resonator, it becomes possible to study properties of a sample with large losses. This method can be used, for example, to study ferromagnetic resonance (FMR). FMR provides information about local internal fields and magnetization of the sample. Frait [164, 165], Soohoo [166] and Bhagat [167] successfully used such microscope to obtain ferromagnetic resonance patterns, while Ikeya [168, 169] applied it to obtain patterns of electron spin

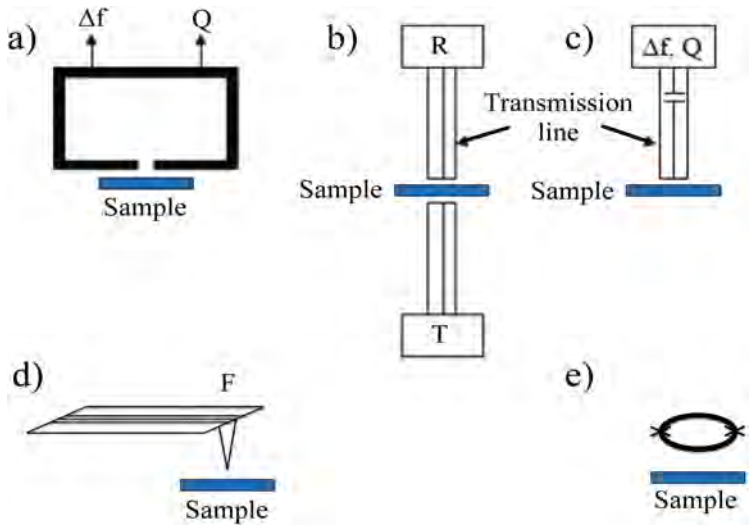

Fig. 12.9 Main types of probe-sample systems used in near-field SHF microscopy

resonance. An important variation of this idea was implemented by Ash and Nicholls [170]. They used an open hemispherical cavity with a flat-parallel reflector. The plate had a small opening inside, and the sample was placed near this opening but outside the resonator. In order to restore excitation signal from the cavity, the distance between the sample and the opening was modulated with fixed frequency. The authors managed to recover the signal reflected from the cavity with phase accuracy to build qualitative pattern of the sample in the course of its scanning under the hole. All these resonance methods use non-propagating methods in order to connect the resonant cavity and the local part of the sample. In this sense, the methods are similar to the aperture method of near-field scanning optical microscopy (NFSOM), where optical conical fiber is used.

Figure 12.9*b* shows a non-resonator circuit, in which the sample is placed at the end or near the end of the microwave transmission line. Complex reflection R or transmission T coefficient is measured, which is used to determine properties of the sample. The most well-known method is measurement of the coefficient of reflection from coaxial transmission line, at the end of which there is a sample (probably with air gap) [171–184]. In variations of this method, waveguides [185–187] with resonator cuts in the walls [188–193] and microstrip lines [194–198] are used during reflection measurements. Transmission tests were also performed in coaxial [180–182, 199–203] and waveguide [193] versions. The listed methods were mostly used for mapping of metal conductivities or surface resistance and dielectric constant. In certain cases, measures were performed quantitatively.

Figure 12.9*c* shows a schematic drawing of one of the most sensitive forms of near-field SHF microscopy. The idea is that the sample is placed near the open end of the cavity at the section of the transmission line, and the changes in resonant frequency and Q-factor are performed as the sample is scanned. The difference of this class of methods from the class shown in Fig. 12.9*a* consists in that it uses the possibility of field amplification at the end of the transmission line instead of insignificant aperture (opening) in the cavity. The feature of field amplification sets the scale for space resolution of this type of microscopes. The first of the structure employing this concept was used to measure moisture content in paper [204]. Other structures made use of transmission lines with samples in contact with the open end of the resonator [205–227] or with an air gap between the probe and the sample [208–225]. Parterns of surface resistance and non-linearity were obtained by the corresponding method for far field with scanning dielectric resonator contacting the sample [228, 229]. It was proven that the method based on using the transmission line with the cavity helps obtain the most accurate quantitative data as compared to all other methods of near-field microscopy. Quantitative presentation of the topography of surface resistance, dielectric constant, dielectric losses and other parameter were obtained. Moreover, the use of the field amplification property helped space resolution of resonance and non-resonance microscopy methods advance into the sub-micrometer region, preserving the quantitative nature of measurements.

Figure 12.9*d* shows a cantilever with pointed top placed above the sample. Such geometry can be used to determine layout of the sample by atomic force microscopy in addition to microwave microscopy results. There are three subslcasses of scanning

probe measurements of material properties at SHF. The first class includes measurement of localized electron spin resonance (ESR) [230]. In this case, the cantilever is used for scanning tunnel microscopy, but the magnetic field is simultaneously applied to the sample. Local signal at the Larmor precession frequency can be extracted from the response from the peak and transformed into the pattern of sample response ESR. The second design option consists in creatio nof a magnetic field gradient according to the sample (e.g., with the help of small magnetic particles on the cantilever) after placing the sample inside alternating magnetic field. The sample in this case locally meets the condition for magnetic resonance and causes power effect on the cantilever [231–233]. The third method consists in the simple use of sharp metallized cantilevers for performance of aperture-free near-field measurements. Sharp end in immediate proximity of the metal sample will locally amplify the radiation induced by focused beam in the far area. If an additional phenomenon can occur in this local region due to increased field strength, and if it can be recorded, then it becomes possible to perform local microscopic study of the physics of this phenomenon. One of important examples of this type of microscopy is apertureless microscopy, in which the signal reflected from the area of the probe top is measured, while the probe periodically oscillates up and down [234].

Figure 12.9*e* shows the probe-sample system used in combination with Superconducting Quantum Interference Device (SQUID). SQUID generates circulating alternating currents when permanent shift is applied to the loop (AC Josephson effect). Frequency of these currents is in direct proportion to the applied displacement voltage. The currents generate alternating magnetic fields, which later penetrate into the sample. In response, the sample generates its own currents, which in turn alter inductances of the SQUID loop. By studying magnetic field of the feedback signal required to maintain permanent magnetic stream in the SQUID, it becomes possible to draw the map of electromagnetic response of the sample [235, 236]. The advantage of this method consists in its applicability in a wide frequency range (in principle – from the frequency of the alternating magnetic field to the frequency corresponding to the energy cut of the superconductor equal to the energy of formation of the Cooper pair, which is used for SQUID creation, 100 GHz and more).

Known methods and devices for control of parameters of dielectric and conductive materials at SHF that go beyond the limits of the presented classification include the ones described in papers [237–242].

Method of [237] for measurement of complex dielectric permittivity of composite materials like carbon fiber-reinforced plastics with coarse surfaces characterized by high values of complex relative dielectric permittivity consists in the following: reference short-circuiting device and two additional reference short-circuiting devices (rough and smooth) are taken; after that, measurement of the complex coefficient of reflection from reference short-circuiting devices and the tested sample is performed, complex reflection coefficients are specified, and measurement results are processed to calculate values of complex relative dielectric permittivity.

Method described in [238] is used for measurement of complex dielectric permittivity and dielectric loss tangent of composite materials of the carbon fiber-reinforced

plastic type. Roughness of the material sample surface is measured; after that, reference short-circuiting device with the same roughness as the measured material is selected, complex coefficient of reflection from the reference short-circuiting device and the tested sample is measured, and measurement results are processed to calculate values of complex dielectric permittivity and dielectric loss tangent.

During measurement of complex dielectric permittivity of radio-absorbing composite materials under heating [239], thermocouples for measurement of temperature profile are inserted into the tested material sample through its entire thickness and at different depths, starting from the surface, and probing high-power electromagnetic wave is used, which simultaneously performs measurement and heating of the sample of the tested material. Measurement of the heating temperature is performed by thermocouples installed through entire thickness of the tested material sample. Measured parameters are the complex reflection or transmission coefficient of the electromagnetic wave and the temperature of sample heating throughout its thickness. Measured parameters are used to determine dielectric permittivity of the measured material at different frequencies.

The method of measurement of magnetic-dielectric parameters and thickness of coatings on metal [240] consists in creation of the electromagnetic field in the volume of the tested dielectric material on the conductive substrate, sequential excitation of slow surface waves: two E-waves at different but similar wavelengths λ_{G1}, λ_{G2} and one H-wave with λ_{G3}, measurement of attenuation of the field strength in normal plane relative to the direction of propagation of the wave with the help of a system of receiving vibrators at different values of the base d between them and calculation of normal attenuation coefficients α_{E1}, α_{E2}, α_{H} from the expression $E(y) = E_0 \exp[-\alpha(y) \cdot y]$ and determination of magnetic and dielectric permittivity and thickness of magnetic-dielectric coating from the formulas:

$$\varepsilon\mu = 1 + \frac{\alpha_{E1}\alpha_{E2}\lambda_{T1}\lambda_{T2}(\alpha_{E1} - \alpha_{E2})}{4\pi^2\left(\alpha_{E2}\lambda_{T1}{}^2 - \alpha_{E1}\lambda_{T2}{}^2\right)}, \tag{12.2}$$

$$\frac{b}{\varepsilon} = 1 + \frac{\alpha_{E1}\lambda_{\Gamma 1}{}^2}{4\pi^2(\varepsilon\mu - 1) - \alpha_{E1}{}^2\lambda_{\Gamma 1}{}^2}, \tag{12.3}$$

$$\mu = \frac{\beta_3}{\alpha_H}\left(\beta_3 b - \frac{\pi}{2}\right) \tag{12.4}$$

where the phase coefficient of the H wave is

$$\beta_3 = \frac{2\pi}{\lambda_{T3}}\sqrt{\varepsilon\mu - 1 - \left(\frac{\alpha_H\lambda_{T3}}{2\pi}\right)^2}. \tag{12.5}$$

SHF method of determining complex permittivity and conductivity of dielectric plates [241] consists in the fact that the directed antenna is used to excite the *E*-wave incident on the dielectric plate. The minimum of the reflected wave field is used to find the Brewster's angle of the incident wave and calculate the value of dielectric permittivity. Power values of incident and reflected waves are measured, the value of reflection coefficient is determined, and the specific conductivity and value of dielectric losses of the dielectric plate are calculated. Angle of incidence of the electromagnetic wave is increased to the value ensuring full internal reflection of the electromagnetic wave, field strength attenuation is measured in normal plane relative to the wave propagation direction, and normal attenuation coefficients and thickness of dielectric plate are calculated. This method helps determine complex permittivity and thickness of dielectric plates without dielectric substrate.

The method of determining thickness of dielectric coatings on conductive base [242] consists in creating electromagnetic field in the volume of tested dielectric material and conductive substrate and subsequent recording of converter properties. Microwave electromagnetic field of traveling surface wave is created above the dielectric-metal surface of the *E* type in the single mode is created, normals of the attenuation coefficients α_{E1} and α_{E2} to the normal of the dielectric-metal surface at two wavelengths λ_{G1} and λ_{G2} respectively are measured, and relative dielectric permittivity and thickness of the coating are determined.

12.1.9 Measurement of Thickness of Nanometer Metal Layers and Conductivity of Semiconductor in Metal-Semiconductor Structures Based on Reflection and Transmission Spectra of Electromagnetic Radiation

The authors of [35] suggest the method of non-destructive multi-parameter control of electrophysical parameters of nanometer metal layers and conductivity of the semiconductor in metal-semiconductor structures based on reflection and transmission spectra of the electromagnetic wave.

Tested structure with the thickness t consists of metal layer with thickness t_m with conductivity σ_m and substrate with thickness t_s with conductivity σ_s. Reflection R and transmission T coefficients of the electromagnetic wave interacting with semiconductor plate (substrate) with applied metal layer are determined by conductivity and thickness of the metal layer, as well as conductivity, thickness and dielectric permittivity of the substrate.

Measurement of thickness t_m of the metal film and conductivity σ_s of the substrate based on reflection $R(\omega)$ and transmission $T(\omega)$ spectra of electromagnetic radiation using the least square method for experimental data processing for this case is based on solving the system of equations

$$\begin{cases} \dfrac{\partial S(t_{\text{м}}, \sigma_{\text{п}})}{\partial t_{\text{м}}} = 0 \\ \dfrac{\partial S(t_{\text{м}}, \sigma_{\text{п}})}{\partial \sigma_{\text{п}}} = 0 \end{cases}, \tag{12.6}$$

$$\text{where } S(t_{\text{м}}, \sigma_{\text{П}}) = \sum \left(|T_{\text{эксп}}|^2 - |T(\omega, t_{\text{м}}, \sigma_{\text{п}})|^2 \right)^2 \tag{12.7}$$

$$\text{or } S(t_{\text{м}}, \sigma_{\text{п}}) = \sum \left(|R_{\text{эксп}}|^2 - |T(\omega, t_{\text{м}}, \sigma_{\text{п}})|^2 \right)^2. \tag{12.8}$$

In order to increase the range of variation of R and T with frequency variation in the selected frequency range (8–12 GHz), a layer of 2 mm thick dielectric with relative dielectric permittivity of 9.6 (Fig. 12.10a) was placed before the tested structure. In this case, the increase in frequency from 8 to 12 GHz saw a significant (almost by two orders) reduction of the reflection coefficient of the electromagnetic wave.

Tested structure (Fig. 12.10b and c) was placed in rectangular waveguide and completely filled its cross-section. Measured R_{1exp}, R_{2exp} and calculated $R_1(\omega, t_{\text{m}}, \sigma_{\text{s}})$, $R_2(\omega, t_{\text{m}}, \sigma_{\text{s}})$ frequency dependencies of the reflection coefficient of the electromagnetic wave incident from the side of the dielectric layer at two different orientations of the tested structure make it possible to build the residual function, which is the function of two variables t_{m}, σ_{s}:

$$S(t_{\text{м}}, \sigma_{\text{п}}) = \sum ||R_{2\text{эксп}} - R_{1\text{эксп}}| - |R_2(\omega_{\text{эксп}}, t_{\text{м}}, \sigma_{\text{п}}) - R(\omega_{\text{эксп}}, t_{\text{м}}, \sigma_{\text{п}})||^2, \tag{12.9}$$

Solution to the Equation (12.6) for the function of two variables S (t_{m},σ_{s}) in the formula (12.9) is the target thickness of metal film $t_{\text{m}\,t}$ and electrical conductivity of the substrate σ_{st}.

During the test, metal-semiconductor structures designed as titanium and vanadium films applied to 480 μm silicon substrates were measured. As a result of solving reverse problem the parameters of tested structures were found based on measured reflection spectra in the frequency range of 8–12 GHz.

Thus, the performed analysis of the contemporary state of studies in the field of control of parameters of dielectric and conductive materials at UHF demonstrates that modern measurement methods are characterized by significant variety and ensure the possibility of determining a number of parameters of metal films, semiconductor and dielectric materials and structures. However, ranges of controlled parameters due to insufficient sensitivity of the used control methods and limitations imposed on used design relations are often insufficient to support the needs of modern production of integrated circuits, microelectronic and nanoelectronic devices of the microwave range.

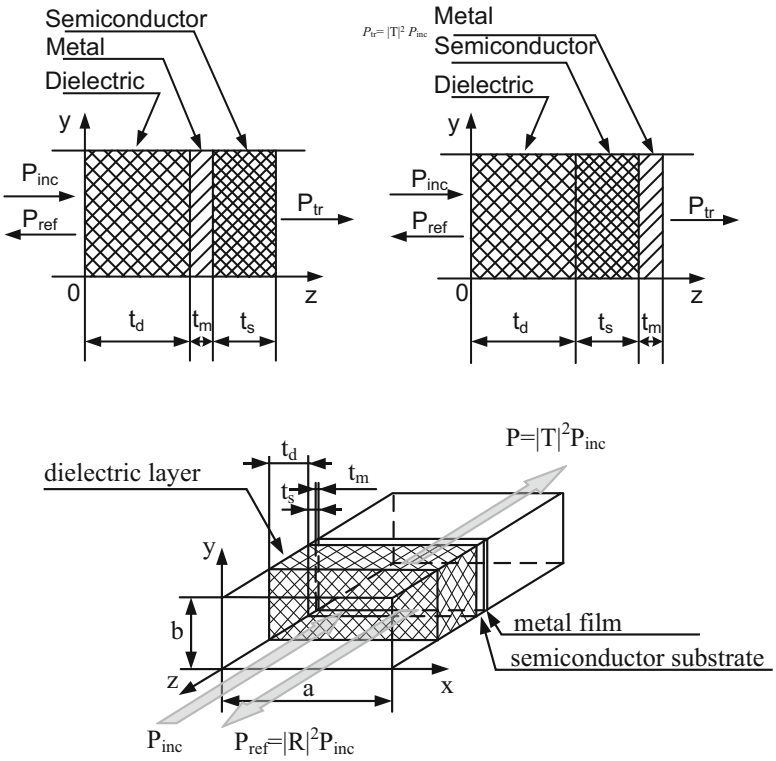

Fig. 12.10 Position of the tested structure

12.2 Mathematical Model and Results of Computer Modeling of the Interaction Between Microwave Radiation with One-Dimensional Waveguide Photonic Structures Including Nanometer, Metal, Dielectric and Semiconductor Layers

12.2.1 Interaction of SHF Radiation with Multi-Layered Structures with Planes of Layers Perpendicular to the Radiation Propagation Direction

Intensive development of nanotechnologies stimulated development and creation of the new class of periodic structures known as photonic crystals. These structures consist of periodically placed components, the dimensions of which are comparable to the wavelength of the electromagnetic radiation propagating in them. Transmission spectrum of such structure contains the frequency domain unavailable for propagation of electromagnetic wave – analog of the gap in crystals. In case of

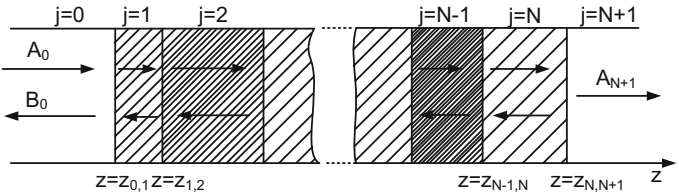

Fig. 12.11 Layered structure consisting of *N* layers

irregularities of the layered structure, narrow transmission windows can occur in the gap of the photonic crystal [51].

In the microwave range, one-dimensional photonic crystal can be implemented with the help of planar transmission lines with periodically changing structure [54, 55]. Microwave photonic structures were used to create band filters, tunable cavities and miniature antennas [53–61]. Known is high sensitivity of the frequency dependence of transmission window in the photonic crystal gap to periodicity irregularities in a layered structure. The authors of [243] demonstrated the possibility of using this property of photonic crystals for control of permittivity of layered dielectrics.

12.2.1.1 Mathematical Model

To calculate reflection and transmission coefficients of the electromagnetic wave in case of its normal incidence on multi-layer structure with planes of layers perpendicular to the radiation propagation direction and completely filling cross-section of the waveguide (Fig. 12.11), we will use the matrix of wave transmission between regions with different values of the constant of electromagnetic wave propagation γ_j and γ_{j+1} [35, 43].

Expressions for field components at different sides of the border between fields with different values of the constant of electromagnetic wave propagation have the following form [6, 244]:

$$\begin{aligned} E_j &= E(x)\left(A_j e^{-\gamma_j z} + B_j e^{\gamma_j z}\right), \\ H_j &= -\gamma_j H(x)\left(A_j e^{-\gamma_j z} - B_j e^{\gamma_j z}\right), \\ E_{j+1} &= E(x)\left(A_{j+1} e^{-\gamma_{j+1} z} + B_{j+1} e^{\gamma_{j+1} z}\right), \\ H_{j+1} &= -\gamma_{j+1} H(x)\left(A_{j+1} e^{-\gamma_{j+1} z} - B_{j+1} e^{\gamma_{j+1} z}\right), \end{aligned} \tag{12.10}$$

Condition of continuity of the field components at the boundary located at the distance of $z_{j,j+1}$ from the structure surface have the following form:

$$\begin{aligned} &A_j e^{-\gamma_j z_{j,j+1}} + B_j e^{\gamma_j z_{j,j+1}} = A_{j+1} e^{-\gamma_{j+1} z_{j,j+1}} + B_{j+1} e^{\gamma_{j+1} z_{j,j+1}}, \\ &-\gamma_j A_j e^{-\gamma_j z_{j,j+1}} + \gamma_j B_j e^{\gamma_j z_{j,j+1}} = -\gamma_{j+1} A_{j+1} e^{-\gamma_{j+1} z_{j,j+1}} + \gamma_{j+1} B_{j+1} e^{\gamma_{j+1} z_{j,j+1}}, \end{aligned} \tag{12.11}$$

Let us multiply the first equation of the system (12.11) by γ_{j+1}, add these equations and subtract the first equation from the second one; as a result, we get:

$$\begin{aligned} &A_j(\gamma_{j+1} - \gamma_j) e^{-\gamma_j z_{j,j+1}} + B_j(\gamma_{j+1} + \gamma_j) e^{\gamma_j z_{j,j+1}} = 2B_{j+1}\gamma_{j+1} e^{\gamma_{j+1} z_{j,j+1}} \\ &A_j(\gamma_{j+1} + \gamma_j) e^{-\gamma_j z_{j,j+1}} + B_j(\gamma_{j+1} - \gamma_j) e^{\gamma_j z_{j,j+1}} = 2A_{j+1}\gamma_{j+1} e^{-\gamma_{j+1} z_{j,j+1}}. \end{aligned} \tag{12.12}$$

After expressing coefficients A_{J+1}, B_{J+1} from this system of equations:

$$\begin{aligned} A_{j+1} &= A_j \frac{\gamma_{j+1} + \gamma_j}{2\gamma_{j+1}} e^{(\gamma_{j+1} - \gamma_j) z_{j,j+1}} + B_j \frac{\gamma_{j+1} - \gamma_j}{2\gamma_{j+1}} e^{(\gamma_{j+1} + \gamma_j) z_{j,j+1}} \\ B_{j+1} &= A_j \frac{\gamma_{j+1} - \gamma_j}{2\gamma_{j+1}} e^{-(\gamma_{j+1} + \gamma_j) z_{j,j+1}} + B_j \frac{\gamma_{j+1} + \gamma_j}{2\gamma_{j+1}} e^{-(\gamma_{j+1} - \gamma_j) z_{j,j+1}} \end{aligned} \tag{12.13}$$

the following expression for components of transmission matrices can be written:

$$T(z_{j,j+1}) = \begin{pmatrix} \frac{\gamma_{j+1} + \gamma_j}{2\gamma_{j+1}} e^{(\gamma_{j+1} - \gamma_j) z_{j,j+1}} & \frac{\gamma_{j+1} - \gamma_j}{2\gamma_{j+1}} e^{(\gamma_{j+1} + \gamma_j) z_{j,j+1}} \\ \frac{\gamma_{j+1} - \gamma_j}{2\gamma_{j+1}} e^{-(\gamma_{j+1} + \gamma_j) z_{j,j+1}} & \frac{\gamma_{j+1} + \gamma_j}{2\gamma_{j+1}} e^{-(\gamma_{j+1} - \gamma_j) z_{j,j+1}} \end{pmatrix}, \tag{12.14}$$

which links the coefficients A_j, B_j, A_{j+1}, B_{j+1} determining amplitudes of incident and reflected waves at both sides of the boundary $z_{j,j+1}$ by the ratio:

$$\begin{pmatrix} A_{j+1} \\ B_{j+1} \end{pmatrix} = T(z_{j,j+1}) \cdot \begin{pmatrix} A_j \\ B_j \end{pmatrix}. \tag{12.15}$$

Coefficients A_{N+1} and B_0 determining the amplitude of the wave that passed through multi-layered structure (Fig. 12.11) and the wave reflected from it are connected to the coefficient A_0 determining the amplitude of the incident wave by the following ratio

$$\begin{pmatrix} A_{N+1} \\ 0 \end{pmatrix} = T_N \cdot \begin{pmatrix} A_0 \\ B_0 \end{pmatrix}, \tag{12.16}$$

where

$$T_N = \begin{pmatrix} T_N[1,1] & T_N[1,2] \\ T_N[2,1] & T_N[2,2] \end{pmatrix} = \prod_{j=N}^{0} T_{j,(j+1)}$$
$$= T(z_{N,N+1}) \cdot T(z_{N-1,N}) \ldots T(z_{1,2}) \cdot T(z_{0,1})$$

is the transmission matrix of a layered structure composed of N layers (Fig. 12.11).

Recording reflection $R = \frac{B_0}{A_0}$ and transmission $T = \frac{A_{N+1}}{A_0}$ coefficients through the transmission elements T_N, in accordance with the ratio we get (12.16)

$$R = -\frac{T_N[2,1]}{T_N[2,2]}, \tag{12.17}$$

$$T = \frac{T_N[1,1] \cdot T_N[2,2] - T_N[1,2] \cdot T_N[2,1]}{T_N[2,2]}. \tag{12.18}$$

The obtained relation can be used to calculate values of transmission and reflection coefficient in case of interaction of the electromagnetic wave with thin metal films, dielectric and semiconductor layers and multi-layered structures.

12.2.1.2 Results of Computer Modeling of Reflection Spectra of Waveguide Photonic Structures in Different Frequency Ranges

The authors carried out computer modelling of one-dimensional photonic structures of the SHF range in waveguide version implemented in the form of structures designed as periodically alternating layers of dielectrics of two types with different values of thickness and permittivity (Fig. 16.11). The structure completely fills the cross-section of the waveguide, and planes of layers of the structure are perpendicular to the direction of propagation of electromagnetic radiation in the waveguide.

For calculation of reflection and transmission coefficients of the electronic wave in case of its incidence on such structure we used the structure described in Sect. 12.2.1.1.

The following structures were considered during computer modeling:

1. 11-layer structure designed as alternating layers of ceramics (Al_2O_3) with thickness of 1 mm and dielectric permittivity of $\varepsilon = 9.6$ (polycore) and foam plastic with thickness of 12 mm and permittivity $\varepsilon = 1.1$ within the frequency range of 8–14 GHz.
2. 19-layer structure designed as alternating layers of Rogers dielectric with thickness of 2.8 mm and dielectric permittivity $\varepsilon_c = 3$ and foam plastic with thickness of 12 mm and permittivity $\varepsilon_f = 1.1$ within the frequency range of 8–12.5 GHz.

3. 11-layer structure designed as alternating layers of ceramics (Al_2O_3) with thickness of 1 mm and dielectric permittivity of $\varepsilon_c = 9.6$ (polycore) and foam plastic with thickness of 2.5 mm and permittivity $\varepsilon_f = 1.1$ within the frequency range of 25–40 GHz.
4. 11-layer structure designed as alternating layers of Rogers dielectric with thickness of 1.5 mm and dielectric permittivity $\varepsilon_c = 3.5$ and foam plastic with thickness of 2.5 mm and permittivity $\varepsilon_f = 1.1$ within the frequency range of 25–40 GHz.
5. 17 -layer structure designed as alternating layers of fluoroplastic with thickness of 2 mm and dielectric permittivity $\varepsilon_c = 1.96$ and foam plastic with thickness of 2.5 mm and permittivity $\varepsilon_f = 1.1$ within the frequency range of 26–40 GHz.
6. 11-layer structure designed as alternating layers of ceramics with thickness of 0.375 mm and dielectric permittivity of $\varepsilon_c = 96$ and foam plastic with thickness of 1 mm and permittivity $\varepsilon_f = 1.1$ within the frequency range of 33.14–33.22 GHz.

Frequency dependencies of the squared absolute value of the reflection coefficient R of the electromagnetic wave from the examined structure during propagation of the wave of the H_{10} type calculated using the expression (12.17) are shown in Fig. 12.12, 12.13, 12.14, 12.15, 12.16, and 12.17 (curves 1). The same figures show results of calculation of the frequency dependence of the reflection coefficient of the examined photonic structure in the presence of irregularity in the form of altered thickness of the middle layer. In this case, a narrow transmission window appears in the reflection spectra, the position of which can be adjusted by changing thickness of the altered layer of dielectric.

It should be noted that, similarly to real crystals, introduction of irregularities in the form of impurity atoms into which creates donor or acceptor levels in the gap, creation of the above irregularities in photonic crystals, as follows from the presented drawings, also leads to appearance of donor transmission windows in the gap, which are located near the upper frequency boundary of the gap (e.g., Fig. 12.12, curve 5), or acceptor windows located near the lower frequency boundary of the gap (e.g., Fig. 12.12, curve 2). Frequency position of the window is determined by irregularity parameters.

Computer modeling of reflection spectra of one-dimensional waveguide crystals of various lengths was performed.

Figure 12.18 shows calculated spectra of reflection of one-dimensional waveguide photonic crystal consisting of alternating layers of ceramics (Al_2O_3) with thickness of 1 mm and permittivity $\varepsilon_c = 9.6$ (polycore) and foam plastic with thickness of 12 mm and permittivity $\varepsilon_f = 1.1$ within the frequency range of 8–14 GHz with different numbers of layers in the periodic structure of the crystal. Irregularity in the form of the thickness of the middle layer reduced to 3 mm was introduced into the crystal.

Figure 12.19 shows calculated spectra of reflection of one-dimensional waveguide photonic crystal consisting of alternating layers of ceramics (Al_2O_3) with thickness of 1 mm and permittivity $\varepsilon_c = 9.6$ (polycore) and foam plastic with thickness of 1 mm and permittivity $\varepsilon_f = 1.1$ within the frequency range of

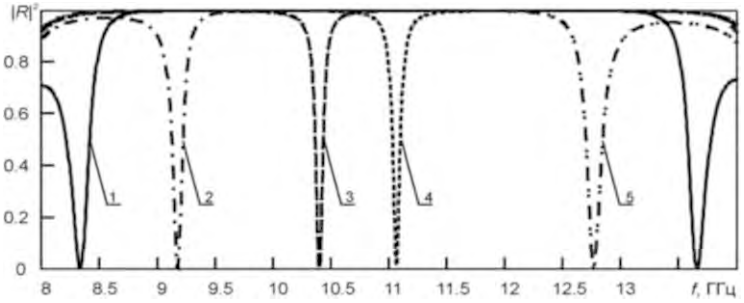

Fig. 12.12 Frequency dependencies of the squared absolute value of the reflection coefficient of the 11-layer photonic crystal "polycore – foam plastic" for different values of thickness d_6 of the altered 6th layer (foam plastic layer)
Curve 1 corresponds to the photonic crystal without irregularities
d_6, mm: 2–7.0; 3–4.0; 4–3.0; 5–1.0

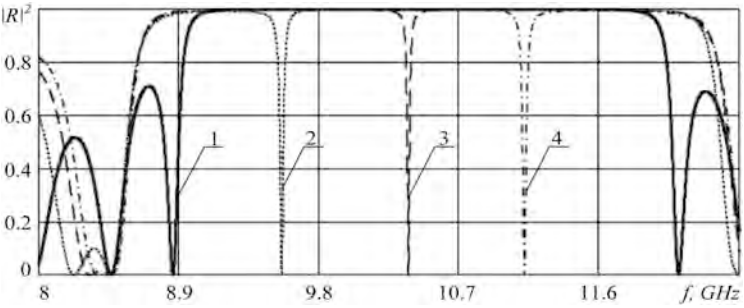

Fig. 12.13 Frequency dependencies of the squared absolute value of the reflection coefficient of the 19-layer photonic crystal "Rogers – foam plastic" for different values of thickness d_{10} of the altered 10th layer (foam plastic layer)
Curve 1 corresponds to the photonic crystal without irregularities
d_{10} , mm: 2–6.0; 3–3.0; 4–1.0

24–46 GHz with different numbers of layers in the periodic structure of the crystal. Irregularity in the form of the thickness of the middle layer increased to 5 mm was introduced into the crystal.

As can be seen from the presented figures, an increase in the number of periods of a one-dimensional waveguide photonic structure increases Q-factor of the transmission window in the crystal gap in the event of insignificant shift of the transmission window towards lower (if the thickness of the altered layer is smaller than the thickness of regular layers) or higher (if the thickness of the altered layer is greater than the thickness of regular layers) frequencies.

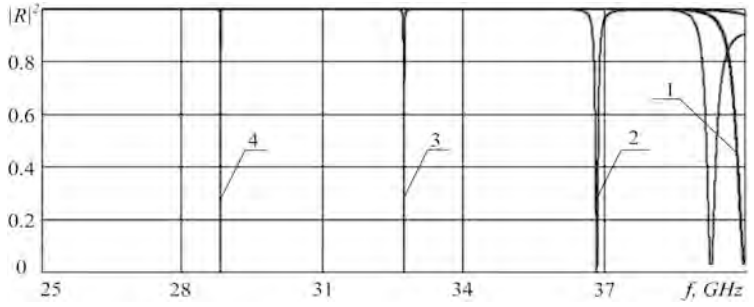

Fig. 12.14 Frequency dependencies of the squared absolute value of the reflection coefficient of the 11-layer photonic crystal "polycore – foam plastic" for different values of thickness d_6 of the altered 6th layer (foam plastic layer)
Curve 1 corresponds to the photonic crystal without irregularities.
d_6, mm: 2–4.0; 3–5.5; 4–7.5.

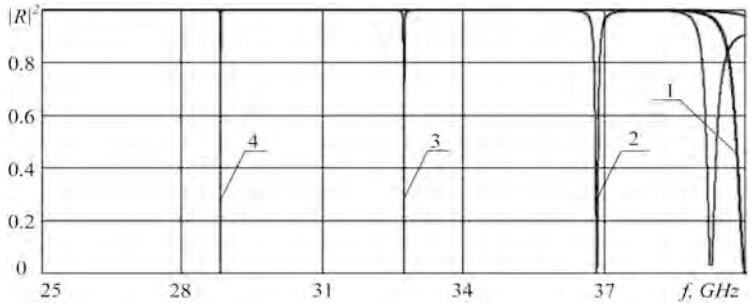

Fig. 12.15 Frequency dependencies of the squared absolute value of the reflection coefficient of the 11-layer photonic crystal "Rogers – foam plastic" for different values of thickness d_6 of the altered 6th layer (foam plastic layer)
Curve 1 corresponds to the photonic crystal without irregularities.
d_6, mm: 2–4.0; 3–5.5; 4–7.0.

12.2.1.3 Results of Computer Modeling of the Dependence of Reflection Spectra of Waveguide Photonic Structures on the Position of Irregularity in the Periodicity of the Photonic Crystal

As noted in the section above, introduction of irregularity into the periodic structure of a one-dimensional photonic crystal leads to emergence of narrow transmission windows in its gap: either donor or acceptor ones.

Studies were performed to examine dependence of the parameters of emerging transmission windows on the position of irregularity in the structure of the photonic structure.

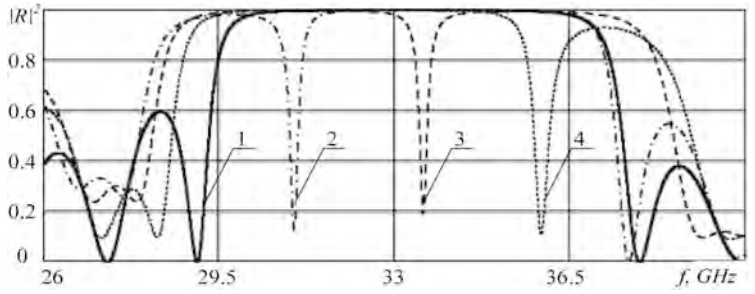

Fig. 12.16 Frequency dependencies of the squared absolute value of the reflection coefficient of the 17-layer photonic crystal "fluoroplastic – foam plastic" for different values of thickness d_9 of the altered 10th layer (foam plastic layer)
Curve 1 corresponds to the photonic crystal without irregularities.
d_{10}, mm: 2–7.5; 3–5.5; 4–4,

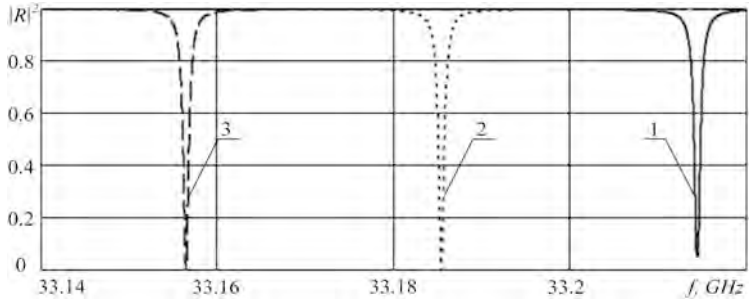

Fig. 12.17 Frequency dependencies of the squared absolute value of the reflection coefficient of the 11-layer photonic crystal "96 ceramics – foam plastic" for different values of thickness d_6 of the altered 6th layer (foam plastic layer)
d_6, mm: 1–5.49; 2–5.5; 3–5.51.

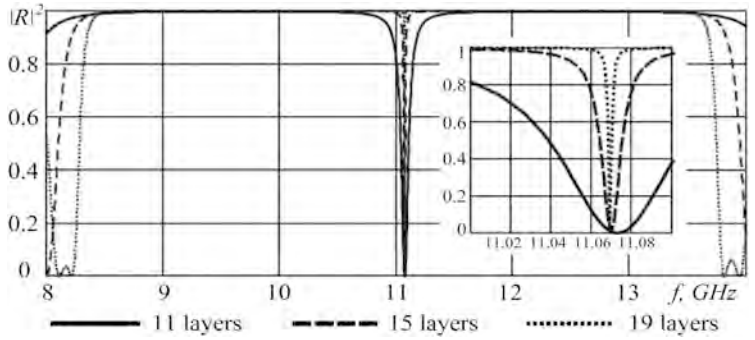

Fig. 12.18 Frequency dependencies of the squared absolute value of reflection of photonic crystals "polycore – foam plastic" in the 3 cm range of wavelengths with irregularities in the form of reduced thickness of middle layer containing different numbers of layers

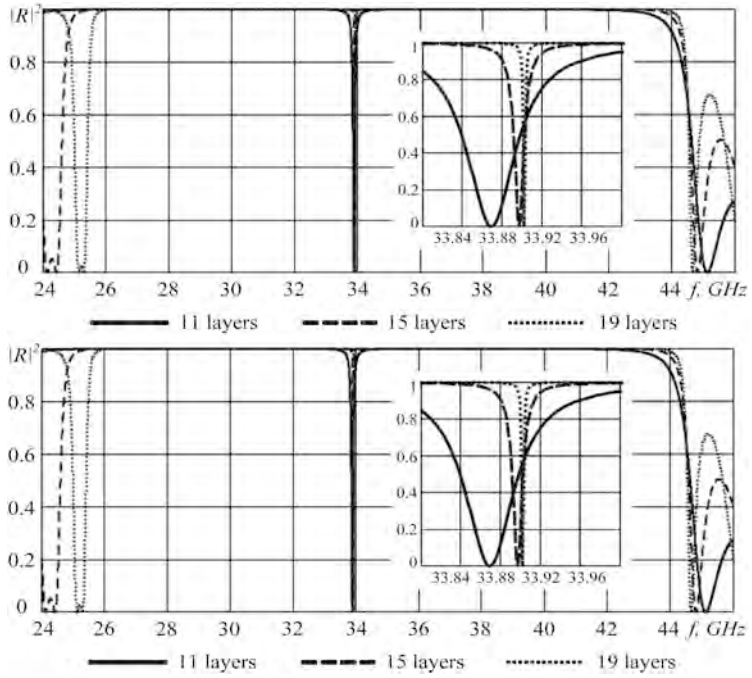

Fig. 12.19 Frequency dependencies of the squared absolute value of reflection of photonic crystals "polycore – foam plastic" in the 8 mm range of wavelengths with irregularities in the form of increased thickness of middle layer containing different numbers of layers

Figure 12.20 shows reflection spectra of 11-layer photonic crystal "polycore-foam plastic" (1 mm thick polycore, 12 mm thick polycore) in the 3-cm range of wavelengths in case of irregularity in the form of the thickness of one of foam plastic layers reduced to 3 mm (*a*) and to 5 mm (*b*).

Figure 12.21 shows reflection spectra of 11-layer photonic crystal "polycore-foam plastic" (1 mm thick polycore, 1 mm thick polycore) in the 8-mm range of wavelengths in case of irregularity in the form of the thickness of one of foam plastic layers reduced to 0.05 mm (*a*) and increased to 5 mm (*b*).

As demonstrated by computer modeling, placement of irregularity in the center of the photonic crystal leads to emergence of the transmission window with the minimum value of reflection coefficient and the maximum Q-factor. Shift of the irregularity from the center of the photonic crystal towards the edge leads to a decrease in the Q-factor of the transmission window and an increase in the reflection coefficient in the minimum of the reflection window up to complete disappearance of the window. In this case, irregularities in positions that are symmetrical in relation to the center are equivalent: reflection spectra for 11-layered photonic structures with irregularities in the second and tenth or in the fourth and eighth layers coincide.

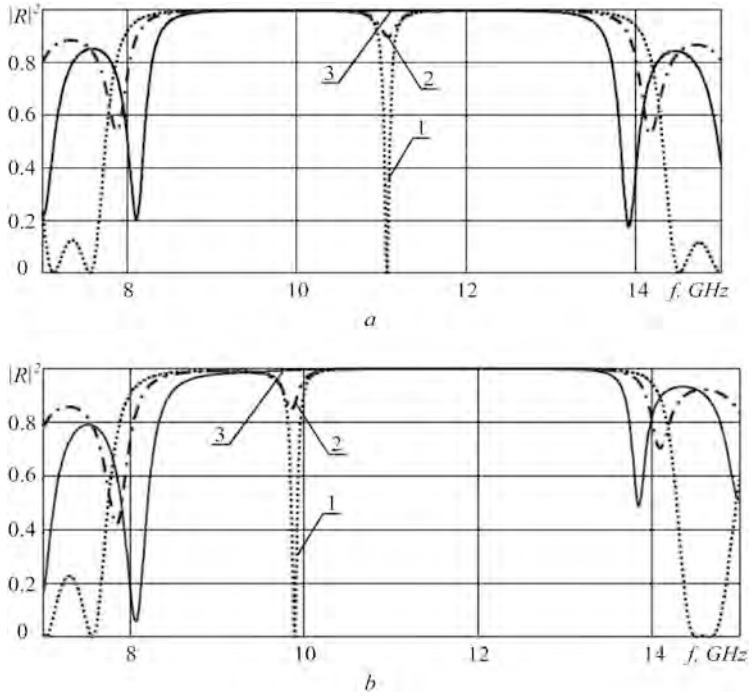

Fig. 12.20 Frequency dependencies of the squared absolute value of the reflection coefficient of 11-layer photonic crystal "polycore – foam plastic" in the presence of irregularity in the form of thickness of one of foam plastic layers reduced to 3 mm (*a*) and 5 mm (*b*)
1 – sixth, 2 – fourth and eighth, 3 – second and tenth

12.2.1.4 Results of Computer Modeling of the Dependence of Reflection Spectra of Waveguide Photonic Structures on Irregularity Parameters

Section 12.2.1.2 demonstrates that introduction of irregularity into a waveguide photonic crystal leads to appearance of narrow transmission windows in its transmission spectrum in the frequency domain of high reflection coefficient. Figures 12.12, 12.13, 12.14, 12.15, 12.16, and 12.17 show that the change in the thickness of the altered layer causes the position of transmission window in the photonic crystal gap to change as well.

If an irregularity in the form of altered dielectric permittivity of one of the layers of the photonic crystal is introduced at the frequency dependence $R(\omega)$, a transmission window appears in its gap, the position of which is determined by dielectric permittivity of the altered layer. Results of calculation of frequency dependencies of the reflection coefficient of 11-layer photonic crystal with transmission window for various values of permittivity ε of the middle (sixth) layer are shown in Fig. 12.22.

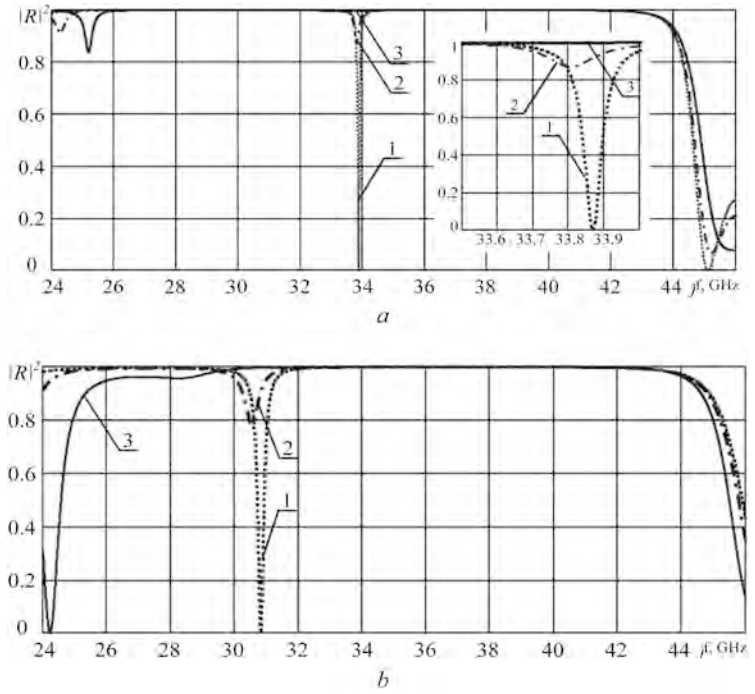

Fig. 12.21 Frequency dependencies of the squared absolute value of the reflection coefficient of 11-layer photonic crystal "polycore – foam plastic" in the presence of irregularity in the form of thickness of one of foam plastic layers reduced to 0.05 mm (**a**) and increased to 5 mm (**b**)
1 – sixth, 2 – fourth and eighth, 3 – second and tenth

Sensitivity of position of the transmission window in the gap of the photonic crystal depends on the thickness of the altered layer. For example, if the 6th layer of the examined structure is reduced to 4 mm, frequency dependencies of the squared absolute value of the reflection coefficient of 11-layer photonic crystal for different values of permittivity ε of the 6th layer will look as follows (Fig. 12.22), specifically: with the change of dielectric permittivity from 1 to 3, position of the transmission window changes from 10.4 to 9.4 GHz.

Moreover, if an irregularity in the form of altered thickness of the middle layer is introduced in the photonic structure, change of the dielectric permittivity of the following layer also causes changes in the frequency position of the transmission window and the value of reflection coefficient in its minimum.

Results of calculation of frequency dependencies of the reflection coefficient of 11-layer photonic crystal with transmission window for various values of permittivity ε of the seventh layer with altered sixth layer are shown in Fig. 12.24.

Analysis of the dependencies shown in Figs. 12.2, 12.3, 12.4, 12.5, 12.6, 12.7, 12.8, 12.9, 12.10, 12.11, 12.12, 12.13, 12.14, 12.15, 12.16, 12.17, 12.18, 12.19, 12.20, 12.21, 12.22, 12.23, and 12.24 allows us to suggest that solving the resverse

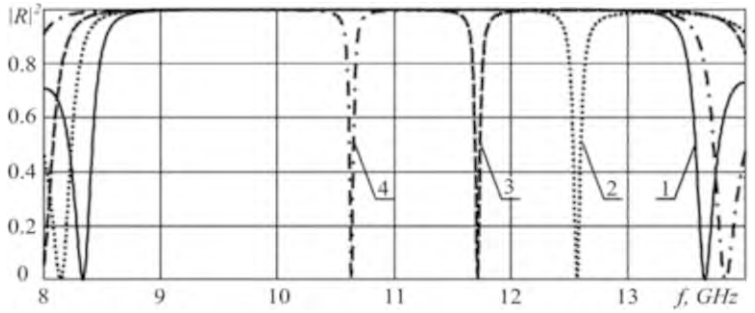

Fig. 12.22 Frequency dependencies of the squared absolute value of the reflection coefficient of the 11-layer photonic crystal for different values of permittivity ε of the altered 6th layer (12 mm thick)
ε, rel. units: 1–1; 2–1.5; 3–2; 4–3

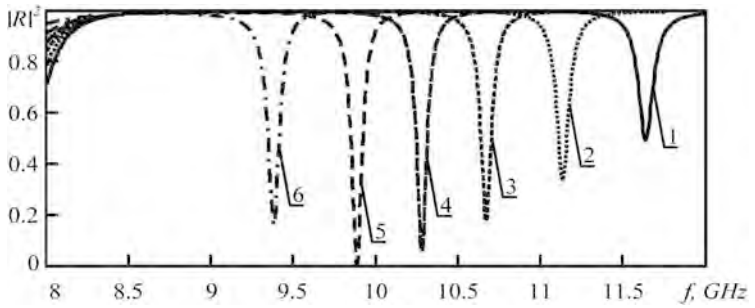

Fig. 12.24 Frequency dependencies of the squared absolute value of the reflection coefficient of the photonic crystal for various values of permittivity ε of the 7th layer with the thickness of the altered 6th layer (foam plastic) equal to ($d_6 = 5$ mm)
ε, rel. units: 1–1; 2–3; 3–5; 4–7; 5–9.6; 6–15

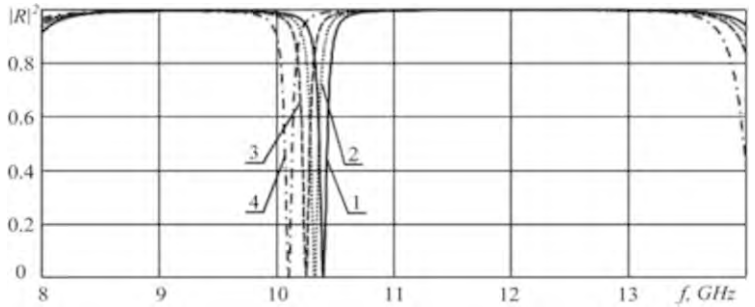

Fig. 12.23 Frequency dependencies of the squared absolute value of the reflection coefficient of the 11-layer photonic crystal for different values of permittivity ε of the altered 6th layer (4 mm thick)
ε, rel. units: 1–1; 2–1.5; 3–2; 4–3

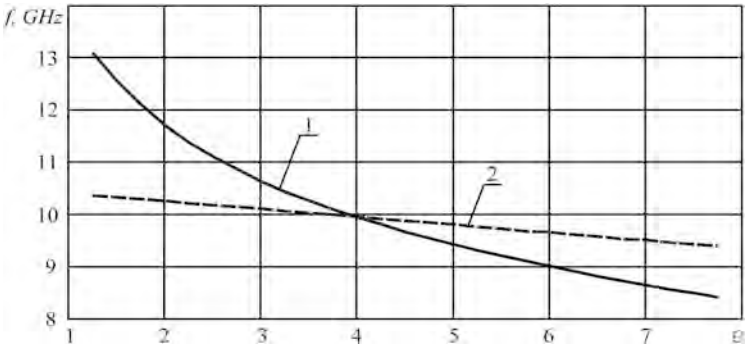

Fig. 12.25 Dependencies of the frequency corresponding to the minimum reflection coefficient in the transmission window on permittivity ε of the 6th (altered) layer; d_6, mm: 1–12; 2–4

problem based on the frequency dependency of the squared absolute value of the reflection coefficient $R(\omega)$ of the photonic crystal can be used to determine permittivity of plates in a wide range of values. The calculations demonstrate that by variation of the thickness of irregular layer and the position of the transmission window in the frequency range it is possible to adjust sensitivity of the reflection coefficient to the parameter ε of the tested plate. Dependencies of the frequency corresponding to the minimum reflection coefficient in the transmission window on the altered layer for two values of thickness of the altered layer are shown in Fig. 12.25 (the altered layers differs from regular ones in terms of both thickness and permittivity) and in Fig. 12.26 (the layer with altered dielectric permittivity follows the layer with altered thickness). If permittivity of the tested sample is known, it is possible to measure its thickness with high sensitivity.

Figure 12.27 shows dependencies of the frequency corresponding to the minimum reflection coefficient in the transmission window on the thickness of the tested sample. As can be seen from the presented dependencies, sensitivity of the frequency corresponding to the minimum reflection coefficient in the transmission window to variation in thickness of the polycore sample with thickness of about 1 mm reaches 1 MHz/μm at frequencies of 12–13 GHz.

12.2.1.5 Results of Computer Modeling of Reflection Spectra of Waveguide Photonic Structures Containing Transmitting Layers

Previous Sects. 12.2 and 12.2.1.4 describe high sensitivity of the frequency position of transmission window of the photonic crystal to the parameters of introduced irregularity. The authors performed studies of reflection spectra of such structures in case of addition of a two-layer structure designed as semiconductor or dielectric plate with applied nanometer metal layer. It can be suggested that frequency

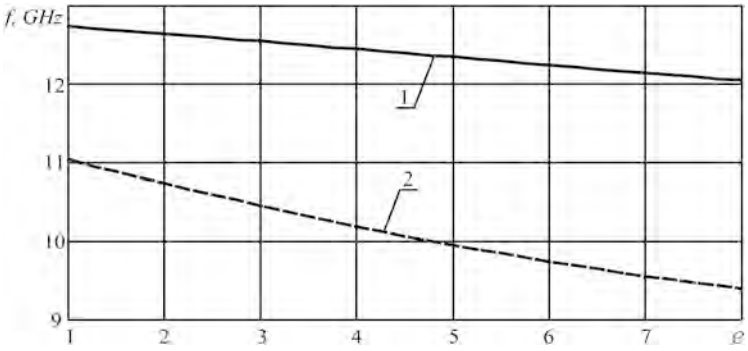

Fig. 12.26 Dependencies of the frequency corresponding to the minimum reflection coefficient in the transmission window on the permittivity ε of the 7th layer (1 mm thick) in the presence of the altered sixth layer in the photonic structure; d_6, mm: 1–2; 2–7

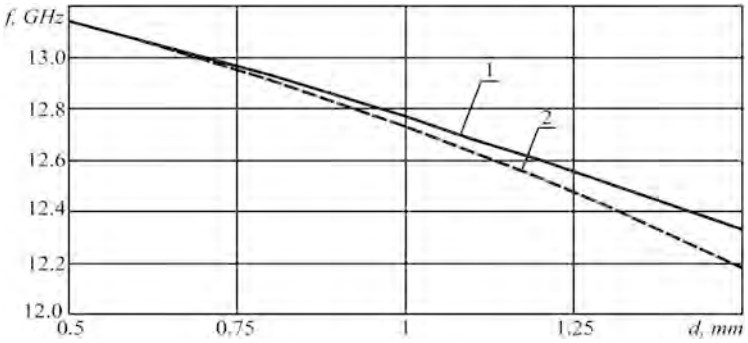

Fig. 12.27 Dependencies of the frequency corresponding to the minimum reflection coefficient in the transmission window on thickness of the 6th (altered) layer; permittivity ε_6, rel. units: 1–2 (fluoroplastic), 2–9.6 (polycore)

dependency of the reflection coefficient in the transmission window of such modified photonic structure will depend on the thickness and conductivity of metal layer in the added two-layer structure.

Figure 12.28 shows calculated frequency dependencies of the reflection coefficient of the photonic crystal designed as alternating layers of ceramics (Al_2O_3) with thickness of 1 mm and permittivity $\varepsilon_c = 9.6$ (polycore) and foam plastic with thickness of 12 mm and permittivity $\varepsilon_f = 1.1$ in the proximity of the transmission window in the presence of irregularity in the form of reduced middle (sixth) layer thickness d_6 for different values of thickness h of the nanometer metal layer in the structure "chrome on polycore" placed after the photonic crystal.

As follows from the results shown in this figure, change in h from 0 to 200 nm causes shift of the transmission window from the original position by ~50 MHz.

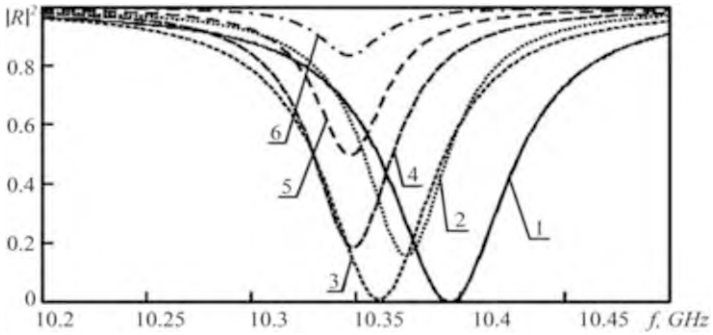

Fig. 12.28 Frequency dependencies of the squared absolute value of reflection coefficient of the photonic structure for different values of thickness h of the nanometer metal layer in case of placement of the photonic crystal before the measured structure
$d_6 = 4$ mm. Curve 1 corresponds to the photonic crystal without measured structure
h, nm: 2–0; 3–4; 4–20; 5–50; 6–200

Dependencies of the squared absolute value of the reflection coefficient $|R(\omega, t_m)|^2$ of the electromagnetic wave on the thickness of metal layer of the tested structure calculated using the relation (12.17) are shown in Fig. 12.29.

As follows from the results of calculations presented in Fig. 12.29, by selecting frequency of probing radiation from the resonance area it is possible to change the range of thicknesses of the metal layer in which rapid change of the frequency coefficient of electromagnetic radiation in the transmission window of the photonic structure is observed.

At the frequency $f_{min1} = 10.375$ GHz corresponding to the minimum of the squared absolute value of the reflection coefficient of the photonic crystal without additional two-layer structure, the reflection coefficient approaches saturation at thickness of the metal (chrome) layer exceeding 40 nm (curve 1 in Fig. 12.29), while at frequency $f_{min2} = 10.35$ GHz corresponding to the minimum reflection coefficient of the photonic crystal with additional structure the reflection coefficient approaches saturation with the thickness of the metal (chrome) layer exceeding 150 nm (curve 3 in Fig. 12.29).

Such character of resonance reflection makes it possible to use frequency dependencies of the reflection coefficient of the photonic crystal in the presence of irregularity in the form of reduced thickness of the middle layer for implementation of the methods of measurement of parameters of nanometer thickness with adjustable sensitivity of the reflection coefficient to changes in the thickness of the nanometer metal layer of the measured structure.

For significant expansion of the thickness range of metal films (up to several thousand nanometers), in which the coefficient of reflection from photonic structure does not reach saturation, modified 11-layer structure of the photonic crystal was considered, which consists of alternating layers of 1 mm ceramics with dielectric permittivity $\varepsilon = 100$ and 1 mm thick foam plastic with dielectric permittivity $\varepsilon = 1.1$.

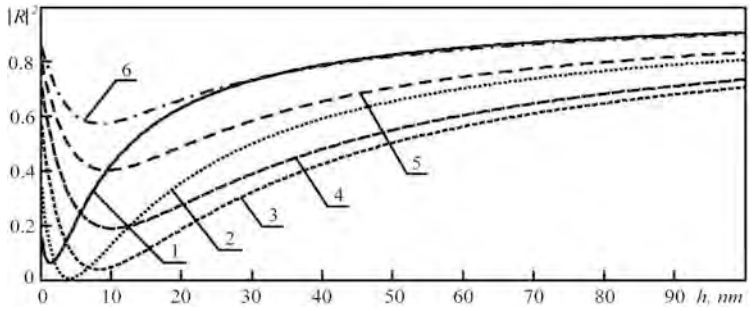

Fig. 12.29 Calculated dependencies of squared absolute values of the reflection coefficients $|R(\omega, t_m)|^2$ of the modifier photonic crystal in the presence of irregularity in the form of the 6th layer of reduced thickness ($d_6 = 4$ mm) on the thickness of metal layer with the photonic crystal placed before the tested structure at different frequencies f
f, GHz: 1–10.375; 2–10.36; 3–10.35; 4–10.34; 5–10.33; 6–10.32

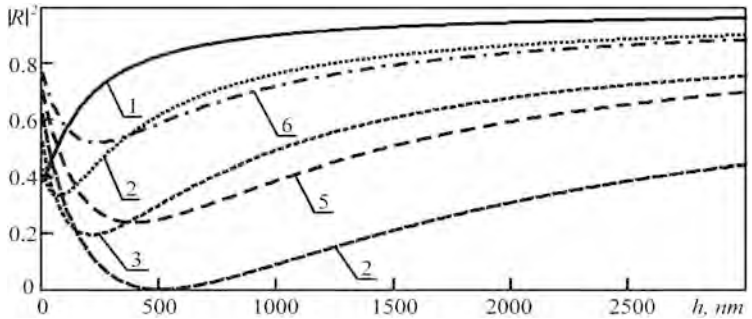

Fig. 12.30 Calculated dependencies of squared absolute values of the reflection coefficients $|R(\omega, t_m)|^2$ of the modified photonic crystal in the presence of irregularity in the form of the 6th layer of reduced thickness ($d_6 = 0.5$ mm) on the thickness of metal layer with the photonic crystal placed before the tested structure at different frequencies f
f, GHz: 1–8995; 2–9,01; 3–9,02; 4–9,03; 5–9,04; 6–9,05

As follows from the results of calculation of $|R|^2$ shown in Fig. 12.30, the coefficient of reflection from the photonic crystal with additional structure designed as dielectric plate with applied metal layer approaches saturation only with the thickness of the metal (chrome) layer exceeding 3000 nm (Fig. 12.30).

The presented curves demonstrate strong dependence of the reflection coefficient of the system "waveguide photonic crystal – tested structure" on the parameters of metal layer, which makes it possible to consider the possibility of determining thickness of the metal film with its known conductivity (or determining conductivity with its known thickness) by solving the reverse problem, for example, by least square method based on known theoretical description (12.17).

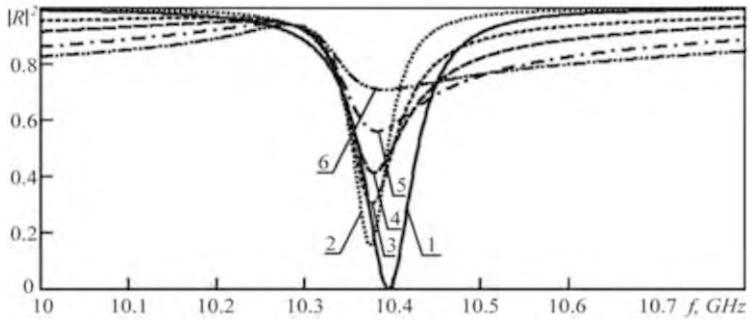

Fig. 12.31 Frequency dependencies of the squared absolute value of the reflection coefficient of the photonic crystal for different values of thickness h of the nanometer metal layer with the tested structure placed before the photonic crystal with thickness of the altered 6th layer (foam plastic) $d_6 = 4$ mm
Curve 1 corresponds to the photonic crystal without measured structure
h, nm: 2–0; 3–2.5; 4–5; 5–10; 6–25

When the tested two-layer structure is placed before the photonic structure, the form of frequency dependence of the reflection coefficient in the region of the transmission window, as follows from the results of calculation shown in Fig. 12.31, also undergoes significant changes with an increase in the thickness of the metal layer. In this case, the greatest change of the value of the squared absolute value of the reflection coefficient in the minimum of dependence $|R(\omega)|^2$ is observed within the range of thicknesses of metal (chrome) layer equal to 0–20 nm.

Thus, computer modeling demonstrated the following:

1. Multi-layer structure designed as periodically alternating layers of dielectrics with different values of permittivity with planes of layers perpendicular to the direction of propagation of the electromagnetic wave in the waveguide has frequency properties of one-dimensional optical photonic structures in the microwave range, in particular:
   (a) There is a frequency range unavailable for propagation of the electromagnetic wave, in which the reflection coefficient is close to or equal to one – analog of the gap in real crystals;
   (b) Creation of irregularities in the examined waveguide photonic crystal leads to appearance of donor or acceptor transmission windows in the transmission zone, and the frequency position of the transmission window is determined by parameters of the irregularity.
2. An increase in the number of periods of a one-dimensional waveguide photonic structure increases Q-factor of the transmission window in the crystal gap in the event of insignificant shift of the transmission window towards lower (if the thickness of the altered layer is smaller than the thickness of regular layers) or higher (if the thickness of the altered layer is greater than the thickness of regular layers) frequencies.

3. Placement of irregularity in the center of the photonic crystal leads to emergence of the transmission window with the minimum value of reflection coefficient and the maximum Q-factor.
4. The use of one-dimensional waveguide photonic crystals with irregularities helps increase sensitivity of methods of testing electrophysical parameters of materials and layered structures based on microwave radiation reflection and transmission spectra.

12.3 Theoretical Basis for the Method of Measurement of SHF Material Parameters Using One-Dimensional Waveguide Photonic Structures

12.3.1 Measurement of Permittivity of Materials

As demonstrated in Sect. 12.2.1.4, determination of such electrophysical parameters of structures as thickness or conductivity of the metal layer, etc. based on the spectrum of transmission $T(\omega)$ or reflection R (ω) of electromagnetic radiation is possible by means of the least square method, which helps found the value of the target parameter p, at which the sum S of squared differences between experimentally obtained ($|T_{exp}|^2$ or $|R_{exp}|^2$) and design ($|T(\omega,d|^2$ or$|R(\omega,d|^2$) of the values of squared absolute values of transmission or reflection coefficient is:

$$S(p) = \sum_{i=1}^{N} \left(|T_{i\ \text{эксп}}|^2 - |T(\omega_{i\ \text{эксп}}, p)|^2 \right)^2$$

or

$$S(p) = \sum_{i=1}^{N} \left(|R_{i\ \text{эксп}}|^2 - |R(\omega_{i\ \text{эксп}}, p)|^2 \right)^2 \tag{12.19}$$

or

$$S(p) = \sum_{i=1}^{N} \left[\left(|T_{i\ \text{эксп}}|^2 - |T(\omega_{i\ \text{эксп}}, p)|^2 \right)^2 + \left(|R_{i\ \text{эксп}}|^2 - |R(\omega_{i\ \text{эксп}}, p)|^2 \right)^2 \right]$$

becomes minimum, where N is the number of experimental points.

Therefore, the target value of the unknown parameter (thickness or conductivity of the metal film) p_t can be found by solving the equation:

$$\frac{\partial S(p)}{\partial p} = 0 \tag{12.20}$$

This equation can be used by numerical method using a computer.

If the task allows to perform optimization of the residual function based on several parameters from the physical point of view, the equation will be replaced with a system of equations. If the target parameter is a complex value (complex permittivity, complex magnetic permittivity, etc.), the problem shall be solved in the complex plane.

If irregularity in the form of altered permittivity of one of the layers is introduced into waveguide photonic crystal, transmission window, the position of which inside the gap area is determined by permittivity of the excited layer, appears in the frequency dependence $R(\omega)$. This makes it possible to use frequency dependence of the reflection coefficient of the system "photonic crystal placed before the measured sample – measured sample" to measure permittivity of the tested sample, solving the reverse problem.

In order to find the target dielectric permittivity $|R(\omega)|^2$, it is possible to use the least square method, during implementation of which such value of the ε_t is found at which the sum $S(\varepsilon_t)$ of squared differences between experimentally obtained $|R_{exp}|^2$ and design $|R(\omega, \varepsilon_d)|^2$ values of squared absolute value of reflection coefficient (12.19), which becomes minimum, in this case takes the following form:

$$S(\varepsilon) = \sum \left(|R_{\text{эксп}}| - |R(\omega, \varepsilon)|^2 \right)^2. \tag{12.21}$$

Target value of permittivity ε of the tested sample is determined by numerical technique as a result of solving the Eq. (12.20), which in this case takes the following form:

$$\frac{\partial S(\varepsilon)}{\partial \varepsilon} = \frac{\partial \left(\sum \left(|R_{\text{эксп}}|^2 - |R(\omega, \varepsilon)|^2 \right) \right)^2}{\partial \varepsilon} = 0. \tag{12.22}$$

Computer modeling was performed to study the possibility of measurement of permittivity of materials based on spectra of reflection of electromagnetic radiation. Modeled was measurement of dielectric permittivity of the dielectric plate with thickness of 4 mm with waveguide photonic crystal composed of 19 alternating layers of 1 mm thick polycore and 12 mm thick foam plastic with the irregularity in the form of thickness of the middle (tenth) layer (foam plastic) reduced to 3 mm placed before the plate. Results of calculation of the direct problem are shown in Fig. 12.32.

Test data were set as values of the squared absolute value of the coefficient of reflection from the structure obtained from the exact solution of (12.17) with the

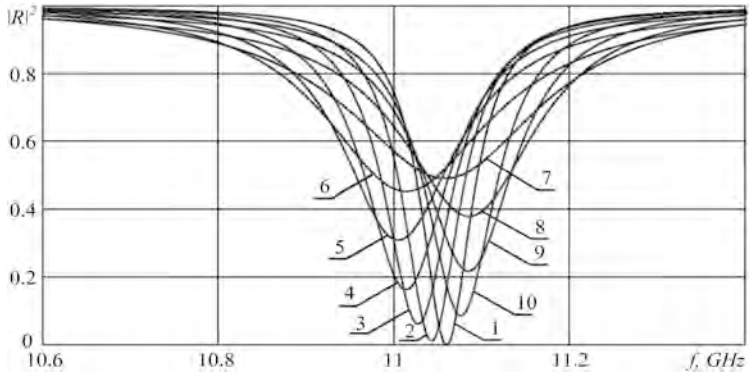

Fig. 12.32 Results of calculation of reflection spectra of the structure "waveguide photonic crystal with irregularity – tested dielectric sample) for different values of dielectric permittivity of the sample
ε: 1–1; 2–2; 3–3; 4–4; 5–5; 6–6; 7–7; 8–8; 9–9; 10–10

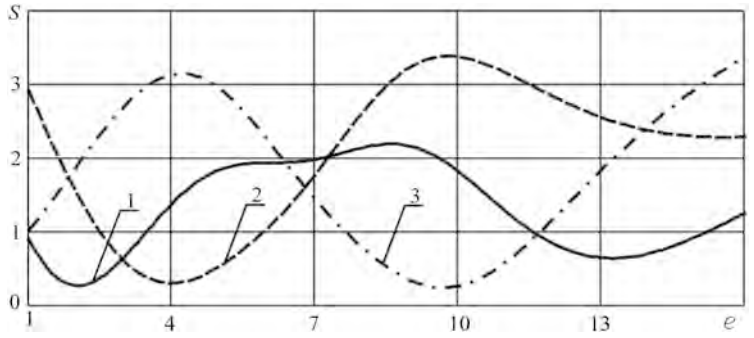

Fig. 12.33 Formula of the residual functions S(ε) determined by the expression (12.21) for different values of dielectric permittivity ε of the tested sample
ε: 1–2; 2–4; 3–9.6

error of ±10% and with the error in frequency setting equal to $\pm\ 0.5{\cdot}10^{-3}\%$. Residual functions $S(\varepsilon)$ determined by the expression (12.32) for different values of dielectric permittivity of the tested sample are shown in Fig. 12.32. The value of the argument ε at which the function $S(\varepsilon)$ reaches its minimum value is the solution to the Eq. (12.32), i.e. the target value of permittivity ε_t of the tested sample. Figure 12.33 shows test (points) and calculated (lines) values of the reflection coefficient obtained with the help of found values of permittivity ε_t of tested samples. Relative error of determination of dielectric permittivity of the sample according to test data amounted to 1–3% (Fig. 12.34).

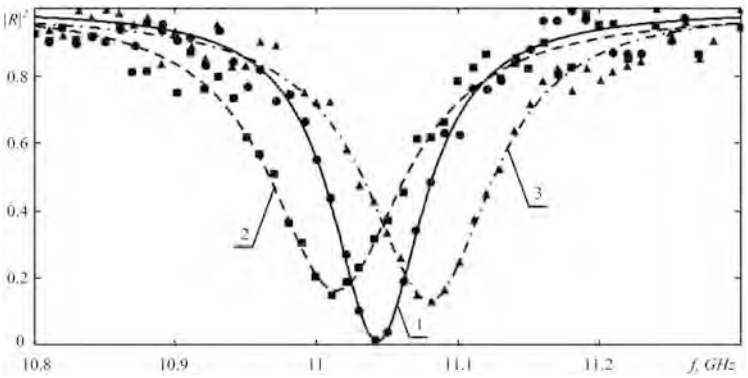

Fig. 12.34 Test (points) and calculated (lines) values of the reflection coefficient obtained using the found values of the parameter ε_t
ε_t: 1–1.9; 2–3.9; 3–9.7

12.3.2 Measurement of Complex Permittivity of Materials with Losses

An important practical task of microelectronics and nanoelectronics is the problem of simultaneous measurement of such parameters of semiconductor plates used as IC substrates as dielectric permittivity ε_s and electrical conductivity σ_s (i.e., complex dielectric permittivity) in the wide range of their variation; at the same time, it is preferable to perform tests using standard equipment without special expensive probes.

Complex permittivity of a material is recorded as:

$$\varepsilon = \varepsilon' - j \cdot \varepsilon'' = \varepsilon_L - j \cdot \frac{\sigma}{\omega \varepsilon_0}, \tag{12.23}$$

where εL is the dielectric permittivity of the lattice, σ is the electrical conductivity of the sample, ω is the circular frequency of the propagating radiation.

Measurement of real and imaginary components of the complex dielectric permittivity of the sample, or its dielectric permittivity ε and conductivity σ based on reflection spectra $R(\omega)$ of electromagnetic radiation in case of using the least square methods for processing of experimental data for this case is based on solving the system of equations

$$\begin{cases} \dfrac{\partial S(\sigma, p)}{\partial \varepsilon} = 0 \\ \dfrac{\partial S(\varepsilon, \sigma)}{\partial \sigma} = 0 \end{cases}, \tag{12.24}$$

for residual function of the form

$$S(\sigma, p) = \sum_{i=1}^{N} \left(|R_{\text{i эксп}}|^2 - |R(\omega_{i\ \text{эксп}}, \varepsilon, \sigma)|^2 \right)^2. \tag{12.25}$$

Computer modeling was performed to study the possibility of measurement of complex permittivity of materials based on spectra of reflection of electromagnetic radiation. Modeling was performed for measurement of permittivity of a silicone plate with thickness of 0.5 mm placed as the central layer of waveguide photonic crystal consisting of 11 alternating layers of 1 mm thick polycore and 1 mm thick foam plastic and manifested as variation of its periodic structure. Results of calculation of the direct problem are shown in Figs. 12.25 and 12.35.

Test data were set as values of the squared absolute value of the coefficient of reflection from the structure obtained from the exact solution of (12.17) with the error of ±5% and with the error in frequency setting equal to ± 0.5·10–3%. Formula for the residual function (12.35) is shown in Fig. 12.36.

Solution to the system of Eq. (12.34) for the function $S(\varepsilon,\sigma)$ presented as (12.35) consists of target dielectric permittivity and conductivity of the sample ε_t and σ_t. Figure 12.37 shows test (points) and calculated (lines) values of the reflection coefficient obtained with the help of found values of parameters ε_t and σ_t. Relative error of determining dielectric permittivity of the sample based on test data reached 15%; relative error of determining conductivity of the sample based on test data reached 7%.

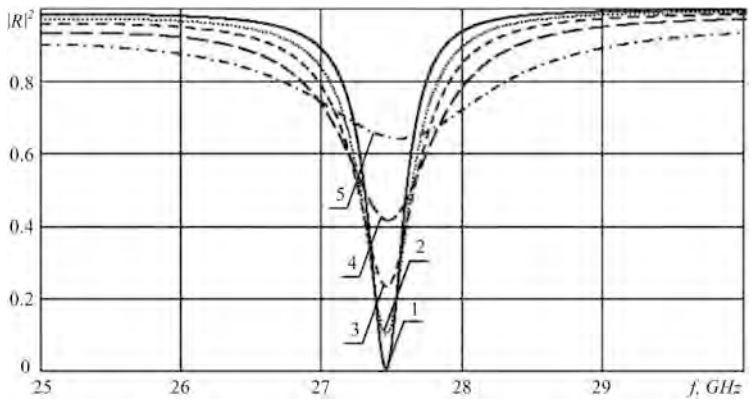

Fig. 12.35 Results of calculation of the reflection spectra of the structure "waveguide photonic structure with irregularity in the form of measured sample – 0.5 mm thick silicon wafer" for different values of silicon conductivity
σ, Ohm_{-1} m_{-1}: 1–1; 2–5; 3–10; 4–20; 5–50

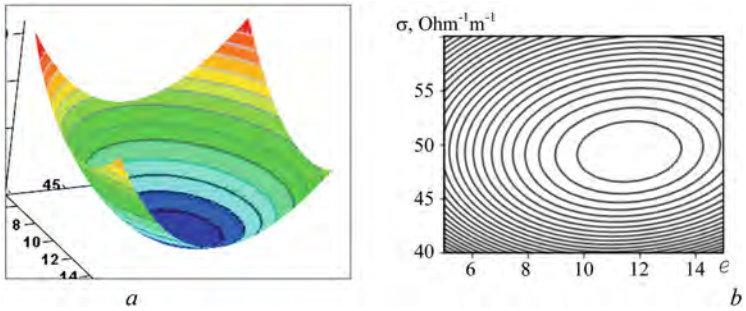

Fig. 12.36 Formula for the residual function in the space of target parameters (**a**) and the contour chart of the residual function in the plane of target parameters (**b**) for silicon sample ($\varepsilon = 12$) with conductivity $\sigma = 50$ Ohm^{-1} m^{-1}

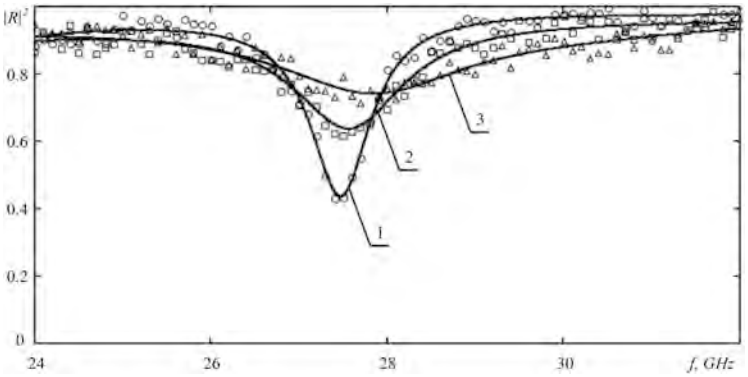

Fig. 12.37 Test (points) and calculated (lines) values of the reflection coefficient obtained with the help of found values of parameters ε_t and σ_t respectively
1–11.8 and 21.3; 2–11.7 and 47.9; 3–10.0 and 97.9

12.3.3 Measurement of Thicknesses of Nanometer Metal Films on Dielectric or Semiconductor Substrates

The use of frequency dependence of the squared absolute value of the coefficient of reflection $|R(\omega)|^2$ of electromagnetic radiation from the photonic structure with tested sample designed as dielectric or semiconductor plate with applied metal layer with known parameters of the substrate helps determine the thickness $t_{m\ t}$ of the nanometer metal film if its conductivity is known (or determine its conductivity if its thickness is known).

In order to find the target thickness t_{mt} of the nanometer metal film based on frequency dependence of $|R(\omega)|^2$ can be performed by using the least square method, the implementation of which helps find such value of the parameter t_{mt} at which the

sum $S(t_{mt})$ of experimentally obtained $|R_{exp}|^2$ and design $|R(\omega, t_{mt})|^2$ squared absolute values of the reflection coefficient (12.19), which in this case has the form

$$S(t_м) = \sum \left(|R_{эксп}|^2 - |R(\omega, t_м)|^2 \right)^2, \tag{12.26}$$

becomes minimal.

Target value of the metal film thickness $t_{m\,t}$ is determined by numerical technique as a result of solving the eq. (12.20), which in this case takes the following form:

$$\frac{\partial S(t_м)}{\partial t_м} = \frac{\partial \left(\sum \left(|R_{эксп}|^2 - |R(\omega, t_м)|^2 \right) \right)^2}{\partial t_м} = 0. \tag{12.27}$$

Similarly, if the film thickness is known, its conductivity can be determined from the solution to the equation

$$\frac{\partial S(\sigma_п)}{\partial \sigma_п} = \frac{\partial \left(\sum \left(|R_{эксп}|^2 - |R(\omega, \sigma_п)|^2 \right) \right)^2}{\partial \sigma_п} = 0. \tag{12.28}$$

Computer modeling was performed to study the possibility of thickness of nanometer metal films based on spectra of reflection of electromagnetic radiation. Modeling was performed for measurement of thickness of the nanometer chrome layer ($\sigma = 2 \cdot 10^6$ cm) applied to 0.5 mm polycore substrate ($\varepsilon = 9.6$). Test data were set as values of the squared absolute value of the coefficient of reflection from the structure obtained from the exact solution of (12.17) with the error of $\pm 10\%$ and with the error in frequency setting equal to $\pm 0.5 \cdot 10^{-3}\%$. Residual functions (12.25) with the waveguide photonic structure consisting of 19 alternating layers of polycore with thickness of 1 mm and foam plastic with thickness of 12 mm with irregularity of the thickness of the middle (10th) layer (foam plastic) reduced to 3 mm placed before the measured structure for different thicknesses of the nanometer chrome layer are shown in Fig. 12.38.

Solution to the Eq. (12.27) for the function $S(t_m)$ in the form of 12.25 is the target thickness of the metal film t_{mt}. Figure 12.29 shows test (points) and calculated (lines) values of the reflection coefficient obtained with the help of found values of the parameter $t_{m\,t}$.

Relative error of determination of the thickness of nanmometer metal film according to test data amounted to 4–14% (Fig. 12.39).

An important practical task of microelectronics and nanoelectronics is the problem of simultaneous determination of substrate conductivity σ_s and metal film thickness t_m of a finished structure, when it is not possible to measure parameters of the semiconductor substrate separately.

Measurement of thickness of the metal film t_m and conductivity of the substrate σ_s based on reflection $R(\omega)$ and transmission $T(\omega)$ spectra of electromagnetic radiation

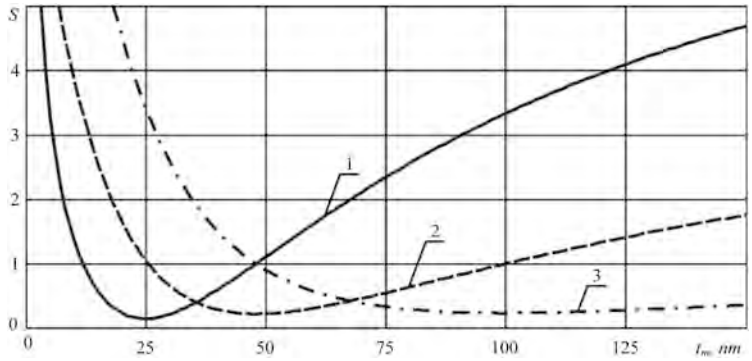

Fig. 12.38 Residual function for various thicknesses t_m of the chrome nanolayer t_m, nm: 1–25; 2–50; 3–100

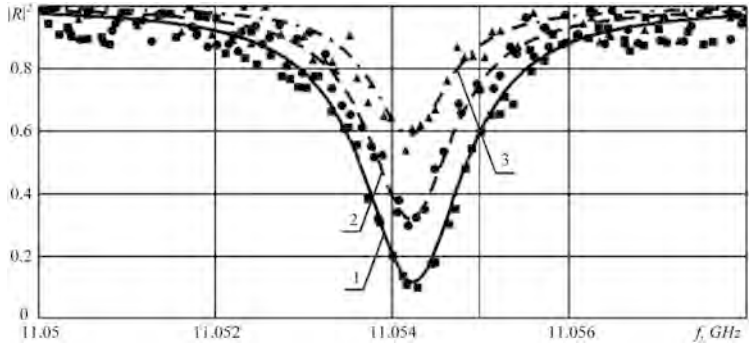

Fig. 12.39 Test (points) and calculated (lines) values of the reflection coefficient obtained with the help of found values of the parameter $t_{m\ t}$, $t_{m\ t}$, nm: 1–26; 2–57; 3–104

by using the least square method for this case is also based on solving the system of Eqs. (12.20). It should be noted that the system of Eq. (12.20) has a solution if the function of two variables of the (12.19) form on the plane (t_m, σ_s) has an express global minimum. Computer modeling and experimental studies demonstrate that in most cases surfaces of the type

$$S(t_м, \sigma_п) = \sum \left(|T_{эксп}|^2 - |T(\omega, t_м, \sigma_п)|^2 \right)^2 \tag{12.29}$$

or

$$S(t_м, \sigma_п) = \sum \left(|R_{эксп}|^2 - |R(\omega, t_м, \sigma_п)|^2 \right)^2 \tag{12.30}$$

in the region of the minimum has the shape of a hollow ravine in the coordinate space (t_m, σ_s, S) (Fig. 12.40).

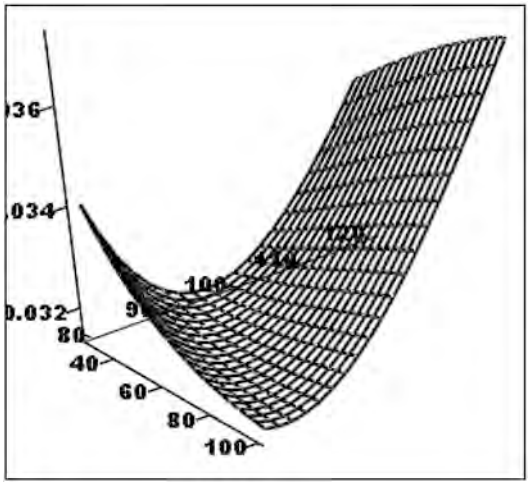

Fig. 12.40 Formula of the residual function (12.27) in the space of target parameters for 130 nm thick metal layer applied to silicon substrate with conductivity $\sigma = 90$ Ohm^{-1} m^{-1}

At the same time, if measurements are performed for two different orientations of the tested structure relative to the photonic crystal (photonic crystal – metal film – semiconductor substrate and photonic crystal – semiconductor substrate – metal film), the residual function with the formula

$$S(t_м, \sigma_п) = \sum ||R_{2\ эксп} - R_{1\ эксп}| - |R_2(\omega_{эксп}, t_м, \sigma_п) - R_1(\omega_{эксп}, t_м, \sigma_п)||^2, \tag{12.31}$$

where $R_{1\ exp}$, $R_{2\ exp}$, are measured, and $R_1(\omega, t_m, \sigma_s)$, $R_2(\omega, t_m, \sigma_s)$ are calculated dependencies of the reflection coefficient of reflection of the electromagnetic wave incident at the side of photonic crystal for two different orientations of the measured structure often have pronounced global minimum (Fig. 12.31), which makes it possible to accurately determine the thickness of the metal film t_m and conductivity of the substrate σ_s, solving the following system of equations:

$$\begin{cases} \dfrac{\partial s(t_м, \sigma_P)}{\partial t_м} = 0 \\ \dfrac{\partial S(t_м, \sigma_p)}{\sigma_п} = 0 \end{cases}. \tag{12.32}$$

Modeling was performed for simultaneous application of the thickness of metal layer applied to the semiconductor substrate with waveguide photonic structure consisting of 11 alternating layers of 1 mm thick polycore and 1 mm thick foam plastic containing irregularity in the form of reduced thickness of the middle layer before tested structure. Test data were set as values of the squared absolute value of the coefficient of reflection from the system obtained from the exact solution of (12.17) with the error of ±5% and with the error in frequency setting equal to ±0.5·10_3% . Formula for the residual function (12.31) is shown in Fig. 12.41.

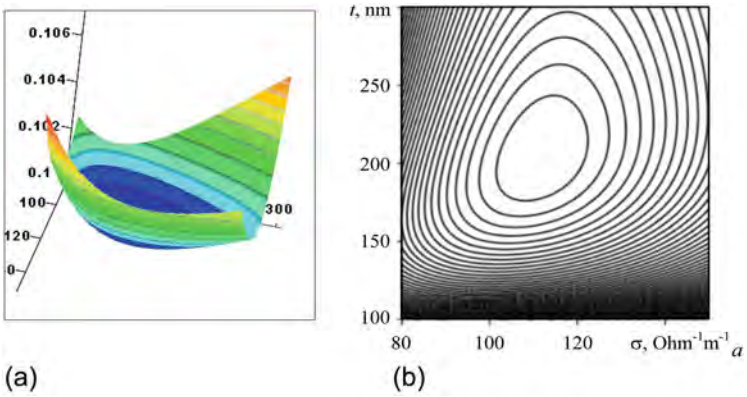

Fig. 12.41 Formula for the residual function (3.13) in the space of target parameters (**a**) and the contour chart of the residual function in the plane of target parameters (**b**) for 130 nm thick metal film applied to silicon substrate with conductivity $\sigma = 90$ Ohm^{-1} m^{-1}

Therefore, the performed computer modeling demonstrates that the use of one-dimensional waveguide photonic crystals makes it possible to implement highly sensitive methods of measurement of electrophysical parameters of materials and layer structures, including the ones containing nanometer metal layers, based on SHF radiation reflection and/or transmission spectra.

12.4 Results of Experimental Study of Interaction of SHF Radiation with One-Dimensional Waveguide Photonic Structures

12.4.1 Results of Experimental Study of Reflection and Transmission Spectra of Waveguide Photonic Crystals

During experimental studies, frequency dependency of the absolute vale of the coefficient of electromagnetic wave reflection from 11-layer structure (Fig. 12.33) composed of alternating layers of polycore ($\varepsilon = 9.6$) and foam plastic ($\varepsilon = 1.1$). Measurements were performed with the help of panoramic VSWR and attenuation measuring device P2–61 and vector circuit analyzer *Agilent N5230A PNA*. Functional circuit of the test unit is illustrated in Figs. 12.42 and 12.43.

Figure 12.44 shows measured frequency dependencies of the squared absolute value of the reflection coefficient $|R_{exp}|^2$ of the electromagnetic wave from the photonic crystal near the transmission window for different values of thickness of the 6th layer (foam plastic).

Fig. 12.42 Test unit

Fig. 12.43 11-layer structure of waveguide photonic crystal

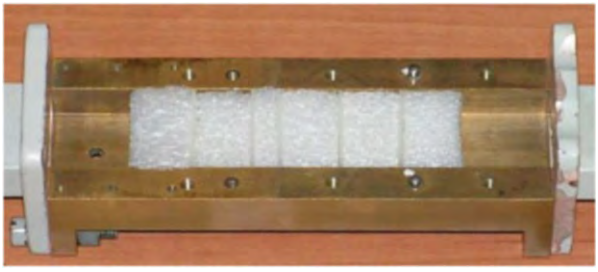

Fig. 12.44 Measured frequency dependencies of the squared absolute value of the reflection coefficient of the photonic crystal for different values of thickness d*6* of the altered 6th layer (foam plastic layer) Curve 1 corresponds to the photonic crystal without irregularities
d_6, mm: 2–7.0; 3–5.0; 4–4.0

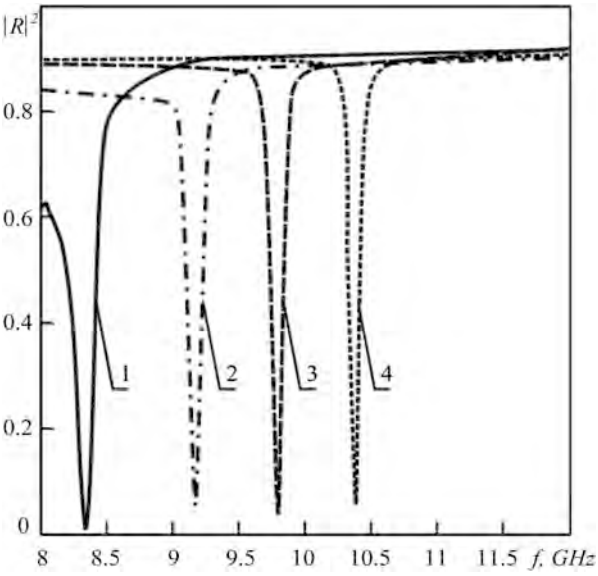

The results shown in Fig. 12.44 confirm the possibility of adjustment of the position of transmission window in the gap of the photonic crystal based on waveguide structures.

12.4.2 Use of Waveguide Photonic Structures for Measurement of Parameters of Nanometer Metal Layers on Semiconductor and Dielectric Substrates

12.4.2.1 Experimental Study of Frequency Dependencies of the Reflection Coefficient of Photonic Structures Containing Nanometer Metal Layers

During experimental studies, frequency dependency of the absolute vale of the coefficient of electromagnetic wave reflection from 11-layer structure composed of alternating layers of polycore ($\varepsilon = 9.6$) and foam plastic ($\varepsilon = 1.1$). The tested structure was designed as polycore substrate with applied nanometer chrome film.

In order to calculate propagation constants of electromagnetic wave γ_0, γ_d, γ_m, γ_s in empty waveguide and waveguides filled with dielectric, metal film and semiconductor respectively, the following expressions were used:

$$\gamma_0 = \sqrt{\frac{\pi^2}{a^2} - \omega^2 \varepsilon_0 \mu_0}, \quad \gamma_{\text{п,м}} = \sqrt{\frac{\pi^2}{a^2} - \omega^2 \varepsilon^*_{\text{п,м}} \varepsilon_0 \mu_{\text{п,м}} \mu_0}, \quad \gamma_{\text{д}} = \sqrt{\frac{\pi^2}{a^2} - \omega^2 \varepsilon_{\text{д}} \varepsilon_0 \mu_0},$$

where $\varepsilon^*_{\text{п,м}} = \varepsilon'_{\text{п,м}} - j\varepsilon''_{\text{п,м}}$ is the complex dielectric permittivity of the semiconductor layer and thin metal film, $\varepsilon'_{\text{п,м}} = \varepsilon_{\text{п,м}} - \frac{\sigma^2_{\text{п,м}} m^*_{\text{п,м}}}{\varepsilon_0 e^2 n_{\text{п,м}}}$, $\varepsilon''_{\text{п,м}} = \frac{\sigma_{\text{п,м}}}{\varepsilon_0 \omega}$ are the real and imaginary parts of complex dielectric permittivity of the semiconductor layer and thin metal film, ε_0 and μ_0 are dielectric and magnetic permittivity values in vacuum, $\varepsilon_{s,\,m}$ and $\mu_{s,\,m}$ are values of relative dielectric and magnetic permittivity of the lattice of the semiconductor substrate and metal layer respectively, $\sigma_{s,\,m}$ are electrical conductivity values of semiconductor substrate and metal layer, $m^*_{\text{п,м}}, n_{\text{п,м}}$ are the effective masses and concentrations of electrons in semiconductor substrate and metal layer, ε_d is the relative dielectric permittivity of the dielectric layer.

Results of measurements of $|R_{ex[}(\omega)|^2$ for different values of thickness of the chrome film applied to polycore substrate with the photonic crystal placed before the tested structure in the presence of irregularity in the form of reduced thickness of the sixth layer d_6 in the crystal are shown in Fig. 12.35. When the chrome layer thickness is increased from zero to 144 nm, the value $|R_{exp}(\omega)|^2$ in the minimum of the transmission window of the photonic crystal varies within 0.03–0.5 (Fig. 12.45).

Results of measurement of $|R_{exp}(\omega)|^2$ for different values of thickness of the chrome film applied to polycore substrate with the tested structure placed before the photonic structure are shown in Fig. 12.36. In this case, the value $|R_{exp}(\omega)|^2$ in the

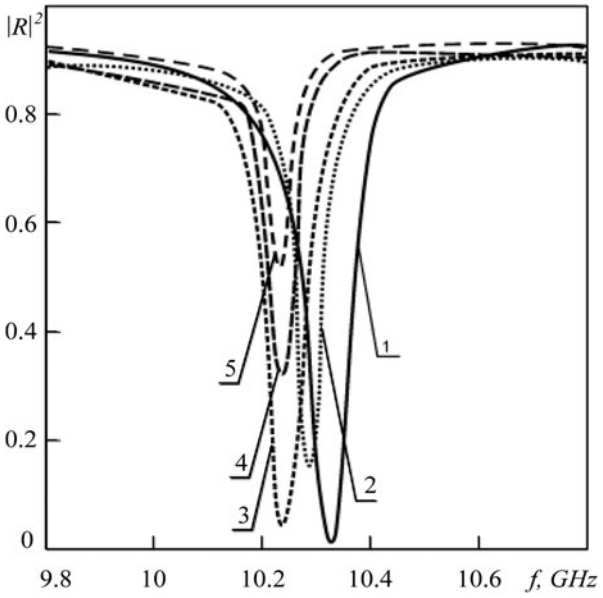

Fig. 12.45 Measured frequency dependencies of the squared absolute value of the reflection coefficient of the photonic crystal in the presence of irregularity in the form of reduced thickness of the 6th layer (foam plastic ($d_6 = 4$ mm) for different values of thickness h of the nanometer metal layer in case of placement of the photonic crystal before the tested structure
Curve 1 corresponds to the photonic crystal without measured structure
h, nm: 2–0; 3–21; 4–76; 5–144

minimum of the transmission window of the photonic structure changes from 0.18 to 0.55 units with the increase in the chrome layer thickness from zero to 20 nm (Fig. 12.46).

12.4.2.2 Measurement of Electrical Conductivity of Metal Films Applied to Dielectric Substrates

Parameters of tantalum films with nitrogen content applied to 0.5 mm polycore substrates were experimentally measured. Transmission coefficient was measured using the vector network analyzer *Agilent PNA N5230A* in the frequency range of 8.5–10.5 GHz. Thicknesses of metal films were measured with atomic-force microscope NTEGRA Spectra.

Tested samples were placed after 11-layer waveguide photonic crystal formed by alternating layers of polycore ($\varepsilon = 9.6$; $\mathrm{tg}\delta = 1 \cdot 10^{-4}$) with a thickness of 1 mm and foam plastic ($\varepsilon = 1.1$; $\mathrm{tg}\delta = 0$) with a thickness of 12 mm. The photonic crystal contained an irregularity in the form of the thickness of the 6th layer (foam plastic) reduced to 4.63 mm. Photo of the measuring system is shown in Fig. 12.38.

Figure 12.47 shows experimentally tested dependencies of squared absolute values of the reflection $|R_{exp}|^2$ (a) and transmission $|T_{exp}|^2(b)$ coefficients of the electromagnetic wave from the tested structure (photonic crystal – tantalum films of various thickness on polycore substrate) on the probe signal frequency (Fig. 12.48).

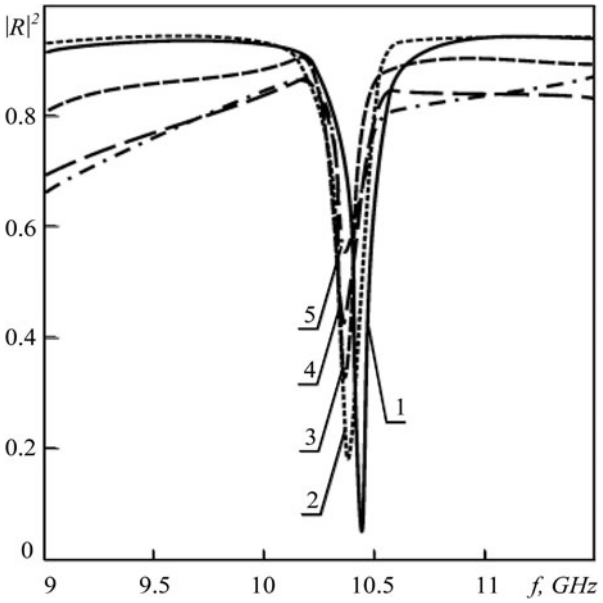

Fig. 12.46 Measured frequency dependencies of the squared absolute value of the reflection coefficient of the photonic crystal in the presence of irregularity in the form of reduced thickness of the 6th layer (foam plastic ($d_6 = 4$ mm) for different values of thickness h of the nanometer metal layer in case of placement of the photonic crystal after the tested structure
Curve 1 corresponds to the photonic crystal without measured structure
h, nm: 2–0; 3–12; 4–18; 5–21

The reverse problem (12.27) of determining electrical conductivity of tantalum films was solved using experimental data. The obtained values of electrical conductivity of films are given in Table 12.1.

Figure 12.49 shows reflection and transmission spectra of the structure "waveguide photonic crystal – tested sample" calculated with the help of the ratio (12.17) at conductivity values determined from the reverse problem (full curves) and obtained experimentally (points).

12.4.2.3 Measurement of Thicknesses of Metal Films Applied to Semiconductor Substrates

Thickness values of nichrome films applied to 0.43 mm thick silicone substrates with electrical conductivity of 45 $\text{Ohm}^{-1}\ \text{m}^{-1}$ were measured experimentally. Electrical conductivity of the films amounted to $1.65 \cdot 10^6\ \text{Ohm}^{-1}\ \text{m}^{-1}$. Transmission coefficient was measured using the vector network analyzer *Agilent PNA N5230A* in the frequency range of 9.3–9.6 GHz.

Tested samples were placed after 11-layer waveguide photonic crystal formed by alternating layers of polycore ($\varepsilon = 9.6$; $\text{tg}\delta = 1 \cdot 10^{-4}$) with a thickness of 1 mm and foam plastic ($\varepsilon = 1.1$; $\text{tg}\delta = 0$) with a thickness of 12 mm. The photonic crystal contained an irregularity in the form of the thickness of the 6th layer (foam plastic) reduced to 6 mm.

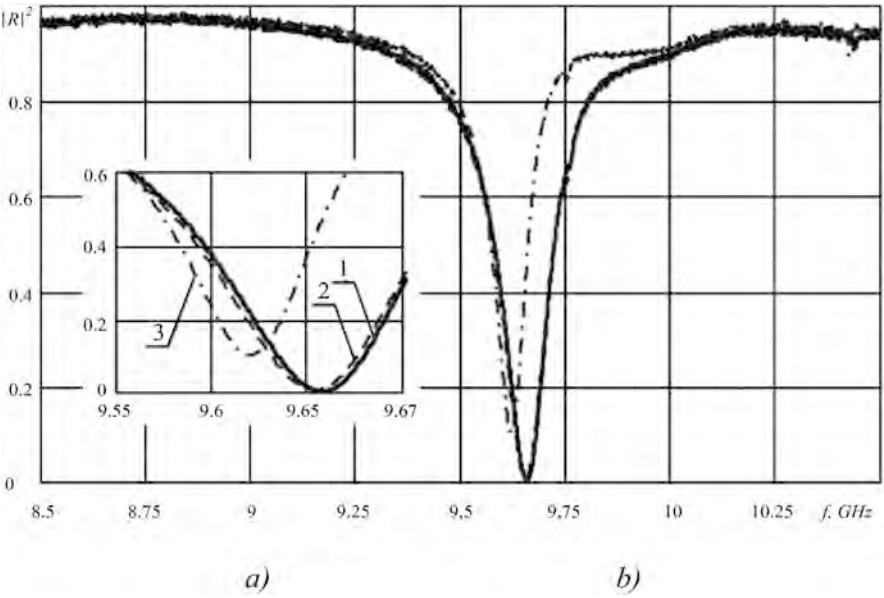

Fig. 12.47 Experimentally tested dependencies of squared absolute values of the reflection $|R_{exp}|^2$ (**a**) and transmission $|T_{exp}|^2$ (**b**) coefficients of the electromagnetic wave from the tested structure (photonic crystal – tantalum films of various thickness on polycore substrate) on the probe signal frequency: curve 1 – tantalum film thickness 10 nm; curve 2 – tantalum film thickness 106 nm; curve 3 – tantalum film thickness 265 nm

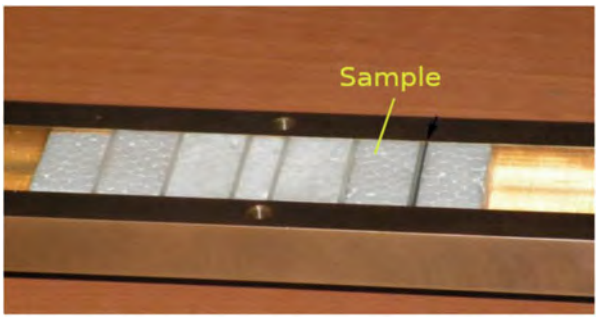

Fig. 12.48 Photo of measurement system

Table 12.1 Test results of the electric conductance of the Tantalum films

	Thickness, nm	Electrical conductivity, $Ohm^{-1} \cdot m^{-1}$
Structure 1	10	$0.449 \cdot 10^6$
Structure 2	106	$0{,}051 \cdot 10^6$
Structure 3	265	$0.199 \cdot 10^6$

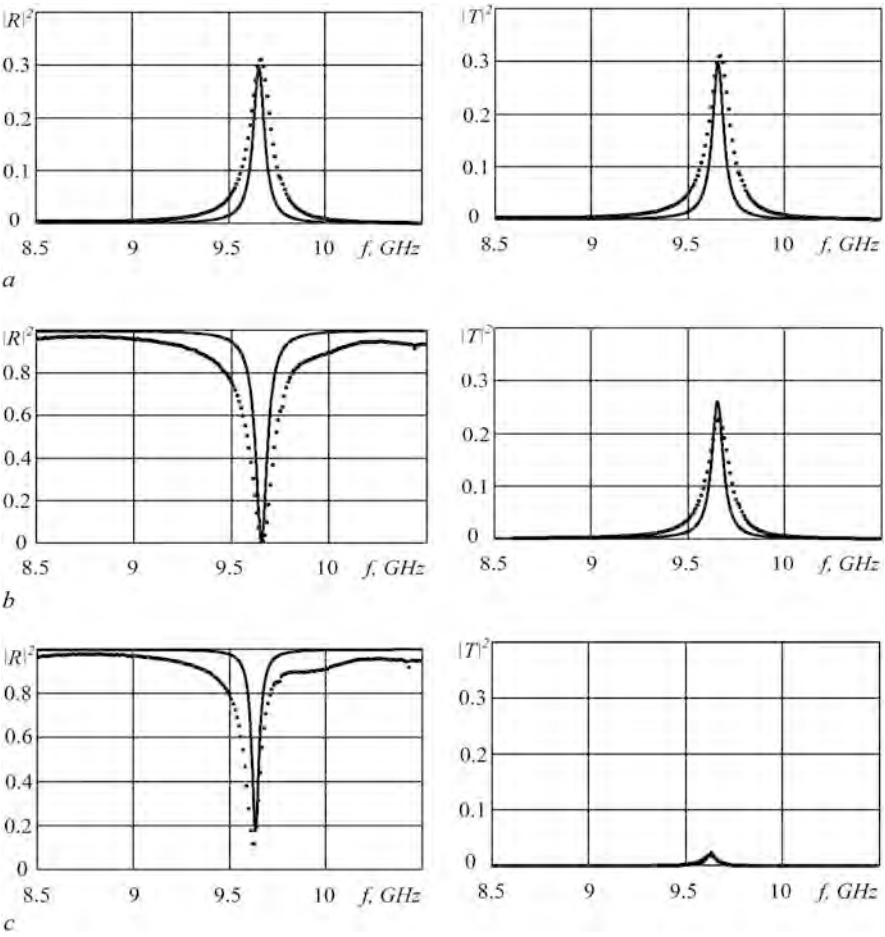

Fig. 12.49 Experimental (points) and calculated (full curves) spectra of reflection (left) and transmission (right) of the "waveguide photonic crystal – tested sample" structure: (**a**) – structure 1, (**b**) – structure 2, (**c**) – structure 3

Figure 12.50 shows experimentally tested dependencies of squared absolute values of the ratio $|R_{exp}|^2$ of the electromagnetic wave from the tested structure (photonic crystal – nichrome films of various thickness on silicon substrate) on the probe signal frequency.

The reverse problem (12.26) of determining thickness of nichrome films was solved using experimental data. The obtained values of film thickness are given in Table 12.2:

Figure 12.51 shows reflection spectra of the structure "waveguide photonic crystal – tested sample"calculated with the help of the ratio (12.17) at film thickness values determined from the reverse problem (full curves) and obtained experimentally (points).

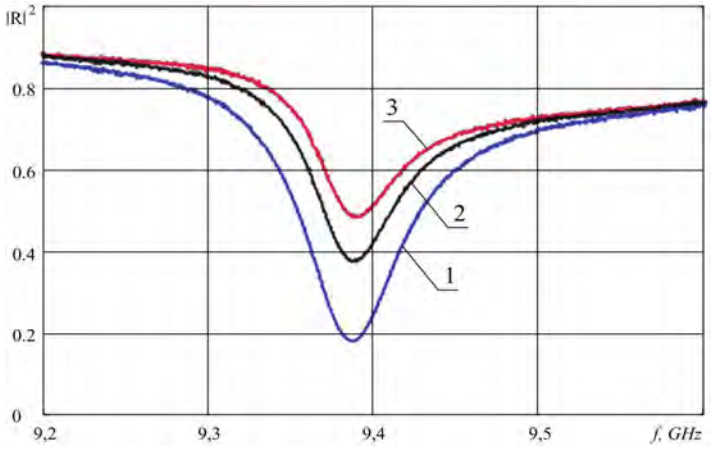

Fig. 12.50 Experimentally tested dependencies of squared absolute values of the ratio $|R_{exp}|^2$ of the electromagnetic wave from the tested structure (photonic crystal – nichrome films of various thickness on silicon substrate) on the probe signal frequency: curve 1 – first film; curve 2 – second film; curve 3 – third film

Table 12.2 Thickness of the films of nichrome

	Thickness, nm
Structure 1	10
Structure 2	54
Structure 3	141

12.4.2.4 Measurement of Thickness of Nanometer Metal Layers and Electrical Conductivity of Semiconductor in Metal-Semiconductor Structures

When developing the structure of creation of metal-semiconductor structures, it is important to know thickness of the metal layer and electrical conductivity of the conductor upon completion of the process cycle.

Experimental measurement of reflection spectra of the electromagnetic wave within the frequency range of 9–10 GHZ was performed in the "waveguide photonic structure – tested semiconductor structure" system. During the test, metal-semiconductor structures designed as nichrome films applied to 430 μm silicon substrates were measured. Transmission coefficient was measured using the vector network analyzer *Agilent PNA N5230A*. Measurements were performed for two different variants of layer alternation: waveguide photonic structure – metal film – semiconductor substrate and waveguide photonic crystal – semiconductor substrate – metal film.

Tested samples were placed after 11-layer waveguide photonic crystal formed by alternating layers of polycore ($\varepsilon = 9.6$; $\text{tg}\delta = 1 \cdot 10^{-4}$) with a thickness of 1 mm and foam plastic ($\varepsilon = 1.1$; $\text{tg}\delta = 0$) with a thickness of 12 mm. The photonic crystal contained an irregularity in the form of the thickness of the 6th layer (foam plastic)

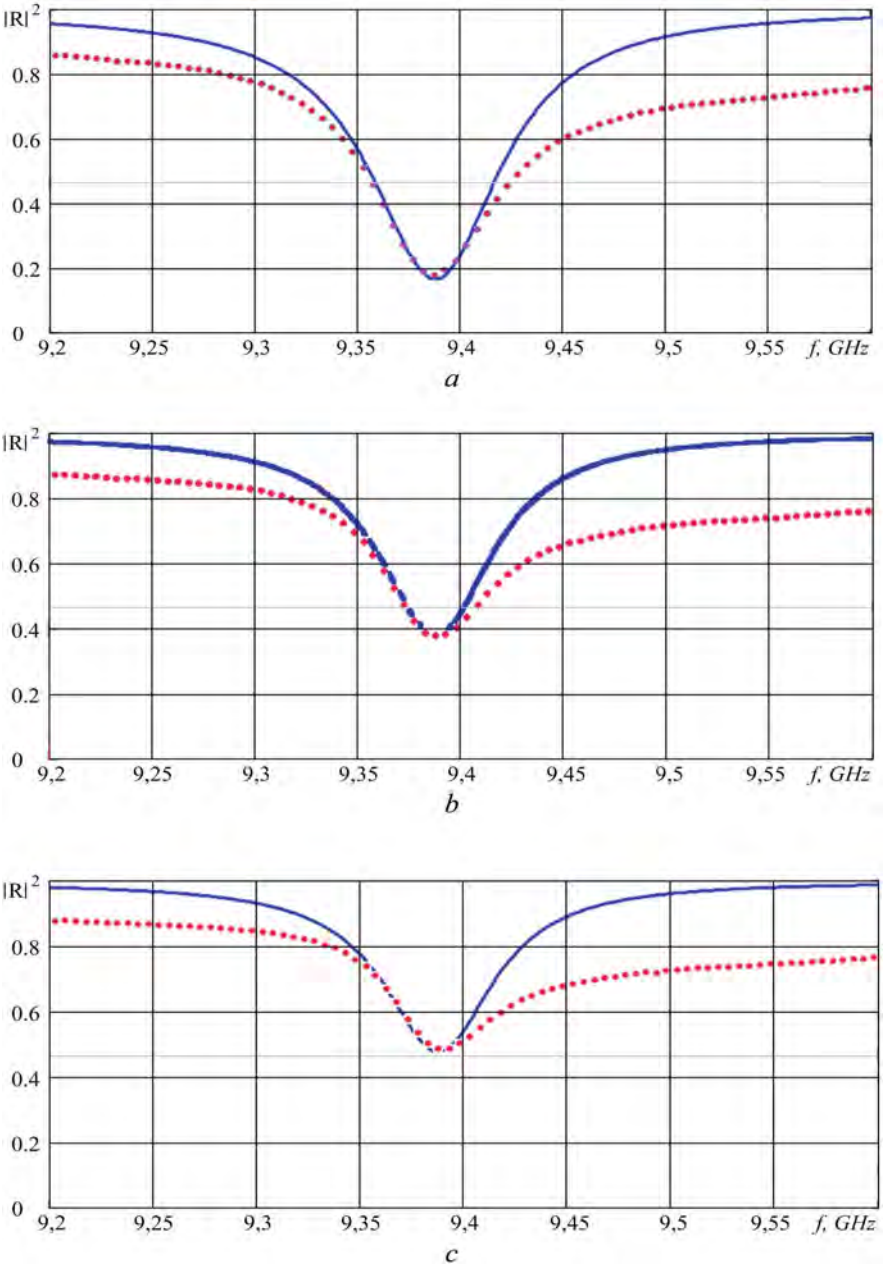

Fig. 12.51 Experimental (points) and calculated (full curves) spectra of reflection of the "waveguide photonic crystal – tested sample" structure: (**a**) – structure 1, (**b**) – structure 2, (**c**) – structure 3

reduced to 6 mm. Experimentally tested dependencies of the reflection coefficient $|R_{exp}|^2$ of the electromagnetic wave on the tested structure (photonic crystal – nichrome films of different thickness on silicone substrate) for two possible orientations of the tested structure are shown in Fig. 12.52.

The residual function $S(t_m, \sigma_s)$ was built based on the results of measurement of reflection spectra and their calculation. Graph of the residual function, e.g. for the third structure, is shown in Figs. 12.52 and 12.53.

As a result of solving the reverse problem with the help of measured reflection spectra in the frequency range of 9–10 GHz parameters of tested structures were determined using the system of Eq. (12.32) and the residual function $S(t_m, \sigma_{si})$ presented as (12.30) (Table 12.3).

Figure 12.54 shows the results of calculations (full lines) of the reflection spectra of the electromagnetic wave incident on the side of the photonic crystal for two different orientations of the measured structure performed using the expression (12.17) at values of thickness of the metal film and electrical conductivity of the substrate that are roots of the system of Eq. (12.32). Experimental curves (points) are presented in the same figures.

Therefore, the use of a photonic crystal ensures change of the reflection coefficient from values close to zero to values close to one in the measured frequency range, which expands the range of measured thicknesses and the class of tested materials, both dielectrics and metal films, and at the same time makes it possible to perform measurements in a narrow frequency range.

12.4.3 Use of Waveguide Photonic Structures for Measurement of Parameters of Dielectric Materials

12.4.3.1 Experimental Study of Frequency Dependencies of the Reflection Coefficient of Photonic Structures Containing Irregularities in the Form of Dielectric Layers

During experimental studies, frequency dependency of the absolute vale of the coefficient of electromagnetic wave reflection from 11-layer photonic structure composed of alternating layers of polycore ($\varepsilon = 9.6$; $tg\delta = 4.7 \cdot 10^{-4}$) with a thickness of 1 mm and foam plastic ($\varepsilon = 1.1$; $tg\delta = 0$) with a thickness of 12 mm were measured within the frequency range of 8–12 GHz. Irregularity in the form of reduced thickness of the 6th layer (foam plastic) was introduced into the photonic structure. The seventh layer (polycore) was replaced with the tested dielectric sample (Fig. 12.55).

Results of measurements of frequency dependencies of the absolute square value of photonic crystal reflection with transmission window for various values of permittivity of the ε7th layer are shown in Fig. 12.45.

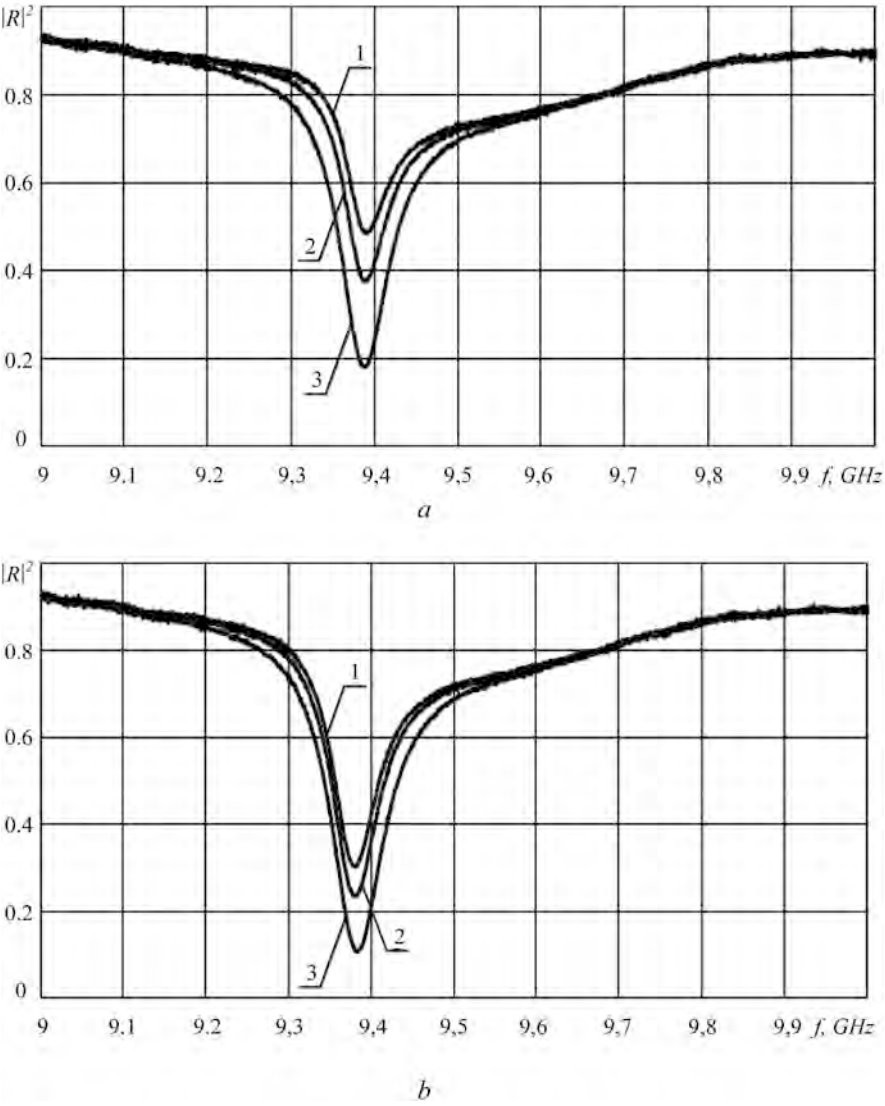

Fig. 12.52 Experimentally tested dependencies of squared absolute values of the electromagnetic wave from the tested structure (photonic crystal – nichrome films of various thickness on silicon substrate) on the probe signal frequency: curve 1 – first structure; curve 2 – second structure; curve 3 – third structure: (**a**) – in the system "waveguide photonic crystal – metal film – semiconductor substrate"; (**b**) – in the system "waveguide photonic crystal – semiconductor substrate – metal film"

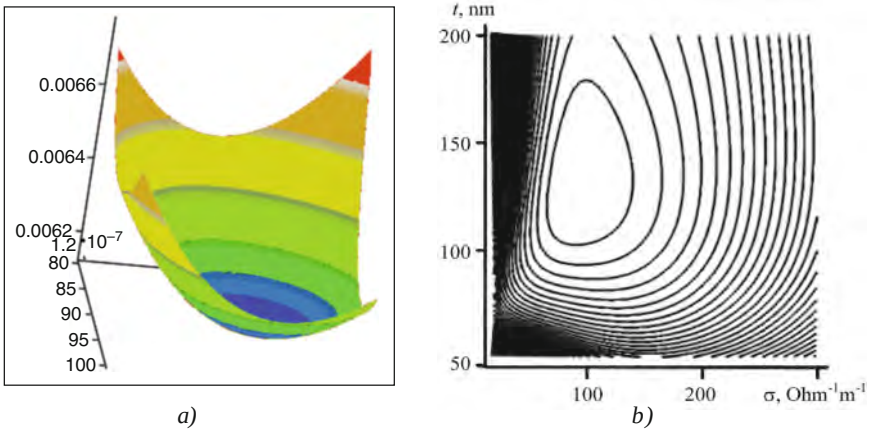

Fig. 12.53 Residual function in the coordinate space (t_m, σ_s, S) (**a**) and outline map in the proximity of the global minimum (**b**)

Table 12.3 The values of the parameters of the structures 1–3

	Metal film thickness $t_{m\ t}$, nm	Substrate conductivity $\sigma_{s\ t}$, Ohm^{-1} m^{-1}
Structure 1	10	50
Structure 2	44	48
Structure 3	110	45.3

The presented dependencies demonstrate high sensitivity of the form of frequency and amplitude characteristics of the transparency window in the gap of the photonic crystal on dielectric permittivity of one of the layers of periodic structure.

12.4.3.2 Measurement of Permittivity of Materials with Low Losses

Parameters of the following materials were tested experimentally: fluoroplastic, plexiglass, vinyl plastic and sitall. Frequency dependency of the absolute value of reflection ratio of the electromagnetic wave on 11-layer photonic structure consisting of alternating polycore layers ($\varepsilon = 9.6$; $\mathrm{tg}\delta = 1 \cdot 10^{-4}$) with thickness of 1 mm and foam plastic ($\varepsilon = 1.1$; $\mathrm{tg}\delta = 0$) with thickness of 12 mm with irregularity in the form of the thickness of the 6th layer reduced to 3.97 mm (foam plastic) was measured within the frequency range of 9.6–10.1 GHz. The tested dielectric layer was placed after the structure in the waveguide immediately adjacent to the last layer of the structure. Measured spectra of reflection of the waveguide photonic crystal "polycore – foam plastic" and the structure "waveguide photonic crystal – measured dielectric" are shown in Fig. 12.56.

Results of measurement of transmission and reflection coefficients of the structure "waveguide photonic crystal – fluoroplastic layer" are shown in Fig. 12.48 (points), structure "waveguide photonic crystal – plexiglass layer" – in Fig. 12.49 (points),

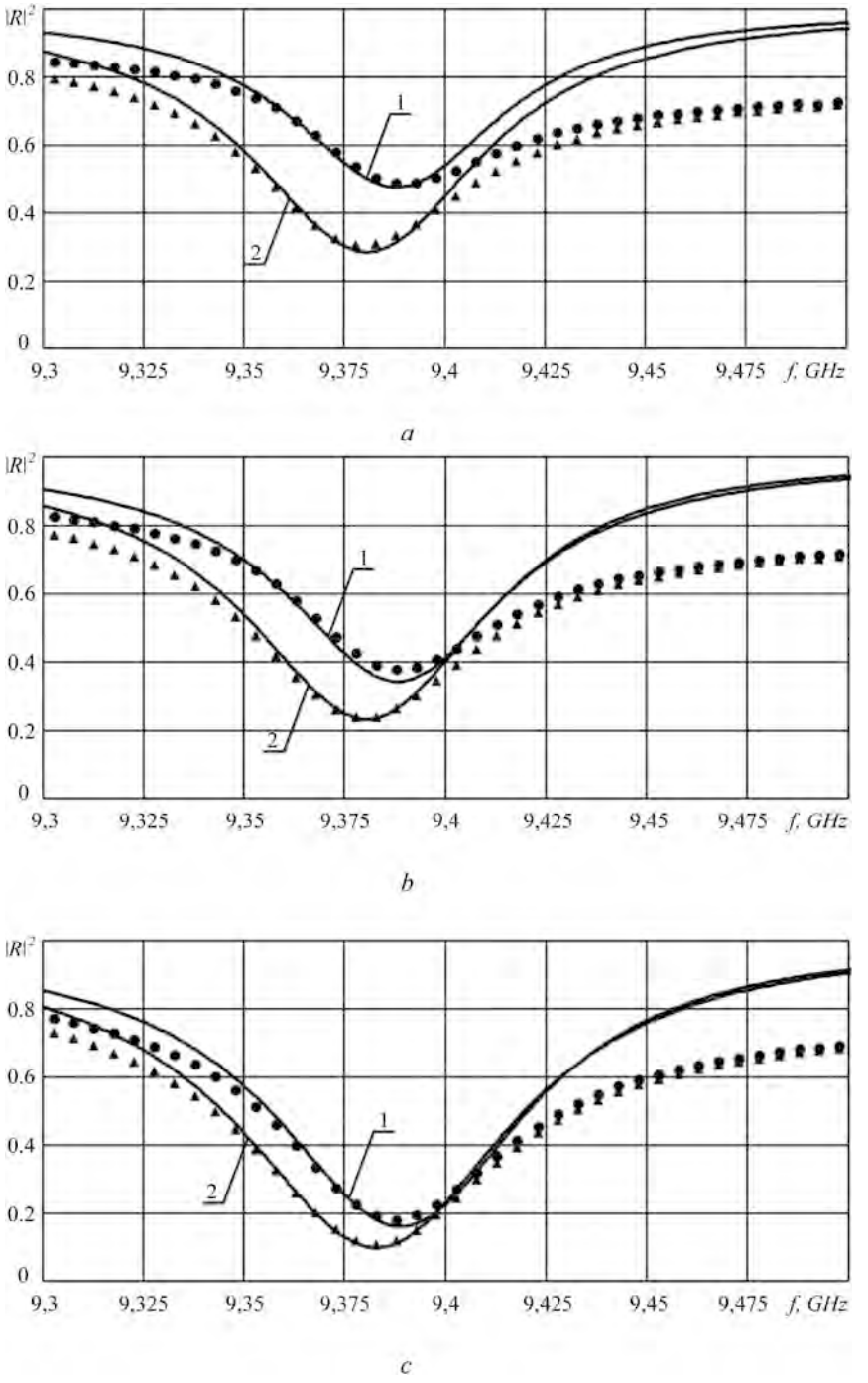

Fig. 12.54 Experimental (points) and calculated (full lines) spectra of reflection from the tested structure: (**a**) – first structure; (**b**) – second structure; (**c**) – third structure; *1* – in the "photonic waveguide crystal – metal film – semiconductor substrate" structure, *2* – in the "photonic waveguide crystal – semiconductor substrate – metal film" structure

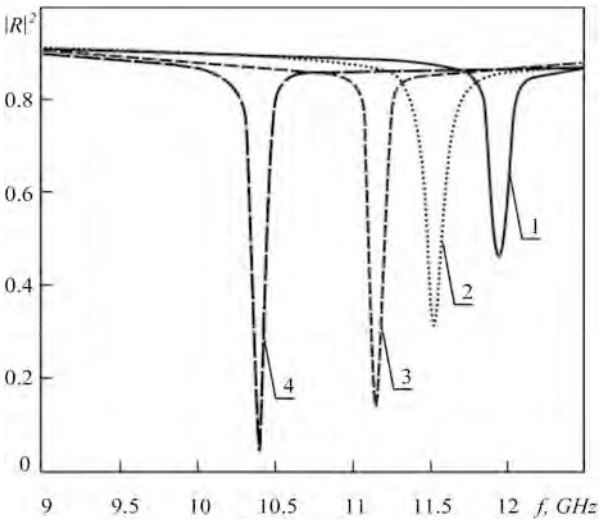

Fig. 12.55 Measured frequency dependencies of the squared absolute value of the reflection coefficient of the 11-layer structure of the photonic crystal for various values of permittivity ε of the 7th layer with the thickness of the altered 6th layer $d_6 = 4$ mm
ε, rel. units: 1–1.0 (air gap); 2–3.0 (ST-3 styrene copolymer); 3–5.0 (ST-5 styrene copolymer); 4–9.6 (polycore).

structure "waveguide photonic crystal – vinyl plastic layer" – in Fig. 12.50 (points), structure "waveguide photonic crystal – sitall layer" – in Fig. 12.48 (points) (Figs. 12.57, 12.58, 12.59, and 12.60).

Permittivity of the tested materials was determined by solving the reverse problem (12.22). The results of solving the reverse problem are shown in Table 12.4.

Corresponding calculated frequency dependencies of absolute values of reflection and transmission coefficients at obtained values of permittivity of the measured samples are shown in Fig. 12.48, 12.19, 12.50, and 12.51 (full lines).

12.4.3.3 Measurement of Real and Imaginary Parts of Complex Dielectric Permittivity of Materials with Losses

Parameters of the following materials were tested experimentally: fabric reinforced laminate, conductive ceramics. Frequency dependency of the absolute value of reflection ratio of the electromagnetic wave on 11-layer photonic structure consisting of alternating polycore layers ($\varepsilon = 9.6$; $\text{tg}\delta = 1 \cdot 10^{-4}$) with thickness of 1 mm and foam plastic ($\varepsilon = 1.1$; $tg\delta = 0$) with thickness of 12 mm with irregularity in the form of the thickness of the 6th layer reduced to 3.97 mm (foam plastic) was measured within the frequency range of 9.6–10.1 GHz. The tested dielectric layer was placed after the structure in the waveguide immediately adjacent to the last layer of the structure. Measured spectra of reflection of the waveguide photonic crystal "polycore – foam plastic" and the structure "waveguide photonic crystal – measured dielectric" are shown in Fig. 12.61.

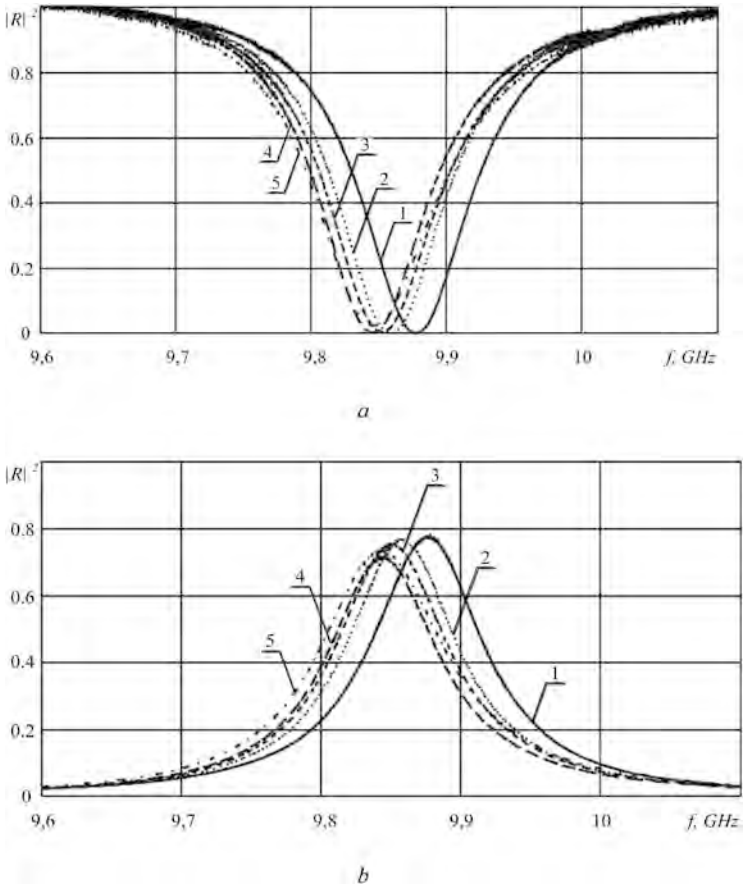

Fig. 12.56 Experimental frequency dependencies of the absolute values of reflection (**a**) and transmission (**b**) coefficients of 11-layer waveguide photonic crystal "polycore – foam plastic" (curve 1) and the structure "waveguide photonic crystal – tested dielectric" (curves 2–7): 2 – fluoroplastic; 3 – sitall; 4 – vinyl plastic; 5 – plexiglass

Results of measurement of reflection and transmission coefficients of the structure "waveguide photonic crystal – fiber-based laminate layer" is shown in Fig. 12.62 (points), of the structure "waveguide photonic crystal – conducting ceramics layer" – in Fig. 12.63 (points).

Solving of the reverse problem (12.23) helped determine dielectric permittivity and tangent of the angle of dielectric losses presented in Table 12.5.

Corresponding calculated frequency dependencies of absolute values of reflection and transmission coefficients at obtained values of permittivity of the measured samples are shown in Figs. 12.53 and 12.54 (full lines).

Therefore, features of interaction of SHF radiation with one-dimensional waveguide photonic structures in the three-centimeter range of wavelengths.

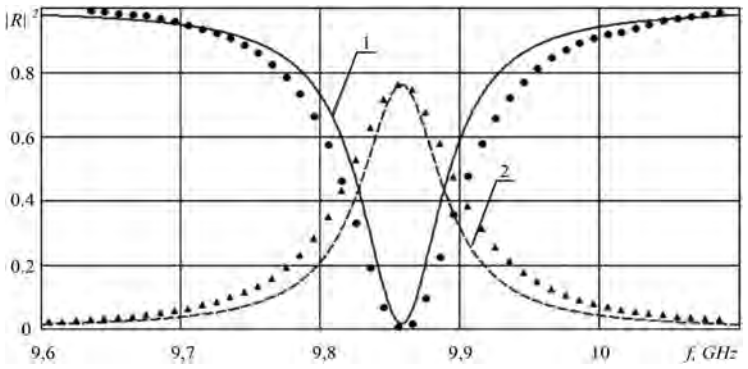

Fig. 12.57 Experimental (points) and calculated (full lines) frequency dependencies of the absolute value of coefficient of reflection (curve 1) and transmission (curve 2) coefficients of the system "11-layer waveguide photonic crystal – measured dielectric (fluoroplastic)"

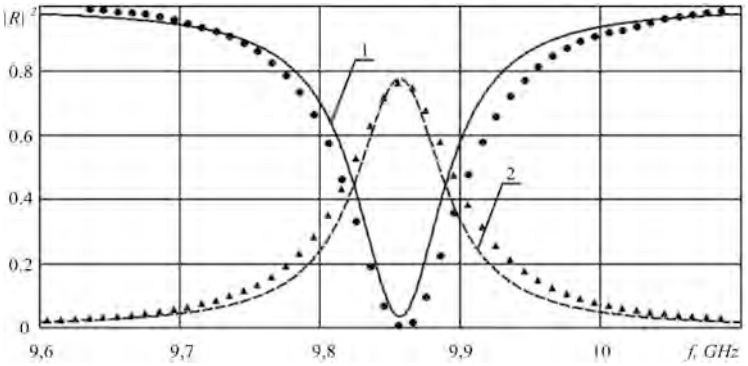

Fig. 12.58 Experimental (points) and calculated (full lines) frequency dependencies of the absolute value of coefficient of reflection (curve 1) and transmission (curve 2) coefficients of the system "11-layer waveguide photonic crystal – measured dielectric (plexiglass)"

Experimentally tested were reflecting and passing spectra of electromagnetic radiation of the microwave range in one-dimensional photonic structures containing irregularities in the form of altered thickness and permittivity of separate layers, as well as one-dimensional waveguide photonic structure placed before the "nanometer metal film – semiconductor or dielectric substrate" structure.

Experimentally implemented were methods of determining complex permittivity of the materials, permittivity and conductivity of semiconductor layers, thickness and electrical conductivity of nanometer metal layers applied to dielectric and semiconductor substrates using reflecting and passing spectra of one-dimensional waveguide photonic crystals.

Therefore, materials of the studies presented in this chapter can be briefly summarized as follows:

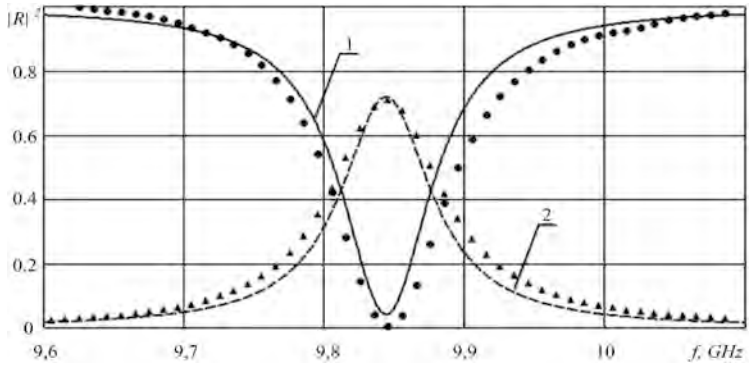

Fig. 12.59 Experimental (points) and calculated (full lines) frequency dependencies of the absolute value of coefficient of reflection (curve 1) and transmission (curve 2) coefficients of the system "11-layer waveguide photonic crystal – measured dielectric (vinyl plastic)"

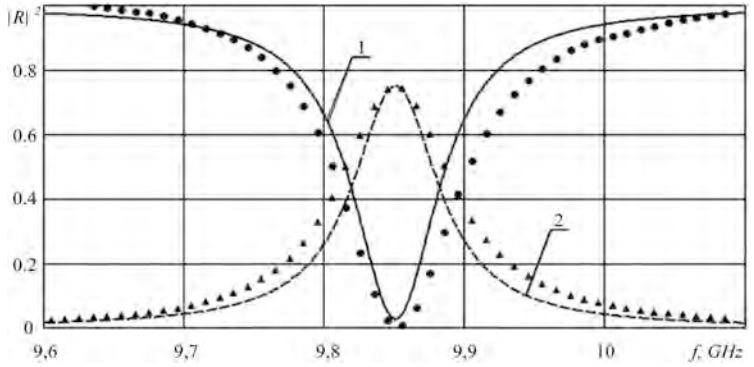

Fig. 12.60 Experimental (points) and calculated (full lines) frequency dependencies of the absolute value of coefficient of reflection (curve 1) and transmission (curve 2) coefficients of the system "11-layer waveguide photonic crystal – measured dielectric (sitall)"

Table 12.4 Dielectric permeability of the studied materials and the value of tgō

Material	ε
Plexiglass	2.032
Vinyl plastic	3.29
Sitall	2.66

1. Mathematical model describing the interaction of electromagnetic radiation of the SHF range with one-dimensional waveguide photonic structures, including the ones containing dielectric and conductive nanometer layers and providing the possibility of calculating SHF reflection and transmission coefficients for such structures, was developed.

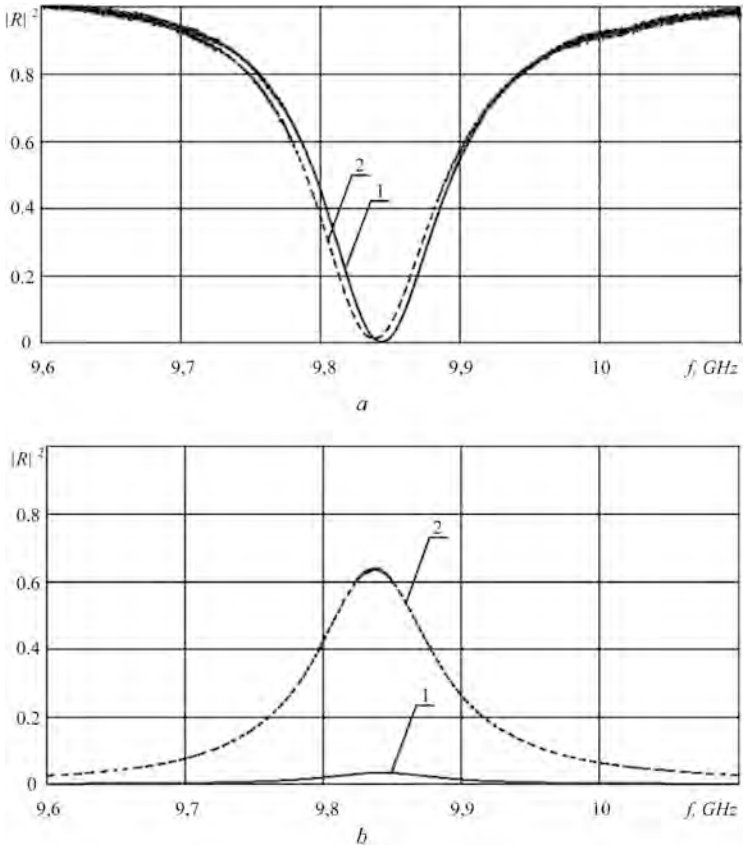

Fig. 12.61 Experimental frequency dependencies of the squared absolute value of the reflection (**a**) and transmission (**b**) coefficients of the structure "waveguide photonic crystal – tested dielectric": 1 – conducting ceramics, 2 – fiber-based laminate

2. Computer modeling of reflection and transmission spectra of one-dimensional photonic crystals of the SHF range in the waveguide range was performed in the presence of irregularities in the form of altered thickness and/or dielectric permittivity of separate layers.
3. It was established that creation of irregularities in the form of modified thickness and/or dielectric permittivity of separate layers in one-dimensional waveguide photonic crystals leads to appearance of donor transmission windows located near the upper frequency boundary of the photonic structure gap or acceptor transmission windows located near the lower frequency boundary of the photonic structure gap. Frequency position of the transmission window – its depth – is determined by parameters of the layer disrupting periodicity.
4. The study of reflection spectra of the photonic crystal with introduced irregularity in the form of two-layer structure designed as semiconductor or dielectric plate

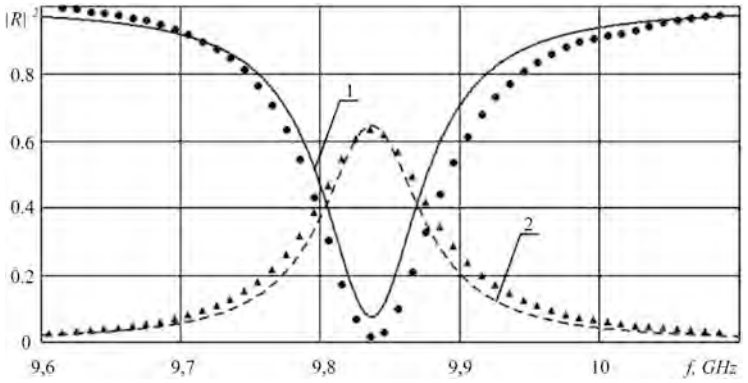

Fig. 12.62 Experimental (points) and calculated (full lines) frequency dependencies of the absolute value of coefficient of reflection (curve 1) and transmission (curve 2) coefficients of the system "11-layer waveguide photonic crystal – measured dielectric (fabric-based laminate)"

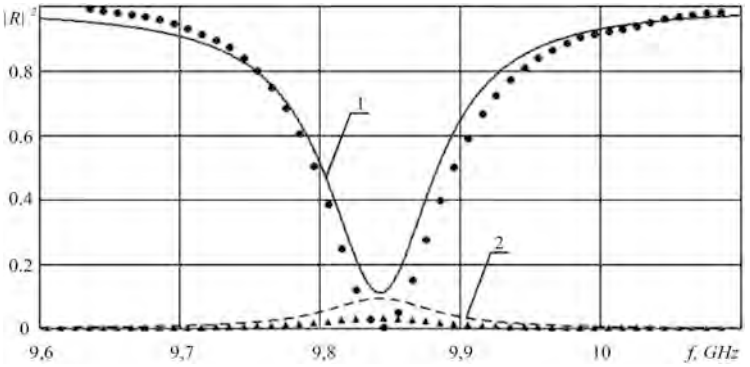

Fig. 12.63 Experimental (points) and calculated (full lines) frequency dependencies of the absolute value of coefficient of reflection (curve 1) and transmission (curve 2) coefficients of the system "11-layer waveguide photonic crystal – measured dielectric (conducting ceramics)"

Table 12.5 Dielectric permeability

Material	ε	tgδ
Fabric-reinforced laminate	4.11	0.13
Conducting ceramics	15.7	0.5

with applied nanometer metal layer was performed. It was demonstrated that frequency dependence of the reflection coefficient in the transmission window of such modified photonic crystal is determined by thickness and conductivity of the metal layer.

5. Dependencies of the reflection coefficient of the photonic crystal containing irregularity in the form of semiconductor or dielectric plate with applied nanometer metal layer on the thickness of this layer were studied. It was demonstrated

that an increase in dielectric permittivity of layers of photonic waveguide crystal expands the ranges of thickness and conductivity of nanometer metal layers included in its composition, in which the coefficient of reflection of microwave electromagnetic radiation from photonic structure does not reach saturation.

6. Theoretical substantiation is presented for the method of measurement of parameters of dielectrics, semiconductors and layered structures of the metal-semiconductor and metal-dielectric structures within a wide range of variation of these parameters in the spectra of reflection and transmission of electromagnetic radiation using one-dimensional waveguide photonic structures.
7. The possibility of solving the reverse problem for determination of complex dielectric permittivity of layer included in the waveguide photonic crystal as irregularities, electrical conductivity and dielectric permittivity of semiconductor plates, as well as conductivity of the semiconductor plate and thickness of the nanometer metal layer applied to it, was demonstrated.
8. The results of experimental studies of interaction of SHF radiation with one-dimensional waveguide photonic structures in the three-centimeter range of wavelengths were presented. Experimentally tested were reflecting and passing spectra of electromagnetic radiation of the microwave range in one-dimensional photonic structures containing irregularities in the form of altered thickness and permittivity of separate layers, as well as one-dimensional waveguide photonic structure placed before the "nanometer metal film – semiconductor or dielectric substrate" structure.
9. Experimentally implemented were methods of determining complex permittivity of the materials, permittivity and conductivity of semiconductor layers, thickness and electrical conductivity of nanometer metal layers applied to dielectric and semiconductor substrates using reflecting and passing spectra of one-dimensional waveguide photonic crystals.

References

1. Chaplygin, Y. A. (Ed.). (2005). *Nanotechnologies in electronics*. Moscow: Tekhnosfera. 448 p.
2. Luchinin, V. V., & Tairov, Y. M. (Eds.). (2006). *Nanotechnology: Physics, Processes, Diagnostics, Devices*. Moscow: Fizmatlit. 552 p.
3. Pavlov, L. V. (1987). *Methods of measurement of semiconductor material parameters*. Moscow: High School. 239 p.
4. Kovtoniuk, N. F., & Kontsevoy, Y. A. (1970). *Measurement of parameters of semiconductor materials*. Moscow: Radio i Svyaz'. 432 p.
5. Blood, P., & Orton, J. (1981). V. Methods of measuring electrical properties of semiconductors. *Foreign Radioelectronics*, p. 1, p. 3–50; p. 2, No. 2, p. 3–49.
6. Usanov, D. A. (1985). *SHF methods of measurement of semiconductor parameters*. Saratov: Saratov University Publishing House. 55 p.
7. https://docviewer.yandex.by/view/0/?page=2&*=%2BonauKxAvQpH4ya6UrvRBiVilTZ7InVybCI6Imh0dHBzOi8vd3d3LnJlc2VhcmNoZ2F0ZS5uZXQvcHJvZmlsZS9BbmF0b2x5X1NrcmlwYWwvcHVibGljYXRpb24vMjU3ODU0ODYxX01lYXN1cmVtZW50X29mX3RoZV9wYXJhbWV0ZXJzX29mX25hbm9tZXRlcl9maWxtc19ieV9vcHRpY2FsX2FuZF9taWNy

b3dhdmVfbWV0aG9kcy9saW5rcy8wMGI0OTUzNmIxZGYwMGRhZDEwMDAwMDAvT
WVhc3VyZW1lbnQtb2YtdGhlLXBhcmFtZXRlcnMtb2YtbmFub21ldGVyLWZpbG1zLWJ5
LW9wdGljYWwtYW5kLW1pY3Jvd2F2ZS1tZXRob2RzLnBkZiIsInRpdGxlIjoiTWVhc3Vy
ZW1lbnQtb2YtdGhlLXBhcmFtZXRlcnMtb2YtbmFub21ldGVyLWZpbG1zLWJ5LW9wdGl
jYWwtYW5kLW1pY3Jvd2F2ZS1tZXRob2RzLnBkZiIsIm5vaWZyYW1lIjp0cnVlLCJ1aWQ
iOiIwIiwidHMiOjE2MDgxMDgyMjc1NzcsInl1IjoiNTM2Njk0NDU0MTU2MzE4MzUxNCI
sInNlcnBQYXJhbXMiOiJsYW5nPWVuJnRtPTE2MDgxMDgxODgmdGxkPWJ5Jm5hbWU
9TWVhc3VyZW1lbnQtb2YtdGhlLXBhcmFtZXRlcnMtb2YtbmFub21ldGVyLWZpbG1zLW
J5LW9wdGljYWwtYW5kLW1pY3Jvd2F2ZS1tZXRob2RzLnBkZiZ0ZXh0PTcuK0dlcnNoZ
XpvbiUyQytFLitNLiUyQytMaXR2YWstR29yc2theWElMkMrTC4rQi4lMkMrUGxva2hvdm
ElMkMrTC4rQS4lMkMrJTI2K1phcnViaW5hJTJDK1QuK1MuKyUyODE5NzAlMjkuKzE0
NTYrTWV0aG9kcytvZitkZXRlcm1pbmluZytwYXJhbWV0ZXJzK29mK3NlbWljb25kdWN
0b3IrZmlsbXMrYXQrU0hGLitJbitFLitBLitGZWRvdG92KyUyOEVkLiUyOSUyQysxNDU
3K1NlbWljb25kdWN0b3IrZGV2aWNlcythbmQrdGhlaXIrYXBwbGljYXRpb24rJTI4cHAu
KzMlRTIlODAlOTM0OCUyQytJc3N1ZSsyMyUyOS4mdXJsPWh0dHBzJTNBLy93d3cucm
VzZWFyY2hnYXRlLm5ldC9wcm9maWxlL0FuYXRvbHlfU2tyaXBhbC9wdWJsaWNhdGlv
bi8yNTc4NTQ4NjFfTWVhc3VyZW1lbnRfb2ZfdGhlX3BhcmFtZXRlcnNfb2ZfbmFub21ldG
VyX2ZpbG1zX2J5X29wdGljYWxfYW5kX21pY3Jvd2F2ZV9tZXRob2RzL2xpbmtzLzAwY
jQ5NTM2YjFkZjAwZGFkMTAwMDAwMC9NZWFzdXJlbWVudC1vZi10aGUtcGFyYW1ld
GVycy1vZi1uYW5vbWV0ZXItZmlsbXMtYnktb3B0aWNhbC1hbmQtbWljcm93YXZlLW1ld
GhvZHMucGRmJmxyPTE1NyZtaW1lPXBkZiZsMTBuPXJ1JnNpZ249MTUxODQ0ZmEyYz
BkNTdkN2UwYThkYjgxMTc4MWJmNjUma2V5bm89MCJ9&lang=en.

8. Arapov, Y. G., & Davydov, A. B. (1978). Waveguide methods of measuring electrophysical parameters of semiconductors at SHF. In *Non-destructive testing* (pp. 63–87). London: E. Arnold. No.11.
9. Usanov, D. A., Skripal, A. V., & Skripal, A. V. (2003). *Physics of semiconductor RF and optical autodynes*. Saratov: Saratov University Publishing House. 312 p.
10. Usanov, D. A., & Skripal, A. V. (1999). *Physics of operation of semiconductor devices in microwave chips*. Saratov: Saratov University Publishing House. 376 p.
11. Afsar, M. N., Birch, J. R., & Clarke, R. N. (1986). The measurement of the properties of materials. *IEEE, 74*(1), 206–220.
12. Yagudin, G. K. (1968). *Measurement of Electrophysical Parameters of Semiconductors Using Electromagnetic Microwave Fields. – Electronic Equipment Reviews* (Series Semiconductor Devices and Microelectronics). Moscow: TsNII Electronics. Issue 21. 68 p.
13. Viktorov, V. A., Lunkin, B. V., & Sovlukov, A. S. (1989). *Radiowave measurements of technological process parameters*. Moscow: Energoatomizdat. 208 p.
14. Sukhorukov, V. V. (Ed.). (1992). *Non-destructive testing. In 5 volumes. Vol. 4. Control by radiations: Practical guide*. Moscow: High School. 321 p.
15. Kluev, V. V. (Ed.). (1986). *Devices for non-destructive testing of materials and products. Reference book. In 2 volumes. Vol. 1*. Moscow: Engineering. 352 p.
16. Baranov, L. I., Gamaniuk, V. B., & Usanov, D. A. (1972). The problem of determining conductivity and dielectric permittivity of semiconductors at SHF. *Radiotechnics and Electronics, 17*(2), 426–428.
17. Atwater. (1961). Measurement of carrier lifetime in microwave semiconductors. *TIRI, 49*(9), 1671–1672.
18. Bhar, J. N. (1963). Microwave techniques in the study of semiconductors. *IEEE, 51*(11), 1597–1605.
19. Zavyalov, A. S., & Dunayevskiy, G. E. (1985). *Measurement of material parameters at superhigh frequencies*. Tomsk: Tomsk University Publishing. 214 p.
20. Champlin, K. S., & Armstrong, D. B. (1962). Explicit forms for the conductivity and permittivity of Bulk semiconductors in wave-guides. *TIRI, 50*(2), 272–273.
21. Holmes, D. A., & Feucht, D. L. (1964). Microwave measurement of conductivity and dielectric constant of semiconductors. *IEEE, 52*(1), 107–108.
22. Gunn, M. W. (1964). Microwave measurement of complex dielectric permittivity of semiconductors. *IEEE, 52*(2), 194.

23. Grigulis, Y. K. (1970). *Electromagnetic method of analysis of layered semiconductor and metal structures*. Zintane: Riga. 272 p.
24. Konev, V. A., Kuleshov, E. M., & Punko, I. N. (1985). In I. S. Kovalev (Ed.), *Radiowave Ellipsometry* (104 p). Minsk, Science and Technology.
25. Jacobs, H., Brand, F. A., Meindl, J. D., et al. (1963). New microwave techniques in surface recombination and lifetime studies. *IEEE, 4*, 608–620.
26. Starikov, V. D. (1972). *Methods of measurement at SHF using measuring lines*. Moscow: Soviet Radio. 144 p.
27. Brandt, A. A. (1963). *Study of dielectrics at super-high frequencies*. Moscow: Fizmatgiz. 147 p.
28. Valitov, R. A., & Sretenskiy, V. N. (1963). *Radiotechnical measurements*. Moscow: Soviet Radio. 102 p.
29. Akhmanaev V.B., Medvedev Y.V., Petrov A.S. Resonator for Contactless Measurement of Specific Resistance of Semiconductor Materials Electronics. Series SHF Electronics. 1981 Issue 4. 49–51.
30. Gordienko, Y. E., Starostenko, V. V., Dudkin, N. A., & Shevchenko, V. E. (1974). Instrument for measurement of thickness of semiconductor epitaxial films on low resistance substrates. *Experiment Instruments and Technology, 4*, 196–199.
31. Yagudin, G. H., Shibaev, A. A., & Ponomarenko, O. N. (1973). *Contactless methods of non-destructive testing of electrophysical parameters of semiconductor structures*. Electronic Technology Reviews. Series Semiconductor Devices, issue 4 (104). 52 p.
32. Steven, M. Anlage, D. E. S, Feenstra, B. J., Vlahacos, C. P., & Wellstood, F. C. (2000). *Near-field microwave microscopy of materials properties*. arXiv:cond-mat/0001075 v2 18 Apr 2000.
33. Grosse, P. (1982). *Free electrons in solids*. Mocsow: Mir. 270 p.
34. Chaplygin, Y. A., Usanov, D. A., Skripal, A. V., Skripal, A. V., Semenov, A. A., Abramov, A. V., & Golishnikov, A. A. (2005). *Radiowave and optical measurements of thickness and conductivity of metal films on semiconductor and dielectric substrates* (pp. 68–77). News of Higher Educational Institutions. Electronics. No.1.
35. Usanov, D. A., Skripal, A. V., Abramov, A. V., & Bogolubov, A. S. (2006). Measurement of thickness of nanometer metal layers and conductivity of semiconductor in metal-semiconductor structures based on reflection and transmission spectra of electromagnetic radiation. *TPJ, 76*(5), 112–117.
36. Chaplygin, Y. A., Skripal, A. V., Abramov, A. V., & Bogolubov, A. S. (2006). Resonant reflection of electromagnetic radiation from structures with nanometer metal layers. *Physics of Wave Processes and Radiotechnical Systems, 9*(3), 59–63.
37. Chaplygin, Y. A., Usanov, D. A., Skripal, A. V., Abramov, A. V., Bogolubov, A. S. (2006). *Methods of measuring conductivity of nanometer metal films in layered structures based on electromagnetic radiation reflection spectra* (pp. 27–35). News of Higher Educational Institutions. Electronics. No. 6.
38. Usanov, D. A., Skripal, A. V., Abramov, A. V., & Bogolubov, A. S. (2007). Changes in the type of resonant radiation in nanometer metal film – Dielectric structures. *Letters to TPJ, 3*(2), 13–22.
39. Usanov, D. A., Skripal, A. V., Abramov, A. V., & Bogolubov, A. S. (2004). *SHF method of measurement of metal films on semiconductor substrates.* In 14th International Crimea Conference "Microwave and telecommunication technology" (CriMiCo'2004). Ukraine, Sevastopol, September 13–17, 2004, pp. 686–687.
40. Usanov, D. A., Skripal, A. V., Abramov, A. V., & Bogolubov, A. S. (2004). *Microwave Measurements of Thickness of Metal Films on Semiconductor Substrates*. In Proceedings of the 9th International Scientific and Technical Conference "Relevant Problems of Solid-State Electronics and Microelectronics". Dvinomorskoye, Russia, September 12–17, 2004. Taganrog: TRTU Publishing. Part 2. pp. 100–103.
41. Usanov, D. A., Skripal, A. V., Abramov, A. V., & Bogolubov, A. S. (2005). *SHF Measurements of Nanometer Metal Films on Semiconductor Substrates*. In 15th International Crimea Conference "Microwave and Telecommunication Technology" (CriMiCo'2005). Sevastopol, September 12–16, 2005: Conference Proceedings. Sevastopol: Veber, pp. 605–606.

42. Abramov, A. V., Usanov, D. A., Skripal, A. V., & Bogolyubov, A. S. (2005). *Microwave measurements of thickness and conductivity of nanometer metal-semiconductor structures*. In Proceedings of 35rd European Microwave Conference. Paris, France. 4–6th October 2005. Vol. 1. pp. 509–512.
43. Usanov, D. A., Skripal, A. V., & Abramov, A. V. (2005). *Measurements of nanometer metal films on semiconductor substrates based on electromagnetic radiation reflection spectra*. In Conference Proceedings. Electronics and Informatics – 2005. V International Science and Technology Conference. Zelenograd, November 23–25, 2005, Moscow, MIET, Part 1. pp. 158–159.
44. Usanov, D. A., Skripal, A. V., Abramov, A. V., Bogolyubov, A. S., & Kalinina, N. V. (2006). *Measurements of thickness of metal films in sandwich structures by the micro- wave reflection spectrum*. In Proceedings of 36rd European Microwave Conference. Manchester, UK, 10–15th September 2006, pp. 509–512.
45. Usanov, D. A., Skripal, A. V., Abramov, A. V., & Bogolubov, A. S. (2006). *SHF method of measuring conductivity of nanometer metal films in layered structures.* In 16th International Crimea Conference "Microwave and Telecommunication Technology" (CriMiCo'2006). Sevastopol, September 12–16, 2005: Conference Proceedings in 2 volumes – Sevastopol: Veber, pp. 773–774.
46. Usanov, D. A., Skripal, A. V., Abramov, A. V., & Bogolubov, A. S. (2006). *Microwave measurements of thickness of nanometer metal layers and conductivity of semiconductor in structures "metal-semiconductor"*. In Proceedings of the XVI International Conference on Microwaves, Radar and Wireless Communications MIKON-2006, Poland, Krakow, May 22–24, 2006, vol. 3, pp. 874–877.
47. Usanov, D. A., Skripal, A. V., Abramov, A. V., Bogolubov, A. S., Skvortsov, V. S, & Merdanov, M. K. (2007). *Measurement of nanometer metal layers on isolating substrates using waveguide photonic structures in the microwave range*. In Materials of the 5th Russian-Japanese Workshop "Equipment, Technologies and Analytical Systems for Material Studies, Microelectronics and Nanoelectronics". MISiS Publishing, Moscow, vol. 1, pp. 466–475.
48. Usanov, D. A., Skripal, A. V., Abramov, A. V., Bogolubov, A. S., Skvortsov, V. S., & Merdanov, M. K. (2007). *Measurement of Nanometer Metal Layers Using Waveguide Photonic Structures*. In Proceedings of the 17th International Crimea Conference "Microwave and Telecommunication Technology", September 10–14, 2007. Sevastopol, Crimea. Ukraine, vol. 2, pp. 549–550.
49. Usanov, D., Skripal, A., Abramov, A., Bogolubov, A., Skvortsov, V., & Merdanov, M. (2007). *Measurement of the metal nanometer layer parameters on dielectric substrates using photonic crystals based on the wave-guide structures with controlled irregularity in the microwave band*. In Proceedings of 37th European Microwave Conference. Munich, Germany, October 8–12, 2007, pp. 198–201.
50. Usanov, D. A., Skripal, A. V., Abramov, A. V., Bogolubov, A. S., Skvortsov, V. S., & Merdanov, M. K. (2007). *Use of Waveguide Photonic Structures for Measurement of Parameters of Nanometer Metal Layers on Insulating Substrates.* News of Higher Educational Institutions. Electronics. No. 6, pp. 25–32.
51. Yablonovitch, E. (1987). Inhibited spontaneous emission in solid-state physics and electronics. *Physical Review Letters, 58*(20), 2059–2062.
52. Yablonovitch, E., Gimitter, T. J., Meade, R. D., et al. (1991). Donor and acceptor modes in photonic band structure. *Physical Review Letters, 67*(24), 3380–3383.
53. Kuriazidou, C. A., Contopanagos, H. F., & Alexopolos, N. G. (2001). Monolithic waveguide filters using printed photonic-bandgap materials. *IEEE Transactions on Microwave Theory and Techniques, 49*(2), 297–306.
54. Duchamp, J. M., Perrier, A. L., & Ferrari, P. (2004). *MS, CPW and Fin-line attenuators and dispersion effects on microwave and millimeter wave PBG structure parameters*. In Proceedings of 34rd European Microwave Conference, Amsterdam, Netherlands, October 12–14, 2004, vol. 2, pp. 877–880.
55. Tae-Yeoul and Kai Chang. (2001). Uniplanar one-dimensional photonic-bandgap structures and resonators. *IEEE Transactions on Microwave Theory and Techniques, 49*(3), 549–553.

56. Kee, C.-S., Kim, J.-E., Park, H. Y., & Lim, H. (1999). Roles of wave impedance and refractive index in photonic crystals with magnetic and dielectric properties. *IEEE Transactions on Microwave Theory and Techniques, 47*(11), 2148–2150.
57. Gulyaev, Y. V., & Nikitov, S. A. (2001). Magnonic crystals – Spin waves in periodic structures. *Rep of RAS, 380*(4), 469–471.
58. Gulyaev, Y. V., & Nikitov, S. A. (2003). Photonic and magnetophotonic crystals – New medium for data transmission. *Radiotechnics, 8*, 26–30.
59. Gulyaev, Y. V., Nikitov, S. A., Zhivotovskiy, L. V., Klimov, A. A., Tayad, F., Presmanes, L., Bonin, K., Tsai, C. S., Vysotskiy, S. L., & Filimonov, Y. A. (2003). Ferromagnetic films with periodic structures with magnon gap – Magnon crystals. *Letters to JETP, 77*(10), 670–674.
60. Belyaev, B. A., Voloshin, A. S., & Shabanov, V. F. (2006). Study of microstrip analogs of band-pass filters on one-dimensional photonic crystals. *Radiotechnics and Electronics, 51*(6), 694–701.
61. Burns, G. W., Thayne, I. G., & Arnold, J. M. (2004). *Improvement of planar antenna efficiency when integrated with a millimetre-wave photonic crystal*. In Proceedings of European Conference on Wireless Technology. Amsterdam, Netherlands, October 11–12, 2004, pp. 229–232.
62. Wu, H.-S., Tzuang, C.-K. C. (2004). *Miniaturized high-gain synthetic rectangular waveguide antenna of near-omnidirectional radiation pattern*. In Proceedings of 34rd European Microwave Conference. Amsterdam, Netherlands, October 12–14, 2004, vol. 2, pp. 1189–1192.
63. Usanov, D. A., Skripal, A. V., Abramov, A. V., Bogolubov, A. S., Skvortsov, V. S., & Merdanov, M. K. (2008) *Application of multilayer metal-dielectric structures for creation of wideband waveguide matched loads*. In XVII International Conference on Microwaves, Radar and Wireless Communications Poland, Wroclaw, May 19–21, 2008, vol.2, pp. 553–556.
64. Dmitry, A. U., Skripal, A. V., Abramov, A V., Bogolubov, A. S., Skvortsov, V. S., & Merdanov, M. K. (2008). *Wideband waveguide matched loads based on photonic crystals with nanometer metal layers*. In Proceedings of the 38th European Microwave Conference. 27–31 October 2008. Amsterdam, The Netherlands, pp. 484–487. 978-2-87487-006-4 © 2008 EuMA.
65. Usanov, D. A., Meschanov, V. P., Skripal, A. V., Abramov, A. V., Bogolubov, A. S., Skvortsov, V. S., & Merdanov, M. K. (2007). *Wideband waveguide matched loads based on layered metal-dielectric structures*. In Proceedings of the 6th International Science and Technology Conference Physics and Technical Applications of Wave Processes, September 17–21, 2007. Kazan, pp. 222–223.
66. Usanov D. A., Skripal A. V., Abramov A. V., Bogolubov A. S., Skvortsov, V. S, & Merdanov, M. K. (2007). *Spectral characteristics of waveguide photonic structures with nanometer metal layer*. In Proceedings of the 6th International Science and Technology Conference Physics and Technical Applications of Wave Processes, September 17–21, 2007. Kazan, pp. 233–234.
67. Usanov, D. A., Skripal, A. V., Abramov, A. V., Bogolubov, A. S., Kulikov, M. Y., Skvortsov, V. S, & Merdanov, M. K. (2008). Use of microstrip and waveguide photonic crystals for measurement of parameters of materials and nanostructures. In L.V. Kozhitov (Ed.). *Advanced Technologies, Equipment and Analytical Systems for Material Science and Nanomaterials: Proceedings of the I International Kazakhstan-Russian-Japanese Scientific Conference and the VI Russian-Japanese Seminar* (pp. 336–344). Moscow: Intercontact Science. Ust-Kamenogorsk: VKGTU. 840 p.
68. Usanov, D. A., Skripal, A. V., Abramov, A. V., Bogolubov, A. S., Kulikov, M. Y., Skvortsov, V. S., & Merdanov, M. K. (2008). SHF photonic structures and their use for measurement of material parameters and creation of functional devices of SHF electronics. *Physics of Wave Processes and Radiotechnical Systems, 11*(3), 51–59.
69. Usanov, D. A., Skripal, A. V., Abramov, A. V., Bogolubov, A. S., Skvortsov, V. S., & Merdanov, V. K. (2009). RF Patent No. 2349904. Method of Measuring Electrophysical Parameters of the Structure "Nanometer Metal Film – Semiconductor or Dielectric Substrate". Publication date: March 20, 2009. Bull. No. 8 (under patent application 2007134232/09 (037404) dated September 13, 2007). IPC G01N 22/00 (2006.01).

70. Usanov, D. A., Skripal, A. V., Abramov, A. V., Bogolubov, A. S., Kulikov, M. Y., Skvortsov, V. S, & Merdanov, M. K. (2008). Photonic structures and their use for measurement of parameters of materials, micrometer and nanometer layers and creation of functional devices of SHF electronics. *International Nanotechnologies Forum*. Moscow, December 3–5, 2008, vol. 1, pp. 152–154.
71. Benedict, T. S., & Shockly, W. (1953). Microwave observation of the collision frequency of electrons in germanium. *Physics Review, 89*, 1152–1153.
72. Gabriel, G. J., & Brodwin, M. E. (1965). The solution of guided waves in Jnhomogeneous anisotropic media by Petru bation and Variational methods. *IEEE Transactions, MTT-13*(5), 364–370.
73. Viktorov, V. A. (2005). RF Patent 2262658 IPC G 01 B 7/06. Method of determining thickness of dielectric coating. Publication date: October 20, 2005. Bull. 29.
74. Kovalev, S. V., Nesterov, S. M., & Skorodumov, I. A. (2000). RF Patent 2069052 IPC G 01 R 29/08, G 01 R 29/12 Method of determining complex dielectric and magnetic permittivity of radar absorbent materials. Publication date: September 27, 2000. Bull. 27.
75. Fedunin, P. A., Dmitriev, D. A., & Fedorov, N. P. (2005). RF Patent 2256168 IPC G 01 N 22/00, G 01 R 27/26. SHF method of determining thickness and complex dielectric permittivity of dielectric coatings. Publication date: July 10, 2005. Bull. 19.
76. Dmitrienko, G. V., & Trefilov, N. A. (2001). RF Patent 2199760 IPC G 01 R 27/04, G 01 R 27/06. Device for measurement of high values of complex dielectric permittivity of heavily absorbing materials at SHF. Application No. 2001106868/09. Application date: March 13, 2001. Publication date: February 27, 2003.
77. Velikotskiy, V. N., Dvadnenko, V. Y., De-Monderik, V. G., Starshinova, E. I., Chizhov, V. V., & Yarmak, I. N. (1994). RF Patent 2012893 IPC G 01 R 27/26. Measuring cell. Application No. 5023918/09. Application date: July 15, 1991. Publication date: May 15, 1994.
78. Dmitrienko, G. V., & Trefilov N. A. (2008). RF Patent 2328008 IPC G 01 R 27/28. Device for measurement of high values of complex dielectric permittivity of low impedance composite materials at SHF. Application No. 2006128859/09. Application date: August 8, 2006. Publication date: June 27, 2008.
79. Dmitrienko, G. V., & Trefilov, N. A. (2008). RF Patent 2321010 IPC G 01 R 27/26. Device for measurement of high values of complex dielectric permittivity of low impedance composite materials at SHF. Application No. 2006128860/09. Application date: August 8, 2006. Publication date: June 27, 2008.
80. Champlin, K. S., Armstrong, D. B., & Gunderson, P. D. Charge carrier inertia in semiconductors. *Proceedings of the IEEE, 52*(6), 720–729.
81. Taketomi, K., & Kawasaki, K. (1970). *Method of measuring complex dielectric constant using microwave bulk resonator.* Gifu Koge Koto Semma Gakkai Kie. No. 3. pp. 33–37.
82. Terselius, B., & Ranby, B. (1978). Cavity perturbation measurements of the dielectric properties of vulcanizing rubber and polyethylene compounds. *Journal of Microwave Power, 13*, 327–335.
83. Parkash, A., Vaid, J. K., & Mansingh, A. (1979). Measurement of dielectric parameters at microwave frequencies by cavity-perturbation technique. *IEEE Transactions on Microwave Theory and Techniques, MTT-27*, 791–795.
84. Matus, L. G., Boss, C. B., & Riddle, A. N. (1983). Tuning and matching the TM010 cavity. *Devices for Scientific Studies, 54*(12), 69–75.
85. Hong, K. H., & Roberts, J. A. (1974). Microwave properties of liquids and solids using a resonant microwave cavity as a probe. *Journal of Applied Physics, 45*, 2452–2456.
86. Li, S., Akyel, C., & Bosisio, R. G. (1981). Precise calculations and measurements on the complex dielectric constant of lossy materials using TM010 cavity perturbation techniques. *IEEE Transactions on Microwave Theory and Techniques, MTT-29*, 1041–1048.
87. Cook, R. J. (1973). Microwave cavity methods. In J. Chamberlain & G. W. Chantry (Eds.), *High frequency dielectric measurement.* (Conf. Proceedings, March 1972) (pp. 12–27). Guildford, U.K.: IPC Science and Technology Press.

88. Ni, E., & Stumper, U. (1985). *Permittivity measurements using a frequency tuned microwave TE01 cavity resonator*. In Proceedings of the Institution of Electrical Engineers, pt. H, 132, (1), 27–32.
89. Usanov, D. A., & Kabanov, L. N. (1981). *Application of the perturbation theory to calculation of cavities partially filled with semiconductors*. Semiconductor Physics and Electronics. Properties and use of semiconductor and dielectric structures (pp. 93–96). Saratov: Saratov University Publishing House.
90. Von Hippel, A. R. (1959). *Dielectric materials and applications*. Moscow/Leningrad: Gosenergoizdat, 336 p.
91. Llewellyn-Jones, D. T. et al. (1980). *New method of measuring low values of loss in the near millimetre wavelength region using untuned cavities*. In Proceedings of the Institution of Electrical Engineers, vol. 127, pt. A, no. 8, pp. 535–540.
92. Birch, J. R., & Clarke, R. N. (1982). Dielectric and optical measurements from 30 to 1000 CHz. *Radio and Electronic Engineer, 52*(11/12), 566–584.
93. Kremer, F., & Izatt, J. R. (1981). Millimetre-wave absorption measurements in low-loss dielectrics using an untuned cavity resonator. *International Journal of Infrared and Millimetre Waves, 2*, 675–694.
94. Izatt, J. R., & Kremer, F. (1981, July). Millimetre wave measurement of both parts of the complex index of refraction using an untuned cavity resonator. *Applied Optics, 20*(14), 2555–2559.
95. Dvinskikh, V. A., Duving, V. G., Usanov, D. A. (1978). Semiconductor oscillator for measurement of dielectric permittivity of materials at SHF. *Electronic Equipment. Series 1. SHF Electronics*. No.8. P. 100–102.
96. Detinko, M. V., Lisuk, Y. V., Medvedev, Y. V., & Skrylnikov, A. A. (1992). Contactless radiowave methods of measuring electrophysical parameters of semiconductor materials. *News of Higher Educational Institutions Physics, 35*(9), 45–63.
97. Dmitrienko, G. V., & Trefilov, N. A. (2005). Patent 2247399 RU, IPC G01 R 27/26. Device for Measurement of High Values of Complex Dielectric Permittivity of Low Impedance Materials at SHF. Application No. 2004101740/28. Application date: January 20, 2004; Publication date: February 27, 2005.
98. Dmitrienko, G. V., & Trefilov, N. A. (2005). Patent 2247400 RU, IPC G01 R 27/26. Device for measurement of complex dielectric permittivity of low impedance materials at SHF. Application No. 2004101742/28. Application date: January 20, 2004; Publication date: February 27, 2005.
99. Yakovenko, N. A., & Levchenko, A. S. (2006). Patent 2284533 RU, IPC G01 R 27/26. Method of non-destructive testing of electrical parameters of thin flat films of non-magnetic impedance or conductive materials and the device for its implementation. Application No. 2005113484/28. Application date: May 3, 2005; Publication date: September 27, 2006.
100. Dmitrienko, G. V, & Trefilov, N. A. (2008). Pat. 2326392 RU, IPC G01 R 27/04. Device for determination of parameters of low impedance materials at SHF using a coaxial resonator. Application No. 2007100792/28. Application date: January 9, 2007. Publication date: June 10, 2008.
101. Duving, V. G. (2002). Pat. 2188433 RU, IPC G01 R 27/26, G01 N 22/04. SHF device for non-destructive Testing of Electrophysical parameters of dielectric materials. Application No. 2001110890/09. Application date: April 19, 2001. Publication date: August 27, 2002.
102. Dunaevskiy, G. E., & Inhireev, A. L. (1995). Pat. 2034276 RU, IPC G01 N 22/00. Device for control of parameters of dielectric materials. Application No. 4878934/09. Appication date: October 29, 1990. Publication date: April 30, 1995.
103. Guillot, T. (1992). Pat. 2672687 FR, IPC G01 R 27/04, G01 R 27/26. Method and device for measuring the electrical conductivity of the elementary grains of a conducting powder. FR19910001391 19910207, 1992-08-14.
104. Gary, C., & Saleh, A. (2008). Pat. WIPO 2008076936 WO, IPC G01 R 27/26. Method and apparatus for sensing composition of flexible fuels. Application No. PCT/US2007/087661. Application date: December 14, 2007. Publication date: June 26, 2008.

105. Dmitrienko, G. V., & Trefilov, N. A. (2005). Pat. 2253123 RU, IPC G 01 R 27/26. Method of measurement of complex dielectric permittivity of low impedance materials at SHF and device for its implementation. Application No. 2004106671/28. Application date: March 5, 2004. Publication date: May 27, 2005.
106. Lebedev, I. V. (1970). *Microwave Technology and Devices: in 2 volumes* (Vol. 1). Moscow: High School. 372 p.
107. Ilchenko, M. E., Vzyatyshev, V. F., Gasanov, L. G. et al. (1989). Dielectric Resonators; Ed. by M. E. Ilchenko. Moscow: Radio and Communication, 328 p.
108. Korobkin, V. A., & Khizhnyak, N. A. (1978). Waveguide dielectric resonance of dielectric sample in rectangular waveguide. *News of Higher Educational Institutions Radiophysics, 21* (4), 558–565.
109. Korobkin, V. A., Pyatak, N. I., Babarika, L. I. et al. (1976). *Determination of parameters of dielectrics at microwave frequency using waveguide-dielectric resonances*. Experiment Instruments and Technology. No.3, pp. 169–171.
110. Usanov, D. A., & Feklistov, V. B. (1981). *Resonance method of testing dielectric permittivity of dielectric sheets at SHF*. Abstracts of the First All-Union Inter-University Science and Technology Conference "Optical and Radiowave Methods and Means of Non-Destructive Quality Control of Materials and Devices". Fergana. October 28–30, 1981. p. 1, pp. 64–66.
111. Usanov, D. A. (1986). *Means of radiowave control based on the effect of autodyne detection in solid-state oscillators*. Abstracts of the Science and Technical Conference "State and Trends of Development of the Metrics of Semiconductor and Dielectric Structures", September 2–5, 1986. Saratov. p. 40.
112. Usanov, D. A., Pisarev, V. V., & Vagarin, A. Y. (1985). Use of autodyne frequency converters based on gunn diodes for contactless measurement of microwave dielectric parameters. *Non-Destructive Testing*. No.5, pp. 82–85.
113. Borodovskiy, P. A., Buldygin, A. F., & Utkin, K. K. (1977). Calculation and experimental study of autodyne frequency converter based on Gunn diode. *News of Higher Educational Institutions of MHSSE USSR. Radioelectronics, 20*(10), 64–70.
114. Bulakhova, L. V., Kukushkin, V. V., & Solyakov, V. N. (1981). On frequency properties of gunn diode-based mixers in the millimeter range. *Radiotechnics, 26*(3), 666–667.
115. Usanov, D. A., & Pisarev, V. V. (1981). Features of operation of generators based on IT diodes in autodyne mode with close frequencies of generation and Signa. *News of Higher Educational Institutions. MHSSE USSR. Radioelectronics, 24*(10), 81–82.
116. Borodovskiy, P. A., Buldygin, A. F., & Utkin, K. K. (1974). Autodyne gunn diode-based mixer. *News of Higher Educational Institutions MHSSE USSR. Radioelectronics, 17*(12), 82–84.
117. Yatsunenko, A. G., & Sokolovskiy, I. I. (1980). Amplifier-transformer based on diode with transfer of electrons. *Radiotechnics, 35*(6), 40–42.
118. Roman, O. A., & Trepanov, V. K. Experimental study of frequency converters based on diodes with electron transmission. *News of Higher Educational Institutions of MHSSE USSR, 23*(10), 80–82.
119. Usanov, D. A., Skripal, A. V., Korotin, B. N., et al. (1994). Study of physical process in semiconductor microwave devices in the conditions of influence of external electromagnetic fields of the SHF range, optical radiation and constant magnetic field. In Y. A. Chaplygin (Ed.), *Modeling and designing of devices and systems of microelectronics and nanoelectronics: Inter-University compilation* (pp. 36–45). Zelenograd: Moscow Institute of Electronic Technology.
120. Usanov, D. A., Skripal, A. V. (1980). Detection by IC Diodes Operating in Active Mode. *Electronic Technology. Ser. 1. SHF Electronics*. Issue 10, pp. 62–63.
121. Usanov, D. A., Skripal, A. V., Avdeev, A. A., & Babayan, A. V. (1996). Effect of autodyne detection in gunn diode-based oscillator with low-frequency oscillating circuit in power line. *Radiotechnics and Electronics, 41*(12), 1497–1500.
122. Usanov, D. A., Bezmenov, A. A., & Orlov, V. B. (1980). Detector effect in amplifiers on avalanche transit-time diodes. *News of Higher Educational Institutions. Radioelectronics, 23* (10), 63–64.

123. Usanov, D. A., Bezmenov, A. A., Vagarin, A. Y., & Loginov, V. M. (1981). Detector effect in SHF amplifiers based on transistors. *Electronic Technology. Series 1. SHF Electronics*. Issue 9, pp. 60–61.
124. Usanov, D. A., Bezmenov, A. A., Vagarin, A. Y., & Loginov, V. M. (1984). Detector effect in SHF amplifiers based on field transistors. *Electronic Technology. Series 1. SHF Electronics*. Issue 1, pp. 32–33.
125. Usanov, D. A., & Bezmenov, A. A. (1986). Detection by SHF field transistors operating in active mode. *Electronic Technology. Series 1. SHF Electronics*. Issue 2, pp. 19–21.
126. Usanov, D. A., Skripal, A. V., Korotin, B. N., & Avdeev, A. A. (1992). *SHF measuring devices based on autodyne detection effect in semiconductor devices with negative resistance. Relevant Problems of Electronic Instrumentation APEP-92*. Abstracts of the International Science and Technology Conference, September 23–26, 1992. Novosibirsk: Novosibirsk Electrotechnical Institute, vol. 5: Measurements in Radiotechnics, pp. 40–44.
127. Usanov, D. A., Tupikin, V. D., Skripal, A. V., & Korotin, B. N. (1995). Using the effect of autodyne detection in semiconductor SHF generators for creation of radiowave control devices. *Non-Destructive Testing*. No.5, pp. 16–20.
128. Usanov, D. A., Bezmenov, A. A., Korotin, B. N. (1986). Device for measurement of thickness of dielectric films sprayed on metal. *Experiment Instruments and Technology*. No.4, pp. 227–228.
129. Usanov, D. A., Skripal, A. V., Korotin, B. N., & Avdeev, A. A. (1997). Pat. 2094811 RU, IPC G01 R 27/26. Gunn Diode-Based device for measurement of parameters of dielectric materials. No. 95115788/09. Application date: September 7, 1995; Publication date: October 27, 1997; Bull. No. 30.
130. Usanov, D. A., Skripal, A. V., Korotin, B. N., & Avdeev, A. A. (1997). Pat. 2096T91 RU, IPC G01 R 27/26. Device for measurement of parameters of dielectric materials. No. 95115711/09. Application date: September 7, 1995; Publication date: November 20, 1997; Bull. No. 32.
131. Usanov, D. A., Vagarin, A. Y., & Korotin, B. N. (1985). AC 1161898 USSR, IPC G01 R 27/26. Device for Measurement of Parameters of Dielectric Materials. No. 3584535/25; Application Date: April 22, 1983; Publication Date: June 15, 1985; Bull. No.22.
132. Usanov, D. A., Posadskiy, V. N., Burening, P. V., et al. (1977). Detector effect in amplifiers based on diodes with transfer of electrons. *Radiotechnics and Electronics, 22*(5), 1085–1086.
133. Usanov, D. A., Vagarin, A. Y., & Bezmenov, A. A. (1981). On using detector effect in generators based on avalanche transit time diodes for measurement of dielectric permittivity of materials. *Non-Destructive Testing*. No. 11, pp. 106–107.
134. Usanov, D. A., & Skripal, A. V. (1987). *Autodyne detection effect in gunn diode-based generators and its use for control of material parameters*. In 42th All-Union Scientific Session Dedicated to the Day of Radio: Abstracts: Moscow: Radio and Communication, p. 2. p. 31.
135. Usanov, D. A., Vagarin, A. Y., & Venig, S. B. (1985). Using the detector effect in gunn diode-based oscillator for measurement of parameters of dielectrics. *Non-Destructive Testing*. No.6, pp. 78–82.
136. Usanov, D. A., & Korotin, B. N. (1985). Device for measurement of thickness of metal films applied to dielectric base. *PTE*. No.1, p. 254.
137. Usanov, D. A., Korotin, B. N., Orlov, V. E. (1987). Using the effect of autodyne detection in SHF generators based on tunnel diodes to determine parameters of dielectrics. *Non-Destructive Testing*. No. 9, pp. 83–84.
138. Usanov, D. A., & Skripal, A. V. (1987). Effect of autodyne detection in Gunn diode-based oscillators and its use for control of thickness and permittivity of materials. *News of Higher Educational Institutions. Radioelectronics, 30*(10), 76–77.
139. Usanov, D. A., Skripal, A. V., Korotin, B. N., & Skripal, A. V. (1986). *SHF thickness gauge*. State and Trends of Development of the Metrics of Semiconductor and Dielectric Structures: Abstracts of Science and Technology Meeting. Moscow: TsNII "Electronics", Ser. 8. Issue 2 (232), p. 43.
140. Usanov, D. A., Skripal, A. V., & Korotin, B. N. et al. (1986). AC 1264109, IPC G01 R 27/26. Device for measurement of parameters of dielectric materials. Publication date: October 15, 1986. Bull. No.38.

141. Usanov, D. A., Tupikin, V. D., Skripal, A. V., & Skripal, A. V. (1986). AC 1448821 USSR, IPC G01 B 15/02./ (USSR). No. 4102803/24–28; Application date: 05.08.86.
142. Usanov, D. A., Pisarev, V. V., Avdeev, A. A., Skripal, A. V. et al. (1988). AC 1831121A1 RU, IPC G01 E 27/26./ No. 4497352/ 09; Application date: October 20, 1988.
143. Usanov, D. A., Skripal, A. V., Korotin, B. N., & Avdeev, A. A. (1997). Pat. 2096791 RU, IPC G01 R 27/26. Device for Measurement of parameters of dielectric materials. Application No. 95115711/09. Application date: September 7, 1995; Publication date: November 20, 1997.
144. Usanov, D. A., Skripal, A. V., Korotin, B. N. et al. (1990). *Radiowave thickness gauges for metal-dielectric structures*. Control of Surface Thicknesses and its Metrological Provision: Abstracts of the 4th All-Union Scientific Conference and Exhibition, September 18–20, 1990. Izhevsk, pp. 8–10.
145. Usanov, D. A., Skripal, A. V., Skripal, A. V. et al. (1993) *Control of parameters of dielectric coatings on color CRT mask*. Transfer Technologies, Complexes and Equipment in Engineering: Abstracts of 2th Annual Meeting for the Section of Innovative Inter-University Science and Technology Program. Saratov: Saratov State University Publishing, pp. 53–54.
146. Usanov, D. A., Skripal, A. V., Korotin, B. N. et al. (1993). *Radiowave control system based on autodyne detection effect in semiconductor devices with negative resistance.* Non-Destructive Physical Methods and Means of Control: Abstracts of the 13th Science and Technology Conference, September 8–12, 1993. Saint Petersburg, p. 58.
147. Usanov, D. A., Skripal, A. V., Skripal, A. V. et al. *Problem of control of thin-film coatings and its solution by methods of non-destructive testing.* Optical, Radiowave and Thermal Methods and Means of Quality Control of Materials, Products and Environment: Abstracts of the 5th Russian Science and Technology Conference, October 26–29, 1993. Ulyanovsk, pp. 8–9.
148. Usanov, D. A., Skripal, A. V., Skripal, A. V. et al. (1994). *Methods of control of parameters of thin-film metal-dielectric structures*. Non-Destructive Testing in Science and Industry-94: Abstracts of the Russian Science and Technology Conference with International Participation, May 31–June 2, 1994. Moscow, pp. 135–137.
149. Usanov, D. A., Skripal, A. V. (1995). *Radiowave control based on autodyne detection effect in semiconductor devices*. Optical, Radiowave and Thermal Methods and Means of Non-Destructive Control: Abstracts of the Russian Science and Technology Conference with International Participation: Abstracts of the Russian Science and Technology Conference with International Participation, September 12–14, 1995. Saratov: Saratov University Publishing House, pp. 5–6.
150. Skripal, A. V. (1996). *Systems and devices of Radiowave control based on the effect of autodyne detection in semiconductor devices*. Problems of Innovative Activities of Scientists, Inventors and Other Creative Workers in Conditions of Reformation of Economy: Abstracts of Regional Conference, April 16, 1996. Saratov: PUNIR Publishing, pp. 35–36.
151. Usanov, D. A., Skripal, A. V., Korotin, B. N. et al. (1988). *Informational and measurement complex for control of coating parameters*. Information Note on a Scientific and Technical Achievement. Saratov, TsNTI.
152. Usanov, D. A., Skripal, A. V., Abramov, A. V., & Pozdnyakov, V. A. (2001). *SHF method of measurement of mobility of free charge carriers*. Abstracts of the All-Russian Science and Technology Remote Conference "Electronics". Zelenograd, November 19–30, 2001. Moscow: MIET, pp. 68–69.
153. Usanov, D. A., Skripal, A. V., Abramov, A. V., & Pozdnyakov, V. A. (2002). *SHF method of measurement of mobility of free charge carriers in semiconductor structures*. In Proceedings of the 8th International Scientific and Technical Conference "Relevant Problems of Solid-State Electronics and Microelectronics". Dvinomorskoye, Russia, September 14–19, 2002. Taganrog: TRTU Publishing House, Part 2, pp. 86–89.
154. Usanov, D. A., Skripal, A. V., Abramov, A. V., & Pozdnyakov, V. A. (2003). *Measurement of mobility of free charge carriers in semiconductor structures with the help of semiconductor synchronized microwave oscillators*. Materials of All-Russian Science and Technology Conference "Relevant Problems of Radioelectronics". Samara, June 30, 2003. S.P. Korolev Samara State Aerospace University. Samara: NTC Publishing, pp. 31–33.

155. Skripal, A. V., Abramov, A. V., & Pozdnyakov, V. A. (2003). *Using a Synchronized Oscillator for Measurement of Mobility of Free Charge Carriers in Semiconductor Structures*. Abstracts of the 2nd International Science and Technology Conference "Physics and Technical Applications of Wave Processes". Samara, September 7–13, 2003. Samara State University. Samara: Samara University Publishing House, p. 353.
156. Usanov, D. A., Skripal, A. V., Abramov, A. V., & Pozdnyakov, V. A. (2003). *Semiconductor synchronized microwave oscillators in the signal subtraction circuit for measurement of mobility of free charge carriers in semiconductor structures*. In Proceedings of the 13th International Crimea Conference "Microwave and Telecommunication Technology" (CriMiCo'2003). Sevastopol, September 8–12, 2003. Sevastopol: Veber, pp. 589–591.
157. Usanov, D. A., Skripal, A. V., Abramov, A. V., & Pozdnyakov, V. A. (2003). *Study of characteristics of semiconductor structures at super-high frequencies using synchronized oscillator.* Works of the Fourth International Science and Technology Conference "Microelectronic Converters and Devices Based on Microelectronic Converters" (MEPP-2003, Baku-Sumqayit). Baku-Sumqayit, December 16–18, 2003. Baku: Mutarjim Publishing, pp. 12–14.
158. Usanov, D. A., Skripal, A. V., Abramov, A. V., & Pozdnyakov, V. A. (2004). SHF method of measurement of mobility of free charge carriers in semiconductor structures. *News of Higher Educational Institutions. Electronics*. No. 2, pp. 76–84.
159. Usanov, D. A., Skripal, A. V., & Ulyanov, D. V. (2000). *Power suppression mode in semiconductor synchronized microwave oscillators*. In Proceedings of 13th International Conference on Microwaves, Radar and Wireless Communications MIKON–2000. Poland, Wroclaw, May 22–24, 2000. vol. 1, pp. 109–112.
160. Usanov, D. A., Skripal, A. V., & Ulyanov, D. V. (2000). Effect of magnetic field on operation of semiconductor synchronized SHF oscillators in power attenuation mode. *News of Higher Educational Institutions. Electronics*. No. 6, pp. 49–54.
161. Usanov, D. A., Skripal, A. V., & Abramov, A. V. (2002). *Optical control of semiconductor synchronized microwave oscillators in the power suppression mode*. In Proceedings of XIV International Conference on Microwaves, Radar and Wireless Communications MIKON-2002. Ploand, Gdansk, May 20–22, 2002. vol. 1. pp. 255–258.
162. Usanov, D. A., Skripal, A. V., & Abramov, A. V. (2002). Optical control of semiconductor synchronized SHF generators operating in signal subtraction circuit. *News of Higher Educational Institutions. Electronics*. No. 5, pp. 31–39.
163. Synge, E. A. (1928). A suggested method for extending microscopic resolution into the ultra-microscopic region. *The Philosophical Magazine, 6*, 356–362.
164. Frait, Z. (1959). The use of high frequency modulation in studying ferromagnetic resonance. *Czechoslovak Journal of Physics, 9*, 403–404.
165. Frait, Z., Kambersky, V., Malek, Z., & Ondris, M. (1960). Local variations of uniaxial anisotropy in thin films. *Czechoslovak Journal of Physics, B10*, 616–617.
166. Soohoo, R. F. (1962). A microwave magnetic microscope. *Journal of Applied Physics, 33*, 1276–1277.
167. Lofland, S. E., Bhagat, S. M., Ju, H. L., Xiong, G. C., Venkatesan, T., & Greene, R. L. (1995). Ferromagnetic resonance and magnetic homogeneity in a giant- magnetoresistance material La2/3Ba1/3MnO3. *Physical Review B, 52*, 15058–15061.
168. Ikeya, M., & Miki, T. (1987). ESR microscopic imaging with microfabricated field gradient coils. *Japanese Journal of Applied Physics, 26*, L929–L931.
169. Ikeya, M., Furusawa, M., & Kasuyai, M. (1990). Near-field scanning electron spin resonance microscopy. *Scanning Microscopy, 4*, 245–248.
170. Ash, E. A., & Nicholls, G. (1972). Super-resolution aperture scanning microscope. *Nature, 237*, 510–512.
171. Bryant, C. A., & Gunn, J. B. (1965). Noncontact technique of the local measurement of semiconductor resistivity. *The Review of Scientific Instruments, 36*, 1614–1617.
172. Xu, Y. S., & Bosisio, R. G. (1992). Nondestructive measurements of the resistivity of thin conductive films and the dielectric constant of thin substrates using an open-ended Coaxila line. *IEE Proceedings H, 139*, 500–506.

173. Stuchly, M. A., & Stuchly, S. S. (1980). Coaxial line reflection methods for measuring dielectric properties of biological substances at radio and Microwave frequencies – A review. *IEEE Transactions on Instrumentation and Measurement, IM-29*, 176–183.
174. Stuchly, M. A., Brady, M. M., Stuchly, S. S., & Gajda, G. (1982). Equivalent circuit of an open-ended coaxial line in a Lossy dielectric. *IEEE Transactions on Instrumentation and Measurement, IM-31*, 116–119.
175. Athey, T. W., Stuchly, M. A., & Stuchly, S. S. (1982). Measurement of radio frequency permittivity of biological tissues with an open-ended coaxial line: Part I. *IEEE Transactions on Microwave Theory and Techniques, MTT-30*, 82–86.
176. Stuchly, M. A., Athey, T. W., Samaras, G. M., & Taylor, G. E. (1982). Measurement of radio frequency permittivity of biological tissues with an open-ended coaxial line: Part II – Experimental results. *IEEE Transactions on Microwave Theory and Techniques, MTT-30*, 87–92.
177. Gajda, G. B., & Stuchly, S. S. (1983). Numerical analysis of open-ended coaxial lines. *IEEE Transactions on Microwave Theory and Techniques, MTT-31*, 380–384.
178. Burdette, E. C., Cain, F. L., & Seals, J. (1980). In vivo probe measurement technique for determining dielectric properties at VHF through Microwave frequencies. *IEEE Transactions on Microwave Theory and Techniques, MTT-28*, 414–427.
179. Fee, M., Chu, S., & Hansch, T. W. (1989). Scanning electromagnetic transmission line microscope with sub-wavelength resolution. *Optics Communications, 69*, 219–224.
180. Stranick, S. J., & Weiss, P. S. (1993). A versatile microwave-frequency-compatible scanning tunneling microscope. *The Review of Scientific Instruments, 64*, 1232–1234.
181. Stranick, S. J., & Weiss, P. S. (1994). A tunable microwave frequency alternating current scanning tunneling microscope. *The Review of Scientific Instruments, 65*, 918–921.
182. Bumm, L. A., & Weiss, P. S. (1995). Small cavity nonresonant tunable microwavefrequency alternating current scanning tunneling microscope. *The Review of Scientific Instruments, 66*, 4140–4145.
183. Jiang, G. Q., Wong, W. H., Raskovich, E. Y., Clark, W. G., Hines, W. A., & Sanny, J. (1993). Openended coaxial-line technique for the measurement of the microwave dielectric constant for low-loss solids and liquids. *The Review of Scientific Instruments, 64*, 1614–1621.
184. Asami, K. (1994). The scanning dielectric microscope. *Measurement Science and Technology, 5*, 589–592.
185. Gutman, R. J., & Borrego, J. M. (1987). *Microwave scanning microscopy for planar structure diagnostics*. In IEEE MTT Digest, pp. 281–284.
186. Bhimnathwala, H., & Borrego, J. M. (1994). Measurement of the sheet resistance of doped layers in semiconductors by microwave reflection. *Journal of Vacuum Science and Technology B, 12*, 395–398.
187. Qaddoumi, N., & Zoughi, R. (1997). Preliminary study of the influences of effective dielectric constant and nonuniform probe apeture field distribution on near field microwave images. *Materials Evaluation, 55*, 1169–1173.
188. Golosovsky, M., & Davidov, D. (1996). Novel millimeter-wave near-field resistivity microscope. *Applied Physics Letters, 68*, 1579–1581.
189. Golosovsky, M., Galkin, A., & Davidov, D. (1996). High-spatial resolution resistivity mapping of large-area YBCO films by a near-field millimeter-wave microscope. *IEEE MTT, 44*, 1390–1392.
190. Golosovsky, M., Lann, A., & Davidov, D. (1998). A millimeter-wave near-field scanning probe with an optical distance control. *Ultramicroscopy, 71*, 133–141.
191. Lann, A. F., Golosovsky, M., Davidov, D., & Frenkel, A. (1998). Combined millimeter-wave near-field microscope and capacitance distance control for the quantitative mapping of sheet resistance of conducting layers. *Applied Physics Letters, 73*, 2832–2834.
192. Lann, A. F., Golosovsky, M., Davidov, D., & Frenkel, A. (1999). Microwave near- field polarimetry. *Applied Physics Letters, 75*, 603–605.
193. Bae, J., Okamoto, T., Fujii, T., Mizuno, K., & Nozokido, T. (1997). Experimental demonstration for scanning near-field optical microscopy using a metal micro-slit probe at millimeter wavelengths. *Applied Physics Letters, 71*, 3581–3583.

194. Tabib-Azar, M., Shoemaker, N., & Harris, S. (1993). Non-destructive characterization of materials by evanescent microwaves. *Measurement Science and Technology, 4*, 583–590.
195. Tabib-Azar, M., Su, D. P., Pohar, A., LeClair, S. R., & Ponchak, G. (1999). 0.4 μm spatial resolution with 1 GHz (λ= 30 cm) evanescent microwave probe. *The Review of Scientific Instruments, 70*, 1725–1729.
196. Tabib-Azar, M., Pathak, P. S., Ponchak, G., & LeClair, S. (1999). Nondestructive superresolution imaging of defects and nonuniformities in metals, semiconductors, dielectrics, composites, and plants using evanescent microwaves. *The Review of Scientific Instruments, 70*, 2783–2792.
197. Tabib-Azar, M., Ciocan, R., Ponchak, G., & LeClair, S. R. (1999). Transient thermography using evanescent microwave microscope. *The Review of Scientific Instruments, 70*, 3387–3390.
198. Ponchak, G., Akinwande, D., Ciocan, R., LeClair, S. R., & Tabib-Azar, M. (1999). *Evanescent microwave probes using coplanar waveguide and Stripline for super-resolution imaging of materials*. In IEEE MTT-S Digest.
199. Keilmann, F. (1989). US Patent 4,994,818, filed Oct. 27, 1989.
200. Merz, R., Keilmann, F., Haug, R. J., & Ploog, K. (1993). Nonequilibrium edge-state transport resolved by far-infrared microscopy. *Physical Review Letters, 70*, 651–653.
201. Keilmann, F. (1995). FIR Microscopy. *Infrared Physics & Technology, 36*, 217–224.
202. Keilmann, F., van der Weide, D. W., Eickelkamp, T., Merz, R., & Stockle, D. (1996). Extreme sub-wavlength resolution with a scanning radio-frequency transmission microscope. *Optics Communications, 129*, 15–18.
203. Knoll, B., Keilmann, F., Kramer, A., & Guckenberger, R. (1997). Contrast of microwave near-field microscopy. *Applied Physics Letters, 70*, 2667–2669.
204. Bosisio, R. G., Giroux, M., & Couderc, D. (1970). Paper sheet moisture measurements by Microwave phase perturbation techniques. *Journal of Microwave Power, 5*, 25–34.
205. Tanabe, E., & Joines, W. T. (1976). A nondestructive method for measuring the complex permittivity of dielectric materials at Microwave frequencies using an open transmission line resonator. *IEEE Transactions on Instrumentation and Measurement, IM-25*, 222–226.
206. Cho, Y., Kirihara, A., & Saeki, T. (1996). Scanning nonlinear dielectric microscope. *The Review of Scientific Instruments, 67*, 2297–2303.
207. Cho, Y., Kazuta, S., & Matsuura, K. (1999). Scanning nonlinear dielectric microscopy with nanometer resolution. *Applied Physics Letters, 75*, 2833–2835.
208. Wei, T., Xiang, X.-D., Wallace-Freedman, W. G., & Schultz, P. G. (1996). Scanning tip microwave near-field microscope. *Applied Physics Letters, 68*, 3506–3508.
209. Lu, Y., Wei, T., Duewer, F., Lu, Y., Ming, N., Schultz, P. G., & Xiang, X.-D. (1997). Nondestructive imaging of dielectric-constant profiles and ferroelectric domains with a scanning-tip Microwave near-field microscope. *Science, 276*, 2004–2006.
210. Gao, C., Wei, T., Duewer, F., Lu, Y., & Xiang, X.-D. (1997). High spatial resolution quantitative microwave impedance microscopy by a scanning tip microwave near-field microscope. *Applied Physics Letters, 71*, 1872–1874.
211. Takeuchi, I., Wei, T., Duewer, F., Yoo, Y. K., Xiang, X.-D., Talyansky, V., Pai, S. P., Chen, G. J., & Venkatesan, T. (1997). Low temperature scanning-tip microwave near-field microscopy of YBCO films. *Applied Physics Letters, 71*, 2026–2028.
212. Chang, H., Gao, C., Takeuchi, I., Yoo, Y., Wang, J., Schultz, P. G., Xiang, X.-D., Sharma, R. P., Downes, M., & Venkatesan, T. (1998). Combinatorial synthesis and high throughput evaluation of ferroelectric/dielectric thin-film libraries for microwave applications. *Applied Physics Letters, 72*, 2185–2187.
213. Gao, C., & Xiang, X.-D. (1998). Quantitative microwave near-field microscopy of dielectric properties. *The Review of Scientific Instruments, 69*, 3846–3851.
214. Vlahacos, C. P., Black, R. C., Anlage, S. M., & Wellstood, F. C. (1996). Near-field scanning Microwave microscope with 100 μm resolution. *Applied Physics Letters, 69*, 3272–3274.
215. Steven, M., Anlage, C. P. V., Dutta, S., & Wellstood, F. C. (1997). Scanning microwave microscopy of active superconducting microwave devices. *IEEE Transactions on Applied Superconductivity, 7*, 3686–3689.

216. Steinhauer, D. E., Vlahacos, C. P., Dutta, S., Wellstood, F. C., & Anlage, S. M. (1997). Surface resistance imaging with a scanning near-field microwave microscope. *Applied Physics Letters, 71*, 1736–1738. cond-mat/9712142.
217. Steinhauer, D. E., Vlahacos, C. P., Dutta, S. K., Feenstra, B. J., Wellstood, F. C., & Anlage, S. M. (1998). Quantitative imaging of sheet resistance with a scanning near-field microwave microscope. *Applied Physics Letters, 72*, 861–863.
218. Steinhauer, D. E., Vlahacos, C. P., Canedy, C., Stanishevski, A., Melngailis, J., Ramesh, R., Wellstood, F. C., & Anlage, S. M. (1999). Imaging of Microwave Permittivity, Tunability, and Damage Recovery in (Ba,Sr)TiO3 Thin Films. *Applied Physics Letters, 75*, 3180–3182.
219. Feenstra, B. J., Vlahacos, C. P., Thanawalla, A. S., Steinhauer, D. E., Dutta, S. K., Wellstood, F. C., & Anlage, S. M. (1998). *Near-field scanning microwave microscopy: Measuring local microwave properties and electric field distributions*. In IEEE MTT-S International Microwave Symposium Digest, pp. 965–966.
220. Anlage, S. M., Vlahacos, C. P., Steinhauer, D. E., Dutta, S. K., Feenstra, B. J., Thanawalla, A., & Wellstood, F. C. (1998). Low power superconducting microwave applications and microwave microscopy. *Particle Accelerators, 61*(321–336), 57–72.
221. Anlage, S. M., Steinhauer, D. E., Vlahacos, C. P., Feenstra, B. J., Thanawalla, A. S., Hu, W., Dutta, S. K., & Wellstood, F. C. (1999). Superconducting material diagnostics using a scanning near-field microwave microscope. *IEEE Transactions on Applied Superconductivity, 9*, 4127–4132.
222. Anlage, S. M., Hu, W., Vlahacos, C. P., Steinhauer, D., Feenstra, B. J., Dutta, S. K., Thanawalla, A., & Wellstood, F. C. (1999). Micro-wave nonlinearities in High-Tc superconductors: The truth is out there. *Journal of Superconductivity, 12*, 353–362.
223. Vlahacos, C. P., Steinhauer, D. E., Dutta, S. K., Feenstra, B. J., Anlage, S. M., & Wellstood, F. C. (2000). Non-contact imaging of dielectric constant with a near-field scanning microwave microscope. *The Americas Microscopy and Analysis, 75*, 13–16.
224. Anlage, S. M., Thanawalla, A. S., Zhuravel', A. P., Hu, W., Vlahacos, C. P., Steinhauer, D. E., Dutta, S. K., & Wellstood, F. C. (1999). Near-field scanning microwave microscopy of superconducting materials and devices. In N. Koshizuka & S. Tajima (Eds.), *Advances in superconductivity* (XI ed., pp. 1079–1084). Tokyo: Springer.
225. Vlahacos, C. P., Steinhauer, D. E., Dutta, S. K., Feenstra, B. J., Anlage, S. M., & Wellstood, F. C. (1998). Quantitative topographic imaging using a near- field scanning microwave microscope. *Applied Physics Letters, 72*, 1778–1780.
226. Werner, M. J., & King, R. J. (1996). *Mapping the "ε"′ of conducting solid films in situ*, MRS Proceeding.
227. U.S. Patent #5,334,941, Microwave reflection resonator sensors. Issued August 2, 1994 to R. J. King.
228. Gallop, J., Hao, L., & Abbas, F. (1997). Spatially resolved measurements of HTS microwave surface impedance. *Physica C, 282–287*, 1579–1580.
229. Hao, L., & Gallop, J. C. (1999). Spatially resolved measurements of HTS Microwave surface impedance. *IEEE Transactions on Applied Superconductivity, 9*, 1944–1947.
230. Manassen, Y. (1994). Scanning probe microscopy and magnetic resonance. *Advanced Materials, 6*, 401–404.
231. Zhang, Z., Hammel, P. C., & Wigen, P. (1996). Observation of ferromagnetic resonance in a microscopic sample using magnetic resonance force microscopy. *Applied Physics Letters, 68*, 2005–2007.
232. Zhang, Z., Hammel, P. C., Midzor, M., Roukes, M. L., & Childress, J. R. (1998). Ferromagnetic resonance force microscopy on microscopic cobalt single layer films. *Applied Physics Letters, 73*, 2036–2038.
233. Wago, K., Botkin, D., Yannoni, C. S., & Rugar, D. (1998). Paramagnetic and ferromagnetic resonance imaging with a tip-on-cantilever magnetic resonance force microscope. *Applied Physics Letters, 72*, 2757–2759.
234. Knoll, B., & Keilmann, F. (1999). Near-field probing of vibrational absorption for chemical microscopy. *Nature, 399*, 134–137.

235. Black, R. C., Wellstood, F. C., Dantsker, E., Miklich, A. H., Nemeth, D. T., Koelle, D., Ludwig, F., & Clarke, J. (1995). Microwave microscopy using a superconducting quantum interference device. *Applied Physics Letters, 66*, 99–101.
236. Black, R. C., Wellstood, F. C., Dantsker, E., Miklich, A. H., Koelle, D., Ludwig, F., & Clarke, J. (1995). High-frequency magnetic microscopy using a high-Tc SQUID. *IEEE Transactions on Applied Superconductivity, 5*, 2137–2141.
237. Dmitrienko, G. V., & Trefilov, N. A. (2004). Pat. 2231078 RU, IPC G01 R 27/04. Method of measurement of high values of complex dielectric permittivity of impedance materials at SHF and device for Its implementation. Application No. 2002133721/09. Application date: December 15, 2002; Publication date: June 20, 2004.
238. Dmitrienko, G. V., & Trefilov, N. A. (2002). Pat. 2194285 RU, IPC G01 R 27/04. Method of measurement of high values of complex dielectric permittivity of impedance materials. Application No. 2001106866/09. Application date: March 13, 2001; Publication date: December 10, 2002.
239. Dmitrienko, G. V., & Trefilov, N. A. (2004). Pat. 2228535 RU, IPC G01 R 27/26. Method of measurement of complex dielectric permittivity of radar-absorbent composite materials during heating. Application No. 2002131754/09. Application date: November 26, 2002; Publication date: May 10, 2004.
240. Fedunin, P. A., Karev, D. V., Dmitriev, D. A, & Kaberov, S. R. (2005). Pat. 2251073 RU, IPC G01 B 15/02, G01 R 27/26. Microwave method of measurement of magnetic-dielectric Parameters and thickness of spin surfaces on metal. Application No. 2002105214/28. Application date: February 26, 2002; Publication date: April 27, 2005.
241. Fedunin, P. A., Kaberov, S. R., Dmitriev, D. A., & Fedorov, N. P. (2005). Pat. 2249178 RU, IPC G01 B 15/02, G01 R 27/26. SHF Method of determining complex dielectric permittivity and thickness of dielectric plates. Application No. 2003106528/28. Application date: March 7, 2003; Publication date: March 27, 2005.
242. Suslin, M. A., Dmitriev, D. A., Kaberov, S. R., Fedunin, P. A., & Karev, D. V. (2002). Pat. 2193184 RU, IPC G01 N 22/00, G01 R 27/26. SHF Method of determining dielectric permittivity and thickness of dielectric coatings on metal. Application No. 2001102116/09. Application date: January 23, 2001; Publication date: November 20, 2002.
243. Oliynik, V., Makarov, D., & Danilov, V. (2005). *Dielectric permeability measurements with waveguide bragg structure usage*. In Proceedings of 15th-International Crimean Conference "Microwave & Telecommunication Technology" (CriMiCo'2005). September 12–16, 2005. Sevastopol, Crimea, Ukraine, pp. 785–786.
244. Brekhovskih, L. M. (1973). *Waves in layered structures*. Moscow: Science, 342 p.

Chapter 13
Radiation Stability of SHF Devices

13.1 Impact of Ionizing Radiation on the Characteristics of Silicon-Germanium Integrated Circuits of the SHF Range

One of the most important directions in development of microelectronics of military and special purpose is creation of a new generation of radiation-tolerant electronic component base (ECB) of wide application range, including LSICs of the SHF range [1].

Compliance with radiation resistance requirements in combination with high functional possibilities and wide frequency range poses a serious scientific and technical task for LSIC developers. One of the promising directions of development of SHF range LSICs is represented by devices based on silicon-germanium (SiGe) [2]. According to the information in possession of the authors, no official certification radiation tests of SiGe SHF ICs designed by national design centers have been performed to date. The results of foreign studies of these devices are far from being fully covered in literature, especially in terms of effect of the pulse ionizing radiation (IR) and issues of SHF IC resistance with their characteristic criteria parameters.

In this connection, it is plausible to study the radiation resistance of the national SiGe elemental base and SHF ICs based on SiGe BiCMOS technology. The main aim of such studies is to determine parameter-criteria of resistance of SiGe SHF ICs as well as absolute and relative resistance parameters as compared to ICs based on different technologies. Customers (military and space industry) are also particularly interested in the degree of adequacy of the existing imitation testing methods.

The object of the number of first studies performed by native specialists [2] was represented by SiGe of heterostructural bipolar transistors of the n-p-n type and SHF ICs based on them: low-noise amplifier (LNA), wideband amplifier (WBA) and voltage controlled oscillator (VCO), designed by FSUE "NIIMA Progress" and manufactured using SGB25V technology with design standards of 0.42 /0.25 μm.

© The Editor(s) (if applicable) and The Author(s), under exclusive license to Springer Nature Switzerland AG 2021

A. Belous, *Handbook of Microwave and Radar Engineering*,
https://doi.org/10.1007/978-3-030-58699-7_13

Tests for impulse effect of IR on these products were performed using the modeling unit “ARSA” and the laser imitator “RADON-5”. Tests for IR dose exposure were performed on the electron accelerator У-31/33 in the bremsstrahlung gamma radiation mode (modeling unit У-31/33) and X-ray simulator REIM-M. Modeling units, laboratory simulators, dosimetry means and measuring equipment were provided by ENPO SPELS JSC.

13.1.1 Heterostructural Bipolar Transistors

Study of radiation degradation of SiGe HBT characteristics was performed for devices of two types: standard (HBT S) and high-voltage (HBT H), which are basic active elements of a SHF IC. Cross section of SiGe HBT manufactured in accordance with the SGB25VD technology is shown in Fig. 13.1, while the main HBT parameters are given in the Table 13.1.

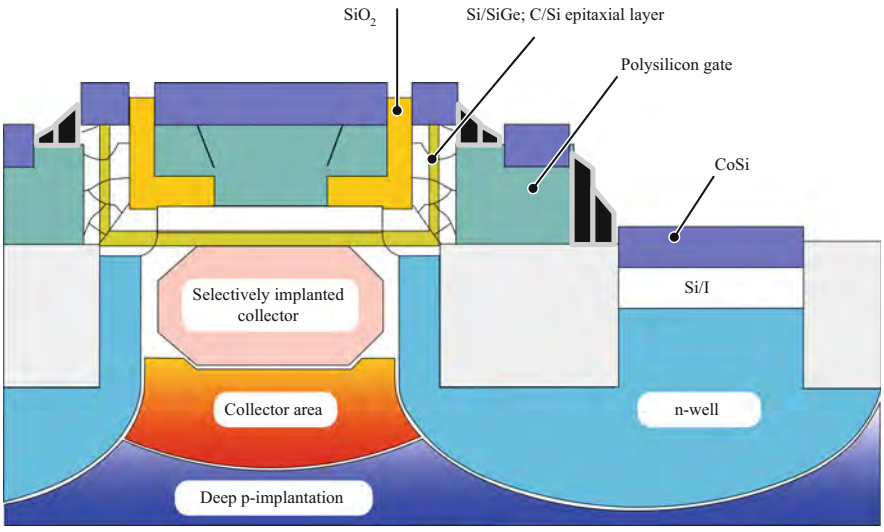

Fig. 13.1 Cross-section of a SiGe heterostructural bipolar transistor [1]

Table 13.1 Main parameters of SiGe HBT

Parameter	Value	
Type of transistor	HBT S	HBT H
Emitter area, μm^2	0.42 × 0.84	0.42 × 0.84
Maximum single frequency amplification, GHz	45	25
Maximum generation frequency, GHz	90	70
Static coefficient of the base current transmission β	190	190
Trip voltage U_{CE0}, V	4.0	7.0

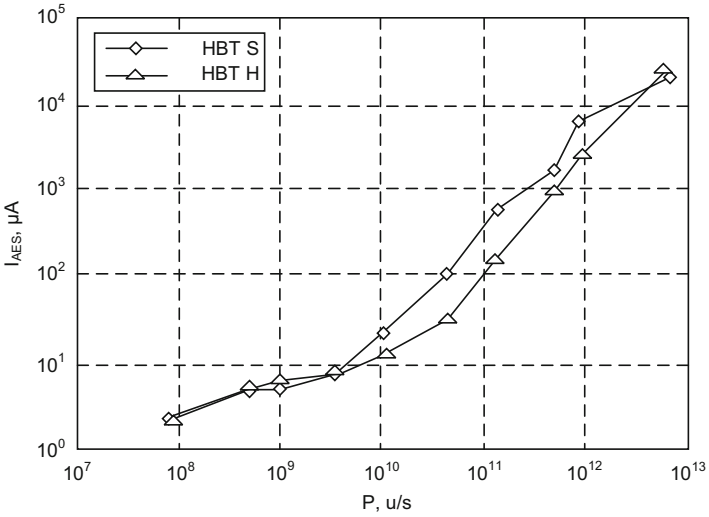

Fig. 13.2 Experimental dependencies of the amplitude value of the pulse reaction of the collector current of SiGe HBT on the dose power [1]

Experimental dependencies of the amplitude value of pulse reaction of the manifold current at $U_{KE} = 2$ V of the dose power are shown in Fig. 13.2. According to the presented results, at the level of pulse effect exceeding 3×10^9 u/m, a dependence is linear, which conforms to the known results for a classic bipolar transistor [3]. In order to ensure maximum level of IR pulse effect equal to 6.5×10^{12} u/s, laser simulation methods with calibration on the modeling unit were used in work. No thyristor effect or catastrophic failures were determined in SiGe HBT within the examined range of dose powers.

Studies of the SiGe HBT characteristics under dose exposure to IR were performed using the modeling unit У-31/33. During exposure, HBTs were in the active static mode ($U_{BE} = 0.7$ V; $U_{CE} = 0$ V) corresponding to the fields of operation in real circuits. During intervals between radiation sessions, the values of base current I_B and collector current I_C of the HBT at $U_{BE} = 0.7$ V and $U_{C3} = 0.9$ V were measured; after that, static coefficient of the base current transmission standardized to the value up to radiation of β/β_0 was calculated. Experimental dependencies of I_B and β/β_0 of the absorbed dose value are presented in Fig. 13.3 for both HBT types.

According to the obtained results, the most critical static parameter of the HBT under dose exposure is the base current, significant increase of which is determined by accumulation of radiation-induced charge in the oxide near the base-emitter transition, which leads to an increase in the carrier recombination rate in the base [4, 5]. In its turn, quick increase in the base current at the values of the absorbed dose exceeding 2×10^5 units at practically unchanged collector current cause significant degradation of β: at exposure level of 1.2×10^6 units, HBT β ГБТ decreases by 40%. while at dose equal to 2×10^7 units HBT base current increased 10 times,

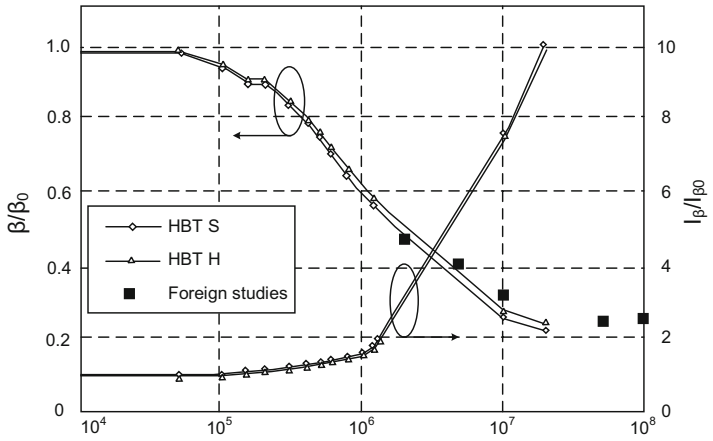

Fig. 13.3 Experimental dependencies of I_B и β/β_0 SiGe of HBT on the value of the absorbed dose [1]

Table 13.2 Basic parameters of the first Russian ICs LNA and WBA

Amplifier type	LNA	WBA
Working frequency range, GHz	0,1...3,0	0,1...3,0
Consumed current, mA	12 or 20	31
Gain factor |S21|, dB	10...20	8...16
Reverse isolation |S12|, dB	−45...−20	−25...−22
Input VSWR	1,5 max.	2,2 max.
Output VSWR	1,5 max.	2,4 max.
Noise coefficient at 1 GHz, dB	2 max.	6 max.
Output power at 1 dB compression at 1 GHz frequency, dBm	+7 min.	+3.5 min.
Supply voltage, V	3	5

which led to the reduction of β to 25% of the initial value. These results are in accordance with the data of foreign studies of dose degradation of SiGe HBTs manufactured according to technology SGB25VD and presented for comparison in Fig. 13.3 [1].

13.1.2 SHF LNA and WBA Chips

First Russian ICs LNA and WBA are based on bipolar transistors: LNA – according to cascade circuit, WBA – according to two-cascade circuit with OE. Main parameters of ICs LNA and WBA are given in Table 13.2. Simplified block diagrams and topologies of IC LNA are shown in Fig. 13.4, IC WBA – in Fig. 13.5.

Results of the experimental study of characteristics of ICs LNA and WBA are shown in Figs. 13.6 and 13.7.

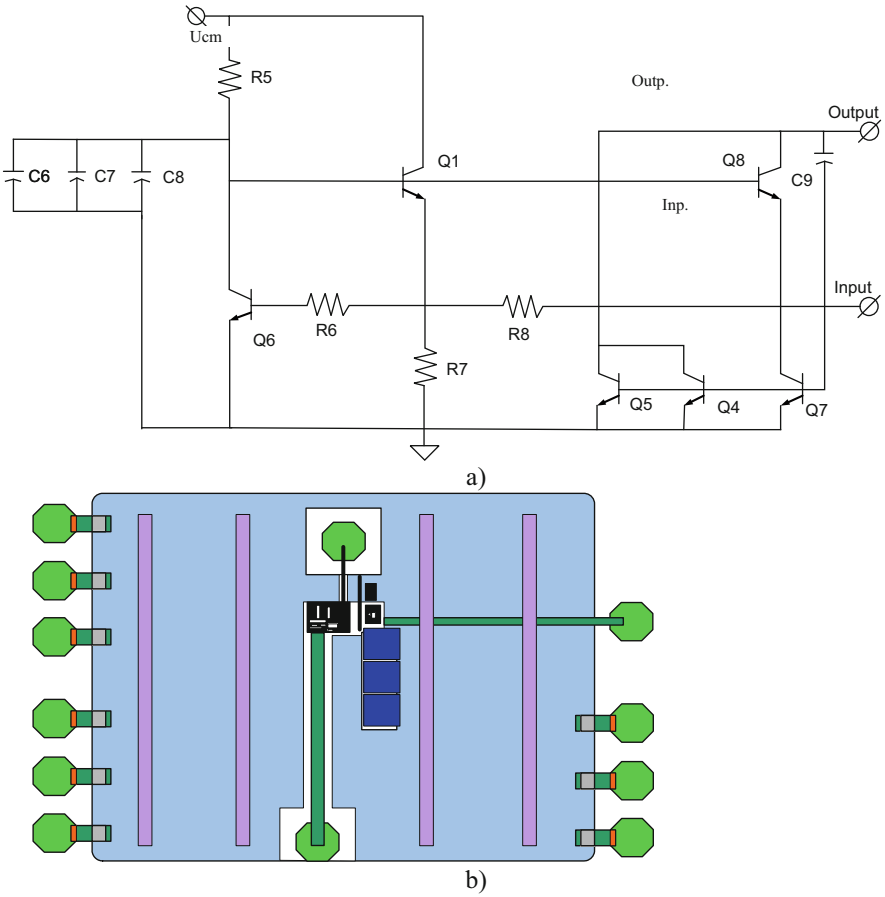

Fig. 13.4 Block diagram (**a**) and topology (**b**) of SiGe IC SHF LNA [1]

Experimental dependencies of the low-signal amplification coefficient *C*a and consumption current I_C of ICs LNA and WBA on the equivalent power of the dose shown in Fig. 13.8 a and b allow us to make

- under pulse effect of IR, parameter-criteria of ICs LNA and WBA behave similarly;
- at the moment of exposure to pulse of IR, *C*a decreases with an increase in the dose power; at effect levels of $4 \times 10^9 \ldots 10^{10}$ u/s, reduction of *C*a at 400 MHz is 100% of the initial value;
- at dose power values exceeding 5×10^9 u/s the amplitude value of I_C increases linearly with the dose power increase; at effect level of 10^10 u/s, the increase in I_C equals to 100% of the mode value;
- the time of workability loss of both ICs by parameters *C*a and I_C at limit levels of effect of $3 \times 10^{10} \ldots 7 \times 10^{10}$ u/s does not exceed 20 μs;
- no thyristor effect or catastrophic failures have been detected.

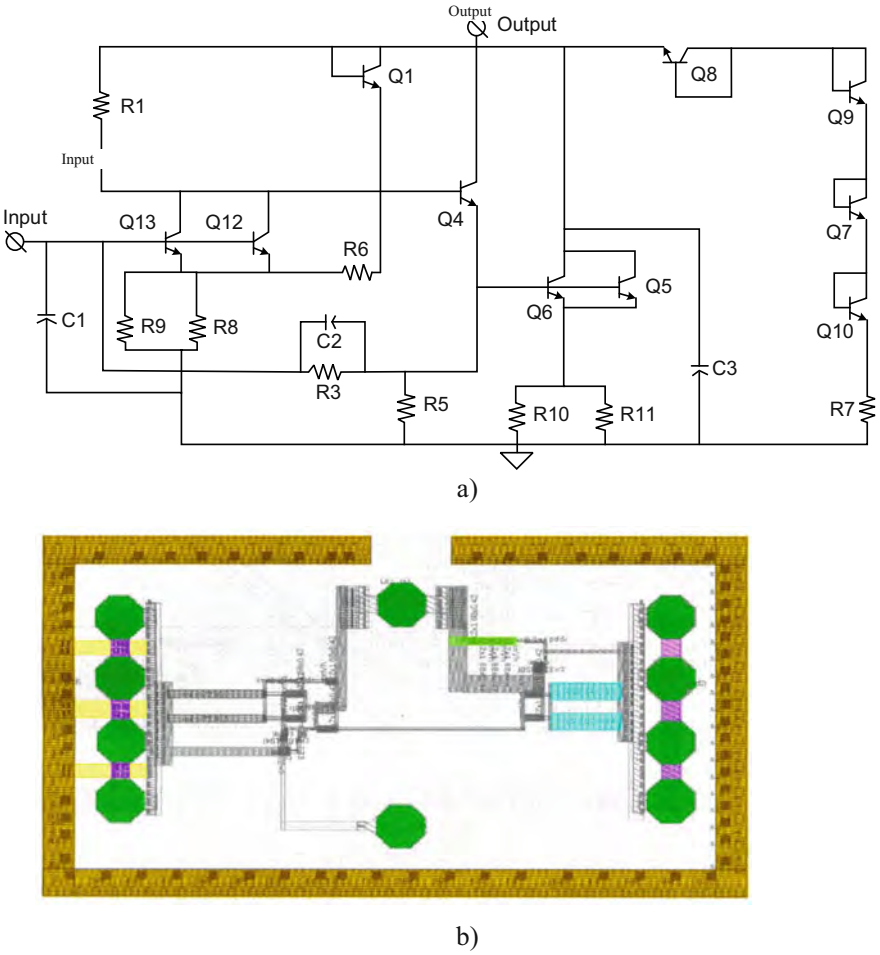

Fig. 13.5 Block diagram (**a**) and topology (**b**) of SiGe IC SHF LNA WBA [1]

The study of IC LNA under dose effect of IR on the modeling unit У-31/33 up to the level of 1.5×10^6 units helped identify the most critical parameters: low-signal amplification coefficient *C*a at frequencies below 0.4 GHz, output power at 1 dB compression P_{1dB} at a frequency of 1 GHs and consumption current I_C in the linear mode. Experimental dependencies of the given parameters on the absorbed dose are shown in Fig. 13.9, according to which all three parameter-criteria decrease with an increase in the absorbed dose. At maximum exposure equal to 1.5×10^6 units their relative change does not exceed 6%. The effect of dependence of the *C*a degradation level on the input signal frequency has been identified, but not properly explained yet: at frequencies higher than 0,5 GHz *C*a remains virtually unchanged at the maximum effect level.

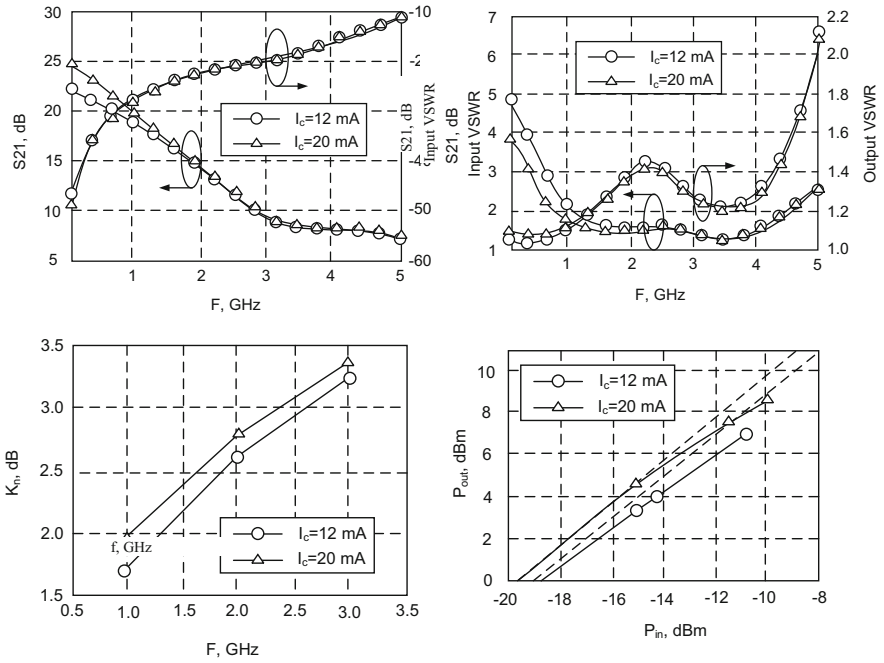

Fig. 13.6 Results of the studies of characteristics of IC LNA

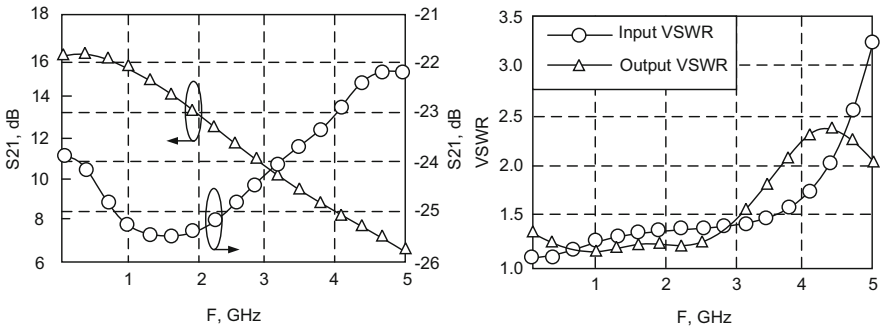

Fig. 13.7 Results of experimental studies of the characteristics of IC WBA [1]

Degradation of other measured parameters (VSWR, C_n and Ca at frequencies higher than 0,5 GHz) has not been identified – their variation is within the tolerable measurement error.

The results presented in Fig. 13.9c in [1] made it possible to obtain preliminary forecast of the threshold dose effect for IC LNA. Based on the linear extrapolation results, 20% reduction of the identified parameter-criteria (Ca, P_{1dB} and I_C) occurs when the values of the absorbed dose are within the range of values of $5 \times 10^6 \ldots 1.2 \times 10^7$ units.

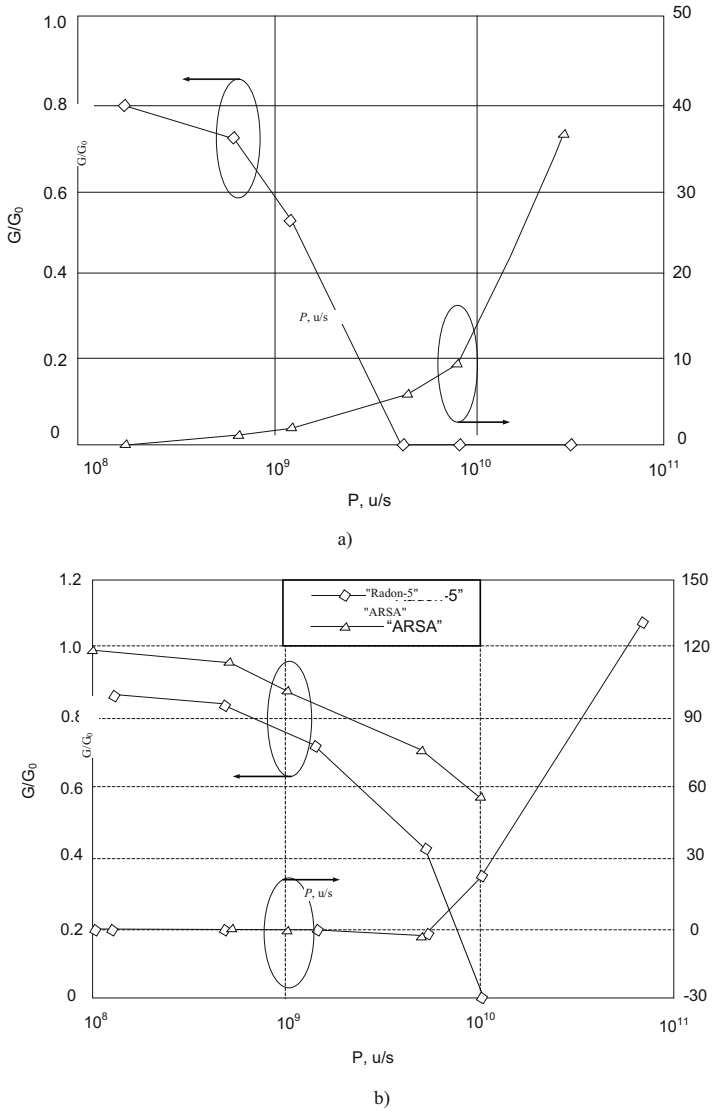

Fig. 13.8 Experimental dependencies of the amplitude value of pulse reaction *C*a and I_C for IC LNA (**a**) and WBA (**b**) on equivalent dose power [1]

Comparative results of studies with the use of X-ray simulator REIM-M demonstrated qualitatively similar character of degradation of parameter-criteria of IC LNA resistance.

Study of the IC BWA under dose exposure to IR performed by the authors of [1] on modeling unit and X-ray simulator demonstrated that the variations of the

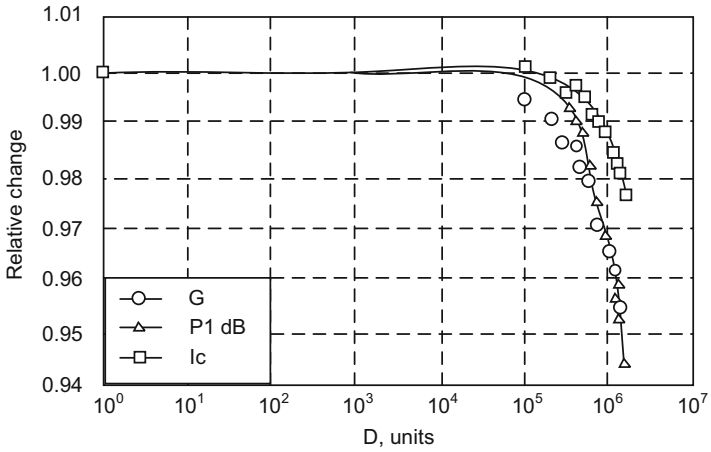

Fig. 13.9 Experimental dependencies of parameter-criteria of IC LNA resistance on the value of the absorbed dose [1]

controlled parameters within the examined range of the dose absorption values of up to 1.2×10^6 units are within the limits of measurement equipment errors.

13.1.3 SHF VCG Chips

Basic diagram and topology of Russian IC VCO are shown in Fig. 13.10. Unlike ICs LNA and WBA, the composition of IC VCO includes, along with SiCe HBT, MOS transistors and varicaps. The core of the IC VCG is formed by the resonator based on integral three-output inductance and MOS varicaps, switched into the DS circuit of the preliminary amplifier based on bipolar transistors. Buffer amplifier is installed at the IC VCG output. Main parameters of IC VCG are given in Table 13.3.

The results of the experimental research of IC VCG characteristics are shown in Fig. 13.11.

Experimental dependencies of the output power level P_{out} and consumption current I_P of IC VCO on the equivalent dose power shown in Fig. 13.12 allow us to make the following conclusions:

- at the moment of the IR pulse effect, output power P_{out} of the IC reduces monotonously with the increasing dose power; with exposure level of 4×10^9u/s, the reduction of P_{out} is 100%;
- consumption current I_C increases linearly with the dose power increase; at effect level of 6×10^9 u/s, the increase in I_C equals to 100% of the mode value;
- the time of workability loss of both IC VCO by parameters P_{out} and I_C at maximum level of effect of 5.4×10^{10} u/s does not exceed 35 μs;
- no thyristor effect or catastrophic failures have been detected.

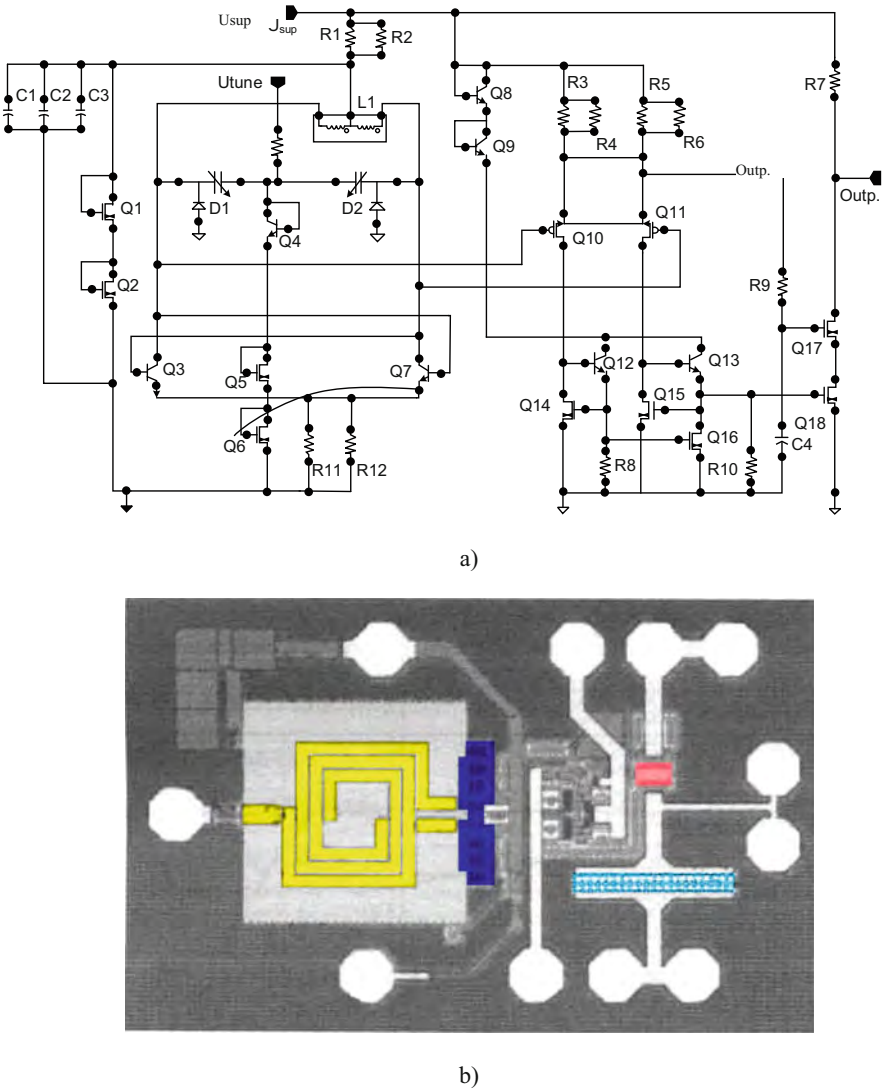

a)

b)

Fig. 13.10 Block diagram (**a**) and topology (**b**) of SiGe IC SHF VCO [1]

As a result of the study of IC VCO characteristics under dose exposure to IR on the modeling unit up to the level of 1.2×10^6 units, the authors of [1] managed to identify the most critical parameters: total consumption current I_C and core consumption current I_{core}. Experimental dependencies of the given parameters on the absorbed dose are shown in Fig. 13.13, according to which both parameter-criteria decrease with an increase in the absorbed dose. At maximum radiation level, their relative change does not exceed 1%. Degradation of other measured parameters

Table 13.3 Basic parameters of IC SHF VCO [1]

Parameter	Value
Retuning frequency range, GHz	3,4...4,6
Output power, dBm	−11...−10
Level of harmonic 2, dBn	−44 max.
Level of harmonic 3, dBn	−46 max
Phase noise during tuning of 100 kHz, dBn/Hz	−100 max.
Control voltage range, V	0...3
Core consumed current, mA	6
Total consumed current, mA	46
Supply voltage, V	5

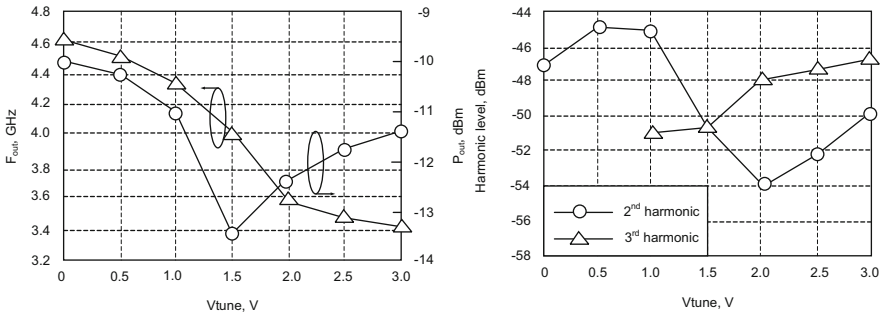

Fig. 13.11 Results of studies of characteristics of IC SHF VCO [1]

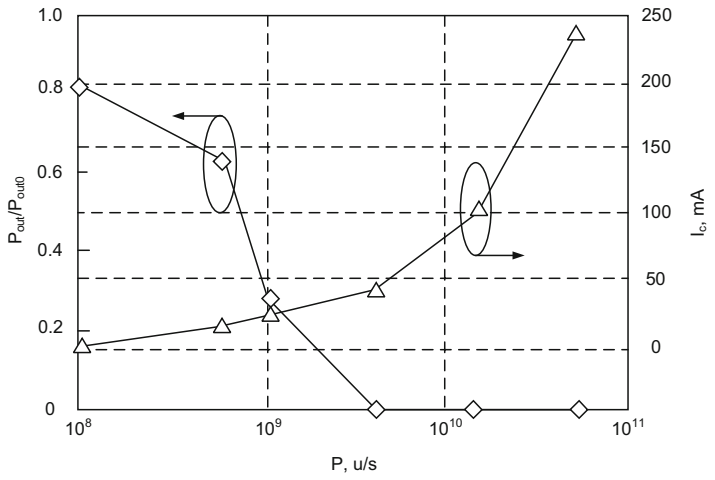

Fig. 13.12 Experimental dependencies of the amplitude value of pulse reaction $P_{out}$and I_C of IC CHF VCO on the equivalent dose power

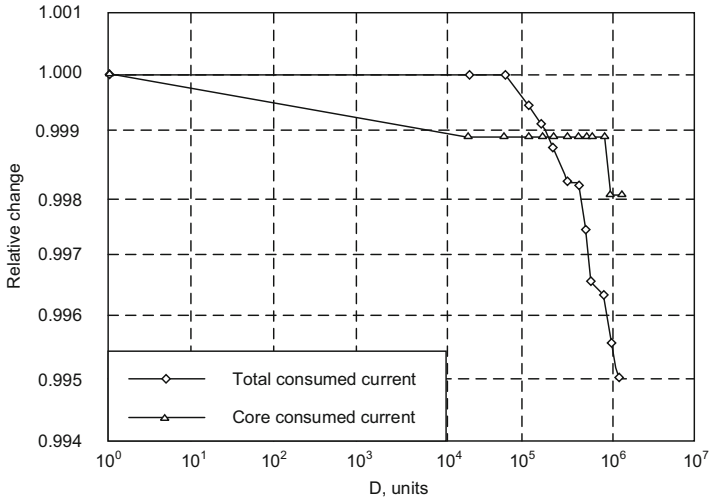

Fig. 13.13 Experimental dependencies of parameter-criteria of IC SHF VCO resistance on the value of the absorbed dose

(output signal frequency P_{out}, level of harmonics, phase noise) was not identified – their measurement is within the measurement error limits.

The results presented in Fig. 13.13 made it possible to obtain preliminary forecast of the threshold dose effect for IC VCO. Based on the linear extrapolation results, 20% reduction of the identified parameter-criteria (I_C and I_{core}) occurs when the values of the absorbed dose are within the range of values from $1.6 \times 10^7 \ldots 4 \times 10^7$ units.

Thus, we have examined only the results of experimental studies of radiation resistance of silicon-germanium heterostructural bipolar transistors and monolithic SHF ICs based on them and designed by national design centers that were published in national "open" information sources.

As a result of these studies, parameter-criteria of SiGe CHF ICs were determined. For example, for ICs of SHF amplifiers, the crucial parameters are: low-signal amplification coefficient *C*a at frequencies below 0.4 GHz, output power at 1 dB compression P_{1dB} at a frequency of 1 GHs and consumption current I_C. For ICs of SHF VCOs, the crucial parameters are: output power level P_{out} total consumption current $I_П$ and core consumption current I_{core}.

Absolute and relative resistance levels of SiGe bipolar SHF ICs to dose and pulse effects of ionizing radiation have been determined. According to the comparative diagram show in Fig. 13.14 a, the level of resistance of SiGe bi-polar SHF ICs to the dose effect of IR exceeds 2×10^6 units and is only inferior to GaAs ICs. Based on the comparative diagram presented in Fig. 13.14 b, the estimated level of resistance of SiGe SHF ICs to pulse effect of IR is 2×10^8 u/s, which corresponds to the resistance level of Si bi-polar and SOS ICs. No thyristor effect or catastrophic failures have been detected.

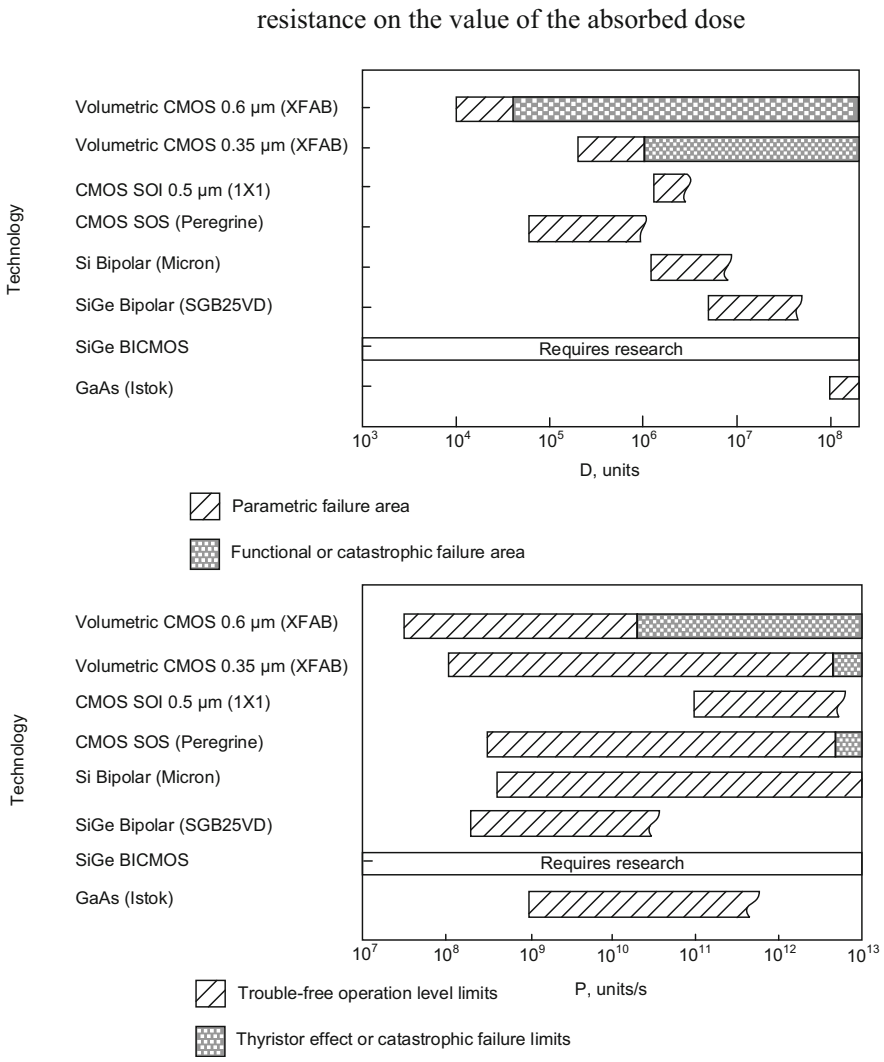

Fig. 13.14 Relative resistance of SiGe SHF ICs to dose (**a**) and pulse (**b**) effect of IR [1]

It has been discovered that under dose exposure, 20% degradation of static parameters (I_B and β/β_0) SiGe of heterostructural bipolar transistors occurs when the level of the absorbed dose reaches $3 \times 10^5 \ldots 5 \times 10^5$ units, which is by order of magnitude lower than the identified threshold values for SHF ICs.

Adequacy of tests of SiGE ICs for resistance to the pulse effect of ICs by means of laser simulation has been experimentally confirmed, which proves the identity of processes of photo and gamma ionization in semiconductor structure of SiGe ICs.

13.2 Design Features of the Radiation-Resistant Library for Designing SHF Functional Units Based on CMOS SOI Technology

As demonstrated in [6], the use of SOI (silicon-on-insulator) structures ensures high radiation resistance of LSICs to pulse effect, which is determined by significant reduction of the ionizing currents, prevention of the latching effect and suppression of spurs between neighboring elements [7, 8]. On the other hand, low spurious capacitances typical of SOI transistors as compared to devices designed according to volumetric CMOS technology as well as high insulation between elements makes SOI technology advantageous for development of SHF range LSICs. An important possible area of application of SHF CMOC SOI LSICs is the satellite navigation equipment of GLONASS and GPS standards within the frequency range of 1.20–1.65 GHz [9, 10].

A number of foreign silicon factories used CMOS SOI technological process allowing the development of analog and digital LSICs of the SHF range [11–13]. Until recent time, national CMOS SOI technologies were only used for development of digital or low-frequency analog-digital LSICs [14, 15]. Due to this, the study of SHF characteristics of the national CMOS SOI with design norms of 0,35 μm for development of a radiation-resistant LCIS of a navigation radio receiver is a very relevant objective.

Key stages in solving this task:

- preliminary study of high-frequency and noise properties of SOI MOS transistors from the standard digital library;
- development of new library elements, such as integral inductors and varicaps, which are absent in the library but necessary for the construction of functional units of the radio receiving device;
- design and production of test chips of the generating, amplifying and mixing functional units with working frequencies of 1.2–1.65 GHz from the composition of SHF path of the radio receiver;
- performance of the experimental study of the characteristics of these crystals and determination of preliminary levels of resistance to dose and pulse effect of the ionizing radiation.

Basic technological process for this research was provided by the Russian CMOS technology by NIIME JSC and Micron factory based on SOI structures with design norms of 0.35 μm. The technology, which is initially designed for development of digital LCISs with supply voltage of 3.3 V, has two levels of polycrystal silicon and two levels of metallization.

Calculational and experimental modeling of SHF and noise properties of SOI MOS transistors, condensers and resistors was performed using elements from the standard library. At the same time, new library elements missing for creation of SHF functional units, such as integral inductors and varicaps, were designed. Test

Table 13.4 Test structures for the study of SHF characteristics of CMOS SOI technology

No	Test structure	Description
1	n-MOS transistor	$L = 0.35$ μm; $W = 400$ μm; A-type
2	LNA on n-MOS transistor	$L = 0.35$ μm; $W = 1000$ μm; A –type; mode: $U_{GS} = 2.5$ V; $U_{GD} = 1.0$ V
3	Varicap on r-MOS transistor in the depletion region	$L = 1.0$ μm; $W = 500$ μm; H-type; mode: $U_C = U_S = 0$ V; $U_{SC} = 3$ V; $U = 0$–3 V
4	Varicap on r-MOS transistor in the saturation region	$L = 0.35$ μm; $W = 500$ μm; H-type; mode: $U_C = U_S = U_{SC} = 1{,}5$ V; $U = 0$–3 V
5	Diffusion resistor	$R = 100$ ohm; $L = 60$ μm; $W = 45$ μm
6	MIM-condenser	$C = 1{,}2$ pF; $L = 140$ μm; $W = 65$ μm
7–11	Set of integral coils of spiral inductances	$L = 1$–14 nH

structures created specifically for the study of standard and new elements are listed in the Table 13.4.

Experimental studies of the tested structures were performed within the frequency range of 0.1–20 GHz by means of SHF probe station Summit 12000B, vector network analyzer E8361A and analyzer of semiconductor device parameters 4156C. Mathematical exclusion of contact areas from the measurement results of test structures was performed by means of de-embedding, using "open" and "short" structures [16].

13.2.1 High-frequency and Noise Properties of Domestic SOI MOS Transistors

Basic element of the first actual Russian CMOS SOI library is the n-channel MOS (n-MOS) transistor. Indicators of high-frequency properties of the transistor are the single amplification frequency (F_t) and maximum generation frequency (F_{max}), of noise properties – noise coefficient (K_{nmin}). For preliminary estimation of F_t and F_{max}, probe measurement was performed to determine L-parameters of vehicle No.1 – SOI n-MOS transistor, the appearance of which is shown in Fig. 13.15a; structural diagram of the stand for probe tests is shown in Fig. 13.15b. Results of calculation and experimental modeling of the frequency dependencies of S-parameters of n-MOS transistor are shown in Fig. 13.5c,d. According to the preliminary estimation, at voltages of $U_{GS} = 1.0$ V and $U_{GD} = 2.5$ V, the values of F_t and F_{max} are at least 15 GHz and 90 GHz respectively, which proves the possibility of realization of amplifier and generator LSICs of the navigation frequency range. The detected significant difference in measured and calculated S-parameters of the tested structures of n-MOS-transistor indicates the necessity to specify parameters of the SPICE model.

One of the shortest way of studying noise properties of a transistor is the determination of the matrix of noise parameters, which is a complex technical task

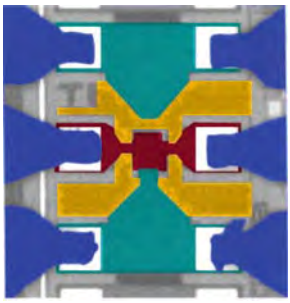

a)

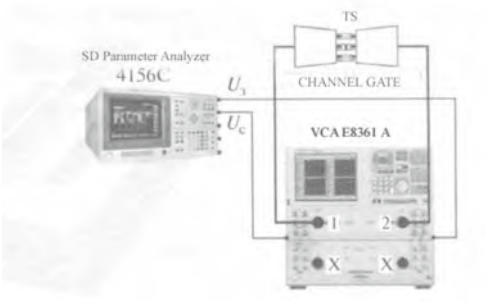

b)

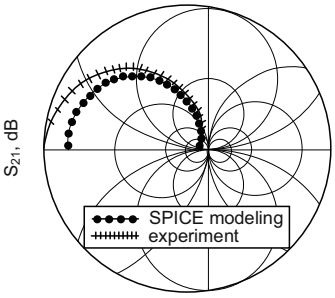

c)

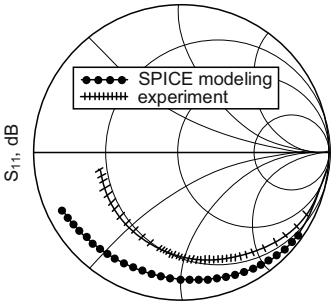

d)

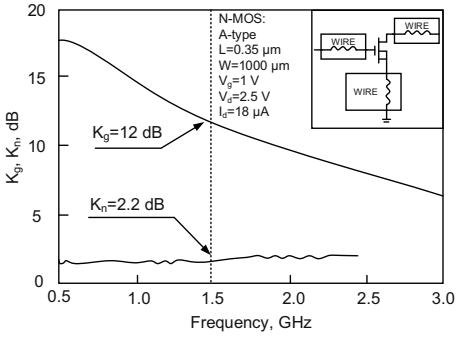

e)

Fig. 13.15 Photograph of the test chip of the test structure No.1 of SOI n-MOS transistor with connected probes (**a**), diagram of the stand for probe tests (**b**); results of the calculation and experimental modeling of S-parameters of the transistor after the procedure of mathematical exclusion of contact areas: S_{21} (**c**), S_{11} (**d**); results of experimental studies of SHF parameters of the test structure of LNA on SOI transistor (**e**) [7]

[17]. Preliminary estimation of noise properties is performed on the basis of the noise coefficient (C_n) of the test structures of the low-noise amplifier based on a n-MOS-transistor (test structure No.2, Fig. 13.15).

Test structure of the low-noise amplifier was designed as a SOI n-MOS transistor connected to the measuring equipment with wires of certain lengths performing the function of matched inductances (Fig. 13.15d). Selection of the wire length in circuits of gate, source and drain is performed by means of calculation and experimentation based on the best match (VSWR minimum) by input/output. Transistor mode during the study of C_n corresponded to the values.

$$U_{GS} = 1.0 \text{ V}; U_{GF} = 2.5\text{B and} I_C = 18 \text{ mA}.$$

According to the measurement results presented in Fig. 13.15e [7], at 1.5 kHz frequency the value of C_n is 2.2 dB at amplification coefficient value (*C*a) of 12 dB. This proves the possibility to use this technology for creation of amplifying units with Ca over 20 dB and C_n of not more than 2 dB, but requires experimental determination of the parameters of the noise model and/or subsequent specification of the SPICE model parameters of n-MOP transistor according to the traditional method.

13.2.2 Instrument Modeling of SOI MOS Transistors

Calculated modeling of high-frequency characteristics of n-MOS transistor and estimation of the values F_t and F_{max} in [7] was performed with application of hardware and software modeling by means of TCAD.

Figure 13.16 a shows the appearance of the transistor structure for modeling [18], basic parameters of which are given in Table 13.5.

Figure 13.16b, c show output and pass-through VACs of the transistor obtained by modeling in TCAD and calculation according to SPICE model that are properly matched with each other.

An important element of radio frequency circuits is represented by transistors with a large gate width (up to hundreds μm) that are based on composite transistors with parallel coupling of certain parameterized elementary transistors with small width. Modeling of the transistor structure was performed in two stages. During the first stage, TCAD means were used for calculation of S-parameters of one elementary transistor. During the second stage, Advanced Design System (ADS) was used for modeling of a composite transistor. Figure 13.17 shows frequency dependencies of the S-parameters of a 400 μm wide composite transistor obtained by modeling in TCAD and calculation according to SPICE model.

Insignificant differences within 1–2 dB are explained by the fact that during modeling of parallel coupling of several elementary transistors in ADS the interaction between them is not taken into account.

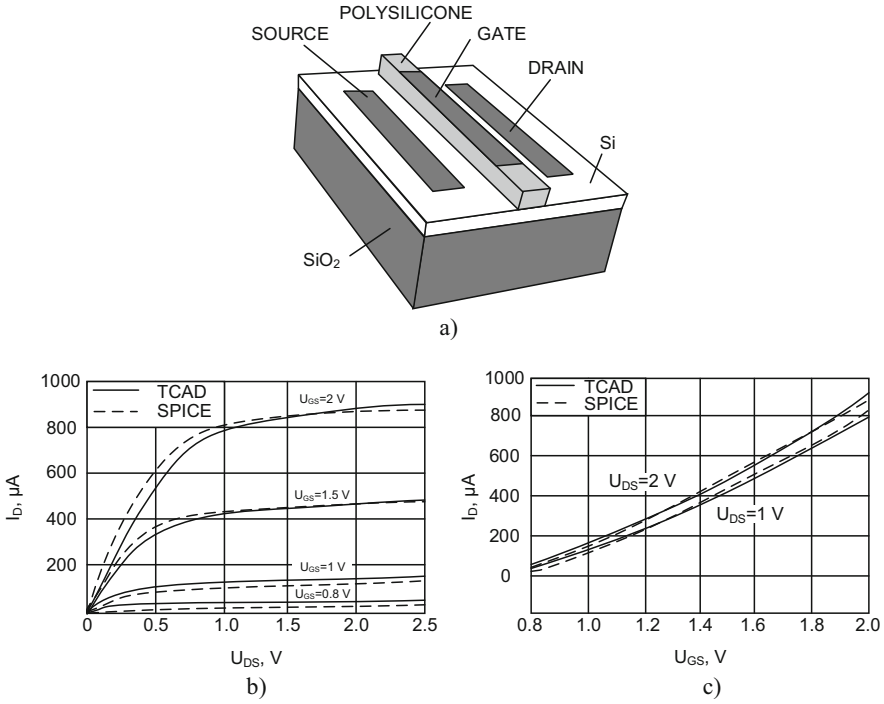

Fig. 13.16 MOS SOI transistor structure (**a**); transistor VAC: (**b**) output, (**c**) pass-through [7]

Table 13.5 Basic parameters of the structure of a SOI MOS transistor

Parameter	Value
Gate oxide thickness, A	70
Source/drain depth, μm	0.25
Impurity concentration in the channel, cm	4.3×10^{17}
Impurity concentration in the source and drain regions, cm	3.5×10^{18}
Impurity concentration in the polycrystal silicon gate, cm^{-3}	3.8×10^{19}
Silicon layer thickness, μm	0.2
Hidden oxide thickness, μm	0.2
Transistor gate length, μm	0.35
Transistor gate width, μm	4.0
Area of transistor source/drain region, μm^2	4.8
Perimeter of the source/drain region, μm	10.4

Estimation of values F_t and F_{max} was performed by two means: Based on S-parameters calculated with the help of TCAD for transistors with varied channel length, and based on analytical ratios [20]:

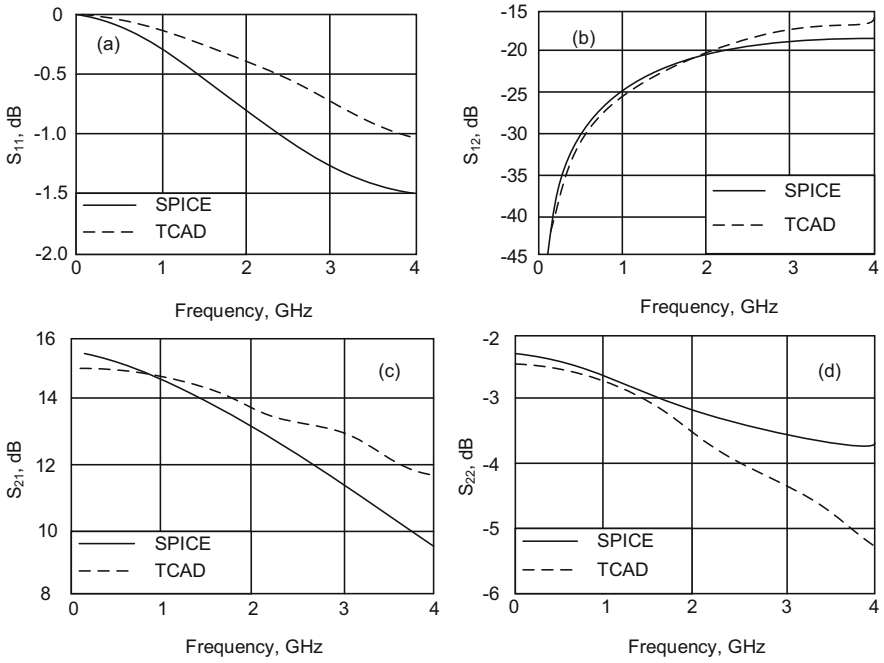

Fig. 13.17 Results of calculation of 5 parameters of the composite l-SOI MOS transistor

$$F_t = \frac{V_S}{2\pi L}, \tag{13.1}$$

$$F_{\text{MAKC}} = \frac{F_t}{2\sqrt{r + F_{t\tau_3}}}, \tag{13.2}$$

where V_s is the saturation speed for electron in the channel (6×10^4 m/s), r is the ratio of input and output resistances (4×10^{-3}), τ_3 is the time constant determined by the gate resistance and the capacitance between drain and gate (1.3 ps), L is the gate length.

Results of calculation of F_t and F_{max} based on S-parameters (Fig. 13.18) properly match analytical dependencies. For a transistor with channel length of 0.35 μm, the value of F_{max}, obtained on the basis of S-parameters is 90 GHz, which is close to the analytical estimation.

The model of 3D structure of a SOI MOS transistor presented in the work [7] allows adequate calculation of VACs and S-parameters at frequencies up to 4 GHz. According to the estimation performed by authors of the model, values of single amplification frequency F_t are ~20 GHz, while the maximum generation frequency F_{max} – 90 GHz. The obtained dependencies properly match the results of calculations based on expressions (13.1) and (13.2), as well as with experimental results.

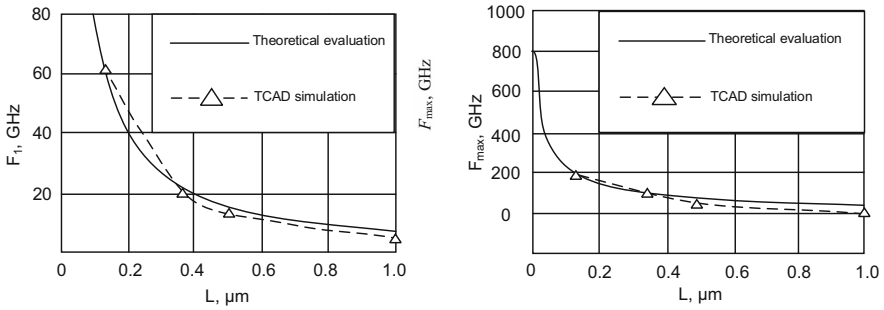

Fig. 13.18 Dependence of the frequency F_t (**a**) and F_{max} (**b**) on the channel length L

13.2.3 MOS VVCs

Frequency retuning in the radio receiver heterodyne unit is ensured by means of an element with smoothly retunable capacitance – varicap, which is absent in a standard SOI library.

The study of plausibility of varicap within CMOS SOI process was performed by local developers in several stages. First, the analysis of various structures was performed [20], after which two versions of varicap test structures were designed on the basis of a standard r-MOS transistor of H-type shown in Fig. 13.19a, b. Geometrical parameters of test varicap structures are given in Table 13.6. In the test structure No.3, MOS transistor is in the depletion mode. Such structure ensures high linearity of re-tuning but has increased sensitivity to substrate noises. In test structure No.4, outputs of source, drain and pocket of the transistor are united, and the capacity retuning can be used both in depletion mode and in saturation mode; at the same time, retuning characteristic of the varicap has strong non-linearity. Control of the capacitance of varicap test structures is performed by changing voltage at the gate within the range of 0. . . + 3 V.

Estimation of values of effective capacitance (C_{eff}) and Q-factor Q retuning range is performed on the basis of the results of probe measurements of S-parameters of varicaps test structures. Values of the main parameters of test structures are given in Table 13.6; Fig. 13.19c, d show dependencies of C_{eff} and ΔC_{eff} on the control voltage at frequency of 1.3 GHz, according to which the capacitance retuning coefficient ΔC_{eff} of the test structure of r-MOS varicaps is not less than 40% at Q of at least 7 units, which is sufficient fro creation of the voltage-controlled generator for the radio receiver heterodyne unit.

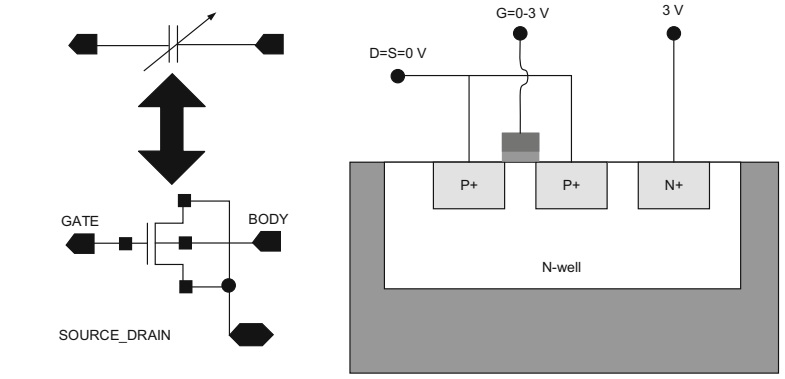

a)

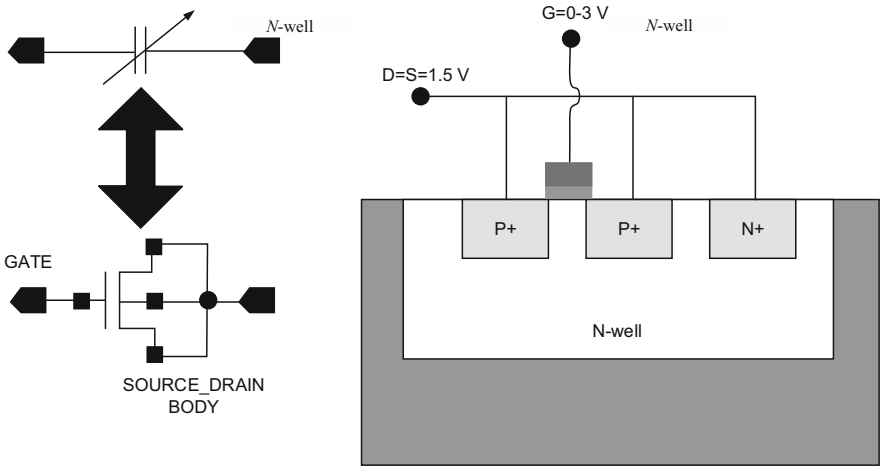

b)

Fig. 13.19 Structures of r-SOI MOS varicaps of test structures Nos. 3 (**a**), 4 (**b**) and results of their experimental studies (**c**), (**d**)

Table 13.6 Comparison of basic parameters of the test structure of r-MOS varicaps

Test structure No.	C_{min}, pF	C_{max}, pF	ΔC_{eff}, pF	R_{eff}, Ohm	Q, u	F_b, GHz*
3	0.73	1.17	0.44	21	7	6
4	0.81	1.22	0.41	14	10	15

Note: * frequency at which ΔC_{eff} is reduced by 20%

13.2.4 R, C, L *Elements*

Integral passive elements, such as resistors with low specific resistance, MIM condensers and spiral inductances with high Q-factor and linearity in the wide range of frequencies are widely used for creation of matching, selective and resonance circuits in amplifying, generating and mixing units of SHF LSICs [21, 22]. High-frequency parameters of the test structures of resistors, condensers and inductance coils (Table 13.4) designed according to the SOI technology were experimentally examined.

Condensers. MIM condenser (test structure No.6) with calculated rating of 1.2 pG is installed in three lower layers of metal and one layer of polycrystal silicon. Comparison of the frequency dependencies of C_{eff} and resistance R_{eff} obtained on the basis of measured S-parameters for three samples of test structures No.6 with the calculation results are shown in Fig. 13.20a, b. According to the presented results, effective measured value of the condenser capacitance is 1.30–1.35 pF, which corresponds to the value of specific capacitance of MIM condensers 0.14–0.15

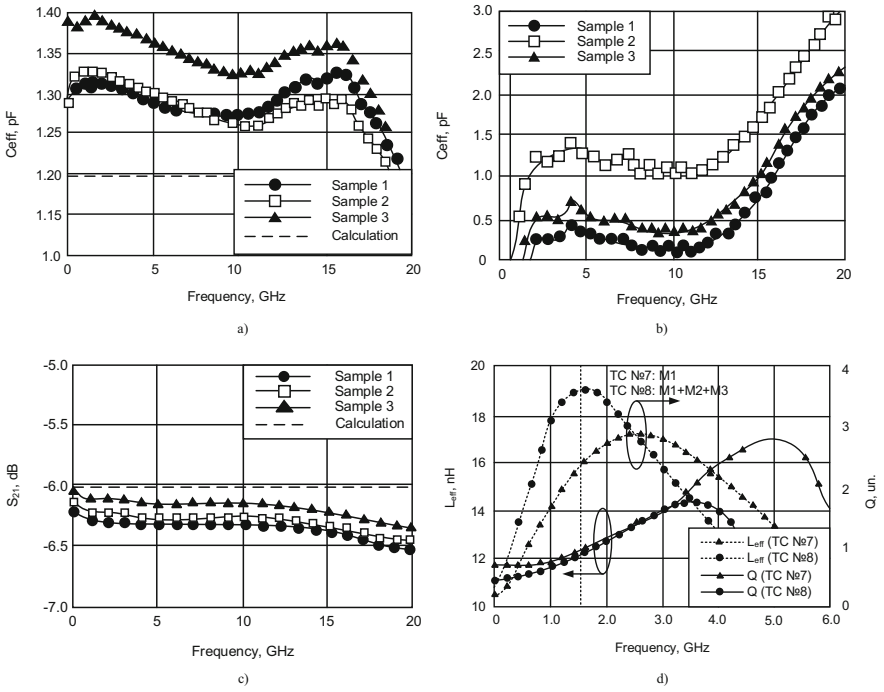

Fig. 13.20 Comparative results of the calculated and experimental modeling of the dependencies C_{eff} (**a**), K_{eff} (**b**) of three sample test structures of the MIM condenser and S_{21} three sample test structures of the resistor (**c**). Results of experimental studies of SHF parameters of test structures of single-layer and multi-layer integral inductances (**d**) [7]

fF/μm^2. In comparison, standard value of the specific capacitance of MIM condensers in foreign radio frequency technologies is not less than 1 fF/μm^2.

Since the difference between calculation based on the ideal condenser model and the results of measurement of C_{eff} does not exceed 10%, it is allowed to use the ideal condenser moder in designing SHF LSICs. Working frequency range of MIM condenser is limited at the top by the value of 12 GHz due to rapid growth of resistance R_{eff}.

Authors of [7] have discovered an unexpectedly wide spread (0.2–1.5 Ohm) in the values of the condenser series resistance within the frequency range up to 12 GHz, which causes uncertainty with the value of Q-factor Q. It is possible that this effect is determined by the spread of effective resistance of the contact between the measuring probe and the contact area of the test structure and thus requires additional study.

Resistors. Test structure No.5 of the resistor with resistance of about 100 Ohm is designed for working currents of units and dozens of mA.

Comparative analysis of the results of measurements and calculations of S-parameters for three samples of the test structure No.5 of the resistor shown in Fig. 13.20c demonstrates satisfactory matching of the calculated (100 Ohm) and experimental (10^3–10^7 Ohm) resistance values. Regardless of the large area of the resistor (60 μm x 45 μm), phase progression does not exceed 3 degrees at 20 GHz, which allows application of the ideal resistor model without taking into account such spurious elements as the substrate capacitance.

Inductance coils

Q. Integral coils missing in the standard library with effective inductance L_{eff} of 1–15 nH and quality factor Q of 3–20 units are necessary for construction of the radio receiver units of the range 1.2–1.6 GHz.

Preliminary estimation of the realized values of L_{eff} and Q was performed by means of probe studies of S-parameters by the designed test structure containing two spiral coils with inductance value of about 12 nH with equivalent topology.

Appearance of the coils is shown in Fig. 13.20d. The first coil with test structure No.7 is installed in one layer of top metal, the second one (test structure No.8) – in three layers of metal connected by means of jumpers.

Frequency dependencies of the inductance L_{eff} and Q-factor Q obtained by calculation based on S-parameters after mathematical exclusion of contact areas are shown in Fig. 13.20 d. Maximum value Q of the coil with test structure is 3 units, while the value Q of the multi-layer coil does not exceed 4 units, which is due to high losses in low-Ohm silicon substrate [21]. Effective resistance of the multi-layer coil of the test structure No.8 is two times less than the resistance of the single-layer coil. Intrinsic resonance frequency is reduced by 1.5 GHz for multi-layer coil due to additional spurious capacitances. According to the preliminary estimation, realization of integral coils with L_{eff} higher than 3 nH and Q higher than 10 units will require the application of the substrate shielding technique [22].

Additionally, [7] included the study of the set of test structures of inductances of various ratings (Table 13.4) installed in three top layers of metal connected by means of jumpers. 3D electromagnetic model of the inductance of test structure No.10 and

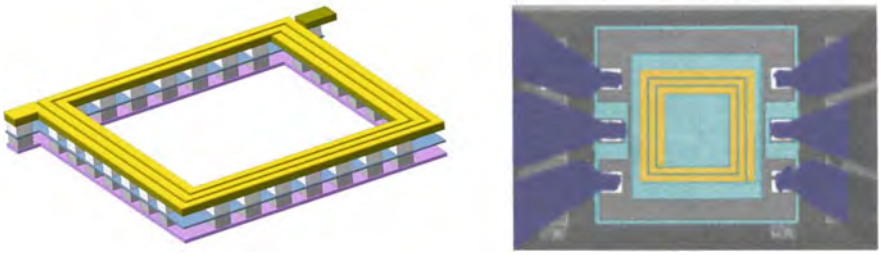

a) (b)

Fig. 13.21 Electromagnetic model of the inductance coil (**a**) and appearance of the chip with installed probes (test structure No.10) (**b**)

Table 13.7 Comparison of parameters of the test structure of spiral inductances [7]

Test structure No.	L_{eff}(1–5 GHz), nH	R_{eff}, Ohm	Q_{max}, u	F_{res}, GHz
9	1.07	1.2	6.8	15.5
10	2.96	2.3	5.7	9.7
11	13.9	13.2	3.8	4.0

appearance of the chip with installed measuring probes are shown in Fig. 13.21. Measured S-parameters were calculated on the basis of the measured S-parameters of test structures of inductances listed in Table 13.7.

13.2.5 Design of Functional Elements of SHF Path

The developed library of SHF elements has undergone practical approbation as part of the test structures of generating, amplifying and mixing functional units of the SHF path of a standard navigation radio receiver designed in the course of work.

Test structure of the voltage-controlled oscillator consists of the core and the buffer amplifier. Core of the voltage-controlled oscillator is based on a classic differential circuit with negative resistance based on *LC*-resonator determining the generation frequency and the differential amplifier [23]. The role of inductive element of the resonator is performed by spiral coils installed in the chip metallization layers; retuning of the generation frequency is performed by means of the control voltage supplied to the varicaps designed in course of this work. Differential amplifier with cross feedback based on SOI MOS transistors compensating losses in the *LC*resonator ensures low level of even harmonics. Buffer amplifier, which is a voltage repeater, reduces the effect of the load on oscillator characteristics and increases the output power level. Experimental values of parameters of the voltage-controlled oscillator at supply voltage of 3.3 V and variation of the control voltage within 0.3–3 V are given in Table 13.8.

Table 13.8 Experimental values of the voltage-controlled oscillator and mixer parameters [7]

Voltage-controlled oscillator		Mixer	
Parameter	Measured value	Parameter	Measured value
Output signal frequency, MHz	1440... 1570	Conversion coefficient, dB	+0.5
Output power, dBm	+ 1... + 3	Linearity by input, dBm	−13
Level of harmonic 3, dBn	−25...−30	Noise coefficient, dB	9
Phase noise (100 kHz), dBn/Hz	−93	VSWR by heterodyne input	2.5
Consumed current, mA	29...32	Consumed current, mA	27

Test structure of a single-cascade amplifier based on n-MOS-transistors [7] contains input and output matching circuits (integral inductances) and blocking condensers.

Test structure of the mixer [7] is based on a differential circuit and consists of the mixing core on Gilbert core and input amplifier [24] designed according to the differential cascade circuit and used to reduce C_n and transformation of the input single-ended signal into the differential signal. Single-ended SHF input has a resistance of 50 Ohm, heterodyne differential input – 100 Ohm. Experimental values of the mixer parameters at supply voltage of 3.3 V and at frequencies $F_{RF} = 1250$ MHz; $F_{HET} = 1415$ MHz; $P_{HET} = +10$ dBm and $F_{IF} = 165$ MHz are given in the Table 13.8.

The determination of the levels of radiation resistance of the functional units of the SHF path of the radio receiver in [7] was carried out on the basis of the test center of ENPO SPELS JSC using the modeling unit ARSA, the laser simulator RADON-5 (pulse effect of IR), electron accelerator ʏ-31/33 in the mode of bremsstrahlung gamma radiation and X-ray simulator REIM-M (dose effect of IR) [20]. Limit level of the pulse effect amounted to 5×10^{12} u/s, dose effect – 1.2×10^{6}. Rated deviation of the parameter-criteria from the initial value during tests was accepted as 20%.

In course of the study of resistance of SOI functional units to pulse effect, control of the following parameters was performed: thyristor effect and catastrophic failures, pulse reaction of the consumption current I_C, output power level P_{out} (VCO), amplification coefficient Ca (amplifier) and conversion coefficient C_C (mixer).

Thyristor effect and catastrophic failures were not found under pulse effect of IR up to the level of 5×10^{12} u/s in any of the examined functional units. Figure 13.22 [7] shows the diagram that helps estimate levels of trouble-free operation of the VCO, amplifier and mixer located in the range of 1×10^{8}–1×10^{9} u/s and determine the resistance parameter-criteria: K_C for the mixer, P_{out} for the VCO and Ka for the amplifier. It has been determined that the time of workability loss for functional units does not exceed 140 μs.

The list of parameter-criteria controlled in [7] during the study of resistance of SHF test functional units to the dose effect of IR are given in Table 13.9 together with resistance levels. The most critical parameter P_{out} was identified for three sample voltage-controlled oscillators. Degradation of other controlled parameters

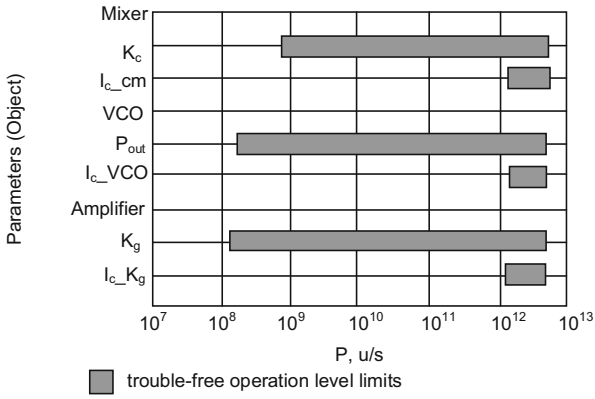

Fig. 13.22 Levels of resistance of SHF units to IR pulse effect

has not been identified; their variation is within the limits of the measurement level. As a preliminary, the level of resistance of the VCO is not less than 10^6 units. The study of the dose degradation of characteristics of five sample amplifiers and three sample mixers identified significant spread of resistance levels among the examined samples, which allows us to conventionally divide them into two groups: "unstable" and "stable". Parameter-criterion determining the resistance of sample amplifier and mixer of the unstable group is the top limit of linearity of the amplitude characteristic (P_{1dBout}). According to the diagram shown in Fig. 13.23a, the level of parametric fault of sample amplifiers from the unstable group is 240×10^3 units, while the relevant dependencies of P_{1dBout} of the amplifier on the absorbed dose are shown in Fig. 13.23b. According to the Table 13.9, resistance level of sample SHF units of stable amplifiers and mixers is not less than 10^6 units.

Thus, studies of high-frequency and noise properties of SOI n-MOS transistors from the library of SOI CMOS technology with design norms of 0.35 μm revealed that the values of frequency of single-time amplification and maximum generation frequency are 15–20 and 90 GHz respectively, which proves the possibility of implementation of amplifying, mixing and generating ICs with working frequency ranges of 1.2–1.65 GHz. Still open are the issues of calculation and experimental determination of noise model parameters for specification of the parameters of SPICE model of n-MOS transistor, as well as the research of feasibility of development of SHF ICs for the frequency range of 2–5 GHz.

In course of the work [7], a set of new library elements was designed: integral inductors and varicaps necessary for creation of SHF functional units of the radio receiver. For integral spiral inductances with ratings of 12 nHn, Q factor does not exceed 3.6. It has been established that implementation of coils with $Q > 5$ can require substrate shielding. A varicap design with capacitance retuning range of at least 40% with Q of 7 was suggested, which is sufficient for creation of functional units of the voltage-controlled oscillator with the required characteristics.

Values of SHF parameters of the national CMOS SOI technology with design norms of 0.35 μm obtained as a result of calculation and experimental studies are shown in Table 13.10 [7].

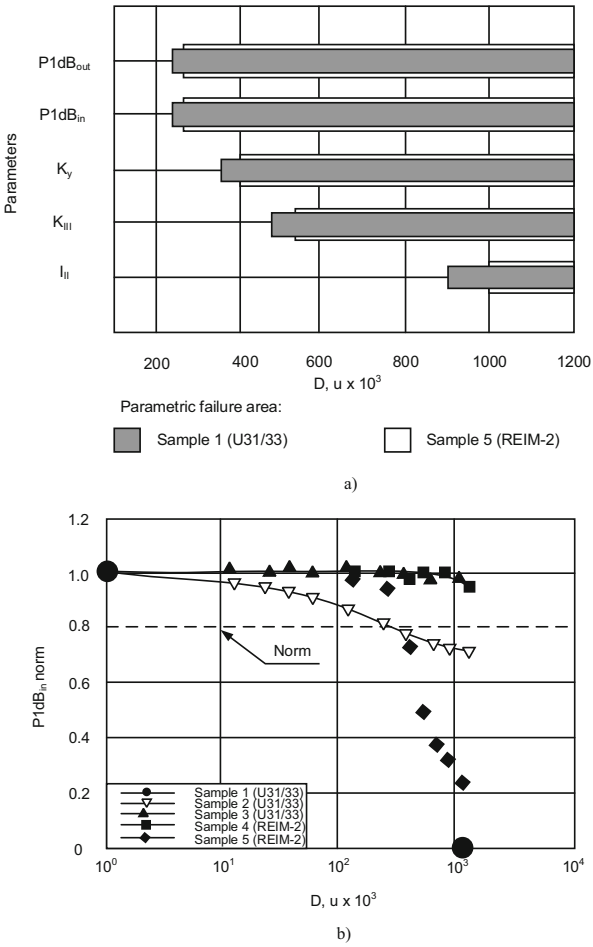

Fig. 13.23 Resistance levels of sample SHF amplifiers from the unstable group (**a**) and experimental dependencies of the top limit of linearity of the output amplitude characteristic P $1dB_{out}$ on the absorbed dose (**b**) [7]

Test chips of the generating, amplifying and mixing units included in the SHF path of the navigation radio receiver have been designed and manufactured. It has been experimentally determined that the test chips of the voltage-controlled oscillator and the mixer are functionally capable of working within the range of 1.2–1.65 GHz, while parameter values are closed to the calculated ones.

Experimental estimation of the resistance levels of the designed functional units to dose and pulse effect of IR has been performed. Thyristor effect and catastrophic failures were not found until the level of 5×10^{12} u/s. During dose exposure to IR, it was determined that the examined sample amplifiers and mixtures can be divided into two groups: "unstable" and "stable". Preliminary resistance level of sample test chips of the "stable" group is not less than 10^6 units.

Table 13.9 Results of tests of SHF test units for dose effect of IR [7]

Test functional unit	Controlled parameters (radiation up to the level of 1.2×10^6 units, norm – 20% deviation of the parameter value)	Parameter-criterion Resistance level	
		"Unstable" group	"Stable" group
VCO	Consumption current I_C, output power P_{out}, output frequency F_{out}, level of the third harmonic P_3, phase noise P_N.	P_{out} 10^6 units min.	Deviation of parameters from the norm over 10^6 units not found
Amplifier	Consumption current /$_c$, linearity by input /FdB_{in} and output P1dB_{out}, amplification coefficient C_a, noise coefficient C_n.	$P1$ dB_{out} 240×10^3units min.	
Mixer	Consumption current /$_c$, top limit of linearity of the amplitude characteristic /fdB conversion coefficient C_c, noise coefficient C_n.	$P1$ dB 360×10^3 units min.	

Table 13.10 SHF parameter values of the elements of SOI CMOS process, 0.35 μm [7]

Active elements	
Transistor	$L = 0.35$ μm; $W = 400$ μm; A-type
Preliminary value of F_t, GHz	15–20
Preliminary value of F_{max}, GHz	90
Noise coefficient C_n, dB	2.2
Varicaps	p-MOS-transistor, N-type
C_{max}/C_{min}	1.5
Q-factor, Q (2 GHz)	10
F_b, GHz	15
Passive elements	
MIM condensers	3 metal layers, 1 polycrystal silicon layer
Specific capacitance, fF/μm^2	0.15
F_b, GHz	12
Resistors	Polycrystal silicon and diffusion
F_b, GHz	15
Inductances	4 metal layers, 0.6–1 μm thick each
Substate conductivity, Ohm cm^2	5–10
Maximum Q-factor Q, units (1 nH)	7
Maximum Q-factor Q, units (10 nH)	4

Thus, the results of the performed studies proved the principal possibility of development of a radiation-resistant monolithic LSIC of radio receiver of satellite navigation onboard equipment based on the national CMOS SOI technology with design norms of 0.35 μm.

13.3 Features of the Mechanisms of Influence of Space Factors on the Formation of Local Radiation Effects

Over the last decade, spacecraft electronic systems have qualitatively changed, being determined by transition to the element-technology basis of microelectronics, which made it possible to drastically increase their functional, technical-economic and operational characteristics. At the same time, it is necessary to prolong the terms of active existence of spacecrafts from 3–5 years (current value) to 10–12 years with installation of radio equipment not in air-sealed containers, but on open spacecraft platforms. This tendency makes the problem of radiation resistance of integral circuits (ICs) come into the forefront, since in many cases radiation-related failures and faults will determine the period of active life of spacecrafts. At the same time, as the integration level increases, local radiation effects that cause failures and faults of ICs due to the effect of separate high-energy nuclear particles come into the forefront [8, 26–28].

Currently, the following basic effects are observed in modern ICs on an experimental basis [8, 16–30]:

- false positives (single faults) of triggers, registers and memory cells;
- multiple faults caused by formation of single faults in several neighboring memory cells;
- short-term pulse signals (needles) at the outputs of analog and digital ICs;
- thyristor effect in four-layer spurious structure, generally in volumetric CMOS ICs;
- secondary trip of p-n transitions, especially for devices working in the pre-trip region;
- long-term conductive channels due to thermal effects in isolating structures (pinholes), in particular – local destruction of the region in the gate dielectric;
- shunting of multi-layer structures (conductive emitter-collector channel in bi-polar structures) and a number of others.

The analysis demonstrates that for modern ICs with high integration level the following local radiation effects are the most critical:

- single faults;
- thyristor effects;
- short-term pulses of ionization reaction (needles).

Calculation and experimental estimation of IC radiation resistance under exposure to the cosmic space factors is divided into a number of stages [26]:

- analysis of the spacecraft functioning conditions;
- estimation of radiation effects directly applied to the IC;
- calculation and experimental estimation of IC parameters of sensitivity to local radiation effects;
- prediction of radiation resistance parameters.

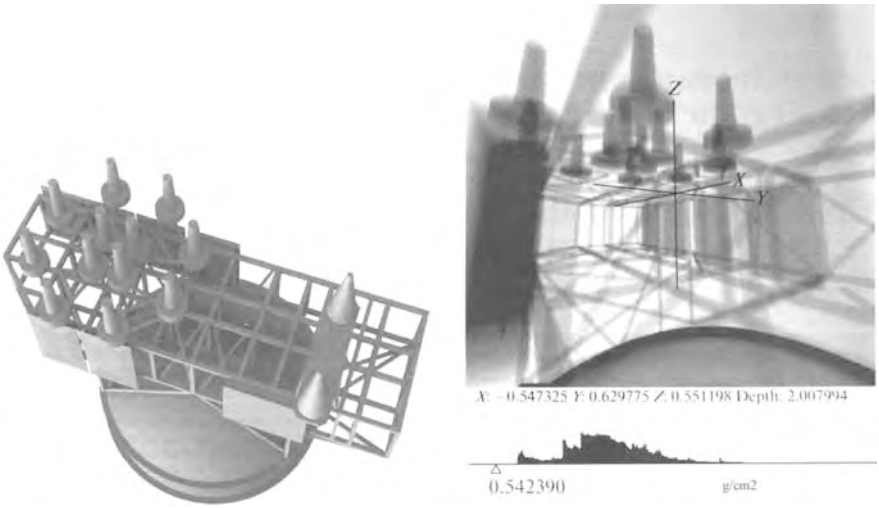

Fig. 13.24 Spacecraft design (**a**) and an example of its optical model (**b**)

Analysis of the spacecraft functioning conditions based on the conditions of its work (orbit parameters and time of functioning) includes the evaluation of external radiation condition. In the analysis of local radiation effects in the IC, it is possible to neglect the effect of electronic radiation, which is incapable of forming large energy releases in the sensitive micro volumes of IC elements. Therefore, within the framework of this task it is necessary to take into account protons of the Earth's radiation belts, as well as protons and ions of solar and galactic cosmic rays. As of now, there is a sufficient number of models and methods that allow performance of such estimations [8, 26–30].

The following stage includes evaluation for the radiation effects acting directly on the sensitive regions of the IC. Calculated estimation of radiation effects shall take into account both real design features of the spacecraft itself and features of the electronic equipment and the IC in the electronic unit. These tasks are performed by the specialized software 3DSPACE [31, 32]. Calculated modeling implemented in the 3DSPACE environment is based on an optical model for the analyzed products obtained by ray method (Fig. 13.24). The degree of shading shows a quantitative picture of radiation protection across the entire solid angle. For the purpose of making correct technical solutions for implementation of possible local protection for the most radiation-sensitive ICs, 3DSPACE environment provides special options showing distribution of thickness of effective protection and the most critical areas. These calculation result in the characteristics of radiation fields acting in the set internal point of the spacecraft directly on the IC chip.

Calculated estimation of IC sensitivity parameters based on local radiation effects even with known technological parameters of IC elements is extremely complicated

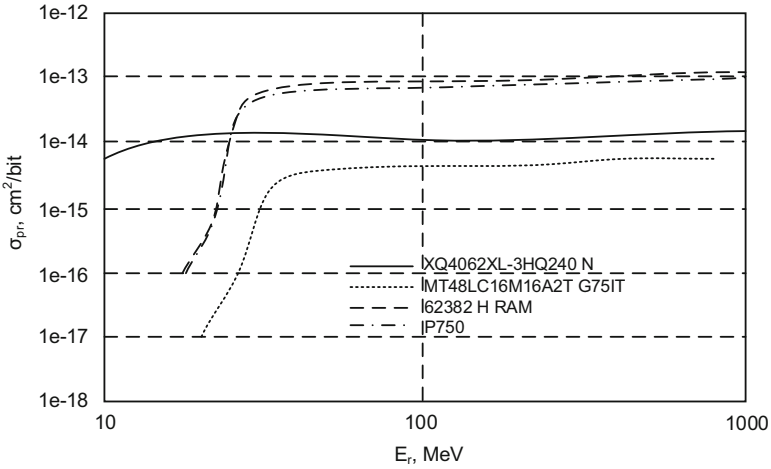

Fig. 13.25 Rated dependencies of cross-sections of single faults on the energy of protons in PLD XQ4062XL-3HQ240N, SDRAM MT48LC16M16A2TG-75IT, RAM 62382H and micro processor P750 [26]

due to the complexity of occurring non-linear and non-stationary processes of formation of ionization reaction from a separate nuclear particle [8]. Therefore, the optimal solution is to determine certain IC sensitivity parameters experimentally and then "recover" their characteristics by calculation methods.

The optimal set of sensitivity parameters to be determined during calculation and experimental studies includes cross-section of saturation of the local radiation effect and threshold value of linear energy losses for ions or energy for protons. When evaluating the sensitivity parameters by the effects like single failures and/or thyristor effects, it is possible to use only two independent parameters: e.g., saturation sections under the effect of ions and protons [33].

The easiest way is to estimate the saturation cross-sections for single IC faults with submicron design norms due to the relatively small energy of the IC appearance (MeV units). Experimental values of saturation cross-sections of single failures can be obtained with proton energy above 200 MeV and linear ion losses over 10 MeV mg/cm^2. In this case, there will be no particular problems during implementation of experimental studies on proton accelerators.

The application of simplified single-parameter model makes it possible to recover dependence of sections of single faults on the proton energy (Fig. 13.25). Based on the result of experimental studies of ICs on proton accelerators, we can make the following conclusions:

– in modern ICs designed according to the volumetric technology wit design norms of 0,5 μm and below, section of single faults is about $10^{-15}...10^{-14}$ cm^2/bit;
– due to the presence of the threshold energy of nuclear reactions in materials from the action of protons, the threshold energy of protons remains almost unchanged

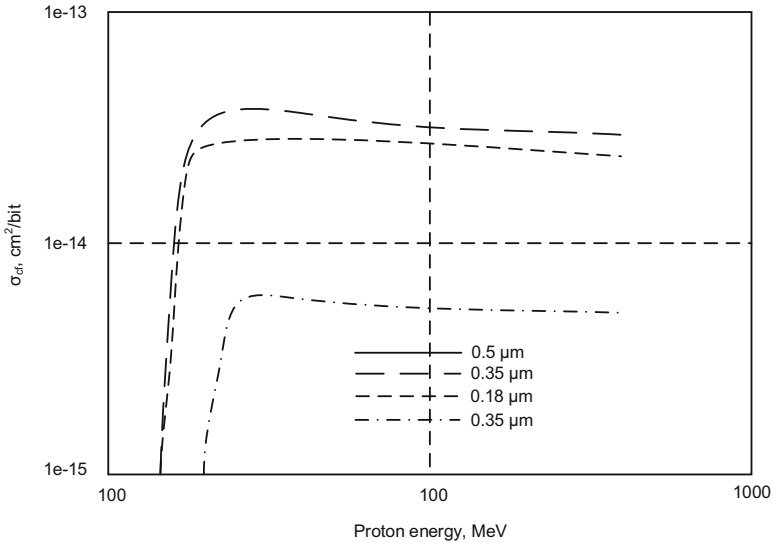

Fig. 13.26 Typical dependencies of cross-sections of single faults from the proton energy for ICs with various design norms [26]

and amounts to about 15 MeV. As the design norms decrease, the dependence of the SF cross-sections on the proton energy approaches a step function;
– with reduced design norms, values of the cross-sections of saturation and threshold energies the switches are reduced insignificantly. For example, in case of twofold reduce of the design norms, the given values will only increase by 30. . .40% (Fig. 13.26).

The situation with estimation of cross-section of saturation of single faults under the effect of ions is a bit more complex. Due to certain difficulties associated with tests on ion accelerators, it is necessary to develop additional methods of evaluation of cross-sections of saturation of single faults. These values can be most adequately determined based on the results of experimental studies in the fields of isotopic sources of spontaneous fission, for example, based on the CF^{252} isotope. However, during this it is necessary to take the following factors into account [26]:

– modern ICs with design norms of 0.5 μm and below have several metallization layers, due to which the thickness of passive near-surface regions can be compared to trips of fission fragments (about 10 μm);
– in modern ICs with design norms of 0.5 μm and below the switch charges become so small that single faults can be caused by alpha particles acting together with fission fragments;
– there is almost complete collection of carriers from a nuclear particle track from an ion, which is a fragment of spontaneous fission.

Another alternative method consists in using focused laser radiation of the picosecond duration during scanning of the entire surface of the IC chip. However, in this case there are also limitations associated with the presence of multi-layer metallization. In principle, this limitation can be removed by using the local laser radiation method, with the help of which it is possible to evaluate the cross-section of saturation of a separate element [34].

Rough estimation of the cross-section of saturation can be based on the analysis of the IC chip surface. Therefore, the analysis of IC solutions in terms of diagrams and topology allows us to conclude that the cross-section of single faults at ICs is about 10% of the area occupied by RAM structures, general purpose registers and other similar structures. In other words, if the RAM IC chip area A_{ic} is known, cross-section of saturation of single faults under the effect of ions σ_{ion} can be estimated as [26]:

$$\sigma_{\text{ИОН}} \approx 0,1 \text{A}_{\text{ИС}} / N_{\text{Оз у}}, \tag{13.3}$$

where N_{ram} is the total informational capacity of the RAM.

More difficult is evaluation of parameters of the IC sensitivity to needle-like effects that determine the faults of analog and combined digital ICs. Unfortunately, it is fairly difficult to predict the possibility of the signal appearance, especially in analog devices. Moreover, signals of various forms and amplitudes can be found at IC outputs (Fig. 13.27). Therefore, the only real way in this case is the experimental determination of IC sensitivity parameters.

Of all the effects, thyristor effect is the most dangerous, as it can cause burning of both IC and secondary power source. Performed calculation and experimental research identified an increase in the CMOS IC sensitivity with reduction of design norms. For example, in CMOS ICs with design norms of 0.5 μm and higher the thyristor effect under exposure to cosmic space protons is very rare, while in ICs with design norms of 0.25 μm and lower it happens nearly always even at normal temperature. Therefore, it is very important to evaluate parameters of CMOS IC sensitivity to this effect.

It should be noted that the presented results for single fault effects do not apply to the estimation of sensitivity parameters based on thyristor effects, as the sensitivity regions are determined by spurious structures. Therefore, even for elements of similar type the values of cross-sections under the effect of ions may vary within 0–10^{-2} cm^2/bit. In this case, effective is the random scanning method for evaluation of dependence of effect sections on energy (equivalent values of linear energy losses) (Fig. 13.28). We should also note that due to relatively long-term development of the thyristor effect (Fig. 13.29) the sensitivity parameters can be estimated with exposure to laser radiation with duration of up to 15 ns. Experimental studies on laser focusing unit with consideration of significant energy losses on optical irregularities make it possible to estimate the threshold energy of the thyristor effect emergence and the area of separate sensitive region (cross-section) (Fig. 13.30).

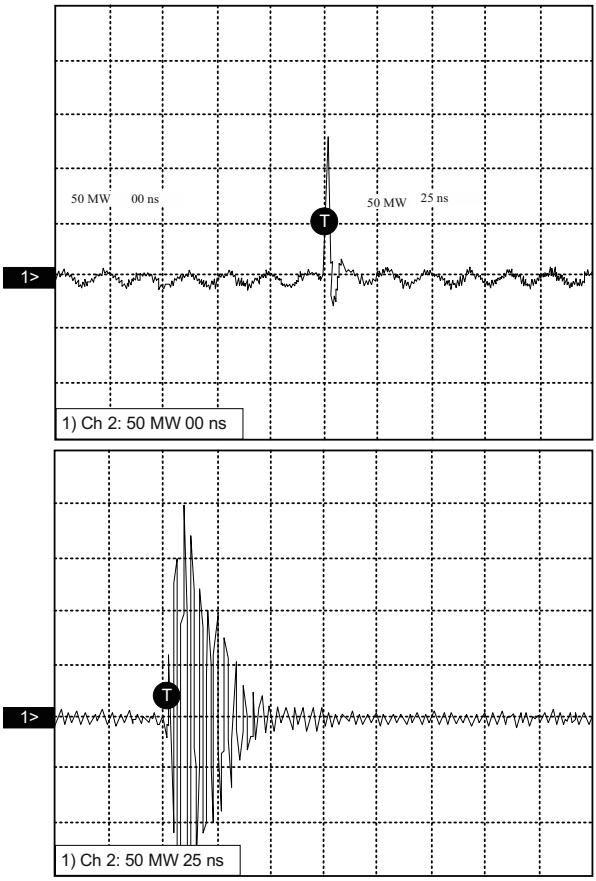

Fig. 13.27 Typical shapes of pulses and needles at the output of the operational amplifier 1484УД1 under radiation with 1 GeV protons [26]

Estimation of the frequency of occurrence of local radiation effects in ICs under the effect of cosmic space factors is usually performed during the last stage with known inner radiation environment and sensitivity parameters. The given analysis shows that the acceptable precision of estimation is ensured by models based on presentation of the sensitive region in the form of a rectangle [30], and, in particular, simplified Peterson model FOM [29]. For example, in geostationary orbit, frequency of single failures in the configuration memory of the PLD XQ4062XL-3HQ240N using RPP and FOM models is estimated as 0.6 events / (IC day) and 0.4 events / (IC day) respectively. Equivalent estimation of thyristor effects leads to the values of 6×10^{-4} events/(IC day) and 3×10^{-3}events/(IC day).

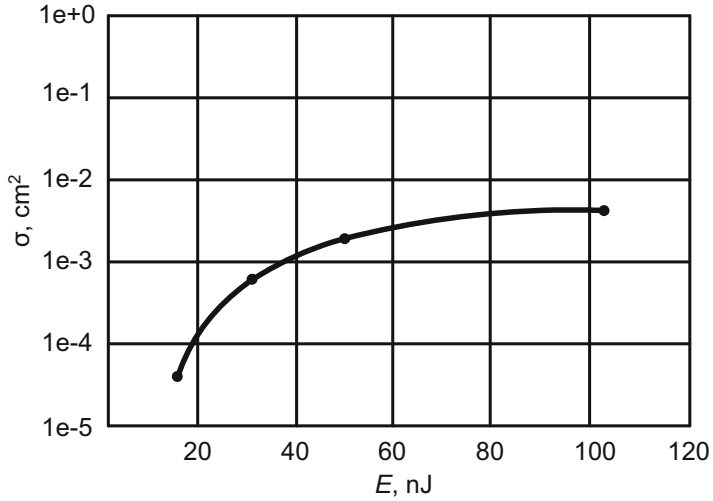

Fig. 13.28 Dependence of the thyristor effect section on LR energy in the chip 98E07A by Fujitsu

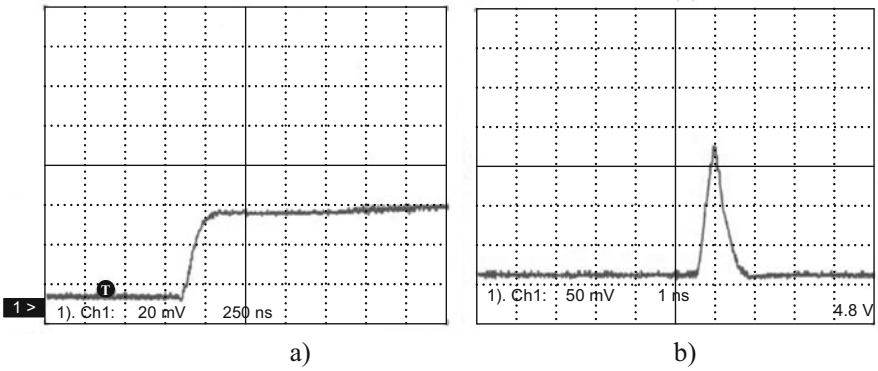

Fig. 13.29 Typical oscillograms of development of thyristor effect in CMOS IC: (**a**) – stationary TE; (**b**) – short-term TE [26]

Thus, the results of the above studies performed by national and foreign authors indicate the possibility of estimation of the frequency of local radiation effects in ICs under the effect of cosmic space factors with the use of the developed modeling means of internal radiation environment and calculation and experimental methods of IC sensitivity parameters based on the results of tests on proton accelerator and laser unit with focused radiation.

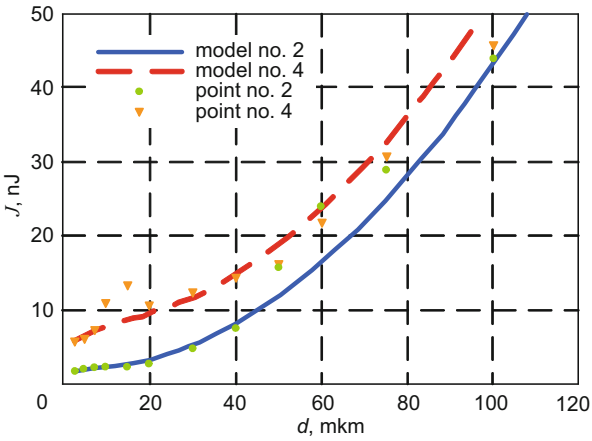

Fig. 13.30 Experimental and calculated dependencies of threshold energy of thyristor effect occurrence in various sensitivity regions from the laser spot diameter in IC A54SX16A-TQ100I [26]

13.4 Features of the Design of Passive Elements for Radiation-Resistant Monolithic Silicon-Germanium SHF ICs

Rapid development of submicron silicon-germanium (SiGe) BiCMOS-technologies with boundary frequencies above 200 GHz and increased resistance to the effect of ionizing radiation opens wide possibilities for their use in communication and radar systems of SHF and millimeter (mm) range [2, 21]. Combination of the full set of functions of a radio frequency (RF) of the transceiver path with processor and memory on single silicon chip is possible on condition of availability of the set of passive SHF elements as part of the process library of BiCMOS process. Passive SHF elements, such as transmission lines, high-Q inductances and transformers are mandatory components for all SHF libraries for mature technologies on semi-isolating substrate (A_3B_5).

Meanwhile, for BiCMOS technologies that are digital and low-frequency in terms of their origin, similar passive elements are new and either presented by a very limited set or overall absent from the library composition [2]. On the other hand, high losses in the conductive silicon substrate can significantly reduce the Q value of passive elements, which in its turn will have an effect on characteristics of the entire SHF LSIC. In this connection, it is plausible to develop design methods for SHF passive elements by means of modern CAD. The methods mentioned in the work [2] were practiced on the example of designing a set of passive elements including a microstrip line, high-Q inductances and balanced transformer and designed for the use as part of monolithic SHF ICs designed according to SiGE BiCOMP technology with topology norms of 0.25 μm and increased resistance to the effect of ionizing radiation.

Requirements for the parameters of passive elements are given in the Table 13.11, where the following designations are adopted: f – frequency, Z_0 – wave resistance;

Table 13.11 Parameters of developed passive elements [21]

Element name	Microstrip transmission line	Inductance	Balance transformer
Requirements for the values of the element parameter	$Z_O = 50$ ohm, $\alpha < 0.5$ dB/mm, $f = 4...6$ GHz	$L = 0.1...0.15$ hH, $Q > 15$, $f = 23...25$ GHz	$N = 2$, $IL < 6$ dB, $RL < 10$ dB, $f = 4...6$ GHz

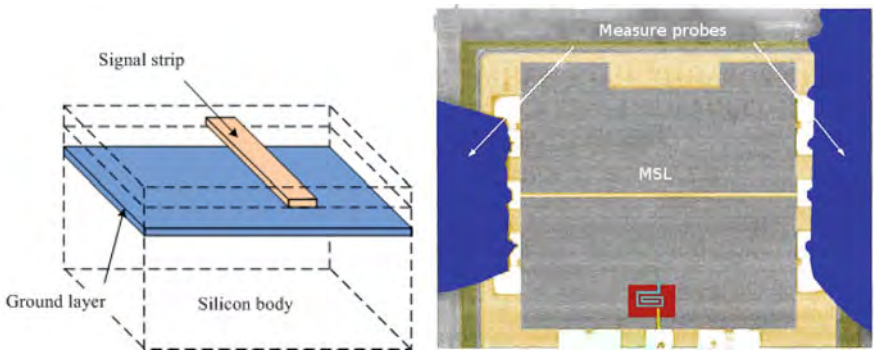

Fig. 13.31 Simplified structure of the microstrip line on silicon substrate (**a**), photo of the test MSL structure with connected SHF probes (**b**) [21]

α – MSL running depletion; L – inductance; Q – Q-factor; N – impedance transformation coefficient, IL – inserted losses, RL – reflection losses.

13.4.1 Microstrip Transmission Line

In monolithic SHF IC, microstrip (MSL) and coplanar lines are used as transmission lines [22]. In the millimeter range, MSLs are used for creation of matching and selective circuits, directional couplers, combiners, etc. The main parameters of the transmission line are wave resistance, effective dielectric penetrability and running depletion. Standard libraries contain scalable models of various transmission lines and their irregularities characterized by low dielectric losses for technologies on semi-isolating substrate. For silicone technologies with multiple metal layers, designing of the transmission line with set wave resistance and low depletion is a separate important task. Simplified MSL structure is shown in Fig. 13.31a [21]. Signal strip is located in the top (as a rule, the thickest) layer of metal, while the ground layer is located in the bottom layer [2]. For such structure, Z_0 of 50 Ohm is obtained at signal strip width (W) of several μm. Initial value of W is calculated based on engineering analytical expressions with the help of the special calculator of the

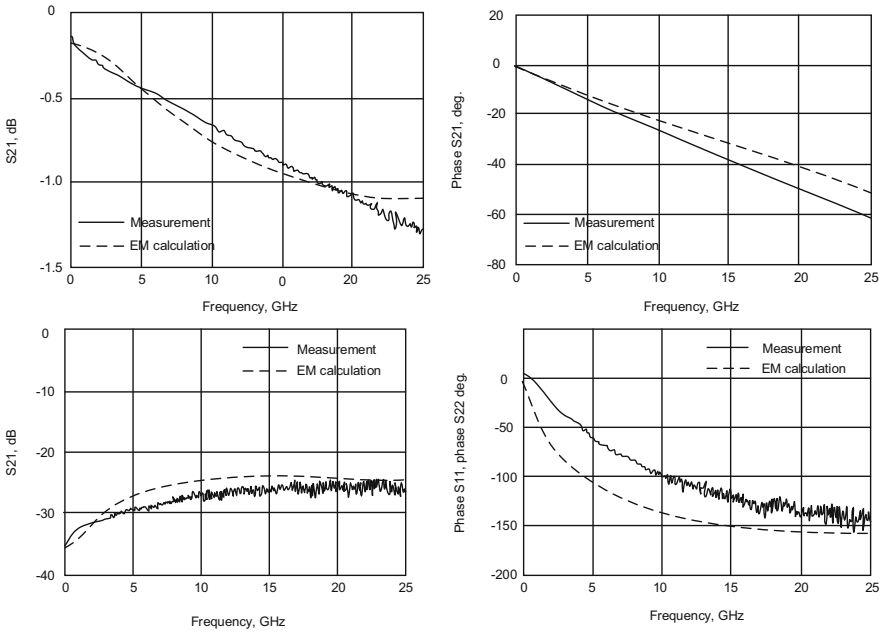

Fig. 13.32 Comparative results of measurements and electromagnetic calculation of the 5 parameters of the MSL test structure [21]

transmission line built into most SHF CADs [22]. Ultimate value of W is determined for a real structure with the help of electromagnetic analysis [2].

According to the given method, test structure shown in Fig. 13.31b [21] including 0.79 mm MSL and contact areas for SHF probes was designed and manufactured for BiCMOS technology with four layers of metal. The thickness of the top metal layer is 2 μm, total dielectric thickness ($Si0_2$) – 4.5 μm, MSL thickness – 8 μm.

Comparative results of measurement of the S-parameters of MSL test structure without exclusion of effect of the contact areas performed by the means of the probe station Summit 12000B and vector analyzer E8361A are shown in Fig. 13.32 together with the electromagnetic calculation results. At frequency of 5 GHz, running value of inserted losses amounts to 0.57 dB/mm. For precise measurements, it is necessary, first of all, to exclude the effect of contact areas, which is ensured by additional calibration structures or the special procedure performed by CAD means (De-embedding).

13.4.2 Integral Inductances

Integral inductances are used in selective, filtering and resonance circuits of SHF systems. Inductances are characterized by effective value of L, Q-factor and intrinsic

resonance frequency [22]. In SHF and millimeter ranges, the required inductance value is from one to deciles of nH, while the resonance frequency is from one to dozens GHz, which is normally ensured by a flat structure with a small (1–3) number of turns.

The technique of inductance synthesis, described in detail in [35], begins with the choice of the structure and the development of its preliminary topology. In this, analytical expressions [22] or inductance models built into most SHF CADs are used. Verification of inductance characteristics and further optimization of parameters is performed with the help of electromagnetic modeling and calculation of S-parameters, on the basis of which the values of L and Q are determined [35]. During the last stage, Spice model of inductance on concentrated elements for CAD is created based on the best matching with the results of the electromagnetic analysis.

According to the given method, three-output inductance of the K-range was designed [21]. In order to increase Q-factor, the inductance is installed in the top metal layer, which has greatest thickness and conductivity. Topology and calculated frequency dependencies L and Q are shown in Fig. 13.33a, b

The designed MSL and inductance were made as test elements and found application in the monolithic voltage-controlled oscillator (VCO) with central frequency of 24 GHz built on heterostructural bipolar transistors (HBT) with the values of maximum generation and single amplification frequency of $F_{max}/F_t = 90/45$ GHz. Simplified block diagram of the OCV shown in Fig. 13.34 [21], a, consists of the core and the buffer amplifier. Core of the voltage-controlled oscillator is based on a classic differential circuit with negative resistance [23] based on LC-resonator determining the generation frequency and the differential amplifier. Retuning of the generation frequency is performed by variation of capacitances of MOS varicaps under the effect of the control voltage. Three-output inductance described above is used as an inductance element of the resonator. Differential amplifier with reverse feedback on HBT compensating losses in the LC-resonator ensures low level of even harmonics [23] and eliminates the effect of spurious inductances in chip packaging [36]. Buffer amplifier, which is a voltage repeater, reduces the effect of the load on oscillator characteristics and increases the output power level. VCO differential outputs are connected to contact areas with the help of MSL described in the first part of the work. Appearance of the topology of VCO test structure is shown in Fig. 13.34 b. According to the results of calculations given in Table 13.12, VOC frequency retuning range exceeds 1.8 GHz, while the output power during operation for differential load of 100 Ohms is not less than +5 dBm.

13.4.3 Balance-to-Unbalance Transformers

Differential circuits improving dynamic characteristics of devices have recently become popular in creation of SHF monolithic amplifiers, mixers, VCOs, modulators, etc. [21]. Meanwhile, most pieces of the existing SHF measuring equipment are fitted with balanced (single-ended) coaxial 50 Ohm inputs and outputs, which

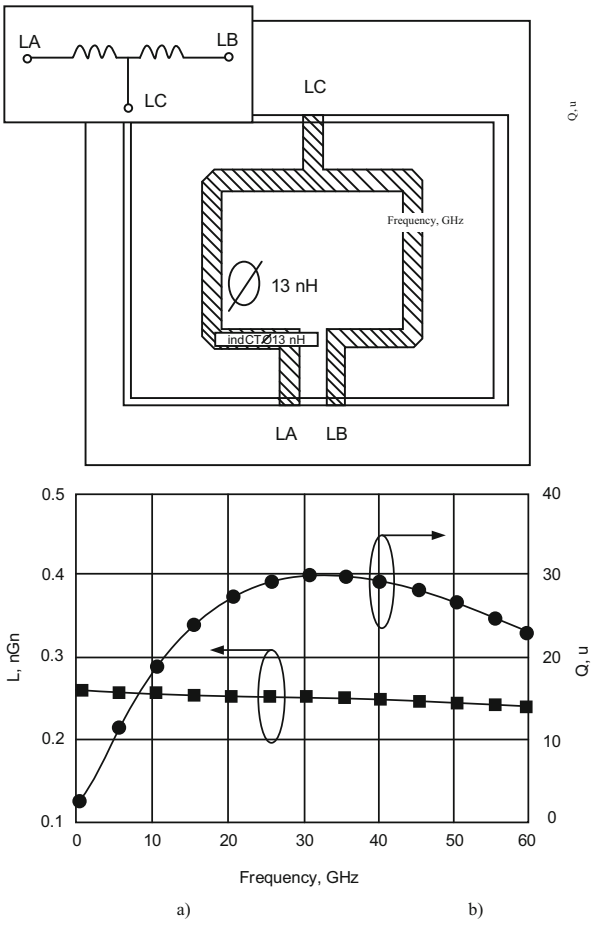

Fig. 13.33 Topology and diagram of three-output inductance (**a**), calculated frequency dependencies L and Q (**b**) [21]

emphasizes the task of conversion of an unbalanced signal into a balanced one by means of special transformers, also known as baluns (balanced → unbalanced).

Currently, a number of SHF transformers and baluns are industrially manufactured in the form of separate elements for surface mounting [37].

These elements, which are designed for drawing of hybrid circuits, have a number of disadvantages: limited frequency range, large dimensions and cost. The solution to this problem lies in application of integrals and baluns.

From the whole variety of baluns for integral installation shown in Fig. 13.35, it is possible to distinguish active and passive baluns on concentrated elements (lattice baluns), as well as baluns on coupled inductances and Marchand baluns on quarter-wave coupled lines [22, 38]. Depending on the relative position of the coils, baluns on coupled inductances can have frontal or lateral electromagnetic coupling. Active baluns have wide frequency ranges, high amplification and small dimensions; however, they also have limited dynamic range and significant level of intrinsic

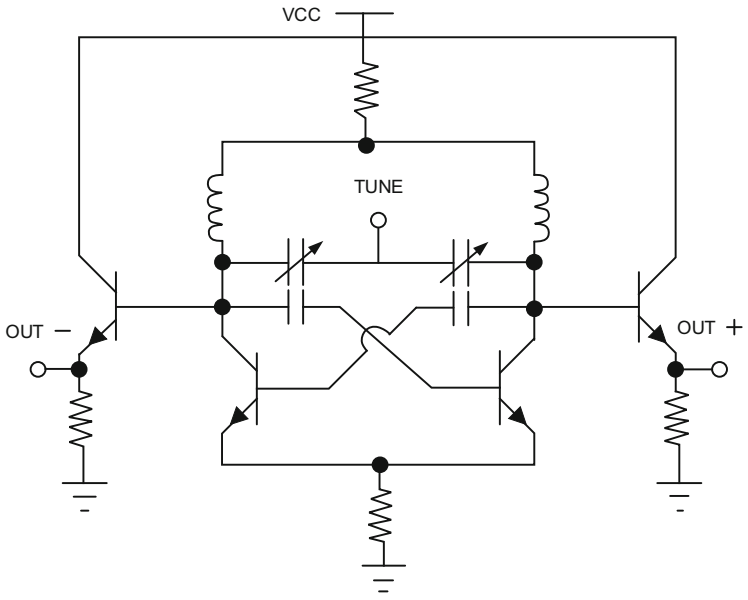

a)

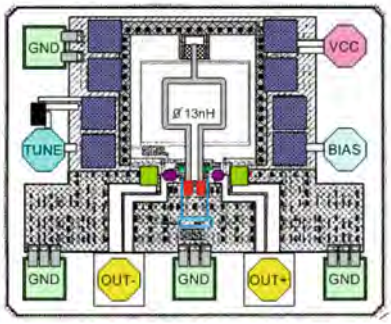

b)

Fig. 13.34 Simplified block diagram (**a**) and test chip topology (**b**) of VCO [21]

Table 13.12 Results of calculation of parameters of SHF VCO

Parameter name	Parameter value
Retuning frequency range, GHz	23,4...25,2
Output power for 100 Ohm load, dBm	+5
Phase noise during tuning of 1 MHz, dBn/Hz	−98
Coefficient of harmonics, dBn	−30
Control voltage retuning range, V	0...3
Consumed current, mA	18
Supply voltage, V	3

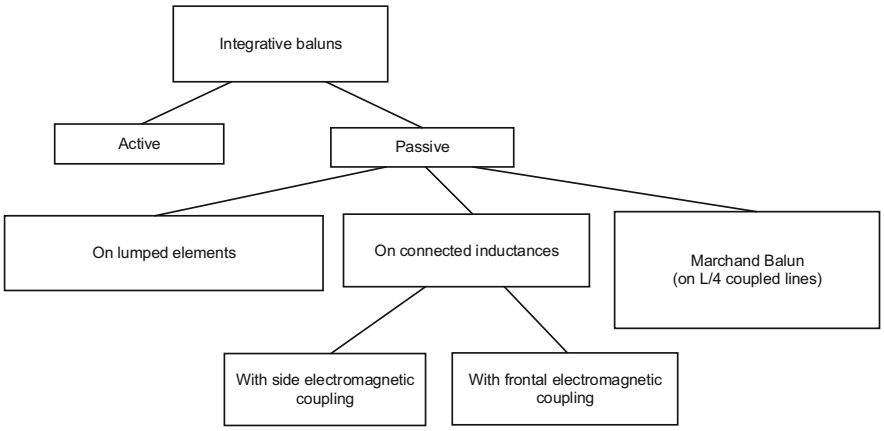

Fig. 13.35 Classification of integral balanced transformers (baluns) [21]

noises and consume additional power. On matched elements, baluns have acceptable dimensions but are narrow-band and only used in the low frequency range. Marchand baluns are wideband and relatively simple for synthesis, but have large dimensions and are used in the millimeter range [38]. Baluns on coupled inductances with frontal coupling characterized by high coefficient of coupling between coils are characterized by small dimensions and low insertion losses. Baluns on coupled inductances are most prospective for the SHF range [39]; their primary and secondary coils are formed by two spiral inductances located in neighboring layers of metallization, one under another. Synthesis of these baluns is performed by iteration optimization of the structure in course of complete electromagnetic modeling. Additional degree of freedom allowing to reduce the time of optimization is achieved thanks to the use of tuned condensers C1, C2 and C3 shown in Fig. 13.36a [40]. This work provides an adjusted method of designing baluns on coupled inductances consisting of four basic operations.

The first stage, based on the required frequency band and impedance transformation coefficient N depending on expressions (13.4) and (13.5), involves evaluation of inductance values of the primary L_P and secondary L_S coils [21]:

$$L_{\Pi} = \frac{Z_{O\Pi}}{2\pi f_o \sqrt{1 - k_{CB}^2}}, \tag{13.4}$$

$$L_B = L_{\Pi} k_{CB}^2 N^2, \tag{13.5}$$

where Z_{PW} is the characteristic impedance of the load connected to the primary coil; f_O is the central part of the working range; k_C is the coefficient of coupling between coils which is equal to 0.7–0.95 for baluns on connected inductances with frontal coupling.

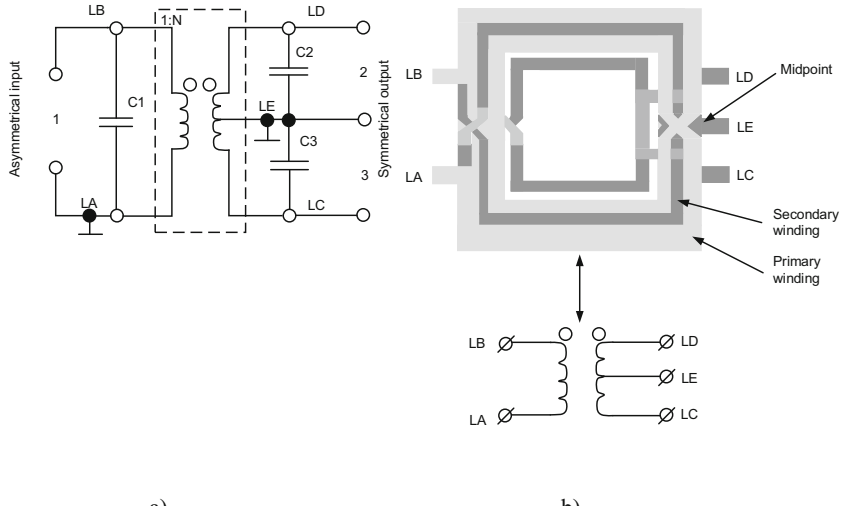

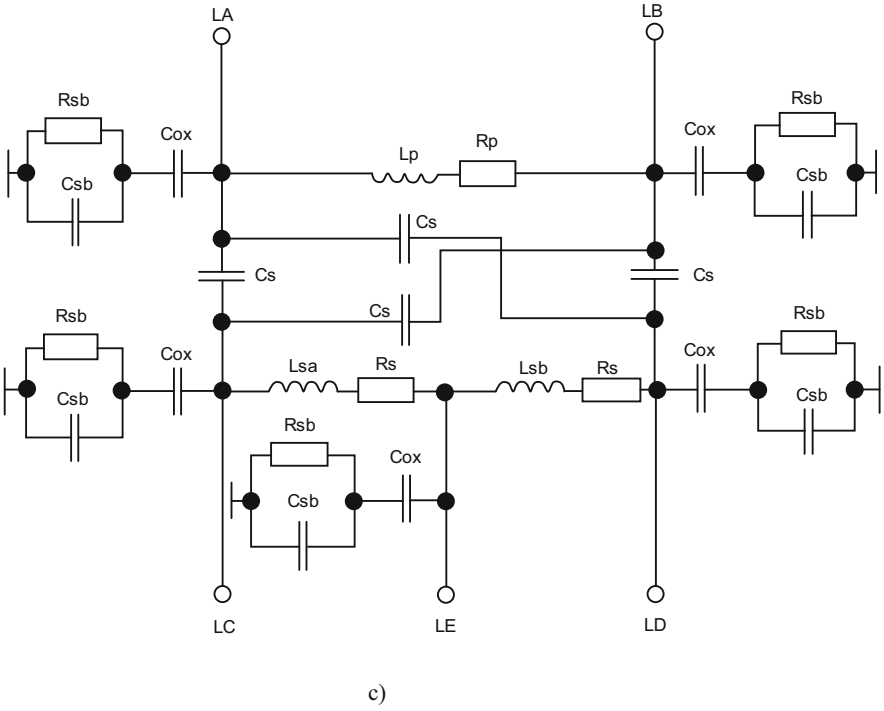

Fig. 13.36 Block diagram (**a**), topology (**b**) and Spice model (**c**) of a balun on coupled inductances [21]

After that, according to the method outlined above in this work [21], inductance topologies are created with ratings of L_P and L_S. High k_C between coils is ensured by balance of inductances, and the evenness of AFCs and FCS – by at least twofold excess of the resonance inductance frequency over the value of f_O [40].

During the third stage, electromagnetic modeling of balun characteristics on connected inductances and minimization of the phase and amplitude imbalance are performed. 180° phase shift at the balun output is ensured by special output (middle point) in the middle of the secondary grounded coil (Fig. 13.36b) [22]. One of the reasons behind unbalance lies in the difference between transformation coefficients $N1$ (coil LB-LA → coil LD-LE) and N2 caused by asymmetry in the structure of baluns on coupled inductances, including due to interlevel connections. Such unbalance is eliminated by equalization of the inductance values of both parts of the secondary coil, which is achieved by the shift of the middle point or variation of topology of the secondary coil [40] at constant coefficients N1 and N2.

Tuning of baluns on coupled inductances to the central frequency f_Q and provision of the required reflection losses is performed during stage four by selection of parallel tuning condensers [39] at the inputs of these baluns (Fig. 13.36a). Condenser value at asymmetric input C1 is evaluated according to the following expression:

$$C1 = \frac{1}{4\pi^2 f_o^2 L_{\Pi}\left(1 - k_{CB}^2\right)}. \tag{13.6}$$

At the final stage, Spice model of connected inductance baluns is created for CAD. Figure 13.36c shows the Spice model taking into account interturn capacities and the effect of the substrate [40].

A balun with frontal coupling for operation in the frequency band of 4. . .6 GHz with parameters given in Table 13.11 was designed for approbation of the given method. Figure 13.37a shows the topology of its test structure designed for probe measurements, Fig. 13.37b, c and d – calculated characteristics, according to which the inserted losses and reflection losses are not higher than −6 dB and − 10 dB accordingly, while phase and amplitude imbalance do not exceed 1° and − 0.2 dB.

Methods for designing of basic passive elements for monolithic silicone-germanium ICs of the SHF range, such as transmission lines, inductances and balanced transformers, were created based on the performed complex of studies. In course of studies, it was determined that due to high dielectric losses and complex multi-layered structure of the passivating dielectric, passive metal elements on silicon substrate can have Q-factors 3–5 times lower than structures on semi-isolating substrates, which causes the necessity to include a separate stage of full electromagnetic analysis into the design methods.

According to these developed techniques, a set of passive elements was designed and manufactured for use in the composition of monolithic SHF SiGe BiCMOS ICs with topological norms of 0.25 μm. Calculated values of the element parameters correspond to the source requirements determined in Table 13.11.

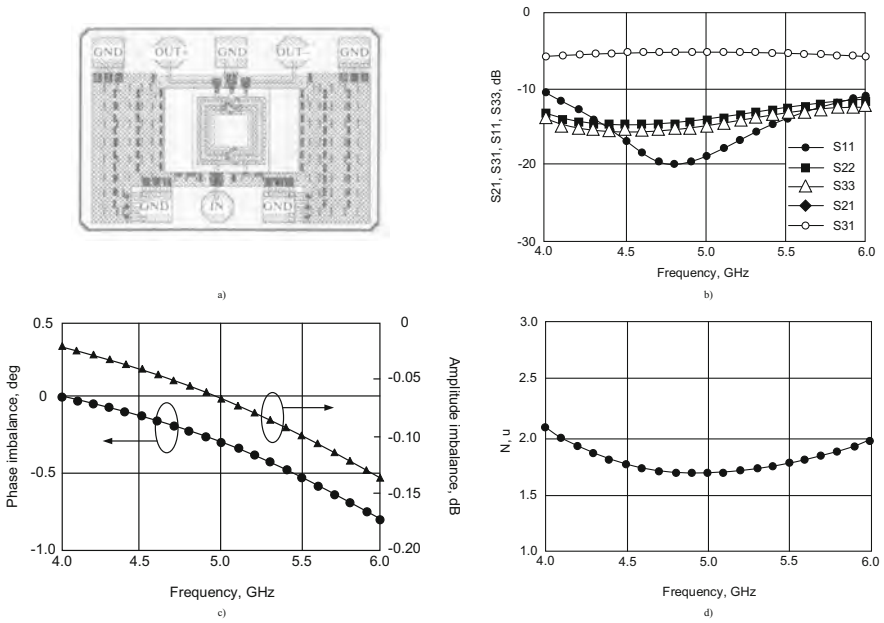

Fig. 13.37 Topology of the test structure of balun on coupled inductances (**a**), calculated dependencies of S-parameters (**b**), phase and amplitude imbalance (**c**) and TV connection coefficient (**d**) [21]

References

1. Elesin, V. V., Chukov, G. V., Gromov, D. V., Repin, V. V., & Vavilov, V. A. (2010). Study of the effect of ionizing radiation on characteristics of silicon-germanium integrated circuits of the microwave range. *Microelectronics, 39*(2), 136–148.
2. Cressler, J. D. (2005). *The Silicon heterostructure handbook: Materials, fabrication, devices, circuits, and applications of SiGe and Si Strained-Layer Epitaxy* (p. 1210). CRC Press.
3. Nikiforov, A. Y., & Skorobogatov, P. K. (2004). Physical basics of laser imitative modeling of 3D ionization effects in ICs and SDs: Linear model. *Microelectronics, 33*(2), 91–107.
4. Diez, S., & Ullan, M. (2008). Elai IHP SiGe:C BiCMOS technologies as a suitable backup solution for the ATLAS upgrade front-end electronics. *IEEE Nuclear Science Symposium Conference Record, N94-4*, 3091–3097.
5. Ullan, M., Diez, S., Campabadal, F., Lozano, M., et al. (2007). Gamma radiation effects on different varieties of SiGe:C RBT technologies. *IEEE Transactions on Nuclear Science, 54*(4), 989–993.
6. A. I. Belous, V.A. Solodukha, & S.V. Shvedov (2015). *Space electronics* (2 volumes, 1184 p). Moscow: Tekhnosfera.
7. Elesin, V. V., Nazarova, G. N., Chukov, G. V., Kabalnov, Y. A., & Titarenko, A. A. (2012). Study of the possibility of development of radiation-immune LSICs of the navigation purpose according to Russian SOI CMOS technology with norms of 0.35 μm. *Microelectronics, 41*(4), 291–303.
8. Chumakov, A. I. (2004). *Effect of Space radiation on integrated circuits*. Moscow: Radio and Communication. 320 p.

9. Elesin, V. V. (2010). Integrated circuits of the SHF range for measurement and information systems. *Sensors and Systems, 3*(130), 61–65.
10. Elesin, V. V., Kuznetsov, A. G., Chukov, G. V., et al. (2010). *Parameters of radiation immunity of Russian Radio Frequency SOI ICs for Navigation Systems* (Radiation Immunity of Electronic Systems – "Immunity-2010": Report at the Russian Scientific Conference, Lytarkino, June 3–4, 2010). Moscow: SPELS-NIIP.
11. Shahidi, G. (2002). SOI technology for the GHz Era. *IBM Journal of Research and Development, 46*(2/3), 121–132.
12. Description for SOS technological process. http://www.psemi.com/content/ultracmos/ultracmos_process_tech.html
13. Taya, T., Ito, S., & Higemot, N. (2004). *RF circuit technology that realizes wireless LSI products* (Special Issue on Technologies that Support the e-Society, Vol. 71. No. 4 Oki Technical Review).
14. Description of technological processes of "NIIME and Mikron". http://www.mikron.sitronics.ru/products/micron/technology
15. Gorbunov, M. S., Zebrev, G. I., & Osipenko, P. N. et al. (2010). *Comparison of different layout versions of SOI MOSFETs for designing of radiation-immune ICs*. Problems of Atomic Science and Technology. Ser.: Physics of Radiation Effect on Radioelectronic Equipment. Issue 1. pp. 39–43.
16. Chukov, G. V. (2010). *Means of connecting chips of SHF units to measuring path* (pp. 155–159). Electronics, microelectronics and Nanoelectronics. Collection of Scientific Works: NRNU MEPhI.
17. Chen, C. H., Wang, Y. L., Bakr, M., & Zeng, Z. (2008). Novel noise parameter determination for on-wafer microwave noise measurements. *IEEE Transactions on Instrumentation & Measurement, 57*(11), 2462–2471.
18. Kuo, J. B., & Ker-Wei, S. U. (1998). *CMOS VLSI engineering: Sili- con-on-insulator (SOI)* (p. 460). Kluwer Academic Publishers.
19. Sze, S. (1984). *Physics of semiconductor devices* (456 p). Moscow: Mir.
20. Garcia, I. G., Melendez, J., & Hernandez, E. (2006). *Design and characterization of integrated varactors for RF applications* (p. 160). Wiley.
21. Elesin, V. V., Nazarova, G. N., & Usachev, N. A. (2010). Design of passive elements for monolithic SiG SHF ICs immune to the effect of ionizing radiations. *Microelectronics, 39*(2), 149–157.
22. Bahl. (2003). *Lumped element for RF and microwave circuits I I Artech house microwave library*.
23. Grebennikov, A. (2007). *RF and microwave transistor oscillator design* (p. 441). Wiley.
24. Maas, S. (1986). *Microwave mixer*. Artech House, Dedham 335.
25. Nikiforov, A. Y., Skorobogatov, P. K., Chumakov, A. I., et al. (2009). Experimental studies of adequacy of laser simulation modeling of 3D ionization effects in integrated circuits and semiconductor devices. *Microelectronics, 38*(1), 4–20.
26. Chumakov, A. I., Vasilyev, A. L., Kozlov, A. A., Koltsov, D. O., Krinitskiy, A. V., Pechenkin, A. A., Tararaksin, A. S., & Yanenko, A. V. (2010). Prediction of local radiation effects in ICs under the effect of cosmic Space factors. *Microelectronics, 39*(2), 85–90.
27. Holmes-Siedle, A., & Adams, L. (1993). *Handbook of radiation effects*. (479 p). New York: Oxford University Press.
28. Messenger G. C., & Ash, M. S. (1997). *Single event phenomena* (368 p). New York: Chapman & Hali.
29. Petersen, E. D. (1997). *Single-event analysis and prediction/1997 IEEE NSREC* (pp. Ill-1–111-160). Short Course: Applying Computer Simulation Tools to Radiation Effects Problems. Snowmass Village, Colorado.
30. Stapor, W. J. (1995). *Single-event effects qualification. 1995 IEEE NSREC IEEE nuclear and space radiation conference* (pp. 11-1–11-68). Short Course: Advanced Qualification Techniques; a Practical Guide for Radiation Testing of Electronics. Madison, Winconsin.

31. Kozlov, A. A., & Chumakov, A. I. (2004). Design estimate of radiation protection of space equipment in 3D approximation. In V. Y. Stenin (Ed.), *Electronics, microelectronics and nanoelectronics. A collection of science papers* (pp. 326–329). Moscow: MEPhI.
32. Kozlov, A. A., & Chumakov, A. I. (2004). *Algorithm of assessment of structural protection of space vehicles/radiation immunity of electronic systems*. "Immunity-2004". Scientific and Technical Compilation. Issue 7. Moscow: MEPhI/SPELS. pp. 21–22.
33. Chumakov, A. I. (1998). Simplified method of assessment of IC immunity to single failures. *Microelectronics, 27*(6), 475–479.
34. Chumakov, A. I., Egorov, A. N., Mavritskiy, O. B., & Yanenko, A. V. (2004). Possibilities of using local laser radiation for modeling of effects from influence of separate nuclear particles in ICs. *Microelectronics, 33*(2), 128–133.
35. Nazarova, G. N. (2008). Electromagnetic modeling of integrated inductances for SHF ICs. In *Electronics, microelectronics and Nanoelectronics. A collection of scientific works* (pp. 121–124). Moscow: MEPhI.
36. Elesin, V. V., & Nazarova, G. N. (2008). Method of optimization of SPDT keys for monolithic phase shifters and attenuators of the SHF range. In *Electronics, microelectronics and Nanoelectronics. A collection of scientific works* (pp. 114–120). Moscow: MEPhI.
37. Multilayer Chip Baiuns. Application Note. www.tdk.co.jp/tefe02/transformer.htm.
38. Glubokoe, A. A., Bondar, D. B., & Shelkovnikov, B. N. (2006). Wideband transformers for integrated circuits in the LTCC technology. *Technologies and Design in Electronic Equipment, 3*, 26–31.
39. Gruner, D., Grustat, H., & Boeck, G. (2008). Fully integrated 5.8 GHz SiGe power amplifier. In *Proceedings of the 38th European Microwave* (pp. 301–304). Amsterdam, The Netherlands. https://product.tdk.com/info/en/products/capacitor/ceramic/mlcc/technote/sog_soft_term.html
40. Kehrer, D. (2000). *Integrated lumped transformers in silicon-based technologies up to 20 GHz*. (p. 85. Techisehen Universitat Wien.

Index

A
Acheson method, 394
Active antenna, 206, 207
Active electronically scanned arrays (AESAs), 460, 467–469, 474, 476, 477, 479, 484, 486, 489, 529–531, 534, 592, 594, 595, 597, 599, 602–604
  A-band AESA, 302
  air-cooled radar, 291
  assessment of reliability, 303
  centralized power supply system, 304
  cost, 291
  energy storage devices, 303
  polyalphaolefin (PAO), 291
  power consumption, 305
  power supply system, 302, 303, 310
  pulse power system, 301
  reliability requirements, 301
  SPN power modules, 304
  transceiver modules, 291, 302
  TRMs, 304
Active shelf life (ASL), 725
ADS software package, 357
Advanced antenna systems
  application, 326
  digital antenna systems, 328
  multi-frequency antennas, 326
  PAA with signal processing, 327
  PAAs with active amplifiers, 327
  PAAs with electronic scanning, 326
  remote probing, 327
  technical solutions, 325
Advanced Design System (ADS), 925
AESA phase shifters, 474
AESA transceiver module, 291
"Aggressor" conductor, 703
Air-based antenna devices, 324
Aircrafts
  air-ground interface, 147
  georadars, 147
  GPRs, 147, 148
  helicopter, 148
  LFM signal, 148
  probing, 148
  specialized air-based radar complexes, 149
Air traffic control radar, 4
"Almaz" program, 121
Amplifying semiconductor crystal (ASC), 786
Amplitude-frequency characteristic (AFC), 47, 666
Analog design library, 353, 354
Analog-to-digital converter (ADC), 49
Anisotropic, 169
Antenna arrays (AA), 97
Antenna devices
  development and improvement, 324
  development in radar sets, 320–322
  direction of development, 323
  of ground-based radars, 324
  requirements, 323
  space-based radiotechnical systems, 324
Antenna efficiency, 199, 200
Antenna-feeder devices (AFD), 710
Antenna manufacturing technologies, 258
Antennas devices
  active antennas, 206, 207
  actual dish antennas, beam pattern, 175
  alternating magnetic field, 193

© The Editor(s) (if applicable) and The Author(s), under exclusive license to Springer Nature Switzerland AG 2021

A. Belous, *Handbook of Microwave and Radar Engineering*,
https://doi.org/10.1007/978-3-030-58699-7

Antennas devices (*cont.*)
antenna efficiency, 199, 200
aperture efficiency, 197
array-shaped, 168
asymmetrical vibrator (monopole), 203
beam width, 170
blade beam, 177
characteristics, 168, 170, 231
circular polarization, 173
cosecant-squared beam pattern, 178, 180–182
dipole beam pattern
in horizontal plane, 194
in vertical plane, 195
dipole radiation pattern, 194
directional antenna, 204, 205
directivity pattern, 169, 194
effective aperture, 171
effective area, 196, 197
electromagnetic waves, 167
front to back intensity ratio, 172
gain factor, 168
half-wave, 174
input impedance (resistance), 197
inverse cosecant-squared beam pattern, 180
linear antenna arrays, 184, 185
linear polarization, 172, 173
lobes, 172
log-periodic antenna, 205, 206
manufacturer documentation, 194
mechanical dimensions, 167
monopulse (*see* Monopulse antennas)
offset antenna, 177, 178
in orthogonal coordinates, 169–171
PAAs, 183, 184
parabolic dish-shaped, 168, 175
planar array
frequency scanned, 186, 187
phase shifter, 187
phased array antenna, 184
planar lattice, 185
in polar coordinates, 169
polarization, 172
purpose, 193
radar and functions, 167
radiation resistance, 197
radiocommunication (*see* Radiocommunication)
receiving and transmitting, 192
and receiving devices, 10
resonant LC circuit, 192
SHF radio systems, 167
side lobes, 170
symmetrical Hertz vibrator, 193
VSWR, 198
Aperture effectiveness, 171
Aperture efficiency, 197
Aperture synthesis, 117
Arithmetical devices (ADs), 77
Atomic force microscopy, 844
Autocompensators, 44
Autodyne methods, 841, 842
Automatic compensator of perturbing radiations (ACPR), 38
component, 46
correlation feedback, 41
dynamic errors, 50
factor, 40
heterodyne, 41, 42
operation algorithm, 40
quadrature, 42, 43
Avionics, 347
Azimuth and range-difference methods, 8
Azimuth devices, 7

B

Balanced Voltage Converter (BVC), 302
Basic radar, 2
Belarusian State University of Informatics and Radioelectronics (BSUIR Minsk), 749
Blade beam antenna, 177
BMEWS (Ballistic Missile Warning Radar), 289
Bridge methods, 833, 834
Buffer amplifier, 932
Bulk acoustic wave filters (BAW), 615, 616

C

Cadence Design System
Analog Artist design system, 348
arrangement and routing system, 352
composer IC design environment, 350
end-to-end IC design, 351
HDL blocks, 351
IC design software, 342
modeling, 352
real designing, 351
synthesis of tests, 352
timing analysis, 352
CAD means, instrumentation and technical modeling, 353, 356
CAD software means, 348
Calculation diagnostics method (CDM), 110

Capacitive crosstalk, 702–705
Cavity methods, 834, 836–839
Cellular communication systems
  parabolic dish printed antenna, 243–248
Central processing unit (CPU), 689
Ceramic capacitors, 737, 738
Charged device model, 755, 756
Chemical vapor deposition (CVD), 396
Chip design techniques, 339
Circuit-based methods, 691–693
Circular polarization, 173
Civilian radars, 252
CMOS SOI technology
  characteristics, 922
  high-frequency and noise properties, 923–925
  high radiation resistance, 922
  instrument modeling, 925–927
  MOS VVCs, 928
  noise properties, 922
  R, C, L elements, 930, 931
  technological process, 922
  test structures, 923
Coaxial low-pass filters, 738, 739, 743
COBRA DANE radar station, 299
Coherent compensation of perturbing radiations (CCPR), 38
Communication engineering, 665
Computer-aided design (CAD) system, 70
Computing resource distribution, 341
Computing system structure, 59
Conical scanning principle, 191
Convolution operation, 83
Cosecant-squared antennas, 178, 180
Cosecant-squared beam pattern, 178, 180–182
Cost optimization, 340
Crosstalk, 700

D

Data processing algorithm, 75
Debugging process, 29
"Delta Estimate", 190
Designing DSP systems
  algorithms, 54
  FFT computers, 56
  hydroacoustic signals, 56
  image processing, 54
  LSIC chip, 58
  methods, 53
  microprocessor, 56
  parallel-pipeline, 53
  sound signals, 54
Designing microprocessor sets, 95
Design libraries, SHF ICs
  analog design library, 353, 354
  CAD means, 356
  design route, mixed-signal ICs, 353, 355
Dielectric materials
  frequency dependency, 884, 886, 888
  measurement, 888, 889, 892–894
  measurement of permittivity, 886, 888, 890, 891
Digital filtration, 81
Digital ICs, 348
Digital processing, 74
Digital processor, 3
Digital signal processor (DSP), 698
Dipole antennas, 200
  beam pattern, 200
  biconical antennas, 201
  directivity pattern, 201
  efficiency, 203
  half-wave dipole, 200, 201
  high radiation resistance, 203
  as nergy converter, 203
  power consumption, 202, 203
  in radioelectronics, 200
  thick dipoles, 201
  thin dipole, 201
  wideband dipoles, 202
Directional antennas, 204, 205
Director-type antennas, 204
Distance gauges, 7
Distributed Bragg reflectors (DBR), 780
Doppler frequency, 36
Double depletion region (DDR), 817, 818
Dry etching, GaN structures, 431
DSP algorithms, 73
  data processing operations, 75
  hardware and software, 76
  macro-operations, 77, 91
  operational devices, 77
  operations and hardware, 78
  performance, 78
  procedures, 76
  propagation medium, 74
  signal parameters, 75
  signal processing, 74
Dynamic errors, 50

E

Earth remote probing
  modern radars, 114
  multiple electronic systems, 115

Earth remote probing (*cont.*)
SARs (*see* Synthesized aperture radars (SARs)
side-looking radars, 116
spatial resolution, 117
special measuring technologies, 114
vehicle radar antenna, 116
Earth remote sensing (ERS), 114
with aperture synthesis, 117
cardinal problem, 115
COSMO ERS SVs, 122
double-purpose COSMO-SkyMed ERS SVs, 123
European Remote Sensing satellite, 117
Lacrosse system, 123
modern commercial ERS SV with SAR, 124, 125
for navigation tasks, 125
"Priroda" ("Nature") module, 122
Space ERS vehicle ENVISAT-1, 120
Effective aperture, 171
Electrical pumping (EP-VECSEL), 787
Electric power supply circuits
capabilities, 733
closed-circuit television systems, 728
equivalent electrical power distribution network, 734
frequency characteristics, 737
impedance-frequency characteristics, 731, 732
negative peaks, 732, 733
output impedance, 733
PDN, 735
power distribution network, 729
printed circuit board, 733
radioelectronic equipment, 728
SHF-system, 729
tantalum capacitor, 733, 735, 736
transmission line, 730
voltage regulator impedance, 730, 731
voltage regulator module, 729
well-balanced power distribution network, 730
wire-circuit board, 736
Electrodynamical system, 828
Electroluminescence, 395
Electromagnetic compatibility (EMC), 478
assessment methods, 671
asymmetric/common-mode interference, 662
characteristics, 661, 671, 677
computer modelling and simulation, 686, 687
design features
buffer capacitors, 684–686
capacitors, 682
ceramic-/quartz-crystal resonator oscillator, 685
common-mode interferences, 683
constant-voltage regulator, 683
distribution of layers, 684
factors, 681
HF electromagnetic interference, 680
HF interference, 686
IC design, 681
IC power buses, 685
interference propagation, 682
microcontroller, 681, 682, 684
microstrip lines, 686
modern microcontroller architectures, 681
multi-layer printed circuit boards, 683
optimization, 684
parameter optimization, 681
power wiring, 683
radiation, 686
electric devices, 670
EMI classification, 668, 669
frequency and time domains, 663
interference signal, 663–665
interference source and receiver, 662
measurements of electromagnetic radiation, 665, 666
methods, 670
national defence products, 671
natural interferences, 661
principal differences, 674, 675
quantity of amplifiers, 677
radiated and conductive interferences, 661
regulations, 671
requirements, 670–673, 676, 679
RES, 667, 668
semiconductor electronics, 661
semiconductor integrated chips, 671
symmetric/differential mode interference, 662
system solutions, 661
technical means and configuration, 678, 680
tests for resistance, 678, 679
validation processes, 679
Electromagnetic environment (EME), 667
Electromagnetic interferences (EMI), 478
Electromagnetic radiation, 831, 847–849
Electromagnetic waves, 16
Electronic component base (ECB), 57, 909
Electronic security systems, 346

Electronic systems, 1
Electron spin resonance (ESR), 843, 845
Electro-optical transformation, 777
Electrophysical parameters, 830–832, 839
Electrostatic discharge immunity, 755, 758
Electrostatic discharges (ESD), 661, 695, 752, 753
Elementary component (EC), 32
Elliptical polarization, 173
Encoders
  Electric Encoder, 311
  position sensors, 310
  pulse coding, 300
Equivalent series inductance (ESL), 709, 733
Equivalent series resistance (ESR), 709, 733
European Committee for Electrical Standardization (CENELEC), 670
European Committee for Standardization (CEN), 670
European Telecommunication Standards Institute (ETSI), 670
External influencing factors (EIF), 725

F
Ferromagnetic resonance (FMR), 843
FFT algorithm, 64
Finite element method (FEM), 253, 279
Finite impulse response (FIR), 84
Fourier coefficients, 65
Fourier, Hadamard and Walsh transform, 55
Fourier transformation, 663, 699
Fourier transforms, 55, 80, 86, 101, 102
Frequency characteristics, 49, 808
Frequency scanned antenna array, 186, 187
F-15SE fighter jet, 33

G
Gallium arsenide metal-semiconductor field-effect transistors (GaAs MESFET), 417
Gallium nitride (GaN)
  comparison, properties, 391
  physicla properties, 391
Gallium nitride heterostructural field transistors (GaN HEMT), 420
Galvanic metallization method, 531
GaN-based power devices
  advantages, 401
  analytics, 401
  characteristics and cost, 401
  commercially available, 401
  diodes, 402
  GaN P-N-diodes, 402
  heterostructural field transistors, 400
  lateral HEMTs, 404, 405
  properties, 400
  Schottky barrier diodes, 402
  silicon carbide and diamond, 400
  silicon field devices, 401
  2D electron gas, 404
  vertical GaN MOSFET, 403
  vertical GaN HEMT, 405
GaN-based SHF transistors
  advantages, 409, 414, 415
  AlGaN/GaN heterostructures, 407
  Arrhenius curve, 413
  commercial success, 415
  companies and institutions, 415
  functional compositions, 408
  and GaAs HEMT transistors, 410
  high-power internally matched transistors, 409
  high-power semiconductor amplifiers, 406
  industrial technologies, 413
  and MICs, 410, 411 (*see also* Monolithic integrated circuits (MIC))
  operating parameters, 414
  parameters, serial GaN-transistors, 408
  properties, 408
  radars, 411
  S-band, 415
  2D electron gas, 407
  40 W GaN MIC amplifier, 412
  wideband communication systems, 415
  X band, 415
GaN device crystals
  advantages, 428
  epitaxy, 428
  etching, semiconductors, 431
  formation of contacts, 429–431
  ion implantation, 429
  isolation of devices, 429
  lithography, 431
  nitride MBE, 429
  sapphire substrates, 428
  surface formation and device passivation, 432, 433
Gate turn off (GTO), 389
Gaussian frequency, 48
Gematronic weather radar, 176
Generalized structural diagram, 31
Generator frequency, 828
Generator with distributed spectrum, 693
Geoinformation system (GIS), 115

Geometrical volume, 31
Georadars, 127
  antennas, 147
  foreign manufacturers, 127
  modernized, 129, 130
  Russian (*see* Russian georadars)
Giante's concept, 227
Global navigation satellite systems (GNSS), 281
Ground instability, 707
Ground penetrating radars (GPRs)
  on aircrafts, 147–150
  aperture synthesis, 109
  CDM, 110, 111
  central frequencies, 108
  design features, 107
  development, 107
  formation and interpretation, radio , images,108
  four-layer environment, 112
  for hidden objects, 107
  with increased resolution
    antenna part, 126
    classic matched filter, 129
    control unit, 126
    georadars, 127
    modernized georadar receiver, 130
    modernized receiver, 129
    narrowband sinewave signal, 127
    operating principle, 127
    organization, pumping signal, 129
    pumping signal synthesis procedure, 129
    recording unit, 126
    Russian georadar "OKO-2", 126
    TWTs with noise factor, 128
    UWB radar location, 127
    UWB signals, 128, 130, 131
    wideband amplifier, 128
  preliminary processing procedures, 108
  radio images, 108
  spectral method, 109
  sub-surface image, 110
  transmitting module, 113
  UWB devices (*see* Ultra-wideband devices (UWB))
  UWB quasi-continuous linear FM signals
    altitude metering, 140
    beating frequencies, 142
    generation and processing path, 142, 144–146
    structure, 140, 142
    superresolution, 141
    VCO, 140
  UWB short-pulse ground penetrating radars, 113
  video pulse ultra-wideband, 111
Gunn-diode based synchronized generator, 842

H
Half-wave antenna, 174
Half-wave dipople, 201
Hardware implementation, 89
Heterostructural bipolar transistors (HBT), 910–913, 947
High electron mobility transistor (HEMT), 390
High Frequency Integrated Vacuum Electronics (HiFIVE), 446, 447, 451, 453, 460, 462
Highlights (HL)
  amplitude and phase relations, 36
  calculation, 35
  local coordinate system, 35
  parameters, 34
  production, 36
  projection, 36
  radar CS, 36
  recalculation process, 34
  RS model, 37
High-power SHF modules
  Ml220 module, 457
  MPM, 454
  power levels, 453
  power source, 456, 457
  solid-state amplifiers, 454
  TWT, 455
High-quality crystalline gallium nitride, 392
High-speed communication systems
  capacitive crosstalk, 702–705
  crosstalk, 700
  formal signal characteristics, 699
  Fourier transformation, 699
  ground instability, 707
  inductive crosstalk, 700–705
  power source interferences, 708–710
  relaxation oscillation, 705–707
  signal integrity, 699, 700
  spectrum of digital signals, 699
High-speed transient (HST) immunity 756–758
Homoepitaxial growth, 428
Horizontal cavity, 777
Hybrid mode resonator, 837
Hydroacoustic signals, 56

I
IC design process, 358, 359
Image processing, 54
Indium-gallium phosphor heterobiopolar transistors (GaInP HBT), 419
Inductance coils, 931
Inductive crosstalk, 700–705
Installable software, 340
Instrumental-process simulation software, 340
Integral circuits (ICs), 937, 938
Integral inductances, 946–948
Integrated chips (IC), 746
Integrated Circuits Electromagnetic Emission Model (ICEM), 694
Integrated gate-commutated thyristor (IGCT), 390
Interactive environment Analog Artist, 348
Intermodulation distortion level (IDL), 761
International Electrotechnical Commission (IEC), 670
International Organization for Standardization (ISO), 670
International Radio Consultative Committee, 666
International Special Committee on Radio Interference (CISPR), 670
Internet, 243, 252, 255
Intolerable electromagnetic interference (IEI), 667
Ion implantation, 429
Ionizing radiation (IR), 909

K
Karhunen–Loeve transform, 55

L
Laboratory of Physics of Nanostructures (LPN), 781
Lagers with the vertical resonator, 777–780
Least square method, 866, 867
Lely sublimation process, 395
LETI method, 395, 396
Line of sight (LoS), 30
Linear antenna array, 100, 184, 185
Linear systolic system, 71
Linearity, 784
Liquid Crystal Surface Emitting Laser (LICSEL), 792
Lithography, 431
Log-periodic antenna, 205, 206
Long-wave alloyed surface-emitting laser
  crystal, 781
  electrical and power characteristics, 782
  InP/InAlCaAs-based active region, 780
  laser generation, 780
  optical amplification, 780
  optical injection synchronization, 781
  radiophotonic devices, 780
  tunnel junction, 780
  vertical structure, 781
Lorentz line, 792
Low-noise amplifier (LNA), 909

M
Machine model, 753, 754
Marconi Martello radar station, 298
Mathematical model, 12, 850–852
Mathematical simulation, 336
Metal films, 878–880
Metal-organic vapor-phase epitaxy (MOVPE), 428
Microcircuits, 56, 96, 97
  classification, 751
  design stage, 748
  discrete semiconductors, 747
  effective shields, 746
  factors, 745, 746
  integrated chips, 748, 749
  integrated circuit, 749
  microelectronic integrated circuits, 747
  microwave, 357
  processing units, 749
  radiation method, 749
  radioactive equipment, 747
  radioelectronic devices, 745
  RESs, 748
  radio frequency interference, 747 (*see also* Radio frequency microcircuits)
  semiconductor devices, 748
  sensibility threshold, 752
  standard design process, 358
  testing technique, 749
  transfer characteristics, 750
  transmission factor, 751
  types, 751
Microcontrollers
  circuit-based methods, 691–693
  electromagnetic field distribution, 688
  EMC characteristics, 694, 695
  measurement, 688
  national omissions, 687
  propagation paths, 689–691

Microcontrollers (*cont.*)
sources of interferences, 689–691
spectrum of interferences, 689
TEM-chamber method, 688
Micro Electro-Mechanical System-VCSEL (MEMS-VCSEL), 792–795
Microelectronic integrated circuit (MIC), 745
Microprocessor, 64, 65
Microstrip transmission line, 945, 946
Microwave devices, 723
Microwave electronics
autodyne methods, 841, 842
conductivity, 847–849
electromagnetic radiation, 847–849
electrophysical parameters, 830–832
measurement of semiconductor parameters, 833, 834, 836–839
nanometer metal layers, 847–849
semiconductor, 827–830
SHF microscopy, 843–847
synchronized oscillators, 842
waveguide dielectric resonance method, 840, 841
waveguide methods, 830–832
Microwave IC CAD systems, 349
Microwave integrated vacuum electronics
beam transportation, 450
cathodes, 448
HiFIVE program, 446, 447, 451
implementation of program, 451–453
MIC technology, 449
multi-stage collector, 448, 450
oscillation modes, 448
takeoff power, 448
technical possibilities, 448
traditional vacuum devices, 447
Microwave power amplifier, 454
Microwave power modules (MPM), 455, 457
block diagram, 455
design and features, 454
development and potential systems, 454
in electronic warfare systems, 458
for EW and communication systems, 442
ground forces, 441
HiFIVE, 453
microwave power amplifier, 454
millimeter range, 441
parameters, MPMs by L-3 Communications EDD, 457
serial production, 457
small TWT, 462
vacuum-semiconductor, 441
Microwave signals, 803, 804
Military aircraft technology, 457
Millimeter and sub-millimeter waves, 16
application, 20
features, 18
frequency distribution, 22
names and conventional boundaries, 17
oscillations, 20
propagation, 18, 19
ranges, 22, 23
waveguide path, 23
Mirror software, 265, 266, 268
Mixed-signal ICs, 353, 355
Mobile radars, 180
MOCVD method, 531, 532
Mode-locked Integrated eXternal-cavity Surface Emitting Laser (MIXSEL), 796
Modern pulse radar, 3
Modern radar systems, 320
Modern radio electronics, 14, 20
Modified Lely method, 396
Molecular beam epitaxy (MBE), 428, 531
Monolithic chips
PLL of SHF synthesizers, 572–573
software, 591–594
wide-band frequency, 587–590
Monolith integrated circuits (MIC)
GaAs MIC technologies, 427
GaN amplifiers, 406, 407, 411
GaN-based transistors, 415
and GaN HEMT, 420
industrial technologies, SHF transistors, 418
mounting, 423
powerful transistors, 419
powerful wideband amplifiers, 417
in radio-technical systems, 416
Monopulse antennas
angular position, classic radars, 189
conical scanning, 191, 192
delta azimuth diagram, 190
elevation angle, 190, 191
four parallel receiver channels, 191
linear antenna array, 189
measurements, 189
operating principle, 190
principle, 189
quadrants, 190
secondary channels, 188
single phase, 188
target fluctuation errors, 189
Multi-layered structure, 851
Multi-more resonator (MMR), 611
Multiple electronic systems, 115

Multi-positional passive radar sets, 8
Multi-task situation, 9

N
Nanoelectronics, 827
Nanometer metal layers, 877–879
Naval Research Laboratory (NRL), 442
Near-field microwave (SHF) microscopy 843–847
Near-field scanning optical microscopy (NFSOM), 844
Netzer angular sensors, 315
Netzer capacitance sensors, 312
Netzer development kit, 317
Netzer Precision Motion Sensors Ltd (Israel), 311
Netzer products, 311
Noise characteristics, 783
Non-contact methods, 828
Non-linear distortions, 48
Non-recursive filters, 85

O
OD operating program, 77
Ohmic contacts, 430, 431
One-dimensional waveguide photonic structures
  dielectric/semiconductor substrates, 871–875
  losses, 869–871
  metal films, 878–880
  metal-semiconductor structures, 882, 884, 885, 887
  nanometer metal layers, 877–879
  permittivity of materials
    computer modeling, 867
    electrophysical parameters, 866
    numerical method, 867
    numerical technique, 867
    parameters, 867
    reflection coefficient, 869
    reflection spectra, 868
    residual functions, 868
    test data, 867
  reflection and transmission spectra, 875–877
  semiconductor substrates, 879, 881, 883
On-line options, 7
Operating speed, 67
Optical injection synchronization, 781
Optical pumping, 787, 796

P
Parabolic (dish) antenna, 175
Parallel-conveyor systems, 68
Parallel-pipeline DSP systems, 57
Parallel-pipeline FFT implementation, 87
Parallel-pipeline (systolic) structures, 82–84
Parallel-pipeline (systolic) systems, 71, 73
Partially depleted absorber (PDA), 818
Passivation, 432, 433
  by epitaxial layers, 433
  functions, 432
  PECVD processes, 432
  preliminary processing, semiconductor surface, 432
  SiN, 433
  SiO_2, 433
  surface treatment, 432
Passive intermodulation (PIM)
  band, coaxial and waveguide transmission lines, 764–766
  directional couplers, 765
  equipment, 769–772
  external, 766, 767
  frequency duplexers, 765
  IDL, 761
  level evaluation methods, 767, 768, 770
  mechanisms, 761, 762
  printed circuit board, 764
  RF connectors, 763, 764
  transformers, 765
Passive location complexes (PLC), 8
Passive mode synchronization lasers (PMS), 796
PC workstations, 340
Perturbing radiations, 37
Phased antenna arrays (PAAs), 3, 183, 184, 288
  active arrays, 290
  advantage, 289
  AESA, 290, 291
  air defense and reconnaissance, 292
  as beam control, 297
  classification, 289
  combat and reconnaissance tasks, 293
  in communication systems, 252
  detection and tracking, 297
  electromagnetic oscillations, 296
  electronic control, 294
  electronic device, 295
  interference, 294
  linear size, 248
  massive BMEWS, 289
  military and reconnaissance purposes, 300
  PAA reflectors, 248–250

Phased antenna arrays (PAAs) (*cont.*)
PAVE PAWS radar station, 299
perpendicular axis, 294
phase control, 288, 297
planar printed structure, 250
pulse coding, 300
reflected signal, 293
on semiconductor elements, 299
standard coding technique, 300
structure and parameters, planar reflector antenna, 251, 252
three-element phase shifters, 296
vertical polarization, 250
wave polarization, 250
Phase detectors (PD), 42, 44
Phase shifters, 295
advantage, varactor, 383
using CAD means, 383–386
communication systems, 380
parameter, 383
principle operation, 380
quality, 382
with smooth phase adjustment, 382
Photocathodes, 439
Photodiodes (PD), 810
DDR, 817, 818
PDA, 818
UTC, 818–821
Photoelectronic cathodes, 439
Photonic crystal, 849, 855, 857, 859
Photonic devices
communication networks, 777
edge-emission laser, 779
inverse optical-electrical conversion, 778
laser heterostructures, 779
laser radiation, 778
local telecommunication networks, 780
long-wave VCSELs, 779
microwave, 778
modern semiconductor technologies, 779
multi-layer reflector, 780
optical radiation, 778
planar-epitaxial technology, 779
principle of operation, 777
quality of life, 777
radiophotonic radar building principle, 778
short-wave VCSEL, 779
SLE, 777
VCSEL technology, 777
Photosensors, 809, 810
Physical diffraction theory, 264, 273
Pipeline MD, 62
Pipeline methods, 90
Pipeline specialized processor, 87
Plancheral theorem, 80
Plasma-chemical deposition (PECVD), 433, 531
Polarization, 172
Positioning systems, antenna
Netzer products, 311
position sensors (encoders), 311–314
principles, 310
rotating antenna systems, 314, 316, 318–320
Power, 171
Power distribution network (PDN), 729, 735
Power electronics
advantages, GaN-based, 401
AESA, 392
application, SiC-based, 399
gallium nitride, 400
HEMT, 390
IGCT, 390
industrial production, SiC
Acheson method, 394
Cree Research Inc., 397
CVD, 396
electroluminescence, 395
evolution, 394
history of discovery, 394
Lely method, 395
LETI method, 395, 396
sublimation sandwich method, 395
lateral HEMTs, 404, 405
lifecycle, semiconductor devices, 390
requirements and directions, development, 389
research activities, 398
Schottky diodes, 402
shape formation, crystals, 394
thyristors, 389
uncontrollable structure, 394
Power semiconductors, 390
comparison, properties, 391
GaN-based blue LEDs, 392
lifecycle, electronics, 390
manufacturers, 390
nitrides, 392
properties, 389
recommended use of Si, GaN, SiC, 392, 393
silicon carbide, 392
Power source interferences, 708–710
Power supply rejection ratio (PSRR), 708
Power Surface Mount (PSM), 744
Primary signal processing, 75
Printed circuit board (PCB), 685, 731

"Priroda" ("Nature") module, 122
Prism 2 software, 159
Processor elements (PEs), 66, 95
Programmable DSP processors, 92
Pulse coding, 299, 300
Pulse generation lasers, 796–798

Q
Quadrature components, 44
Quadrature phase shifter, 43
Quantum dots (QD), 797
Quantum wells (QW), 797
"Quasi-directional" transmission, 227
Quasi-optical transmission lines, 27

R
Radar cross-section (RCS), 114
Radar location devices
  georadiolocation, 127, 161
  remote probing, 116
  SARs, 121
  UWB, 127, 137
Radars, 1, 346
  interference immunity, 6
  mean time, failures, 6
  operational efficiency, 6
  probability, 4
  random errors, 5
  range resolution, 4
  RMS error, 5
  systematic errors, 5
  tactical and technical parameters, 4
  technical parameter, 6
  throughput capacity, 6
Radar sets, 467, 529, 539, 594, 595, 604
  HF and SHF components
    acoustic wave-based microwave filters, 614–618
    active PAAs, 625–630
    cable sealing glands, 618–623
    ceramic capacitors, 649–650
    line filters and film capacitors, 651–654
    microstrip filters, 611–614
    microwave filters, 611
    radar sets, 618, 626
    radioelectronic equipment, 657–659
    Russian powerful stripline, 623–625
    SASP (*see* Spectrum advanced specialty products (SASP))
    specialty connectors and cabling, 654–657
    high and low power SHF amplifiers, 499–503
    high speed hybrid converters, 525–529
    Russian active GaAs elements, 482–491
    ultra-wideband microwave power amplifiers, 494–497
    wideband silicon carbide-based power amplifiers, 490–494
Radar stations, 116, 128
Radar systems, 1, 55
Radar targets, 1
Radiation propagation direction
  computer modelling, 852–857
  irregularity parameters, 858–862
  mathematical model, 850–852
  photonic crystal, 849, 855, 857, 859
  planar transmission lines, 850
  reflection spectra, 861, 863–866
  transmission spectrum, 849
  transmitting layers, 861, 863–866
Radiation resistance, 197
Radiation stability
  balance-to-unbalance transformers 947–950, 952
  BiCMOS technologies, 944
  HBT, 910–913
  heterostructural bipolar transistors, 909
  impulse effect, 910
  integral inductances, 946–948
  LNA, 912, 914, 915, 917
  microelectronics, 909
  microstrip transmission line, 945, 946
  parameters of passive elements, 944
  radio frequency (RF), 944
  resistance requirements, 909
  silicon-germanium (SiGe), 944
  VCG chips, 914–920
  WBA, 912, 914, 915, 917
Radiocommunication
  in antennas, 210
  capacitor voltage divider/D-Dot-sensor, 225
  energy absorption, 225
  flat reflective printed antenna (*see* Cellular communication systems)
  HFSS ANSYS environment, 208
  log-spiral antennas, 281–288
  man-portable devices, 226–229
  microstrip antennas on thin substrate, 234, 235, 237–243
  mirror dish antennas, 264–280
  multiband patch antenna, 207, 230–235
  three-range slot antenna, 253–255, 257

Radiocommunication (*cont.*)
Vivaldi antenna on ceramic substrate, 255, 257–263
wideband microstrip antenna, 210–215
wideband SHF travelling-wave antenna, 215–223
wireless systems WiMAX and WLAN, 207, 208, 210
Radioelectronic devices, 15, 17
Radioelectronic equipment (REE), 778
Radio electronic systems (RES), 666–668, 746
connection, ADS model, 336
Mouser Electronic, 369–373
Multisim Blue Software, 366, 367, 369
narrow-band interference, 337
physical device, 337
physical model, 336, 337
principle of automated generation, 338
Ultiboard Component Evaluator, 373, 374, 378
Radio frequency microcircuits
algorythmic/in-circuit approaches, 336
analytical laboratories, 343
application, SHF chips, 344, 346
cloning department, 343, 345
design department
chip techniques, 339
computing equipment and software, 340, 342
computing resources, 340, 341
hardware structure, typical chip design center, 339
instrumental-process simulation software, 340
PC workstations, 340
typical hardware, 339
documentation and archiving department, 344
ECB development, 335
end-to-end simulation, 335
LSI model, 336
mathematical simulation, 336
measurement and test department
adapter production and debugging, 341, 343
companies, 340
hardware components, 341
IC functional control, 341
organization, 341, 343
standard design center, 340
standard list of equipment, 342, 344
military equipment, 346, 347
model, 335
quality control department, 344
VHDL methods, 336
Radio frequency resource (RFR), 666
Radio-frequency VLSI, 335
Radiolocations, 1
antenna and receiver, 2, 3
digital processor, 3
physical basis, 2
signals, 1
software complex, 29
stations/radio locators, 1
systems, 1
UWB radar set, 3
Radio navigation systems, 21
Radiophotonics
active delay line, 801–803
ASC, 786
continuous-mode VCSELs, 792
electrical and power characteristics, 791
EP-VECSEL, 787, 788
functional devices, 799, 800
InCaAsP/InGaAlAs, 787
LICSEL, 793, 795, 796
linearity, 784
Lorentz line, 792
low-signal frequency-modulation characteristics, 782, 783
measurement and calibration means, 807, 808
microwave p-i-n photoelectric detectors, 809–814
microwave signals, 803, 804
noise characteristics, 783, 792
optical and microwave signals, 800
optical pumping, 791
OP-VECSEL, 787, 789
photons, 791
p-i-n-photodiode, 814–817
pulse generation lasers, 796–798
radar equipment, 801
radio signals, 805, 806
RIN, 791
semiconductor lasers, 793
spectral and tuning characteristics, 784–786
spectral characteristics, 793
VCSEL, 786
Radio signals, 805, 806
Radiosystem, 20
Random measurement errors, 6
Range-difference algorithm, 8
Range-difference devices, 7
Receiver protection device, 292
Receiver sensors, 115

Recording-recovery-interpretation, 108
Rectangular waveguide, 23
Reflected signal (RS), 29
Reflection spectra, 861, 863–866
Relative intensity noise (RIN), 783, 791
Relaxation oscillation, 705–707
Remote surveying, 115
Remotely piloted aircrafts (RPA), 457, 458
Resistors, 931
Resonance reflection, 863
Resonant arrays, 716
RF integrated circuits, 348
Root-mean-square errors, 12
Rotating antenna systems, 318
Russian georadars
  archaeology, 150
  design, 150
  environmental protection, 150
  geology, 150
  GPRs of "Loza" Series, 153, 154, 156–158
  industrial and civil construction, 150
  "OKO" georadars, 160, 161
  "OKO-2", 126
  as search technical and forensic tool, 150
  transport construction, 150
  "Zond-2" georadars, 158, 159

S
Schottky contact, 430
Secondary power supply system
  DC/DC converters, 597–600
  electromagnetic processes, 602–605
  principles of building, 594–597
  SynQor converters, 600–602
Self-synchronizing systems, 68
Self-tuning errors, 50
Semiconductor, 663, 827–830
Semiconductor devices (SD), 745, 746
Semiconductor laser emitters (SLE), 777
Semiconductor protective devices
  advantages, 714, 716
  behaviour, 719
  development, 714, 719, 720
  electrodynamic systems, 714
  equivalent circuit, 721
  five-layer diode structure, 719, 720
  frequency barrier, 719
  "hysteresis", 719
  lumped design, 718
  "makeup", 714, 715
  parallel connection of diodes, 715, 717
  parallel-serial connection, 718
  parameters, 720
  resonant arrays, 716
  semi-array, 716
  serial connection of diodes, 715, 716
  series-parallel connection, 716
  series-parallel switching, 715
  transistor power, 719
  waveguide structure, 714
Semiconductor Saturable Absorber Mirror (SESAM), 796
Serial digital filtration processor, 82
Serial surveillance radars, 175
SHF chips
  attenuators
    analog control, 555–556, 568
    attenuation-frequency dependence, 555
    balanced amplifier, 562, 563
    deferent control voltage, 568, 570, 572
    digital control, 556–559
    digitally controlled amplifiers, 571
    fixed attenuation, 552, 553
    functional diagram of chip, 560, 563, 571
    functional parts, 550
    functional structure, 569
    gain factor dependence, 569
    gallium-arsenide (GaAs) field-effect transistors, 562
    ICs automatic gain control, 568
    integrated chips, 550
    maximum output power, 561
    operating frequency and temperature, 561
    parameters, 554
    SHF heterotransition germanium silicon transistors, 560
    typical gain factor-frequency dependence, 564
    ultra-wideband amplifier, 565, 566
    ultra-wideband chip, 565
    variable gain amplifiers, 568
    wideband amplifier, 567
  synthesizers
    HMC983 and HMC984, 580–586
    monolithic chips (*see* Monolithic chips)
    three-band monolithic microcircuits, 575–577
    wide-band monolithic microcircuits, 576–578
SHF devices
  AESA transceiver modules (*see* Secondary power supply system)
  application, 723

SHF devices (*cont.*)
attenuators, 467–472
bioman, 753, 754
buffer amplifier, 932
capacitance, 934
ceramic capacitors, 737, 738
characteristics, 934
charged device model, 755, 756
chip metallization layers, 932
chips (*see* SHF chips)
coaxial low-pass filters, 738, 739, 743
coefficient, 724
communication, 710–712
commutator failure tree, 726
commutator operation, 726
designing SAW frequency, 511–517
electronic and mechanical switch reliability, 728
electronic devices, 723
electrostatic discharge immunity, 755, 758
ESD, 752, 753
GaAs
microwave transistors, 506–511
protective devices, 504, 506
transistor amplifiers, 499–506
GaN
AESA TRMs, 529–531
microcircuits, 535–541
monolithic GaN microwave PA, 531–533
SHF microcircuits, 533–534
SHF transistors, 535
gas discharge protective devices, 712, 714
and HF
attenuators, 549–550
double balanced mixers, 545–547
frequency mixers, 548–552
integrated monolithic amplifiers, 543–545
multi-purpose high-frequency amplifiers, 546–549
and noise properties, 934
HST, 756–758
integral spiral inductances, 934
IR pulse effect, 934, 936
low noise amplifiers, 476–481
machine model, 753, 754
mechanical components, 727
microwave devices, 727
microwave radio receivers, 518–525
microwave switch reliability indicators, 727, 729
mixer parameters, 933
n-MOS-transistors, 933
noise-suppressing filters, 478–480
“normal conditions”, 724
parameters, 933
phase shifter (*see* AESA phase shifters)
power amplifier (PA), 476–481
preamplifiers of transceivers, 476
radar location, 710–712
radar sets (*see* Radar sets)
radiation resistance, 933
radio receiver, 934
reliability indicators, 727
requirements, 727
resistance, 752, 753, 935
resource assessment methods, 723
SOI CMOS process, 936
space technology, 723
spiral inductances, 932
surface mount filters, 743, 744
surge immunity test, 758, 759, 761
technical conditions, 724
test chips, 935
testing methods, 757
test structures, 932
thyristor effect and catastrophic failures, 933, 935
two-pole switches, 470–472
vacuum protective devices, 721, 722
voltage-controlled oscillator, 932, 933
Ship movement control systems, 180
SiC-based power electronics devices
companies, 398
fields of application, 399
history, 397
non-conductive sapphire Al_2O_3, 398
Russian enterprises and companies, 397
use, 398
wide-gap materials, 398
Side-looking radars, 115, 116
Signal filtering, 79
Signal processing, 74
Signal-to-noise ratio, 13
Signal weighting, 79
Silicon carbide (SiC)
comparison, properties, 391
industrial production (*see* Power electronics)
physicla properties, 391
super-fast high-voltage Schottky diodes, 392
Silicon carbide metal-semiconductor field-effect transistors (SiC MESFET), 419

Silicon-germanium (SiGe), 909
Silicon lateral double-diffused MOS transistors (Si LDMOS), 417
Silicon-on-insulator (SOI) structures, 922
Simulated radiolocation object, 31
Simultaneously Switching Noises (SSN), 690
Smith chart, 236
Solid-state microelectronics, 827
Sound signals, 54
Space factors
  experimental studies, 941
  integral circuits (ICs), 937, 938
  laser radiation, 941
  limitations, 941
  local radiation effects, 942
  LR energy, 943
  microelectronics, 937
  operational amplifier, 942
  optical model, 938
  parameters, 941
  proton accelerators, 939
  proton energy, 939, 940
  RAM, 941
  spacecraft design, 938
  thyristor effect, 943, 944
Spatial resolution, 117
Spectrum advanced specialty products (SASP)
  coaxial filters, 631
  combined D-subs (filtered combo D-sub), 646
  development and production, 649
  easy mate filter plates series, 637
  electrical characteristics, 646
  filter assemblies, 632
  filter plates, 633, 634
  hermetically sealed threaded case filters, 642
  intercomponent connections, 631
  LC filters, 643
  low pass filters (LPF), 639
  micro D-sub, 648
  miniature filters, 640
  power SMD filters, 632
  rectangular connectors, 642
  resin sealed bolt-in filters, 640
  solder-in filters (non-sealed filters), 639
  solder-in filters (sealed filters), 640
  Spectrum Control, 630
  surface mount filters, 631
  terminals, 632, 636
Spectrum Control, 737
SPICE parameters, 357
Spontaneous electromagnetic interferences (SEI), 666, 667
Square Surface Mount (SSM), 744
SSN-noises, 695
Standalone devices, 7
Standard design workstation, 339
Standard source data, 101
Standard waveguides, 24, 26
Sublimation sandwich method, 395
Superconducting Quantum Interference Device (SQUID), 845
Superwide band devices, *see* Ultra-wideband devices (UWB)
Surface-acoustic-wave (SAW) filters, 614–616
Surface mount filters, 743, 744
Surge immunity test, 758, 759, 761
Surveillance radars, 7
Synchronized oscillators, 842
Synthesized aperture radars (SARs)
  "Almaz" program, 121, 122
  high quality, 114
  modernization, 115
  multi-channel multi-functional, 115
  orbital parameters and technical characteristics, RS SVs, 118
  radiolocation images, 114
  Russian hardware base, 114
  space-based, 116
Systolic algorithms, 69
  and structures, 70
Systolic and parallel-pipeline systems, 71
Systolic structure, 68
Systolic systems
  programmability, 70

T
Technical Conditions, 724
Technological process, RF and SHF products
  BCDMOS, 347
  BiCMOS, 347
  BJT, 347
  CMOS, 347
  digital ICs, 348
Telecommunication optic fiber (TCOF) systems, 777
Temporal filtration, 79
Thermoelectric micro-cooler (TEMC), 790
Thermoelectronic cathodes, 438
Thompson model, 60
Tracking radars, 7

Transceiver module (TRM), 468, 470, 476–478, 484–487, 489, 490, 519–521, 529, 531, 534, 595, 596, 599, 602, 604
Transmission Line Model (TLM), 686
Transmission lines, 28
Transmission matrix, 852
Transmission spectrum, 829
Transmitting layers, 861, 863–866
Travelling wave tube (TWT)
  bandwidth, 455
  on coupled resonators, 442
  dimensions and weight, 455
  gyroscopic, 445
  gyroTWT, 442
  helical micro-TWT, 462
  helical TWT, 443
  L-3 Communications, 459
  medium-power, 460
  mini-TWT, 455
  MPM, 441, 461
  Q-band, 462
  reliability, 456
  space TWTs, 459
  special pulsed helical TWTs, 458
  super-linear helical, 444
  traditional applications, 459
  ultra-wideband, 443
  with power source and MPM, 456
  MPM, 455
2D systolic structure, 82

U
Ultra-wideband devices (UWB)
  bandwidth factor, 107
  characteristics, 132
  classification
    medical, 134
    mobile (portable) systems, 134–136
    radio communication devices, 137
    stationary radars, 134
    stationary systems, 134
    sub-surface probing, 133
    through-the-wall radars, 134
  dvelopment in Russia companies, 138
  procedure, device registration, 132
  radar location, 127
  Russian manufacturers, 139
  video pulse signals, 108
Uniform wave systems (UWS), 130
Unipolar heterojunction photodiode (UTC), 818–821
US Department of Defense, 671

V
Vacuum electronics
  cathode, 438
  classes of devices, 438
  continual environment, 437
  electronics, 437
  emitter/cathode, 437
  free electrons in continual , environment,437
  history, 437
  information signal carrier, 437
  military services
    national security, 440
    NRL, 442
    US Air Force, 441
    US ground forces, 441
    VTDs (*see* Vacuum tube devices (VTD))
  photocathodes, 439
  rapid development, 439
  tasks, 438
  thermoelectronic cathodes, 438
  three-electrode tube (triode), 437
  typical device (tube), 437, 438
  vacuum nanotechnology, 439
  vacuum tube devices, 439
Vacuum microwave devices, 454, 459, 460
Vacuum protective devices, 721, 722
Vacuum-semiconductor MPM, 441
Vacuum SHF devices
  centimeter range, 459, 460
  millimeter and terahertz ranges, 460–463
Vacuum tube devices (VTD)
  electronic weapon systems, 441
  gyroscopic devices, 445
  military systems, 440
  national laboratories, 440
  sales, 440
  SHF power modules, 444
  small-sized klystrons, 445
  and solid-state devices, 444
  TWTs, 443–444
  US Air Force, 441
  US ground forces, 441, 442
Vertical-cavity surface-emitting laser (VCSEL), 777

Vertical External Cavity Surface-Emitting Laser (VECSEL), 786
Vertical heterotransition field-emission transistors (VHFET), 405
Vertical micro-cavity, 777
Very large scale integrated circuits (VLSIs), 63, 93, 335, 353, 356
  data I/O protocols, 60
  development, 57
  LSIC chips, 67
  macro-programmable, 94
  packaging, 67
  proportionality factor, 58
  synchronization problem, 68
VHDL language, 353, 354, 356
Vicselonics, 777
Virtual waveguide, 248
Vivaldi antennas, 255, 257, 258, 261, 262
VLSI-based computing systems, 57, 68
VLSI model, 60
Voltage-controlled oscillator (VCO), 140, 909, 947
Voltage-current characteristic (VAC), 763
Voltage regulator module (VRM), 729
Voltage standing-wave ratio (VSWR), 198, 199, 208, 231, 234, 251, 283

W
Waveguide dielectric resonance method, 840, 841
Waveguide methods, 830–832
Waveguides, 25, 27
Wet etching, GaN structures, 431
Wideband amplifier (WBA), 909
Wideband transistor power amplifiers
  as active transistor elements, 416
  CHPA0618-2 amplifier, 425
  complex design, 416
  dynamic characteristics, 421
  electromagnetic compatibility testing, 417
  GaAs MESFET, 417
  GaAs MIC technologies, 427
  GaInP HBT, 419
  GaN HEMT, 420
  high-power wideband amplifiers, 425
  industrial technologies, 418
  matching circuits (MC), 416
  MESFET technology, 418
  monolithic amplifier TGA2570, 422
  operating frequencies, 416
  packaged GaN transistors, 427
  parameters, 423
  pHEMT transistors, 418
  production advantages, 421
  radioelectronic suppression, 417
  SiC MESFET, 419
  Si LDMOS, 417
  transistor SHF amplifiers, 423
Wide-gap semiconductors
  properties, 408
  SHF devices, 406
Wired communication systems
  common-mode voltage, 696
  data-transmission rates, 696
  EMC characteristics, 698
  frequency ranges, 696
  measurements, 696
  signal spectrum, 697
  subscriber devices, 696
  system design stage, 697
  typical block diagram, 698
Wireless man-portable devices (WBAN), 226–228